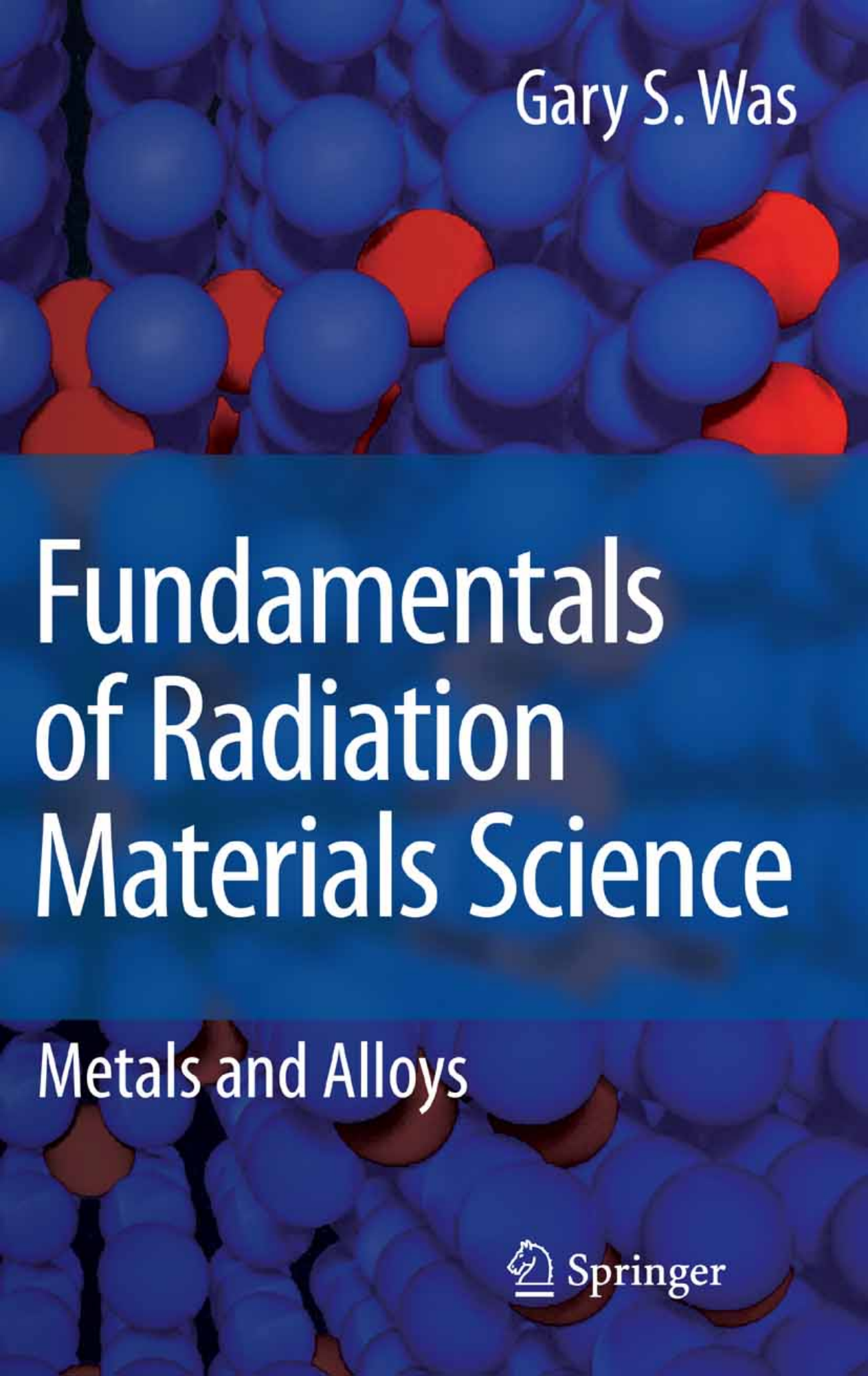
Gary S. Was
Fundamentals of Radiation Materials Science
Metals and Alloys
Springer

Fundamentals of Radiation Materials Science

Gary S. Was

Fundamentals of Radiation Materials Science

Metals and Alloys

With 381 Figures

Springer

Gary S. Was
Nuclear Engineering and Radiological Sciences
Materials Science and Engineering
University of Michigan
1921 Cooley Bldg.
2355 Bonisteel Blvd.
Ann Arbor, MI 48109-2104, USA
e-mail: gsw@umich.edu

Library of Congress Control Number: 2007922926

ISBN 978-3-540-49471-3 Springer Berlin Heidelberg New York

Typesetting and production: LE-TEX Jelonek, Schmidt & Vöckler GbR, Leipzig
Cover design: eStudio Calamar S.L., F. Steinen-Broo, Girona, Spain

Printed on acid-free paper 54/3180/YL – 5 4 3 2 1 0

This book is dedicated to my wife,
LeeAnn

Preface

The purpose of this text is to provide a foundation for understanding the theory and mechanisms behind the effects of irradiation on metals and alloys. The subject is divided into three parts, each of which is subdivided into individual chapters that together, provide a unified picture of how radiation interacts with, and alters the structure and properties of metallic materials. Part I consists of three chapters and focuses on the *radiation damage process* and provides the formalism for the prediction of the amount and spatial configuration of the damage produced by bombarding particles. Chapter 1 treats the interactions between particles that result in the transfer of energy from the incident particle to the target atoms. Chapter 2 focuses on determination of the number of displacements produced by the bombarding particles, and Chap. 3 describes the spatial configurations of the resulting defects.

While radiation damage describes the state of the irradiated material, radiation effects are concerned with defect behavior in the solid after formation. Part II (Chaps. 4–11) covers the *physical effects* of irradiation on metals. Chapter 4 provides background on the equilibrium concentration of point defects and their diffusion. Chapter 5 treats diffusion and reactions between point defects under irradiation that are fundamental to all of the observable effects. Chapter 6 describes radiation-induced segregation, which is a direct consequence of radiation-enhanced diffusion. Chapters 7 and 8 address the nucleation and growth of dislocation loops and voids, the defect aggregates that determine much of the behavior of irradiated alloys. Chapter 9 covers the stability of phases under irradiation and irradiation-induced precipitation and precipitate dissolution. Chapter 10 extends the effects of irradiation to the unique effects resulting from ion irradiation such as composition changes, sputtering, exfoliation, etc. Finally, Chap. 11 describes the application of ion irradiation to simulate the effects of neutron irradiation.

Mechanical effects of radiation damage (Part III) are distinguished from physical effects by the application of stress. Hardening and deformation of alloys under irradiation are discussed in Chap. 12. The effect of irradiation on crack nucleation and propagation resulting either from static or fatigue loading is discussed in Chap. 13. Finally, creep deformation and growth are treated in Chap. 14. Irradiation also has a profound effect on corrosion and stress corrosion cracking and these degradation modes may prove to be limiting processes for many reactor designs. Chapter 15 combines the effects of irradiation with the processes of corrosion and stress corrosion cracking to examine how irradiation and the media can combine to degrade alloy behavior.

The chapters contain examples and illustrations of radiation effects and sample calculations to quantify and describe the observations. Problems at the end of each chapter are designed to reinforce the main concepts of each chapter and to challenge the reader on his or her comprehension of the topics covered within. Taken together, the chapter text, examples, illustrations and end-of-chapter problems provide a comprehensive treatment of the effects of irradiation on metals and alloys.

The subject matter in this text will likely require two academic terms to complete. Many of the topics rely on a basic knowledge of disciplines that constitute the underlying basis for irradiation effects: thermodynamics and kinetics of solids, crystal structure, defects and dislocations, physical metallurgy, elasticity and plasticity, deformation and fracture and corrosion and stress corrosion cracking. The text either presents the requisite background for each of these topics, or provides references of other sources where good treatments can be found.

This book should also be useful to researchers who would like to learn more about the subject, or who would like a more complete and integrated treatment of the topics than can be found in individual papers on the subject. While the chapters are integrated with one another and each chapter builds upon the sum of the previous chapters, it is possible to read selected chapters for just that topic.

As a final comment, the author would like to note that this book was written by sorting, organizing and condensing information from several texts and numerous journal and conference papers in order to arrive at a comprehensive description of the processes constituting radiation materials science. A conscientious effort was made to acknowledge and give credit to the original sources of the ideas, theories, mathematical developments and drawings contained herein. For occasional oversights that may have occurred during the condensation process, the author offers his apologies. He is indebted to the many authors and publishers who provided material and illustrations for this text.

Finally, the author wishes to acknowledge the many colleagues, students and friends who aided and advised him in this work. In particular, special thanks go to Jeremy Busby, Todd Allen, Michael Atzmon, Roger Stoller, Yuri Osetsky, Ian Robertson and Brian Wirth, for their substantive contributions to the content, to Elaine West, Brian Wagner and Sean Lemecha for their work on the illustrations, to Cherilyn Davis and Ovidiu Toader for their help in manuscript and movie preparation, to Lynn Rehn, Don Olander, Arthur Motta, Michael Nastasi, Steve Zinkle, K. Linga Murty, Lou Mansur and Peter Andresen for their chapter reviews, and to John King and Arden Bement for providing the inspiration to the author to pursue this field many years ago.

Ann Arbor, May 2007 *Gary S. Was*

Introduction

Radiation materials science describes the interaction of radiation with matter—a broad subject covering many forms of irradiation and of matter. Some of the most profound effects of irradiation on materials occur in the core of nuclear power reactors where atoms comprising the structural components are displaced numerous times over the course of their engineering lifetimes. The consequences of radiation to core components includes changes in shape and volume by tens of percent, increases in hardness by factors of five or more, severe reduction in ductility and increased embrittlement, and susceptibility to environmentally induced cracking. For these structures to fulfill their purpose, a firm understanding of the effect of radiation on materials is required in order to account for irradiation effects in design, to mitigate its effect by changing operating conditions, or to serve as a guide for creating new, more radiation-tolerant materials that can better serve their purpose.

The attractiveness of nuclear power as a present day and future energy source is due to the vast improvements that have been made in the way reactors are operated and in our understanding of how these engineering systems degrade and fail. But the attractiveness of nuclear power is also driven by new concepts for advanced reactors that offer improvements in safety and reliability, radioactive waste production, energy efficiency and cost effectiveness. Nuclear power holds the promise for producing hydrogen in a clean and low cost process that would power a future hydrogen economy. Yet all of these improvements come at a cost. That cost is a greater demand on the materials used to build and operate these reactors. New concepts that promise better performance from this energy source also include more aggressive environments, higher temperatures and greater levels of irradiation. In his article in *Nature*, Butler [1] summarizes the challenges facing several promising advanced reactor concepts. In all but one, material behavior is the *leading* challenge in bridging the gap from concept to reality. The pivotal role of material behavior in the unique radiation environment created in a reactor core makes radiation materials science of paramount importance in the future of nuclear energy in the world. It is with this perspective that the objective of this text was formulated, to provide a sound, fundamental understanding of radiation effects in structural materials.

Structural materials in reactor systems are predominantly crystalline, metallic alloys. Virtually all of the structural materials in reactors are metallic, and many of the materials proposed for the more aggressive conditions in advanced reactor concepts are metals as well. The types of radiation that can alter structural materials

consist of neutrons, ions, electrons and gamma rays. All of these forms of radiation have the capability to displace atoms from their lattice sites, which is the fundamental process that drives the changes in structural metals described earlier. The inclusion of ions among the irradiating particles provides a tie-in to other fields and disciplines such as the use of accelerators for the transmutation of nuclear waste, or in the creation of new materials by ion implantation, ion beam mixing, plasma assisted ion implantation and ion beam assisted deposition. All of the concepts developed in this text for the interactions of ions with solids are applicable to these fields as well.

The effect of irradiation on materials is rooted in the initial event in which an energetic projectile strikes a target. While the *event* is made up of several steps or processes, the primary result is the displacement of an atom from its lattice site. This book will address primarily crystalline solids in which the atom locations are defined by the crystalline structure. Irradiation displaces an atom from its site, leaving a vacant site behind (a *vacancy*) and the displaced atom eventually comes to rest in a location that is between lattice sites, becoming an *interstitial* atom. The vacancy-interstitial pair is central to radiation effects in crystalline solids and is known as a *Frenkel pair* (FP). The presence of the Frenkel pair and other consequences of irradiation damage determine the physical effects, and with the application of stress, the mechanical effects of irradiation.

The radiation damage event, detailed in Chap. 1, is concluded when the displaced atom (also known as the *primary knock-on atom*, PKA) comes to rest in the lattice as an interstitial. This event consumes about 10^{-11} s. Subsequent events are classified as physical effects of irradiation. These effects include such phenomena as swelling, growth, phase change, segregation, etc. For example, it is possible to take a block of pure nickel, 1 cm on a side, irradiate it in a reactor (to a fluence of say, 10^{22} n/cm^2) and measure it to be 1.06 cm on a side, representing a volume change of 20%! The volume change, or swelling, is isotropic and is due to the formation of voids in the solid (see for example, Fig. 8.1).

Another example is irradiation growth. One can irradiate a cylindrical rod of uranium, 10 cm in length and 1 cm in diameter (7.85 cm^3) to a fluence of $\sim 10^{20}$ n/cm^2 and measure it to be 30 cm in length and 0.58 cm in diameter. The volume is unchanged (7.85 cm^3), but the shape is highly distorted. Distortion at constant volume under irradiation is referred to as growth.

Phase changes under irradiation are also common. A Ni–12.8at%Al, solid solution alloy irradiated with 5 MeV Ni^+ ions to 10^{16} cm^{-2} will result in the formation of a Ni_3Al phase, which is separate and distinct from the parent phase (see for example, Fig. 9.3). The formation of a new phase is known as irradiation-induced phase formation and is of great significance in both ion and neutron irradiations.

A last example of physical changes of irradiation is segregation. If a Ni–1at%Si alloy is bombarded with Ni^+ ions at 525 °C and to a dose of one displacement per atom, the result is an enrichment of Si on the surface and at grain boundaries to values that are 20 to 60 times the amount in the bulk (see for example, Fig. 6.5). This redistribution of alloying elements to specific sites in the microstructure is

known as radiation-induced segregation and occurs in many alloys to a significant extent when irradiated at high temperatures.

Irradiation-induced physical changes can indeed be dramatic. But how do they alter the structural integrity of components? This is the realm of mechanical effects of irradiation. Mechanical effects manifest themselves only under the application of a stress. The result is that alloys behave much differently than their unirradiated counterparts. For example, the impact energy of an irradiated steel can be drastically reduced. For unirradiated steels, the energy absorbed is a strong function of temperature, where at low temperatures, little energy is absorbed and the steel becomes very brittle, but with increasing temperature, the energy absorbing capacity of the steel increases dramatically. Irradiation of a steel with neutrons can cause a marked reduction in the strain and a several-fold increase in the strength of the steel. The result is an increase in strength by a factor of five and a decrease in ductility by over a factor of ten. Irradiation can also influence the way in which materials deform at high temperature. Under a constant load, there is almost a complete loss of creep strength due to severe embrittlement arising from irradiation.

Finally, irradiation to a neutron fluence of $>5 \times 10^{20}\,\mathrm{n/cm^2}$ ($E > 1\,\mathrm{MeV}$) results in accelerated intergranular cracking of iron- and nickel-base austenitic alloys in light water reactors. This cracking phenomenon is very pervasive in that it affects most all austenitic alloys in all types of water reactors. Clearly, any of these effects will have profound consequences on reactor component integrity. Understanding how they work is the key to designing around their detrimental effects or to developing new alloys that are more radiation tolerant. As it turns out, almost all of these effects have a common link: defects such as isolated vacancies and interstitials, clusters of vacancies and interstitials, dislocation loops and lines and voids and bubbles. The reader should keep these defect types in mind as we move from the radiation damage event through the physical effects to the mechanical effects.

We will address the radiation damage event first as this is the basis for understanding all effects of irradiation. We will start by quantifying the extent of radiation damage and develop a physical description of the interaction process. In quantifying the displacement process, what we are seeking is a quantitative description of the number of vacancies and interstitials produced by an incoming projectile. Unless we can do this, we have no hope of understanding the extent of the damage. The importance of determining the effect of irradiation in terms of the production of defects is discussed in Chaps. 2 and 3, and is shown here with a simple illustration. The number of displacements created by a neutron flux is a complicated function of the energy dependence of that flux. Note in the top graph in Fig. I.1 that the dependence of the yield strength of a 316 stainless steel alloy on the neutron fluence is highly dependent on the particular neutron flux spectrum [2]. OWR is a test reactor with a typical LWR neutron spectrum, RTNS-II produced a pure 14 MeV source of neutrons and LASREF had a broad spectrum of high neutron energies. However, if the yield strength is plotted as a function of the displacement damage in the alloy (dpa = displacements per atom in the solid), then data from all three neutron sources collapses beautifully onto a single trend line (bottom graph in Fig. I.1) that

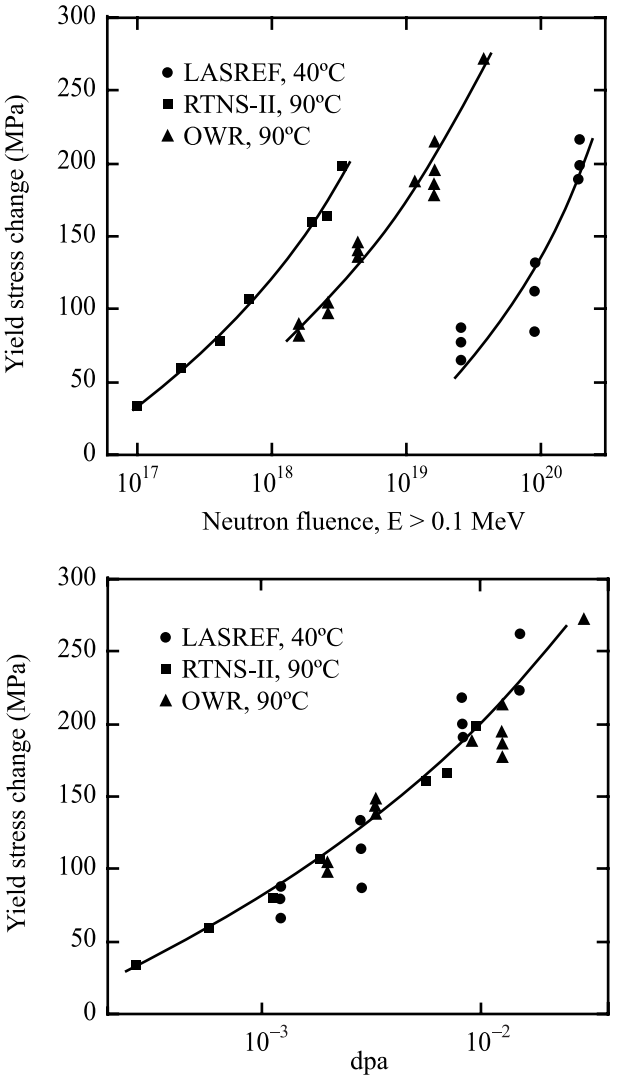

Fig. I.1. Comparison of yield stress change in 316 stainless steel irradiated in three facilities with very different neutron energy flux spectra. While there is little correlation in terms of neutron fluence, the yield stress changes correlate well against displacements per atom, dpa (after [2])

is independent of the flux spectrum. The independence of the yield strength-dpa correlation on the neutron spectrum indicates that dpa is a better representation of the effect of irradiation on materials properties than is the fluence, giving rise to our first objective. That is the determination of the quantity R, the number of displacements per unit volume per unit time:

$$R \equiv \frac{\#\text{displacements}}{\text{cm}^3\text{s}} = N \int_{\check{E}}^{\hat{E}} \phi(E_\text{i}) \sigma_D(E_\text{i}) \, \text{d}E_\text{i} \,, \tag{I.1}$$

where N is the atom number density, $\hat{E}$ is the maximum energy of the incoming particle, $\check{E}$ is the minimum energy of the incoming particle, $\phi(E_\text{i})$ is the energy dependent particle flux, and $\sigma_\text{D}(E_\text{i})$ is the energy dependent displacement cross section:

$$\sigma_\text{D}(E_\text{i}) = \int_{\check{T}}^{\hat{T}} \sigma(E_\text{i}) \nu(T) \, \text{d}T \,, \tag{I.2}$$

where $\hat{T}$ is the maximum energy transferred in a collision of a particle of energy E_i and a lattice atom, $\check{T}$ is the minimum energy transferred in a collision of a particle of energy E_i and a lattice atom, $\sigma(E_\text{i}, T)$ is the cross section for the collision of a particle of energy E_i that results in a transfer of energy T to the struck atom, $\nu(T)$ is the number of displacements per primary knock-on atom. So, ultimately, we want to determine:

$$R = N \int_{\check{E}}^{\hat{E}} \int_{\check{T}}^{\hat{T}} \phi(E_\text{i}) \sigma(E_\text{i}, T) \nu(T) \, \text{d}T \, \text{d}E_\text{i} \,. \tag{I.3}$$

The two key variables in this equation are $\sigma(E_\text{i}, T)$ and $\nu(T)$. The term $\sigma(E_\text{i}, T)$ describes the transfer of energy from the incoming particle to the first atom it encounters in the target, the primary knock-on atom (PKA). Determination of this quantity is the goal of Chap. 1. The second quantity is $\nu(T)$, the total number of displacements that the PKA goes on to make in the solid, and its determination is described in detail in Chap. 2. Taken together, they describe the total number of displacements caused by an incoming particle of energy E_i, and Eq. (I.3) accounts for the energy distribution of the incoming particles. The result is the total number of displacements in the target from a flux of particles with a known energy distribution. We will return to this equation often, as it is the essence of the quantification of radiation damage in solids.

References

1. Butler D (2004) Nuclear Power's New Dawn. Nature 429:238–240
2. Greenwood LR (1994) J Nucl Mater 216:29–44

Contents

Movies accompanying the text are located at: www.sitemaker.umich.edu/was.

Part I Radiation Damage

Part I

Radiation Damage

1 The Radiation Damage Event

The radiation damage event is defined as the transfer of energy from an incident projectile to the solid and the resulting distribution of target atoms after completion of the event. The radiation damage event is actually composed of several distinct processes. These processes and their order of occurrence are as follows:

1. The interaction of an energetic incident particle with a lattice atom
2. The transfer of kinetic energy to the lattice atom giving birth to a primary knock-on atom (PKA)
3. The displacement of the atom from its lattice site
4. The passage of the displaced atom through the lattice and the accompanying creation of additional knock-on atoms
5. The production of a displacement cascade (collection of point defects created by the PKA)
6. The termination of the PKA as an interstitial

The radiation damage event is concluded when the PKA comes to rest in the lattice as an interstitial. The result of a radiation damage event is the creation of a collection of point defects (vacancies and interstitials) and clusters of these defects in the crystal lattice. It is worth noting that this entire chain of events consumes only about 10^{-11} s (see Table 1.1). Subsequent events involving the migration of the point defects and defect clusters and additional clustering or dissolution of the clusters are classified as *radiation damage effects*.

What we first need to know in order to understand and quantify radiation damage, is how to describe the interaction between a particle and a solid that produces displacements, and later on, how to quantify this process. The most simple model is one that approximates the event as colliding hard spheres with displacement occurring when the transferred energy is high enough to knock the struck atom off its lattice site. In addition to energy transfer by hard-sphere collisions, the moving atom loses energy by interactions with electrons, the Coulomb field of nearby atoms, the periodicity of the crystalline lattice, etc. The problem is reduced to the following. If we can describe the energy-dependent flux of the incident particle and the energy transfer cross sections (probabilities) for collisions between atoms, then we can quantify the PKA production in a differential energy range and utilize this to determine the number of displaced atoms.

In this chapter, we will concentrate on quantifying the energy transferred between interacting bodies as well as describing the energy transfer cross section. We

Table 1.1. Approximate time-scale for the production of defects in irradiated metals (from [1])

Time (s)	Event	Result
10^{-18}	Energy transfer from the incident particle	Creation of a primary knock-on atom (PKA)
10^{-13}	Displacement of lattice atoms by the PKA	Displacement cascade
10^{-11}	Energy dissipation, spontaneous recombination and clustering	Stable Frenkel pairs (single interstitial atoms (SIA) and vacancies) and defect clusters
$> 10^{-8}$	Defect reactions by thermal migration	SIA and vacancy recombination, clustering, trapping, defect emission

will begin with neutron–nucleus reactions since the neutrality of the neutron makes the interaction particularly straightforward. Following creation of the PKA, subsequent interactions occur between atoms, and the positive charge of the nucleus and the negative charge of the electron cloud become important in understanding how atoms interact. In fact, atom–atom interaction is the low-energy limit of ion–atom interactions that occur in reactor cores and via ion irradiation using accelerators over a wide energy range and can lead to the last type of interaction: ionization collisions.

1.1 Neutron–Nucleus Interactions

1.1.1 Elastic Scattering

By virtue of their electrical neutrality, elastic collisions between neutrons and nuclei can be represented as colliding hard spheres. When neutrons pass through a solid, there is a finite probability that they will collide with a lattice atom, imparting a recoil energy to the struck atom. This probability is defined by the double differential scattering cross section (in energy and angle), $\sigma_s(E_i, E_f, \Omega)$, where, E_i and E_f are the incident and final energies and Ω is the solid angle into which the neutron is scattered. We are often only interested in the scattering probability as a function of E_i and the scattering angle. The single differential scattering cross section is:

$$\sigma_s(E_i, \Omega) = \int \sigma_s(E_i, E_f, \Omega)\, dE_f . \tag{1.1}$$

The total scattering probability for neutrons of energy E_i is:

$$\sigma_s(E_i) = \int \sigma_s(E_i, \Omega)\, d\Omega . \tag{1.2}$$

In the study of irradiation effects, we are interested in the behavior of the struck atom. So we are seeking $\sigma_s(E_i, T)$; the energy transfer cross section, or the probability that a neutron of energy E_i elastically scattering against an atom of mass M, will impart a recoil energy T to the struck atom. But first it is necessary to find T in terms of the neutron energy and the scattering angle. To do this, let us consider the dynamics of binary elastic collisions in the center-of-mass and laboratory frames.

Figure 1.1a shows the trajectories of a neutron and the target nucleus before and after scattering, as seen from both the laboratory reference system and the center-of-mass system. The easiest way to obtain a relationship between the incident neutron energy, scattering angle and transferred energy is to analyze the dynamics of the collision in the center-of-mass (CM) system. When the collision is viewed in the center-of-mass system, the recoiling particles appear to move away from each other in opposite directions. Momentum conservation along the axes of approach and departure yield:

$$\begin{aligned} v_c m - V_c M &= 0 \\ v_c' m - V_c' M &= 0\,, \end{aligned} \tag{1.3}$$

and conservation of kinetic energy requires that:

$$\frac{1}{2}mv_c^2 + \frac{1}{2}MV_c^2 = \frac{1}{2}mv_c'^2 + \frac{1}{2}MV_c'^2\,. \tag{1.4}$$

Using Eq. (1.3) to eliminate v_c and v_c', we get:

$$\left[\frac{1}{2}m\left(\frac{M}{m}\right)^2 + \frac{1}{2}M\right]V_c^2 = \left[\frac{1}{2}m\left(\frac{M}{m}\right)^2 + \frac{1}{2}M\right]V_c'^2\,. \tag{1.5}$$

Therefore,

$$\begin{aligned} &V_c = V_c'\,, \text{ and hence,} \\ &v_c = v_c'\,. \end{aligned} \tag{1.6}$$

Since the target nucleus is at rest in the lab system and moving to the left with speed V_c in the CM system, the CM system itself must be moving to the right relative to the lab system with the same speed, V_c. Thus, if we use V_{CM} to denote the speed of the CM system relative to the laboratory system, the magnitudes of V_{CM} and V_c are the same (but opposite in direction). This can be restated as follows:

$$v_c = v_\ell - V_{CM} = v_\ell - V_c\,, \tag{1.7}$$

and using Eq. (1.3), we find that:

$$V_{CM} = \left(\frac{m}{M+m}\right)v_\ell\,. \tag{1.8}$$

Recall that we want to relate T, the energy transferred to the struck atom, to ϕ, the scattering angle in the CM system. Using vector addition we can relate the recoil

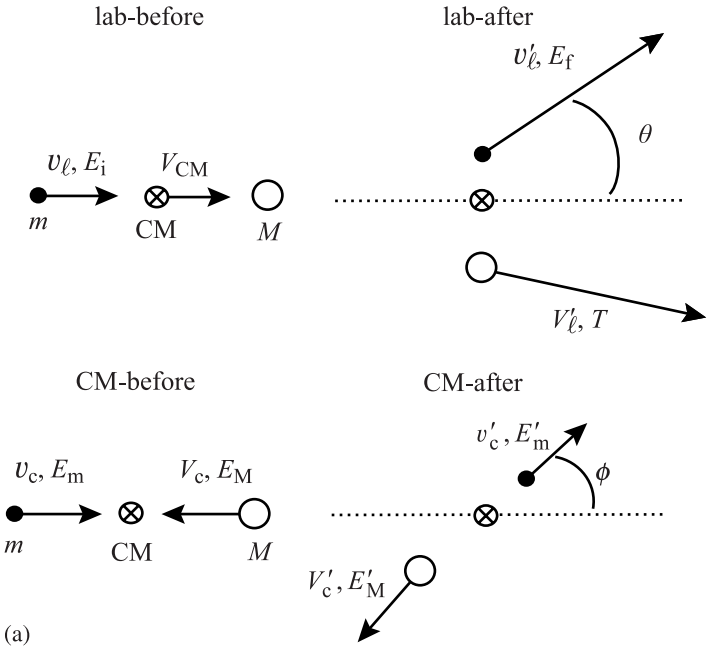

Fig. 1.1. Vector velocities (a) in the laboratory and center-of-mass (CM) systems, and (b) composite diagram relating velocities in the two systems

target nucleus velocity in the lab system, V'_ℓ, to ϕ as shown in Fig. 1.1b, which is a composite of the interaction in the lab and CM systems shown in Fig. 1.1a. Using the law of cosines:

$$V'^2_\ell = V^2_\mathrm{CM} + V'^2_\mathrm{c} - 2V_\mathrm{CM}V'_\mathrm{c}\cos\phi\,, \tag{1.9}$$

and re-writing the velocities in Eq. (1.9) in terms of energy gives:

$$V'^2_\ell = \frac{2T}{M}, \quad V^2_\mathrm{CM} = \frac{2E_\mathrm{i}}{m}\left(\frac{m}{m+M}\right)^2, \quad \text{and} \quad V'^2_\mathrm{c} = \frac{2m}{M^2}E'_\mathrm{m}\,,$$

and substituting these expressions into Eq. (1.9) gives:

$$T = \frac{mM}{(m+M)^2}E_\mathrm{i} + \frac{m}{M}E'_\mathrm{m} - 2\left(\frac{m}{m+M}\right)\left(E_\mathrm{i}E'_\mathrm{m}\right)^{1/2}\cos\phi\,, \tag{1.10a}$$

or

$$T = \eta_1\eta_2 E_\mathrm{i} + \frac{\eta_1}{\eta_2}E'_\mathrm{m} - 2\eta_1\left(E_\mathrm{i}E'_\mathrm{m}\right)^{1/2}\cos\phi\,, \tag{1.10b}$$

where $\eta_1 = m/(m+M)$ and $\eta_2 = M/(m+M)$.

Since we want to find the energy transferred, T as a function of initial energy and scattering angle only, we use the relationship between E_i and E'_m to eliminate E'_m. From Eqs. (1.7) and (1.8), we know that:

$$v'_\mathrm{c} = v_\ell - \left(\frac{m}{m+M}\right)v_\ell = v_\ell\left(\frac{M}{m+M}\right). \tag{1.11}$$

Writing Eq. (1.11) in terms of energy gives:

$$E'_\mathrm{m} = E_\mathrm{i}\left(\frac{M}{m+M}\right)^2 = \eta_2^2 E_\mathrm{i}\,. \tag{1.12}$$

Substituting into Eq. (1.10b) and simplifying gives:

$$T = \frac{\gamma}{2}E_\mathrm{i}(1-\cos\phi)\,, \tag{1.13}$$

where we define

$$\gamma = \frac{4mM}{(M+m)^2} = \frac{4A}{(1+A)^2}\,, \tag{1.14}$$

where $1 = m$ and $A = M$. Hence, T depends upon only one unknown, ϕ. Note the angular dependence of T on ϕ as shown in Fig. 1.2. The energy transferred rises from 0 at $\phi = 0$ to a maximum of γE_i at $\phi = \pi$, or $T_\mathrm{min} = \check{T} = 0$ and $T_\mathrm{max} = \hat{T} = 0$. That is, the energy transferred is a maximum when the particle backscatters and is a minimum when it misses the target, resulting in no change in course ($\phi = 0$).

Example 1.1. For a neutron incident on a hydrogen atom, $\hat{T}_\text{n-H}/E_\mathrm{i} = 1.0$. But for a neutron incident on a uranium atom, $\hat{T}_\text{n-U}/E_\mathrm{i} = 0.017$. Conversely, comparing the interaction of an iron atom with 100 keV Xe^+ ions or electrons, the value of γ for the Xe–Fe interaction is 0.83, yielding a $\hat{T}$ of 83,000 eV. However, the value of γ for e^-–Fe interaction is 0.00004, giving a $\hat{T}$ of only 4 eV, which, as we will see in Chap. 2, is not enough to displace an iron atom from its lattice site.

The scattering angles in the lab system for the incident particle (θ) and the struck atom (α) can be written in terms of the scattering angle in the center-

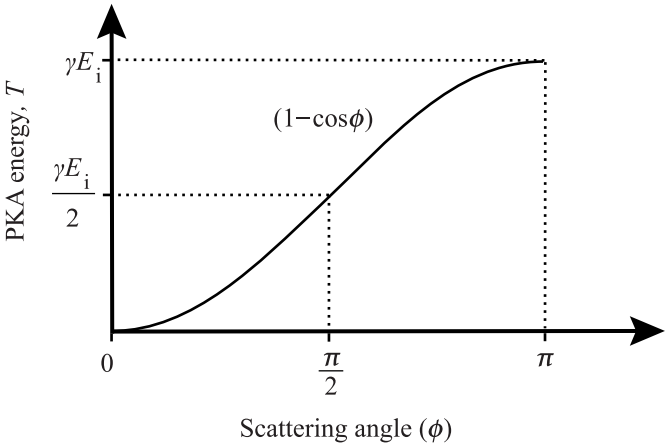

Fig. 1.2. Energy transfer as a function of center-of-mass scattering angle

of-mass system (ϕ) using the vector diagram in Fig. 1.1b. Applying the law of sines to Fig. 1.1b for the *scattered particle*:

$$\frac{v'_\ell}{\sin(\pi-\theta)} = \frac{v'_c}{\sin\theta},$$

where v'_c is given by Eqs. (1.6) and (1.7):

$$v'_c = V_{CM}\left(\frac{v_\ell}{V_{CM}} - 1\right),$$

and using Eq. (1.8), we have:

$$v'_c = V_{CM}\frac{M}{m}.$$

Applying the law of cosines to the same triangle gives:

$$v'^2_\ell = v'^2_c + V^2_{CM} - 2V_{CM}v'_c\cos(\pi-\phi),$$

and combining the last three equations to express θ as a function of ϕ yields:

$$\tan\theta = \frac{(M/m)\sin\phi}{1+(M/m)\cos\phi}.$$

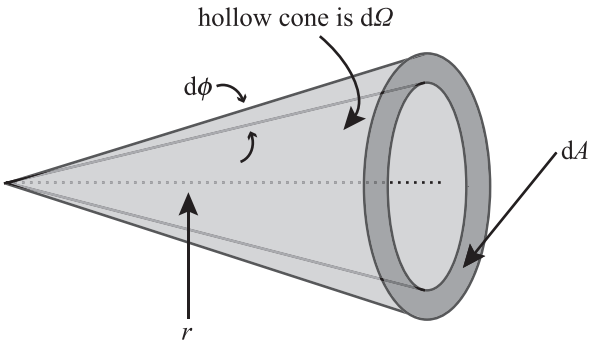

Fig. 1.3. Scattering into the solid angular element $\mathrm{d}\Omega$ defined by $\mathrm{d}A/r^2$

Applying the law of sines to the vector diagram in Fig. 1.1b for the *struck atom* gives:

$$\frac{V_{\mathrm{c}}'}{\sin\alpha} = \frac{V_{\ell}'}{\sin\phi}\,,$$

and combining this result with Eqs. (1.6) and (1.9) where the energies are written in terms of velocities gives:

$$\tan\alpha = \frac{\sin\phi}{1-\cos\phi}\,.$$

We are still interested in obtaining the probability that a given T will be imparted to the recoil atom. This depends on the differential cross section. We define $\sigma_{\mathrm{s}}(E_{\mathrm{i}},\phi)\,\mathrm{d}\Omega$ as the probability of a collision that scatters the incident particle into a center-of-mass angle in the range $(\phi,\ \mathrm{d}\Omega\ )$ where $\mathrm{d}\Omega$ is an element of solid angle about the scattering direction ϕ. Since differential probabilities written in transformed variables are equivalent, $\sigma_{\mathrm{s}}(E_{\mathrm{i}},\phi)$ can be written in terms of CM variables:

$$\sigma_{\mathrm{s}}(E_{\mathrm{i}},T)\,\mathrm{d}T = \sigma_{\mathrm{s}}(E_{\mathrm{i}},\phi)\,\mathrm{d}\Omega\,. \tag{1.15}$$

Using Fig. 1.3 to relate $\mathrm{d}\Omega$ to $\mathrm{d}\phi$, we have by definition:

$$\mathrm{d}\Omega = \mathrm{d}A/r^2\,, \tag{1.16}$$

and from Fig. 1.4, we have:

$$\mathrm{d}\Omega = \frac{r\,\mathrm{d}\phi\,(2\pi r\sin\phi)}{r^2} = 2\pi\sin\phi\,\mathrm{d}\phi\,. \tag{1.17}$$

Substituting Eq. (1.17) into Eq. (1.15) yields:

$$\sigma_{\mathrm{s}}(E_{\mathrm{i}},T)\,\mathrm{d}T = \sigma_{\mathrm{s}}(E_{\mathrm{i}},\phi)\,\mathrm{d}\Omega = 2\pi\sigma_{\mathrm{s}}(E_{\mathrm{i}},\phi)\sin\phi\,\mathrm{d}\phi\,. \tag{1.18}$$

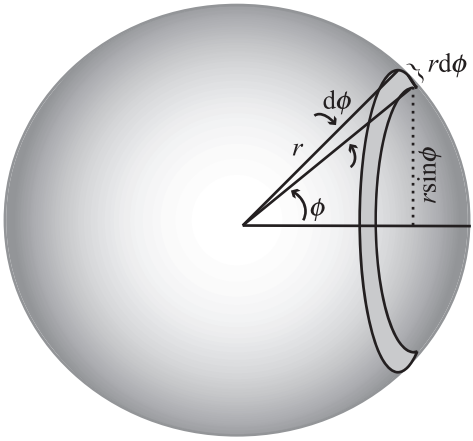

Fig. 1.4. The solid angle $d\Omega$ subtended at the scattering angle ϕ by the incremental angle $d\phi$

And since $T = \frac{\gamma}{2}E_i(1-\cos\phi)$ then $dT = \frac{\gamma}{2}E_i \sin\phi\, d\phi$, then we have:

$$\sigma_s(E_i, T) = \frac{4\pi}{\gamma E_i}\sigma_s(E_i, \phi)\,. \tag{1.19}$$

Figure 1.5 shows the difference in the differential scattering cross section in units of area per unit solid angle vs. area per unit angle as in Eq. (1.18). Although the number of atoms scattered through an angle increment $d\phi$ about $\phi = \pi/2$ is greater than that through an angular increment $d\phi$ about $\phi = 0$ or π (Fig. 1.5a), the number intercepting the spherical surface per unit of solid angle is constant over all angles, ϕ (Fig. 1.5b). Hence $dT/d\phi$ varies in a sinusoidal manner with ϕ but $dT/d\Omega$ is independent of ϕ.

Using Eqs. (1.2) and (1.18), the total elastic scattering cross section is:

$$\sigma_s(E_i) = \int \sigma_s(E_i, \phi)\, d\Omega = 2\pi \int \sigma_s(E_i, \phi)\sin\phi\, d\phi\,.$$

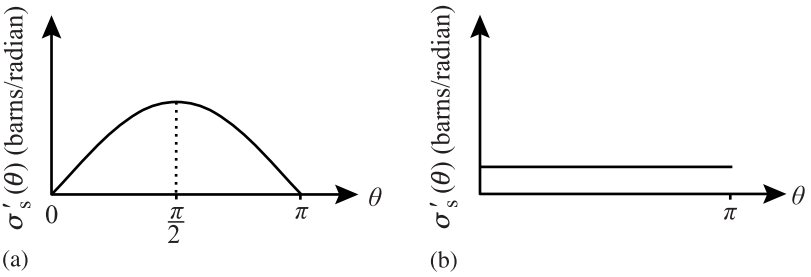

Fig. 1.5. Isotropic differential scattering cross sections in units of (a) area per unit scattering angle and (b) area per unit solid angle

If we assume that elastic scattering in the CM system is independent of scattering angle (i.e., scattering is isotropic), Fig. 1.6, then:

$$\sigma_s(E_i) = \int \sigma_s(E_i,\phi)\,d\Omega = 2\pi\sigma_s(E_i,\phi)\int \sin\phi\,d\phi = 4\pi\sigma_s(E_i,\phi) \tag{1.20}$$

and

$$\sigma_s(E_i,T) = \frac{\sigma_s(E_i)}{\gamma E_i}, \tag{1.21}$$

which is independent of T! That is, $\sigma_s(E_i,T)$, the probability that a neutron of energy E_i, elastically scattering against an atom of mass M, will impart a recoil energy T to the struck atom does not depend on the recoil energy. Now the average recoil energy can be calculated:

$$\bar{T} = \frac{\int_{\check{T}}^{\hat{T}} T\sigma_s(E_i,T)\,dT}{\int_{\check{T}}^{\hat{T}} \sigma_s(E_i,T)\,dT} = \frac{\check{T}+\hat{T}}{2} \approx \frac{\hat{T}}{2} = \frac{\gamma E_i}{2}. \tag{1.22}$$

Applying Eq. (1.22) to the case of a 1 MeV neutron incident on elements of varying mass, we have the following:

1 MeV n on C: $\gamma = 0.28$ $\bar{T} = 0.14$ MeV
1 MeV n on Fe: $\gamma = 0.069$ $\bar{T} = 0.035$ MeV
1 MeV n on U: $\gamma = 0.017$ $\bar{T} = 0.009$ MeV

In addition to the elastic scattering just discussed, we can have energy transfer by inelastic scattering, (n, 2n) reactions and (n, γ) reactions. The first two reactions become important above neutron energies of about 1.0 and 8.0 MeV, respectively, while the latter occurs at thermal neutron energies in ^{235}U.

1.1.2 Inelastic Scattering

Inelastic scattering is characterized by a reaction in which the emitted particle is experimentally the same as the captured particle, but there is a loss of kinetic energy in the system. The energy is found in the excitation energy of the product nucleus, e.g., N^{14}(p, p')N^{14^*} or C^{14}(n, n')C^{14^*}. The differences in the energies of groups of scattered particles correspond to the energy separations of excited levels in the product nucleus:

$$Q = \sum_f KE_f - \sum_i KE_i = \sum_f M_f c^2 - \sum_i M_i c^2.$$

In an inelastic collision, a neutron is absorbed by the nucleus, forming a compound nucleus, which emits a neutron and a γ-ray. There may be more than one γ emitted and the nucleus may remain in an excited state during the course of an interaction. The inelastic scattering cross section can be divided into resolved and unresolved

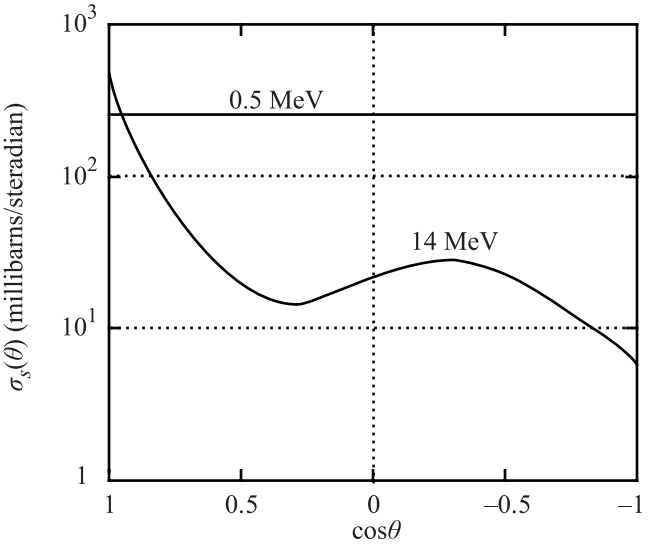

Fig. 1.6. Differential elastic scattering cross sections for C^{12} at 0.5 MeV and 14 MeV neutrons as a function of the cosine of the center-of-mass scattering angle (from [2])

resonance components [3]. For a given resonance (jth resonance) of the target nucleus, the scattering cross section will be a function of Q_j, the γ decay energy of the residual nucleus that is always negative. Analogous to Eq. (1.15) we can write differential equalities $\sigma_{sj}(E_i, Q_j, T)\,dT = \sigma_{sj}(E_i, Q_j, \phi)\,d\Omega$, so that:

$$\sigma_{sj}(E_i, Q_j, T) = \sigma_{sj}(E_i, Q_j, \phi)\,2\pi \sin\phi \frac{d\phi}{dT}. \tag{1.23}$$

However, the expression for T in Eq. (1.13) is not valid for inelastic collisions since kinetic energy is not conserved. Instead we focus on the conservation of total energy. If the target nucleus M is at rest in the lab system and the particle m has energy E_i, then the energy balance in CM coordinates is:

$$\frac{M}{M+m}E_i + Q_j = E'_m + E'_M, \tag{1.24}$$

where Q_j is the reaction energy and E'_m and E'_M are the kinetic energies in CM coordinates of the exit particle and nucleus, respectively. In order that momentum is conserved:

$$mE'_m = ME'_M, \tag{1.25}$$

and combining Eq. (1.24) with Eq. (1.25) (assuming that the masses of the projectile and target are unchanged after the reaction), yields:

$$E'_m = \frac{M}{M+m}\left(Q_j + \frac{M}{M+m}E_i\right)$$

or

$$E'_{\mathrm{m}} = \eta_2 \left(Q_j + \eta_2 E_{\mathrm{i}}\right) . \tag{1.26}$$

Recalling the general expression for T, Eq. (1.10b):

$$T = \eta_1 \eta_2 E_{\mathrm{i}} + \frac{\eta_1}{\eta_2} E'_{\mathrm{m}} - 2\eta_1 \left(E_{\mathrm{i}} E'_{\mathrm{m}}\right)^{172} \cos\phi ,$$

and substituting in for E'_{m} from Eq. (1.26) yields

$$T\left(E_{\mathrm{i}}, Q_j, \phi\right) = \frac{\gamma}{2} E_{\mathrm{i}} - \frac{\gamma}{2} \left[E_{\mathrm{i}} \left(E_{\mathrm{i}} + Q_j \frac{A+1}{A}\right)\right]^{1/2} \cos\phi + \frac{Q_j}{A+1} . \tag{1.27}$$

Now, the expression for $\mathrm{d}T/\mathrm{d}\phi$ becomes:

$$\frac{\mathrm{d}T\left(E_{\mathrm{i}}, Q_j, \phi\right)}{\mathrm{d}\phi} = \frac{\gamma}{2} E_{\mathrm{i}} \left[1 + \frac{Q_j}{E_{\mathrm{i}}} \frac{A+1}{A}\right]^{1/2} \sin\phi . \tag{1.28}$$

Note that in the case of elastic collisions, $Q_j = 0$ and Eq. (1.27) reduces to Eq. (1.13).

If we now assume that inelastic scattering is isotropic in the CM system, then we have:

$$\sigma_{\mathrm{s}j}\left(E_{\mathrm{i}}, Q_j\right) = \int \sigma_{\mathrm{s}j}\left(E_{\mathrm{i}}, Q_j, \phi\right) \mathrm{d}\Omega = 4\pi \sigma_{\mathrm{s}j}\left(E_{\mathrm{i}}, Q_j, \phi\right) . \tag{1.29}$$

Substituting Eqs. (1.28) and (1.29) into (1.23) yields:

$$\sigma_{\mathrm{s}j}\left(E_{\mathrm{i}}, Q_j, T\right) = \frac{\sigma_{\mathrm{s}j}\left(E_{\mathrm{i}}, Q_j\right)}{\gamma E_{\mathrm{i}} \left(1 + \dfrac{Q_j}{E_{\mathrm{i}}} \dfrac{A+1}{A}\right)^{1/2}} . \tag{1.30}$$

for inelastic collisions in the resolved resonance region.

When the compound nucleus is excited to high enough energies, the resonance levels overlap and are no longer individually distinguishable. The inelastic scattering cross section is treated as a continuum and is described by an evaporation model [3] with:

$$\sigma_{\mathrm{is}}\left(E_{\mathrm{i}}, E'_{\mathrm{m}}, T\right) = \sigma_{\mathrm{is}}\left(E_{\mathrm{i}}\right) \frac{f\left(E_{\mathrm{i}}, E'_{\mathrm{m}}\right)}{4\dfrac{1}{A+1}\left(E_{\mathrm{i}} E'_{\mathrm{m}}\right)^{1/2}} , \quad \text{and}$$

$$\sigma_{\mathrm{is}}\left(E_{\mathrm{i}}, T\right) = \sigma_{\mathrm{is}}\left(E_{\mathrm{i}}\right) \int_0^{E'^{\max}_{\mathrm{m}}} \frac{f\left(E_{\mathrm{i}}, E'_{\mathrm{m}}\right)}{4\dfrac{1}{A+1}\left(E_{\mathrm{i}} E'_{\mathrm{m}}\right)^{1/2}} \mathrm{d}E'_{\mathrm{m}} , \tag{1.31}$$

where $f\left(E_{\mathrm{i}}, E'_{\mathrm{m}}\right)$ is a distribution function for the energy E'_{m} of the scattered neutron in the CM system that represents the probability that a neutron is evaporated from the moving compound nucleus, whose value in the CM system is a Maxwellian of

nuclear temperature $E_D = kT$:

$$f\left(E_\mathrm{i}, E'_\mathrm{m}\right) = \frac{E'_\mathrm{m}}{I\left(E_\mathrm{i}\right)} \mathrm{e}^{\left(-E'_\mathrm{m}/E_\mathrm{D}\right)}, \tag{1.32}$$

and

$$I\left(E_\mathrm{i}\right) = E_\mathrm{D}^2 \left[1 - \left(1 + \frac{E'^{\max}_\mathrm{m}}{E_\mathrm{D}}\right) \mathrm{e}^{-E'^{\max}_\mathrm{m}/E_\mathrm{D}}\right], \tag{1.33}$$

is a normalization factor such that

$$\int_0^{E'^{\max}_\mathrm{m}} f\left(E_\mathrm{i}, E'_\mathrm{m}\right) \mathrm{d}E'_\mathrm{m} = 1\,. \tag{1.34}$$

The maximum value of E'_m is given by Eq. (1.26) with $Q = Q_1$, the lowest energy level, and the minimum value of E'_m is zero.

1.1.3 (n, 2n) Reactions

Reactions such as the (n, 2n) reaction are important in radiation effects since they produce additional neutrons that can either cause damage or transmutation reactions in components of interest. Following the 2n model, which is based on work by Odette [4] and Segev [5], a second neutron can only be emitted if the residual excitation of the nucleus after emission of the first neutron exceeds the binding energy of a neutron in the mass-M nuclide. The recoil energy after emission of the first neutron is taken to be the average value ($\cos\phi = 0$ in Eq. (1.10b)) and is shown in Fig. 1.7a in the lab system. We next analyze the second reaction (emission) in the CM system described in Fig. 1.7b. We begin by using the law of cosines to relate V''_c to ϕ:

$$V''^2_\ell = V'^2_\ell + V''^2_\mathrm{c} - 2V'_\ell V''_\mathrm{c} \cos\phi\,. \tag{1.35}$$

From Fig. 1.7a, we have:

$$\frac{1}{2} M V'^2_\ell = \bar{T}_\ell \quad \text{or} \quad V'^2_\ell = \frac{2\bar{T}_\ell}{M},$$

and from Fig. 1.7b we have:

$$\frac{1}{2}(M-m) V''^2_\mathrm{c} = E''_\mathrm{M} \quad \text{or} \quad V''^2_\mathrm{c} = \frac{2E''_\mathrm{M}}{M-m}\,.$$

Conservation of momentum requires:

$$(M-m)V''_\mathrm{c} = m v''_\mathrm{c}\,, \tag{1.36}$$

and squaring gives:

$$V_{\mathrm{c}}''^2 = \left(\frac{m}{M-m}\right)^2 v_{\mathrm{c}}''^2 = \frac{2m}{(M-m)^2} E_{\mathrm{m}}''. \tag{1.37}$$

Substituting into the law of cosines, Eq. (1.35), gives:

$$V_{\ell}''^2 = \frac{2\bar{T}_{\ell}}{M} + \frac{2m}{(M-m)^2} E_{\mathrm{m}}'' - 2\left(\frac{2m}{(M-m)^2}\frac{2}{M} E_{\mathrm{m}}'' \bar{T}_{\ell}\right)^{1/2} \cos\phi\,, \tag{1.38}$$

where $\bar{T}_{\ell} = \eta_1\eta_2 E_{\mathrm{i}} + (\eta_1/\eta_2) E_{\mathrm{m}}'$ is the mean recoil energy after emission of the first neutron. Writing $V_{\ell}''^2$ in terms of energy gives the recoil energy following the second emission:

$$\begin{aligned} T &= \frac{1}{2}(M-m) V_{\ell}''^2 \\ &= \frac{M-m}{M}\bar{T}_{\ell} + \frac{m}{M-m} E_{\mathrm{m}}'' - 2\left(\frac{m}{M}\right)^{1/2} (E_{\mathrm{m}}'' \bar{T}_{\ell})^{1/2} \cos\phi \\ &= \frac{A-1}{A}\bar{T}_{\ell} + \frac{1}{A-1} E_{\mathrm{m}}'' - 2\left(\frac{1}{A}\right)^{1/2} \left(\bar{T}_{\ell} E_{\mathrm{m}}''\right)^{1/2} \cos\phi \\ &= \frac{A}{A-1}\frac{\eta_1}{\eta_2} E_{\mathrm{m}}'' + \frac{A-1}{A}\bar{T}_{\ell} - 2\left(\frac{\eta_1}{\eta_2}\right)^{1/2} \left(\bar{T}_{\ell} E_{\mathrm{m}}''\right)^{1/2} \cos\phi\,. \end{aligned} \tag{1.39}$$

The (n, 2n) reaction cross section is a special case of the inelastic scattering cross section given in Eq. (1.31):

$$\begin{aligned} &\sigma_{\mathrm{n,2n}}\left(E_{\mathrm{i}}, E_{\mathrm{m}}', E_{\mathrm{m}}'', T\right) \\ &\quad = \sigma_{\mathrm{n,2n}}(E_{\mathrm{i}}) \frac{E_{\mathrm{m}}'}{I(E_{\mathrm{i}})} \mathrm{e}^{-E_{\mathrm{m}}'/E_{\mathrm{D}}} \frac{E_{\mathrm{m}}''}{I(E_{\mathrm{i}}, E_{\mathrm{m}}')} \mathrm{e}^{-E_{\mathrm{m}}''/E_{\mathrm{D}}}, \quad \text{and} \\ &\sigma_{\mathrm{n,2n}}(E_{\mathrm{i}}, T) \\ &\quad = \int_0^{E_{\mathrm{i}}-U} \frac{E_{\mathrm{m}}'}{I(E_{\mathrm{i}})} \mathrm{e}^{-E_{\mathrm{m}}'/E_{\mathrm{D}}} \int_0^{E_{\mathrm{i}}-U-E_{\mathrm{m}}'} \frac{E_{\mathrm{m}}''}{I(E_{\mathrm{i}}, E_{\mathrm{m}}')} \mathrm{e}^{-E_{\mathrm{m}}''/E_{\mathrm{D}}} \,\mathrm{d}E_{\mathrm{m}}' \,\mathrm{d}E_{\mathrm{m}}'', \end{aligned} \tag{1.40}$$

where $I(E_{\mathrm{i}})$ is given in Eq. (1.33) with $E_{\mathrm{m}}'^{\max} = E_{\mathrm{i}} - U$ and $I(E_{\mathrm{i}}, E_{\mathrm{m}}')$ is Eq. (1.33) with $E_{\mathrm{m}}'^{\max}$ replaced by $E_{\mathrm{m}}''^{\max} = E_{\mathrm{i}} - U - E_{\mathrm{m}}'$, and for (n, 2n) reactions, $U = 0$ [3].

1.1.4 (n, γ) Reactions

Another class of reactions that can affect the extent of radiation damage involves photon emission. This reaction is important since the energy of the recoiling nucleus is sufficient to displace an atom. As we will see later, this type of displacement is particularly important in radiation damage in reactor pressure vessels in which the gamma flux is more comparable to the fast neutron flux than in the reactor core. Recalling the momentum and energy conservation laws of Eqs. (1.3) and (1.4) and

After 1st collision (reaction) After 2nd reaction

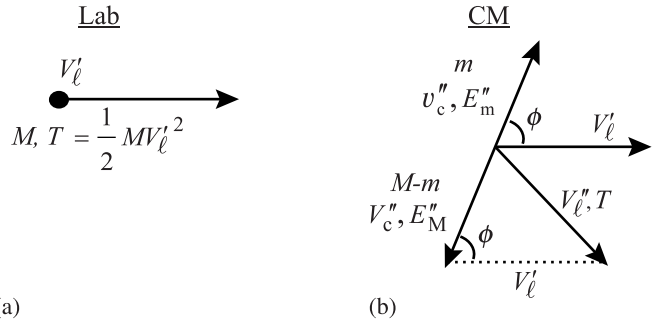

(a) (b)

Fig. 1.7. Vector velocities for the (n, 2n) reaction in (a) the lab system and (b) the center-of-mass system

Fig. 1.1, which for (n, γ) reactions, $E_i \sim 0$ (since these reactions occur with thermal neutrons of energy 0.025 eV), $E_f \equiv 0$ (since there is no scattered neutron) and Q is the equivalent of the mass difference between the initial particles and the compound nucleus. When the compound nucleus (CN) de-excites, it emits a γ-ray with this energy. Conservation of momentum says that the nucleus must recoil with momentum:

$$(m+M)\,V'_c = \frac{E_\gamma}{c}\,. \tag{1.41}$$

Note that this is an approximation since we have not subtracted the mass defect from the compound nucleus. Squaring both sides of Eq. (1.41) and dividing by $2(m+M)$ gives:

$$\frac{1}{2}(m+M)V'^2_c = \frac{E^2_\gamma}{2(m+M)c^2}\,.$$

As in the case of elastic scattering, T is given by:

$$T = \left(V^2_{CM} + V'^2_c - 2V_{CM}V'_c\cos\phi\right)\left(\frac{M+m}{2}\right),$$

but $V_{CM} \ll V'_c$ so to a good estimate:

$$T \cong \left(\frac{m+M}{2}\right)V'^2_c = \frac{E^2_\gamma}{2(M+m)c^2}\,.$$

We will assume further that this value of T represents the maximum recoil energy. But since not all of Q will be emitted in a single γ-ray, we approximate the average recoil energy as half the value of the maximum recoil energy, giving:

$$\bar{T} \cong \frac{E^2_\gamma}{4(M+m)c^2}\,. \tag{1.42}$$

The radiative capture cross section is derived from the Breit–Wigner single-level formula when the target nucleus has zero intrinsic angular momentum and the compound nucleus has a neutron width Γ_n and a radiation width Γ_g, and a total width Γ, and E_0 is the resonance energy and λ is the wavelength [6]:

$$\sigma_{n,\gamma}(E_i) = \pi\lambda^2 \frac{\Gamma_n \Gamma_\gamma}{(E_i - E_0)^2 + (\Gamma/2)^2}. \tag{1.43}$$

Expressing Eq. (1.43) in terms of σ_0, the maximum value of the radiative capture cross section (at $E = E_0$) and taking the Γ_n proportional to $1/\lambda$ and to $\sqrt{E}$ gives:

$$\sigma_{n,\gamma}(E_i) = \sigma_0 \sqrt{\frac{E_0}{E_i}} \left\{ \frac{1}{[(E_i - E_0)/(\Gamma/2)]^2 + 1} \right\}. \tag{1.44}$$

Table 1.2 provides a summary of the energy transfer and the energy transfer cross sections for the various types of reactions covered in Sect. 1.1.

1.2 Interactions Between Ions and Atoms

Ion–atom or atom–atom collisions are governed by interactions between the electron clouds, the electron cloud and the nucleus, and between the nuclei. These interactions are described by what are known as interatomic potentials. In order to develop descriptions of energy transfer cross sections for interactions between atoms, we need descriptions of the potential function that governs that interaction. Unfortunately, there exists no single function that describes all interactions, but rather, the nature of the interaction is a strong function of the atom energies, and hence their distance of closest approach of their nuclei. The following section provides a summary of interatomic potentials adapted from Chadderton [7].

1.2.1 Interatomic Potentials

The end product of the neutron–nuclear interaction is the creation of the primary knock-on atom with some amount of kinetic energy. This atom will, of course, make subsequent collisions with other atoms in the solid. Knowledge of the forces acting between two colliding atoms represents the most fundamental aspect of radiation damage, without which a proper description of the primary event and the ensuing defect structure is impossible. Our interest lies in the forces between like atoms, unlike atoms, or ions and atoms. The description of interactions between atoms is done using potential functions. Recall that the atoms are (usually) electrically neutral but are composed of positive and negative components that do not cancel at all points in space. It is well known that the potential energy between two point

Table 1.2. Energy transfer and energy transfer cross sections for various types of neutron–nuclear collisions

Type of collision	Energy transfer and energy transfer cross section	Equation in text
Elastic scattering	$T = \frac{\gamma}{2} E_\mathrm{i}(1-\cos\phi)$	(1.13)
	$\sigma_\mathrm{s}(E_\mathrm{i},T) = \frac{\sigma_\mathrm{s}(E_\mathrm{i})}{\gamma E_\mathrm{i}}$	(1.21)
Inelastic scattering	$T(E_\mathrm{i},Q_j,\phi) = \frac{\gamma}{2}E_\mathrm{i} - \frac{\gamma}{2}\left[E_\mathrm{i}\left(E_\mathrm{i}+Q_\mathrm{i}\frac{A+1}{A}\right)\right]^{1/2}\cos\phi + \frac{Q_j}{A+1}$	(1.27)
	resonance region $\sigma_{\mathrm{s},j}(E_\mathrm{i},Q_j,T) = \frac{\sigma_{\mathrm{s},j}(E_\mathrm{i},Q_j)}{\gamma E_\mathrm{i}\left(1+\frac{Q_j}{E_\mathrm{i}}\frac{l+A}{A}\right)^{1/2}}$	(1.30)
	unresolved resonance region $\sigma_\mathrm{is}(E_\mathrm{i},T) = \sigma_\mathrm{is}(E_\mathrm{i})\int_0^{E'^{\max}_\mathrm{m}} \frac{f(E_\mathrm{i},E'_\mathrm{m})}{4\frac{1}{A+1}\left(E_\mathrm{i}E'_\mathrm{m}\right)^{1/2}}\,\mathrm{d}E'_\mathrm{m}$	(1.31)
(n, 2n)	$T = \frac{A}{A-1}\frac{\eta_1}{\eta_2}E''_\mathrm{m} + \frac{A-1}{A}\bar{T}_\ell - 2\left(\frac{\eta_1}{\eta_2}\right)^{1/2}\left(\bar{T}_\ell E''_\mathrm{m}\right)^{1/2}\cos\phi$	(1.39)
	$\sigma_\mathrm{n,2n}(E_\mathrm{i},T) = \int_0^{E_\mathrm{i}-U}\frac{E'_\mathrm{m}}{I(E_\mathrm{i})}\mathrm{e}^{-E'_\mathrm{m}/E_\mathrm{D}} \times \int_0^{E_\mathrm{i}-U-E'_\mathrm{m}}\frac{E''_\mathrm{m}}{I(E_\mathrm{i},E'_\mathrm{m})}\mathrm{e}^{-E''_\mathrm{m}/E_\mathrm{D}}\,\mathrm{d}E'_\mathrm{m}\,\mathrm{d}E''_\mathrm{m}$	(1.40)
(n, γ)	$\bar{T} \cong \frac{E_\gamma^2}{4(M+m)c^2}$	(1.42)
	$\sigma_{\mathrm{n},\gamma}(E_\mathrm{i}) = \sigma_0\sqrt{\frac{E_0}{E_\mathrm{i}}}\left\{\frac{1}{[(E_\mathrm{i}-E_0)/(\Gamma/2)]^2+1}\right\}$	(1.44)

charges of the same sign separated by a distance r is described by the well know Coulomb equation:

$$V(r) = \frac{\varepsilon^2}{r}, \tag{1.45}$$

where ε is a single unit charge. However, in the case of atoms, we have a charged nucleus surrounded by an electron cloud of opposite charge. It is evident that the potential function describing the interaction between atoms is far more complicated. Even in the simplest cases, $V(r)$ has never been determined exactly, but some simple considerations show that it must be dominated by two distinct contributions over the

range of separation in which we are interested. Perhaps the simplest of all potential functions is the "hard-sphere" approximation. This potential is described as follows:

$$V(r) = \begin{cases} 0 & \text{for} \quad r > r_0 \\ \infty & \text{for} \quad r < r_0 \,. \end{cases} \tag{1.46}$$

This potential function describes an interaction with an infinitely sharp cut-off at the atomic radius r_0. At distances greater than this radius the interaction vanishes, while at distances less than r_0 the magnitude is infinity. This description is analogous to the behavior of billiard balls and hence, the atoms in this model are described as acting as such. Clearly this is not a very realistic description of atom–atom interaction since we know that the electron shells can overlap.

Figure 1.8 shows how the interatomic potential actually varies with separation. At large separation, the principal interaction is supplied by the Coulomb forces while for smaller separations, the central field repulsive force is dominant. A similar relationship applies to all crystals regardless of the nature of binding. In all cases there is a smooth curve with a minimum at the separation distance corresponding to the nearest neighbor distance in the lattice, r_e (also referred to as D).

In describing the interaction between atoms, we will use two yardsticks for points of reference. One is the Bohr radius of the hydrogen atom, $a_0 = 0.053\,\text{nm}$, which provides a measure of the position of the atomic shells. The other is r_e, the spacing between nearest neighbors in the crystal (typically $\sim 0.25\,\text{nm}$). When $r \ll r_e$, electrons populate the lowest energy levels (closed shells) of the individual atoms and only the outer valence shells will have empty levels. As two atoms are brought together, the valence shells begin to overlap and weak attractive forces such as van de Waals forces may develop. When $a_0 < r \leq r_e$ the closed inner shells begin to overlap. Since the Pauli exclusion principle demands that some electrons change their levels, and hence move to higher energy levels, the extra energy supplied in forcing the atoms together constitutes a positive potential energy of interaction. This is known as closed shell repulsion and the potential that most accurately describes

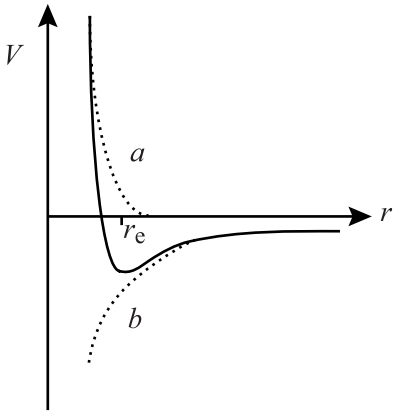

Fig. 1.8. Variation of interatomic potential with separation, r. Coulomb forces dominate at large separations (b) and the central repulsive force dominates at small separations (a), and at intermediate distances, there is a smooth transition between the two extremes with a minimum corresponding to the equilibrium separation distance, r_e or D

this region is the Born–Mayer potential:

$$V(r) = A\exp(-r/B)\,, \tag{1.47}$$

where A and B are constants determined from the elastic moduli [8]. Although this function was first used by Born and Mayer to represent core ion repulsion in their theory of ionic crystals, it is perfectly valid for separations on the order of the equilibrium separation, r_e, and is useful in treatments of threshold or near-threshold collisions where the impact parameter is of the order r_e.

When $r \ll a_0$, Coulomb interaction between the nuclei dominates all other terms in $V(r)$:

$$V(r) = \frac{Z_1 Z_2 \varepsilon^2}{r}\,. \tag{1.48}$$

At slightly larger distances, the nuclear charges are electrostatically "screened" by the space charge of the innermost electron shells that have entered the internuclear space. The potential describing this behavior is known as the screened Coulomb potential [8, 9, 10, 11, 12]:

$$V(r) = \left(\frac{Z_1 Z_2 \varepsilon^2}{r}\right)\exp(-r/a)\,, \tag{1.49}$$

where $a = \dfrac{Ca_0}{\left(Z_1^{2/3} + Z_2^{2/3}\right)^{1/2}}$ or $a = \dfrac{Ca_0}{(Z_1 Z_2)^{1/6}}$, $C = 0.8853$ and a_0 is the Bohr radius of the hydrogen atom. More generally, screening by the electron cloud is described by a screening function, $\chi(r)$ that is defined as the ratio of the actual atomic potential at a radius r to the Coulomb potential. The function of $\chi(r)$ is to moderate the Coulomb potential to describe the interaction between atoms at all separation distances. For large distances, $\chi(r)$ will tend toward zero, and at very small distances, $\chi(r)$ will tend toward unity. This is one way in which a single interatomic potential function can be used to describe all collisions.

We have now described two regimes of interaction. At small separations ($r \ll a_0$) the screened Coulomb term dominates all others, with the screening effect decaying exponentially with the separation distance. In the region $a_0 < r \leq r_e$ electronic interaction dominates and is best described by the Born–Mayer potential. At intermediate separations there is no satisfactory description of the nature of atomic interaction. Unfortunately, it is exactly in this region where information is needed to provide a proper analytical description of radiation damage.

Nevertheless, we may make a first approximation to the total potential by summing the controlling potentials at large and small separations:

$$V(r) = \frac{Z_1 Z_2 \varepsilon^2}{r}\exp(-r/a) + A\exp(-r/B)\,, \tag{1.50}$$

where $A = 2.58 \times 10^{-5}(Z_1 Z_2)^{11/4}$ eV, $B = 1.5a_0/(Z_1 Z_2)^{1/6}$ are empirical formulae suggested by Brinkman [11], consistent with observed compressibilities and elastic

moduli in the noble metals Cu, Ag and Au. Unfortunately, there is a little experimental information about the forces between metal atoms, which is our primary interest. Figure 1.9 shows that the first term dominates for small separation and the second for large.

Brinkman suggested a model for the interaction between two identical atoms in which the nucleus is surrounded by a rigid charge distribution ρ_ε and it is assumed that both atoms supply a screened Coulomb field of the same type:

$$V(r) = \frac{Z^2\varepsilon^2}{r}\,\mathrm{e}^{-r/a}\left(1-\frac{r}{2a}\right). \tag{1.51}$$

This relation approaches the Coulomb repulsion as r approaches zero and changes sign at $r = 2a$, becoming a weak attractive potential with a minimum at $r = a(1+\sqrt{3})$. However, this potential predicts a strong interaction energy at large distances and may not represent the true physical picture for metals. Brinkman formulated a new potential function:

$$V(r) = \frac{AZ_1Z_2\varepsilon^2\exp(-Br)}{1-\exp(-Ar)}. \tag{1.52}$$

Note that for small values of r the potential closely approximates the Coulomb repulsive interaction, i.e.,

$$\lim_{r\to\infty} V(r) \to \frac{Z_1Z_2\varepsilon^2}{r},$$

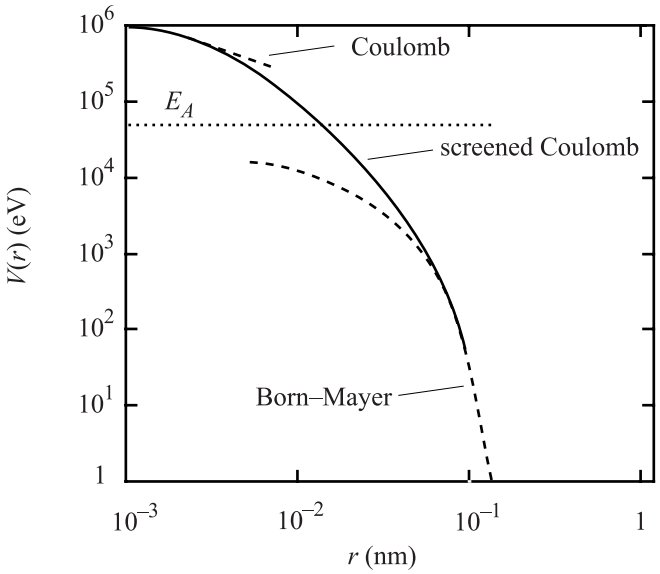

Fig. 1.9. Behavior of various potential functions over a range of separation distances between copper atoms

and at large separation, the potential equation approximates the exponential repulsion of the Born–Mayer type:

$$\lim_{r\to\infty} V(r) \to AZ_1Z_2\varepsilon^2 \exp(-Br)\,.$$

The constant B is defined as $B = Z_{\text{eff}}^{1/3}/Ca_0$, where $Z_{\text{eff}} = (Z_1Z_2)^{1/2}$, and C is of the order 1.0 or 1.5. The constant A depends on the compressibility and bulk modulus, which depend on the overlap of closed electron shells. An empirical expression for A is $A = \dfrac{0.95\times10^{-6}}{a_0} Z_{\text{eff}}^{7/6}$. Substituting for A, B and C (= 1.5) into Eq. (1.52) gives:

$$V(r) = 1.9\times10^{-6} Z_{\text{eff}}^{1/2} E_{\text{R}} \frac{\exp\left(-Z_{\text{eff}}^{1/3} r/1.5a_0\right)}{1-\exp\left(-0.95\times10^{-6} Z_{\text{eff}}^{7/6} r/a_0\right)}\,, \tag{1.53}$$

where $E_{\text{R}} = \varepsilon^2/2a_0$ is the Rydberg energy (13.6 eV).

It should be noted that although the potential is a reasonably reliable function for all metals whose atomic number exceeds 25 over the range $r < 0.7r_{\text{e}}$, it should not be used near $r = r_e$ since in the derivation it has been implicitly assumed that all interatomic distances are close to those of Cu, Ag and Au. It is therefore not a valid potential to use in calculating formation and migration energies of point defects.

Two other potentials should be discussed. The first is the Firsov or Thomas–Fermi two-center potential. This potential function is an improvement over the screened Coulomb potential by virtue of the fact it takes into account the change in electron energy connected with the mutual approach of the nuclei. The potential can be written as:

$$V(r) = \frac{\chi(r)}{r}\,,$$

where $\chi(r)$ is the screening function. In the case of the screened Coulomb potential:

$$\begin{aligned} \chi(r) &= \chi_{\text{B}}(r) \quad \text{and} \\ \chi_{\text{B}}(r) &= Z_1Z_2\varepsilon^2 \exp(-r/a)\,, \end{aligned} \tag{1.54}$$

while in the Firsov potential:

$$\chi(r) = \chi_{\text{TF}}(r/a) = \chi\left[\left(Z_1^{1/2} + Z_2^{1/2}\right)^{2/3} \frac{r}{a}\right], \tag{1.55}$$

so that we have:

$$V(r) = \frac{Z_1Z_2\varepsilon^2}{r}\chi\left[\left(Z_1^{1/2} + Z_2^{1/2}\right)^{2/3} \frac{r}{a}\right], \tag{1.56}$$

where

$$\chi\left[\left(Z_1^{1/2}+Z_2^{1/2}\right)^{2/3}\frac{r}{a}\right]$$

is a screening function.

The second potential of interest is the Thomas–Fermi–Dirac two-center potential (TFD). The Thomas–Fermi–Dirac statistical model of the atom was employed to calculate a potential from first principles. As a consequence, this potential takes into account exchange effects and places a finite boundary, defined by r_b, on the spatial distribution of the electron cloud density ρ_ε. The potential obtained for like atoms is:

$$\bar{V}(r)=\frac{Z^2\varepsilon^2}{r}\chi\left(Z^{1/3}\frac{r}{a}\right)-\alpha Z+\bar{\Lambda}\,, \tag{1.57}$$

where $\alpha\cong 3.16\times 10^{-3}\dfrac{\varepsilon^2}{a_0}$ and $\bar{\Lambda}$ is a set of integrals over exact single-center electron densities. Calculations using this potential have shown that for very small separations of less than $\sim 0.3a_0$, $\bar{V}(r)$ agrees well with other theoretical curves and with experiment, while in the range $\sim 0.3a_0$ to $3a_0$, $V(r)$ agrees with other theoretical and experiment results better than the screened Coulomb potential or the Firsov potential [7].

In selecting the appropriate potential for a specific collision problem, the range of separation can be determined by equating the available kinetic energy to the potential and hence obtaining the smallest separation. The important interaction terms for the calculated separation can then be determined. For interactions between metal atoms at low kinetic energies, 10^{-1} to 10^3 eV, the Born–Mayer term alone is sufficient with constants given in Eq. (1.50). In cases of atom–atom collisions in the collision cascade, where energies from 10^3 to 10^5 eV are involved, an inverse power potential is extremely convenient. Such a potential can be formulated by fitting a function C/r^s to one of the above potential functions over a limited range of r. For example, one can fit an inverse square ($s=2$) function to the screened Coulomb potential at $r=a$, obtaining the same slope, ordinate and curvature. This function is [13]:

$$V(r)=\frac{Z_1Z_2\varepsilon^2 a}{r^2}e^{-1}\,. \tag{1.58}$$

For a limited range of r, this can be used as an approximate potential. Re-writing using the expression in Eq. (1.49) for a gives:

$$V(r)=\frac{2E_R}{e}\left(Z_1Z_2\right)^{5/6}\left(\frac{a_0}{r}\right)^2\,. \tag{1.59}$$

A convenient alternative for numerical calculations uses the fact that $\frac{2E_R}{e} \cong 10\,\text{eV}$, hence:

$$V(r) = 10\,(Z_1 Z_2)^{5/6} \left(\frac{a_0}{r}\right)^2 \text{eV}. \tag{1.60}$$

This potential also applies to heavy ion bombardment in the energy range 10^3 to 10^5 eV. In the case of light ions at high energy, such as 5 MeV protons, the simple Coulomb potential is adequate.

Table 1.3 summarizes the various potential functions and their regions of applicability. But how do we go about verifying a potential function? For example, how do we determine the constants A and B in the Born–Mayer potential for a specific element? Since the Born–Mayer potential is based on small displacements from equilibrium (i.e., r_e), we can obtain these constants from bulk property measurement of the solid, e.g., compressibility, elastic moduli, etc. If we expand the potential $\phi(r)$ as $\phi_0 + \left(\frac{d\phi}{dr}\right)_0 r + 1/2 \left(\frac{d^2\phi}{dr^2}\right)_0 r^2 + \cdots$, then the coefficient of $\left(\frac{d^2\phi}{dr^2}\right)_0$ is the curvature of the energy–distance curve at $r = r_e$ shown in Fig. 1.8.

How then do we know that a given potential does or does not properly describe the interaction in a region of r? We can make this determination by scattering measurements or by measuring the range of ions in solids. Since $V(r)$ describes the nature of the interaction, it will also tell us about $\sigma_s(E_i)$, that can be determined by scattering experiments. Also, range measurements give a good indication of how many interactions must have occurred in order to place the ion in its deposited location. Both of these sets of experiments will provide information on the adequacy of the chosen potential function to accurately describe the interaction between atoms in the solid.

With some appreciation for the way in which neutral atoms or atoms and ions interact, we are now prepared to describe a collision between these species, which is in some ways very similar to, and in other ways very different from neutron–nuclear collisions. The resulting formalism will provide us with the tools to determine the energy transferred from the incident atom to the struck atom along with the energy transfer cross section. The following treatment is adapted from Thompson [13].

1.2.2 Collision Kinematics

The orbits of two colliding atoms are shown in Fig. 1.10 relative to the center of mass of the masses M_1 and M_2. Particle locations are most conveniently denoted in polar coordinates (r_1, ψ) and (r_2, ψ) for masses M_1 and M_2, respectively. The impact parameter is b, ψ is the scattering angle of the struck atom in the lab system and ϕ is the asymptotic scattering angle when the interparticle spacing approaches infinity. The impact parameter is defined as the distance between the asymptotic trajectories of the colliding particles as shown in Fig. 1.10. We are interested in determining the detailed orbits by expressing ϕ is a function of b. This result will then be used to determine the scattering cross section.

Table 1.3. Summary of potential functions

Potential	Equation for $V(r) =$	Range of applicability	Definitions	Eq. in text
Hard-sphere	$0 \quad \text{for} \quad r > r_0$ $\infty \quad \text{for} \quad r < r_0$	$10^{-1} < T < 10^3\,\text{eV}$	$r_0 =$ Size of atom	(1.46)
Born–Mayer	$V(r) = A\exp(-r/B)$	$10^{-1} < T < 10^3\,\text{eV}$ $a_0 < r \leq r_e$	A, B determined from elastic moduli	(1.47)
Simple Coulomb	$\dfrac{Z_1 Z_2 \varepsilon^2}{r}$	Light ions of high energy $r \ll a_0$		(1.48)
Screened Coulomb	$\left(\dfrac{Z_1 Z_2 \varepsilon^2}{r}\right)\exp(-r/a)$	Light ions $R < a_0$	$a_0 =$ Bohr radius $a =$ Screening radius	(1.49)
Brinkman I	$\dfrac{Z^2\varepsilon^2}{r}\mathrm{e}^{(-r/a)}\left(1-\dfrac{r}{2a}\right)$	$r < a$	$a \cong \quad a_0/Z^{1/3}$	(1.51)
Brinkman II	$\dfrac{AZ_1Z_2\varepsilon^2\exp(-Br)}{1-\exp(-Ar)}$	$Z > 25$ $r < 0.7r_e$	$A = \dfrac{0.95\times10^{-6}}{a_0}Z_{\text{eff}}^{7/6}$ $B = Z_{\text{eff}}^{1/3}/Ca_0$ $C \cong 1.5$	(1.52)
Firsov	$\dfrac{Z_1Z_2\varepsilon^2}{r}\chi\left[\left(Z_1^{1/2}+Z_2^{1/2}\right)^{2/3}\dfrac{r}{a}\right]$	$r \leq a_0$	χ is screening function	(1.56)
TFD two-center	$\dfrac{Z^2\varepsilon^2}{r}\chi\left(Z^{1/3}\dfrac{r}{a}\right)-\alpha Z+\bar{\Lambda}$	$r < r_b(3a_0)$	$r_b =$ Radius at which the electron cloud density vanishes	(1.57)
Inverse square	$\dfrac{2E_r}{e}(Z_1Z_2)^{5/6}\left(\dfrac{a_0}{r}\right)^2$	$a/2 < r < 5a$	$E_R =$ Rydberg energy $= 13.6\,\text{eV}$	(1.59)

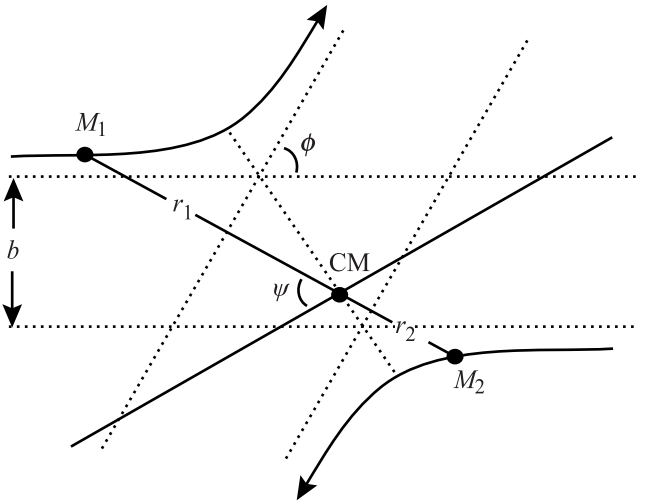

Fig. 1.10. Collision orbits in the center-of-mass system

The radial and transverse velocity of mass M_1 are $\dot{r}_1$ and $r_1\dot{\psi}$ in polar coordinates, and the resultant velocity is $(\dot{r}_1^2 + r_1^2\dot{\psi}^2)^{1/2}$. The velocity components are the same for mass M_2 with the subscript 2 substituted for 1. Conservation of energy requires that the total energy of any system remain constant. The energy in the lab reference system is just $E_\mathrm{i} = \dfrac{1}{2}M_1 v_\ell^2 = E_\mathrm{T}$. Recall that $V_\mathrm{CM} = \dfrac{M_1}{M_1 + M_2} v_\ell$, and that the kinetic energy of the center of mass itself (in the lab system) is:

$$E_\mathrm{CM} = \frac{1}{2}(M_1 + M_2) V_\mathrm{CM}^2 = \left(\frac{M_1}{M_1 + M_2}\right) E_\mathrm{i}\,.$$

Hence, the energy in the CM system that is available for transformation is the total kinetic energy less the motion energy of the CM system:

$$E = E_\mathrm{T} - E_\mathrm{CM} = E_\mathrm{i} - E_\mathrm{CM} = E_\mathrm{i}\left(\frac{M_2}{M^1 + M_2}\right). \tag{1.61}$$

In an elastic collision, the sum of the potential and kinetic energies at any point in the orbit must equal the asymptotic sum of kinetic energies, so:

$$\underset{\text{asymptotic energy}}{E_\mathrm{i}\left(\frac{M_2}{M_1 + M_2}\right)} = \underset{\text{sum of kinetic energy at any point in orbit}}{\frac{1}{2}M_1\left(\dot{r}_1^2 + r_1^2\dot{\psi}^2\right) + \frac{1}{2}M_2\left(\dot{r}_2^2 + r_2^2\dot{\psi}^2\right)} + \underset{\text{potential energy}}{V(r_1 + r_2)}. \tag{1.62}$$

Letting $r = r_1 + r_2$ be the total separation distance, and $r_1 = \dfrac{M_2}{M_1+M_2}r$, $r_2 = \dfrac{M_1}{M_1+M_2}r$, and the energy balance of Eq. (1.62) simplifies to:

$$\eta E_\mathrm{i} = \frac{1}{2}\mu\left(\dot{r}^2 + r^2\dot{\psi}^2\right) + V(r)\,, \tag{1.63}$$

where $\eta = \dfrac{M_2}{M_1+M_2}$ and $\mu = \dfrac{M_1M_2}{M_1+M_2}$ is the reduced mass.

The law of conservation of angular momentum demands that the value at any point in the orbit must equal the asymptotic value. Recall that:

$$v_\ell = v_\ell - V_\mathrm{CM} = v_\ell\left(\frac{M_2}{M_1+M_2}\right) \quad \text{and} \quad V_2 = V_\mathrm{CM} = v_\ell\left(\frac{M_1}{M_1+M_2}\right),$$

so that the asymptotic value of the angular momentum is given by:

$$M_1v_1b_1 + M_2v_2b_2 = \frac{M_1M_2}{M_1+M_2}v_\ell(b_1+b_2) = \mu b v_\ell\,. \tag{1.64}$$

The angular momentum at any point is given by:

$$\begin{aligned} M_1r_1^2\dot{\psi} + M_2r_2^2\dot{\psi} &= \left[M_1\left(\frac{M_2}{M_1+M_2}r\right)^2 + M_2\left(\frac{M_1}{M_1+M_2}r\right)^2\right]\dot{\psi} \\ &= \mu r^2\dot{\psi}\,, \end{aligned} \tag{1.65}$$

hence:

$$\mu r^2\dot{\psi} = \mu b v_\ell\,. \tag{1.66}$$

Substituting from Eq. (1.66) into Eq. (1.63) to eliminate $\dot{\psi}$ and solving for $\dot{r}$, we obtain:

$$\dot{r} = \left(\frac{2}{\mu}\right)^{1/2}\left[\eta E_\mathrm{i}\left(1 - \frac{b^2}{r^2}\right) - V(r)\right]^{1/2}. \tag{1.67}$$

The algebra for this step is as follows. Multiplying out the terms of Eq. (1.63) gives:

$$\eta E_\mathrm{i} - \frac{1}{2}\mu\dot{r}^2 = \frac{1}{2}\mu\frac{v_\ell^2b^2}{r^2} + V(r)\,,$$

and re-arranging gives:

$$\eta E_\mathrm{i} - \frac{1}{2}\mu\frac{v_\ell^2b^2}{r^2} = \frac{1}{2}\mu\dot{r}^2 + V(r)\,. \tag{1.68}$$

Recall that $E_\mathrm{i} = 1/2 M_1 v_\ell^2$ and therefore, $v_\ell^2 = 2E_\mathrm{i}/M_1$ and we can eliminate v_ℓ so that the second term on the left hand side of Eq. (1.68) becomes $-\dfrac{\mu b^2 E_\mathrm{i}}{M_1 r^2}$. Since $\mu = \dfrac{M_1 M_2}{M_1 + M_2}$ and $\mu/M_1 = \eta$, then:

$$\eta E_\mathrm{i} - \eta E_\mathrm{i} \frac{b^2}{r^2} = \frac{\mu \dot{r}^2}{2} + V(r), \quad \text{and} \quad \eta E_\mathrm{i} \left(1 - \frac{b^2}{r^2}\right) = \frac{\mu \dot{r}^2}{2} + V(r),$$

or

$$\dot{r} = \left(\frac{2}{\mu}\right)^{1/2} \left[\eta E_\mathrm{i} \left(1 - \frac{b^2}{r^2}\right) - V(r)\right]^{1/2},$$

which is the same as in Eq. (1.67). Note that r reaches the distance of closest approach when $\dot{r} = 0$. At this point:

$$V(r) = \eta E_\mathrm{i} \left(1 - \frac{b^2}{r^2}\right), \tag{1.69}$$

and $V_\mathrm{max} = \eta E_\mathrm{i}$ (at $b = 0$) which represents a "head-on" collision. So if a particle strikes a target atom of equal mass, then $V_\mathrm{max} = 1/2 E_\mathrm{i}$.

When $r \to \infty$, $V(r) \to 0$ and $\dot{r}^2 = \left(\dfrac{2}{\mu}\right) \eta E_\mathrm{i}$, or $\dot{r}^2 = 2E_\mathrm{i}/M_1$, $E_\mathrm{i} = 1/2 M_1 \dot{r}^2$ (and $\dot{r} = v_\ell$ at $r \to \infty$), so $E_\mathrm{i} = 1/2 M_1 v_\ell^2$.

Recall that we are looking for ϕ as a function of b. Going back to Eq. (1.67) and dividing $\dot{r}$ in Eq. (1.67) by $\dot{\psi}$ from Eq. (1.66) we have:

$$\frac{\dot{r}}{\dot{\psi}} = \frac{\mathrm{d}r}{\mathrm{d}\psi} = -\left(\frac{2}{\mu}\right)^{1/2} \left[\mu E_\mathrm{i} \left(1 - \frac{b^2}{r^2}\right) - V(r)\right]^{1/2} \frac{r^2}{v_\ell b}. \tag{1.70}$$

The minus sign in front of the quantity to the right of the equality is because for the first half of the orbit, $\dot{r}$ decreases as ψ increases. Bringing the term r^2 under the square root gives:

$$\frac{\mathrm{d}r}{\mathrm{d}\psi} = -\frac{1}{v_\ell b} \left(\frac{2}{\mu}\right)^{1/2} \left[\mu E_\mathrm{i} \left(r^4 - r^2 b^2\right) - r^4 V(r)\right]^{1/2}. \tag{1.71}$$

Dividing terms under the square root by $\eta E_\mathrm{i} b^2$ to bring this term out of the square root gives:

$$\frac{\mathrm{d}r}{\mathrm{d}\psi} = -\frac{1}{v_\ell b} \left(\frac{2}{\mu}\right)^{1/2} (\eta E_\mathrm{i})^{1/2} b \left[\frac{r^4}{b^2} \left(1 - \frac{V(r)}{\eta E_\mathrm{i}}\right) - r^2\right]^{1/2}. \tag{1.72}$$

Since $1/2M_1v_\ell^2 = E_\mathrm{i}$, then $v_\ell = (2E_\mathrm{i}/M_1)^{1/2}$, and substituting for v_ℓ gives:

$$\begin{aligned}\frac{\mathrm{d}r}{\mathrm{d}\psi} &= -\left(\frac{2}{\mu}\frac{M_1}{2E_\mathrm{i}}\eta E_\mathrm{i}\right)^{1/2}\left[\frac{r^4}{b^2}\left(1-\frac{V(r)}{\eta E_\mathrm{i}}\right)-r^2\right]^{1/2}\\ &= -\left(\frac{M_1}{\mu}\eta\right)^{1/2}\left[\frac{r^4}{b^2}\left(1-\frac{V(r)}{\eta E_\mathrm{i}}\right)-r^2\right]^{1/2}\\ &= -\left[\frac{r^4}{b^2}\left(1-\frac{V(r)}{\eta E_\mathrm{i}}\right)-r^2\right]^{1/2}. \end{aligned} \tag{1.73}$$

Substituting for $x = 1/r$ gives:

$$\frac{\mathrm{d}x}{\mathrm{d}\psi} = \left[\frac{1}{b^2}\left(1-\frac{V(x)}{\eta E_\mathrm{i}}\right)-x^2\right]^{1/2}. \tag{1.74}$$

This is the equation of orbit ($\psi = f(x)$).

The scattering angle ϕ is found by expressing $\mathrm{d}\psi$ as a function of x and $\mathrm{d}x$ and integrating from the limits on ψ corresponding to $x = 0$ and $1/\rho$. These limits are $\phi/2$ and $\pi/2$, respectively, as shown in Fig. 1.10. Performing this integration for the first half of the orbit yields:

$$\int_{\phi/2}^{\pi/2}\mathrm{d}\psi = \int_0^{1/\rho}\left[\frac{1}{b^2}\left(1-\frac{V(x)}{\eta E_\mathrm{i}}\right)-x^2\right]^{-1/2}\mathrm{d}x \tag{1.75}$$

and

$$\phi = \pi - 2\int_0^{1/\rho}\left[\frac{1}{b^2}\left(1-\frac{V(x)}{\eta E_\mathrm{i}}\right)-x^2\right]^{-1/2}\mathrm{d}x. \tag{1.76}$$

The quantity ρ in the upper limit of x is the value of r when $\psi = \pi/2$ and hence is the distance of closest approach, Since $\mathrm{d}x/\mathrm{d}\psi = 0$ when $\psi = \pi/2$, ρ is given from Eq. (1.74) by:

$$\eta E_\mathrm{i} = \frac{V(\rho)}{1-\dfrac{b^2}{\rho^2}}. \tag{1.77}$$

Equations (1.76) and (1.77) provide the relation between ϕ and b.

We have yet to determine the cross section for our scattering event. This may be done as follows. If particles M_1 are bombarding target atoms M_2, then in Fig. 1.11, those ions which cross an area $2\pi b\,\mathrm{d}b$ enclosed by circles of radii b and $b + \mathrm{d}b$ will be scattered into $\mathrm{d}\phi$ about ϕ. Since the relation between $\mathrm{d}b$ and $\mathrm{d}\phi$ can be obtained from Eq. (1.76) by differentiation, the differential cross section is

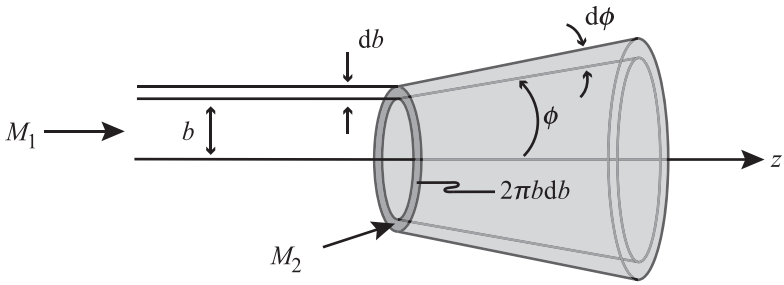

Fig. 1.11. Scattering of ions crossing an area $2\pi b\,\mathrm{d}b$ into an angular element $\mathrm{d}\phi$ about ϕ

given by:

$$\sigma(E_\mathrm{i},T)\,\mathrm{d}T = 2\pi b\,\mathrm{d}b \quad \text{and} \quad \sigma(E_\mathrm{i},T) = 2\pi b\frac{\mathrm{d}b}{\mathrm{d}\phi}\frac{\mathrm{d}\phi}{\mathrm{d}T}\,. \tag{1.78}$$

Knowing $V(r)$ enables ϕ to be written in terms of b^2 using Eq. (1.76) and then in terms of T using Eq. (1.13). Differentiating gives $2\pi b\,\mathrm{d}b$ as a function of T and $\mathrm{d}T$. Then from Eq. (1.78) the differential cross section for collisions having recoils in $\mathrm{d}T$ about T follows. The total cross section for collisions with T anywhere in the range $\check{T}$ to γE_i is:

$$\sigma(E_\mathrm{i}) = \int_{\check{T}}^{\gamma E_\mathrm{i}} \sigma(E_\mathrm{i},T)\,\mathrm{d}T\,. \tag{1.79}$$

The process for finding the energy transfer cross section can be summarized as follows:

1. Select a potential function $V(r)$.
2. Use Eq. (1.76) to obtain b as a function of ϕ, $b = f(\phi)$.
3. Use Eq. (1.13) to obtain ϕ as a function of T, $\phi = g(T)$.
4. Use the relations between b and ϕ and between ϕ and T in Eq. (1.78) to obtain the energy transfer cross section.

The preceding description of the energy transfer cross section emphasizes the importance of knowing the potential function describing the particular ion–atom or atom–atom interaction of interest. Without accurate knowledge of the potential function, further description of the collision process and the ensuing defect structure become impossible. Unfortunately, explicit evaluation of the integral in Eq. (1.76) is possible only for simple potential functions. But before looking further at the various potential functions and their application in determining the energy transfer cross section, we need first to consider the different possible classes of ions and their corresponding energies.

Classification of Ions

There are three important classes of ions in ion–atom collisions. The first is light energetic ions with $E_i > 1\,\text{MeV}$. The second is highly energetic ($E_i \sim 10^2\,\text{MeV}$) heavy ions such as fission fragments ($M \sim 10^2$). The third is lower energy heavy ions that may be produced by an accelerator or appear as a recoil that result from an earlier high-energy collision. The energy of these recoils is generally less than 1 MeV.

For each of these interactions, we must decide on the most appropriate potential function. A convenient guide is ρ/a, the ratio of the distance of closest approach to the screening radius as a function of the recoil energy, T. A rough graph of ρ vs. T is provided in Fig 1.12 to aid in the selection of the most appropriate potential. The three curves represent ions of each of the three classes just discussed: (1) 20 MeV protons, (2) 70 MeV fission fragments, and (3) 50 keV Cu ions. Curve (1) collisions apply to the regime where $\rho \ll a$ and the simple Coulomb potential is adequate. Curve (2) collisions that are head-on will have $\rho \ll a$ also. But for glancing collisions, $\rho \sim a$ and the screened Coulomb potential is most appropriate. Curve (3) represents the region where $a < \rho \ll 5a$ and the inverse square potential or Brinkman potential would apply since both the Born–Mayer and screened Coulomb terms must be accounted for.

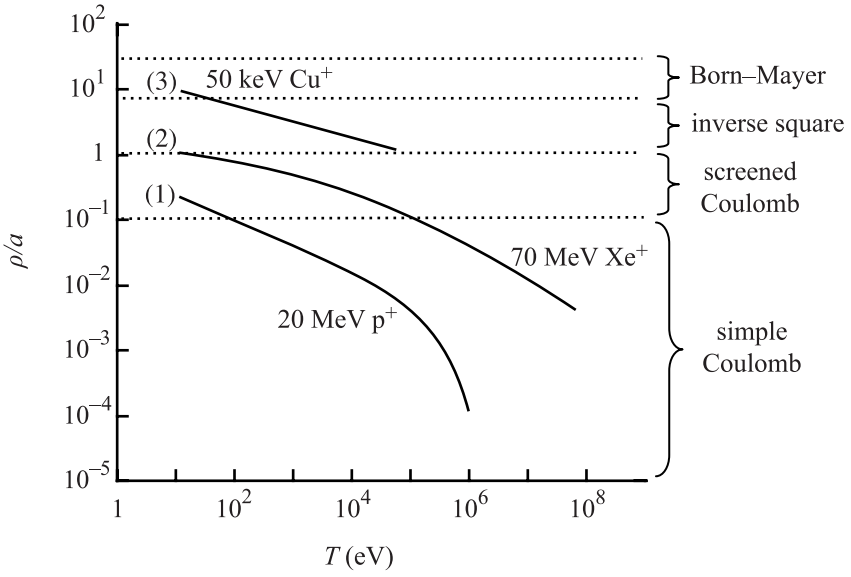

Fig. 1.12. Distance of closest approach r, as a function of T for (1) 20 MeV protons in Cu, (2) 70 MeV Xe^+ ions in Cu, and (3) 50 keV Cu^+ recoils in Cu (from [12])

Hard-sphere Type Collisions

The hard-sphere potential is appropriate for ion energies below about 50 keV and for near head-on elastic collisions. Here, $\rho \sim r_e$ and atoms will act like hard spheres. In a head-on collision, $b = 0$ and from Eq. (1.77) we have:

$$\eta E_i = V(\rho)\,. \tag{1.80}$$

When b is not quite zero, the collision may be pictured as in Fig. 1.13 where we define $R_1 = \rho \dfrac{M_2}{M_1 + M_2}$ and $R_2 = \rho \dfrac{M_1}{M_1 + M_2}$. If ρ is known, then from the figure:

$$b = \rho \cos \frac{\phi}{2}\,. \tag{1.81}$$

Now, recalling that:

$$\sigma_s(E_i, T)\,\mathrm{d}T = 2\pi b\,\mathrm{d}b$$

$$\sigma_s(E_i, T) = 2\pi b \frac{\mathrm{d}b}{\mathrm{d}\phi}\frac{\mathrm{d}\phi}{\mathrm{d}T}\,, \tag{1.82}$$

where $\dfrac{\mathrm{d}b}{\mathrm{d}\phi} = 1/2\rho \sin\phi/2$ from $b = \rho\cos\phi/2$, and $\dfrac{\mathrm{d}\phi}{\mathrm{d}T} = \dfrac{2}{\gamma E_i \sin\phi}$ from $T = \dfrac{\gamma E_i}{2}(1 - \cos\phi)$. Then $\sigma(E_i, T) = 2\pi\rho\cos\phi/2 \dfrac{\rho}{2}\sin\phi/2 \dfrac{2}{\gamma E_i \sin\phi}$, and

$$\sigma_s(E_i, T) = \frac{\pi\rho^2}{\gamma E_i}\,. \tag{1.83}$$

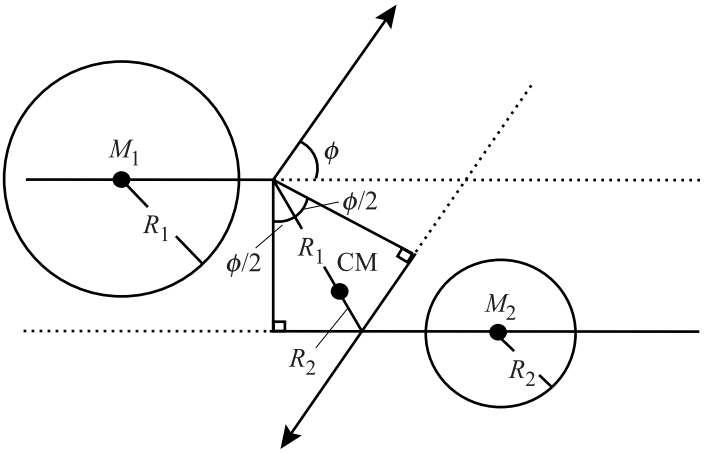

Fig. 1.13. Schematic of colliding atoms obeying the hard-sphere approximation for collisions

Recall that for neutron–nuclear interactions, $\sigma_s(E_i,T) = \sigma_s(E_i)/\gamma E_i$. Using this relation, we can obtain an idea of the size of the energy transfer cross section for neutron–nuclear interactions vs. atom–atom interactions: $\dfrac{\sigma(E_i,T)^{a-a}}{\sigma(E_i,T)^{\text{n-nuclear}}} = \dfrac{\pi\rho^2}{\sigma_s(E_i)} \sim \dfrac{\pi(10^{-8})^2}{10^{-24}} \sim 10^8$, and so the energy transfer cross section for atom–atom interactions is about eight orders of magnitude greater than that for neutron–nuclear interactions.

The total scattering cross section is:

$$\sigma_s(E_i) = \int_{\check{T}}^{\gamma E_i} \sigma_s(E_i,T)\,dT = \int_{\check{T}}^{\gamma E_i} \frac{\pi\rho^2}{\gamma E_i}\,dT = \frac{\pi\rho^2}{\gamma E_i}\left[\gamma E_i - \check{T}\right] = \pi\rho^2 . \tag{1.84}$$

Note that $\sigma_s(E_i)$ is independent of E_i (because $\rho \neq f(E_i)$), and that $\sigma_s(E_i,T)\alpha 1/E_i$ and is independent of T. We can find $\sigma_s(E_i,T)$ explicitly by applying the appropriate potential function to find a value of ρ (determined by $V(r)$). Recall from our discussions in Sect. 1.2.1 that for collisions in which the impact parameter is on the order of the equilibrium separation of the atoms, the Born–Mayer potential is most appropriate. This corresponds to energies below about 10 keV. (Note that this means that we are also backing off from a pure hard-sphere model.) Hence, we will use $V(r) = A\exp(-r/B)$, where A and B are defined in Eq. (1.47). Using Eq. (1.80) gives:

$$V(\rho) = A\exp(-\rho/B) = \eta E_i \tag{1.85}$$

or

$$\rho = B\ln\left(\frac{A}{\eta E_i}\right), \tag{1.86}$$

and since $b = \rho\cos\phi/2 = B\ln(A/\eta E_i)\cos\phi/2$, the energy transfer cross section is:

$$\sigma_s(E_i,T) = \frac{\pi B^2}{\gamma E_i}\left[\ln\frac{A}{\eta E_i}\right]^2 . \tag{1.87}$$

The total scattering cross section is then the integral of the energy transfer cross section between the limits $\check{T}$ and γE_i:

$$\sigma_s(E_i) = \int_{\check{T}}^{\gamma E_i} \pi B^2\left[\ln\frac{A}{\eta E_i}\right]^2 \frac{1}{\gamma E_i}\,dT . \tag{1.88}$$

From this expression, we will be able to calculate the total cross section for displacement scattering events for all allowed T. Note that the total scattering cross section depends on E_i. Also, for typical values of A, B and $\check{T}$ (25 eV), the value of $\sigma_s(E_i)$ for atom–atom interactions is about 10^8 times that for neutron–nuclear events.

Rutherford Scattering

Let us turn now to a second example in which we will use the pure Coulomb scattering potential to demonstrate Rutherford scattering. From our classification of ions according to ion energy and mass, type 1 collisions involve light ($m \sim 1$ to 4) energetic ($E >$ MeV) ions where $\rho \ll a$. Collisions of this sort are adequately represented by the simple Coulomb potential, which from Eq. (1.48) is:

$$V(r) = \frac{Z_1 Z_2 \varepsilon^2}{r}.$$

We will assume that Z_1 and Z_2 represent the nuclear charges and that this collision occurs at high energies so that electrons are stripped from the nuclei and the only interaction is between the nuclei.

In our description of the trajectories of the particles in the CM system, we found that at the point of closest approach, $\mathrm{d}x/\mathrm{d}\psi = 0$ and from Eq. (1.77):

$$\eta E_\mathrm{i} = \frac{V(\rho)}{1 - \dfrac{b^2}{\rho^2}}.$$

Substituting in for $V(r)$ gives:

$$\frac{Z_1 Z_2 \varepsilon^2}{\rho} = \eta E_\mathrm{i} \left(1 - \frac{b^2}{\rho^2}\right). \tag{1.89}$$

Defining:

$$b_0 = \left(\frac{Z_1 Z_2 \varepsilon^2}{\eta E_\mathrm{i}}\right), \tag{1.90}$$

it follows that:

$$\frac{b_0}{\rho} = 1 - \frac{b^2}{\rho^2}, \tag{1.91}$$

and

$$\rho = \frac{b_0}{2}\left[1 + \left(1 + \frac{4b^2}{b_0^2}\right)\right]^{1/2}. \tag{1.92}$$

Hence, the distance of closest approach is a function of the impact parameter b, as expected. For head-on collisions, $b = 0$ and the minimum value of ρ depends on E_i:

$$\rho\,(b = 0) = \rho_0 = b_0 = \frac{Z_1 Z_2 \varepsilon^2}{\eta E_\mathrm{i}}. \tag{1.93}$$

Note that for this type of collision, ρ depends on E_i, in contrast to independence of E_i in the hard-sphere model. Going back to the orbital equation (1.75), we will now evaluate it as a definite integral:

$$\int_{\pi/2}^{\phi/2} \mathrm{d}\psi = \int_{1/\rho}^{0} \left[\frac{1}{b^2} - \frac{b_0}{b^2}x - x^2\right]^{-1/2} \mathrm{d}x. \tag{1.94}$$

Since $\psi = \pi/2$ when $r = \rho (x = 1/\rho)$ and $\psi = \phi/2$ when $r = \infty$ $(x = 0)$, letting $y = x + \dfrac{b_0}{2b^2}$, gives:

$$\phi/2 - \pi/2 = \int_{\frac{1}{\rho}+\frac{b_0}{2b^2}}^{\frac{b_0}{2b^2}} \left[c^2 - y^2\right]^{-1/2} \mathrm{d}y, \tag{1.95}$$

where $c^2 = \left(\dfrac{1}{b^2} + \dfrac{b_0^2}{4b^4}\right)$. The orbits are then:

$$\begin{aligned}\phi/2 - \pi/2 &= \left[\sin^{-1}\frac{y}{c}\right]_{\frac{1}{\rho}+\frac{b_0}{2b^2}}^{\frac{b_0}{2b^2}} \\ &= \sin^{-1}\frac{b_0}{2b^2} - \sin^{-1}\frac{1}{c}\left(\frac{1}{\rho} + \frac{b_0}{2b^2}\right).\end{aligned} \tag{1.96}$$

Since $\sin^{-1}\dfrac{1}{c}\left(\dfrac{1}{\rho} + \dfrac{b_0}{2b^2}\right) = \sin^{-1}(1) = \pi/2$, then:

$$\sin\phi/2 = \frac{b_0}{2b^2 c}. \tag{1.97}$$

Substituting for c (from above) into Eq. (1.97) yields:

$$\sin^2\phi/2 = \frac{1}{1 + \dfrac{4b^2}{b_0^2}}. \tag{1.98}$$

Using trigonometric relations for $\sin^2\phi/2$, we have:

$$b = \frac{b_0}{2}\cot\phi/2. \tag{1.99}$$

We now have a relationship between the impact parameter, b and the asymptotic scattering angle, ϕ. Note that b is a function of E_i through b_0 (Eq. (1.93)).

We now want an expression for the scattering cross section. Using Eq. (1.82) for $\sigma_s(E_i, T)$, we have:

$$\sigma_s(E_i, T)\,\mathrm{d}T = \sigma_s(E_i, \phi)\,\mathrm{d}\Omega = 2\pi b\,\mathrm{d}b = \pi b_0 \cot\frac{\phi}{2}\,\mathrm{d}b\,, \tag{1.100}$$

and substituting for $\mathrm{d}b$ from Eq. (1.99) gives:

$$\sigma_s(E_i, \phi) = \left(\frac{b_0}{4}\right)^2 \frac{1}{\sin^4(\phi/2)}\,, \tag{1.101}$$

which is the Rutherford inverse fourth power scattering law. The cross section for recoil is exactly the same as for elastic collisions, Eq. (1.13), and since:

$$\sigma_s(E_i, T) = \sigma_s(E_i, \phi)\,\frac{\mathrm{d}\Omega}{\mathrm{d}T}\,,$$

we have:

$$\sigma_s(E_i, T) = \frac{\pi b_0^2}{4}\frac{E_i\gamma}{T^2}\,. \tag{1.102}$$

Note that unlike neutron–nuclear collisions and hard-sphere scattering in general, the Rutherford scattering cross section is a strong function of T. This expression also shows that the scattering cross section $\sigma_s(E_i, T) \to \infty$ as $T \to 0$. But this is just a reflection of the fact that as $\phi \to 0$, $b \to \infty$ and is representative of long-range Coulomb interactions. In reality, there is a cut-off in b and hence in ϕ due to electron screening. As we will see later, this cut-off is E_d, the displacement energy. The average energy transferred is then:

$$\bar{T} = \frac{\int_{\check{T}}^{\hat{T}} T\,\sigma_s(E_i, T)\,\mathrm{d}T}{\int_{\check{T}}^{\hat{T}} \sigma_s(E_i, T)\,\mathrm{d}T} = \frac{\check{T}\ln(\hat{T}/\check{T})}{1 - \dfrac{\check{T}}{\hat{T}}}\,. \tag{1.103}$$

For $\hat{T} = \gamma E_i$ and $\check{T} = E_d$ and since $\gamma E_i \gg E_d$, then:

$$\bar{T} \approx E_d \ln\left(\frac{\gamma E_i}{E_d}\right)\,. \tag{1.104}$$

which is quite small for all energies E_i, reflecting the strong $1/T^2$ dependence in Eq. (1.102).

The integral of Eq. (1.102) over T gives the total cross section for displacement events by an ion of energy E_i:

$$\sigma_s(E_i) = \frac{\pi}{4} b_0^2 \hat{T} \int_{E_d}^{\hat{T}} \frac{\mathrm{d}T}{T^2} = \frac{\pi b_0^2}{4}\left(\frac{\hat{T}}{E_d} - 1\right)\,, \tag{1.105}$$

and since at high energies $\hat{T}/E_{\rm d} \gg 1$ then we have for $\hat{T} = \gamma E_{\rm i}$:

$$\sigma_{\rm s}(E_{\rm i}) \approx \frac{\pi b_0^2}{4}\frac{\gamma E_{\rm i}}{E_{\rm d}}, \tag{1.106}$$

which is quite large.

A critical question in applying the above results is under what conditions can Rutherford scattering be applied? The answer is that we must require that during an encounter, the major part of scattering occurs in the region where $r \ll a$. But this is a qualitative measure. What is needed is a means for determining quantitatively, when Rutherford scattering applies. To address this question, we consider two cases.

Case 1: Near "head-on" collisions high T. For near head-on collision, $\rho_0 \ll a$ or $E_{\rm i} \gg E_a$, where E_a is the value of $E_{\rm i}$ that would give $\rho_0 = a$ assuming a screened Coulomb potential:

$$E_a = 2E_{\rm R}(Z_1 Z_2)^{7/6}(M_1 + M_2)/(M_2 e), \tag{1.107}$$

which is obtained by re-writing the screened Coulomb potential (Eq. (1.49)) in an inverse square law form (Eq. (1.59)), with $\varepsilon^2 = 2a_0 E_{\rm R}$ and equating at $r = a$ and setting $V(r) = \eta E_{\rm i} = \dfrac{M_2}{M_1 + M_2} E_{\rm i}$ for a head-on collision.

Case 2: Glancing collisions (low T). Here we only consider those collisions in which $b \le a$, or that result in an energy transfer $\check{T} \sim E_{\rm d}$ for $b = a$. For a simple Coulomb collision with $b = a$, we have from Eqs. (1.98) and (1.13):

$$T = \frac{\varepsilon^2 \gamma E_a^2}{4E_{\rm i}}, \quad \text{or} \quad E_{\rm i} = \frac{\varepsilon^2 \gamma E_a^2}{4T}, \tag{1.108}$$

and giving this value of $E_{\rm i}$ the name E_b at $T = \check{T}$, we have

$$E_b = \frac{\varepsilon^2 \gamma E_a^2}{4\check{T}}, \quad \text{where} \quad \check{T} = E_{\rm d}, \tag{1.109}$$

and this equation is valid for all $E_{\rm i} \gg E_b$. Essentially, E_b is the value of $E_{\rm i}$ that results in a transfer of energy $T \ge E_{\rm d}$ at $b = a$. Or looking at it another way, values of $E_b < E_{\rm i}$ give $T \ll \check{T}$ and can be neglected since $\rho \ge a$, and these encounters can be neglected. Table 1.4 provides examples of the values of E_a and E_b for different particle–target atom combinations and energies.

From Table 1.4, since $E_a < E_b$, we can use the criterion that $E_{\rm i}$ must be $\gg E_b$ as an extreme test of the validity of the simple Coulomb scattering description.

In summary, if $E_{\rm i} \gg E_a$, the simple Coulomb potential may be used for near head-on collisions. If $E_{\rm i} \gg E_b$, it can be used for all collisions of interest in radiation damage. Light charged particles such as protons and alphas with $E_{\rm i} > 1$ MeV fall into this category, while fission fragments are in the regime $E_a < E_{\rm i} < E_b$ and recoils have $E_{\rm i} \le E_a$. These will be discussed next. But first, we present an example of Rutherford scattering.

Table 1.4. Values of E_a and E_b for various particle–target atom combinations and energies (from [13])

Incident particle	Target atom	E_a (eV)	E_b (eV)
C	C	2×10^3	8×10^5
Al	Al	1×10^4	2×10^7
Cu	Cu	7×10^4	1×10^9
Au	Au	7×10^5	1×10^{11}
Xe	U	5×10^5	3×10^{10}
D^+	C	1.5×10^2	2×10^3
D^+	Cu	1×10^3	2×10^4
D^+	U	4×10^3	1×10^5

Example 1.2. 2 MeV protons on aluminum
For this case,

$$\hat{T} = \gamma E_\mathrm{i} = \frac{4(27)}{(27+1)^2}2\,\mathrm{MeV} = 0.28\,\mathrm{MeV}$$

$$\check{T} = 25\,\mathrm{eV}$$

$$\bar{T} = E_\mathrm{d}\ln\left(\frac{\gamma E_\mathrm{i}}{E_\mathrm{d}}\right) = 233\,\mathrm{eV}$$

We can also calculate $E_a \sim 200\,\mathrm{eV}$ and $E_b \sim 4000\,\mathrm{eV}$. (For comparison, 2 MeV He^+ on Al, $E_a \sim 1\,\mathrm{keV}$ and $E_b \sim 25\,\mathrm{keV}$. Also, for 2 MeV H^+ on Au, $E_a \sim 1.6\,\mathrm{keV}$ and $E_b \sim 38\,\mathrm{keV}$, and for 2 MeV He^+ on Au, $E_a \sim 8\,\mathrm{keV}$ and $E_b \sim 69\,\mathrm{keV}$.) Since $E_\mathrm{i} \gg E_b$, the simple Coulomb law is valid for this type of collision. Incidentally, $\sigma(E_\mathrm{i}) \sim 4\times10^{-22}\,\mathrm{cm}^2$ and since the mean free path between collisions is $\lambda = 1/\sigma N$ and $N \sim 6\times10^{22}\,\mathrm{a/cm}^3$, then $\lambda \sim 0.04\,\mathrm{cm}$ or about 400 μm, or about 10 times the length of a 2 MeV proton track in Al. This means that there is on average, only one Rutherford scattering collision for every 10 protons incident on Al.

Now, lets investigate the other classes of ion–atom collisions such as heavy, energetic ions, heavy, slow ions and high-energy electrons.

Heavy, Energetic Ions

For heavy, energetic ions such as fission fragments, Fig. 1.12 shows that an appropriate potential must account for both screened Coulomb and closed shell repulsion. Let us look first at the simple Coulomb potential as a rough approximation, knowing that its use is only justified for recoil energies approaching γE_i which is where

$\rho \ll a$. Recall that $\sigma(E_\mathrm{i}) = \dfrac{\pi b_0^2}{4}\dfrac{\gamma E_\mathrm{i}}{E_\mathrm{d}}$, and $b_0 \alpha \dfrac{Z_1}{\gamma E_\mathrm{i}}$, $\gamma = \dfrac{4M_1M_2}{(M_1+M_2)^2}$, $\eta = \dfrac{M_2}{M_1+M_2}$, which gives an increase in the cross section compared to the light ion by a factor of

$$\frac{\sigma_\mathrm{heavy}}{\sigma_\mathrm{light}} = \frac{\left.\dfrac{z_1^2 M_1}{E_\mathrm{i}}\right|_\mathrm{heavy}}{\left.\dfrac{z_1^2 M_1}{E_\mathrm{i}}\right|_\mathrm{light}} \approx 10^6$$

for the fission fragments at the peaks of the fission yield of uranium, $M_1^\mathrm{light} \simeq 96\,\mathrm{amu}$, $E_1^\mathrm{light} \simeq 95\,\mathrm{MeV}$ and $M_1^\mathrm{heavy} \simeq 137\,\mathrm{amu}$, $E_1^\mathrm{heavy} \simeq 55\,\mathrm{MeV}$. Comparing to the example of the 2 MeV proton on Al, fission fragments have a cross section that is larger by a factor of 10^4! Therefore, the mean free path is 10^{-4} that of a proton in Al.

Recall that $\sigma(E_\mathrm{i}, T)$ varies as $1/T^2$. But this is only true near $\gamma E_\mathrm{i} (\rho \ll a)$. At lower energies screening will reduce the sensitivity to energy. So we must use a better description of the interaction between energetic, heavy ions and target atoms.

Brinkman's expression, Eq. (1.50), includes both terms and if this is used in the impulse approximation (see [13]), the result is:

$$T = \frac{M_1}{M_2}\frac{A^2}{E_\mathrm{i}}\left[F\left(\alpha, \frac{b}{B}\right) - (1-\alpha)F\left(1+\alpha, \frac{b}{B}\right)\right]^2, \tag{1.110}$$

where A, B are given in Eq. (1.50) and

$$\begin{aligned} F\left(\alpha, \frac{b}{B}\right) &= \frac{b}{B}\int_{b/a}^{\infty} \frac{-\mathrm{e}^{-x}\,\mathrm{d}x}{(x^2 - b^2/a^2)^{1/2}(1-\mathrm{e}^{-\alpha x})^2} \\ &= \frac{b}{B}\sum_{n=0}^{\infty}(n+1)\,K_0\left\{\frac{b}{B}(1+n\alpha)\right\}, \end{aligned} \tag{1.111}$$

where $K_0(y)$ is a Bessel function of the third kind. The term α is the ratio of Born–Mayer and screened Coulomb terms at $r = a$, so in general, $\alpha < 1$. T can be found from b and Eq. (1.110), and by inversion, b is obtained as a function of T. Differentiation gives $\sigma = 2\pi b\,\mathrm{d}b$. However, because of the complexity of Eq. (1.110), numerical solutions are required. Nevertheless, we may calculate $\mathrm{d}N$, the number of recoils in $\mathrm{d}T$ at T produced by the fission fragment in slowing down to rest. This is found by:

$$\mathrm{d}N = n\sigma\,\mathrm{d}x = n\frac{\mathrm{d}\sigma}{\mathrm{d}T}\left(-\frac{\mathrm{d}E}{\mathrm{d}x}\right)^{-1}\mathrm{d}E\,\mathrm{d}T, \tag{1.112}$$

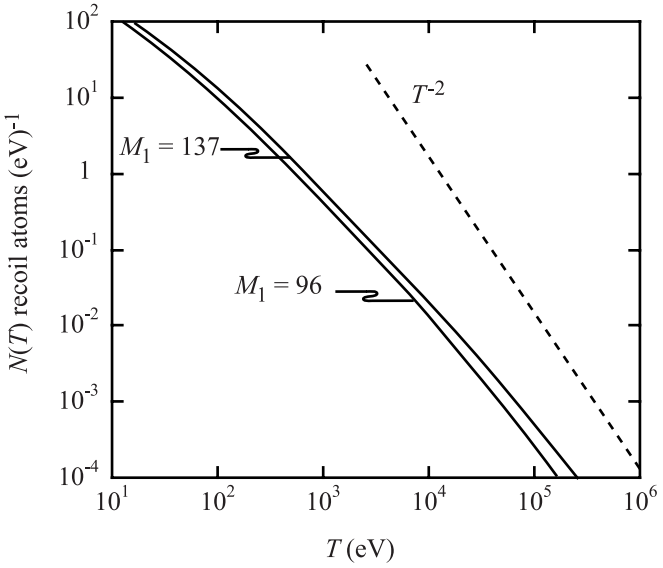

Fig. 1.14. The energy spectrum of recoils $N(T)\,\mathrm{d}T$ produced by fission fragments slowing down to rest in uranium. Two cases are shown: $M_1 = 96$, $E_1 = 95\,\mathrm{MeV}$ and $M_1 = 137$, $E_1 = 55\,\mathrm{MeV}$ (from [13])

where n is the density of atoms, and

$$N(T)\,\mathrm{d}T = n\int_0^{E_\mathrm{i}} \frac{\sigma}{\mathrm{d}T}\left(\frac{\mathrm{d}E}{\mathrm{d}X}\right)^{-1}\mathrm{d}E\,\mathrm{d}T\,. \tag{1.113}$$

Brinkman carried out these calculations for light and heavy fragments from ^{235}U fission slowing down in uranium. The results are shown in Fig. 1.14. Note that $N(T)$ decreases more rapidly than T^{-1} and hence the majority of displaced atoms are produced by low-energy recoils. Therefore, high-energy recoils can be neglected altogether. Another way of looking at this is that the simple Coulomb potential is only valid in an energy range that does not contribute significantly to displacements.

Heavy, Slow Ions

These ions are classified by the curve labeled "3" in Fig. 1.12. This is a very important class of collisions as it covers most of the applications of kV ion implanters and low MeVaccelerators in the fields of materials science and radiation damage that includes such topics as ion implantation and heavy ion radiation effects simulation. The figure shows that collisions must be dealt with over the range $a < \rho < 10a$. The formalism used for fission fragments in the previous section applies to glancing collisions but for head-on collisions, another approach is needed. The appropriate

potential for $a/5 \leq \rho \leq 5a$ is the inverse square approximation. We use a potential of the form:

$$V(r) = \frac{2E_R}{e}(Z_1 Z_2)^{5/6}\left(\frac{a_0}{r}\right)^2,$$

which is obtained by fitting a screened Coulomb potential to the inverse square potential and equating at $r = a$, Eq. (1.59). Substituting this potential function into the orbital equation (1.76) gives:

$$\frac{\phi}{\pi} = 1 - \left(1 + \frac{a^2 E_a}{b^2 E_\mathrm{i}}\right)^{-1/2}. \tag{1.114}$$

Using Eq. (1.13) to express ϕ in terms of T gives:

$$T = \gamma E_\mathrm{i} \cos^2\left[\frac{\pi}{2}\left(1 + \frac{a^2 E_a}{b^2 E_\mathrm{i}}\right)^{-1/2}\right]. \tag{1.115}$$

Expressing b in terms of T and differentiating gives:

$$\sigma_\mathrm{s}(E_\mathrm{i}, T) = \frac{4E_a a^2 \alpha}{\gamma E_\mathrm{i}^2 (1 - 4\alpha^2)^2 [x(1-x)]^{1/2}}, \tag{1.116}$$

where $x = \dfrac{T}{\gamma E_\mathrm{i}}$ and $\pi\alpha = \cos^{-1} x^{1/2}$.

For small x (low-energy transfer), we have:

$$\sigma_\mathrm{s}(E_\mathrm{i}, T) = \frac{\pi^2 a^2 E_a \gamma^{1/2}}{8 E_\mathrm{i}^{1/2} T^{3/2}}. \tag{1.117}$$

Note that the energy transfer cross section is dependent on T. The mean recoil energy is:

$$\bar{T} = \frac{\int_{\check{T}}^{\gamma E_\mathrm{i}} T \sigma_\mathrm{s}(E_\mathrm{i}, T)\,\mathrm{d}T}{\int_{\check{T}}^{\gamma E_\mathrm{i}} \sigma_\mathrm{s}(E_\mathrm{i}, T)\,\mathrm{d}T} = \left(\gamma E_\mathrm{i} \check{T}\right)^{1/2}. \tag{1.118}$$

The total cross section for displacement is:

$$\sigma_\mathrm{s}(E_\mathrm{i}) = \int_{\check{T}}^{\gamma E_\mathrm{i}} \sigma_\mathrm{s}(E_\mathrm{i}, T)\,\mathrm{d}T = \frac{\pi^2 a^2 E_a \gamma^{1/2}}{4\left(E_\mathrm{i}\check{T}\right)^{1/2}}. \tag{1.119}$$

Relativistic Electrons

Radiation damage from electrons is not so important in reactor core materials, but more so in the laboratory as they are commonly used in electron microscopes for radiation damage studies. Due to the low mass of the electron, very high energies

must be attained in order to cause displacements of a lattice atom. These energies are high enough such that relativistic quantum mechanics must be used to describe the collision. Even so, the energy transferred is large enough to displace only the struck atoms with no secondary displacements.

In relativistic form, the momentum of an electron with rest mass m_0 and kinetic energy E_i is:

$$p_\mathrm{e}^2 = \frac{E_\mathrm{i}}{c^2}\left(E_\mathrm{i} + 2m_0c^2\right). \tag{1.120}$$

Since the struck atom recoils non-relativistically, the recoil expression is that given in Eq. (1.9):

$$V_\ell'^2 = V_\mathrm{CM}^2 + V_\mathrm{c}'^2 - 2V_\mathrm{CM}V_\mathrm{c}'\cos\phi = 2V_\mathrm{CM}^2\left(1-\cos\phi\right) = 4V_\mathrm{CM}^2\sin^2\frac{\phi}{2},$$

and conservation of momentum gives:

$$p_\mathrm{e} = \left(m_0 + M\right)V_\mathrm{CM} \cong MV_\mathrm{CM}.$$

Replacing the velocity terms with energies in the expression for $V_\ell'^2$ yields:

$$T = \frac{2E_\mathrm{i}}{Mc^2}\left(E_\mathrm{i} + 2m_0c^2\right)\sin^2\frac{\phi}{2}, \tag{1.121}$$

or

$$\hat{T} = \frac{2E_\mathrm{i}}{Mc^2}\left(E_\mathrm{i} + 2m_0c^2\right). \tag{1.122}$$

An approximate expression for the Dirac equation for light ions [13] yields the differential scattering cross section:

$$\begin{aligned}\sigma_\mathrm{s}\left(E_1,\phi\right) = {} & \frac{4\pi a_0^2Z_2^2E_\mathrm{R}^2}{m_0^2c^4}\frac{1-\beta^2}{\beta^4} \\ & \times\left[1-\beta^2\sin^2\left(\phi/2\right)+\pi\alpha\beta\sin\left(\phi/2\right)\left(1-\sin\left(\phi/2\right)\right)\right] \\ & \times\cos\left(\phi/2\right)\csc^3\left(\phi/2\right),\end{aligned} \tag{1.123}$$

where $\beta = v/c$ and $\alpha = Z_2/137$. This expression approaches the Rutherford scattering law for small β. Using Eqs. (1.121) and (1.122), the differential scattering cross section is written in terms of T and $\hat{T}$:

$$\sigma_\mathrm{s}\left(E_\mathrm{i},T\right) = \frac{4\pi a_0^2Z_2^2E_\mathrm{R}^2}{m_0^2c^4}\frac{1-\beta^2}{\beta^4}\left[1-\beta^2\frac{T}{\hat{T}}+\pi\frac{\alpha}{\beta}\left\{\left(\frac{T}{\hat{T}}\right)^{1/2}-\frac{T}{\hat{T}}\right\}\right]\frac{\hat{T}}{T^2}. \tag{1.124}$$

The total cross section is found by integrating Eq. (1.124) from $\check{T}$ to $\hat{T}$:

$$\sigma_{\mathrm{s}}(E_{\mathrm{i}}) = \frac{4\pi a_0^2 Z_2^2 E_{\mathrm{R}}^2}{m_0^2 c^4} \frac{1-\beta^2}{\beta^4} \left(\frac{\hat{T}}{\check{T}} - 1 \right) - \beta^2 \log \frac{\hat{T}}{\check{T}} + \alpha\beta 2 \left(\frac{\hat{T}}{\check{T}} \right)^{1/2} - 1 - \log \frac{\hat{T}}{\check{T}} . \tag{1.125}$$

For electrons with energies above the damage threshold and $\hat{T}/\check{T}$ slightly greater than unity:

$$\sigma_{\mathrm{s}}(E_{\mathrm{i}}) \cong \frac{4\pi a_0^2 Z_2^2 E_{\mathrm{R}}^2}{m_0^2 c^4} \left(\frac{1-\beta^2}{\beta^4} \right)^2 \left[\frac{\hat{T}}{\check{T}} - 1 \right] . \tag{1.126}$$

Figure 1.15 shows that at high enough energies, $\sigma(E_{\mathrm{i}})$ approaches an asymptotic value:

$$\sigma_{\mathrm{s}}(E_{\mathrm{i}}) \to \frac{8\pi a_0^2 Z_2^2 E_{\mathrm{R}}^2}{\check{T} M_2 c^2} \tag{1.127}$$

when $E_{\mathrm{i}} \gg m_0 c^2$. It should be emphasized, however, that these cross sections are most accurate for light elements but seriously underestimate $\sigma_{\mathrm{s}}(E_{\mathrm{i}})$ for heavy elements ($Z > 50$). Table 1.5 provides a summary of the energy transfer and the energy transfer cross sections for the various types of atom–atom interactions discussed in Sect. 1.2.

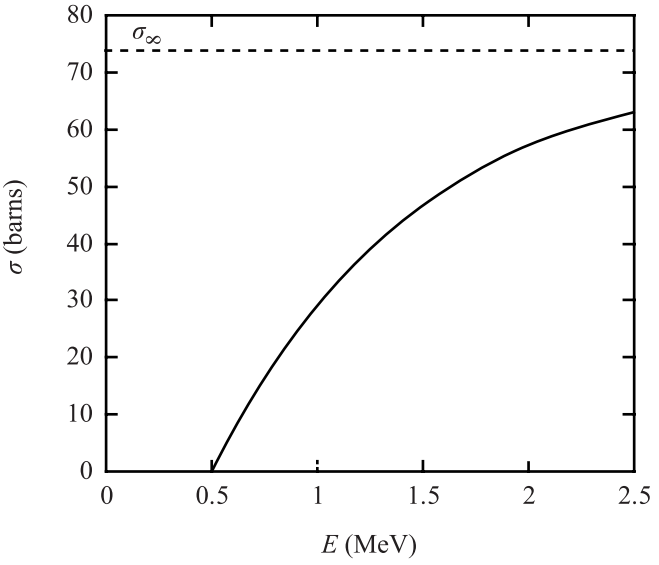

Fig. 1.15. Damage cross section for electrons bombarding copper where $E_{\mathrm{d}} = 25\,\mathrm{eV}$ (from [13])

Table 1.5. Energy transfer and energy transfer cross sections for various types of atom–atom collisions

Type of collision	Energy transfer and energy transfer cross section	Equation in text
Hard-sphere type (Born–Mayer potential) $\rho \sim r_e$	$\sigma_s(E_i,T) = \dfrac{\pi B^2}{\gamma E_i}\left[\ln\dfrac{A}{\eta E_i}\right]^2$	(1.87)
	$\bar{T} = \gamma E_i/2$	(1.13)
Rutherford scattering (simple Coulomb potential) $\rho \ll a$	$\sigma_s(E_i,T) = \dfrac{\pi b_0^2}{4}\dfrac{E_i\gamma}{T^2}$	(1.102)
	$\bar{T} \approx E_d \ln\left(\dfrac{\gamma E_i}{E_d}\right)$	(1.104)
Heavy ion (inverse square) $a/5 \le \rho \le 5a$	$\sigma_s(E_i,T) = \dfrac{\pi^2 a^2 E_a \gamma^{1/2}}{8E_i^{1/2}T^{3/2}}$	(1.117)
	$\bar{T} = \left(\gamma E_i \hat{T}\right)^{1/2}$	(1.118)
Relativistic electrons	$\sigma(E_i,T) = \dfrac{4\pi a_0^2 Z_2^2 E_R^2}{m_0^2 c^4}\dfrac{1-\beta^2}{\beta^4}$ $\times\left[1-\beta^2\dfrac{T}{\hat{T}}+\pi\dfrac{\alpha}{\beta}\left\{\left(\dfrac{T}{\hat{T}}\right)^{1/2}-\dfrac{T}{\hat{T}}\right\}\right]\dfrac{\hat{T}}{T^2}$	(1.124)

1.3 Ionization Collisions

Up to this point, we have been treating collisions as discrete events. However, besides collision with or between nuclei, an ion or atom traveling through the lattice may lose energy by electronic excitation, by ionization or by Bremsstrahlung (loss of energy of an electron passing through the Coulomb field of a nucleus by emission of X-rays). These events may be viewed as more or less continuous events. What follows is a treatment of energy loss in solids.

1.3.1 Energy Loss Theory

We are interested in finding the differential energy loss of an ion or atom traveling through a lattice. We begin by defining the energy loss per unit length as $-\mathrm{d}E/\mathrm{d}x$ (or $NS(E)$ where N is the atom number density and S is the stopping power in units of energy $\times$ distance squared) so that the total energy loss can then be approximated by a sum of these components:

$$\left(-\frac{\mathrm{d}E}{\mathrm{d}x}\right)_{\text{total}} = \left(-\frac{\mathrm{d}E}{\mathrm{d}x}\right)_{\text{n}} + \left(-\frac{\mathrm{d}E}{\mathrm{d}x}\right)_{\text{e}} + \left(-\frac{\mathrm{d}E}{\mathrm{d}x}\right)_{\text{r}}, \tag{1.128}$$

where the subscripts are defined as follows:

n = elastic
e = electronic
r = radiation

For most of the applications in which we will be interested, energy loss by radiation will be small and will be neglected.

From our discussion in Sect. 1.2.1 it is evident that in order to accurately describe the slowing down of an ion or atom over the entire energy range from $\hat{T}$ to $\check{T}$, where $\hat{T}$ may be in MeVand $\check{T} \sim 10\,\text{eV}$, several potential functions would need to be "pieced" together (see Fig. 1.9). This would cause problems because of discontinuities at the cuts. Moreover, the cut-off points of these functions often differ depending on M and Z.

However, we can separate or subdivide stopping power according to the type of interaction and hence, the energy regime. In the high-energy regime, $\rho \ll a$ and $S_\text{e} \gg S_\text{n}$ and these interactions are treated as pure Coulomb collisions. In the low-energy regime, $\rho \approx a$ and $S_\text{n} > S_\text{e}$. This is the region of importance in the deposition of displacement energy. In either case, we can establish a formalism for calculating stopping power, $\mathrm{d}E/\mathrm{d}x = NS(E)$.

If we know the energy transfer cross section $\sigma(E_\text{i}, T)$ for either S_n or S_e, then we can calculate the average energy transfer:

$$\bar{T} = \frac{\int T\sigma\,\mathrm{d}T}{\int \sigma\,\mathrm{d}T} = \text{energy lost or transferred},$$

and the mean free path (mfp) between collisions is $\lambda = \dfrac{1}{N\sigma}$. Then the ratio of these two quantities is the energy loss per unit length:

$$\begin{aligned}\frac{\mathrm{d}E}{\mathrm{d}x} = \frac{\bar{T}}{\lambda} &= \frac{\int_{\check{T}}^{\hat{T}} T\sigma(E_\text{i}, T)\,\mathrm{d}T}{\int_{\check{T}}^{\hat{T}} \sigma(E_\text{i}, T)\,\mathrm{d}T} \cdot N\int_{\check{T}}^{\hat{T}} \sigma(E_\text{i}, T)\,\mathrm{d}T \\ &= N\int_{\check{T}}^{\hat{T}} T\sigma(E_\text{i}, T)\,\mathrm{d}T\,, \end{aligned} \tag{1.129}$$

where N is the target number density.

Another way to look at this is as follows: Consider a projectile incident on an amorphous target containing an average of N atoms/unit volume (Fig. 1.16). In traversing the slab of material between x and $x + \Delta x$, the projectile will come within a distance b_1 of $N\Delta x 2\pi b_1\,\mathrm{d}b$ target particles and transfer an energy $T(E_\text{i}, b)$ to each. The total energy transferred to all target particles in the slab is obtained by integrating over all possible impact parameters:

$$\Delta E = N\Delta x\int_0^\infty T 2\pi b\,\mathrm{d}b.$$

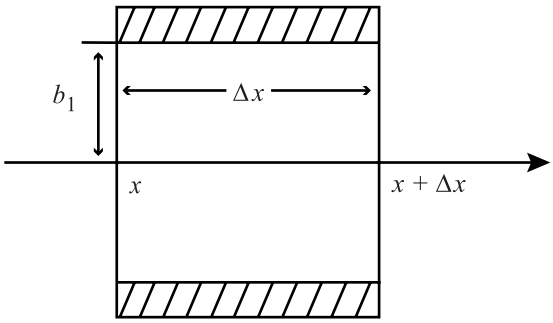

Fig. 1.16. Schematic of an incident projectile of energy E passing within a distance b_1 of an annular ring containing $N\Delta x 2\pi b_1 \,\mathrm{d}b$ atoms

Assuming $\Delta E \ll E$ and dividing by Δx and taking the limit as $x \to 0$, we obtain:

$$\left.\frac{\Delta E}{\Delta x}\right|_{\lim x\to 0} = \frac{\mathrm{d}E}{\mathrm{d}x} = N\int_0^\infty T 2\pi b\,\mathrm{d}b\,.$$

We know that $\sigma(E_\mathrm{i}, T)\,\mathrm{d}T = 2\pi b\,\mathrm{d}b$, so:

$$\frac{\mathrm{d}E}{\mathrm{d}x} = N\int_{\check{T}}^{\hat{T}} T\sigma(E_\mathrm{i}, T)\,\mathrm{d}T\,,$$

which is the same result as from Eq. (1.129). Let us first consider nuclear stopping, or energy loss from elastic collisions.

Nuclear Stopping Power

We define $\left(-\frac{\mathrm{d}E}{\mathrm{d}x}\right)_\mathrm{n}$ or $NS_\mathrm{n}(E_\mathrm{i})$ as the energy lost to target nuclei when a projectile of energy E_i traverses a differential thickness $\mathrm{d}x$ of a target of unit density. A simple formulation of $\left(-\frac{\mathrm{d}E}{\mathrm{d}x}\right)_\mathrm{n}$ can be made if we assume that each target nucleus acts independently of every other target nucleus in slowing down a projectile. In essence, we are neglecting any possible interactions between nuclei. This is a fair approximation for amorphous targets and a good first approximation for crystalline targets also.

Case 1: High-energy Elastic Collisions, $\rho \ll a$.

Rutherford scattering describes this type of interaction accurately. Recall that for simple Coulomb scattering, the energy transfer cross section (Eq. (1.102)) is:

$$\sigma_\mathrm{s}(E_\mathrm{i}, T) = \frac{\pi b_0^2}{4}\frac{\gamma E_\mathrm{i}}{T^2}\,.$$

Therefore the stopping power becomes:

$$\left.\frac{\mathrm{d}E}{\mathrm{d}x}\right|_{\mathrm{n}} = NS_{\mathrm{n}}(E_{\mathrm{i}}) = N\int_{\check{T}}^{\gamma E_{\mathrm{i}}} T\,\frac{\pi b_0^2}{4}\,\frac{\gamma E_{\mathrm{i}}}{T^2}\,\mathrm{d}T$$
$$= \frac{N\pi b_0^2}{4}\gamma E_{\mathrm{i}} \ln\left(\frac{\gamma E_{\mathrm{i}}}{\check{T}}\right), \tag{1.130}$$

where $\hat{T} = \gamma E_{\mathrm{i}}$ and $\check{T}$ is the value of T which yields $b = a$ or $\check{T}_b = \dfrac{\varepsilon^2 \gamma E_a^2}{4E_{\mathrm{i}}}$.

Substituting for b_0 from Eq. (1.93) gives:

$$\left.\frac{\mathrm{d}E}{\mathrm{d}x}\right|_{\mathrm{n}} = NS_{\mathrm{n}}(E_{\mathrm{i}}) = \frac{N\pi Z_1^2 Z_2^2 \varepsilon^4}{E_{\mathrm{i}}}\,\frac{M_1}{M_2}\ln\left(\frac{\gamma E_{\mathrm{i}}}{\check{T}_b}\right). \tag{1.131}$$

Note that for like atoms, $\gamma = 1$ and $M_1 = M_2$, so:

$$NS_{\mathrm{n}}(E_{\mathrm{i}}) = \frac{N\pi Z_1^2 Z_2^2 \varepsilon^4}{E_{\mathrm{i}}}\ln\left(\frac{E_{\mathrm{i}}}{\check{T}_b}\right). \tag{1.132}$$

Substituting for E_a from Eq. (1.107) into the expression for $\check{T}_b$ gives:

$$\check{T}_b = \frac{4E_{\mathrm{R}}^2 (Z_1 Z_2)^2 (Z_1 Z_2)^{2/6}}{E_{\mathrm{i}}}. \tag{1.133}$$

Using $a = a_0/(z_1 z_2)^{1/6}$ and substituting for $(z_1 z_2)^{1/6}$ gives:

$$\check{T}_b = \frac{4E_{\mathrm{R}}^2 a_0^2 Z^4}{a^2 E_{\mathrm{i}}},$$

for $z_1 = z_2$, and since $\varepsilon^2 = 2a_0 E_{\mathrm{R}}$, then Eq. (1.132) becomes:

$$NS_{\mathrm{n}}(E_{\mathrm{i}}) = \frac{4N\pi Z^4 a_0^2 E_{\mathrm{R}}^2}{E_{\mathrm{i}}}\ln\left(\frac{E_{\mathrm{i}}}{\check{T}_b}\right)$$
$$= \frac{4N\pi Z^4 a_0^2 E_{\mathrm{R}}^2}{E_{\mathrm{i}}}\ln\left(\frac{a^2 E_{\mathrm{i}}^2}{4a_0^2 E_{\mathrm{R}}^2 Z^4}\right) \tag{1.134}$$

Case 2: Low-energy elastic collisions, $\rho \sim a$.

At intermediate and lower energies, pure Coulomb scattering will not correctly capture the interaction. Here we must use a screened Coulomb function to account for the effects of the electrons in the internuclear space. Lindhard, Nielsen and Scharff [14] proposed a universal, one-parameter, differential scattering cross section in reduced notation:

$$\sigma = \frac{-\pi a^2}{2}\,\frac{f\left(t^{1/2}\right)}{t^{3/2}} \tag{1.135}$$

where t is a dimensionless collision parameter defined by:

$$t = \in^2 \frac{T}{\hat{T}}, \tag{1.136}$$

and $\in$ is dimensionless energy defined as:

$$\in = \frac{aM_2}{Z_1 Z_2 \varepsilon^2 (M_1 + M_2)} E_\mathrm{i}. \tag{1.137}$$

Lindhard et al. [14] treated $f\left(t^{1/2}\right)$ to be a simple scaling function where t was a measure of the depth of penetration into an atom during a collision and large t represents close approach. The function $f\left(t^{1/2}\right)$ is plotted as the thick solid line in Fig. 1.17. The analytical expression for the function developed by Winterbon et al. [15] is:

$$f\left(t^{1/2}\right) = \lambda' t^{1/6} \left[1 + (2\lambda' t^{2/3})^{2/3}\right]^{-3/2}, \tag{1.138}$$

where $\lambda' = 1.309$. A generalization of Eq. (1.138) for power law scattering is:

$$f\left(t^{1/2}\right) = \lambda_\mathrm{m} t \frac{1}{2} - \mathrm{m}, \tag{1.139}$$

where $\lambda_{1/3} = 1.309$, $\lambda_{1/2} = 0.327$, and $\lambda_1 = 0.5$. Equation (1.139) approximately describes scattering from a potential of the form $V(r)\alpha r^{-\mathrm{s}} = r^{-1/\mathrm{m}}$, where s is the

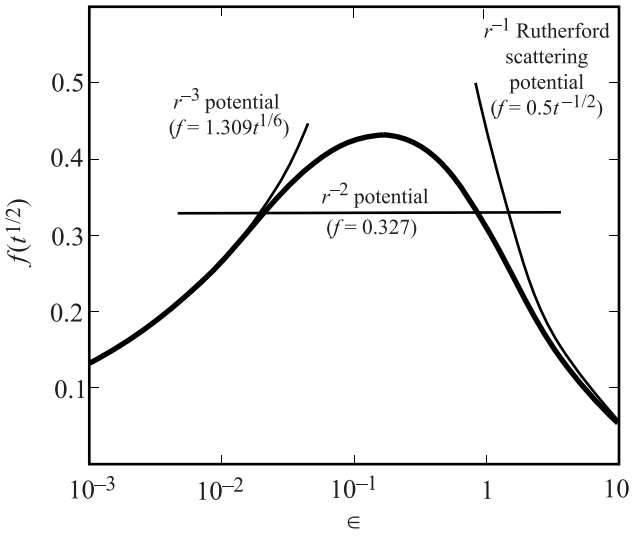

Fig. 1.17. Reduced differential cross section calculated from the Thomas–Fermi potential. The thick solid line ranging over $10^{-3} < \in < 10$ is from Eq. (1.135). The thin solid lines at left and right and the horizontal line in the middle are calculated using the power law cross section, Eq. (1.139) (from [15])

power law exponent. At low energies (low $\in$), there is little penetration during the collision (t is small) and collisions are described by a power law with $V(r)\alpha r^{-3}$, and $m = 1/3$, yielding a $t^{1/6}$ dependence. At higher energies, screening effects are minimal and are described by a $V(r)\alpha r^{-1}$ potential and $m = 1$, giving $t^{-1/2}$ behavior. At intermediate energies, the function (cross section) is slowly varying and is best described by a power law potential for the form, $V(r)\alpha r^{-2}$, with $m = 1/2$ giving no dependence on t, which means that the cross section is independent of $\in$.

For screened Coulomb potentials, the differential energy transfer cross section, defined in reduced notation in Eq. (1.135), is used to determine the nuclear stopping power as:

$$\left(\frac{\mathrm{d}E}{\mathrm{d}x}\right)_{\mathrm{n}} = \frac{-N\pi a^2 \hat{T}}{\in^2} \int_0^{\hat{T}} f(t^{1/2})\,\mathrm{d}t^{1/2}. \tag{1.140}$$

This expression can be written in a universal format by [16]:

$$\rho_{\mathrm{R}} = \frac{N4\pi a^2 M_1 M_2}{(M_1 + M_2)^2} R, \tag{1.141}$$

where R is a measure of length in the lab system. Nastasi et al. [17] provided a relationship between $S_{\mathrm{n}}(E)$ and $S_{\mathrm{n}}(\in)$:

$$S_{\mathrm{n}}(\in) = \frac{M_1 + M_2}{M_1} \frac{1}{4\pi a Z_1 Z_2 \varepsilon^2} S_{\mathrm{n}}(E) = \frac{\in}{\pi a^2 \gamma E_{\mathrm{i}}} S_{\mathrm{n}}(E), \tag{1.142}$$

which, combined with Eq. (1.140), yields an expression for:

$$\left(\frac{\mathrm{d}\in}{\mathrm{d}\rho}\right) \equiv S_{\mathrm{n}}(\in) = \frac{1}{\in} \int_0^{\in} f\left(t^{1/2}\right)\,\mathrm{d}t^{1/2}, \tag{1.143}$$

that must be solved numerically. The result is plotted in Fig. 1.18 as the reduced nuclear stopping function. Equation (1.143) can be solved exactly for the power law approximation to $f\left(t^{1/2}\right)$ (Eq. (1.139)) giving:

$$S_{\mathrm{n}}(\in) = \frac{\lambda_{\mathrm{m}}}{2(1-m)} \in^{1-2\mathrm{m}}, \tag{1.144}$$

where λ_{m} is given with Eq. (1.139). Substituting the screening length, a, for a universal screening length, a_{U}, $S_{\mathrm{n}}(\in)$ in Eq. (1.142) can be re-written as:

$$S_{\mathrm{n}}(\in) = \frac{\in}{\pi a_{\mathrm{U}}^2 \gamma E_{\mathrm{i}}} \int_0^{\hat{T}} T\sigma(E,T)\,\mathrm{d}T, \tag{1.145}$$

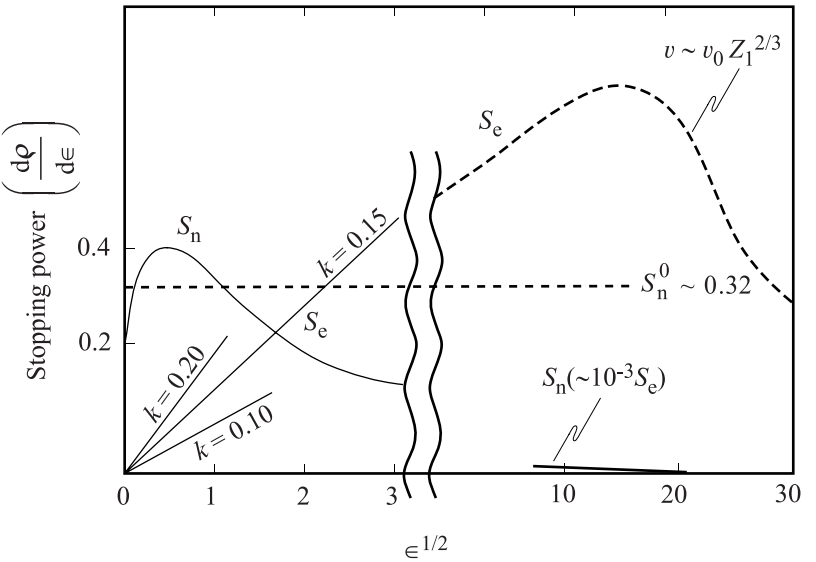

Fig. 1.18. The reduced nuclear and electronic stopping cross sections as a function of $\epsilon^{1/2}$

and using the identity:

$$\int_0^{\hat{T}} \sigma(E,T)\,\mathrm{d}T = \int_0^{b_{\max}} 2\pi b\,\mathrm{d}b, \tag{1.146}$$

we have an expression for the nuclear stopping cross section in reduced notation:

$$S_n(\epsilon) = \frac{\epsilon}{a_U^2} \int_0^{\infty} \sin^2 \frac{\phi}{2}\,\mathrm{d}b^2. \tag{1.147}$$

Ziegler et al. [18] used the universal screening function (Fig. 1.19):

$$\chi_U = 0.1818e^{-3.2x} + 0.5099e^{-0.9423x} + 0.2802e^{-0.4029x} + 0.02817e^{-0.2016x}, \tag{1.148}$$

and the numerical integration of Eq. (1.76) and Eq. (1.147) to calculate a universal, reduced nuclear stopping cross section, the ZBL cross section shown in Fig. 1.20. An expression for the fit is:

$$S_n(\epsilon) = \frac{0.5\ln(1 + 1.1383\,\epsilon)}{(\epsilon + 0.01321\,\epsilon^{0.21226} + 0.19593\,\epsilon^{0.5})}, \tag{1.149}$$

and for practical calculations, the ZBL universal nuclear stopping for an ion with energy E_i in the lab system is:

$$S_n(E_i) = \frac{8.462 \times 10^{-15} Z_1 Z_2 M_1 S_n(\epsilon)}{(M_1 + M_2)(Z_1^{0.23} + Z_2^{0.23})} \frac{\mathrm{eVcm}^2}{\mathrm{atom}}, \tag{1.150}$$

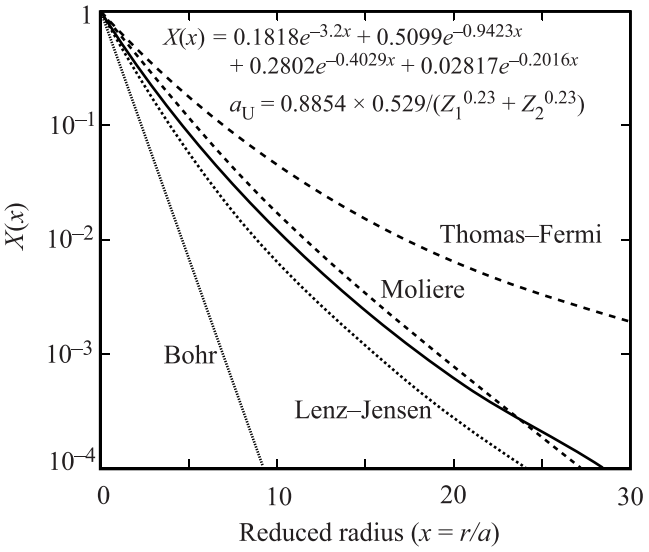

Fig. 1.19. The universal screening function χ_U (solid thick line) from Eq. (1.148) as a function of $x = r/a_U$, where a_U is the universal screening length defined by $a_U = 0.8854a_0/(Z_1^{0.23} + Z_2^{0.23})$, along with several other screening functions (from [17])

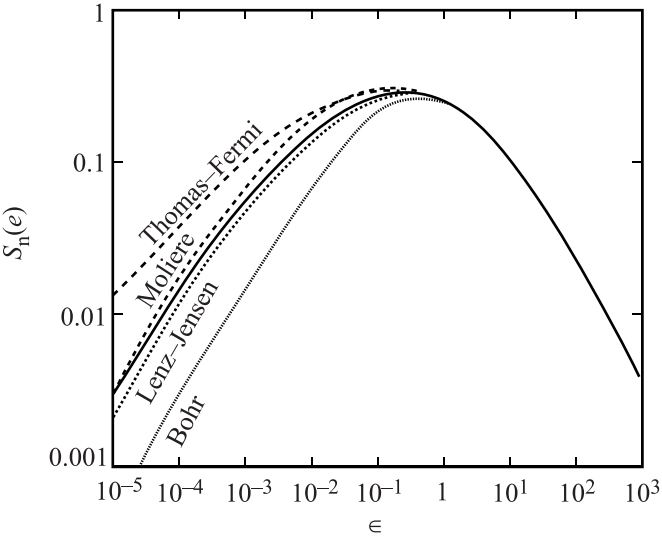

Fig. 1.20. Nuclear stopping power in reduced units from Eq. (1.149)

where the ZBL reduced energy is:

$$\in = \frac{32.53 M_2 E_\mathrm{i}}{Z_1 Z_2 (M_1 + M_2)(Z_1^{0.23} + Z_2^{0.23})} . \tag{1.151}$$

Two approximations to $S_\mathrm{n}(E_\mathrm{i})$ for collisions in the intermediate energy regime are considered. The first involves use of the inverse square potential, Eq. (1.59). Exact solutions of the orbits is possible [16], and Eq. (1.76) yields:

$$\frac{\phi}{\pi} = 1 - \frac{1}{\left(1 + \dfrac{a^2 E_a}{b^2 E_\mathrm{i}}\right)^{1/2}} . \tag{1.152}$$

Using Eq. (1.13) to determine T gives:

$$T = \gamma E_\mathrm{i} \cos^2 \left[\frac{\pi}{2} \left(1 + \frac{a^2 E_a}{b^2 E_\mathrm{i}} \right)^{1/2} \right] . \tag{1.153}$$

Expressing b^2 in terms of T and differentiating, and using the relation between $\sigma(E_\mathrm{i}, T)$ and b from Eq. (1.78) gives:

$$\sigma_\mathrm{s}(E_\mathrm{i}, T) = \frac{4 E_a a^2 \alpha}{\gamma E_\mathrm{i}^2 (1 - 4\alpha^2)^2 (x(1-x))^{1/2}} , \tag{1.154}$$

where $x = T/E_\mathrm{i}$, $\pi\alpha = \cos^{-1}\sqrt{x}$, and for small x (T/E_i), Eq. (1.154) has the form:

$$\sigma_\mathrm{s}(E_\mathrm{i}, T) = \frac{\pi^2 a^2 E_a \gamma^{1/2}}{8 E_\mathrm{i}^{1/2} T^{3/2}} . \tag{1.155}$$

The total cross section and mean recoil energy are calculated from Eq. (1.155) taking a cut-off to zero at $\bar{T} = \gamma E_\mathrm{i}$:

$$\bar{T} = \left(\gamma E_\mathrm{i} \check{T}\right)^{1/2} , \tag{1.156}$$

$$\sigma_\mathrm{s}(E_\mathrm{i}) = \frac{\pi^2 a^2 E_a \gamma^{1/2}}{4 \left(E_\mathrm{i} \check{T}\right)^{1/2}} . \tag{1.157}$$

The stopping power is then determined using:

$$S_\mathrm{n}(E_\mathrm{i}) = \int_{\check{T}}^{\hat{T}} T \sigma(E_\mathrm{i}, T)\, \mathrm{d}T ,$$

and substituting the energy transfer cross section from Eq. (1.155) yields:

$$\left(\frac{\mathrm{d}E}{\mathrm{d}x}\right)_\mathrm{n} = N S_\mathrm{n}(E_\mathrm{i}) = \frac{\pi^2}{4} a^2 N E_a \gamma . \tag{1.158}$$

This same result is obtained using the fact that:

$$\frac{\mathrm{d}E}{\mathrm{d}x} = \frac{\bar{T}}{\lambda} = N\sigma_\mathrm{s}\bar{T}\,, \tag{1.159}$$

where $\lambda = \dfrac{1}{N\sigma_\mathrm{s}}$ is the mean free path between collisions, and substituting for σ_s and $\bar{T}$ from Eqs. (1.156) and (1.157).

The second approximation of $S_\mathrm{n}(E_\mathrm{i})$, uses the Thomas–Fermi screening function. We will assume that a series of small angle scattering events are responsible for most of the energy loss of a projectile in a target. When this is true, the energy transferred, T, can be expressed as a function of E_i and b by solving Eq. (1.76) for ϕ using the Thomas–Fermi screening function, Eq. (1.49), and expanding the solution on the assumption that ϕ is small. Proceeding, we find:

$$\phi = \pi - 2\int_0^{\hat{x}} \left[\frac{1}{b^2}\left(1 - \frac{V(x)}{\eta E_\mathrm{i}} - b^2x^2\right)\right]^{-1/2} \mathrm{d}x\,, \tag{1.160}$$

for $V(r) = \dfrac{Z_1Z_2\varepsilon^2}{r} f(r/a)$, where $f(r/a) = r/a$.

The solution is:

$$\phi = \pi - b\left[b^2 + \frac{Z_1Z_2\varepsilon^2 a}{E_\mathrm{R}}\right]^{-1/2}. \tag{1.161}$$

Solving for b and substituting in the expression:

$$\sigma(E_\mathrm{i},\phi)\,\mathrm{d}\Omega = 2\pi b\,\mathrm{d}b\,,$$

and using Eq. (1.13) to obtain $\sigma_\mathrm{s}(E_\mathrm{i},T)\,\mathrm{d}T$, we then can find $S_\mathrm{n}(E_\mathrm{i})$ from Eq. (1.129). The result is:

$$S_\mathrm{n}^0 = K\frac{Z_1Z_2}{Z^{1/3}}\frac{M_1}{M_1+M_2}\mathrm{eV\,cm^2} \tag{1.162}$$

(where $Z^{1/3} = \left(Z_1^{2/3} + Z_2^{2/3}\right)^{1/2}$ and $K = 1.158\pi\varepsilon^2 a_0 = 2.8\times10^{-15}\mathrm{eV\,cm^2}$), which is referred to as the standard stopping power and is shown in Fig. 1.18. Note that S_n^0 is independent of the projectile energy to a first approximation. Ranges estimated from S_n^0 will be reasonably close when small-angle scattering predominates.

Recall that the key assumption in deriving Eq. (1.162) was that energy loss of a projectile can be represented as a series of small angle scattering events, allowing us to then assume that ϕ remains small. Table 1.6 gives the scattering angles and energy loss for a 50 keV silicon projectile incident on a silicon target atom. Note that for $\rho/a \geq 1$, this assumption is clearly valid. Let us now look at electronic energy loss.

Table 1.6. Scattering angles and energy loss for a 50 keV silicon projectile and a silicon target atom

$\rho/a =$	10	1	0.1
ϕ (Radians)	0.004π	0.26π	0.89π
θ (Degrees)	0.36	23.4	80.5
T/E	4×10^{-5}	0.16	0.973
T (keV)	0.002	8	49

Electronic Stopping Power

The theoretical computation of electronic stopping power is a much more complicated problem than the calculation of S_n. For the description of collisions between ions and electrons, we may use the classical equation (Eq. (1.106)). But here we must consider that the binary collision is between a heavy moving ion and an electron in a solid. This approach is valid as long as all electrons participate and the ion velocity exceeds the velocity of the tightest bound electron. We may define T by:

$$\hat{T} \cong \gamma_e E_i \,, \tag{1.163}$$

where $\gamma_e = \dfrac{4m_e M}{(m_e + M)^2}$ and hence $\hat{T}$ is very small. We will also define a lower limit for ion-electron interactions as the effective mean excitation-ionization level $\bar{I}$.[1] We also note that we must use the electron density, which is just Z_2 times the atom density,

$$n = NZ_2 \,. \tag{1.164}$$

Writing an expression for stopping power due to excitation-ionization interactions that is equivalent to Eq. (1.130) yields:

$$\begin{aligned}\left(\frac{\mathrm{d}E}{\mathrm{d}x}\right)_e &= \frac{n}{Z_2}\int_{\bar{I}}^{\gamma_e E_i} T\,\sigma_s\left(E_i, T\right)\mathrm{d}T \\ &= \frac{n}{Z_2}\frac{\pi b_0^2}{4}\gamma_e E_i \ln\left(\frac{\gamma_e E_i}{\bar{I}}\right) \\ &= N\pi\frac{Z_1^2 Z_2 \varepsilon^4}{E_i}\frac{M}{m_e}\ln\left(\frac{\gamma_e E_i}{\bar{I}}\right) .\end{aligned} \tag{1.165}$$

This formula is however only approximate. A more exact expression is obtained from a quantum mechanical treatment based on the Born approximation, which is interpreted physically to mean that the perturbation due to the incident particle does not seriously disturb the electronic motion for large impact parameters. The result

[1] To a first approximation, $\bar{I} = kZ_2$ where $k = 11.5\,\mathrm{eV}$.

of this analysis is the addition of a factor of 2, which comes from the small-energy transfer processes where free Coulomb scattering is invalid. The Bethe–Bloch formula is a good approximation:

$$\left(-\frac{\mathrm{d}E}{\mathrm{d}x}\right)_{\mathrm{e}} = \frac{N2\pi Z_1^2 Z_2 \varepsilon^4}{E_{\mathrm{i}}} \frac{M}{m_{\mathrm{e}}} \ln\left(\frac{\gamma_{\mathrm{e}} E_{\mathrm{i}}}{\bar{I}}\right) = \frac{2\pi N Z_1^2 M \varepsilon^4}{m_{\mathrm{e}} E_{\mathrm{i}}} B, \tag{1.166}$$

where $B = Z_2 \ln\left(\frac{\gamma_{\mathrm{e}} E_{\mathrm{i}}}{\bar{I}}\right)$ is the stopping number. For relativistic velocities:

$$B = Z_2 \left\{ \ln\left(\frac{\gamma_{\mathrm{e}} E_{\mathrm{i}}}{\bar{I}}\right) - \ln\left(1-\beta^2\right) - \beta^2 \right\}, \tag{1.167}$$

where $\beta = v/c$ and c is the speed of light. Note that at high energies, S_{n} and S_{e} vary as $1/E_{\mathrm{i}}$ very nearly.

$$\frac{S_{\mathrm{e}}}{S_{\mathrm{n}}} = \frac{2M_2}{m_{\mathrm{e}} Z_2} \frac{\ln\left(\frac{\gamma_{\mathrm{e}} E_{\mathrm{i}}}{\bar{I}}\right)}{\ln\left(\frac{\gamma E_{\mathrm{i}}}{E_{\mathrm{d}}}\right)}. \tag{1.168}$$

Applying Eq. (1.168) to the case of MeV protons, the value is ~2000 for $\bar{I} \sim 11.5 Z_2$ eV, or the electronic stopping power is 2000 times that of the nuclear stopping power.

At low velocities, electrons in the inner shells contribute less to the stopping power. Also, the neutralization probability becomes so large that the collision between the projectiles and the surrounding electrons is almost elastic. The energy loss becomes proportional to the projectile velocity. Lindhard, Scharff, Schiott (LSS), and Firsov gave theoretical descriptions for this energy region. The LSS expression is based on elastic scattering of free target electrons in the static field of a screened point charge. Firsov's is based on a simple geometric model of momentum exchange between the projectile and target atom during interpenetration of electron clouds. Lindhard and Winther [19] have shown that as long as the ion velocity is less than the velocity of an electron having an energy equal to the Fermi energy, E_{f} of the free electron gas, S_{e} will be proportional to the velocity of the ion or the one-half power of its energy. Using a potential of the form:

$$V(r) = \frac{2(Z_1 Z_2)^{1/2} \varepsilon^2}{r} \chi_{\mathrm{TF}} \left[1.13 \left(Z_1^{2/3} + Z_2^{2/3} \right)^{1/2} \frac{r}{a_0} \right], \tag{1.169}$$

the Lindhard–Scharff stopping cross section becomes:

$$S_{\mathrm{e}}(E) = k' E^{1/2}, \tag{1.170}$$

$$k' = 3.83 \frac{Z_1^{7/6} Z_2}{M_1^{1/2} \left(Z_1^{2/3} + Z_2^{2/3} \right)^{3/2}}, \tag{1.171}$$

where $S_e(E)$ is given in units of $10^{-15}\,\mathrm{eV\,cm^2/atom}$ and E is in keV. Expressing the stopping cross section in reduced notation gives:

$$S_e(\in) = \left(\frac{d\in}{d\rho}\right)_e = k\in^{1/2}, \quad \text{where}$$

$$k = \frac{0.07937 Z_1^{2/3} Z_2^{1/2} \left(1+\frac{M_2}{M_1}\right)^{3/2}}{\left(Z_1^{2/3}+Z_2^{2/3}\right)^{3/4} M_2^{1/2}}. \tag{1.172}$$

The universal nuclear stopping cross section is shown in Fig. 1.18 where a single curve represents all possible projectile–atom collisions, and the electronic stopping cross section of Eq. (1.172) results in a family of lines or one for each combination of projectile and target atom.

An approximate treatment that results in an analytical expression is obtained in the following analysis. Consider an atom of mass M_1, moving with velocity v_1, which makes a head-on collision with an electron moving in the opposite direction with velocity v_e. The relative initial speed of the two particles is:

$$v_{r0} = v_1 + v_e\,. \tag{1.173}$$

After collision, the velocity vector changes but not the magnitude:

$$v_{rf} = -\left(v_1 + v_e\right). \tag{1.174}$$

The speed of the atom following the collision with the electron is given by:

$$\begin{aligned} v_{1f} &= V_{CM} + \left(\frac{m_e}{m_e+M_1}\right) v_{rf} \\ &= \frac{M_1 v_1 - m_e v_e}{M_1+m_e} - \left(\frac{m_e}{M_1+m_e}\right)(v_1+v_e) \\ &\cong v_1 - \frac{2m_e v_e}{M_1} \end{aligned} \tag{1.175}$$

where m_e is neglected compared to M_1. The change in the energy of the atom due to the collision is:

$$\Delta E = \Delta\left(\frac{1}{2}M_1 v_1^2\right) \cong M_1 v_1\left(v_1 - v_{1f}\right) = 2m_e v_e v_1\,. \tag{1.176}$$

The electron velocity after the collision is given as:

$$\begin{aligned} v_{ef} &= V_{CM} - \left(\frac{M_1}{M_1+m_e}\right) v_{rf} \\ &= \frac{M_1 v_1 - m_e v_e}{M_1+m_e} + \left(\frac{M_1}{M_1+m_e}\right)(v_1+v_e) = 2v_1 + v_e \end{aligned} \tag{1.177}$$

or the increase in the electron velocity is:

$$\Delta v_e = v_{ef} - v_e = 2v_1 \,. \tag{1.178}$$

The number of conduction electrons in a metal is approximately equal to the atom number density N. But only those electrons with velocities lying in the range Δv_e of the Fermi velocity v_f are able to participate in the slowing down process. Therefore, the effective density of electrons in the metal is:

$$n_e \cong N\left(\frac{\Delta v_e/2}{v_f}\right) = \left(\frac{v_1}{v_f}\right)N \,. \tag{1.179}$$

The current of effective electrons impinging on the atom is:

$$I_e = n_e v_{ro} = n_e\left(v_1 + v_e\right) \cong n_e v_e \,, \tag{1.180}$$

and the collision rate of effective electrons with a single atom is $\sigma_e I_e$, where σ_e is the cross section for interaction of the moving atom with conduction electrons. The stopping power is then the energy loss rate of a moving atom to effective electrons divided by the velocity of the atom:

$$\left(-\frac{dE}{dx}\right)_e = \frac{-\sigma_e I_e \Delta E}{v_1} \,. \tag{1.181}$$

Substituting Eqs. (1.176), (1.179) and (1.180) into the above expression and writing v_e and v_1 as $(2E_f/m_e)^{1/2}$ and $(2E/M_1)^{1/2}$, respectively, yields:

$$\left(-\frac{dE}{dx}\right)_e = -8\sigma_e N\left(\frac{m_e}{M_1}\right)^{1/2} E^{1/2} = kE^{1/2} \,, \tag{1.182}$$

where

$$k = 8\sigma_e N\left(\frac{m_e}{M_1}\right)^{1/2} \,, \tag{1.183}$$

where $k = 0.03NZ^{2/3}\,\mathrm{eV}^{1/2}/\mathrm{nm}$ for like atoms, or $S_e = k'E^{1/2}$ where $k' = 3 \times 10^{-15}Z^{2/3}\,\mathrm{eV}^{1/2}\mathrm{cm}^2$ for like atoms. Both equations are valid for $0 < E\,(\mathrm{keV}) < 37Z^{7/3}$. For example, for $M_2 = \mathrm{Si}, k'_{\mathrm{Si}} \sim 0.2 \times 10^{-15}\,\mathrm{eV}^{1/2}\mathrm{cm}$. Table 1.7 summarizes the nuclear and electronic stopping powers for the various types of interactions used in Sect. 1.3.1.

1.3.2 Range Calculations

We have developed expressions for the two major forms of energy loss: (1) collisions of the ion with the target nuclei, and (2) interactions of the ion with the electrons in the solid. We will now assume that these two forms of energy loss are independent

Table 1.7. Summary of stopping powers for various types of interactions

Type of interaction	Nuclear stopping power NS_n		Electronic stopping power NS_e	
High E Coulomb	$\frac{4N\pi Z^4 a_0^2 E_R^2}{E_i} \ln\left(\frac{a^2 E_i^2}{4a_0^2 E_R^2 Z^4}\right)$	(1.134)	$N\pi \frac{Z_1^2 Z_2 \varepsilon^4}{E_i} \frac{M}{m_e} \ln\left(\frac{\gamma_e E_i}{\bar{I}}\right)$	(1.165)
Low E	General expression:		$\left(\frac{dE}{dx}\right)_e = k' E_i^{1/2}$	(1.170)
	$\frac{8.462\times 10^{-15} Z_1 Z_2 M_1 S_n(\in)}{(M_1+M_2)(Z_1^{0.23}+Z_2^{0.23})}$	(1.150)	$k' = 3.83 \frac{Z_1^{7/6} Z_2}{M_1^{1/2}\left(Z_1^{2/3}+Z_2^{2/3}\right)^{3/2}}.$	
	Inverse square:			
	$\frac{\pi^2}{4} a^2 N E_a \gamma$	(1.158)	$\left(\frac{dE}{dx}\right)_e = kE^{1/2}$	(1.182)
	Thomas–Fermi screening:			
	$K \frac{Z_1 Z_2}{Z^{1/3}} \frac{M_1}{M_1+M_2}$	(1.162)	$k = 8\sigma_e N \left(\frac{m_e}{M_1}\right)^{1/2}$	
	$Z^{1/3} = \left(Z_1^{2/3}+Z_2^{2/3}\right)^{1/2}$		valid for $0 < E\ (\text{keV}) < 37Z^{7/3}$	
	$K = 1.158\pi\varepsilon^2 a_0 = 2.8\times 10^{-15}$ eV cm			

of each other. Because of this approximation, we may write the total energy loss of a single projectile as the sum of the individual contributions:

$$S_T = N\left[S_n(E) + S_e(E)\right], \tag{1.184}$$

This expression can be integrated to give the total distance R that a projectile of initial energy E_i will travel before coming to rest:

$$R = \int_0^R dx = \frac{1}{N}\int_0^{E_i} \frac{dE}{\left[S_n(E) + S_e(E)\right]}. \tag{1.185}$$

This distance is called the average total range and is a useful quantity for making estimates of the average penetration depths of ions in amorphous targets. An example of an estimate of the total path length using the inverse square potential (see Eq. (1.155)) is:

$$\begin{aligned}\frac{dE}{dx} &= N\int_{\check{T}}^{\gamma E_i} T\sigma(E_i,T)\,dT \quad \text{where} \quad \sigma(E_i,T) = \frac{\pi^2 a^2 E_a \gamma^{1/2}}{8E_i^{1/2}T^{3/2}} \\ &= \frac{\pi^2}{4} a^2 N E_a \gamma,\end{aligned} \tag{1.186}$$

so,

$$\bar{x} = \bar{R}_{\text{total}} = \int_0^{E_\text{i}} \frac{\mathrm{d}E'}{(\mathrm{d}E/\mathrm{d}x)_n} = \int_0^{E_\text{i}} \frac{\mathrm{d}E'}{\frac{\pi^2}{4} a^2 N E_a \gamma}$$

$$= \frac{4E_\text{i}}{\pi^2 a^2 N E_a \gamma} \quad \text{where} \quad E_\text{i} \leq E_a \,. \tag{1.187}$$

The quantity of interest is, however, the projection of the total range on the initial direction of the particle path (Fig. 1.21). In addition, we want to know the deviation in the projected range, which arises from the fact that all particles do not suffer the same sequence of collisions. We then define:

$\overline{R_\text{p}} =$ mean projected range
$\overline{\Delta R_\text{p}} =$ standard deviation of the projected range.

Methods for computing $\overline{R_\text{p}}$ have been developed by Lindhard et al. [16]. In cases where the energy transfer T is small compared to the total energy of the particle, the differential equation for $\overline{R_\text{p}}$ has the solution:

$$\overline{R_\text{p}} = \int_0^{E_\text{i}} \frac{\mathrm{d}E'}{\beta_1 (E')} \exp\left[\int_{E_\text{i}}^{E'} \frac{\alpha_1 (x)\, \mathrm{d}x}{\beta_1 (x)}\right], \tag{1.188}$$

where $\alpha_1 (E) = \dfrac{\mu}{2} N \dfrac{S_\text{n} (E)}{E}$, and

$$\beta_1 (E) = N\left[S_\text{n} (E) + S_\text{e} (E) - \frac{\mu}{2} \frac{\Omega_\text{n}^2 (E)}{E}\right], \tag{1.189}$$

and $\Omega_\text{n}^2 (E) = \int_0^\infty T_\text{n}^2 2\pi b\, \mathrm{d}b$.

The standard deviation is computed by defining the quantities R_c (chord range) and $R_\perp$ (range perpendicular to the initial direction) so that, from Fig. 1.22, we have

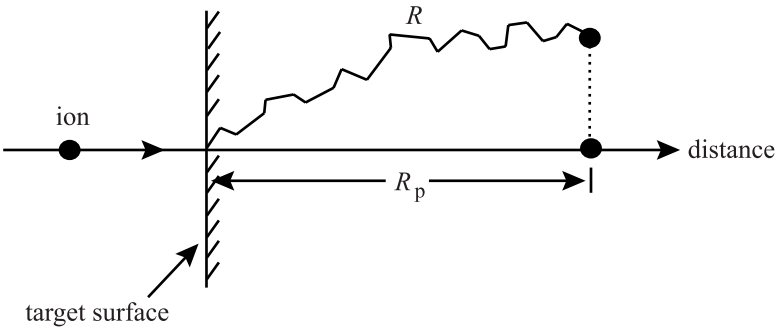

Fig. 1.21. Total path length R and projected range R_p for an ion incident on a target

the following relation:

$$\overline{R_{\mathrm{c}}^2} = \overline{R_{\mathrm{p}}^2} + \overline{R_{\perp}^2}\,, \tag{1.190}$$

and a related quantity:

$$\overline{R_{\mathrm{r}}^2} = \overline{R_{\mathrm{p}}^2} - \frac{1}{2}\overline{R_{\perp}^2}\,, \tag{1.191}$$

and, for cases where $T \ll E$,

$$\overline{R_{\mathrm{r}}^2(E)} = \int_0^E \frac{2\overline{R_{\mathrm{p}}(E')}\,\mathrm{d}E'}{\beta_2(E')} \exp\left[\int_E^{E'} \frac{3\alpha_2(x)}{\beta_2(x)}\,\mathrm{d}x\right], \tag{1.192}$$

and

$$\overline{R_{\mathrm{c}}^2(E)} = \int_0^E \frac{2\overline{R_{\mathrm{p}}(E')}\,\mathrm{d}E'}{N\left[S_{\mathrm{n}}(E') + S_{\mathrm{e}}(E')\right]}\,, \tag{1.193}$$

and then $\overline{\Delta R_{\mathrm{p}}}$ is found from

$$\left(\overline{\Delta R_{\mathrm{p}}}\right)^2 = \frac{2\overline{R_{\mathrm{r}}^2}(E) + \overline{R_{\mathrm{c}}^2}(E)}{3} - \left(\overline{R_{\mathrm{p}}}\right)^2\,, \tag{1.194}$$

where $\alpha_2(E) = \alpha_1(E)/2$, $\beta_2(E) = \beta_1(E) - \dfrac{N\mu\Omega_{\mathrm{n}}^2(E)}{E}$.

The integrals can be evaluated numerically for the Thomas–Fermi potential or analytically if the approximate values of S_{n} and S_{e} are used together with the value:

$$\Omega_{\mathrm{n}}^2(E) = \frac{4M_1M_2}{3(M_1+M_2)} S_{\mathrm{n}}^0 E\,. \tag{1.195}$$

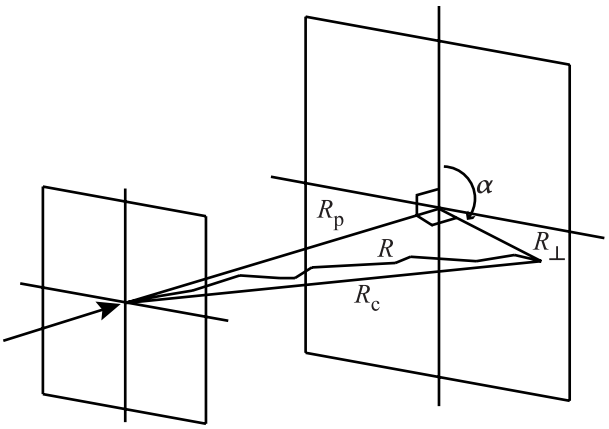

Fig. 1.22. Schematic of the definition of range parameters R, R_{p}, R_{c}, $R_{\perp}$

In LSS formalism, the average total path length can be calculated from:

$$\rho_{\mathrm{R}} = \int_0^{\in} \frac{\mathrm{d}\in}{[S_{\mathrm{n}}(\in) + S_{\mathrm{e}}(\in)]} = \int_0^{\in} \frac{\mathrm{d}\in}{\left[S_{\mathrm{n}}(\in) + k\in^{1/2}\right]}. \tag{1.196}$$

This expression must be integrated numerically using different values of k. For a particular Z_1, Z_2 and E_{i}, we calculate $\in$ and k and then read off the value of ρ_{R} from Fig. 1.23 and convert to R using Eqs. (1.141), (1.137) and $\rho_{\mathrm{R}} = 3.06\varepsilon$:

$$R(nm) = \frac{6EM_2(M_1+M_2)\left(Z_1^{2/3}+Z_2^{2/3}\right)^{1/2}}{\rho Z_1 Z_2 M_1}, \tag{1.197}$$

where E is in keV and ρ is in g/cm^3. The most interesting range quantity of interest is the average projected range, R_{p}, and this is what is usually measured. At high energies, $S_{\mathrm{e}} \gg S_{\mathrm{n}}$ and $R \sim R_{\mathrm{p}}$. At low energies where $S_{\mathrm{n}} \sim S_{\mathrm{e}}$, then $R_{\mathrm{p}} < R$. This difference gets larger with M_2/M_1. LSS theory also analyzed this problem.

At low $\in$ or ρ_{R} (and small values of k):

For $M_2/M_1 = \frac{1}{2}$; $R/R_{\mathrm{p}} \sim 1.2$ (at low $\in$, k)

$M_2/M_1 = 1$; $R/R_{\mathrm{p}} \sim 1.6$

and $M_2/M_1 = 2$; $R/R_{\mathrm{p}} \sim 2.2$.

At high energies ($\in$ large), $R/R_{\mathrm{p}} \to 1$ for all k. Finally as a general approximation [16]:

$$\frac{R}{R_{\mathrm{p}}} \cong 1 + B\frac{M_2}{M_1}, \tag{1.198}$$

where B is a slowly varying function of E and R. In the energy region where nuclear stopping dominates and $M_1 > M_2$, $B = 1/3$. Increased electronic stopping at higher energies leads to smaller values of B. When $M_1 < M_2$, large angle scattering

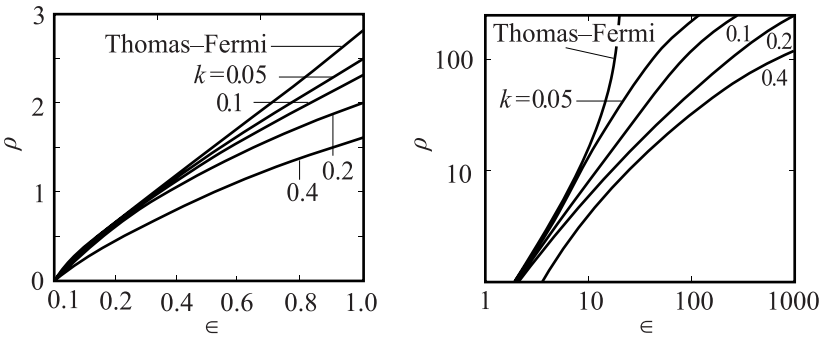

Fig. 1.23. Reduced range-energy plots for various values of the electronic stopping parameter, k

increases the difference between R and R_p. However, for these collisions, electronic stopping is appreciable and partially offsets the increase in the difference. Therefore, $B = 1/3$ is a reasonable approximation for a wide range of conditions, giving:

$$R_p \cong \frac{R}{1 + (M_2/3M_1)} . \tag{1.199}$$

Range straggling can be calculated using the theory of Lindhard et al. [16]. For the case where nuclear stopping dominates and $M_1 > M_2$, i.e., small angle scattering:

$$2.5\Delta R_p \cong 1.1 R_p \left[\frac{2(M_1 M_2)^{1/2}}{M_1 + M_2} \right] , \tag{1.200}$$

or

$$\Delta R_p \cong R_p / 2.5 . \tag{1.201}$$

For a high-energy ion, the slowing down path is essentially a straight line in the original direction of motion, since the stopping is electronic with a small amount of straggle at the end due to nuclear collisions (Fig. 1.24a). At lower energies where S_n

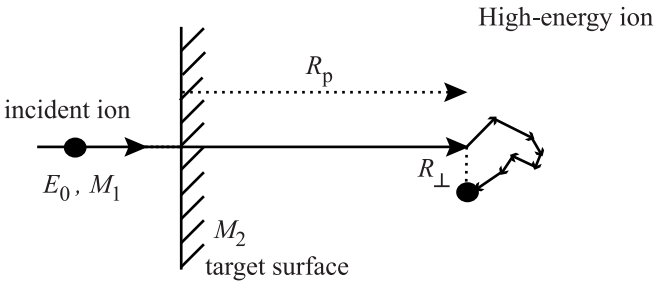

(a)

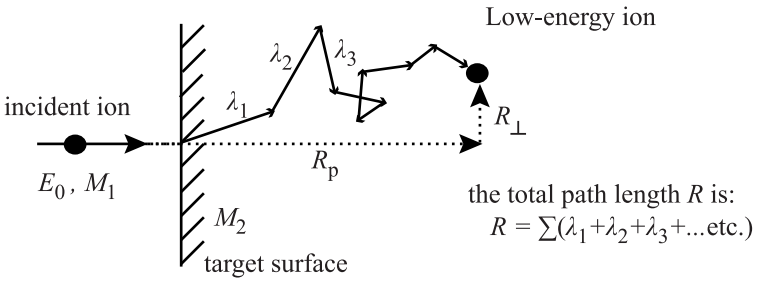

(b)

Fig. 1.24. Total path length, projected range and perpendicular range for (a) high-energy ions and (b) low-energy ions incident on a target

and S_e are more comparable, the ion path follows a zigzag course with many large deflections with the distance between collisions decreasing as the energy decreases and the cross section increases (Fig 1.24b). The stopping positions are distributed according to a Gaussian as

$$N(x) = N_p e^{-1/2X^2}, \tag{1.202}$$

where $X = \dfrac{x - R_p}{\Delta R_p}$ and ΔR_p is the standard deviation (Fig. 1.25). If the peak concentration is N_p at R_p, then this will fall to $\dfrac{1}{e^{1/2}} N_p$ at distances $x = R_p \pm \Delta R_p$. If we view the target perpendicularly through its surface, then the number of implanted ions per unit area will be N_s, given by:

$$N_s = \int_{-\infty}^{+\infty} N(x)\,\mathrm{d}x, \tag{1.203}$$

or since $\mathrm{d}x = \Delta R_p\,\mathrm{d}X$ and the Gaussian curve is symmetrical, then:

$$N_s = 2\Delta R_p N_p \int_0^{\infty} e^{-1/2X^2}\,\mathrm{d}X, \tag{1.204}$$

which can be written:

$$N_s = \Delta R_p N_p \sqrt{2\pi} \left\{ \sqrt{\frac{2}{\pi}} \int_0^{\infty} e^{-1/2X^2}\,\mathrm{d}X \right\}. \tag{1.205}$$

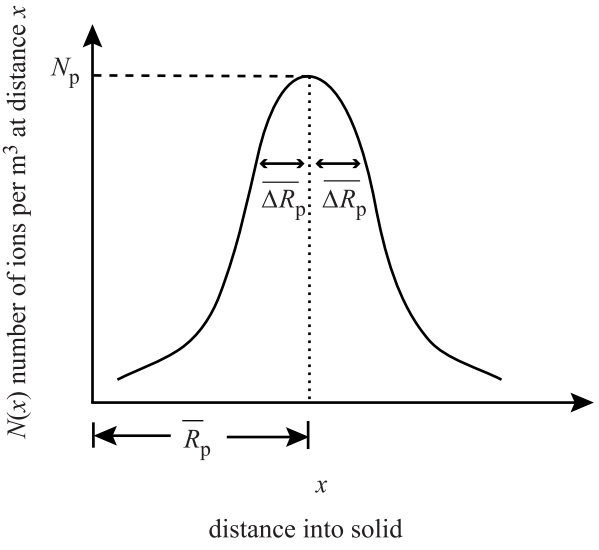

Fig. 1.25. Parameters of the Gaussian distribution applied to an ion implantation profile showing the projected range, $\bar{R}_p$, the straggling or standard deviation, $\overline{\Delta R}_p$, and the maximum concentration, N_p of the implanted ion

The integral inside the bracket is the error function and tends to unity as $X \rightarrow \infty$, so that if N_s is the number of ions/cm^2 implanted into the target, we have:

$$N_p = \frac{N_s}{\sqrt{2\pi}\Delta R_p} \cong \frac{0.4 N_s}{\Delta R_p}, \tag{1.206}$$

so the density of implanted ions is:

$$N(x) = \frac{0.4 N_s}{\Delta R_p} \exp\left(-1/2\left\{\frac{x - R_p}{\Delta R_p}\right\}^2\right). \tag{1.207}$$

As an example, if we implant 5×10^{15} ions/cm^2 of 40 keV B into Si, then $R_p \sim 160$ nm, $\Delta R_p \sim 54$ nm and $N_p \sim 4 \times 10^{20}$ atoms/cm^2. Note that from the properties of the Gaussian, the concentration will fall by one decade at $x \simeq R_p \pm 2\Delta R_p$ and by 2 decades at $x \simeq R_p \pm 3\Delta R_p$, etc.

Using the LSS treatment to describe electronic and nuclear stopping, Littmark and Ziegler have solved for the ranges of atoms with atomic number between 1 and 92 in all elements. Their work is published in Volume 6 of *The Stopping and Ranges of Ions in Matter* [20]. For each atom serving as the target, the mean ion depth, longitudinal straggling and transverse straggling is compiled in graphs for projectiles with $1 \leq Z \leq 92$ and over a wide energy range. The following example is taken from this handbook.

Example 1.3. MeV He implantation into Si
Zeigler [18] plots and tabulates the range parameters for a wide range of ions and target atoms. For 2 MeV He incident on a Si target, the range and straggling are 7.32 μm and 0.215 μm, respectively. If we assume a dose of 10^{15} He ions/cm^2, then applying Eq. (1.204) gives a peak concentration of $\sim 1.86 \times 10^{19}$ He atoms/cm^3 at a depth of 7.32 μm, which is approximately 620 appm. Equation (1.205) gives the distribution of deposited He atoms as:

$$N(x) = 1.86 \times 10^{19} \exp\left(-1/2\left\{\frac{x - 7.32}{0.215}\right\}^2\right) \text{He/cm}^3,$$

where x is in units of μm.

In addition to a tabulation of range data, Ziegler has developed a Monte Carlo based computer program for calculating the transport of ions in matter [18]. The program is available on the web at http://www.srim.org and the reader is encouraged to try some examples using the SRIM simulation software. This program is downloadable at no cost to the user (subject to the terms of use posted on the site) and may be executed on your personal computer. The following example uses data taken from the SRIM program.

Example 1.4. Implantation of Al into Ni
A similar example can be worked for lower energy implantation of a heavier element such as Al, into a nickel target. In this case, we use the output of the TRIM program. Selecting 200 keV Al in Ni results in a projected range of ~135 nm with a longitudinal straggling of 44 nm. Substitution into Eq. (1.204) yields a peak concentration 9.1×10^{19} Al/cm^3 for a dose of 10^{15} Al$^+$/cm^2. The TRIM software also yields a quantity that allows the user to determine concentration. The unit of concentration in the ion range plot is [atoms/cm^3/atoms cm^2] and the range of the implanted ion distribution on this plot has a maximum of $\sim 8 \times 10^4$ atoms/cm^3/atoms cm^2. Multiplying this value by the dose of 10^{15} Al$^+$/cm^2 gives $\sim 8 \times 10^{19}$ Al/cm^3 which is close to the analytical solution.

Chapter Review

The chapter began with a description of neutron–nuclear collisions, utilizing the absence of charge on the neutron to describe the interaction using a hard-sphere approximation. Expressions for the energy transfer in elastic and inelastic scattering collisions were developed and (n, 2n) and (n, γ) reactions were analyzed as well to determine the energy transferred. Table 1.2 summarizes the energy transfer and energy transfer cross sections for these types of reactions. The description of projectile-target interaction was broadened to include ion–atom and atom–atom collisions which are relevant for two important cases: ion irradiation or implantation and the interaction between atoms in a lattice after the initial collision with a neutron in reactor materials. Interatomic potentials form the basis for describing the interaction between atoms and also for determining the energy transfer cross section. Table 1.3 summarizes the important potentials used to describe these interactions.

Collision kinematics was then used to develop a description of the orbit of colliding atoms and hence, the transferred energy and the energy transfer cross section. Because there is not one single interatomic potential that describes the interaction over the entire distance (energy) range, the energy transfer and energy transfer cross sections are analyzed in various energy ranges and for various classes of interactions. Rutherford scattering is used to describe light energetic ions and slow heavy ions, energetic heavy ions, and relativistic electrons are all treated separately. Table 1.5 summarizes the energy transfer and energy transfer cross section for various atom–atom collisions.

Energy loss theory is developed in order to determine the energy loss of energetic atoms/ions to the solid by elastic/nuclear collisions and by collisions with the electrons of the target. Collisions are analyzed in terms of their energy range for both nuclear stopping and electronic stopping. Table 1.7 summarizes the stopping

powers for various types of interactions. Finally, the stopping powers are used to develop expressions for the range and projected range of ions in solids so that their penetration depth and concentration distribution can be determined.

Nomenclature

a	Screening radius
a_0	Bohr radius of the hydrogen atom
a_{U}	Universal screening length
A	Atomic mass
A	Pre-exponential constant in Born–Mayer relation, Eq. (1.47)
b	Impact parameter
B	Constant in exponent in Born–Mayer relation, Eq. (1.47)
C	Constant in screened Coulomb potential, Eq. (1.49) = 0.8853
c	Speed of light
D	Nearest neighbor spacing between atoms
E_{a}	Value of E_i that yields $\rho_0 = a$
E_{b}	Value of E_i that gives $T \geq E_{\mathrm{d}}$ at $b = a$
E_{d}	Displacement energy
E_{D}	Maxwellian nuclear temperature = kT
E_{f}	Final energy
E_γ	Gamma ray energy
E_{i}	Incoming particle energy
$E_{\mathrm{v,i}}^{f}$	Vacancy and interstitial formation energy
$E_{\mathrm{v,i}}^{m}$	Vacancy and interstitial migration energy
E'_{m}	Kinetic energy of incoming particle in CM system
E''_{m}	Energy of neutron after (n, 2n) reaction
E'_{M}	Kinetic energy of target particle in CM system
E''_{M}	Energy of CM after (n, 2n) reaction
E_{R}	Rydberg energy
E_{T}	Total energy
$\bar{I}$	Excitation-ionization level
m	Mass of incoming particle
M	Mass of target
N	Atom number density
N_{p}	Peak implanted ion concentration
N_{s}	Implanted ion density in ions/unit area
p_{e}	Momentum of electron
Q	Excitation energy of nucleus
r_{e}	Nearest neighbor spacing between atoms
$\dot{r}$	Radial velocity in polar coordinates
R	Range of ion
R_{eff}	Recombination radius

R_p	Projected range
ΔR_p	Standard deviation of projected range
s	Power law exponent
S_e	Electronic stopping power
S_n	Nuclear stopping power
t	Time
t	Dimensionless collision parameter, Eq. (1.136)
T	Energy transferred in collision
$\check{T}$	Minimum energy transferred
$\hat{T}$	Maximum energy transferred
$\bar{T}$	Average energy transferred
T_ℓ	Energy transferred to target atom after (n, 2n) reaction
$V(r)$	Potential energy
v_c	Velocity of incoming particle in CM system
V_c	Velocity of target particle in CM system
v'_c	Velocity of incoming particle in CM system after collision
V'_c	Velocity of target atom in CM system after collision
v''_c	Velocity of neutron in CM system after (n, 2n) reaction
V''_c	Velocity of target atom in CM system after (n, 2n) reaction
V_CM	Velocity of CM in lab system
v_ℓ	Velocity of incoming particle in lab system
v'_ℓ	Velocity of incoming particle in lab system after collision
V'_ℓ	Velocity of target atom in lab system after collision
V''_ℓ	Velocity of target atom in lab system after (n, 2n) reaction
Z	Atomic number
β	v/c
$\chi(r)$	Screening function
χ_U	Universal screening function
ε	Unit charge
$\in$	Dimensionless, reduced energy parameter, Eq. (1.137)
ϕ	Asymptotic scattering angle at infinity separation
ϕ	Scattering angle in CM system
$\dot{\psi}$	Angular velocity in polar coordinates
ψ	Scattering angle of struck atom in lab system
λ	Mean free path between collisions
λ_m	See Eq. (1.139)
λ'	1.309, Eq. (1.138)
μ	Reduced mass, Eq. (1.63)
$\nu(T)$	Displacement function
θ	Scattering angle in lab system
ρ	Distance between atom centers in a collision
ρ_e	Electron cloud density
ρ_0	Distance of closest approach; value of r when $\psi = \pi/2$
ρ_r	Dimensionless, reduced distance parameter, Eq. (1.141)

$\sigma(E_i)$	Total atomic collision cross section
$\sigma(E_i, T)$	Differential energy transfer cross section
$\sigma(E_i, \phi)$	Differential angular collision cross section
$\sigma(E_i, E_\phi, \Omega)$	Double differential collision cross section
$\sigma(E_i, Q_j, \phi)$	Differential angular cross section for inelastic collisions
$\sigma(E_i, Q_j, T)$	Differential energy transfer cross section for inelastic collisions
Ω	Solid angle into which incoming particle is scattered
$d\Omega$	Differential solid angular element
ξ_e	$Z_1^{1/6}$

Problems

1.1 A 0.5 MeV neutron strikes a target atom with mass A, which is initially at rest. Calculate the velocity and energy of both particles in the laboratory reference frame after a head-on collision for $A = 27$ (Al) and $A = 207.2$ (Pb).

1.2 A detector of 100% efficiency (i.e., every particle entering the detector is registered) and area of $1\,cm^2$ is placed a distance r from a target (taken to be of zero dimension, i.e., a point). The target is bombarded with neutrons. Assuming that only elastic scattering occurs, that scattering is azimuthally symmetric and that the scattering cross section is isotropic:

a) What is the ratio of the number of particles detected by the detector at positions 1 and 2 shown in the figure?

b) What is the ratio of the number of particles scattered through an angular increment of 10° about $\theta_1 = 5°$ and $\theta_2 = 85°$?

c) Repeat parts (a) and (b) assuming that instead of being isotropic, the differential scattering cross section varies as $\sigma_s(E_i, \theta) = \cos\theta$.

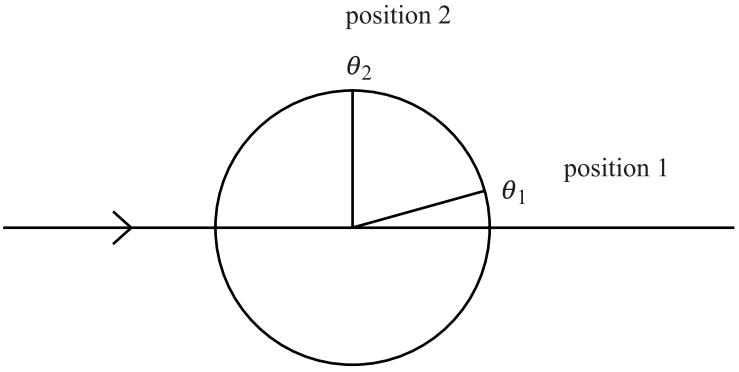

$d\theta$ = Increment of scattering angle
$d\Omega$ = Increment of solid angle about θ
θ = Scattering angle in the center-of-mass system

1.3 A Ti plate is bombarded with 10^{14} neutrons per cm^2 per second at perpendicular incidence. The entire plate is hit by the beam.
   a) Calculate the number of particles scattered per second at
      i) $85^\circ \leq \theta = 86^\circ$ and
      ii) $5^\circ \leq \theta = 6^\circ$.
      The plate size is $1\,\text{cm}^2$ by 0.6 mm. Scattering is isotropic with a total scattering cross section of 2.87 barns ($1\,\text{barn} = 10^{-24}\,\text{cm}^2$).
   b) The same target is bombarded with particles such that the differential angular scattering cross section is proportional to θ^2. Calculate the ratio of the atomic flux in interval (i) above to that in interval (ii).
      In both cases, perform full integration of the differential cross section.
   c) Approximate the integrals in (b) by assuming the differential angular scattering cross section to be constant in each integration interval and equal to the value at the interval's center.

1.4 Derive the kinematic factor K, defined as $K = E_\text{f}/E_\text{i}$, where E_i is the projectile energy before the collision and E_f is the projectile energy after the collision.

1.5 The following formula relates the scattering angles θ and ϕ in the lab and center-of-mass frames, respectively:

$$\tan\theta = (M/m)\sin\phi/[1 + (M/m)\cos\phi]$$

where m and M are the masses of the projectile and target, respectively. Discuss this expression for the following three cases: $m = M$, $m \gg M$ and $m \ll M$.

1.6 Derive Eq. (1.24) in the text.

1.7 Derive Eq. (1.39) in the text.

1.8 For two colliding particles write expressions for:
   a) E_T, the total energy of a system of n particles
   b) E_CM, the energy of the center of mass (determined by V_CM and the total mass of the system)
   c) and E, the total energy in the CM system.
   Show that $E = E_\text{T} - E_\text{CM}$ (Eq. (1.61))

1.9 Derive a relation between b and ϕ from Eq. (1.76) for the hard-sphere potential:

$$\begin{aligned} V_\text{HS}(r) &= 0 \qquad r \geq r_0 \\ &= \infty \qquad r < r_0 \end{aligned}$$

Make sure your answer is correct for $b > r_0$.

1.10 As a means of describing atom–atom interaction at intermediate separation, i.e., between Coulombic repulsion and closed shell repulsion, an inverse power potential is often employed of the form

$$V(r) = \text{constant}/r^n .$$

For example, one can fit an inverse square ($n = 2$) function to the screened Coulomb potential at $r = a$ obtaining the same slope, ordinate and curvature.

This function is

$$V(r) = z_1 z_2 \varepsilon^2 a / \left(r^2 \exp[1]\right) .$$

Formulate the cross sections $\sigma_s(E_i, T)$ and $\sigma_s(E_i, \phi)$ for atom–atom interactions obeying the inverse square potential function.

1.11 Compare your result in Problem 1.10 to that obtained using a Born–Mayer potential and a simple Coulomb potential. Comment on the similarities and differences.

1.12 Calculate the average energy transfer from a 100 keV Ni atom colliding with another Ni atom, using:
a) The hard-sphere potential
b) The inverse square potential.

1.13 Explain, in physical terms, why the scattering cross section resulting from Coulombic repulsion depends on the transferred energy, T, while that for neutron–nuclear interaction does not.

1.14 Assuming a pure Coulomb potential, determine the distance of closest approach for a 100 keV boron atom on silicon for an impact parameter, $b = 1$ nm. What is the significance of your answer?

1.15 1 MeV Al^+ ions are accelerated toward a pure Ni target. The ions are directed normal to the sample surface.
a) Calculate the total path length and provide an estimate for the mean projected range of the ions.
b) For a dose of 10^{16} ions/cm^2, estimate the maximum Al concentration and the FWHM of the Al distribution. Use $S_e = kE^{1/2}$, where $k = 2 \times 10^{-16}$ eV$^{1/2}$cm^2.

1.16 A 10 MeV Si ion penetrates a Si crystal.
a) Calculate its energy as a function of distance traveled and its penetration depth. Assume that electronic stopping dominates.
b) Write an expression for the depth distribution of implanted Si ions and give the straggling.

1.17 Calculate the energy threshold above which the Rutherford scattering cross section can be used for: (i) near head-on collisions, and (ii) all collisions of He^{++} and H^+ in Si and Pd.

1.18 2 MeV He^{++} ions are backscattered ($\theta = 180°$) off of a 25 nm thick gold foil. Determine the highest and lowest energy values of the backscattered ions as measured in a detector placed at 180° with respect to the incoming beam. Use $k = 0.14 \times 10^{-15}$ eV$^{1/2}$ cm^2.
Determine the stopping power by interpolation or extrapolation based on the following values of $1/N(\mathrm{d}E/\mathrm{d}x)$ (in eV/(10^{15} atoms/cm^2)):

Energy (MeV):	1.6	2.0
Au	122.3	115.5
Al	47.5	44.25

1.19 Assume the stopping power can be described by the following function:

$S = C + KE^{1/2}$ where C and K are constants.

a) Derive an equation for the particle range as a function of energy.
b) Does the range increase or decrease as:
   i) Energy increases
   ii) K increases
   iii) C increases.

1.20 Which increases the high-energy electronic stopping power the most, increased charge, energy, or mass of the projectile ion?

1.21 A 2 MeV proton travels through lead.
a) Assuming elastic collisions, calculate the maximum energy that can be transferred from the proton to the lead.
b) What energy would a Pb ion need to have the same maximum energy transfer in a Pb–Pb collision as the proton–Pb collision in part (a)?

1.22 An Fe particle is fired at a block of natural uranium. To get the Fe as close to the uranium particle as possible, would you be better off using a higher charge state of Fe or a lighter isotope? Assume Coulomb potentials can be used.

1.23 A thin film containing F^{19} is bombarded with 1.85 MeV protons. The following reaction takes place:

$$F^{19} + p \rightarrow O^{16} + \alpha .$$

The reaction has a Q value of 8.13 MeV.
After interaction, an alpha particle is seen to emerge at a right angle to the incident proton beam. What are the energies of the alpha particle and the oxygen atom? What is the maximum energy each of these particles could transfer to a stationary Fe atom?

1.24 A helium atom at 1 MeV is sent into iron. Assuming the electronic stopping cross section is a constant $88\,\text{eV}/(10^{15}\,\text{atoms/cm}^2)$, what is the energy of the helium atom after it travels 500 nm? If the He atom collides with an Fe atom after traveling 500 nm, what is the maximum energy transferred? Assume an atomic density of $8.5 \times 10^{22}\,\text{atoms/cm}^3$ for Fe. Was an assumption of constant stopping power valid?

References

1. Ullmaier H, Schilling W (1980) Radiation damage in metallic reactor materials. In: Physics of Modern Materials, vol. I. IAEA, Vienna
2. Lamarsh JR (1971) Introduction to Nuclear Reactor Theory. Addison-Wesley, Reading, MA
3. Doran DG (1977) Nucl Sci Eng 49:130
4. Odette GR (1972) Trans Am Nucl Soc 15:464
5. Segev M (1971) Inelastic Matrices in Multigroup Calculation, ANL-7710. Argonne National Lab, Argonne, IL, p 374
6. Evans RD (1955) The Atomic Nucleus. McGraw-Hill, New York
7. Chadderton LT (1965) Radiation Damage in Crystals. Methuen, London

8. Born M, Mayer JE (1932) Z Physik 75:1
9. Firsov OB (1957) Zh eksper. teor. Fiz 32:1464
10. Firsov OB (1957) Zh eksper. teor. Fiz 33:696
11. Brinkman JA (ed) (1962) Radiation Damage in Solids. Academic, New York
12. Abrahamson AA (1963) Phys Rev 130:693
13. Thompson MW (1969) Defects and Radiation Damage in Metals. Cambridge University Press, Cambridge
14. Lindhard J, Nielsen V, Scharff M (1968) Approximation method in classical scattering by screened Coulomb fields. Mat. Fys. Medd. Dan Vid. Selsk. 36(10)
15. Winterbon KB, Sigmund P, Sanders JB (1970) Spatial distribution of energy deposited by atomic particles in elastic collisions. Mat. Fys. Medd. Dan Vid. Selsk. 37(14)
16. Lindhard J, Scharff M, Schiott HE (1963) Range concepts and heavy ion ranges. Mat. Fys. Medd. Dan Vid. Selsk. 33(14):3
17. Nastasi M, Mayer JW, Hirvonen JK (1996) Ion-Solid Interactions: Fundamentals and Applications. Cambridge University Press, Cambridge
18. Ziegler JF, Biersack JP, Littmark U (1996) The Stopping and Range of Ions in Solids. Pergamon, New York
19. Lindhard J, Winther A (1964) Mat. Fys. Medd. Dan Vid. Selsk. 34:1
20. Littmark U, Ziegler JF (1980) Handbook of Range Distributions of Energetic Ions in all Elements. Pergamon, New York

2 The Displacement of Atoms

2.1 Elementary Displacement Theory

The struck lattice atom of energy T, is referred to as a primary knock-on atom, or PKA. This atom moves through the lattice encountering other lattice atoms. Such encounters may result in sufficient energy transfer to displace this lattice atom from its site resulting in two displaced atoms. If this collision sequence continues, a series of tertiary knock-ons is produced resulting in a collision cascade. A cascade is a spatial cluster of lattice vacancies and atoms residing as interstitials in a localized region of the lattice. Such a phenomenon can have a profound effect on the physical and mechanical properties of the alloy, as will become evident later. Here we are concerned with being able to quantify the displacement cascade. That is, for a neutron of energy E_{i}, striking a lattice atom, how many lattice atom displacements will result? We have already discussed in detail the nature of neutron–nucleus and atom–atom collisions. Now, we will develop a model for determining the number of atoms displaced by a PKA of energy T.

Recall that to quantify radiation damage, we require a solution to the damage rate equation:

$$R_{\mathrm{d}} = N \int_{\check{E}}^{\hat{E}} \phi\left(E_{\mathrm{i}}\right) \sigma_{\mathrm{D}}\left(E_{\mathrm{i}}\right) \mathrm{d}E_{\mathrm{i}} \,, \tag{2.1}$$

where N is the lattice atom density, $\phi\left(E_{\mathrm{i}}\right)$ is the energy-dependent particle flux and $\sigma_{\mathrm{D}}\left(E_{\mathrm{i}}\right)$ is the energy-dependent displacement cross section. The displacement cross section is a probability for the displacement of lattice atoms by incident particles:

$$\sigma_{\mathrm{D}}\left(E_{\mathrm{i}}\right) = \int_{\check{T}}^{\hat{T}} \sigma\left(E_{\mathrm{i}}, T\right) \nu(T) \mathrm{d}T \,, \tag{2.2}$$

where $\sigma\left(E_{\mathrm{i}}, T\right)$ is the probability that a particle of energy E_{i} will impart a recoil energy T to a struck lattice atom, and $\nu(T)$ is the number of displaced atoms resulting from such a collision. Chapter 1 provided the energy transfer cross section appearing in Eq. (2.2) for various types of particles in various energy ranges. This chapter will be devoted to supplying the second term in the integrand, $\nu(T)$, the number of atom displacements resulting from a primary recoil atom of energy T, and the limits of T between which displacements occur. Finally, we will develop the displacement cross section and an expression for the displacement rate.

2.1.1 Displacement Probability

As a first step, we define $P_d(T)$ as the probability that a struck atom is displaced upon receipt of energy T. Clearly, there is some minimum energy that must be transferred in order to produce a displacement. We will call this energy, E_d. The magnitude of E_d is dependent upon the crystallographic structure of the lattice, the direction of the incident PKA, the thermal energy of the lattice atom, etc. These considerations will be discussed in detail later. By definition of E_d, the probability of displacement for $T < E_d$ is zero. If E_d is a fixed value under all conditions then the probability of displacement for $T > E_d$ is one. Hence our simplest model for the displacement probability is a step function:

$$\begin{aligned} P_d(T) &= 0 \qquad \text{for} \quad T < E_d \\ &= 1 \qquad \text{for} \quad T > E_d \,. \end{aligned} \tag{2.3}$$

and is shown in Fig. 2.1. However, E_d is not constant for all collisions due to the factors mentioned earlier. The effect of atomic vibrations of the lattice atoms would be expected to lower the value of E_d or introduce a natural "width" of the order kT to the displacement probability. Further, as will be discussed later, the effect of crystallinity will also contribute strongly to the blurring effect on E_d. In fact, the picture in Fig. 2.1 and Eq. (2.3) is only strictly true for an amorphous solid at 0 K. A more realistic representation is shown in Fig. 2.2 and is represented as:

$$\begin{aligned} P_d(T) &= 0 \qquad\quad \text{for} \quad T < E_{d_{min}} \\ &= f(T) \qquad \text{for} \quad E_{d_{min}} < T < E_{d_{max}} \\ &= 1 \qquad\quad \text{for} \quad T > E_{d_{max}} \,, \end{aligned} \tag{2.4}$$

where $f(T)$ is a smoothly varying function between 0 and 1. Given the displacement probability, the next task is to find the number of displacements as a function of the energy transferred. Kinchin and Pease [1] developed a simple theory to find the average number of displaced atoms initially created by a PKA of energy T in a given solid lattice. Their analysis is based on the following assumptions:

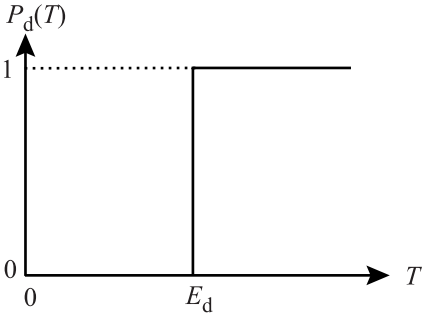

Fig. 2.1. The displacement probability $P_d(T)$ as a function of the kinetic energy transferred to a lattice atom, assuming a sharp displacement threshold

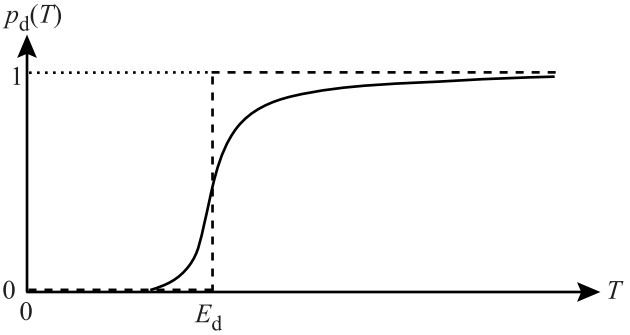

Fig. 2.2. The displacement probability as a function of the kinetic energy transferred to the lattice atom allowing for a blurring of the threshold due to atomic vibrations, impurity atoms, etc.

1. The cascade is created by a sequence of two-body elastic collisions between atoms.
2. The displacement probability is 1 for $T > E_d$ as given by Eq. (2.4).
3. When an atom with initial energy T emerges from a collision with energy T' and generates a new recoil with energy ε, it is assumed that no energy passes to the lattice and $T = T' + \varepsilon$.
4. Energy loss by electron stopping is given by a cut-off energy E_c. If the PKA energy is greater than E_c no additional displacements occur until electron energy losses reduce the PKA energy to E_c. For all energies less than E_c electronic stopping is ignored, and only atomic collisions occur.
5. The energy transfer cross section is given by the hard-sphere model.
6. The arrangement of the atoms in the solid is random; effects due to crystal structure are neglected.

Assumption 1 is fundamental to all theories of a cascade consisting of isolated point defects. Elimination of this restriction allows the cascade to be represented by a displacement spike discussed in Chapt. 3. Assumption 2 neglects crystallinity and atomic vibrations, which will add a natural width or "blurring" effect to the distribution. Later on, we will relax Assumptions 3, 4, 5 and 6.

2.1.2 The Kinchin and Pease Model for Atom Displacements

Consider the two moving atoms created when a PKA first strikes a stationary atom. After the collision, the PKA has residual energy $T - \varepsilon$ and the struck atom receives an energy $\varepsilon - E_d$, giving:

$$\nu(T) = \nu(T - \varepsilon) + \nu(\varepsilon - E_d) \,, \tag{2.5}$$

where E_d is the energy consumed in the reaction. By neglecting E_d relative to ε, i.e., $\varepsilon \gg E_d$ according to Assumption 3, then Eq. (2.5) becomes:

$$\nu(T) = \nu(T - \varepsilon) + \nu(\varepsilon) \,. \tag{2.6}$$

Equation (2.6) is not sufficient to determine $\nu(T)$ because the energy transfer ε is unknown. Since the PKA and lattice atoms are identical, ε may lie anywhere between 0 and T. However, if we know the probability of transferring energy in the range $(\varepsilon, \mathrm{d}\varepsilon)$ in a collision, we can multiply Eq. (2.6) by this probability and integrate over all allowable values of ε. This will yield the average number of displacements.

Using the hard-sphere Assumption 5 the energy transfer cross section is:

$$\sigma(T,\varepsilon) = \frac{\sigma(T)}{\gamma T} = \frac{\sigma(T)}{T} \quad \text{for like atoms}\,, \tag{2.7}$$

and the probability that a PKA of energy T transfers energy in the range $(\varepsilon, \mathrm{d}\varepsilon)$ to the struck atom is:

$$\frac{\sigma(T,\varepsilon)\,\mathrm{d}\varepsilon}{\sigma(T)} = \frac{\mathrm{d}\varepsilon}{T}\,, \tag{2.8}$$

and for $\gamma = 1$ (like atoms). Multiplying the right hand side of Eq. (2.6) by $\mathrm{d}\varepsilon/\mathrm{d}T$ and integrating from 0 to T yields:

$$\begin{aligned} \nu(T) &= \frac{1}{T}\int_0^T [\nu(T-\varepsilon)+\nu(\varepsilon)]\,\mathrm{d}\varepsilon \\ &= \frac{1}{T}\left[\int_0^T \nu(T-\varepsilon)\,\mathrm{d}\varepsilon + \int_0^T \nu(\varepsilon)\,\mathrm{d}\varepsilon\right]\,. \end{aligned} \tag{2.9}$$

A change in variables from ε to $\varepsilon' = T-\varepsilon$ in the first integral and Eq. (2.9) gives:

$$\nu(T) = \frac{1}{T}\int_0^T \nu(\varepsilon')\,\mathrm{d}\varepsilon' + \frac{1}{T}\int_0^T \nu(\varepsilon)\,\mathrm{d}\varepsilon\,, \tag{2.10}$$

which is really a sum of two identical integrals. Therefore:

$$\nu(T) = \frac{2}{T}\int_0^T \nu(\varepsilon)\,\mathrm{d}\varepsilon\,. \tag{2.11}$$

Before solving Eq. (2.11), let us examine the behavior of $\nu(\varepsilon)$ near the displacement threshold, E_d. Clearly when $T < E_\mathrm{d}$ there are no displacements and:

$$\nu(T) = 0 \quad \text{for} \quad 0 < T < E_\mathrm{d}\,. \tag{2.12}$$

If T is greater than E_d but less than $2E_\mathrm{d}$, two results are possible. The first is that the struck atom is displaced from its lattice site and the PKA, now left with energy less than E_d, falls into its place. However, if the original PKA does not transfer E_d, the struck atom remains in place and no displacement occurs. In either case, only one displacement in total is possible from a PKA with energy between E_d and $2E_\mathrm{d}$, and:

$$\nu(T) = 1 \quad \text{for} \quad E_\mathrm{d} < T < 2E_\mathrm{d}\,. \tag{2.13}$$

Using Eqs. (2.12) and (2.13) we may split the integral in Eq. (2.11) into ranges from 0 to E_d, E_d to $2E_\mathrm{d}$, and $2E_\mathrm{d}$ to T and evaluate:

$$\nu(T) = \frac{2}{T}\left[\int_0^{E_\mathrm{d}} 0\,\mathrm{d}\varepsilon + \int_{E_\mathrm{d}}^{2E_\mathrm{d}} 1\,\mathrm{d}\varepsilon + \int_{2E_\mathrm{d}}^{T} \nu(\varepsilon)\,\mathrm{d}\varepsilon\right]\,,$$

yielding:

$$\nu(T) = \frac{2E_\mathrm{d}}{T} + \frac{2}{T}\int_{2E_\mathrm{d}}^{T} \nu(\varepsilon)\,\mathrm{d}\varepsilon \ . \tag{2.14}$$

We can solve Eq. (2.14) by multiplying by T and differentiating with respect to T giving:

$$T\frac{\mathrm{d}\nu}{\mathrm{d}T} = \nu \ , \tag{2.15}$$

with the solution:

$$\nu = CT \ . \tag{2.16}$$

Substituting Eq. (2.16) into Eq. (2.14) gives:

$$C = \frac{1}{E_\mathrm{d}} \ , \tag{2.17}$$

and therefore:

$$\nu(T) = \frac{T}{2E_\mathrm{d}} \quad \text{for } 2E_\mathrm{d} < T < E_\mathrm{c} \ . \tag{2.18}$$

The upper limit is set by E_c (Assumption 4). When a PKA is born with $T > E_\mathrm{c}$, the number of displacements is $\nu(T) = E_\mathrm{c}/2E_\mathrm{d}$ for $T > E_\mathrm{c}$. So the full Kinchin–Pease (K–P) result is:

$$\nu(T) = \begin{cases} 0 & \text{for } T < E_\mathrm{d} \\ 1 & \text{for } E_\mathrm{d} < T < 2E_\mathrm{d} \\ \dfrac{T}{2E_\mathrm{d}} & \text{for } 2E_\mathrm{d} < T < E_\mathrm{c} \\ \dfrac{E_\mathrm{c}}{2E_\mathrm{d}} & \text{for } T \geq E_\mathrm{c} \end{cases} \ . \tag{2.19}$$

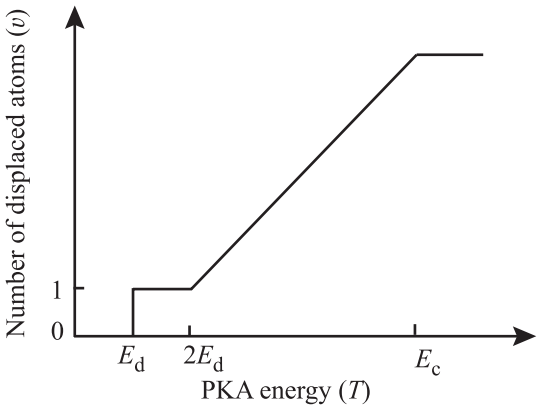

Fig. 2.3. The number of displaced atoms in the cascade as a function of the PKA energy according to the model of Kinchin and Pease

Note that $T/2E_d$ is a true average since the number of displacements can range from 0 (no energy transfers above E_d) to $T/E_d - 1$ (every collision transfers just enough) and for large T, ν approaches T/E_d. So the maximum value of $\nu(T)$ is $2(T/2E_d) = T/E_d$. The full displacement function described by Eq. (2.19) is shown in Fig. 2.3.

2.1.3 The Displacement Energy

A lattice atom must receive a minimum amount of energy in the collision in order to be displaced from its lattice site. This is the displacement energy or displacement threshold, E_d. If the energy transferred, T, is less than E_d, the struck atom will vibrate about its equilibrium position but will not be displaced. These vibrations will be transmitted to neighboring atoms through the interaction of their potential fields and the energy will appear as heat. Hence, the potential fields of the atoms in the lattice form a barrier over which the stuck atom must pass in order to be displaced. This is the source of the displacement threshold energy.

Since metals are crystallographic in structure, the potential barrier surrounding an equilibrium lattice site is not uniform in all directions. In fact, there are directions in which the surrounding atoms will remove large amounts of energy from the struck atom yielding a high potential barrier. Along directions of high symmetry there exist open directions along which the threshold displacement energy is low. Since the direction of the recoil is determined from the collision event which is itself a random process, the recoil direction is entirely random. The single value often quoted for displacement energy in radiation damage calculations then represents a spherical average of the potential barrier surrounding the equilibrium lattice site.

The value of E_d may be roughly estimated using an argument by Seitz [2]. The energy of sublimation, E_s, for most metals is about 5–6 eV. Since half as many bonds are broken by removing an atom from the surface of a crystal as opposed to the interior, the energy to remove an atom from the interior is then 10–12 eV. If an atom is moved from its lattice site to an interstitial position in the direction of least resistance and time is allowed for neighboring atoms to relax (an adiabatic movement), an energy of $2E_c$ is needed. Since in reality, the struck atom is not always projected in the direction of least resistance and time is not allowed for the relaxation of neighboring atoms, a greater amount of energy (perhaps 4–5 E_c) is needed. Thus we would expect E_d to be 20–25 eV.

Accurate determinations of the displacement energy can be made if the interaction potential between lattice atoms is known. This is accomplished by moving the atom in a given direction and summing the interaction energies between the moving atom and all other nearest neighbors along the trajectory of the struck atom. When the total potential energy reaches a maximum, the position corresponds to a saddle point and the difference between the energy of the atom at the saddle point, E^*, and its energy in the equilibrium position, E_{eq}, represents the displacement threshold for the particular direction. Since the interaction energy in these collisions is only tens of eV, the Born–Mayer potential would be the most appropriate potential to use in

describing the interaction. These calculations can be carried out over all directions and averaged to obtain a mean E_d for a particular solid.

To appreciate the significance of the variation in interaction energies or potential barriers with crystal direction we will consider the case of copper. In the cubic lattice there are three crystallographic directions that may be considered easy directions for displacement; ⟨100⟩, ⟨110⟩ and ⟨111⟩. In particular, ⟨110⟩ is the close-packed direction in the fcc lattice and ⟨111⟩ is the close-packed direction in the bcc lattice. Figure 2.4 shows how an atom is displaced along each of these directions in the fcc lattice. In each case, the displaced atom K passes through the midpoint of a set of "barrier atoms" B, in the direction of the L atom, with the atom configuration dependent on the direction. For a K atom displaced in the ⟨110⟩ direction, the atoms are located at the corners of a rectangle to which the path of K is perpendicular. When the K atom passes through the barrier, it loses kinetic energy in glancing collisions, which initially becomes potential energy of the barrier atoms. The energy need not be shared equally between the four B atoms. This is illustrated by drawing a set of contours of constant E_d in the place of the B atoms (Fig. 2.5). Then if K only receives a quantity of energy E_d ⟨110⟩ in the collision event, it will be displaced if its initial direction is contained within a small cone of solid angle centered about the ⟨110⟩ direction. For small energies, the cone intersects the B atom plane in a circle but as the energy transferred increases, the intersection deviates significantly from a right circular cone (Fig. 2.5). The contours are in fact, generated by the intersection of a complex but symmetrical three-dimensional surface with a sphere which is described about the atom K as center. This contour pattern can be constructed by accounting for the interaction between the K atom

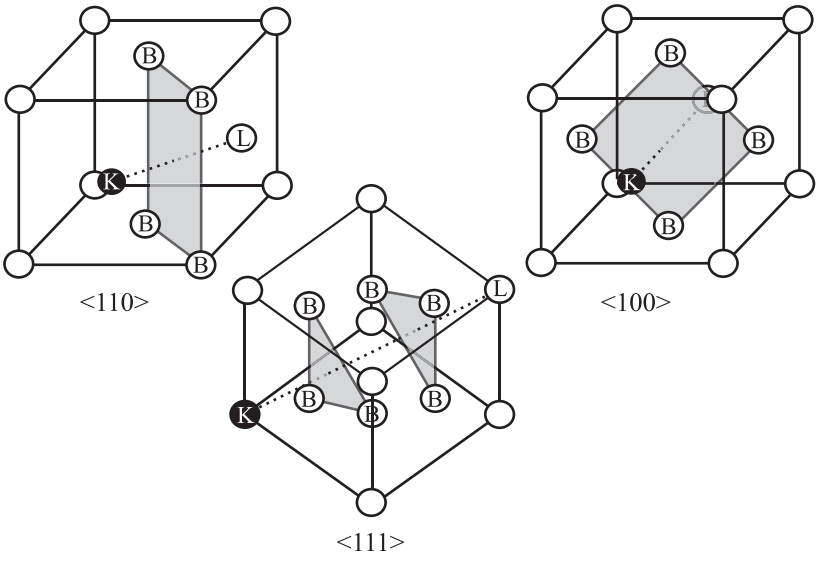

Fig. 2.4. Struck atom, *K*, and barrier atoms *B* for various directions of the struck atom in the fcc lattice

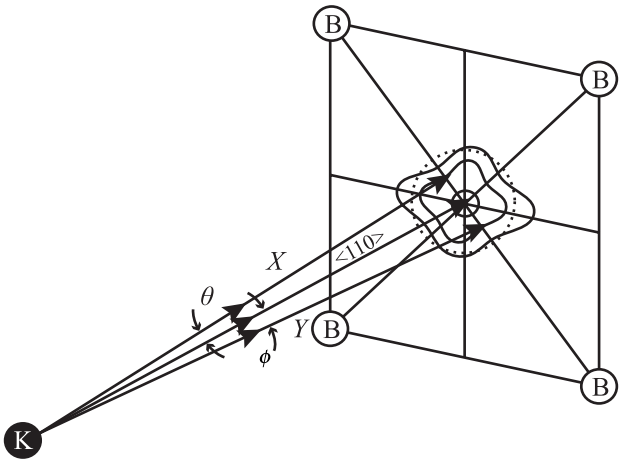

Fig. 2.5. Equipotential contours in the barrier plane for a struck atom, *K*, traveling close to the ⟨110⟩ direction and heading toward the barrier plane defined by the barrier atoms, *B* (after [3])

and each of the B atoms at every point in time while simultaneously accounting for interactions between each of these five atoms and other atoms in the surrounding region of the crystal. This is a very difficult problem, the solution of which depends heavily on the interaction potential. In principle, at least, we can obtain all the information we need about the directional dependence of the thresholds. Figure 2.6 shows the displacement threshold as a function of direction in fcc copper and gold. Note that displacement threshold energies along ⟨100⟩ and ⟨110⟩ are low, but the value along ⟨111⟩ is high due to the large distance between barrier atoms in this direction and the two sets of barriers between the atoms on the body diagonal of the unit cell.

This dependence will be further illustrated in an example using the fcc lattice and a parabolic repulsion function. Figure 2.7 shows a lattice atom on the face of a unit cell in an fcc crystal receiving energy from a collision. Its flight trajectory is in the ⟨100⟩ direction, which is equidistant from four atoms located on the faces of the unit cell. In an fcc lattice, each atom is surrounded by 12 nearest neighbors. Displacement will be dependent on several important factors. They are the number of barrier atoms, B, the impact parameter, z (the distance of closest approach to the B atoms), and the distance from the K atom in its lattice site to the barrier, y. These quantities are given in Table 2.1 for the fcc lattice. The energy required to displace an atom will increase with B and y and decrease with z. Since z is smallest for the ⟨111⟩ direction, this will be the most difficult to penetrate. Also $z_{100} < z_{110}$ and $y_{100} > y_{110}$, so both factors will make displacement along ⟨110⟩ easier then along ⟨100⟩. Lets take the specific example of displacement in the ⟨100⟩ direction of the fcc example and calculate a value for E_{d}.

The energy of a single atom in a normal lattice site is:

$$E_{\mathrm{eq}} = -12U \,, \tag{2.20}$$

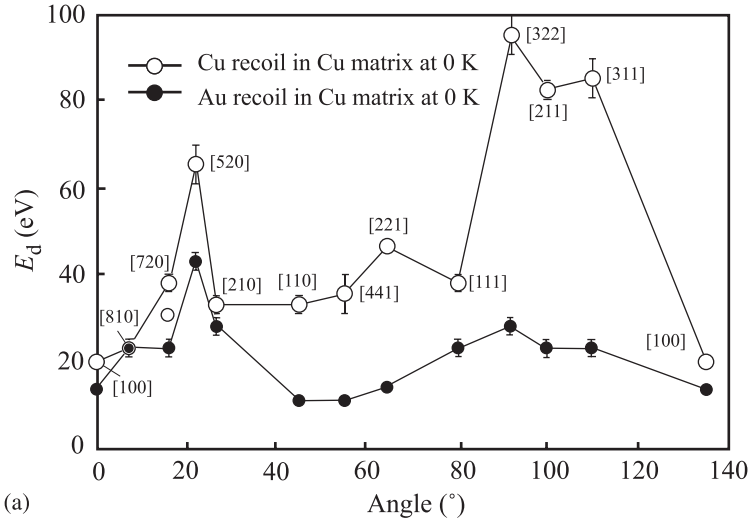

(a)

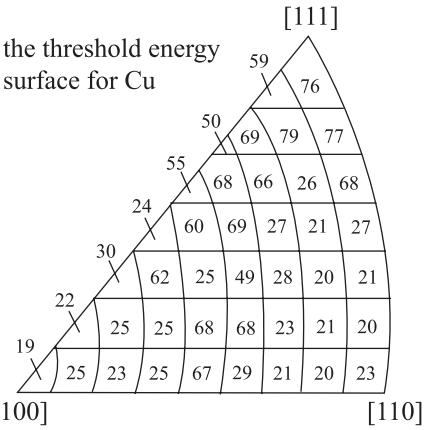

(b)

Fig. 2.6. Displacement energy as a function of direction in (a) fcc Cu and Au crystal (after [3]), and (b) in copper (after [4])

where U is the energy per atom of the crystal. Since only half as many bonds are broken in the sublimation process, this energy is just:

$$E_s \cong 6U \ , \tag{2.21}$$

and since $E_s \sim 4-5\,\text{eV}$, U is about 1 eV.

To describe the interaction of the lattice atoms as they are pushed together in the solid, we will use a simple parabolic repulsion as opposed to the Born–Mayer

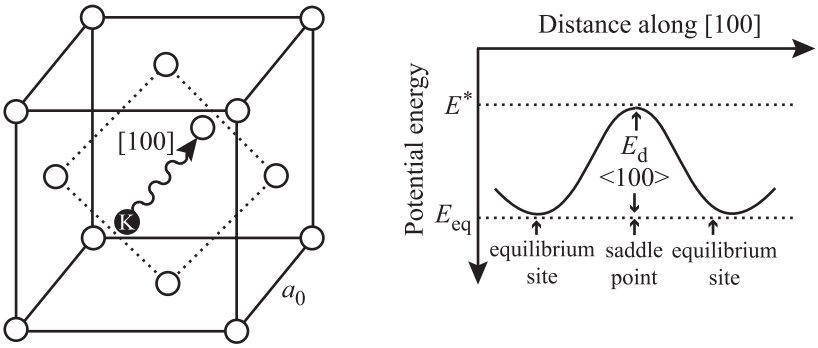

Fig. 2.7. Displacement of a lattice atom along the ⟨100⟩ direction in the fcc lattice and the variation of energy of the atom with position along its path (after [5])

potential:

$$V(r) = -U + \frac{1}{2}k(r_{eq} - r)^2 \quad r < r_{eq}$$
$$V(r) = 0 \quad r > r_{eq}\,, \tag{2.22}$$

where k is the force constant characterizing the repulsive position of the potential. The force constant can be expressed as [5]:

$$ka^2 = \frac{3v}{\beta}\,, \tag{2.23}$$

where

k = force constant
a = lattice constant
$v = a^3/4$ = specific volume of an atom
β = compressibility.

In our example, the equilibrium spacing of the struck atom and the four atoms forming the square barrier is $r_{eq} = a/\sqrt{2}$. When the atom is at the center of the square, it interacts with the four atoms at the corners a distance $a/2$ away. Hence, the energy

Table 2.1. Parameters used for the determination of E_d in the fcc lattice

Direction	# B atoms	Impact parameter, z	Distance to barrier, y
⟨100⟩	4	$\frac{a}{2}$	$\frac{a}{2}$
⟨110⟩	4	$\frac{\sqrt{6}}{4}a$	$\frac{\sqrt{2}}{4}a$
⟨111⟩	3	$\frac{a}{\sqrt{6}}$	$\frac{a}{3}$

Table 2.2. Recommended values of the effective displacement energy for use in displacement calculations (from [6])

Metal	Lattice (c/a)	$E_{d,min}$ (eV)	E_d (eV)
Al	fcc	16	25
Ti	hcp (1.59)	19	30
V	bcc	–	40
Cr	bcc	28	40
Mn	bcc	–	40
Fe	bcc	20	40
Co	fcc	22	40
Ni	fcc	23	40
Cu	fcc	19	30
Zr	hcp	21	40
Nb	bcc	36	60
Mo	bcc	33	60
Ta	bcc	34	90
W	bcc	40	90
Pb	fcc	14	25
Stainless steel	fcc		40

at the saddle point is:

$$E^* = 4V\left(\frac{a}{2}\right) = 4\left[-D + \frac{1}{2}(ka^2)\left(\frac{1}{\sqrt{2}} - \frac{1}{2}\right)^2\right] . \tag{2.24}$$

The displacement energy in the $\langle 100\rangle$ direction is then:

$$E_d\langle 100\rangle = \varepsilon^* - \varepsilon_{eq} = 8D + 2\left(ka^2\right)\left(\frac{1}{\sqrt{2}} - \frac{1}{2}\right)^2 . \tag{2.25}$$

Typical values for ka^2 and U for metals are 60 eV and 1 eV, respectively, yielding $E_d\langle 100\rangle \cong 13.1$ eV. This value is in reasonable agreement with that given in Fig. 2.6. Table 2.2 gives values of E_d for various metals [6]. Note that for the transition metals, the accepted value of E_d is 40 eV.

2.1.4 The Electron Energy Loss Limit

Now that we have established a lower limit on the energy transfer necessary to cause a displacement, E_d, lets turn our attention to the high-energy regime of collisions. Recall that at low energies ($T < 10^3$ eV), $S_n \gg S_e$, and we may assume that nearly all of the energy loss of the PKA goes toward elastic collisions (Fig. 1.18). However, as the PKA energy increases, the fraction of the total energy loss that is due to electron excitation and ionization increases until above the crossover energy, E_x, $S_e > S_n$.

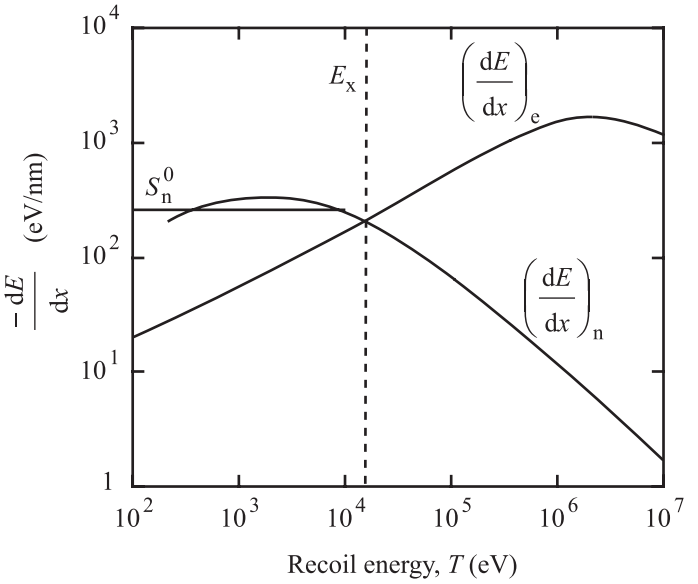

Fig. 2.8. Energy loss from electronic and nuclear stopping as a function of energy (after [7])

Our expression for $\nu(T)$ in Eq. (2.19) must therefore be modified to account for this variation in the amount of kinetic energy available for displacement collisions.

Figure 2.8 shows $(\mathrm{d}E/\mathrm{d}x)_n$ for carbon recoils in graphite using Eq. (1.162) and Lindhard's Thomas–Fermi result, the latter showing that Eq. (1.162), which predicts a constant value of 250 eV/nm is a good approximation for energies up to at least E_a. Note that at high energies ($T \gg E_x$) electronic energy losses predominate by several orders of magnitude. However at low energies ($T \ll E_x$) the situation is reversed.

Fortunately, because of departures from the hard-sphere model, the primary recoil creates secondaries with average energies far below $\frac{1}{2}\hat{T}$. These will almost always be in the range where electronic excitation can be neglected. To obtain $\nu(T)$ to a fair approximation we calculate the energy E_c, dissipated in elastic collisions by the PKA:

$$E_\mathrm{c} = \int_0^{\check{T}} \frac{(\mathrm{d}E/\mathrm{d}x)_n \,\mathrm{d}E}{(\mathrm{d}E/\mathrm{d}x)_n + (\mathrm{d}E/\mathrm{d}x)_e} \,. \tag{2.26}$$

We can then use Eq. (1.182) for $(\mathrm{d}E/\mathrm{d}x)_e$ and Eq. (1.130) for $(\mathrm{d}E/\mathrm{d}x)_n$ with $\check{T} = E_\mathrm{a}$. The modified damage function is the original Eq. (2.19) with T replaced by E_c:

$$\nu(T) = \frac{E_\mathrm{c}}{2E_\mathrm{d}} \,. \tag{2.27}$$

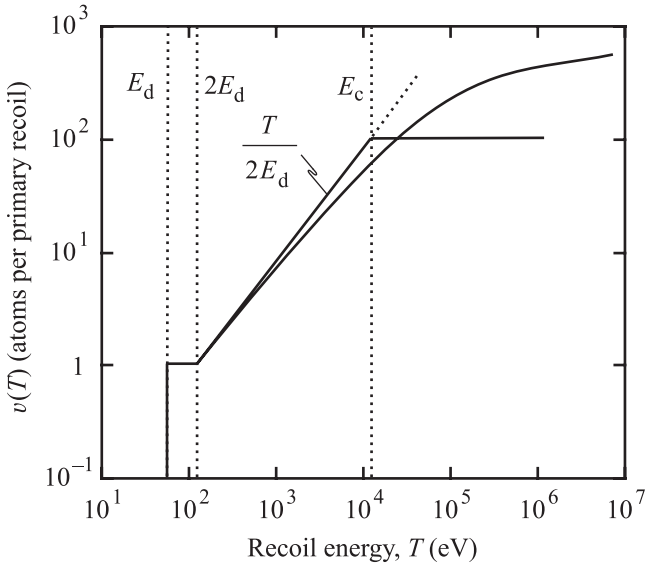

Fig. 2.9. Number of displaced atoms per primary recoil compared to the simple K–P result of $T/2E_d$ (after [7])

As an estimate of E_c we can use the maximum energy a moving atom (of energy E) can transfer to an electron as:

$$\frac{4m_e}{M}E\,, \tag{2.28}$$

and equating this with the ionization energy of the struck electron belonging to the target atom we have:

$$E_c = \frac{M}{4m_e}I\,. \tag{2.29}$$

Kinchin and Pease [1] equated E_c and E_x, implying that all energy above E_x is lost in electron excitation, and displacements account for all the energy loss below E_c. Figure 2.9 shows $\nu(T)$ for graphite using Lindhard's $(\mathrm{d}E/\mathrm{d}x)_n$. Note that for recoils with energy below E_c, the simple theory gives a fair description, but for $T > E_c$, the losses in electron excitation are important.

2.2 Modifications to the K–P Displacement Model

2.2.1 Consideration of E_d in the Energy Balance

Snyder and Neufeld [8] make the assumption that an energy E_d is consumed in each collision such that the relation in Assumption 3 of the K–P displacement model will

read:

$$T = T' + \varepsilon + E_{\mathrm{d}}\,, \tag{2.30}$$

and both atoms move off after collision, no matter how small their energy. When compared with the Kinchin–Pease model, it may be expected that $\nu(T)$ would decrease since an energy loss term is added. However, because atoms are allowed to leave the collision with energy less than E_{d}, an increase in $\nu(T)$ will occur. Since these two changes to $\nu(T)$ nearly cancel, the result is very similar to the K–P model:

$$\nu(T) = 0.56\left(1 + \frac{T}{E_{\mathrm{d}}}\right) \quad \text{for } T > 4E_{\mathrm{d}}\,. \tag{2.31}$$

2.2.2 Realistic Energy Transfer Cross Sections

The weakest point of the K–P displacement model is the assumption of hard-sphere collisions (Assumption 5). In fact, more realistic energy transfer cross sections can be used while still maintaining the proportionality of Eq. (2.19). Sanders [9] solved Eq. (2.5) using an inverse power potential (r^{-s}) to obtain:

$$\nu(T) = s\left(2^{\frac{1}{s+1}} - 1\right)\frac{T}{2E_{\mathrm{d}}}\,, \tag{2.32}$$

which for the inverse square potential becomes:

$$\nu(T) = 0.52\frac{T}{2E_{\mathrm{d}}}\,, \tag{2.33}$$

reducing the Kinchin–Pease result by a factor of 2.

However, the use of this potential has its shortcomings because it is applied to all collisions in the cascade while its region of validity is limited to those values of T such that $\rho < 5a$. Physically, the effect of realistic scattering is to make a larger number collisions generate T in the subthreshold regions below E_{d} where they are removed from multiplication chain.

For many years, investigators have been intrigued that Eq. (2.19) appears to overestimate $\nu(T)$ in metals by a factor of 2 to 10 [10] and yet attempts to measure the energy dependence of $\nu(T)$ over a large energy range (50–200 keV recoil atoms in gold) gave a quadratic rather than linear relationship. In 1969 Sigmund [11] took a different approach to this problem by considering the *recoil density* $F(T,\varepsilon)\,\mathrm{d}\varepsilon$ defined as the average number of atoms recoiling with an energy in $(\varepsilon, \varepsilon + \mathrm{d}\varepsilon)$ as a consequence of a primary ion slowing down from T to zero energy. The recoil density can be expressed in a form that uses the power law approximation of the Thomas–Fermi differential cross section [12]:

$$\sigma(T,E) \propto T^{-m}\varepsilon^{-1-m}\,, \tag{2.34}$$

where $0 \leq m \leq 1$, giving:

$$F(T,\varepsilon) = \frac{m}{\psi(1)-\psi(1-m)} \frac{T}{(\varepsilon+U)^{1-m}\varepsilon^{1+m}} , \tag{2.35}$$

for $T \gg \varepsilon \gg U$, where

$$\psi(x) = \mathrm{d}[\ln\Gamma(x)]/\mathrm{d}x , \tag{2.36}$$

U is the binding energy lost by an atom when leaving a lattice site, and $\Gamma(x)$ is the gamma function or the generalized factorial function. Since a recoiling atom is displaced when $\varepsilon > E_\mathrm{d}$ we obtain:

$$\nu(T) = \int_{E_\mathrm{d}}^{T} \mathrm{d}\varepsilon F(T,\varepsilon) = \frac{(1+U/E_\mathrm{d})^m - 1}{\psi(1)-\psi(1-m)} \left(\frac{T}{U}\right) \tag{2.37}$$

for $T \gg E_\mathrm{d} \gg U$. The value of m is chosen in such a way [13] that $\sigma(T,\varepsilon)$ describes collisions at *low* energies, i.e., $2E_\mathrm{d} \leq T \leq 100E_\mathrm{d}$. This constrains $m \leq 4$. For $m = 0$, Eq. (2.37) reads:

$$\nu(T) = \frac{6}{\pi^2}\frac{T}{U}\ln(1+U/E_\mathrm{d}) . \tag{2.38}$$

This is an upper limit for displacement processes since loss of defects by replacement collisions has been neglected.

A characteristic feature of displacements in metals is the large recombination volume of an isolated point defect, of the order of 100 atomic volumes or more. Hence, E_d is the energy lost to the environment by an atom trying to escape the recombination volume. This has the consequence that in cascades, many defects are lost by replacement collisions [14]. The binding energy U is only a few eV and thus negligible as compared to E_d, reducing Eq. (2.38) to:

$$\nu(T) = \frac{6}{\pi^2}\frac{T}{E_\mathrm{d}} = 1.22\left(\frac{T}{2E_\mathrm{d}}\right) , \tag{2.39}$$

which is about 22% greater than the result of Eq. (2.19) which accounted for replacement collisions.

2.2.3 Energy Loss by Electronic Excitation

Even for $E > E_\mathrm{c}$, collisions of the PKA with electrons compete for energy loss against collisions with lattice atoms. These two processes can be treated independently, and each can be represented by separate energy transfer cross sections. The formulation originally presented by Lindhard et al. [15] is summarized here as presented by Olander in [5] as a more realistic treatment of energy loss by electronic excitation (Assumption 4).

As a PKA traverses a distance dx of a solid, three things may happen: (1) it collides with an electron, (2) it collides with an atom, or (3) nothing. Let $p_e\,d\varepsilon_e$ be the probability that a collision between the PKA and an electron in the interval dx transfers energy in the range (ε_e, $d\varepsilon_e$) to the electron:

$$p_e\,d\varepsilon_e = N\sigma_e(T,\varepsilon_e)\,d\varepsilon_e\,dx\,, \tag{2.40}$$

where $\sigma_e(T,\varepsilon_e)$ is the energy transfer cross section from the PKA to the electron. Similarly, for a PKA and lattice atom:

$$p_a\,d\varepsilon_a = N\sigma_a(T,\varepsilon_a)\,d\varepsilon_a\,dx\,, \tag{2.41}$$

and the probability that nothing happens in dx is:

$$\begin{aligned} p_o &= 1 - \int_0^{\varepsilon_{e,max}} p_e\,d\varepsilon_e - \int_0^{\varepsilon_{a,max}} p_a\,d\varepsilon_a \\ &= 1 - N\,dx[\sigma_e(T) - \sigma_a(T)]\,, \end{aligned} \tag{2.42}$$

and $\varepsilon_{e,max}$, $\varepsilon_{a,max}$ are the maximum energies transferable to an electron and atom by a PKA of energy T. We re-write the conservation equation for $\nu(T)$ by weighting with the appropriate probability for the process by which it is created and integrating over the permissible ranges of energy transfers:

$$\begin{aligned} \nu(T) = &\int_0^{\varepsilon_{a,max}} [\nu(T-\varepsilon_a) + \nu(\varepsilon_a)]p_a\,d\varepsilon_a \\ &+ \int_0^{\varepsilon_{e,max}} \nu(T-\varepsilon_e)p_e\,d\varepsilon_e + p_0\nu(T)\,. \end{aligned} \tag{2.43}$$

Substituting for p_e, p_a and p_0 yields:

$$\begin{aligned} [\sigma_a(T) + \sigma_e(T)]\nu(T) = &\int_0^{\varepsilon_{a,max}} [\nu(T-\varepsilon_a) + \nu(\varepsilon_a)]\sigma_a(T,\varepsilon_a)\,d\varepsilon_a \\ &+ \int_0^{\varepsilon_{e,max}} \nu(T-\varepsilon_e)\sigma_e(T,\varepsilon_e)\,d\varepsilon_e\,. \end{aligned} \tag{2.44}$$

Since the maximum energy transferred to an electron is very small compared to T, $\nu(T-\varepsilon_e)$ can be expanded in a Taylor series and truncated after the second term:

$$\nu(T-\varepsilon_e) = \nu(T) - \frac{d\nu}{dT}\varepsilon_e\,, \tag{2.45}$$

and the last term in Eq. (2.44) can be written as:

$$\begin{aligned} \int_0^{\varepsilon_{e,max}} \nu(T-\varepsilon_e)\sigma_e(T,\varepsilon_e)\,d\varepsilon_e = &\nu(T)\int_0^{\varepsilon_{e,max}} \sigma_e(T,\varepsilon_e)\,d\varepsilon_e \\ &- \frac{d\nu}{dT}\int_0^{\varepsilon_{e,max}} \varepsilon_e\sigma_e(T,\varepsilon_e)\,d\varepsilon_e\,. \end{aligned} \tag{2.46}$$

The first integral on the right in Eq. (2.46) is the total cross section for collisions of the PKA with the electron, and cancels the corresponding term on the left in Eq. (2.44). The second integral on the right of Eq. (2.46) is the electronic stopping power of the solid divided by the atom density. Substituting Eq. (2.46) using Eq. (2.45), we have:

$$\nu(T) + \left[\frac{(\mathrm{d}T/\mathrm{d}x)_\mathrm{e}}{N\sigma(T)}\right]\frac{\mathrm{d}\nu}{\mathrm{d}T} = \int_0^{T_\mathrm{max}} [\nu(T-\varepsilon)+\nu(\varepsilon)]\left[\frac{\sigma(T,\varepsilon)}{\sigma(T)}\right]\mathrm{d}\varepsilon\ , \tag{2.47}$$

where the subscript "a" on T and σ has been dropped with the understanding that these quantities refer to atomic collisions. Equation (2.47) can be solved using the hard-sphere assumption, but where $\left(\frac{\mathrm{d}E}{\mathrm{d}x}\right)_\mathrm{e}$ is given by Eq. (1.182), i.e., $\left(\frac{\mathrm{d}E}{\mathrm{d}x}\right)_\mathrm{e} = kE^{1/2}$, giving:

$$\nu(T) = \frac{2E_\mathrm{d}}{T} + \frac{2}{T}\int_{2E_\mathrm{d}}^{T}\nu(\varepsilon)\,\mathrm{d}\varepsilon - \frac{kT^{1/2}}{\sigma N}\frac{\mathrm{d}\nu}{\mathrm{d}T}\ . \tag{2.48}$$

After simplification, the final result is:

$$\nu(T) = \left[1 - \frac{4k}{\sigma N(2E_\mathrm{d})^{1/2}}\right]\left(\frac{T}{2E_\mathrm{d}}\right)\ , \quad \text{for } T \gg E_\mathrm{d}\ , \tag{2.49}$$

where k is a constant depending on the atom number density, N, and the atomic number. The term σ is the energy-independent hard-sphere collision cross section. Note that when electronic stopping is properly accounted for in the basic integral equation, the entire concept of a definite energy, E_c, separating regimes of electronic energy loss from atomic collisions can be dismissed.

However, Eq. (2.49) is still plagued by the use of the hard-sphere assumption. Lindhard realized that in order to ensure that reliable predictions are obtained, a realistic energy transfer cross section must be used. Lindhard also realized that the parameter $\nu(T)$ need not be interpreted solely as the number of displacements produced per PKA, but could be taken to be that part of the original PKA energy, which is transferred to the atoms of the lattice (rather than the electrons) in slowing down. In reality, collisions of the PKA with atoms compete with collisions with electrons. But the processes can be treated as independent events. Nevertheless, the expression for $\nu(T)$ needs to be reformulated. According to Lindhard's energy partitioning theory:

$$\nu(T) = \xi(T)\left(\frac{T}{2E_\mathrm{d}}\right)\ , \tag{2.50}$$

where

$$\xi(T) = \frac{1}{1 + 0.13(3.4\varepsilon_\mathrm{T}^{1/6} + 0.4\varepsilon_\mathrm{T}^{3/4} + \varepsilon_\mathrm{T})}\ , \tag{2.51}$$

ε_T is a reduced PKA energy:

$$\varepsilon_T = \frac{T}{2Z^2\varepsilon^2/a} , \tag{2.52}$$

and a is the screening radius

$$a = \frac{0.8853a_0}{Z^{1/3}} .$$

The damage energy efficiency function $\xi(T)$ is given as a function of PKA energy, T, and as a function of Z (various elements) in Fig. 2.10.

In 1975, Norgett, Robinson and Torrens [17] proposed essentially this model to calculate the number of displacements, N_d according to:

$$N_d = \frac{\kappa E_D}{2E_d} = \frac{\kappa(T-\eta)}{2E_d} , \tag{2.53}$$

where T is the total energy of the PKA, η is the energy lost in the cascade by electron excitation, and E_D is the energy available to generate atomic displacements by elastic collisions, and is known as the *damage energy*. The displacement efficiency, κ is 0.8 and is independent of M_2, T or temperature. The quantity E_D is defined by:

$$E_D = \frac{T}{[1+k_N g(\varepsilon_N)]} , \tag{2.54}$$

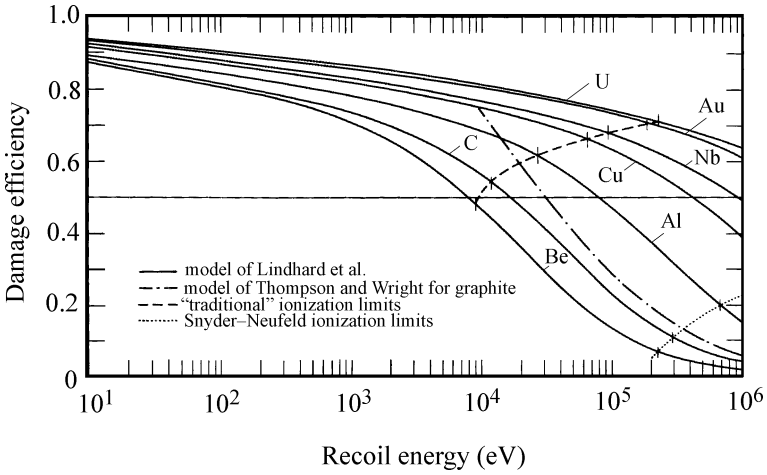

Fig. 2.10. The effect of electronic energy losses on the energy available for atomic displacements (from [16])

and inelastic energy loss is calculated according to the method of Lindhard using a numerical approximation to the universal function, $g(\varepsilon_N)$:

$$\begin{aligned} g(\varepsilon_N) &= 3.4008\varepsilon_N^{1/6} + 0.40244\varepsilon_N^{3/4} + \varepsilon_N \\ k_N &= 0.1337 Z_1^{1/6} \left(\frac{Z_1}{A_1}\right)^{1/2} \\ \varepsilon_N &= \left(\frac{A_2 T}{(A_1 + A_2)}\right)\left(\frac{a}{Z_1 Z_2 \varepsilon^2}\right) \\ a &= \left(\frac{9\pi^2}{128}\right)^{1/3} a_0 \left(Z_1^{2/3} + Z_2^{2/3}\right)^{-1/2} \end{aligned} \tag{2.55}$$

where a_0 is the Bohr radius and ε is the unit electronic charge. If $E_d \sim 40\,\text{eV}$, then $N_d = 10E_D$, where E_D is in keV.

2.2.4 Effects of Crystallinity

The analysis thus far has assumed that the cascade occurs in a solid composed of a random array of atoms. However, when the order of a crystal structure is imposed (Assumption 6), two important effects occur that can alter the number of displacements produced by a PKA; focusing and channeling. *Focusing* is the transfer of energy and/or atoms by near head-on collisions along a row of atoms. *Channeling* is the long-range displacement of atoms along open directions (channels) in a crystal structure in which an atom travels by making glancing collisions with the walls of the channel which are just rows of atoms. Both processes can result in long-range transport of interstitials away from the initial PKA or the cascade. Both processes also reduce the number of displacements per PKA, $\nu(T)$, as calculated from the simple Kinchin–Pease model.

Focusing

The effects of focusing were first seen in the directional dependence of the threshold energy, E_d. In an fcc lattice, for example, displacements occur in the $\langle 100 \rangle$ and $\langle 110 \rangle$ directions with the lowest energy transfer of any crystalline direction. Since the direction of the primary knock-on is random, focusing must be possible for a sizable range of polar angles off the close packed direction. If exact head-on collision were required to produce a linear collision chain, the phenomenon would be of little practical significance since this probability is extremely low.

Focusing along an atomic row can be analyzed using the hard-sphere approximation. The distance between atoms along a particular crystallographic is denoted by D. Figure 2.11 shows two atoms of such a row in which a collision sequence is initiated by the atom which was initially centered at A. This atom receives energy T and moves off at an angle θ_0 to the atomic row. The dashed circle shows the atom position at the instant it strikes the next atom in the row. The radius of the colliding

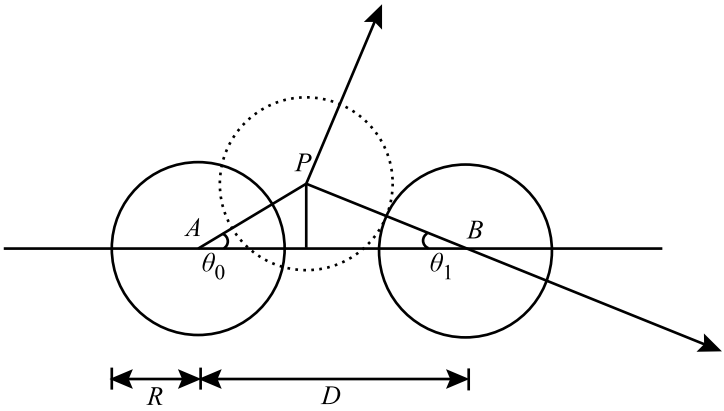

Fig. 2.11. The simple focusing effect assuming hard-sphere collisions

sphere, R, is obtained from the Born–Mayer potential. The impact transfers some of T to the second atom, which then moves off in the direction of the line joining P and B at an angle θ_1 to the row. From Fig. 2.11 we can also show that:

$$\overline{AP}\sin\theta_0 = \overline{PB}\sin\theta_1 \,. \tag{2.56}$$

If θ_0 and θ_1 are small, Eq. (2.56) can be approximated by:

$$\overline{AP}\theta_0 \approx \overline{PB}\theta_1 \,, \tag{2.57}$$

and if θ_0 and θ_1 are very small, then

$$\overline{AP} \approx \overline{AB} - \overline{PB} = D - 2R \,, \quad \text{and since } \overline{PB} = 2R \tag{2.58}$$

$$(D-2R)\theta_0 = 2R\theta_1 \,, \quad \text{and}$$

$$\theta_0(D-2R) = \theta_1(2R) \,. \tag{2.59}$$

If we further define a focusing parameter:

$$f \equiv \theta_1/\theta_0 \,, \tag{2.60}$$

then by Eq. (2.59):

$$f = \frac{D}{2R} - 1 \,. \tag{2.61}$$

This permits us to write the following inequalities:

$$\begin{aligned} &\text{for } f > 1 \,, \quad D > 4R \quad \text{and} \quad |\theta_0| < |\theta_1| \\ &\text{for } f < 1 \,, \quad D < 4R \quad \text{and} \quad |\theta_0| > |\theta_1| \,. \end{aligned} \tag{2.62}$$

Considering further collisions, by the time the momentum pulse reaches atom n, the relation between angles is given by:

$$\begin{aligned}\theta_n &= f\theta_{n-1} \\ &= f^2\theta_{n-2} \\ &= f^3\theta_{n-3} \\ &\vdots \\ &\vdots \\ &= f^n\theta_0 = \left(\frac{D}{2R} - 1\right)^n \theta_0 \,,\end{aligned} \tag{2.63}$$

or finally

$$\theta_n = (f)^n\theta_0 = \left(\frac{D}{2R} - 1\right)^n \theta_0 \,. \tag{2.64}$$

This last relation shows that if $D > 4R$, the focusing parameter f is greater than unity so that the angles θ_n will increase in successive collisions. Conversely, if $D < 4R$, f is less than unity and the angles θ_n converge to zero.

A set of conditions also exist under which the scattering angle θ_n will neither diverge nor converge after successive collisions. These are the conditions for critical focusing ($\theta_n = \theta_{n+1} = \ldots$) which can be determined as follows. The recoil angle of atom B can be related to the initial direction of atom A by applying the law of sines to triangle $\underline{APB}$:

$$\frac{\sin(\pi - \theta_0 - \theta_1)}{\sin\theta_0} = \frac{D}{2R} \,, \tag{2.65}$$

which simplifies to:

$$\frac{\sin(\theta_0 + \theta_1)}{\sin\theta_0} = \frac{D}{2R} \,. \tag{2.66}$$

The condition for critical focusing is $\theta_1 = \theta_0$. Applying this equality in Eq. (2.66) gives:

$$\frac{\sin 2\theta_0}{\sin\theta_0} = 2\cos\theta_0 = \frac{D}{2R} \,, \tag{2.67}$$

and

$$\cos\theta_0 = \cos\theta_c = \frac{D}{4R} \,, \tag{2.68}$$

or focusing will occur when $\cos\theta_0 \leq \dfrac{D}{4R}$ and

$$\cos\theta_c = \frac{D}{4R} \,. \tag{2.69}$$

Equation (2.60) also shows that focusing of momentum is favored along rows of atoms in the $\langle hkl \rangle$ directions for which the separation distance D^{hkl} is a minimum, or the close-packed directions.

If we treat the atoms as having an energy-dependent radius, we can determine the maximum possible energy for focusing at any given collision angle. The key is to allow the potential between atoms to vary with separation. The critical focusing energy, E_{f}^{hkl}, is defined as that energy below which $f < 1$, $D < 4R$ and focusing is possible. In the hard-sphere model the relation between kinetic energy E, and potential energy $V(r)$ for a head on collision is given by Eq. (1.80) as $V(2R) = \frac{1}{2}E$. If $V(r)$ is given in the Born–Mayer potential, Eq. (1.47), $V(r) = A\exp(-Br)$, then:

$$E = 2A\exp(-2R/B)\,. \tag{2.70}$$

For a head-on collision, $\theta_{\mathrm{c}} = 0$, so $\cos\theta_{\mathrm{c}} = \dfrac{D}{4R} = 1$, and we have:

$$E_{\mathrm{fc}} = 2A\exp\left(\frac{-D}{2B}\right)\,. \tag{2.71}$$

This means that any angle greater than zero will result in defocusing for $E \geq> E_{\mathrm{c}}$, or that focusing at an energy E_{fc} can only occur for $\theta = 0^{\circ}$. Clearly then, the critical focusing angle depends on the energy of the projectile. The relation between angle and energy is developed by writing the expression for E_{fc} in terms of D:

$$D = 2B\ln\left(\frac{2A}{E_{\mathrm{fc}}}\right)\,. \tag{2.72}$$

Now, for any atom of energy T reaching a separation of $4R$ gives:

$$4R = 2B\ln\left(\frac{2A}{T}\right)\,. \tag{2.73}$$

Combining these equations gives:

$$\frac{D}{4R} = \cos\theta_{\mathrm{c}} = \frac{\ln(2A/E_{\mathrm{fc}})}{\ln(2A/T)}\,, \quad T < E_{\mathrm{fc}}\,. \tag{2.74}$$

Note that the condition of critical focusing can be expressed in two ways:

1. $E_{\mathrm{fc}} = 2A\exp\left(\dfrac{-D}{2B}\right)$: This condition gives the energy E_{fc} for which focusing occurs for a head-on collision ($\theta_{\mathrm{c}} = 0$).
2. $\cos\theta_{\mathrm{c}} = \dfrac{\ln(2A/E_{\mathrm{fc}})}{\ln(2A/T)}$: This condition gives the maximum angular deviation from a head-on collision θ_{c}, at which a PKA of energy T can initiate a focused sequence.

From the first expression, it should be apparent that focusing is a function of crystallographic direction since D is a function of crystal structure. That is:

$$E_{\mathrm{f}}^{hkl} = 2A \exp\left(\frac{-D^{hkl}}{2B}\right) . \tag{2.75}$$

For example, in the fcc lattice, we have:

$$D^{\langle 100\rangle} = a$$
$$D^{\langle 110\rangle} = \frac{\sqrt{2}}{2}a$$
$$D^{\langle 111\rangle} = \sqrt{3}a$$

therefore, since $D^{\langle 110\rangle} < D^{\langle 100\rangle} < D^{\langle 111\rangle}$, we have $E_{\mathrm{f}}^{\langle 110\rangle} > E_{\mathrm{f}}^{\langle 100\rangle} > E_{\mathrm{f}}^{\langle 111\rangle}$.

Typical values for E_{f} are 80 eV for $E_{\mathrm{f}}^{\langle 110\rangle}$ in copper and 600 eV for gold. In any case, E_{f} is much less than initial PKA energies.

From the preceding discussion, it should be apparent that focusing is only applicable if a scattered atom is within an angle θ_{c} of an atomic row. Then a focused sequence can result. It is therefore important to determine the probability that the initial direction of a struck atom is within a cone of apex θ_{c} about an atomic row. For a random starting direction, the probability of generating a focused collision sequence at energy T is:

$$P_{\mathrm{f}}(T) = \frac{\theta_{\mathrm{c}}^2}{4} . \tag{2.76}$$

Expanding $\cos\theta_{\mathrm{c}}$ in Eq. (2.69) gives:
$1 - \frac{1}{2}\theta_{\mathrm{c}}^2 \approx \frac{D}{4R}$, for small θ_{c}. Substituting from Eq. (2.75) gives:

$$P_{\mathrm{f}}(T) = \frac{1}{2}\left(1 - \frac{D}{4R}\right) \tag{2.77}$$

or

$$\begin{aligned} P_{\mathrm{f}}(T) &= \frac{1}{2}\left[1 - \frac{\ln(2A/E_{\mathrm{fc}})}{\ln(2A/T)}\right] \\ &= \frac{1}{2}\left[\frac{\ln(2T/E_{\mathrm{fc}})}{\ln(E_{\mathrm{fc}}/2A) + \ln(T/E_{\mathrm{fc}})}\right] . \end{aligned} \tag{2.78}$$

Since $E_{\mathrm{fc}}/2A \gg 1$ and $T/E_{\mathrm{fc}} \sim 1$, then:

$$\begin{aligned} P_{\mathrm{f}}(T) &= \frac{1}{2}\frac{\ln(T/E_{\mathrm{fc}})}{\ln(E_{\mathrm{fc}}/A)} \quad T < E_{\mathrm{fc}} \\ &= 0 \quad T > E_{\mathrm{fc}} \end{aligned} \tag{2.79}$$

For n equivalent directions in the crystal:

$$P_{\mathrm{f}}(T) = n\frac{\ln(T/E_{\mathrm{c}})}{\ln(E_{\mathrm{c}}/A)} \,. \tag{2.80}$$

For example, in copper $E_{\mathrm{fc}} \sim 80\,\mathrm{eV}$, and for $A \sim 20{,}000\,\mathrm{eV}$, $P_{\mathrm{f}}(60\,\mathrm{eV}) \sim 0.026n$. For $n = 12$, then $P_{\mathrm{f}} \sim 0.3$ or 30%. Focusing refers to the transfer of energy by elastic collisions along a line, but without involving the transfer of mass. We will next discuss replacement collisions in which both energy and mass are transferred.

Replacement Collisions

In addition to energy transfer, mass can be transferred by replacement of the struck atom with the striking atom if the center of the first atom moves beyond the midpoint of the two atoms as they reside in the lattice. In our analysis of focusing we assumed hard-sphere collisions. However, if we assume that there is a softness to the atom, three things occur:

1. The hard-sphere model overestimates the angle of scattering for a particular impact parameter and hence the amount of focusing must be overestimated.
2. Atoms is the row feel the influence of the oncoming disturbance long before it gets there so the atom is already moving. Since D is decreased, focusing is enhanced.
3. Replacement becomes possible.

Referring to Fig. 2.12, as the collision proceeds, the distance x between atoms A_n and A_{n+l} decreases continuously. The velocity of the center of mass (CM) is:

$$V_{\mathrm{CM}} = \left(\frac{M_1}{M_1+M_2}\right)v_1 + \left(\frac{M_2}{M_1+M_2}\right)v_2 \,,$$

where v_1 and v_2 are in the lab system. The relative speed, defined by $g = v_1 - v_2$ gives:

$$v_1 = V_{\mathrm{CM}} + \left(\frac{M_2}{M_1+M_2}\right)g$$
$$v_2 = V_{\mathrm{CM}} + \left(\frac{M_1}{M_1+M_2}\right)g \,,$$

and the total kinetic energy of the two particles is:

$$KE = 1/2M_1v_1^2 + 1/2M_2v_2^2 \,,$$

and in terms of g and V_{CM} is:

$$KE = 1/2(M_1+M_2)V_{CM}^2 + 1/2\mu g^2 \,,$$

where μ is the reduced mass = $\left(\frac{M_1M_2}{M_1+M_2}\right)$. The total kinetic energy is divided into two parts: one due to the motion of the system and another due to the relative motion

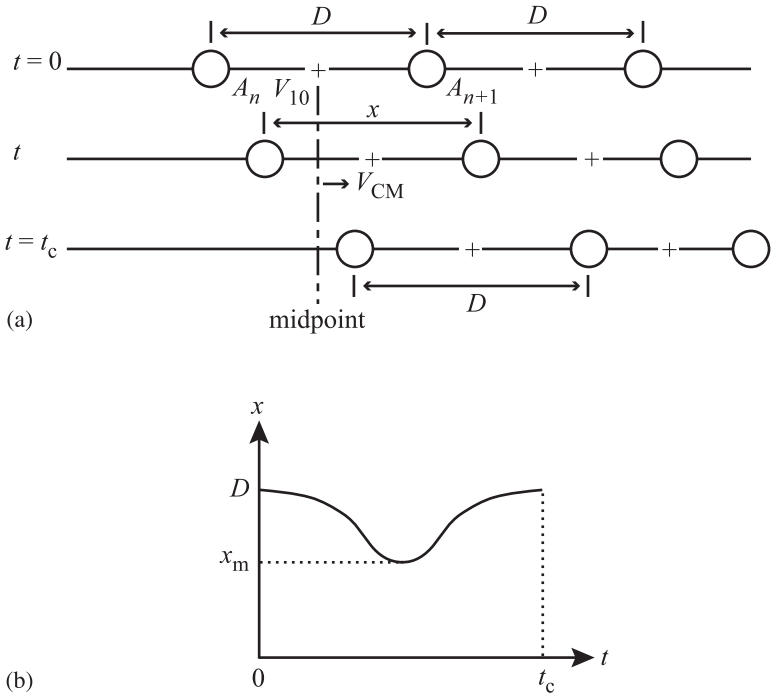

Fig. 2.12. Head-on collisions in a focused chain when the interaction potential acts continuously during the collision. (a) Atom positions during the collision initiated by the atom *on the left*. (b) Separation of atoms A_n and A_{n+1} during the collision (after [5])

of the two particles. Conservation of total energy is given as $E_\mathrm{r} + V(x) = E_{\mathrm{r}0}$, where $V(x)$ is the potential energy at a head-on separation distance of x, $E_{\mathrm{r}0}$ is the relative kinetic energy at infinite (initial) separation, and E_r is the relative kinetic energy at any point. Rewriting the kinetic energy in terms of g gives:

$$\frac{1}{2}\mu g^2 + V(x) = \frac{1}{2}\mu g_0^2$$

and

$$g_0 = v_{10}\ ,$$

where g_0 is the initial speed. This equation should be recognizable from our earlier analysis in Chap. 1, Sect. 1.2.2. Recall that at $x = x_{\min}$, $V(x_{\min}) = 1/2\mu g_0^2$, and for $M_1 = M_2$, then $g_0 = v_{10}$ and $V = E/2$.

We also assume that the interaction energy at the initial separation is $V(D) \ll \frac{1}{2}\mu g_0^2$. The time rate of change of the separation distance is equal to the relative speed:

$$\frac{\mathrm{d}x}{\mathrm{d}t} = -g\ . \tag{2.81}$$

Taking the collision time as twice the time needed to reach the distance of closest approach:

$$t_c = -2\int_D^{x_m} \frac{dx}{g} = -2\int_{V(D)}^{V(x_m)} \frac{dV}{g\,dV/dx}\,, \tag{2.82}$$

where x_m is the distance of closest approach.

Since $V(x) = A\exp(-x/B)$, then

$$\frac{dV}{dx} = -\frac{A}{B}\exp(-x/B) = -\frac{V}{B}\,, \tag{2.83}$$

and:

$$\begin{aligned} g &= \left\{\left[\frac{1}{2}\mu g_0^2 - V(x)\right]\frac{4}{M}\right\}^{1/2} \\ &= \left\{\left[\frac{E}{2} - V\right]\frac{4}{M}\right\}^{1/2} \\ &= 2\left\{\frac{E}{2M} - \frac{V}{M}\right\}^{1/2}\,, \end{aligned} \tag{2.84}$$

where $\mu = M/2$ for like atoms and $1/2\mu g_0^2 = 1/4Mv_{10}^2 = E/2$. Substitution of Eqs. (2.83) and (2.84) into Eq. (2.82) yields:

$$t_c = B\left(\frac{2M}{E}\right)^{1/2}\int_{V(D)}^{E/2} \frac{dV}{V(1-2V/E)^{1/2}} \tag{2.85}$$

$$= 2B\left(\frac{2M}{E}\right)^{1/2}\tanh^{-1}\left[1 - \frac{2V(D)}{E}\right]^{1/2}\,. \tag{2.86}$$

Note that the definition of a hard-sphere radius has been used for the upper limit, i.e., x_m is taken to be $2R(E)$. For $V(D)/E \ll 1$,

$$t_c = B\left(\frac{2M}{E}\right)^{1/2}\ln\left[\frac{2E}{V(D)}\right]\,. \tag{2.87}$$

Since the speed of the center of mass is $\dfrac{v_{10}}{2} = \left(\dfrac{E}{2M}\right)^{1/2}$, the distance moved by the CM during the collision time, t_c, is:

$$x = t_c\left(\frac{E}{2M}\right)^{1/2}\,. \tag{2.88}$$

If $x > D/2$, atom A_n will end up to the right of the initial halfway point and replacement will occur and A_n will occupy the lattice site occupied by atom A_{n+1}. Relating

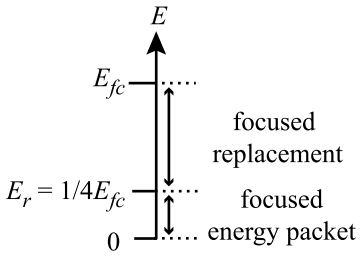

Fig. 2.13. Energy scale for focused energy transfer and focused replacement sequence

the distance x to energy by substituting for t_c from Eq. (2.87) into Eq. (2.88) gives:

$$\frac{x}{B} = \ln\left(\frac{2E_r}{V(D)}\right) . \tag{2.89}$$

For $x = D/2$:

$$\exp\left(\frac{D}{2B}\right) = \frac{2E_r}{A\exp(-D/B)} ,$$

and the replacement energy becomes:

$$E_r = \frac{A}{2}\exp\left(\frac{-D}{2B}\right) . \tag{2.90}$$

According to the above arguments, and comparing to Eq. (2.71), focused replacement is possible when the energy transported in the collision chain satisfies:

$$E > E_r = \frac{1}{2}A\exp\left(\frac{-D}{2B}\right) = \frac{1}{4}E_{fc} . \tag{2.91}$$

Therefore, we get focused replacement, or

$E_{fc}/4 < T < E_{fc}$: focused replacement
$T < E_{fc}/4$: focused momentum/energy packet .

Hence mass transfer can occur when E is between $E_r = E_{fc}/4$ and E_{fc}, which from our previous example is about the same or slightly less than the displacement energy, E_d. Figure 2.13 shows where focusing and replacement collisions fall on the energy spectrum of the PKA.

Assisted Focusing

In our analysis of focusing, we have not accounted for the effects of surrounding atoms or nearest neighbors. Due to their repulsion of the moving atom, they tend to act as a lens and aid in the focusing process. The net result of this assisted focusing is to increase the critical energy for focusing, E_{fc}, rendering focusing more probable. Second, the ring of atoms surrounding a focusing event also tend to dissipate energy by glancing collisions. This effect is augmented by the vibrational motion of the atom rings, which can be increased with temperature. The length of

the replacement chain and the number of collisions in the chain decrease as the temperature increases. The increased motion of the surrounding atoms increases the energy loss from the collision sequence. Other effects that destroy the sequence are alloying elements and defects such as interstitials, vacancies and dislocations. Figure 2.14 shows the number of collisions in a focused chain of initial energy E in room-temperature copper along with the focusing probability. Table 2.3 from Chadderton [18] gives the focusing and replacement energies in various directions in fcc and bcc lattices as modified by surrounding atoms (assisted focusing). Note that in all cases, the focusing energies are larger when the surrounding atoms aid in the focusing process.

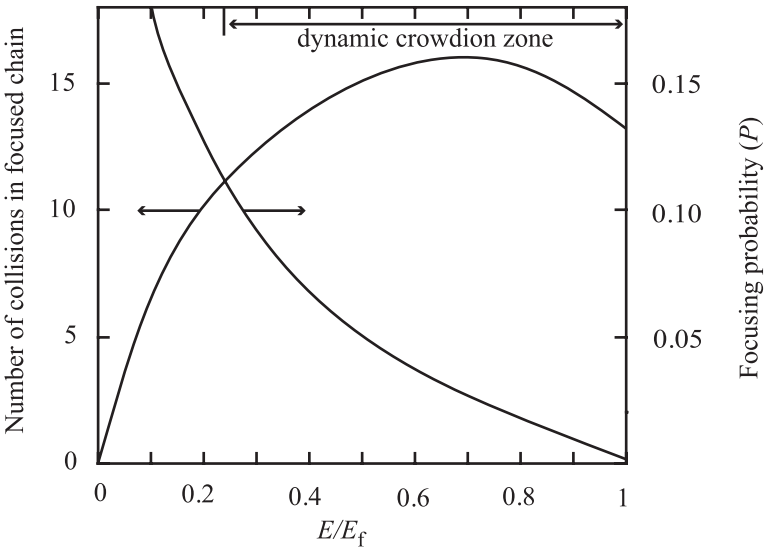

Fig. 2.14. Length and probability of the collision chain in a ⟨110⟩ collision sequence in copper at room temperature (after [5])

Table 2.3a Equations for focusing energies (E_{fc}^{hkl}) in the fcc and bcc lattices (after [18])

⟨*hkl*⟩	Face-centered cubic	Body-centered cubic
⟨100⟩	$\dfrac{A(D^{110})^2}{2D^2}\exp\left(-\dfrac{D^{110}}{4B}\right)^{\uparrow}$	$2A\exp\left(-\dfrac{D^{111}}{B\sqrt{3}}\right)$
⟨110⟩	$2A\exp\left(-\dfrac{D^{110}}{2B}\right)$	$\dfrac{4\sqrt{2}(D^{111})^2A}{15B^2}\exp\left(-\dfrac{D^{111}\sqrt{5}}{2\sqrt{3}B}\right)^{\uparrow\uparrow}$
⟨111⟩	$\left(\dfrac{6}{19}\right)^{1/2}\dfrac{A(D^{110})^2A}{D^2}\exp\left(-\dfrac{D^{110}}{2B}\left(\dfrac{19}{12}\right)^{1/2}\right)^{\uparrow}$	$2A\exp\left(-\dfrac{D^{111}}{2B}\right)$

Table 2.3b Equations for replacement energies (E_r^{hkl}) in the fcc and bcc lattices (after [18])

$\langle hkl \rangle$	Face-centered cubic	Body-centered cubic
$\langle 100 \rangle$	$5A \exp\left(-\frac{D^{110}}{D\sqrt{2}}\right)$	$\frac{A}{2} \exp\left(-\frac{D^{100}}{2B}\right)$
$\langle 110 \rangle$	$\frac{A}{2} \exp\left(-\frac{D^{110}}{2B}\right)$	$3A \exp\left(-\frac{D^{110}}{2B}\right)$
$\langle 111 \rangle$	$4A \exp\left(-\frac{D^{110}}{B\sqrt{3}}\right)$	$2A \exp\left(-\frac{D^{111}}{2B}\right)$

↑ In the (110) plane only
↑↑ Assisted focusing

Channeling

Channeling is the long distance displacement of energetic knock-on atoms down an open direction in the crystal lattice. Figure 2.15a shows a schematic of an atom spiraling down an open channel in a crystal lattice and Fig. 2.15b shows axial and planar channels along specific crystallographic directions in the fcc lattice. The walls of the passageway consist of atomic rows. If the rows surrounding the channel are close-packed, discrete repulsive forces between atoms are "smeared out" and the atom appears to be traveling in a long cylindrical tube with radius R_{ch}. The value of R_{ch} can be determined by equating πR_{ch}^2 with the cross sectional area of the channel. If the amplitude of the lateral oscillations of the moving atom is small compared to R_{ch}, the potential well provided by the channel wall is roughly parabolic in the direction transverse to the channel axis.

The interaction of the moving atom with a channel wall (Fig. 2.16) can be described by a harmonic channel potential:

$$V_{ch}(r) = kr \,, \tag{2.92}$$

where r is the lateral distance from the axis, and k is the force constant which depends on the potential function describing atom–atom repulsion and channel dimension R_{ch}. Using the Born–Mayer potential to describe atom–atom interactions in this energy regime, k becomes:

$$k = \frac{A}{DB}\left(\frac{2\pi R_{ch}}{B}\right) \exp\left(\frac{-R_{ch}}{B}\right) \,, \tag{2.93}$$

where D is the atom spacing in the rows forming the channels. Moving atoms enter the channel with a velocity component along the channel axis (Fig. 2.16) given by:

$$V_{z0} = \left(\frac{2E}{M}\right)^{1/2} \cos\theta_0 \,, \tag{2.94}$$

where $(2E/M)^{1/2} = V_0$. The axial velocity is gradually reduced by inelastic energy loss to the electron cloud. The moving atom undergoes simple harmonic motion in

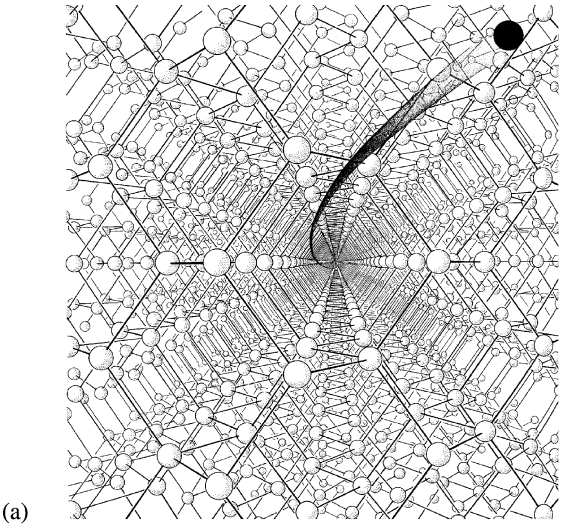

(a)

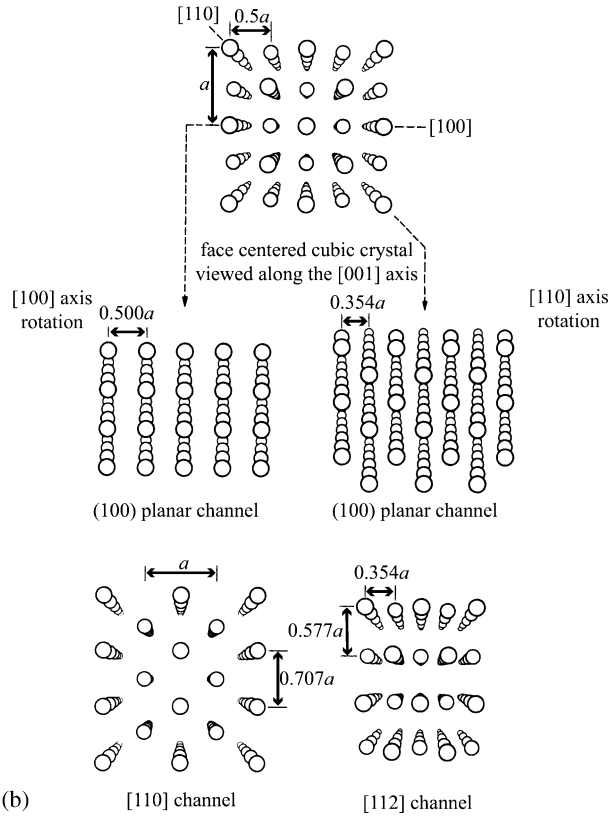

(b)

Fig. 2.15. (a) Schematic of an atom moving in a channel in a crystal lattice (after [19]). (b) Axial and planar channels in the fcc lattice (after [20])

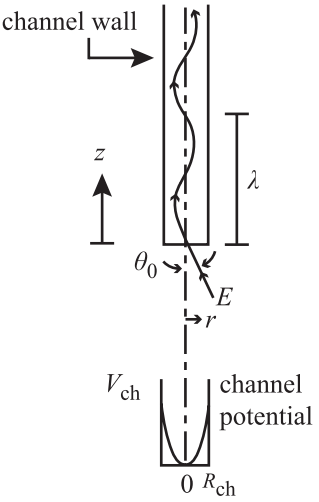

Fig. 2.16. Trajectory of a channeled atom (after [5])

the r direction with period τ given by:

$$\tau = 2\pi \left(\frac{M}{2k}\right)^{1/2} \tag{2.95}$$

and the initial wavelength of the oscillation is equal to $V_{z0}\tau$ for $\theta_0 = 0$ or:

$$\lambda = 2\pi \left(\frac{E}{k}\right)^{1/2} . \tag{2.96}$$

The amplitude of lateral oscillation is determined by the injection angle, θ_0 and the kinetic energy of the injected atom, E. The r component of the atom velocity as it enters the channel is:

$$V_{r0} = \left(\frac{2E}{M}\right)^{1/2} \sin\theta_0 \cong \left(\frac{2E}{M}\right)^{1/2} \theta_0 . \tag{2.97}$$

So the radial component of the kinetic energy is $E\theta_0^2$, which is equal to the potential energy at the transverse amplitude, $kr_{\max}^2$. Equating kinetic and potential energies and solving for $r_{\max}$ gives:

$$r_{\max} = \left(\frac{E}{k}\right)^{1/2} \theta_0 , \tag{2.98}$$

and the trajectory of the channeled atom is:

$$r = \theta_0 \left(\frac{E}{k}\right)^{1/2} \sin\left[\left(\frac{k}{E}\right)^{1/2} Z\right] . \tag{2.99}$$

The critical angle beyond which channeling cannot occur, θ_{ch}, is obtained by equating the transverse amplitude, r_{max}, and the channel radius, R_{ch}:

$$\theta_{ch} = R_{ch}\left(\frac{k}{E}\right)^{1/2} . \tag{2.100}$$

Note that θ_{ch} decreases as E increases, as expected. When the mean free path between collisions is of the order of a few atom spacings, large-angle collisions become probable and channeling dissipates. The channeling probability is difficult to determine since we must knock an atom into the channel, but there are no atoms near the channel axis. The event probably starts with an impact on an atom forming the channel wall. If the entrance angle is small enough, it may begin to channel.

There is no upper limit on energy for channeling. Instead, θ_{ch} just becomes smaller as E increases. The minimum channeling energy occurs when the wavelength is $\sim nD$ or a few atom spacings ($n \sim 2$). Essentially, there develops a resonance between impulses from channel walls and transverse oscillations. The trajectory terminates in a violent collision. Recall that our treatment is only valid if $\lambda \gg D$. Solving for E in Eq. (2.96) and letting $\lambda = 2D$ yields $E_{ch} \sim 0.1\,\mathrm{kD}^2$. For copper, E_{ch} is about 300 eV. E_{ch} is larger for large mass because k increases with mass. Channeling is a high-energy phenomenon and is most significant for light atoms, while focusing is a low-energy phenomenon that is most significant for heavy atoms.

Effect of Focusing and Channeling on Displacements

The probability of a crystal effect is a function of recoil energy. $P(T)$ is used for either P_f or P_{ch}, but since $E_f \sim 100\,\mathrm{eV}$, P_f is quite small. The equation governing cascade effects can be modified to account for crystal effects by modifying Eq. (2.14):

$$\nu(T) = P(T) + [1 - P(T)]\left[\frac{2E_d}{T} + \frac{2}{T}\int_{2E_d}^{T} \nu(\varepsilon)\,\mathrm{d}\varepsilon\right] . \tag{2.101}$$

The first term on the right in Eq. (2.101) represents the lone displaced atom, which results if the PKA is channeled or focused on the first collision. The second term gives the number of displacements created by a PKA that makes an ordinary displacement on the first collision. Assuming $P \neq P(T)$, Eq. (2.101) is differentiated with respect T to yield:

$$T\frac{\mathrm{d}\nu}{\mathrm{d}t} = (1 - 2P)\nu + P . \tag{2.102}$$

Integration gives

$$\nu(T) = \frac{CT^{(1-2P)} - P}{1 - 2P} \tag{2.103}$$

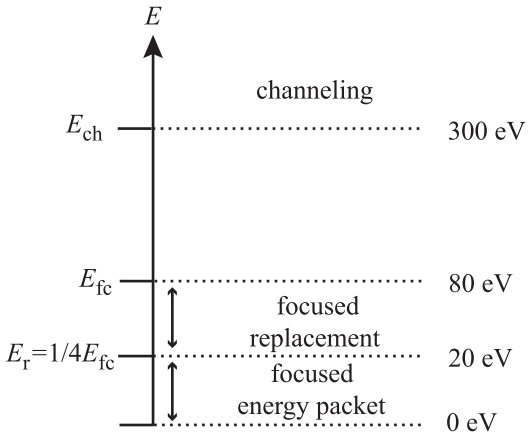

Fig. 2.17. Energy scale showing focused energy transfer, focused replacement sequence and channeling

and the constant C can be found by substitution into Eq. (2.82):

$$C = \frac{1-P}{(2E_{\mathrm{d}})^{(1-2P)}} ,$$

resulting in the final solution:

$$\nu(T) = \frac{1-P}{1-2P}\left(\frac{T}{2E_{\mathrm{d}}}\right)^{(1-2P)} - \frac{P}{1-2P} . \tag{2.104}$$

For small P, $\nu(T)$ can be approximated by:

$$\nu(T) = \left(\frac{T}{2E_{\mathrm{d}}}\right)^{(1-2P)} . \tag{2.105}$$

It should be noted that the most important crystal effect is channeling which is most important at high energies. For example, for $P = 7\%$, a 10 keV PKA in iron produces 100 displacements or about half the amount with $P = 0$. Figure 2.17 shows where channeling occurs on the PKA energy scale. Note that channeling is a high-energy phenomenon and that there is a gap between the replacement energy, below which replacements or focused energy transfer occur, and the channeling energy, above which channeling occurs. Given the K–P model for displacement and the various modifications to the basic model, we now turn to the determination of the number of displaced atoms.

2.3 The Displacement Cross Section

The results of previous sections may now be used to define the displacement cross section as:

$$\sigma_{\mathrm{D}}(E_{\mathrm{i}}) = \int_{\check{T}}^{\hat{T}} \nu(T)\sigma(E_{\mathrm{i}}, Q_j, T)\,\mathrm{d}T , \tag{2.106}$$

where $\nu(T)$ is the number of displacements caused by a PKA of energy T, $\sigma(E_i, Q_j, T)$ is the general form of the energy transfer cross section, and $\check{T}$ and $\hat{T}$ are the minimum and maximum transfer energies. This quantity was first presented in Eq. (2.2) and gives the average number of displacements produced by an incoming neutron of energy E_i. We can apply this expression to the various regimes of scattering in order to determine their individual contributions to the total number of displacements. We will first determine $\sigma_D(E_i)$ for each type of interaction using the basic K–P result and then go back and add in the modifications.

2.3.1 Elastic Scattering

Consider $\sigma_s(E_i, T)$ for elastic scattering. From Eq. (1.19),

$$\sigma_s(E_i, T) = \frac{4\pi}{\gamma E_i}\sigma_s(E_i, \phi) .$$

In the case of isotropic scattering:

$$\sigma_s(E_i, \phi) = \frac{\sigma_s(E_i)}{4\pi} ; \quad \sigma_s(E_i, T) = \frac{\sigma_s(E_i)}{\gamma E_i} ,$$

therefore:

$$\sigma_{Ds}(E_i) = \frac{\sigma_s(E_i)}{\gamma E_i}\int_{E_d}^{\gamma E_i} \nu(T)\,dT . \tag{2.107}$$

Should we wish to consider anisotropic elastic scattering in systems such as fast reactors, the angular dependence of the elastic scattering cross section can be written in a series of Legendre polynomials:

$$\sigma_s(E_i, \phi) = \frac{\sigma_s(E_i)}{4\pi}\sum_{\ell=0}^{\infty} a_\ell(E_i) P_\ell(\cos\phi) , \tag{2.108}$$

where $\sigma_s(E_i)$ is the total elastic scattering cross section for incident neutrons of energy E_i, P_ℓ is the ℓth Legendre polynomial, and values of a_ℓ are the energy-dependent coefficients of the cross section expansion. At neutron energies encountered in thermal or fast reactors, it is sufficient to retain only the first two terms, $\ell = 0$ and $\ell = 1$. Since $P_0 = 1$ and $P_1 = \cos\phi$:

$$\sigma_s(E_i, \phi) = \frac{\sigma_s(E_i)}{4\pi}\left[1 + a_1(E_i)\cos\phi\right] . \tag{2.109}$$

Also, given that $\cos\phi = 1 - 2T/\gamma E_i$, and substituting Eq. (2.109) into Eq. (2.106) gives:

$$\sigma_{Ds}(E_i) = \frac{\sigma_s(E_i)}{\gamma E_i}\int_{E_d}^{\gamma E_i} \nu(T)\left[1 + a_1(E_i)\left(1 - \frac{2T}{\gamma E_i}\right)\right] dT . \tag{2.110}$$

2.3.2 Inelastic Scattering

Since inelastic scattering is isotropic in the center-of-mass system:

$$\sigma_{sj}(E_i, Q_j, \phi) = \frac{\sigma_{sj}(E_i, Q_j)}{4\pi} . \tag{2.111}$$

Equation (1.30) gives the energy transfer cross section for inelastic scattering in the resonance region as:

$$\sigma_{sj}(E_i, Q_j, T) = \frac{\sigma_{sj}(E_i, Q_j)}{\gamma E_i} \left[1 + \frac{Q_i}{E_i}\left(\frac{1+A}{A}\right)\right]^{-1/2} ,$$

so that

$$\sigma_{Dsj}(E_i) = \sum_j \frac{\sigma_{sj}(E_i, Q_j)}{\gamma E_i} \left[1 + \frac{Q_j}{E_i}\left(\frac{1+A}{A}\right)\right]^{-1/2} \int_{\check{T}_j}^{\hat{T}_j} \nu(T)\,dT , \tag{2.112}$$

where the minimum and maximum values of $T(E_i, Q_j, \phi)$ are given by Eq. (1.27) and setting $\cos\phi = -1$ and 1, respectively, gives:

$$\hat{T}_j = \frac{\gamma E_i}{2}\left[1 + \frac{1+A}{2A}\frac{Q_j}{E_i} + \left(1 + \frac{Q_j}{E_i}\frac{1+A}{A}\right)^{1/2}\right]$$

$$\check{T}_j = \frac{\gamma E_i}{2}\left[1 + \frac{1+A}{2A}\frac{Q_j}{E_i} - \left(1 + \frac{Q_j}{E_i}\frac{1+A}{A}\right)^{1/2}\right] .$$

2.3.3 (n, 2n) and (n, γ) Displacements

The displacement cross section for (n,2n) reactions can be written as:

$$\sigma_{D(n,2n)}(E_i) = \int_0^{E_i - E'_m} \sigma_{(n,2n)}(E_i T)\frac{T}{2E_d}\,dT , \tag{2.113}$$

where $\sigma_{(n,2n)}(E_i, T)$ is given by Eq. (1.40).

The displacement cross section due to (n, γ) reactions can be written as:

$$\sigma_{D\gamma}(E_i) = \sigma_\gamma \int_0^{\hat{T}} \frac{T}{2E_d}\,dT . \tag{2.114}$$

However, since we have assumed that the lattice atom recoils with an average energy

$$\overline{T} = \frac{\hat{T}}{2} = \frac{E_\gamma^2}{4(A+1)c^2} ,$$

and that E_γ for a given isotope is either known or can be measured, Eq. (2.114) can be simplified to:

$$\sigma_{D\gamma} = \sigma_\gamma \frac{\overline{T}}{2E_d} = \frac{E_\gamma^2}{8E_d(A+1)c^2} . \tag{2.115}$$

The total displacement cross section due to these forms of neutron interaction then becomes:

$$\begin{aligned}\sigma_{\mathrm{D}}(E_{\mathrm{i}}) =& \sigma_{\mathrm{Ds}}(E_{\mathrm{i}}) + \sigma_{\mathrm{Ds}j}(E_{\mathrm{i}}) + \sigma_{\mathrm{D(n,2n)}}(E_{\mathrm{i}}) + \sigma_{\mathrm{D}\gamma} \\ =& \frac{\sigma_{\mathrm{s}}(E_{\mathrm{i}})}{\gamma E_{\mathrm{i}}} \int_{E_{\mathrm{d}}}^{\gamma E_{\mathrm{i}}} \frac{T}{2E_{\mathrm{d}}} \left[1 + a_1(E_{\mathrm{i}}) \left(1 - \frac{2T}{\gamma E_{\mathrm{i}}}\right)\right] \mathrm{d}T \\ &+ \sum_j \frac{\sigma_{\mathrm{s}j}(E_{\mathrm{i}}, Q_j)}{\gamma E_{\mathrm{i}}} \left[1 + \frac{Q_j}{E_{\mathrm{i}}} \left(\frac{1+A}{A}\right)\right]^{-1/2} \int_{\check{T}_j}^{\hat{T}_j} \frac{T}{2E_{\mathrm{d}}} \mathrm{d}T \\ &+ \int_0^{E_{\mathrm{i}} - E'_{\mathrm{m}}} \sigma_{(\mathrm{n,2n})}(E_{\mathrm{i}}, T) \frac{T}{2E_{\mathrm{d}}} \mathrm{d}T \\ &+ \sigma_\gamma \frac{E_\gamma^2}{8E_{\mathrm{d}}(A+1)c^2} \,, \end{aligned} \tag{2.116}$$

where the terms are for elastic scattering, inelastic scattering in the resonance region, (n,2n) reactions and (n,γ) reactions, respectively.

2.3.4 Modifications to the K–P Model and Total Displacement Cross Section

The displacement cross section can be modified to account for the relaxation of the various assumptions made to the basic K–P model as in Sect. 2.2. These modifications are as follows summarized in Table 2.4. Applying these correction terms to the basic K–P result by consolidating Assumptions 1 and 3 into a single constant C' and using Eq. (2.104) for the effect of crystallinity, transforms Eq. (2.116) to read:

$$\begin{aligned}\sigma_{\mathrm{D}} =& \frac{\sigma_{\mathrm{s}}(E_{\mathrm{i}})}{\gamma E_{\mathrm{i}}} \int_{E_{\mathrm{d}}}^{\gamma E_{\mathrm{i}}} \left[\frac{1-P}{1-2P} \left(C'\xi(T) \frac{T}{2E_{\mathrm{d}}}\right)^{(1-2P)} - \frac{P}{1-2P}\right] \\ &\times \left[1 + a_1(E_{\mathrm{i}}) \left(1 - \frac{2T}{\gamma E_{\mathrm{i}}}\right)\right] \mathrm{d}T \\ &+ \sum_j \frac{\sigma_{\mathrm{s}j}(E_{\mathrm{i}}, Q_j)}{\gamma E_{\mathrm{i}}} \left[1 + \frac{Q_j}{E_{\mathrm{i}}} \left(\frac{1+A}{A}\right)\right]^{-1/2} \\ &\times \int_{\check{T}_j}^{\hat{T}_j} \left[\frac{1-P}{1-2P} \left(C'\xi(T) \frac{T}{2E_{\mathrm{d}}}\right)^{(1-2P)} - \frac{P}{1-2P}\right] \mathrm{d}T \\ &+ \int_0^{E_{\mathrm{i}} - E'_{\mathrm{m}}} \sigma_{(\mathrm{n,2n})}(E_{\mathrm{i}}, T) \left[\frac{1-P}{1-2P} \left(C'\xi(T) \frac{T}{2E_{\mathrm{d}}}\right)^{(1-2P)} - \frac{P}{1-2P}\right] \mathrm{d}T \\ &+ \sigma_\gamma \left[\frac{1-P}{1-2P} \left(C'\xi(T) \frac{E_\gamma^2}{8E_{\mathrm{d}}(A+1)c^2}\right)^{1-2P} - \frac{P}{1-2P}\right] . \end{aligned} \tag{2.117}$$

Table 2.4. Modifications to the displacement cross section

Assumption	Correction to $\nu(T)$	Equation in text
3: Loss of E_d	$0.56\left(1+\dfrac{T}{2E_\mathrm{d}}\right)$	Eq. (2.31)
4: Electronic energy loss cut-off	$\xi(T)\left(\dfrac{T}{2E_\mathrm{d}}\right)$	Eq. (2.50)
5: Realistic energy transfer cross section	$C\dfrac{T}{2E_\mathrm{d}}\,, \quad 0.52 < C \leq 1.22$	Eqs. (2.33), (2.39)
6: Crystallinity	$\dfrac{1-P}{1-2P}\left(\dfrac{T}{2E_\mathrm{d}}\right)^{(1-2P)} - \dfrac{P}{1-2P}$	Eq. (2.104)
	$\sim \left(\dfrac{T}{2E_\mathrm{d}}\right)^{(1-2P)}$	Eq. (2.105)

Using the more simplified expression for the effect of crystallinity Eq. (2.104) reduces Eq. (2.117) to:

$$\begin{aligned}\sigma_\mathrm{D} = {} & \frac{\sigma_\mathrm{s}(E_\mathrm{i})}{\gamma E_\mathrm{i}} \int_{E_\mathrm{d}}^{\gamma E_\mathrm{i}} \left[\left(C'\xi(T)\frac{T}{2E_\mathrm{d}}\right)^{(1-2P)}\right]\left[1+a_1(E_\mathrm{i})\left(1-\frac{2T}{\gamma E_\mathrm{i}}\right)\right]\mathrm{d}T \\ & + \sum_j \frac{\sigma_{\mathrm{s}j}(E_\mathrm{i},Q_j)}{\gamma E_\mathrm{i}}\left[1+\frac{Q_j}{E_\mathrm{i}}\left(\frac{1+A}{A}\right)\right]^{-1/2} \int_{\check{T}_j}^{\hat{T}_j}\left(C'\xi(T)\frac{T}{2E_\mathrm{d}}\right)^{(1-2P)}\mathrm{d}T \\ & + \int_0^{E_\mathrm{i}-E'_\mathrm{m}} \sigma_{(\mathrm{n},2\mathrm{n})}(E_\mathrm{i},T)\left(C'\xi(T)\frac{T}{2E_\mathrm{d}}\right)^{(1-2P)}\mathrm{d}T \\ & + \sigma_\gamma\left(C'\xi(T)\frac{E_\gamma^2}{8E_\mathrm{d}(A+1)c^2}\right)^{1-2P}\,, \end{aligned} \tag{2.118}$$

or,

$$\sigma_\mathrm{D} = \sigma_{\mathrm{Ds}} + \sigma_{\mathrm{Di}} + \sigma_{\mathrm{D(n,2n)}} + \sigma_{\mathrm{D}\gamma}\,. \tag{2.119}$$

The displacement cross section for stainless steel was calculated by Doran [21] using the energy partition theory of Lindhard and is shown in Fig. 2.18.

2.4 Displacement Rates

Recall that the displacement rate was given in Eq. (2.1) as:

$$R = \int_{\check{T}}^{\hat{T}} N\phi(E_\mathrm{i})\sigma_\mathrm{D}(E_\mathrm{i})\,\mathrm{d}E_\mathrm{i}\,.$$

This is the displacement rate density or total number of displacements per unit volume per unit time [#/cm^3 s]. To get a rough estimate of the order of magnitude of

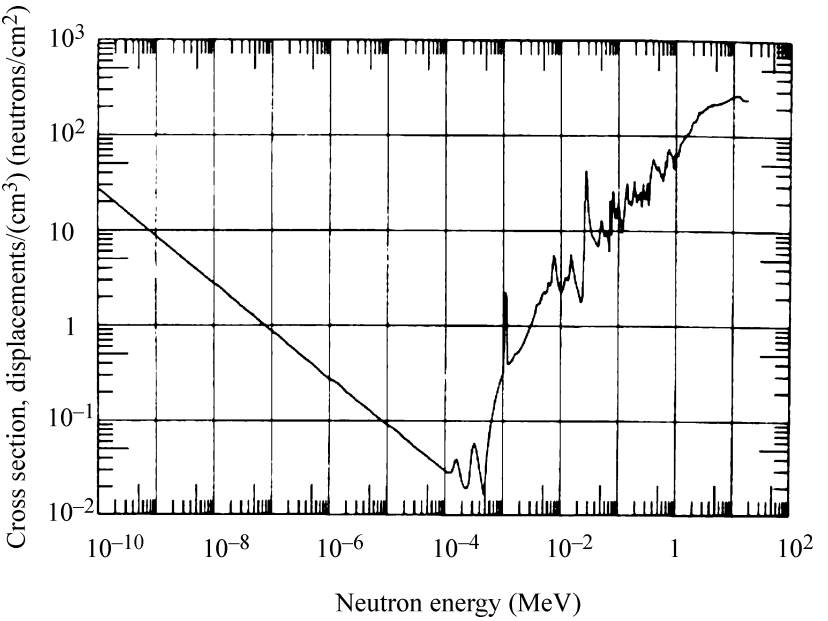

Fig. 2.18. The displacement cross section for stainless steel based on a Lindhard model and ENDF/B scattering cross sections (after [21])

this number, let us simplify the displacement cross sections as follows. Neglecting (n,2n) and (n,γ) contributions to displacements, all modifications to the simple K–P displacement model (i.e., using $\nu(T) = T/2E_\mathrm{d}$), and neglecting E_d relative to E_i, the displacement cross section due to elastic and inelastically scattered neutrons only becomes:

$$\begin{aligned}\sigma_\mathrm{D}(E_\mathrm{i}) = {} & \frac{\sigma_\mathrm{s}(E_\mathrm{i})}{\gamma E_\mathrm{i}} \int_{E_\mathrm{d}}^{\gamma E_\mathrm{i}} \frac{T}{2E_\mathrm{d}} \left[1 + a_1(E_\mathrm{i}) \left(1 - \frac{2T}{\gamma E_\mathrm{i}}\right)\right] \mathrm{d}T \\ & + \sum_j \frac{\sigma_{\mathrm{s}j}(E_\mathrm{i}, Q_j)}{\gamma E_\mathrm{i}} \left[1 + \frac{Q_j}{E_\mathrm{i}} \left(\frac{1+A}{A}\right)\right]^{-1/2} \int_{\check{T}_j}^{\hat{T}_j} \frac{T}{2E_\mathrm{d}} \mathrm{d}T \,.\end{aligned} \tag{2.120}$$

Assuming that elastic scattering is isotropic ($a_1 = 0$), neglecting inelastic scattering and integrating between the limits E_d and γE_i gives:

$$\sigma_\mathrm{D}(E_\mathrm{i}) = \frac{\sigma_\mathrm{s}(E_\mathrm{i})}{\gamma E_\mathrm{i}} \int_{E_\mathrm{d}}^{\gamma E_\mathrm{i}} \frac{T}{2E_\mathrm{d}} \mathrm{d}T \,, \tag{2.121}$$

and if $\gamma E_\mathrm{i} > E_\mathrm{c}$, then:

$$\begin{aligned}\sigma_\mathrm{D}(E_\mathrm{i}) &= \frac{\sigma_\mathrm{s}(E_\mathrm{i})}{\gamma E_\mathrm{i}} \left[\int_{E_\mathrm{d}}^{2E_\mathrm{d}} \mathrm{d}T + \int_{2E_\mathrm{d}}^{E_\mathrm{c}} \frac{T}{2E_\mathrm{d}} \mathrm{d}T + \int_{E_\mathrm{c}}^{\gamma E_\mathrm{i}} \frac{E_\mathrm{c}}{2E_\mathrm{d}} \mathrm{d}T\right] \\ &= \frac{\sigma_\mathrm{s}(E_\mathrm{i})}{2\gamma E_\mathrm{i} E_\mathrm{d}} \left[E_\mathrm{d} + \frac{(\gamma E_\mathrm{i})^2}{2} - \frac{E_\mathrm{d}^2}{2} + \gamma E_\mathrm{i} E_\mathrm{c} - E_\mathrm{c}^2\right] \,.\end{aligned} \tag{2.122}$$

If we choose $\gamma E_\mathrm{i} \sim E_\mathrm{c}$ and neglecting terms in E_d or E_d^2 gives:

$$\sigma_\mathrm{D}(E_\mathrm{i}) \approx \left(\frac{\gamma E_\mathrm{i}}{4E_\mathrm{d}}\right) \sigma_\mathrm{s}(E_\mathrm{i}) \,, \tag{2.123}$$

and Eq. (2.2) becomes:

$$R = \frac{N\gamma}{4E_\mathrm{d}} \int_{E_\mathrm{d}/\gamma}^{\infty} \sigma_\mathrm{s}(E_\mathrm{i}) E_\mathrm{i} \phi(E_\mathrm{i}) \,\mathrm{d}E_\mathrm{i} \tag{2.124}$$

$$= N\sigma_\mathrm{s} \left(\frac{\gamma \bar{E}_\mathrm{i}}{4E_\mathrm{d}}\right) \Phi \,, \tag{2.125}$$

where $\bar{E}_\mathrm{i}$ is an average neutron energy and Φ is the total neutron flux above energy E_d/γ, and the term in brackets is the number of displacements (Frenkel pairs) produced per neutron. The validity of assuming isotropic scattering and neglecting inelastic scattering is shown in Figs. 2.19 and 2.20. Essentially, both approximations are reasonable at energies below one to a few MeV.

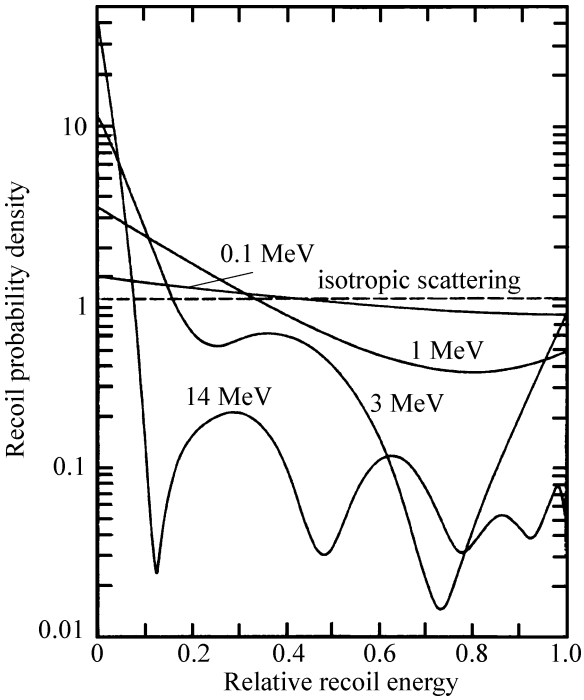

Fig. 2.19. Recoil energy spectra from the elastic scattering of fast neutrons using data from ENDF/B files (after [22])

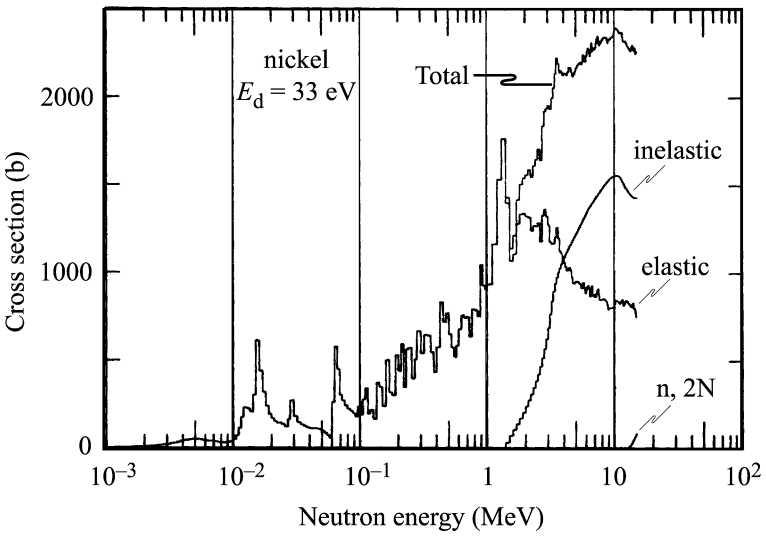

Fig. 2.20. Displacement cross section for nickel showing the elastic and inelastic components (after [21])

Example 2.1. Neutron irradiation of iron. As an example, let us look at the damage caused by 0.5 MeV neutrons in Fe in a fast flux that may be representative of the core of a fast reactor:

$$N = 0.85 \times 10^{23}\,\text{atoms/cm}^3$$
$$\sigma_s = 3 \times 10^{-24}\,\text{cm}^2$$
$$\Phi = 10^{15}\,\text{neutrons cm}^{-2}\,\text{s}^{-1}$$
$$\frac{\gamma E_i}{4E_d} = 350\ \text{displaced atoms/neutron}$$

R is 9×10^{16} displaced atoms per cm^3 per second, or dividing R by N gives $\sim 10^{-6}$ dpa/s. This is equivalent to each atom being displaced from a normal lattice site once every 12 days.

A second example can be worked for the displacement rate in the aluminum fuel plates in an MTR-type thermal neutron research reactor. In this case, we have:

$$E_i \sim 0.5\,\text{MeV}$$
$$N = 0.6 \times 10^{23}\,\text{atoms/cm}^3$$
$$\sigma_s = 3 \times 10^{-24}\,\text{cm}^2$$
$$\Phi = 3 \times 10^{13}\,\text{neutrons cm}^{-2}\,\text{s}^{-1}$$

$$\frac{\gamma E_{\mathrm{i}}}{4E_{\mathrm{d}}} = 690 \text{ displaced atoms/neutron}$$

R is 4×10^{15} displaced atoms per cm^3 per second, or dividing R by N gives $\sim 7 \times 10^{-8}$ dpa/s, or about 2/yr. Note that even though the number of displacements per neutron is almost a factor of 2 higher in Al than in Fe, the damage rate is significantly lower because of the much lower fast flux in this type of reactor.

2.5 Correlation of Property Changes and Irradiation Dose

The ultimate objective of the calculation of R_{d} is to provide a prediction of the extent of change of a particular property of the material under irradiation. The mechanical property may be yield strength, swelling, degree of embrittlement, etc. Recall in the Introduction that the determination of the number of displaced atoms was motivated by the inability of particle fluence to account for property changes (see Fig. I.1 in the Introduction). While an improvement over units of exposure such as neutron fluence, displacement rate alone cannot alone account for the macroscopic changes observed, and a semi-empirical method of correlating damage with macroscopic property changes has evolved known as the damage function method. In this method the atom displacement rate is replaced with the change in some macroscopic property after a time t of irradiation. The displacement cross section is replaced by the damage function for the particular mechanical property, $G_{\mathrm{i}}(E)$, hence:

$$\Delta P_{ij} = \int \int G_{\mathrm{i}}(E)\phi_j(E,t)\,\mathrm{d}E\,\mathrm{d}t \ , \tag{2.126}$$

where ΔP_{ij} is the change in the property labeled by the index i, during an irradiation time of t and in a neutron flux where $\phi_j(E,t)$ is the jth neutron differential spectrum. Assuming energy-time separability, $\phi_j(E,t) = \phi_j(E)t$, then Eq. (2.126) can be rewritten as:

$$\Delta P_{ij}^{(k)} = t \cdot \int G_{\mathrm{i}}^{(k)}(E)\phi_j(E)\,\mathrm{d}E \ , \tag{2.127}$$

where the superscript refers to the kth cycle of iteration.

The objective is to deduce a single function $G_{\mathrm{i}}(E)$ from a set of measured ΔP_{i} values. Given $\Delta P_{ij}^{(k)}$ and $\phi_j(E)$ as input along with an initial approximation of $G_{\mathrm{i}}(E)$ or $G_{\mathrm{i}}^{(0)}(E)$, a computer code is used to generate iterative solutions $G_{\mathrm{i}}^{(k)}(E)$. An appropriate solution is obtained when the standard deviation of the ratios of all measured-to-calculated values $\Delta P_{ij}/\Delta P_{ij}^{(k)}$ reaches a lower value that is consistent with experimental uncertainties. As it turns out, the resultant damage function is

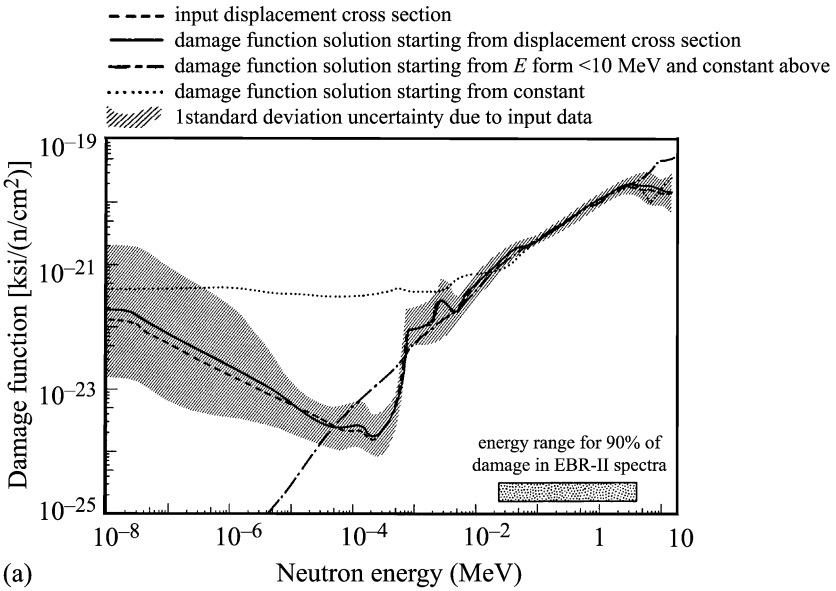

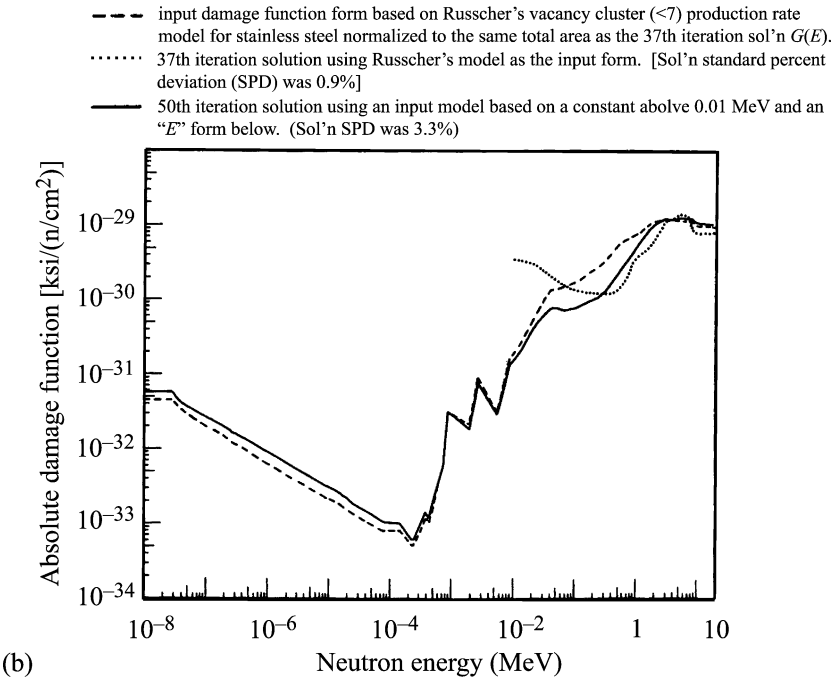

Fig. 2.21. (a) A 60 ksi yield strength damage function for 304 stainless steel irradiated and tested at 480 °C (after [23]). (b) Damage function for a $2.0 \times 10^{-8}\,\mathrm{psi}^{-1}\bar{\varepsilon}/\bar{\sigma}$ property change for stainless steel (after [24])

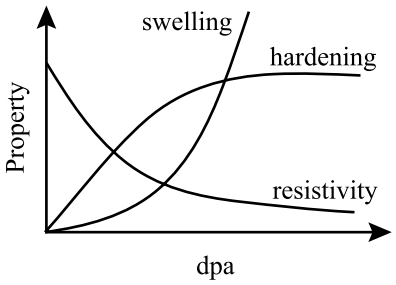

Fig. 2.22. Dose dependence of swelling, resistivity and radiation-induced segregation

highly sensitive to the initial approximation as shown in Fig. 2.21. But note that since the shape of $G_{\mathrm{i}}(E)$ is the same as the displacement function, it is clear that they are related. However, this result tells us that we cannot fully understand radiation effects by only calculating the number of displaced atoms. We cannot treat radiation effects as a black box. Rather, in order to understand the effect of the damage on the properties of the material, we must understand the fate of these defects after they are formed. This realization is reinforced by the property dependence on dose shown in Fig. 2.22. Note that for the three property changes, resistivity, radiation-induced segregation and hardening, the functional dependence on dose is strikingly different between them. While property change certainly relates to displacement damage, the nature of the change is not uniform but varies considerably depending on the property measured. The next chapter explores the spatial and temporal distribution of radiation damage. But before we examine the damage zone in detail, let us complete our picture of the production of displacements by addressing the damage created by charged particles such as ions and electrons.

2.6 Displacements from Charged Particle Irradiation

Displacements from charged particles differ from those due to neutrons because as they travel through the lattice, they lose energy via electronic excitation in addition to via elastic collisions. Figure 2.23 shows the trade-off in energy loss mechanism dominance with energy in the energy range of relevance for ion–solid interaction, and Fig. 2.24 shows the residual ion energy as a function of ion penetration depth. Note that electronic stopping will dominate at short depths, but elastic collisions

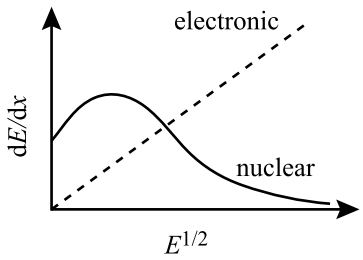

Fig. 2.23. Variation in nuclear and electronic stopping powers over the energy range of relevance to ion–solid interactions

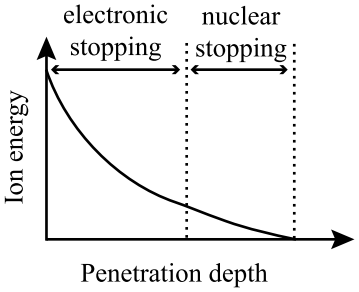

Fig. 2.24. Residual range of an ion incident on a target and the regimes of electronic and nuclear stopping dominance

will dominate near the end of range. An expression for the number of displacements from a charged particle can be derived from the analysis of energy lost from the PKA by electronic excitation given in Sect. 2.2.3 and described by Eq. (2.40) through Eq. (2.49). Equation (2.44) describes the loss of energy to both atoms and electrons in the target by the PKA. We can revisit this analysis assuming that the particle we are tracking is the incident ion. As was done in Eq. (2.45), we can expand the terms for $\nu(T-\varepsilon_\mathrm{a})$ and $\nu(T-\varepsilon_\mathrm{e})$ in a Taylor series and truncate the series after the second term, giving:

$$\begin{aligned}\nu(T-\varepsilon_\mathrm{a}) &= \nu(T) - \frac{\mathrm{d}\nu}{\mathrm{d}T}\varepsilon_\mathrm{a}\,,\\ \nu(T-\varepsilon_\mathrm{e}) &= \nu(T) - \frac{\mathrm{d}\nu}{\mathrm{d}T}\varepsilon_\mathrm{e}\,,\end{aligned} \tag{2.128}$$

and the integrals involving the terms $\nu(T-\varepsilon_\mathrm{a})$ and $\nu(T-\varepsilon_\mathrm{e})$ can both be written in the general form:

$$\begin{aligned}\int_0^{\varepsilon_\mathrm{max}} \nu(T-\varepsilon)\sigma(T,\varepsilon)\,\mathrm{d}\varepsilon &= \nu(T)\int_0^{\varepsilon_\mathrm{max}} \sigma(T,\varepsilon)\,\mathrm{d}\varepsilon - \frac{\mathrm{d}\nu}{\mathrm{d}T}\int_0^{\varepsilon_\mathrm{max}} \varepsilon\sigma(T,\varepsilon)\,\mathrm{d}\varepsilon\\ &= \nu(T)\sigma(T) - \frac{\mathrm{d}\nu(T)}{\mathrm{d}T}S(T)\,.\end{aligned} \tag{2.129}$$

Since in this treatment, the ion is the incoming projectile, we will re-write Eq. (2.129) using our established convention that the incoming particle is of energy E_i and it transfers energy T to the target atoms and electrons, and the maximum energy transfer is $\hat{T}$:

$$\begin{aligned}\int_0^{\hat{T}} \nu(E_\mathrm{i}-T)\sigma(E_\mathrm{i},T)\,\mathrm{d}T &= \nu(E_\mathrm{i})\int_0^{\hat{T}} \sigma(E_\mathrm{i},T)\,\mathrm{d}T - \frac{\mathrm{d}\nu}{\mathrm{d}E}\int_0^{\hat{T}} T\sigma(E_\mathrm{i},T)\,\mathrm{d}T\\ &= \nu(E_\mathrm{i})\sigma(E_\mathrm{i}) - \frac{\mathrm{d}\nu(E_\mathrm{i})}{\mathrm{d}E}S(E_\mathrm{i})\,,\end{aligned} \tag{2.130}$$

where Eq. (1.79) is used to transform the integral of the differential energy transfer cross section, $\sigma(E_\mathrm{i},T)$ to the total collision cross section $\sigma(E_\mathrm{i})$, and Eq. (1.129) is used to transform the integral of $T\sigma(E_\mathrm{i},T)$ into the stopping cross section $S(E_\mathrm{i})$.

Applying the results of Eqs. (2.129) and (2.130) into Eq. (2.44) gives:

$$\mathrm{d}\nu(E_\mathrm{i}) = \frac{\mathrm{d}E}{S(E_\mathrm{i})}\int_0^{\hat{T}} \nu(T)\sigma(E_\mathrm{i},T)\,\mathrm{d}T\ . \tag{2.131}$$

Since we are concerned with the total number of displacements over the entire range of the ion rather than the specific number of displacements over a distance $\mathrm{d}x$ of the sample, we can integrate Eq. (2.131) over the entire range of ion energy loss to obtain the number of displacements resulting from an incident ion with initial energy E_i:

$$\begin{aligned}\nu(E_\mathrm{i}) &= \int_0^{E_\mathrm{i}} \frac{\mathrm{d}E'}{S(E')}\int_{E_\mathrm{d}}^{\hat{T}} \nu(T)\sigma(E',T)\,\mathrm{d}T \\ &= \int_0^{E_\mathrm{i}} \sigma_\mathrm{d}(E')\frac{\mathrm{d}E'}{S(E')}\ ,\end{aligned} \tag{2.132}$$

and

$$\int_{E_\mathrm{d}}^{\hat{T}} \nu(T)\sigma(E',T)\,\mathrm{d}T \equiv \sigma_\mathrm{d}(E')\ , \tag{2.133}$$

where $E' = E'(x)$ is the ion energy as a function of the traveled path length x as the ion travels down to zero energy. We can work a simple example using an approximation to the treatment given above. We are interested in the number of collisions made by an ion as it passes through a solid. We will take I as the ion flux in units of ions/cm^2 and we can write the number of collisions per second in a volume element of unit cross sectional area and thickness $\mathrm{d}x$ which transfer energy in the range $(T, \mathrm{d}T)$ to atoms of this element as:

$$NI\sigma(E,T)\,\mathrm{d}x\ . \tag{2.134}$$

The number of collisions per unit volume per unit time which transfer energy in $(T, \mathrm{d}T)$ at depth x is $NI\sigma(E,T)$ [collisions/cm^3 s]. The number of displaced atoms for each collision that produces a PKA of energy T is $\nu(T)$. Therefore, the production rate of displaced atoms at depth x is:

$$R_\mathrm{d}(x) = NI\int_{E_\mathrm{d}}^{\gamma E} \sigma(E,T)\nu(T)\,\mathrm{d}T \quad [\text{displacements/cm}^3\,\text{s}]\ . \tag{2.135}$$

(Note that we have not accounted for the fact that I is a function of x (or E) and that $I(x) \neq I_0$.) E is a function of x since the ion slows down by loss of energy to the electrons of the target. The functional form of $E(x)$ can be estimated using $\mathrm{d}E/\mathrm{d}x = kE^{1/2}$ as:

$$E(x) = [(E_\mathrm{i})^{1/2} - 1/2kx]^2\ , \tag{2.136}$$

where E_i is the initial energy of the ion when it strikes the target. The number of displaced atoms/atom/s is $R_\mathrm{d}(x)/N$ and the $\dfrac{\text{dpa}}{(\text{ions/cm}^2)}$ at a depth x is $R_\mathrm{d}(x)/NI$.

We will assume that $\sigma(E,T)$ can be described by Rutherford scattering and using the Lindhard treatment for $\nu(T)$ from the K–P model, and assuming $\xi = 0.5$ gives:

$$\begin{aligned}\frac{R_\mathrm{d}}{NI} &= \int_{E_\mathrm{d}}^{\gamma E_\mathrm{i}} \frac{1}{2}\frac{\pi Z_1^2 Z_2^2 \varepsilon^4}{4}\left(\frac{M+M_\mathrm{i}}{M}\right)^2 \frac{1}{E_\mathrm{i}}\frac{4M_\mathrm{i}M}{(M+M_\mathrm{i})^2}\frac{1}{T^2}\frac{T}{2E_\mathrm{d}}\,\mathrm{d}T \\ &= \frac{\pi Z_1^2 Z_2^2 \varepsilon^4}{4E_\mathrm{i}E_\mathrm{d}}\left(\frac{M_\mathrm{i}}{M}\right)\ln\frac{\gamma E_\mathrm{i}}{E_\mathrm{d}}\,\frac{\mathrm{dpa}}{\mathrm{ion/cm^2}}\,.\end{aligned} \tag{2.137}$$

Applying this result to 0.5 MeV protons in iron gives $\sim 10^{-18}\,\mathrm{dpa/(ions/cm^2)}$ at the surface. 20 MeV C^+ ions incident on nickel produce $\sim 3\times10^{-18}\,\mathrm{dpa/(ions/cm^2)}$ at the surface, but 50 times this amount at the damage peak. These values can be compared to the damage rate from 0.5 MeV neutrons in iron:

$$\begin{aligned}\frac{R_\mathrm{d}}{N\phi} &= \left(\frac{\gamma E_\mathrm{i}}{4E_\mathrm{d}}\right)\sigma_\mathrm{s} \\ &= 350\times 3\times10^{-24} \\ &= 1\times10^{-21}\,\frac{\mathrm{displacements}}{\mathrm{n/cm^2\,s}}\,.\end{aligned} \tag{2.138}$$

Comparing 0.5 MeV neutrons to 20 MeV C^+ ions shows that over their range C^+ ions produce 3000 times more displacements than do neutrons. Figure 2.25 com-

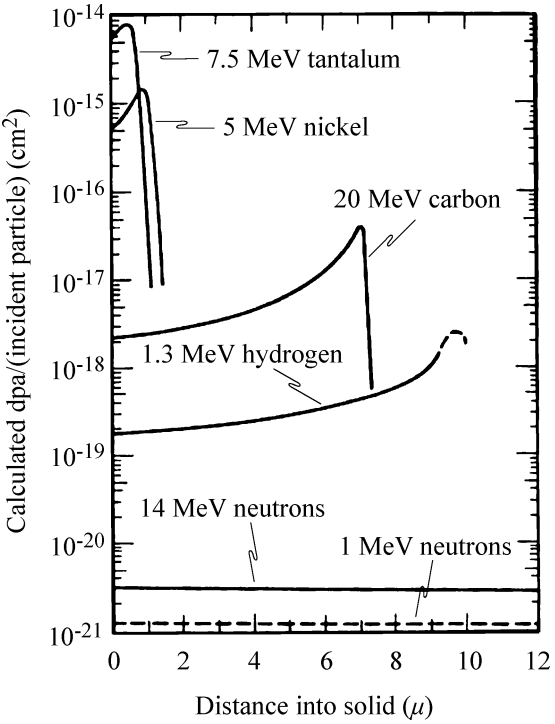

Fig. 2.25. Displacement-damage effectiveness for various energetic particles in nickel (after [25])

pares the displacement rates as a function of penetration depth for ions of various mass and energy. As expected, for the same energy, ions of heavier mass deposit their energy over a shorter distance resulting in higher damage rates. Note that due to the large collision mean free path of a neutron as compared to an ion, the neutron damage energy is low and constant over distances of millimeters.

Nomenclature

a	Lattice constant
a_0	Bohr radius of the hydrogen atom
A	Atomic mass
A	Pre-exponential constant in Born–Mayer relation, Eq. (1.47)
B	Spacing between barrier atoms in crystal lattice
B	Constant in exponent in Born–Mayer relation, Eq. (1.47)
c	Speed of light
D	Nearest neighbor spacing between atoms
E_c	Cut-off energy; critical energy for focusing
E_ch	Critical energy for channeling
E_fc	Critical focusing energy
E_d	Displacement energy
E_D	Damage energy
E_i	Projectile energy
E_r	Critical energy for replacement collisions; relative kinetic energy
E_s	Sublimation energy
E_γ	Gamma ray energy
$E_\mathrm{i,}$	Incoming particle energy
E'_m	Kinetic energy of incoming particle in CM system
E''_m	Energy of neutron after (n, 2n) reaction
E^*	Saddle point energy
E_eq	Energy of atom in equilibrium lattice site
f	Focusing parameter
g	Relative speed $v_1 - v_2$
G	Damage function
$\bar{I}$	Excitation-ionization level
k	Force constant; constant in the electronic energy loss term, $kE^{1/2}$
m	Mass of incoming particle; $1/\mathrm{s}$
m_e	Mass of the electron
M_1	Mass of projectile
M_2	Mass of target
N	Atom number density
$p, p_\mathrm{e}, p_\mathrm{a}$	Probability, refers to electron, refers to atom
P_ch	Channeling probability
P_d	Displacement probability
P_f	Focusing probability

Q	Excitation energy of nucleus
r_{eq}	Equilibrium spacing between atoms
$r_{\max}$	Transverse amplitude of channeled atom
R	Atomic radius
R_{ch}	Radius of channel
R_{d}	Displacement rate [#/cm^3 s]
S	Exponent in the power law approximation
$S, S_{\mathrm{e}}, S_{\mathrm{n}}$	Stopping power; electronic; nuclear
t_{c}	Collision time
T	Energy transferred in collision
$\check{T}$	Minimum energy transferred
$\hat{T}$	Maximum energy transferred
$\bar{T}$	Average energy transferred
T_{ℓ}	Energy transferred to target atom after (n,2n) reaction
U	Energy per atom in a crystal
V	Energy per atom in a crystal
$V(r)$	Potential energy
ν	Specific volume of the atom
V_{CM}	Velocity of CM in lab system
v_1	Velocity of projectile in lab system
v_2	Velocity of target in lab system
V_{CM}	Velocity of center of mass
Y	Distance to atom barrier
z	Impact parameter
Z	Atomic number

β	Compressibility
ε	Secondary atom knock-on energy; unit charge Eq. (2.52)
$\varepsilon_{\mathrm{eq}}$	Energy of atom in a normal lattice site
ε	Reduced PKA energy
ε^*	Energy of atom at saddle point
ϕ, Φ	Neutron flux
γ	$4M_1M_2/(M_1+M_2)^2$
η	Energy lost to electronic excitation in the NRT model
κ	Displacement efficiency
μ	Reduced mass
ν	specific volume of an atom
$\nu(T)$	Displacement function
θ	Scattering angle in lab system
θ_{c}	Critical focusing angle
θ_{ch}	Critical channeling angle
$\sigma(E_{\mathrm{i}})$	Total atomic collision cross section
$\sigma(E_{\mathrm{i}}, T)$	Differential energy transfer cross section
σ_{D}	Displacement cross section
σ_{s}	Scattering cross section

σ_{sj}	Inelastic scattering cross section for the jth resonance
$\sigma_{(n,2n)}$	Cross section for (n,2n) reactions
σ_γ	Cross section for (n,γ) reactions
τ	Period for oscillation for a channeled atom
ξ	Damage energy efficiency, Eq. (2.50)

Problems

2.1 a) Using the simple K–P model and assuming only elastic, isotropic scattering, calculate the number of displacements per atom (dpa) in nickel subjected to a fast neutron (2 MeV) fluence of $10^{22}\,\mathrm{n/cm^2}$.
b) Using the relativistic expression for the electron–atom energy transfer, calculate the minimum electron energy required to displace an atom in (i) Al and (ii) W.

2.2 In a (n, 2n) reaction, a second neutron can only be emitted if the residual excitation of the nucleus after emission of the first neutron exceeds the binding energy of a neutron in the mass M nuclide. The recoil energy after emission of the first neutron is taken to be the average value ($\cos\phi = 0$). Write an expression for the recoil energy following the second emission.

2.3 An ^{56}Fe nucleus undergoes an (n,γ) reaction resulting in the release of a single 7 MeV gamma ray, on average. If a steel component is located in a reactor where the peak thermal flux is $1\times10^{14}\,\mathrm{n/cm^2}$ and the thermal/fast flux ratio is one (where $E_{ave}^{fast} \geq 1\,\mathrm{MeV}$), determine the relative displacement rates by fast neutrons, recoil nuclei and gamma rays which undergo Compton scattering. Assume $\sigma_{(n,\gamma)} \sim 4b$, $\sigma_s \sim 3b$.

2.4 A slab of iron is exposed to a 20 MeV gamma source.
a) What is the most probable interaction between the gamma and the electrons in the Fe?
b) Assume the reaction you chose in part (a) occurs. Can this lead to the displacement of an Fe atom if the displacement energy is 40 eV?

2.5 A thermal neutron causes the following reaction

$$^{27}\mathrm{Al} + n \rightarrow {}^{28}\mathrm{Al} + \gamma\,.$$

The gamma energy is 1.1 keV. The gamma will interact with lattice electrons. What is the most probable event? For this event, what is the maximum energy transferred? Does the resultant electron have enough energy to displace an aluminum atom (assume the displacement energy is 25 eV). Can the recoil Al atom displace another aluminum atom?

2.6 The (n,γ) reaction in ^{56}Fe releases a prompt gamma ray of $E_\gamma = 7\,\mathrm{MeV}$.
a) What is the recoil energy of the ^{57}Fe product nucleus?
b) Determine the number of displaced atoms per ^{57}Fe recoil assuming $E_d = 40\,\mathrm{eV}$.
c) If the thermal component of the neutron flux in a fast reactor is $10^{13}\,\mathrm{n/cm^2\,s}$ what is the damage production rate due to the (n,γ) reaction in ^{56}Fe?

d) If the fast flux is given by: $\phi_f(E_n) = 10^{15}\delta(E_n - 0.5)$, where E_n is in MeV, what is the damage production rate due to the fast flux in iron?

Use the K–P displacement formula in (c) and (d). The scattering cross section for 0.5 MeV neutrons is 3 barns. Also, $\sigma_a^{56} \sim 2.5$ barns for part (c).

2.7 Assuming that atom–atom interactions can be treated as near head-on collisions, the appropriate potential function is then the Born–Mayer potential. Write an expression for the threshold energy for unassisted critical focusing along the [110] direction in fcc nickel in terms of the lattice constant, a.

2.8 For iron (equilibrium phase for 400 °C), assuming a focusing collision occurs, how much does the closest approach (the allowed equivalent hard-sphere radius calculated using a Born–Mayer potential) change between a [100] collision chain and a [110] collision chain?

2.9 a) Calculate the focusing energy of the $\langle 111 \rangle$ direction for gold under the condition of assisted focusing.

b) Will focusing occur along the $\langle 111 \rangle$ direction in the absence of assisted focusing? Why?

c) The experimental focusing energy of gold is 21,000 eV for the $\langle 111 \rangle$ direction. Compare your answer with this value.

2.10 a) Determine the critical focusing energy for the $\langle 111 \rangle$, $\langle 110 \rangle$ and $\langle 100 \rangle$ directions in fcc copper and iron.

b) Plot θ_c as a function of $T < E_c$ for the $\langle 111 \rangle$ directions in Ni and Fe. Comment on similarities and differences.

c) Do the same for the $\langle 110 \rangle$ direction of each.

d) Repeat parts (a) and (b) using the inverse square potential, $V(r) = A/r^2$, where $A = 1.25\,\text{eV}\,\text{nm}^2$.

e) Over what energy range does focused replacement occur? How about focused energy packets only?

2.11 For the focusing process as described in Problem 2.10, give a physical explanation of why the critical angle for focusing, θ_c, should depend on the projectile energy.

2.12 A 30 keV ion enters a channel in the solid lattice and loses energy only by electronic excitation. Using the Lindhard stopping power formula Eq. (1.170), determine the distance traveled by the ion before it is dechanneled. The minimum channeling energy is 300 eV. Use $k = 0.003NZ^{2/3}\,\text{eV}^{1/2}/\text{nm}$, where N is the atomic density of the metal in nm^{-3}.

2.13 Show that when channeling is accounted for in the collision cascade, the average number of displaced atoms $\nu(T)$ is:

$$\nu(T) - (T/2E_d)^{1-2p} ,$$

where p is the probability that an atom with energy E being channeled is lost to the cascade. Assume that $p \neq f(E)$, $T \gg E_d$, and $p \ll 1$.

Assuming that all energy is lost by elastic collisions for 100 keV protons in nickel determine:

a) The energy loss per unit length in the solid, dE/dx

b) The range in the solid.

2.14 A crystal of copper is bombarded with monoenergetic (2 MeV) neutrons.
   a) Calculate the mean atomic displacement rate (displacements/cm^3 s) using the simple Kinchen–Pease model and the following data:
   Lattice parameter, Cu = 0.361 nm
   Atomic weight of Cu = 63.54 amu
   Displacement energy for Cu = 40 eV
   $\phi = 10^{13}$ n/cm^2 s (2 MeV)
   $\sigma_s = 0.5 \times 10^{-24}$ cm^2 (2 MeV)
   b) Repeat part (a) but instead of 2 MeV neutrons, use a monoenergetic thermal neutron beam where $\phi_{th} = \phi_{fast}$, $\sigma_{th} = 3.78 \times 10^{-24}$ cm^2 and the recoil energy, $E_R \sim 382$ eV.
   c) What would be the effect on your answer to part (a) by including Lindhard's damage energy function $\xi(T)$?
   d) How would your answer in part (a) be affected by assuming that the channeling probability is 1%, 5%, 10%?

2.15 For the 2 MeV neutron bombardment problem describe in Problem 2.14, how would you go about calculating the threshold energy for unassisted critical focusing along the [110] direction?

2.16 Assume that the copper target in Problem 2.14 was bombarded by a beam of 2 MeV He ions instead of a beam of 2 MeV neutrons. Calculate the displacement rate at the surface of the sample and compare to your result for Problem 2.14.

2.17 The same copper sample as in Problem 2.14 is bombarded with 500 keV Cu^+ ions at a flux of 10^{15} cm^{-2} s^{-1}. Calculate:
   a) The displacement rate at the surface
   b) The location of the damage peak.
   Use a linear interpolation between the values of dE/dx as given on the attached sheet.

References

1. Kinchin GH, Pease RS (1955) Rep Prog Phys 17:1
2. Seitz F (1949) Disc Faraday Soc 5:271
3. Bacon DJ, Deng HF, Gao F (1993) J Nucl Mater 205:84
4. King WE, Merkle KL, Meshii M (1983) J Nucl Mater 117:12–25
5. Olander DR (1976) Fundamental Aspects of Nuclear Reactor Fuel Elements. US DOE, Washington, DC
6. ASTM E521 (1996) Standard Practice for Neutron Radiation Damage Simulation by Charged-Particle Irradiation. Annual Book of ASTM Standards, vol. 12.02. American Society for Testing and Materials, Philadelphia, PA
7. Robinson MT (1969) Defects and Radiation Damage in Metals. Cambridge University Press, Cambridge
8. Snyder WS, Neufeld J (1955) Phys Rev 97(6):1636
9. Sanders JB (1967) Dissertation, University of Leiden
10. Kohler W, Schilling W (1965) Nukleonik 7:389

11. Sigmund P (1969) Appl Phys Lett 14(3):114
12. Lindhard J, Nielsen V, Scharff M (1968) Kgl Dan Vidnsk Selsk Mat Fyf Medd 36(10)
13. Sigmund P (1969) Rad Eff 1:15–18
14. Erginsoy C, Vineyard GH, Englert A (1964) Phys Rev 133A:595
15. Lindhard J, Nielsen V, Scharff M, Thomsen PV (1963) Dan Vidnsk Selsk Mat Fyf Medd 33:1
16. Robinson MT (1972) The dependence of radiation effects on the primary recoil energy. In: Corbett JW, Ianiello LC (eds) Proceedings of Radiation-Induced Voids in Metals, CONF-710601, USAEC Technical Information Center, Oak Ridge, TN, 1972, p 397
17. Norgett MJ, Robinson MT, Torrens IM (1975) Nucl Eng Des 33:50–54
18. Chadderton LT (1965) Radiation Damage in Crystals. Wiley, New York
19. Brandt W (1968) Sci Amer 218:90
20. Datz S, Noggle TS, Moak CT (1965) Nucl Instr Meth 38:221
21. Doran DG (1971) Displacement Cross Sections for Stainless Steel and Tantalum Based on A Lindhard Model, USAEC Report, HEDL-TME-71-42. WADCO Corporation, Hanford Engineering Development Laboratory, April 1971
22. Robinson MT (1996) J Nucl Mater 216:1–28
23. Simmons RL, McElroy WN, Blackburn LD (1972) Nucl Technol 16:14
24. McElroy WN, Dahl RE, Gilbert ER (1970) Nucl Eng Des 14:319
25. Kulcinski GL, Brimhall JL, Kissinger HE (1972) Production of voids in pure metals by high-energy heavy-ion bombardment. In: Corbett JW, Ianiello LC (eds) Proceedings of Radiation-Induced Voids in Metals, CONF-710601, USAEC Technical Information Center, Oak Ridge, TN, 1972, p 453

3 The Damage Cascade

3.1 Displacement Mean Free Path

In our discussion of cascade development, no consideration was given to the spatial arrangement of displaced atoms. We assumed that every Frenkel pair created was preserved and that no annihilation occurred. However, the spatial arrangement of these Frenkel pairs is crucial in determining the number that survive annihilation or immobilization by clustering. In order to understand what the damaged region looks like, we need to know if the displacements are concentrated or distributed. A helpful tool in this regard is the mean free path for displacement collisions, i.e., collisions in which the energy transferred is greater than E_d. This will tell us how far apart the displacements occur and hence, the separation distance between Frenkel pairs.

By definition, the mean free path, $\lambda = \dfrac{1}{N\sigma}$ and the corresponding displacement cross section is:

$$\sigma_\mathrm{d}'(E) = \int_{E_\mathrm{d}}^{E} \sigma(E,T)\,\mathrm{d}T \ . \tag{3.1}$$

This is the cross section for the transfer of energy in excess of E_d and is given in terms of the differential energy transfer cross section between lattice atoms. Note that σ_d' has nothing to do with the projectile, be it a neutron or an ion, or the source of the damage in general. Using the equivalent hard-sphere model to evaluate σ_d' gives:

$$\sigma(E,T) = \frac{\sigma(E)}{\gamma E} \ ,$$

but $\gamma = 1$, so substituting into Eq. (3.1) and integrating yields:

$$\sigma_\mathrm{d}'(E) = \int_{E_\mathrm{d}}^{E} \frac{\sigma(E)}{E}\,\mathrm{d}T = \sigma(E)\left(1 - \frac{E_\mathrm{d}}{E}\right) \ , \tag{3.2}$$

where $\sigma(E) = 4\pi r^2$ is the total collision cross section between lattice atoms, so:

$$\sigma_\mathrm{d}'(E) = 4\pi r^2\left(1 - \frac{E_\mathrm{d}}{E}\right) \ , \tag{3.3}$$

and r is the energy-dependent, equivalent hard-sphere radius, which, using the Born–Mayer potential gives:

$$\sigma_\mathrm{d}'(E) = \pi B^2\left[\ln\left(\frac{2A}{E}\right)\right]^2\left(1 - \frac{E_\mathrm{d}}{E}\right) \ , \tag{3.4}$$

and the mean free path, λ becomes:

$$\lambda = \frac{1}{N\pi B^2 \left[\ln\left(\frac{2A}{E}\right)\right]^2 \left(1 - \frac{E_\mathrm{d}}{E}\right)} \,. \tag{3.5}$$

The mean free path and the total collision cross section are plotted in Fig. 3.1 for copper atoms in copper, and show that as the energy of the moving atom drops, the cross section increases slowly but the mean free path becomes very small at energies just above E_d. Note that the critical region ($\lambda \sim 0.3$–$1.0\,\mathrm{nm}$), or the region in which every lattice atom in the path of the knock-on is displaced, lies in the energy range ~ 50–$100\,\mathrm{eV}$.

The mean free paths for primary recoil atoms of 300 keV and 1 MeV resulting from self-ion irradiations of Si, Cu and Au are shown in Fig. 3.2. Recall that $\bar{T} = \frac{\gamma E_\mathrm{i}}{2} \cong \frac{2E_\mathrm{i}}{A}$ (for n-Cu interactions), where E_i is the neutron energy and A is the atomic mass. Typically, $E_\mathrm{i} \sim 0.5\,\mathrm{MeV}$ (for a thermal or fast reactor) and $A \sim 60$ (stainless steel), giving $\bar{T} \sim 15\,\mathrm{keV}$. So at large recoil energies, the displacements are well separated ($\sim 100\,\mathrm{nm}$ at 15 keV), but as the recoil energy decreases, the spacing approaches the atomic spacing, at which point each atom along the recoil path is displaced.

3.2 Primary Recoil Spectrum

The analysis of displacement mean free path gives us a first glimpse of what the spatial distribution of defects might look like. Brinkman [3] was the first to picture the cascade as a *displacement spike* with a high core density of vacancies surrounded by an interstitial shell (Fig. 3.3). Seeger [4] modified the picture to account for crystallinity such as focused energy packets (focusons), and long-range transport of mass by replacement collisions and channeling, and termed the vacancy core a *depleted zone* (Fig. 3.4).

Two additional quantities are helpful in developing a picture of the distribution of damage energy. The first is the deposited energy depth distribution, $F_\mathrm{D}(x)$, defined by:

$$F_\mathrm{D}(x)\,\mathrm{d}x = \mathrm{d}E = NS_n E(x)\,\mathrm{d}x \,. \tag{3.6}$$

Using the nuclear stopping power and range given by the power law potential [5] results in a simple form for $F_\mathrm{D}(x)$:

$$F_\mathrm{D}(x) = \frac{T}{2mR}(1 - x/R)^{\frac{1}{2m}-1} \,, \tag{3.7}$$

where T is the PKA energy, R is the PKA range and $m = 1/s$ where s is the power law exponent. If $N_\mathrm{d}(x)$ is the number of displacements per unit depth at a depth x, then using the modified K–P model or the NRT model (e.g., Eq. (2.53)) with $\kappa = 0.8$

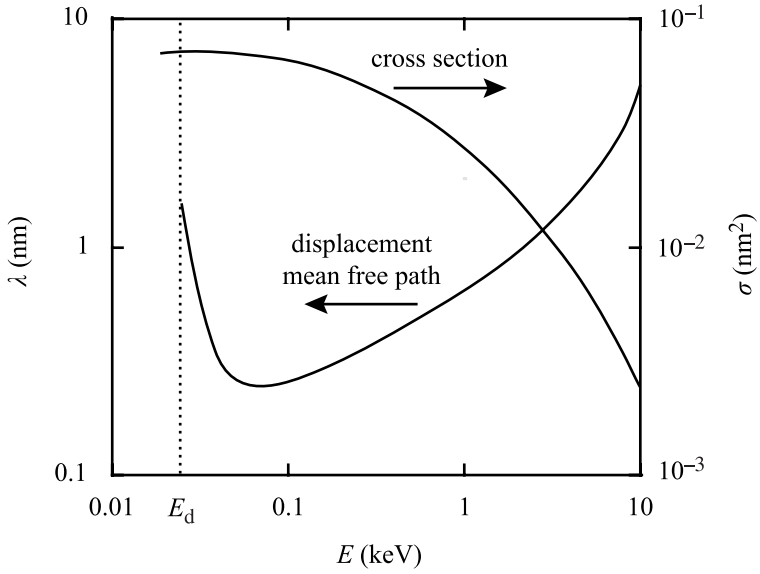

Fig. 3.1. Displacement mean free path and total collision cross section for copper atoms moving in copper (after [1])

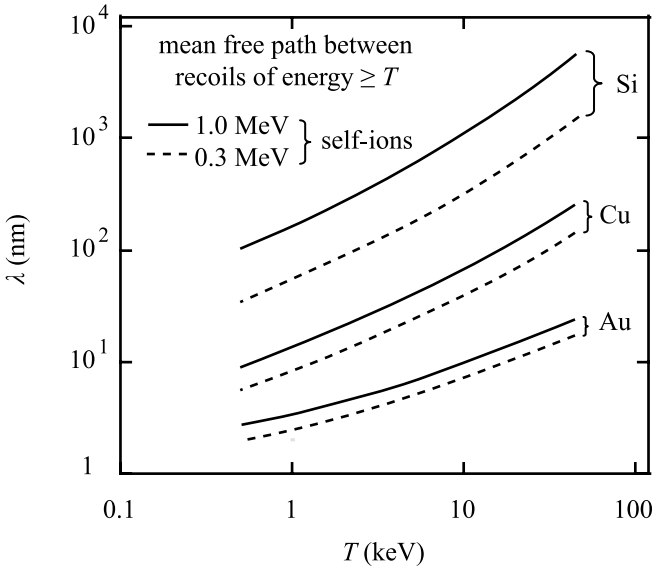

Fig. 3.2. Mean free paths of primary recoil atoms of 300 keV and 1 MeV, self-ion irradiations of Si, Cu and Au (after [2])

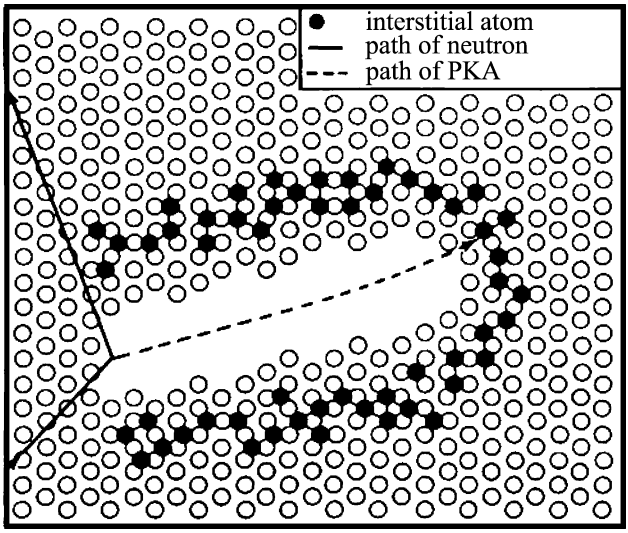

Fig. 3.3. Original version of the displacement spike as drawn by Brinkman (after [3])

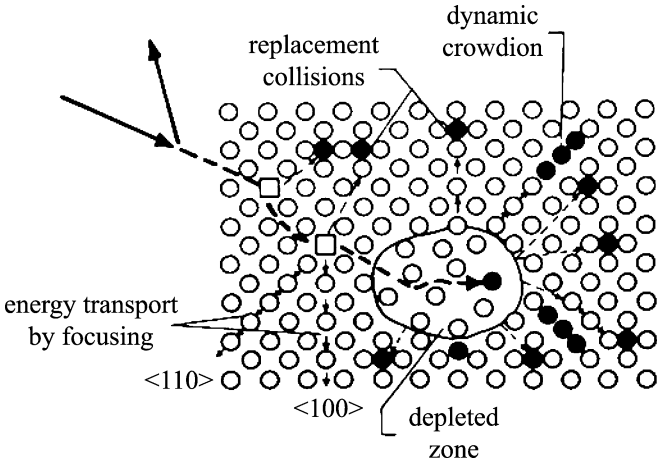

Fig. 3.4. Revised version of Brinkman's displacement spike as drawn by Seger (after [4]) accounting for crystallinity in the damage cascade

and with $F_{\mathrm{D}}(x)$ replacing E_{D}, we can write that:

$$\frac{N_{\mathrm{d}}(x)}{\phi} = \frac{0.8F_{\mathrm{D}}(x)}{2E_{\mathrm{d}}}\,, \tag{3.8}$$

and the displacement rate as a function of depth in units of dpa becomes:

$$\mathrm{dpa}(x) = \frac{N_{\mathrm{d}}(x)}{N} = \frac{0.4F_{\mathrm{D}}(x)}{NE_{\mathrm{d}}}\phi\,. \tag{3.9}$$

The *total dpa* produced over the range of the recoil can be estimated by replacing $F_D(x)$ with the damage energy E_D from Eq. (2.54) over the range of the recoil, R:

$$\text{dpa} \cong \frac{\phi 0.4 E_D}{N R E_d} \,. \tag{3.10}$$

The second important concept is the primary recoil spectrum. The density of recoil atoms with energies between T and $T + dT$ that occur during irradiation is an important quantity in radiation damage. The recoil density depends on the projectile energy and mass and gives a measure of the density of displacement damage in the target. The density of recoils as a function of recoil energy is known as the primary recoil spectrum and is given as:

$$P(E_i, T) = \frac{1}{N} \int_{E_d}^{T} \sigma(E_i, T')\, dT' \,, \tag{3.11}$$

which is the fractional number of recoils between the minimum displacement energy E_d, and energy T, and N is the total number of primary recoils, and $\sigma(E_i, T)$ is the energy transfer cross section for a particle of energy E_i to create a recoil of energy T. The fraction of recoils is shown in Fig. 3.5 for 1 MeV projectiles of various mass incident on a copper target. Note that while higher mass projectiles produce more recoils at higher energy, the difference does not appear to be large.

For defect production, it is not the number of recoils of a particular energy that is of greatest importance, rather it is the fraction of damage energy that are produced

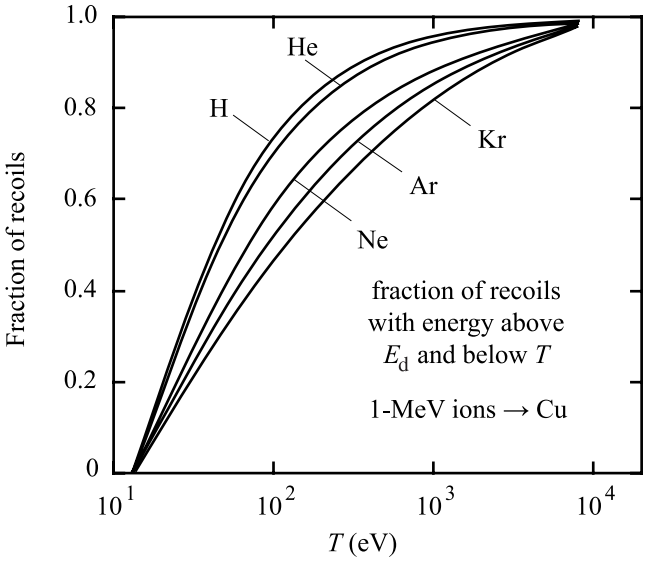

Fig. 3.5. Integral primary recoil spectra for 1 MeV particles in copper. Curves plotted are the integral fractions of primary recoils between the threshold energy and energy, T from Eq. (3.11) (after [2])

in recoils of a particular energy. This quantity is given by "weighting" the recoil spectra by the number of defects or the damage energy produced in each recoil:

$$W(E_\mathrm{i},T)=\frac{1}{E_\mathrm{D}(E_\mathrm{i})}\int_{E_\mathrm{d}}^{T}\sigma(E_\mathrm{i},T')E_\mathrm{D}(T')\,\mathrm{d}T'\,, \tag{3.12}$$

where $E_\mathrm{D}(T)$ is the damage energy created by a recoil of energy T:

$$E_\mathrm{D}(E_\mathrm{i})=\int_{E_\mathrm{c}}^{\hat{T}}\sigma(E_\mathrm{i},T')E_\mathrm{D}(T')\,\mathrm{d}T'\,, \tag{3.13}$$

and $\hat{T}=\gamma E_\mathrm{i}$.

For the extremes of Coulomb and hard-sphere interactions, the differential energy-transfer cross sections are:

$$\sigma_\mathrm{Coul}(E_\mathrm{i},T)=\frac{\pi M_1(Z_1Z_2\varepsilon^2)^2}{E_\mathrm{i}T^2}\,, \tag{3.14}$$

and

$$\sigma_\mathrm{HS}(E_\mathrm{i},T)=\frac{A}{E_\mathrm{i}}\,. \tag{3.15}$$

Ignoring electron excitations and allowing $E_\mathrm{D}(T)=T$, and substituting Eqs. (3.14) and (3.15) into Eq. (3.12) gives the weighted average recoil spectra for each type of interaction:

$$W_\mathrm{Coul}(T)=\frac{\ln T-\ln\check{T}}{\ln\hat{T}-\ln\check{T}}\,, \tag{3.16}$$

and

$$W_\mathrm{HS}(T)=\frac{T^2-\check{T}^2}{\hat{T}^2} \tag{3.17}$$

where $\check{T}=E_\mathrm{d}$. Equations (3.16) and (3.17) are graphed in Fig. 3.6 for 1 MeV particle irradiations of copper. The Coulomb potential is a good approximation for proton irradiation while the hard-sphere potential is a good approximation for neutron irradiation. The Coulomb forces extend to infinity and slowly increase as the particle approaches the target. In a hard-sphere interaction, the particles and target do not "feel" each other until their separation reaches the hard-sphere radius at which point the repulsive force goes to infinity. A screened Coulomb is most appropriate for heavy ion irradiation. The result is that Coulomb interactions tend to create many PKAs with low energy while hard-sphere collisions create fewer PKAs but with higher energy. Note the large difference in $W(T)$ between the various types of irradiations in Fig. 3.6. While heavy ions come closer to reproducing the energy distribution of recoils of neutrons than do light ions, neither is accurate in the "tails" of the distribution. This does not mean that ions are poor simulations of radiation

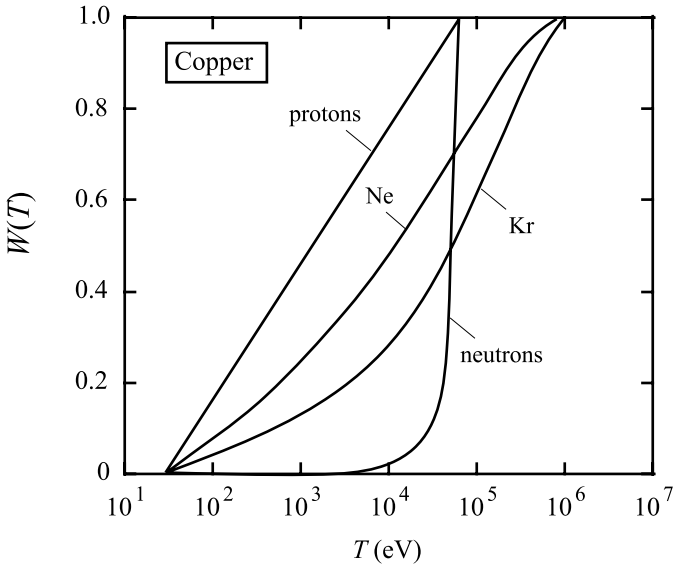

Fig. 3.6. Weighted recoil spectra for 1 MeV particles in copper, (after [2]). Curves representing protons and neutrons are calculated using Eqs. (3.14) and (3.15), respectively. $W(T)$ for other particles were calculated using Lindhard cross sections and include electronic excitation

damage, but it does mean that damage is produced differently and that this needs to be considered when assessing the microchemical and microstructural changes due to irradiation.

Figure 3.7 illustrates the difference in the types of damage that is produced by different types of particles. Light ions such as electrons and protons will produce damage as isolated Frenkel pairs or in small clusters while heavy ions and neutrons produce damage in large clusters. For 1 MeV particle irradiation of nickel, half the recoils for protons are produced with energies less than $\sim$ 1 keV but with an average energy of 60 eV while the same number for Kr occurs at about 30 keV with an average energy of 5 keV. Recoils are weighted toward lower energies because of the screened Coulomb potential that controls the interactions of charged particles. For an unscreened Coulomb interaction, the probability of creating a recoil of energy T varies as $1/T^2$. Because neutrons interact as hard spheres, the probability of a creating a recoil of energy T is independent of recoil energy.

3.3 Cascade Damage Energy and Cascade Volume

The energy density in a cascade of volume V_{cas} formed by an energetic projectile of energy E_{i} is given by [7]:

$$\bar{\Theta}_{\mathrm{D}} \cong \frac{E_{\mathrm{D}}}{NV_{\mathrm{cas}}} , \tag{3.18}$$

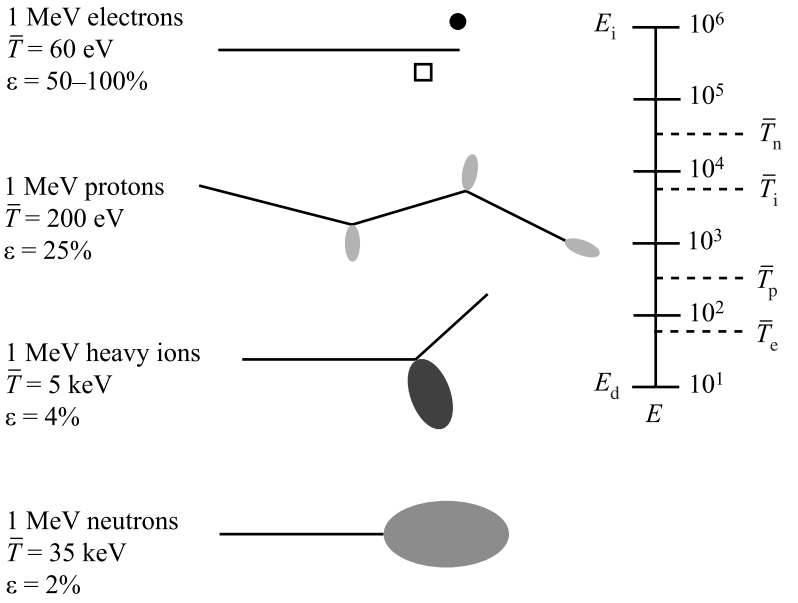

Fig. 3.7. Difference in damage morphology, displacement efficiency and average recoil energy for 1 MeV particles of different type incident on nickel (after [6])

where E_D is the damage energy defined in Eq. (2.54) and N is the atom density of the target. To find the volume of the cascade requires knowledge of the depth distribution of the damage energy. Averback [2] showed that the volume of the cascade can be approximated by:

$$V_{cas} = \frac{4\pi}{3}((\delta\Delta X)^2 + 2(\delta Y)^2)^{3/2} , \tag{3.19}$$

where $(\Delta X)^2$ and Y^2 are the longitudinal and transverse moments of the deposited damage energy distribution for an individual cascade, and δ is a contraction factor that accounts for the difference between an individual cascade and the average cascade determined by transport theory.

While Eqs. (3.18) and (3.19) provide a description of the spatial extent of a cascade, other characteristics of the cascade are the temperature and temporal lifetime. The effective temperature of the cascade can be estimated by the relation:

$$3k_B T_{max} = \bar{\Theta}_D , \tag{3.20}$$

where k_B is Boltmann's constant. The lifetime of the cascade or *thermal spike* can be estimated by solving the heat equation for the spread of energy from a point source in three dimensions. The variance in the temperature profile, R^2, is given by:

$$R^2 = 4D\tau , \tag{3.21}$$

where τ is the cascade lifetime and D is the thermal diffusivity $= \kappa_T/C_p$, where κ_T is the thermal conductivity and C_p is the specific heat capacity. The cascade energy is then:

$$E_D = \frac{4}{3}\pi R^3 U_a N \,, \tag{3.22}$$

where U_a is the energy per atom. The cascade lifetime is determined by combining Eqs. (3.21) and (3.22) to solve for τ:

$$\tau = \frac{1}{4D}\left(\frac{3E_D}{4\pi N U_a}\right) \,. \tag{3.23}$$

If we estimate U_a from the melting temperature of the target, then $U_a \sim 0.3\,\text{eV}$ and $D \sim 10^{12}\,\text{nm}^2/\text{s}$, then the lifetime of a 1 keV cascade is of the order 10^{-12} s, or a few lattice vibration periods.

3.4 Computer Simulations of Radiation Damage

Analytical solutions to the space and time dependence of damage caused by an energetic particle incident on a target can take us only so far. And as we will see later, excellent instrumentation exists to observe defect clusters such as transmission electron microscopy, X-ray scattering, small angle neutron scattering and positron annihilation spectroscopy. But these instruments do not have the resolution to image individual defects and they cannot capture the temporal development of the cascade. To gain a better understanding of the spatial and temporal development of the cascade, we must turn to computer simulation. There are three principal techniques used to model the behavior of atoms in a displacement cascade; the binary collision approximation (BCA) method, the molecular dynamics (MD) method and the kinetic Monte Carlo (KMC) method [8]. Each will be briefly discussed.

3.4.1 Binary Collision Approximation (BCA) Method

BCA simulations are useful for examining the collisional stages of high-energy cascades in statistically significant numbers. BCA simulations consider only the interactions between two colliding atoms at a time and in sequence [8]. The computation follows only the atoms having significant energies and are thus very efficient. The BCA approach provides a good approximation to the collision stage, since the neglected many-body interactions make little contribution to the atom trajectories at collision energies well above the atom displacement energy. At energies near or even less than the displacement energy, ballistic features of cascades such as replacement-collision sequences and focused-collision sequences (focusons) can be reasonably captured by BCA calculations. At primary recoil energies above approximately 20 keV, cascades may have more than one damage region. Because the mean free path between high-energy collisions of a recoil atom increases with energy,

higher energy cascades will consist of multiple damage regions or *subcascades* that are well separated in space due to high-energy collisions. Channeling of primary or high-energy secondary recoils also contributes to subcascade formation when the channeled recoils lose energy and de-channel.

There are two distinct types of BCA models. Those for crystalline targets are termed BC or binary crystal models and resemble MD models in that they assign all atoms to well-defined initial positions [9]. Models for materials without long-range order (amorphous solids) are termed MC or Monte Carlo models and use stochastic methods to locate target atoms and to determine collision parameters. The MC models are similar to transport theory models used in analytical theory to track neutron populations in a medium.

An example of a BC model is the MARLOW code [10]. The program models crystalline targets with no restrictions on the crystal symmetry or on the chemical composition. All collision parameters are calculated from the particle positions. Several interatomic potentials are available for selection to describe atom collisions. Inelastic energy losses may be included in either local or non-local form, but the loses are limited to the velocity-proportional ($E^{1/2}$) range of kinetic energies. Figure 3.8 shows the spatial configuration of defects from an early computer simulation using the MARLOWE code for the case of a 200 keV cascade in copper. This is a very energetic cascade that would only be expected from extremely energetic neutrons such as are generated in a fusion reactor. The PKA is generated in the lower

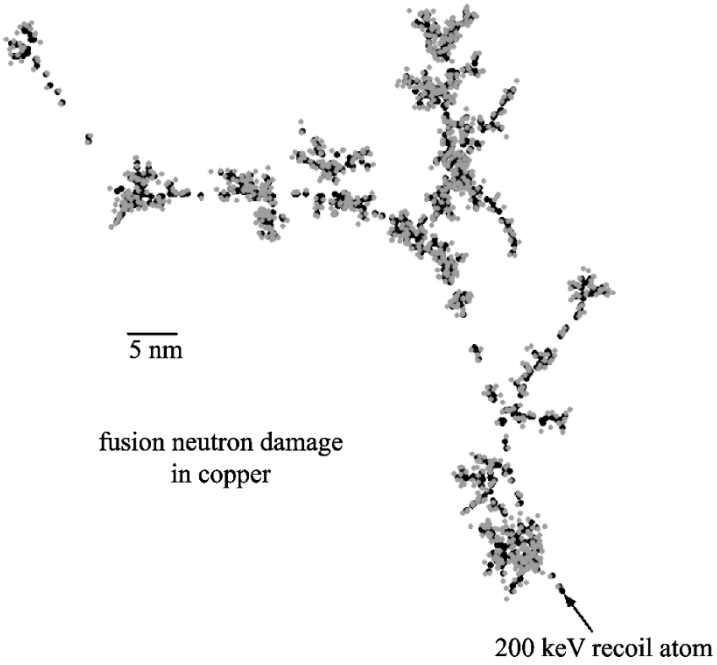

Fig. 3.8. Collisional stage of a 200 keV cascade in copper simulated using the binary collision approximation in MARLOWE (after [8])

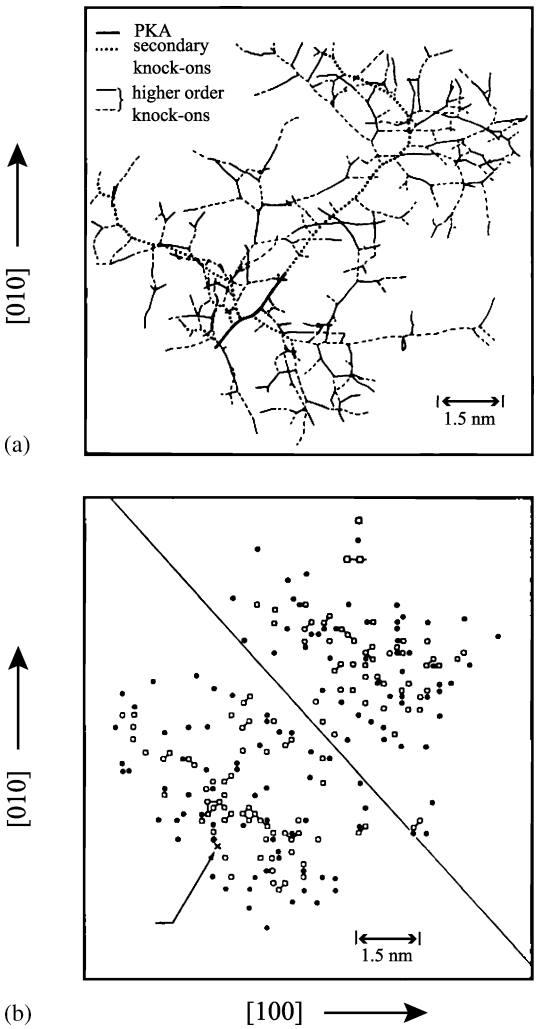

Fig. 3.9. Computer simulation of a displacement spike due to a 5 keV PKA in iron. All out-of-plane damage has been projected onto the ⟨001⟩ plane shown in the figure. (a) Recoil trajectories and (b) vacancies and interstitial atoms at the end of the collision cascade (0 K). The *diagonal line* in (b) shows the effect of channeling of a secondary knock-on atom (after [11])

right hand corner (arrow) and proceeds to the left with a kinetic energy of 200 keV. The dark spheres are displaced atoms and the lighter spheres are vacant lattice sites. Note that the full cascade consists of several subcascades.

A second example, shown in Fig. 3.9 shows how the cascade can become extended in space. The recoil trajectories and final configuration of interstitials and vacancies in bcc iron is shown after interaction with a 5 keV PKA at a temperature of 0 K [11]. All vacancies and interstitials within a sphere containing 30 lattice atom sites were assumed to recombine spontaneously. Note in Fig. 3.9a, that the secondary knock-on in the center of the spike undergoes channeling, making possible the extension of the cascade into the upper right half of the lattice shown in Fig. 3.9b. Essentially, all of the damage to the upper right of the diagonal is due to channeling of the secondary knock-on.

TRIM [12] is another BCA code that uses Monte Carlo techniques to describe the trajectory of the incident particle and the damage created by that particle in amorphous solids and was discussed briefly in Chap. 1. TRIM uses a maximum impact parameter set by the density of the medium and a constant mean free path between collisions which is related to this. Stochastic methods are used to select the impact parameter for each collision and to determine the scattering plane. The barycentric scattering angle is determined by a "magic" formula, tested against published integral tables and represents the scattering from the ZBL "universal" potential. Inelastic energy losses are based on the effective charge formalism, using tables distributed with the code. Figure 3.10 shows a simulation of 3 MeV protons incident on a nickel target. Figure 3.10a shows the trajectories of the incident particles for 10,000 cases (MC runs), and Fig. 3.10b shows the ion concentration profile and the displacement rate profile as a function of depth.

3.4.2 Molecular Dynamics (MD) Method

Molecular dynamics is the second major type of methodology used to describe collision cascades. MD is a computationally intensive method for modeling atomic systems on the appropriate scale for the simulation of displacement cascades and provides the most realistic description of atomic interactions in cascades [8]. Using realistic interatomic potentials and appropriate boundary conditions, the fate of all atoms in a volume containing the cascade can be described through the various stages of cascade development. The analytical interatomic potential functions must describe the force on an atom as a function of the distance between it and the other atoms in the system. It must account for both attractive and repulsive forces in order to obtain stable lattice configurations. In MD simulations, the total energy of the system of atoms being simulated is calculated by summing over all the atoms. The forces on the atoms are used to calculate acceleration according to $F = ma$, yielding the equations of motions for the atoms. The computer code solves these equations numerically over very small time steps, and then recalculates the forces at the end of the time step, to be applied in the calculations in the next time step. The process is repeated until the desired state is achieved. Time steps in MD simulation must be very small ($5-10\times10^{-15}$ s), so MD simulations are generally run for no more than 100 ps. As the initial primary kinetic energy E increases, larger and larger numerical crystallites are required to contain the event. The size of the crystallite is roughly proportional to E. The required computing time-scales roughly as E^2. The demand on computing time limits the statistical capabilities of MD simulation. However, they provide a detailed view of the spatial extent of the damage process on an atomic level that is not afforded by other techniques.

A cascade simulation begins by thermally equilibrating a block of atoms that constitutes the system to be studied. This process allows the determination of the lattice vibrations for the simulated temperature. Next, the cascade simulation is initiated by giving one of the atoms a specified amount of kinetic energy and an initial direction. Several cascades must be run in order to have results that can

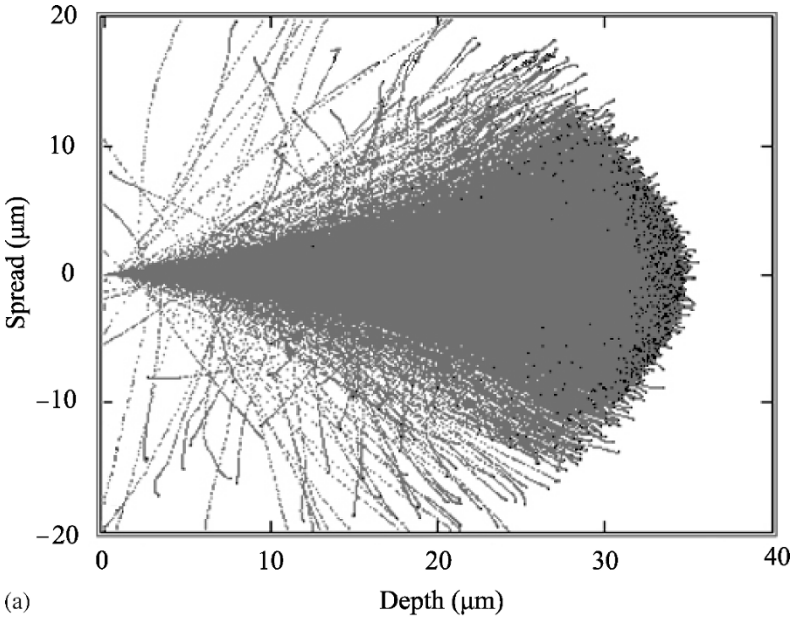

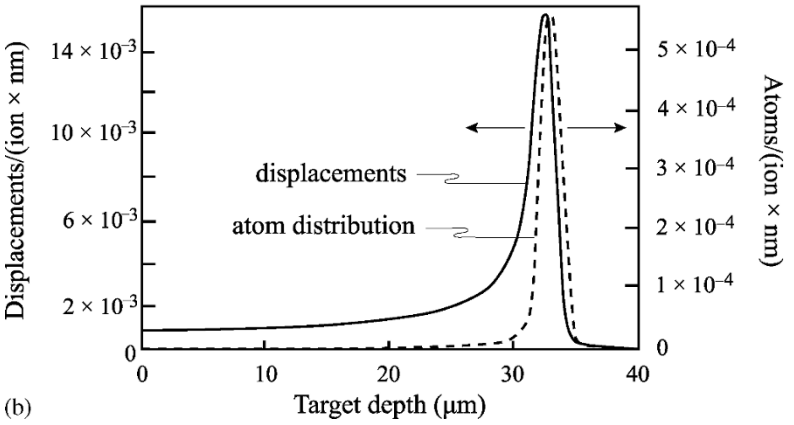

Fig. 3.10. A 3 MeV proton incident on nickel as modeled by the TRIM code: (a) trajectory, (b) concentration profile and displacement profile

be used to represent the average behavior of the system at any energy and temperature. One such code used for MD simulations is the MOLDY code written by Finnis [13] and uses interatomic potentials developed by Finnis and Sinclair [13], and later modified by Calder and Bacon for cascade simulations [14]. The code only describes elastic collisions between atoms, and does not account for energy loss mechanisms such as electronic excitation and ionization. The energy given

to the PKA in the MD simulation is that corresponding to the value of the displacement energy E_D, given in Eq. (2.54). Stoller [15] conducted an MD simulation for iron and generated the cascade parameters shown in Table 3.1. Note that with increasing energy, the difference between the MD cascade energy and the PKA energy increases. Figure 3.11 shows typical point defect configurations from a 1 keV MD cascade simulation in iron at 100 K. Figure 3.11a shows the cascade at the point of peak disorder and Fig. 3.11b shows the cascade following in-cascade recombination. Note the sizable reduction in the residual damage between 0.18 ps and 9.5 ps. This result shows that the actual damage resulting from the PKA is much less than the total aggregate number of displacements calculated from the K–P or NRT models. While "still" images of the stages of the cascade are useful in understanding how the cascade develops, a much better appreciation is gained by viewing the temporal evolution of the cascade directly. This can be done by viewing Movie 3.1 via the website at www.sitemaker.umich.edu/was. This MD simulation shows the development of a cascade from a 200 keV recoil in iron at 100 K through to cascade quench at 21.6 ps. Note the extension of the cascade to the lower right hand corner that is probably do to a crystallographic effect involving channeling. Also note the striking difference in the defect density between the peak ballistic stage (~ 0.7 ps) and the end of the quench at 21.6 ps.

3.4.3 Kinetic Monte Carlo (KMC) Method

Our objective is to simulate the dynamical evolution of systems of atoms during and immediately following the displacement event. The most robust tool in this class of atomistic simulation methods is molecular dynamics. Integrating the classical equations of motion forward in time, the behavior of the system emerges naturally, requiring no intuition or further input from the user. A serious limitation, however, is that accurate integration requires time steps short enough ($\sim 10^{-15}$ s) to resolve the atomic vibrations. Consequently, the total simulation time is typically limited to less than one nanosecond, while processes we wish to study (e.g., diffusion and annihilation of defects after a cascade event) often take place on much longer timescales. This is the "time-scale problem".

Kinetic Monte Carlo attempts to overcome this limitation by exploiting the fact that the long-time dynamics of this kind of system typically consists of diffusive jumps from state to state. Rather than following the trajectory through every vibrational period, these state-to-state transitions are treated directly. Given a set of rate constants connecting states of a system, KMC offers a way to propagate dynamically correct trajectories through the state space. If the rate catalog is constructed properly, the easily implemented KMC dynamics can give exact state-to-state evolution of the system, in the sense that it will be statistically indistinguishable from a long molecular dynamics simulation. KMC is the most powerful approach available for making dynamical predictions at the mesoscale without resorting to more dubious model assumptions. It can also be used to provide input to and/or verification for higher-level treatments such as rate theory models

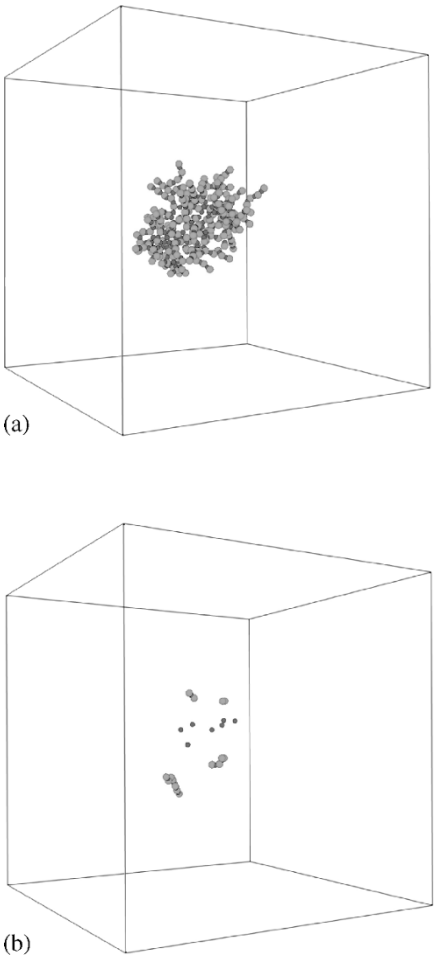

Fig. 3.11. Typical point defect configurations from a 1 keV MD simulation in iron at 100 K at (a) the time of peak disorder (0.18 ps) and (b) following in-cascade recombination (9.5 ps). The larger, lighter spheres are interstitials, and the smaller, darker spheres are vacancies (after [15])

Table 3.1. Typical MD cascade parameters and required atom block sizes (from [15])

Cascade energy $E_{MD} \sim E_D$ (keV)	Corresponding PKA energy (keV)	NRT defects (ν_{NRT})	Atom block size (atoms)
0.1	0.116	1	3456
0.2	0.236	2	6750
0.5	0.605	5	6750
1.0	1.24	10	54,000
2.0	2.54	20	54,000
5.0	6.61	50	128,000
10.0	13.7	100	250,000
20.0	28.8	200	250,000
50.0	61.3	400	1,024,000

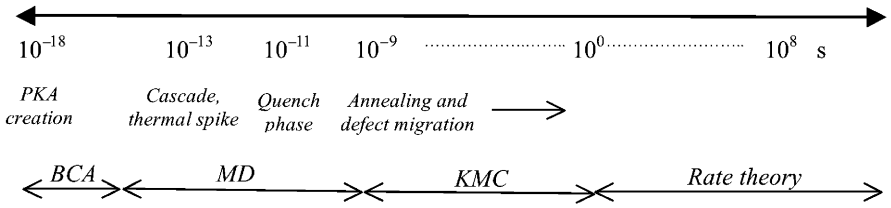

Fig. 3.12. Time-scale for radiation damage evolution and the corresponding simulation methodologies

or finite-element simulations. Moreover, even in situations where a more accurate simulation would be feasible (e.g., using accelerated molecular dynamics or on-the-fly kinetic Monte Carlo), the extreme efficiency of KMC makes it ideal for rapid scans over different conditions, for example, and for model studies. The result is that KMC can reach vastly longer time-scales, typically seconds and often well beyond.

An example of the capability of KMC to capture processes on a larger time-scale is given in Movie 3.2, which shows a KMC simulation of a 20 keV cascade in Fe–0.2Cu–0.6Si–0.7Ni–12.4Mn (similar to a pressure vessel steel) at 327 °C. The simulation shows the enrichment of Ni (green), Mn (black), Si (blue) and Cu (red) at cascade debris (vacancies in yellow) covering a time period out to several years, or many orders of magnitude longer than the cascade quench time. Note the pairing of Ni and Si and the accumulation of solute atoms at the vacancy clusters.

Taken together, the MD and KMC methods cover the radiation time-scale as shown in Fig. 3.12. MD simulations are practical up to the ns range, and KMC simulations extend the range to the second [s] regime. Much occurs after this time-scale and this is generally modeled using rate theory, which will be discussed in Chap. 5 and beyond.

3.5 Stages of Cascade Development

The final state of the cascade is extremely important because the end of the cascade is the starting point for defect diffusion, agglomeration and destruction that forms the basis for the observable effects of irradiation to be covered in Part II of this text. Figure 3.13 shows another example in which a 2D cross section of a cascade is shown at times that correspond to the early stages of the cascade and near the final state. Here again, the damage state has relaxed to a very large degree between 2 ps (Fig. 3.13a) and 18 ps (Fig. 3.13b). Figure 3.14 shows the radial pair correlation function for the two times. The pair correlation function describes the separation of atoms and will appear as a series of spikes for crystalline solids (by virtue of their long-range order) and as a smoothly varying function for a liquid or amorphous solid (in which there is only nearest and second nearest neighbor correlation). As shown in the figure, the atom arrangement in the core of the displace-

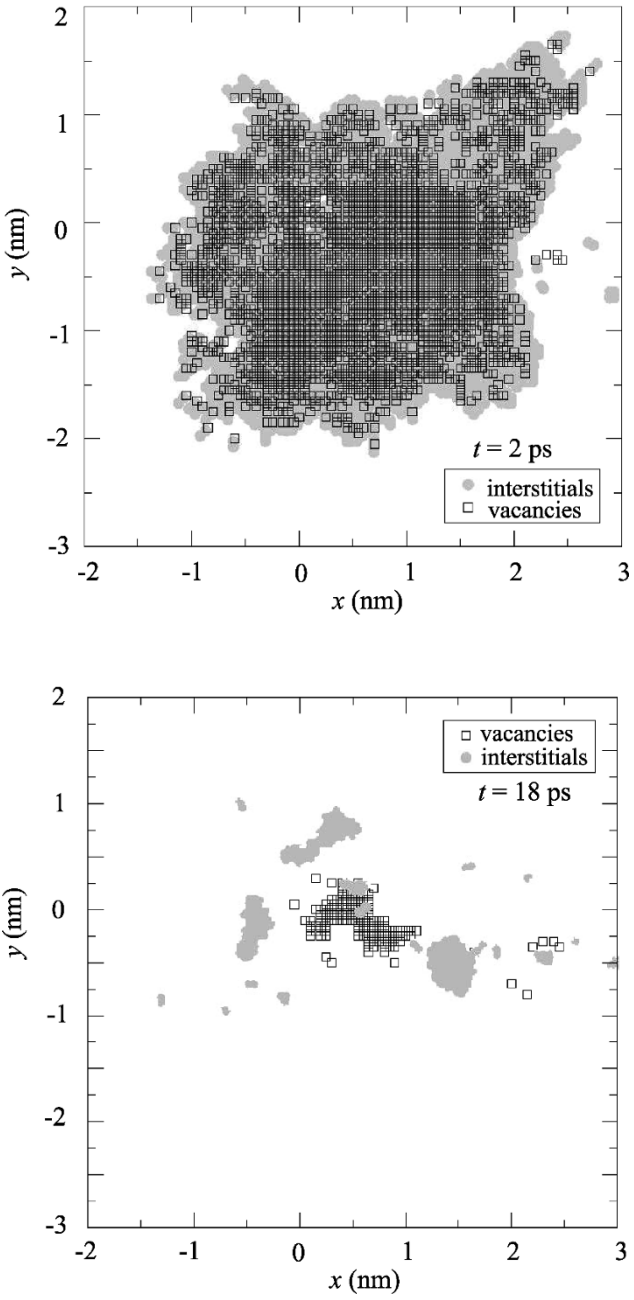

Fig. 3.13. MD simulation of a 30 keV displacement cascade in Cu at 300 K at 2 ps and 18 ps into the collision (calculations performed at the Barcelona Supercomputer center, courtesy of M. Catula and Tomas Diaz de la Rubia)

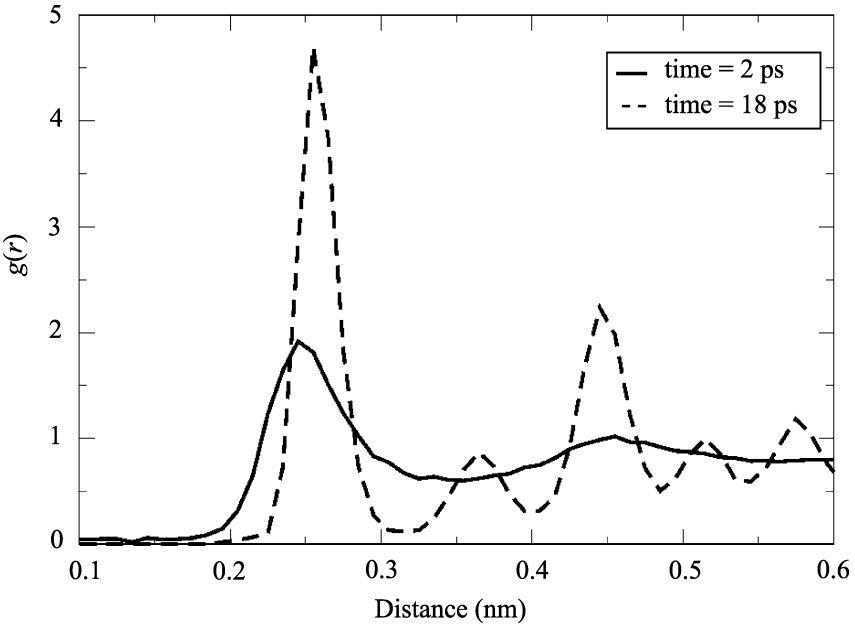

Fig. 3.14. Pair correlation function for the collision cascades in Fig. 3.13, showing the amorphous-like character of the displacement cascade zone at 2 ps and the considerable degree of recovery by 18 ps (calculations performed at the Barcelona Supercomputer center, courtesy of M. Catula and Tomas Diaz de la Rubia)

ment spike at short times is similar to that of a liquid, while the final arrangement is recovering its crystalline configuration. Figure 3.15 shows that the mean square atomic displacement of atoms in the cascade also increases dramatically with time, indicating that the bulk of the aggregate movement of atoms in the displacement cascade occurs *after* the time to reach peak damage! Taken together, the results of Figs. 3.13–3.15 tell us that damage is *annealing* out with time. This annealing is occurring as the energy of the cascade is dropping. In fact, annealing occurs at the tail end of the period during which the cascade energy drops, called the *quench* stage.

We now have a picture of how the cascade develops in time that we can describe. Cascades evolve in stages given as follows:

1. Collisional
2. Thermal spike
3. Quenching
4. Annealing

In the collisional stage (1), the primary recoil atom initiates a cascade of displacive collisions that continues until no atom contains enough energy to create further displacements. At the end of this stage (lasting < 1 ps), the damage consists of energetic displaced atoms and vacant lattice sites. However, stable lattice defects have

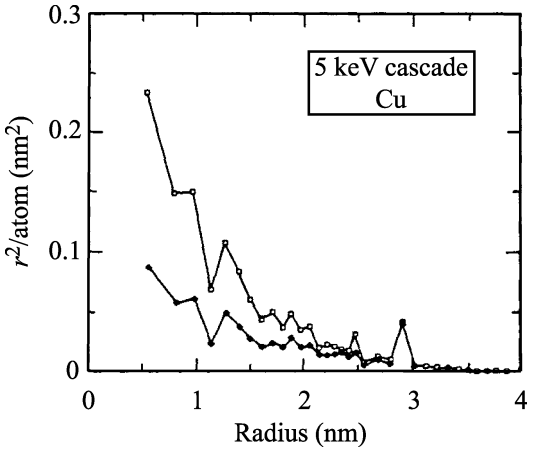

Fig. 3.15. Integrated diffusion coefficient as a function of distance from the center of the cascade at the end of the collisional phase, $t = 0.12$ ps (*solid diamonds*) and at the end of the cooling phase, $t = 10$ ps (*open squares*), for a 5 keV cascade in copper (after [16])

not yet had time to form. During the thermal spike stage (2), the collisional energy of the displaced atoms is shared among their neighboring atoms in the region of high deposited energy density. The development of the spike requires about 0.1 ps, and the spike may occupy several zones in which the energy is high enough so that the atoms resemble molten material. As energy is transferred to the surrounding atoms, the molten zones return to the condensed, or quenched stage (3), and thermodynamic equilibrium is established (~ 10 ps). The quenching stage may take several ps and during this time, stable lattice defects form either as point defects or as defect clusters. But the total number of defects at this stage is much less than the number of atoms displaced in the collisional stage. The annealing stage involves further rearrangement and interaction of defects and occurs by thermally activated diffusion of mobile lattice defects. By definition, the annealing stage (4) lasts until all mobile defects escape the cascade region or another cascade occurs within it. Thus, the timescale extends from nanoseconds to months, depending on the temperature and the irradiation conditions. The annealing stage is the subject of the next part on Physical Effects of Radiation Damage (Part II) and is the link between the damage cascade and the observable effects of irradiation.

3.6 Behavior of Defects within the Cascade

The actual number of defects that survive the displacement cascade and their spatial distribution in the solid will determine their effect on the irradiated microstructure. We define the *displacement efficiency* ξ, as the fraction of the "ballistically" produced Frenkel pairs (NRT dpa) that survive the cascade quench. MD simulation of the displacement cascade provides the recoil dependence of the displacement effi-

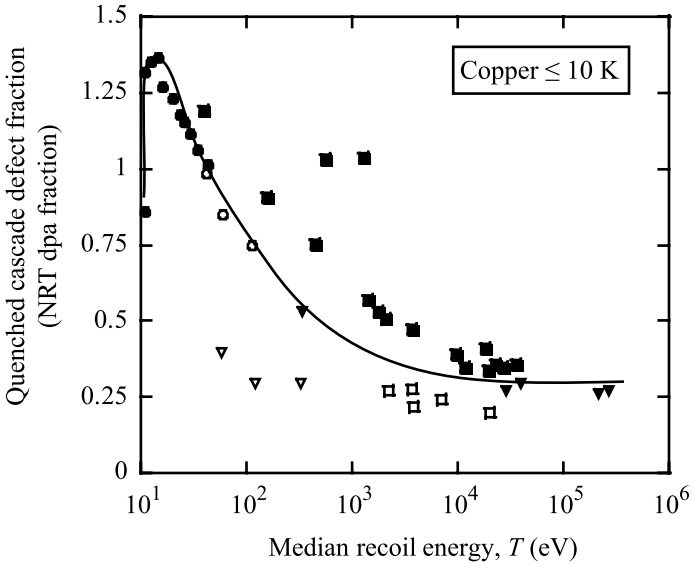

Fig. 3.16. Dependence of the displacement efficiency on median PKA in copper. *Open symbols* refer to MD calculations and *filled symbols* refer to experimental measurements as the result of electron (•), ion (■), fission fragment (⧫) and neutron (▼) irradiation at low temperatures (after [17])

ciency in copper irradiated at low temperature (Fig. 3.16). The value of ξ increases rapidly from zero to > 1 at very low recoil energies. That ξ exceeds 1.0 is attributed to the inability of the modified K–P model to describe displacements in a polycrystalline material at recoil energies near the threshold displacement energy, E_d, due to the strong dependence of E_d on crystallographic orientation [17]. With increasing energy, ξ steadily decreases to a value of about 0.3 for 5 keV cascades in copper. The formation of multiple subcascades at high PKA energies (above ~ 20 keV) causes ξ to remain nearly constant for PKA energies up to 500 keV. Comparing this plot to the recoil and weighted recoil spectra given in Figs. 3.5 and 3.6 shows that electrons and light ions with a low PKA energy will generate values of ξ close to 1, while heavy ions and neutrons that produce high PKA energies will result in ξ at the asymptotic value of 0.3.

The displacement cascade efficiency, ξ is comprised of several components:

$\gamma_{i,v}$ The isolated point defect fraction
$\delta_{i,v}$ Clustered fraction including mobile defect clusters such as di-interstitials
ζ Fraction initially in isolated or clustered form after the cascade quench that is annihilated during subsequent short term ($> 10^{-11}$ s) intracascade thermal diffusion

They are related as follows:

$$\xi = \delta_i + \gamma_i + \zeta = \delta_v + \gamma_v + \zeta \,. \tag{3.24}$$

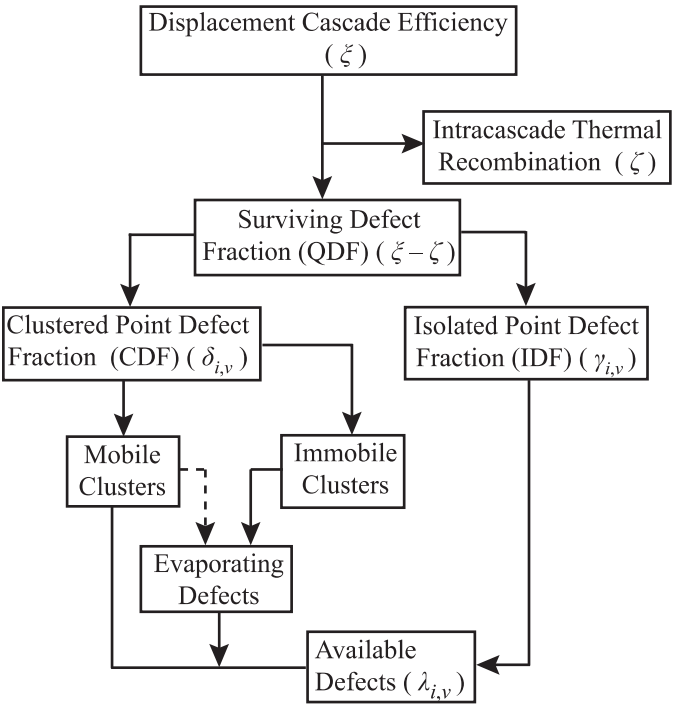

Fig. 3.17. Interdependence of isolated point defects, mobile defect clusters, and thermally evaporating defect clusters that contribute to the fraction of surviving defects that are "available" for radiation effects (after [17])

Figure 3.17 shows the history of defects born according to the NRT model as vacancies and interstitials. The fraction of defects that will be annihilated after the cascade quench by recombination events among defect clusters and point defects within the same cascade (intracascade recombination), ζ is about 0.07, for a displacement efficiency of 0.3. The clustered fraction, δ includes large, sessile clusters and small defect clusters that may be mobile at a given irradiation temperature and will be different for vacancies and interstitials. For a 5 keV cascade, δ_i is about 0.06 and δ_v is closer to 0.18. Some of these defects may be able to "evaporate" or escape the cluster and become "available" defects (Fig. 3.17).

This leaves γ, the isolated point defect fraction as yet to be determined. These defects are available to migrate to sinks, to form clusters, to interact with existing clusters and to participate in the defect flow to grain boundaries that gives rise to radiation-induced segregation. Because of their potential to so strongly influence the irradiated microstructure, defects in this category, along with defects freed from clusters, make up the *freely migrating defects* (FMD). Recall that electrons and light ions produce a large fraction of their defects as isolated Frenkel pairs, thus increasing the likelihood that they remain as isolated defects rather than in clusters. Despite the equivalence in energy among the four particle types described in Fig. 3.7, the

average energy transferred and the defect production efficiencies vary by almost two orders of magnitude! This is explained by the differences in the cascade morphology among the different particle types. Neutrons and heavy ions produce dense cascades that result in substantial recombination during the cooling or quenching phase. However, electrons are just capable of producing a few widely spaced Frenkel pairs (FP) that have a low probability of recombination. Protons produce small widely spaced cascades and many isolated FPs due to the Coulomb interaction and therefore, fall between the extremes in displacement efficiency defined by electrons and neutrons.

The value of γ has been estimated to range from 0.01 to 0.10 depending on PKA energy and irradiation temperature, with higher temperatures resulting in the lower values. Because of the importance of this parameter, we will estimate the freely migrating defect fraction using an analytical treatment by Naundorf [18] that is based on two factors. The first is that energy transfer to atoms is only sufficient to create a single Frenkel pair. The second is that the Frenkel pair lies outside a recombination (interaction) radius so that the nearby FPs neither recombine nor cluster. The model follows each generation of the collision and calculates the fraction of all defects produced that remain free. According to Naundorf, the free single FPs are classified according to the generation i in which they were produced, i.e., the relative amount η_1 is that amount that is produced by primary collisions (first generation), while η_2 is the relative amount produced by secondary collisions (second generation). Thus the total number of free single FPs produced is:

$$\eta = \sum_i \eta_i \,, \tag{3.25}$$

where that produced by primary collisions is:

$$\eta_1 = (\beta_\mathrm{p}/\sigma_\mathrm{d}) \int_{E_\mathrm{d}}^{\gamma E} \sigma(E_\mathrm{i}, T)\, \mathrm{d}T \,, \tag{3.26}$$

and that produced by secondary collisions is:

$$\eta_2 = (1/\sigma_\mathrm{d}) \int_{E_\mathrm{d}}^{\gamma E} \sigma(E_\mathrm{i}, T)[Z(T)\beta_\mathrm{A}(T)/\sigma_\mathrm{A}(T)]\, \mathrm{d}T \int_{E_\mathrm{d}}^{2.5E_\mathrm{d}} \sigma(T, T')\, \mathrm{d}T' \,, \tag{3.27}$$

where $\sigma(E_\mathrm{i}, T)$ is the energy transfer cross section for an incident particle to a lattice atom and $\sigma(T, T')$ is the energy transfer cross section between like atoms in the solid, $Z(T)$ is the total number of secondary collisions produced above E_d by a PKA of energy T along its path. The primary displacement cross section for the incident ion, σ_p, is:

$$\sigma_\mathrm{p} = \int_{E_\mathrm{d}}^{\gamma E} \sigma(E_\mathrm{i}, T)\, \mathrm{d}T \,, \tag{3.28}$$

and the total displacement cross section σ_d is given in the Kinchin–Pease model by:

$$\sigma_\mathrm{d} = \int_{E_\mathrm{d}}^{\gamma E} \sigma(E_\mathrm{i}, T)\nu(T)\, \mathrm{d}T \,. \tag{3.29}$$

The distance λ between two primary collisions is distributed according to an exponential law:

$$W(\lambda) = 1/\lambda_p \exp(-\lambda/\lambda_p) \,, \tag{3.30}$$

with the mean distance:

$$\lambda_p = \Omega/\sigma_p \,, \tag{3.31}$$

where Ω is the atomic volume. The condition that the distance between two consecutive collisions must be larger than an appropriate interaction radius, r_{iv} (so that FPs produced near each other neither recombine nor cluster) reduces the amount of all possible free single FPs by:

$$\beta_p = \exp(-r_{iv}/\lambda_p) \,, \tag{3.32}$$

and is illustrated in Fig. 3.18 [19]. The model provides the efficiency for the production of freely migrating defects. Results of this calculation are shown in Table 3.2 for several ions of varying mass and energy. Values of η range between 24% for proton irradiation to 3% for heavy ion (krypton) irradiation.

Applying this model to our illustration in Fig. 3.7 yields the following values for η:

MeV electrons:	1.0
3.4 MeV protons:	0.2
5.0 MeV Ni^{++} ions:	0.04
Neutrons (fission spectrum):	0.02

These results can also be compared to those calculated by Rehn et al. [20] determined from analysis of experiments and are shown in Fig. 3.19. The data in this

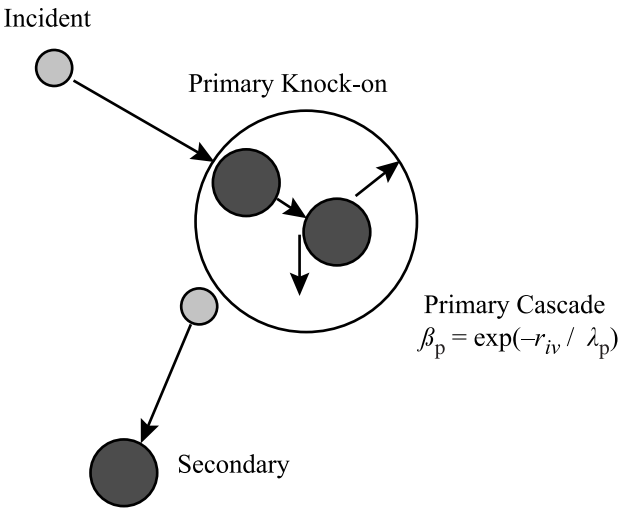

Fig. 3.18. Illustration of the effect of the interaction radius on single Frenkel pair production

Table 3.2. Calculated values for σ_p/σ_d and of the relative amounts η_{calc} of FP production in nickel by different kinds of irradiations ($E_d = 40\,eV$, $r_{iv} = 0.7\,nm$) using Lindhard's analytical differential collision cross section (from [18])

Irradiation	σ_p/σ_d (%)	η_{calc} (%)
1 MeV H^+	37.0	24.0
2 MeV H^+	30.0	19.2
2 MeV Li^+	27.0	16.9
1.8 MeV Ne^+	16.0	8.7
300 keV Ni^+	5.1	2.3
3 MeV Ni^+	7.5	3.8
3.5 MeV Kr^+	5.9	3.0
2 keV O^+	42.0	9.8

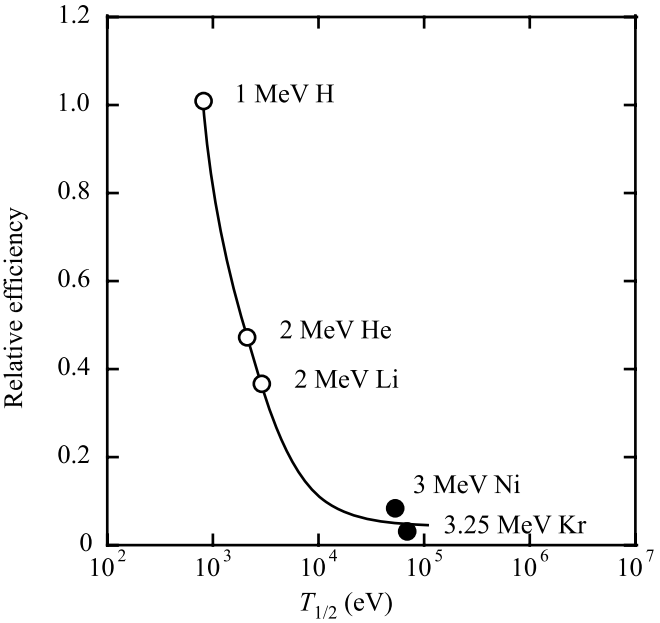

Fig. 3.19. Relative efficiency of freely migrating defect production for ions of various mass and energy (after [20])

figure are arbitrarily normalized to 1.0 for 1 MeV protons. This data along with the results just presented show that at low recoil energies, the fraction of defects that are freely migrating approaches 1.0 and as the recoil energy increases, that fraction drops to values in the range 0.02 to 0.05.

Recent results [21], however, have shown that the low values of FMD efficiency for heavy ion or neutron irradiation cannot be explained by defect annihilation within the parent cascade (*intra*cascade annihilation). In fact, cascade damage generates vacancy and interstitial clusters that act as annihilation sites for FMD,

reducing the efficiency of FMD production. Thus, the cascade remnants result in an increase in the sink strength for point defects and along with recombination in the original cascade, account for the low FMD efficiency measured by experiment.

While the NRT description of atom displacements provides an estimation of the number of Frenkel pairs produced by the PKA, it does not accurately describe atomic interactions in the thermal spike and hence, is inadequate for describing the true configuration of defects. MD simulations can be used for this purpose and have confirmed that defect production by displacement cascades is not as efficient as predicted by the NRT formula. In fact, ν is about 20 to 40% of υ_{NRT} for cascades with energy greater than 1–2 keV. From analysis of MD results for several metals [22], the number of Frenkel pairs is found to depend on the kinetic energy of the PKA, T as:

$$\nu_{\mathrm{MD}} = AT^n \,, \tag{3.33}$$

where A and n are constants that are only weakly dependent on the metal and temperature. Figure 3.20 shows the dependence of ν_{MD} on T for various metals. Note that the behavior of Frenkel pair production is well represented by this function over a large damage energy range. Also note that the results all fall below the NRT value as shown by the solid line in the figure. The lower efficiency is likely the result of SIA production at the periphery of the disordered core dominating that at the end of focused collision chains such that the close proximity to the vacancies and the high kinetic energy of the core during the thermal spike assist in SIA-vacancy recombination.

From the results shown in Fig. 3.20, there is no noticeable dependence on the crystal structure, as there are three fcc metals (Al, Ni, Cu), two hcp metals (Ti, Zr), one bcc metal (Fe) and one ordered $L1_2$ structure (Ni_3Al), and yet the magnitude of ν_{FP} is not separated along crystal structure lines. Second, there is a dependence on atomic mass of the metal as noted in the dependence of ν_{MD} and A on T. The dependence of n on atomic mass is weaker, though evident. The decrease in efficiency with atomic mass is likely due to the enhanced recombination due to thermal spike effects. As cascade energy increases, there is a tendency for cascades to break up into subcascades. Since one cascade produces fewer defects than two separate cascades of the same total energy, subcascade formation will increase the slope of the plots in Fig. 3.20. The transition to subcascades occurs at lower energy in lighter metals and may be the cause for the mass-dependence on efficiency. Note that n is only weakly dependent on mass.

MD simulation has also been applied to the study of defect production in alloys [23, 24]. One might expect that the mass difference between solute atoms in an alloy will interrupt crystallographic processes such as focusing and channeling and result in the production of more Frenkel pairs as compared to the pure metal case. MD simulations in copper containing up to 15 at% gold in solution shows that the larger Au atoms decrease the length of focused displacement events in the ballistic phase and thereby enhance the intensity and lifetime of the disorder and temperature of the thermal spike. However, ν_{FP} was found to be independent on

the alloy composition over a wide range of T. Similar studies conducted on Fe–Cu alloys substantiated these results. Movie 3.3 shows cascade formation and cooling in an Fe–10%Cr alloy in which the yellow balls are vacancies, the grey are iron interstitials and the green are chromium interstitials. In this simulation chromium is modeled as the larger solute, and after cooling, the remaining interstitial population is predominantly iron atoms as their distortion of the lattice is less than that from the oversized chromium atoms.

The results shown in Fig. 3.20 are for MD calculations at or below a temperature of 100 K. Irradiation temperature has a strong effect on the evolution of radiation damage in metals because of its effect on the motion of defects and their stability as clusters. Irradiation temperature also has an effect on the formation of Frenkel pairs. Figure 3.21 shows the Frenkel pair production as a function of temperature in α-iron up through 900 K (627 °C) and for several values of PKA energy. Note that there is a small but consistent effect of temperature in that higher irradiation temperatures produce fewer Frenkel pairs. The lower Frenkel pair production is believed to be due to the increase in the lifetime of the thermal spike as T_{irr} increases, which allows for more defect motion before cooling and hence, more vacancy-interstitial recombination within the cascade region. A contributing factor may be the shorter length of the focused collision sequences (due to the higher kinetic energy of the atoms) that results in a reduction of the vacancy-interstitial separation distance.

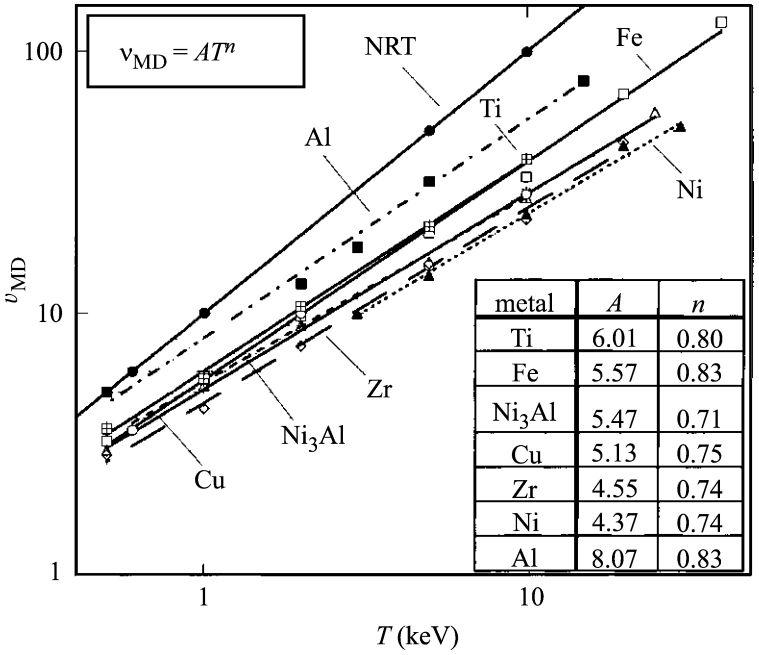

Fig. 3.20. Number of Frenkel pairs produced as a function of damage energy, T for Cu, Fe, Ti, Zr and Ni_3Al at 100 K and for Al and Ni at 10 K (after [22])

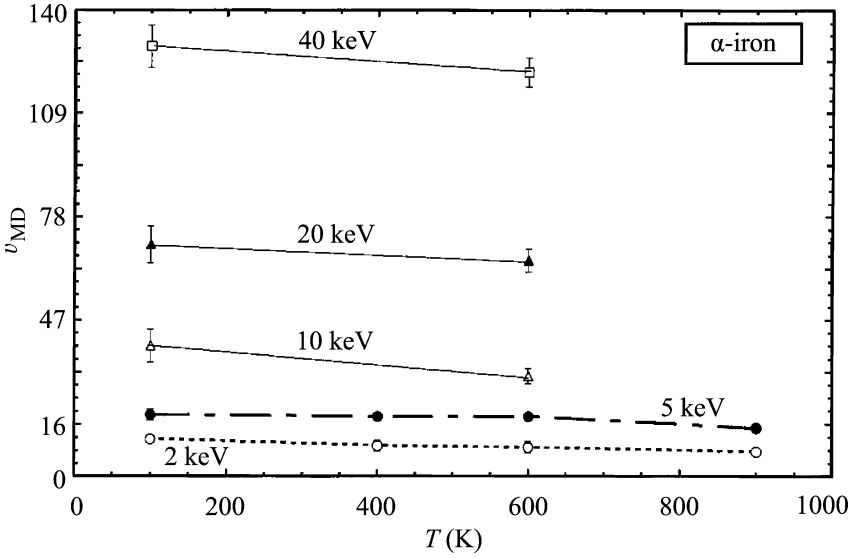

Fig. 3.21. Number of Frenkel pairs produced per cascade as a function of the PKA energy and irradiation temperature in α-iron (after [22])

In ordered alloys such as Ni_3Al (Fig. 3.20), the Frenkel pair production is similar to that in the pure metal (compare with Ni, for example). In addition to Frenkel pairs, anti-site defects or amorphization can occur in these systems. Anti-site defects consist of atoms of the wrong type occupying regular sites in the sublattice. These anti-site defects are observed to increase with T to the 1.25 power rather than to the 0.75 power as in the case of Frenkel pairs. If the amount of disorder is large enough, amorphization can occur. That the anti-site defects form in the molten core confirm that the thermal spike is important in the formation of these defects. The effect of increasing irradiation temperature on defect production in an ordered structure is to increase the number of anti-site defects, primarily due to the reduced length of focused collision sequences.

We now have the description of the damage state that we need in order to begin to describe the development of the physical and mechanical effects of irradiation. The K–P/NRT models along with the energy transfer cross sections provide a means to calculate the number of displacements occurring in a solid from an incident particle of some mass and energy. The spatial, temporal and thermal descriptions of the resulting cascade provide us with a means to estimate the number of defects surviving the cascade quench phase, that are available to influence the microstructure at longer times. To this point, we have focused on developing both a physical and quantitative description of the state of the material at the end of the quench phase of the cascade that is completed within ~ 10 ps of the initial collision event. From that point forward in time, we will be concerned with the development of the microstructure. This development will continue to occur for weeks, months and even

years in a reactor core, spanning some 18 orders of magnitude in time, and constitutes the Physical Effects of Radiation Damage, which is the focus of Part II of this text.

Nomenclature

A	Atomic mass; pre-exponential constant in Born–Mayer relation, Eq. (1.47)
B	Constant in exponent in Born–Mayer relation, Eq. (1.47)
C_p	Specitic heat capacity
D	Thermal diffusivity
E_a	Energy per atom
E_d	Displacement energy
E_D	Damage energy
E_i	Projectile energy
F_D	Energy depth distribution
k_B	Boltzmann's constant
m	1/s
M_1	Mass of projectile
M_2	Mass of target
N	Atom number density
N_d	Number of displacements per unit depth
$P(E_\mathrm{i}, T)$	Primary recoil spectrum
r_{iv}	Recombination radius
R	Ion/atom range in the lattice
s	Exponent in power law relationship
T	Energy transferred in collision
$\check{T}$	Minimum energy transferred
$\hat{T}$	Maximum energy transferred
$\bar{T}$	Average energy transferred
U_a	Energy per atom
V_cas	Cascade volume
$W(\lambda)$	Function for distance between primary collisions
$W(E_\mathrm{i}, T)$	Weighted primary recoil spectrum
ΔX	Longitudinal moment of the cascade
Y	Transverse moment of the cascade
Z	Atomic number
$Z(T)$	Fraction of secondary collisions produced above E_d by a PKA of energy T
β_p	Reduction factor in FPs due to recombination within r_{iv}
δ	Cascade contraction factor
$\delta_\mathrm{i,v}$	Clustered fraction of vacancies and interstitials

ε	Unit charge
ϕ	Neutron flux
γ	$4M_1M_2/(M_1+M_2)^2$
$\gamma_{i,v}$	Isolated point defect fraction
η	Energy lost to electronic excitation in the NRT model; total # free FPs produced in cascade
η_1	Fraction of defects produced by primary collisions
η_2	Fraction of defects produced by secondary collisions
λ	Mean free path
$\nu(T)$	Displacement function
ν_{FP}	Number of Frenkel pairs
Θ	Cascade energy density
$\sigma(E,T)$	Differential energy transfer cross section
$\sigma'_D(E)$	Displacement cross section for collisions between atoms
σ_d	Total displacement cross section
σ_p	Primary displacement cross section for incident ion
τ	Cascade lifetime
ξ	Displacement efficiency
ζ	Fraction of vacancies and interstitials initially clustered that are subsequently annihilated in the cascade

Problems

3.1 Plot the mean free path for Ni between the energies of 1 and 10,000 eV, making calculations at each decade. At what energy is the mean free path the smallest? Use Eq. (1.50) to determine the Born–Mayer constants and a value of 40 eV for E_d.

3.2 What is the implication of the difference in shape in the weighted recoil spectra for neutrons and protons in the morphology of the damage cascade?

3.3 For 1 MeV neutrons incident on nickel, determine
   a) The damage energy
   b) The effective cascade temperature
   c) The cascade lifetime
   using $U_a \sim 0.3$ eV and $D \sim 10^{12}$ nm^2/s.

3.4 You would like to model displacement cascades. What is the appropriate modeling tool, kinetic Monte Carlo or molecular dynamics? Why?

3.5 Based on your expertise using SRIM, you decide to irradiate a steel sample (Fe–18Cr–9Ni) with nickel ions. You have the choice of examining the sample near the surface of the sample or near the damage peak. You are worried that all the implanted nickel ions will change the local chemistry of the sample. To mitigate this concern, should you look in the region closer to the sample surface or the damage peak? Why?

References

1. Olander DR (1976) Fundamental Aspects of Nuclear Reactor Fuel Elements, TID-26711-P1. Technical Information Service, Springfield, VA
2. Averback RS (1994) J Nucl Mater 216:49
3. Brinkman JA (1956) Amer J Phys 24:251
4. Seeger A (1958) On the theory of radiation damage and radiation hardening. In: Proceedings of the Second United Nations International Conference on the Peaceful Uses of Atomic Energy, Geneva, 1958, Vol. 6, p 250, United Nations, New York
5. Nastasi M, Mayer JW, Hirvonen JK (1996) Ion-Solid Interactions: Fundamentals and Applications. Cambridge University Press, Cambridge
6. Was GS, Allen TR (1994) Mater Character 32:239
7. Sigmund P (1981) Sputtering by ion bombardment: theoretical concepts. In: Behrisch R (ed) Sputtering by Particle Bombardment, Springer, Berlin Heidelberg New York, p 9
8. Heinisch HL (1996) J Metals Dec:38
9. Robinson MT (1994) J Nucl Mater 216:1
10. Robinson MT, Torrens IM (1974) Phys Rev B 9:5008
11. Beeler JR (1966) Phys Rev 150:470
12. Ziegler JF, Biersack JP, Littmark U (1996) The Stopping and Range of Ions in Solids. Pergamon, New York
13. Finnis MW, Sinclair JE (1984) Phil Mag A50:45–55; (1986) Erratum Phil Mag A53:161
14. Calder AF, Bacon DJ (1993) J Nucl Mater 207:25–45
15. Stoller RE (1996) J Metals Dec:23
16. Diaz de la Rubia T, Averback RS, Benedek R, King WE (1987) Phys Rev Lett 59(19):1930
17. Zinkle SJ, Singh BN (1993) J Nucl Mater 199:173
18. Naundorf V (1991) J Nucl Mater 182:254
19. Was GS, Allen TR (2007) In: Radiation Effects in Solids, Sickafus KE, Kotomin EA, Uberoage BP, eds, NATO Science Series, Springer 235:65–98
20. Rehn LE, Okamoto PR, Averback RS (1984) Phys Rev B 30(6):3073
21. Iwase A, Rehn LE, Baldo PM, Funk L (1996) J Nucl Mater 238:224–236
22. Bacon DJ, Gao F, Osetsky YuN (2000) J Nucl Mater 276:1–12
23. Deng HF, Bacon DJ (1996) Phys Rev B 54:11376
24. Calder AF, Bacon DJ (1997) In: Proceedings of Symposium on Microstructure Evolution During Irradiation, Vol. 439. Materials Research Society, Pittsburgh, PA, p 521

4 Point Defect Formation and Diffusion

The first step in understanding the effects of irradiation on materials is to understand, on the atomic level, the nature of radiation damage. In the previous chapters we developed a quantitative description of the process of displacing an atom from its lattice site by the transfer of kinetic energy from a high-energy particle. The recoiling lattice atom travels through the crystal, colliding with its neighbors and displacing these also from their sites. A cascade of atomic collisions is created by the original particle with the end result being a number of vacant lattice sites and an equal number of displaced atoms wedged into the interstices of the lattice. The basic *defects* (vacancies and interstitials) form the foundation for *all* observed effects of irradiation on the physical and mechanical properties of materials. Determination of the concentration and diffusion of these basic defects is the subject of this chapter.

4.1 Properties of Irradiation-Induced Defects

Various types of defects exist in any crystalline lattice. These include:

- Point defects (0D): vacancies and interstitials
- Line defects (1D): dislocation lines
- Planar defects (2D): dislocation loops
- Volume defects (3D): voids, bubbles, stacking fault tetrahedra

The most basic of these are point defects. Following [1], we will start with interstitials.

4.1.1 Interstitials

An interstitial is an atom that is located in a position of a crystal that is not a regular lattice site. There are two broad classifications of interstitial sites in the various cubic crystal lattices: octahedral sites and tetrahedral sites, and these will be briefly reviewed. The fcc lattice is cubic with unit cell of length a (lattice constant) and with atoms located at the corners and the faces of the cube (Fig. 4.1). Each corner atom is shared by eight unit cells and each face atom is shared by two unit cells, so the number of atoms per unit cell is 8 corner atoms $\times 1/8$ atom/unit cell $+$ 6 face atoms $\times 1/2$ atoms/unit cell $= 4$. Octahedral sites are interstitial positions that are

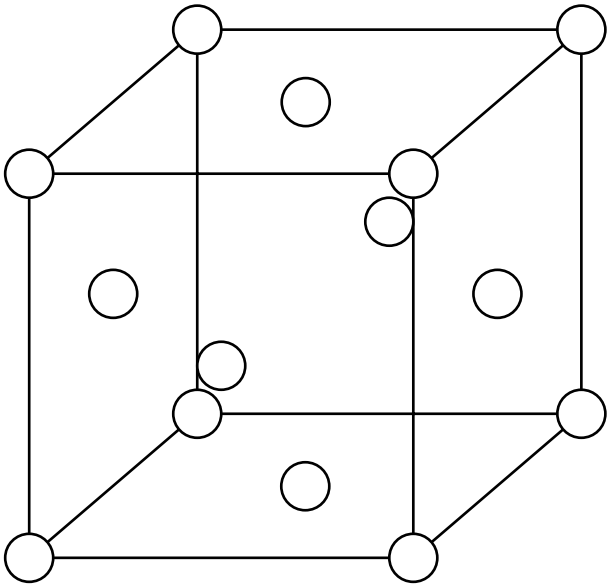

Fig. 4.1. Face-centered cubic (fcc) lattice unit cell

surrounded by an octahedron where the lattice atoms make up the six vertices of an octahedron. There are four octahedral sites per unit cell in the fcc lattice, the center of the unit cell and the edges. The center site is wholly within the unit cell, but the sites on the edges are each shared by four unit cells (Fig. 4.2a). So the total number of octahedral interstitial sites per unit cell is $1 + 12$ edge sites $\times 1/4$ site per unit cell $= 4$ sites. There are also tetrahedral interstitial sites in the fcc lattice in which the atom is located inside a tetrahedron formed by lattice atoms. These are located in side the corners of the unit cell (Fig. 4.2b). There are a total of 8 tetrahedral sites (one for each corner) in the fcc unit cell.

In the bcc lattice, the atoms reside at the corners of the unit cell with one in the center of the cell for a total of two atoms per unit cell; $1 + 8$ corner sites $\times 1/8$ site/unit cell $= 2$ sites (Fig. 4.3). Octahedral interstitial sites are located on the faces and the edges of the unit cell giving 6 faces $\times 1/2$ site per face $+12$ edges $\times 1/4$ sites

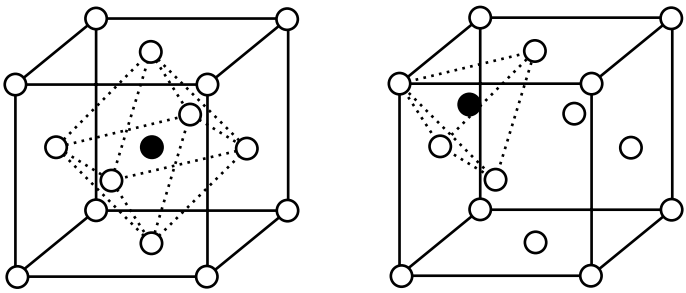

Fig. 4.2. Interstitial positions in the fcc unit cell

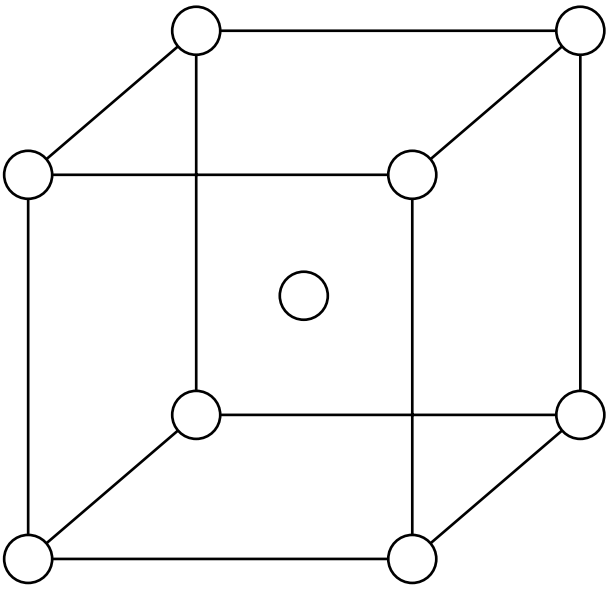

Fig. 4.3. Body-centered cubic (bcc) lattice unit cell

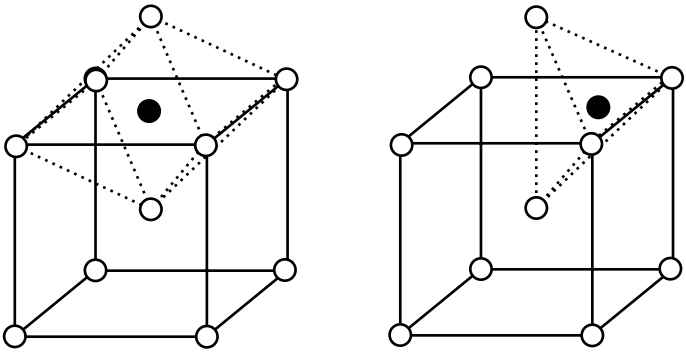

Fig. 4.4. Interstitial positions in the bcc unit cell

per edge = 6 sites per unit cell (Fig. 4.4a). Tetrahedral interstitial sites are located on the faces and in the corners of the faces. There are 6 faces $\times$ 4 locations per face $\times$ 1/2 sites/face = 12 tetrahedral sites (Fig. 4.4b).

The hcp unit cell is not cubic but rather hexagonal and is defined by the c/a ratio where a is the length of a side of the regular hexagon and c is the height of the cell (Fig. 4.5). There are six atoms per unit cell in the hcp lattice; twelve on the corners shared by six cells (= 2) plus two on the faces shared by two cells (= 1) plus three inside the cell at a height of $1/2c$ (= 3). There are six octahedral sites per unit cell, all wholly contained within the unit cell (Fig. 4.6a). There are also six tetrahedral sites per unit cell, four wholly contained within the unit cell and six that are shared by each of three cells (Fig. 4.6b).

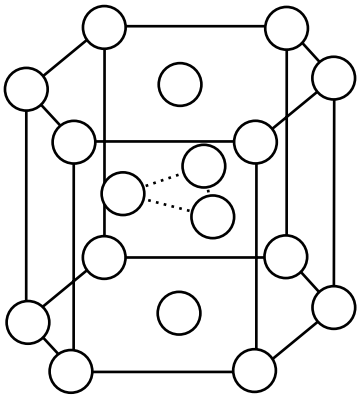

Fig. 4.5. Hexagonal close packed (hcp) unit cell

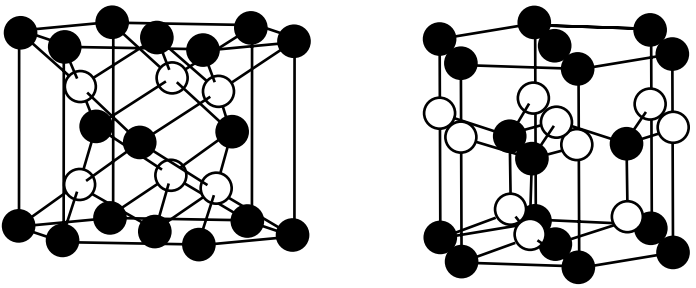

Fig. 4.6. Interstitial positions in the hcp unit cell

Our simple picture of interstitials is not a true physical picture because the stable configuration of self-interstitial atoms (SIA) in metals is the dumbbell or split-interstitial configuration where two atoms are associated with or "share" a single lattice site. Since the atom cores repel each other, the atoms arrange themselves in the lowest energy orientation. This turns out to be with the dumbbell axis along the $\langle 100 \rangle$ direction for fcc metals, the $\langle 110 \rangle$ direction for bcc metals and the $\langle 0001 \rangle$ direction for hcp crystals (Fig. 4.7).

To accommodate two atoms in one lattice site, atoms adjacent to the dumbbell are displaced slightly off their lattice positions which then perturbs neighboring atoms and so on. These displacements emanate from the defect, forming an elastic displacement field. The symmetry of the displacement field is reflected by the SIA configuration in the bcc lattice (Fig. 4.8).

Consider a $\langle 100 \rangle$ dumbbell interstitial configuration in fcc aluminum. The separation distance of the two dumbbells is about $0.6a$. The nearest neighbor spacing in the fcc lattice is along $\langle 110 \rangle$ and is $(a/\sqrt{2})$. So the separation distance of a $\langle 100 \rangle$ dumbell is about 20% smaller than the nearest neighbor distance in the undistorted lattice. The four nearest neighbors to each dumbbell are displaced outwards by about $0.1a$ and the total relaxation volume is about 2Ω, where Ω is the atomic volume. The relaxation volume is determined by treating the crystal as an elastic continuum and inserting an atom as an interstitial (or removing one to create a vacancy) and

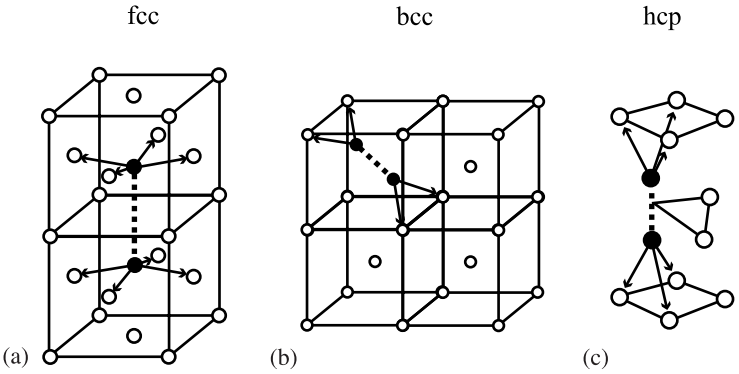

Fig. 4.7. Configurations of SIAs in (a) fcc, (b) bcc and (c) hcp lattices

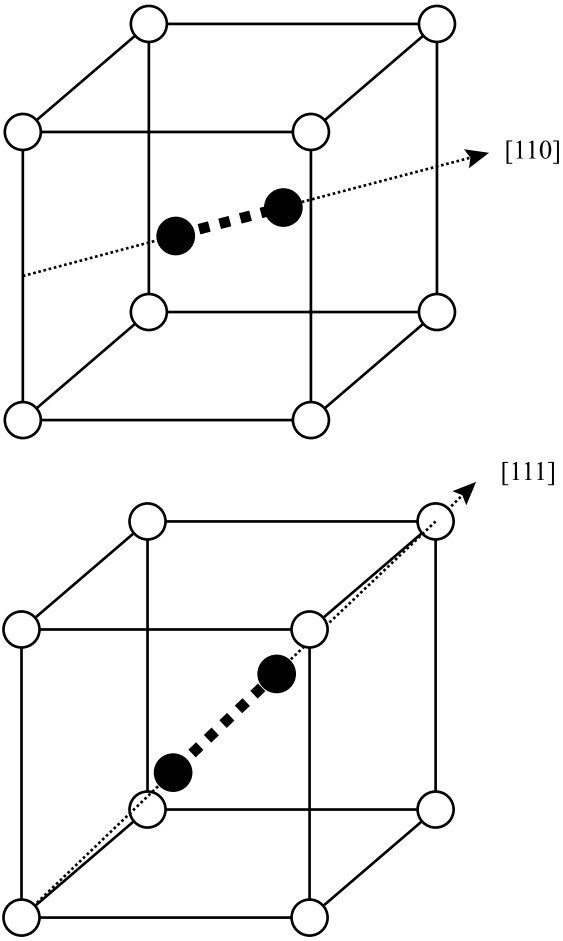

Fig. 4.8. Split interstitials in the bcc lattice

Table 4.1. Numerical values, compiled from different sources for some quantities characterizing properties of radiation-induced point defects in metals (from [1])

	Symbol	Unit	Al	Cu	Pt	Mo	W
Interstitials							
Relaxation volume	V^{i}_{relax}	Atomic vol.	1.9	1.4	2.0	1.1	
Formation energy	E^{i}_{f}	eV	3.2	2.2	3.5		
Equilibrium concentration at T^{*}_{m}	$C_{i}(T_{m})$	–	10^{-18}	10^{-7}	10^{-6}		
Migration energy	E^{i}_{m}	eV	0.12	0.12	0.06		0.054
Vacancies							
Relaxation volume	V^{v}_{relax}	Atomic vol.	0.05	−0.2	−0.4		
Formation energy	E^{v}_{f}	eV	0.66	1.27	1.51	3.2	3.8
Formation entropy	S^{v}_{f}	k	0.7	2.4			2
Equilibrium concentration at T^{*}_{m}	$C_{v}(T_{m})$	–	9×10^{-6}	2×10^{-6}			4×10^{-5}
Migration energy	E^{v}_{m}	eV	0.62	0.8	1.43	1.3	1.8
Activation energy for self-diffusion	Q_{vSD}	eV Q_{a}	1.28	2.07	2.9	4.5	5.7
Frenkel pairs							
Formation energy	E^{FP}_{f}	eV	3.9	3.5	5		

determining the amount of distortion resulting in the lattice. The high relaxation volumes due to SIAs cause large lattice distortions, which lead to strong interaction with other SIAs and with other lattice defects (dislocation, impurity atoms). The net effect of this elastic interaction is an attraction of mobile SIAs to these defects. Experimental values for the relaxation volume in several metals appear in Table 4.1.

4.1.2 Multiple Interstitials

Multiple interstitials form by the agglomeration of mobile SIAs at elevated temperatures. Multiple interstitials have a high binding energy on the order of 1 eV. Since the energy needed to dissociate a SIA from a large cluster approaches the SIA formation energy (2–4 eV), SIA clusters are very stable against dissociation at low temperatures.

Computer simulation predicts that the stable configuration of a di-interstitial in fcc metals is two parallel dumbbells on nearest neighbor sites (Fig. 4.9). The stable structure of tri-interstitials in fcc metals is predicted by computer simulation to be three orthogonal ⟨100⟩ dumbbells on nearest neighbor sites. The anticipated configuration of di-interstitials in the bcc lattice is two ⟨110⟩ dumbbells on nearest neighbor sites.

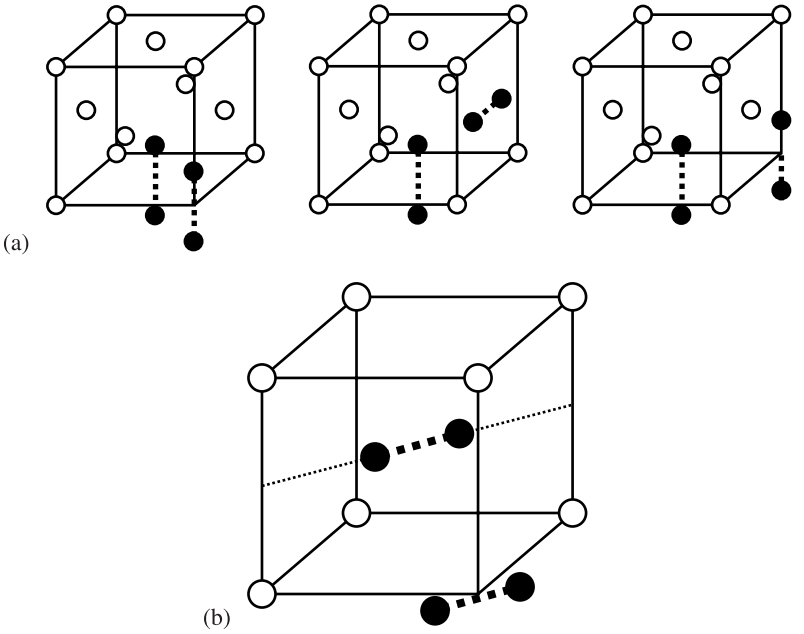

Fig. 4.9. Di-interstitials in the (a) fcc lattice in stable, metastable and new stable positions, and (b) in the bcc lattice

4.1.3 Interstitial–Impurity Complexes

Impurity atoms in metals are efficient traps for SIAs. Stable complexes consisting of undersized atoms and interstitials do not dissociate thermally below a temperature where vacancies become mobile. One possible configuration is the mixed dumbbell where one of the dumbbell atoms is replaced by the impurity atom (Fig. 4.10a). Binding energies are of the order of 0.5 – 1.0 eV. Weaker trapping is observed with oversized impurities (Fig. 4.10b).

Interstitial–impurity complexes require only a small activation energy to re-orient themselves by so-called cage motion. Shown in Fig. 4.10a, the impurity can jump between the indicated positions of the central octahedron, forming a new mixed dumbbell with the adjacent host atom. Since all of the mixed dumbbells have the impurity end toward the center of the cage, no long-range motion is associated with cage motion. The activation energy of the re-orientation jump in the cage is about 0.01 eV.

Movies 4.1 and 4.2 show the behavior of iron and chromium in an Fe–10%Cr alloy following a displacement cascade as a function of the relative sizes of the solutes. In Movie 4.1, chromium is modeled as an oversized solute and in Movie 4.2, chromium is undersized. Note the difference in the interstitial clusters following the cascade cooling period. The undersize Cr (Movie 4.2) undergoes stronger trapping by the iron interstitials than in the case of oversize Cr (Movie 4.1), resulting is a greater number of small interstitial clusters containing Cr.

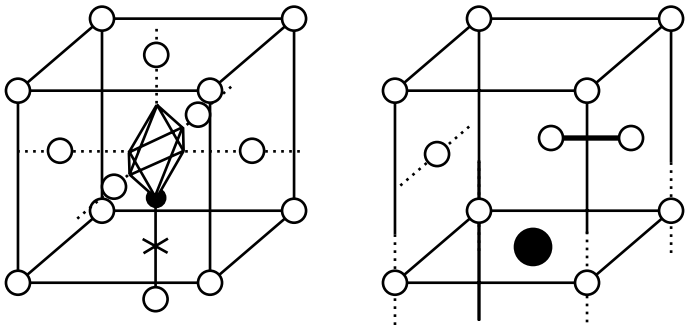

Fig. 4.10. (a) Mixed dumbbell configuration in the fcc lattice formed by an undersized impurity and an atom of the host lattice. The vertices of the octahedron are the other locations of the impurity as it makes a dumbbell with the other "face" atoms in the unit cell. (b) Trapping of an interstitial to make a dumbbell with an oversized impurity in the fcc lattice

4.1.4 Vacancies

The vacancy, or missing lattice atom, is the simplest point defect in metal lattices. All calculations and computer simulations show that the single vacancy structure is a missing lattice atom with the nearest neighbors relaxing inward toward the vacancy.

SIAs have a high formation energy ($> 2.0\,\text{eV}$), a large relaxation volume ($\sim 2\,\Omega$) and a low migration energy ($< 0.15\,\text{eV}$) leading to a high mobility. Vacancies, on the other hand, have low formation energies ($< 2\,\text{eV}$), low relaxation volume (0.1–$0.5\,\Omega$) and high migration energy ($> 0.5\,\text{eV}$) and are therefore much less mobile than SIAs (Table 4.1). Further, the strain field of vacancies is isotropic in cubic metals making them hard to investigate.

4.1.5 Multiple Vacancies

Multiple vacancies have small binding energies compared to interstitial clusters (0.1 eV) but are often observed in irradiated metals. The configuration of multiple vacancy clusters is shown for the fcc lattice in Fig. 4.11a, and for the bcc lattice in Fig. 4.11b. The migration energy of di-vacancies is less than for single vacancies (0.9 eV vs. 1.32 eV for Ni) but increases with increasing cluster size. It appears that since the tetra-vacancy can only migrate by dissociation, it is the first stable nucleus for further clustering.

4.1.6 Solute–Defect and Impurity–Defect Clusters

Vacancies can bind to oversize solute or oversize impurity atoms in order to lower the overall free energy of the solid. Estimates of the binding energy of a vacancy to an oversize solute in the fcc lattice range from 0.2 to 1.0 eV [2]. Hence, these solutes can act as efficient traps for vacancies in the lattice.

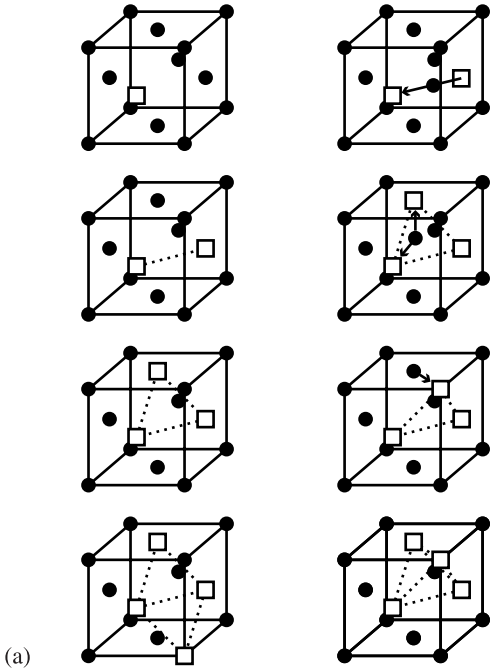

(a)

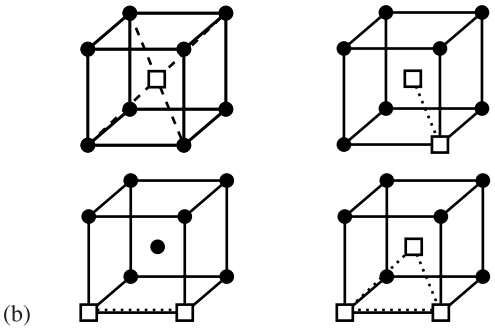

(b)

Fig. 4.11. Configurations of multiple vacancies in the (a) fcc lattice, and (b) bcc lattice

4.2 Thermodynamics of Point Defect Formation

Even in the absence of irradiation, a crystal cannot exist at finite a temperature in a state of absolute perfection. Statistically, there is a finite probability that sufficient energy will be concentrated, by local fluctuations, to form a defect in the crystal lattice. For most purposes, it is fair to assume that the volume of the crystal is constant, for which the Helmholtz free energy function applies. Following [3], if the system is at constant pressure then:

$$F \cong G = U + pV - TS = H - TS \,, \tag{4.1}$$

where U is the internal energy, H is the total enthalpy of the N atoms comprising the system. S represents the disorder (entropy) in the system which can be characterized by:

$$S = k \ln w \,, \tag{4.2}$$

where w is the number of possible different configurations of atoms and k is Boltzmann's constant.

Suppose that a crystal has n defects with N available sites. The increase in free energy is:

$$\Delta G_{\mathrm{f}} = n\Delta H_{\mathrm{f}} - T\Delta S \,, \tag{4.3}$$

where ΔH_{f} is the increase in enthalpy brought about by the introduction (formation) of the defect and ΔS is the change in total entropy, determined as follows.

For one defect, there are N available sites and hence N possible configurations. For n defects, there are N for the first, $(N-1)$ for the second, $(N-2)$ for the third, etc., up to $(N-n+1)$ for the nth. This leads to $N(N-1)(N-2)\ldots(N-n+1)$ configurations in all. But because these are not all distinct and defects are indistinguishable, the number above allows for $n!$ ways of distributing N defects among n sites. Hence, the number of possible different configurations is:

$$w = \frac{N(N-1)(N-2)\ldots(N-n+1)}{n!} \,, \tag{4.4}$$

or

$$w = \frac{N!}{n!(N-n)!} \,. \tag{4.5}$$

The *mixing entropy* is then:

$$\Delta S_{\mathrm{mix}} = k\left[\ln N! - \ln n! - \ln(N-n)!\right] \,. \tag{4.6}$$

Using Stirling's approximation of $\ln x! \simeq x \ln x$ for large x gives:

$$\Delta S_{\mathrm{mix}} = k \ln w \cong \left[N \ln N - n \ln n - (N-n)\ln(N-n)\right] \,. \tag{4.7}$$

In addition to ΔS_{mix} there is a contribution to ΔS from the vibrational disorder of the presence of the defects. According to the Einstein model of lattice motion, the atoms are represented as $3N$ independent linear harmonic oscillators and the associated entropy is:

$$S_{\text{f}} = 3k \ln\left(\frac{kT}{\hbar \nu_{\text{E}}}\right) , \tag{4.8}$$

where ν_{E} is the natural frequency of the oscillator and $\hbar$ is Planck's constant. If each defect changes the vibration frequency of z neighbors to ν_{r}, the entropy is:

$$S'_{\text{f}} = 3kz \ln\left(\frac{kT}{\hbar \nu_{\text{r}}}\right) = 3kz \left[\ln\left(\frac{kT}{\hbar \nu_{\text{E}}}\right) + \ln\left(\frac{\nu_{\text{E}}}{\nu_{\text{r}}}\right)\right] , \tag{4.9}$$

and for n defects, the total change in entropy due to vibrational disorder is:

$$n(S'_{\text{f}} - zS_{\text{f}}) = \Delta S_{\text{f}} = 3nkz \ln\left(\frac{\nu_{\text{E}}}{\nu_{\text{r}}}\right) . \tag{4.10}$$

Taking both contributions to the entropy change and inserting them into the free energy equation gives:

$$\Delta G_{\text{f}} = n\Delta H_{\text{f}} - kT \left[N \ln N - n \ln n - (N-n)\ln(n-N) + n \ln\left(\frac{\nu_{\text{E}}}{\nu_{\text{r}}}\right)^{3z}\right] . \tag{4.11}$$

In equilibrium, n will be such that it satisfies $\mathrm{d}\Delta G_{\text{f}}/\mathrm{d}n = 0$ giving:

$$\frac{\Delta H_{\text{f}}}{kT} = \ln\left[\frac{N-n}{n}\left(\frac{\nu_{\text{E}}}{\nu_{\text{r}}}\right)^{3z}\right] . \tag{4.12}$$

Assuming $n \ll N$ and letting $n/N = C$ (concentration):

$$C = \left(\frac{\nu_{\text{E}}}{\nu_{\text{r}}}\right)^{3z} \exp\left(\frac{-\Delta H_{\text{f}}}{kT}\right) . \tag{4.13}$$

Writing $\left(\frac{\nu_{\text{E}}}{\nu_{\text{r}}}\right)^{3z}$ in terms of entropy gives the familiar equation:

$$C = \frac{n}{N} = \exp\frac{\Delta S_{\text{f}}}{k} \exp\frac{-\Delta H_{\text{f}}}{kT} = \exp\left(\frac{-\Delta G_{\text{f}}}{kt}\right) . \tag{4.14}$$

For vacancies we have:

$$C_{\text{v}} = \exp\left(\frac{S_{\text{f}}^{\text{v}}}{k}\right) \exp\left(\frac{-E_{\text{f}}^{\text{v}}}{kT}\right) , \tag{4.15}$$

and for interstitials:

$$C_\mathrm{i} = \exp\left(\frac{S_\mathrm{f}^\mathrm{i}}{k}\right)\exp\left(\frac{-E_\mathrm{f}^\mathrm{i}}{kT}\right), \tag{4.16}$$

where $E_\mathrm{f}^\mathrm{v} = \Delta H_\mathrm{f}^\mathrm{v}$ and $E_\mathrm{f}^\mathrm{i} = \Delta H_\mathrm{f}^\mathrm{i}$ and E_f^v, E_f^i are the formation energies for the respective defect type, and $\Delta S_\mathrm{f}^\mathrm{v} = S_\mathrm{f}^\mathrm{v}$, $\Delta S_\mathrm{f}^\mathrm{i} = S_\mathrm{f}^\mathrm{i}$. In metals, typical values for E_f^v are $\sim 1\,\mathrm{eV}$, and for $E_\mathrm{f}^\mathrm{i} \sim 4\,\mathrm{eV}$. Hence the formation of vacancies requires considerably less energy than the formation of interstitials (see Table 4.1) and so at thermal equilibrium, $C_\mathrm{v} \gg C_\mathrm{i}$. Let us look at an example.

Example 4.1. Calculate the equilibrium concentration of vacancies and interstitials in aluminum at room temperature and $10\,°C$ *below the melting point.*

a) $RT \simeq 20\,°\mathrm{C}$ or $293\,\mathrm{K}$
From Table 4.1, we have:

$$E_\mathrm{f}^\mathrm{v} \cong 0.66\,\mathrm{eV} \qquad S_\mathrm{f}^\mathrm{v} \sim 0.7\,\mathrm{k}$$
$$E_\mathrm{f}^\mathrm{i} \cong 3.2\,\mathrm{eV} \qquad S_\mathrm{f}^\mathrm{i} \sim 8\,\mathrm{k}\,,$$

and inserting into Eqs. (4.14) and (4.15) yields:

$$C_\mathrm{v} = \exp\left(S_\mathrm{f}^\mathrm{v}/k\right)\exp\left(-E_\mathrm{f}^\mathrm{v}/kT\right) \sim 1.6\times10^{-11}$$
$$C_\mathrm{i} = \exp\left(S_\mathrm{f}^\mathrm{i}/k\right)\exp\left(-E_\mathrm{f}^\mathrm{i}/kT\right) \sim 5.0\times10^{-51}\,.$$

b) At $10\,°\mathrm{C}$ below T_m' or $650\,°\mathrm{C}$ ($923\,\mathrm{K}$)
Eqs. (4.15) and (4.16) yield:

$$C_\mathrm{v} = \exp\left(S_\mathrm{f}^\mathrm{v}/k\right)\exp\left(-E_\mathrm{f}^\mathrm{v}/kT\right) \sim 5.0\times10^{-4}$$
$$C_\mathrm{i} = \exp\left(S_\mathrm{f}^\mathrm{i}/k\right)\exp\left(-E_\mathrm{f}^\mathrm{i}/kT\right) \sim 9.8\times10^{-15}\,.$$

Besides doing an experiment, how do we go about obtaining an estimate for E_f^v? Suppose we create a small cavity in a rigid crystal that has a volume $\Omega = 4/3\pi r_\mathrm{a}^3$ equal to the volume occupied by one atom, where Ω is the atom volume and r_a is the atom radius. Since we must conserve volume, we spread the material from the cavity uniformly over the surface of a crystal. If the crystal is a sphere, we have:

$$R' = R + \Delta R\,. \tag{4.17}$$

Since the crystal is a rigid medium and volume is conserved:

$$4\pi R^2 \Delta R = 4/3\pi r_\mathrm{a}^3\,, \tag{4.18}$$

and if the crystal is large compared to the size of the atom, then $R \gg r_a$ and $\Delta R \ll R$ and:

$$\Delta R = r_a^3/3R^2 \,. \tag{4.19}$$

If E_f^v is the difference in surface energy of the crystal with and without a cavity and σ is the surface energy per unit area, then:

$$\begin{aligned} E_f^v &= 4\pi r_a^2\sigma + 4\pi\gamma(R+\Delta R)^2 - 4\pi R^2\sigma \\ &\sim 4\pi\sigma(r_a^2 + 2R\Delta R)^2 \,, \end{aligned} \tag{4.20}$$

where the first two terms on the right hand side of the equation are the energies associated with the inner and outer surfaces after formation of the vacancy and the last term is the energy of the surface of the crystal before formation of the vacancy, and the ΔR^2 term has been neglected. Substituting for ΔR from Eq. (4.19) gives:

$$\begin{aligned} E_f^v &= 4\pi\sigma\left(r_a^2 + \frac{2}{3}\frac{r_a^3}{R}\right) \\ &= 4\pi\sigma r_a^2\left(1 + \frac{2}{3}\frac{r_a}{R}\right) \,, \end{aligned} \tag{4.21}$$

and since $r_a \ll R$, we have:

$$E_f^v \sim 4\pi\sigma r_a^2 \,. \tag{4.22}$$

In most metals, $\sigma \sim 10\,\mathrm{eV/nm^2}$ and $r_a \sim 0.15\,\mathrm{nm}$, so $E_f^v \sim 2\,\mathrm{eV}$.

If we treat the crystal as an elastic continuum, we get a different expression for E_f^v:

$$E_f^v = 4\pi r_a^2\sigma - 12\pi r_a\frac{\sigma^2}{\mu} + 6\pi r_a\frac{\sigma^2}{\mu} \,, \tag{4.23}$$

where the first term is the surface energy of the cavity, the second term is the reduction in surface energy due to contraction of the surface by the surface tension, and the third term is the elastic energy stored in the solid, μ is the shear modulus of the crystal, and $E_f^v \sim 1\,\mathrm{eV}$. Note that an interstitial will cause a displacement that is greater than r_a, resulting in a greater formation energy as we have seen already.

4.3 Diffusion of Point Defects

Atoms in a lattice are in a constant state of motion due to thermal vibration, and this means that point defects in the lattice are also in motion. The random nature of thermal vibration gives rise to random walk of the atoms via the defects that are in thermal equilibrium with their surroundings, known as *self-diffusion*. If foreign atoms are present in a pure metal, their diffusion is known as *heterodiffusion*.

Self-diffusion arises when a local concentration gradient of defects appears in the crystal, driving atoms to move in the direction that eliminates the gradient. Diffusion is driven by forces other than the concentration gradient, such as stress or strain, electric fields, temperature, etc. Diffusion in a polycrystal is a complex mechanism due to the presence of grain boundaries, internal surfaces, dislocations, etc. We will follow the analysis in [4] by starting with diffusion in a single crystal and then expanding our treatment to include the polycrystalline case later on.

4.3.1 Macroscopic Description of Diffusion

Diffusion is governed by two fundamental laws derived by Fick in 1880. They apply to any state of matter due to their general character regarding macroscopic diffusion processes. The first law is a relationship between the flux, J, and the concentration gradient of the diffusing specie:

$$J = -D\nabla C\,, \tag{4.24}$$

where D is the diffusion coefficient and ∇C is the composition gradient. For diffusion in one dimension:

$$J = -D\frac{\partial C}{\partial x}\,. \tag{4.25}$$

The minus sign indicates that diffusion takes place in the direction of *decreasing* concentration of the diffusing specie. D is generally given in units of cm^2/s or m^2/s and for solids between 20 and 1500 °C, $10^{-20}\,\mathrm{cm}^2/\mathrm{s} < D < 10^{-4}\,\mathrm{cm}^2/\mathrm{s}$.

Fick's second law gives a relation between the concentration gradient and the rate of change of concentration caused by diffusion at a given point in the system:

$$\frac{\partial C}{\partial t} = -\nabla\cdot J = -\nabla\cdot D\nabla C\,,$$

which, in one dimension simplifies to

$$\frac{\partial C}{\partial t} = -\frac{\partial}{\partial x}\left(D\frac{\partial C}{\partial x}\right)\,. \tag{4.26}$$

If D is not a function of the concentration, then we can write Eq. (4.26) as:

$$\begin{aligned}\frac{\partial C}{\partial t} &= -D\nabla^2 C \\ &= -D\frac{\partial^2 C}{\partial x^2}\,.\end{aligned} \tag{4.27}$$

Equations (4.26) or (4.27) can be solved for certain limiting conditions enabling D to be determined on the basis of various measurements.

While Fick's laws provide a description of diffusion on the macroscopic scale, we would like to understand diffusion on the microscopic level as well. Diffusion occurs by several possible mechanisms depending on the nature of the diffusing specie and the host lattice. We will examine these mechanisms and then derive a description of diffusion on the microscopic level.

4.3.2 Mechanisms of Diffusion

To obtain a theoretical description of diffusion, we first consider the elementary act of a jump of an atom from one stable position to another in the lattice. There are several mechanisms of lattice diffusion, some requiring the presence of defects, others not. The following types [5] can be distinguished.

Exchange and ring mechanisms: The exchange mechanism (Fig. 4.12) consists of the exchange of lattice positions involving two atoms located in adjacent crystal sites. It does not require the presence of defects, and it is highly improbable in close packed crystals since it requires considerable deformation and hence, an enormous activation energy. The ring mechanism (Fig. 4.13) is less energy intensive but requires the coordinated movement of three to five atoms. Since the probability of this is low and the energy required is still high, both the exchange and ring mechanisms are unimportant in crystals containing defects.

Vacancy mechanism: This is the simplest mechanism of diffusion and occurs in metals and alloys (Fig. 4.14). Diffusion occurs by the jump of an atom from its lattice site to a vacant site. For an atom to move by this mechanism the presence of a neighboring vacancy is required. Since movement of the vacancy is opposite that of the atom, vacancy-type diffusion is regarded as either a movement of the atom

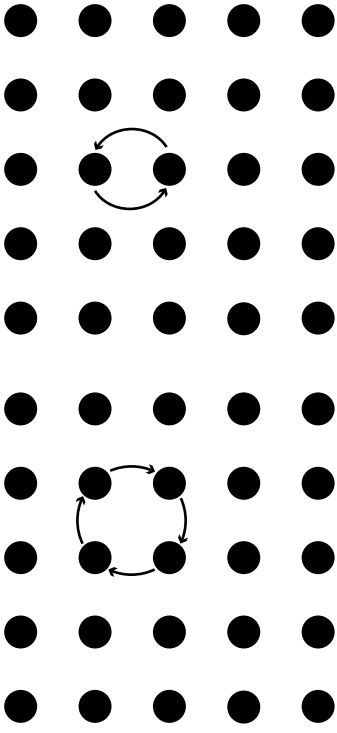

Fig. 4.12. Exchange mechanism of diffusion

Fig. 4.13. Ring mechanism of diffusion

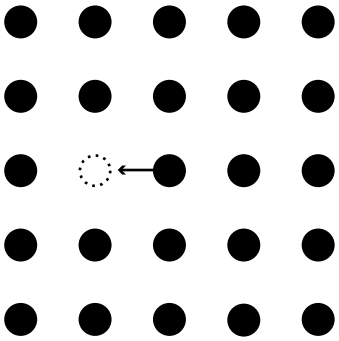

Fig. 4.14. Vacancy mechanism of diffusion

or the equivalent movement of the vacancy. However, as we will see, the diffusion coefficient for vacancy diffusion is *not* equal to that for atom diffusion.

Interstitial mechanism: This mechanism involves the movement of an atom from one interstitial position to another (Fig. 4.15). It requires considerable energy in order to push its way through the barrier atoms separating the interstitial sites in the crystal (recall the role of barrier atoms in our calculation of displacement energy in Chap. 2). In reality, this mechanism only occurs when the diffusing specie is of an atom type that is smaller than the host lattice atoms.

Interstitialcy mechanism: This mechanism involves the displacement of nearby lattice atoms to an interstitial site and generally occurs when atom diameters are comparable. There are two variants of this mechanism: the collinear variant in which displaced atoms move along a straight line (Fig. 4.16a) and the non-collinear variant in which the displaced atom moves to the interstitial position at an angle to the direction of movement of the displacing atom (Fig. 4.16b).

Dumbbell interstitial mechanism: This process involves the symmetrical placement of an interstitial and a lattice atom about a single lattice site such that they share the lattice site. Figure 4.17 shows a 2D schematic of the sharing of a single lattice site by two atoms. Recall from our discussion in Sect. 4.1, that the dumbbell is a very stable configuration for the interstitial and that there are preferred directions for the dumbbell that depend on the lattice, and minimize the energy.

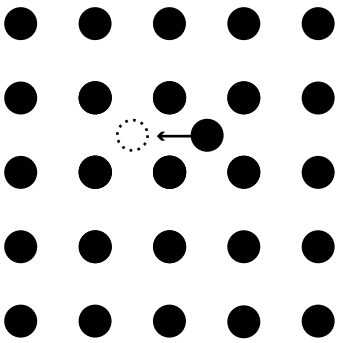

Fig. 4.15. Interstitial mechanism of diffusion

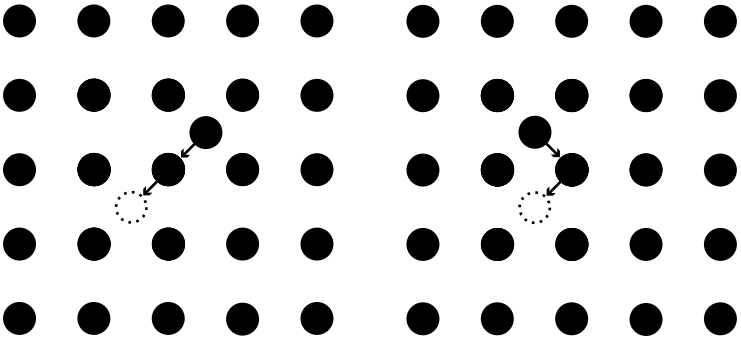

Fig. 4.16. Interstitialcy mechanism of diffusion, (a) collinear variant, (b) non-collinear variant

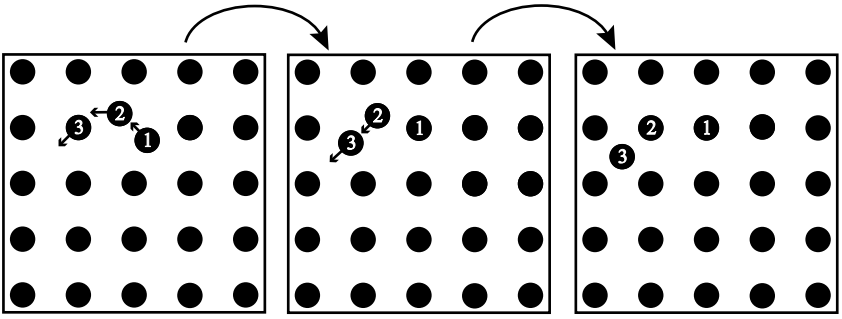

Fig. 4.17. Dumbbell interstitial mechanism of diffusion

Crowding (crowdion) mechanism: This mechanism occurs when an atom is added to a lattice plane but it does not reside in an interstitial position. To accommodate the atom, lattice atoms over, perhaps, 10 lattice constants are all shifted with respect to their lattice sites. The configuration can be thought of as a dumbbell spread over 10 atoms along a row, rather than two (Fig. 4.18). Actually, we have already seen a crowdion in our discussion of focusing collisions. Re-examine Fig. 3.4 and you will see a crowdion emanating from the displacement spike. This configuration is not a stable configuration and exists only temporarily as the energy for the knock-on atoms is expended.

Despite the numerous mechanism for diffusion of atoms in a solid, diffusion usually occurs by either the vacancy or interstitialcy mechanisms. Ultimately, we want to obtain a mathematical relation between the macroscopic parameters for diffusion (i.e., the self-diffusion coefficient) and the elementary acts of defect jumps represented by the coefficients of diffusion for defects, or the microscopic process. We will assume that the self-diffusion process consists of a completely random walk of defects, i.e., there is no correlation between successive jumps of the defects. Although this is reasonable for defect diffusion, it is not strictly true for atom diffusion.

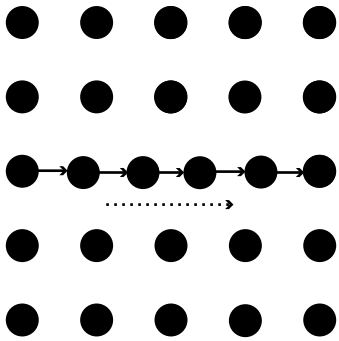

Fig. 4.18. Crowdion mechanism of diffusion

As mentioned earlier, jumps of defects and hence, atoms, are due to thermal vibrations of very high frequency. The Debye frequency is $\sim 10^{13}\,\mathrm{s}^{-1}$. The frequency of atom jumps is orders of magnitude lower, $\sim 10^{8}\,\mathrm{s}^{-1}$ at say, 700 °C. This means that once every 10^5 vibrations, a thermal fluctuation is large enough for an atom to overcome the energy barrier separating it from the next stable position. Let us take a closer look at the jumping process.

4.3.3 Microscopic Description of Diffusion

Suppose that at time zero, a single impurity atom is placed in a position in a crystal which is designated as the origin. The atom proceeds to jump from one site to another in a completely random manner. Each jump is of distance λ, but since the medium is assumed to be isotropic, each jump is arbitrary and independent of previous jumps. After a time t, the displacement, r, of the particle from the origin is measured. If the experiment is repeated several times, r will not be the same because of the stochastic nature of the process. Rather, the displacements will be distributed according to a function $P_\mathrm{t}(r)$ where $P_\mathrm{t}d^3r$ is the probability of finding the atom in a volume element d^3r a distance r from the origin after time t. The quantity that best describes the extent of migration is the mean square displacement, $\overline{r^2}$, which is given by the second moment of the distribution:

$$\overline{r^2} = \int\limits_{\text{all space}} r^2 P_\mathrm{t}(r) d^3r = 4\pi \int_0^\infty r^4 P_\mathrm{t}(r) dr \,. \tag{4.28}$$

We will first compute $\overline{r^2}$ without knowledge of $P_\mathrm{t}(r)$.

If the atom makes Γ jumps per unit time, the time interval t corresponds to a number of n jumps given by:

$$n = \Gamma t \,. \tag{4.29}$$

Each jump is represented by a vector $\underline{\lambda}_\mathrm{i}$, where the subscript, i, refers to the jump number. The vectors are all of the same length, λ_i, but of random direction. The

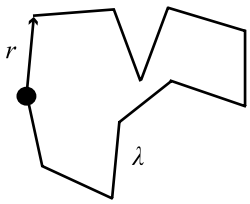

Fig. 4.19. Random jump of a defect in an isotropic solid

position of the diffusing atom after n jumps (Fig. 4.19) is the vector sum of the $\underline{\lambda}_{\mathrm{i}}$ or:

$$\underline{r} = \underline{\lambda}_1 + \underline{\lambda}_2 + .\underline{\lambda}_3 \ldots + \underline{\lambda}_n \, . \tag{4.30}$$

The magnitude of the square of the displacement is obtained by taking the scalar product of $\underline{r}$ with itself:

$$r^2 = \underline{r} \cdot \underline{r} = (\underline{\lambda}_1 + \underline{\lambda}_2 + .\underline{\lambda}_3 \ldots + \underline{\lambda}_n) \cdot (\underline{\lambda}_1 + \underline{\lambda}_2 + .\underline{\lambda}_3 \ldots + \underline{\lambda}_n) \, . \tag{4.31}$$

The scalar product of two sums is equivalent to squaring the sums, giving:

$$r^2 = \sum_{i=1}^{n} \underline{\lambda}_{\mathrm{i}} \cdot \underline{\lambda}_{\mathrm{i}} + 2 \sum_{i=1}^{n-1} \sum_{j \neq i}^{n} \underline{\lambda}_{\mathrm{i}} \cdot \underline{\lambda}_j \, . \tag{4.32}$$

The first term is equal to $n\lambda^2$ and the second term can be rewritten as:

$$\underline{\lambda}_{\mathrm{i}} \cdot \underline{\lambda}_j = \lambda^2 \cos\theta_{ij} \, , \tag{4.33}$$

and

$$r^2 = n\lambda^2 + 2\lambda^2 \sum_{i-1}^{n-1} \sum_{j \neq i}^{n} \cos\theta_{ij} \, , \tag{4.34}$$

or

$$r^2 = n\lambda^2 \left(1 + \frac{2}{n} \sum_{i=1}^{n-1} \sum_{j \neq i}^{n} \cos\theta_{ij} \right) \, . \tag{4.35}$$

The mean square displacement is obtained by averaging r^2 over a large number of experiments. The term $\cos\theta_{ij}$ can range from -1 to 1, and by nature of the random hopping process, the average value of $\cos\theta_{ij}$ for any ij combination is zero. Hence, the last term disappears and:

$$\overline{r^2} = n\lambda^2 \, , \tag{4.36}$$

or

$$\overline{r^2} = \lambda^2 \Gamma t \, . \tag{4.37}$$

Equation (4.37) relates the mean square displacement to the microscopic properties of jump distance and jump frequency. Now, we wish to compute $\overline{r^2}$ from a macroscopic viewpoint.

At $t = 0$, N impurity atoms are introduced into a restricted region of a host crystal. As a consequence of diffusion (random hopping), the N atoms spread out from the origin in a manner described by $C(r,t)$ which is obtained by solving Fick's second law (assuming D is not a function of concentration):

$$\frac{\partial C}{\partial t} = D\frac{1}{r^2}\frac{\partial}{\partial r}\left(r^2\frac{\partial C}{\partial r}\right) , \tag{4.38}$$

with initial condition $C(r,0) = 0$, for $r \neq 0$. Since the N atoms remain in the crystal, $C(r,t)$ is subject to the constraint:

$$\int_0^\infty 4\pi r^2 C(r,t)\,\mathrm{d}r = N , \tag{4.39}$$

with boundary condition that the concentration drops to 0 at infinity, $C(\infty,t) = 0$. The solution to Eq. (4.38) subject to the initial and boundary conditions becomes:

$$C(r,t) = N\frac{\exp\left(-r^2/4Dt\right)}{(4\pi Dt)^{3/2}} . \tag{4.40}$$

The probability of finding the single atom in a spherical shell between r and $r + \mathrm{d}r$ after time t, is equivalent (in the macroscopic diffusion description of the problem) to the fraction of the N atoms located in the same volume element after time t. $P_\mathrm{r}(r)$ and $C(r,t)$ are related by:

$$P_\mathrm{t}(r) = \frac{C(r,t)}{N} = \frac{\exp\left(-r^2/4Dt\right)}{(4\pi Dt)^{3/2}} . \tag{4.41}$$

The mean square displacement is:

$$\begin{aligned}\overline{r^2} &= 4\pi\int_0^\infty r^4 P_\mathrm{t}(r)\,\mathrm{d}r \\ &= \frac{4\pi}{(4\pi Dt)^{3/2}}\int_0^\infty r^4\exp\left(-r^2/4Dt\right) ,\end{aligned} \tag{4.42}$$

or

$$\overline{r^2} = 6Dt . \tag{4.43}$$

Comparing to $\overline{r^2} = \lambda^2\Gamma t$ from our microscopic solution Eq. (4.37), we have:

$$D = 1/6\lambda^2\Gamma , \tag{4.44}$$

which is the Einstein formula and is the link between the microscopic diffusion parameters λ and Γ, and the macroscopic diffusion parameter, D.

4.3.4 Jump Frequency, Γ

We define Γ as the total number of jumps per second for an atom. Therefore, in a time increment δt, we expect $\Gamma\delta t$ jumps. The quantity $\Gamma\delta t$ is proportional to z,

the number of nearest neighbors (sites), p_v, the probability that a given neighboring site is vacant, and ω, the frequency with which an atom jumps to a particular site. Thus, the frequency with which an atom jumps to any neighboring equilibrium site, Γ, is the product of the jump frequency to a single site, ω, the number of nearest neighbor sites, z, and the probability that one site is vacant, p_v, or:

$$\Gamma = z p_v \omega \,, \tag{4.45}$$

and

$$D_a^v = 1/6 z \lambda^2 p_v \omega \,. \tag{4.46}$$

where we have properly included the subscript a and superscript v to indicate that this is the diffusion coefficient for *atom diffusion* via vacancies. Also note that the jump distance λ is related to the lattice constant by $\lambda = Aa$, where the coefficient, A, depends on the diffusion mechanism and the crystal structure. The terms $1/6zA^2$ are often lumped together into a single parameter, α, such that:

$$D_a^v = \alpha a^2 p_v \omega \,, \tag{4.47}$$

and if vacancy motion is random, then $p_v = N_v$ and:

$$D_a^v = \alpha a^2 N_v \omega \,. \tag{4.48}$$

Let us look at an example of how to determine α for a specific diffusion process and crystal structure.

Example 4.2. Vacancy diffusion in the bcc and fcc lattices
In the case of the vacancy mechanism of diffusion in a bcc structure, each atom has eight nearest neighbors ($z = 8$). The jump distance is related to a by $A = \frac{\sqrt{3}}{2}$, and hence, $\alpha = 1$. For the simple interstitial diffusion mechanism in a bcc lattice, $z = 4$ and $A = 1/2$ giving $\alpha = 1/6$. For the fcc lattice, $z = 12$ and $A = \frac{1}{\sqrt{2}}$, giving $\alpha = 1$. For interstitials in the fcc lattice, $z = 12$ and $A = 1/2$ and $\alpha = 1/2$.

Before continuing, it is instructive to point out the difference between vacancy diffusion and atom diffusion via a vacancy mechanism (vacancy self-diffusion). In determining the components of Γ, we noted that Γ depends on the probability, p_v, that a neighboring lattice site is vacant. This is a necessary condition for an atom jump via a vacancy. However, if we are following the migration of the vacancy, then Γ depends on the probability that a neighboring lattice site to the vacancy is filled by an atom. Since in all but the most extreme cases, this probability is ~ 1, and the equation for vacancy diffusion is given as follows:

$$D_v = \alpha a^2 \omega \,, \tag{4.49}$$

and differs from that for vacancy self-diffusion by the factor N_v.

4.3.5 Jump Frequency, ω

In calculating ω we will ignore detailed atomic movements and instead deal in terms of "activated complexes" or regions containing an atom midway between two equilibrium sites (Fig. 4.20). The number of atoms diffusing per second is then obtained by multiplying the number of activated complexes (n_m) by the average velocity of the atoms moving through this barrier ($\bar{\nu}$) divided by the width of this barrier (δ). The jump frequency is then:

$$\omega = \frac{N_m \bar{\nu}}{\delta} , \tag{4.50}$$

where N_m is the mole fraction of activated complexes. The work done in moving an atom across this barrier is equal to the change in Gibbs free energy for the region, ΔG_m:

$$\Delta G_m = \Delta H_m - T\Delta S_m . \tag{4.51}$$

Using ΔG_m, the equilibrium mole fraction of atoms in the region of the saddle point in Fig. 4.20, N_m can be calculated in the same way we calculated N_v. Instead of mixing vacancies to raise the free energy by ΔG_v per mole, we are mixing complexes to raise the free energy an amount ΔG_m per mole. The ideal entropy of mixing is the same for vacancies as for complexes so, at equilibrium, n_m out of N atoms will be in the neighborhood of the saddle point at any instant and:

$$\frac{n_m}{N} = N_m = \exp\left(\frac{-\Delta H_m + T\Delta S_m}{kT}\right) = \exp\left(\frac{-\Delta G_m}{kT}\right) . \tag{4.52}$$

From Eq. (4.50), $\omega = \dfrac{N_m \bar{\nu}}{\delta}$ and $\bar{\nu}/\delta$ is the frequency (call it ν) at which atoms at the saddle point jump to the new site. Thus $N_m \nu$ out of N atoms will jump from one

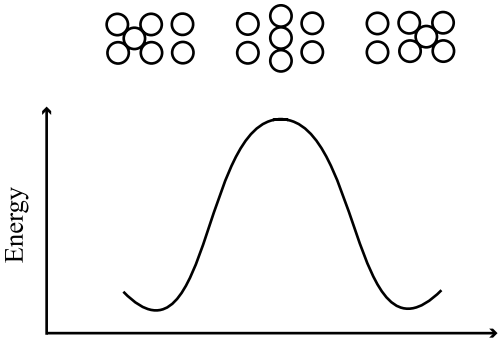

Fig. 4.20. Passage of the "activated complex" from one stable position, through a saddle point, to another stable position

site to a given site per second, and the average jump frequency is:

$$\begin{aligned}\frac{n_{\mathrm{m}}\nu}{N} = \omega &= \nu \exp\left(\frac{-\Delta G_{\mathrm{m}}}{kT}\right) = \nu \exp\left(\frac{\Delta S_{\mathrm{m}}}{k}\right) \exp\left(\frac{-\Delta H_{\mathrm{m}}}{kT}\right) \\ &= \nu \exp\left(\frac{S_{\mathrm{m}}}{k}\right) \exp\left(\frac{-E_{\mathrm{m}}}{kT}\right) ,\end{aligned} \tag{4.53}$$

where ν is the Debye frequency ($\sim 10^{13}\,\mathrm{s}^{-1}$) and $E_{\mathrm{m}} = \Delta H_{\mathrm{m}}$ and $S_{\mathrm{m}} = \Delta S_{\mathrm{m}}$.

4.3.6 Equations for *D*

We are now in a position to write the expressions for the diffusion coefficients for the motion of the defects, and of the atoms by way of the defects:

1. The vacancy diffusion coefficient is given by:

   $$D_{\mathrm{v}} = \alpha a^2 \omega$$

   where

   $$\omega = \nu \exp\left(\frac{-\Delta G^{\mathrm{v}}_{\mathrm{m}}}{kT}\right) = \nu \exp\left(\frac{S^{\mathrm{v}}_{\mathrm{m}}}{k}\right) \exp\left(\frac{-E^{\mathrm{v}}_{\mathrm{m}}}{kT}\right) ,$$

   then

   $$D_{\mathrm{v}} = \alpha a^2 \omega = \alpha a^2 \nu \exp\left(\frac{S^{\mathrm{v}}_{\mathrm{m}}}{k}\right) \exp\left(\frac{-E^{\mathrm{v}}_{\mathrm{m}}}{kT}\right) \tag{4.54}$$

2. The vacancy self-diffusion coefficient is the product of the vacancy diffusion coefficient and the probability that the nearest neighbor site is vacant, N_{v}:

   $$D^{\mathrm{v}}_{\mathrm{a}} = \alpha a^2 N_{\mathrm{v}} \omega ,$$

   where

   $$N_{\mathrm{V}} = \exp\left(\frac{-\Delta G^{\mathrm{v}}_{\mathrm{f}}}{kT}\right) = \exp\left(\frac{S^{\mathrm{v}}_{\mathrm{f}}}{k}\right) \exp\left(\frac{E^{\mathrm{v}}_{\mathrm{f}}}{kT}\right) ,$$

   giving:

   $$D^{\mathrm{v}}_{\mathrm{a}} = \alpha a^2 \nu \exp\left(\frac{S^{\mathrm{v}}_{\mathrm{f}} + S^{\mathrm{m}}_{\mathrm{v}}}{k}\right) \exp\left(\frac{-E^{\mathrm{v}}_{\mathrm{f}} - E^{\mathrm{v}}_{\mathrm{m}}}{kT}\right) . \tag{4.55}$$

3. The interstitial diffusion coefficient is:

   $$D_{\mathrm{i}} = \alpha a^2 \omega ,$$

   or

   $$D_{\mathrm{i}} = \alpha a^2 \nu \exp\left(\frac{S^{\mathrm{i}}_{\mathrm{m}}}{k}\right) \exp\left(\frac{-E^{\mathrm{i}}_{\mathrm{m}}}{kT}\right) . \tag{4.56}$$

4. The interstitial self-diffusion coefficient is the interstitial diffusion coefficient times the probability that a neighboring site contains an interstitial, N_i:

$$D_\mathrm{a}^\mathrm{i} = \alpha a^2 N_\mathrm{i} \omega \,,$$

where

$$N_\mathrm{i} = \exp\left(\frac{-\Delta G_\mathrm{f}^\mathrm{i}}{kT}\right) = \exp\left(\frac{S_\mathrm{f}^\mathrm{i}}{k}\right)\exp\left(\frac{-E_\mathrm{f}^\mathrm{i}}{kT}\right) \,,$$

giving

$$D_\mathrm{a}^\mathrm{i} = \alpha a^2 \nu \exp\left(\frac{S_\mathrm{f}^\mathrm{i} + S_\mathrm{m}^\mathrm{i}}{k}\right)\exp\left(\frac{-E_\mathrm{f}^\mathrm{i} + -E_\mathrm{m}^\mathrm{i}}{kT}\right) \,. \tag{4.57}$$

The diffusion coefficients are all different in detail, but similar in form as they consist of two factors; a constant that is independent of temperature and an exponential of temperature containing an energy term. All equations for D can be rewritten in the form:

$$D = D_0 \exp(-Q/kT) \,, \tag{4.58}$$

where $D_0 = \alpha a^2 \nu$ is the temperature independent term and Q is the activation energy. For vacancy diffusion we have:

$$Q_\mathrm{v} = E_\mathrm{m}^\mathrm{v} \,, \tag{4.59}$$

and for vacancy self-diffusion we have:

$$Q_\mathrm{a}^\mathrm{v} = E_\mathrm{f}^\mathrm{v} + E_\mathrm{m}^\mathrm{v} \,. \tag{4.60}$$

For interstitials we have:

$$\text{and } Q_\mathrm{i} = E_\mathrm{m}^\mathrm{i} \,, \tag{4.61}$$

and for interstitial self-diffusion we have:

$$Q_\mathrm{a}^\mathrm{i} = E_\mathrm{f}^\mathrm{i} + E_\mathrm{m}^\mathrm{i} \,. \tag{4.62}$$

It follows that the activation energy for diffusion of atoms in a crystal depends on both the energy of formation of defects and the energy required for their migration in the periodic field of the crystal lattice. Experiments can be conducted to confirm the temperature dependence of D and also the values of Q. The terms in the pre-exponential factor for the various diffusion mechanisms are provided in Table 4.2 for the fcc and bcc lattices.

Example 4.3. Determination of D_a^v and D_a^i for fcc copper at 500 °C

For copper:

$$\begin{aligned} E_\mathrm{f}^\mathrm{v} &= 1.27\,\mathrm{eV} \,, & E_\mathrm{f}^\mathrm{i} &= 2.2\,\mathrm{eV} \\ E_\mathrm{m}^\mathrm{v} &= 0.8\,\mathrm{eV} \,, & E_\mathrm{m}^\mathrm{i} &= 0.12\,\mathrm{eV} \\ S_\mathrm{f}^\mathrm{v} &= 2.4\,\mathrm{k} \,, & S_\mathrm{f}^\mathrm{i} &\sim 0 \end{aligned}$$

and we neglect S_m^v and S_m^i.

For the fcc lattice, $z = 12$, $A = 1/\sqrt{2}$, and $a \sim 3\,\text{nm}$, giving:

$$D_\text{v} = \alpha a^2 \nu \exp\left(\frac{-0.8}{kT}\right)$$
$$\cong 5 \times 10^{-6}\,\text{cm}^2/\text{s}$$
$$D_\text{i} = \alpha a^2 \nu \exp\left(\frac{-0.12}{kT}\right)$$
$$\cong 7 \times 10^{-2}\,\text{cm}^2/\text{s}$$

$$D_\text{a}^\text{v} = \alpha a^2 \nu \exp\left(\frac{2.4k}{k}\right) \exp\left(\frac{-1.27-0.8}{kT}\right)$$
$$\cong 3 \times 10^{-13}\,\text{cm}^2/\text{s}$$
$$D_\text{a}^\text{i} = \alpha a^2 \nu \exp\left(\frac{-2.2-0.12}{kT}\right)$$
$$\cong 3 \times 10^{-16}\,\text{cm}^2/\text{s}$$

Note that while $D_\text{i}/D_\text{v} \sim 10^4$ due to the smaller migration energy for interstitials than for vacancies, but $D_\text{a}^\text{i}/D_\text{a}^\text{v} \sim 10^{-3}$ because of the very high interstitial formation energy compared to that for vacancies. Plots of the diffusion coefficients are shown in Fig. 4.21. Note that the vacancy diffusion coefficient is larger than the vacancy self-diffusion coefficient and has a smaller slope.

Table 4.2. Parameters in the expression for the diffusion coefficient, $D = \alpha a^2 N \omega$, where $\alpha = 1/6zA^2$ for the various diffusion mechanisms in the fcc and bcc lattices

Diffusion mechanism	z	A	α	N	D
		fcc			
Vacancy	12	$1/\sqrt{2}$	1	1	$a^2\omega$
Vacancy self-diffusion	12	$1/\sqrt{2}$	1	N_v	$a^2 N_\text{v}\omega$
Interstitial	12	1/2	1/2	1	$1/2a^2\omega$
Interstitial self-diffusion	12	1/2	1/2	N_i	$1/2a^2 N_\text{i}\omega$
		bcc			
Vacancy	8	$\sqrt{3}/2$	1	1	$a^2\omega$
Vacancy self-diffusion	8	$\sqrt{3}/2$	1	N_v	$a^2 N_\text{v}\omega$
Interstitial	4	1/2	1/6	1	$a^2\omega$
Interstitial self-diffusion	4	1/2	1/6	N_i	$1/6a^2 N_\text{i}\omega$

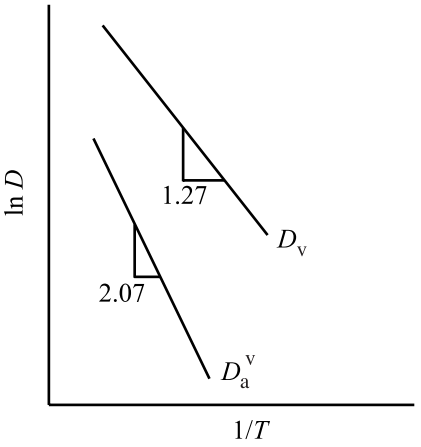

Fig. 4.21. Comparison of plots of $\ln D$ vs. $1/T$ for vacancy diffusion and vacancy self-diffusion

The behavior of self-interstitial atoms in bcc iron at 323 °C is illustrated in Movie 4.3. In this movie, the green balls are the interstitials and the red ball is the vacant lattice site, and together they form a SIA dumbbell in which the two green atoms share a single lattice site. The SIA originates as a ⟨110⟩ split-dumbbell interstitial and then rotates into a ⟨111⟩ interstitial and moves in one-dimension through the ⟨111⟩ crowdion saddle position. Movie 4.4 shows a di-SIA consisting of two parallel ⟨111⟩ split-dumbbells that migrates along the ⟨111⟩ direction and also rotates to different ⟨111⟩-type orientations.

4.4 Correlated Diffusion

Earlier we assumed that irrespective of the kinds of defects present in a crystal lattice, successive jumps of atoms are completely random or uncorrelated. This means that after n jumps, all possible directions for the $(n+1)$th jump are equally probable. This is true for vacancies or interstitials since all structural elements surrounding them are at all times identical. Since the vibrational frequency of a lattice atom is several orders of magnitude greater than the jump frequency, equilibrium in the region surrounding the defect is rapidly established between successive jumps and the next jump occurs with no effect of the previous jump on its direction. But this does not always hold true for atom diffusion as described in [5] and in the following.

If we consider the case of a radioactive tracer to track atom diffusion, a tracer will make a jump if a vacancy is in its immediate vicinity. The second jump is uncorrelated with the first if the probability of the second jump is the same for all directions. However, the tracer arrives from a position that is vacant at the time of its arrival. Hence, when it is "preparing" for the next jump, the chance that the position from which it has arrived is unoccupied is greater than for any other position around the atom. The two jumps are correlated since the probability of the tracer returning to its former position is higher than for making a jump in any other direction. In

other words, the tracer has a greater tendency to move in the direction from which it came than in the direction it is headed, or from Eq. (4.35), $\overline{\cos\theta}_2 < 0$.

Since jumps in the direction from which it came are most probable, the tracer will have traveled a shorter (net) distance than that traveled by the vacancy. Therefore, the self-diffusion coefficient of the tracer (which is a measure of the rate of this process) is smaller than that of the atoms constituting the lattice, since the self-diffusion of the tracer is a correlated random walk whereas the movement of the vacancies and consequently of the atoms constituting the lattice are not correlated.

The correlation effect is absent in the simple interstitial mechanism, but there is correlation of motion by the interstitialcy mechanism. In both the vacancy and the interstitialcy mechanisms, $D_{\text{tracer}} < D_{\text{lattice}}$ and:

$$f = \frac{D_{\text{tracer}}}{D_{\text{lattice}}}\,, \tag{4.63}$$

and f is known as the *Haven coefficient* and is a measure of the degree to which diffusion is random. Recall our earlier discussion of the measurement of the square of the displacement by random walk given by Eq. (4.35):

$$r^2 = n\lambda^2\left(1 + \frac{2}{n}\sum_{i=1}^{n-1}\sum_{j\neq i}^{n}\cos\theta_{ij}\right)\,,$$

where the mean square displacement is obtained by averaging over all values of $\cos\theta_{ij}$. In this expression the term in brackets is f and the value of f for random walk is 1 since the average over all $\cos\theta_{ij}$ is 0. But when there is correlation between successive jumps, f is $\neq 1$. For the vacancy mechanism of diffusion of a tracer in a regular lattice [5]:

$$f_{\text{v}} = \frac{1+\overline{\cos\theta}}{1-\overline{\cos\theta}}\,, \tag{4.64}$$

and for interstitial diffusion,

$$f_{\text{i}} = 1 + \overline{\cos\theta}\,. \tag{4.65}$$

Since in both cases, $\overline{\cos\theta} < 0$, then $f < 1$.

A simpler treatment of f_{v} is that $f_{\text{v}} = \dfrac{1-P}{1+P}$, where P is the probability of a jump of a tracer to a neighboring vacancy, and $1-P$ is the probability that a neighboring vacancy will move away as a result of jumps of lattice atoms. To a first approximation, P is equal to the reciprocal of the number of nearest lattice sites, z, around the tracer. Therefore:

$$f = \frac{1-1/z}{1+1/z} = \frac{z-1}{z+1}\,. \tag{4.66}$$

For the fcc lattice:

$$f = \frac{1-1/12}{1+1/12} = \frac{12-1}{12+1} = 0.85 .$$

For the bcc lattice:

$$f = \frac{1-1/8}{1+1/8} = \frac{8-1}{8+1} = 0.78 .$$

For the simple cubic (sc) lattice:

$$f = \frac{1-1/6}{1+1/6} = \frac{6-1}{6+1} = 0.71 .$$

So, in our microscopic description of the diffusion coefficient D, Eq. (4.44), we account for correlated diffusion by including the correlation coefficient:

$$D = 1/6 f \lambda^2 \Gamma = f \alpha a^2 \omega . \tag{4.67}$$

As an aside, the true correlation coefficient, f, actually consists of two terms, f' and f'' such that $f = f'\, f''$. The quantity f'' was described in the previous section (as f) and f' is related to the difference between the distances traveled during the elementary act by the tracer atom and the defect:

$$f' = \frac{\lambda_{\text{tracer}}}{\lambda_{\text{defect}}} , \tag{4.68}$$

In the case of a vacancy, $f' = 1$ since $\lambda_{\text{tracer}} = \lambda_{\text{vacancy}}$, or the distance traveled by the tracer and the defect are equal in one jump. The same is true for the simple interstitial mechanism. But in the case of the interstitialcy mechanism, the tracer moves from an interstitial position to a lattice site (or vice versa). In both cases, it travels a distance λ_{tracer}. However, the passage of a lattice atom from an interstitial position to a lattice site is equivalent to the appearance of an identical atom displaced from the lattice site in a neighboring interstitial position. Therefore, the jump of a lattice atom from the interstitial position to a lattice site requires (for the collinear case) a displacement of the lattice atom by a distance $2\lambda_{\text{tracer}}$, or $f' = \lambda_{\text{tracer}}/2\lambda_{\text{tracer}} = 0.5$. For the non-collinear case, $f' = \lambda_{\text{tracer}}/1.6\lambda_{\text{tracer}} = 2/3$. Table 4.3 summarizes the correlation coefficient for various diffusion mechanisms in the common crystal lattices.

4.5 Diffusion in Multicomponent Systems

Our discussion on diffusion so far has applied only to pure or single-component systems. We have not accounted for multiple components such as impurities in a pure metal and alloys. Diffusion in these systems was treated in experiments conducted by Smigelskas and Kirkendall in 1947 [6] and analyzed by Darken in 1948 [7]. The

Table 4.3. Correlation coefficients for the most common diffusion mechanisms in the various crystal lattices (from [5])

Crystal lattice	Diffusion mechanism	Correlation factor
Simple cubic	Vacancy	0.65311
	Interstitial	
	Collinear	0.80000
	Non-collinear	0.96970
Face-centered cubic	Vacancy	0.72722
	Interstitial	
	Collinear	0.66666
	Non-collinear	0.72740
Body-centered cubic	Vacancy	0.72722
Hexagonal close packed	Vacancy	0.78121

result is that the diffusion coefficients of the two components in a binary (A–B) system can be expressed as:

$$\tilde{D} = D_A N_A + D_B N_B \ , \tag{4.69}$$

where $D_{A,B}$ are the intrinsic diffusion coefficients and are functions of composition, and $\tilde{D}$ is the interdiffusion coefficient. Since the partial diffusion coefficients depend on the alloy composition, $\tilde{D}$ is a complex, non-linear function of concentration. However, in the case of dilute solutions ($N_B \rightarrow 0$, $N_A \rightarrow 1$), the interdiffusion coefficient is approximately equal to the partial diffusion coefficient of the solute.

The significance of this result can be appreciated by a brief review of the elegance and implications of the experiment. In Kirkendall's experiment, molybdenum wires were wound around a block of brass (70Cu–30Zn) which was then plated with a thick coating of copper. The molybdenum wires are insoluble in copper and act as inert markers to locate the original interface. When the assembly is heated in a furnace, the wire markers on opposite sides of the brass moved toward each other, indicating that more material has left the brass than entered it, implying that the diffusion coefficient of zinc is greater than that of copper.

The vacancy mechanism is the only diffusion mechanism that can account for marker motion. If zinc diffuses by a vacancy mechanism, then the flux of zinc atoms in one direction must equal the flux of vacancies in the opposite direction and the number of zinc atoms leaving the brass is balanced by an equal number of vacancies entering the brass. But the vacancies are absorbed by internal sinks, so the result is that the volume of the brass diminishes and the markers move closer together. The concept of a flux of atoms giving rise to a flux of defects will be explored in depth in Chap. 6 on Radiation-Induced Segregation, which occurs by the *inverse* Kirkendall effect.

4.6 Diffusion along High Diffusivity Paths

Metals and alloys used as structural engineering materials are polycrystals and are thus, inhomogeneous, as they contain grain boundaries, dislocations, internal interfaces due to precipitates or second phases, etc. To understand diffusion in these systems, we must discuss the effect of these linear, planar and area defects on the diffusion process. The primary difference between mono- and polycrystals is that the latter consists of aggregates of crystals oriented (generally) at random. This latter type of structure rarely shows anisotropy of diffusion. The important difference is that linear and planar defects represent high diffusivity paths along which diffusion can occur much faster than via point defects (bulk diffusion).

Grain boundaries are important high diffusivity paths since the atom packing density is lower. There exist several models of grain boundary diffusion, and all assume that the boundary has of width, $\delta \sim 0.3\text{–}0.5\,\text{nm}$. One model that is based on the dislocation model of grain boundaries deserves special attention. In this model, the grain boundary is regarded as a number of edge dislocations. The dislocation density (#/unit length) increases with increasing misorientation angle θ, between two grains in contact (Fig. 4.22). From the figure:

$$d \sin \frac{\theta}{2} = \frac{b}{2} \,. \tag{4.70}$$

Hence, the distance between neighboring dislocations decreases with increasing misorientation angle. A low angle grain boundary consisting of many edge dislocations can be regarded as a row of parallel channels in which packing of atoms is loosest. In this region, the strain is high and the packing of atoms is loose, and the diffusion coefficient will be the highest along the dislocation lines (cores). According to this model, diffusion along grain boundaries should be anisotropic, and depend on the angle θ. The grain boundary described as a slab of uniform thickness δ and diffusion coefficient D_{gb}, can also be viewed as a planar array of pipes of radius p and spacing d. Grain boundary diffusion is related to diffusion along dislocation cores (also known as *pipe diffusion*), described by D_{p}, by the following relation:

$$D_{\text{gb}}\delta = D_{\text{p}}(\pi p^2/d) \,, \tag{4.71}$$

and substituting for d from Eq. (4.70) gives:

$$= D_{\text{p}}\pi p^2 \left(\frac{2 \sin \theta/2}{b} \right)$$

$$\cong \frac{D_{\text{p}}\pi p^2 \theta}{b} \,. \tag{4.72}$$

The dislocation model of the grain boundary shown in Fig. 4.22 is expanded in Fig. 4.23 to show that the extra half planes of atoms can be regarded as edge dislocations. In fact, the rate of diffusion along the grain boundary increases with increasing misorientation angle, θ, and reaches a maximum at $\theta = 45^\circ$ (Fig. 4.24).

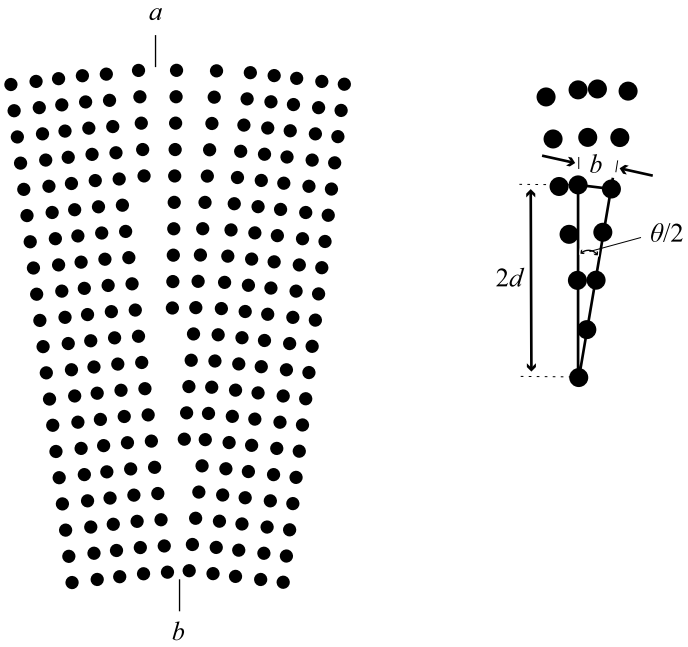

Fig. 4.22. Dislocation model of a small angle grain boundary and the geometrical relationship between the angle of tilt, θ, the Burgers vector, b, and the spacing between the dislocations, d

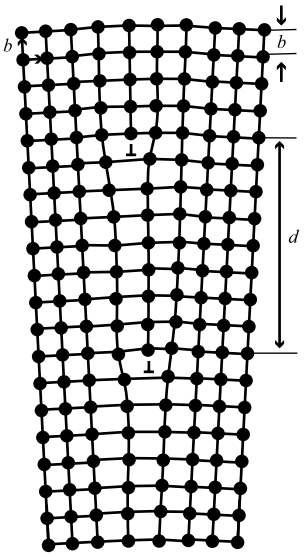

Fig. 4.23. Expanded view of the dislocation model of the grain boundary shown in Fig. 4.22

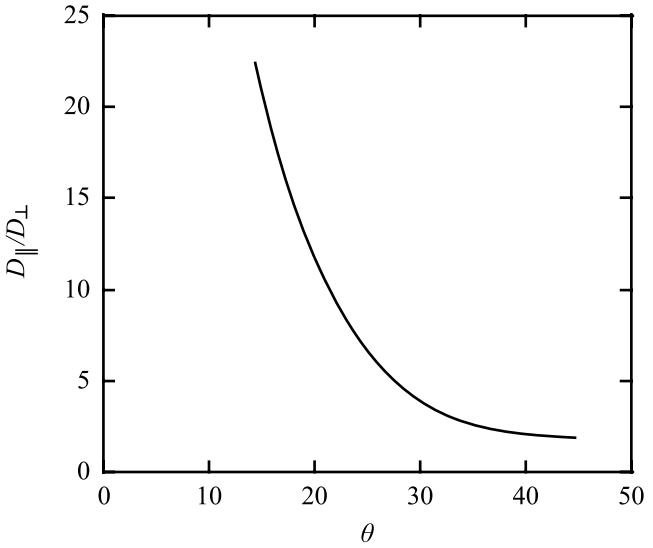

Fig. 4.24. Effect of grain boundary misorientation angle on the diffusion of atoms along grain boundaries (after [5])

At angles greater than 45°, the dislocation model of grain boundaries breaks down since the distance between dislocations, d, would have to be smaller than the lattice constant.

This result also indicates that there should be a relationship between the mean value of the diffusion coefficient, $\bar{D}$, in a polycrystalline material and the grain size, d, since as the grain size decreases, the grain boundary area per unit volume increases. Therefore, $\bar{D}$ should increase with decreasing grain size as shown in Fig. 4.25. We can write the diffusion coefficient of a solid in which diffusion occurs by bulk diffusion (vacancy mechanism) and grain boundary diffusion as:

$$\bar{D} = D_a^{\mathrm{v}} \exp\left(\frac{-Q_{\mathrm{a}}^{\mathrm{v}}}{kT}\right) + D_{\mathrm{gb}} \exp\left(\frac{-Q_{\mathrm{gb}}}{kT}\right) , \tag{4.73}$$

where $D_{\mathrm{a}}^{\mathrm{v}}$ and $Q_{\mathrm{a}}^{\mathrm{v}}$ refer to vacancy self-diffusion and D_{gb} and Q_{gb} refer to grain boundary diffusion. In most metals, $Q_{\mathrm{a}}^{\mathrm{v}} \sim 2Q_{\mathrm{gb}}$, so at low temperature, grain boundary diffusion dominates and at high temperature, diffusion is dominated by bulk, or volume diffusion (Fig. 4.25).

Pipe diffusion along dislocation cores can also influence low temperature lattice diffusion and the total diffusion coefficient can be estimated simply by:

$$\bar{D} = fD_{\mathrm{p}} + (1-f)D_{\mathrm{a}}^{\mathrm{v}} , \tag{4.74}$$

where $\bar{D}$ is the mean diffusion coefficient, D_{p} is the diffusion coefficient for dislocations and $D_{\mathrm{a}}^{\mathrm{v}}$ is the self-diffusion coefficient and f is the fraction of time that the diffusing atom spends within the dislocation. As the dislocation density increases, f increases, and since $D_{\mathrm{p}} > D_{\mathrm{a}}^{\mathrm{v}}$, then D increases as well.

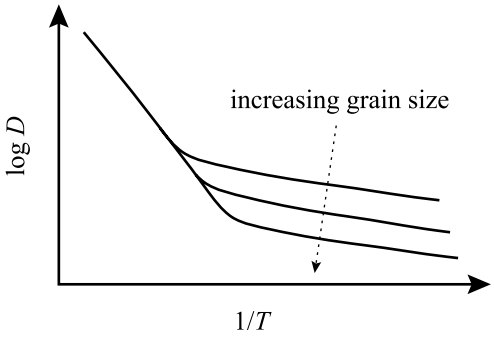

Fig. 4.25. The effect of grain size on the character of diffusion in polycrystalline solids

This general formulation can also be applied to interface or surface diffusion occurring on external and internal surfaces of solids. In general, for defects in the lattice, the more loosely bound the atoms, the lower is the activation energy and the higher is the diffusion coefficient. So surface diffusion requires a lower activation energy than that for other forms of diffusion since each surface atom has only half the nearest neighbors as it does in the bulk, and generally:

$$Q_{\text{surface}} < Q_{\text{gb}} < Q_{\text{p}} < Q_{\text{a}}^{\text{v}} , \quad \text{and so} \quad D_{\text{surface}} > D_{\text{gb}} > D_{\text{p}} > D_{\text{a}}^{\text{v}} . \tag{4.75}$$

Nomenclature

a	Lattice constant
A	Factor depending on geometry and diffusion mechanism
C	Concentration
D_x^y	Diffusion coefficient of species x via y
D_{gb}	Diffusion coefficient for grain boundary diffusion
$\tilde{D}$	Interdiffusion coefficient
D_{lattice}	Diffusion coefficient of lattice atom
D_{p}	Diffusion coefficient for pipe diffusion
D_{tracer}	Diffusion coefficient of tracer atom
E	Energy
f	Correlation (Haven) coefficient
F	Helmholtz free energy
G	Gibbs free energy
H	Enthalpy
J	Flux [cm^{-2}]
k	Boltzmann's constant
n	Number of defects
n_{m}	Number of activated complexes
N	Number of sites
p_{v}	Probability that a lattice site is vacant
P	Pressure

Q	Activation energy
R	Radius
r_a	Radius of an atom
S	Entropy
T	Temperature
U	internal energy
$\bar{v}$	Average velocity of atoms moving through barrier in activated complex, Eq. (4.50)
V	Volume
z	Number of nearest neighbors
α	$1/6zA^2$
δ	Width of the barrier in an activated complex Eq. (4.50); grain boundary width
γ	Stacking fault energy
Γ	Jump frequency
Λ	Jump distance
μ	Shear modulus
ν	Frequency; Poisson's ratio
ν_E	Natural frequency of an oscillator
ν_r	Perturbed frequency of an oscillator
σ	Surface energy
ω	Jump frequency to a single site
Ω	Volume of an atom

Subscripts

a	Atomic
E	Natural component to ν
f	Formation
gb	Grain boundary
i,v	Interstitials, vacancies
m	Migration
p	Pipe
r	Vibrational contribution to ν
th	Thermal

Superscripts

FP	Frenkel pair
i,v	Interstitials, vacancies
mix	Mixing

Acronyms

SIA	Single interstitial atom

Problems

4.1 Many metals occur with both bcc and fcc structure, and it is observed that the transition from one structure to the other involves only insignificant volume change. Assuming *no* volume change, find the ratio $D_{\text{fcc}}/D_{\text{bcc}}$ where D_{fcc} and D_{bcc} are the closest distances between metal atoms in the respective structures.

4.2 For a Ni lattice, calculate the following parameters for atomic chains along the (110) direction:
- a) the number of atoms per unit chain length
- b) the number of chains per unit area
- c) the product of the two. What is this product?

4.3 In the past, investigators have sometimes considered an interstitial atom as having been produced by the transfer of an atom from a normal lattice site to an interstitial site, thus resulting in a one-to-one correspondence between the concentrations of vacancies and interstitials. However, the equilibrium number of vacancies is generally orders of magnitude greater than the equilibrium number of interstitials at a given temperature. Explain.

4.4 The magnitude of the relaxation volume, $|V|$ is greater than 1.0 for interstitials and is less than 1.0 for vacancies. Explain.

4.5 In terms of the jump frequency to a particular neighboring site, ω, and the lattice constant, a, what is the diffusion coefficient for impurity atoms whose equilibrium position is the octahedral interstitial site in:
- a) the fcc lattice
- b) the bcc lattice?

4.6 Consider a rigid crystal in the shape of a sphere of radius R. We create a small cavity of radius r (one atomic volume) in the center of the sphere. The material that was in this volume is spread uniformly over the surface of the sphere (assuming this can be done), increasing the radius of the sphere to R'.
- a) Show that for an atomic radius of 0.15 nm and an intrinsic surface energy, $\sigma \sim 10\,\text{eV}/\text{nm}^2$, the formation energy of a vacancy is of order $\simeq 2\,\text{eV}$.
- b) If instead of a rigid solid, the crystal is treated as an elastic continuum, how would this affect the value of E_{f}^{v} you calculated for part (a)? Why?

4.7 Calculate the diffusivity of interstitials and vacancies in a piece of copper at 484 °C. Neglect the contributions of mixing entropy. Use 0.361 nm for the lattice constant. Also, calculate the diffusion coefficient for diffusion of atoms by vacancy self-diffusion. Why is this so much lower than the diffusivity of vacancies? Take $\gamma = 1$.

4.8 In a laboratory experiment conducted at 10 °C below the melting point of copper, 0.02% of the atom sites are vacant. At 500 °C, the vacant atom fraction was 5.7×10^{-8}.
- a) What is the vacancy formation energy?
- b) How many vacancies are there per cm^3 at 800 °C?

References

1. Ullmaier H, Schilling W (1980) Radiation damage in metallic reactor materials. In: Physics of Modern Materials, vol. I. IAEA, Vienna
2. Hackett MJ, Was GS, Simonen EP (2005) J ASTM Int 2(7)
3. Thompson MW (1969) Defects and Radiation Damage in Metals. Cambridge University Press, Cambridge
4. Shewmon PG (1989) Diffusion in Solids. The Minerals, Metals and Materials Society, Warrendale, PA
5. Mrowec S (1980) Defects and Diffusion in Solids, an Introduction. Elsevier, New York
6. Smigelskas A, Kirkendall E (1947) Trans AIME 171:130
7. Darken L (1948) Trans AIME 175:184–201

5 Radiation-Enhanced Diffusion and Defect Reaction Rate Theory

We have developed an understanding of the formation of point defects, their motion or diffusion in a solid, and the configurations of some of the common types of defect clusters encountered in irradiated and unirradiated metals. Clearly, the formation, growth and dissolution of defect aggregates such as voids, dislocation loops, etc., depend upon the diffusion of point defects and their reaction with the defect aggregates. But they also depend upon the concentration of point defects in the solid. The concentration at any point and time is a balance between the production rate, and the loss rate of point defects and is adequately described by the *point defect balance equations*. The increase in diffusion or enhancement of atom mobility in an irradiated metal is due to two factors: (1) the enhanced concentration of the defects, and (2) the creation of new defect species.

Recall that the diffusion of lattice atoms by way of the vacancy mechanism is given by:

$$D_{\mathrm{a}}^{\mathrm{v}} = f_{\mathrm{v}} D_{\mathrm{v}} C_{\mathrm{v}} \ ,$$

where D_{v} is the vacancy diffusion coefficient, C_{v} is the vacancy concentration and f_{v} is the correlation coefficient. Thus, increasing the concentration of vacancies will increase the diffusion coefficient for the atoms in the metal. However, if other mechanisms of diffusion are operative, such as interstitials or di-vacancies, then the total diffusion coefficient for atoms, D_{a} is written as:

$$D_{\mathrm{a}} = f_{\mathrm{v}} D_{\mathrm{v}} C_{\mathrm{v}} + f_{\mathrm{i}} D_{\mathrm{i}} C_{\mathrm{i}} + f_{2\mathrm{v}} D_{2\mathrm{v}} C_{2\mathrm{v}} + \ldots$$

and diffusion of atoms in the metal is increased by opening new channels via defect species which are usually not present in significant concentration at thermal equilibrium. Under irradiation, D_{a} is also written as D_{rad}.

In this chapter, we will develop the transient and steady state solutions to the point defect balance equations in different temperature and microstructural regimes within the framework of radiation-enhanced diffusion [1, 2]. The solutions to the equations are used to determine the radiation-enhanced diffusion coefficient. Reaction rate theory is then presented to develop an understanding of how point defects interact with the various defect aggregates. Radiation-enhanced diffusion and defect reaction rate theory are essential to understanding the evolution of the irradiated microstructure developed in Chaps. 6–10.

5.1 Point Defect Balance Equations

The development of radiation-induced vacancy and interstitial concentrations occurs due to competing processes. Frenkel defects are created from the collisions between high-energy particles and lattice atoms. These defects can be lost either through recombination of vacancies and interstitials or by reaction with a defect sink (void, dislocation, dislocation loop, grain boundary or precipitate). The local change in defect concentration of the various defect species can be written as the net result of (1) the local production rate, (2) reaction with other species, and (3) diffusion into or out of the local volume or the divergence of the flow. The main reactions we will focus on in this treatment are vacancy–interstitial recombination ($v + i \rightarrow \square$, where $\square$ represents a lattice site) and point defect reactions with sinks ($v + s \rightarrow s$, and $i + s \rightarrow s$). These competing processes can be mathematically described by the *chemical rate equations*:

$$\begin{aligned} \frac{\mathrm{d}C_\mathrm{v}}{\mathrm{d}t} &= K_0 - K_\mathrm{iv}C_\mathrm{i}C_\mathrm{v} - K_\mathrm{vs}C_\mathrm{v}C_\mathrm{s} \\ \frac{\mathrm{d}C_\mathrm{i}}{\mathrm{d}t} &= K_0 - K_\mathrm{iv}C_\mathrm{i}C_\mathrm{v} - K_\mathrm{is}C_\mathrm{i}C_\mathrm{s}\ , \end{aligned} \tag{5.1}$$

where

C_v = vacancy concentration
C_i = interstitial concentration
K_0 = defect production rate
K_iv = vacancy–interstitial recombination rate coefficient
K_vs = vacancy–sink reaction rate coefficient
K_is = interstitial–sink reaction rate coefficient

The terms K_iv, K_vs, K_is are rate constants of the general form, K_{jX} that describe the loss rate of point defects, j per unit point defect concentration to sinks of type, X. Similar equations can be written for defect agglomerates such as di- and tri-vacancies and interstitials. Note that the equations are non-linear differential equations and they are not mutually symmetric with respect to vacancy and interstitial concentrations because of the difference in K_is and K_vs, making an analytical solution difficult. The term "chemical" refers to homogeneous reactions, where the rate depends only on concentration ("law of mass action") and not on the local distribution $C(r)$ of the reactants. Thus, uniformity and thereby chemical kinetics require that $\nabla C \approx 0$. This gives rise to a problem when considering localized sinks, e.g., dislocations, grain boundaries, voids, precipitate interfaces, etc. Such local sinks violate the supposition of spatial uniformity in the host metal in that there is now locally, a directed net flow of mobile point defects toward the closest sinks. The divergence of the flow is equivalent to another "reaction" term, $\nabla \cdot D\nabla C$ in the kinetic balance equations. The locally valid rate equations are:

$$\begin{aligned} \frac{\partial C_\mathrm{v}}{\partial t} &= K_0 - K_\mathrm{iv}C_\mathrm{i}C_\mathrm{v} - K_\mathrm{vs}C_\mathrm{v}C_\mathrm{s} + \nabla \cdot D_\mathrm{v}\nabla C_\mathrm{v} \\ \frac{\partial C_\mathrm{i}}{\partial t} &= K_0 - K_\mathrm{iv}C_\mathrm{i}C_\mathrm{v} - K_\mathrm{is}C_\mathrm{i}C_\mathrm{s} + \nabla \cdot D_\mathrm{i}\nabla C_\mathrm{i}\ . \end{aligned} \tag{5.2}$$

The solution to these equations requires the statement of boundary conditions in addition to the initial local concentrations of the mobile defects (vacancies and interstitials). However, we can assume that $\nabla C \approx 0$ if the mean defect separation is greater than the mean distance between sinks, that is, the sink density is higher than the defect density. This amounts to treating the sink as being uniformly distributed and Eq. (5.1) applies.

We consider the following model for the solution to Eq. (5.1). A pure metal is irradiated to produce only single vacancies and single interstitials in equal numbers with no spatial correlation of the interstitial with its vacancy. The interstitials and vacancies migrate by random walk diffusion, annihilating each other by mutual recombination or at unsaturable fixed sinks. Sinks and defects are distributed homogeneously in the metal. The diffusion coefficient of the metal is given by the sum of terms due to its diffusion by vacancies and interstitials. The model will have the following limitations:

1. The model applies to a pure metal. Binding of defects to atomic species and limitation of defect motion due to binding and correlation effects are neglected, $f = 1$.
2. The sink concentrations and strengths are time-independent, or unsaturable.
3. Other than mutual recombination, defect–defect interactions (e.g., the formation of di-vacancies or di-interstitials) are ignored.
4. Bias factors for diffusion of defects to sinks are set to unity (no preferential absorption of specific point defects at specific sinks).
5. Diffusion terms in and out of a specific volume are not considered.
6. The thermal equilibrium vacancy concentration is neglected.

The rate constants are as follows:

$$K_{\mathrm{iv}} = 4\pi r_{\mathrm{iv}} (D_{\mathrm{i}} + D_{\mathrm{v}}) \approx 4\pi r_{\mathrm{iv}} D_{\mathrm{i}} \tag{5.3}$$

since $D_{\mathrm{i}} \gg D_{\mathrm{v}}$,

$$K_{\mathrm{is}} = 4\pi r_{\mathrm{is}} D_{\mathrm{i}} \tag{5.4}$$

$$K_{\mathrm{vs}} = 4\pi r_{\mathrm{vs}} D_{\mathrm{v}} \ , \tag{5.5}$$

where r_{iv}, r_{vs} and r_{is} are interaction radii for the reaction between the species given by the subscripts and represent the radii of surfaces such that if crossed by the defect, it is annihilated. The terms D_{i} and D_{v} are the interstitial and vacancy diffusion coefficients, respectively. The production term, K_0, is the *effective* point defect production rate in that it refers to the production of only freely migrating defects that can give rise to long-range diffusion (see Chap. 3). The derivations of the terms in Eqs. (5.3) and (5.4) will be given in the Sect. 5.3.

Note that since the rate constants can differ by several orders of magnitude, the equations are stiff. That is, the time increment needed to follow interstitial motion is orders of magnitude too small to show any vacancy motion. Therefore, the equations must be solved using numerical techniques for stiff equations. But we can gain

insight into the processes by looking at analytical solutions to limiting cases. For example, the defect concentrations initially increase linearly with $C_v = C_i = K_0 t$. Further development depends on the values of the temperature and sink concentration, C_s. We will develop analytical solutions to Eq. (5.1) for four different regimes (combinations of T and C_s); (1) low T and low C_s, (2) low T and intermediate C_s, (3) low T and high C_s, and (4) high T.

5.1.1 Case 1: Low Temperature, Low Sink Density

The approximate solutions to Eq. (5.1) for low temperature and low sink density are given in Fig. 5.1. Initially, defect concentrations build up according to $dC/dt = K_0$ with $C_i \sim C_v$, so $C_i = C_v = C = K_0 t$. Initially, the concentrations are too low for either recombination or sinks to have an effect on the buildup. The buildup of point defects will start to level off when the production rate is compensated by the recombination rate. In the time regime where the production rate is balanced by the recombination rate, we drop the last two terms from Eq. (5.1) and solve for the "quasi-steady state" concentrations:

$$\frac{dC}{dt} = K_0 - K_{iv} C^2 = 0 \quad (C = C_i = C_v)\,, \tag{5.6}$$

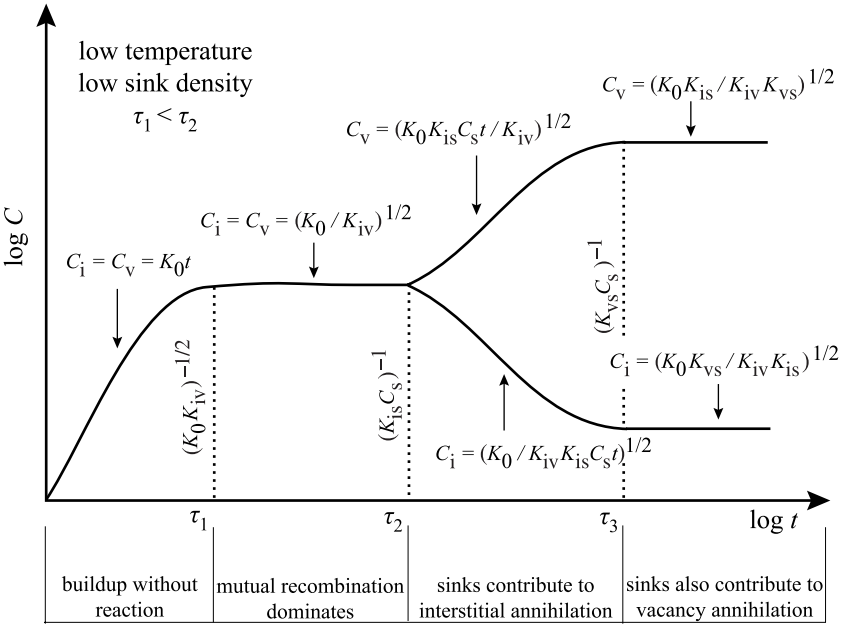

Fig. 5.1. Log-log plot of vacancy and interstitial concentration vs. time for case (1) low temperature and low sink density (after [2])

with the solution:

$$C = \left(\frac{K_0}{K_{iv}}\right)^{1/2} . \tag{5.7}$$

Equating this concentration with that during the buildup phase:

$$K_0 t = \left(\frac{K_0}{K_{iv}}\right)^{1/2} , \tag{5.8}$$

yields the time at which losses to recombination compensate for the production rate from irradiation:

$$t = \tau_1 = (K_0 K_{iv})^{-1/2} , \tag{5.9}$$

where τ_1 is a time constant or characteristic time for the *onset of mutual recombination*.

Eventually, the interstitials (first) and then the vacancies (later) will begin to find the sinks and sinks will start to contribute to annihilation. C_i and C_v remain approximately equal until a time τ_2, which is the time constant for the process of interstitials reacting with the sinks. Because $D_i > D_v$, more interstitials are lost to sinks than vacancies, which is described by:

$$\frac{dC_i}{dt} = -K_{is} C_i C_s , \tag{5.10}$$

so the interstitial concentration will decay and the vacancy concentration will rise (since their only sink is interstitials and interstitials are being lost to sinks), yielding:

$$\begin{aligned} C_v(t) &= \left[\frac{K_0 K_{is} C_s t}{K_{iv}}\right]^{1/2} \\ C_i(t) &= \left[\frac{K_0}{K_{iv} K_{is} C_s t}\right]^{1/2} . \end{aligned} \tag{5.11}$$

(The derivation of Eq. (5.11) is Problem 5.15 at the end of the chapter.) The time at which these equalities occur is obtained by equating the concentrations in the bounding time regimes of quasi-steady state and buildup of interstitials/decay of vacancies (Fig. 5.1):

$$\begin{aligned} C_v &= \left(\frac{K_0}{K_{iv}}\right)^{1/2} = \left[\frac{K_0 K_{is} C_s t}{K_{iv}}\right]^{1/2} \\ C_i &= \left(\frac{K_0}{K_{iv}}\right)^{1/2} = \left[\frac{K_0}{K_{iv} K_{is} C_s t}\right]^{1/2} , \end{aligned} \tag{5.12}$$

and solving for the time yields the time constant for the *onset of the buildup regime*:

$$t = \tau_2 = (K_{is} C_s)^{-1} . \tag{5.13}$$

After a while, at time τ_3, true steady state will be achieved. τ_3 is the time constant for the slowest process, which is the interaction of vacancies with sinks. Solving Eq. (5.1) for the steady state concentration of vacancies and interstitials by setting $dC_v/dt = dC_i/dt = 0$ gives:

$$\begin{aligned} C_v^{ss} &= -\frac{K_{is}C_s}{2K_{iv}} + \left[\frac{K_0K_{is}}{K_{iv}K_{vs}} + \frac{K_{is}^2C_s^2}{4K_{iv}^2}\right]^{1/2} \\ C_i^{ss} &= -\frac{K_{vs}C_s}{2K_{iv}} + \left[\frac{K_0K_{vs}}{K_{iv}K_{is}} + \frac{K_{vs}^2C_s^2}{4K_{iv}^2}\right]^{1/2} \end{aligned} \quad . \tag{5.14}$$

Since vacancies and interstitials are produced in equal numbers and equal numbers are lost to recombination, the loss of each to sinks must be equal at steady state, and:

$$K_{vs}C_v = K_{is}C_i \; . \tag{5.15}$$

For the case of low temperature and low sink density, C_s is small, and the vacancy and interstitial concentrations in Eq. (5.14) are approximated as:

$$C_v^{ss} \cong \sqrt{\frac{K_0K_{is}}{K_{iv}K_{vs}}} \; ; \quad C_i^{ss} \cong \sqrt{\frac{K_0K_{vs}}{K_{iv}K_{is}}} \; . \tag{5.16}$$

Equating these expressions to those from the previous (buildup) region gives:

$$C_v = \left[\frac{K_0K_{is}C_st}{K_{iv}}\right]^{1/2} = \left[\frac{K_0K_{is}}{K_{iv}K_{iv}}\right]^{1/2} \; . \tag{5.17}$$

and solving for the time gives the time constant for the *onset of steady state*:

$$t = \tau_3 = (K_{vs}C_s)^{-1} \; . \tag{5.18}$$

The buildup shown in Fig. 5.1 is really a schematic and not the actual buildup. The transitions between regimes are not so sudden. For example, if the sink density is assumed to be zero, the exact solution to Eq. (5.1) is:

$$C_v(t) = \sqrt{\frac{K_0}{K_{iv}}} \tanh\left(\sqrt{K_{iv}K_0}t\right) \; . \tag{5.19}$$

5.1.2 Case 2: Low Temperature, Intermediate Sink Density

Increasing the sink density has the effect of bringing τ_2 closer to τ_1 (see Fig. 5.2). That is, the region of mutual recombination is shrunk at the expense of annihilation at sinks. In fact, when:

$$\tau_1 = \tau_2 \text{ or } (K_0K_{iv})^{-1/2} = (K_{is}C_s)^{-1} \; , \tag{5.20}$$

the plateau disappears.

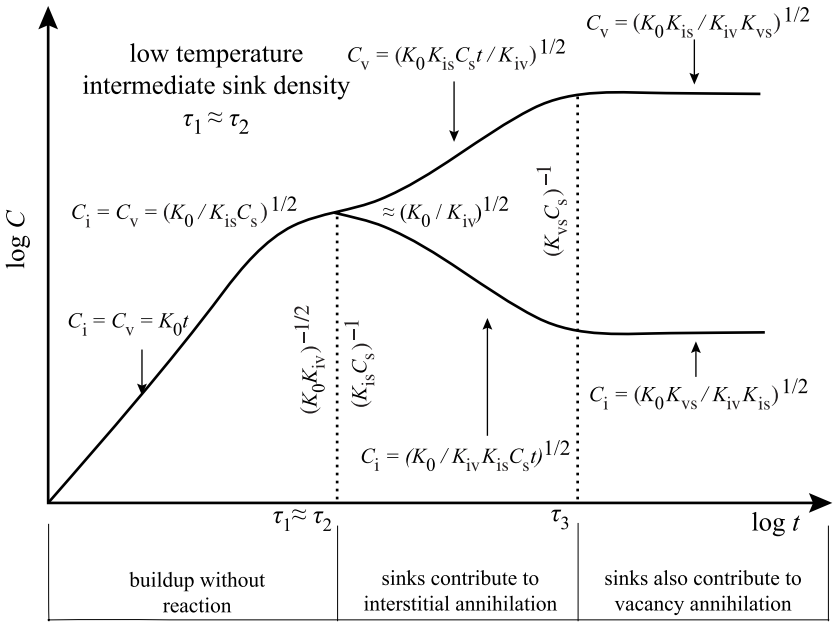

Fig. 5.2. Log-log plot of vacancy and interstitial concentration vs. time for case (2) low temperature and intermediate sink density (after [2])

5.1.3 Case 3: Low Temperature, High Sink Density

The main effect of a high sink density is that interstitials find the sinks before they find vacancies because $C_s \gg C_v$ at short time (Fig. 5.3). That is, the time to reach linear buildup (loss of interstitials to sinks), τ_2, becomes shorter than the time to reach quasi-steady state due to vacancy–interstitial interaction, τ_1. In this case, the interstitial concentration comes into a quasi-steady state with production and annihilation at sinks:

$$\frac{dC_i}{dt} = 0 = K_0 - K_{is} C_i C_s \,, \tag{5.21}$$

resulting in the quasi-steady state concentration:

$$C_i = \frac{K_0}{K_{is} C_s} \,. \tag{5.22}$$

Equating interstitial concentrations in the linear buildup regime with the quasi-steady state regime:

$$K_0 t = \frac{K_0}{K_{is} C_s} \,, \tag{5.23}$$

and solving for t gives the value for the time constant τ_2:

$$t = \tau_2 = (K_{is} C_s)^{-1} \,. \tag{5.24}$$

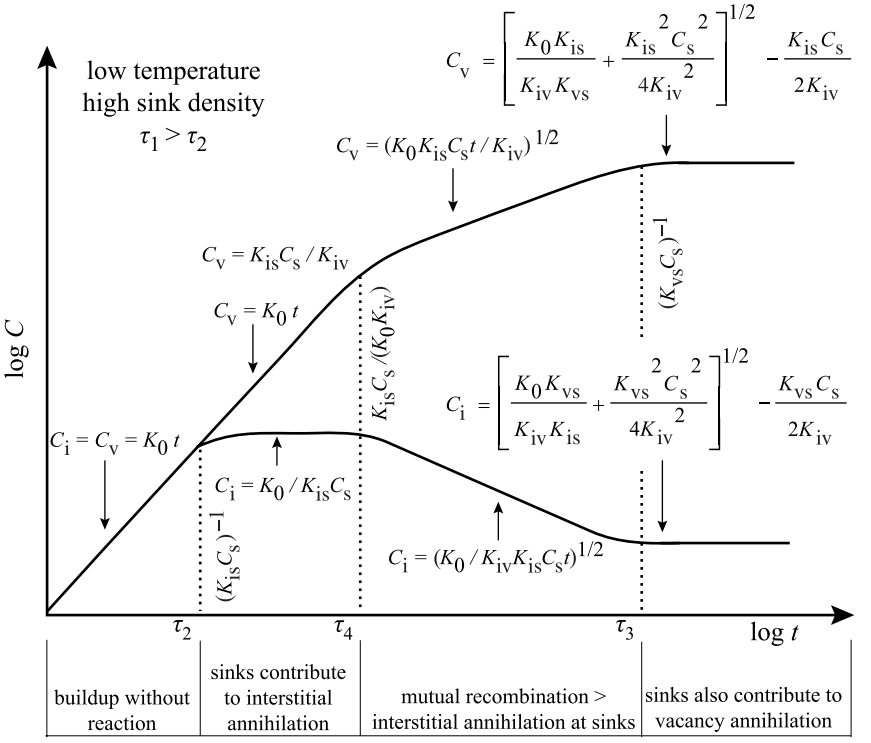

Fig. 5.3. Log-log plot of vacancy and interstitial concentration vs. time for case (3) low temperature and high sink density (after [2])

Note that since interstitials have found the sinks before finding the slower vacancies, the vacancy concentration continues to rise according to $C_v = K_0 t$. A competition soon arises between annihilation of interstitials at sinks and recombination with vacancies:

$$K_{is} C_i C_s = K_{iv} C_i C_v \cong K_{iv} C_i K_0 t \,, \tag{5.25}$$

yielding the time constant for the transition between the regimes where interstitials go to sinks and mutual recombination dominates:

$$t = \tau_4 = \frac{K_{is} C_s}{K_{iv} K_0} \,. \tag{5.26}$$

In the regime following τ_4, C_v rises but more slowly, and C_i decreases slowly according to:

$$\begin{aligned} C_v &= (K_0 K_{is} C_s t / K_{iv})^{1/2} \\ C_i &= (K_0 / K_{is} K_{iv} C_s t)^{1/2} \,. \end{aligned} \tag{5.27}$$

Steady state arrives at:

$$\tau_3 = \frac{1}{K_{\mathrm{vs}} C_{\mathrm{s}}} \,, \tag{5.28}$$

with

$$\begin{aligned} C_{\mathrm{v}}^{ss} &= -\frac{K_{\mathrm{is}} C_{\mathrm{s}}}{2K_{\mathrm{iv}}} + \left[\frac{K_0 K_{\mathrm{is}}}{K_{\mathrm{iv}} K_{\mathrm{vs}}} + \frac{K_{\mathrm{is}}^2 C_{\mathrm{s}}^2}{4K_{\mathrm{iv}}^2} \right]^{1/2} \\ C_{\mathrm{i}}^{ss} &= -\frac{K_{\mathrm{vs}} C_{\mathrm{s}}}{2K_{\mathrm{iv}}} + \left[\frac{K_0 K_{\mathrm{vs}}}{K_{\mathrm{iv}} K_{\mathrm{is}}} + \frac{K_{\mathrm{vs}}^2 C_{\mathrm{s}}^2}{4K_{\mathrm{iv}}^2} \right]^{1/2} . \end{aligned} \tag{5.29}$$

Note that the steady state concentrations are the same as Eq. (5.14) given earlier in case (1), but without the simplification of dropping the terms in C_{s} since in this case, the sink density is high and cannot be neglected.

5.1.4 Case 4: High Temperature

At high temperature, the defect annihilation rate at the sinks keeps the concentration of interstitials low (Fig. 5.4). Since recombination does not contribute much, the rate equations become:

$$\begin{aligned} \frac{\mathrm{d}C_{\mathrm{v}}}{\mathrm{d}t} &= K_0 - K_{\mathrm{vs}} C_{\mathrm{s}} C_{\mathrm{v}} \\ \frac{\mathrm{d}C_{\mathrm{i}}}{\mathrm{d}t} &= K_0 - K_{\mathrm{is}} C_{\mathrm{s}} C_{\mathrm{i}} \,, \end{aligned} \tag{5.30}$$

with steady state solutions:

$$C_{\mathrm{v}} = \frac{K_0}{K_{\mathrm{vs}} C_{\mathrm{s}}} \,, \quad C_{\mathrm{i}} = \frac{K_0}{K_{\mathrm{is}} C_{\mathrm{s}}} \,, \tag{5.31}$$

with characteristic times given by:

$$\text{interstitial annihilation at sinks:} \quad K_0 t = \frac{K_0}{K_{\mathrm{is}} C_{\mathrm{s}}} \Rightarrow t = \tau_2 = (K_{\mathrm{is}} C_{\mathrm{s}})^{-1} \tag{5.32}$$

$$\text{vacancy annihilation at sinks:} \quad K_0 t = \frac{K_0}{K_{\mathrm{vs}} C_{\mathrm{s}}} \Rightarrow t = \tau_3 = (K_{\mathrm{vs}} C_{\mathrm{s}})^{-1} \,. \tag{5.33}$$

The time evolution of vacancy and interstitial concentrations displayed in Fig. 5.4 ignores the presence of thermal vacancies, which may be significant at higher temperatures. The buildup of radiation-induced vacancies and interstitials at high temperature, including an initial presence of thermal equilibrium vacancies is shown in Fig. 5.5. Note the effect of sink (dislocation) density and defect production rate.

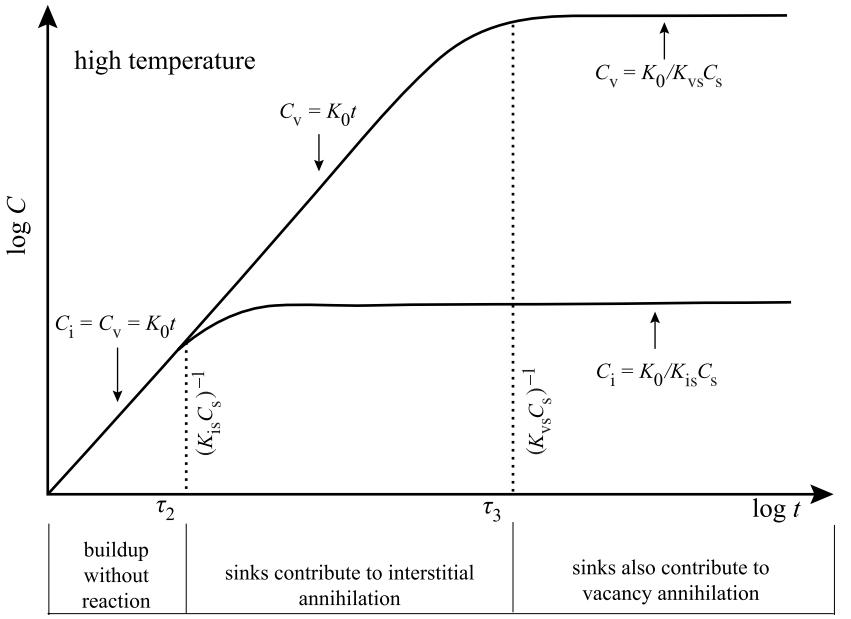

Fig. 5.4. Log-log plot of vacancy and interstitial concentration vs. time for case (4) high temperature (after [2])

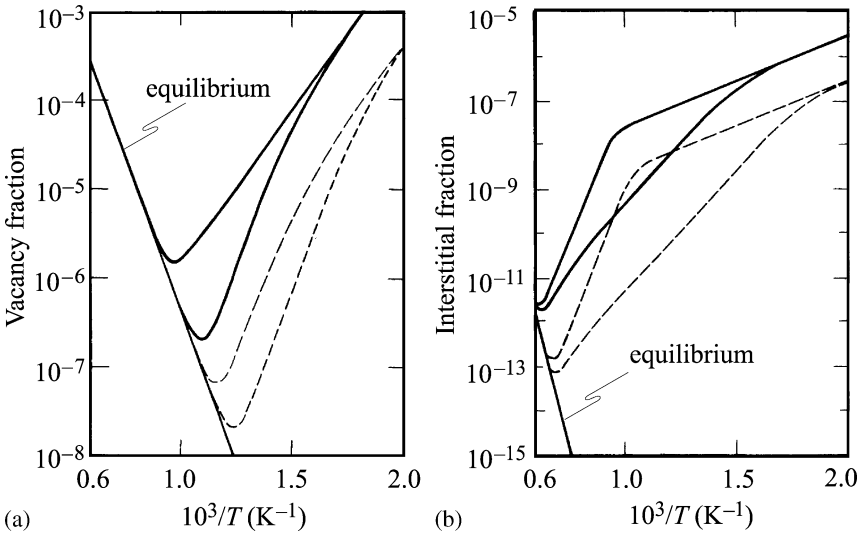

Fig. 5.5. Steady state (a) vacancy and (b) interstitial concentrations in an irradiated metal at a high production rate (*solid line*) and at a low defect production rate (*dashed line*). The *upper* and *lower curves* for each defect production rate represent small and large dislocation densities, respectively (after [3])

Table 5.1. Time constants for rate-limiting processes in the point defect balance equations

Time constant	Value	Process
τ_1	$(K_0 K_{iv})^{-1/2}$	Onset of mutual recombination
τ_2	$(K_{is} C_s)^{-1}$	Onset of interstitial loss to sinks
τ_3	$(K_{vs} C_s)^{-1}$	Onset of vacancy loss to sinks
τ_4	$\tau_1^2/\tau_2 = \dfrac{K_{is} C_s}{K_0 K_{iv}}$	Mutual recombination dominates interstitial loss to sinks

Figure 5.5a shows that increasing the sink density lowers the vacancy concentration since sinks absorb the vacancies (loss term is proportional to K_{vs}). Also for a fixed sink density, a higher displacement rate results in a higher vacancy concentration because the production rate is higher than the loss rate to sinks. The same is true for interstitials shown in Fig. 5.5b. The kinks in the interstitial concentration curves correspond to the temperature at which vacancies become mobile and contribute to interstitial loss by mutual recombination as in Fig. 5.3. Comparing Figs. 5.5a,b shows that the equilibrium concentration of interstitials is negligible over the practical range of reactor component temperatures, while this is not the case for vacancies.

The main objective of solving the point defect balance equations is to obtain values for C_i and C_v to determine D_{rad}, which is just the sum of $C_i D_i$ and $C_v D_v$. The preceding discussion shows that we can interpret radiation-enhanced diffusion experiments after an isothermal irradiation at a constant flux for a time t in terms of characteristic times. Table 5.1 summarizes the time constants for the various rate-limiting mechanisms. For low sink density, recombination dominates at short times, followed by interstitial annihilation at sinks and then vacancy annihilation at sinks, which is the slowest process and controls the achievement of steady state. At high sink density, interstitial annihilation at sinks dominates early, followed by mutual recombination and then vacancy loss to sinks. As a rule, when $\tau_1 < \tau_2$, mutual recombination dominates and when $\tau_2 < \tau_1$, sinks dominate. In summary, the key factors affecting C_i and C_v are production rate, defect mobility and sink concentration.

5.1.5 Properties of the Point Defect Balance Equations

The point defect balance equations and their solutions possess interesting properties, which provide further insight into the behavior of vacancies and interstitials in the diffusion of lattice atoms. They are the following:

1. The vacancy concentration referred to in the last section is really $C_v - C_v^0$ where C_v^0 is the thermal equilibrium concentration of vacancies. In high-temperature irradiations ($T/T_m \geq 0.5$), this concentration is non-negligible. However, over all irradiation temperatures of interest, $C_i^0/C_i \ll 1$.

2. In the absence of sinks and thermal vacancies, C_v can be exchanged with C_i, that is, $C_v = C_i$ at any instant:

$$\begin{aligned} \frac{dC_v}{dt} &= K_0 - K_{iv}C_iC_v \\ \frac{dC_i}{dt} &= K_0 - K_{iv}C_iC_v \ . \end{aligned} \tag{5.34}$$

Since $D_{rad} = D_iC_i + D_vC_v$, and $C_i = C_v$, but since $D_i \gg D_v$, then interstitials contribute much more to atom mobility than do vacancies.

3. If there is only one type of sink, then at steady state:

$$\begin{aligned} K_0 &= K_{iv}C_iC_v + K_{vs}C_vC_s \\ K_0 &= K_{iv}C_iC_v + K_{is}C_iC_s \ , \end{aligned} \tag{5.35}$$

or

$$K_{vs}C_v = K_{is}C_i \ , \tag{5.36}$$

and the absorption rate of interstitials and vacancies at sinks is equal, or the net absorption rate at the sink is zero. Even for the case of multiple sink types, if the sinks have the same "strength" for vacancies and interstitials, then the net flow to any sink is zero.

4. Inclusion of sink terms violates the symmetry with respect to C_i and C_v because of the different values of K ($K_{vs} \neq K_{is}$). Symmetry *is* present in the steady state with regard to D_iC_i and D_vC_v (since $K_{is}\alpha D_i$ and $K_{vs}\alpha D_v$). The physical consequence is that vacancies and interstitials contribute to atom mobility to the same extent and their actions cannot be discriminated. At steady state:

$$\begin{aligned} 0 &= K_0 - K_{iv}C_iC_v - K'_{vs}D_vC_vC_s \\ 0 &= K_0 - K_{iv}C_iC_v + K'_{is}D_iC_iC_s \ , \end{aligned} \tag{5.37}$$

where the K terms have been written as $K = K'D$, giving:

$$D_vC_vK'_{vs}C_s = D_iC_iK'_{is}C_s \ . \tag{5.38}$$

So if $K'_{vs} \sim K'_{is}$, then $D_iC_i = D_vC_v$ which means that vacancies and interstitials contribute *equally* to atom mobility. Even though the steady state concentration of interstitials is much lower than the steady state concentration of vacancies, they each contribute equally to atom mobility because of the faster rate of diffusion of interstitials. For any particular sink to grow, it must have a net bias for either vacancies or interstitials. In real metals, K_{vs} and K_{is} are not equal. Specific sinks have a bias for certain point defects, allowing that sink to grow. This behavior is described in more detail Sect. 5.3.

5.1.6 Deficiencies of the Simple Point Defect Balance Model

The simple point defect model neglects numerous features of realistic systems that must be incorporated in order to obtain accurate results. For example, no account is taken for changing sink strengths, which occur as dose buildup continues due to the formation of depleted zones and defect clusters. Also, sink bias is neglected. Bias is an important factor affecting the development of the irradiated microstructure as will become evident in Chaps. 7 and 8. Defect–defect interaction and defect–impurity interaction have also been neglected. Defect–defect interaction will be important in the formation of void and interstitial loop nuclei and cannot be neglected if larger clusters are to be properly accounted for. These small clusters will serve as traps or sinks for mobile defects. In fact, vacancy clusters have been found to increase D_{rad} in the mutual-recombination range, but are insignificant for high sink concentrations and temperatures where annealing to fixed sinks dominates [4]. Finally, the equations are unable to account for defect gradients (and in the simple form, for concentration gradients). These become very important in processes such as radiation-induced segregation (Chap. 6), in which defect fluxes give rise to concentration gradients in the alloying elements. Such processes may significantly alter the behavior of sinks and the bias of the sinks.

5.2 Radiation-Enhanced Diffusion

In a pure metal, the diffusion coefficient under radiation is given by:

$$D_{\mathrm{rad}} = D_{\mathrm{v}} C_{\mathrm{v}} + D_{\mathrm{i}} C_{\mathrm{i}} \,. \tag{5.39}$$

Because the concentrations of vacancies and interstitials under irradiation are much greater than those produced thermally, the radiation-enhanced diffusion coefficients are much larger than thermal diffusion coefficients. Despite the shortcomings, it is interesting to see how well the simple point defect balance equations are able to estimate the effect of irradiation on diffusion. Figure 5.6 is a plot of $\log D_{\mathrm{rad}}$ vs. $\log t$ for the case of annealed Ag-30% Zn at 40 °C irradiated with 2.5 MeV electrons at a flux of $3.7 \times 10^{15}\,\mathrm{m^{-2}s^{-1}}$ [2]. The thin solid lines are the interstitial and vacancy concentrations and the thick solid line is the their sum as calculated from Eq. (5.35) by Sizeman [2] and the dashed line is the experimental data. The experiment actually measures the Zener relaxation time, τ_z (see [1]), which is proportional to D_{rad}. The experimental result confirms the existence of a maximum in D_{rad} as in case (1) for low temperature and low sink density. This result also shows that the interstitial component dominates at times less than that to achieve steady state, τ_3, since $D_{\mathrm{i}} > D_{\mathrm{v}}$ (by assumption) and $C_{\mathrm{i}} > C_{\mathrm{v}}$ for $\tau < \tau_3$.

Another excellent example of calculation of D_{rad} vs. measurement is provided by Rothman [5.1] for self-diffusion in copper at 200 °C in a crystal containing a dislocation density of $10^{11}\,\mathrm{m^{-2}}$ under irradiation with a net damage rate,

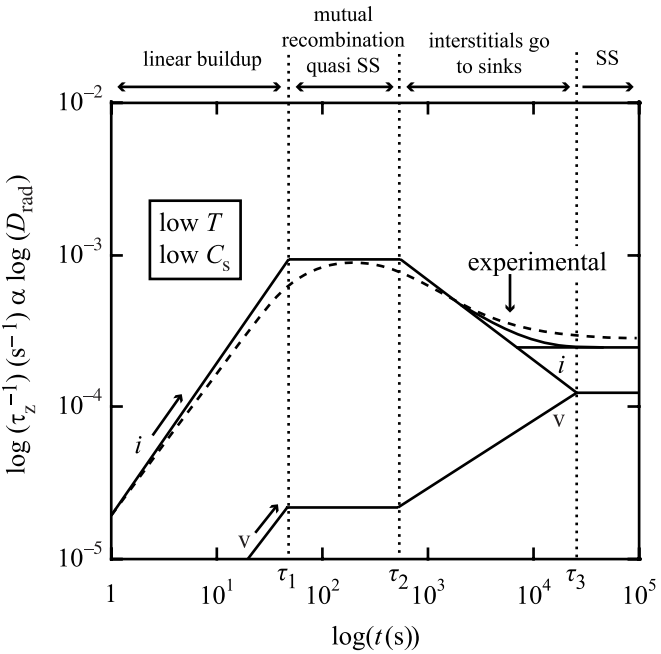

Fig. 5.6. Time dependence of D_{rad} vs. ln$t$ for both calculation (*solid line*) and measurement (*dashed line*). *Thin solid lines* are for the vacancy and interstitial components and the *heavy solid line* is the sum of the components (after [2])

$K_0 = 10^{-6}\,\text{dpa/s}$ (similar to that experienced by a fast reactor core structural material). In this case, $D_{\text{rad}} \sim 6.5 \times 10^{-21}\,\text{m}^2\,\text{s}^{-1}$. Given that the thermal diffusion coefficient is $\sim 1.4 \times 10^{-27}\,\text{m}^2\,\text{s}^{-1}$, this represents an extremely large ($> 10^6$) increase due to irradiation. Figure 5.7 shows that at temperatures below 575 °C, D_{rad} exceeds the thermal equilibrium self-diffusion coefficient for this defect production rate (curve 1). The various curves in Fig. 5.7 represent different combinations of production rates and defect densities. Note that at low temperature, mutual recombination dominates and D_{rad} has an activation energy of $E_{\text{m}}^{\text{v}}/2$ (all curves). At low sink density (10^{11} dislocations m^{-2} (curve 1), where $\rho_{\text{d}} \sim 4\pi r_{\text{vs}} C_{\text{s}} = 4\pi r_{\text{is}} C_{\text{s}}$) the mutual recombination region ties indirectly to diffusion by thermal equilibrium vacancies with increasing temperature. At high sink densities, ($10^{14}\,\text{m}^{-2}$ (curve 2) and $10^{15}\,\text{m}^{-2}$ (curve 3)), mutual recombination gives way to annealing at fixed sinks at a critical temperature, determined as follows.

According to Eq. (5.36), for a single sink type:

$$C_{\text{i}} K_{\text{is}} = C_{\text{v}} K_{\text{vs}} \quad \text{or} \quad C_{\text{i}} = \frac{C_{\text{v}} K_{\text{vs}}}{K_{\text{is}}} \,. \tag{5.40}$$

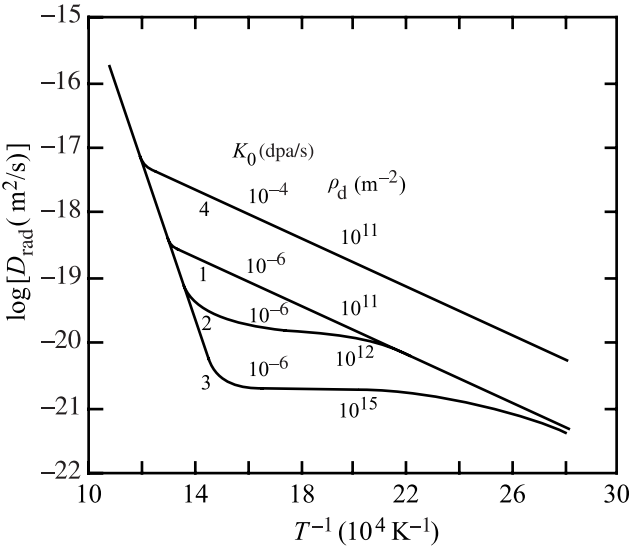

Fig. 5.7. Calculated D_{rad} for self-diffusion of copper as a function of temperature for different combinations of defect production rates and dislocation densities. *1*: $K_0 = 10^{-6}$ dpa/s, $\rho_d = 10^{11}$ m^{-2}, *2*: $K_0 = 10^{-6}$ dpa/s, $\rho_d = 10^{14}$ m^{-2}, *3*: $K_0 = 10^{-6}$ dpa/s, $\rho_d = 10^{15}$ m^{-2}, *4*: $K_0 = 10^{-4}$ dpa/s, $\rho_d = 10^{11}$ m^{-2} (after [1])

At steady state, Eq. (5.29) apply and they can be re-written in the following form:

$$C_v = \frac{K_{is}C_s}{2K_{iv}}\left[\left(1+\frac{4K_0K_{iv}}{K_{is}K_{vs}C_s^2}\right)^{1/2}-1\right]$$
$$C_i = \frac{K_{vs}C_s}{2K_{iv}}\left[\left(1+\frac{4K_0K_{iv}}{K_{is}K_{vs}C_s^2}\right)^{1/2}-1\right] . \tag{5.41}$$

We define a parameter, η, such that:

$$\eta = \frac{4K_0K_{iv}}{K_{vs}K_{iv}C_s^2} . \tag{5.42}$$

Then using Eq. (5.41) C_v can be written as:

$$C_v = \frac{F(\eta)K_0}{K_{vs}C_s} , \text{ or } C_vK_{vs}C_s = F(\eta)K_0 . \tag{5.43}$$

where:

$$F(\eta) = \frac{2}{\eta}[(1+\eta)^{1/2}-1] . \tag{5.44}$$

Equation (5.43) shows that $F(\eta)$ determines the number of defects absorbed by sinks in relation to the total rate of formation of the defects. If $\eta \to 0$, then

$F(\eta) \rightarrow 1$, i.e., all of the defects are lost to sinks and none to recombination. In the limit of large η, $F(\eta) \sim 2/\eta^{1/2}$ and $F(\eta) \rightarrow 0$, indicating that mutual recombination dominates defect loss. When $F(\eta) = 1/2$, the loss of defects to sinks and recombination is equal. This occurs at a value of η of:

$$\eta = 8 = \frac{4K_0K_{iv}}{K_{vs}K_{is}C_s^2} \,. \tag{5.45}$$

Equation (5.45) can be solved for the critical temperature below which mutual recombination will dominate, and above which loss to sinks will dominate. (The term η will be revisited in Chap. 8 in describing the effect of recombination on void growth). Using Eqs. (5.3), (5.4), and (5.5) for K_{iv}, K_{is} and K_{vs}, and defining $K'_{iv} = 4\pi r_{iv}$, $K'_{is} = 4\pi r_{vs}$ and $K'_{vs} = 4\pi r_{iv}$, gives:

$$8 = \frac{4K_0K'_{iv}D_0^i \exp\left(\dfrac{-E_m^i}{kT}\right)}{K'_{vs}D_0^v \exp\left(\dfrac{-E_m^v}{kT}\right) K'_{is}D_0^i \exp\left(\dfrac{-E_m^i}{kT}\right) C_s^2} \,, \tag{5.46}$$

where $E_{i,m}^v$ is the migration energy and $D_0^{i,v}$ is the pre-exponential factor in the diffusion coefficient for interstitials and vacancies, respectively. Equation (5.46) simplifies to:

$$T_c = \frac{E_m^v}{k \ln\left[\dfrac{2D_0^v C_s^2 K'_{is} K'_{vs}}{K_0 K'_{iv}}\right]} \,. \tag{5.47}$$

At the highest temperatures, D_{rad} is overwhelmed by thermal vacancies (all curves in Fig. 5.7), and increasing K_0 to 10^{-4} dpa/s (curve 4) raises D_{rad} in the mutual recombination range by a factor of 10.

Figure 5.8 shows the radiation-enhanced diffusion coefficient calculated for a sample of nickel undergoing irradiation at a rate of 10^{-6} dpa/s for different sink annihilation probabilities, p, where p^{-1} is the average number of jumps of a defect between creation and annihilation at a sink [5]. The diffusion coefficient describing radiation-enhanced diffusion, D_{rad}, is shown by the solid line. The dashed line to the left is the thermal diffusion coefficient and the solid horizontal line at the right is the diffusion coefficient due to ballistic mixing, D_m [6], and will be discussed in Chap. 10. The difference between the curves for D_{rad} and D_{th} is the effect of radiation-enhanced diffusion. As shown, irradiation can result in a several orders of magnitude increase in the diffusion coefficient.

5.3 Defect Reactions

Each of the terms in the point defect balance equation represents a reaction. The rate at which the reaction occurs will depend on the nature of the reacting species.

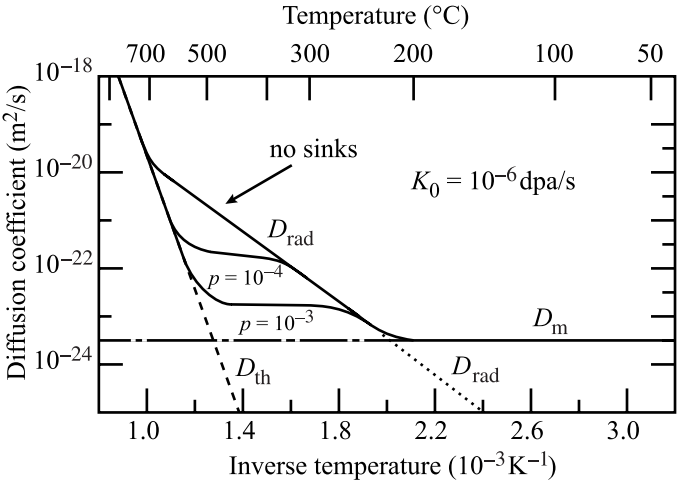

Fig. 5.8. Diffusion coefficient as a function of $1/T$ for a nickel-base alloy during irradiation at a displacement rate of 10^{-6} dpa/s. D_{rad} is calculated from rate theory for various sink annihilation probabilities, p. The diffusion coefficient from displacement mixing is D_m and the thermal diffusion coefficient is D_{th} (from [5])

Following [3], we will develop expressions for the rates of each of the reactions in the point defect balance equation, as they will be used in describing processes such as void growth, dislocation climb, etc. We have seen that the motion of mobile point defects can be considered a random walk process. When one of these defects encounters a specie in the crystal to which it becomes tightly bound, one or both of the partners in the encounter is considered to disappear from the solid. Examples include a vacancy or interstitial intersecting a free surface, grain boundary, dislocation, void, etc., or a vacancy encountering a vacancy, an interstitial encountering an interstitial, or a vacancy encountering an interstitial. Clearly the rate of such reactions is proportional to the concentrations of both species, or:

$$\text{reaction rate of } A \text{ and } B = K_{AB} C_A C_B \text{reactions}/\text{cm}^3\,\text{s}\,, \tag{5.48}$$

where C_A and C_B are the concentration of species A and B in units of particles/cm^3, and K_{AB} is the rate constant of the reaction in cm^3/s. Reactions can be between two mobile particles (vacancy and interstitial at high temperature) or between one mobile and one stationary defect, e.g., low temperature where vacancies are immobile and interstitials are mobile, or between interstitials and dislocation, grain boundaries, voids, etc.

There are two types of processes that will be of interest in dealing with the reaction between point defects and sinks. They are *reaction rate-controlled* and *diffusion-controlled* processes. In reaction rate-governed processes, there must be no macroscopic concentration gradients of either partner. If one partner is large compared to the atomic sized reactant, or if one is a strong sink, a concentration gradient may be established in the vicinity of the stationary defect. Reactions between point defects are examples of reaction rate-controlled processes. If a defect

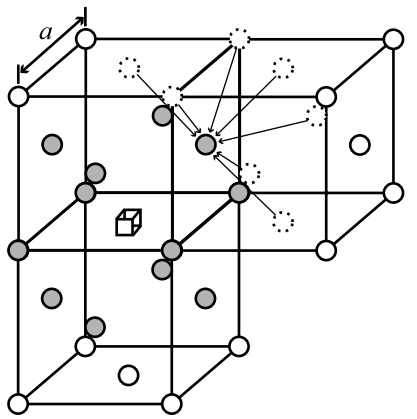

Fig. 5.9. Locations of nearest neighbors for the formation of a di-vacancy in the fcc lattice (after [3])

concentration gradient is established, the overall process is governed by the rate of diffusion of the mobile species to the stationary sink. This is the case with free surfaces, voids and grain boundaries. These defects are usually not treated by reaction rate theory.

As a first example of a reaction rate-controlled process, let us look at the vacancy–vacancy reaction. Consider the reaction:

$$\mathrm{v} + \mathrm{v} \rightarrow \mathrm{v}_2 \,, \tag{5.49}$$

that proceeds in the forward direction only and is characterized by the rate constant $K_{2\mathrm{v}}$. In this example, one vacancy is assumed to be stationary and the other is mobile. The rate of di-vacancy formation per cm^3 is:

$$R_{2\mathrm{v}} = P_{2\mathrm{v}} C_{\mathrm{v}} \tag{5.50}$$

where C_{v} is the concentration of monovacancies and $P_{2\mathrm{v}}$ is the probability per second that another vacancy jumps into a site that is a nearest neighbor to a particular vacancy (Fig. 5.9). A di-vacancy will form if a nearest neighbor site to a vacancy is occupied by another vacancy, thus $P_{2\mathrm{v}}$ depends on the crystal structure. Taking the fcc lattice, all 12 nearest neighbor sites are equivalent, yielding:

$$P_{2\mathrm{v}} = 12 P_x \,, \tag{5.51}$$

where P_x is the probability per second that another vacancy jumps into one of the nearest neighbor positions surrounding the vacancy. P_x is proportional to:

1. The number of sites surrounding the nearest neighbor site from which another vacancy could jump (seven sites as shown by the dashed atoms in Fig. 5.9)

2. The probability that one of these lattice positions is occupied by a vacancy, N_v
3. The jump frequency of a vacancy, ω, or

$$P_x = 7N_v\omega_v \ , \tag{5.52}$$

and we can write the vacancy site fraction as $N_v = C_v\Omega$, where C_v is the volumetric vacancy concentration and Ω is the atomic volume. Back substitution of Eqs. (5.51) and (5.52) into Eq. (5.50) yields:

$$R_{2v} = 84\omega\Omega C_v^2 \ [\mathrm{cm}^{-3}\,\mathrm{s}^{-1}] \ . \tag{5.53}$$

Comparison with the definition of the reaction rate, Eq. (5.48) gives the reaction rate constant K_{2v}:

$$K_{2v} = 84\omega\Omega \ . \tag{5.54}$$

In the fcc lattice, $D_v = a^2\omega$, then

$$K_{2v} = \frac{84\Omega D_v}{a^2} \ . \tag{5.55}$$

Although the expression for the rate constant was derived for a vacancy–vacancy reaction, the same formulation applies to any reaction between any specie (e.g., impurity) that occupies substitutional positions in the fcc lattice. It can also be used for other lattice types, but the factor, 84, called the combinatorial factor is dependent on the crystal structure. The combinatorial factor is the solid state analog of the cross section in particle interactions.

In the previous example, we forced one of the reactants to be stationary. When the reaction is between two mobile species, the rate is $(K_{AB} + K_{BA})C_AC_B$, where K_{AB} is the rate constant calculated assuming that B is immobile and vice versa for K_{BA}. Therefore, if both vacancies are mobile, the result would be multiplied by a factor of 2; $K_{2v} + K_{2v} = 2K_{2v}$. Given this background, we now turn our attention to the various terms in the point defect balance equations in order to develop expressions for the reaction rate coefficients.

5.3.1 Defect Production

The first term in the defect balance equations of Eq. (5.1) is the production rate of vacancies and interstitials and this was determined in Chap. 2, Eq. (2.125), where the term in brackets is given the designation, υ_{FP}:

$$K_0 = \xi\,\nu_{FP}\sigma_s N\phi\,[\mathrm{cm}^{-3}\,\mathrm{s}^{-1}] \ . \tag{5.56}$$

For stainless steel, $\nu_{FP} \sim 30$ Frenkel pairs per collision, $\sigma_s \sim 3\times10^{-24}\,\mathrm{cm}^2$ and $N \sim 7\times10^{22}\,\mathrm{cm}^{-3}$. The term, ξ, is the displacement efficiency (Chap. 3) that accounts for the reduction in freely migrating point defects due to in-cascade recombination and clustering.

5.3.2 Recombination

The second term in Eq. (5.1), $K_{\mathrm{iv}} C_{\mathrm{v}} C_{\mathrm{i}}$ is the recombination rate. The rate constant K_{iv} is the same for both vacancies and interstitials since they must recombine with each other at the same rate. Reactions between vacancies and interstitials are of great importance since the result is mutual annihilation or return to the perfect lattice. Assuming a stationary vacancy and a mobile interstitial, and that recombination only occurs when the interstitial jumps into a site that is nearest neighbor to the vacancy, we can determine the recombination rate constant for an octahedral interstitial in the fcc lattice. There are six octahedral sites as nearest neighbors to the vacant lattice site and each lattice site has eight octahedral nearest neighbors, giving a value of 48 for the combinatorial factor:

$$K_{\mathrm{iv}} = \frac{48 \Omega D_{\mathrm{i}}}{a^2} \,. \tag{5.57}$$

However, this is a bit unrealistic since (1) the stable form of the interstitial is the split interstitial, and (2) the vacancy and interstitial are attracted to each other by virtue of their strain fields, causing spontaneous recombination to occur over distances greater than the nearest neighbor spacing. Therefore, a more realistic estimate of the combinatorial factor, z_{iv} is ~ 500:

$$K_{\mathrm{iv}} = \frac{z_{\mathrm{iv}} \Omega D_{\mathrm{i}}}{a^2} \,, \text{ and } z_{\mathrm{iv}} \sim 500 \,. \tag{5.58}$$

5.3.3 Loss to Sinks

The loss term represents all the possible sinks for vacancy and interstitial loss. These sinks can be divided into three categories:

1. *Neutral* (*unbiased*) *sinks* show no preference for capturing one type of defect over the other type. The rate of absorption is proportional to the product of the diffusion coefficient of the point defect and the difference in the concentrations of the point defect in the bulk metal and at the sink surface. The types of sinks in this category are voids, incoherent precipitates and grain boundaries.
2. *Biased sinks* exhibit preferential attraction for one defect type over the other. Dislocations exhibit a stronger preference for interstitials than for vacancies. The bias is due to the drift of interstitials down the stress gradient near the dislocation core. Since absorption of interstitials enhances dislocation climb, the dislocation is an unsaturable sink. Two types of dislocations are considered; networks in unirradiated metal and from unfaulted Frank loops, and interstitial dislocation loops.
3. *Variable bias sinks* such as coherent precipitates act as traps, which capture a defect but preserve its identity until it is annihilated by the opposite type defect. Impurity atoms and coherent precipitates act as recombination centers with a limited capacity.

5.3.4 Sink Strengths

Reaction rate constants describe the reaction and are designated a point defect and a sink (which may be another point defect), and are designated K_{jX} where j is the mobile point defect and X is the sink. As such, they include the diffusion coefficient of the point defect as well as a description of the tendency for the reaction to occur. It is often useful to describe the tendency of a sink to absorb defects that is independent of the defect properties. The *sink strength*, with units of cm^{-2}, is such a description and it reflects the *strength* or affinity of a sink for defects. Sink strength is independent of defect properties for neutral sinks. The sink strength is defined as:

$$\text{absorption rate } = K_{jX} C_j C_X = k_{jX}^2 C_j D_j \,, \tag{5.59}$$

so

$$k_{jX}^2 = \frac{K_{jX} C_X}{D_j} \,, \tag{5.60}$$

or

$$k_j^2 = \sum_X k_{jX}^2 \,. \tag{5.61}$$

Both the rate constant and the sink strength are terms commonly used to describe the action of sinks on the defects in the solid. Physically, k_j^{-1} is the mean distance a free defect of type j travels in the solid before becoming trapped.

Before we treat the various sink types, we will first look at the rate constants for the two basic reaction processes; reaction rate-controlled processes and diffusion-limited processes. We begin with reaction rate-controlled processes.

5.4 Reaction Rate-Controlled Processes

5.4.1 Defect–Void Interaction

For reactions where capture is controlled by the rate at which the point defects enter the trap site, we can use Eq. (5.58). For defect–void reactions, the term to be determined is the combinatorial factor. For a void, the number of lattice points on the surface of the sphere is $4\pi R^2/a^2$, where the area occupied by a lattice point is approximated at a^2. The rate constant then becomes:

$$K_{\text{vV}} = \frac{4\pi R^2 \Omega D_\text{v}}{a^4} = \frac{4\pi R^2 D_\text{v}}{a} \,, \quad \text{where} \quad \Omega \sim a^3, k_\text{V}^2 = \frac{4\pi R^2 \rho_\text{V}}{a} \,, \tag{5.62}$$

where ρ_V is the concentration of voids in the solid.

5.4.2 Defect–Dislocation Interaction

Consider a cylinder about a dislocation line whose axis is coincident with the dislocation line such that capture is certain for any vacancy entering the cylinder (Fig. 5.10). The cylinder consists of z_{vd} atomic sites on each of the crystal planes intersected by the dislocation line. The cylinder defines the capture radius of the dislocation, or the radius inside which entering defects are lost to the sink. If the spacing between atom planes in the lattice is $\sim a$, then there are z_{vd}/a capture sites per unit length of dislocation. Letting ρ_d be the density of dislocation lines in the crystal (in units of centimeters of dislocation line per cm^3 of solid or cm^{-2}), then there are $z_{vd}\rho_d/a$ capture sites per unit volume. If the concentration of vacancies per unit volume is C_v, then the vacancy site fraction is $C_v\Omega$. For a vacancy jump rate of ω, the rate of vacancy capture rate by the dislocation per cm^3 is:

$$R_{vd} = \frac{z_{vd}\rho_d}{a} C_v \Omega \omega [\mathrm{cm}^{-3}\,\mathrm{s}^{-1}] \,. \tag{5.63}$$

Since $\Omega \sim a^3$ and $D_v = a^2\omega$, we have:

$$\begin{aligned} &R_{vd} = D_v z_{vd} \rho_d C_v \ \text{ and reaction rate constant } \ K_{vd} = D_v z_{vd} \,, k_{vd}^2 = z_{vd}\rho_d \\ &R_{id} = D_i z_{id} \rho_d C_i \ \text{ and reaction rate constant } \ K_{id} = D_i z_{id} \,, k_{id}^2 = z_{id}\rho_d \end{aligned} \tag{5.64}$$

and $z_{vd} \neq z_{id}$.

5.5 Diffusion-Limited Reactions

Reactions between defects and sinks cannot always be characterized as reaction rate-limited. Reactions driven by defect concentration gradients are diffusion-limited and must be treated differently. Such reactions are defect–void, defect–grain boundary and sometimes defect–dislocation interactions. Following [3], these reactions are addressed here starting with defect–void reactions.

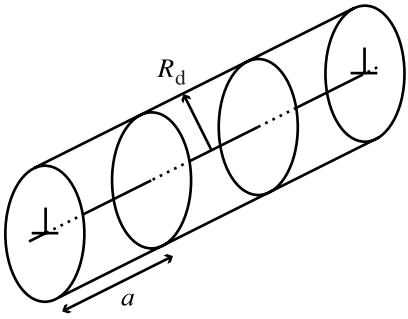

Fig. 5.10. Capture volume around a dislocation line, defined by the cylinder of radius R_d and with sink sites lying on crystal planes separated by a distance a

5.5.1 Defect–Void Reactions

Consider the case of ρ_V voids per unit volume, each of radius, R, which absorb a particular type of point defect present in the solid and between the spherical sinks. Focusing on a single sphere, the unit cell or capture volume surrounding each sphere is defined as the portion of the solid that can be associated with each sphere. The radius of the capture volume (see Fig. 5.11) around each sphere is defined by:

$$\left(\frac{4}{3}\pi\mathcal{R}^3\right)\rho_V = 1\,. \tag{5.65}$$

The diffusion equation for the point defects will be solved in the spherical shell $R \leq r \leq \mathcal{R}$. The concentration of point defects at a radial position r in the capture volume at time t is denoted by $C(r,t)$. The definition of the capture volume implies that there is no net flux of point defects across the boundary at $r = \mathcal{R}$ which is written as:

$$\left(\frac{\partial C}{\partial r}\right)_{\mathcal{R}} = 0\,, \tag{5.66}$$

and the point defect concentration at the surface of the sphere is:

$$C(R,t) = C_R\,. \tag{5.67}$$

The value of C_R depends on the process. For insoluble gas atoms where the spheres represent gas bubbles, $C_R = 0$. For bubbles or voids where the point defects are vacancies or interstitials, $C_R = C^0_{v,i}$, the thermal equilibrium defect concentration.

If the defects are created uniformly in the capture volume and no sinks other than the sphere are present, then the concentration $C(r,t)$ is determined by solution of the volumetric diffusion equation with a volumetric source term:

$$\frac{\partial C}{\partial t} = \frac{D}{r^2}\frac{\partial}{\partial r}\left(r^2\frac{\partial C}{\mathrm{d}r}\right) + K_0\,, \tag{5.68}$$

where D is the diffusion coefficient of the defects (assumed to be independent of concentration) and K_0 is the defect production rate per unit volume given by Eq. (5.56).

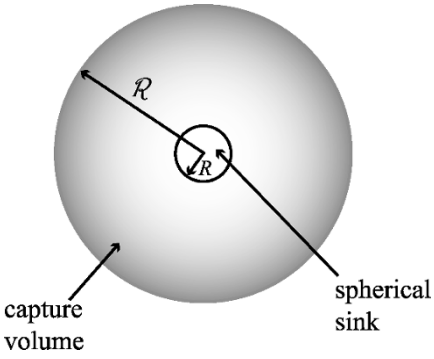

Fig. 5.11. The unit cell for determination of the diffusion-controlled rate constant for defect absorption by a spherical sink

When a solid is irradiated at a temperature where point defects are mobile, the loss of particles to the sink is partially compensated by the production rate so the concentration changes slowly with time $\left(\frac{\partial C}{\partial t} \sim 0\right)$ and Eq. (5.61) can be approximated as:

$$\frac{D}{r^2}\frac{\mathrm{d}}{\mathrm{d}r}\left(r^2\frac{\mathrm{d}C}{\mathrm{d}r}\right) = -K_0 \,. \tag{5.69}$$

The solution to Eq. (5.69) subject to the boundary conditions given by Eqs. (5.66) and (5.67) is:

$$C(r) = C_R + \frac{K_0}{6D}\left[\frac{2\mathcal{R}^2(r-R)}{rR} - \left(r^2 - R^2\right)\right] \,. \tag{5.70}$$

Since in many cases, the capture volume radius is much larger than the sink radius and the defect concentration changes rapidly only very close to the sink, the capture volume is divided into two regions (Fig. 5.12). In region 1 the diffusion term is much greater than the source term and Eq. (5.69) can be approximated by:

$$\frac{1}{r^2}\frac{\mathrm{d}}{\mathrm{d}r}\left(r^2\frac{\mathrm{d}C}{\mathrm{d}r}\right) = 0 \,, \tag{5.71}$$

with boundary conditions:

$$C(R) = C_R \tag{5.72}$$

$$C(\infty) = C(\mathcal{R}) \,. \tag{5.73}$$

The solution of Eq. (5.71) subject to the boundary conditions given by Eqs. (5.72) and (5.73) gives:

$$C(r) = C_R + [C(\mathcal{R}) - C_R]\left[1 - \left(\frac{R}{r}\right)\right] \,. \tag{5.74}$$

The flux of particles at the void surface is defined by:

$$J = -D\left(\frac{\mathrm{d}C}{\mathrm{d}r}\right)_R \,. \tag{5.75}$$

Using Eq. (5.70) gives:

$$J = \frac{-D[C(\mathcal{R}) - C_R]}{R} \,. \tag{5.76}$$

The absorption rate of point defects by the void is:

$$-(4\pi R^2)J = 4\pi RD[C(\mathcal{R}) - C_R] \,. \tag{5.77}$$

Requiring that point defects produced in the capture volume be absorbed by the void gives:

$$\frac{4}{3}\pi(\mathcal{R}^3 - R^3)K_0 = 4\pi RD[C(\mathcal{R}) - C_R] \,. \tag{5.78}$$

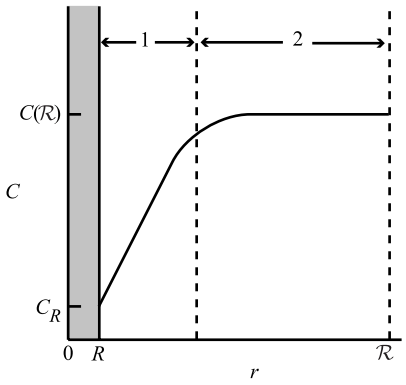

Fig. 5.12. Regions of interest in the solution of the diffusion equation in a spherical shell with a uniform volumetric production rate of defects

If $\mathcal{R}^3 \gg R^3$, the balance becomes:

$$C(\mathcal{R}) = C_R + \frac{K_0 \mathcal{R}^3}{3RD} \,. \tag{5.79}$$

Assuming that $C(\mathcal{R}) \gg C_R$ in Eq. (5.56) and replacing $C(\mathcal{R})$ by C, we obtain the total rate of diffusion-controlled absorption of point defects by the void by multiplying Eq. (5.77) by the number of voids per unit volume ρ_{V}:

$$\text{Rate of absorption/cm}^3 = 4\pi RD\rho_{\mathrm{V}} C \,. \tag{5.80}$$

The rate constant for diffusion-controlled reaction of point defects and a perfect spherical sink of radius R is then:

$$\begin{aligned} K_{\mathrm{iV}} &= 4\pi RD_{\mathrm{i}} \,, \\ K_{\mathrm{vV}} &= 4\pi RD_{\mathrm{v}} \,, \\ k_{\mathrm{V}}^2 &= 4\pi R\rho_{\mathrm{V}} \,, \end{aligned} \tag{5.81}$$

where the subscripts of K refer to the reacting species, vacancies or interstitials (v, i) and voids, V.

5.5.2 Defect–Dislocation Reactions

Diffusion-controlled reactions between defects and dislocations occur in much the same way as in the case of spherical sinks, but in cylindrical coordinates. Taking the capture radius of the sink to be R_{d} and the dislocation density to be ρ_{d}, we define the unit cell such that:

$$(\pi\mathcal{R}^2)\rho_{\mathrm{d}} = 1 \,. \tag{5.82}$$

The diffusion equation is:

$$\frac{D}{r}\frac{\mathrm{d}}{\mathrm{d}r}\left(r\frac{\mathrm{d}C}{\mathrm{d}r}\right) + K_0 = 1 \tag{5.83}$$

with boundary conditions:

$$C(R_\mathrm{d}) = C_\mathrm{Rd} \tag{5.84}$$

$$\left(\frac{\mathrm{d}C}{\mathrm{d}r}\right)_{\mathcal{R}} = 0\,, \tag{5.85}$$

and solution:

$$C(r) = C_{R_\mathrm{d}} + \frac{K_0\mathcal{R}^2}{2D}\left[\ln\left(\frac{r}{R_\mathrm{d}}\right) - 1/2\left(\frac{r^2 - R_\mathrm{d}^2}{\mathcal{R}^2}\right)\right]\,. \tag{5.86}$$

Analogous to the case for spherical sinks, in region 1, but in cylindrical geometry instead, the diffusion equation is:

$$\frac{1}{r}\frac{\mathrm{d}}{\mathrm{d}r}\left(r\frac{\mathrm{d}C}{\mathrm{d}r}\right) = 0\,, \tag{5.87}$$

with boundary conditions:

$$C(R_\mathrm{d}) = C_\mathrm{Rd} \tag{5.88}$$

$$C(\mathcal{R}) = C\,, \tag{5.89}$$

with solution:

$$C(r) = C_{R_\mathrm{d}} + [C(\mathcal{R}) - C_{R_\mathrm{d}}]\frac{\ln(r/R_\mathrm{d})}{\ln(\mathcal{R}/R_\mathrm{d})}\,. \tag{5.90}$$

The flux of defects to the dislocation line is:

$$J = -D\left(\frac{\mathrm{d}C}{\mathrm{d}r}\right)_{R_\mathrm{d}} = \frac{-D[C(\mathcal{R}) - C_{R_\mathrm{d}}]}{R_\mathrm{d}\ln(\mathcal{R}/R_\mathrm{d})}\,. \tag{5.91}$$

The absorption rate per unit length of dislocation line $= -(2\pi R_\mathrm{d})J$

$$= \frac{2\pi D[C(\mathcal{R}) - C_{R_\mathrm{d}}]}{\ln(\mathcal{R}/R_\mathrm{d})}\,. \tag{5.92}$$

The rate of defect production in the capture volume

$$= \pi(\mathcal{R}^2 - R_\mathrm{d}^2)K_0\,, \tag{5.93}$$

and since all defects produced in the capture volume are captured by the dislocation:

$$\frac{2\pi D[C(\mathcal{R}) - C_{R_\mathrm{d}}]}{\ln(\mathcal{R}/R_\mathrm{d})} = \pi(\mathcal{R}^2 - R_\mathrm{d}^2)K_0\,, \tag{5.94}$$

and

$$C(\mathcal{R}) = C_{R_\mathrm{d}} + \frac{K_0\mathcal{R}^2}{2D}\ln(\mathcal{R}/R_\mathrm{d}) \text{ for } R_\mathrm{d}/\mathcal{R} \ll 1\,, \tag{5.95}$$

so from Eq. (5.91) the rate of defect capture by dislocations per unit volume $= \dfrac{2\pi D\rho_{\mathrm{d}}C}{\ln(\mathcal{R}/R_{\mathrm{d}})}$, and the rate constants for vacancies and interstitials are:

$$\begin{aligned} K_{\mathrm{vd}} &= \frac{2\pi D_{\mathrm{v}}}{\ln(\mathcal{R}/R_{\mathrm{vd}})} \\ K_{\mathrm{id}} &= \frac{2\pi D_{\mathrm{i}}}{\ln(\mathcal{R}/R_{\mathrm{id}})} \,, \end{aligned} \tag{5.96}$$

and

$$\begin{aligned} k^2_{\mathrm{vd}} &= \frac{2\pi\rho_{\mathrm{d}}}{\ln(\mathcal{R}/R_{\mathrm{vd}})} \\ k^2_{\mathrm{id}} &= \frac{2\pi\rho_{\mathrm{d}}}{\ln(\mathcal{R}/R_{\mathrm{id}})} \,. \end{aligned} \tag{5.97}$$

Note that the combinatorial factors for vacancies and interstitials differ by the capture radius. The capture radius for interstitials is slightly greater than that for vacancies and is the origin of the dislocation bias for interstitials.

5.6 Mixed Rate Control

Mixed rate control occurs when the reaction rate is determined by a combination of processes. We can determine the rate constant for the combined processes by adding the reciprocals of the rate constants to give the resistance due to series steps of diffusion and surface attachment. For the case of voids, we use the rate constants given by Eqs. (5.62) and (5.81), and:

$$\frac{1}{K_{\mathrm{eff}}} = \frac{1}{K_{\mathrm{reaction}}} + \frac{1}{K_{\mathrm{diffusion}}} \,, \tag{5.98}$$

to yield the effective rate constant:

$$K_{\mathrm{eff}} = \frac{4\pi RD}{1+\dfrac{a}{R}} \,, \quad k^2_{\mathrm{eff}} = \frac{4\pi R\rho_{\mathrm{V}}}{1+\dfrac{a}{R}} \,. \tag{5.99}$$

For large spheres, $a/R \to 0$ and the rate constant is that for diffusion only. This result shows that reaction rate limitations to capture kinetics for spherical sinks are only significant if the sphere radius is small, approaching the lattice constant.

For dislocations, the capture rates calculated from a diffusion-controlled process vs. a reaction rate-controlled process are:

$$\begin{aligned} K_{\mathrm{diffusion}} &= \frac{2\pi D}{\ln(\mathcal{R}/R_{\mathrm{d}})} \\ K_{\mathrm{reaction}} &= z_{\mathrm{d}}D \,, \end{aligned} \tag{5.100}$$

giving the effective rate constant for mixed-control:

$$K_{\text{eff}} = \frac{D}{\dfrac{1}{z_{\text{d}}} + \dfrac{\ln(\mathcal{R}/R_{\text{d}})}{2\pi}} \,, \quad k^2_{\text{eff}} = \frac{\rho_{\text{d}}}{\dfrac{1}{z_{\text{d}}} + \dfrac{\ln(\mathcal{R}/R_{\text{d}})}{2\pi}} \,. \tag{5.101}$$

Consider z_{d} to be the area of a circular region of radius R_{d} divided by the number of atoms per unit area. For the (100) plane of the fcc lattice, the number of atoms/unit area is $2/a^2$ a/cm^2 and:

$$K_{\text{reaction}}/D = z_{\text{d}}/D = \frac{2\pi R_{\text{d}}^2}{a^2} = 24 \text{ for } R_{\text{d}} \sim 0.6\,\text{nm and } a \sim 0.3\,\text{nm} \,. \tag{5.102}$$

For a dislocation line density of $10^{10}\,\text{cm}^{-2}$, $K_{\text{diffusion}}/D = \dfrac{2\pi}{\ln(\mathcal{R}/R_{\text{d}})} = 1.4$. So capture of defects by dislocations is diffusion-controlled.

5.7 Defect–Grain Boundary Reactions

Interactions between point defects and grain boundaries are important in the case of radiation-induced segregation, discussed in Chap. 6. Following the analysis of Heald and Harbottle [7], the sink strength of the grain boundary is determined by considering a spherical grain of radius a, with grain boundary defect concentration equal to the thermal equilibrium value, which will be neglected compared to the irradiated-induced concentration. The loss to sinks *within* the grain is:

$$k^2 DC = (z_{\text{d}}\rho_{\text{d}} + 4\pi R_{\text{V}}\rho_{\text{V}})DC \,, \tag{5.103}$$

where k^2 is the sink strength for the grain interior due to dislocations and voids, and the diffusion equation is:

$$\frac{\text{d}^2 C}{\text{d}r^2} + \frac{2}{r}\frac{\text{d}C}{\text{d}r} + \frac{K_0}{D} - k^2 C = 0 \,, \tag{5.104}$$

subject to boundary conditions $C(r = a) = 0$ and $C(r = 0) =$ finite. The solution to Eq. (5.104) subject to the boundary conditions is:

$$C(r) = \frac{K_0}{Dk^2}\left[1 - \frac{a\sinh(kr)}{r\sinh(ka)}\right] \,, \tag{5.105}$$

and the total flow of point defects to the grain boundary, A is:

$$A = -4\pi r^2 D \left.\frac{\partial C}{\partial r}\right|_{r=a} = \frac{4\pi K_0 a}{k^2}\left[ka\cot(ka) - 1\right] \,. \tag{5.106}$$

Written in rate theory formalism, Eq. (5.106) becomes:

$$A = z_{\mathrm{gb}} D C_0 \,, \tag{5.107}$$

where z_{gb} is the sink strength for an individual grain boundary and C_0 is the concentration at the grain center ($r = 0$):

$$C_0 = C(r=0) = \frac{K_0}{Dk^2}\left[1 - \frac{ka}{\sinh(ka)}\right] \,. \tag{5.108}$$

From Eqs. (5.106), (5.107), and (5.108), the grain boundary sink strength, z_{gb} is

$$z_{\mathrm{gb}} = 4\pi a\left[\frac{ka\cosh(ka) - \sinh(ka)}{\sinh(ka) - ka}\right] \,. \tag{5.109}$$

For small grains and low sink strengths, $ka \to 0$, and:

$$z_{\mathrm{gb}}(ka \to 0) = 8\pi a = 4\pi d \,, \tag{5.110}$$

where $d(= 2a)$ is the grain diameter. When sink strength is large, $ka \to \infty$, and:

$$z_{\mathrm{gb}}(ka \to \infty) = 4\pi k a^2 = \pi k d^2 \,. \tag{5.111}$$

The grain boundary sink strength is the product of z_{gb} and the grain density in grains per unit volume, or $\rho_{\mathrm{gb}} = 6/\pi d^3$, giving:

$$k^2_{\mathrm{gb}}(ka \to 0) = 24/d^2 \,, \quad K_{j\mathrm{gb}} = 4\pi D_j d \,, \tag{5.112}$$

and

$$k^2_{\mathrm{gb}}(ka \to \infty) = 6k/d \,, \quad K_{j\mathrm{gb}} = \pi k D_j d^2 \,, \tag{5.113}$$

where $j =$ i or v.

Generally, $k^2 \sim 10^{11}\,\mathrm{cm}^{-2}$ and $d > 10^{-3}\,\mathrm{cm}$ so that Eq. (5.113) is the appropriate expression for the grain boundary sink strength. In fact, the grain boundary sink strength is given by Eq. (5.113) whenever $(z_{\mathrm{d}}\rho_{\mathrm{d}} + 4\pi R_{\mathrm{V}}\rho_{\mathrm{V}}) > 1/d$.

5.8 Coherent Precipitates and Solutes

These types of sinks are known as variable bias sinks in that they act as traps for vacancies and interstitials rather than as infinite sinks in which the defect loses its identity after being absorbed. The source of the attraction of vacancies and interstitials to the trap is the relief of the strain field produced by the coherency between the trap and the lattice. The coherent precipitate is of a structure in which the lattice planes of the precipitate are continuous with those of the matrix, but due to the difference in lattice parameters, there is a strain field at the interface where the lattice planes from each are forced to match. The over- or undersized solute is a limiting

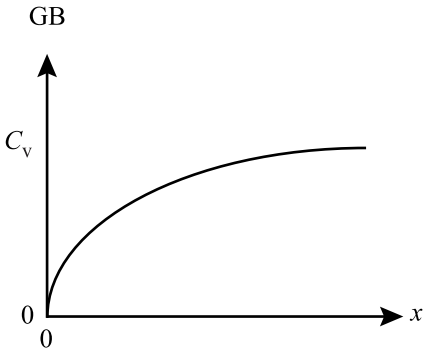

Fig. 5.13. Diffusion-controlled reaction between vacancies and a grain boundary

case of a coherent precipitate. The trap strength is limited by the capacity of the interface to hold or trap a defect until the anti-defect arrives and results in annihilation. Hence, no matter accumulates at this defect and thermal emission does not occur. The interface *does* exhibit a bias for defects and this bias is a function of the biased sinks in the solid. For example, if the biased sinks in the solid favor interstitials, then $k_i^2 > k_v^2$ and the trap interface will acquire slightly more vacancies than interstitials. This excess of vacancies then causes the trap surface to become a more effective sink for interstitials than for vacancies. The biases for the trap are denoted by Y_v and Y_i (Brailsford and Bullough [8] and Olander [3] provide detailed analyses of the bias factors), and the absorption rates of vacancies and interstitials at the trap is given by:

$$\begin{aligned} A_v^{CP} &= 4\pi R_{CP} D_v C_v \rho_{CP} Y_v = K_{vCP} C_v \rho_{CP} \\ A_i^{CP} &= 4\pi R_{CP} D_i C_i \rho_{CP} Y_i = K_{iCP} C_i \rho_{CP} \, . \end{aligned} \tag{5.114}$$

If there can be no steady state accumulation of defects at the trap, then there is no net matter flow to or from the sinks and:

$$4\pi R_{CP} \rho_{CP} C_v Y_v = 4\pi R_{CP} \rho_{CP} C_i Y_i \, , \tag{5.115}$$

so

$$Y_i = \frac{D_v C_v}{D_i C_i} Y_v \, , \tag{5.116}$$

and the rate constants and sink strengths are:

$$\begin{aligned} K_{vCP} &= 4\pi R_{CP} D_v Y_v \, ; \quad k_{vCP}^2 = 4\pi R_{CP} \rho_{CP} Y_v \\ K_{iCP} &= 4\pi R_{CP} D_i Y_i \, ; \quad k_{iCP}^2 = 4\pi R_{CP} \rho_{CP} Y_i \, . \end{aligned} \tag{5.117}$$

So variable bias sinks play an interesting role in that they adjust their preference for point defects in response to the relative sink strengths in the bulk.

The reaction rate constants for the various reactions are summarized in Table 5.2 for the various defect–defect, and defect–sink reactions.

Table 5.2. Reaction rate constants for defect–sink reactions

Reaction	Rate constant	Sink strength	Eq. #
v + v	$K_{2\mathrm{v}} = \dfrac{z_{2\mathrm{v}}\Omega D_{\mathrm{v}}}{a^2}$	–	Eq. (5.55)
i + i	$K_{2\mathrm{i}} = \dfrac{z_{2i}\Omega D_{\mathrm{i}}}{a^2}$	–	Eq. (5.55)
v + i	$K_{\mathrm{iv}} = \dfrac{z_{\mathrm{iv}}\Omega D_{\mathrm{i}}}{a^2}$	–	Eq. (5.58)
v,i + void			
Reaction rate control	$K_{\mathrm{vV}} = \dfrac{4\pi R^2 D_{\mathrm{v}}}{a}$ $K_{\mathrm{iV}} = \dfrac{4\pi R^2 D_{\mathrm{i}}}{a}$	$k_{\mathrm{V}}^2 = \dfrac{4\pi R^2 \rho_V}{a}$	Eq. (5.62)
Diffusion control	$= 4\pi R D_{\mathrm{v}}$ $= 4\pi R D_{\mathrm{i}}$	$= 4\pi R \rho_V$	Eq. (5.81)
Mixed rate control	$= \dfrac{4\pi R D_{\mathrm{v}}}{1 + \dfrac{a}{R}}$ $= \dfrac{4\pi R D_{\mathrm{i}}}{1 + \dfrac{a}{R}}$	$= \dfrac{4\pi R \rho_{\mathrm{V}}}{1 + \dfrac{a}{R}}$	Eq. (5.99)
v,i + dislocation			
Diffusion control	$K_{\mathrm{vd}} = \dfrac{2\pi D_{\mathrm{v}}}{\ln(\mathcal{R}/R_{\mathrm{vd}})}$ $K_{\mathrm{id}} = \dfrac{2\pi D_{\mathrm{i}}}{\ln(\mathcal{R}/R_{\mathrm{id}})}$	$k_{\mathrm{vd}}^2 = \dfrac{2\pi \rho_d}{\ln(\mathcal{R}/R_{\mathrm{vd}})}$ $k_{\mathrm{id}}^2 = \dfrac{2\pi \rho_{\mathrm{d}}}{\ln(\mathcal{R}/R_{\mathrm{id}})}$	Eqs. (5.96), (5.97)
Reaction rate control	$= z_{\mathrm{vd}} D_{\mathrm{v}}$ $= z_{\mathrm{id}} D_{\mathrm{i}}$	$= z_{\mathrm{vd}} \rho_{\mathrm{d}}$ $= z_{\mathrm{id}} \rho_{\mathrm{d}}$	Eq. (5.64)
Mixed rate control	$= \dfrac{D_{\mathrm{v}}}{\dfrac{1}{z_{\mathrm{vd}}} + \dfrac{\ln(\mathcal{R}/R_{\mathrm{vd}})}{2\pi}}$ $= \dfrac{D_{\mathrm{i}}}{\dfrac{1}{z_{\mathrm{id}}} + \dfrac{\ln(\mathcal{R}/R_{\mathrm{id}})}{2\pi}}$	$= \dfrac{\rho_{\mathrm{d}}}{\dfrac{1}{z_{\mathrm{vd}}} + \dfrac{\ln(\mathcal{R}/R_{\mathrm{vd}})}{2\pi}}$ $= \dfrac{\rho_{\mathrm{d}}}{\dfrac{1}{z_{\mathrm{id}}} + \dfrac{\ln(\mathcal{R}/R_{\mathrm{id}})}{2\pi}}$	Eq. (5.101)
v,i + grain boundary			
Diffusion control	$k_{\mathrm{vgb}} = \dfrac{2}{3} D_{\mathrm{v}} d^4$ $k_{\mathrm{igb}} = \dfrac{2}{3} D_{\mathrm{i}} d^4$	$k_{\mathrm{gb}}^2 = 24/d^2,\ d < 10^{-3}\,\mathrm{cm}$	Eq. (5.112)
	$K_{\mathrm{vgb}} = 6k D_{\mathrm{v}} d^5$ $K_{\mathrm{igb}} = 6k D_{\mathrm{i}} d^5$	$k_{\mathrm{gb}}^2 = 6k/d,\ d > 10^{-3}\,\mathrm{cm}$	Eq. (5.113)
v,i + coherent ppt	$K_{\mathrm{vCP}} = 4\pi R_{\mathrm{CP}} D_{\mathrm{v}} Y_{\mathrm{v}}$, $K_{\mathrm{iCP}} = 4\pi R_{\mathrm{CP}} D_{\mathrm{i}} Y_{\mathrm{i}}$	$k_{\mathrm{vCP}}^2 = 4\pi R_{\mathrm{CP}} \rho_{\mathrm{CP}} Y_{\mathrm{v}}$, $k_{\mathrm{iCP}}^2 = 4\pi R_{\mathrm{CP}} \rho_{\mathrm{CP}} Y_{\mathrm{i}}$	Eq. (5.117)

Nomenclature

A	Flow rate of defects to sink
a	Lattice constant, grain radius
C	Concentration
C_{iv}	Interstitial, vacancy concentration
C_{R}	Vacancy concentration at void boundary
C_{s}	Sink concentration
D	Grain diameter
D_{rad}	Radiation enhanced diffusion coefficient
D_{th}	Thermal diffusion coefficient
D_{m}	Ballistic mixing diffusion coefficient
D_0^y	Pre-exponential factor in the diffusion coefficient via defect y
D_x^y	Diffusion coefficient for species x via y
E_{m}^y	Migration energy of defect y
f	Correlation coefficient
i	Interstitial designation
v	Vacancy designation
s	Sink designation
J_x	Flux of atom or defect x across a marker plane
k	Boltzmann's constant
k_X^2	Sink strength of sink X
K_0	Defect production rate
K_{gb}	Rate constant for defect–grain boundary interaction
K_{id}	Rate constant for interstitial–dislocation interaction
K_{iv}	Vacancy–interstitial recombination rate constant
K_{is}	Interstitial–sink reaction rate constant
K_{vd}	Rate constant for vacancy–dislocation interaction
K_{vs}	Vacancy–sink reaction rate constant
$K_{2\mathrm{v}}$	Di-vacancy formation rate constant
N	Atom fraction
r_{iv}	Vacancy–interstitial recombination radius
r_{is}	Interstitial–sink recombination radius
r_{vs}	Vacancy–sink recombination radius
p	Sink annihilation probability
$P_{2\mathrm{v}}$	Probability/second of forming a di-vacancy
P_x	Probability/second that a vacancy jumps to a nearest neighbor to a vacancy
R_{d}	Dislocation core radius
R_{id}	Reaction rate between interstitials and dislocations
R_{vd}	Reaction rate between vacancies and dislocations
$R_{2\mathrm{v}}$	Rate of di-vacancy formation

R	Radius of unit cell or capture volume surrounding a spherical sink
t	Time
T	Temperature
T_c	Critical temperature defined by Eq. (5.47)
ν_2	Di-vacancy designation
z_{gb}	Sink strength for an individual grain boundary
z_{xy}	Combinatorial number for a reaction between x and y
ϕ	Particle flux
ρ_d	Dislocation density
η	Parameter defined by Eq. (5.45)
σ_s	Microscopic scattering cross section
τ_x	Time constant for process x
ω	Jump frequency
Ω	Atomic volume
ξ	Production efficiency term

Subscripts

a	Atoms
CP	Coherent precipitate
d	Dislocation
gb	Grain boundary
i, v	Interstitials, vacancies
m	Migration
rad	Under irradiation
R	Void radius
s	Sink
V	Void

Superscripts

i, v	Interstitials, vacancies

Problems

5.1 Point defect concentration build up during irradiation can be described by:

$$\frac{dC_v}{dt} = K_0 - K_{iv}C_iC_v - K_{vs}C_vC_s + \nabla \cdot (D_v \nabla C_v)$$
$$\frac{dC_i}{dt} = K_0 - K_{iv}C_iC_v - K_{is}C_iC_s + \nabla \cdot (D_i \nabla C_i)$$

How do these equations simplify if you are irradiating a single crystal with no defects present? In that case, what is the relationship between vacancy and interstitial concentrations? Do the vacancy and interstitial concentrations differ if you start with a sample that contains defects?

5.2 For pure nickel irradiated at 500 °C:

a) calculate the steady state concentration of vacancies and interstitials.

$$K_0 = 5 \times 10^{-4}\,\text{dpa/s} \quad \Delta H_m^v = 0.82\,\text{eV}$$
$$C_s = 10^9\,\text{cm}^{-3} \quad \Delta H_m^i = 0.12\,\text{eV}$$
$$r_{iv} = r_{is} = r_{vs} = 10a \quad \Delta S_m^v = \Delta S_m^i = 0$$
$$\nu = 10^{13}\,\text{s}^{-1}$$

b) for a dislocation density of $10^{12}\,\text{cm}^{-2}$, determine the temperature at which mutual recombination gives way to annealing at fixed sinks.

5.3 A perfect, single crystal Cu wire (cylinder) of radius $R = 10\,\text{nm}$ and length $L \gg R$ is irradiated at 400 °C. The only sink present is the surface.

a) Assuming negligible recombination, solve the diffusion equation

$$\frac{\partial C_x}{\partial t} = K_0 + D_x \nabla^2 C_x$$

at steady state for $x =$ interstitial or vacancy, to obtain the vacancy and interstitial concentration profiles. What boundary condition do you use at the surface? When you solve the equation, pay attention to the symmetry of the problem to eliminate terms in the expression for $\nabla^2 C_x$.

b) Calculate the rates of absorption (number of defects per unit area and time) at the surface.
(Hint: remember that $\nabla^2 C$ is continuous.)

5.4 Calculate the steady state radiation-enhanced diffusion coefficient for copper at $T/T_m = 0.5$ in terms of K_0, the defect production rate, and ρ_d, the dislocation sink density.

5.5 Assume for a metal of interest that the interstitial–sink interaction radius and the vacancy–sink interaction radius are equal. Two irradiations are performed at low, but non-negligible sink density. The displacement rate is the same for both irradiations. In the second irradiation, a minor alloying addition doubles the diffusion coefficient of interstitials but does not change the diffusion coefficient for vacancies. By how much does the ratio of the steady state vacancy to interstitial concentrations change? Explain physically what happens to the point defects.

5.6 A sample of aluminum is held at room temperature (20 °C) and irradiated with a monoenergetic beam of 1 MeV neutrons at a flux of $10^{14}\,\text{n/cm}^2\,\text{s}$. Assume that the capture radii $r_{iv} = r_{is} = r_{vs}$ are all approximately $10a$.

a) At what sink density does defect annihilation at sinks overtake mutual recombination?

b) What is the value of the radiation-enhanced steady state diffusion coefficient of aluminum atoms? How does this compare to the diffusion coefficient in the absence of irradiation?

c) Verify that your calculations in part (b) do indeed represent a steady state condition, i.e., $dC_v/dt = dC_i/dt = 0$.

5.7 A defect-free Al crystal is irradiated at a displacement rate of 10^{-5} dpa/s.
   a) Calculate the steady state concentration of point defects at $T = 100\,^{\circ}\text{C}$ and 500 °C.
   b) Once steady state is reached, the irradiation is stopped. Calculate the time constant for recombination as a function of temperature.
   c) One wishes to measure the defect concentration in the irradiated Al, a process assumed to take 100 s. Determine the temperature range for which the defect concentration can be kept within 1% of its value at the end of the irradiation for this length of time.
   Assume the combinatorial factor, $z = 500$.

5.8 Following the analysis for the diffusion rate of point defects to spherical sinks, derive an expression for the vacancy concentration profile around a dislocation. What is the vacancy capture rate by dislocations?

5.9 For fcc nickel, determine whether vacancy capture by dislocations is a diffusion-controlled or reaction rate-controlled process. What about interstitial capture by dislocations?
   z_d = Area of the circular region about the dislocation (defined by the capture radius) divided by the number of atoms per unit area
   r_{vd} = Capture radius for vacancies = 0.6 nm
   r_{id} = Capture radius for interstitials = 0.7 nm

5.10 It can be shown that the time constant (characteristic time) for the process $v + s \rightarrow s$ is $t_3 = (K_{vs}C_s)^{-1}$. At sufficiently high temperature, vacancies may be sufficiently mobile so that the reaction $v + v \rightarrow v_2$ may terminate the increase in vacancy concentration with time. If the consumption rate of vacancies in di-vacancy formation is $K_{vv}C_v^2$, determine the time constant for the onset of steady state.

5.11 A sample of fcc copper with a low sink density ($\tau_1 < \tau_2$) is irradiated at low temperature ($T/T_m = 0.3$) until steady state is reached. Some time later, all sinks instantly disappear and a new steady state is reached. Determine the magnitude of the change in C_v and C_i between the two steady states.

5.12 Explain the reason (or likely reasons) for the following observations:
   a) The displacement rate at the surface of a copper sample is 1000 times higher when irradiated with 1 MeV Cu^+ ions than with 1 MeV protons at the same flux.
   b) A scattering experiment using 3 MeV B^+ ions on Cu produces yields that disagree sharply with calculations using the Rutherford scattering formula. Why?
   c) A single crystal of copper is irradiated with 2 MeV He^+ ions and the backscatter yield is only 5% of that of a polycrystal.
   d) Irradiation of a metal with a high neutron flux does not produce a measurable increase in the atom diffusion coefficient.
   e) Two metals are pressed together and heated to $0.5T_m$. It is observed that atoms from the metals intermix at the interface. Attempts to determine the

defect(s) responsible for the intermixing reveal that vacancies account for 100% of the atom mixing. True or false? Why?

5.13 Two engineers are arguing over how to test the effect of the high point defect concentration developed during irradiation on the deformation rate of nickel at 500 °C. Engineer #1 maintains that one can irradiate the sample to the appropriate fluence at the temperature of interest, remove it from the reactor, and heat it back up to temperature to perform the test. Engineer #2 insists that the concentration of point defects decays almost immediately after irradiation ceases and therefore, tests must be performed in situ. Who is right? Why?
(Hint: consider the point defect equation for the slowest defect (vacancy) only neglect recombination and consider that the only sinks present are dislocations at a concentration of $10^9\,\mathrm{cm}^{-2}$).

$$D_{\mathrm{v}}^{\mathrm{Ni}}(500\,^{\circ}\mathrm{C}) \sim 10^{-8}\,\mathrm{cm}^2/\mathrm{s}$$
$$a \sim 0.3\,\mathrm{nm}$$

5.14 Assume a solid containing defect sinks is irradiated at a temperature T_0, at which only vacancies are mobile.
a) For the case of a high sink density, estimate the time, t_1 at which sinks will contribute to vacancy annihilation. Neglect recombination.
b) For the case of a low sink density, estimate the time, t_2 at which recombination will contribute to vacancy annihilation. Neglect the effect of sinks.
c) Describe what changes can be made in either the irradiation process or the material microstructure to force $t_1 = t_2$.

Assume a quasi-steady state condition exists, beginning at t_1 in part (a) and at t_2 in part (b).

5.15 Show that, for a metal with a low sink density undergoing neutron irradiation at low temperature ($T/T_{\mathrm{m}} < 0.2$), when sinks contribute to interstitial annihilation, the vacancy and interstitial concentrations as a function of time can be written Eq. (5.11) as:

$$C_{\mathrm{v}} = (K_0 K_{\mathrm{is}} C_{\mathrm{s}} t / K_{\mathrm{iv}})^{1/2}$$
$$C_{\mathrm{i}} = (K_0 / K_{\mathrm{iv}} K_{\mathrm{is}} C_{\mathrm{s}} t)^{1/2}$$

(Hint: consider this case to be intermediary to the quasi-steady state and steady state cases such that $\mathrm{d}C_{\mathrm{i}}/\mathrm{d}t < 0$ and $\mathrm{d}C_{\mathrm{v}}/\mathrm{d}t > 0$ and write the point defect balance equations as inequalities.)

5.16 Two bi-layer samples with a low sink strength are being irradiated at low temperature as part of a radiation-enhanced diffusion experiment. If the displacement rate of the second sample is five times that of the first sample, what is the difference in the radiation-enhanced diffusion coefficient?

References

1. Rothman SJ (1983) Effects of irradiation and diffusion in metals and alloys. In: Nolfi FV (ed) Phase Transformations During Irradiation. Applied Science, New York, pp 189–211
2. Sizemann R (1978) J Nucl Mater 69/70:386–412
3. Olander DR (1976) Fundamental Aspects of Nuclear Reactor Fuel Elements, TID-26711-P1. Technical Information Service, Springfield, VA
4. Lam NQ (1975) J Nucl Mater 56:125–135
5. Wiedersich H (1986) In: Johnson RA, Orlov AN (eds) Physics of Radiation Effects in Crystals. Elsevier Science, New York, p 237
6. Matteson S, Roth J, Nicolet M (1979) Rad Eff 42:217–226
7. Heald PT, Harbottle JE (1977) J Nucl Mater 67:229–233
8. Brailsford AD, Bullough R (1972) J Nucl Mater 44:121–135

Part II

Physical Effects of Radiation Damage

6 Radiation-Induced Segregation

A profound consequence of irradiation at elevated temperature is the spatial redistribution of solute and impurity elements in the metal. This phenomenon leads to enrichment or depletion of alloying elements in regions near surfaces, dislocations, voids, grain boundaries, and phase boundaries. Figure 6.1 shows a plot of solute element profiles across a grain boundary in stainless steel irradiated in a reactor to a dose of several dpa at about 300 °C. Note that there is significant depletion of chromium, molybdenum and iron and enrichment of nickel and silicon. Such drastic changes at the grain boundary will cause changes in the local properties of the solid and may induce susceptibility to a host of processes that can degrade the integrity of the component. For this reason, understanding radiation-induced segregation (RIS) is of great importance for reactor performance.

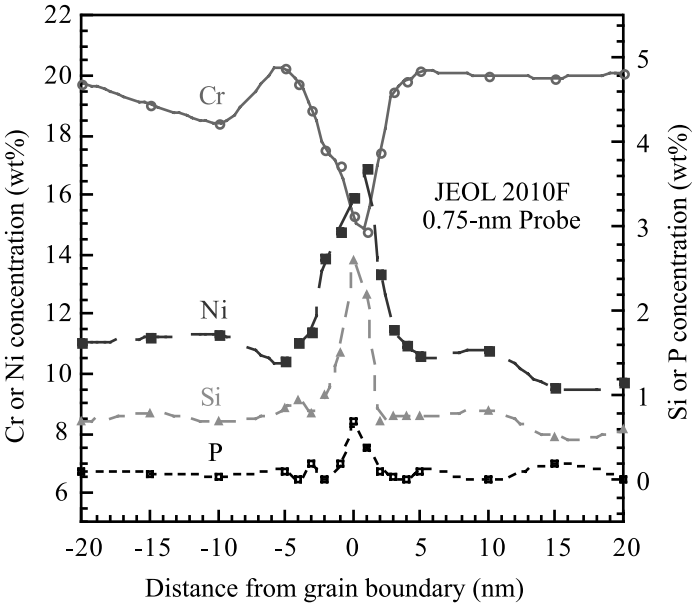

Fig. 6.1. Radiation-induced segregation of Cr, Ni, Si and P at the grain boundary of a 300 series stainless steel irradiated in a light water reactor core to several dpa at $\sim 300\,^{\circ}\mathrm{C}$ (after [1])

First postulated by Anthony in 1972 [2], and observed by Okamoto and Weidersich in 1973 [3], RIS has its origin in the coupling between defect fluxes and fluxes of alloying elements. Irradiation produces point defects and defect clusters with an approximately random distribution throughout the material. Those defects that are mobile and escape recombination are re-incorporated into the crystal structure at dislocations, grain boundaries and other defect sinks. As shown in Chap. 5, point defects flow to spatially discrete sinks. Since the motion of atoms causes the motion of defects, atom fluxes are associated with defect fluxes. Any preferential association of defects with a particular alloying component and/or preferential participation of a component in defect diffusion will couple a net flux of the alloying element to the defect fluxes. The flux of an element causes its buildup or depletion in the vicinity of defect sinks and, therefore, concentration gradients in initially homogeneous alloy phases. The concentration gradients induce back diffusion of the segregating elements, and a quasi-steady state may be set up during irradiation whenever the defect-driven alloying element fluxes are balanced by diffusion-driven back diffusion.

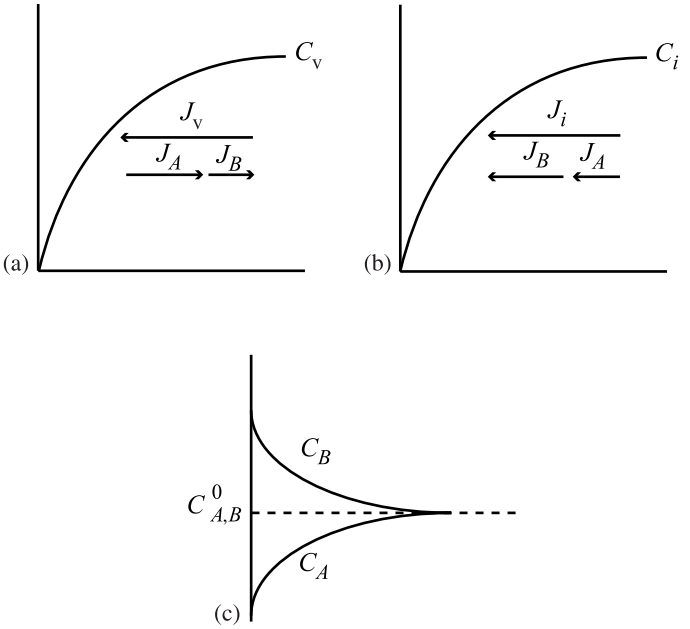

Fig. 6.2. Schematic of radiation-induced segregation in a binary, 50% A–50% B system showing (a) the development of the vacancy concentration profile by the flow of vacancies to the grain boundary balanced by an equal and opposite flow of A and B atoms, but not necessarily in equal numbers, (b) the development of the interstitial concentration profile by the flow of interstitials to the grain boundary balanced by an equal and flow of A and B atoms migrating as interstitials, but not necessarily in equal numbers, (c) the resulting concentration profiles for A and B

Figure 6.2 presents a schematic of processes driving segregation in a binary, 50%A–50%B alloy, under irradiation at an elevated temperature. As described in Chap. 5, vacancies and interstitials flow to the grain boundary causing a concentration profile to develop. In the case of vacancies (Fig. 6.2a) the flux of vacancies to the grain boundary is balanced by an equal flux of atoms in the opposite direction. However, if the participation of A atoms in the vacancy flux is larger than the atom fraction in the alloy (and consequently the participation of B atoms is less), then there will be a net loss of A atoms, and a net gain of B atoms at the boundary, giving rise to concentration gradients, such as shown in Fig. 6.2c. Considering interstitials, their flux to the grain boundary is also made up of a flux of A and B atoms. If the participation of B atoms in the interstitial flux is greater than the atom fraction in the alloy (and necessarily, the participation of A atoms in the flux is less than the atom fraction in the alloy) then a net increase in B atoms and a corresponding net decrease in A atoms will result. These processes are shown in Fig. 6.2b. This example shows that both vacancy and interstitial flow to the grain boundary can result in the net accumulation of one alloying element and a corresponding depletion of the other alloying element. Whether element A enriches or depletes when both processes are included depends on the relative strengths of atom association with the respective defect fluxes.

In this chapter, we will focus on radiation-induced segregation in concentrated binary and ternary alloy systems and we will explore the dependence of RIS on temperature, dose and dose rate.

6.1 Radiation-Induced Segregation in Concentrated Binary Alloys

To distinguish a concentrated alloy from a dilute alloy, it will be assumed that a concentrated alloy is one in which the substitutional solute concentration is above a few percent. The following segregation model is also well-suited to describe alloy systems with significant atomic size differences, including the limit in which the undersized component is present in dilute solution.

The model for solute segregation as developed by Wiedersich [4] follows. We will consider a binary solid solution of elements A and B which are distributed randomly throughout the solid. Due to irradiation the local vacancy and interstitial concentrations change with time according to the point defect balance equations:

$$\begin{aligned} \frac{\partial C_\mathrm{v}}{\partial t} &= -\nabla J_\mathrm{v} + K_0 - R \\ \frac{\partial C_\mathrm{i}}{\partial t} &= -\nabla J_\mathrm{i} + K_0 - R\,, \end{aligned} \tag{6.1}$$

where $-\nabla J_\mathrm{v}$ and $-\nabla J_\mathrm{i}$ are the divergences of the vacancy and interstitial fluxes, respectively, K_0 is the Frenkel pair production rate and $R = K_\mathrm{iv} C_\mathrm{i} C_\mathrm{v}$, is the rate of

recombination of vacancies and interstitials. Note also that we have dropped the vector notation for sake of simplicity and thus, we will need to keep track of direction. Equations (6.1) are identical to Eq. (5.1) in the absence of sinks and with the gradient term included. The conservation equations for the alloying elements A and B are:

$$\frac{\partial C_{\mathrm{A}}}{\partial t} = -\nabla J_{\mathrm{A}}$$
$$\frac{\partial C_{\mathrm{B}}}{\partial t} = -\nabla J_{\mathrm{B}} \; . \tag{6.2}$$

The defect and atom fluxes in Eqs. (6.1) and (6.2) arise from forces due to chemical potential gradients. In reality, the equations should be solved for chemical potential, but for simplicity, we will use relations between fluxes and concentration gradients. The coupling between atom and defect fluxes is based on simple physical models. Note that in the case of self-ion bombardment, we would also include a production term due to the implanted element concentration.

It is assumed that diffusive motions of A and B atoms occur only by vacancy and by interstitial jumps. An important coupling between atom and defect fluxes is that a flux of interstitials drives a flux of A and B atoms, equal in size and direction to that of the interstitials, across any fixed lattice or "marker" plane:

$$J_{\mathrm{i}} = J_{\mathrm{A}}^{\mathrm{i}} + J_{\mathrm{B}}^{\mathrm{i}} \; , \tag{6.3}$$

and, similarly, a flux of vacancies drives a flux of A and B atoms equal in size, but opposite in direction, across the marker plane:

$$J_{\mathrm{v}} = -\left(J_{\mathrm{A}}^{\mathrm{v}} + J_{\mathrm{B}}^{\mathrm{v}}\right) \; . \tag{6.4}$$

In Eqs. (6.3) and (6.4) and in subsequent notation, the subscripts indicate the species of flux considered, and superscripts the complementary species by which the flux occurs. In general, the division of vacancy and interstitial fluxes via A and B atoms will not be in the same proportion as the atom fractions in the alloy, N_{A}, N_{B}. That is, vacancies may migrate preferentially via B atoms and interstitials via A atoms, as described earlier and shown in Fig. 6.2.

The fluxes of atoms and defects can be expressed in terms of the gradients of the different species by the *partial diffusion coefficient*:

$$D_{\mathrm{A}}^{\mathrm{v}} = \frac{1}{6}\lambda_{\mathrm{v}}^2 z_{\mathrm{v}} N_{\mathrm{v}} \omega_{\mathrm{A}}^{\mathrm{v}} f_{\mathrm{A}}^{\mathrm{v}} \; , \tag{6.5}$$

where $\omega_{\mathrm{A}}^{\mathrm{v}}$ is the jump frequency with which an A atom exchanges with a vacancy on a given neighboring site, N_{v} is the atomic fraction of vacancies, z_{v} is the number of nearest neighbors to the A atom, and λ_{v} is the jump distance. The term $f_{\mathrm{A}}^{\mathrm{v}}$ is the correlation factor for A atoms migrating by vacancies, which accounts for the greater than random probability that after an initial jump, subsequent jumps of the A atom will have a displacement component opposite to that of the initial jump.

In alloys, f is highly composition-dependent and is neglected in the following for simplicity, giving:

$$D_{\mathrm{A}}^{\mathrm{v}} = \frac{1}{6}\lambda_{\mathrm{v}}^2 z_{\mathrm{v}} N_{\mathrm{v}} \omega_{\mathrm{A}}^{\mathrm{v}} \,, \tag{6.6}$$

and the partial diffusion coefficient for vacancies via A atoms is:

$$D_{\mathrm{v}}^{\mathrm{A}} = \frac{1}{6}\lambda_{\mathrm{v}}^2 z_{\mathrm{v}} N_{\mathrm{v}} \omega_{\mathrm{v}}^{\mathrm{A}} \,. \tag{6.7}$$

Note than $\omega_{\mathrm{A}}^{\mathrm{v}} = \omega_{\mathrm{v}}^{\mathrm{A}} (= \omega_{\mathrm{Av}})$ since either jump frequency involves the exchange of a given A atom–vacancy pair. Combining those factors on the RHS of Eqs. (6.6) and (6.7) that are common to both, the *diffusivity coefficient* is defined as:

$$d_{\mathrm{Av}} = \frac{1}{6}\lambda_{\mathrm{v}}^2 z_{\mathrm{v}} \omega_{\mathrm{Av}} \,, \tag{6.8}$$

so that we have:

$$\begin{aligned} D_{\mathrm{A}}^{\mathrm{v}} &= d_{\mathrm{Av}} N_{\mathrm{v}} \\ D_{\mathrm{v}}^{\mathrm{A}} &= d_{\mathrm{Av}} N_{\mathrm{A}} \,. \end{aligned} \tag{6.9}$$

For B atoms, the complementary equations are;

$$\begin{aligned} D_{\mathrm{B}}^{\mathrm{v}} &= d_{\mathrm{Bv}} N_{\mathrm{v}} \\ D_{\mathrm{v}}^{\mathrm{B}} &= d_{\mathrm{Bv}} N_{\mathrm{B}} \end{aligned} \tag{6.10}$$

with

$$d_{\mathrm{Bv}} = \frac{1}{6}\lambda_{\mathrm{v}}^2 z_{\mathrm{v}} \omega_{\mathrm{Bv}} \,, \tag{6.11}$$

where ω_{Bv} is the effective exchange-jump frequency of a B atom–vacancy pair that includes a factor accounting for possible binding or repulsion between vacancies and B atoms.

The partial diffusion coefficients of A and B atoms via interstitials, and interstitials via the elements, provided migration occurs by an interstitial mechanism, are similarly:

$$D_{\mathrm{A}}^{\mathrm{i}} = \frac{1}{6}\lambda_{\mathrm{i}}^2 z_{\mathrm{i}} N_{\mathrm{i}} \omega_{\mathrm{A}}^{\mathrm{i}} \,, \tag{6.12}$$

which is analogous to Eq. (6.6) We are, however, neglecting the fact that interstitial migration is more complex because more than one atom is significantly involved in any interstitial jump. The partial diffusion coefficients for interstitials are thus:

$$\begin{aligned} D_{\mathrm{A}}^{\mathrm{i}} &= d_{\mathrm{Ai}} N_{\mathrm{i}} \\ D_{\mathrm{i}}^{\mathrm{A}} &= d_{\mathrm{Ai}} N_{\mathrm{A}} \end{aligned} \tag{6.13}$$

and

$$D_{\mathrm{B}}^{\mathrm{i}} = d_{\mathrm{Bi}} N_{\mathrm{i}}$$
$$D_{\mathrm{i}}^{\mathrm{B}} = d_{\mathrm{Bi}} N_{\mathrm{B}} \,. \tag{6.14}$$

The expression for d_{Ai} and d_{Bi} will depend on the interstitialcy mechanism and will be more complicated than Eqs. (6.8) and (6.11). In writing the partial diffusion coefficients in the form $D = \mathrm{d}N$, we further assume that the spatial dependence resides in the factor N, whereas the ds are composition-independent.

The "average" or "total" diffusion coefficients for the various species are

$$D_{\mathrm{v}} = d_{\mathrm{Av}} N_{\mathrm{A}} + d_{\mathrm{Bv}} N_{\mathrm{B}}$$
$$D_{\mathrm{i}} = d_{\mathrm{Ai}} N_{\mathrm{A}} + d_{\mathrm{Bi}} N_{\mathrm{B}} \tag{6.15}$$
$$D_{\mathrm{A}} = d_{\mathrm{Av}} N_{\mathrm{v}} + d_{\mathrm{Ai}} N_{\mathrm{i}}$$
$$D_{\mathrm{B}} = d_{\mathrm{Bv}} N_{\mathrm{v}} + d_{\mathrm{Bi}} N_{\mathrm{i}} \,. \tag{6.16}$$

Using the partial and total diffusion coefficients we can write the fluxes of atoms and defects with respect to a coordinate system fixed on the crystal lattice:

$$\begin{aligned} J_{\mathrm{A}} &= -D_{\mathrm{A}} \chi \nabla \mathrm{C}_{\mathrm{A}} + d_{\mathrm{Av}} N_{\mathrm{A}} \nabla C_{\mathrm{v}} - d_{\mathrm{Ai}} N_{\mathrm{A}} \nabla C_{\mathrm{i}} \\ J_{\mathrm{B}} &= -D_{\mathrm{B}} \chi \nabla \mathrm{C}_{\mathrm{B}} + d_{\mathrm{Bv}} N_{\mathrm{B}} \nabla C_{\mathrm{v}} - d_{\mathrm{Bi}} N_{\mathrm{B}} \nabla C_{\mathrm{i}} \end{aligned} \tag{6.17}$$

$$\begin{aligned} J_{\mathrm{v}} &= d_{\mathrm{Av}} N_{\mathrm{v}} \chi \nabla C_{\mathrm{A}} + d_{\mathrm{Bv}} N_{\mathrm{v}} \chi \nabla C_{\mathrm{B}} - D_{\mathrm{v}} \nabla C_{\mathrm{v}} \\ &= (d_{\mathrm{Av}} - d_{\mathrm{Bv}}) N_{\mathrm{v}} \chi \nabla C_{\mathrm{A}} - D_{\mathrm{v}} \nabla C_{\mathrm{v}} \\ J_{\mathrm{i}} &= -d_{\mathrm{Ai}} N_{\mathrm{i}} \chi \nabla C_{\mathrm{A}} - d_{\mathrm{Bi}} N_{\mathrm{i}} \chi \nabla C_{\mathrm{B}} - D_{\mathrm{i}} \nabla C_{\mathrm{i}} \\ &= -(d_{\mathrm{Ai}} - d_{\mathrm{Bi}}) N_{\mathrm{i}} \chi \nabla C_{\mathrm{A}} - D_{\mathrm{i}} \nabla C_{\mathrm{i}} \end{aligned} \tag{6.18}$$

where $\chi = \left(1 + \dfrac{\partial \ln \gamma_{\mathrm{A}}}{\partial \ln N_{\mathrm{A}}}\right) = \left(1 + \dfrac{\partial \ln \gamma_{\mathrm{B}}}{\partial \ln N_{\mathrm{B}}}\right)$, accounts for the difference between the chemical potential gradient (the true driving force for the diffusion of A and B atoms) and the concentration gradient, and γ_{A} and γ_{B} are activity coefficients. The second equality in the expressions for J_{v} and J_{i} is obtained by neglecting small perturbations arising from the presence of defects, so that $\nabla C_{\mathrm{B}} = -\nabla C_{\mathrm{A}}$. This equality describes the Kirkendall effect from the vacancy and interstitial mechanisms, respectively. That is, the difference in the A atom and B atom fluxes in opposite directions past a marker plane must be made up by an appropriate defect flux.

Of the four flux equations, Eq. (6.17) to Eq. (6.18), only three are independent because atom fluxes and defect fluxes through a marker plane must balance:

$$J_{\mathrm{A}} + J_{\mathrm{B}} = -J_{\mathrm{v}} + J_{\mathrm{i}} \,. \tag{6.19}$$

To obtain the atom and defect distributions in time and space, the set of coupled partial differential equations in Eq. (6.1) must be solved for the appropriate initial and boundary conditions. Inserting the fluxes given in Eq. (6.17) to Eq. (6.19) into

Eq. (6.1) gives:

$$\begin{aligned}
\frac{\partial C_\mathrm{v}}{\partial t} &= \nabla\left[-\left(d_{\mathrm{Av}} - d_{\mathrm{Bv}}\right)\chi\Omega C_\mathrm{v}\nabla C_\mathrm{A} + D_\mathrm{v}\nabla C_\mathrm{v}\right] + K_0 - R \\
\frac{\partial C_\mathrm{i}}{\partial t} &= \nabla\left[\left(d_{\mathrm{Ai}} - d_{\mathrm{Bi}}\right)\chi\Omega C_\mathrm{i}\nabla C_\mathrm{A} + D_\mathrm{i}\nabla C_\mathrm{i}\right] + K_0 - R \\
\frac{\partial C_\mathrm{A}}{\partial t} &= \nabla\left[D_\mathrm{A}\chi\nabla C_\mathrm{A} + \Omega C_\mathrm{A}\left(d_{\mathrm{Ai}}\nabla C_\mathrm{i} - d_{\mathrm{Av}}\nabla C_\mathrm{v}\right)\right] .
\end{aligned} \tag{6.20}$$

Note that the terms in brackets are just the fluxes, J, of the respective species. The atomic fractions, N have been corrected to volume concentration according to $N = \Omega C$, where Ω is the average atomic volume of the alloy. The equation for element B is $C_\mathrm{B} = 1 - C_\mathrm{A}$ when small defect concentrations are neglected.

Assuming that steady state has been reached, we can make some qualitative conclusions about the flux equations in Eq. (6.17) to Eq. (6.19). As steady state:

$$J_\mathrm{A} = J_\mathrm{B} = 0 , \tag{6.21}$$

and neglecting defect bias effects in the solid:

$$J_\mathrm{i} = J_\mathrm{v} , \tag{6.22}$$

since vacancies and interstitials are produced and recombine in equal numbers. Eliminating ∇C_i in the relation for J_A in Eq. (6.17) using Eqs. (6.19), (6.21) and (6.22) gives:

$$\nabla C_\mathrm{A} = \frac{N_\mathrm{A}N_\mathrm{B}d_{\mathrm{Bi}}d_{\mathrm{Ai}}}{\chi\left(d_{\mathrm{Bi}}N_\mathrm{B}D_\mathrm{A} + d_{\mathrm{Ai}}N_\mathrm{A}D_\mathrm{B}\right)}\left(\frac{d_{\mathrm{Av}}}{d_{\mathrm{Bv}}} - \frac{d_{\mathrm{Ai}}}{d_{\mathrm{Bi}}}\right)\nabla C_\mathrm{v} . \tag{6.23}$$

Equation (6.23) is a relation between the vacancy concentration gradient and the A atom concentration gradient. It is evident that the relation between the direction of the gradient of alloy component A and that of the vacancy gradient is determined by the relative magnitude of the ratios $\frac{d_{\mathrm{Av}}}{d_{\mathrm{Bv}}}$ and $\frac{d_{\mathrm{Ai}}}{d_{\mathrm{Bi}}}$. Recall from Eqs. (6.8) and (6.11) that:

$$\begin{aligned}
d_{\mathrm{Av}} &= \frac{1}{6}\lambda_\mathrm{v}^2 z_\mathrm{v}\omega_{\mathrm{Av}} \\
d_{\mathrm{Bv}} &= \frac{1}{6}\lambda_\mathrm{v}^2 z_\mathrm{v}\omega_{\mathrm{Bv}} ,
\end{aligned}$$

and

$$\omega_{\mathrm{Av}} = \nu\exp\left(\frac{\Delta S_\mathrm{m}^{\mathrm{Av}}}{k}\right)\exp\left(\frac{-E_\mathrm{m}^{\mathrm{Av}}}{kT}\right) , \quad \omega_{\mathrm{Bv}} = \nu\exp\left(\frac{\Delta S_\mathrm{m}^{\mathrm{Bv}}}{k}\right)\exp\left(\frac{-E_\mathrm{m}^{\mathrm{Bv}}}{kT}\right) ,$$

therefore:

$$\frac{d_{\mathrm{Av}}}{d_{\mathrm{Bv}}} \approx \exp\left(\frac{E_\mathrm{m}^{\mathrm{Bv}} - E_\mathrm{m}^{\mathrm{Av}}}{kT}\right) , \tag{6.24}$$

since differences in ΔS_m between A and B atoms are small. Similarly:

$$\frac{d_{Ai}}{d_{Bi}} \approx \exp\left(\frac{E_m^{Bi} - E_m^{Ai}}{kT}\right) . \tag{6.25}$$

During irradiation, the vacancy concentration always decreases towards a defect sink, and Eq. (6.23) predicts that the element A becomes enriched at sinks if $\frac{d_{Ai}}{d_{Bi}} > \frac{d_{Av}}{d_{Bv}}$, i.e., if preferential transport of A atoms via interstitials outweighs preferential transport via vacancies and vice versa.

Example 6.1. Segregation in a B–25%A alloy
Let us look at a B–25%A alloy (where B = Ni and A = Cu), and assume that there is no preferential association of defects with either A or B atoms. Given the following values for migration energies of the two components via vacancies and interstitials:

$$E_m^{Av} \sim 0.77\,\text{eV} \qquad E_m^{Ai} \sim 0.10\,\text{eV}$$
$$E_m^{Bv} \sim 1.28\,\text{eV} \qquad E_m^{Bv} \sim 0.15\,\text{eV} ,$$

Then, from Eqs. (6.24) and (6.25) we have:

$$\begin{aligned}\left(\frac{d_{Av}}{d_{Bv}} - \frac{d_{Ai}}{d_{Bi}}\right) &= \exp\left(\frac{1.28 - 0.77}{kT}\right) - \exp\left(\frac{0.15 - 0.1}{kT}\right) \\ &= \exp\left(\frac{0.51}{kT}\right) - \exp\left(\frac{0.05}{kT}\right) \\ &\gg 0\end{aligned}$$

Since $\left(\frac{d_{Av}}{d_{Bv}} - \frac{d_{Ai}}{d_{Bi}}\right)$ is positive and the concentration gradient of A follows that of vacancies, we have depletion of A at the sink. If this sink is a free surface, then A is depleted at the surface. If it is a grain boundary, then A is depleted at the grain boundary. More A atoms move away from the sink via vacancies than to the sink via interstitials. Figure 6.3 shows the behavior of the A concentration at a temperature of 500 °C and a dose rate of 10^{-3} dpa/s. Note that the drop in the concentration of A at the sink surface is balanced by a buildup behind the depleted zone. With increasing dose the depleted zone increases in depth and width until back diffusion due to the large concentration gradient causes a leveling off and the establishment of a "steady state" condition at $t > 10^4$ s.

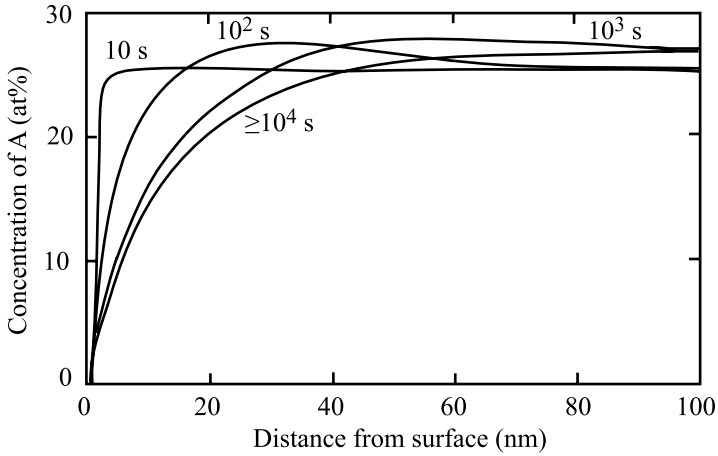

Fig. 6.3. Concentration profiles of element A in a B–25%A alloy as a function of irradiation time at a temperature of 500 °C and for a displacement rate of 10^{-3} dpa/s; $E_m^{Av} = 0.77$ eV, $E_m^{Bv} = 1.28$ eV, $E_m^{Ai} = 0.10$ eV, $E_m^{Bi} = 0.15$ eV (after [4])

6.1.1 Solution to the Coupled Partial Differential Equations

Solution to the system of partial differential equations given in Eq. (6.20) must be obtained numerically. Solutions can be obtained in either planar geometry (free surface) or spherical geometry (grain boundary). In the Perks code [5], segregation of the alloying elements is modeled adjacent to a plane, which is a perfect sink for point defects, such as a grain boundary or a free surface. Another plane is sufficiently far away to model the conditions in the middle of the grain where there are no concentration gradients. The model calculates the concentrations of the major elements by considering the fluxes of each species caused by the migration of point defects created thermally and by irradiation. Point defect losses occur due to mutual recombination and annihilation at fixed sinks, the boundary surfaces and a uniform and time-independent distribution of dislocations. The detailed radiation-induced microstructure is not considered explicitly, but the sink strength can be adjusted with dose to simulate the buildup of sinks in the microstructure.

Once the fluxes are calculated, the divergences can be used to perform the time integration required by the continuity equations in Eq. (6.20). The program calculates the concentration of each species independently. An advantage of this method is that any errors in the calculations are evident when the partial concentrations are summed.

The deep boundary condition is representative of the bulk material where there are no concentration gradients for atomic and defect species so that the next flux of each species is always zero. The surface or grain boundary is created as a perfect sink for point defects, thus their concentration at the sink is maintained at their initial values ($\mathrm{d}C_k/\mathrm{d}t = 0$). In order to conserve atoms in the solid, the atomic fluxes at the boundary are all zero.

6.1.2 Interstitial Binding

Undersize solutes can tightly bind to interstitials forming interstitial-solute complexes that migrate as solute interstitials. The RIS model described in Sect. 6.1 can account for solute-interstitial binding by accounting for the non-random occupation of interstitials by A and B atoms in the diffusivity coefficients, d_{Ai} and d_{Bi}, respectively [4]. The concentrations of A and B interstitials are given as:

$$C_{\mathrm{Ai}} = C_{\mathrm{i}} \frac{C_{\mathrm{A}} \exp(E_{\mathrm{b}}^{\mathrm{Ai}}/kT)}{C_{\mathrm{A}} \exp(E_{\mathrm{b}}^{\mathrm{Ai}}/kT) + C_{\mathrm{B}}} , \tag{6.26}$$

$$C_{\mathrm{Bi}} = C_{\mathrm{i}} \frac{C_{\mathrm{B}}}{C_{\mathrm{A}} \exp(E_{\mathrm{b}}^{\mathrm{Ai}}/kT) + C_{\mathrm{B}}} , \tag{6.27}$$

where $E_{\mathrm{b}}^{\mathrm{Ai}}$ is the average energy gained by converting a B interstitial into an A interstitial. The term $E_{\mathrm{b}}^{\mathrm{Ai}}$ is referred to as the effective A interstitial binding energy. Clearly, solutes that bind to interstitials will undergo enrichment at sinks by virtue of the flow of interstitials to the sink.

Example 6.2. Segregation with interstitial binding in Ni–Si
Segregation will occur in systems where strong binding of the interstitials to undersize atoms occurs. Consider the system of B–5%A where B is Ni and A is Si and preferential interstitial association with A atoms occurs. Figure 6.4 shows the calculated concentration profile of alloy component A (Si) for an irradiation temperature of 500 °C. Note that element A strongly segregates to the surface. This can be understood by referring to the parameters of Eq. (6.27). We have chosen $E_{\mathrm{m}}^{\mathrm{Av}} = E_{\mathrm{m}}^{\mathrm{Bv}} = 1.28\,\mathrm{eV}$ and $E_{\mathrm{m}}^{\mathrm{Ai}} = 0.9\,\mathrm{eV}$, $E_{\mathrm{m}}^{\mathrm{Bi}} = 0.15\,\mathrm{eV}$ and a binding energy of $E_{\mathrm{b}}^{\mathrm{Ai}} = 1.0\,\mathrm{eV}$ so that:

$$\frac{d_{\mathrm{Av}}}{d_{\mathrm{Bv}}} - \frac{d_{\mathrm{Ai}}}{d_{\mathrm{Bi}}} = 1 - \exp\left[\left(E_{\mathrm{b}}^{\mathrm{Ai}} - E_{\mathrm{mi}}^{\mathrm{Ai}} + E_{\mathrm{m}}^{\mathrm{Bi}}\right)/kT\right] < 0$$

and from Eq. (6.23) the surface becomes strongly enriched in Si. The binding energy in part results from the size difference between Ni and Si. Here the solute atom, Si is considerably smaller and is expected to segregate to the surface according to the argument given in Sect. 6.1.3. Results are supported by the preceding calculation and confirmed by experiment. Figure 6.5 shows that segregation of silicon to the surface does indeed occur in a Ni–1%Si alloy irradiated at moderate temperature. It should also be noted that in the Ni–Si system, the solubility limit for Si is ~ 10 at%, and that segregation of Si to values of above the solubility limit will result in precipitation of Ni_3Si. Hence one important result of irradiation-induced segregation is that it can lead to local solute concentration that exceeds the solubility limit and results in precipitation. Irradiation can also act to stabilize a second phase that would otherwise not be present in thermodynamic equilibrium and vice versa. These processes are discussed in Chap. 9.

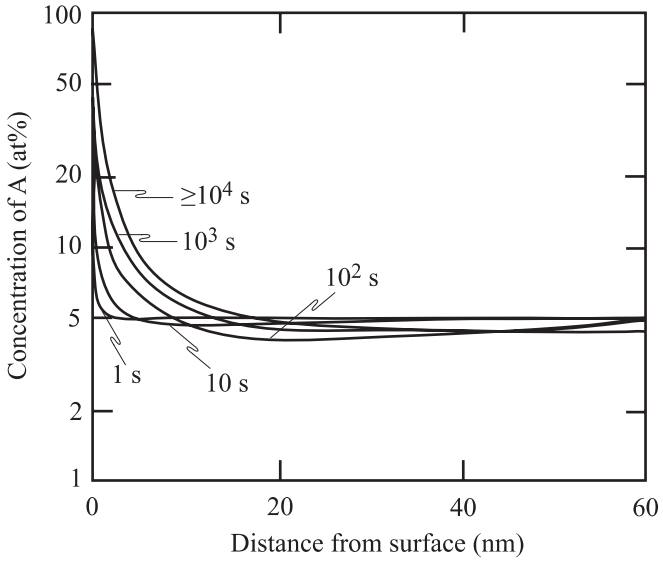

Fig. 6.4. Concentration profiles of element A in a B–5%A alloy as a function of irradiation time at temperature of 500 °C and for a displacement rate of 10^{-3} dpa/s; $E_m^{Av} = E_m^{Bv} = 1.28\,eV$, $E_b^{Ai} = 1.0\,eV$, $E_m^{Ai} = 0.90\,eV$, $E_m^{Bi} = 0.15\,eV$ (after [4])

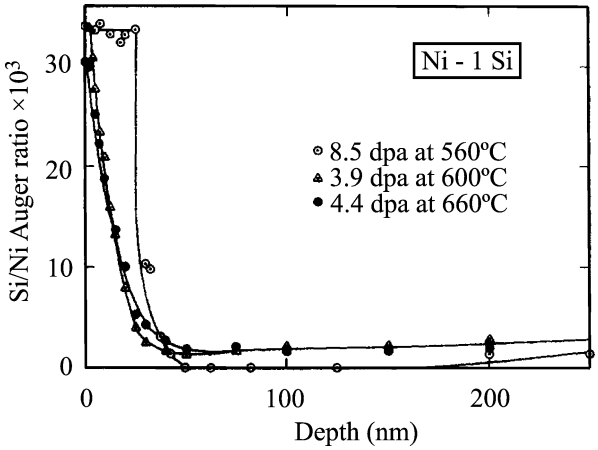

Fig. 6.5. Measured concentration vs. depth profiles for a Ni–1%Si alloy irradiated to doses between 3.9 and 8.5 dpa at temperatures between 560 and 660 °C with 3.5 MeV $^{58}Ni^+$ ions at a displacement rate of $\sim 10^{-3}$ dpa/s at the sample surface (after [6])

6.1.3 Solute Size Effect

Size difference between solute atoms plays a major role in determining the magnitude and direction of segregation [6]. To reduce the strain energy stored in the lat-

tice, undersize solute substitutional atoms will preferentially exchange with solvent atoms in interstitial positions, whereas oversize solute atoms will tend to remain on, or return to, substitutional sites. Strain-energy considerations also predict that vacancies will preferentially exchange with oversize solute atoms. During irradiation at elevated temperatures, the fraction of undersize solute atoms migrating as interstitials, or of oversize solute atoms migrating against the vacancy flux, may therefore greatly exceed the fraction of solute in the alloy. In other words, any variation in size between solute and solvent atoms will cause the chemical composition of the irradiation-induced interstitial and vacancy fluxes toward sinks to differ from the chemical composition of the alloy. This disproportionate participation of misfitting solute atoms in the defect fluxes to sinks will cause a redistribution of solute, which will produce an enrichment of undersize solute and a depletion of oversize solute near defect sinks. Since the surface of an irradiated solid serves as an unsaturable sink for both vacancy and interstitial-type defects, concentration gradients will be created near the surface of alloys that contain misfitting solute atoms during irradiation at appropriate temperatures. Table 6.1 shows the volume misfit for several solute–solvent combinations and the predicted and observed direction of segregation under irradiation. Note that positive misfits should result in depletion (−) at sinks while negative misfits should result in enrichment (+) at sinks.

Example 6.3. Segregation driven by the size effect in Ni–1%Al
An example of the size effect is the Ni–Al system. According to Table 6.1, Al is an oversized solute in the Ni lattice, and E_m^{Al-v} will be less than E_m^{Ni-v} since the oversize Al atoms will preferentially exchange with vacancies. According to Eqs. (6.24) and (6.25), $\frac{d_{Av}}{d_{Bv}} > \frac{d_{Ai}}{d_{Bi}}$ and depletion at the surface is predicted. In fact, measurement of the segregation of Al in Ni–1%Al irradiated to 10.3 dpa at 510 °C and to 10.7 dpa at 620 °C shows strong depletion of Al at the surface followed by redistribution behind the surface (Fig. 6.6). The buildup of Al just below the surface results in an Al concentration that exceeds the solubility limit and induces second phase formation as discussed in detail in Chap. 9.

6.1.4 Effect of Temperature

The temperature dependence of RIS is shown in Fig. 6.7 for a B–25% A alloy, as determined by solution of Eq. (6.20). Note that with increasing temperatures, the profile flattens. This is because the difference between $\frac{d_{Av}}{d_{Bv}}$ and $\frac{d_{Ai}}{d_{Bi}}$ decreases with increasing temperature. Figure 6.8 shows that the steady state concentration at the sink surface passes through a minimum as a function of temperature and can be explained as follows. At high temperatures, a large thermal vacancy concentration

Table 6.1. Effect of solute size on radiation-induced segregation (from [7, 8, 9])

Solute–solvent	Volume misfit (%)	Predicted direction of segregation	Observed direction of segregation
Pd–Cu	−20	+	+
Pd–Fe	−27	+	+
Pd–Mo	−3	+	+
Pd–Ni	−26	+	+
Pd–W	−2	+	+
Al–Ge	−37	+	+
Al–Si	−45	+	+
Al–Zn	−19	+	+
Fe–Cr	+4	−	−
Mg–Cd	−19	+	+
Ti–Al	−3	+	+
Ti–V	−26	+	+
Ni–Al	+52	−	−
Ni–Au	+55	−	−
Ni–Be	−29	+	+
Ni–Cr	+1	−	−
Ni–Ge	−5	+	+
Ni–Mn	+32	−	−
Ni–Mo	+31	−	−
Ni–Sb	+21	−	−
Ni–Si	−16	+	+
Ni–Ti	+57	−	−
Cu–Ag	+44	−	−
Cu–Be	−34	+	+
Cu–Fe	−8	+	+
Cu–Ni	−7	+	+
*SS–Ni	−3	+	+
*SS–Cr	+5	−	−
*SS–Si	−3	+	+
*SS–C	+54	−	
*SS–Mn	+3	−	−
*SS–Mo	+36	−	−
*SS–Cu	+9	−	

* SS refers to 316 stainless steel from [8]

leads to a high diffusion rate of alloying elements as well as to a high defect recombination rate; the latter reduces the defect fluxes to sinks, and hence, the amount of solute segregation, while the former increases the back diffusion of segregated alloying elements. At low temperatures, the vacancy mobility is low, the radiation-induced excess vacancy concentration is correspondingly high so that defect recombination becomes dominant, and hence the defect fluxes to sinks decrease and segregation is

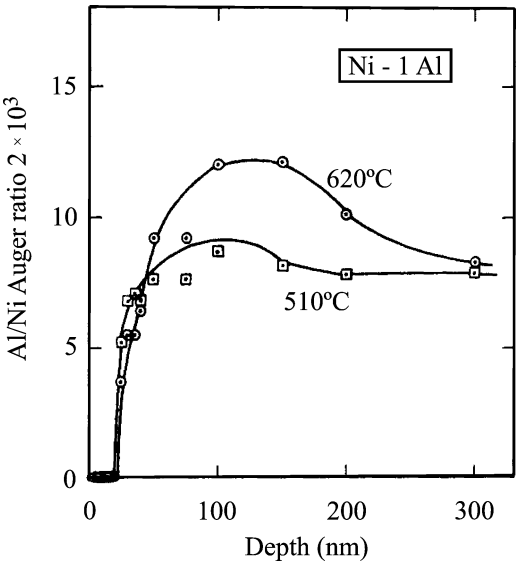

Fig. 6.6. Measured concentration vs. depth profiles for a Ni–1%Al alloy irradiated to 10.3 dpa at 510 °C and to 10.7 dpa at 620 °C with 3.5 MeV $^{58}Ni^{+}$ ions at a displacement rate of $\sim 10^{-3}$ dpa/s at the sample surface (after [6])

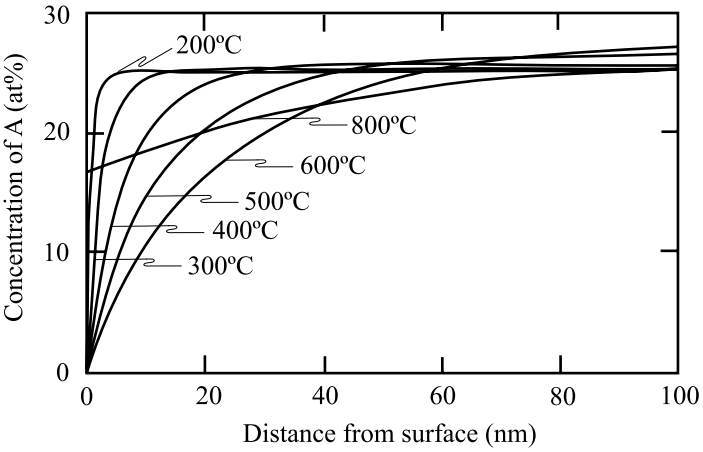

Fig. 6.7. Steady state concentration profiles of element A as a function of temperature for the same alloy and irradiation conditions as shown in Fig. 6.3 (after [4])

reduced. At intermediate temperatures, the thermal vacancy concentration becomes insignificant and the radiation-induced excess vacancy concentration is relatively low. The defect recombination rate is low, and hence defects migrate predominantly to sinks and significant segregation occurs.

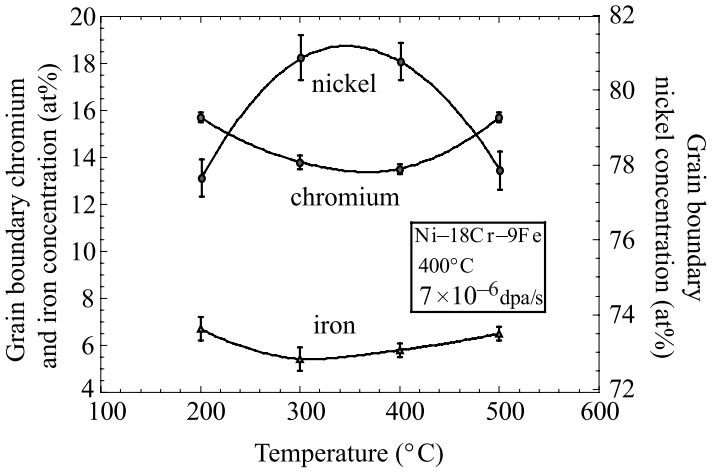

Fig. 6.8. Temperature dependence of grain boundary segregation of Ni, Cr and Fe in a Ni–18Cr–9Fe alloy irradiated with 3.4 MeV protons at 400 °C to 1 dpa and at a displacement rate of 7×10^{-6} dpa/s (after [10])

6.1.5 Effect of Dose Rate

Decreasing the dose rate will shift the temperature dependence of RIS to lower temperatures as shown in Fig. 6.9. The shift of the curve toward lower temperatures for lower displacement rates can be explained as follows. At a given temperature, a lower point defect generation rate K_0 means the vacancies and interstitials are added to the lattice more slowly, or more widely spaced in time. However, their thermal mobility is unchanged and with the lower numbers of defects in the lattice, the probability of finding a sink vs. recombination is increased. Thus, at a given temperature, lower displacement rates tend to increase the role of the sink over the

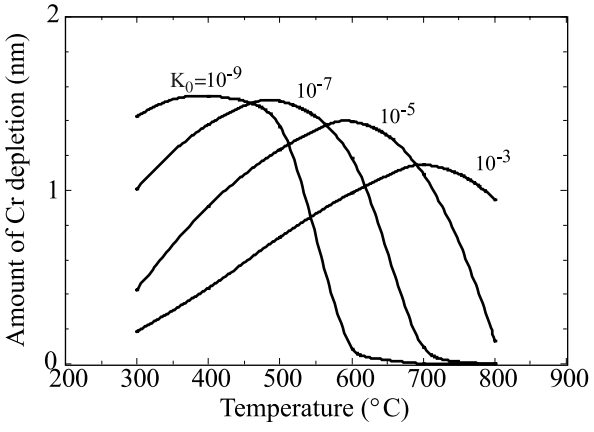

Fig. 6.9. Dose rate dependence of grain boundary chromium depletion calculated using the MIK model for RIS (after [11] and [12])

role of recombination, resulting in greater segregation. At high temperatures, a lower displacement rate means that irradiation-produced vacancies will have less of an impact, so that their effect on segregation is less than that at higher dose rate and the amount of segregation drops with decreasing dose rate.

6.2 RIS in Ternary Alloys

Engineering alloys are rarely simple binary alloys. Most structural alloys contain many solutes, each with a specific role in the properties of the alloy. Because of the significance of structural stainless steels that are predominantly composed of iron, chromium and nickel, we will reproduce the development of the time and space-dependent concentration equations for a ternary alloy under irradiation. The following description is a condensation of that given by Lam et al. [13] for a ternary alloy whose components A, B and C are present in concentrations C_A, C_B and C_C (number of atoms per unit volume). We start by writing the defect fluxes partitioned into those occurring via A, B and C atoms in the alloy according to:

$$\begin{aligned} J_i &= J_i^A + J_i^B + J_i^C \\ J_v &= J_v^A + J_v^B + J_v^C \,, \end{aligned} \tag{6.28}$$

where the subscripts indicate the species of flux (interstitial or vacancy) and the superscripts indicate the complementary species by which the flux occurs (atom A, B, or C). The partial interstitial fluxes are in the same direction as the corresponding atom fluxes while the partial vacancy fluxes are in the opposite direction to the atom fluxes:

$$\begin{aligned} &J_i^A = J_A^i \,; \quad J_i^B = J_B^i \,; \quad J_i^C = J_C^i \\ &J_v^A = -J_A^v \,; \quad J_v^B = -J_B^v \,; \quad J_v^C = -J_C^v \,, \end{aligned} \tag{6.29}$$

and Eq. (6.25) can be written as:

$$\begin{aligned} J_i &= J_A^i + J_B^i + J_C^i \\ J_v &= -\left(J_A^v + J_B^v + J_C^v\right) \,. \end{aligned} \tag{6.30}$$

These equations express the coupling between defect and atom fluxes across any fixed lattice plane.

As with the defect compositions, the alloy composition in time and space can be described by the conservation equations:

$$\begin{aligned} \frac{\partial C_A}{\partial t} &= -\nabla \cdot J_A \\ \frac{\partial C_B}{\partial t} &= -\nabla \cdot J_B \\ \frac{\partial C_C}{\partial t} &= -\nabla \cdot J_C \,, \end{aligned} \tag{6.31}$$

where J_A, J_B and J_C are the total fluxes of the alloying elements, which can be partitioned into partial fluxes occurring by vacancies and interstitials:

$$\begin{aligned} J_A &= J_A^v + J_A^i \\ J_B &= J_B^v + J_B^i \\ J_C &= J_C^v + J_C^i \,. \end{aligned} \tag{6.32}$$

The defect and atom fluxes are expressed in terms of the concentration gradients of the different species:

$$\begin{aligned} J_k^i (\equiv J_i^k) &= -D_k^i \chi \nabla C_k - D_i^k \nabla C_i \\ J_k^v (\equiv -J_v^k) &= -D_k^v \chi \nabla C_k + D_v^k \nabla C_v \,, \end{aligned} \tag{6.33}$$

where $k = $ A, B or C, χ is the thermodynamic factor which relates the concentration gradient to the chemical potential gradient of atoms (as in Eqs. (6.17) and (6.18)), and $D_k^i D_k^v$, D_i^k and D_v^k are the partial diffusion coefficients of atoms k by interstitials, and vacancies, and of interstitials and vacancies by atoms, respectively. The partial diffusion coefficients have the form:

$$\begin{aligned} D_k^j &= d_{kj} N_j \\ D_j^k &= d_{kj} N_k \,, \end{aligned} \tag{6.34}$$

where $j = $ i or v, $N_j = \Omega C_j$ and $N_k = \Omega C_k$ are the atomic fractions of defects and of k atoms, respectively, Ω is the average atomic volume in the alloy, and d_{kj} are the diffusivity coefficients for conjugate atom-defect pairs kj:

$$d_{kj} = \frac{1}{6} \lambda_k^2 z_k \omega_{kj}^{\text{eff}} \,. \tag{6.35}$$

Here λ_k is the jump distance, z_k the coordination number, and ω_{kj}^{eff} the effective jump or exchange frequency of the pair. The total diffusion coefficients for interstitials and vacancies are defined as:

$$\begin{aligned} D_i &= \sum_k d_{ki} N_k \\ D_v &= \sum_k d_{kv} N_k \,, \end{aligned} \tag{6.36}$$

and for atoms:

$$D_k = d_{ki} N_i + d_{kv} N_v \,. \tag{6.37}$$

For alloy systems in which atoms of one alloy component interact with interstitials to form bound atom–interstitial complexes, the non-random occupation of interstitials by A, B, and C atoms is accounted for in the same manner as for a binary alloy system. For preferential A atom–interstitial binding, we have by analogy with Eqs. (6.26) and (6.27):

$$
\begin{aligned}
C_{\mathrm{Ai}} &= C_{\mathrm{i}} \frac{C_{\mathrm{A}} \exp(E_{\mathrm{b}}^{\mathrm{Ai}}/kT)}{C_{\mathrm{A}} \exp(E_{\mathrm{b}}^{Ai}/kT) + C_{\mathrm{B}} + C_{\mathrm{C}}} \,, \\
C_{\mathrm{Bi}} &= C_{\mathrm{i}} \frac{C_{\mathrm{B}}}{C_{\mathrm{A}} \exp(E_{\mathrm{b}}^{\mathrm{Ai}}/kT) + C_{\mathrm{B}} + C_{\mathrm{C}}} \,, \\
C_{\mathrm{Ci}} &= C_{\mathrm{i}} \frac{C_{\mathrm{C}}}{C_{\mathrm{A}} \exp(E_{\mathrm{b}}^{\mathrm{Ai}}/kT) + C_{\mathrm{B}} + C_{\mathrm{C}}} \,,
\end{aligned}
\tag{6.38}
$$

where $E_{\mathrm{b}}^{\mathrm{Ai}}$ is the average energy gained by converting a B interstitial or a C interstitial into an A interstitial. From Eqs. (6.31), (6.33), (6.34), (6.35) and (6.28), the defect and atom fluxes with respect to a coordinate system fixed on the crystal lattice are:

$$
\begin{aligned}
J_{\mathrm{i}} &= -(d_{\mathrm{Ai}} - d_{\mathrm{Ci}})\Omega C_{\mathrm{i}} \chi \nabla C_{\mathrm{A}} - (d_{\mathrm{Bi}} - d_{\mathrm{Ci}})\Omega C_{\mathrm{i}} \chi \nabla C_{\mathrm{B}} - D_{\mathrm{i}} \nabla C_{\mathrm{i}} \\
J_{\mathrm{v}} &= (d_{\mathrm{Av}} - d_{\mathrm{Cv}})\Omega C_{\mathrm{v}} \chi \nabla C_{\mathrm{A}} + (d_{\mathrm{Bv}} - d_{\mathrm{Cv}})\Omega C_{\mathrm{v}} \chi \nabla C_{\mathrm{B}} - D_{\mathrm{v}} \nabla C_{\mathrm{v}} \\
J_{\mathrm{A}} &= -D_{\mathrm{A}} \chi \nabla C_{\mathrm{A}} + d_{\mathrm{Av}} \Omega C_{\mathrm{A}} \nabla C_{\mathrm{v}} - d_{\mathrm{Vi}} \Omega C_{\mathrm{A}} \nabla C_{\mathrm{i}} \\
J_{\mathrm{B}} &= -D_{\mathrm{B}} \chi \nabla C_{\mathrm{B}} + d_{\mathrm{Bv}} \Omega C_{\mathrm{B}} \nabla C_{\mathrm{v}} - d_{\mathrm{Vi}} \Omega C_{\mathrm{B}} \nabla C_{\mathrm{i}} \\
J_{\mathrm{C}} &= -D_{\mathrm{C}} \chi \nabla C_{\mathrm{C}} + d_{\mathrm{Vv}} \Omega C_{\mathrm{C}} \nabla C_{\mathrm{v}} - d_{\mathrm{Ci}} \Omega C_{\mathrm{C}} \nabla C_{\mathrm{i}} \,.
\end{aligned}
\tag{6.39}
$$

Small perturbations arising from the presence of point defects are neglected so that $C_{\mathrm{A}} + C_{\mathrm{B}} + C_{\mathrm{C}} = 1$ and $\nabla C_{\mathrm{C}} = -(\nabla C_{\mathrm{A}} + \nabla C_{\mathrm{B}})$. Of the five fluxes in Eq. (6.39), only four are independent because the defect and atom fluxes across a marker plane must balance:

$$
J_{\mathrm{A}} + J_{\mathrm{B}} + J_{\mathrm{C}} = J_{\mathrm{i}} - J_{\mathrm{v}} \,. \tag{6.40}
$$

A system of four coupled partial differential equations describing the space and time dependence of the atoms and defects in the solid is determined by substituting the defect and atom fluxes given by Eq. (6.39) into Eqs. (6.31) and (6.1):

$$
\begin{aligned}
\frac{\partial C_{\mathrm{v}}}{\partial t} &= \nabla \cdot [-(d_{\mathrm{Av}} - d_{\mathrm{Cv}})\Omega C_{\mathrm{v}} \chi \nabla C_{\mathrm{A}} - (d_{\mathrm{Bv}} - d_{\mathrm{Cv}})\Omega C_{\mathrm{v}} \chi \nabla C_{\mathrm{B}} + D_{\mathrm{v}} \nabla C_{\mathrm{v}}] + K - R \\
\frac{\partial C_{\mathrm{i}}}{\partial t} &= \nabla \cdot [(d_{\mathrm{Ai}} - d_{\mathrm{Ci}})\Omega C_{\mathrm{i}} \chi \nabla C_{\mathrm{A}} + (d_{\mathrm{Bi}} - d_{\mathrm{Ci}})\Omega C_{\mathrm{i}} \chi \nabla C_{\mathrm{B}} + D_{\mathrm{i}} \nabla C_{\mathrm{i}}] + K - R \\
\frac{\partial C_{\mathrm{A}}}{\partial t} &= \nabla \cdot [D_{\mathrm{A}} \chi \nabla C_{\mathrm{A}} + \Omega C_{\mathrm{A}} (d_{\mathrm{Ai}} \nabla C_{\mathrm{i}} - d_{\mathrm{Av}} \nabla C_{\mathrm{v}})] \\
\frac{\partial C_{\mathrm{B}}}{\partial t} &= \nabla \cdot [D_{\mathrm{B}} \chi \nabla C_{\mathrm{B}} + \Omega C_{\mathrm{B}} (d_{\mathrm{Bi}} \nabla C_{\mathrm{i}} - d_{\mathrm{Bv}} \nabla C_{\mathrm{v}})] \,.
\end{aligned}
\tag{6.41}
$$

Numerical solutions of Eq. (6.41) are obtained for a planar sample under irradiation. The grain boundary is equated to a free surface and the calculations are performed for only a single grain, taking advantage of the symmetry of the problem. The initial conditions are those for thermodynamic equilibrium of the alloy. Conditions at the boundary are defined as follows. At the grain center, all

concentration gradients are set equal to zero. At the grain boundary, the concentrations of interstitials and vacancies are fixed at their thermal equilibrium values. The grain boundary atom concentrations are determined by the conservation of the numbers of atoms in the specimen. Atom concentrations are assumed to be initially uniform. Parameters used in the calculation of segregation in Fe–Cr–Ni alloys are given in [13] for the Lam model and in [5] for the Perks model.

Equations (6.41) can be solved at steady state to provide a relationship between the vacancy gradient and the atom gradient. This relationship is known as a determinant, M and is a function of the concentrations and diffusivities. The determinant for a three-component alloy is determined in the same way as was done for the binary alloy case Eq. (6.23) and is given by [14]:

$$M_j = \frac{\nabla C_j}{\nabla C_\mathrm{v}} = \frac{\dfrac{d_{j\mathrm{v}}C_j}{D_j}\displaystyle\sum_{k\neq j}\frac{d_{ki}C_k}{D_k} - \frac{d_{ji}C_j}{D_j}\sum_{k\neq j}\frac{d_{k\mathrm{v}}C_k}{D_k}}{\chi\displaystyle\sum_k \frac{d_{ki}C_k}{D_k}} . \tag{6.42}$$

The determinant can be used to help determine the primary mechanism of segregation in Fe–Cr–Ni alloys. Table 6.2 shows the determinant calculated for Cr, Fe, and Ni for a total of seven alloys *assuming that preferential coupling with the vacancy flux causes the segregation*, i.e., setting the interstitial diffusion coefficients for Cr, Fe, and Ni to be equal to each other. The segregation trends (enrichment or depletion at the grain boundary) for Cr, Fe, and Ni that were measured on the grain boundaries of these alloys by Auger electron spectroscopy (AES) and energy dispersive spectroscopy in scanning transmission electron microscopy (STEM/EDS) are also listed. For each alloy where the determinant for the element is positive, depletion occurs; where the determinant is negative enrichment occurs. Note that for each element in each of the seven alloys studied, the sign of the determinant agrees with the measurement (by either STEM/EDS or AES) and calculation. This example also shows that while chromium always depletes and nickel always enriches, iron can either enrich or deplete depending on the relative concentrations of nickel and chromium.

Table 6.2. Segregation behavior in Ni–Cr–Fe and Fe–Cr–Ni alloys compared to inverse Kirkendall predictions. Determinants (M) calculated using Eq. (6.42)

Alloy	M_Cr	M_Fe	M_Ni	Ref.	Cr	Fe	Ni	Analysis method
Ni–18Cr	3.9	—	−3.9	[14]	Depletes	—	Enriches	AES&STEM/EDS
Ni–18Cr–9Fe	5.0	0.4	−5.4	[15]	Depletes	Depletes	Enriches	AES&STEM/EDS
Fe–16Cr–24Ni	4.0	3.6	−7.6	[16]	Depletes	Depletes	Enriches	AES
Fe–20Cr–24Ni	5.0	2.4	−7.4	[16]	Depletes	Depletes	Enriches	AES&STEM/EDS
Fe–24Cr–24Ni	6.3	1.8	−8.5	[16]	Depletes	Depletes	Enriches	AES
Fe–24Cr–19Ni	6.5	−1.8	−4.7	[16]	Depletes	Enriches	Enriches	AES
Fe–20Cr–9Ni	5.0	−3.0	−2.0	[16]	Depletes	Enriches	Enriches	AES&STEM/EDS

In the Fe–Cr–Ni system, Cr is the fast diffuser and Ni is the slow diffuser and Fe is between the two. When the nickel level is high relative to the Cr level, the large amount of enrichment of Ni at the grain boundary cannot be fully compensated by depletion of Cr, so Fe also must deplete. But when the Cr level is high relative to Ni the reverse occurs and Fe enriches. Note that Cr and Ni do not exactly cancel as can be seen in the case of the Fe–24Cr–24Ni alloy in which Ni enrichment is stronger than Cr depletion and Fe must also deplete.

This example exposes a key process in RIS, the role of composition in the segregation behavior. When the composition near a sink starts to change, the diffusivities of the elements in that region will change also as diffusion is composition-dependent. The effect of changing local composition needs to be accounted for in order to properly determine the extent of RIS, as will be covered in the next section.

6.3 Effect of Local Composition Changes on RIS

We have established that RIS occurs because of differences in the coupling of the various solutes with defects. Further, the difference in the strength of the coupling influences the degree of segregation. Therefore, when the concentration near the sink is significantly different from that in the bulk, the diffusivities of the solutes will change as well, and this change needs to be accounted for in order to accurately determine the composition profile [12]. The Perks model can be modified to include both composition-dependent diffusivities.

In the Perks model, the rate of segregation of element k by defect j is described by a diffusivity of the general form given by Eq. (6.24):

$$d_{\mathrm{kj}} = 1/6\lambda_{\mathrm{j}}^2 z_{\mathrm{j}} \nu \exp\left(\frac{S_{\mathrm{m}}^{\mathrm{j}}}{k}\right) \exp\left(\frac{-E_{\mathrm{m}}^{\mathrm{kj}}}{kT}\right) ,$$

or in simplified notation:

$$d_{\mathrm{kj}} = d_0^{\mathrm{kj}} \exp\left(\frac{-E_{\mathrm{m}}^{\mathrm{kj}}}{kT}\right) , \tag{6.43}$$

where the pre-exponential terms are lumped into a single term, d_0^{kj}. In most solutions to Eq. (6.41), the migration energies for each element are assumed to be equal, with differences in segregation rates arising from differences in the pre-exponential factors. To account for diffusion in a solution of varying composition, the migration energy term in the exponential must be described as a function of composition [11, 15, 16] as presented in the following paragraphs.

For an atom to migrate (Cr migrating in a Fe–Cr–Ni lattice will be used as an example), it must move from its equilibrium position in the lattice (with equilibrium energy $d_{\mathrm{kj}} = d_0^{\mathrm{kj}} \exp\left(\frac{-E_{\mathrm{m}}^{\mathrm{kj}}}{kT}\right)$) and travel through a position of maximum potential

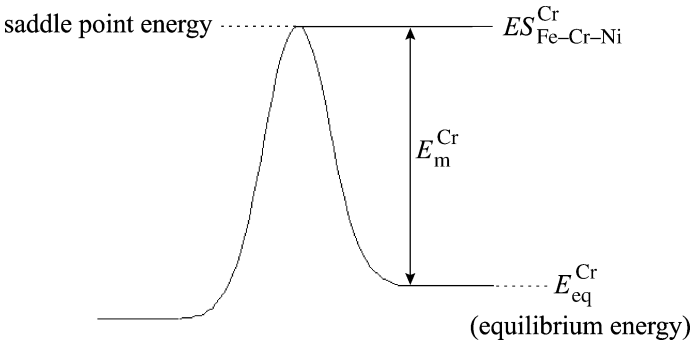

Fig. 6.10. Determination of the migration energy for an atom–vacancy exchange in an Fe–Cr–Ni alloy (after [12])

(known as the saddle point, with saddle point energy $d_{kj} = d_0^{kj} \exp\left(\frac{-E_m^{kj}}{kT}\right)$), before moving to a new lattice site. This relationship between the energies is shown schematically in Fig. 6.10. For atom – vacancy exchnge the migration energy is the difference between the saddle point energy and the equilibrium energy:

$$E_m^{Cr\text{-}v} = ES^{Cr}_{Fe\text{-}Cr\text{-}Ni} - E_{eq}^{Cr} \,. \tag{6.44}$$

In a simple model, the equilibrium energy can be described as the interaction energy between nearest neighbors:

$$E_{eq}^{Cr\text{-}v} = Z\left[C_{Cr}E_{CrCr} + C_{Ni}E_{NiCr} + C_{Fe}E_{FeCr} + C_vE_{Cr\text{-}v}\right] \,, \tag{6.45}$$

where Z is the number of nearest neighbors, C is the atomic concentration of atoms and/or defects, and E_{kj} is the pair interaction energy between an atom k and an atom or vacancy j. Pair interaction energies between unlike neighbors are defined to be a linear average of the like atom pair energies minus any ordering energy:

$$E_{NiCr} = \frac{E_{NiNi} + E_{CrCr}}{2} - E^{ord}_{NiCr} \,. \tag{6.46}$$

Combining Eq. (6.44) to Eq. (6.46) and requiring that $C_{Fe} + C_{Cr} + C_{Ni} = 1$, the migration energy for Cr, Ni and Fe via vacancies can be expressed as:

$$E_m^{Cr\text{-}v} = ES^{Cr}_{Fe–Cr–Ni} - Z\left[\frac{1}{2}\left(C_{Cr}+1\right)E_{CrCr} + \frac{C_{Ni}}{2}E_{NiNi} + \frac{C_{Fe}}{2}E_{FeFe} + C_vE_{Cr\text{-}v}\right] + ZC_{Ni}E^{ord}_{NiCr} + ZC_{Fe}E^{ord}_{FeCr} \tag{6.47a}$$

$$E_m^{Ni\text{-}v} = ES^{Ni}_{Fe\text{-}Cr\text{-}Ni} - Z\left[\frac{1}{2}\left(C_{Ni}+1\right)E_{NiNi} + \frac{C_{Cr}}{2}E_{CrCr} + \frac{C_{Fe}}{2}E_{FeFe} + C_vE_{Ni\text{-}v}\right] + ZC_{Cr}E^{ord}_{NiCr} + ZC_{Fe}E^{ord}_{FeNi} \tag{6.47b}$$

$$E_{\mathrm{m}}^{\mathrm{Fe\text{-}v}} = ES_{\mathrm{Fe\text{-}Cr\text{-}Ni}}^{\mathrm{Fe}} - Z\left[\frac{1}{2}\left(C_{\mathrm{Fe}}+1\right)E_{\mathrm{FeFe}} + \frac{C_{\mathrm{Cr}}}{2}E_{\mathrm{CrCr}} + \frac{C_{\mathrm{Fe}}}{2}E_{\mathrm{NiNiFe\text{-}v}} + C_{\mathrm{v}}E_{\mathrm{Ni\text{-}v}}\right] + ZC_{\mathrm{Fe}}E_{\mathrm{FeCr}}^{\mathrm{ord}} + ZC_{\mathrm{Ni}}E_{\mathrm{FeNi}}^{\mathrm{ord}} \tag{6.47c}$$

In order to determine the migration energies in Eq. (6.47), pair interaction energies and saddle point energies must be calculated. For like atoms, the pair interaction energy is the cohesive energy, E_{coh} divided by the number of nearest neighbor bond pairs:

$$E_{\mathrm{CrCr}} = E_{\mathrm{coh}}^{\mathrm{Cr}}/(Z/2)\,, \tag{6.48a}$$

$$E_{\mathrm{FeFe}} = E_{\mathrm{coh}}^{\mathrm{Fe}}/(Z/2)\,, \tag{6.48b}$$

$$E_{\mathrm{NiNi}} = E_{\mathrm{coh}}^{\mathrm{Ni}}/(Z/2)\,. \tag{6.48c}$$

Since pure Fe and pure Cr occur in the bcc structure, the energy required to convert Fe and Cr to the fcc structure for application to stainless steels must be included in the determination of E_{CrCr} and E_{FeFe} to properly describe the equilibrium energy:

$$E_{\mathrm{CrCr}}^{fcc} = E_{\mathrm{CrCr}}^{bcc} + \Delta G_{\mathrm{Cr}}^{bcc\rightarrow fcc}\,, \tag{6.49a}$$

$$E_{\mathrm{FeFe}}^{fcc} = E_{\mathrm{FeFe}}^{bcc} + \Delta G_{\mathrm{Fe}}^{bcc\rightarrow fcc}\,. \tag{6.49b}$$

Pair interaction energies between unlike atoms are determined from the average value of the like-atom pair energies less any ordering energy:

$$E_{\mathrm{NiCr}} = \frac{\left(E_{\mathrm{NiNi}}+E_{\mathrm{CrCr}}\right)}{2} - E_{\mathrm{NiCr}}^{\mathrm{ord}}\,, \tag{6.50a}$$

$$E_{\mathrm{FeCr}} = \frac{\left(E_{\mathrm{FeFe}}+E_{\mathrm{CrCr}}\right)}{2} - E_{\mathrm{FeCr}}^{\mathrm{ord}}\,, \tag{6.50b}$$

$$E_{\mathrm{FeNi}} = \frac{\left(E_{\mathrm{FeFe}}+E_{\mathrm{NiNi}}\right)}{2} - E_{\mathrm{FeNi}}^{\mathrm{ord}}\,. \tag{6.50c}$$

Finally, the pair interaction energy for atoms and vacancies is fitted to the formation energy of the pure metal and is given by:

$$E_{\mathrm{Cr\text{-}v}} = \left(\frac{E_{\mathrm{coh}}^{\mathrm{Cr}} + E_{\mathrm{f}}^{\mathrm{Cr\text{-}v}}}{Z}\right)\,, \tag{6.51a}$$

$$E_{\mathrm{Ni\text{-}v}} = \left(\frac{E_{\mathrm{coh}}^{\mathrm{Ni}} + E_{\mathrm{f}}^{\mathrm{Ni\text{-}v}}}{Z}\right)\,, \tag{6.51b}$$

$$E_{\mathrm{Fe\text{-}v}} = \left(\frac{E_{\mathrm{coh}}^{\mathrm{Fe}} + E_{\mathrm{f}}^{\mathrm{Fe\text{-}v}}}{Z}\right)\,, \tag{6.51c}$$

where $E_{\mathrm{f}}^{\mathrm{k\text{-}v}}$ is the vacancy formation energy in pure k.

The last quantity remaining to be determined is the saddle point energy, which is calculated using the saddle point energy of pure Fe, Cr, and Ni. The saddle point

energy in the pure metal is calculated to reproduce the vacancy migration energy in the pure metal. For example, assuming that in pure Cr both an atom and a vacancy are extracted and placed at a saddle point, then the energy to extract the Cr atom is given by:

$$E_{\mathrm{Cr}} = Z(C_{\mathrm{Cr}}E_{\mathrm{CrCr}} + C_{\mathrm{v}}E_{\mathrm{Cr\text{-}v}}) \,. \tag{6.52}$$

The energy to extract the vacancy is:

$$E_{\mathrm{v}} = Z(C_{\mathrm{v}}E_{\mathrm{vv}} + C_{\mathrm{Cr}}E_{\mathrm{Cr\text{-}v}}) \tag{6.53}$$

Since $C_{\mathrm{Cr}} + C_{\mathrm{v}} = 1$ in a pure metal and since $C_{\mathrm{v}} \ll C_{\mathrm{Cr}}$, the sum of $E_{\mathrm{Cr}} + E_{\mathrm{v}}$ becomes:

$$E_{\mathrm{Cr}} + E_{\mathrm{v}} = Z(E_{\mathrm{CrCr}} + E_{\mathrm{Cr\text{-}v}}) \,. \tag{6.54}$$

Equation (6.54) represents the equilibrium energy for pure Cr. We want to place the atom at a saddle point with an energy such that:

$$E_{\mathrm{m}}^{\mathrm{Cr\text{-}v}} = ES_{\mathrm{pure}}^{\mathrm{Cr}} - (E_{\mathrm{Cr}} + E_{\mathrm{v}}) = ES_{\mathrm{pure}}^{\mathrm{Cr}} - Z(E_{\mathrm{CrCr}} + E_{\mathrm{Cr\text{-}v}}) \,. \tag{6.55}$$

The saddle point energy in the pure metal is then given as:

$$ES_{\mathrm{pure}}^{\mathrm{Cr}} = E_{\mathrm{m}}^{\mathrm{Cr\text{-}v}} + Z(E_{\mathrm{CrCr}} + E_{\mathrm{Cr\text{-}v}}) \,. \tag{6.56}$$

This approach, described in the modified inverse Kirkendall (Perks) model called the MIK model [12], was used to model RIS and results were compared to measurements taken on a range of Fe-base and Ni-base austenitic alloys irradiated at temperatures from 200 to 600 °C and at doses up to 3 dpa. The RIS results shown in Fig. 6.11 clearly demonstrate the importance of accounting for composition changes near the sinks in the determination of the RIS composition profiles. The MIK model calculations agree with AES measurements of grain boundary nickel concentration in irradiated Fe–20Cr–24Ni much better than the original Perks model. Also, over a range of alloys, doses and irradiation temperatures (Fig. 6.12) the inclusion of local composition changes on RIS results in much better agreement with the data. These data also serve to illustrate the importance of vacancies in RIS in Fe–Cr–Ni alloys at intermediate temperatures. The MIK model calculations did *not* include either interstitial binding (that is, $E_{\mathrm{b}}^{\mathrm{ik}} = 0$) or preferential participation of any of the alloying elements in the interstitial flux. Excellent agreement between model and measurement is achieved solely by preferential participation of alloying elements in the vacancy flux. Hence, in the Fe–Cr–Ni system, atom migration via vacancies appears to be the dominant mechanism of RIS.

6.4 Effect of Solutes on RIS

The presence of impurities in a solid can influence the propensity for RIS at the grain boundary. It has been hypothesized that solutes that are oversized or undersized with

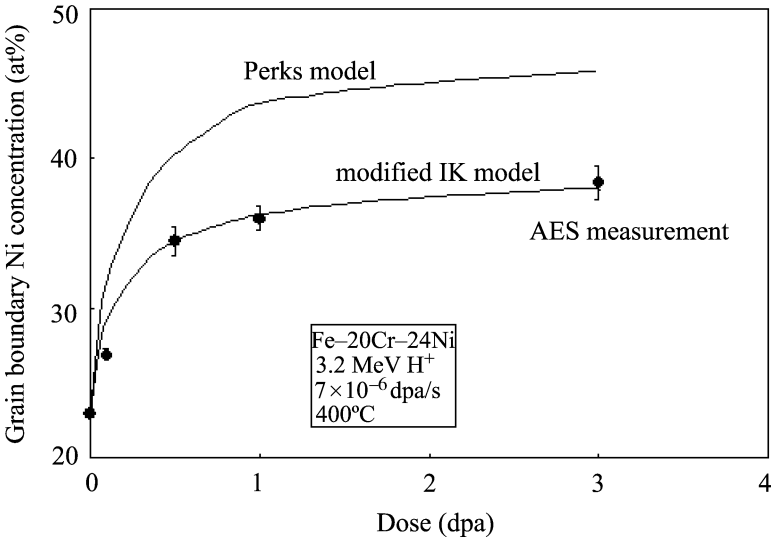

Fig. 6.11. The modified inverse Kirkendall (MIK) model result compared to the Perks model result and to measurement showing the importance in accounting for the changing local composition at sinks in RIS. Experiment was conducted on Fe–20Cr–24Ni using 3.2 MeV protons at 400 °C and at a displacement rate of 7×10^{-6} dpa/s (after [12])

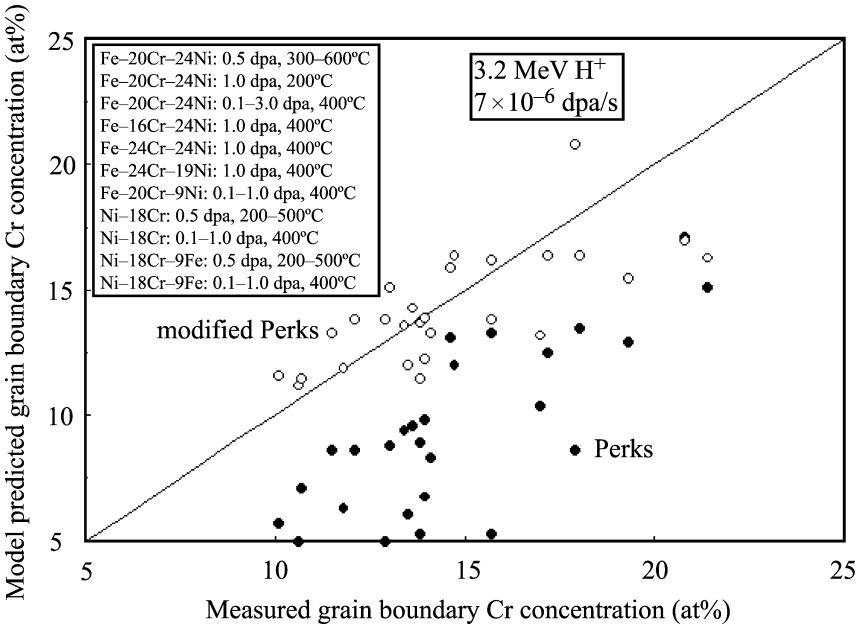

Fig. 6.12. MIK model applied to several alloys under a range of doses and temperatures and comparison to measurement (after [2])

respect to the lattice atoms can act as traps for vacancies or interstitials. Trapping of point defects by solutes could increase the fraction of vacancies and interstitials undergoing mutual recombination, thus reducing the fraction flowing to sinks, and hence, the degree of segregation. Mansur and Yoo [17] generalized the point defect balance equations to include point defect trapping. Trapping is accommodated by subtracting and adding terms corresponding to trapping and recombination at traps, and the release of point defects from traps. In addition, equations describing the conservation of the trapped defects are also added. As a result, the point defect balances, from Eq. (6.1), are given as follows:

Free vacancies:

$$\begin{aligned}\frac{\partial C_{\mathrm{v}}}{\partial t} &= \nabla \cdot D_{\mathrm{v}} \nabla C_{\mathrm{v}} + K_0 - K_{\mathrm{iv}} C_{\mathrm{i}} C_{\mathrm{v}} \\ &\quad + \sum_l \tau_{\mathrm{v}l}^{-1} C_{\mathrm{v}l} - C_{\mathrm{v}} \sum_l K_{\mathrm{i}l} C'_{\mathrm{i}l} - C_{\mathrm{v}} \sum_l \kappa_{\mathrm{v}l} (C_{\mathrm{l}}^t - C'_{\mathrm{v}l} - C'_{\mathrm{i}l}) - K_{\mathrm{v}} C_{\mathrm{v}} \,.\end{aligned} \tag{6.57}$$

Free interstitials:

$$\begin{aligned}\frac{\partial C_{\mathrm{i}}}{\partial t} &= \nabla \cdot D_{\mathrm{i}} \nabla C_{\mathrm{i}} + K_0 - K_{\mathrm{iv}} C_{\mathrm{i}} C_{\mathrm{v}} \\ &\quad + \sum_l \tau_{\mathrm{i}l}^{-1} C_{\mathrm{i}l} - C_{\mathrm{i}} \sum_l K_{\mathrm{v}l} C'_{\mathrm{v}l} - C_{\mathrm{i}} \sum_l \kappa_{\mathrm{i}l} (C_{\mathrm{l}}^t - C'_{\mathrm{v}l} - C'_{\mathrm{i}l}) - K_{\mathrm{i}} C_{\mathrm{i}} \,.\end{aligned} \tag{6.58}$$

In Eqs. (6.57) and (6.58), the summations extend over the $l = 1, 2, \ldots, n$ types of traps. Similarly, the following equations apply to each of the $l = 1, 2, \ldots, n$ types of traps.

Traps (concentration in general is a function of position and time):

$$\frac{\partial C_{\mathrm{l}}^t}{\partial t} = f_{\mathrm{l}}(r,t) \,. \tag{6.59}$$

Trapped vacancies:

$$\frac{\partial C_{\mathrm{v}l}^t}{\partial t} = C_{\mathrm{v}} \kappa_{\mathrm{v}l} (C_{\mathrm{l}}^t - C'_{\mathrm{v}l} - C'_{\mathrm{i}l}) - \tau_{\mathrm{v}l}^{-1} C'_{\mathrm{v}l} - C_{\mathrm{i}} K_{\mathrm{v}l} C'_{\mathrm{v}l} \,. \tag{6.60}$$

Trapped interstitials:

$$\frac{\partial C_{\mathrm{i}l}^t}{\partial t} = C_{\mathrm{i}} \kappa_{\mathrm{i}l} (C_l^t - C'_{\mathrm{v}l} - C'_{\mathrm{i}l}) - \tau_{\mathrm{i}l}^{-1} C'_{\mathrm{i}l} - C_{\mathrm{v}} K_{\mathrm{i}l} C'_{\mathrm{i}l} \,. \tag{6.61}$$

In Eqs. (6.57) and (6.58), the first three terms are the same as in Eq. (6.1). The remaining terms have the following meaning. Referring to the equation for free vacancies, the fourth term is the release of trapped vacancies from the sink and the variable $\tau_{\mathrm{v}l}^{-1}$ is the mean time that the vacancy is trapped at the lth trapping site. The mean trapping time is denoted by $\tau_{jl} = (b^2/D_j^0)\exp[(E_{\mathrm{b}}^{jl} + E_{\mathrm{m}}^j)/kT]$, where j denotes i or v, D_j^0 is the pre-exponential of the diffusion coefficient $[D_j = D_j^0 \exp(-E_{\mathrm{m}}^j/kT)]$, b is the order of atomic distance, E_{b}^{jl} is the binding energy of the point defect at

the lth type trap, and E_{m}^{j} is the point defect migration energy. The fifth term is the recombination rate of vacancies with trapped interstitials, where $K_{\mathrm{i}l}$ is the recombination rate constant for that reaction and is given by $K_{\mathrm{i}l} = 4\pi r_{\mathrm{i}l} D_{\mathrm{v}}$ or $K_{\mathrm{v}l} = 4\pi r_{\mathrm{v}l} D_{\mathrm{i}}$, where $r_{\mathrm{i}l}$ and $r_{\mathrm{v}l}$ denote the respective radii of the recombination volumes. The sixth term describes the trapping of free vacancies at a trap of type l. The concentration difference $(C_l^t - C'_{\mathrm{v}l} - C'_{\mathrm{i}l})$ accounts for the fact that the fraction $C'_{\mathrm{v}l}/C_l^t + C'_{\mathrm{i}l}/C_l^t$ traps of type l are already occupied by vacancies and interstitials and hence, are not available as traps for free defects. It also accounts for the fact that a given trap may have a binding energy for both vacancies and interstitials but would not trap both simultaneously, since when one is trapped, the site is then a recombination center. The terms $\kappa_{\mathrm{v}l} = 4\pi r'_{\mathrm{v}l} D_{\mathrm{v}}$ and $\kappa_{\mathrm{i}l} = 4\pi r'_{\mathrm{i}l} D_{\mathrm{i}}$ denote the capture coefficients similar to recombination coefficients, and the $r'_{\mathrm{v}l}$ and $r'_{\mathrm{i}l}$ are the capture radii of the trap type l for the respective point defects. Finally, the seventh term is the loss of defects to all internal sinks and K_{v} describes the rate constant for all sinks.

Equation (6.57) through Eq. (6.61) are substituted for the vacancy and interstitial concentrations in Eq. (6.41) and solved in the same manner as before in a version of the MIK code designated MIK-T. The results of trapping in Fe–16Cr–13Ni containing an oversized solute concentration of 1% is shown in the plot of grain boundary chromium content vs. dose for the case of irradiation at a dose rate of 10^{-5} dpa/s at a temperature of 400 °C and for interstitial and vacancy binding energies up 1.0 eV (Fig. 6.13a). Note that high binding energies on the order 1.0 eV are required for trapping to reduce the amount of RIS. The main effect is a reduction in the amount of grain boundary Cr depletion, but a secondary effect is a slowing of the rate of segregation with dose. Figure 6.13b shows that trapping moves the temperature at which RIS is a maximum to a slightly lower temperature. Figure 6.14 shows the effect of oversize solute addition on grain boundary chromium depletion and nickel enrichment in Fe–Cr–Ni alloys irradiated with protons, and that experimental results qualitatively follow those of the model.

As successful as these models are in predicting the direction and magnitude of segregation, they are very incomplete. The models have been developed for binary and ternary systems only, whereas real engineering alloys may contain 10–20 alloying elements. Even though some may be present in very small quantities, they can exert a very large influence on the behavior of the alloy. The Perks and MIK models apply only to solute atoms and not to small interstitial atoms such as B, C and N. Further, many of the thermodynamic parameters required for accurate simulation of RIS are unknown and must be estimated, introducing uncertainty into the results. Despite these shortcomings, they can serve to rationalize to RIS in real systems.

6.5 Examples of RIS in Austenitic Alloys

As stated earlier, RIS is an extremely important problem in structural materials exposed to irradiation at elevated temperatures. The changes in grain boundary composition can give rise to microstructure changes (precipitation, dislocation loop structure, void structure) in addition to changes in susceptibility to processes such as

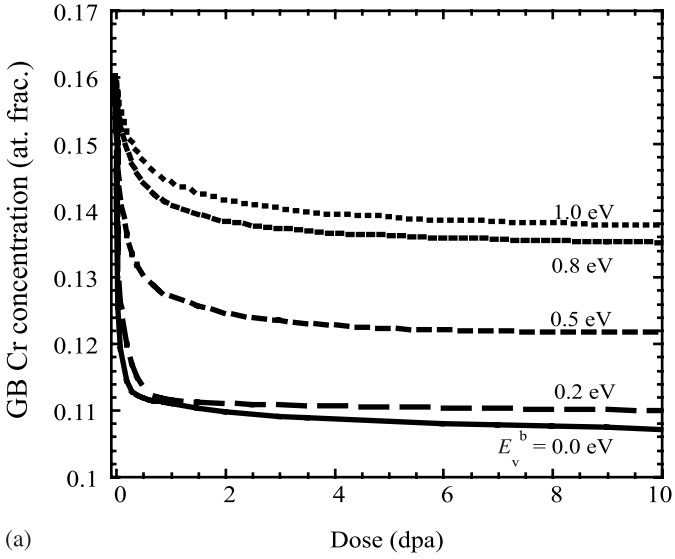

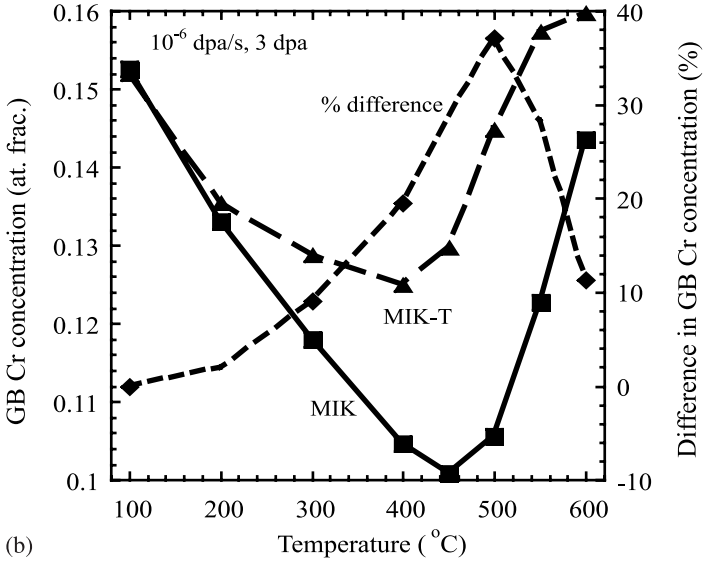

Fig. 6.13. Calculated grain boundary Cr composition (a) as a function of binding energy for the MIK-T model at 400 °C and 1×10^{-5} dpa/s for Fe–16Cr–13Ni, and (b) as a function of temperature at a constant dose rate of 10^{-5} dpa/s at 3 dpa. Percent difference calculated by (MIK-T – MIK)/MIK*100% (after [18])

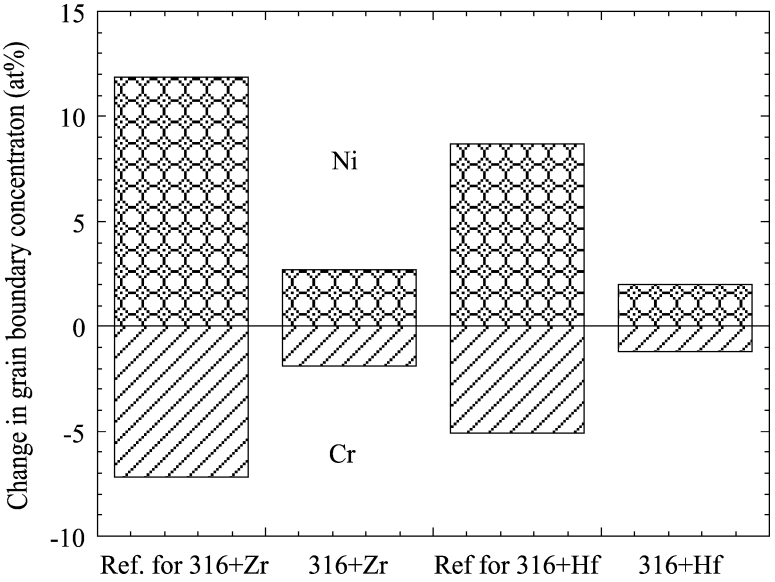

Fig. 6.14. Grain boundary Cr and Ni composition for reference and oversize impurity-doped Fe–Cr–Ni alloys irradiated at 400 °C to 3.0 dpa (Zr) and 2.5 dpa (Hf) (after [18] and [19])

intergranular corrosion and stress corrosion cracking. For example, we determined that Cr always depletes in irradiated stainless steels, and the loss of chromium at grain boundaries could cause an increased susceptibility to intergranular corrosion and intergranular stress corrosion cracking, since chromium provides *passivity* to the alloy by forming a very thin, protective, Cr_2O_3 film. As will be discussed in Chap. 15, with increases in dose above some *pseudo-threshold* level, the amount of intergranular stress corrosion cracking (IGSCC), measured as the percentage of the fracture surface that displays intergranular facets, increases steeply in slow strain rate tests in 288 °C normal water chemistry used in boiling water reactors (BWR). Figure 6.15 shows that the grain boundary Cr content also decreases rapidly with dose due to RIS. The loss of Cr may raise the susceptibility of the alloy to IASCC, although other changes are occurring in the microstructure at the same time.

Silicon is also observed to segregate very strongly with dose, as shown in Fig. 6.16 for austenitic stainless steels irradiated at $\sim$ 288 °C. These measurements of high levels of Si were made by STEM/EDS. Due to the spatial resolution limit of this technique, the actual grain boundary level of Si may be underestimated by as much as a factor of 3–5, giving concentrations of over 20% Si at the grain boundary. Since Si is soluble in high-temperature water, it is possible that it could be enhancing dissolution at the grain boundary giving rise to increased rates of intergranular corrosion (IGC) and IGSCC.

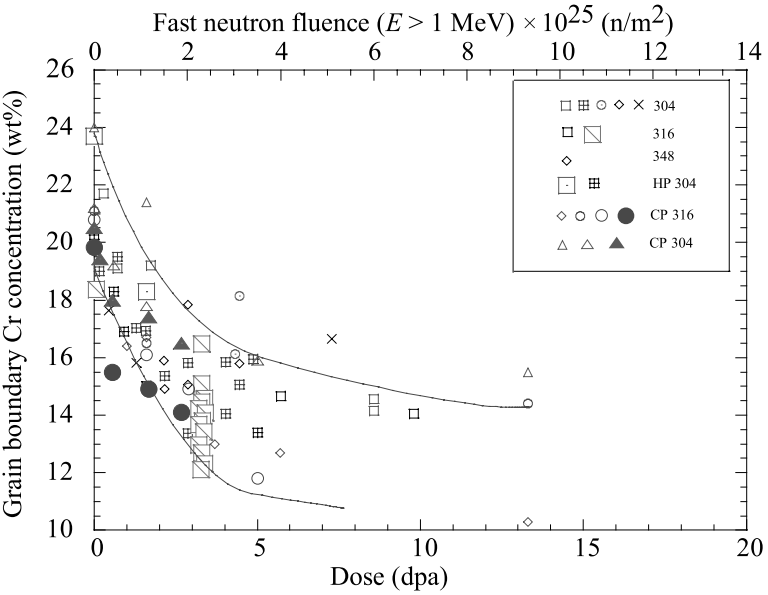

Fig. 6.15. Dependence of grain boundary chromium concentration on dose for a range of 300 series stainless steels irradiated under various conditions. Note that RIS increases with dose through about 5 dpa after which the change is minimal (after [20])

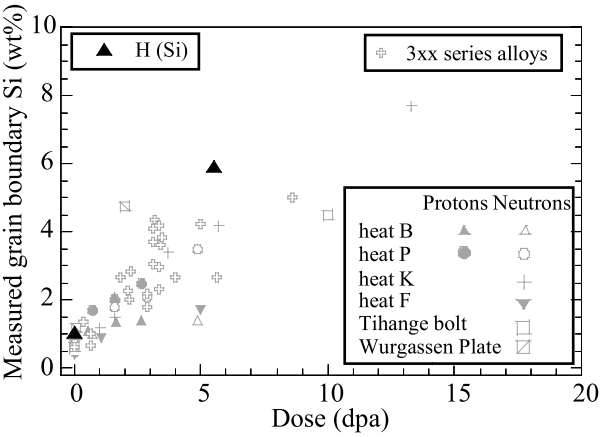

Fig. 6.16. Grain boundary segregation of silicon in 300 series austenitic alloys irradiated with neutrons or protons to 13 dpa

6.6 RIS in Ferritic Alloys

RIS is also of significance in ferritic steels, particularly pressure vessel steels where the grain boundary segregation of interstitial impurities such as P can have significant consequences for grain boundary embrittlement. Compared to austenitic steels, little work has been done on the segregation of alloying elements in ferritic alloys. Segregation models for interstitial impurities are not as well-developed as for sub-

stitutional solutes. Faulkner [21] has reviewed the segregation data and mechanisms and suggests that RIS in ferritic steels is by defect–impurity complexes and that site competition by other elements at the boundary plays a significant role determining in the amount of segregation of a particular impurity. Focusing on the behavior of P, it is assumed that migration by self-interstitial phosphorus complexes is fast such that the concentration remains uniform across the grain boundary plane. The maximum grain boundary concentration of phosphorus is given by:

$$C_{\mathrm{P}}^{\max} = C_{\mathrm{g}} \frac{E_{\mathrm{b}}}{E_{\mathrm{f}}} \left[\frac{C_{\mathrm{g}}^{j} \exp\left(E_{\mathrm{b}}^{j}/kT\right)}{\sum_{j} C_{\mathrm{g}}^{j} \exp\left(E_{\mathrm{b}}^{j}/kT\right)} \right] \left[1 + \frac{\xi K_0 F(\eta)}{ADk^2} \exp\left(E_{\mathrm{f}}^{\mathrm{i}}/kT\right) \right] , \tag{6.62}$$

where C_{g} is the total impurity concentration in the grain, E_{b}^{j} is the binding energy between the point defect, the self-interstitial and the impurity atom, E_{f} is the interstitial formation energy and C_{g}^{j} is the concentration of impurity atom, j in the grains. The denominator of the first bracket is the sum of point defect binding energy terms for all of the elements entering into the site competition process. In the second bracket, ξ is the defect production efficiency, $F(\eta)$ is a recombination term, K_0 is the defect production rate, A is associated with the vibrational entropy of the atoms surrounding the point defect, D is the defect diffusion coefficient, and k^2 is the sink efficiency.

Following segregation to the boundary, the impurity concentration will be determined by site competition at the boundary where the concentration of phosphorus is given by:

$$C_{\mathrm{P}}^{*} = C_{\mathrm{P}}^{\max} \frac{C_{\mathrm{g}}^{\mathrm{P}} \exp(Q_{\mathrm{P}}/kT)}{C_{\mathrm{g}}^{j} \exp(Q_j/kT) + C_{\mathrm{g}}^{\mathrm{P}} \exp(Q_{\mathrm{P}}/kT)} , \tag{6.63}$$

where $C_{\mathrm{g}}^{\mathrm{P}}$ is the concentration of P and $C_{\mathrm{g}}^{\mathrm{j}}$ is the concentration of the other impurity elements in the grains, and Q_{P} and Q_j are the solute grain boundary binding energies for P and for the other elements, respectively. The value of C_{P}^{*} is the maximum expected segregation at steady state. Before steady state is reached, the grain boundary concentration depends on time according to:

$$\frac{C_{\mathrm{P}}(t) - C_{\mathrm{g}}}{C_{\mathrm{P}}^{*} - C_{\mathrm{g}}} = 1 - \exp\left(\frac{4D_{\mathrm{c}}t}{\alpha^2 d^2}\right) \operatorname{erfc}\left(\frac{2\sqrt{D_{\mathrm{c}}t}}{\alpha d}\right) , \tag{6.64}$$

where D_{c} is the point defect–impurity complex diffusion coefficient, α is the enrichment ratio and d is the grain boundary width. Experimental measurements of P segregation in ferritic steels are shown in Fig. 6.17. Note that while the P concentration increases with dose, it varies significantly with the specific alloy. This variation is likely due to site competition with other impurities, most important of which is carbon. The A533 B steel shown has a high grain boundary P level because it has a low C content. Figure 6.18 shows the competition between P and C at the grain boundary and the P segregation is highest when the C level is low.

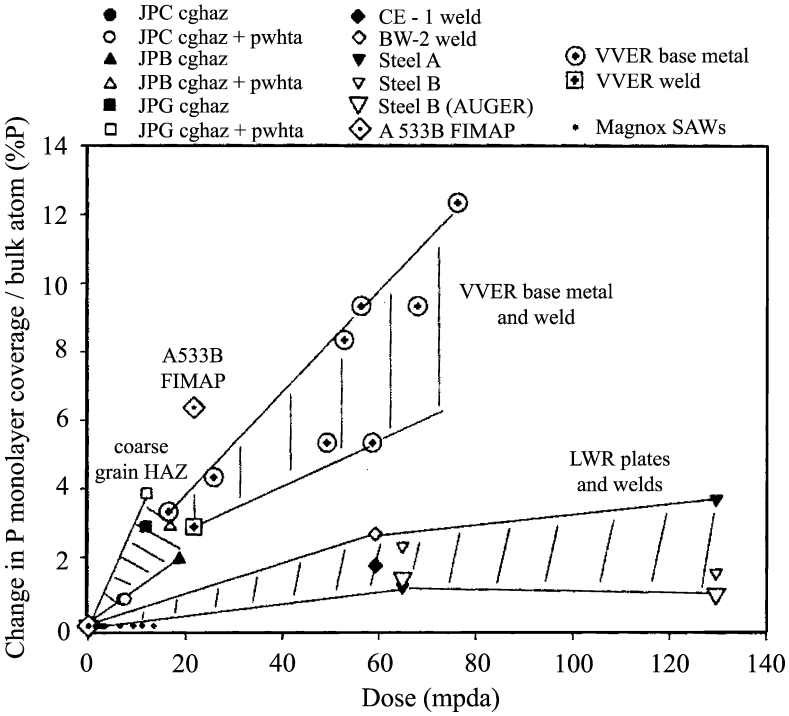

Fig. 6.17. Dose dependence of the irradiation-induced change in grain boundary phosphorus monolayer coverage normalized with respect to the bulk atomic phosphorus concentration for C-Mn LWR plates, welds and coarse HAZ structure and VVER base metal and weld. All irradiation temperatures are 275–290 °C except for the Magnox SAWs, which cover the range 186–311 °C (after [21])

In the higher Cr alloys such as the 9–12%Cr ferritic-martensitic alloys, the behavior of Cr at the grain boundary is of concern because of the potential for the formation of brittle, chromium-rich phases. While Cr depletes in austenitic alloys, recent results have shown that it enriches in F-M alloys, behaving like an undersize solute [22]. Although this behavior is not yet understood, experiments have indeed shown that enrichment of Cr at the grain boundary can be substantial. Figure 6.19 shows that Cr *enriches* at the grain boundary of a Fe–9Cr alloy (T91) by almost 5 wt% following irradiation with 2 MeV protons to 10 dpa at 450 °C. If such enrichment leads to the formation of Cr-rich phases, grain boundary embrittlement could result.

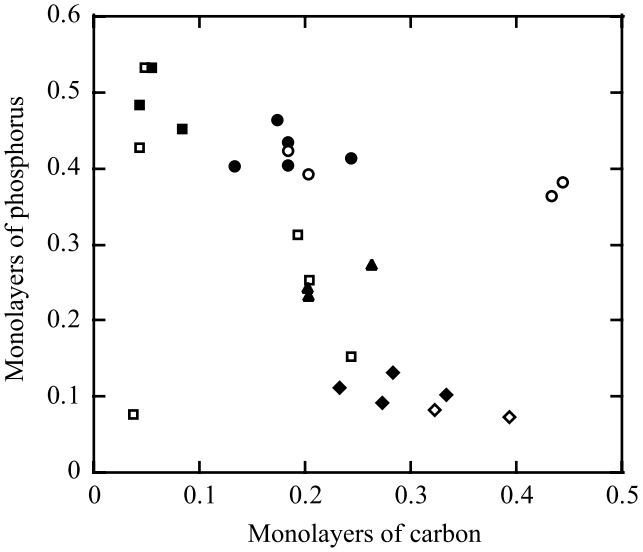

Fig. 6.18. Variation of phosphorus and carbon monolayer coverage at grain boundaries of thermally aged and irradiated ferritic alloys (after [21])

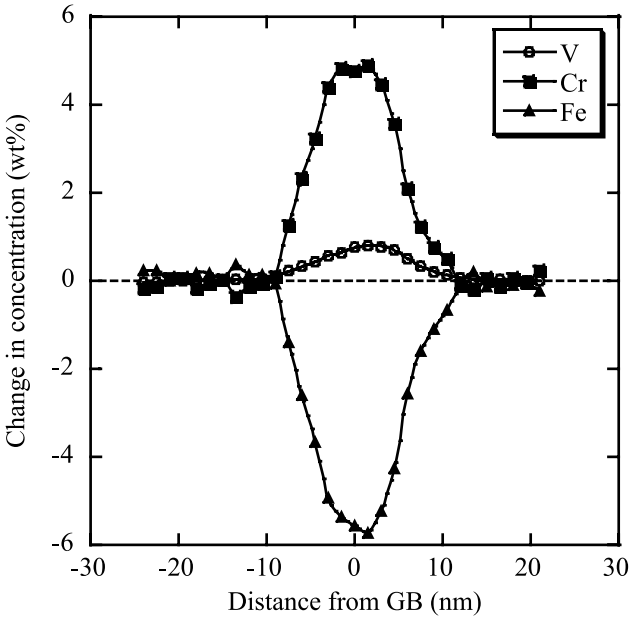

Fig. 6.19. Grain boundary composition of a ferritic-martensitic Fe–9Cr steel containing 0.2%V and irradiated with 2MeV protons at 450°C to 10dpa (after [22])

Nomenclature

A	Term associated with vibrational entropy, see Eq. (6.62)
C_x	Concentration of specie x
C_{P}^{*}	Maximum grain boundary segregation of P at steady state in ferritic steels
d	Grain size
d_{xy}	Partial diffusion coefficient divided by N_y
d_0^x	Pre-exponential term for diffusion of specie x
D	Diffusion coefficient
D_x^y	Partial diffusion coefficient for migration of x via y
E_{eq}^x	Equilibrium energy for specie x
E_{b}^{xz}	Binding energy of specie x to defect z
E_{f}^x	Formation energy of specie x
E_{m}^{xz}	Migration energy of specie x migrating via defect z
E_{xy}	Interaction energy between species x and y
E_{xy}^{ord}	Ordering energy for species x and y
ES_{alloy}^x	Saddle point energy for element x in alloy
f	Correlation coefficient
$F(\eta)$	Recombination term in Eq. (6.62)
i	Interstitial designation
k	Boltzmann's constant
k^2	Sink efficiency
v	Vacancy designation
s	Sink designation
J_x	Flux of atom or defect x across a marker plane
K_0	Defect production rate
K_{xy}	Reaction rate constant for x and y
M_j	Determinant for specie j (defined in Eqs. (6.23) and (6.39))
N_x	Atom fraction of specie x
Q_{Sj}	Grain boundary binding energy for solute j
r_{xy}	Capture radius for defect x by sink/trap y
R	Recombination rate
S_{m}^x	Entropy of migration for specie x
t	Time
T	Temperature
z	Number of nearest neighbors
α	Enrichment ratio
γ_x	Activity coefficient of specie x
κ_{xy}	Capture coefficient of defect x by sink/trap y
λ	Jump distance
ω	Jump frequency
Ω	Atomic volume

τ	Time constant
ξ	Defect production efficiency

Subscripts

eq	Equilibrium
f	Formation
g	Impurity
l	Trap type
m	Migration

Superscripts

j	Specie or defect
k	solute
ord	Ordering
t	Trap

Acronyms

AES	Auger electron spectroscopy
BWR	Boiling water reactor
F-M	Ferritic-martensitic
IASCC	Irradiation assisted stress corrosion cracking
IGSCC	Intergranular stress corrosion cracking
IGC	Intergranular cracking
IK	Inverse Kirkendall
MIK	Modified inverse Kirkendall
MIK-T	Modified inverse Kirkendall-trapping
RIS	Radiation-induced segregation
STEM-EDS	Scanning transmission electron microscopy-energy dispersive spectrometry

Problems

6.1 A sample of Cu–20%Al is irradiated at 500 °C.
   a) Will aluminum segregate to or from the surface? Explain. (Assume that association of defects with Al and Cu atoms is non-preferential.)
   b) If there is strong binding (a preferential association) of interstitials to the undersized atom, how would your answer to part (a) change? (Take $E_b^{\text{Cu-i}} = 1\,\text{eV}$.)
   c) Repeat part (a) for $T = 100\,°\text{C}$. (Here, vacancies are immobile.)

6.2 A Ni–18Cr alloy is irradiated at 400 °C.
   a) The chromium concentration is measured at the grain boundary and is found to deplete. What is the sign of the determinant for chromium?

b) The bulk concentration of nickel decreases from 82 to 70 wt%. Assuming nothing else changes, what happens to the determinant of chromium? State your assumptions.
c) If the diffusion coefficient of chromium vacancies decreases, what happens to the Cr segregation profile?

6.3 An Fe–18Cr–8Ni alloy is irradiated and radiation-induced segregation changes the grain boundary composition. Calculate the Ni and Cr equivalents for the bulk alloy and at the grain boundary assuming $\Delta Cr = -5$ and $\Delta Ni = +3$. In terms of the Schaeffler diagram, how is the grain boundary area different than the bulk? If an Fe–18Cr–20Ni alloy was irradiated under the same conditions, what changes?

6.4 For the ternary alloy Fe–18Cr–20Ni, determine if iron enriches or depletes during irradiation at 500 °C.

6.5 For the Fe–18Cr–20Ni alloy in Problem 6.4, determine the migration energy for chromium via vacancies, $E_m^{Cr\text{-}v}$ at the grain boundary when the grain boundary composition is Fe–10Cr–30Ni.

$$E_{coh}^{Cr} = -4.10\,eV$$
$$E_{coh}^{Fe} = -1.28\,eV$$
$$E_{coh}^{Ni} = -4.44\,eV$$
$$E_f^{Cr\text{-}v} = 1.60\,eV$$
$$E_f^{Fe\text{-}v} = 1.40\,eV$$
$$E_f^{Ni\text{-}v} = 1.79\,eV$$
$$E_{NiCr}^{ord} = 0.005\,eV$$
$$E_{FeCr}^{ord} = 0.003\,eV$$

References

1. Bruemmer SM, Simonen EP, Scott PM, Andresen PL, Was GS, Nelson LJ (1999) J Nucl Mater 274:299–314
2. Anthony TR (1972) In: Corbett JW, Ianniello LC (eds) Radiation-Induced Voids in Metals and Alloys, AEC Symposium Series, Conf-701601, p 630
3. Okamoto PR, Harkness SD, Laidler JJ (1973) ANS Trans 16:70
4. Wiedersich H, Okamoto PR, Lam NQ (1979) J Nucl Mater 83:98–108
5. Perks JM, Marwick AD, English CA (1986) AERE R 12121 (June)
6. Rehn LE, Okamoto PR, Potter DI, Wiedersich H (1978) J Nucl Mater 74:242–251
7. Rehn LE (1982) In: Picraux ST, Choyke WJ (eds) Metastable Materials Formation by Ion Implantation. Elsevier Science, New York, p 17
8. Okamoto PR, Wiedersich H (1974) J Nucl Mater 53:336–345
9. Kornblit L, Ignatiev A (1984) J Nucl Mater 126:77–78
10. Was GS, Allen TR, Busby IT, Gan I, Damcott D, Carter D, Atzmor M, Konik EA (1999) J Nucl Mater 270:96–114

11. Was GS, Allen TR (1993) J Nucl Mater 205:332–338
12. Allen TR, Was GS (1998) Acta Metal 46:3697
13. Lam NQ, Kumar A, Wiedersich H (1982) In: Brager HR, Perrin JS (eds) Effects of Radiation on Materials, 11th Conference, ASTM STP 782, American Society for Testing and Materials, pp 985–1007
14. Watanabe S, Takahashi H (1994) J Nucl Mater 208:191
15. Grandjean Y, Bellon P, Martin G (1994) Phys Rev B 50:4228
16. Nastar M, Martin G (1999) Mater Sci Forum 294–296:83
17. Mansur LK, Yoo MH (1978) J Nucl Mater 74:228–241
18. Hackett MJ, Was GS, Simonen EP (2005) J ASTM Int 2(7)
19. Fournier L, Sencer BH, Wang Y, Was GS, Gan J, Bruemmer SM, Simonen EP, Allen TR, Cole JI (2002) In: Proceedings of the 10th International Conference on Environmental Degradation of Materials in Nuclear Power Systems: Water Reactors, NACE International, Houston, TX
20. Was GS (2004) Recent developments in understanding irradiation assisted stress corrosion cracking. In: Proceedings of the 11th International Conference on Environmental Degradation of Materials in Nuclear Power Systems: Water Reactors, American Nuclear Society, La Grange Park, IL, pp 965–985
21. Faulkner RG, Jones RB, Lu Z, Flewitt PEJ (2005) Phil Mag 85(19):2065–2099
22. Gupta G, Jiao Z, Ham AN, Busby JT, Was GS (2006) J Nucl Mater 351(1–3):162–173

7 Dislocation Microstructure

One of the most profound consequences of irradiation on the microstructure of materials is the formation of dislocation loops. Dislocation loops have a bias for interstitials and thus have a strong impact on the development of the irradiated microstructure. They also influence the deformation behavior and consequently, the ductility and hardening of irradiated materials, as will be discussed in Chap. 12. In this chapter, we will review the origin and character of dislocations, their mobility and multiplication and their stresses, strains and energies. The character of dislocation loops will be examined and models for nucleation and growth will be presented. Finally, the stacking fault tetrahedron will be discussed. For a more in-depth treatment of dislocations, the reader is referred to [1, 2, 3, 4].

7.1 Dislocation Lines

The discovery of dislocations in crystals has its origin in the discrepancy between the measured and theoretical stress needed to cause shear in a crystal. Consider the stress required to shear a crystal along a given atomic plane. A shear of one atomic distance requires that atoms above the plane all move one lattice spacing relative to those below (Fig. 7.1). To reach the saddle point, each atom must move horizontally a distance of one atom radius, a. Since the separation of two planes is $\sim 2a$, the shear strain at the saddle point is $\gamma \approx a/2a \sim 1/2$. In a perfectly elastic crystal, the ratio of shear stress to shear strain is the shear modulus:

$$\frac{\sigma_s}{\gamma} = \mu \, . \tag{7.1}$$

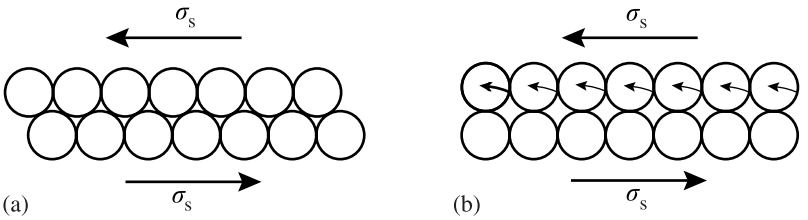

Fig. 7.1. Initial position of atoms above and below a slip plane, and the motion of the atoms above the slip plane required to cause slip

For a typical shear modulus of 17 GPa and a shear strain of $1/2$, the shear stress from Eq. (7.1) is ~ 8.5 GPa. However, experiments, for example on magnesium, produce deformation at shear stresses of ~ 1 MPa, which is different from theory by a factor of 10^4! The reason is the existence of dislocations that provide for much reduced shear stresses in crystals.

A *dislocation* is a line that forms a boundary between a region of the crystal that has slipped and one that has not. The two basic types of dislocations lines are the edge and the screw. In an *edge dislocation*, atoms over the cut surface are shifted in a direction *perpendicular* to the dislocation line. An edge dislocation can also be thought of as the insertion of an extra half plane of atoms (Fig. 7.2). In a *screw dislocation*, the atoms over the cut surface are shifted in a direction *parallel* to the dislocation line (Fig. 7.3a). The screw dislocation itself is a pole about which a spiral ramp of planes circles (analogous to a parking garage ramp) (Fig. 7.3b). There also exist *mixed dislocations* in which the shift is neither parallel nor perpendicular to the dislocation line, but at some arbitrary angle. Figure 7.4 shows a mixed dislocation in a crystal in which the dislocation line is curved. Note that the boundary separating slipped and unslipped regions is circular. At point A (front face), the dislocation is of pure edge character. At point B (side face), the dislocation is of pure screw character. In between, the dislocation is *mixed* with the proportion of screw and edge character varying continuously with distance along the line. Figure 7.5 shows the construction of a mixed dislocation.

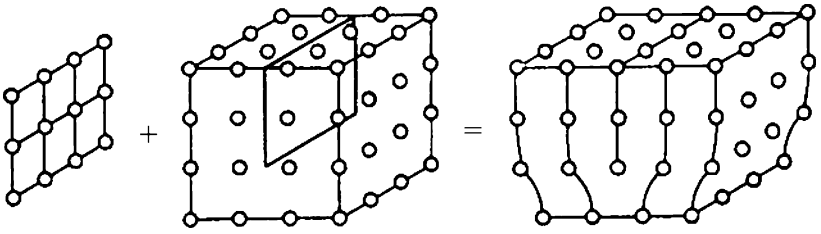

Fig. 7.2. An edge dislocation described as an extra half plane of atoms above the slip plane

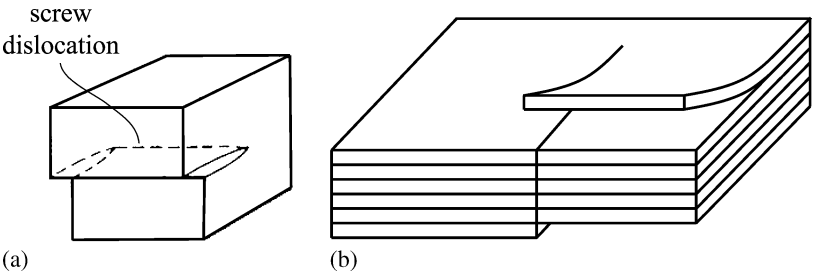

Fig. 7.3. (a) A screw dislocation formed by a cut and a shift of atoms in a direction parallel to the *cut line*. (b) A schematic showing the "parking ramp" nature of a screw dislocation in which atom planes spiral about the dislocation line

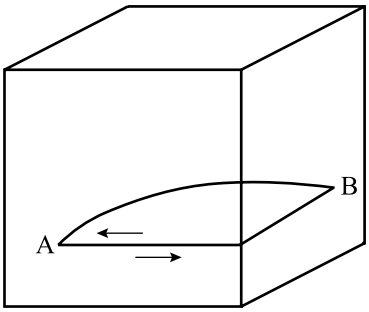

Fig. 7.4. Curved dislocation line with pure screw character at point A, pure edge character at point B and mixed character along the length of the dislocation

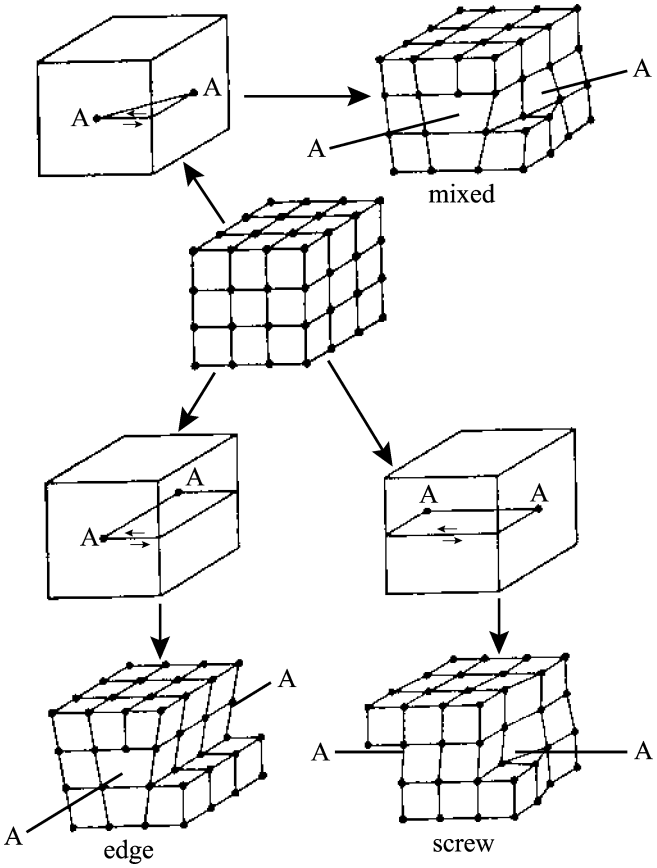

Fig. 7.5. Construction of a dislocation line with mixed character

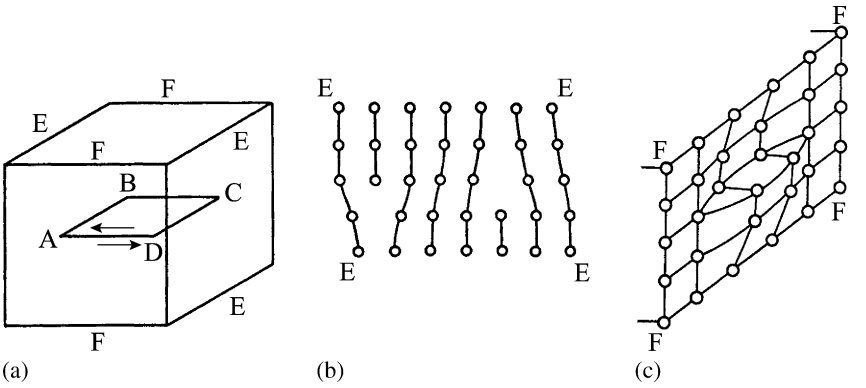

Fig. 7.6. A perfect dislocation loop in a crystal in which the character of the loop varies with position long the loop

A dislocation line can also be made in the form of a closed loop rather than a line that terminates at the crystal surface. Following Fig. 7.6, we make a cut along *ABCD* and shift the atoms parallel to the plane and then rejoin them. Note that segments *AB* and *DC* have edge character and segments *BC* and *AD* have screw character. Segments *AB* and *DC* have opposite sign in that one has a half plane above the cut and one has the half plane below it. The same is true with segments *BC* and *AD*. This loop is termed a *perfect* dislocation loop.

Now suppose that instead of shifting atoms parallel to the plane as we did in the example of a perfect loop, we fill up the cut with more atoms. The shift of atoms on each side of the cut is *perpendicular* to the surface. Figure 7.7 shows that by insertion of a disk of atoms into the cut, that every segment of the dislocation loop has pure edge character. This is very different from the perfect loop with edge and screw character. This dislocation loop is called a *prismatic* or *Frank* loop. One variation is to remove a disk of atoms from the cut rather than insert an extra plane of atoms.

7.1.1 Dislocation Motion

Dislocations can move in two modes: glide and climb. Glide is the motion of a dislocation on its slip plane and is conservative motion in that it requires no long-range mass transport in order to occur. Experiments have shown that the logarithm of the dislocation velocity is proportional to the logarithm of the shear stress causing glide:

$$\ln v_{\mathrm{g}} \alpha \ln \sigma_{\mathrm{s}} \,, \tag{7.2}$$

which implies a power law relationship between shear stress and dislocation velocity:

$$v_{\mathrm{g}} = \left(\frac{\sigma_{\mathrm{s}}}{\sigma_{\mathrm{D}}} \right)^{m} \,, \tag{7.3}$$

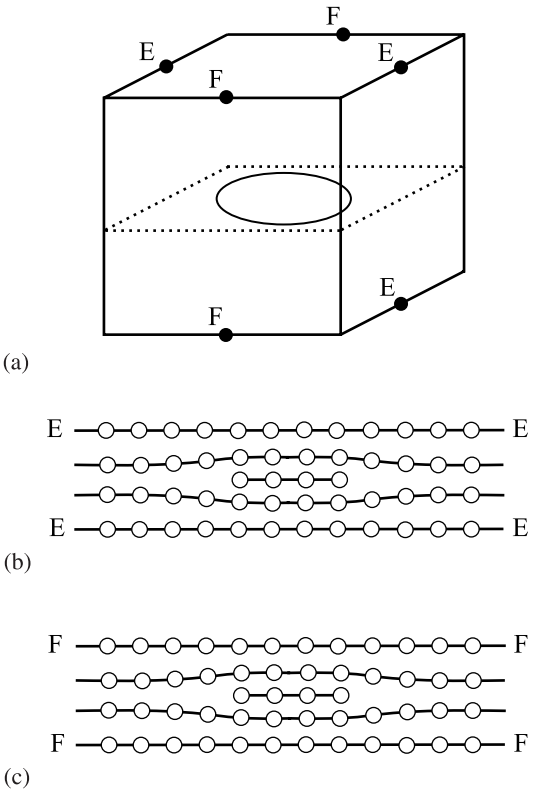

Fig. 7.7. A Frank dislocation loop formed by insertion of a circular plane of atoms between existing planes in the lattice

where m is the stress exponent (~ 1.65) and σ_D is the value of the stress that yields a dislocation velocity of 0.01 m/s [5]. Experiments also show that the logarithm of the dislocation velocity is proportional to the reciprocal of the absolute temperature, T:

$$\ln v_g \alpha \frac{1}{T} , \tag{7.4}$$

leading to the following description of the velocity of a gliding dislocation in terms of stress and temperature:

$$v_g = f(\sigma) \exp(-E/kT) . \tag{7.5}$$

When dislocations glide, they displace the crystal above the slip plane relative to that below. Figure 7.8 shows that if an edge dislocation glides to the surface, the result is a step on the surface of magnitude equal to the Burgers vector. Screw dislocations will also produce a step on the surface, but on a face that is perpendicular to the dislocation line (Fig. 7.9). The perfect loop described in the last section will also

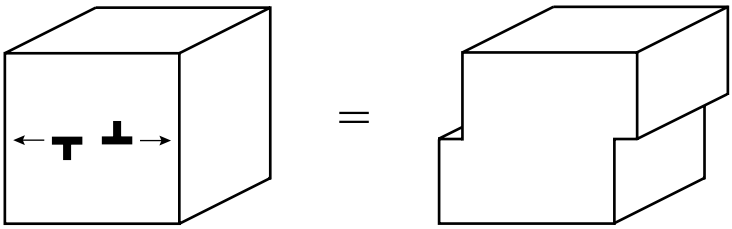

Fig. 7.8. Slip produced by movement of edge dislocations to the surface of a crystal

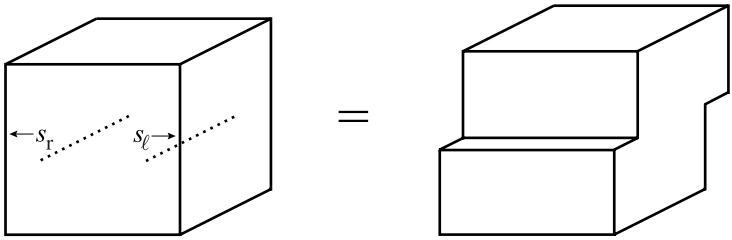

Fig. 7.9. Slip produced by movement of a screw dislocation to the surface of a crystal

result in displacement of the crystal when it reaches the surface. Figure 7.10 shows the displacement of the crystal above the slip plane relative to that below. Note that the displacements are entirely consistent with the character of the dislocation where it intersects the surface as shown in Figs. 7.8 and 7.9.

A Frank loop is essentially an edge dislocation. The slip plane for this type of loop is defined by the intersection of the loop edge and the adjacent crystal and consists of a cylindrical surface projecting above and below the plane of the loop. Figure 7.11 shows how surface atoms would be displaced if the loop were to glide to the surface. However, this mode of motion is not energetically favorable and this loop is more likely to move by climb rather than glide.

Dislocations also move by a non-conservative process called *climb*. Climb is an important process for edge dislocations and prismatic loops, since unlike screw dislocations that can glide on *any* plane containing the dislocation, there is only

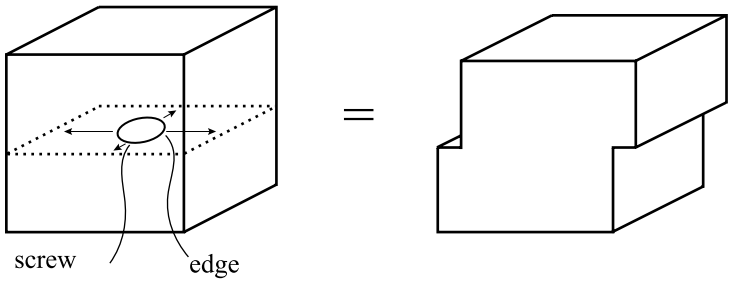

Fig. 7.10. Slip produced by movement of a perfect dislocation loop to the surface of a crystal

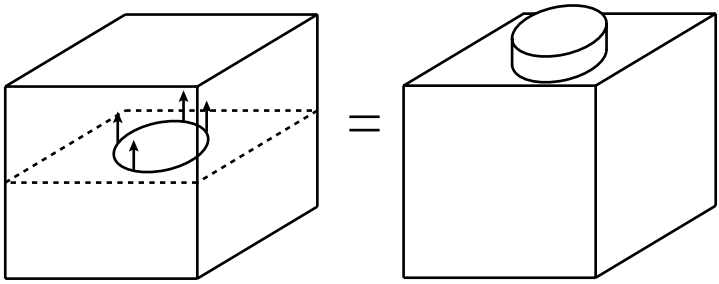

Fig. 7.11. Slip produced by movement of a Frank loop to the surface of a crystal

one possible slip plane for an edge dislocation to glide. Climb is the extension or recession of the extra half plane of atoms by absorption or emission of a vacancy, absorption of an interstitial atom or emission/absorption of clusters of vacancies or SIAs. Figure 7.12 shows the positive climb of an edge dislocation by absorption of a vacancy at the dislocation core. In order for the edge dislocation to move up one lattice spacing, all of the atoms along the edge (into the paper) must absorb a vacancy. Positive climb results in a decrease in the size of the extra half plane, while negative climb results in the increase in the size of the extra half plane. Positive climb is associated with a compressive strain and will be promoted by a compressive stress component perpendicular to the extra plane. Similarly, a tensile stress applied perpendicular to the extra plan promotes growth of the plane and thus, negative climb. Since they are essentially edge dislocations, Frank loops climb in the same manner, where positive climb results in loop shrinkage and negative climb results in loop growth. Note that there is a fundamental difference between the nature of the stress that produces slip and that which produces climb. Slip occurs as the result of shear stress, and climb occurs as a result of a normal stress.

Since climb requires that vacancies move through the lattice either to or away from the extra half plane, the rate of climb will be dependent on both the diffusion coefficient of vacancies and their concentration. In unirradiated solids, this means that climb will be most important at high temperature. However, in irradiated solids, the increased population of vacancies will make climb more important at lower tem-

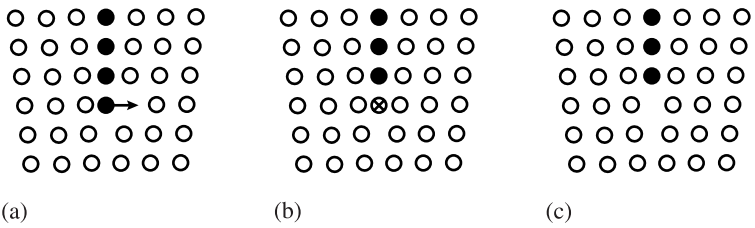

Fig. 7.12. Positive climb of an edge dislocation by absorption of vacancies at its core

peratures. Further, the elevated concentration of interstitials means that they too can contribute to climb in a direction that is opposite to that of vacancies.

7.1.2 Description of a Dislocation

A description of a dislocation consists of the specification of the vector defining the line direction, $\boldsymbol{s}$ and the Burgers vector defining the atom shift, $\boldsymbol{b}$. The Burgers vector is defined as follows:

1. Define a positive direction, $\boldsymbol{s}$, along the dislocation line (e.g., into the paper).
2. Construct a plane perpendicular to the dislocation line.
3. Starting in a region of perfect crystal (away from the dislocation core), complete a counterclockwise circuit around the dislocation line (in the plane of the paper)
4. The Burgers vector, $\boldsymbol{b}$ is the vector needed to close the circuit.

The rule is shown schematically in Fig. 7.13 for a screw dislocation. Following this convention, the Burgers vector of an edge dislocation is *perpendicular* to the dislocation line. The Burgers vector of a screw dislocation is *parallel* to the dislocation line.

For an edge dislocation, we can determine the Burgers vector in the following manner. Sighting down the dislocation line (along the positive $\boldsymbol{s}$ direction), we make a counterclockwise circuit around the dislocation. The vector connecting the end point to the origin is the Burgers vector. Figure 7.14 shows an example of the determination of the Burgers vector using the construction rule. (Note that it does not matter which direction is called positive, but we need to adopt a convention in order to determine the orientation of the line and the extra half plane in the crystal. If we sighted in the opposite direction, $\boldsymbol{b}$ will be in the opposite direction. What matters is the specification of $\boldsymbol{s}$ *relative to* $\boldsymbol{b}$.) Following the convention, Fig. 7.15a shows a dislocation with line direction, $\boldsymbol{s}$ pointing into the paper and $\boldsymbol{b}$ pointing to the left. The dislocation in Fig. 7.15b is identical to that in Fig. 7.15a since the relationship between $\boldsymbol{s}$ and $\boldsymbol{b}$ is the same. However, the dislocation shown in Fig. 7.15c is of opposite sign.

For a screw dislocation, we consider a left handed screw (counterclockwise rotation; see Fig. 7.16). With this convention, $\boldsymbol{s}$ and $\boldsymbol{b}$ are in the same direction. Figure 7.17a shows a screw dislocation with Burgers vector in the same direction as $\boldsymbol{s}$.

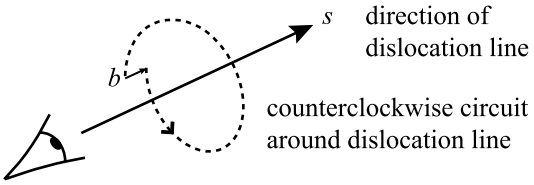

Fig. 7.13. Convention for finding the Burgers vector of a dislocation line characterized by direction $\boldsymbol{s}$

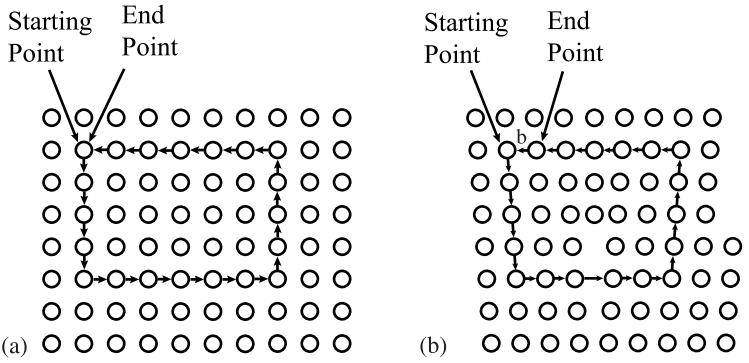

Fig. 7.14. The Burgers circuit for an edge dislocation following the convention shown in Fig. 7.13

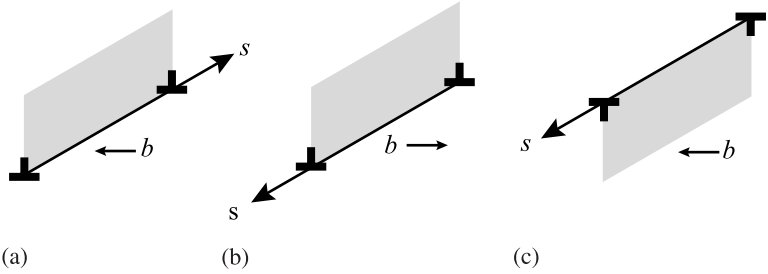

Fig. 7.15. Examples of identical edge dislocations (a) and (b) and an edge dislocation of opposite sign (c)

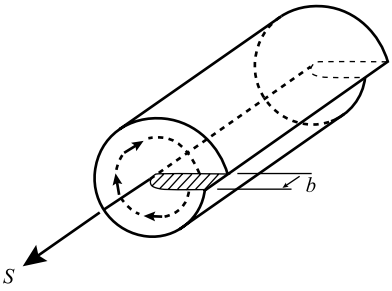

Fig. 7.16. The Burgers circuit for a screw dislocation following the convention shown in Fig. 7.13

The dislocation shown in Fig. 7.17b is identical to that in Fig. 7.17a, but the dislocation shown in Fig. 7.17c is of opposite sign as the other two.

An edge dislocation glides in the direction of its Burgers vector. A screw dislocation glides in a direction *perpendicular to* its Burgers vector. We adopt the following convention to determine the direction of motion of a dislocation line: *The positive direction of motion is obtained by a counterclockwise rotation on a plane parallel*

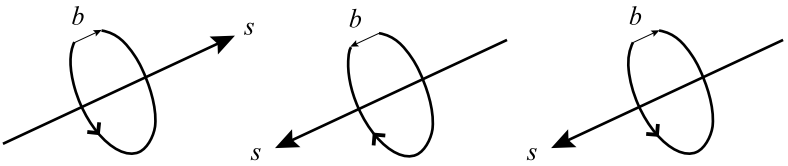

(a) (b) (c)

Fig. 7.17. Examples of identical screw dislocations (a) and (b), and a screw dislocation of opposite sign (c)

to the slip plane, *and through* 90° *from the positive direction of the dislocation line itself*. The rule is shown by the illustration in Fig. 7.18a. Figures 7.18b,c show the positive direction of motion for an edge and screw dislocation, respectively. Figure 7.19 shows the direction of motion for a dislocation loop that is characterized by a single Burgers vector (perfect loop) and changes character along the dislocation line.

7.1.3 Displacements, Strains and Stresses

Dislocations interact with each other and with other microstructure features through their stress fields. Therefore, it is important to establish the stress and strain fields around a dislocation as well as the energy associated with the dislocation line. We will begin with the screw dislocation and then treat the edge dislocation. Recall the orientation of the screw dislocation is one in which the Burgers vector is parallel to the dislocation line, which means that the displacement of atoms is in the direction of the dislocation line. If we describe the dislocation in cylindrical coordinates, Fig. 7.20, then there is no displacement along the r or θ directions so that:

$$u_r = u_\theta = 0 \,. \tag{7.6}$$

In Cartesian coordinates, the displacement in the x–y plane is zero. The only displacement is in the z-direction, and from inspection, we have in cylindrical coordinates:

$$u_z = \frac{b}{2\pi}\theta \,, \quad u_r = u_\theta = 0 \,, \tag{7.7}$$

and in Cartesian coordinates:

$$u_z = \frac{b}{2\pi}\tan^{-1}\frac{y}{x} \,, \tag{7.8}$$

where b is the magnitude of the Burgers vector. From elasticity theory, we can calculate the strain from the displacement as:

$$\varepsilon_{\theta z} = \frac{1}{r}\left(\frac{\partial u_z}{\partial \theta}\right) = \frac{b}{2\pi r} \,, \quad \varepsilon_{\mathrm{rr}} = \varepsilon_{\theta\theta} = \varepsilon_{zz} = \varepsilon_{r\theta} = \varepsilon_{rz} = 0 \,, \tag{7.9}$$

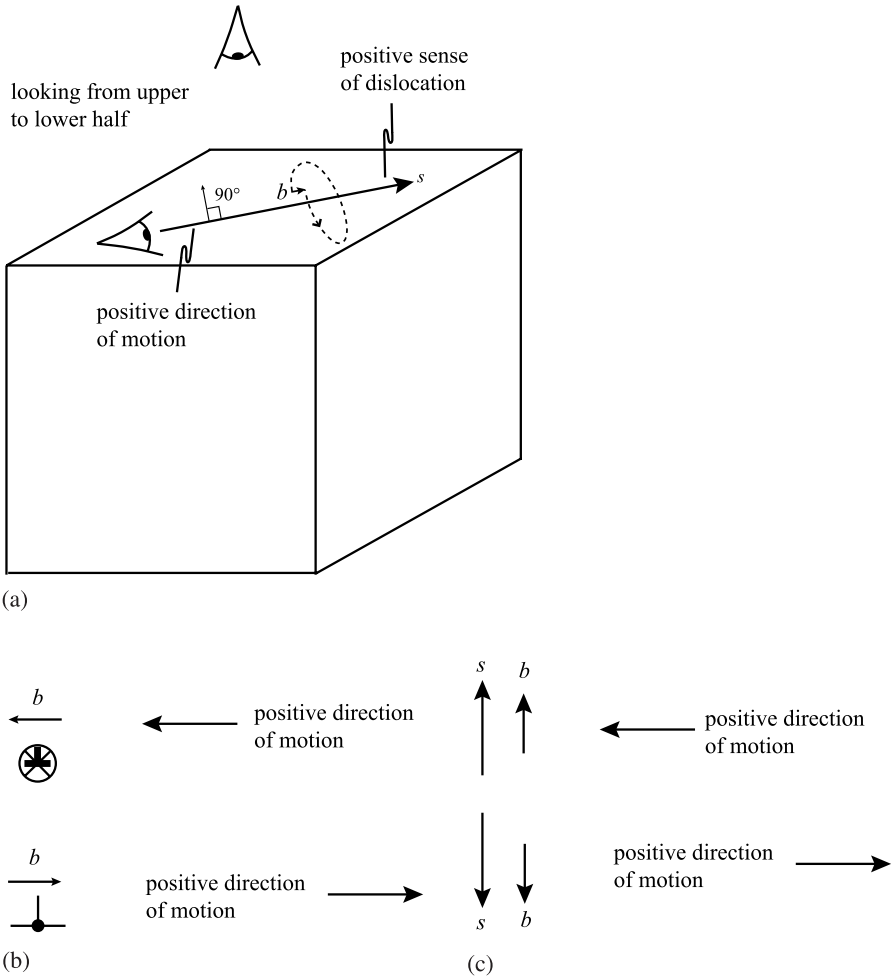

Fig. 7.18. (a) Rule for determination of the direction of motion of a dislocation on its slip plane and examples of the positive direction of motion for (b) edge and (c) screw dislocations

and in Cartesian coordinates:

$$\begin{aligned}
\varepsilon_{xz} &= \frac{b}{2\pi}\frac{y}{x^2+y^2} = \frac{b}{2\pi r}\sin\theta \\
\varepsilon_{yz} &= -\frac{b}{2\pi}\frac{x}{x^2+y^2} = -\frac{b}{2\pi r}\cos\theta \\
\varepsilon_{xx} &= \varepsilon_{yy} = \varepsilon_{zz} = \varepsilon_{xy} = 0\,.
\end{aligned} \tag{7.10}$$

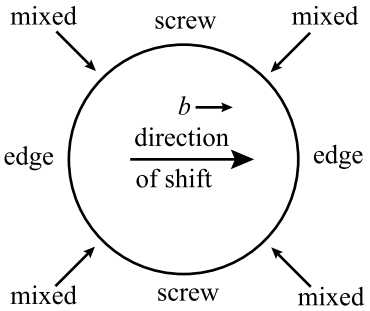

Fig. 7.19. Positive direction of motion of a perfect loop characterized by a single Burgers vector

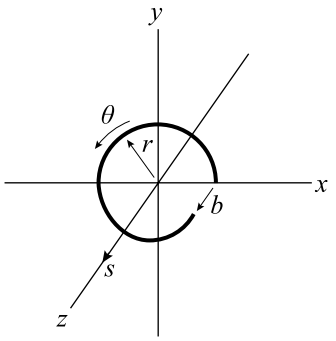

Fig. 7.20. Screw dislocation in the Cartesian coordinate system

The stress field of the screw dislocation is determined from the relation between stress and strain:

$$\sigma_{\theta z} = \mu \varepsilon_{\theta z} = \frac{\mu b}{2\pi r}\,, \quad \sigma_{rr} = \sigma_{\theta\theta} = \sigma_{zz} = \sigma_{r\theta} = \sigma_{rz} = 0\,, \tag{7.11}$$

and:

$$\begin{aligned} \sigma_{xz} &= \frac{\mu b}{2\pi}\frac{y}{x^2+y^2} = \frac{\mu b}{2\pi r}\sin\theta \\ \sigma_{yz} &= -\frac{\mu b}{2\pi}\frac{x}{x^2+y^2} = -\frac{\mu b}{2\pi r}\cos\theta \\ \sigma_{xx} &= \sigma_{yy} = \sigma_{zz} = \sigma_{xy} = 0\,. \end{aligned} \tag{7.12}$$

For an edge dislocation as shown in Fig. 7.21, the displacement of atoms is in the x-direction. The displacement is not so simple here, but we know that the dislocation will be similar at any point along the z-axis and hence, the stress state is one of plane stress. The displacement field around the edge dislocation in Cartesian coordinates is:

$$\begin{aligned} u_x &= \frac{b}{2\pi}\left[\tan^{-1}\frac{y}{x} + \frac{\lambda+\mu}{\lambda+2\mu}\frac{xy}{x^2+y^2}\right] \\ u_y &= \frac{b}{2\pi}\left[\frac{-\mu}{2(\lambda+2\mu)}\log\frac{x^2+y^2}{c} + \frac{\lambda+\mu}{\lambda+2\mu}\frac{y^2}{x^2+y^2}\right] \\ u_z &= 0\,, \end{aligned} \tag{7.13}$$

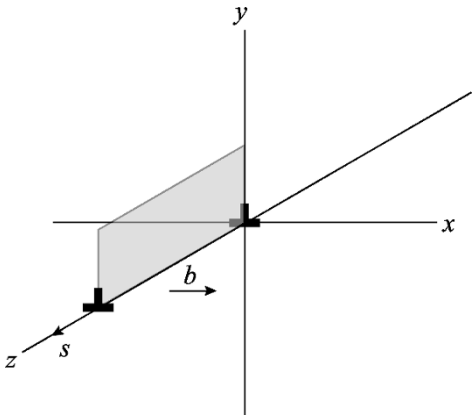

Fig. 7.21. Edge dislocation in the Cartesian coordinate system

where the constant c is added to make the log term dimensionless, but is irrelevant since stresses and strains are derivatives of the displacements. The resulting strains are:

$$\begin{aligned}
\varepsilon_{xx} &= -\frac{by}{2\pi}\frac{\mu y^2+(2\lambda+3\mu)x^2}{(\lambda+2\mu)(x^2+y^2)^2}\\
\varepsilon_{yy} &= \frac{by}{2\pi}\frac{(2\lambda+\mu)x^2-\mu y^2}{(\lambda+2\mu)(x^2+y^2)^2}\\
\varepsilon_{xy} &= \frac{b}{2\pi(1-\nu)}\frac{x(x^2-y^2)}{(x^2+y^2)^2}\\
\varepsilon_{zz} &= \varepsilon_{xz}=\varepsilon_{yz}=0\,,
\end{aligned} \tag{7.14}$$

where ν is Poisson's ratio, λ is the Lamé constant and $\nu = \dfrac{\lambda}{2(\lambda+\mu)}$. The stresses around an edge dislocation are then:

$$\begin{aligned}
\sigma_{xx} &= \frac{-\mu b}{2\pi(1-\nu)}\frac{y(3x^2+y^2)}{(x^2+y^2)^2} = \frac{-\mu b}{\pi(1-\nu)r}\sin\theta(2+\cos 2\theta)\\
\sigma_{yy} &= \frac{\mu b}{2\pi(1-\nu)}\frac{y(x^2-y^2)}{(x^2+y^2)^2} = \frac{\mu b}{\pi(1-\nu)r}\sin\theta\cos 2\theta\\
\sigma_{xy} &= -\frac{\mu b}{2\pi(1-\nu)}\frac{x(x^2-y^2)}{(x^2+y^2)^2} = \frac{\mu b}{\pi(1-\nu)r}\cos\theta\cos 2\theta\\
\sigma_{zz} &= \nu(\sigma_{xx}+\sigma_{yy}) = \frac{\mu\nu by}{\pi(1-\nu)(x^2+y^2)} = \frac{-2\mu\nu b}{\pi(1-\nu)r}\sin\theta\\
\sigma_{xz} &= \sigma_{yz}=0\,.
\end{aligned} \tag{7.15}$$

The stresses in cylindrical coordinates are:

$$\begin{aligned}
\sigma_{rr} &= \sigma_{\theta\theta} = \frac{\mu b}{2\pi(1-\nu)}\frac{\sin\theta}{r} \\
\sigma_{r\theta} &= \frac{-\mu b}{2\pi(1-\nu)}\frac{\cos\theta}{r} \\
\sigma_{zz} &= \frac{-\mu \nu b}{2\pi(1-\nu)}\frac{\sin\theta}{r} \\
\sigma_{\theta z} &= \sigma_{rz} = 0 \,.
\end{aligned} \tag{7.16}$$

7.1.4 Energy of a Dislocation

Energy is stored in any elastic medium that is stressed. Applying a tensile stress to a rod produces a tensile strain, which is proportional to the stress in an elastic solid. Consider a unit cube within the rod. A stress, σ is the total force applied across a face of the cube. The strain is the fractional distance the cube elongates in the direction of the stress. So the work done (energy/unit volume) on the cube is the force times the distance, or:

$$W = \int_0^{\varepsilon_{\max}} \sigma \, \mathrm{d}\varepsilon \,, \tag{7.17}$$

and from Fig. 7.22, we have:

$$W = 1/2 \sigma_{\max} \varepsilon_{\max} \,. \tag{7.18}$$

For a generalized stress field, the stored energy per unit volume is:

$$W = 1/2(\sigma_{xx}\varepsilon_{xx} + \sigma_{yy}\varepsilon_{yy} + \sigma_{zz}\varepsilon_{zz} + \sigma_{xy}\varepsilon_{xy} + \sigma_{xz}\varepsilon_{xz} + \sigma_{yz}\varepsilon_{yz}) \,, \tag{7.19}$$

and in cylindrical coordinates:

$$W = 1/2(\sigma_{rr}\varepsilon_{rr} + \sigma_{\theta\theta}\varepsilon_{\theta\theta} + \sigma_{zz}\varepsilon_{zz} + \sigma_{r\theta}\varepsilon_{r\theta} + \sigma_{rz}\varepsilon_{rz} + \sigma_{\theta z}\varepsilon_{\theta z}) \,, \tag{7.20}$$

where $\sigma_{ij} = \sigma_{ji}$.

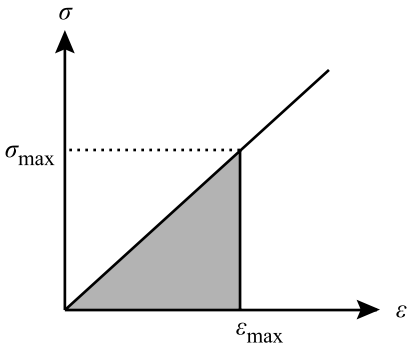

Fig. 7.22. Elastic stress-strain curve showing the stored energy in the strain field

Applying Eq. (7.20) to the screw dislocation gives:

$$W = 1/2(\sigma_{\theta z}\varepsilon_{\theta z}) = \frac{\mu b^2}{8\pi^2 r^2} \,. \tag{7.21}$$

The elastic energy per unit length of the dislocation line is:

$$E_l = \int_{r_c}^{R} W 2\pi r \,\mathrm{d}r = \frac{\mu b^2}{4\pi} \int_{r_c}^{R} \frac{\mathrm{d}r}{r} = \frac{\mu b^2}{4\pi} \ln\left(\frac{R}{r_c}\right) + \varepsilon_c \,. \tag{7.22}$$

The limits on the integral are the dislocation core radius, r_c, and R. The dislocation core radius is that distance below which linear elasticity does not hold and is generally taken to be several Burgers vectors in magnitude. R is the outer dimension of the crystal, or for polycrystalline materials, R could be taken to be the grain radius. However, a further constraining condition is the presence of other dislocations, which is the case even in a well-annealed metal in which the dislocation density is still $\sim 10^8\,\mathrm{cm}^{-2}$. So R is often taken to be the distance midway to the next dislocation. However, the elastic energy is not highly sensitive to R since it appears in the ln term. The term ε_c is the energy of the dislocation core radius, which is not included in the integral since linear continuum elasticity theory breaks down in this region. Assuming that the stress level in the core is $\mu/30$, then for a dislocation core radius of $5b$, the value of ε_c is approximately $\mu b^2/10$, which is about 10–20% of the value of that in the elastic strain field (ln term).

For an edge dislocation, the elastic energy per unit length determined in the same way as for the screw dislocation is:

$$E_l = \frac{\mu b^2}{4\pi(1-\nu)} \ln\left(\frac{R}{r_c}\right) + \varepsilon_c \,, \tag{7.23}$$

which is different from the screw dislocation by a factor of $(1-\nu)$ in the denominator of the first term, or a factor of about 1.6 for $\nu \sim 0.3$. For typical values of R and r_c, $\frac{\mu b^2}{2} \le E_l \le \mu b^2$. The elastic energy per unit length of dislocation line is also called the line tension and is denoted by Γ. Generally, Γ is taken to have the value $\frac{\mu b^2}{2}$.

7.1.5 Line Tension of a Dislocation

Under a uniform applied shear stress, σ_s, an element of dislocation line, $\mathrm{d}s$, is displaced in a direction normal to $\mathrm{d}s$ by an amount $\mathrm{d}l$ (Fig. 7.23). The area swept out by the dislocation line element, $\mathrm{d}s$, is $\mathrm{d}s\,\mathrm{d}l$. The average displacement of the crystal above the slip plane relative to that below is by an element:

$$\mathrm{d}x = \left(\frac{\mathrm{d}s\,\mathrm{d}l}{A}\right) b \,, \tag{7.24}$$

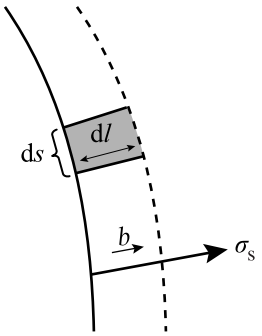

Fig. 7.23. Dislocation line segment ds sweeping out an area ds dl in the direction of the Burgers vector

where A is the area of the slip plane. The force creating the shear stress is $\sigma_s A$, and the work done is:

$$\begin{aligned} \mathrm{d}W = F\,\mathrm{d}x &= \sigma_s A\left(\frac{\mathrm{d}s\,\mathrm{d}l}{A}\right)b \\ &= \sigma_s\,\mathrm{d}s\,\mathrm{d}l b\,. \end{aligned} \tag{7.25}$$

Since force is work divided by the distance over which it is applied:

$$F = \frac{\mathrm{d}W}{\mathrm{d}l} = \sigma_s\,\mathrm{d}s b\,, \tag{7.26}$$

and the force per unit length is:

$$F_l = \frac{\mathrm{d}W/\mathrm{d}l}{\mathrm{d}s} = \sigma_s b\,. \tag{7.27}$$

Consider a curved dislocation line. The line tension produces an inward radial force that tends to straighten out the dislocation line. The dislocation will only remain curved if a shear stress exists to resist the line tension. We wish to determine the shear stress required to maintain the curvature. Consider a segment of a dislocation line as shown in Fig. 7.24. The outward force due to the shear stress is:

$$\sigma_s b\,\mathrm{d}s = 2\sigma_s b R\,\mathrm{d}\theta\,. \tag{7.28}$$

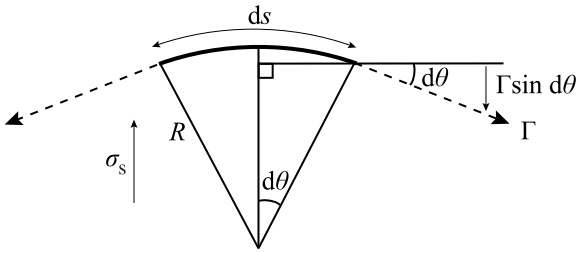

Fig. 7.24. Inward restraining force on a dislocation line segment ds due to a shear stress σ_s

The inward restraining force is:

$$\Gamma \sin(\mathrm{d}\theta) \sim 2\Gamma\,\mathrm{d}\theta\ . \tag{7.29}$$

From Eqs. (7.28) and (7.29) we have the force balance:

$$2\Gamma\,\mathrm{d}\theta = 2\sigma_{\mathrm{s}} bR\,\mathrm{d}\theta\ , \tag{7.30}$$

and solving for σ_{s} yields the shear stress in terms of the line tension:

$$\sigma_{\mathrm{s}} = \frac{\Gamma}{bR}\ . \tag{7.31}$$

For:

$$\Gamma \approx \frac{\mu b^2}{2}\ , \quad \text{then} \quad \sigma_{\mathrm{s}} = \frac{\mu b}{2R}\ , \tag{7.32a}$$

and for

$$\Gamma \approx \mu b^2\ , \quad \text{then} \quad \sigma_{\mathrm{s}} = \frac{\mu b}{R}\ . \tag{7.32b}$$

One mechanism of formation of dislocations in solids is the Frank–Read mechanism. The mechanism is shown in Fig. 7.25 and occurs as follows. A dislocation line segment defined by *ABCD* and Burgers vector $\boldsymbol{b}$ is such that segments *AB* and *DC* are immobile and only segment *BC* lies in a slip plane. The dislocation segment *BC* is pinned at the points *B* and *C*. The temperature is assumed to be low enough that that climb is not an option. Under an applied stress, the segment BC bows out slightly in response to the stress and adopts the curvature as prescribed by the line tension on the dislocation given in Eq. (7.32b) $\sigma_{\mathrm{s}} = \dfrac{\mu b}{2R}$, and for $l = 2R$, $\sigma_{\mathrm{s}} \approx \dfrac{\mu b}{l}$. When the force arising from the curvature of the dislocation line can no longer balance the force produced by the applied stress, becomes unstable and bows out to adopt the configuration shown in Fig. 7.25c. Note that at this point, the line segments *P* and *P′* have opposite character and as the dislocation continues to bow out they come in contact with each other and annihilate, leaving a region of perfect crystal and a perfect loop. The applied shear stress will cause the loop to expand and will also start the process of creating a new loop from the same *BC* segment. This process can continue to occur and one such pinned dislocation can produce many loops and will continue as long as the loops are able to expand away from the source. Figure 7.26 shows a micrograph of a Frank–Reed source in a silicon crystal. Eventually, the back stress caused by the previous loops will produce a retarding force on the source and it will shut down. Back stress due to dislocation pileup is discussed in Chap. 12.

7.1.6 Forces on a Dislocation

Application of a shear stress, σ_{xy}, on a solid containing an edge dislocation (Fig. 7.27) produces motion in the $+x$ direction. In moving a dislocation a distance *L*, the external applied stress will have done an amount of work/unit length of

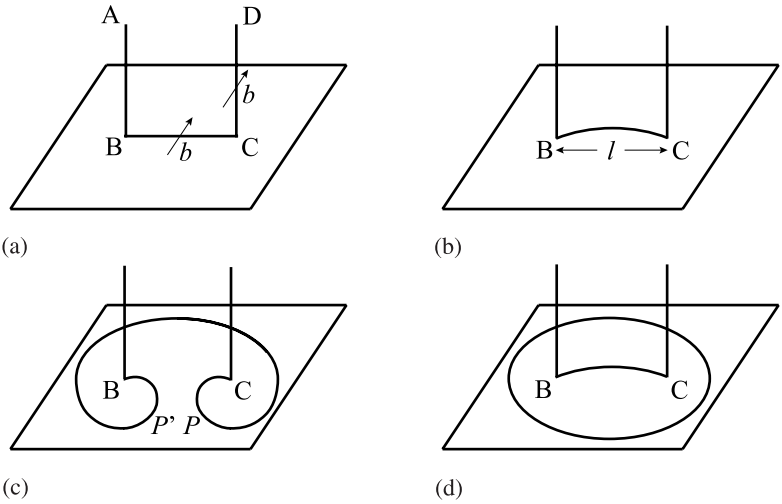

Fig. 7.25. Frank–Read source for the production of dislocations

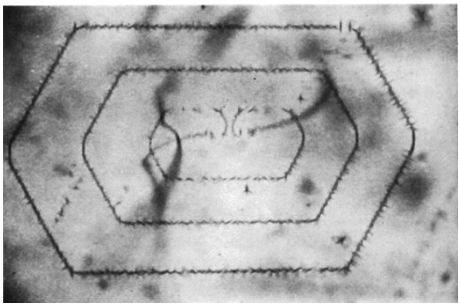

Fig. 7.26. Micrograph of a Frank–Read source in a silicon crystal (from [6])

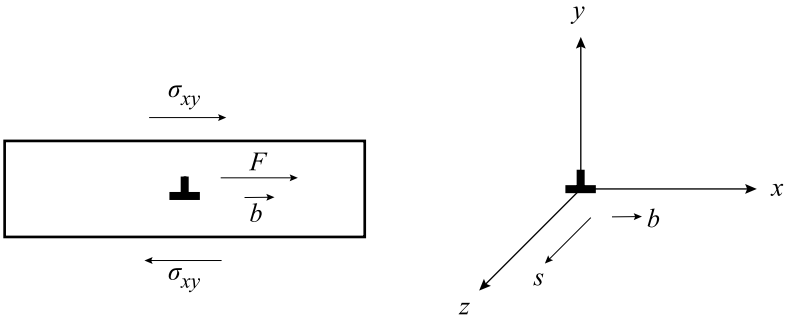

Fig. 7.27. Force on an edge dislocation with character $\boldsymbol{s}|001|$, $\boldsymbol{b}|100|$ due to a shear stress σ_{xy}

dislocation line equal to $\sigma_{xy}bL$. Then the force is $F = \sigma_{xy}b$. Note that the force is in the $+x$ direction.

For a screw dislocation, application of a shear stress, σ_{yz}, results in a force $\sigma_{yz}b$, where the force is in the $+x$ direction (Fig. 7.28). Application of a shear stress σ_{xz} produces a force $-\sigma_{xz}b$, where the force is in the $-y$ direction, and motion is perpendicular to the slip plane.

What if we apply a stress to an edge dislocation that produces a force in a direction perpendicular to the slip plane? A tensile stress, σ_{xx}, applied to the edge dislocation in Fig. 7.29 will produce a downward force on the dislocation equal to $-\sigma_{xx}b$. The only way that the dislocation can respond to this stress is to climb.

Forces on mixed dislocations are more complicated. If a dislocation is oriented along the $+z$-direction and its slip plane is perpendicular to the y-axis, then the Burgers vector can be described by:

$$\boldsymbol{b} = b_x\boldsymbol{i} + b_z\boldsymbol{k}\,, \tag{7.33}$$

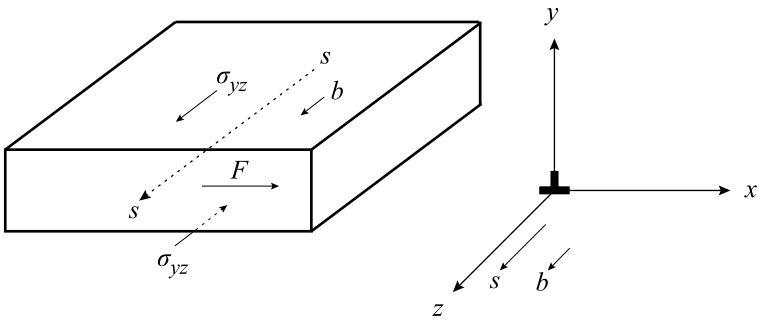

Fig. 7.28. Force on a screw dislocation with character $\boldsymbol{s}|001|$, $\boldsymbol{b}|001|$ due to a shear stress σ_{yz}

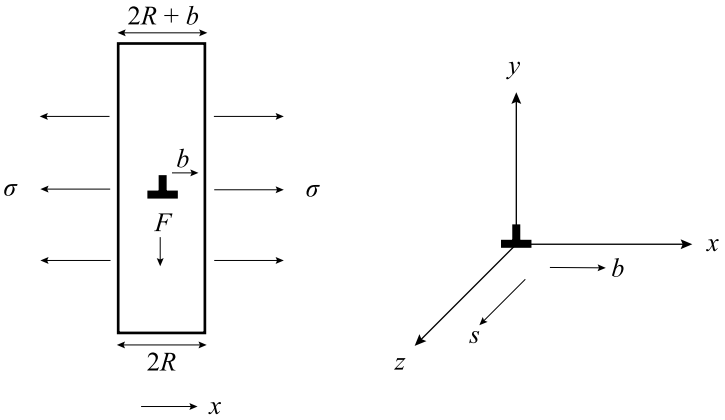

Fig. 7.29. Force on an edge dislocation with character $\boldsymbol{s}|001|$, $\boldsymbol{b}|100|$ due to a normal stress σ_{xx}

where b_x and b_z are edge and screw components of the Burgers vector and $\boldsymbol{i}$ and $\boldsymbol{k}$ are unit vectors in the x and z-directions, respectively. An external stress placed on the surfaces of a crystal containing a dislocation includes six components; $\sigma_{xx}, \sigma_{yy}, \sigma_{zz}, \sigma_{xy}, \sigma_{xz}$ and σ_{yz}. Of these six stress components, only σ_{yz} and σ_{xy} can exert a force on an edge dislocation that will cause motion *in* the slip plane. Stress components σ_{xz} and σ_{xx} causes motion perpendicular to the slip plane. The term σ_{zz} does no work, nor does σ_{yy}. The total force on a unit length of dislocation line is then:

$$\boldsymbol{F} = (\sigma_{xy} b_x + \sigma_{yz} b_z)\boldsymbol{i} - (\sigma_{xx} b_x + \sigma_{xz} b_z)\boldsymbol{j} \,, \tag{7.34}$$

where the first term is the force component parallel to the slip plane and the second term is the force component normal to the slip plane, and $\boldsymbol{n} = (i, j, k)$ defines the unit vector.

As an example of forces between dislocations, let us take the case of parallel screw dislocations. The force, $\boldsymbol{F}$ that a screw dislocation situated at the origin (with Burgers vector $\boldsymbol{b}$) exerts on a parallel screw dislocation at a position (r, θ) (with Burgers vector $\boldsymbol{b}'$) is:

$$\begin{aligned} \boldsymbol{F} &= \sigma_{yz} b_z \cdot \boldsymbol{i} - \sigma_{xz} b_z \cdot \boldsymbol{j} \\ &= \frac{\mu b r \cos\theta}{2\pi r^2} b' + \frac{\mu b r \sin\theta}{2\pi r^2} b' \\ &= \frac{\mu b b' r}{2\pi r^2} (\cos\theta \cdot \boldsymbol{i} + \sin\theta \cdot \boldsymbol{j}) \,. \end{aligned} \tag{7.35}$$

The force is in a direction that is perpendicular to the dislocation lines. It is repulsive if the dislocations are of the same sign, and attractive if the dislocations are of opposite sign. The force on the dislocation at the origin due to the dislocation at (r, θ) is equal in magnitude but opposite in sign from the force on the dislocation at (r, θ) due to that at the origin. The force components in the xy-plane are shown in Fig. 7.30a and the magnitude of the forces as a function of θ are shown in Fig. 7.30b.

A dislocation of mixed character represents the generalized case of a force on a dislocation. For a mixed dislocation, the Burgers vector is:

$$\begin{aligned} \boldsymbol{b} &= b_x \boldsymbol{i} + b_y \boldsymbol{j} + b_z \boldsymbol{k} \\ &= b_1 \boldsymbol{i} + b_2 \boldsymbol{j} + b_3 \boldsymbol{k} \,. \end{aligned} \tag{7.36}$$

Therefore, we write the incremental work done on a dislocation of Burgers vector described by Eq. (7.36) due to an arbitrary stress σ_{ij}, as:

$$\delta W = \sum_{\substack{i=1 \\ j=1}}^{3} b_i \sigma_{ij} n_j \, \mathrm{d}A \,, \tag{7.37}$$

or in matrix notation:

$$\mathrm{d}W = \underline{b}\,\underline{\underline{\sigma}}\,\underline{n}\,\mathrm{d}A \,, \tag{7.38}$$

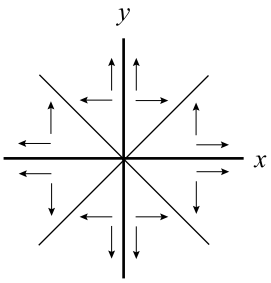

(a)

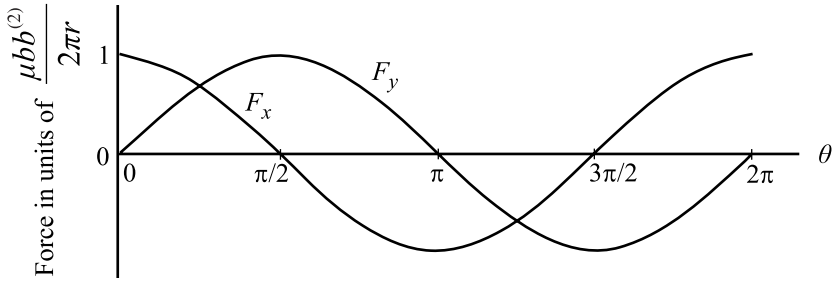

(b)

Fig. 7.30. The x and y-components of the force on a screw dislocation due to another dislocation (a) in the x–y plane, and (b) as a function of θ

where $\underline{\underline{\sigma}}$ is the stress tensor, $\underline{n}$ is the unit vector perpendicular to the slip plane and $\underline{b}$ is the Burgers vector. Actually, $\underline{b}$ is a column vector so that Eq. (7.38) is written as:

$$\mathrm{d}W = \underline{\boldsymbol{b}}^T \underline{\underline{\sigma}} \cdot \underline{n}\,\mathrm{d}A\,. \tag{7.39}$$

The term $\underline{n}\,\mathrm{d}A$ can be written as $\mathrm{d}\boldsymbol{A}$ which is just

$$L(\boldsymbol{s} \times \mathrm{d}\boldsymbol{l})\,, \tag{7.40}$$

where $\boldsymbol{s}$ is the unit vector in the direction of the dislocation line, L is the length of the dislocation line and $\mathrm{d}\boldsymbol{l}$ $(= \mathrm{d}x\boldsymbol{i} + \mathrm{d}y\boldsymbol{j} + \mathrm{d}z\boldsymbol{k})$ is the unit vector in the slip plane and is normal to $\boldsymbol{s}$ and $\boldsymbol{n}$. Recall that $\boldsymbol{b} = b_x\boldsymbol{i} + b_y\boldsymbol{j} + b_z\boldsymbol{k}$, so $\boldsymbol{b}$ has a component only in the direction $\mathrm{d}\boldsymbol{l}$. Since $\boldsymbol{A} \cdot \boldsymbol{B} \times \boldsymbol{C} = \boldsymbol{A} \times \boldsymbol{B} \cdot \boldsymbol{C}$, then:

$$\mathrm{d}W = \underline{\boldsymbol{b}}^{\boldsymbol{T}} \underline{\underline{\sigma}} \times \boldsymbol{s} \cdot \mathrm{d}\boldsymbol{l}L\,, \tag{7.41}$$

and:

$$\frac{1}{L}\mathrm{d}W = \underline{\boldsymbol{b}}^{\boldsymbol{T}} \underline{\underline{\sigma}} \times \boldsymbol{s} \cdot \mathrm{d}\boldsymbol{l}\,. \tag{7.42}$$

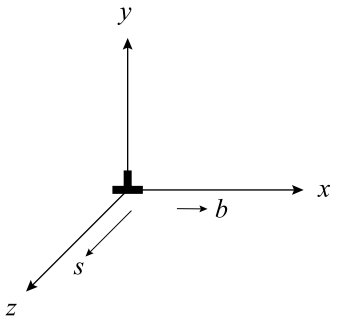

Fig. 7.31. Orientation of an edge dislocation for the determination of the forces due to a generalized stress field

The term $\underline{\boldsymbol{b}}^{\boldsymbol{T}}\underline{\underline{\sigma}}\times\boldsymbol{s}$ in Eq. (7.42) is the force per unit length on a dislocation due to an external stress which tends to displace the dislocation, and is designated:

$$\boldsymbol{f}=\underline{\boldsymbol{b}}^{\boldsymbol{T}}\underline{\underline{\sigma}}\times\boldsymbol{s}\,, \tag{7.43}$$

and is known as the *Peach–Koehler* equation.

Let us apply the Peach–Koehler equation to the case of an edge dislocation described by Burgers vector and direction: $b\begin{vmatrix}1\\0\\0\end{vmatrix}$ and $s\begin{vmatrix}0\\0\\1\end{vmatrix}$ and shown in Fig. 7.31. We write the first quantity in Eq. (7.43) as:

$$\underline{\boldsymbol{b}}^{\boldsymbol{T}}\underline{\underline{\sigma}}=b|100|\begin{vmatrix}\sigma_{xx}&\sigma_{xy}&\sigma_{xz}\\\sigma_{yx}&\sigma_{yy}&\sigma_{yz}\\\sigma_{zx}&\sigma_{zy}&\sigma_{zz}\end{vmatrix}=b|\sigma_{xx}\sigma_{xy}\sigma_{xz}|\,, \tag{7.44}$$

and then taking the cross product with $\boldsymbol{s}$ gives:

$$\underline{\boldsymbol{b}}^{\boldsymbol{T}}\underline{\underline{\sigma}}\times\boldsymbol{s}=b\begin{vmatrix}\boldsymbol{i}&\boldsymbol{j}&\boldsymbol{k}\\\sigma_{xx}&\sigma_{xy}&\sigma_{xz}\\0&0&1\end{vmatrix}\,. \tag{7.45}$$

The cross product, or determinant is $b\sigma_{xy}\boldsymbol{i}-b\sigma_{xx}\boldsymbol{j}$, and the force on the dislocation is:

$$\boldsymbol{f}=b\sigma_{xy}\boldsymbol{i}-b\sigma_{xx}\boldsymbol{j}\,. \tag{7.46}$$

Note that $f_x=b\sigma_{xy}$ is a *glide* force in the $+x$-direction and the force component $f_y=-b\sigma_{xx}$ is the *climb* force in the $-y$-direction. Only σ_{xy} and σ_{xx} can exert forces on a dislocation with Burgers vector and direction defined as in this example.

For a screw dislocation with Burgers vector and direction given by: $b\begin{vmatrix}0\\0\\1\end{vmatrix}$ and $s\begin{vmatrix}0\\0\\1\end{vmatrix}$, and shown in Fig. 7.32, we have:

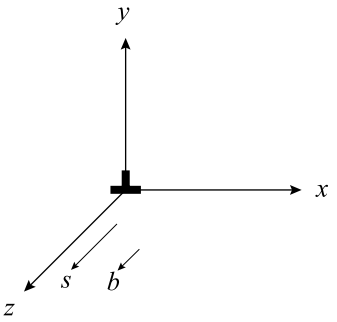

Fig. 7.32. Orientation of a screw dislocation for the determination of the forces due to a generalized stress field

$$\underline{\boldsymbol{b}}^{\boldsymbol{T}}\,\underline{\underline{\sigma}} = b|001|\begin{vmatrix}\sigma_{xx} & \sigma_{xy} & \sigma_{xz}\\ \sigma_{yx} & \sigma_{yy} & \sigma_{yz}\\ \sigma_{zx} & \sigma_{zy} & \sigma_{zz}\end{vmatrix} = b|\sigma_{xz}\sigma_{yz}\sigma_{zz}|\,, \tag{7.47}$$

and then taking the cross product with $\boldsymbol{s}$ gives:

$$\boldsymbol{f} = \underline{\boldsymbol{b}}^{\boldsymbol{T}}\,\underline{\underline{\sigma}} \times \boldsymbol{s} = b\begin{vmatrix}\boldsymbol{i} & \boldsymbol{j} & \boldsymbol{k}\\ \sigma_{xz} & \sigma_{yz} & \sigma_{zz}\\ 0 & 0 & 1\end{vmatrix} = b\sigma_{yz}\boldsymbol{i} - b\sigma_{xz}\boldsymbol{j}\,, \tag{7.48}$$

and $f_x = b\sigma_{yz}$ and $f_y = -b\sigma_{xz}$. Note that only σ_{yz} and σ_{xz} can exert a force on a dislocation defined in this example.

7.1.7 Interactions Between Dislocations

Let us examine interactions between dislocations. We will look at edge–edge, screw–screw, and edge–screw interactions. We will begin with the edge–edge interaction.

Edge–edge interaction

To find the force on dislocation (2) due to the presence of dislocation (1), we locate dislocation (1) at the origin of our coordinate axes and dislocation (2) at some arbitrary position (Fig. 7.33a). According to the Peach–Koehler equation, the force is: $\boldsymbol{f} = \underset{(2)}{\underline{\boldsymbol{b}}}^{\,T}\,\underset{(1)}{\underline{\underline{\sigma}}} \times \underset{(2)}{\boldsymbol{s}}$, where the Burgers vector and direction are those of dislocation (2), and the stress is due to dislocation (1). The first term in the cross product then becomes:

$$\underline{\boldsymbol{b}}^{\boldsymbol{T}}\,\underline{\underline{\sigma}} = \underbrace{b|100|}_{(2)}\underbrace{\begin{vmatrix}\sigma_{xx} & \sigma_{xy} & 0\\ \sigma_{yx} & \sigma_{yy} & 0\\ 0 & 0 & \sigma_{zz}\end{vmatrix}}_{(1)} = b|\sigma_{xx}\sigma_{xy}0|;, \tag{7.49}$$

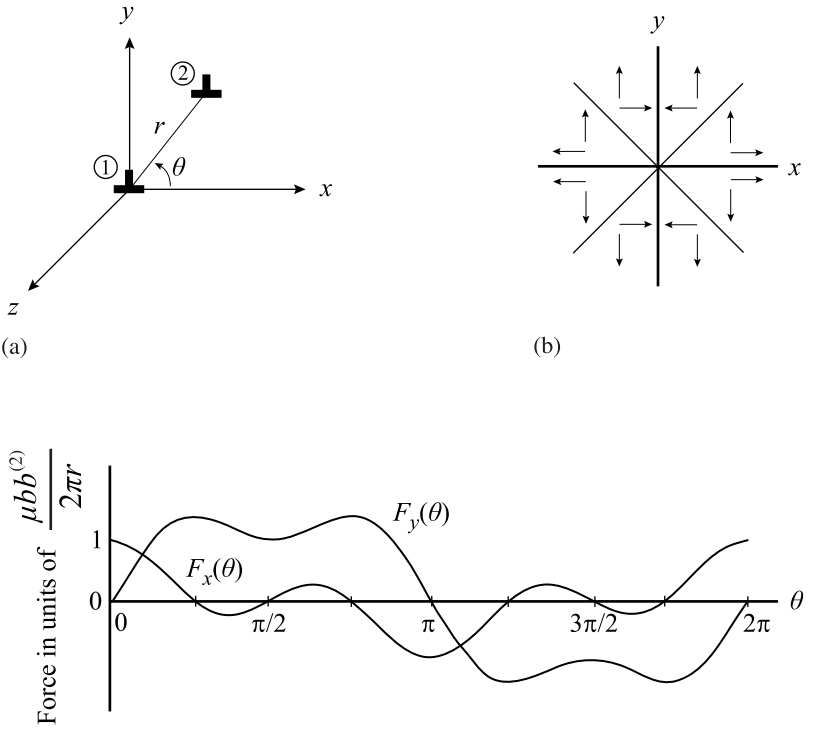

Fig. 7.33. (a) Orientation of dislocations to determine the force on edge dislocation (*2*) due to edge dislocation (*1*), and *x* and *y*-components of the force (b) in the *x*–*y* plane, and (c) as a function of θ

and

$$\boldsymbol{f} = \underline{\boldsymbol{b}}^{\boldsymbol{T}}\,\underline{\underline{\boldsymbol{\sigma}}} \times \underset{(2)}{\boldsymbol{s}} = b \begin{vmatrix} \boldsymbol{i} & \boldsymbol{j} & \boldsymbol{k} \\ \sigma_{xx} & \sigma_{xy} & 0 \\ 0 & 0 & 1 \end{vmatrix} = b\sigma_{xy}\boldsymbol{i} - b\sigma_{xx}\boldsymbol{j}\,. \tag{7.50}$$

The force on dislocation (2) can be written as:

$$\boldsymbol{F} = \underbrace{\frac{\mu b b^{(2)}}{2\pi(1-\nu)r}(\cos\theta\cos 2\theta)\boldsymbol{i}}_{F_x(\theta)} - \underbrace{\frac{\mu b b^{(2)}}{2\pi(1-\nu)r}\sin\theta(2+\cos 2\theta)\boldsymbol{j}}_{F_y(\theta)}\,, \tag{7.51}$$

and the force components in the *x*–*y* plane are shown in Fig. 7.33b, and as a function of θ in Fig. 7.33c.

Note that if dislocation (2) has the same $\boldsymbol{s}$ but the Burgers vector is in the opposite direction, then the net effect on the resultant force is simply a change in sign of

each of the terms in Eq. (7.51) but preservation of the magnitudes. If dislocation (2) has Burgers vector $b\begin{vmatrix}0\\1\\0\end{vmatrix}$, then the preceding analysis becomes:

$$\underset{(2)}{\underline{\boldsymbol{b}}^{\boldsymbol{T}}}\,\underline{\underline{\boldsymbol{\sigma}}} = \underbrace{b|010|}_{(2)}\underbrace{\begin{vmatrix}\sigma_{xx} & \sigma_{xy} & 0\\ \sigma_{yx} & \sigma_{yy} & 0\\ 0 & 0 & \sigma_{zz}\end{vmatrix}}_{(1)} = b|\sigma_{xy}\sigma_{yy}0|\,, \tag{7.52}$$

$$\boldsymbol{f} = \underset{(2)}{\underline{\boldsymbol{b}}^{\boldsymbol{T}}}\,\underline{\underline{\boldsymbol{\sigma}}}\times\underset{(2)}{\boldsymbol{s}} = b\begin{vmatrix}\boldsymbol{i} & \boldsymbol{j} & \boldsymbol{k}\\ \sigma_{xy} & \sigma_{yy} & 0\\ 0 & 0 & 1\end{vmatrix} = b\sigma_{yy}\boldsymbol{i} - b\sigma_{xy}\boldsymbol{j}\,. \tag{7.53}$$

In this case, the x-component of the force produces a positive climb force to the right, and the y-component of the force produces a negative (downward) glide force.

Screw–screw interaction

For two screw dislocations as shown in Fig. 7.34, the force on dislocation (2) due to dislocation (1) is:

$$\boldsymbol{f} = \underset{(2)}{\underline{\boldsymbol{b}}^{\boldsymbol{T}}}\,\underline{\underline{\boldsymbol{\sigma}}}\times\underset{(2)}{\boldsymbol{s}} = b\begin{vmatrix}\boldsymbol{i} & \boldsymbol{j} & \boldsymbol{k}\\ \sigma_{xz} & \sigma_{yz} & 0\\ 0 & 0 & 1\end{vmatrix} = b\sigma_{yz}\boldsymbol{i} - b\sigma_{xz}\boldsymbol{j}\,, \tag{7.54}$$

where the x-component of the force, $b\sigma_{yz}$ is to the right, and the y-component of the force, $-b\sigma_{xz}$ is downward in Fig. 7.34. The force on dislocation (2) can be written as:

$$\boldsymbol{F} = \frac{\mu b b^{(2)}}{2\pi r}\cos\theta\boldsymbol{i} + \sin\theta\boldsymbol{j}\,, \tag{7.55}$$

and the force components in the x–y plane have already been shown in Fig. 7.30a, and as a function of θ in Fig. 7.30b.

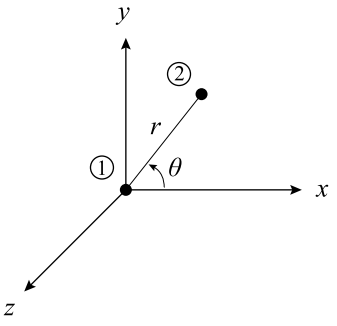

Fig. 7.34. Orientation of dislocations to determine the force on screw dislocation (*2*) due to screw dislocation (*1*)

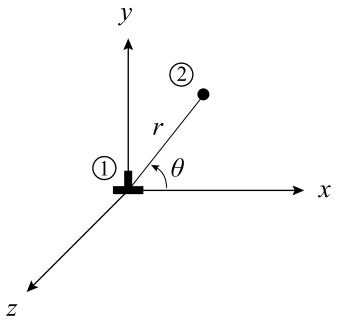

Fig. 7.35. Orientation of dislocations to determine the force on screw dislocation (*2*) due to edge dislocation (*1*)

Edge–screw interaction

The last example is the determination of the force between an edge and a screw dislocation as defined in Fig. 7.35. We know that an edge dislocation has no xz or yz stress components, which are needed to move a screw dislocation. So we can state the following rules: For an edge dislocation with $b \begin{vmatrix} 1 \\ 0 \\ 0 \end{vmatrix}$ and $s \begin{vmatrix} 0 \\ 0 \\ 1 \end{vmatrix}$, the only stresses that produce a force on it are σ_{xx} and σ_{xy}. The stress field around the dislocation has components σ_{xx}, σ_{yy}, σ_{zz} and σ_{xy}. For a screw dislocation with $b \begin{vmatrix} 0 \\ 0 \\ 1 \end{vmatrix}$ and $s \begin{vmatrix} 0 \\ 0 \\ 1 \end{vmatrix}$, the only stresses that produce a force on it are σ_{xz} and σ_{yz}. The stress field around the dislocation has components σ_{xz} and σ_{yz}.

7.1.8 Extended Dislocations

Slip occurs in the fcc lattice on (111) planes and in the $\langle 110 \rangle$ direction. The Burgers vector is $a/2[110]$, which is the shortest lattice vector connecting an atom at the cube corner with a neighboring atom at the center of a cube face. However, the atom arrangement on the $\{111\}$ slip plane is such that slip in the [110] direction is not the easiest path. Figure 7.36a shows the atom arrangement on a close-packed (111) plane. The $\{111\}$ planes are stacked in the sequence ABC ABC…, such that the centers of the A plane of atoms fall on top of each other, and similarly for the B and C planes of atoms. The vector $b_1 = a/2[10\bar{1}]$ shown in Fig. 7.36a is the observed slip direction. However, if atoms are considered as hard spheres, this direction represents a high-energy path as atoms moving from one B site to another must climb over the A atoms. A simpler path is by way of vectors b_2 and b_3, which is along the "valleys" between the A atoms. This dislocation reaction is given by: $b_1 \rightarrow b_2 + b_3$, $a/2[10\bar{1}] \rightarrow a/6[2\bar{1}\bar{1}] + a/6[11\bar{2}]$. Essentially, the Burgers vector, b_1 of the total dislocation has been dissociated into two *partial dislocations* b_2 and b_3. Figure 7.36b shows the atom arrangement of the partial dislocations on the $\{111\}$ plane and Fig. 7.36c shows the vector diagram

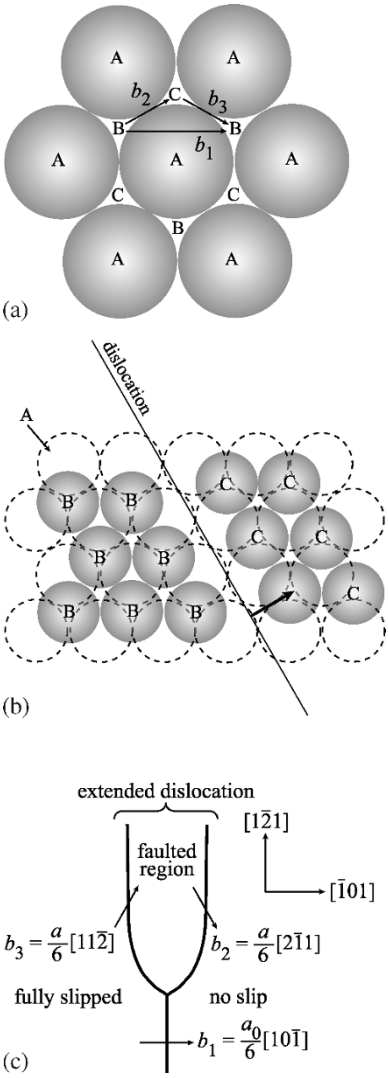

Fig. 7.36. Slip on the close-packed (111) plane in the fcc lattice. (a) Slip directions. (b) Location of atoms in a Shockley partial. (c) Dislocation dissociation into to partial dislocations

of the dissociation of the total dislocation into two partial dislocations. The partials are often called *Shockley partials* and the combination of the two partials is termed an *extended dislocation*. Dissociation is independent of dislocation character and the partial dislocations move as a unit that maintains the equilibrium width between them. The space between the partials is referred to as the faulted region or the *stacking fault* and its size is determined by the *stacking fault energy*, SFE. The lower the SFE, the greater the separation of the partials and the higher the energy, the closer they are together. Stacking faults are important in cross slip as the partials must recombine in order for cross slip to occur. Ex-

tended dislocations also occur in hcp lattices, but are not commonly observed in bcc metals.

7.1.9 Kinks and Jogs

Both edge and screw dislocations can acquire jogs, or steps in the dislocation line by interaction with other dislocations. The jogs are of two types. A jog that lies in the slip plane instead of normal to it is called a kink. Figure 7.37a shows an edge dislocation with a kink of screw character that lies in the slip plane of the edge dislocation, and Fig. 7.37b shows a screw dislocation with a kink of edge orientation. Kinks are unstable as they can line up and annihilate during glide. A second type of jog is shown in Fig. 7.37c in which the jog and the dislocation are of edge orientation. These types of jogs are able to glide since they lie in the slip plane of the dislocation. The only difference between the motion of the jogged edge dislocation and the ordinary edge dislocation is that instead of gliding along a single plane, it glides over a stepped surface. Another type of jog is the most important in plastic deformation and is shown in Fig. 7.37d. This is a screw dislocation containing a job with an edge orientation. The only way the screw dislocation can move to a new position and take its jog with it is by climb of the jog. Figure 7.37e shows the movement of a jogged screw dislocation as the segments between jogs bow out in the slip plane under an applied stress producing a trail of vacancies left behind the jog as the dislocation moves in its slip plane.

7.2 Faulted Loops and Stacking Fault Tetrahedra

Because of their importance in irradiated materials, we will discuss Frank loops at greater length. Frank loops are important in irradiated materials because they are often nucleated in a displacement cascade. Recall that the cascade consists of a core of vacancies surrounded by a shell of interstitials (Figs. 3.3 and 3.9). If the vacancy core or the interstitial shell collapse (condense) onto a close-packed plane, Frank loops may be generated. In both cases, a stacking fault results. Vacancy condensation produces an intrinsic fault and interstitial condensation results in an extrinsic stacking fault. The faults are described as follows.

In regular, close-packed lattices such as fcc and bcc, atom layers follow a regular stacking sequence. In the fcc lattice, the stacking sequence is ABCABCABC…, indicating that every third layer lies over the first layer. Removal of a layer of atoms results in a break or a fault in the stacking sequence. Removal of a plane of atoms produces an intrinsic stacking fault, which is also known as a single fault, and the dislocations attached to the single fault are S-dislocations, giving an S-Frank dislocation (Fig. 7.38a). For example, the sequence is modified to ABCAB/ABCABC…, where "/" denotes the fault or missing plane of atoms. Insertion of an extra plane of atoms produces a double fault in the stacking sequence; ABCAB/A/CABC…. (Fig. 7.38b). This is an extrinsic or double fault and the dislocations are D-dislocations giving a D-Frank loop. The Burgers vector of the S-Frank

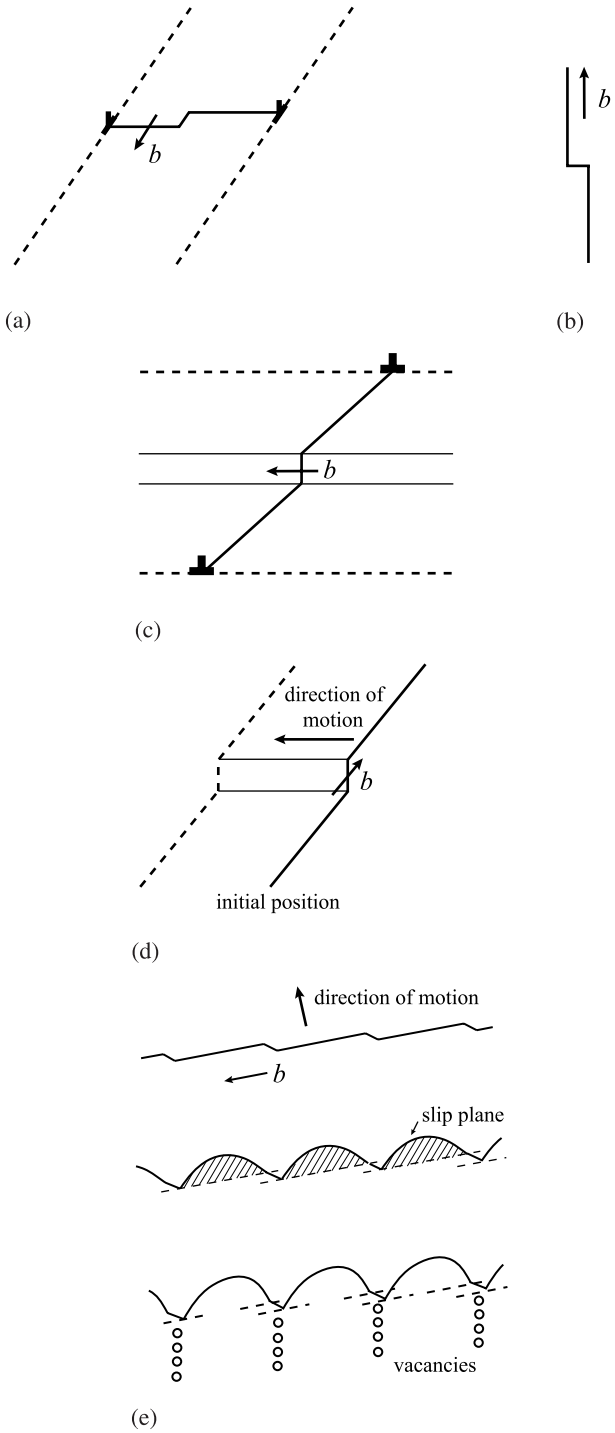

Fig. 7.37. Kinks and jogs in dislocations. (a) Edge dislocation with a kink of screw character. (b) Screw dislocation with a kink of edge orientation. (c) Edge jog in an edge dislocation. (d) Edge jog in a screw dislocation and direction of motion of the dislocation. (e) Movement of a jogged screw dislocation of part (d) showing bowing of the segments between jogs and the trail of vacancies left behind the trail of jogs (after [7])

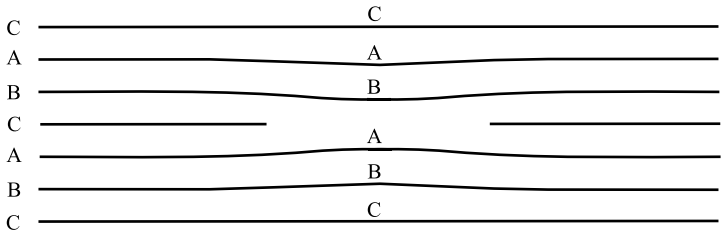

(a)

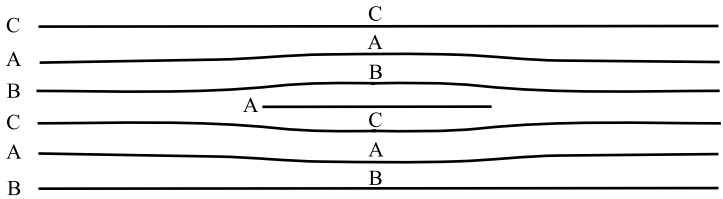

(b)

Fig. 7.38. Schematic of an (a) intrinsic stacking fault and an (b) extrinsic stacking fault

and D-Frank loops are identical. Since a Frank loop results from addition or removal of close-packed planes, $\boldsymbol{b}$ must be directed normal to the (111) plane and has a length equal to the spacing between planes, $a/\sqrt{3}$, then the Burgers vector is described by $\boldsymbol{b} = a/3[111]$. Since it is extremely difficult to move on its slip plane (the glide plane is actually a cylinder defined by the edge of the loop), the Frank loop is considered to be *sessile* or immobile since its glide plane is a *cylinder* defined by the projection of the loop perimeter in a direction perpendicular to, and above or below the plane of the loop. A Frank loop can also unfault either autocatalytically or by reaction with a dislocation line to form a perfect loop. This process is described in Chap. 12.

Another dislocation configuration that can form in irradiated metals is the stacking fault tetrahedron (SFT). A SFT is a three-dimensional stacking fault configuration that is in the shape of a tetrahedron. SFTs are believed to evolve directly from vacancy clusters produced in cascades. They are also believed to evolve from Frank loops. A Frank loop will always line on a (111) plane in an fcc lattice. Figure 7.39a shows a loop of triangular shape on a (111) plane with edges parallel to [110] directions. A Frank dislocation that is parallel to a [110] direction can lower its energy by splitting into a Shockley dislocation, $a/6[211]$ and a stair-rod dislocation. The slip plane of the Shockley dislocation is also a (111) plane but it is different from that containing the Frank loop. Figure 7.39b shows two of the three Shockley dislocations formed from the three sides of the Frank loop, moving up (111) planes. Each Shockley has left behind it a stair-rod dislo-

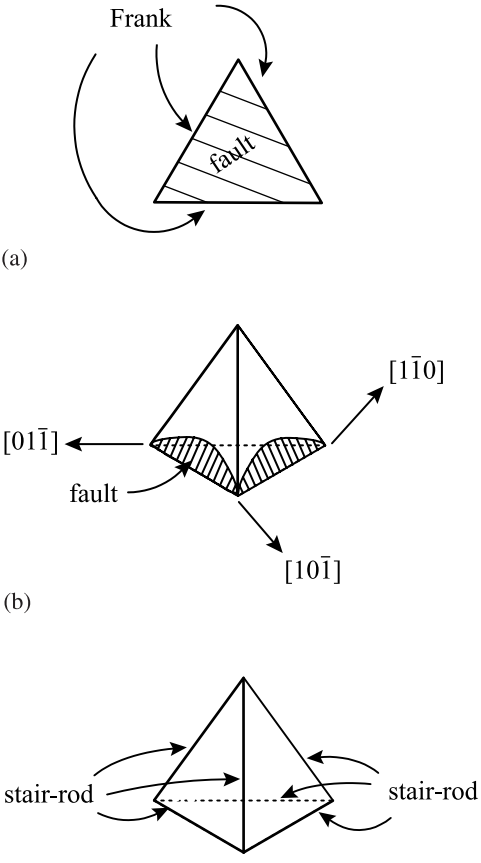

Fig. 7.39. A stacking fault tetrahedron (SFT) formed by faults on each of the faces of the tetrahedron (after [1])

cation, $a/6[110]$ in the position formerly occupied by a side of the Frank dislocation loop (edge of the triangle). The stacking fault contained in the Frank loop now bends at the stair-rod dislocation and extends up onto the close-packed (111) planes of the Shockley dislocations. As the Shockley dislocations move up the planes shown in Fig. 7.39b, they eventually meet at the intersections of their slip planes and the intersections of Shockley dislocations result in other stair-rod dislocations along the remaining three edges of the tetrahedron. The final configuration is a tetrahedron whose sides are stacking faults and whose edges are stair-rod dislocations (Fig. 7.39c). The Frank dislocation and the Shockley dislocations no longer exist.

Dislocations can also interact with SFTs. MD simulation of the interaction of a dissociated $a/2[110]$ dislocation (into two Shockley partials, $a/6[121]$) on the (111) glide plane shows that several types of interaction are possible [8]. When the SFT is in the slip plane of the dislocation, the SFT may be cut by the dislocation

and recovers by a shift of the structure above the glide plane to regain its original shape. The interaction can also create ledges in the SFT that can reduce stability and lead to dissolution. TEM observations show that SFTs can be cut multiple times by dislocations in channels.

7.3 Defect Clusters

As described in Chap. 3, the fraction of defects produced in a cascade is between 20 and 40% of that predicted by the NRT model due to intracascade recombination. Of these, not all appear as single interstitial atoms or isolated vacancies. A significant fraction of defects are created in the form of clusters, rather than as single defects. Vacancy clusters may grow to form voids, which are an important microstructure feature that influences both dimensional (Chap. 8) and mechanical (Chap. 12) properties of materials. If the clusters are stable, they may also migrate away from the cascade region and be absorbed at sinks such as dislocations and grain boundaries. Interstitial and vacancy clusters must be treated separately since in general, interstitial clusters are stable and vacancy clusters are not. Their mobilities differ as well with interstitial clusters exhibiting greater mobility than their vacancy counterparts.

7.3.1 Fraction of Defects Forming Clusters

In-cascade clustering of defects is important because it promotes nucleation of extended defects. Interstitial clustering can occur in one of two ways. In the first, interstitial clusters are created in the transition between the collisional and thermal spike phases in which atoms that are displaced from the cascade center due to the initial shock wave are pushed into interstitial locations. Alternatively, clusters can occur during the thermal spike phase by short-range diffusion driven by the elastic interaction between neighboring interstitials. The probability of clustering and the size of the clusters tend to increase with increasing PKA energy and a higher proportion of SIA form clusters than do vacancies [9]. Figure 7.40 shows the fraction of interstitials that form clusters as a function of the PKA energy in several metals and at 100 K, as determined by MD simulation [10]. Note that the clustered fraction increases quickly with T as damage transitions from single displacements to cascade morphology. In contrast to the Frenkel pair production efficiency (Fig. 3.20) the clustered fraction varies with the metal, and while there are only 5 metals shown here, the clustering appears to occur according to the crystal structure with the highest clustering fraction occurring for the fcc structure and the lowest for the bcc structure with the hcp structure in between.

While MD results show that the fraction of interstitials in clusters is larger in copper than in α-iron by ~ 70 to 45% at 100 and 600 K for PKA energies above 5 keV [11], experimental evidence shows that the cluster density in copper is as much as 10^3 higher than that in Fe [12]. While the size of this difference is not

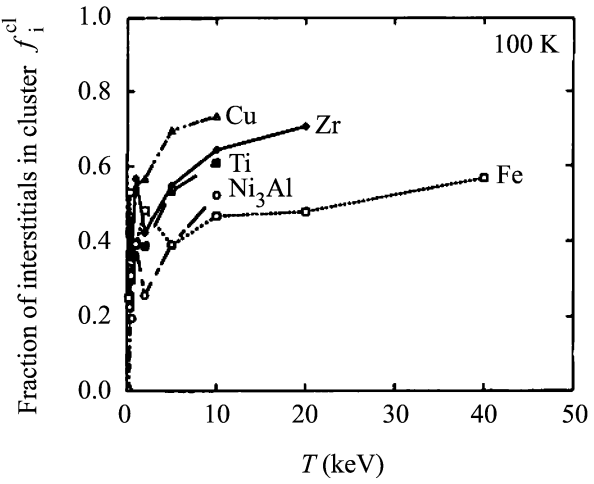

Fig. 7.40. The fraction, f_i^{cl}, of SIAs that survive as clusters containing at least two interstitials in several metals and Ni_3Al at 100 K (after [10])

understood, it may have its origins in the nature of the cluster as discussed in the next section.

Interstitial clustering depends on the irradiation temperature [9, 10, 13]. Figure 7.41 shows that with increasing temperature, the fraction of interstitials in clusters in α-iron decreases for damage energies between 5 and 40 keV. Actually, interstitial clustering increases at higher temperatures due to the more compact nature and longer lifetime of the cascade at higher temperature, providing more time for interstitials to diffuse and interact. Recall from Sect. 3.6 and Fig. 3.21 that the Frenkel pair production decreases slightly with temperature. Combining these results, the effect of temperature can be described as resulting in an increasing fraction of the decreasing population of interstitials forming clusters as the temperature increases, yielding a net decrease in f_i^d.

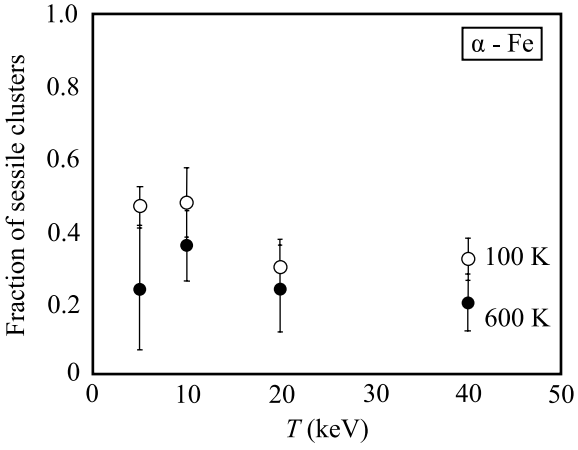

Fig. 7.41. The fraction of SIA clusters formed in a sessile configuration in α-iron at the end of the thermal spike as a function of PKA energy and irradiation temperature (after [10])

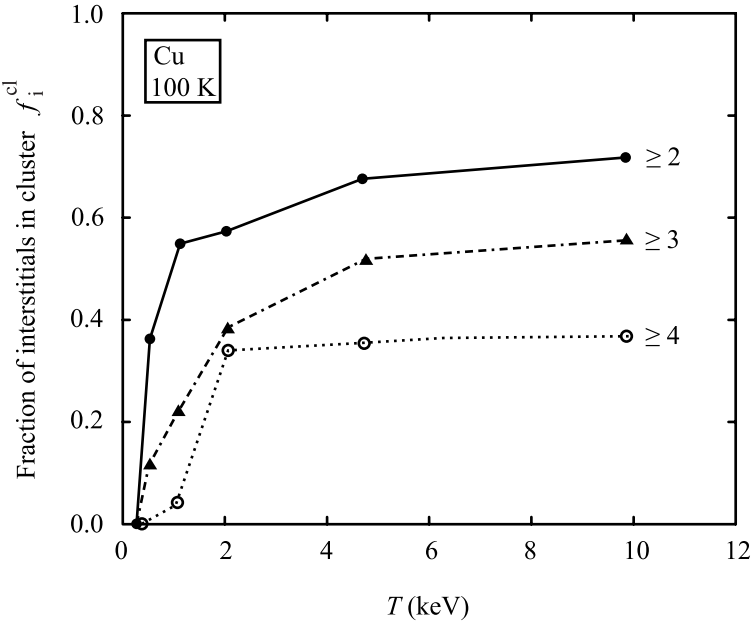

Fig. 7.42. The fraction f_i^{cl}, of SIAs that survive in clusters of two or more, three or more and four or more in copper at 100 K (after [10])

Finally, the clustered fraction can be broken down according to cluster size to reveal the dependence of clustering on cluster size. Figure 7.42 shows the fraction of SIAs in clusters of sizes $\simeq 2$, $\simeq 3$ and $\simeq 4$ in copper as a function of damage energy for an irradiation temperature of 100 K. Note that the cluster fraction is very sensitive to minimum cluster size, especially at lower damage energies, yielding a net decrease in f_i^{cl}.

Clustering of vacancies occurs within the core of the cascade as well and the extent of clustering varies with the host lattice. Based on measurements of size and number density of vacancy clusters in irradiated metals, the fraction of vacancies in clusters is estimated to be less than 15%. The true fraction may be larger because of the invisibility of small clusters, but also the fact that vacancy clusters are not nearly as stable as interstitial clusters as will be shown in the next section.

7.3.2 Types of Clusters

The structure of the cluster is a strong function of the crystal structure [12, 14]. In α-Fe, MD simulation shows that the most stable configuration of small clusters (< 10 SIAs) is a set of $\langle 111 \rangle$ crowdions. Next in stability is the $\langle 110 \rangle$ crowdion. As the cluster size grows (> 7 SIAs) only two configurations are stable, the $\langle 111 \rangle$ and $\langle 110 \rangle$ crowdions. These crowdions also may act as nuclei for the formation of

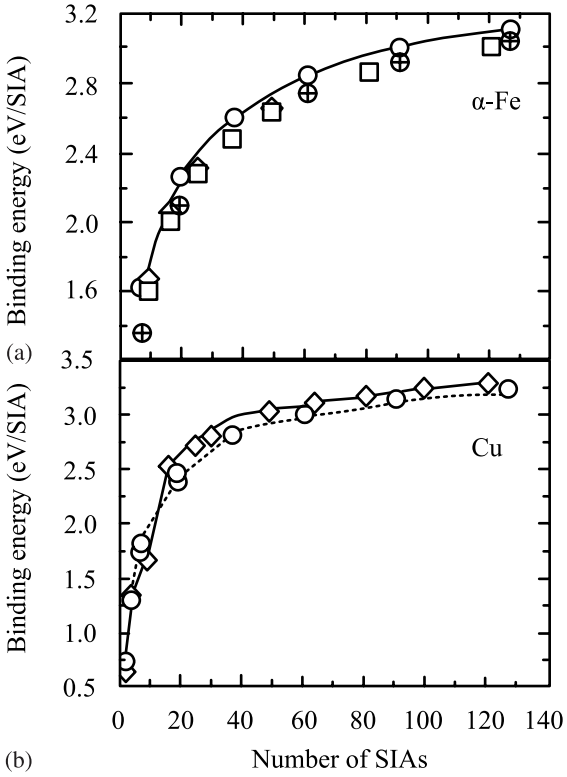

Fig. 7.43. Binding energy for SIA loops of different shapes and Burgers vectors (a) in α-Fe, and (b) in copper (after [12])

perfect interstitial dislocation loops with Burgers vector $1/2\langle 111\rangle$ or $\langle 100\rangle$, respectively.

In fcc copper, the $\langle 100\rangle$ dumbbell is the stable configuration of the SIA and the smallest cluster is of the form of two $\langle 100\rangle$ dumbbells. Larger clusters can have two configurations: a set of $\langle 100\rangle$ dumbbells or a set of $\langle 110\rangle$ crowdions, each with $\{111\}$ as the habit plane. During growth, the clusters transform into faulted Frank loops with Burgers vector $1/3\langle 111\rangle$, and perfect loops with Burgers vector $1/2\langle 110\rangle$. The binding energy of SIA loops in Fe and in Cu is shown in Fig. 7.43a,b, respectively. Note that the binding energy for SIA loops in Cu is slightly higher than for SIA loops in α-Fe, in agreement with the higher clustering fraction predicted by MD modeling. Figure 7.44 shows a micrograph of interstitial clusters and small interstitial loops in a copper foil after irradiation with 30 keV Cu^+ ions. Note that these defect clusters are only a few nanometers in size. Cluster densities can reach very high levels as shown in Fig. 7.45.

The stability of vacancy clusters is low relative to interstitial clusters. The most stable configurations for vacancy clusters in α-Fe are either a set of di-vacancies concentrated on two adjacent $\{100\}$ planes, or a set of first nearest neighbor vacancies on a $\{110\}$ plane. During cluster growth, the first type results in a perfect dislocation loop with Burgers vector $\langle 100\rangle$ and the second unfaults into a perfect

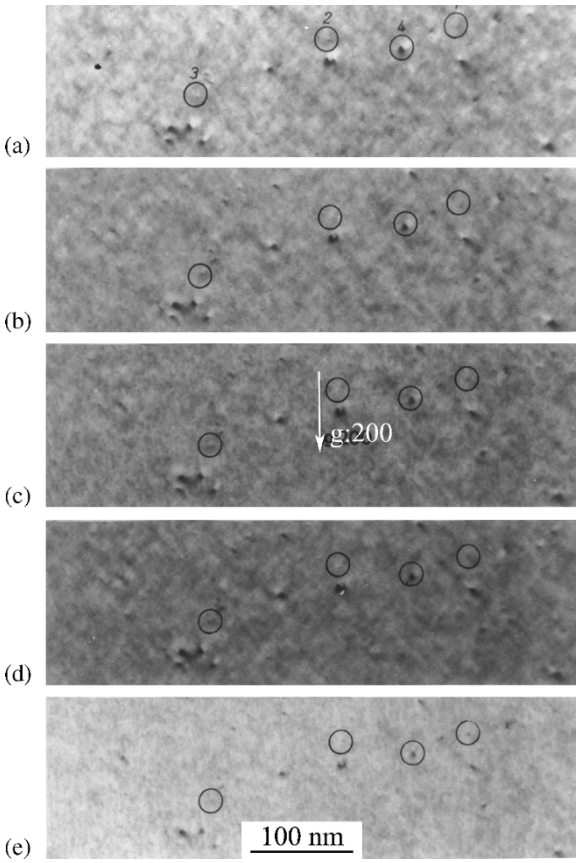

Fig. 7.44. Micrograph of interstitial clusters and small interstitial loops in copper irradiated with 30 keV Cu^{+}. Defects are highlighted by the circles on the micrographs (after [15])

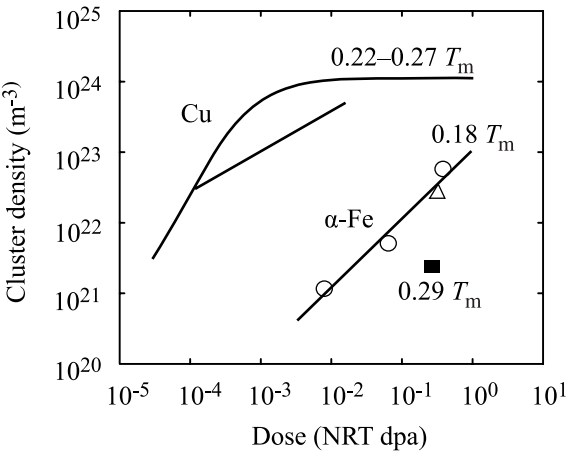

Fig. 7.45. Dose dependence of cluster densities measured in α-iron and copper irradiated with fission neutrons at temperatures below 0.3 T_m (after [12])

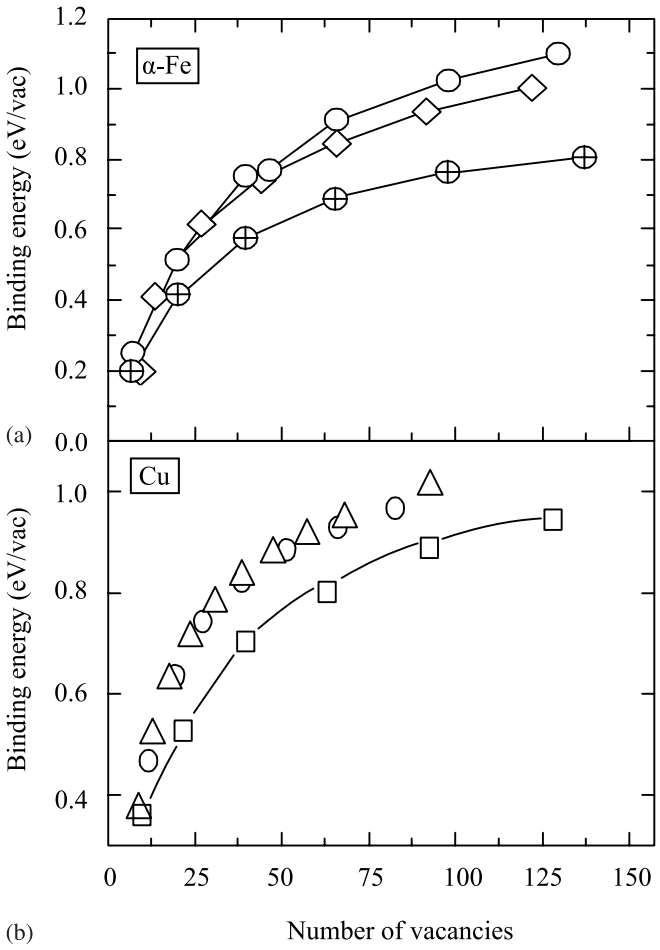

Fig. 7.46. Binding energy of vacancy loops of different shapes and Burgers vectors in (a) α-Fe, and (b) copper (after [12])

loop with Burgers vector $1/2\langle 111\rangle$. Vacancy loops can also exist in the faulted configuration. The loops will generally unfault to form perfect loops when the number of vacancies reaches about 40 [12].

In fcc Cu, the most stable configurations of a vacancy cluster are the stacking fault tetrahedron (SFT) and faulted clusters on $\{111\}$ planes that form Frank loops with Burgers vector $1/3\langle 111\rangle$. Binding energies of the various vacancy configurations in α-Fe and Cu are shown in Fig. 7.46a,b. Note that the binding energy of vacancies in the cluster is much less than that for interstitials shown in Fig. 7.43a,b. The binding energy per defect for a four-defect cluster is less than 0.4 eV for vacancies, but is about 1.2 eV for interstitials. Observation by transmission electron microscopy [16] reveals that vacancy dislocation loops and SFT a few nanometers in size are formed by cascades in many metals (Fig. 7.47).

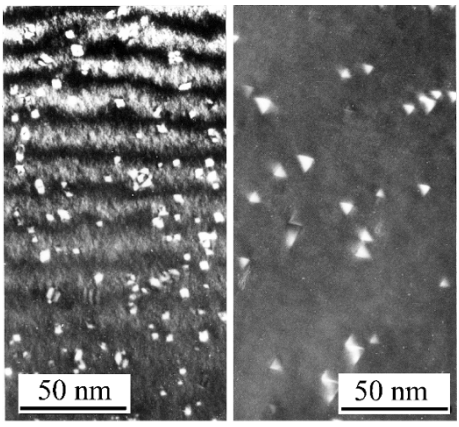

Fig. 7.47. Transmission electron micrograph of (a) defect clusters in gold irradiated to $1.1 \times 10^{22}\,\mathrm{n/m^2}$ at 200 °C and (b) stacking fault tetrahedra in silver irradiated to $4.4 \times 10^{21}\,\mathrm{n/m^2}$ at 400 °C (after [16])

7.3.3 Cluster Mobility

Clustered SIAs formed in cascades exhibit high mobility and can migrate over atomic scale distances during the lifetime of the cascade ($\sim 10\,\mathrm{ps}$). However, not all clusters are glissile. Besides stable, faulted Frank loops, SIAs may form metastable arrangement of SIAs that do not reorganize into a stable, glissile form by the end of the thermal spike. They are significant because they do not migrate away from the cascade, they may act as nucleation sites for the growth of extended defects. Figure 7.41 indicates that the fraction of SIA clusters in a metastable sessile configuration by the end of the thermal spike phase is between 30 and 50% at 100 K and somewhat less at 600 K. The form of these clusters varies with crystal structure. In hcp metals, small sessile clusters form a triangular arrangement of closely-packed atoms on the basal plane. In α-iron, three SIAs can form a triangle that is parallel to but displaced from the $\{111\}$ plane. If clusters form as faulted dislocation loops, such as $\boldsymbol{b} = 1/3\langle 111\rangle$ in fcc, $1/2\langle 110\rangle$ in bcc and $1/2\langle 0001\rangle$ in hcp, then they are intrinsically sessile and cannot exhibit glide. The ability to move arises from the clustered crowdion form of these extended defects. They have a form best described as small perfect interstitial dislocation loops with Burgers vector $\boldsymbol{b} = 1/2\langle 110\rangle$ in fcc, $1/2\langle 111\rangle$ and $\langle 100\rangle$ in bcc and $1/3\langle 11\bar{2}0\rangle$ in hcp. Table 7.1 summarizes the Burgers vectors of the glissile and sessile dislocation loops formed by vacancy and interstitial clusters.

Mobile clusters can interact with other clusters or with impurity atoms such as helium. The behavior of small interstitial clusters in the presence of impurity helium atoms and vacancies is illustrated in Movies 7.1–7.3. In Movie 7.1 a SIA (green spheres) in bcc iron interacts with two substitutional He (light blue spheres) atoms and the interaction leads to recombination and ejection of the He into in an interstitial position from which it migrates and traps the other He substitutional atom. Movie 7.2 shows the interaction between a 6-SIA cluster and three substitutional He atoms. In this case, recombination and He ejection occurs with two of the three He atoms resulting in a cluster consisting of 4-SIA and one interstitial He atom, and

Table 7.1. Summary of Burgers vectors of glissile and sessile loops in fcc, bcc and hcp lattices (after [10])

Crystal structure	Burgers vector	Cluster mobility
fcc	$\boldsymbol{b} = 1/2\langle 110\rangle$	Glissile
	$\boldsymbol{b} = 1/3\langle 111\rangle$	Sessile
	SFT (vacancy)	Sessile
bcc	$\boldsymbol{b} = 1/2\langle 111\rangle$, $\langle 100\rangle$	Glissile
	$\boldsymbol{b} = 1/2\langle 110\rangle$	Sessile
hcp	$\boldsymbol{b} = 1/3\langle 11\bar{2}0\rangle$	Glissile
	$\boldsymbol{b} = 1/2\langle 10\bar{1}0\rangle$, $1/2\langle 0001\rangle$	Sessile

a cluster consisting of one interstitial He and one substituional He. Movie 7.3 shows the interaction between a 6-SIA cluster and a 4-He/6-vacancy cluster. Vacancies are denoted by the red spheres. The interaction causes the recombination and rejection of He resulting in a 4-He/1-SIA cluster.

The majority of SIA clusters are glissile. Di- and tri-interstitial clusters in both α-iron and copper undergo one-dimensional glide along the crowdion direction [12]. In these small clusters, the crowdion can rotate such that glide occurs in an equivalent direction. This rotation results in essentially three-dimensional motion. The rotation frequency is lower for tri-interstitials and increases with temperature for both defects. Larger clusters are essentially perfect dislocation loops with a Burgers vector along the crowdion axis, so that their movement can be considered as thermally-assisted glide in one-dimension. Figure 7.48 shows 19 and 91-interstitial clusters in α-iron. Both loops extend over six (220) planes as shown in the figures at the right of each cluster. The motion of these clusters is one-dimensional and along $\langle 111\rangle$. A feature of cluster motion is that the effective correlation factor is greater than unity, i.e., a cluster that has moved one step has a high probability of making the next step in the same direction. Movie 7.4 is an MD simulation of a 19-SIA cluster in bcc iron at 287 °C. The cluster exhibits one-dimensional motion in the direction of the Burgers vector.

The activation energy for cluster motion is between 0.022 and 0.026 eV in α-iron and between 0.024 and 0.030 eV in copper [12]. The activation energy is weakly dependent on the size of the cluster, allowing the cluster jump frequency to be expressed as:

$$\nu_n = \nu_0 n^{-S} \exp(-\langle E_\mathrm{m}\rangle / kT) \,, \tag{7.56}$$

where $\langle E_\mathrm{m}\rangle$ is the average effective activation energy, ν_0 is the size-independent, pre-exponential factor, and the term n^{-S} is the cluster size dependence, where a value of ~ 0.65 for s describes the cluster size dependence of the pre-exponential factor for both α-iron and copper. Figure 7.49 shows the total pre-exponential factor as a function of cluster size. This dependence is likely due to enhanced focusing of the crowdion configuration for SIAs in a cluster, which results in increased probability of successive jumps.

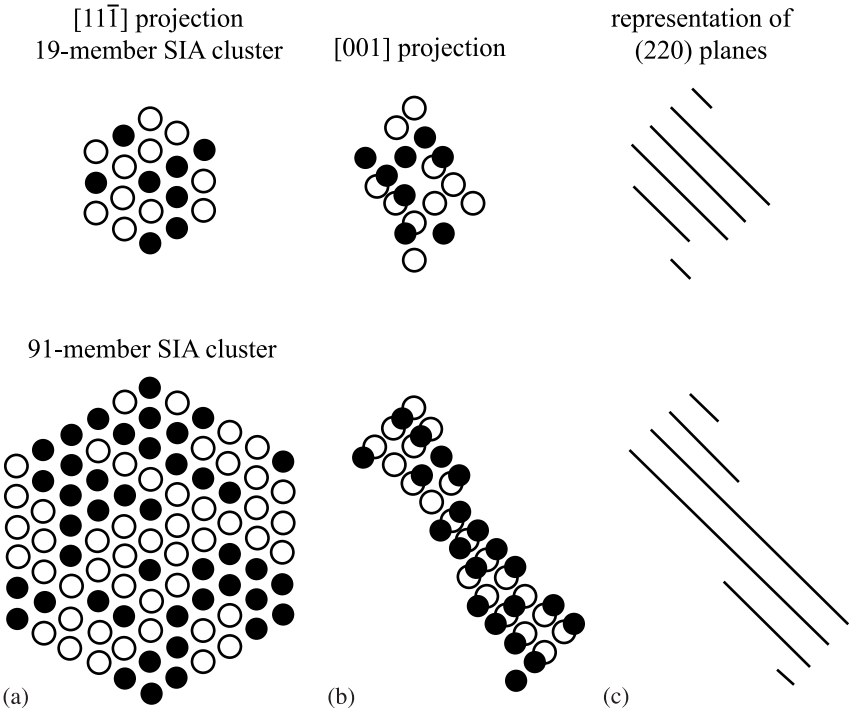

Fig. 7.48. A 19 and 91-interstitial cluster in (a) [11$\bar{1}$] and (b) [001] projections. Filled and open circles represent the centers of mass of $\langle 111 \rangle$ crowdions and split dumbbells, respectively. (c) Additional (220) lattice planes occupied by the clusters (after [17])

Vacancy clusters that form perfect dislocation loops are also intrinsically glissile. MD simulation shows that the mobility of perfect vacancy loops with $\boldsymbol{b} = 1/2\langle 110 \rangle$ and $1/2\langle 111 \rangle$ in Cu and α-iron respectively, is only slightly lower than that of a cluster of the same number of interstitial crowdions [12]. The result is shown in Fig. 7.50 for a 37-defect cluster. As long as they are in the form of perfect loops, they are mobile. Vacancy clusters that do not collapse to a dislocation structure or that form a Frank loop or SFT are immobile.

7.4 Extended Defects

As described in the previous sections, vacancies and interstitials can cluster to form other types of defects that will be important in defining the effect of irradiation on both physical and mechanical properties of the solid. In principle a cluster of point defects could be one-dimensional (a line), two-dimensional (a disc), or three-dimensional (a void). Vacancies and interstitials that cluster in numbers greater than those discussed earlier will agglomerate into specific configurations in the crystal lattice. In particular they will take up the minimum energy configuration, which in

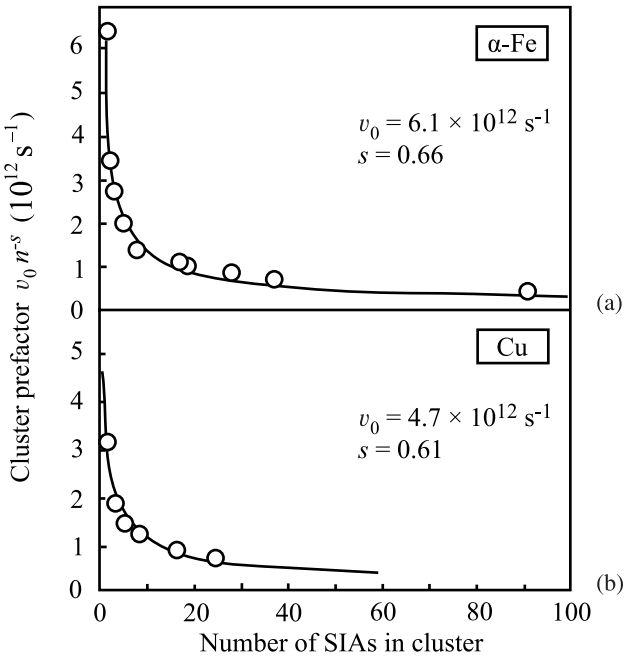

Fig. 7.49. Size dependence of the pre-exponential factor in Eq. (7.56) in (a) α-Fe and (b) Cu (after [12])

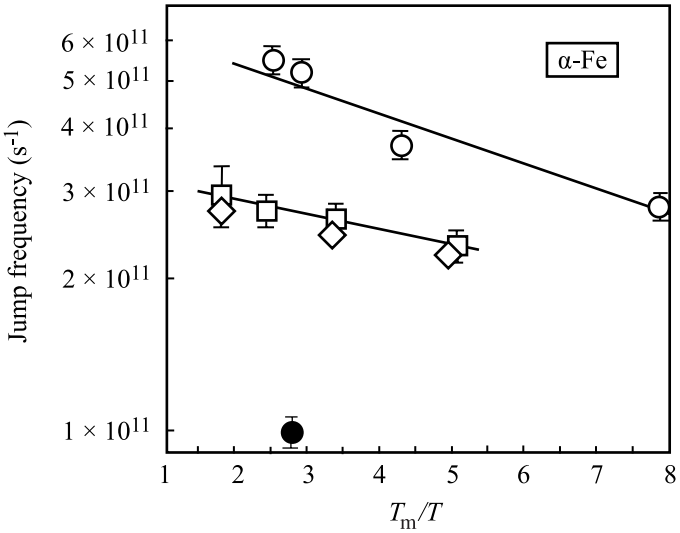

Fig. 7.50. Jump frequency vs. reciprocal temperature for vacancy loops (*squares* and *diamonds*) and SIA loops (*circles*) in Fe at 375 °C (after [12])

three dimensions is a void, and in two dimensions is a loop or platelet with a thickness of magnitude equal to one Burgers vector and lying between adjacent close-packed planes.

It may be envisioned that following the radiation damage event, the core of the displacement spike collapses (or the vacancies condense) onto the $\{111\}$ plane, forming a vacancy disc. The energy of the disc can be written as:

$$E_{\mathrm{d}} = 2\pi r_{\mathrm{d}}^2 \gamma \,, \tag{7.57}$$

where r_{d} is the disc radius and γ is the surface energy of the metal. For a small number of vacancies, the aggregate form with the least energy is the spherical void. The energy of the spherical void of radius r_{V} is:

$$E_{\mathrm{V}} = 4\pi r_{\mathrm{V}}^2 \gamma \,. \tag{7.58}$$

If Ω is the atomic volume then the number of vacancies in the void is:

$$n_{\mathrm{V}} = \frac{4}{3}\frac{\pi r_{\mathrm{V}}^3}{\Omega} \,. \tag{7.59}$$

The energy of the void written in terms of the number of vacancies is:

$$E_{\mathrm{S}} = 4\pi \left(\frac{3n_{\mathrm{v}}\Omega}{4\pi}\right)^{2/3} \gamma = (6n_{\mathrm{v}}\Omega\sqrt{\pi})^{2/3}\gamma \,. \tag{7.60}$$

For a large number of vacancies, the planar loop is a more stable configuration and this will be discussed shortly.

Another possible configuration of a cluster of vacancies is the stacking fault tetrahedron as described in Sect. 7.2. The energy of the stacking fault tetrahedron, or SFT, is given by [4, 18, 19]:

$$E_{\mathrm{SFT}} = \frac{\mu L b^2}{6\pi(1-\nu)}\left[\ln\left(\frac{4L}{a}\right) + 1.017 + 0.97\nu\right] + \sqrt{3}L^2\gamma_{\mathrm{SFE}} \,, \tag{7.61}$$

where ν is Poisson's ratio, a is the lattice parameter, γ_{SFE} is the energy of the stacking fault and L is the length of the edge of the tetrahedron and $L = a(n/3)^{1/2}$.

A similar process involving interstitial condensation may occur around the edges of the depleted zone where high interstitial concentrations may exist. The condensation of interstitials onto a close-packed plane produces an extra layer of atoms and two breaks in the stacking sequence, as described in Sect. 7.2 For a disc of radius r_{L}, the energy of a faulted loop (vacancy or interstitial) is:

$$E_{\mathrm{L}} = 2\pi r_{\mathrm{L}}\Gamma + \pi r_{\mathrm{L}}^2\gamma_{\mathrm{SFE}} \,, \tag{7.62}$$

where the first term is the energy of the dislocation line and the second term is the energy associated with the stacking fault, and Γ is the energy per unit length of dislocation line. In the fcc lattice, faulted loops lie on the $\{111\}$ planes, which have

an atom density of $4/\sqrt{3}a^2$, or an area per atom of $\sqrt{3}a^2/4$. So the radius of a loop consisting of n vacancies (or interstitials) is:

$$r_{\mathrm{L}} = \left(\frac{\sqrt{3}a^2 n}{4\pi} \right)^{1/2} . \tag{7.63}$$

Approximating Γ with μb^2, Eq. (7.32b) where μ is the shear modulus and b is the Burgers vector, Eq. (7.62) becomes:

$$E_{\mathrm{L}} = 2\pi\mu b^2 \left(\frac{\sqrt{3}a^2 n}{4\pi} \right)^{1/2} + \pi \left(\frac{\sqrt{3}a^2 n}{4\pi} \right) \gamma_{\mathrm{SFE}} . \tag{7.64}$$

More precise expressions for the energy of faulted and perfect loops are given in [4, 6, 18, 19, 20] and from [20], the energy of the faulted Frank loop is:

$$E_{\mathrm{F}} = \frac{2}{3} \frac{1}{(1-\nu)} \mu b^2 r_{\mathrm{L}} \ln \left[\frac{4r_{\mathrm{L}}}{r_{\mathrm{c}}} - 2 \right] + \pi r_{\mathrm{L}}^2 \gamma_{\mathrm{SFE}} . \tag{7.65}$$

The energy of a perfect loop [16] is:

$$E_{\mathrm{P}} = \frac{2}{3} \frac{1}{(1-\nu)} + \frac{1}{3} \left(\frac{2-\nu}{2(1-\nu)} \right) \mu b^2 r_{\mathrm{L}} \ln \left[\frac{4r_{\mathrm{L}}}{r_{\mathrm{c}}} - 2 \right] , \tag{7.66}$$

where r_{c} is the dislocation core radius. Equations (7.65) and (7.66) refer to both interstitial and vacancy loops and from these equations, the difference in energy between a perfect loop and a Frank loop is:

$$\Delta E = \pi r_{\mathrm{L}}^2 \gamma_{\mathrm{SFE}} - \frac{1}{3} \left(\frac{2-\nu}{2(1-\nu)} \right) \mu b^2 r_{\mathrm{L}} \ln \left[\frac{4r_{\mathrm{L}}}{r_{\mathrm{c}}} - 2 \right] . \tag{7.67}$$

Therefore, unfaulting is favorable if:

$$\gamma_{\mathrm{SFE}} > \frac{\mu b^2}{3\pi r_{\mathrm{L}}} \left(\frac{2-\nu}{2(1-\nu)} \right) \ln \left[\frac{4r_{\mathrm{L}}}{r_{\mathrm{c}}} - 2 \right] . \tag{7.68}$$

Equations for a disc, void, perfect loop, faulted loop and SFT are plotted in Fig. 7.51a,b for 316 stainless steel and zirconium respectively. The values of the materials parameters are provided in the caption. Note that in general, faulted defects are more stable in zirconium than in stainless steel and voids are more stable in stainless steel than in zirconium. In stainless steel, voids are stable to relatively large sizes and the energy of the faulted loop remains below that of the perfect loop to large defect sizes. In zirconium, faulted loops and SFTs are more stable than voids. The high susceptibility to void swelling in stainless steel and the absence of voids in zirconium are in qualitative agreement with the formation energies for these extended defects according to Fig. 7.51.

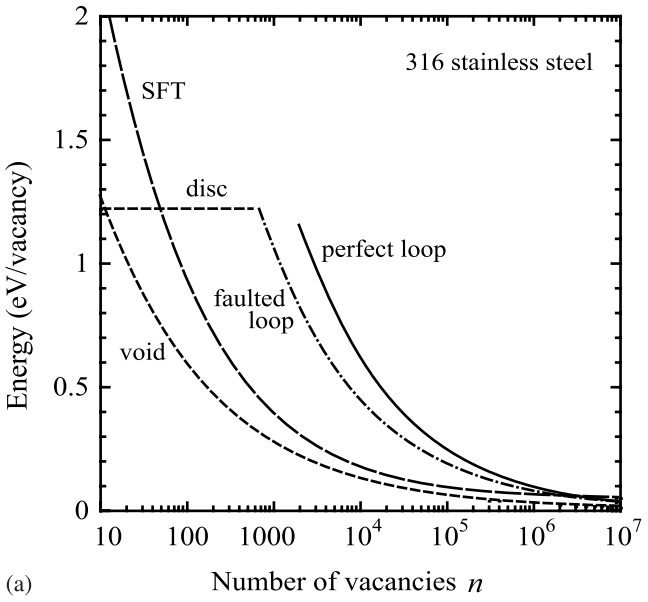

(a)

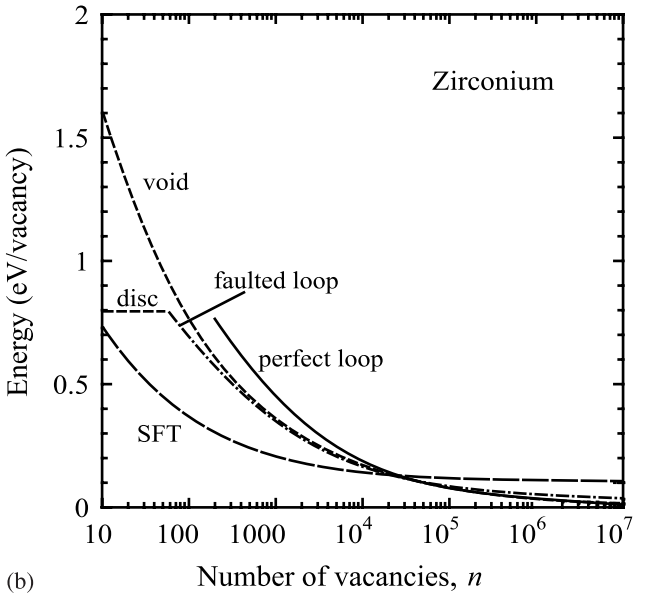

(b)

Fig. 7.51. Formation energy for various vacancy cluster defects in (a) 316 stainless steel, and (b) zirconium as a function of the log of the number of vacancies in the cluster. Material parameters for stainless steel are $\gamma_{SFE} = 35\,mJ/m^2$, $\gamma = 1.75\,J/m^2$, $\mu = 82\,GPa$. Material parameters for zirconium are $\gamma_{SFE} = 102\,mJ/m^2$, $\gamma = 1.40\,J/m^2$, $\mu = 33\,GPa$

Since we have just shown that the void is a stable configuration only for small numbers of vacancies, how then can we observe large voids with the number of vacancies exceeding several orders of magnitude? It is well-established that for most metals, irradiation at low temperatures ($< 0.2T/T_m$) results in aggregation of vacancies and interstitials to form clusters that are bound by dislocations, i.e., loops and stacking fault tetrahedra (in metals with low SFE). At higher temperatures, vacancies can also aggregate to form voids. Voids appear in a band of temperatures ranging from about $1/3 < T/T_m < 1/2$ where insoluble gases such as helium have a strong effect on stabilizing voids. At temperatures less than $1/3T/T_m$, vacancies are not mobile enough to reach the voids before annihilation with migrating interstitials. Also, loops formed by vacancy collapse of cascades are stable against thermal dissociation at low temperatures and hence, reduce the number of vacancies available for void growth. At very high temperature, the thermal equilibrium vacancy concentration becomes comparable with the radiation-induced vacancy concentration and voids tend to shrink by vacancy emission. The subject of void and bubble nucleation and growth will be discussed in more detail in Chap. 8.

7.5 Effective Defect Production

With a better understanding of the importance of defect clusters, we can expand and refine our description of defect production. Microstructure evolution is ultimately controlled by the migrating defect fractions of vacancies and interstitials, $MDF_{v,i}$. The most straightforward component of the MDF is the isolated point defect fraction, $IDF_{v,i}$ (discussed in Chap. 3), which is produced directly in the displacement cascade. A second component is the mobile cluster fraction, $MCF_{i,v}$ (discussed in Sect. 7.3.3) and is composed of mobile interstitial defect clusters and mobile vacancy clusters. The third component is defects released from clusters by evaporation, $EDF_{v,i}$, and is most important for vacancies, and interstitials at very high temperatures. Taken together, these three sources of isolated defects comprise the migrating defect fraction, $MDF_{v,i}$. Zinkle and Singh [21] constructed a flow chart to show the evolution of the various defect forms (Fig. 7.52), which is an expansion of the more simplistic case shown in Fig. 3.16 by inclusion of the processes in dashed boxes. Zinkle and Singh summarized experiments from which values for $MDF_{v,i}$ could be determined, and found that in general, $3\% < MDF_i < 10\%$, and $1\% < MDF_v < 10\%$ where the percentages refer to the calculated NRT production rate. While there is considerable uncertainly regarding the quantitative values deduced from experiments, the range can be used to bound the expected available defect fraction.

The significance of these processes is that they are not often addressed in traditional rate theory models of microstructure evolution. To create an accurate physical model of defect production and accumulation under cascade damage conditions, the following must be included:

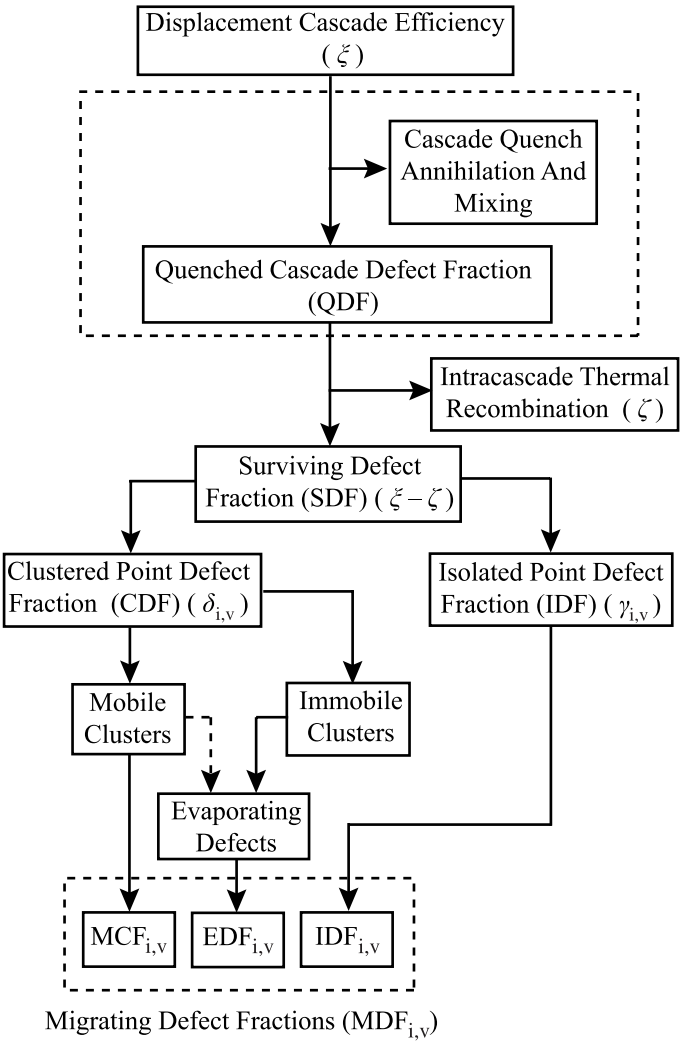

Fig. 7.52. Flow chart giving the contributions to the migrating defect fraction from isolated defects, mobile defect clusters and evaporating defects (after [19])

1. The production of a large fraction of defects heterogeneously in the form of vacancy and interstitial clusters with the remainder as isolated vacancies and interstitials
2. The bias for absorption of mobile interstitial clusters and freely migrating interstitials at sinks
3. The fractions of interstitials and vacancies in clustered or isolated forms that are not necessarily equal, which is equivalent to an asymmetric production of freely migrating fractions of vacancies and interstitials

4. Vacancy evaporation from clusters formed during the cascade quench that results in a temperature-dependent contribution to the fraction of freely migrating vacancies

As will be shown in subsequent sections and in the discussion of void formation and growth in Chap. 8, intracascade clustering and the thermal stability of interstitial and vacancy clusters cause an *asymmetry* in the supply of migrating vacancies and interstitials, termed the *production bias* and this bias represents a strong driving force for loop and void nucleation and growth.

7.6 Nucleation and Growth of Dislocation Loops

Dislocation loops resulting from vacancy and interstitial condensation are created from clusters of the respective defects, and either shrink or grow depending on the flux of defects reaching the embryo. Once they have reached a critical size, the loops become stable and grow until they unfault by interaction with other loops or with the network dislocation density. The following sections describe the processes of loop nucleation, growth and unfaulting that determine the dislocation microstructure of a metal under irradiation.

7.6.1 Loop Nucleation

Various attempts have been made to determine the nucleation rate of dislocation loops and voids. We will follow a treatment that is based on steady sate concentrations of vacancies and interstitials and assumes dilute solution thermodynamics, as develop by Russell et al. [22]. In this treatment, the effects of cascades are ignored. We will then introduce clustering theory and show how it can be applied to the loop nucleation problem to account for the formation of defect clusters in addition to point defects.

We begin by expressing the nucleation rate of a defect cluster of size n as the flux of clusters between adjacent size classes in a phase space of cluster size. Considering only one type of defect (vacancies, for example), the flux between any two adjacent size classes can be written as:

$$J_n = \beta_v(n)\rho(n) - \alpha_v(n+1)\rho(n+1)\,, \tag{7.69}$$

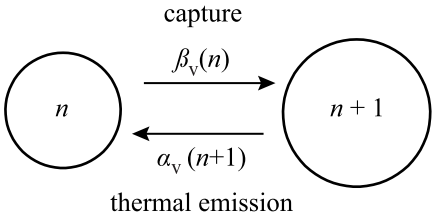

Fig. 7.53. Illustration of the capture and emission processes governing the flux of clusters between adjacent size classes in a phase space of cluster size

where $\rho(n)$ and $\rho(n+1)$ are the number of n-mers (loops containing n vacancies) and $(n+1)$-mers per unit volume. $\beta_v(n)$ is the rate of vacancy capture by a n-mer, and $\alpha_v(n+1)$is the rate of vacancy loss by a $(n+1)$-mer. The first term in Eq. (7.69) represents an addition to the $n+1$ size class by capture of a vacancy by a void n-mer size class. The second term is a loss from the $(n+1)$-mer size class by emission of a vacancy. Figure 7.53 shows the various processes described by Eq. (7.69) in phase space. At steady state, $J_n = 0$ and Eq. (7.69) becomes:

$$\alpha_v(n+1) = \beta_v(n)\frac{\rho^0(n)}{\rho^0(n+1)}\,, \tag{7.70}$$

where $\rho^0(n)$ is the equilibrium concentration of n-mer vacancy loops. Substituting for $\alpha_v(n+1)$ from Eq. (7.69) into the expression for the nucleation rate, Eq. (7.70) yields:

$$\begin{aligned} J_n &= \beta_v(n)\left[\rho(n) - \rho(n+1)\frac{\rho^0(n)}{\rho^0(n+1)}\right] \\ &= -\beta_v(n)\rho^0(n)\left[\frac{\rho(n+1)}{\rho^0(n+1)} - \frac{\rho(n)}{\rho^0(n)}\right]\,, \end{aligned} \tag{7.71}$$

and the term in brackets is just the derivative of the ratio $\rho(n)/\rho^0(n)$, or $\dfrac{\partial\left[\rho(n)/\rho^0(n)\right]}{\partial n}$. The nucleation rate then becomes:

$$J_n = -\beta_v(n)\rho^0(n)\frac{\partial\left[\rho(n)/\rho^0(n)\right]}{\partial n}\,, \tag{7.72}$$

where

$$\rho^0(n) = N_0\exp(-\Delta G_n^0/kT)\,, \tag{7.73}$$

and N_0 is the number of nucleation sites per unit volume, and ΔG_n^0 is the free energy of forming the n-mer vacancy loop.

The steady state nucleation rate of vacancy loops (consisting of k vacancies) can also be described as the product of the loop concentration, the jump frequency of the vacancy to the loop and the jump distance, and is given by:

$$J_k = \rho_k^0\beta_k Z\,, \tag{7.74}$$

where ρ_k^0 and β_k are the values of $\rho^0(n)$ and $\beta_v(n)$ at the critical size, k, and Z is the Zeldovich factor that depends on the curvature of ΔG_n^0 near the maximum, at the critical size. If ΔG_n^0 is approximated by a parabola in this region (lower curve in Fig. 7.54), then:

$$Z = \left[-\frac{1}{2\pi kT}\frac{\partial^2\Delta G_n^0}{\partial n^2}\right]_{n_k}^{1/2}\,, \tag{7.75}$$

where the derivative is evaluated at the critical loop size, n_k. Its value is the width of ΔG_k^0 at kT units below the maximum and is on the order of 0.05.

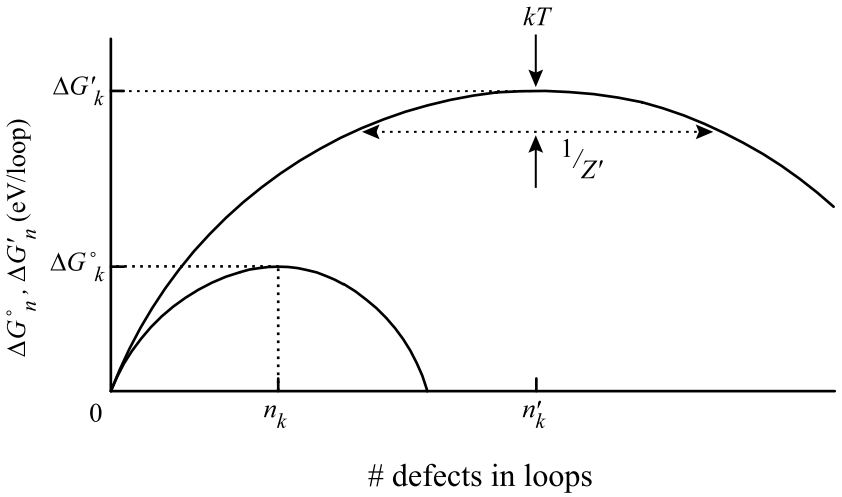

Fig. 7.54. Schematic nucleation curves showing the various parameters which are important in cluster nucleation. ΔG_k^0 is the activation barrier to nucleation if interstitials are not present, while $\Delta G_k'$ is the same quantity if interstitials are present during the vacancy cluster nucleation process (after [22])

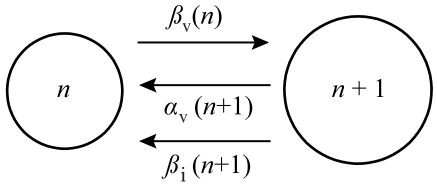

Fig. 7.55. Illustration of the capture and emission processes governing the flux of clusters between adjacent size classes in a phase space of cluster size and including the effect of interstitial capture

Consider now the presence of interstitials in the vacancy loop nucleation formulation. The flux between any two size classes, say n and $n+1$, now becomes:

$$J_n = \beta_v(n)\rho(n) - \alpha_v(n+1)\rho(n+1) - \beta_i(n+1)\rho(n+1)\,, \tag{7.76}$$

where all terms are as previously defined, and $\beta_v(n+1)$ is the rate of interstitial capture by a $(n+1)$-mer. Interstitial emission is of low probability and is neglected. Figure 7.55 shows the various processes described by Eq. (7.76) in phase space.

The rate of vacancy emission from a vacancy loop will be governed by temperature, size and lattice energetics. Since the defect fractions are as high as 10^{-4}, a cluster has a defect in its immediate vicinity only this small fraction of time. The emission probability should be affected only slightly during this time interval and not at all otherwise. Therefore we conclude that α_v is a value characteristic of a system without interstitials. Setting $J = 0$ in Eq. (7.76) is equivalent to equilibrating the size classes since there is no net flux between size classes. If we neglect interstitials, then from Eq. (7.76) we can write:

$$\alpha_v(n+1) = \frac{\beta_v(n)\rho^0(n)}{\rho^0(n+1)}\,. \tag{7.77}$$

Combining Eqs. (7.76) and (7.77) gives:

$$J_n = \beta_v(n)\left\{\rho(n) - \rho(n+1)\left[\frac{\rho^0(n)}{\rho^0(n+1)} + \frac{\beta_i(n+1)}{\beta_v(n)}\right]\right\} . \tag{7.78}$$

Since $\rho^0(n) = N_0 \exp(-\Delta G_n^0/kT)$, then we note that:

$$\frac{\rho^0(n)}{\rho^0(n+1)} = \exp\left(\frac{\delta G_n^0}{kT}\right) , \tag{7.79}$$

where $\delta G_n^0 \equiv \Delta G_{n+1}^0 - \Delta G_n^0$. The term δG_n^0 is the difference between the free energies of creating loops of $j+1$ and j vacancies from single vacancies at the prevailing supersaturation. We now define new functions of n, $\rho'(n)$ and $\delta G_n'$ such that by analogy with Eq. (7.79):

$$\frac{\rho'(n)}{\rho'(n+1)} = \frac{\rho^0(n)}{\rho^0(n+1)} + \frac{\beta_i(n+1)}{\beta_i(n)} = \exp(\delta G_n'/kT) , \tag{7.80}$$

where

$$\delta G_n' = \Delta G_{n+1}' - \Delta G_n' , \tag{7.81}$$

and $\Delta G_n'$ is not generally a free energy because of the term $\dfrac{\beta_i(n+1)}{\beta_i(n)}$ in Eq. (7.81). Using the expression in Eq. (7.81), we can re-write the equation for J_n in terms of $\dfrac{\rho'(n)}{\rho'(n+1)}$ by substituting Eqs. (7.80) into (7.78) to give:

$$J_n = \beta_v(n)\left\{\rho(n) - \rho(n+1)\,\frac{\rho'(n)}{\rho'(n+1)}\right\} . \tag{7.82}$$

Re-arranging Eq. (7.82) gives:

$$J_n = -\beta_v(n)\rho'(n)\frac{\rho(n+1)}{\rho'(n+1)} - \left[\frac{\rho(n)}{\rho'(n)}\right] , \tag{7.83}$$

and noting that:

$$\frac{\left[\dfrac{\rho(n+1)}{\rho'(n+1)} - \dfrac{\rho(n)}{\rho'(n)}\right]}{\Delta n} = \frac{\partial\left(\dfrac{\rho(n)}{\rho'(n)}\right)}{\partial n} , \tag{7.84}$$

gives:

$$J_n = -\beta_v(n)\rho'(n)\frac{\partial\left[\rho(n)/\rho'(n)\right]}{\partial n} , \tag{7.85}$$

which is the basic flux equation. Re-arranging Eq. (7.85) by taking the natural log of both sides and summing from $j = 0$ to $n-1$ gives:

$$\sum_{j=0}^{n-1} \ln\left(\frac{\rho'(j)}{\rho'(j+1)}\right) = \sum_{j=0}^{n-1}\left\{-\ln\left[\frac{\beta_i(j+1)}{\beta_v(j)} + \exp\left(\frac{\delta G_j^0}{kT}\right)\right]\right\} , \tag{7.86}$$

and

$$\ln\left(\frac{\rho'(n)}{\rho'(0)}\right) = \sum_{j=0}^{n-1}\left\{-\ln\left[\frac{\beta_i(j+1)}{\beta_v(j)} + \exp\left(\frac{\delta G_j^0}{kT}\right)\right]\right\} . \tag{7.87}$$

We can identify two boundary conditions. The first is the quantity $\rho'(0)$, which may be evaluated by noting that as $\beta_i(n)/\beta_v(n) \to 0$, $\rho'(0) = \rho^0(0)$ and that $\rho^0(0) \to N_0$, is simply the number of nucleation sites per unit volume. Since N_0 (and hence $\rho'(0)$) is independent of void concentration, we can write:

$$\ln\left(\frac{\rho'(n)}{\rho'(0)}\right) = \sum_{j=0}^{n-1}\left\{-\ln\left[\frac{\beta_i(j+1)}{\beta_v(j)} + \exp\left(\frac{\delta G_j^0}{kT}\right)\right]\right\} = \frac{-\Delta G_n'}{kT} , \tag{7.88}$$

and

$$\Delta G_n' = kT\sum_{j=0}^{n-1}\ln\left[\frac{\beta_i(j+1)}{\beta_v(j)} + \exp\left(\frac{\delta G_j^0}{kT}\right)\right] . \tag{7.89}$$

Since as $\beta_i(n)/\beta_v(n) \to 0$, $\rho'(0) \to \rho^0(0)$ and $\rho^0(0)$ is just N_0, the number of nucleation sites per unit volume, we have then:

$$\rho'(n) = N_0 \exp\left(\frac{-\Delta G_n'}{kT}\right) , \tag{7.90}$$

and

ΔG_n^0 = activation barrier without interstitials
$\Delta G_n'$ = activation barrier with interstitials.

The upper curve in Fig. 7.54 shows $\Delta G_n'$ as functions of n. Note that $\Delta G_n'$ is larger than ΔG_k^0, and requires a larger loop size due to the hindering effect of interstitials on the loop nucleation process. The maxima in the two curves occur at n_k, ΔG_k^0 and n_k', $\Delta G_k'$.

Now, the steady state loop nucleation rate may be calculated from the expression for J_n in Eq. (7.85):

$$J_k = Z'\beta_k\rho_k' , \tag{7.91}$$

which is the rate at which loops escape over the potential barrier of height $\Delta G_k'$ in units of loops/cm^3 s. The term β_k, is the rate of single vacancy impingement on a loop of size n_k'. The term Z' is:

$$Z' = \left[-\frac{1}{2\pi kT}\frac{\partial^2\Delta G_n'}{\partial n^2}\right]_{n_k'}^{1/2} . \tag{7.92}$$

The subscript indicates that the second derivative is to be evaluated at $n = n_k'$. As with Z in Eq. (7.75), its value is the width of $\Delta G_k'$at kT units below the maximum and is of the order of 0.05. The second derivative is found from Eq. (7.69) to be:

$$\frac{1}{kT}\left(\frac{\partial^2\Delta G_n'}{\partial n^2}\right)_{n_k'} = \left\{\left[\frac{1}{kT}\frac{\partial^2\Delta G_n^0}{\partial n^2}\right]\left[\exp\left(\frac{1}{kT}\frac{\partial\Delta G^0}{\partial n}\right)\right]\right\}_{n_k'} , \tag{7.93}$$

giving:

$$\rho'_k = N_0 \exp\left(-\Delta G'_k / kT\right) , \tag{7.94}$$

where $\Delta G'_k$ is determined by evaluating Eq. (7.89) at n'_k.

The steady state nucleation rate will not be established immediately after a sudden change in supersaturation or temperature, but will lag by a characteristic time, τ, known as the incubation time and is given by [22]:

$$\tau = 2(\beta_k Z'^2)^{-1} . \tag{7.95}$$

Equations (7.89) and (7.94) also apply for interstitial loop nucleation except that Z', β_k and ρ'_k are for interstitial loops rather than for vacancy loops, and $\Delta G'_n$ for interstitial loops is:

$$\Delta G'_n = kT \sum_{j=0}^{n-1} \ln \left[\frac{\beta_v(j+1)}{\beta_i(j)} + \exp\left(\frac{\delta G_j^0}{kT} \right) \right] , \tag{7.96}$$

where δG_j^0 is now the difference between the free energies of forming dislocation loops of $j+1$ and of j interstitials (in the absence of vacancies), β_k is the gross rate of interstitial capture by the loop of critical size and $1/Z'$ is the width of $\Delta G'_n$ (for interstitials) a distance kT below the maximum at $\Delta G'_k$, and the net number of interstitials in the critical nucleus is denoted by n'_k. The critical loop size, n'_k occurs at the maximum of $\Delta G'_n$ and is determined by solving $\partial \Delta G'_n / \partial n = 0$ for n'_k.

More recent treatments of the nucleation rate call for setting the all the fluxes in Eq. (7.69) equal to the steady state flux, J_{ss}, leading to a family of equations [23]:

$$J_1 = \beta_v(1)\rho(1) - \alpha(2)\rho(2) = J_{ss} \tag{7.97}$$

$$J_2 = \beta_v(2)\rho(2) - \alpha(3)\rho(3) = J_{ss} \tag{7.98}$$

$$J_3 = \beta_v(3)\rho(3) - \alpha(4)\rho(4) = J_{ss} \tag{7.99}$$

$$\vdots$$

$$J_{n-1} = \beta_v(n-1)\rho(n-1) - \alpha(n)\rho(n) \tag{7.100}$$

where $n = n_v^{max}$. Letting the ratio of shrinkage to growth, $\alpha_k / \beta_v^k = r_k$ for all $k \leq 2$, and letting $r_1 = 1$, the system of equations can be solved by multiplying the equations for J_k by the product of all the r_k with $k \leq i$. That is, Eq. (7.98) is multiplied by r_2, Eq. (7.99) is multiplied by both r_2 and r_3, and so on. If the resulting set of equations is summed, all the r_k are eliminated except r_1 and r_n to yield:

$$J_1 = J_{ss} = \frac{\beta_v(1)\rho(1) - \alpha(n)\rho(n) \prod_{j=2}^{n-1} r_j}{1 + \sum_{k=2}^{n-1} \prod_{j=2}^{k} r_j} . \tag{7.101}$$

The product term in the numerator is eliminated by noting that (1) for a nucleation problem, the concentration of the monodefect, $\rho(1)$ will be much greater than $\rho(n)$,

and (2) the ratio of the shrinkage to growth terms r_j is less than unity for $n > n_v^*$. Therefore, Eq. (7.101) becomes:

$$J_{ss} = \beta_v(1)\rho(1)\left[1 + \sum_{k=2}^{n-1}\prod_{j=2}^{k} r_j\right]^{-1} . \tag{7.102}$$

The advantage of this method to compute J_{ss} is the elimination of the Zeldovich factor and the approximations that must be made to compute it.

Russell [22] determined that based on vacancy and interstitial parameters and their likely supersaturations in a solid under irradiation, that interstitial loop nucleation is easier than vacancy loop nucleation because interstitial loop nucleation is much less sensitive to vacancy involvement than is vacancy loop nucleation to interstitial involvement. The primary reason is that S_i is expected to be several orders of magnitude greater than S_v during irradiation because of the very low equilibrium concentration of interstitials. Nevertheless, nucleation by this mechanism has been found to be difficult for both vacancy and interstitial loops, in contrast to the observation of stable loop growth after fairly low doses.

7.6.2 Clustering Theory

The nucleation of loops is essentially a clustering process in which enough of one type of defect needs to cluster, in the presence of the other type of defect, to result in a critical size embryo that will survive and grow. The cluster will shrink or grow depending on the net condensation rate of defects on clusters. Generalizing the description of cluster behavior in phase space given in the last section, and taking a vacancy loop as an example, vacancy clusters, v_j consisting of j vacancies will shrink or grow according to:

$$\begin{aligned}\frac{dv_j}{dt} = {} & K_{0j} - \sum_{n-1}^{\infty}[\beta_{v_n}(j) + \beta_{i_n}(j)]v_j - \sum_{n=1}^{j}\alpha_{v_n}(j)v_j \\ & + \sum_{n=1}^{j-1}\beta_{v_n}(j-n)v_{j-n} + \sum_{n=1}^{\infty}\beta_{i_n}(j-n)v_{j+n} \\ & + \sum_{n=1}^{\infty}\alpha_{v_n}(j+n)v_{j+n} + \text{additional loss terms}\end{aligned} \tag{7.103}$$

where β_{v_n} and β_{i_n} are the capture rates of migrating defect clusters v_n or i_n by a cluster of size v_j, and α_{v_n} is the corresponding emission or thermal dissolution rate. The first term on the RHS is the direct production of clusters of size j. The second term is the loss of clusters from size class j due to absorption of a vacancy or an interstitial cluster of size n, where $1 \simeq n \simeq \infty$. The third term is the loss of clusters from size class j due to emission of vacancy clusters of size n. The fourth and fifth terms are the addition of clusters to size class j due to absorption of vacancy clusters by smaller size classes, and the absorption of interstitial

clusters by larger size classes. The sixth term is the addition of clusters to the size class j by loss of vacancy clusters from larger size classes and the "additional loss terms" allow for other mechanisms of contributing to the number of clusters in size class j.

Equation (7.103) can be solved numerically without further simplification. But for large clusters and long irradiation times, the number of equations required would be extremely large. A major simplification is to require clusters to grow or shrink by only the addition or loss of single point defects, resulting in:

$$\begin{aligned}\frac{\mathrm{d}\nu_j(t)}{\mathrm{d}t} &= K_{0j} + \beta(j-1,j)\nu_{j-1}(t) + \alpha(j+1,j)\nu_{j+1}(t) \\ &\quad - [\beta(j,j+1) + \alpha(j,j-1)]\nu_j(t)\,, \quad j \geq 2\,. \end{aligned} \tag{7.104}$$

If it is assumed that j is a continuous variable and a Taylor series expansion is used in Eq. (7.104) to relate all functions to their values at size j, the simplified description is a continuum diffusional approximation in size space, known as a *Fokker–Planck equation*:

$$\begin{aligned}\frac{\partial \nu_j(t)}{\partial t} &= K_{0j}(t) - \frac{\partial}{\partial j}\left\{\nu_j(t)\left[\beta(j,j+1) - \alpha(j,j-1)\right]\right\} \\ &\quad + \frac{1}{2}\frac{\partial^2}{\partial j^2}\left\{\nu_j(t)[\beta(j,j-1) + \alpha(j,j+1)]\right\}\,, \end{aligned} \tag{7.105}$$

which is further simplified to:

$$\begin{aligned}\frac{\partial \nu_j(t)}{\partial t} &= K_{0j}(t) - \frac{\partial}{\partial j}F_{\mathrm{v}_j}\nu_j(t) + \frac{\partial^2}{\partial j^2}D_{\mathrm{v}_j}\nu_j(t) \\ &= K_{0j}(t) - \frac{\partial}{\partial j}\left(F_{\mathrm{v}_j}\nu_j(t) - \frac{\partial}{\partial j}D_{\mathrm{v}_j}\nu_j(t)\right)\,. \end{aligned} \tag{7.106}$$

The first term on the RHS of Eq. (7.106) is the direct production rate of clusters of size j. The second term is the *drift* in size space driven by the excess condensation of one point defect type over another:

$$F_{\mathrm{v}_j} = (z_{\mathrm{v}}D_{\mathrm{v}}C_{\mathrm{v}} - z_{\mathrm{i}}D_{\mathrm{i}}C_{\mathrm{i}}) \tag{7.107}$$

The drift term is responsible for the shift of the cluster size distribution to larger sizes. The drift term ensures that a large cluster will inevitably grow in a radiation field, but due to the evolving microstructure, the drift contribution is not constant with dose. Cluster evolution is also very sensitive to the ratio of the concentration of vacancies and interstitials, as F_{v} contains the difference in their contribution and can change sign. The result is that the sign of F_{v} depends on the overall microstructure.

The third term is the *diffusion* in size space and D_{v_j} is the irradiation-enhanced diffusion coefficient given by:

$$D_{\mathrm{v}_j} = 1/2(z_{\mathrm{v}}D_{\mathrm{v}}C_{\mathrm{v}} + z_{\mathrm{i}}D_{\mathrm{i}}C_{\mathrm{i}})\,. \tag{7.108}$$

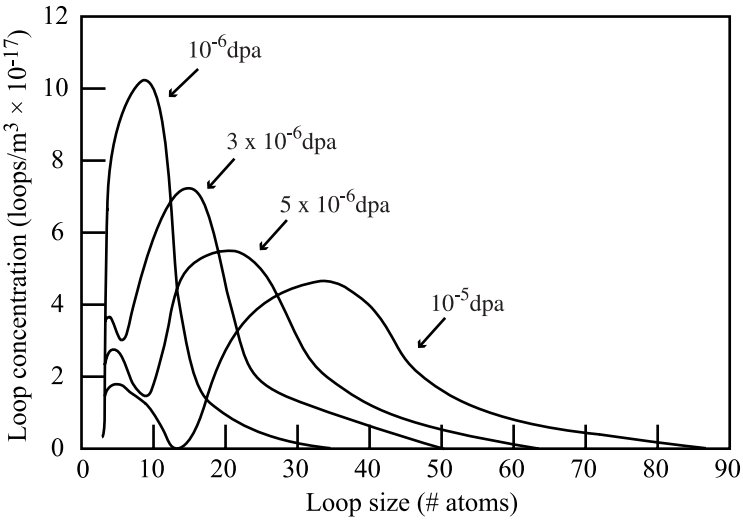

Fig. 7.56. Development of the interstitial loop size distribution with dose in 316 stainless steel irradiated at a dose rate of 10^{-6} dpa/s and a temperature of 550 °C with $\rho_d = 10^{13}\,m^{-2}$ (after [25])

The diffusion term causes the cluster size distribution to broaden with dose. The diffusion term accounts for the fact that two different clusters introduced at the same time at the same size may differ in size at a later time due to random encounters with point defects.

Algorithms for the approximate solution of Eq. (7.106) are discussed by Golubov et al. [24]. The features of the Fokker–Planck equation are illustrated in Fig. 7.56 for the development of the interstitial loop size distribution for 316 stainless steel with initial dislocation density of $10^{13}\,m^{-2}$, irradiated at 550 °C at a dose rate of 10^{-6} dpa/s. Note that with increasing dose, the mean loop size increases (drift term in Eq. (7.106)) and the size distribution broadens (diffusion term in Eq. (7.106)). As small clusters grow and their geometry changes, so does the capture efficiency for freely migrating defects. For very large cluster sizes, the Fokker–Planck equation is too simple as the defect production and cluster growth depend on the microstructure. The effect of the damage microstructure in the evolution of defect clusters must be accounted for in order to accurately predict their behavior.

7.6.3 Production Bias-Driven Cluster Nucleation

As discussed both in Chap. 3 and in the Sects. 7.3 and 7.4 of this chapter, a significant fraction of point defects produced under cascade damage irradiation are in the form of mobile and immobile vacancy and interstitial clusters such that freely migrating interstitials and vacancies are produced in unequal numbers. This has led to the concept of *production bias* as a major driving force for microstructure evolution under cascade-producing irradiation, and is based on the premise that defects

in clusters do not behave as freely migrating defects. In fact, as we have seen, interstitial clusters can be mobile and exhibit 1D and 3D glide. In some cases, the clusters remain mobile to very large size, though generally, there is a tendency toward the sessile state with increasing size. This picture of defect formation describes an asymmetry, or bias, in the production of freely migrating point defects under cascade damage conditions due to two sources: (1) the difference in the proportion of vacancies and interstitials that agglomerate into primary clusters, and (2) the difference in the thermal stability and mobility of the vacancy and interstitial clusters. Under cascade conditions, in addition to the probabilistic nature of point defect jumps, the random production, in space and time, of clusters also introduces fluctuations in the point defect fluxes to the sinks. The *production bias model* (PBM) is a framework for considering this added complication in the evolution of the microstructure under irradiation.

Semenov and Woo [26] utilized the Fokker–Planck treatment of cluster dynamics presented in the last section to produce a revised description of the loop nucleation rate that incorporates the effect of small interstitial cluster generation in the collision cascade produced randomly in time and space. They considered that small, immobile interstitial clusters are continuously generated in collision cascades, and that these clusters can be treated as small dislocation loops. The probability density, P of an interstitial cluster with a size of n_0 interstitials at a time t_0, to grow to a size of n interstitials at time t is:

$$\frac{\partial P_{\mathrm{i}}(n,t)}{\partial t} = -\frac{\partial}{\partial n}\left(F_{\mathrm{i}}(n) - \frac{\partial}{\partial n}D_{\mathrm{i}}(n)\right)P_{\mathrm{i}}\,, \tag{7.109}$$

where the *diffusion* term, $D_{\mathrm{i}}(n)$ describes the spreading of the size distribution of interstitial loops in time due to random fluctuations in the isolated and clustered point defect fluxes and is given by:

$$D_{\mathrm{i}}(n) = D_{\mathrm{i}}^{\mathrm{s}}(n) + D_{\mathrm{i}}^{\mathrm{cl}}(n)\,, \tag{7.110}$$

with superscripts *s* and *cl* denoting single defects and clusters, respectively, and:

$$D_{\mathrm{i}}^{\mathrm{s}}(n) = \left(\frac{\pi n}{\Omega b}\right)^{1/2}(z_{\mathrm{v}}D_{\mathrm{v}}C_{\mathrm{v}} + z_{\mathrm{i}}D_{\mathrm{i}}C_{\mathrm{i}})\,, \tag{7.111}$$

$$D_{\mathrm{i}}^{\mathrm{cl}} = \frac{N_{\mathrm{d}}K_0 n}{4b}\left(z_{\mathrm{v}}^2\frac{\langle N_{\mathrm{dv}}^2\rangle}{k_{\mathrm{v}}N_{\mathrm{d}}^2} + z_{\mathrm{i}}^2\frac{\langle N_{\mathrm{di}}^2\rangle}{k_{\mathrm{i}}N_{\mathrm{d}}^2}\right)\,. \tag{7.112}$$

In the preceding, K_0 is the effective point defect generation rate (cluster and free), N_{d} is the average number of point defects generated per cascade and $\langle N_{\mathrm{dv,i}}^2\rangle$ is the average of the square of the quantity, $k_{\mathrm{v,i}}^2$ are the total sink strengths for vacancies and interstitials, z_{vi} are the bias factors for vacancies and interstitials, and b is the magnitude of the Burgers vector.

The *drift* term has two components, $F_{\mathrm{i}}^{\mathrm{s}}(n)$, and $F_{\mathrm{i}}^{c}(n)$.

$$F_{\mathrm{i}}^{\mathrm{s}}(n) = \frac{2\pi r_{\mathrm{i}}(n)}{\Omega}(z_{\mathrm{i}}D_{\mathrm{i}}C_{\mathrm{i}} - z_{\mathrm{v}}D_{\mathrm{v}}C_{\mathrm{v}})\,, \tag{7.113}$$

is the term that drives the growth rate of loops and the loop radius:$r_\mathrm{i} = (n_\mathrm{i}\Omega/\pi b)^{1/2}$ and $C_\mathrm{i,v}$ and $D_\mathrm{i,v}$ are the average concentration and diffusion coefficient of the defects.

$$F_\mathrm{i}^\mathrm{c}(n) = \frac{2\pi r_\mathrm{i}(n)}{\Omega}\int_{n_0}^{n} x f_\mathrm{il}(x,t)W(x,n)\,\mathrm{d}x\,, \tag{7.114}$$

is the rate of change in the loop size due to the absorption of smaller interstitial loops by coalescence. The function $f_\mathrm{il}(n,t)$ is the distribution of interstitial loops which is related to the total loop number density, $N_\mathrm{il}(t)$ by:

$$N_\mathrm{il}(t) = \int_{n_\mathrm{min}}^{n_\mathrm{max}} f_\mathrm{il}(n,t)\,\mathrm{d}n\,, \tag{7.115}$$

and n_min is the size of the interstitial clusters at which they become mobile and n_max is the size at which they join the network. The term $W(n',n)$ describes the coalescence between loops of sizes n' and n ($n' < n$):

$$W(n',n) = \frac{4r_\mathrm{i}(n')}{\lambda_\mathrm{d}}\left[D_\ell(n) + \left(D_\ell^2(n) + \frac{v_\ell^2(n)\lambda_\mathrm{d}^2}{4}\right)^{1/2}\right]\,, \tag{7.116}$$

where λ_d is the mean free path between two consecutive coalescing events, v_ℓ is the climb velocity and $D_\ell(n)$ is the climb diffusion coefficient due to the fluctuating point defect fluxes and is given as:

$$D_\ell(n) = D_\ell^\mathrm{s}(n) + D_\ell^\mathrm{cl}(n)\,, \tag{7.117}$$

with:

$$D_\ell^\mathrm{s}(n) = \frac{\Omega}{4\pi b^2 r_\mathrm{i}(n)}(z_\mathrm{v}D_\mathrm{v}C_\mathrm{v} - z_\mathrm{i}D_\mathrm{i}C_\mathrm{i})\,, \tag{7.118}$$

$$D_\ell^\mathrm{cl} = \frac{N_\mathrm{d}K_0\Omega}{16\pi b^2}\left(z_\mathrm{v}^2\frac{\langle N_\mathrm{dv}^2\rangle}{k_\mathrm{v}N_\mathrm{d}^2} + z_i^2\frac{\langle N_\mathrm{di}^2\rangle}{k_\mathrm{i}N_\mathrm{d}^2}\right). \tag{7.119}$$

Subject to the boundary conditions:

$$P_\mathrm{i}(n_\mathrm{min},t)|_{n_0,t_0} = P_\mathrm{i}(n_\mathrm{m},t)|_{n_0,t_0} = 0\,, \tag{7.120}$$

the solution to Eq. (7.109) is given by Semenov and Woo [26] to be:

$$P_\mathrm{m} = \frac{\int_{n_\mathrm{min}}^{n_0}\exp\left(-\int_{n_\mathrm{min}}^{x}\frac{F_\mathrm{i}^\mathrm{s}(x')}{D_\mathrm{i}(x')}\,\mathrm{d}x'\right)\mathrm{d}x}{\int_{n_\mathrm{min}}^{n_0}\exp\left(-(1-\alpha^*)\int_{n_\mathrm{min}}^{x}\frac{F_\mathrm{i}^\mathrm{s}(x')}{D_\mathrm{i}(x')}\,\mathrm{d}x'\right)\mathrm{d}x}\,, \tag{7.121}$$

where

$$\alpha^* = \frac{F_\mathrm{i}^c(n_\ell)}{F_\mathrm{i}^\mathrm{s}(n_\ell)}(n_\mathrm{min} < n_\ell < n^* < n_\mathrm{m})\,. \tag{7.122}$$

The term α^* is the ratio of the rate of loop size change due to cluster coalescence to that due to point defect absorption, or essentially, the relative importance of cluster coalescence compared to defect absorption. Semenov writes the integrals in the exponential functions in Eq. (7.120) as:

$$\int_n \frac{F_{\rm i}^{\rm s}(x)}{D_{\rm i}(x)}\,{\rm d}x = \frac{2f_{\rm s}}{d_{\rm cl}}\left[n^{1/2} - \frac{d_{\rm s}}{d_{\rm cl}}\ln\left(\frac{d_{\rm s}}{d_{\rm cl}}n^{1/2}+1\right)\right]\,, \tag{7.123}$$

where

$$f_{\rm s} = \frac{F_{\rm i}^{\rm s}(n)}{n^{1/2}}\,,\quad d_{\rm s} = \frac{D_{\rm i}^{\rm s}(n)}{n^{1/2}}\,,\quad d_{\rm cl} = \frac{D_{\rm i}^{\rm cl}(n)}{n^{1/2}}\,. \tag{7.124}$$

The two limiting cases are when defect absorption is unimportant, $d_{\rm cl}\to 0$, and when cluster coalescence is minimal, $d_{\rm s}\to 0$. For the case $d_{\rm cl}\to 0$, Eq. (7.121) becomes:

$$\begin{aligned} P_{\rm m} = (1-\alpha^*)&\frac{\exp(-f_{\rm s}n_0/d_{\rm s}) - \exp(-f_{\rm s}n_{\rm min}/d_{\rm s})}{\exp(-f_{\rm s}n_{\rm m}(1-\alpha^*)/d_{\rm s}) - \exp(-f_{\rm s}n_{\rm min}(1-\alpha^*)/d_{\rm s})} \\ &\times \exp(\alpha^* f_{\rm s}n_{\rm min}/d_{\rm s})\,, \end{aligned} \tag{7.125}$$

and for the case $d_{\rm s}\to 0$, Eq. (7.121) becomes:

$$\begin{aligned} P_{\rm m} = &\left\{(1-\alpha^*)^2\exp\left(2\alpha^* f_{\rm s}n_{\rm min}^{1/2}/d_{\rm cl}\right)\left[\left(1+2f_{\rm s}n_0^{1/2}/d_{\rm cl}\right)\exp\left(-2f_{\rm s}n_0^{1/2}/d_{\rm cl}\right)\right.\right. \\ &\left.\left. - \left(1+2f_{\rm s}n_{\rm min}^{1/2}/d_{\rm cl}\right)\exp\left(-2f_{\rm s}n_{\rm min}^{1/2}/d_{\rm cl}\right)\right]\right\} \\ &/\left\{\left(1+2(1-\alpha^*)f_{\rm s}n_{\rm min}^{1/2}/d_{\rm cl}\right)\exp\left(-2(1-\alpha^*)f_{\rm s}n_{\rm min}^{1/2}/d_{\rm cl}\right)\right. \\ &\left. - \left(1+2(1-\alpha^*)f_{\rm s}n_{\rm min}^{1/2}/d_{\rm cl}\right)\exp\left(-2(1-\alpha^*)f_{\rm s}n_{\rm min}^{1/2}/d_{\rm cl}\right)\right\}\,. \end{aligned} \tag{7.126}$$

The behavior of $P_{\rm m}$ as a function of the number of interstitials in the cluster is shown in Fig. 7.57. In this case, $\alpha^* = 0$ and the solid lines are for the case where $d_{\rm s}\to 0$, Eq. (7.126), and the dashed lines are for the case were $d_{\rm cl}\to 0$, Eq. (7.125). The dashed line at the lower left in the figure resulted when clusters are ignored. However, when clustering is considered (solid lines) the nucleation probability increases substantially. In fact, if we define ε_{i0} to be the fraction of interstitials produced in cascades in the form of immobile clusters, and K_0 is the interstitial production rate, then $\varepsilon_{i0}K_0/n_0$ is the production rate of interstitial clusters in the cascade, and the nucleation rate of interstitial loops is:

$$J_\ell = \frac{\varepsilon_{i0}K_0P_{\rm m}}{\Omega n_0}\,. \tag{7.127}$$

Choosing the following values; $\varepsilon_{i0} = 0.4$, $P_{\rm m}\sim 10^{-6}$, $\Omega\sim 10^{-29}\,{\rm m}^3$, $n_0\sim 8$, gives $\sim 5\times 10^{21}\,{\rm loops/m}^3$ per NRT dpa. Given that loop densities are observed to be about this value, then the incubation dose is on the order of 1 NRT dpa. However, this value for the nucleation incubation time is high as small loops are readily observed in transmission electron microscopy of irradiated materials at fractions of a dpa.

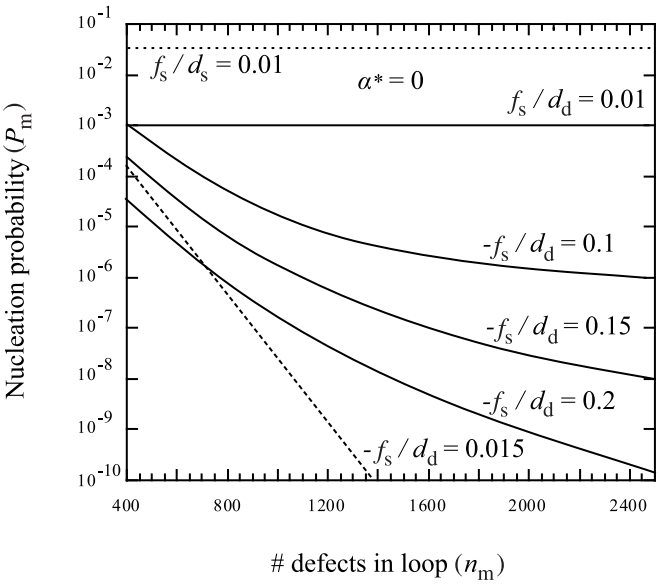

Fig. 7.57. Interstitial cluster nucleation probability as a function of loop size. In this figure, $\alpha^* = 0$ and the *solid lines* are for the case where $d_s \to 0$, Eq. (7.126), and the dashed lines are for the case were $d_c \to 0$, Eq. (7.125). The *dashed line* at the *lower left* in the figure is result when clusters are ignored (after [26])

7.7 Dislocation Loop Growth

The growth of loops can also be determined from the Fokker–Planck equations that provide the size distribution of loops of all sizes (see Fig. 7.56). Applying Eq. (7.104) to the case of interstitial loops gives an equation of the form:

$$\frac{\mathrm{d}i_j}{\mathrm{d}t} = K_{0j} + [\beta_v(j+1) + \alpha_i(j+1)]i_{j+1} - [\beta_v(j) + \beta_i(j) + \alpha_i(j)]i_j + \beta_i(j-1)i_{j-1} \,, \tag{7.128}$$

where i_j is the concentration of interstitial loops of size j and the term on the LHS of Eq. (7.128) is the time rate of change of the population of interstitial loops of size j. The terms $\beta_k(j)$ and $\alpha_k(j)$ are the absorption and emission rates of defects of type k from loops of size j. The first term on the RHS of the equality is the direct production rate of clusters of size j. Practically, this term is different from zero up to the tetrahedral cluster ($j = 4$). The first term in square brackets is the production of clusters of size j by the emission of an interstitial or absorption of a vacancy by clusters of size $j + 1$. The second term in square brackets is the loss of clusters of size j by absorption of a vacancy or an interstitial, or emission of an intertstitial. The last term is the addition of clusters of size j by capture of an interstitials by clusters

of size $j-1$. Solution of Eq. (7.128) results in the loop size distribution as a function of time, which describes the evolution of interstitial loops with dose or time.

Pokor et al. [27] used the Fokker–Planck formalism to model the evolution of a population of loops via chemical rate theory in a homogeneous medium. In their treatment, they allowed for production of clusters in the cascade containing up to four defects, and solved a set of equations for the concentration of defect clusters consisting of two equations for individual vacancies or interstitials and $2N$ equations for the population of loops up to size N. The physics of the formulation is contained in the expressions for the defect capture rates, β, and emission rates, α for each defect type, k as a function of the cluster size, given as [27]:

$$\beta_{\mathrm{k}}(j) = 2\pi r(j) z_{\mathrm{c}}(j) D_{\mathrm{k}} C_{\mathrm{k}} \,, \tag{7.129}$$

$$\alpha_{\mathrm{k}}(j) = 2\pi r(j) z_{\mathrm{c}}(j) \frac{D_{\mathrm{k}}}{\Omega} \exp(-E_{\mathrm{bk}}(j)/kT) \,, \tag{7.130}$$

where $r(j)$ is the radius of an interstitial loop of size j, D_k andC_k are the diffusion coefficient and concentration of defect k, $z_{\mathrm{c}}(j)$ is the bias factor for the interstitial loop of size j and $E_{\mathrm{bk}}(j)$ is the binding energy of for a cluster of j defects of type k. Pokor [27] gives the following expressions for $z_{\mathrm{c}}(j)$ and E_{bi}:

$$z_{\mathrm{c}}(j) = z_{\mathrm{i}} + \left(\sqrt{\frac{b}{8\pi a}} z_{\mathrm{li}} - z_{\mathrm{i}} \right) \frac{1}{j^{a_{\mathrm{li}}/2}} \,, \tag{7.131}$$

$$E_{\mathrm{b}}^{\mathrm{i}} = E_{\mathrm{f}}^{\mathrm{i}} + \frac{E_{\mathrm{b}}^{2i} - E_{\mathrm{f}}^{i}}{2^{0.8} - 1} (j^{0.8} - (j-1)^{0.8}) \,, \tag{7.132}$$

where z_{i} is the bias factor for a straight dislocation line for interstitials, a is the lattice parameter and b is the Burgers vector, z_{li} and a_{li} are parameters used to describe the evolution of the bias with cluster size [28]. For the binding energy term, E_{f}^{i} is the formation energy of an interstitial point defect Eq. (4.16), E_{b}^{2i} is the binding energy of a two-interstitial cluster and j is the number of defects in a cluster of size j and the expression comes from molecular dynamics simulations [29, 30].

In order to account for the effect of the annihilation of the network dislocation density with dose, they assumed that the rate of change of the density was proportional to $\rho^{3/2}$, giving $\mathrm{d}\rho/\mathrm{d}t = -Kb^2\rho^{3/2}$, and resulting in a dislocation density that decreases as $1/t^2$ (see next section). The network dislocation density in irradiated metals evolves toward a saturation value with increasing dose. In stainless steel, it has been observed to reach a saturation value of $\sim 6\times10^{-10}\,\mathrm{cm}^{-2}$ over a temperature range that spans 400 to 600 ℃ [31]. Cluster model results of the loop density and size for three grades of stainless steel irradiated at 330 ℃ and to doses up to 40 dpa calculated using Eqs. (7.128)–(7.132) are compared against measurements in Fig. 7.58 and show relatively good agreement. Dislocation recovery plays an important role in microstructure evolution as it represents a change in sink density. Failure to account for the recovery of the initial dislocation network would lead to a faster saturation of the loop structure in the 316 alloys. The most sensitive param-

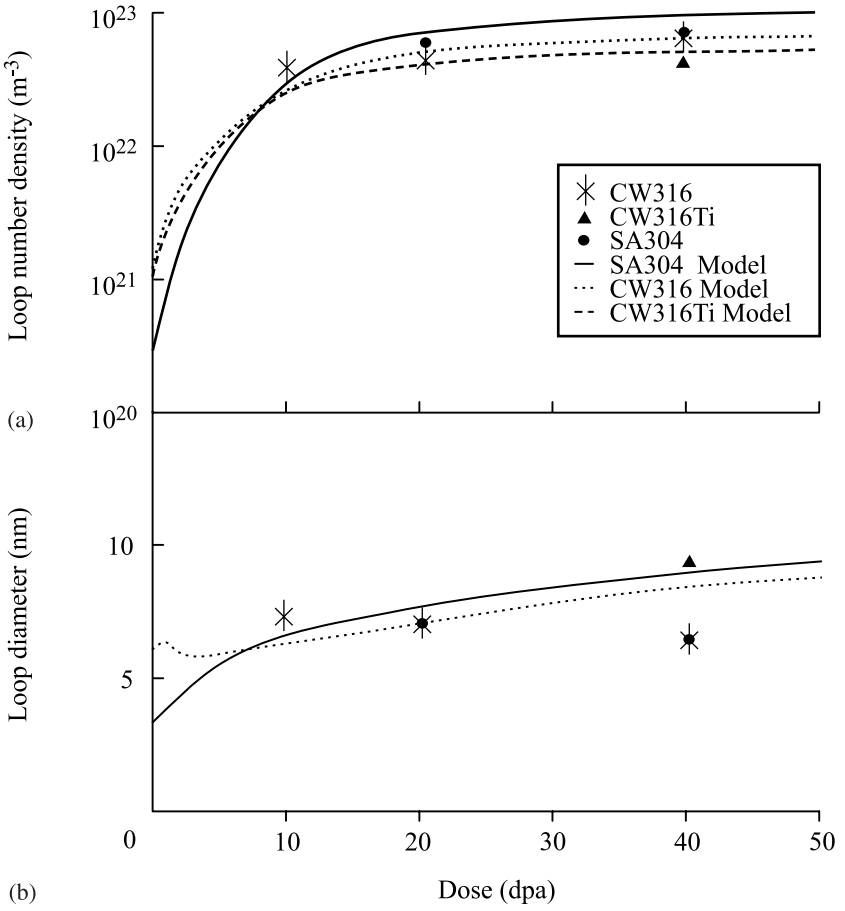

Fig. 7.58. Evolution of the Frank loop (a) density and (b) size for 330 °C irradiation to high dose according to the cluster dynamics model of Pokor et al. (after [27])

eters controlling the irradiation microstructure are the temperature, dose, materials constants and the initial network dislocation density.

Simpler treatments for determining the loop size distribution can be made by neglecting the formation of defect clusters larger than the tetra-interstitial, limiting the number of size classes and simplifying the cluster description. Stoller et al. [32] described the evolution of larger loops by the equation:

$$\frac{\mathrm{d}i_j}{\mathrm{d}t} = i_{j-1}\tau_j^{-1} - i_j\tau_{j+1}^{-1}\,, \tag{7.133}$$

where i_j is the number of loops in a given size class with radius r_L, and the τ_j is the lifetime of a loop of size j against growth to the next larger size class:

$$\tau_j = \int_{r_j}^{r_{j+1}} \left(\frac{\mathrm{d}r_\mathrm{L}}{\mathrm{d}t}\right)^{-1} \mathrm{d}r_\mathrm{L}\,, \tag{7.134}$$

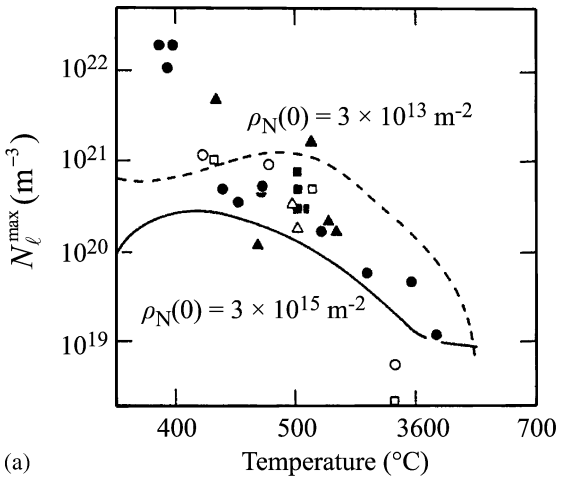

(a)

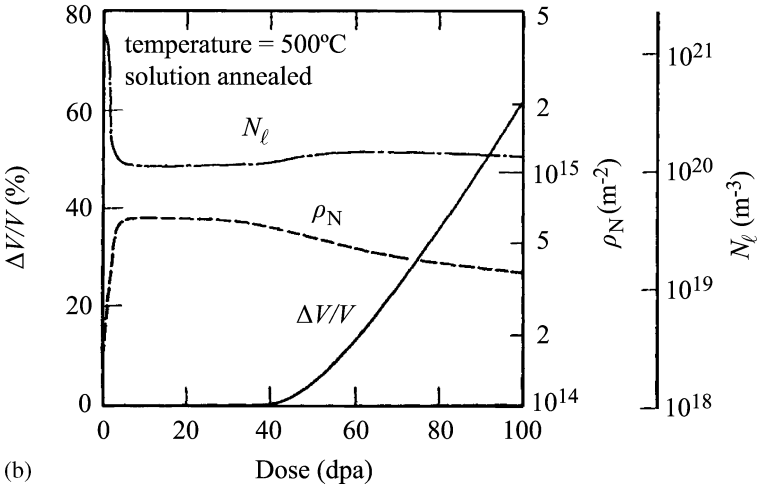

(b)

Fig. 7.59. (a) Comparison of calculated maximum faulted loop density and low fluence fast reactor data as a function of temperature. (b) Dose dependence of faulted loop density for irradiation of solution annealed stainless steel at 500 °C (after [32])

and

$$\frac{\mathrm{d}r_\mathrm{L}}{\mathrm{d}t} = \frac{\Omega}{b}[z_\mathrm{iL}(r_\mathrm{L})D_\mathrm{i}C_\mathrm{i} - z_\mathrm{vL}(r_\mathrm{L})D_\mathrm{v}(C_\mathrm{v} - C_\mathrm{vL})]\,, \tag{7.135}$$

where z_iL and z_vL are given by Eq. (5.97) and $C_\mathrm{vL} = C_\mathrm{v}^0 \exp(E_\mathrm{F}\Omega/kT)$, where E_F is the energy of a faulted loop from Eq. (7.65). Figure 7.59a shows a comparison of the temperature dependence of the calculated maximum faulted loop density and

low fluence fast reactor data for 316 stainless steel with initial network dislocation densities of $3\times10^{15}\,\mathrm{m}^{-2}$ (solid line) and $3\times10^{13}\,\mathrm{m}^{-2}$ (dashed line). Figure 7.59b shows the dose dependence of the loop density for solution annealed 316 irradiated at 500 ℃.

Semenov and Woo [26] accounted for the effect of production bias by writing Eq. (7.135) for the rate of change in loop size to include terms due to interstitial cluster and vacancy cluster absorption:

$$\frac{\mathrm{d}r_\mathrm{L}}{\mathrm{d}t}=\frac{\Omega}{b}[J_\mathrm{i}-J_\mathrm{v}+J_\mathrm{v}^e+J_\mathrm{i}^{cl}-J_\mathrm{v}^{cl}]\,, \tag{7.136}$$

where the Js are the fluxes due to single interstitials, single vacancies, vacancy thermal emission, interstitial clusters and vacancy clusters, respectively, and τ_d is the lifetime of the dislocation loop. Substituting for the fluxes [32] results in:

$$\frac{\mathrm{d}r_\mathrm{L}}{\mathrm{d}t}=\frac{K_0}{(\rho_N+\rho_\mathrm{L})b}\left(\frac{k_\mathrm{V}^2(\varepsilon_\mathrm{i}-\varepsilon_\mathrm{v}')+k_\mathrm{d}^2\bar{z}(1-\varepsilon_\mathrm{i})}{k^2}-\frac{K^e}{K_0}\right)\,, \tag{7.137}$$

where K_0 is the defect production rate, K^e is the vacancy thermal emission rate, ρ_n and ρ_L are network and loop dislocation densities, $\varepsilon_\mathrm{i,v}$ are the fraction of interstitials and vacancies, respectively, that are immobilized by intracascade clustering, $\varepsilon_\mathrm{v}'=\varepsilon_\mathrm{v}-K^e/K_0$, z_d is the dislocation bias, $k_\mathrm{V,d}^2$ are the sink strengths of voids and dislocations, k^2 is the total sink strength and $\bar{z}=\dfrac{z_\mathrm{d}k_\mathrm{c}^2}{k^2+z_\mathrm{d}k_\mathrm{d}^2}$. The steady state interstitial loop growth rate for 316 stainless steel with an effective point defect production rate of $10^{-7}\,\mathrm{dpa/s}$ is shown as a function of temperature in Fig. 7.60. The growth rate is in units of Burgers vector, b per dpa. Note that the loop growth rate is low at low and high temperatures and peaks at an intermediate temperature of about 500 ℃.

7.8 Recovery

Growing dislocation loops eventually encounter either network dislocations or each other. The maximum radius to which a loop can grow, R_max, is governed by the loop density, ρ_L as given by $\dfrac{4\pi}{3}\rho_\mathrm{L}R_\mathrm{max}^3=1$. When loops interact, they coalesce and contribute to the network dislocation density. Interaction between individual dislocations and loops results in loop unfaulting that also contributes to the network (discussed in Chap. 12, Sect. 12.3). As the dislocation density increases, the rate of loop interaction with the network increases and the loop radius is further limited by the network dislocation density as described by Eq. (5.82), $(\pi R_\mathrm{max}^2)\rho_N=1$.

However, observations of irradiated microstructures confirm that the dislocation density saturates, implying that there must also be a process for removal of network dislocations limiting their buildup. The process of recovery can explain the behavior of the dislocation density with irradiation. The rate of change of the dislocation

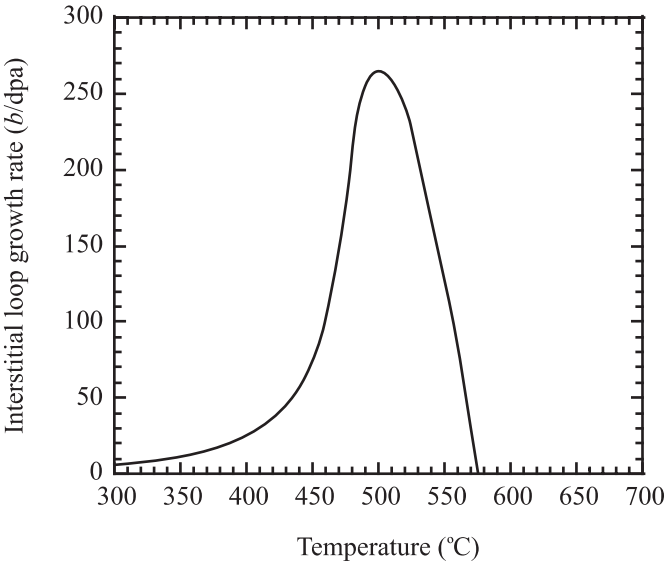

Fig. 7.60. Interstitial loop growth rate in units of Burgers vector, b per dpa as a function of temperature for a 316 stainless steel (after [33])

density in a solid under stress at high temperature is assumed to behave according to:

$$\dot{\rho} = B\rho - A\rho^2 \,, \tag{7.138}$$

where ρ is the density of mobile dislocations and A and B are constants. (Note that while the rate of dislocation density change given by Eq. (7.138) is phenomenological by nature, a more accurate description of the physical process is provided by Eq. (7.133)). The first term of Eq. (7.138) is the production rate of dislocations and the second term is the annihilation rate. The loss term is assumed to occur due to mutual annihilation of pairs of dislocations of opposite sign, which implies a reaction rate that is proportional to the square of the number of dislocations present at a given time. Garner and Wolfer [34] showed that the generation rate of dislocations is proportional to $b^2\phi\rho^{1/2}$, so that Eq. (7.138) can be written as:

$$\dot{\rho} = B\rho^{1/2} - A\rho^{3/2} \,, \tag{7.139}$$

where $B \sim b^2\phi$ and $A \sim v_c$, where v_c is the climb velocity of the dislocation (see Chap. 14). At steady state ($\mathrm{d}\rho/\mathrm{d}t = 0$), and the saturation density is $\rho_s = B/A$. The solution to Eq. (7.138) is given as:

$$\frac{\rho(t)}{\rho_s} = \frac{1 - e^{-x} + \sqrt{\rho_0/\rho_s}(1 + e^{-x})}{1 + e^{-x} + \sqrt{\rho_0/\rho_s}(1 - e^{-x})} \,, \tag{7.140}$$

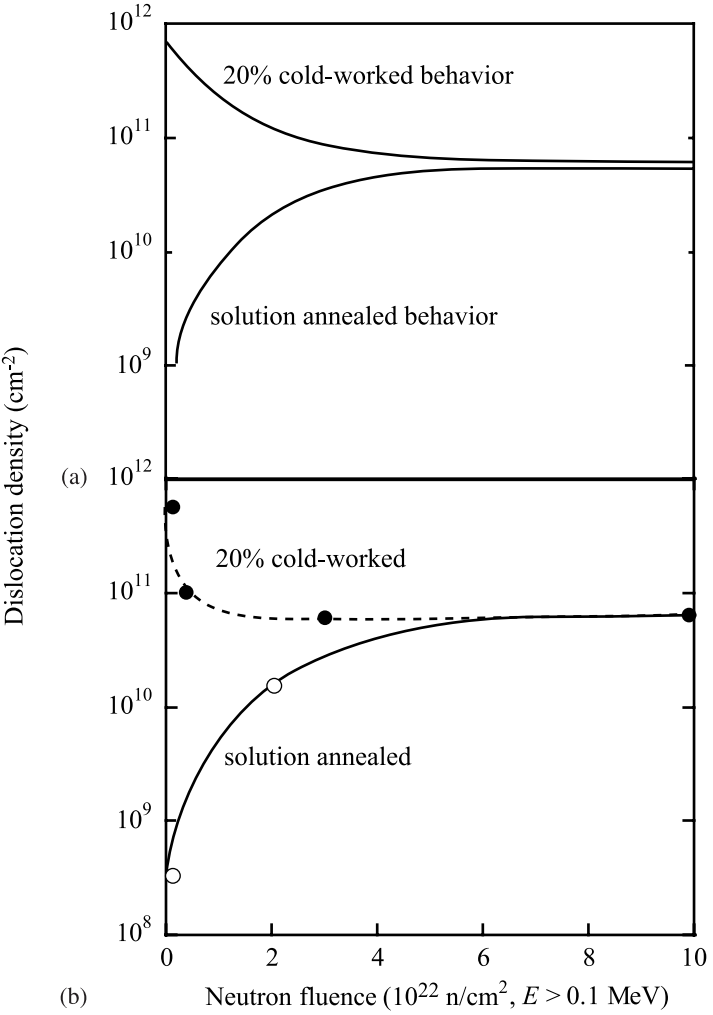

Fig. 7.61. (a) Calculated dislocation density evolution in 316SS at 500 °C using Eq. (7.139), for starting densities of $7 \times 10^{11}\,\mathrm{cm}^{-2}$ and $4 \times 10^{8}\,\mathrm{cm}^{-2}$, for cold-worked and annealed conditions, respectively (after [34]). (b) Measured dislocation density in 20% cold-worked and annealed 316SS after irradiation in EBR-II at 500 °C (after [35])

where ρ_0 is the initial dislocation density and

$$x = A\sqrt{\rho_s}t = \sqrt{\rho_s}v_c t\ . \tag{7.141}$$

Using a saturation density, ρ_s of $6 \times 10^{10}\,\mathrm{cm}^{-2}$, and initial dislocation densities, ρ_0 of $3 \times 10^{8}\,\mathrm{cm}^{-2}$ for annealed 316 SS and $7 \times 10^{11}\,\mathrm{cm}^{-2}$ for 20% CW 316 SS, the dislocation densities calculated from Eq. (7.139) are shown in Fig. 7.61a. The relationship between x in Eq. (7.140) and fluence was defined by the case where

the dislocation density for annealed 316 SS reached a value of $2 \times 10^{10}\,\mathrm{cm}^{-2}$ at $2 \times 10^{22}\,\mathrm{n/cm}^2$. Data are plotted in Fig. 7.61b. Note how well the model results of Fig. 7.61a agree with the data. This agreement also establishes that the original dislocations are no different from those produced during the irradiation with regard to their ability to absorb point defects.

7.9 Evolution of the Interstitial Loop Microstructure

The evolution of the interstitial loop population can be described in terms of its response to temperature and dose. The temperature regime that is important for LWR operation is between 270 and 340 °C. Higher temperatures may be reached from gamma heating in certain thick components such as PWR baffle plates. This temperature range represents a transition region between what is commonly termed as low-temperature (50–300 °C) and high-temperature (300–700 °C) behavior. Below 300 °C, the dislocation microstructure is characterized by a high density of "black dots" (defect clusters that are too small to resolve in the TEM, $< 2\,\mathrm{nm}$), network dislocations and a low density of Frank loops. A very small percentage of the small loops in stainless steels are observed to be SFT, which is much less than the 25–50% of clusters in nickel or copper [10]. Near 300 °C, the radiation-induced microstructure changes from one dominated by small dislocation loops to one containing larger faulted loops and network dislocations (Fig. 7.62). Figure 7.63 shows large dislocation loops after irradiation at high temperatures. Above

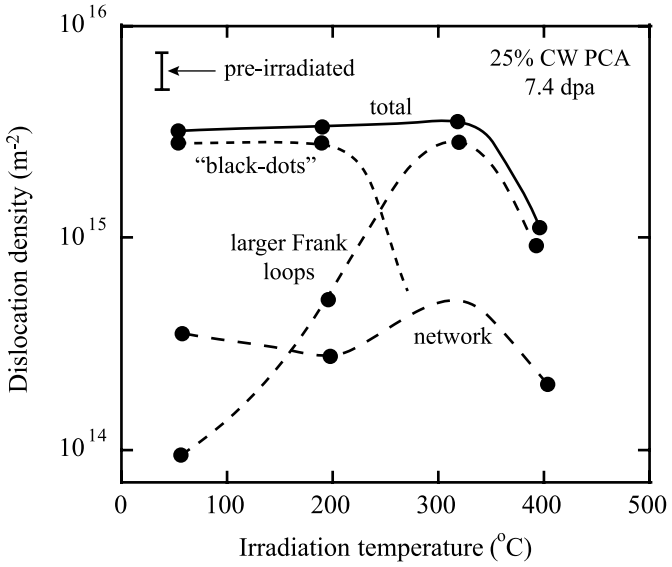

Fig. 7.62. Effect of irradiation temperature in the range 50–400 °C on the components of the dislocation density in neutron-irradiated austenitic stainless steel (after [36])

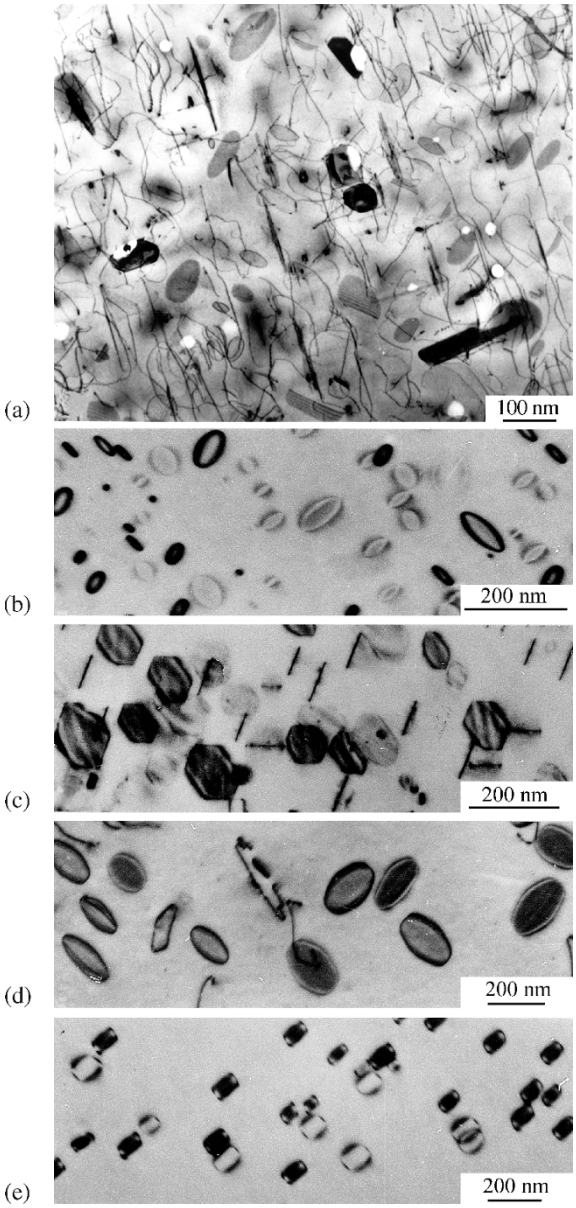

Fig. 7.63. Images of large Frank loops in (a) a 300 series stainless steel irradiated at 500 °C to a dose of 10 dpa (from [37]), and (b-e) in irradiated aluminum, copper, nickel and iron, respectively (after [16])

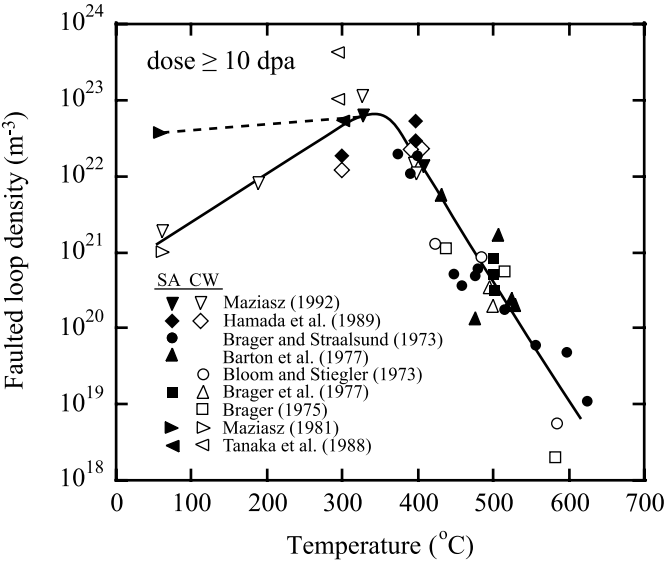

Fig. 7.64. Effect of temperature on the Frank loop density in the intermediate temperature region, 400–600 °C, for neutron-irradiated austenitic stainless steel (after [36])

300 °C, the Frank loop population begins to decrease. Figure 7.64 shows the sharp decrease in faulted loop density by a factor of over 1000 between 400 and 600 °C in neutron-irradiated austenitic stainless steels. The loop size increases with increasing temperature that eventually leads to an increase in the loop unfaulting rate which contributes to the reduction in Frank loop population at high temperature.

Loop density increases rapidly to saturation at low irradiation temperatures. Figure 7.65 shows the increase in loop density in austenitic stainless steels irradiated near 300 °C. Loop size is relatively insensitive to fluence below about 300 °C. At these low temperatures, loop sizes and densities become dynamically stable as a population when a balance is reached between new loop formation and the destruction of existing loops. With increasing temperature in the low-temperature regime, the density of fine loops decreases and the loop size increases.

The dislocation microstructure evolves into one composed of Frank loops and network dislocations above about 300 °C. Loop density saturates at a few dpa and the density is maintained (in a dynamic sense) at higher doses. The dislocation network density increases in proportion to the faulted loop density as temperature is increased though the overall dislocation density is expected to stay fairly constant between 300 and 370 °C. In the higher temperature regime (400–600 °C), the population consists of a low density of Frank loops and a dislocation network. Evolution may actually occur more slowly if other microstructural processes are also occurring such as void and bubble nucleation and growth.

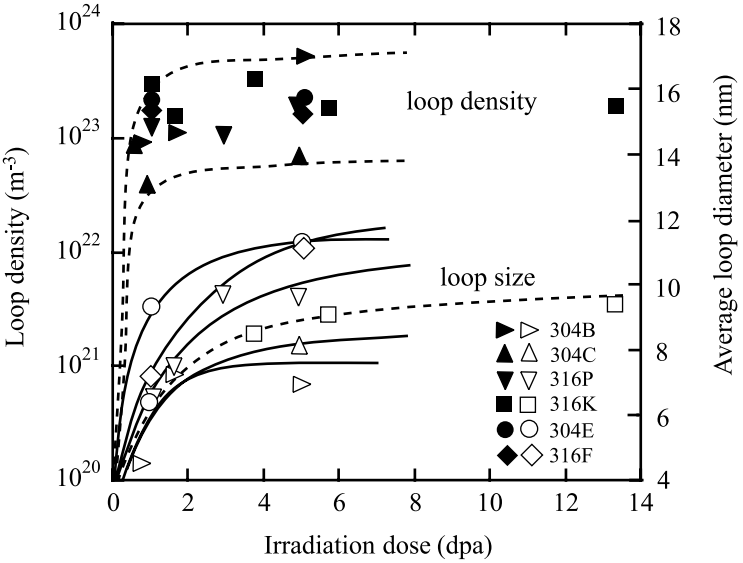

Fig. 7.65. Evolution of the Frank loop density and size in various austenitic stainless steels following irradiation to doses of up to 13 dpa at a temperature near 300 °C (after [38])

The description of defect cluster nucleation and evolution provides a backdrop for understanding the phenomenon of void growth discussed in the next chapter. As will be shown, void formation and growth is intimately linked to the production of defect clusters and their growth into loops, as these microstructures constitute critical sinks that will govern the fate of voids.

Nomenclature

a	Lattice constant
A	Area of slip plane
$\boldsymbol{b}$	Burgers vector
$C_{\mathrm{v,i}}$	Concentration of vacancies, interstitials
$C^0_{\mathrm{v,i}}$	Thermal equilibrium concentration of vacancies, interstitials
d^x	Strength of diffusive spread for clusters by the x process
$D_{\mathrm{v,i}}$	Diffusion coefficient of vacancies, interstitials
D_{k_j}	Diffusion term in size space of defect k and cluster size j, Eq. (7.106)
D_l	Climb diffusion coefficient
E	Energy
E_{b}	Binding energy
E_{f}	Formation energy
E_l	Dislocation loop energy

E_{m}	Migration energy
$\langle E_{\mathrm{m}} \rangle$	Effective activation energy for cluster motion
F_{k_j}	Drift velocity in size space of defect k and cluster size j Eq. (7.106)
G_{j}	Effective Frenkel pair production rate of species j
ΔG	Change in free energy
G_0	Standard free energy
i_n	Cluster of n interstitials
k	Boltzmann's constant
$k^2_{\mathrm{v,i}}$	Total sink strength for vacancies, interstitials
l	Length of dislocation line segment
L	Length of edge of stacking fault tetrahedron
J	Nucleation current. Also flux
K_0	Defect production rate
K^e	Vacancy thermal emission rate
m	Stress exponent in relation between dislocation velocity and shear stress
$\boldsymbol{n}$	Unit vector
n_k, n'_k	Critical cluster size
N_{d}	Average number of defects generated in a single cascade
N_{il}	Number density of interstitial loop
N_0	Number of lattice sites per unit volume. Also number of nucleation sites
$P_{\mathrm{i}}(n,t)$	Probability of growing an interstitial cluster to size n in time t
P_{m}	Loop nucleation probability
r	Defect cluster radius
r_{c}	Dislocation core radius
r_{L}	Loop radius
r_{k}	Critical cluster radius
$\boldsymbol{s}$	Positive direction of the dislocation line
T	Temperature. Also PKA energy
$S_{\mathrm{v,i}}$	Supersaturation of vacancies, interstitials
u_{ij}	Components of the displacement vector
v_{g}	Dislocation glide velocity
v_n	Cluster of n vacancies
V	Volume
W	Work
$z_{\mathrm{v,i}}$	Vacancy, interstitial bias factor
Z	Zeldovich factor Eq. (7.75)
α_j	Emission rate of species j
β_j	Absorption rate of species j
γ	Shear strain,. Also surface energy
γ_{SFE}	Stacking fault energy
δ	Thickness of void shell

ε_c	Strain associated with the dislocation core
ε_{ij}	Components of strain
ε_{i0}	Fraction of interstitials produced in cascades in the form of immobile clusters
Γ	Dislocation line tension
λ	Lamé constant
λ_d	Mean free path between consecutive interstitial cluster coalescing events
μ	Shear modulus
ν	Poisson's ratio. Also jump frequency
$\rho(n)$	Number density of defect clusters of size n
ν_s	Strength of drift term for clusters, by absorption of single defects
Ω	Atomic volume
ρ_x	Density of entity x
σ, σ_{ij}	Stress and components of stress
σ_s	Shear stress
σ_{sD}	Value of shear stress that yields a dislocation velocity of $0.01\,\mathrm{m/s}$
τ	Incubation time Eq. (7.95)
τ_d	Lifetime of dislocation loop

Subscripts

c	Dislocation core
d	Dislocation
i	Interstitial
k	Critical cluster size
L	Loop
F	Frank loop
N	Dislocation network
P	Perfect loop
v	Vacancy
0	Initial

Superscripts

c	Coalescence
cl	Clusters
s	Single defects

Acronyms

EDF	Evaporating defect fraction
IDF	Isolated point defect fraction
MCF	Mobile cluster fraction
MDF	Mobile defect fraction

PBM	Production bias model
PKA	Primary knock-on atom
SFE	Stacking fault energy
SIA	Single interstitial atom

Problems

7.1 Draw billiard ball models of the extra half sheet of atoms which constitute the following dislocations:
   a) The $a/2[110]$ edge dislocation in the (111) plane of the fcc lattice
   b) The $a/2[111]$ edge dislocation on the (110) plane of the bcc lattice.

7.2 It is found experimentally that a certain material does not change in volume when subjected to an elastic state of stress. What is Poisson's ratio for this material?

7.3 Determine the volume of a 10 cm diameter copper sphere that is subjected to a fluid pressure of 12 MPa.

7.4 Assuming that atoms are hard elastic spheres, show that Poisson's ratio for a close-packed array of spheres is $1/3$.

7.5 For a circular shaped disc lying on the (111) plane of an fcc crystal:
   a) Determine the energy as a function of the number of vacancies.
   b) How many vacancies could a spherical void have before it would spontaneously convert to a vacancy disc?

7.6 It is known that the amount of stored energy in a solid can be increased with the addition of dislocations.
   a) Calculate this energy for aluminum with a dislocation density of $10^8\,\mathrm{cm}^{-2}$.
   b) It has also been suggested that this energy can be increased by application of a shear stress, σ_s. Given that the straight edge dislocations in part (a) are in the form of an equally spaced cubic shaped network, determine the shear stress, σ_s, needed to bow each dislocation segment into a half circle and calculate the increase in stored energy resulting.

7.7 Calculate the net density of edge dislocations in a thin simple cubic crystal with lattice parameter $a = 2 \times 10^{-8}$ cm if it is bent to have a radius of curvature of 10 cm. (The thickness of the crystal is no greater than 1 mm.)

7.8 In the circular shear loop shown in the figure below, let the x-axis be the direction of the Burgers vector shown in the drawing, the x-axis be in the plane of the loop but perpendicular to the direction of the Burgers vector, and the y-axis be perpendicular to the plane of the loop. Let θ be the polar angle of the circle measured from point A. At any point θ on the loop, the Burgers vector has an edge component b_e that is perpendicular to the dislocation line at that position and a screw component b_s that is parallel to the line.
   a) Using the fact that the vector $\boldsymbol{b}$ with these components is constant (in magnitude and direction) at all points on the loop, derive expressions for b_e and b_s as functions of θ.

b) Suppose a shear stress σ_{xy} is applied to the loop. Show that the resultant force on the dislocation line is always radially directed and has a magnitude $\sigma_{xy}b$.

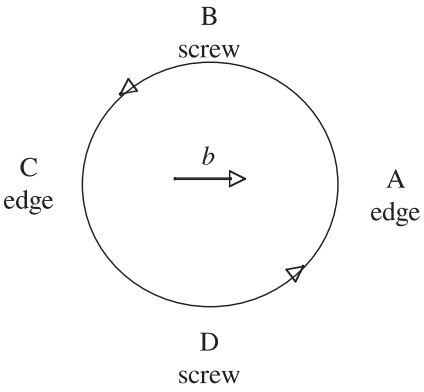

7.9 Plot the stress fields surrounding an edge and screw dislocation as a function of θ. Specifically, plot the following:
a) σ_{xx}, σ_{yy} and σ_{xy} vs. θ for an edge dislocation
b) σ_{xz} and σ_{yz} vs. θ for a screw dislocation

7.10 For the dislocations in the figure below:
a) Calculate the magnitude of the components of force on dislocation (2) due to dislocation (1).
b) Repeat part (a) for angles of 0°, 30°, 45° and 90°.
c) At $\theta = 30°$, will dislocation (2)
i) glide toward or away from dislocation (1)?
ii) tend to climb up or down? Why?

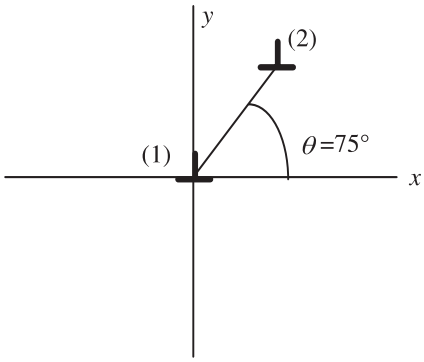

7.11 For the dislocations given in the sketch, find:
a) The force on dislocation (2) due to dislocation (1)
b) In which direction will dislocation (2) climb and/or glide?
c) Describe the stress and temperature dependence of these two processes and under what circumstances each will contribute to creep.

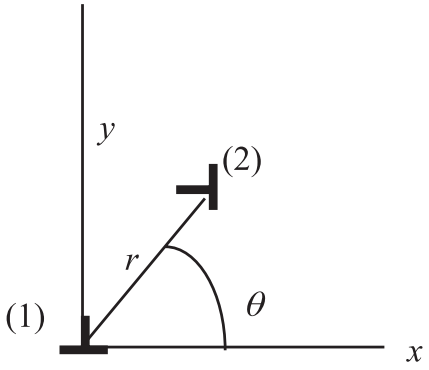

(1) $\boldsymbol{s} = |001|, \boldsymbol{b} = b|100|$
(2) $\boldsymbol{s} = |00\bar{1}|, \boldsymbol{b} = b|0\bar{1}0|$

7.12 An edge dislocation having the properties $\boldsymbol{s} = \boldsymbol{k}$, and $\boldsymbol{b} = b\boldsymbol{j}$ is on a plane $x = X$. Calculate the y-coordinates of the maxima and minima of the glide and climb forces (separately) that it would experience due to a fixed dislocation at the origin ($\boldsymbol{s} = \boldsymbol{k}$) for the following three cases:
a) $\boldsymbol{b} = b\boldsymbol{i}$
b) $\boldsymbol{b} = b\boldsymbol{j}$
c) $\boldsymbol{b} = b(1/2\boldsymbol{i} + \sqrt{3}/2\boldsymbol{j})$.

7.13 An edge dislocation (1) with $\boldsymbol{s} = [001]$ and $\boldsymbol{b} = [100]$ is located a the origin of a coordinate system. Another edge dislocation (2) with $\boldsymbol{s} = [001]$ and $\boldsymbol{b} = [\sqrt{2}\sqrt{2}0]$ is located a distance r away from (1) and 45° CCW from the x-axis.
a) Calculate the glide and climb force on dislocation (2) due to dislocation (1).
b) Make a graph of the force on dislocation (2) as a function of θ (for a given r) for $0 \leq \theta \leq 2\pi$.

7.14 Compute the local force on dislocation (2) due to dislocation (1) for the four examples of interaction between two perpendicular dislocations listed below:

$$\boldsymbol{s}_1 = [001] \qquad \boldsymbol{s}_2 = [010]$$

$$\boldsymbol{b}_1 = \begin{cases} [100] \\ [100] \\ [100] \\ [010] \end{cases} \qquad \boldsymbol{b}_2 = \begin{cases} [100] \\ [010] \\ [001] \\ [010] \end{cases}$$

where the first dislocation passes through $x = y = 0$ and is parallel to the z-axis, and the second dislocation passes through $x = X$, $z = 0$ and is parallel to the y-axis.

a) Show that the total force on dislocation (2) vanishes in all cases.
b) If dislocation is able to flex, sketch the shape it is likely to assume, provided the fist dislocation passing through the origin remains straight.

References

1. Weertman J, Weertman J (1964) Elementary Dislocation Theory. Macmillian, London
2. Hull D, Bacon DJ (1984) Introduction to Dislocations. Pergamon, Oxford
3. Friedel J (1964) Dislocations. Pergamon, New York
4. Hirth JP, Lothe J (1982) Dislocations in Crystals, 2nd edn. Wiley Interscience, New York
5. Reed-Hill RE, Abbaschian R (1994) Physical Metallurgy Principles, 4th edn. PWS, Boston
6. Hull D, Bacon DJ (2001) Introduction to Dislocations, 4th edn. Butterworth Heinemann, Philadelphia
7. Dieter GE (1976) Mechanical Metallurgy, 2nd edn. McGraw-Hill, New York, p 180
8. Osetsky YuN, Stoller RE, Matsukawa Y (2004) J Nucl Mater 329–333:1228–1232
9. Bacon DJ, Osetsky YuN, Stoller RE, Voskoboinikov RE (2003) J Nucl Mater 323:152–162
10. Bacon DJ, Gao F, Osetsky YuN (2000) J Nucl Mater 276:1–12
11. Phythian WJ, Stoller RE, Foreman AJE, Calder AF, Bacon DJ (1995) J Nucl Mater 223:245–261
12. Osetsky YuN, Bacon DJ, Serra A, Singh BN, Golubov SI (2000) J Nucl Mater 276:65–77
13. Osetsky YuN, Bacon DJ, Singh BN, Wirth B (2002) J Nucl Mater 307–311:852–861
14. Stoller RE (2000) J Nucl Mater 276:22–32
15. Jenkins ML, Kirk MA (2001) Characterization of Radiation Damage by Transmission Electron Microscopy. Institute of Physics, Philadelphia, PA
16. Kiritani M (1994) J Nucl Mater 216:200–264
17. Wirth BD, Odette GR, Marondas D, Lucas GE (2000) J Nucl Mater 276:33–40
18. Johnson RA (1967) Phil Mag 16(141):553
19. Jossang T, Hirth JP (1966) Phil Mag 13:657
20. Kelly BT (1966) Irradiation Damage to Solids. Pergamon, New York
21. Zinkle SJ, Singh BN (1993) J Nucl Mater 199:173–191
22. Russell KC, Powell RW (1973) Acta Meta 21:187
23. Stoller RE, Odette GR (1987) In: Gerner FA, Packan NH, Kumar AS (eds) Radiation-Induced Changes in Microstructure: 13th International Symposium (Part I), ASTM STP 955. American Society for Testing and Materials, Philadelphia, PA, pp 358–370
24. Golubov SI, Ovcharenko AM, Barashev AV, Singh BN (2001) Phil Mag A 81(3):643–658
25. Ghoniem NM, Sharafat S (1980) J Nucl Mater 92:121–135
26. Semenov AA, Woo CH (2003) Phil Mag 813:3765–3782
27. Pokor C, Brecht Y, Dubuisson P, Massoud JP, Barbu A (2004) J Nucl Mater 326:19–29
28. Duparc AH, Moingeon C, Smetniansky-de-Grande N, Barbu A (2002) J Nucl Mater 302:143
29. Soneda N, Diaz de la Rubia T (1998) Phil Mag A 78(5):995

30. Osetsky YN, Serra A, Victoria M, Golubov SI, Priego V (1999) Phil Mag A 79(9):2285
31. Garner FA, Kumar AS (1987) Radiation-Induced Changes in Microstructure: 13th International Symposium (Part I), ASTM STP 955. American Society for Testing and Materials, Philadelphia, PA, pp 289–314
32. Stoller RE, Odette GR (1987) In: Garner FA, Packan NH, Kumar AS (eds) Radiation-Induced Changes in Microstructure: 13th International Symposium (Part I), ASTM STP 955. American Society for Testing and Materials, Philadelphia, PA, p 371
33. Eyre BL, Bullough R (1965) Phil Mag 12:31
34. Garner FA, Wolfer WG (1982) In: Brager HR, Perrin JS (eds) Effects of Radiation on Materials: 11th Conference, ASTM STP 782. American Society for Testing and Materials, West Conshohocken, PA, p 1073
35. Garner FA (1994) In: Frost BRT (ed) Materials Science and Technology, chap 6, vol 10A. VCH, New York, p 419
36. Zinkle SJ, Maziasz PJ, Stoller RE (1993) J Nucl Mater 206:266–286
37. Mansur LK (1994) J Nucl Mater 216:97–123
38. Edwards DJ, Simonen EP, Bruemmer SM (2003) J Nucl Mater 317:13–31

8 Irradiation-Induced Voids and Bubbles

The formation and growth of *voids* and *bubbles* is of intense interest for material performance in radiation environments at elevated temperature. The first observation of voids in irradiated metals was published by Cauthorne and Fulton in 1967 [1]. Voids can have a profound influence on material properties because solids undergo *volumetric swelling* when voids form and grow. It has been suggested that the US breeder reactor program experienced a setback of nearly a decade by this surprising observation, as scientists scrambled to understand this phenomenon and the consequences to reactor internals. Since that time, a great deal of effort has been expended toward understanding their formation and growth. Figure 8.1 shows examples of voids in irradiated stainless steel, aluminum and magnesium. Voids of this size and number density can cause tens of percent increases in volume, translating into significant changes in linear dimensions as well. The challenge of designing a reactor to accommodate swelling of this magnitude quickly becomes monumental.

The formation and growth of voids shares much in common with bubbles. Yet because of their nature—a void is essentially an empty cavity—bubble mechanics are more complicated. It is by virtue of the fact that insoluble gases are formed by transmutation when certain metals are irradiated that drew attention to the subject of bubbles in irradiated metals. Under irradiation, it is possible for large numbers of inert gas bubbles to form, which significantly alter the physical and mechanical properties of metals. Fast and thermal spectrum reactors generate helium via transmutation, and the first wall of a fusion reactor is susceptible to bubble formation due to the high gas loading from reaction products in the plasma. Numerous examples exist in reactor systems where bubbles form and alter material properties, one of the most important being the structural materials of fission reactors. This chapter will address the theory of void and bubble nucleation and growth, along with elucidating the most important factors affecting these processes in reactor systems.

8.1 Void Nucleation

The driving force for the formation of voids in solids is the supersaturation of vacancies due to irradiation defined by:

$$S_{\mathrm{v}} = \frac{C_{\mathrm{v}}}{C_{\mathrm{v}}^{0}} , \tag{8.1}$$

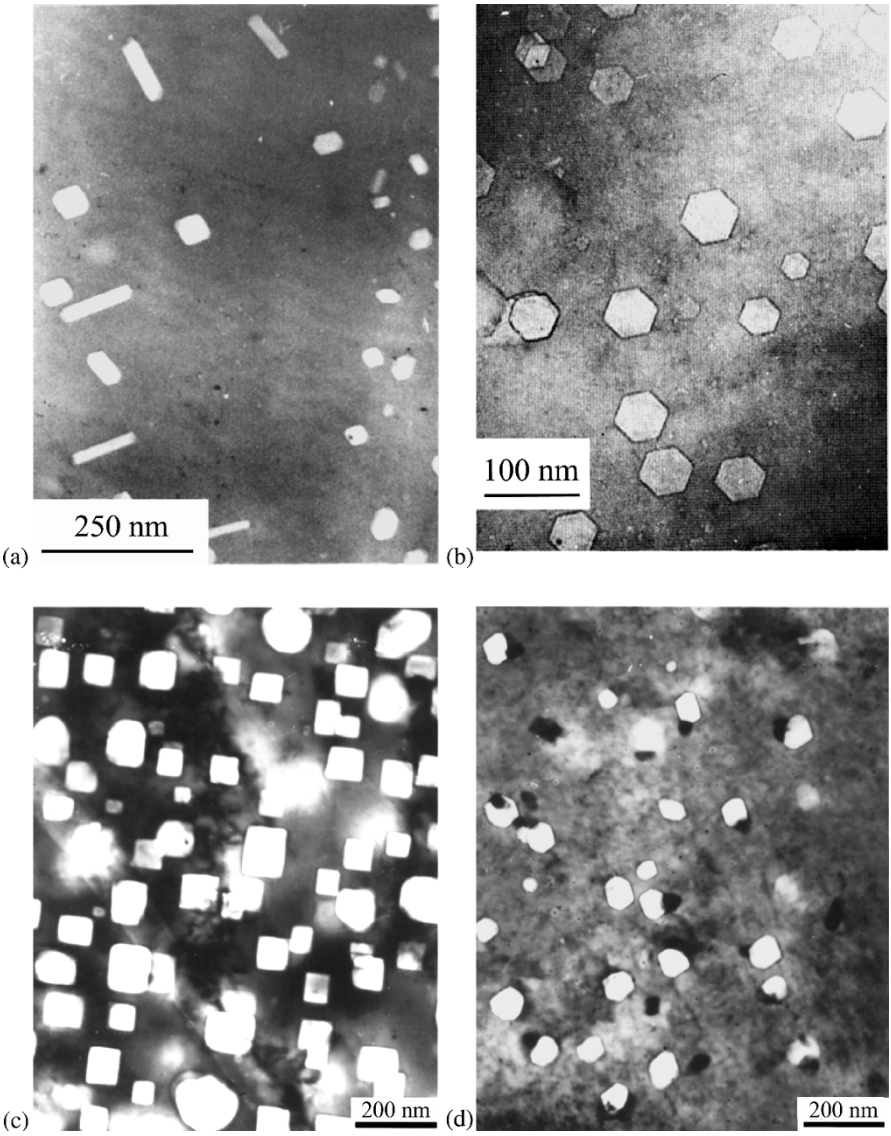

Fig. 8.1. Micrographs of irradiation-induced voids in (a) stainless steel, (b) aluminum (c) and (d) magnesium [2, 3]

where C_v^0 is the thermal equilibrium concentration of vacancies. During irradiation, defects react to form clusters and the clusters either grow by absorption of defects of the same type, or shrink by absorption of defects of the opposite type. For a cluster of vacancies to grow into a void, there must be a net increase in the number of vacancies absorbed over the number of interstitials absorbed. Thus, we will be inter-

ested in the equilibrium void distribution function, $\rho^0(n)$ (where n is the number of vacancies in the void), which is developed by a supersaturation of vacancies in the solid. The distribution function gives the number of vacancy clusters in each size class. Under non-equilibrium conditions, there will be a net flux, J, of voids from one size class to the next larger size class. This is the nucleation current and is the quantity we are interested in finding. The presence of an inert gas in the nucleation process is then considered.

8.1.1 Equilibrium Void Size Distribution

Analogous to the case of point defects (discussed in Chap. 4) and following the derivation in [4], the equilibrium void size distribution is determined from the change in Gibbs free energy of a system containing a distribution $\rho^0(n)$ of vacancy clusters:

$$G = G_0 + \sum_n \rho^0(n) G_n - kT \sum_n \ln w_n \,, \tag{8.2}$$

where G_0 is the free energy of the perfect lattice, the second term is the work to form a void distribution, and the last term is the entropy contribution to the number of ways that the voids can be distributed in a lattice. The quantity G_n is the Gibbs free energy (reversible work) required to form a void of size n:

$$G_n = H_n - TS_n = E_n + pv_n - TS_n \,, \tag{8.3}$$

where $E_n =$ the energy required to form a void of n vacancies
$v_n =$ volume change $(= n\Omega)$
$p =$ hydrostatic stress
$S_n =$ the excess entropy associated with the process
$w_n =$ the number of ways of removing $\rho^0(n)$ voids of size n from the solid
Neglecting the last two terms on the right, G_n reduces to $G_n \cong E_n$.

For large values of n, the energy of the void can adequately be represented by the surface energy:

$$E_\mathrm{V} = 4\pi R_\mathrm{V}^2 \gamma \,, \tag{8.4}$$

where γ is the surface energy of the solid per unit area and R_V is the void radius which is related to the number of vacancies in the void by:

$$n = \frac{4\pi R_\mathrm{V}^3}{3\Omega} \,, \tag{8.5}$$

where Ω is the atomic volume. The reader should note that the expression in Eq. (8.4) is the same as was developed in Eq. (7.58) and for the limiting case of a vacancy, Eq. (4.22). Equation (8.4) is, however, an approximation since the energy should properly include terms for the contraction of the surface and for the elastic energy stored in the solid (see Eq. (4.23)). Combining Eqs. (8.4) and (8.5)

gives:

$$E_n = (36\pi\Omega^2)^{1/3}\gamma n^{2/3} \,. \tag{8.6}$$

The last term in Eq. (8.2) is the product of the temperature and the mixing entropy. It can be obtained by calculating the number of ways in which voids can be distributed in a crystal containing N_0 lattice sites per unit volume. The procedure is the same as that used for vacancies in Sect. 4.2 and results in:

$$w_n = \frac{n^{\rho^0(n)}(N_0/n)!}{(N_0/n-\rho^0(n))!(\rho^0(n))!} \,. \tag{8.7}$$

We now define the chemical potential of a void of size n as μ_n that is related to the Gibbs free energy by:

$$\mu_n = \left.\frac{\partial G}{\partial \rho^0_{(n)}}\right|_{T,p,n} \,. \tag{8.8}$$

Substituting Eq. (8.7) into Eq. (8.2), using Stirling's approximation for the factorial term in Eq. (8.7), and taking the derivative as required by Eq. (8.8) ($\partial G = \partial \Delta G$ since $\Delta G = G - G_0$) gives:

$$\mu_n = E_n + kT \ln\left[\frac{\rho^0(n)}{N_0}\right] \,. \tag{8.9}$$

We have neglected $\rho^0(n)$ compared to N_0 because the void concentration is low. For monovacancies ($n = 1$), and Eq. (8.9) reduces to:

$$\mu_\mathrm{v} = E_\mathrm{v} + kT \ln\left(\frac{C_\mathrm{v}}{N_0}\right) \,. \tag{8.10}$$

Since the equilibrium concentration of vacancies in a solid is given by:

$$C^0_\mathrm{v} = N_0 \exp\left(\frac{-E^\mathrm{v}_\mathrm{f}}{kT}\right) \,, \tag{8.11}$$

substituting for N_0 from Eq. (8.11) into Eq. (8.10) gives:

$$\mu_\mathrm{v} = kT \ln\left(\frac{C_\mathrm{v}}{C^0_\mathrm{v}}\right) = kT \ln S_\mathrm{v} \,. \tag{8.12}$$

The criterion for chemical equilibrium is that the chemical potential of reactants and products in the system be the same, i.e.,

$$n\mu_\mathrm{v} = \mu_n \,. \tag{8.13}$$

Substituting Eqs. (8.9) and (8.12) into the criterion for chemical equilibrium, Eq. (8.13) gives:

$$\rho^0(n) = N_0 \exp(n \ln S_\mathrm{v} - \xi n^{2/3}) \,, \tag{8.14}$$

where

$$\xi = (36\pi\Omega^2)^{1/3}\frac{\gamma}{kT}\,. \tag{8.15}$$

Substituting Eq. (8.15) into Eq. (8.14) and considering only the term inside the exponent, we have:

$$n\ln S_{\rm v} - \xi n^{2/3} = n\ln S_{\rm v} - \frac{(36\pi\Omega^2)^{1/3}\gamma n^{2/3}}{kT}\,. \tag{8.16}$$

Expressing Eq. (8.14) as $\rho^0(n) = N_0\exp(-\Delta G_n^0/kT)$ gives the following expression for

$$\Delta G_n^0:$$
$$\Delta G_n^0 = -nkT\ln S_{\rm v} + (36\pi\Omega^2)^{1/3}\gamma n^{2/3}\,, \tag{8.17}$$

which is just the free energy change in the solid on forming a spherical void consisting of n vacancies on some particular site. A schematic of Eq. (8.17) is shown in Fig. 8.2 in which the free energy is plotted as a function of the number of vacancies in a void. Note that the first term decreases linearly with n while the second term increases as $n^{2/3}$. Accounting for the magnitude of the factors in each term, the resulting sum is a curve with a maximum at a value of n^*. This is the critical size of a void embryo which must be achieved in order for the embryo to grow into a void. At the critical point, vacancy addition and removal both cause a reduction in

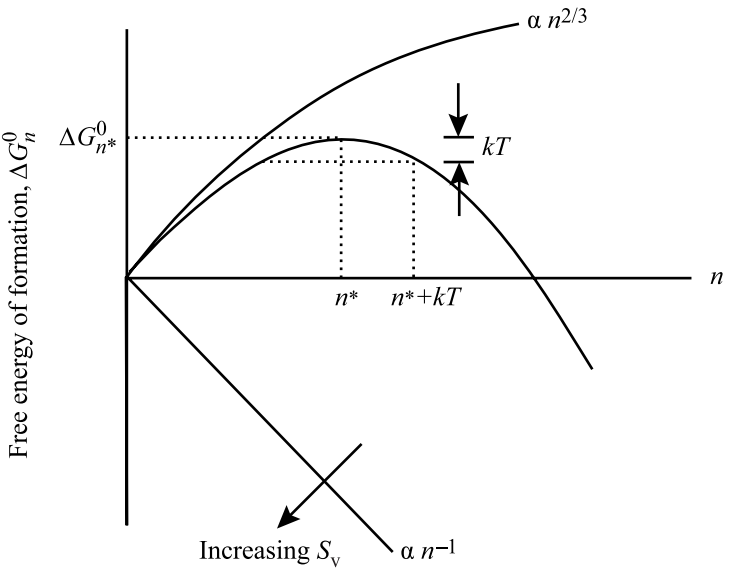

Fig. 8.2. Schematic illustration of ΔG_n^0, the free energy of formation of a spherical void consisting of n vacancies and the effect of thermal fluctuations on the critical size void embryo

the Gibbs free energy of the system, so this is an unstable point. Above the critical size, addition of vacancies to the embryo causes a decrease in the free energy, which means that void growth is favored, while loss of vacancies causes an increase in the free energy, so this reaction is not favored. Note also that thermal fluctuations add an increment to the embryo size, pushing the critical size to a higher value, and thus making it more difficult to nucleate a stable void.

8.1.2 Void Nucleation Rate

The nucleation rate of void embryos (consisting of n vacancies) can be described using the same formalism that was used to describe vacancy loop nucleation in Chap. 7 and developed in [5, 6, 7]. However, for the sake of continuity, that derivation will be repeated here for the case of void embryos. Recall from Eq. (7.74) that the nucleation rate of a void embryo of size n is given by:

$$J_n = \rho^0(n)\beta_{\mathrm{v}}(n)Z\,, \tag{8.18}$$

where $\rho^0(n)$ is the concentration of voids of size n vacancies, $\beta_{\mathrm{v}}(n)$ is the absorption rate and Z, the Zeldovich factor (defined in Sect. 7.6.1) and the void concentration is given by:

$$\rho^0(n) = N_0 \exp\left(\frac{-\Delta G_n^0}{kT}\right)\,, \tag{8.19}$$

where N_0 is the number of sites on which voids can be formed, and ΔG_n^0 is the change in free energy in the solid upon formation of the void and is given in Eq. (8.17). The value of ΔG_n^0 for the critical void embryo size, ΔG_k^0 (for embryo size n_k), is the activation barrier for void formation shown in Fig. 8.3 by the lower curve and is given as:

$$\Delta G_k^0 = -n_k kT \ln S_{\mathrm{v}} + (36\pi\Omega^2)^{1/3}\gamma n_k^{2/3}\,. \tag{8.20}$$

The void nucleation rate is the nucleation current given in Eq. (8.18). The void nucleation current, J_n, and activation barrier, ΔG_k^0, apply to the case where only vacancies are present. However, under irradiation, vacancies and interstitials are produced in equal numbers so the presence of interstitials must be accounted for. We now consider the case where interstitials can also impinge on voids. The analysis is similar to that just presented, but more complicated due to the introduction of another specie that will make void nucleation more difficult.

Consider now, the nucleation of vacancy clusters on one particular kind of attractive site [4, 5, 6] such as the compressive stress field around a dislocation. The following assumptions are made:

1. The lattice is in thermal and dynamic equilibrium, which are minimally affected by displacement and thermal spikes.
2. Monovacancies and solvent monointerstitials are the only mobile point defects present.

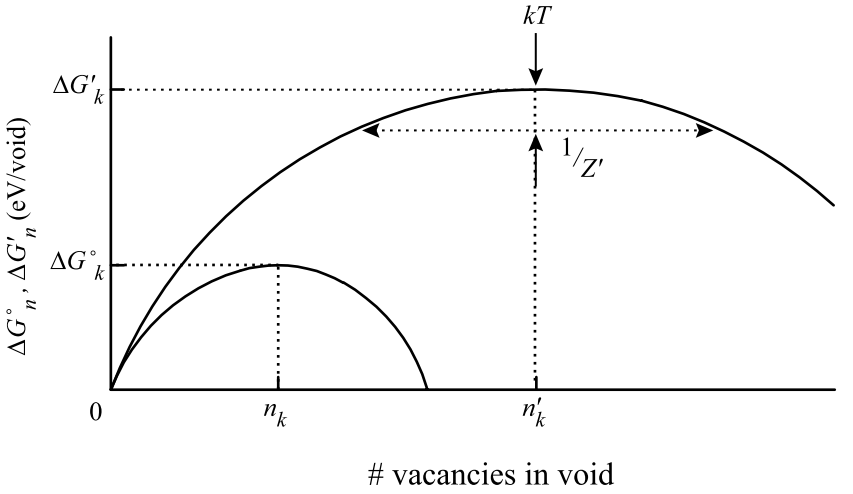

Fig. 8.3. Schematic nucleation curves showing the various parameters which are important in void nucleation. ΔG_k^0 is the activation barrier to nucleation if interstitials are not present, while $\Delta G_k'$ is the same quantity if interstitials are present during the nucleation process (after [6])

3. The defects obey dilute solution thermodynamics.
4. A steady state concentration of vacancies and interstitials exist.

Assumption (1) is reasonable as thermal spike lifetimes are very short (10^{-12} s) and dynamical equilibrium should be attained in similar time intervals. Assumption (2) is generally not valid since gas atoms are often present and are known to play an important role in nucleation (treated in Sect. 8.1.3). Assumption (3) should be valid for low defect concentration ($\leq 10^{-4}$ atomic fraction). The final assumption is a gross oversimplification since the microstructure continues to evolve with increasing dose causing sink strength, and therefore defect concentrations, to continually change.

The following derivation of the void nucleation rate from kinetic considerations is similar to that for loops, in which the nucleation rate is expressed as the flux of clusters between adjacent size classes in a phase space of cluster size. A flux is the concentration times velocity or the product of concentration, jump frequency and jump distance. The flux between any two size classes, say n and $n+1$, is:

$$J_n = \beta_v(n)\rho(n) - \alpha_v(n+1)\rho(n+1) - \beta_i(n+1)\rho(n+1)\,, \tag{8.21}$$

where $\rho(n)$ and $\rho(n+1)$ are the number of n-mer (voids containing a net of n vacancies) and $(n+1)$-mers per unit volume. $\beta_v(n)$ is the rate of vacancy capture by a n-mer, $\alpha_v(n+1)$ and $\beta_v(n+1)$ are the rates of loss and interstitial capture by a $(n+1)$-mer. The first term in Eq. (8.21) represents an addition to the $n+1$ size class by capture of a vacancy by a void of n-mer size class. The second term is a loss from the $(n+1)$-mer size class by loss of a vacancy, and the third term is a loss from the $(n+1)$-mer size class by capture of an interstitial. Interstitial emission is of low

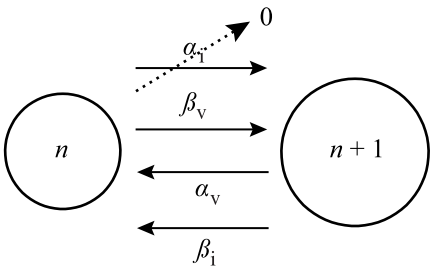

Fig. 8.4. Illustration of the processes governing the flux of between adjacent void sizes in a phase space of void size

probability and is neglected. Figure 8.4 shows the various processes described by Eq. (8.21) in phase space.

Setting $J = 0$ in Eq. (8.21) is equivalent to equilibrating the size classes since there is no net flux between size classes (as we did in Sect. 7.6). If we neglect interstitials, then we can write Eq. (8.21) as:

$$\alpha_v(n+1) = \frac{\beta_v(n)\rho^0(n)}{\rho^0(n+1)} \,. \tag{8.22}$$

Combining Eqs. (8.21) and (8.22) gives:

$$J_n = \beta_v(n)\left\{\rho(n) - \rho(n+1)\left[\frac{\rho^0(n)}{\rho^0(n+1)} + \frac{\beta_i(n+1)}{\beta_v(n)}\right]\right\} \,. \tag{8.23}$$

Since $\rho^0(n) = N_0 \exp(-\Delta G_n^0/kT)$, then we note that:

$$\frac{\rho^0(n)}{\rho^0(n+1)} = \exp\left(\frac{\delta G_n^0}{kT}\right) \,, \tag{8.24}$$

where $\delta G_n^0 \equiv \Delta G_{n+1}^0 - \Delta G_n^0$. We now define new functions of n, $\rho'(n)$ and $\delta G_n'$ such that by analogy with Eq. (8.24):

$$\frac{\rho'(n)}{\rho'(n+1)} = \frac{\rho^0(n)}{\rho^0(n+1)} + \frac{\beta_i(n+1)}{\beta_i(n)} = \exp(\delta G_n'/kT) \,, \tag{8.25}$$

where

$$\delta G_n' = \Delta G_{n+1}' - \Delta G_n' \,, \tag{8.26}$$

and $\Delta G_n'$ is not generally a free energy because of the term $\dfrac{\beta_i(n+1)}{\beta_i(n)}$ in Eq. (8.25). Using the expression in Eq. (8.25), we can re-write the equation for J_n in terms of $\dfrac{\rho'(n)}{\rho'(n+1)}$ by substituting Eq. (8.25) into Eq. (8.23) to give:

$$J_n = \beta_v(n)\left\{\rho(n) - \rho(n+1)\frac{\rho'(n)}{\rho'(n+1)}\right\} \,. \tag{8.27}$$

Re-arranging Eq. (8.27) gives:

$$J_n = -\beta_{\rm v}(n)\rho'(n)\left[\frac{\rho(n)}{\rho'(n)} - \frac{\rho(n+1)}{\rho'(n+1)}\right] , \tag{8.28}$$

and noting that:

$$\frac{\left[\dfrac{\rho(n)}{\rho'(n)} - \dfrac{\rho(n+1)}{\rho'(n+1)}\right]}{\Delta n} = \frac{\partial\left(\dfrac{\rho(n)}{\rho'(n)}\right)}{\partial n} , \tag{8.29}$$

gives:

$$J_n = -\beta_{\rm v}(n)\rho'(n)\frac{\partial\left[\rho(n)/\rho'(n)\right]}{\partial n} , \tag{8.30}$$

which is the basic flux equation. Re-arranging Eq. (8.25) by taking the natural log of both sides and summing from $j = 0$ to $n-1$ gives:

$$\sum_{j=0}^{n-1} \ln\left(\frac{\rho'(j)}{\rho'(j+1)}\right) = \sum_{j=0}^{n-1}\left\{-\ln\left[\frac{\beta_{\rm i}(j+1)}{\beta_{\rm v}(j)} + \exp\left(\frac{\delta G_j^0}{kT}\right)\right]\right\} , \tag{8.31}$$

and:

$$\ln\left(\frac{\rho'(n)}{\rho'(0)}\right) = \sum_{j=0}^{n-1}\left\{-\ln\left[\frac{\beta_{\rm i}(j+1)}{\beta_{\rm v}(j)} + \exp\left(\frac{\delta G_j^0}{kT}\right)\right]\right\} . \tag{8.32}$$

We can identify two boundary conditions. The first is the quantity $\rho'(0)$, which may be evaluated by noting that as $\beta_{\rm i}(n)/\beta_{\rm v}(n) \to 0$, $\rho'(0) = \rho^0(0)$ and that $\rho^0(0) \to N_0$, is simply the number of nucleation sites per unit volume. Since N_0 (and hence $\rho'(0)$) is independent of void concentration, we can write:

$$\begin{aligned}\ln\left(\frac{\rho'(n)}{\rho'(0)}\right) &= \sum_{j=0}^{n-1}\left\{-\ln\left[\frac{\beta_{\rm i}(j+1)}{\beta_{\rm v}(j)} + \exp\left(\frac{\delta G_j^0}{kT}\right)\right]\right\} \\ &= \frac{-\Delta G_n'}{kT} .\end{aligned} \tag{8.33}$$

Since as $\beta_{\rm i}(n)/\beta_{\rm v}(n) \to 0$, $\rho'(0) \to \rho^0(0)$ and $\rho^0(0)$ is just N_0, the number of nucleation sites per unit volume, we have then:

$$\rho'(n) = N_0 \exp\left(\frac{-\Delta G_n'}{kT}\right) , \tag{8.34}$$

and

$\Delta G_n^0 =$ activation barrier without interstitials,
$\Delta G_n' =$ activation barrier with interstitials.

The upper curve in Fig. 8.2 shows $\Delta G'_n$ as functions of n. Note that $\Delta G'_n$ is larger than ΔG^0_k, and requires a larger void size due to the hindering effect of interstitials on the void nucleation process. The maxima in the two curves occur at n_k, ΔG^0_k and n'_k, $\Delta G'_k$.

Now, the steady state void nucleation rate may be calculated from the expression for J_n in Eq. (8.30):

$$J_k = Z' \beta_k \rho'_k \,, \tag{8.35}$$

which is the rate at which voids escape over the potential barrier of height $\Delta G'_k$ in units of $\left[\text{voids/cm}^3\, s\right]$. The term β_k, is the rate of single vacancy impingement on a void of size n'_k. If clusters are assumed to be spherical, then the vacancy impingement rate is expressed by the rate constant for point-defect absorption by spherical sinks, Eq. (5.99). Since void embryos are small, the capture rate is of mixed-control type in which both diffusion and reaction rate limitations are of comparable magnitude:

$$\beta_{\text{v}}(n) = \frac{4\pi R_{\text{V}} D_{\text{v}} C_{\text{v}}}{1 + a/R_{\text{V}}} \,, \tag{8.36}$$

were a is the lattice parameter, and assuming that the rate at which vacancies leave a void depends on the size of the void but not on the concentration of vacancies or interstitials or details of the dynamics. Note that for large voids, $a/R_{\text{V}} \to 0$ and $\beta_{\text{v}}(n)$ has a pure diffusion character.

The term Z', analogous to Z but in the presence of interstitials, is:

$$Z' = \left[-\frac{1}{2\pi kT} \frac{\partial^2 \Delta G'_n}{\partial n^2} \right]^{1/2}_{n'_k} \,. \tag{8.37}$$

The subscript indicates that the second derivative is to be evaluated at $n = n'_k$. Its value is the width of $\Delta G'_k$ at kT units below the maximum and is on the order of 0.05. The second derivative is found from Eq. (8.25) to be:

$$\frac{1}{kT} \left(\frac{\partial^2 \Delta G'_n}{\partial n^2} \right)_{n'_k} = \left\{ \left[\frac{1}{kT} \frac{\partial^2 \Delta G^0_n}{\partial n^2} \right] \left[\exp\left(\frac{1}{kT} \frac{\partial \Delta G^0}{\partial n} \right) \right] \right\}_{n'_k} \,, \tag{8.38}$$

giving:

$$\rho'_k = N_0 \exp\left(-\Delta G'_k / kT\right) \,, \tag{8.39}$$

where $\Delta G'_k$ is determined by evaluating Eq. (8.33) at n'_k.

Since the critical void nucleus size is taken as the maximum of the $\Delta G'_n$ curve, differentiating Eq. (8.17) and substituting the result into Eq. (8.33) permits evaluation of $\Delta G'_n$. The maximum in $\Delta G'_n$ is determined by setting $\partial \Delta G'_n / \partial n = 0$ and

solving for n:

$$n'_k = \frac{36\pi\gamma^3\Omega^2}{3(kT)^3\left[\ln\left(\dfrac{\beta_v(n)-\beta_i(n+1)}{\beta_v^0(n)}\right)\right]^3}, \tag{8.40}$$

where $C_v/C_{v,}^0 = \beta_v(n)/\beta_v^0(n)$. Since $R_V = \left(\dfrac{3}{4}\dfrac{n\Omega}{\pi}\right)^{1/3}$, the radius corresponding to n'_k is:

$$r'_k = \frac{2\gamma\Omega}{kT\ln\left[\left(\dfrac{\beta_v(n)-\beta_i(n+1)}{\beta_v^0(n)}\right)\right]}. \tag{8.41}$$

Note that as $\beta_i \to \beta_v$, $r'_k \to \infty$, which says that if the capture rate for vacancies and interstitials is the same, then the critical void embryo size would need to be ∞.

Figure 8.5 plots $\rho'(n)$ as a function of cluster size n for various values of β_i/β_v for $S_v = 430$ and $T = 623\,^\circ$C. Note the effect of increasing the interstitial arrival rate for a fixed vacancy arrival rate. With increasing arrival rate ratio, (β_i/β_v) the slope of the distribution, $d\rho/dn$ decreases everywhere. The reason is that increasing the interstitial flux increases the fraction of embryos of a given size n which actually shrink to the next smallest size $(n-1)$, whereas to maintain the constrained distribution requires that the increased fraction be balanced by a decreased concentration of nuclei of size n relative to that of size $(n-1)$.

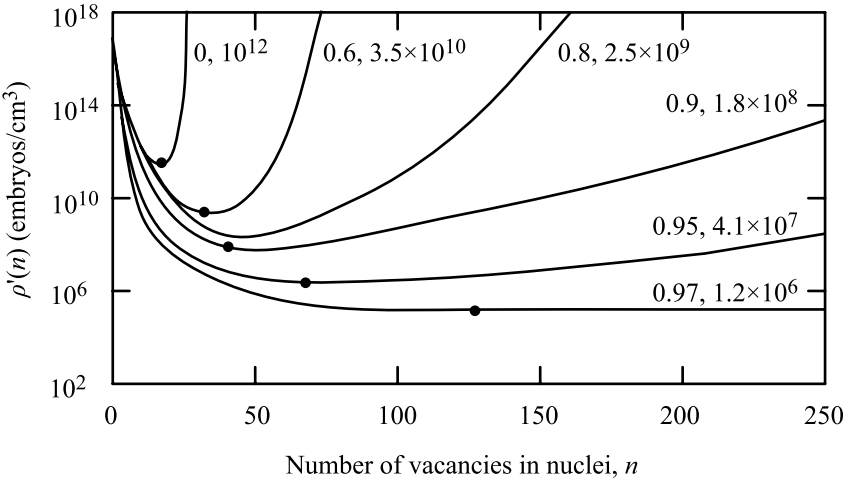

Fig. 8.5. Concentration of void embryos as a function of their size when the net flow of embryos is constrained to be zero. The parameters are the arrival rate ratios β_i/β_v, and the nucleation rates (in s^{-1} cm^{-3}) of the unconstrained system. For this example, $T = 623\,^\circ$C and $S_v = 430$. *Solid circles* indicate the minima of $n(x)$ (from [8])

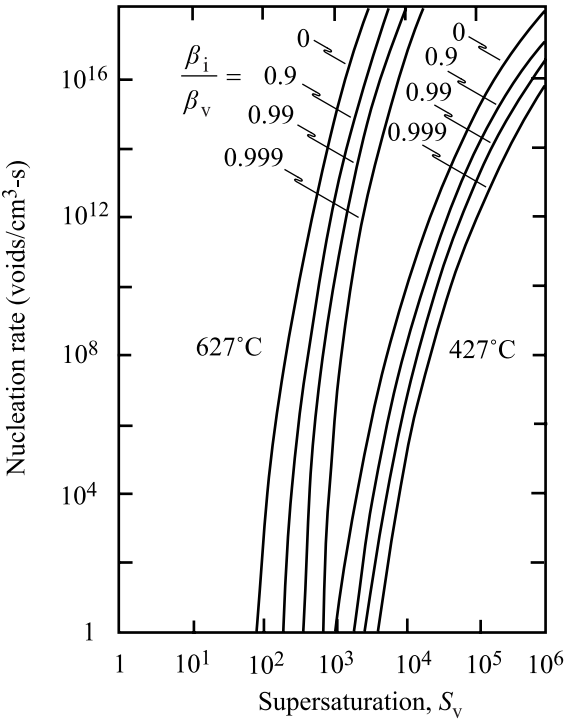

Fig. 8.6. Nucleation rate as a function of the vacancy supersaturation. The parameters are the arrival rate ratios, β_i/β_v and the temperature (after [8])

Increasing the arrival rate ratio also shifts the minimum in the distribution $\rho'(n)$ to larger sizes and to lower concentrations. Since the nucleation rate is proportional to $\rho'(n)$, it decreases tremendously by the deepening and widening of the minimum in $\rho(n)$ as the arrival rate ratio increases. The nucleation rate in Fig 8.5 decreases about 6 orders of magnitude as the arrival rate ratio is increases from 0 to 0.97.

To obtain void nucleation as β_i/β_v approaches 1 requires higher vacancy supersaturation. The strong dependence of nucleation on vacancy supersaturation is affected only very slightly by the arrival rate ratio. Figure 8.6 shows that a factor of 10 increase in supersaturation causes the nucleation rate to increase from 1 to 10^{15} nuclei/cm^3/s at 627 °C.

The effect of temperature on the vacancy concentration, C^* required to give a fixed nucleation rate is shown in Fig. 8.7 by the set of curves identified by the arrival rate ratios, β_i/β_v. Over most of the temperature range, C^* increases with increasing temperature even though the supersaturation $S_v = C_v/C_v^0$ decreases. Note that C_v is high at low temperature where the diffusion coefficient is small and there is not much loss. C_v is small at intermediate temperature where annihilation and loss to sinks is great. But C_v is high again at high temperature where $C_v^0 \sim C_v$. The parameter p is the probability per defect jump that the defect is annihilated at a sink. The values of p range from 10^{-7}, typical of an annealed metal to 10^{-3}, which is typical of a heavily cold worked metal.

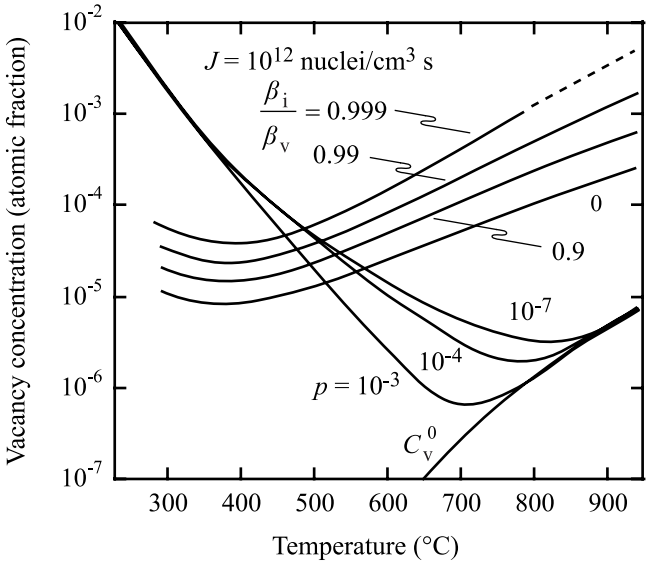

Fig. 8.7. Steady state vacancy concentration caused by a production rate of $K_0 = 10^{-3}$ atom fraction of defect pairs per second. The parameter p on the curves is the probability per jump that a defect is annihilated at existing sinks, such as dislocations. The curve labeled C_v^0 is the thermal equilibrium concentration of vacancies. The set of curves labeled by the arrival rate ratio, β_i/β_v indicates the vacancy concentration required to give a nucleation rate of 10^{12} void nuclei/cm^{3}s. This nucleation rate is obtained at the temperature and vacancy concentration at the intersection of the curves under the conditions characterized by the curve parameters. The nucleation rate will be higher (*lower*) at temperatures below (*above*) the intersection temperature at fixed values of the parameters (after [8])

Figure 8.8 gives the steady state vacancy concentrations for several defect production rates, K_0 and several nucleation rates J and for a sink-annihilation probability of 10^{-7} and an arrival rate ratio of 0.99. The intersection of the defect production rate and the nucleation rate provides the vacancy concentration at the temperature of the intersection. Higher vacancy production rates promote greater vacancy concentration and a higher nucleation rate.

In summary, the void nucleation rate is a function of the height of the activation barrier. Inclusion of interstitials raises the activation barrier and reduces the nucleation rate. The critical void size radius for survival and growth as a void is a function of the activation barrier height with greater heights requiring larger critical void sizes. Nucleation rate is strongly increased by vacancy supersaturation and a reduced interstitial-to-vacancy arrival rate ratio.

8.1.3 Effect of Inert Gas

Up to this point, we have assumed that a supersaturation of vacancies was sufficient to create a void embryo. It is well-known that inert gas atoms may act to

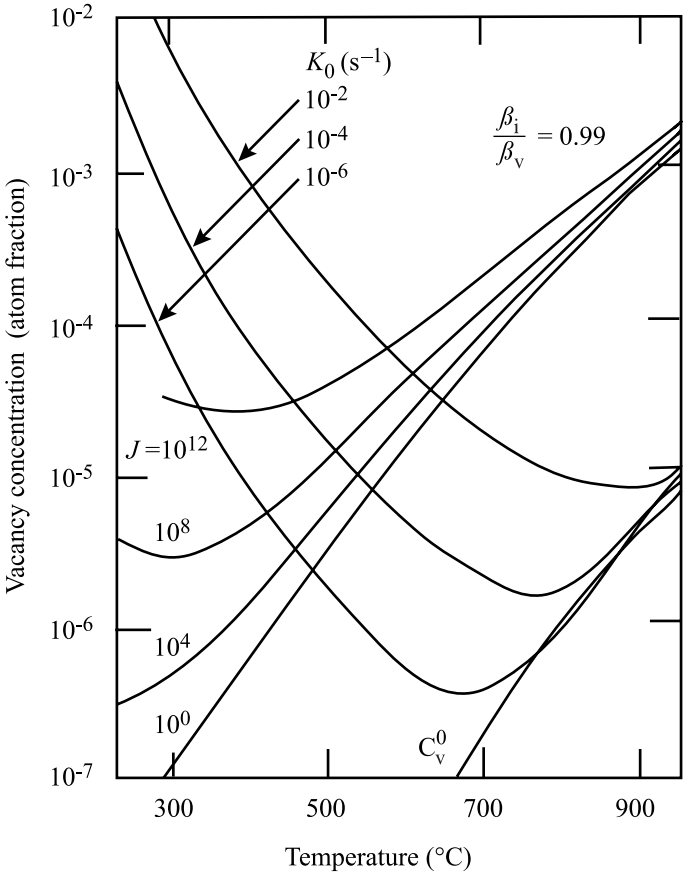

Fig. 8.8. Steady state vacancy concentrations for several defect production rates and a sink annihilation probability $p = 10^{-7}$, and vacancy concentrations required for several nucleation rates J (in cm^{-3} s^{-1}) at an arrival rate ratio of 0.99. Such nucleation rates are obtained at the indicated defect production rates at the temperature where the curves intersect (after [8])

stabilize a void embryo and assist in the nucleation process. In fact, there is evidence to suggest that gas atoms are *always* involved in the void nucleation process [6, 7, 8, 9, 10]. Hence, several theories have been proposed that involve void nucleation in the presence of inert and non-inert gases [9, 11]. Here we will consider a simple treatment [4, 9] of an immobile, inert gas, which is just as extension of the theory already developed. We will focus on helium since it is commonly produced by transmutation reactions in core structural materials.

Helium is very immobile compared to vacancies or interstitials in the temperature range of void formation. Once helium is trapped by a void embryo, its return to the matrix is very unlikely. Therefore, nucleation in the presence of helium does not require us to consider the interaction between helium atoms, vacancies and in-

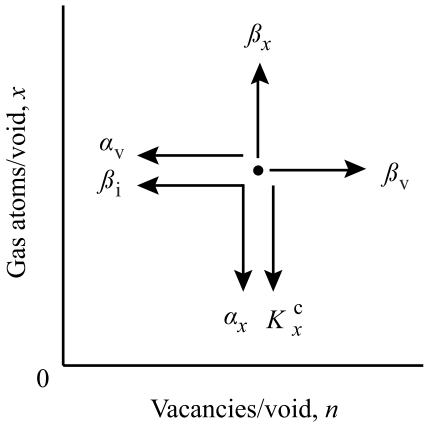

Fig. 8.9. Phase space for void nucleation showing movements of a void following point defect capture (β_i, β_v, β_x) or loss (α_v, α_x, K_x^c) (after [6])

terstitials in the formation of a void embryo. We may analyze the problem instead, by treating the inert gas atoms as sites for the formation of void embryos by migration of the point defects. In essence, this is a form of heterogeneous void nucleation rather than the homogeneous process described in Sect. 8.1.2.

The phase space description of the gas-containing void behavior is similar to that given in Sect. 8.1.2 and in [6]. The void is assigned coordinates specifying its vacancy content (n) and the number of gas atoms it contains (x) (Fig. 8.9). The void moves in the $+n$ direction by capturing vacancies and in the opposite direction by either thermal emission of vacancies or capture of interstitials:

$$\dot{n} = \beta_v^0 n^{1/3} - \alpha_v - \beta_i^0 n^{1/3} , \tag{8.42}$$

where β_v^0 and β_i^0 are the arrival rates of vacancies and interstitials to the void, α_v is the emission rate of vacancies from the void and the factor $n^{1/3}$ accounts for the dependence of the capture rate on the void size. Similarly, movement in the positive x-direction occurs by gas atom capture and in the opposite direction by re-solution of gas atoms (return of the gas atom to the matrix due to knock-out by irradiation) or by thermal emission of gas atoms:

$$\dot{x} = \beta_x^0 n^{1/3} - \alpha_x - x K_x^c , \tag{8.43}$$

where β_x^0 is the arrival rate of gas atoms, α_x is the emission rate of gas atoms and K_x^c is the rate of gas atom re-solution.

For the case where the voids are in equilibrium with the vacancy and gas atom concentrations, the distribution of gas-filled void embryos containing n vacancies and x gas atoms is:

$$\rho^0(n,x) = N \exp\left(\frac{-\Delta G^0(n,x)}{kT}\right) , \tag{8.44}$$

where $\Delta G^0(n,x)$ is the free energy of formation of the gas-filled void, also referred to as an (n,x)-mer. For every $(n-1,x)$-mer capturing a vacancy, a (n,x)-mer will

emit a vacancy, and for every $(n,x-1)$-mer capturing a gas atom, a (n,x)-mer will emit one. Then:

$$\rho^0(n-1,x)\beta_{\rm v}^0(n-1)^{1/3} = \rho^0(n,x)\alpha_{\rm v}(n,x)\ , \tag{8.45}$$

and

$$\rho^0(n,x-1)\beta_x^0(x-1)^{1/3} = \rho^0(n,x)\alpha_x(n,x)\ , \tag{8.46}$$

and substituting Eqs. (8.45) and (8.46) into Eq. (8.42) to eliminate $\alpha_{\rm v}(n,x)$ and $\alpha_x(n,x)$ gives:

$$\dot{n} = \beta_{\rm v}^0 n^{1/3}\left[1 - \frac{\beta_{\rm i}^0}{\beta_{\rm v}^0} - \exp\left(\frac{1}{kT}\frac{\partial \Delta G^0(n,x)}{\partial n}\right)\right] \tag{8.47}$$

$$\dot{x} = \beta_x^0 n^{1/3}\left[1 - \frac{xK_x^c}{\beta_x^0 n^{1/3}} - \exp\left(\frac{1}{kT}\frac{\partial \Delta G^0(n,x)}{\partial x}\right)\right]\ , \tag{8.48}$$

which are the velocities of the void in (n,x) phase space. However, we are interested in the nucleation rate, which requires more development and is described in detail in [4].

We start with a distribution of gas-atom clusters, M_x, which is the number of gas-atom clusters per unit volume composed of x gas atoms. The total helium concentration in the solid is:

$$M = \sum_{x=1} xM_x\ , \tag{8.49}$$

and is determined by the helium production rate due to transmutation reactions. We assume that nucleation of voids occurs independently and simultaneously on each of the gas atom clusters characterized by M_x nucleation sites per unit volume. Nucleation is driven by the vacancy and interstitial supersaturation. In addition to heterogeneous nucleation at gas cluster sites, homogenous nucleation is assumed to occur also on the N_0 lattice sites in the solid. The total nucleation rate is the sum of the contributions of the homogeneous and heterogeneous nucleation rates:

$$J = J_{\rm hom} + \sum_{x=1} J_x\ , \tag{8.50}$$

where $J_{\rm hom}$ is given by Eq. (8.35). In order to obtain the total nucleation rate, we need to determine the heterogeneous nucleation rate J_x on the M_x gas cluster sites.

The distribution of helium void embryos containing n vacancies and x gas atoms, $\rho^0(n,x)$ is governed by the reaction:

$$n{\rm v} = {\rm v}_{nx}\ , \tag{8.51}$$

where ${\rm v}_{nx}$ denotes a void consisting of n vacancies and x gas atoms. Since helium is immobile, there is no chemical reaction expressing the equilibration of gas atoms

between the voids and the bulk. The criterion of chemical equilibrium is then:

$$n\mu_{\rm v} = \mu_{nx} \,, \tag{8.52}$$

and the chemical potential of a void with n vacancies and x gas atoms is:

$$\mu_{nx} = \frac{\partial G}{\partial \rho^0(n,x)} \,. \tag{8.53}$$

The formulation of the total Gibbs free energy for the gas-vacancy cluster is similar to the analysis presented earlier for vacancies alone. Analogous to Eq. (8.2) for voids, the total Gibbs free energy is:

$$G = G_0 + \sum_x \sum_n \left[\rho^0(n,x) G_{nx} - kT \ln w_{nx}\right] \,. \tag{8.54}$$

As before, w_{nx} is the number of ways of arranging $\rho^0(n,x)$ voids on $M_{\rm i}$ sites:

$$w_{nx} = \frac{M_x(M_x-1)\ldots\left\{M_x - \left[\rho^0(n,x)-1\right]\right\}}{[\rho^0(n,x)]!} = \frac{M_x!}{[M_x-\rho^0(n,x)]![\rho^0(n,x)]!} \,. \tag{8.55}$$

Using Eq. (8.55) in Eq. (8.54) and using Eq. (8.54) to determine the chemical potential as given in Eq. (8.53) yields:

$$\mu_{nx} = G_{nx} + kT \ln\left[\frac{\rho^0(n,x)}{M_x}\right] \,. \tag{8.56}$$

The reversible work to form a void embryo from n vacancies and x gas atoms is [4, 12]:

$$G_{nx} = (36\pi\Omega^2)^{1/3}\gamma n^{2/3} - xkT \ln\left(\frac{MHn\Omega}{xkT}\right) \,. \tag{8.57}$$

The first term is the work to create a gas-free void consisting of n vacancies, and is the same as that given in Eq. (8.6) for void formation. The second term is work to move the helium from the solid into the void. H in the second term is the Henry's law constant for the dissolution of helium in the metal. The expressions for G_{nx} in Eq. (8.57) is substituted into the expression for the chemical potential of a void with n vacancies and x gas atoms, Eq. (8.56). Using the equality in Eq. (8.52) with $\mu_{\rm v}$ given by Eq. (8.12) and solving for $\rho^0(n,x)$gives:

$$\rho^0(n,x) = M_x \exp\left[n\ln S_{\rm v} - \xi n^{2/3} + x\ln\left(\frac{MHn\Omega}{xkT}\right)\right] \,. \tag{8.58}$$

which is identical to Eq. (8.14) except for the extra term in the exponent and the pre-exponential factor. In fact, for $x = 0$ and $M_x = N_0$ the result reduces to Eq. (8.14).

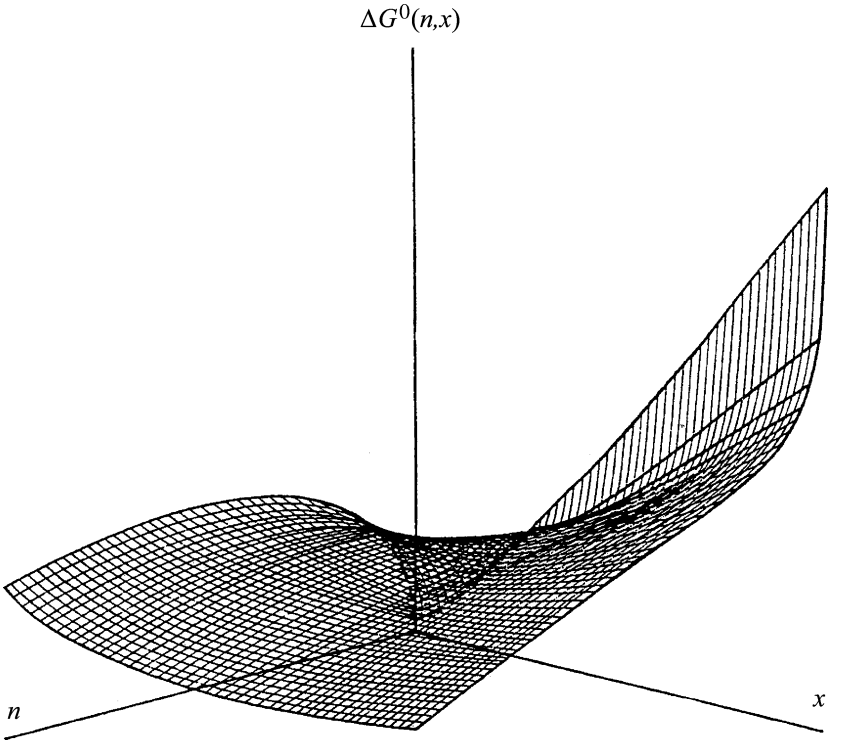

Fig. 8.10. Plot of the free energy of void formation as a function of the number of vacancies (n) and the number of gas atoms (x) in the void. Conditions are: $S_v = 600$, $p_0 = 507\,\text{MPa}$, $T = 500\,^\circ\text{C}$, $\gamma = 1\,\text{J/m}^2$ (after [12])

Using Eq. (8.44) with M_x substituted for N_0 gives:

$$\Delta G^0(n,x) = -nkT \ln S_v + (36\pi\Omega^2)^{1/3}\gamma n^{2/3} - xkT \ln\left(\frac{MHn\Omega}{xkT}\right) . \tag{8.59}$$

Figure 8.10 shows the free energy of void formation as a function of n and x. The intercept of this surface at $x = 0$ (no gas) corresponds to the $\beta_i/\beta_v = 0$ curve in Fig. 8.5 in which ρ' is plotted as a function of n in Eq. (8.34), $\rho'(n) = N_0 \exp(-\Delta G'_k/kT)$, and for $\beta_i/\beta_v = 0$, then $\Delta G'_n = \Delta G(n, x = 0)$. Note that gas atoms in the void reduce the energy barrier for nucleation below that value characteristic of gas-free voids. The saddle point on the surface shown in Fig. 8.10 occurs at $n = 11$ and $x = 6$. The plot, however, does *not* include interstitials (as would a plot of $\Delta G'_n$), which are included in the analysis in exactly the same manner as in the case of homogeneous nucleation.

The determination of the nucleation rate is done in the same manner as for homogeneous nucleation, resulting in a nucleation current:

$$J_{k,x} = Z'_x \beta_{kx} \rho'_k(n,x) , \tag{8.60}$$

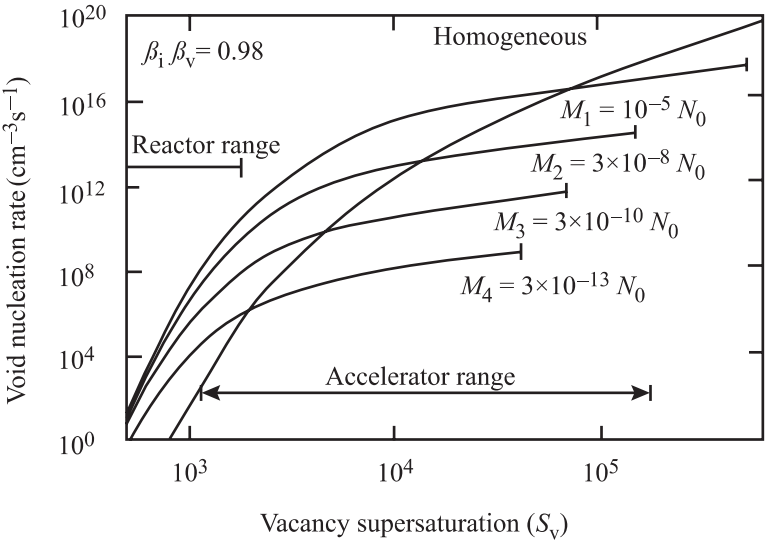

Fig. 8.11. Void nucleation rates (J) on helium atom clusters and the homogeneous nucleation rate (J_{hom}) as functions of vacancy supersaturation at 500 °C. Total helium content of 10 ppm (after [13])

where

$$Z'_x = \left[\frac{-1}{2\pi kT}\frac{\partial^2 \Delta G'(n,x)}{\partial n^2}\right]^{1/2}_{n=n_k}, \tag{8.61}$$

$$\rho'(n,x) = M_x \exp(-\Delta G'(n,x)/kT)\,, \tag{8.62}$$

and

$$\Delta G'(n,x) = kT\sum_{x=0}^{n}\left[\ln\left(\frac{\beta_i^0}{\beta_v^0}\right) + \exp\left(\frac{1}{kT}\frac{\partial \Delta G^0(n,x)}{\partial n}\right)\right], \tag{8.63}$$

and the values of z'_k and $\rho'(n_k,x)$ are evaluated at the critical void size, n_k, and β_{kx} is the rate of impingement of vacancies on a critical size void.

To determine the nucleation rate on the gas-atom clusters in the metal, we must estimate the distribution of the available gas (M atoms/cm^3) among the various cluster sizes. For simplicity, the distribution $M_x = M_1^{-(x+1)}$ is assumed. This distribution must satisfy Eq. (8.49). Figure 8.11 shows the results of calculations based on Eq. (8.60) to Eq. (8.62) and Eq. (8.60) for M equivalent to 10 ppm helium (equivalent to the amount of helium expected in stainless steel cladding after a fluence of 5×10^{22} n/cm^2). Note that in the regime of vacancy supersaturation expected in a reactor, heterogeneous nucleation on helium-atom clusters far outweighs homogeneous nucleation. This behavior constitutes theoretical confirmation of the often-observed enhancement of void nucleation of helium. The relative importance of

homogeneous and heterogeneous nucleation shifts according to the helium concentration because $J_{\text{hom}}(n)$ is proportional to N_0 whereas $J_x(n)$ is proportional to M_x. At low fluence, homogeneous nucleation is dominant because there is not enough helium to drive heterogeneous nucleation. However, since J_{hom} is quite low, no voids are observed until sufficient helium has been generated by transmutation reactions to give the high heterogeneous nucleation rate. This incubation time is physically the relaxation time for the approach to steady state after a step increase in supersaturation. For void formation with or without the presence of gas:

$$\tau = (2\beta_k Z')^{-1} . \tag{8.64}$$

This value is equivalent to a fluence of $10^{22}\,\text{n/cm}^2$ for fast reactor irradiation conditions.

In summary, the effect of gas atoms is to substantially increase the void nucleation rate by lowering the critical radius for a stable void embryo below that for a gas-free void. Therefore, gas atom introduction into the lattice (either by transmutation or accelerator injection) promotes the formation of voids relative to the pristine lattice.

8.1.4 Void Nucleation with Production Bias

The kinetic equation for dislocation loop evolution under cascade damage conditions was developed in Sect. 7.6.3 for interstitial clusters. We can use the same formulation with some changes to the terms to make the formulation specific to void nucleation [14]. Given that the number of vacancies in a spherical void can be written as:

$$\frac{\mathrm{d}n_\text{v}}{\mathrm{d}t} = \frac{3n_\text{v}^{1/3}}{a^2}[D_\text{v}C_\text{v} - D_\text{i}C_\text{i} - D_\text{v}C_\text{v}^0] \tag{8.65}$$

$$C_\text{v}^\text{V} = C_\text{v}^0 \exp(2\gamma\Omega/kTR_\text{V}) , \tag{8.66}$$

where $a = (3\Omega/4\pi)^{1/3}$, n_v is the number of vacancies in a void, $R_\text{v} = an_\text{v}^{1/3}$ and Ω is the atomic volume, the drift velocity, $F(n)$ (from the Fokker–Planck treatment) is now a single term equal to the RHS of Eq. (8.65). The diffusive spread, described by the term $D(n)$ is a sum of contributions due to single defect jumps, cascades, and vacancy emission as:

$$D(n) = D^s(n) + D^c(n) + D^e(n) , \tag{8.67}$$

where

$$D^s(n) = \frac{3n^{1/3}}{2a^2}[D_\text{v}(C_\text{v} - C_\text{v}^0) + D_\text{i}C_\text{i}] , \tag{8.68}$$

$$D^c(n) = \frac{3n^{2/3}}{4a}\left[\frac{K_\text{v}^\text{eff}\langle N_\text{dv}^2\rangle}{k_\text{v}N_\text{dv}} + \frac{K_\text{i}^\text{eff}\langle N_\text{di}^2\rangle}{k_\text{i}N_\text{di}}\right] , \tag{8.69}$$

$$D^e(n) = \frac{9D_\text{v}C_\text{v}^0 n^{2/3}}{2a^2} , \tag{8.70}$$

and K_j^{eff} is the effective generation rate of free point defects, N_{dj} and $\left\langle N_{dj}^2 \right\rangle$ are the average number and the average square number of free point defects generated in a single cascade, respectively, and k_j^2 is the total sink strength for point defects of the type j. The solution to the general kinetic equation is similar to that for the case of interstitial clusters and is given in [14]. For the case of small critical vacancy size, the solution is:

$$P_{\text{m}} \cong \left[\frac{\beta}{6\pi R_{\text{cr}} n_{\text{cr}}} \frac{(D_{\text{v}} C_{\text{v}} - D_{\text{i}} C_{\text{i}})}{D_{\text{i}} C_{\text{i}} (1 + d n_{\text{cr}}^{1/3})} (n_0 - n_{\text{v}\,0}) \right]^{1/2} \times \exp\left(- \frac{\eta(\beta / R_{\text{cr}}) n_{\text{cr}}^{2/3} - n_0^{2/3}}{1 + 1/(d^e n_{\text{cr}}^{1/3}) + d^c / d^e} \right) , \tag{8.71}$$

where n_0 is the initial void embryo size (generally ~ 4 vacancies), n_{v0} is a minimum size of a void embryo below which it is no longer a void (generally ~ 2–3 vacancies), $d = d^{\text{c}} + d^{\text{e}}$, $\beta = 2\gamma\Omega / kT$ and R_{cr} and n_{cr} are the size and vacancy content of the critical size embryo. The term R_{cr} is determined from Eqs. (8.65) and (8.66) under that condition that a void will grow if it receives a net vacancy flux ($D_{\text{v}} C_{\text{v}} > D_{\text{i}} C_{\text{i}}$):

$$R_{\text{cr}} = \frac{\beta D_{\text{v}} C_{\text{v}}^{\text{V}}}{D_{\text{v}} C_{\text{v}} - D_{\text{i}} C_{\text{i}} - D_{\text{v}} C_{\text{v}}^{\text{V}}} , \tag{8.72}$$

and $R(n) = a n^{1/3}$. The terms d^{c} and d^{e} are strengths of the diffusive spread for clusters and for vacancy emission relative to single point defects:

$$d^{\text{c}} = \frac{D^{\text{c}}(n_{\text{cr}})}{n_{\text{cr}}^{1/3} D^{\text{s}}(n_{\text{cr}})} , \quad d^{\text{e}} = \frac{D^{\text{e}}(n_{\text{cr}})}{n_{\text{cr}}^{1/3} D^{\text{s}}(n_{\text{cr}})} , \tag{8.73}$$

and the function η has a value between 0.55 and 0.84.

Application of Eq. (8.71) for various values of d^{c} and d^{e} and for a void embryo size of 4 vacancies leads to nucleation probabilities in the range 10^{-6} to 10^{-4} for critical vacancy clusters of size ~ 100 vacancies (Fig. 8.12). The nucleation rate is then:

$$J \cong \frac{K_{\text{cl}}^{\text{eff}}}{N_{\text{d}}} P_{\text{m}} , \tag{8.74}$$

where $K_{\text{cl}}^{\text{eff}}$ is the effective generation rate of point defects in cluster and free form and N_{d} is the average total number of point defects generated in a single cascade and ε_{i} is the fraction of interstitials produced in cascades in the form of immobile clusters. Figure 8.13 shows the void nucleation rate calculated for annealed copper compared with experimental data at 250, 300 and 350 °C and different surface energies, γ_{s} and for different values of d^{e}. In terms of void nuclei created $\text{cm}^{-3}\,\text{s}^{-1}$, the nucleation rate is in the range 10^{15} to 10^{18}, which is larger than what was predicted by conventional nucleation theory. Thus, the effect of production bias is to increase the nucleation rate.

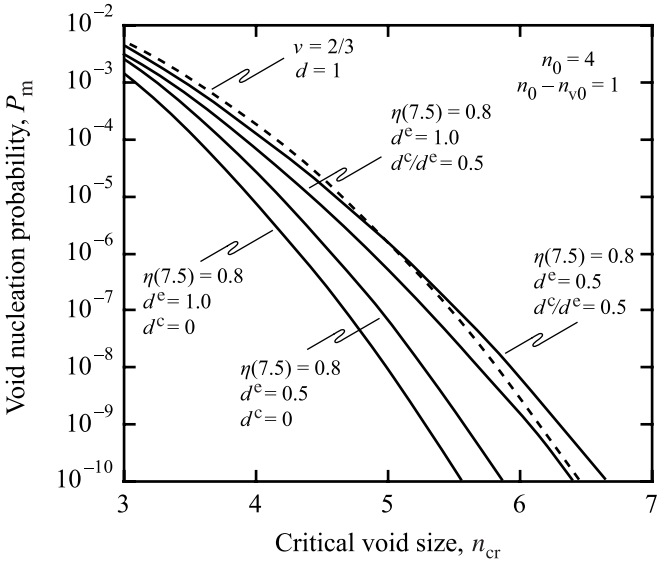

Fig. 8.12. Nucleation probability plotted from Eq. (8.71) for initial void size of four vacancies and minimum size of one vacancy and for different values of d^c and d^e vs. the critical void size, n_{cr}. The term $\nu = \dfrac{(D_v C_v - D_i C_i)[1 - \exp(-\beta/R_{cr})]}{D_i C_i}$ (after [14])

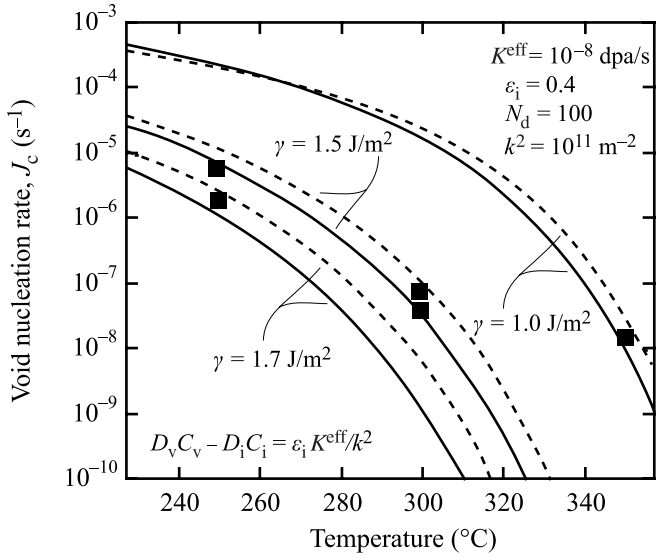

Fig. 8.13. Void nucleation rate vs. irradiation temperature for the case of copper under a displacement rate of 10^{-8} dpa/s (after [14])

8.2 Void Growth

Having determined expressions for the rate at which voids are nucleated in the solid, we now turn to determining the rate at which the void nuclei grow into stable voids. As mentioned earlier, we will assume that the nucleation and growth stages are separated in time and that only when the void embryos are established does growth begin. Of course, this is a simplification of the true in-reactor situation in which the growth of stable nuclei is occurring simultaneously with nucleation.

Void growth is determined by solving the point defect balance equations developed in Chap. 5. These equations provide the vacancy and interstitial supersaturations that drive the nucleation and growth processes. The concentrations of vacancies and interstitials in the solid are determined by equating the rates of defect production and removal by all mechanisms. By doing so, the time derivatives are removed and the resulting solution has the form of a steady state solution. However, since the defect concentrations are changing with time (dose), the *steady state* solution is valid over only short time periods, and is termed *quasi-steady state*. The quasi-steady state solution has value because the changes in sink strength due to microstructure evolution is slow compared to the response time of the defect populations. So in essence, the problem can be solved by assuming an initial condition that properly characterizes the sink strengths, solving the point defect balance equations for those sink strengths, then updating the sink strengths and iterating.

Rates of production and removal are assumed to be uniform throughout the metal. Clearly, strong gradients will exist close to the sink. But they can be neglected by *homogenizing* or *smearing* the sink strengths, that is, by replacing discrete sinks by spatially uniform absorbers of point defects so that the aggregate effect on defect absorption is the same in the homogenized sink case as in the heterogeneous sink case. The sink strengths are those described in Chap. 5. Void growth is then calculated according to rate theory as developed by Brailsford and Bullough [14] subject to the following simplifications:

1. Discrete sinks are replaced by a continuous or *smeared* distribution of sinks.
2. Each sink is given a *strength* so that the current of defects to the *smeared* sink is the same as the current to the actual sinks in the real material.
3. Steps 1 and 2 remove the spatial dependence of C_v and C_i and the point defect balance equations become:

$$\frac{\partial C_\mathrm{v}}{\partial t} = K_0 - \sum_j A_\mathrm{v}^j - R_\mathrm{iv}$$
$$\frac{\partial C_\mathrm{i}}{\partial t} = K_0 - \sum_j A_\mathrm{i}^j - R_\mathrm{iv}\,, \tag{8.75}$$

   where the first term on the right is the production rate of vacancies and interstitials, the second term is the loss rate to all sinks and the last term is the loss rate due to vacancy–interstitial recombination.
4. Vacancy and interstitial concentrations, C_v and C_i are calculated from Eq. (8.75). The change in sink strength due to the flow of defects to the sink is calculated,

and the process, starting with step 1, is iterated in order to advance in time and dose.

Reaction rate constants for defect–sink reactions and sink strengths for the relevant sinks were determined in Chap. 5 and summarized in Table 5.1. Recall that sinks are classified as neutral (voids, grain boundaries, incoherent precipitates), biased (dislocation network and dislocation loops) or variable biased (coherent precipitates and over/undersized solutes). For all sink types, the defect absorption rate is proportional to the diffusion coefficient of the point defect and the difference in defect concentration between the bulk and the sink surface. With the exception of dislocation loops, the interstitial concentration at the sink surface is insignificant compared to the bulk value and may be neglected. In the case of vacancies, their concentration at the network dislocation core is maintained at the equilibrium concentration. For voids and loops, the vacancy concentration at the sink surfaces must also be determined. Once the sink strengths and the defect concentrations at the sink surfaces are all known, then we can determine the net absorption rate of defects by void nuclei and use this information to determine the growth rate of the voids.

8.2.1 Defect Absorption Rates and Concentrations at Sink Surfaces

We seek to determine expressions for the absorption rates of defects for each of the relevant of sinks, categorized according to sink type. The general form of the absorption rate is:

$$A_j^X = k_X^2 D_j (C_j - C_j^X) = k_X^2 D_j C_j - L_j^X \ , \tag{8.76}$$

where A_j^X is the absorption rate of defect j by sink X, k_X^2 is the strength of sink X, D_j is the diffusion coefficient of defect j, C_j and C_j^X are the bulk concentration and sink surface concentration of defect j, and L_j^X is the thermal emission rate of defect j by sink X. Note that for neutral sinks, the sink strengths are dependent only on the character of the sink and not the defect. This is the advantage of writing the loss terms using sink strengths rather than reaction rate constants.

Neutral Sinks

The loss rate of point defects to voids can be written as:

$$\begin{aligned} A_\mathrm{v}^\mathrm{V} &= k_\mathrm{V}^2 D_\mathrm{v} (C_\mathrm{v} - C_\mathrm{v}^\mathrm{V}) = k_\mathrm{V}^2 D_\mathrm{v} C_\mathrm{v} - L_\mathrm{v}^\mathrm{V} \\ A_\mathrm{i}^\mathrm{V} &= k_\mathrm{V}^2 D_\mathrm{i} C_\mathrm{i} \ , \end{aligned} \tag{8.77}$$

where k_V^2 is the sink strength of a void given in Table 5.1, C_v^V is the vacancy concentration at the void surface, L_v^V is the thermal emission rate of vacancies at the sink surface and all voids are assumed to be the same size. The loss rate of defects to incoherent precipitates is:

$$\begin{aligned} A_\mathrm{v}^\mathrm{IP} &= k_\mathrm{IP}^2 D_\mathrm{v} C_\mathrm{v} \\ A_\mathrm{i}^\mathrm{IP} &= k_\mathrm{IP}^2 D_\mathrm{i} C_\mathrm{i} \ , \end{aligned} \tag{8.78}$$

and to grain boundaries the rate is:

$$\begin{aligned} A_{\mathrm{v}}^{\mathrm{gb}} &= k_{\mathrm{gb}}^2 D_{\mathrm{v}} C_{\mathrm{v}} \\ A_{\mathrm{i}}^{\mathrm{gb}} &= k_{\mathrm{gb}}^2 D_{\mathrm{i}} C_{\mathrm{i}} \,, \end{aligned} \tag{8.79}$$

where the sink strengths are given in Table 5.1, and thermal emission terms have been neglected.

Among Eqs. (8.77), (8.78), and (8.79), the term that is yet to be determined is the vacancy concentration at the void surface, $C_{\mathrm{v}}^{\mathrm{V}}$. This is done as follows. Recall from Eq. (4.14) that the thermal equilibrium concentration of vacancies in a solid is:

$$C_{\mathrm{v}}^0 = \frac{1}{\Omega} \exp\left(\frac{S_{\mathrm{f}}}{k}\right) \exp\left(\frac{H_{\mathrm{f}}}{kT}\right) \,,$$

where

$$H_{\mathrm{f}} = E_{\mathrm{f}} + p\Omega \,, \tag{8.80}$$

and the $p\Omega$ term was neglected for single vacancies embedded in the lattice. This simplification does not hold in the solid surrounding a void where forces such as surface tension, pressure due to gas in the void and an external hydrostatic stress are acting. For example, the existence of a void surface produces a surface tension that can be determined, using Fig. 8.14, as follows:

$$\frac{\text{Force}}{\text{unit area}} = \frac{2\pi r\gamma \sin\theta}{A} \cong \frac{2\pi r\gamma}{\pi r^2}\theta = \frac{2\pi r\gamma}{\pi r^2}\left(\frac{r}{R}\right) = \frac{2\gamma}{R} \,, \tag{8.81}$$

where the approximation is that $\sin\theta$ is replaced with θ for small θ. Hence, the p term in Eq. (8.80) becomes:

$$p = -\frac{2\gamma}{R} \,, \tag{8.82}$$

where the minus sign enters because the surface tension acts in an inward direction to shrink the void. The vacancy concentration at the void surface then becomes:

$$C_{\mathrm{v}}^{\mathrm{V}} = \frac{1}{\Omega} \exp\left(\frac{S_{\mathrm{f}}}{k}\right) \exp\left(-\frac{E_{\mathrm{f}}}{kT}\right) \exp\left(-\frac{p\Omega}{kT}\right) \,, \tag{8.83}$$

where:

$$C_{\mathrm{v}}^0 = \frac{1}{\Omega} \exp\left(\frac{S_{\mathrm{f}}}{k}\right) \exp\left(-\frac{E_{\mathrm{f}}}{kT}\right) \,, \tag{8.84}$$

and substituting for $p\Omega$ from Eq. (8.82) gives:

$$C_{\mathrm{v}}^{\mathrm{V}} = C_{\mathrm{v}}^0 \exp\left(\frac{2\gamma\Omega}{RkT}\right) \,, \tag{8.85}$$

and Eq. (8.77) becomes:

$$A_{\mathrm{v}}^{\mathrm{V}} = k_{\mathrm{V}}^2 D_{\mathrm{v}} \left[C_{\mathrm{v}} - C_{\mathrm{v}}^0 \exp\left(\frac{2\gamma\Omega}{RkT}\right)\right] \,. \tag{8.86}$$

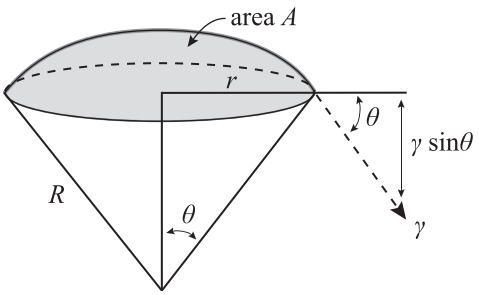

Fig. 8.14. Schematic of the surface tension on a void of radius r

Biased Sinks

The defect loss rate to network dislocations is given by:

$$\begin{aligned} A_{\mathrm{v}}^{\mathrm{d}} &= k_{\mathrm{vd}}^2 D_{\mathrm{v}}(C_{\mathrm{v}} - C_{\mathrm{v}}^0) = k_{\mathrm{vd}}^2 D_{\mathrm{v}} C_{\mathrm{v}} - L_{\mathrm{v}}^{\mathrm{d}} \\ A_{\mathrm{i}}^{\mathrm{d}} &= k_{\mathrm{id}}^2 D_{\mathrm{i}} C_{\mathrm{i}} \,, \end{aligned} \tag{8.87}$$

where the sink strengths are given in Table 5.1 and the term C_{v}^0 is the thermal equilibrium concentration of vacancies. For interstitial dislocation loops, the loss term is:

$$\begin{aligned} A_{\mathrm{v}}^{\mathrm{L}} &= k_{\mathrm{vd}}^2 D_{\mathrm{v}}(C_{\mathrm{v}} - C_{\mathrm{v}}^{\mathrm{L}}) = k_{\mathrm{vL}}^2 D_{\mathrm{v}} C_{\mathrm{v}} - L_{\mathrm{v}}^{\mathrm{L}} \\ A_{\mathrm{i}}^{\mathrm{L}} &= k_{\mathrm{id}}^2 D_{\mathrm{i}}(C_{\mathrm{i}} - C_{\mathrm{i}}^{\mathrm{L}}) = k_{\mathrm{iL}}^2 D_{\mathrm{i}} C_{\mathrm{i}} - L_{\mathrm{i}}^{\mathrm{L}} \,, \end{aligned} \tag{8.88}$$

where the sink strengths are the same as for network dislocations since the dislocation core is the same. However, the defect concentration at the sink surface is different from the thermal equilibrium value because addition of a vacancy or an interstitial to the dislocation loop contracts or expands, respectively, the size of the loop and this requires a change in energy. The concentration of vacancies and interstitials in equilibrium with a loop are $C_{\mathrm{v}}^{\mathrm{L}}$ and $C_{\mathrm{i}}^{\mathrm{L}}$, respectively. Following the analysis in [4] the defect concentration in equilibrium with the loop is determined by considering the Gibbs free energy of a piece of metal containing n_{v} vacancies and n_{i} interstitials at concentrations $C_{\mathrm{v}}^{\mathrm{L}}$ and $C_{\mathrm{i}}^{\mathrm{L}}$, and a single interstitial loop containing m_{i} interstitials:

$$G = G_0 + E_{\mathrm{L}}(m_{\mathrm{i}}) + n_{\mathrm{v}}\mu_{\mathrm{v}} + n_{\mathrm{i}}\mu_{\mathrm{i}} \,, \tag{8.89}$$

where G_0 is the free energy of solid without the loop but with C_{v} and C_{i} defects, $E_{\mathrm{L}}(m_{\mathrm{i}})$ is the energy of the loop, and $\mu_{\mathrm{i,v}}$ are the chemical potentials of interstitials and vacancies in the solid. For the system to be in chemical equilibrium, the transfer of point defects between the solid and the loop must cause no change in the free energy of the system:

$$\delta G = \left(\frac{\mathrm{d}E_{\mathrm{L}}}{\mathrm{d}m_{\mathrm{i}}}\right)\delta m_{\mathrm{i}} + \mu_{\mathrm{v}}\delta n_{\mathrm{v}} + \mu_{\mathrm{i}}\delta n_{\mathrm{i}} = 0 \,, \tag{8.90}$$

and

$$\delta m_{\mathrm{i}} = \delta n_{\mathrm{v}} - \delta n_{\mathrm{i}} \,, \tag{8.91}$$

since the number of interstitials in the loop must come from the bulk. Eliminating δm_{i} from Eqs. (8.91) and (8.92) gives:

$$\left(\frac{\mathrm{d}E_{\mathrm{L}}}{\mathrm{d}m_{\mathrm{i}}}\right)\delta n_{\mathrm{v}} - \left(\frac{\mathrm{d}E_{\mathrm{L}}}{\mathrm{d}m_{\mathrm{i}}}\right)\delta n_{\mathrm{i}} + \mu_{\mathrm{v}}\delta n_{\mathrm{v}} + \mu_{\mathrm{i}}\delta n_{\mathrm{i}} = 0 \,. \tag{8.92}$$

Since changes in vacancy and interstitial concentrations are arbitrary and independent of each other, the coefficients of both changes are set equal to zero, leading to:

$$\begin{aligned} &\frac{\mathrm{d}E_{\mathrm{L}}}{\mathrm{d}m_{\mathrm{i}}} + \mu_{\mathrm{v}} = 0 \\ &\frac{\mathrm{d}E_{\mathrm{L}}}{\mathrm{d}m_{\mathrm{i}}} - \mu_{\mathrm{i}} = 0 \,. \end{aligned} \tag{8.93}$$

From Eq. (8.12), the chemical potential of vacancies and interstitials in a solid with concentrations $C_{\mathrm{v}}^{\mathrm{L}}$ and $C_{\mathrm{i}}^{\mathrm{L}}$ is:

$$\begin{aligned} \mu_{\mathrm{v}} &= kT \ln \frac{C_{\mathrm{v}}^{\mathrm{L}}}{C_{\mathrm{v}}^{0}} \\ \mu_{\mathrm{i}} &= kT \ln \frac{C_{\mathrm{i}}^{\mathrm{L}}}{C_{\mathrm{i}}^{0}} \,. \end{aligned} \tag{8.94}$$

For vacancies and interstitials in equilibrium:

$$C_{\mathrm{v}}^{\mathrm{L}} C_{\mathrm{i}}^{\mathrm{L}} = C_{\mathrm{v}}^{0} C_{\mathrm{i}}^{0} \,, \tag{8.95}$$

or from Eq. (8.94):

$$\mu_{\mathrm{v}} = -\mu_{\mathrm{i}} \,. \tag{8.96}$$

Combining Eqs. (8.93) and (8.94) for vacancies and then for interstitials, yields:

$$\begin{aligned} C_{\mathrm{v}}^{\mathrm{L}} &= C_{\mathrm{v}}^{0} \exp\left(-\frac{\mathrm{d}E_{\mathrm{L}}/\mathrm{d}m_{\mathrm{i}}}{kT}\right) \\ C_{\mathrm{i}}^{\mathrm{L}} &= C_{\mathrm{i}}^{0} \exp\left(\frac{\mathrm{d}E_{\mathrm{L}}/\mathrm{d}m_{\mathrm{i}}}{kT}\right) \,. \end{aligned} \tag{8.97}$$

Using Eq. (7.62) for the energy of a Frank loop:

$$E_{\mathrm{L}} = 2\pi\mu b^2 \left(\frac{\sqrt{3}a^2 m_{\mathrm{i}}}{4\pi}\right)^{1/2} + \pi\left(\frac{\sqrt{3}a^2 m_{\mathrm{i}}}{4\pi}\right)\gamma_{\mathrm{SFE}} \,,$$

and dropping the second term for simplicity, then $\mathrm{d}E_\mathrm{L}/\mathrm{d}m_\mathrm{i}$ becomes:

$$\frac{\mathrm{d}E_\mathrm{L}}{\mathrm{d}m_\mathrm{i}} = \frac{\Theta}{2\sqrt{m_\mathrm{i}}}\,, \tag{8.98}$$

where Θ is $2\pi\mu b^2\left(\dfrac{\sqrt{3}a^2}{4\pi}\right)^{1/2}$. Substituting into Eq. (8.97) yields:

$$\begin{aligned} C_\mathrm{v}^\mathrm{L} &= C_\mathrm{v}^0 \exp\left(-\frac{\Theta}{2\sqrt{m_\mathrm{i}}kT}\right) \\ C_\mathrm{i}^\mathrm{L} &= C_\mathrm{i}^0 \exp\left(\frac{\Theta}{2\sqrt{m_\mathrm{i}}kT}\right)\,. \end{aligned} \tag{8.99}$$

Note that the vacancy concentration in equilibrium with an interstitial loop is less than the equilibrium vacancy concentration in the solid while the reverse is true for interstitials. The absorption rates of vacancies and interstitials at loops then becomes, from Eq. (8.88):

$$\begin{aligned} A_\mathrm{v}^\mathrm{L} &= z_\mathrm{v} D_\mathrm{v} \rho_\mathrm{L}\left[C_\mathrm{v} - C_\mathrm{v}^0 \exp\left(-\frac{\Theta}{2\sqrt{m_\mathrm{i}}kT}\right)\right] \\ A_\mathrm{i}^\mathrm{L} &= z_\mathrm{i} D_\mathrm{i} \rho_\mathrm{L}\left[C_\mathrm{i} - C_\mathrm{i}^0 \exp\left(\frac{\Theta}{2\sqrt{m_\mathrm{i}}kT}\right)\right]\,. \end{aligned} \tag{8.100}$$

Variable Biased Sinks

The sink strengths for variable biased sinks are given in Eq. (5.117) and are:

$$\begin{aligned} k_\mathrm{vCP}^2 &= 4\pi R_\mathrm{CP}\rho_\mathrm{CP} Y_\mathrm{v} \\ k_\mathrm{iCP}^2 &= 4\pi R_\mathrm{CP}\rho_\mathrm{CP} Y_\mathrm{i}\,, \end{aligned}$$

where $Y_\mathrm{v,i}$ are sink strengths for coherent precipitates for vacancies and interstitials and the loss rate of point defects to coherent precipitates is:

$$\begin{aligned} A_\mathrm{v}^\mathrm{CP} &= k_\mathrm{vCP}^2 D_\mathrm{v} C_\mathrm{v} = 4\pi R_\mathrm{CP}\rho_\mathrm{CP} C_\mathrm{v} Y_\mathrm{v} \\ A_\mathrm{i}^\mathrm{CP} &= k_\mathrm{iCP}^2 D_\mathrm{i} C_\mathrm{i} = 4\pi R_\mathrm{CP}\rho_\mathrm{CP} C_\mathrm{i} Y_\mathrm{i}\,. \end{aligned} \tag{8.101}$$

8.2.2 Point Defect Balances

Now that we have expressions for the absorption rates of defects for each type of sink, we can construct the steady state, point defect balances for the solid under irradiation:

$$\begin{aligned} K_0 - \sum_j A_\mathrm{v}^j - R_\mathrm{iv} &= 0 \\ K_0 - \sum_j A_\mathrm{i}^j - R_\mathrm{iv} &= 0\,, \end{aligned} \tag{8.102}$$

and in the most general form:

$$\begin{aligned} K_0 - k_{\mathrm{v}}^2 D_{\mathrm{v}}(C_{\mathrm{v}} - C_{\mathrm{v}}^X) - K_{\mathrm{iv}} C_{\mathrm{v}} C_{\mathrm{i}} &= 0 \\ K_0 - k_{\mathrm{i}}^2 D_{\mathrm{i}}(C_{\mathrm{i}} - C_{\mathrm{i}}^X) - K_{\mathrm{iv}} C_{\mathrm{v}} C_{\mathrm{i}} &= 0 \,, \end{aligned} \tag{8.103}$$

where k_{v}^2 and k_{i}^2 are the total sink strengths for vacancy and interstitial loss:

$$\begin{aligned} k_{\mathrm{v}}^2 &= k_{\mathrm{vV}}^2 + k_{\mathrm{vIP}}^2 + k_{\mathrm{vgb}}^2 + k_{\mathrm{vN}}^2 + k_{\mathrm{vL}}^2 + k_{\mathrm{vCP}}^2 \\ k_{\mathrm{i}}^2 &= k_{\mathrm{iV}}^2 + k_{\mathrm{iIP}}^2 + k_{\mathrm{igb}}^2 + k_{\mathrm{iN}}^2 + k_{\mathrm{iL}}^2 + k_{\mathrm{iCP}}^2 \,, \end{aligned} \tag{8.104}$$

and the C_{v}^X and C_{i}^X are concentrations of vacancies and interstitials at the sink surface. Now, since defect production rates and recombination rates in Eq. (8.103) are equal and there is no net accumulation of point defects at coherent precipitates, then:

$$\sum_j A_{\mathrm{v}}^j = \sum_j A_{\mathrm{i}}^j \,, \tag{8.105}$$

or

$$A_{\mathrm{v}}^{\mathrm{V}} + A_{\mathrm{v}}^{\mathrm{IP}} + A_{\mathrm{v}}^{\mathrm{gb}} + A_{\mathrm{v}}^{\mathrm{d}} + A_{\mathrm{v}}^{\mathrm{L}} = A_{\mathrm{i}}^{\mathrm{V}} + A_{\mathrm{i}}^{\mathrm{IP}} + A_{\mathrm{i}}^{\mathrm{gb}} + A_{\mathrm{i}}^{\mathrm{d}} + A_{\mathrm{i}}^{\mathrm{L}} \,, \tag{8.106}$$

and therefore:

$$\begin{aligned} &(k_{\mathrm{vV}}^2 + k_{\mathrm{vIP}}^2 + k_{\mathrm{vgb}}^2 + k_{\mathrm{vN}}^2 + k_{\mathrm{vL}}^2 + k_{\mathrm{vCP}}^2) D_{\mathrm{v}} C_{\mathrm{v}} - L_{\mathrm{v}}^{\mathrm{V}} - L_{\mathrm{v}}^{N} - L_{\mathrm{v}}^{\mathrm{L}} \\ &= (k_{\mathrm{iV}}^2 + k_{\mathrm{iIP}}^2 + k_{\mathrm{igb}}^2 + k_{\mathrm{iN}}^2 + k_{\mathrm{iL}}^2 + k_{\mathrm{iCP}}^2) D_{\mathrm{i}} C_{\mathrm{i}} - L_{\mathrm{i}}^{\mathrm{L}} \,. \end{aligned} \tag{8.107}$$

where the L terms are the thermal emission of the defect from the sink.

Substituting in for the expressions for sink strength and thermal emission from the respective equations in Chaps. 5 and 7 gives:

$$\begin{aligned} &4\pi R_{\mathrm{V}} \rho_{\mathrm{V}} D_{\mathrm{v}} \left[C_{\mathrm{v}} - C_{\mathrm{v}}^0 \exp\left(\frac{2\gamma\Omega}{RkT} \right) \right] + z_{\mathrm{v}} \rho_N D_{\mathrm{v}} \left(C_{\mathrm{v}} - C_{\mathrm{v}}^0 \right) + 4\pi R_{\mathrm{CP}} \rho_{\mathrm{CP}} D_{\mathrm{v}} C_{\mathrm{v}} Y_{\mathrm{v}} \\ &\quad + z_{\mathrm{v}} \rho_{\mathrm{L}} D_{\mathrm{v}} \left[C_{\mathrm{v}} - C_{\mathrm{v}}^0 \exp\left(-\frac{\Theta}{2\sqrt{m_{\mathrm{i}}} kT} \right) \right] \\ &= \pi R_{\mathrm{V}} \rho_{\mathrm{V}} D_{\mathrm{i}} C_{\mathrm{i}} + z_{\mathrm{i}} \rho_{\mathrm{N}} D_{\mathrm{i}} C_{\mathrm{i}} + 4\pi R_{CP} \rho_{\mathrm{CP}} D_{\mathrm{v}} C_{\mathrm{v}} Y_{\mathrm{i}} \\ &\quad + z_{\mathrm{i}} \rho_{\mathrm{L}} D_{\mathrm{i}} \left[C_{\mathrm{i}} - C_{\mathrm{i}}^0 \exp\left(\frac{\Theta}{2\sqrt{m_{\mathrm{i}}} kT} \right) \right] \,, \end{aligned} \tag{8.108}$$

where terms for grain boundaries and incoherent precipitates are neglected for simplicity. Since the thermal equilibrium interstitial concentration, C_{i}^0 is extremely small, the thermal emission of interstitials from loops can be neglected.

8.3 Void Growth Equation

Now that we have determined the absorption rate of defects for each sink in the solid, we focus on the void with the objective of developing an expression describing its rate of growth. The void growth equation has its origins in the net flux of vacancies to a void embryo. The *net* rate of absorption of vacancies by a void is:

$$A_{\text{net}}^{\text{V}} = A_{\text{v}}^{\text{V}} - A_{\text{i}}^{\text{V}} = 4\pi R D_{\text{v}} \left(C_{\text{v}} - C_{\text{v}}^{\text{V}}\right) - 4\pi R D_{\text{i}} \left(C_{\text{i}} - C_{\text{i}}^{\text{V}}\right) , \tag{8.109}$$

where

R = void radius (we have dropped the subscript V for simplicity)

$C_{\text{v,i}}$ = vacancy/interstitial concentration in the solid

C_{v}^{V} = vacancy concentration at the void surface, and thermal emission of interstitials from loops is neglected

The rate of change in volume of the void is just the net absorption rate times the defect volume, Ω:

$$\frac{\text{d}V}{\text{d}t} = 4\pi R \Omega \left[D_{\text{v}} \left(C_{\text{v}} - C_{\text{v}}^{\text{V}}\right) - D_{\text{i}} C_{\text{i}}\right] , \tag{8.110}$$

and since,

$$V = \frac{4}{3}\pi R^3 , \tag{8.111}$$

we obtain the common form of the void growth equation:

$$\frac{\text{d}R}{\text{d}t} = \dot{R} = \frac{\Omega}{R} \left[D_{\text{v}} \left(C_{\text{v}} - C_{\text{v}}^{\text{V}}\right) - D_{\text{i}} C_{\text{i}}\right] . \tag{8.112}$$

Our objective is to determine an expression for the void growth equation, which amounts to determining the values for C_{v},C_{i}, and C_{v}^{V}. The general solution procedure is thus to solve the point defect balance equations in Eq. (8.75) for C_{v} and C_{i} at some initial value of the void radius, $R(0)$ and then to use those values of C_{v} and C_{i} in Eq. (8.112) to increment the void size from R to R'. Since sink strength changes with void size, updated values of C_{v} and C_{i} must be obtained for the next void growth increment. The process is then iterated to describe the change in void size with time or dose. This process can be carried out numerically and with small time steps in order to minimize the time increment over which the sink strengths are assumed to be constant. In solving for void size in this way, changes to the microstructure can also be incorporated at the time step boundaries.

While a numerical solution of the void growth equation will produce the most accurate result, it provides no insight into the governing processes during void growth. Brailsford and Bullough [15] inserted the solution of Eq. (8.75), into Eq. (8.112) to obtain an approximate analytical result that provides an excellent tool for understanding the parameters governing void growth. Mansur [5, 16] advanced the analysis to develop expressions for the dependence on critical parameters affecting void growth. We begin by returning to the point defect balance equations

at steady state in order to determine the bulk concentrations of vacancies and interstitials, C_v and C_i. Setting the time rate of change of the vacancy and interstitial concentrations equal to zero in Eq. (8.75) gives:

$$\begin{aligned} K_0 - \sum_j A_v^j - R_{iv} &= 0 \\ K_0 - \sum_j A_i^j - R_{iv} &= 0 \,, \end{aligned} \tag{8.113}$$

or

$$\begin{aligned} K_0 - K_{iv} C_i C_v - K_{vs} C_v C_s &= 0 \\ K_0 - K_{iv} C_i C_v - K_{is} C_i C_s &= 0 \,, \end{aligned} \tag{8.114}$$

with solutions:

$$\begin{aligned} C_v &= \frac{-K_{is} C_s}{2K_{iv}} + \left[\frac{K_0 K_{vs}}{K_{iv} K_{is}} + \frac{K_{vs}^2 C_s^2}{4K_{iv}} \right]^{1/2} \\ C_i &= \frac{-K_{vs} C_s}{2K_{iv}} + \left[\frac{K_0 K_{is}}{K_{iv} K_{vs}} + \frac{K_{is}^2 C_s^2}{4K_{iv}} \right]^{1/2} \,, \end{aligned} \tag{8.115}$$

where C_s is the sink concentration. Using Table 5.1 to write the reaction rate constants for vacancies and interstitials at sinks as sink strengths gives:

$$\begin{aligned} C_v &= \frac{-k_i^2}{2K_{iv}} + \left[\frac{K_0 k_v^2 D_i}{K_{iv} k_i^2 D_v} + \frac{k_v^2 D_v^2}{4K_{iv}} \right]^{1/2} \\ C_i &= \frac{-k_v^2}{2K_{iv}} + \left[\frac{K_0 k_i^2 D_v}{K_{iv} k_v^2 D_i} + \frac{k_i^2 D_i^2}{4K_{iv}} \right]^{1/2} . \end{aligned} \tag{8.116}$$

Defining:

$$\eta = \frac{4K_{iv} K_0}{D_i D_v k_v^2 k_i^2} \,, \tag{8.117}$$

and

$$\begin{aligned} k_v^2 &= z_v \rho_d + 4\pi R \rho_V + 4\pi R_{CP} \rho_{CP} \\ k_i^2 &= z_i \rho_d + 4\pi R \rho_V + 4\pi R_{CP} \rho_{CP} \,, \end{aligned} \tag{8.118}$$

where, for simplicity, we have neglected grain boundaries, incoherent precipitates and bias factors on voids and coherent precipitates, and the network dislocations and dislocation loops are represented by a single term with density $\rho_d = \rho_N + \rho_L$. Using Eqs. (8.117) and (8.118), then Eq. (8.116) can be written as:

$$\begin{aligned} C_v &= \frac{D_i k_i^2}{2K_{iv}} \left[(\eta + 1)^{1/2} - 1 \right] \\ C_i &= \frac{D_v k_v^2}{2K_{iv}} \left[(\eta + 1)^{1/2} - 1 \right] . \end{aligned} \tag{8.119}$$

The void growth rate from Eq. (8.112) can be written in the form:

$$\dot{R} = \dot{R}_0 X(\eta) \,, \tag{8.120}$$

where

$$\dot{R}_0 = \frac{\dfrac{K_0(z_\mathrm{i} - z_\mathrm{v})\rho_\mathrm{d}\Omega}{R(z_\mathrm{v}\rho_\mathrm{d} + 4\pi R\rho_\mathrm{V})}}{z_\mathrm{i}\rho_\mathrm{d} + 4\pi R\rho_\mathrm{V} + 4\pi R_\mathrm{CP}\rho_\mathrm{CP}\left[1 + \dfrac{(z_\mathrm{i} - z_\mathrm{v})\rho_\mathrm{d}}{z_\mathrm{v}\rho_\mathrm{d} + 4\pi R\rho_\mathrm{V}}\right]} \,. \tag{8.121}$$

Equation (8.121) can be simplified by dropping the last term in the square brackets in the denominator, since the difference $(z_\mathrm{i} - z_\mathrm{v})$ is small, giving:

$$\dot{R}_0 = \frac{K_0(z_\mathrm{i} - z_\mathrm{v})\rho_\mathrm{d}\Omega}{R(z_\mathrm{v}\rho_\mathrm{d} + 4\pi R\rho_\mathrm{V})(z_\mathrm{i}\rho_\mathrm{d} + 4\pi R\rho_\mathrm{V} + 4\pi R_\mathrm{CP}\rho_\mathrm{CP})} \,. \tag{8.122}$$

This growth term is independent of temperature and is proportional to the dislocation bias for interstitials $(z_\mathrm{i} - z_\mathrm{v})$ and the defect production rate. Note that $\dot{R}_0$ is:

- Independent of temperature
- Proportional to the dislocation bias $(z_\mathrm{i} - z_\mathrm{v})$
- Proportional to the defect production rate, K_0

The term $X(\eta)$ is given by:

$$X(\eta) = F(\eta) - 2\zeta \,, \tag{8.123}$$

where:

$$F(\eta) = \frac{2}{\eta}\left[(\eta + 1)^{1/2} - 1\right] \,, \tag{8.124}$$

and η is a dimensionless parameter defined in Eq. (8.117). Substituting Eq. (8.123) into Eq. (8.120) gives:

$$\dot{R} = \dot{R}_0 F(\eta) - 2\dot{R}_0\zeta \,. \tag{8.125}$$

The quantity η in the function $F(\eta)$ can be simplified by substituting in for k_v^2 and k_i^2 from Eq. (8.104) (or Table 5.1), giving:

$$\eta = \frac{4K_\mathrm{iv}K_0}{D_\mathrm{i}D_\mathrm{v}(z_\mathrm{i}\rho_\mathrm{D} + 4\pi R\rho_\mathrm{V} + 4\pi R_\mathrm{CP}\rho_\mathrm{CP})(z_\mathrm{v}\rho_\mathrm{d} + 4\pi R\rho_\mathrm{V} + 4\pi R_\mathrm{CP}\rho_\mathrm{CP})} \,. \tag{8.126}$$

Using the approximation that $z_\mathrm{i} \cong z_\mathrm{v}$, and eliminating K_iv by using Eq. (5.57) gives:

$$\eta = \frac{4z_\mathrm{iv}K_0\Omega}{D_\mathrm{i}D_\mathrm{v}(z\rho_\mathrm{D} + 4\pi R\rho_\mathrm{V} + 4\pi R_\mathrm{CP}\rho_\mathrm{CP})^2} \,. \tag{8.127}$$

The expression for η is substituted into Eq. (8.124) to obtain an expression for $F(\eta)$. This function describes the effect of homogeneous recombination on void growth

(Fig. 8.15). When recombination is negligible $K_{iv} \to 0$ and $\eta \to 0$, and $F \to 1$, or $\lim_{\eta \to 0} F(\eta) = 1$.

Turning now to the second term in Eq. (8.125), we define for simplicity:

$$\dot{R}_{th} = -2\dot{R}_0 \zeta \,, \tag{8.128}$$

so that Eq. (8.125) can now be written as:

$$\dot{R} = \dot{R}_0 F(\eta) + \dot{R}_{th} \,, \tag{8.129}$$

The term ζ is a function of temperature and is expressed as:

$$\begin{aligned} \zeta = \zeta(T) = {} & \frac{D_v(z_v\rho_d + 4\pi R\rho_V)\left[z_i\rho_d + 4\pi(R\rho_V + R_{CP}\rho_{CP})\right]}{2K_0(z_i - z_v)\left[z_v p_d + 4\pi(R\rho_V + R_{CP}\rho_{CP})\right]} \\ & \times \left[4\pi R_{CP}\rho_{CP}C_v^V + z_v\left\{\rho_N\left(C_v^V - C_v^0\right) + \rho_L\left(C_v^V - C_v^L\right)\right\}\right] \,. \end{aligned} \tag{8.130}$$

so that:

$$\begin{aligned} \dot{R}_{th} = -2\dot{R}_0\zeta = {} & \frac{-2D_v(z_v\rho_d + 4\pi R\rho_V)\left[z_i\rho_d + 4\pi(R\rho_V + R_{CP}\rho_{CP})\right]}{2K_0(z_i - z_v)\rho_d\left[z_v\rho_d + 4\pi(R\rho_V + R_{CP}\rho_{CP})\right]} \\ & \times \frac{\dfrac{K_0(z_i - z_v)\rho_d\Omega}{R(z_v\rho_d + 4\pi R\rho_V)}}{z_i\rho_d + 4\pi R\rho_V + 4\pi R_{CP}\rho_{CP}\left[1 + \dfrac{(z_i - z_v)\rho_d}{z_v\rho_d + 4\pi R\rho_V}\right]} \\ & \times \left[4\pi R_{CP}\rho_{CP}C_v^V + z_v\left[\rho_N\left(C_v^V - C_v^0\right) + \rho_L\left(C_v^V - C_v^L\right)\right]\right] . \end{aligned} \tag{8.131}$$

By approximating $z_i \cong z_v$, numerous terms in Eq. (8.131) cancel, leaving:

$$\begin{aligned} \dot{R}_{th} = {} & \frac{-D_v\Omega}{R(z_i\rho_d + 4\pi R\rho_V + 4\pi R_{CP}\rho_{CP})} \\ & \times \left[4\pi R_{CP}\rho_{CP}C_v^V + z_v\left[\rho_N\left(C_v^V - C_v^0\right) + \rho_L\left(C_v^V - C_v^L\right)\right]\right] \,. \end{aligned} \tag{8.132}$$

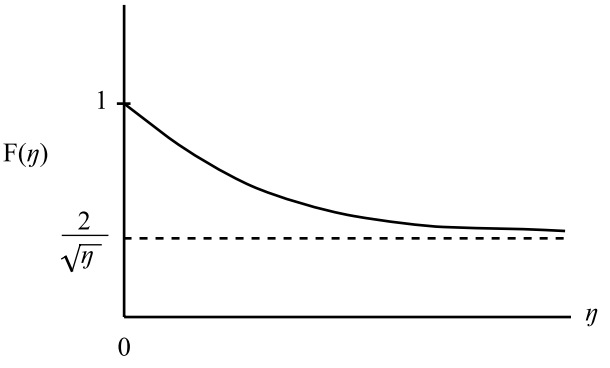

Fig. 8.15. The behavior of the function $F(\eta)$ in Eq. (8.124) as a function of η

Substituting in for C_v^V and C_v^L from Eqs. (8.85) and (8.99), respectively, gives:

$$\dot{R}_{th} = \frac{-D_v \Omega}{R(z_i\rho_d + 4\pi R\rho_V + 4\pi R_{CP}\rho_{CP})} \times \left[4\pi R_{CP}\rho_{CP}C_v^0 \exp\left(\frac{2\gamma\Omega}{RkT}\right) + z_v\left[\rho_N\left(C_v^0 \exp\left(\frac{2\gamma\Omega}{RkT}\right) - C_v^0\right)\right.\right. \\ \left.\left. + \rho_L\left(C_v^0 \exp\left(\frac{2\gamma\Omega}{RkT}\right) - C_v^0 \exp\left(-\frac{\Theta}{2\sqrt{m_i}kT}\right)\right)\right]\right] . \quad (8.133)$$

Approximating $\exp(x) \sim x + 1$ for small x, in the exponential terms of Eq. (8.133) gives:

$$\dot{R}_{th} = \frac{-D_v \Omega}{R(z_i\rho_d + 4\pi R\rho_V + 4\pi R_{CP}\rho_{CP})} \times \left[4\pi R_{CP}\rho_{CP}C_v^0 \exp\left(\frac{2\gamma\Omega}{RkT}\right)\right. \\ \left. + z_v C_v^0\left[\rho_N\frac{2\gamma\Omega}{RkT} + \rho_L\left(\frac{2\gamma\Omega}{RkT} + \frac{\Theta}{2\sqrt{m_i}kT}\right)\right]\right] , \quad (8.134)$$

and pulling the term C_v^0 out into the coefficient yields:

$$\dot{R}_{th} = \frac{-D_v \Omega C_v^0}{R(z_i\rho_d + 4\pi R\rho_V + 4\pi R_{CP}\rho_{CP})} \times \left[4\pi R_{CP}\rho_{CP} \exp\left(\frac{2\gamma\Omega}{RkT}\right) + z_v\rho_N\frac{2\gamma\Omega}{RkT} + z_v\rho_L\left(\frac{2\gamma\Omega}{RkT} + \frac{A}{2\sqrt{m_i}kT}\right)\right] , \quad (8.135)$$

which is the simplified expression for the thermal emission term. This term represents the thermal emission of defects from sinks. It is independent of defect production rate and is strongly temperature-dependent. Note that at very low temperature, $\dot{R}_{th} \to 0$, because of the terms D_v and C_v^0.

The rate of change in the void radius with time, $\dot{R}$, determined from Eq. (8.120), can be used to determine the volumetric swelling rate:

$$\frac{dV}{dt} = 4\pi R^2 \dot{R} . \quad (8.136)$$

Void swelling can be represented in terms of the void size distribution as follows. If $\rho_V(R)\,dR$ is the number of voids/cm^3 with radii between R and $R + dR$, then the total void number density is:

$$\rho_V = \int_0^\infty \rho_V(R)\,dR , \quad (8.137)$$

the average void size is:

$$\overline{R} = \frac{1}{\rho_V}\int_0^\infty R\rho_V(R)\,dR , \quad (8.138)$$

and the amount of void swelling is defined by the change in volume of the solid:

$$\frac{\Delta V}{V} = \frac{4}{3}\pi \int_0^\infty R^3 \rho_V(R)\, dR \,. \tag{8.139}$$

If the void distribution is narrow, then we can approximate the integral in Eq. (8.139) with:

$$\frac{\Delta V}{V} = \frac{4}{3}\pi \overline{R}^3 \rho_V \,. \tag{8.140}$$

The equations provided in this section allow the determination of the rate of growth of voids in a solid under irradiation, and consequently, the rate of swelling of that solid. The following sections address the effects of various parameters on void growth.

8.3.1 Temperature Dependence

Figure 8.16 provides a typical plot of void swelling as a function of temperature. Note that swelling is characterized by a peak at intermediate temperature. This behavior should look familiar from the temperature dependence of RIS since the origin is essentially the same. Low defect mobility limits void growth at low temperature, and the approach of the defect concentration to the thermal equilibrium value, and hence the loss of supersaturation, limits void growth at high temperature. In the preceding analysis of the void growth equation, the two highly temperature sensitive parameters are the vacancy diffusion coefficient D_v and the equilibrium vacancy concentration C_v^0. The temperature dependence of the term $\dot{R}_0 F(\eta)$ is contained in the parameter η, which is controlled by D_v. At low temperatures, swelling is low because vacancies are practically immobile. A low value of D_v makes η large and forces F to become small, resulting in a low value for the term $\dot{R}_0 F(\eta)$. The term $\dot{R}_{th}$ approaches zero since it is proportional to $D_v C_v^0$. Since both $F'(\eta)$ and $\dot{R}_{th}$ become small at low temperature, void growth ceases. Under these conditions, the concentration of vacancies builds up and vacancies and interstitials are lost to recombination.

At high temperature, the emission of vacancies by voids counterbalances the net vacancy influx driven by irradiation and suppresses swelling. When in the void growth equation η becomes small and F approaches unity, the term $\dot{R}_{th}$ also increases (but in the negative direction) and dominates at the highest temperatures. Hence a maximum in the growth rate is predicted at intermediate temperature where both thermal emission and mutual recombination are less important and the net flow of vacancies to voids is maximized. Figure 8.17 shows how the components of the void growth rate combine to result in a peak at intermediate temperature. This is found to be true with all metals.

Figure 8.18a shows an example of the sharp dependence of void swelling on temperature in an Fe–Cr–Ni alloy irradiated in the BN-350 reactor as a function

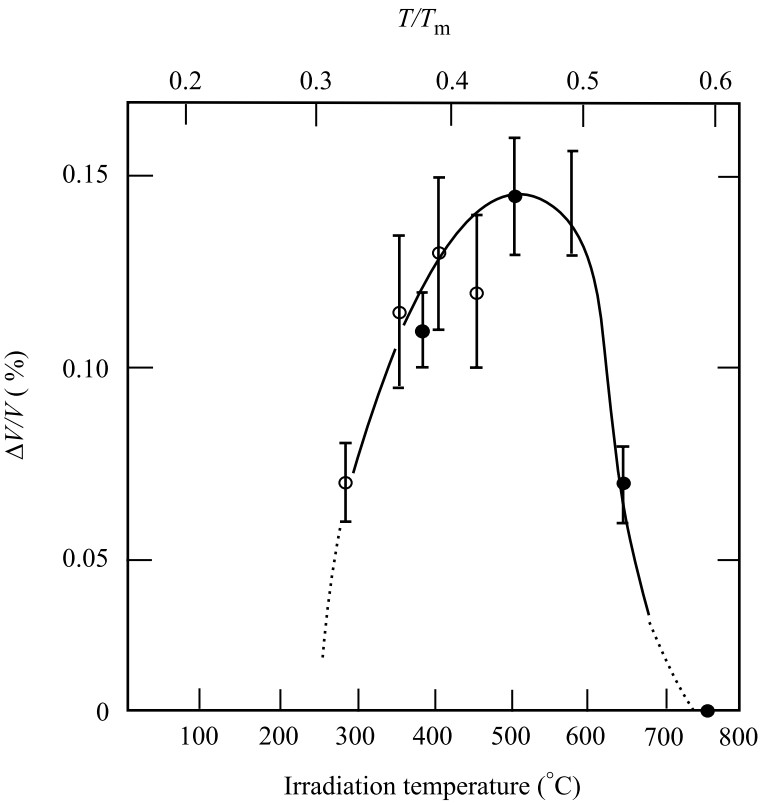

Fig. 8.16. Swelling in nickel as a function of irradiation temperature for a fluence of 5×10^{19} n/cm^2 (after [17])

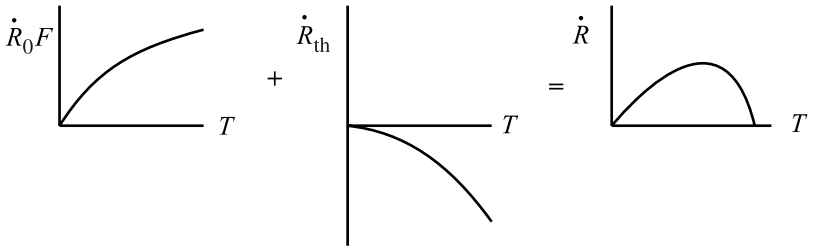

Fig. 8.17. Construction of the total void swelling rate $\dot{R}$ from its components $\dot{R}_0 F$ and $\dot{R}_{th}$

of dose and temperature. All the data were for irradiation over a fixed time period, reflecting the variation of dose rates with position in the core. Closed symbols represent samples in which voids were found and open symbols were samples that exhibited no voids. Note that despite the differing doses and dose rates, void nucleation occurs with a very sharp temperature threshold at about 302–307 °C, illustrating the high sensitivity of void formation to temperature. The gen-

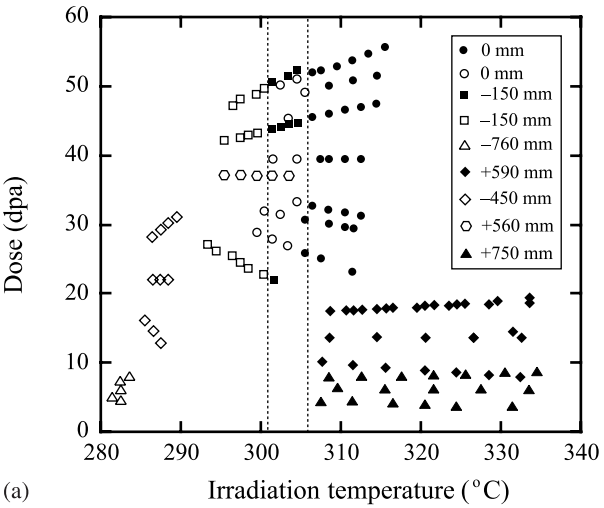

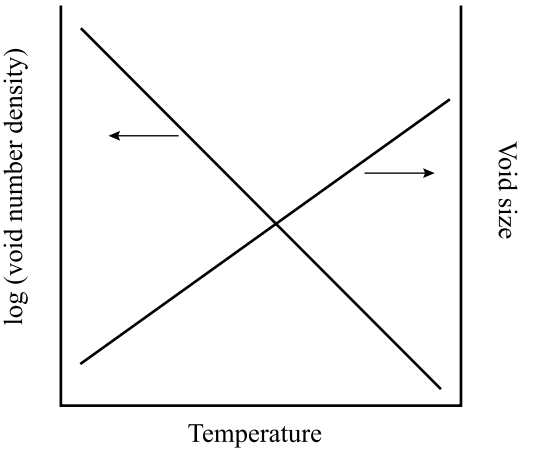

Fig. 8.18. (a) Dose-temperature plot of swelling in a Fe–Cr–Ni alloy irradiated in the BN-350 fast reactor showing the sharp temperature threshold for swelling (after [18]). (b) Schematic of the temperature dependence of void density and void size

eral behavior of the void number density and size with temperature is shown in Fig. 8.18b. With increasing temperature, the void density falls logarithmically and the size increases, which is the typical behavior for a process that is dominated by nucleation at low temperatures where the void growth is slow, and by growth at high temperature where the free energy difference driving void growth is small.

Figure 8.19 shows images of the microstructure in a baffle bolt used to secure baffle former plates against the baffle in a pressurized water reactor. In this case, the head was closest to the core (received the highest dose), and was exposed to the coolant, hence the lowest temperature. Gamma heating caused the temperature to exceed the coolant temperature ($\sim 320\,^{\circ}\mathrm{C}$) along the length of the bolt. While the

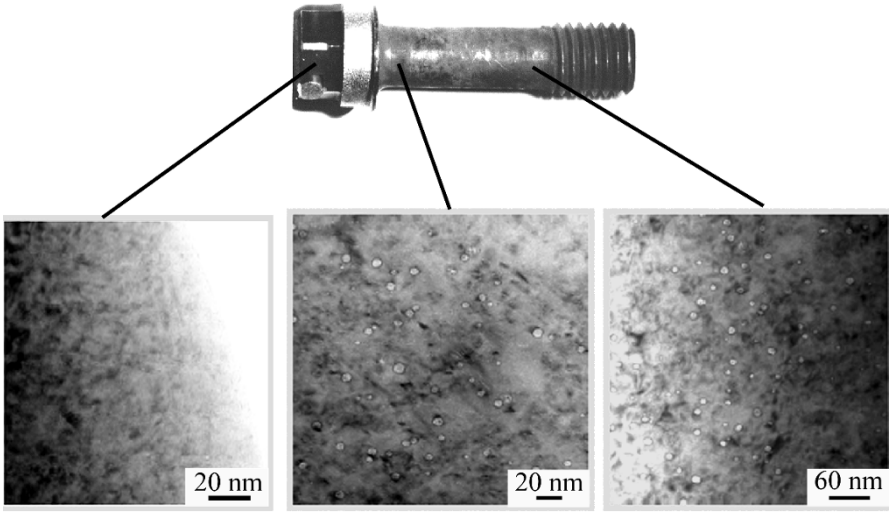

Fig. 8.19. Swelling in a cold-worked 316 SS baffle bolt in a PWR as a function of position along the bolt length. The bolt head was closest to the core and the temperature distribution is caused by a combination of gamma heating and whether the bolt was exposed to the coolant (courtesy S.M. Bruemmer and Garner FA, PNNL)

doses differ somewhat, the dominant influence of temperature is noted by both the lack of voids in the lowest temperature location (head) and the largest void size at the highest temperature (top shank).

8.3.2 Dose Dependence

Understanding how swelling depends on dose is critical in the design and operation of components in radiation environments in which voids have the potential to form and grow. From the discussion in the previous section, the dependence is complicated by the occurrence of the defect production rate, K_0, in the terms $\dot{R}_0$ and $F(\eta)$. So we will take a different approach in determining the void growth rate dependence on dose, following that of Mansur [5]. Recall the expressions for C_v and C_i given in Eq. (8.119):

$$C_v = \frac{D_i k_i^2}{2K_{iv}} \left[(\eta + 1)^{1/2} - 1 \right]$$
$$C_i = \frac{D_v k_v^2}{2K_{iv}} \left[(\eta + 1)^{1/2} - 1 \right] ,$$

and for η as given in Eq. (8.117):

$$\eta = \frac{4K_{\mathrm{iv}}K_0}{D_{\mathrm{i}}D_{\mathrm{v}}k_{\mathrm{v}}^2k_{\mathrm{i}}^2}\,.$$

We can write the term in brackets in Eq. (8.119) as:

$$\left[(\eta+1)^{1/2}-1\right] = \left[\left(1+\frac{4K_{\mathrm{iv}}K_0}{D_{\mathrm{i}}D_{\mathrm{v}}k_{\mathrm{v}}^2k_{\mathrm{i}}^2}\right)^{1/2}-1\right]\,. \tag{8.141}$$

Then, $D_{\mathrm{v}}C_{\mathrm{v}}$ and $D_{\mathrm{i}}C_{\mathrm{i}}$ can be written as:

$$\begin{aligned} D_{\mathrm{v}}C_{\mathrm{v}} &= \frac{D_{\mathrm{v}}D_{\mathrm{i}}k_{\mathrm{i}}^2z_{\mathrm{v}}}{2K_{\mathrm{iv}}}\left[\left(1+\frac{4K_{\mathrm{iv}}K_0}{D_{\mathrm{i}}D_{\mathrm{v}}k_{\mathrm{v}}^2k_{\mathrm{i}}^2}\right)^{1/2}-1\right] \\ D_{\mathrm{i}}C_{\mathrm{i}} &= \frac{D_{\mathrm{v}}D_{\mathrm{i}}k_{\mathrm{v}}^2z_{\mathrm{i}}}{2K_{\mathrm{iv}}}\left[\left(1+\frac{4K_{\mathrm{iv}}K_0}{D_{\mathrm{i}}D_{\mathrm{v}}k_{\mathrm{v}}^2k_{\mathrm{i}}^2}\right)^{1/2}-1\right]\,. \end{aligned} \tag{8.142}$$

Neglecting thermal emission, and substituting into Eq. (8.112) gives:

$$\dot{R} = \frac{\Omega D_{\mathrm{v}}D_{\mathrm{i}}}{2RK_{\mathrm{iv}}}\left[\left(1+\frac{4K_{\mathrm{iv}}K_0}{D_{\mathrm{i}}D_{\mathrm{v}}k_{\mathrm{v}}^2k_{\mathrm{i}}^2}\right)^{1/2}-1\right]\left(k_{\mathrm{v}}^2z_{\mathrm{v}}-k_{\mathrm{i}}^2z_{\mathrm{i}}\right)\,. \tag{8.143}$$

Substituting for k_{v}^2 and k_{i}^2 from Eq. (8.104) and considering only coherent precipitates, network dislocations and loops gives:

$$\begin{aligned} \dot{R} = {} & \frac{\Omega D_{\mathrm{v}}D_{\mathrm{i}}}{2RK_{\mathrm{iv}}}\left[\left(1+\frac{4K_{\mathrm{iv}}K_0}{D_{\mathrm{i}}D_{\mathrm{v}}k_{\mathrm{v}}^2k_{\mathrm{i}}^2}\right)^{1/2}-1\right] \\ & \times\left[4\pi R_{\mathrm{CP}}\rho_{\mathrm{CP}}\left(z_{\mathrm{i}}^{CP}z_{\mathrm{v}}-z_{\mathrm{v}}^{CP}z_{\mathrm{i}}\right)+\rho_{\mathrm{L}}\left(z_{\mathrm{i}}^{\mathrm{L}}z_{\mathrm{v}}-z_{\mathrm{v}}^{\mathrm{L}}z_{\mathrm{i}}\right)+\rho_{\mathrm{N}}\left(z_{\mathrm{i}}^{N}z_{\mathrm{v}}-z_{\mathrm{v}}^{N}z_{\mathrm{i}}\right)\right]\,. \end{aligned} \tag{8.144}$$

Simplifying Eq. (8.144) for the case of voids and total dislocation density only, we have:

$$\dot{R} = \frac{\Omega D_{\mathrm{v}}D_{\mathrm{i}}}{2RK_{\mathrm{iv}}}\left[\left(1+\frac{4K_{\mathrm{iv}}K_0}{D_{\mathrm{i}}D_{\mathrm{v}}k_{\mathrm{v}}^2k_{\mathrm{i}}^2}\right)^{1/2}-1\right]\rho_{\mathrm{d}}\left(z_{\mathrm{i}}^{\mathrm{d}}z_{\mathrm{v}}-z_{\mathrm{v}}^{\mathrm{d}}z_{\mathrm{i}}\right)\,. \tag{8.145}$$

The term $\left(z_{\mathrm{i}}^{\mathrm{d}}z_{\mathrm{v}}-z_{\mathrm{v}}^{\mathrm{d}}z_{\mathrm{i}}\right)$ is the bias of dislocations vs. that for voids and is the determinant of the propensity for a void to grow or shrink. Growth will occur if $z_{\mathrm{i}}^{\mathrm{d}}z_{\mathrm{v}} > z_{\mathrm{v}}^{\mathrm{d}}z_{\mathrm{i}}$, or stated as ratios, $\dfrac{z_{\mathrm{i}}^{\mathrm{d}}}{z_{\mathrm{v}}^{\mathrm{d}}} > \dfrac{z_{\mathrm{v}}}{z_{\mathrm{i}}}$ and shrinkage will occur if the inequality is in the other direction. The presence of other sinks will affect swelling through their inclusion in the terms k_{v}^2 and k_{i}^2. The larger the sink strengths, the lower will be the void growth rate due to the loss of defects to those sinks.

The limiting behaviors of Eq. (8.145) are the cases in which recombination dominates $\frac{4K_{\mathrm{iv}}K_0}{D_{\mathrm{i}}D_{\mathrm{v}}k_{\mathrm{v}}^2k_{\mathrm{i}}^2} \gg 1$ (loss of defects to recombination is much larger than that lost to sinks) and loss to sinks dominates $\frac{4K_{\mathrm{iv}}K_0}{D_{\mathrm{i}}D_{\mathrm{v}}k_{\mathrm{v}}^2k_{\mathrm{i}}^2} \ll 1$ [5]. Assuming that the only sinks besides voids are network dislocations, we have:

$$\dot{R} = \frac{\Omega}{R}\left(\frac{D_{\mathrm{i}}D_{\mathrm{v}}K_0}{z_{\mathrm{i}}^N z_{\mathrm{v}}^N K_{\mathrm{iv}}}\right)^{1/2} \frac{Q_{\mathrm{i}}^{1/2}Q_{\mathrm{v}}^{1/2}\left(z_{\mathrm{i}}^N z_{\mathrm{v}} - z_{\mathrm{v}}^N z_{\mathrm{i}}\right)}{(1+Q_{\mathrm{v}})^{1/2}(1+Q_{\mathrm{i}})^{1/2}} : \text{ recombination dominant} \tag{8.146}$$

$$\dot{R} = \frac{\Omega K_0 Q_{\mathrm{i}} Q_{\mathrm{v}}}{R\rho_{\mathrm{N}}(1+Q_{\mathrm{v}})(1+Q_{\mathrm{i}})}\left(z_{\mathrm{i}}^N z_{\mathrm{v}} - z_{\mathrm{v}}^N z_{\mathrm{i}}\right) : \text{ sink dominant}\,, \tag{8.147}$$

where:

$$Q_{\mathrm{i,v}} = \frac{z_{\mathrm{i,v}}^N \rho_{\mathrm{N}}}{4\pi R \rho_{\mathrm{v}} z_{\mathrm{i,v}}} \tag{8.148}$$

is the ratio of dislocation sink strength to void sink strength. Note that the growth rate is dependent on $K_0^{1/2}$ when recombination is dominant, Eq. (8.146). However, when sinks are dominant, Eq. (8.147) shows that the growth rate is proportional to K_0. Multiplying Eq. (8.147) by $4\pi R^2 \rho_{\mathrm{V}}$ and given that $\Omega = 1/N_0$, the site density, gives the volume swelling rate:

$$\frac{\mathrm{d}(\Delta V/V)}{\mathrm{d}t} = K_0\left(\frac{z_{\mathrm{i}} - z_{\mathrm{v}}}{z_{\mathrm{v}}}\right)\frac{Q}{(1+Q)^2}\,. \tag{8.149}$$

This is the same expression that can be obtained from Eq. (8.122) by neglecting the effect of coherent precipitates. For $Q = 1$ and $z_{\mathrm{i}} - z_{\mathrm{v}} = 0.01$, we have:

$$\frac{\Delta V}{V}\% \cong 1/4 \times (\text{dose in dpa})\,. \tag{8.150}$$

Garner [19] has shown that over a wide dose range, the steady state swelling rate is of the order of $\sim 1\%$/dpa (Fig. 8.20). The linear dependence is consistent with a sink-dominated process, but the magnitude of the coefficient is a factor of four greater than that predicted by Eq. (8.150). The discrepancy is likely due to the effect of clusters that is not accounted for in the rate theory model. A closer look at the behavior of vacancies and interstitials in the cascade shows that the fraction of vacancies and interstitials that form clusters is larger than has been accounted for thus far. Vacancy clusters form near the cascade core and interstitial clusters form near the cascade periphery. Mobile interstitial clusters can reach sinks by migration of the cluster as a whole. Vacancies emitted by vacancy clusters by thermal emission are also free to reach sinks. Since the fraction of interstitials and vacancies in clusters is not the same, nor is their thermal stability, the difference between vacancy and interstitial clusters results in a difference in the effective production rates of vacancies

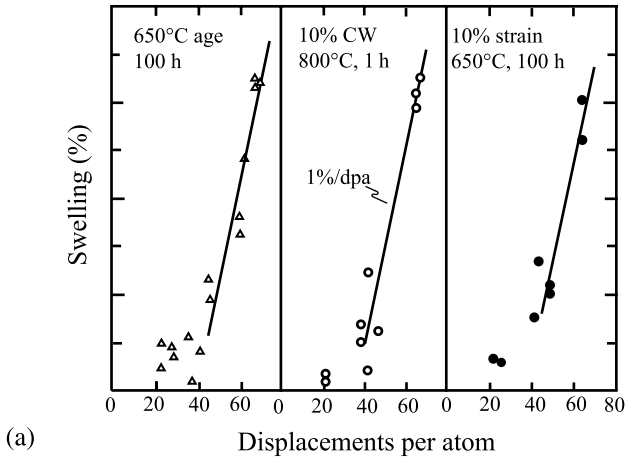

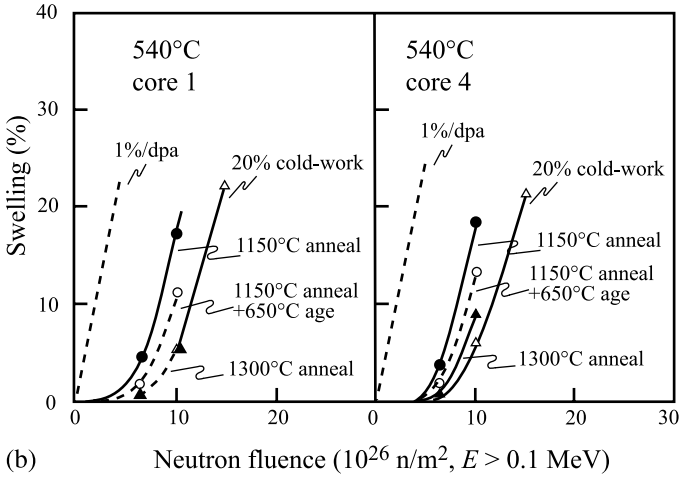

Fig. 8.20. (a) Early development of 1%/dpa swelling rates in aged OKH16N15M3B steel during irradiation in the BOR-60 reactor at 400–550 °C (after [20]). (b) Variations in swelling at 540 °C in EBR-II for two nominally similar heats of 316 stainless steel as a function of starting condition (after [21])

compared to that of interstitials, termed the *production bias*, and can influence void swelling. The net result is that the sink strength of the clusters is much greater than that of the measurable dislocation loops, resulting in a much greater driving force for void swelling than is accounted for by the rate equation formulation. This is one of the reasons that the observed steady state swelling dependence on dose is greater than that predicted by the rate equation formulation.

8.3.3 Role of Dislocations as Biased Sinks

The dislocation structure of an alloy can exert a profound effect on the swelling behavior. Equation (8.122) demonstrates that both a biased sink (e.g., dislocations) and a neutral sink are necessary for void growth. If the bias was removed, $z_i = z_v$, then $\dot{R}_0 = 0$ and swelling will not occur as defects will flow equally to each sink.

The Q-dependence of $\dot{R}_0$ is shown in Fig. 8.21. Note that $\dot{R}_0$ is a maximum at $Q = 1$, or when the flow of vacancies to voids and dislocations is equal. The regime $Q < 1$ is representative of the low dose regime in which both R and ρ_V are small, so vacancy loss to the existing dislocation network dominates. This is why cold-worked alloys swell less. When $Q \sim 1$, then the flow of vacancies to voids and dislocations is approximately equal. This is the regime where bias exerts its greatest influence. If the flow of vacancies and interstitials to sinks is equal, and more interstitials go to dislocations, then more vacancies must flow to voids. At $Q \sim 1$, the flows are equal so the bias is most effective in promoting void growth. When $Q > 1$, defect flow to voids dominates the loss terms and since few defects flow to dislocations, the bias is not very effective in creating an imbalance in point defect fluxes, so the flow of vacancies and interstitials to voids is similar in magnitude and void growth slows or ceases. Although dislocations exhibit a slight preference for interstitials $\left(\frac{\beta_d}{\beta_V} \geq 1\right)$, in a cold-worked material, the dislocations provide so many sinks for vacancies that the effect of a vacancy supersaturation is essentially multiplied, resulting in low void nucleation and growth rates. By the same mechanism, grain boundaries provide *unbiased* sinks for point defects and will keep the vacancy supersaturation too low for growth provided the grain boundary area is large enough (i.e., very small grains). Figure 8.22 shows a plot of swelling rate vs. the sink strength ratio, Q for several austenitic stainless steels and verifies that indeed, the dependence shown in Fig. 8.21 is obeyed in practice.

The effect of cold-work on swelling in reactor exposures is shown in Fig. 8.23. Figure 8.23a shows the effect of cold-work on swelling in 316 stainless steel ir-

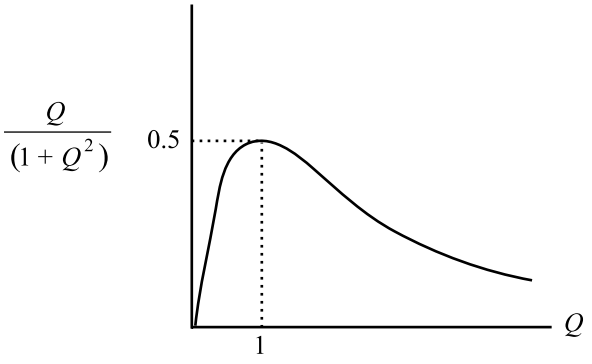

Fig. 8.21. Dependence of swelling on the dislocation/void sink strength ratio, Q in Eq. (8.149)

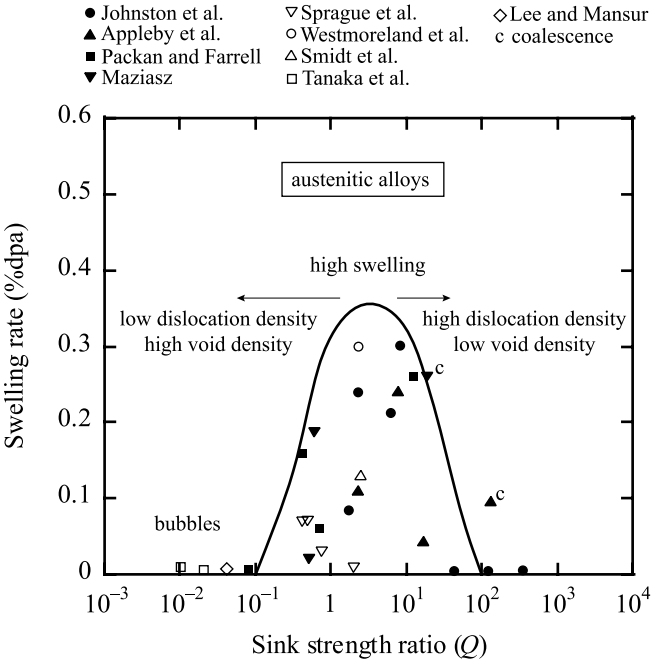

Fig. 8.22. Experimentally observed swelling rates as a function of Q for austenitic stainless steels (after [5])

radiated in EBR-II at 650 °C to levels of 33 and 50 dpa. Note that for both cases, the amount of swelling decreases with increasing cold-work. Figure 8.23b shows that cold-work affects the temperature dependence of swelling by suppressing the magnitude of the swelling peak with increasing levels of cold-work. The data are taken from a stainless steel irradiated to doses of 20–61 dpa in the RAPSODIE reactor. Figure 8.23c shows the effect of cold-work on the dose dependence of swelling in 304 stainless steel, and that increasing cold-work decreases the amount of swelling, but at reduced rates as the amount of cold-work increases. Note also that these data show that the primary effect of cold-work is to extend the transient swelling regime, rather than to alter the steady state swelling rate.

8.3.4 Dose Rate Dependence

The location of the peak swelling temperature depends on the dose rate, sink strength and the predominant mode of defect loss. When the dose rate increases, more point defects are created, but their migration velocities are unchanged. To remove defects at the higher rate at steady state requires point defect concentrations to be higher, resulting in greater recombination and a reduction in the net absorption of vacancies by voids, and hence, a reduction in the void growth rate. As a result,

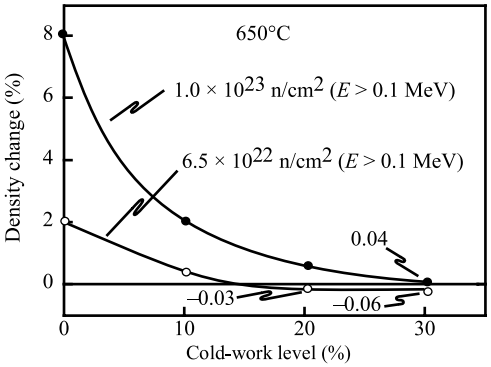

(a)

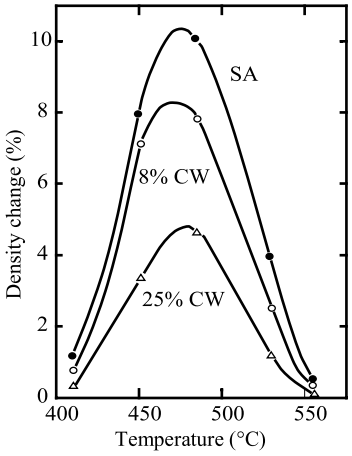

(b)

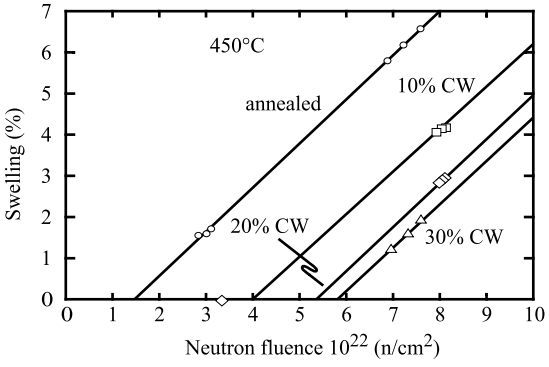

(c)

Fig. 8.23. (a) Effect of cold-work level on the swelling of 316 stainless steel irradiated at 650 °C in EBR-II to 33 and 50 dpa (after [22]). (b) Dependence of swelling on cold-work for various temperatures for 316 stainless steel irradiated in the RAPSODIE reactor to doses of 20–71 dpa (after [23]). (c) Effect of cold-work on swelling in 304 stainless steel at 450 °C in EBR-II (after [24])

the *bell-shaped* swelling curve is displaced to higher temperatures with increasing dose rate. Figure 8.24 is a plot of the temperature dependence of the term $F(\eta)$ in Eq. (8.125), and illustrates the shift of the swelling peak with dose rate, K_0. Alternatively, at a given temperature, the void growth rate decreases for increasing dose rate. At temperatures where thermal emission is non-negligible, the void growth rate is a complicated function of dose rate. Nevertheless, the experimental data substantiate the effect of dose rate on swelling. Figure 8.25 shows swelling in annealed and

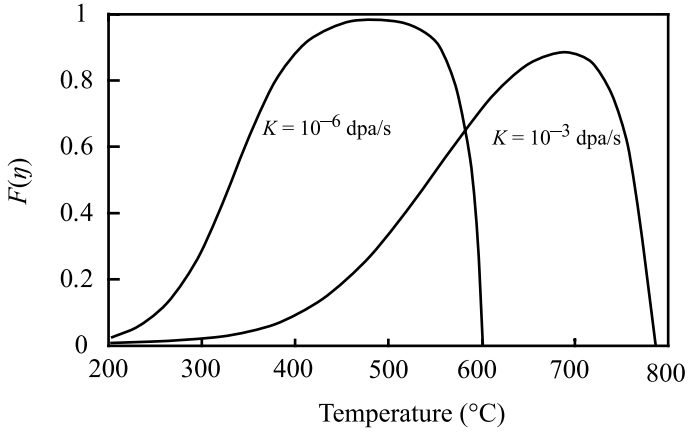

Fig. 8.24. Variation of the function $F(\eta)$ in Eq. (8.124) with temperature, illustrating the shift of the peak with dose rate, K_0. Parameters used to construct the curves are as follows: $\rho_d = 10^9\,\mathrm{cm}^{-2}$, $E_f^v = 1.6\,\mathrm{eV}$, $z_i - z_v = 0.01$, $z_v = 1$, $4\pi R\rho_V = 10^{-11}\,\mathrm{cm}^{-2}$, $D_v = \exp(-1.4\,\mathrm{eV}/kT)\,\mathrm{cm}^2\,\mathrm{s}^{-1}$ (after [15])

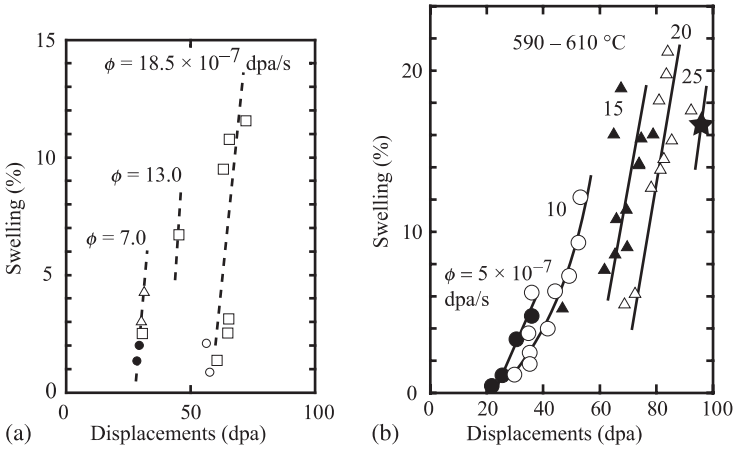

Fig. 8.25. (a) Effect of displacement rate on swelling of annealed 316 stainless steel in the RAPSODIE reactor fuel pin cladding at 562 °C. (b) Swelling in cold-worked 316 stainless steel in the PHENIX reactor fuel pin cladding at 590–610 °C (after [25] and [26])

cold-worked 316 stainless steel at temperatures between 562 and 610 °C over a range of dose rates. Note that increasing dose rate has the effect of reducing the swelling rate at a given dose, but that at steady state, all data have a similar slope, indicating that the primary effect of dose rate is on the duration of the swelling transition period.

If we move up the temperature scale, we can restore the same relative ratio of recombination rate to absorption rate at sinks. In fact, by requiring that this ratio be invariant, we can obtain a relationship between temperature and dose rate, termed the *temperature shift*.

8.3.5 Irradiation Variable Shifts

The concept of variable shifts was developed to provide a better understanding of the relationship between variables in swelling [16]. The idea is that when one irradiation variable is changed, a shift in other variables can be determined that will preserve a physical quantity describing the behavior of defects during irradiation. There are two such quantities that pertain to the limiting case where recombination dominates defect loss. The number of defects per unit volume that have recombined up to a time τ is:

$$N_{\mathrm{R}} = K_{\mathrm{iv}} \int_0^{\tau} C_{\mathrm{i}} C_{\mathrm{v}} \, \mathrm{d}t \; . \tag{8.151}$$

When the solid is at steady state and defect concentrations are controlled by recombination, Eq. (8.116) give:

$$\begin{aligned} C_{\mathrm{v}} &= \left(\frac{K_0}{K_{\mathrm{iv}}} \frac{z_{\mathrm{i}} D_{\mathrm{i}}}{z_{\mathrm{v}} D_{\mathrm{v}}} \right)^{1/2} \\ C_{\mathrm{i}} &= \left(\frac{K_0}{K_{\mathrm{iv}}} \frac{z_{\mathrm{v}} D_{\mathrm{v}}}{z_{\mathrm{i}} D_{\mathrm{i}}} \right)^{1/2} \; , \end{aligned} \tag{8.152}$$

and substituting into Eq. (8.151) yields:

$$N_{\mathrm{R}} = K_0 \tau \; . \tag{8.153}$$

The number of defects lost to sinks per unit volume up to a time τ is:

$$N_{\mathrm{Sj}} = \int_0^{\tau} K_j C_j \, \mathrm{d}t \; , \tag{8.154}$$

where the subscript j denotes the defect type. Substituting Eq. (8.152) into Eq. (8.154) gives for vacancies:

$$N_{\mathrm{Sv}} = \frac{K_{\mathrm{V}}}{(K_0 K_{\mathrm{iv}})^{1/2}} \left(\frac{z_{\mathrm{i}} D_{\mathrm{i}}}{z_{\mathrm{v}} D_{\mathrm{v}}} \right)^{1/2} \Phi \; , \tag{8.155}$$

where Φ is the dose, and the expression for interstitials is identical.

These definitions can be used to determine relationships between any two of the three variables: temperature, dose and dose rate, taking the third to be constant. For example, in the steady state recombination-dominated regime, we may require N_s to be equal for dose 1 and dose rate 1 to that for dose 2 and dose rate 2 at a *fixed temperature*:

$$\frac{K_V}{(K_{0_1}K_{iv})^{1/2}}\left(\frac{z_i D_i}{z_v D_v}\right)^{1/2}\Phi_1 = \frac{K_V}{(K_{0_2}K_{iv})^{1/2}}\left(\frac{z_i D_i}{z_v D_v}\right)^{1/2}\Phi_2 ,$$

and canceling terms in the equality gives:

$$\frac{\Phi_2}{\Phi_1} = \left(\frac{K_{0_1}}{K_{0_2}}\right)^{1/2} . \tag{8.156}$$

For a given change in dose rate, the shift in temperature required at constant dose to keep N_s invariant is determined by equating the same terms, but with *fixed dose*, resulting in:

$$\left(\frac{D_v}{K_0}\right)_1^{1/2} = \left(\frac{D_v}{K_0}\right)_2^{1/2} , \tag{8.157}$$

or substituting in for D_v from Eq. (4.54), $D_v = D_0 \exp(-E_m^v/kT)$:

$$T_2 - T_1 = \frac{\dfrac{kT_1^2}{E_m^v}\ln\left(\dfrac{K_{0_2}}{K_{0_1}}\right)}{1 - \dfrac{kT_1}{E_m^v}\ln\left(\dfrac{K_{0_2}}{K_{0_1}}\right)} . \tag{8.158}$$

For a change in dose, the shift in temperature required to maintain N_s invariant at *fixed dose rate* is:

$$(D_v^{1/2}\Phi)_1 = (D_v^{1/2}\Phi)_2 , \tag{8.159}$$

and substituting in for D_v:

$$\frac{\Phi_2}{\Phi_1} = \exp\left[\frac{E_m^v}{2k}\left(\frac{1}{T_2} - \frac{1}{T_1}\right)\right] , \tag{8.160}$$

and re-arranging gives:

$$T_2 - T_1 = \frac{\dfrac{-2kT_1^2}{E_m^v}\ln\dfrac{\Phi_2}{\Phi_1}}{1 + \dfrac{2kT_1}{E_m^v}\ln\dfrac{\Phi_2}{\Phi_1}} . \tag{8.161}$$

There is another important temperature shift that, instead of requiring that N_s be invariant, requires the net flux of vacancies over interstitials to a particular type

of sink (voids in this case) to be invariant, where the net flux is relevant to void swelling. The temperature shift derived in this way for the recombination-dominated regime to keep swelling rate (N_R) invariant is [16]:

$$T_2 - T_1 = \frac{\dfrac{kT_1^2}{E_m^v + 2E_f^v} \ln \dfrac{K_{0_2}}{K_{0_1}}}{1 - \dfrac{kT_1}{E_m^v + 2E_f^v} \ln \dfrac{K_{0_2}}{K_{0_1}}} \,. \tag{8.162}$$

where E_f^v is the vacancy formation energy.

The various variable shifts described in this section are shown in the following figures. Figure 8.26 shows the relationship between dose vs. dose rate dependence at a reference temperature of 200 °C for the case of N_s invariant, Eq. (8.156). Figure 8.27 shows the temperature shift as a function of dose rate at constant dose for three values of vacancy migration energy for N_s invariant, Eq. (8.158), and Fig. 8.28 shows the same relationship for the constant dose rate case, Eq. (8.161). Figure 8.29 shows the temperature shift as a function of dose for constant dose rate to keep the swelling rate, N_R invariant, Eq. (8.162). Figure 8.30 shows that the temperature shift concept works well in describing the shift in the peak in the swelling vs. temperature curve in nickel over more than five orders of magnitude in the dose rate as given by Eq. (8.162).

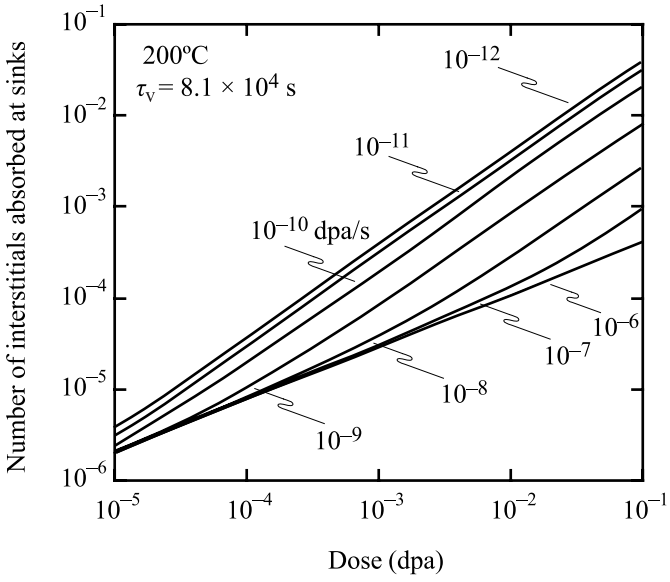

Fig. 8.26. Number of interstitials absorbed at sinks as a function of dose at 200 °C for different dose rates (after [27])

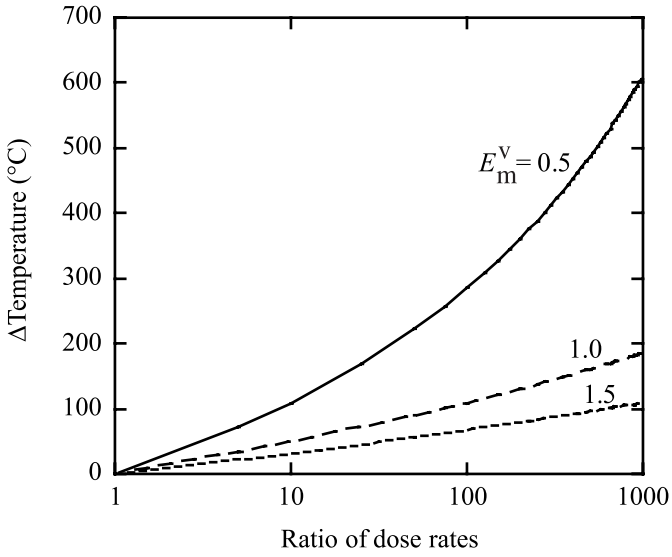

Fig. 8.27. Temperature shift from the reference 200 °C required at constant dose in order to maintain the same point defect absorption at sinks as a function of dose rate, normalized to initial dose rate. Results are shown for three different vacancy migration energies (after [8.27])

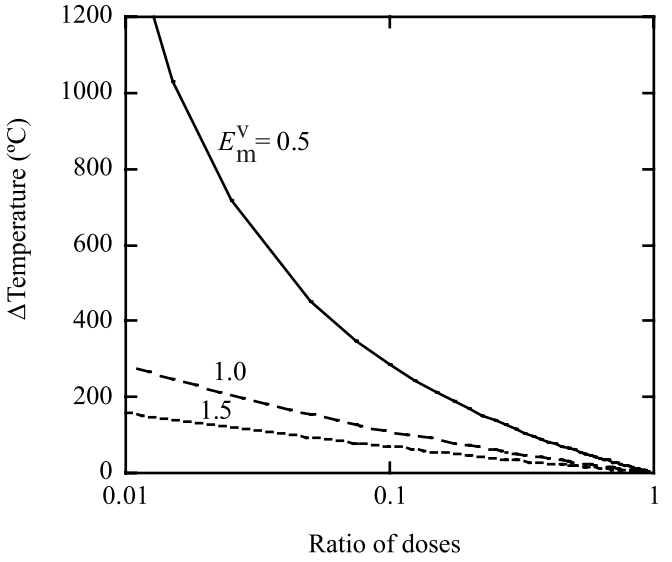

Fig. 8.28. Temperature shift from the reference 200 °C required at constant dose rate in order to maintain the same point defect absorption at sinks as a function of dose, normalized to initial dose. Results are shown for three different vacancy migration energies (after [8.27])

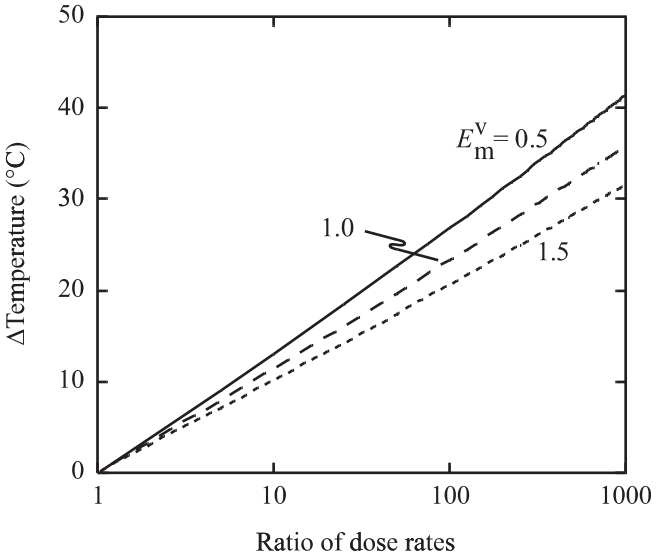

Fig. 8.29. Temperature shift from the reference 200 °C required at constant dose in order to maintain swelling invariance as a function of dose rate, normalized to initial dose rate. Results are shown for three different vacancy migration energies and a formation energy of 1.5 eV

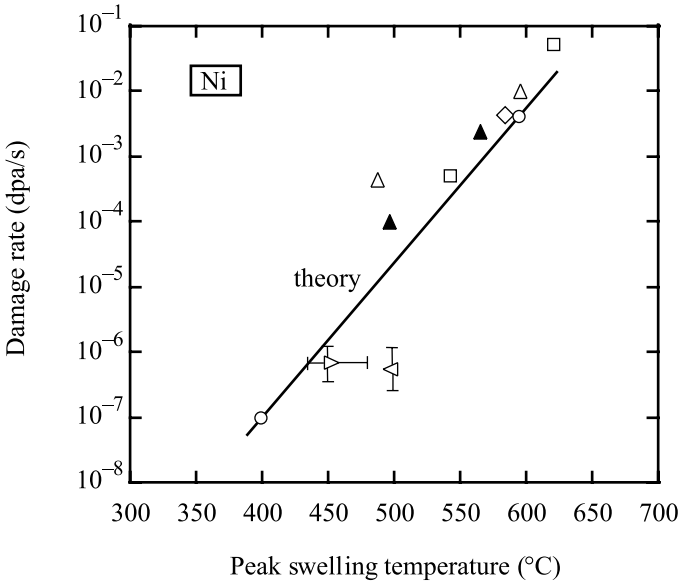

Fig. 8.30. Temperature shift of peak swelling as a function of dose rate. *Points* are experimental data and the *line* is from theory (after [5])

8.3.6 Stress Dependence

Equation (8.125) shows that the void growth rate consists of two components. $\dot{R}_{\text{th}}$ is the thermal emission terms and hence is the only part affected by the state of stress or internal gas pressure. Consequently, the internal gas pressure and stress begin to affect the growth rate only when $\dot{R}_{\text{th}}$ becomes significant, i.e., for temperatures greater than the peak swelling temperature. When the solid is under a hydrostatic stress and when voids contain gas that exerts a pressure on the void surface, the equilibrium vacancy concentration at voids and dislocations will be different from that in the stress-free, gas-free state. Brailsford and Bullough showed that the pressure, but not the external stress, will affect the concentration of vacancies in equilibrium with the void. Hence, the force balance for the void surface of a bubble in mechanical equilibrium, Eq. (8.82), becomes:

$$\sigma = p - \frac{2\gamma}{R}\,, \tag{8.163}$$

where σ is the hydrostatic stress and p is the gas pressure in the void. (In the case of a non-equilibrium bubble, the appropriate stress is the radial component of the stress tensor, σ_{r}.) The vacancy concentration at the surface of the void, given by Eq. (8.85) in the gas-free case, becomes:

$$C_{\text{v}}^{\text{V}} = C_{\text{v}}^{0} \exp\left[-\frac{\Omega}{kT}\left(p - \frac{2\gamma}{R}\right)\right]\,. \tag{8.164}$$

Similarly, the equilibrium vacancy concentration adjacent to the network dislocations becomes:

$$C_{\text{v}}^{N} = C_{\text{v}}^{0} \exp\left[-\frac{\sigma\Omega}{kT}\right]\,. \tag{8.165}$$

Repeating the solution to the void growth equation using the equilibrium vacancy concentration at the void surface given by Eq. (8.164) and the equilibrium vacancy concentration at the network dislocations given by Eq. (8.165) revises the thermal emission term, R_{th} in Eq. (8.135) (with $\rho_{\text{CP}} = \rho_{\text{L}} = 0$) as follows:

$$\dot{R}_{\text{th}} = \frac{D_{\text{v}} C_{\text{v}}^{0} \Omega^{2} z_{\text{v}} \rho_{\text{d}} \left(\sigma + p - \dfrac{2\gamma}{R}\right)}{RkT\left(z_{\text{v}}\rho_{d} + 4\pi R \rho_{\text{V}}\right)}\,. \tag{8.166}$$

Note that shrinkage due to thermal emission becomes instead, stress-enhanced growth when the sum of the external stress and gas pressure exceed the stress due to surface tension:

$$\sigma + p > \frac{2\gamma}{R}\,. \tag{8.167}$$

Note that for a stressed solid containing no gas, stress-enhanced growth will occur when $\sigma > \dfrac{2\gamma}{R}$. For a void containing x gas atoms, Eq. (8.167) becomes:

$$\sigma = \frac{2\gamma}{R} - \left(\frac{3xkT}{4\pi R^{3}}\right)\,. \tag{8.168}$$

The void radius at which $\frac{d\sigma}{dR} = 0$ is called the critical void radius and is given by:

$$R_{cr} = \left(\frac{9xkT}{8\pi\gamma}\right)^{1/2}, \tag{8.169}$$

and substituting into Eq. (8.165) gives the stress at the critical void size, which is the critical stress for unlimited void growth:

$$\sigma_{cr} = \frac{4\gamma}{3}\left(\frac{8\pi\gamma}{9xkT}\right)^{1/2}. \tag{8.170}$$

The effect of stress on void growth in steel is given in Fig. 8.31. Note that there is little effect of stress out to high dose when the stress is low. But when stress is increased, the swelling increases rapidly at relatively lower doses. Figure 8.32 also accounts for the presence of helium in the growth of voids under stress.

However, this formulation predicts that the void growth rate is proportional to stress, which is counter to the 1%/dpa observations. Also, as shown in Fig. 8.32, the effect of stress is only significant at very high temperatures. Experimental data have since shown that the prime role of stress is on shortening the transient swelling regime, rather than increasing the swelling rate in the steady state regime. Figure 8.33 shows the effect of stress on swelling in modified 316 stainless steel alloys irradiated in the PHENIX reactor. Note that with increasing stress, the swelling rate (slope) approaches a constant value at lower doses. Stress can also affect the stability of void nuclei, which would explain the observation of more rapid nucleation.

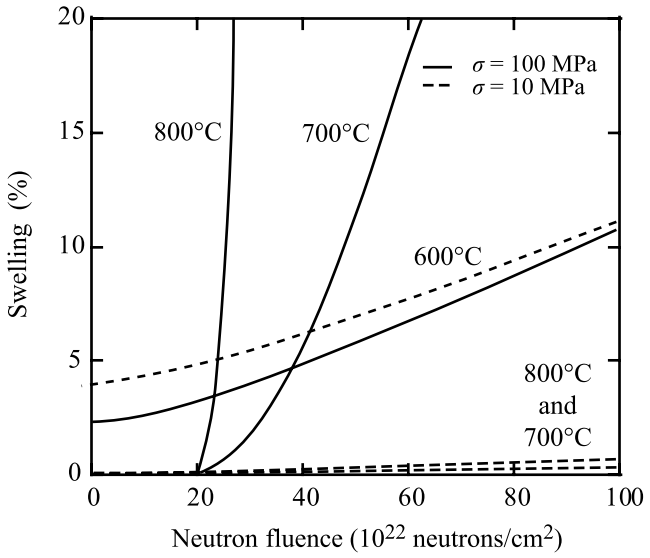

Fig. 8.31. Stress-enhanced swelling for various stress levels and temperatures as a function of fluence (after [28])

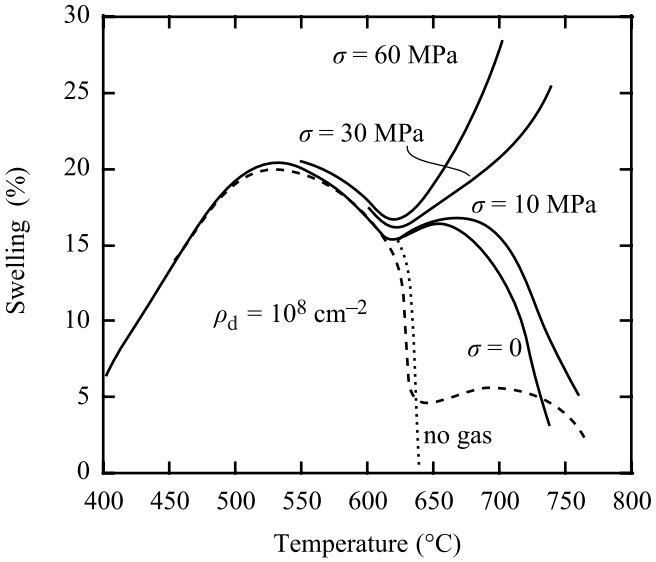

Fig. 8.32. Temperature dependence of stress-enhanced void growth in steel. The solid curves apply to a dislocation density of $10^9\,\mathrm{cm}^{-2}$. And a helium production rate of $10^{-6}\,\mathrm{appm/s}$ (after [29])

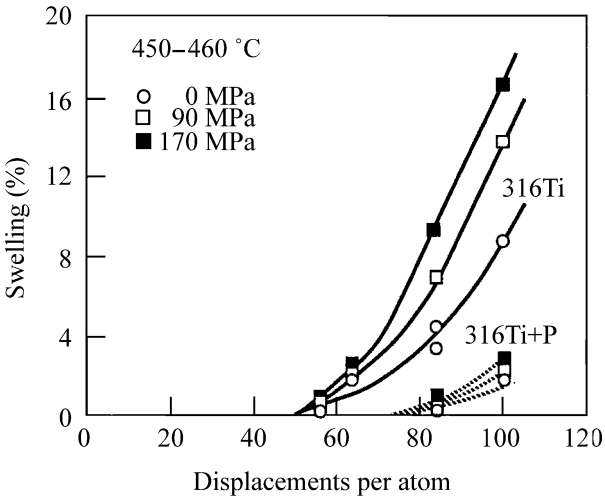

Fig. 8.33. Effect of stress on swelling of two modified 316 stainless steels irradiated in the form of pressurized tubes in the PHENIX reactor (after [30])

In the development of the nucleation rate of voids, the nucleation current and number density of voids of size n was described by Eqs. (8.18) and (8.19), respectively, for the case of vacancy condensation excluding interstitials:

$$J_n = Z\beta N_0 \exp\left(\frac{-\Delta G_n^0}{kT}\right), \quad \text{and} \quad \rho^0(n) = N_0 \exp\left(\frac{-\Delta G_n^0}{kT}\right).$$

with the free energy of formation of void of size n given by Eq. (8.17):

$$\Delta G_n^0 = -nkT \ln S_v + (36\pi\Omega^2)^{1/3}\gamma n^{2/3} .$$

Accounting for the application of an external hydrostatic stress, σ_h, gives:

$$\Delta G_n^0(\sigma_h) = -nkT \ln S_v + (36\pi\Omega^2)^{1/3}\gamma n^{2/3} - n\sigma_h\Omega , \tag{8.171}$$

and

$$\Delta G_n^0(\sigma_h) = \Delta G_n^0(0) + n\sigma_h\Omega . \tag{8.172}$$

Note that the effect of gas pressure, p, in the void can also be accounted for by addition of a term, $np\Omega$.

When interstitials are present, the free energy is given by Eq. (8.33):

$$\Delta G_n' = kT \sum_{j=0}^{n-1} \ln \left[\frac{\beta_i (j+1)}{\beta_v (j)} + \exp\left(\frac{\delta G_j^0}{kT} \right) \right] ,$$

where δG_j^0/kT is the increment in free energy of a void in going from j vacancies to $j+1$ vacancies if no interstitials are present. By assuming that stress affects only the free energy barrier (and not the critical nucleus size), and that the stress contribution of the energy per atom is not dependent on the number of atoms in the cluster, then we can approximate the free energy in Eq. (8.33) in a manner similar to that done in Eq. (8.172) [31]:

$$\Delta G_n'(\sigma_h) = \Delta G_n'(0) + n\sigma_h\Omega . \tag{8.173}$$

Then, from Eq. (8.35), the ratio of stressed to unstressed steady state nucleation rates in a homogeneous, co-precipitation environment is:

$$\frac{J_n(\sigma_h)}{J_n(0)} = \frac{\exp[-(\Delta G_n' - n\sigma_h\Omega)/kT]}{\exp[-\Delta G_n'/kT]} . \tag{8.174}$$

Using Eqs. (8.22) and (8.23) to write the ratio of nucleation currents in terms of the ratio of void number densities in the stressed and unstressed state gives:

$$\frac{J_n(\sigma_h)}{J_n(0)} = \frac{Z'(\sigma_h)\beta_n(\sigma_h)\rho_n(\sigma_h)}{Z'(0)\beta_n(0)\rho_n(0)} = \frac{Z'(\sigma_h)\beta_n(\sigma_h)\exp[-(\Delta G_n'(\sigma_h))]}{Z'(0)\beta_n(0)\exp[-\Delta G_n'(0)]} , \tag{8.175}$$

and provided that neither the arrival rate ratio, $\beta_n(\sigma_h)/\beta_n(0)$, nor Z' is sensitive to the stress level [32], then Eq. (8.175) becomes:

$$\frac{\rho_n(\sigma_h)}{\rho_n(0)} \approx \exp(n\sigma_n\Omega/kT) . \tag{8.176}$$

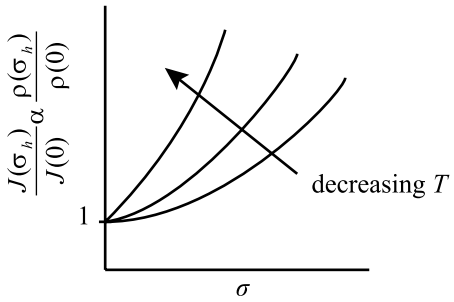

Fig. 8.34. Variation of the void nucleation rate and the void number density as a function of stress and temperature, as described by Eq. (8.176)

Example 8.1. Effect of stress on void density
Assuming an external stress of 100 MPa and a void cluster size of ~ 15 at a temperature of 450℃, Eq. (8.176) gives an increase in the void number density by a factor of ~ 6. However, for a stress of 200 MPa, the increase is 34 and for 300 MPa, the factor becomes ~ 200. Since both stress and temperature appear in the exponent, the factor rises rapidly with an increase in stress and with a decrease in temperature (Fig. 8.34). Referring back to Fig. 8.33, the decreasing time to reach the steady state swelling rate as stress is increased, is explainable by stress-enhanced nucleation, which will be more important at lower temperatures, contrary to the effect of stress on the steady state swelling rate.

8.3.7 Effect of RIS

Recall from Chap. 6, Sect. 6.4, that RIS (radiation-induced segregation) of the major elements occurs at sinks, which can include voids. The result is a *coated void* in which the void develops a shell of composition that is different from that in the matrix. As we have seen, for austenitic stainless steels, the void coating is enriched in nickel and depleted in chromium relative to the matrix. A primary effect of the composition change is a change in diffusion coefficient leading to a change in the void capture efficiency. The capture efficiency for the vacancy in the shell is [16, 33]:

$$z_{\mathrm{v}}^{\mathrm{V}}(r_{\mathrm{V}}) = \frac{1+\delta/r_{\mathrm{V}}}{1+D_{\mathrm{v}}\delta/D_{\mathrm{v}}^{\mathrm{S}}r_{\mathrm{V}}}\,, \tag{8.177}$$

where δ is the thickness of the shell and $D_{\mathrm{v}}^{\mathrm{S}}$ is the vacancy diffusion coefficient in the shell. Recall that an expression for the composition dependence of D_{v} in the shell, $D_{\mathrm{v}}^{\mathrm{S}}$ was determined in Sect. 6.4 of Chap. 6. Using the expression for the capture efficiency in the void growth equations results in a reduction in void growth if $D_{\mathrm{v}}^{\mathrm{S}} < D_{\mathrm{v}}$ and $D_{\mathrm{i}}^{\mathrm{S}} \sim D_{\mathrm{i}}$.

A more important effect of the coating is the elastic interaction between a point defect and a void surrounded with a coating that has different elastic constants than

the matrix. The result is a change in capture efficiency of the void for defects. The capture efficiency due to a difference in elastic constants is given as:

$$z_{\mathrm{i,v}}^{\mathrm{V}}(r_{\mathrm{V}}) = \left[\frac{r_{\mathrm{V}}}{r_{\mathrm{c}}} + \frac{r_{\mathrm{V}}}{(r_{\mathrm{c}}+\delta)^2}\frac{D_{\mathrm{i,v}}}{w_{\mathrm{i,v}}}\right]^{-1}, \tag{8.178}$$

where r_{c} is the void plus coating radius and the transfer velocity, $w_{\mathrm{i,v}}$ is:

$$w_{\mathrm{i,v}} = \frac{D_{\mathrm{i,v}}\exp(-E_{\mathrm{i,v}}^{*}/kT)}{a}, \tag{8.179}$$

where a is the lattice parameter and E^{*} is the repulsive interaction energy at its largest positive value. The sign of E^{*} is positive (repulsion) if the matrix of the shell is stiffer than that of the matrix. Since E^{*} is proportional to the square of the point defect relaxation volume, the sink efficiency is much smaller for the interstitial than for the vacancy due to the larger repulsion for the interstitial. So the stiffer shell results in a repulsion that is greater for the interstitial than for the vacancy, making void nucleation and growth more rapid in the case of a coated void (Fig. 8.35).

A change in the shear modulus or lattice parameter in the shell can also alter the preference of the void for vacancies and interstitials [34] by creating a barrier to defect diffusion through the shell due to a change in the strain energy. When segregation leads to a shell with a shear modulus or lattice parameter only slightly higher than in the surrounding matrix, the void becomes a highly preferential sink for vacancies and swelling is increased. Conversely, a reduction in the shear modulus and

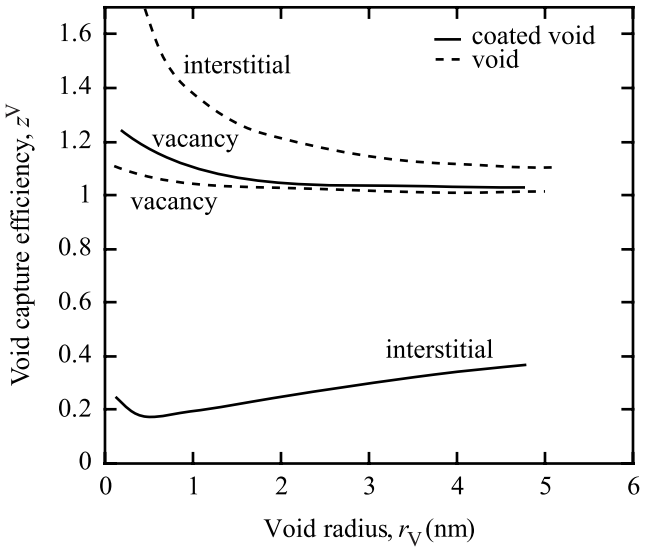

Fig. 8.35. Capture efficiencies for point defects diffusion to a void and a coated void as a function of void radius, r_{V}. The void prefers interstitials, especially at small void sizes. The preference is reversed for the coated void (after [16])

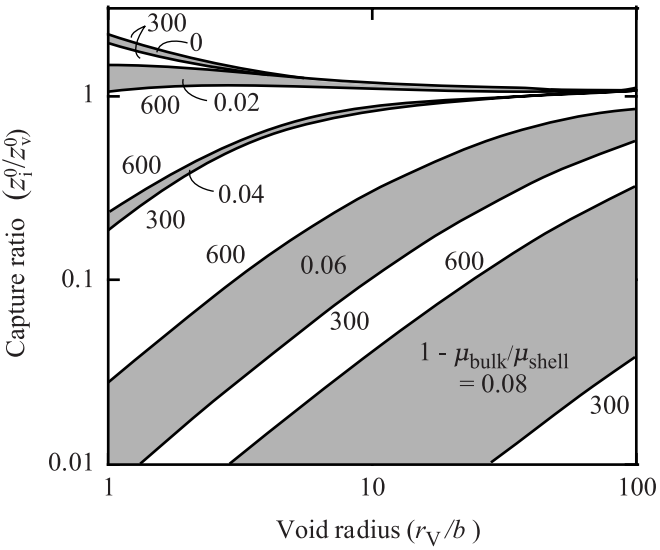

Fig. 8.36. Capture ratio z_i^0/z_v^0 for coated voids with a shell thickness of two atomic layers and zero surface stress (after [34])

lattice parameter should result in reduced void swelling. Figure 8.36 shows the effect of the shear modulus $(1-\mu_{\text{bulk}}/\mu_{\text{shell}})$ on the interstitial/vacancy capture ratio. For small voids, a few percent change in the shear modulus can result in orders of magnitude change in the capture ratio. Allen et al. [35] compared the swelling and RIS behavior of a range of alloys with different nickel content. Calculation of the lattice parameter for the void shell composition shows that the swelling behavior can be explained by a decrease in lattice parameter at the void surface (Fig. 8.37). In fact, segregation leads to a smaller lattice parameter with a lower shear modulus, and the *softer* shell reduces void swelling.

8.3.8 Effect of Production Bias

Our formulation of swelling was developed under the assumption that only single vacancies and interstitials contribute to the growth or shrinkage of the void. If we wish to include the effect of interstitial clustering and mobility in the damage cascade in this picture, then the most straightforward way to do this is to return to clustering theory and describe the evolution of the void embryo with consideration of interstitial clusters. Numerical solution to the Fokker–Planck equation will yield the void size distribution as a function of time or dose. (An example of the results of such an analysis was presented in Chap. 7 for interstitial loops.) However, numerical solutions are not of much value in understanding the process and the importance of various parameters in the evolution of the void population. Another approach is to consider the effect of the asymmetric production of vacancies and interstitials (production bias) due to differences in the fractions that agglomerate into clusters and

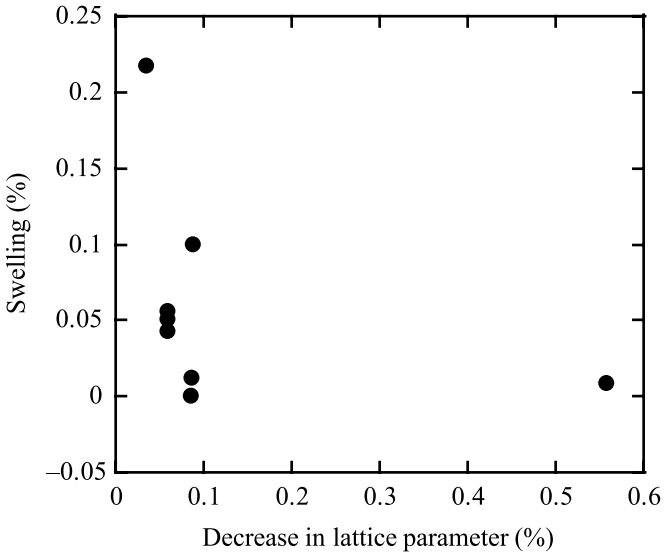

Fig. 8.37. Decrease in swelling as a function of changing lattice parameter. Swelling decreases with decreasing lattice parameter, which is caused by RIS at the void surface (after [35])

differences in the thermal stability and mobility of vacancy and interstitial clusters. So we will consider the case when the interaction of the glissile loops with vacancy and SIA loops is negligibly small, in which case, we can develop an analytical expression for swelling which still captures the effect of clustering [36, 37].

Under cascade conditions where clustering is expected to occur, we modify the vacancy and interstitial steady state point defect balance equations by adding in glissile SIA clusters with the following result:

$$(1-\varepsilon_{\rm i}^{\rm g})K_0^{\rm eff} = D_{\rm i}C_{\rm i}(z_{\rm i}k_{\rm v}^2 + z_{\rm i}^{\rm d}\rho_{\rm d}) + K_{\rm iv}D_{\rm i}C_{\rm i}C_{\rm v} + z_{\rm v}^{\rm ic}D_{\rm v}C_{\rm v}k_{ni}^2 + z_{\rm i}^{\rm vc}D_{\rm i}C_{\rm i}k_{n{\rm v}}^2 \tag{8.180}$$

$$K_0^{\rm eff} = D_{\rm v}C_{\rm v}(z_{\rm v}k_{\rm v}^2 + z_{\rm v}^{\rm d}\rho_{\rm d}) + K_{\rm iv}D_{\rm i}C_{\rm i}C_{\rm v} + z_{\rm v}^{\rm ic}D_{\rm v}C_{\rm v}k_{ni}^2 + z_{\rm i}^{\rm vc}D_{\rm i}C_{\rm i}k_{n{\rm v}}^2 \tag{8.181}$$

$$\varepsilon_{\rm i}^{\rm g}K_0^{\rm eff}/x_{\rm g} = D_{\rm g}C_{\rm g}k_{\rm g}^2\,, \tag{8.182}$$

where $K_0^{\rm eff} = (1-\varepsilon_T)K_0$ is the effective Frenkel pair generation rate obtained from the NRT rate by accounting for the fraction of Frenkel pairs, $\varepsilon_{\rm T}$, recombining during cascade cooling, and $z_{\rm v}^{\rm ic}k_{ni}^2$ and $z_i^{\rm vc}k_{n{\rm v}}^2$ are the sink strengths of sessile SIA clusters (ic) and vacancy clusters (vc) for the absorption of vacancies (v) and SIA clusters (i), respectivly. The quantity, g refers to glissile clusters, $\varepsilon_{\rm i}^{\rm g}$ is the fraction of SIAs in glissile clusters and $x_{\rm g}$ is the mean cluster size. The term $k_{\rm g}^2$ is the total sink strength for the 1D diffusing SIA clusters:

$$k_{\rm g} = \frac{\pi\rho d_{\rm abs}}{4} + \left(\frac{2}{l(2R_{\rm g}-l)}\right)^{1/2} + \pi R^2\rho_{\rm V}\ , \tag{8.183}$$

where $d_{\rm abs}$ is the effective diameter of dislocations for absorbing glissile SIA cluster, $R_{\rm g}$ and l are the grain radius and distance from the cluster to the grain boundary, respectively.

Under cascade damage conditions that allow for intracascade clustering of SIAs and also cluster removal by 1D diffusion of glissile SIA cluster, the void swelling rate is determined by the fluxes of point defects and glissile SIA clusters to voids. Equation (8.110) then becomes:

$$\frac{{\rm d}(\Delta V/V)}{{\rm d}t} = (D_{\rm v}C_{\rm v}z_{\rm v} - D_{\rm i}C_{\rm i}z_{\rm i})k_{\rm v}^2 - D_{\rm g}C_{\rm g}x_{\rm g}k_{\rm g}\pi R^2\rho_{\rm V}\ . \tag{8.184}$$

The second term in Eq. (8.184) comes from Eq. (8.182). Under cascade damage conditions, the difference in the point defect fluxes to dislocations due to dislocation bias as well as the recombination and effect of cluster terms in Eqs. (8.180) and (8.181) cause only small perturbations in the swelling rate at steady state. Neglecting recombination and defect cluster terms in Eqs. (8.180) and (8.181), then Eq. (8.184) becomes:

$$\frac{{\rm d}(\Delta V/V)}{{\rm d}t} = K_0^{\rm eff}\left[\varepsilon_{\rm i}^{\rm g}\left(\frac{z_{\rm v}k_{\rm v}^2}{z_{\rm v}k_{\rm v}^2 + z_{\rm v}^{\rm d}\rho_{\rm d}} - \frac{\pi R^2\rho_{\rm V}}{k_{\rm g}}\right) + (1-\varepsilon_{\rm i}^{\rm g})p_l\frac{z_{\rm v}k_{\rm v}^2 z_{\rm v}^{\rm d}\rho_{\rm d}}{(z_{\rm i}k_{\rm v}^2 + z_{\rm i}^{\rm d}\rho_{\rm d})(z_{\rm v}k_{\rm v}^2 + z_{\rm v}^{\rm d}\rho_{\rm d})}\right]\ , \tag{8.185}$$

where $p_l = (z_{\rm i}^{\rm d}/z_{\rm v}^{\rm d} - z_{\rm i}/z_{\rm v}) \approx (z_{\rm i}^{\rm d}/z_{\rm v}^{\rm d} - 1)$, and $z_v + z_i = 1$.

The swelling rate is proportional to the effective generation rate and the damage efficiency. The first term in square brackets in Eq. (8.185) is the contribution of the production bias to swelling and is proportional to the glissile cluster fraction explicitly. The second term is due to conventional dislocation bias controlled by single point defects, as is evident by its $(1-\varepsilon_{\rm i}^{\rm g})$ proportionality. For the limiting case of single Frenkel pair production, where no clusters are formed, $\varepsilon_{\rm i}^{\rm g} = 0$, the first term vanishes and the swelling rate is driven by single point defect absorption controlled by dislocation bias. The resulting expression is the same as that given in Eq. (8.122) (neglecting coherent precipitates). Conversely, when $\varepsilon_{\rm i}^{\rm g}$ is close to 1.0, the conventional dislocation bias contribution is small compared to that due to production bias.

When both single SIAs and SIA clusters exhibit 3D diffusion, the swelling rate follows an expression analogous to that determined for the single defect, dislocation bias case, Eq. (8.122); however, an SIA cluster term is now included that is analogous to that for single SIAs and can be written as:

$$\frac{{\rm d}(\Delta V/V)}{{\rm d}t} = K_0^{\rm eff}\frac{z_{\rm v}k_{\rm v}^2 z_{\rm v}^{\rm d}\rho_{\rm d}}{(z_{\rm v}k_{\rm v}^2 + z_{\rm v}^{\rm d}\rho_{\rm d})}\left[\frac{\varepsilon_{\rm i}^{\rm g}p_{cl}}{z_{\rm cl}k_{\rm v}^2 + z_{\rm v}^{\rm d}\rho_{\rm d}} + \frac{(1-\varepsilon_{\rm i}^{\rm g})p_\ell}{(z_{\rm v}k_{\rm v}^2 + z_{\rm v}^{\rm d}\rho_{\rm d})}\right]\ , \tag{8.186}$$

where $p_{\rm cl} = (z_{\rm cl}^{\rm d}/z_{\rm v}^{\rm d} - z_{\rm cl}/z_{\rm v})$ is the bias factor for SIA clusters. Equation (8.186) results in a positive swelling rate for 3D cluster reaction kinetics for any microstructure, similar that in the single defect, dislocation bias formulation, meaning that saturation of swelling will not occur.

A permanently positive swelling rate is not physically plausible as swelling is known to saturate at high doses and high values of swelling. In fact, the general behavior of the solution of the Fokker–Planck equation is a gradual broadening of the size distribution until steady state is reached as cascade damage limits further growth of interstitial clusters. According to Eq. (8.185), the swelling rate decreases with increasing void size because of their increasing efficiency for capturing glissile SIA clusters, and the swelling rate will drop to zero when a maximum void size, $R^{\max}$, is reached. Under this condition, and if the void density remains constant, the swelling rate saturates when the swelling reaches some value, $(\Delta V/V)^{\max}$. In the case where production bias dominates, the saturation void size and saturation swelling become, from Eq. (8.185):

$$R^{\max} = \pi d_{\text{abs}}/z_{\text{v}}^{\text{d}}\,, (\Delta V/V)^{\max} = \frac{4\pi}{3}(R^{\max})^3\rho_{\text{V}}\,. \tag{8.187}$$

Note that neither $R^{\max}$ nor $(\Delta V/V)^{\max}$ depend on cascade parameters $\varepsilon_{\text{i}}^{\text{g}}$ or ε_{T}, and $R^{\max}$ is even independent of the void number density, ρ_{V}. If cluster formation is ignored in Eq. (8.185), then the swelling rate does not vanish. The saturation of swelling is an intrinsic property of production bias under cascade damage conditions.

As presented in the description of clusters using the Fokker–Planck formulation (Sect. 7.6), it was noted that the cluster size distribution is broadened by the parameter D and shifted by the parameter F. Thus, with increasing dose, the solution to the Fokker–Planck equation describes the broadening of the void size distribution and the increase in the mean void size of the distribution with dose. This general behavior can be compared with experimental swelling results for Fe–Cr–Ni irradiated at 650 °C. Figure 8.38 shows that the mean size of the distribution increases from about 11 nm at 9 dpa to over 50 nm by 80 dpa with a corresponding broadening of the distribution. Since swelling is mainly sensitive to the shift of the mean size of the distribution, linear swelling ($\Delta V/V\alpha$ dose) is obtained when the growth rate is large compared to the diffusional broadening, in which case the swelling rate is then given by the drift force alone.

8.3.9 Void Lattices

Voids have also been found to organize themselves in periodic arrays, or lattices in a metal under irradiation. Figure 8.39a shows a void lattice in bcc Nb following irradiation with 8.5 MeV Ta^+ to a dose of 300 dpa at 800 °C, and Fig. 8.39b shows one in Mo irradiated with 2 MeV N^+ ions to a dose of 100 dpa at 870 °C. The lattices are much easier to form in bcc metals than in fcc metals, though lattices have been observed in Ni, Al and stainless steel. Void lattices are a form of self-organization that occurs as responses of complex systems to external stimuli. It is believed that self-organization results from the collective interaction between system components under external forces that drive the system far from equilibrium. In irradiated solids, the void patterns are believed to be linked to the collective action of the point defects on the lattice structure.

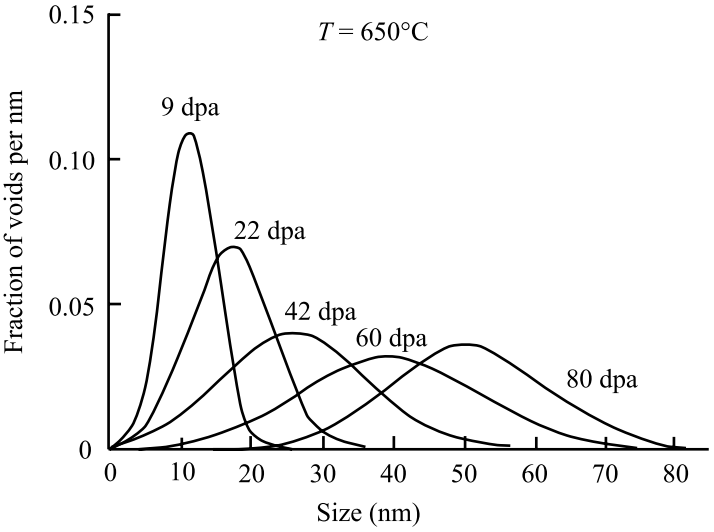

Fig. 8.38. Experimentally measured void size distribution in a Fe–Cr–Ni alloy irradiated at 650 °C (after [36])

A full understanding of the formation of void lattices is still lacking, but the theory is able to account for many of the parametric effects in lattice formation. Kinetic rate theory and the determination of an instability threshold can explain many of the observations to date. In general, ordered defect structures form when the following general conditions are satisfied [39]:

1. Agglomeration of vacancies into clusters during the collisional phase of cascade cooling
2. A bias for dislocations towards preferential absorption of interstitials over vacancies
3. An asymmetry in the production and diffusion of mobile point defects (production bias)
4. Some degree of anisotropy during the evolution of clustered defects. This could either be triggered by diffusional anisotropies of point defects, or by anisotropic elastic interaction between defect clusters during the latter stages of their evolution.

The occurrence of void lattice formation under cascade damage conditions (neutron or ion irradiation) and its absence under single Frenkel pair production (electron irradiation) is strong evidence for a key role of the 1D motion of thermally stable SIA clusters directly produced in cascades. In fact, it has been shown that when there is anisotropic transport of self-interstitial atoms by the crowdion mechanism (i.e., transport in which some crystal directions are preferred over others), voids occupying spatial positions that form a regular lattice grow faster, on average, than the randomly distributed voids [40]. However, for the void lattice to

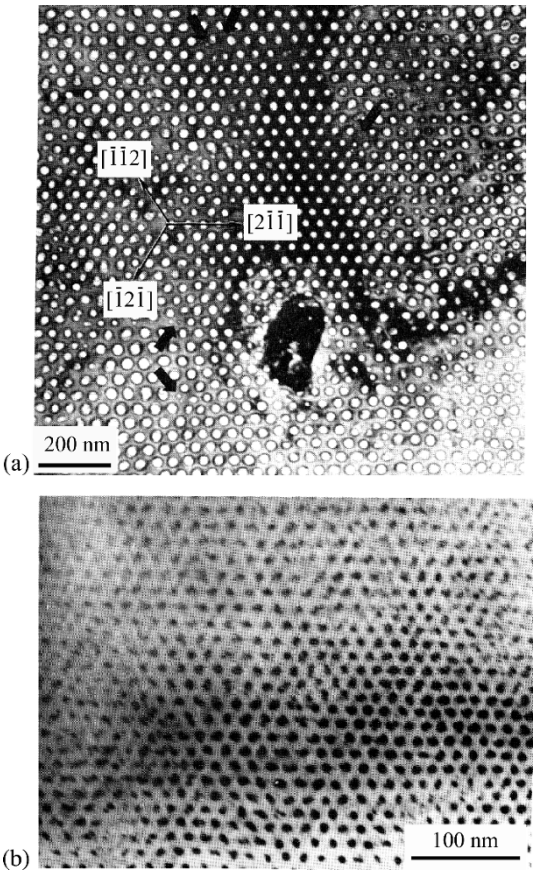

Fig. 8.39. Void lattice in (a) Nb irradiated with 8.5 MeV Ta^+ at 800 °C to 300 dpa, and helium bubble lattice in (b) Mo irradiated with 2 MeV N^+ ions to a dose of 100 dpa at 870 °C (after [39])

form, randomly distributed voids have to disappear. This can occur through stochastic void coarsening. Since void evolution in this case is sensitive to the spatial variations in the void growth rate, even a small fraction of interstitials moving as crowdions can significantly affect the spatial behavior of the void ensemble, resulting in the dissolution of randomly distributed voids with lower growth rates by stochastic fluctuations, and the nucleation and growth of voids forming a regular lattice.

8.3.10 Effect of Microstructure and Composition

The alloy microstructure can exert significant effects on void nucleation and growth. Microstructure features such as composition, solute addition and precipitate structure are among the most important in influencing void behavior.

Major Element Composition

In simple Fe–Cr–Ni austenitic alloys, swelling drops dramatically with increasing nickel content, reaching a minimum at about 50 at%. Figure 8.40 shows that the swelling dependence of nickel holds for various particle irradiations. The effect of Ni content on swelling is primarily due to the change in incubation dose as shown in Fig. 8.41. In fact, the data in Fig. 8.42 shows that at steady state, the swelling rate is the same over a wide range of nickel content.

Chromium content also affects swelling of austenitic alloys. Figure 8.43 shows that increasing chromium over the range 15 to 30% results in greater swelling. Less data is available on the systematic effect of Cr than for Ni, but the available data suggests swelling increases monotonically with Cr content. Swelling is much less of a problem in ferritic alloys, but reaches a maximum with a chromium content of about 15 at%. Figure 8.44 summarizes the effect of Ni and Cr on swelling in Fe–Cr–Ni alloys at 675 °C.

Solute Additions

Void swelling should be inhibited by additions of minor elements that bind either vacancies or interstitials with sufficient strength to reduce the effective mobility, thus preventing defects from reaching sinks and promoting recombination. The effect of solutes on the point defect balance equations was presented in Chap. 6, Sect. 6.4. The effect of solute addition on void swelling behavior can be determined by solving Eq. (6.57) through Eq. (6.61) and the nucleation rate, Eq. (8.35), and the void

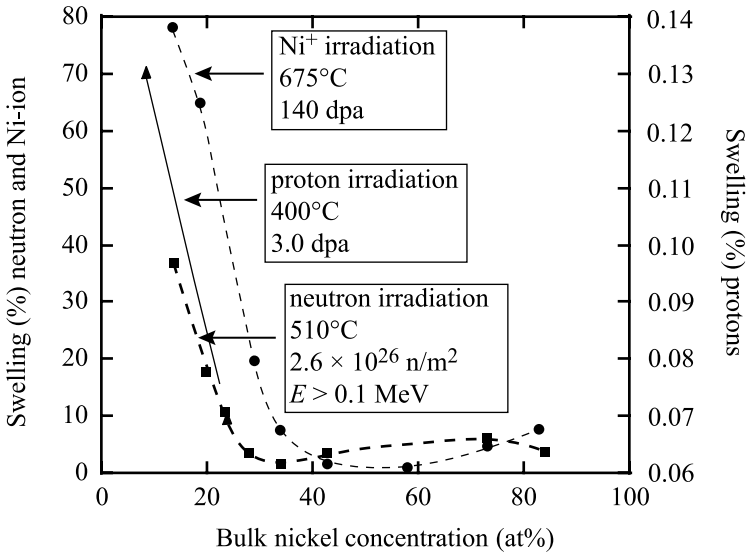

Fig. 8.40. The effect of bulk nickel concentration on swelling resulting from irradiation with different particles: neutrons, nickel ions and protons (after [35])

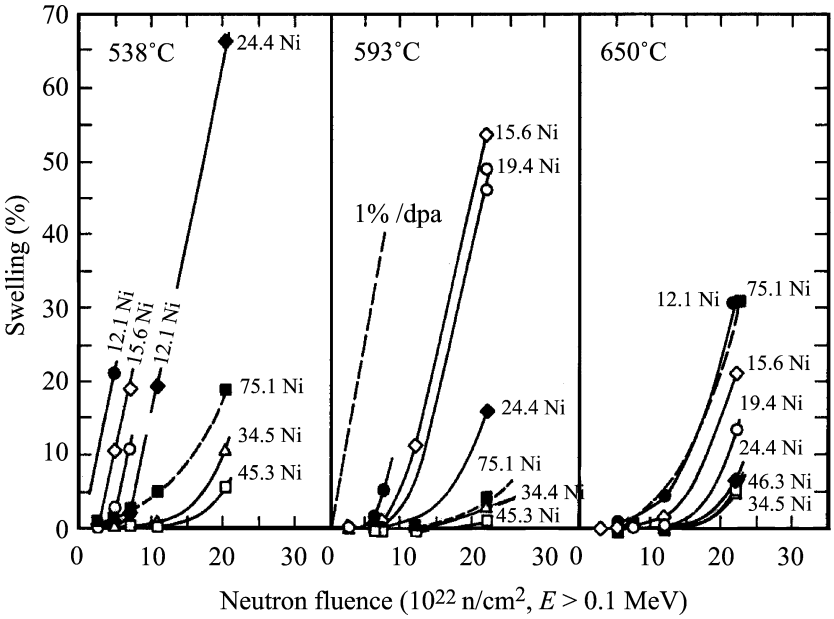

Fig. 8.41. The influence of temperature and nickel content on swelling of ternary Fe–15Cr–*x*Ni alloys in EBR-II (after [41])

swelling rate, Eq. (8.112). Results of numerical methods solution [42] show that with increasing values of binding energy, the activation energy for void nucleation increases (Fig. 8.45). The void swelling rate decreases with increasing binding energy as shown in Fig. 8.46. The net effect of solute addition on void swelling is shown in Fig. 8.47 which indicates that for increased solute concentration and binding energy, void swelling decreases. Data on the role of solutes in swelling is in general agreement with the model. Figure 8.48 shows that Si and P strongly influence the swelling of austenitic stainless steels. In fact, Si is a fast diffuser and is known to alter the ratio of diffusivities of the solvent atoms. As shown in Fig. 8.49, the effect of P on swelling is indeed in extending the incubation period to larger doses. Oversize solutes such as Hf have a similar effect in suppressing the nucleation of voids in stainless steels irradiated at ~ 300 °C. While other factors are important, Fig. 8.50 shows that the addition of ~ 1 wt% Hf to 316 stainless steel results in the suppression of void formation during Ni^{++} ion irradiation at 500 °C through a dose of 50 dpa, compared to an incubation dose of only 2 dpa for the reference 316 stainless steel alloy.

Precipitates

Precipitates can act as recombination sites for vacancy–interstitial annihilation to reduce void swelling. Precipitates can also inhibit dislocation climb necessary for dislocations to act as a preferential sink for interstitials and hence, retard void growth.

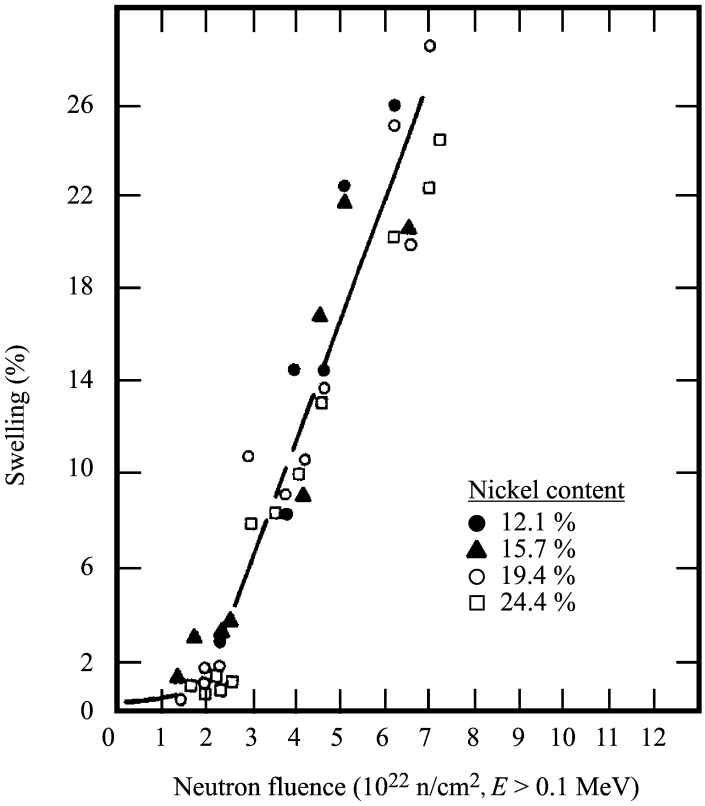

Fig. 8.42. Swelling of Fe–15Cr–Ni ternary alloys in EBR-II at temperatures between 400 and 510°C for nickel levels between 12.1 and 24.4 wt% (after [41])

In fact, precipitates can affect cavity growth in three ways [46]. The first is a direct effect in which voids that are attached to precipitates can undergo large growth rates because the precipitate acts as a collector of point defects. Precipitates can indirectly affect void growth by changing the overall sink strength of the solid, or by changing the characteristics of the matrix.

As discussed in Sect. 5.8, the coherent precipitate is considered to be a site where constrained recombination of defects occurs due to the distribution of saturable traps that acquire a steady state occupation probability as a result of a balance between defect capture, defect thermal release and extrinsic recombination with the anti-defect. However, incoherent precipitates accept any excess point defect flux that happens to impinge on it. These precipitates can accumulate defects and may act as sites for rapid transport of defects, similar to grain boundaries. In fact, they can serve as sites for the collection of defects which are then channeled to voids.

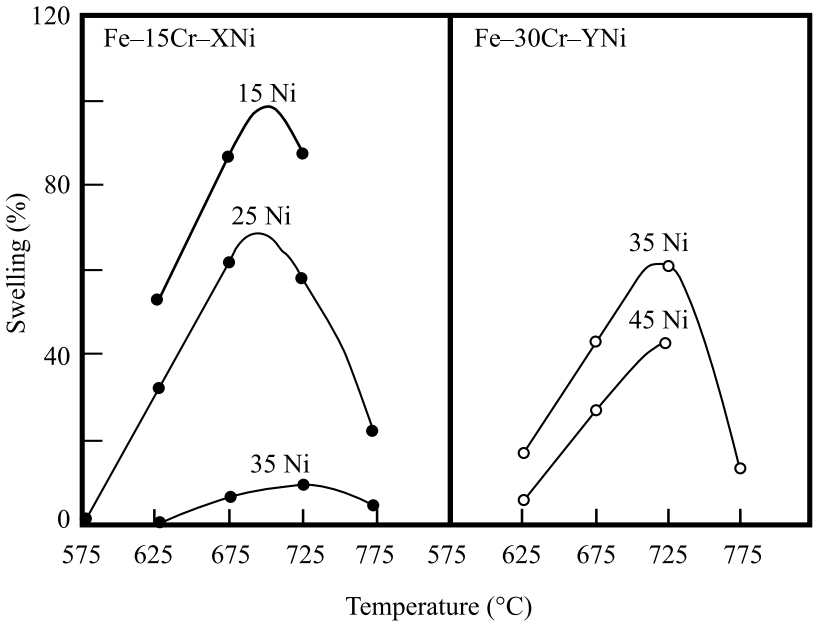

Fig. 8.43. Effect of chromium content on swelling in Fe–Cr–Ni alloys following 5 MeV Ni^+ ion irradiations to a dose of 140 dpa (after [19])

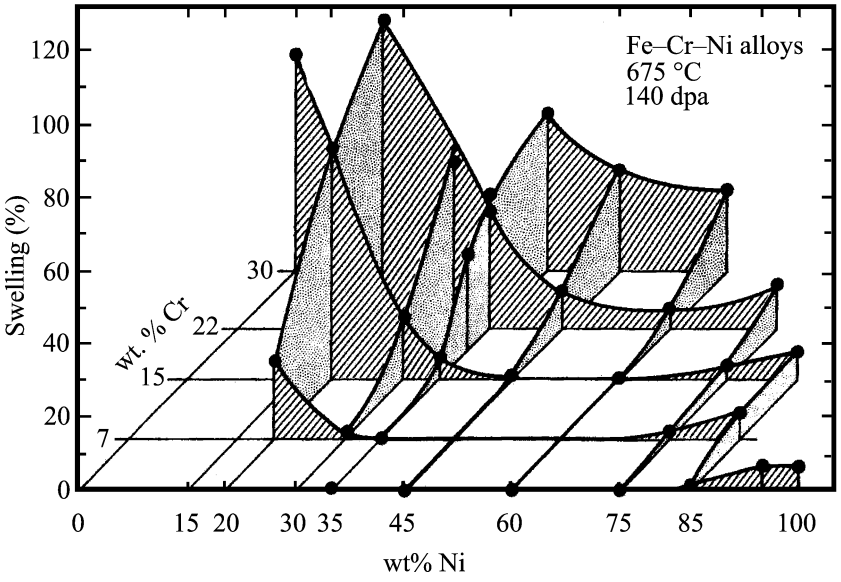

Fig. 8.44. Two-dimensional plot of the nickel and chromium dependence of swelling in Fe–Cr–Ni alloys irradiated with 5 MeV Ni^+ ions at 675 °C to a dose of 140 dpa. Swelling was measured by the step-height technique (after [19])

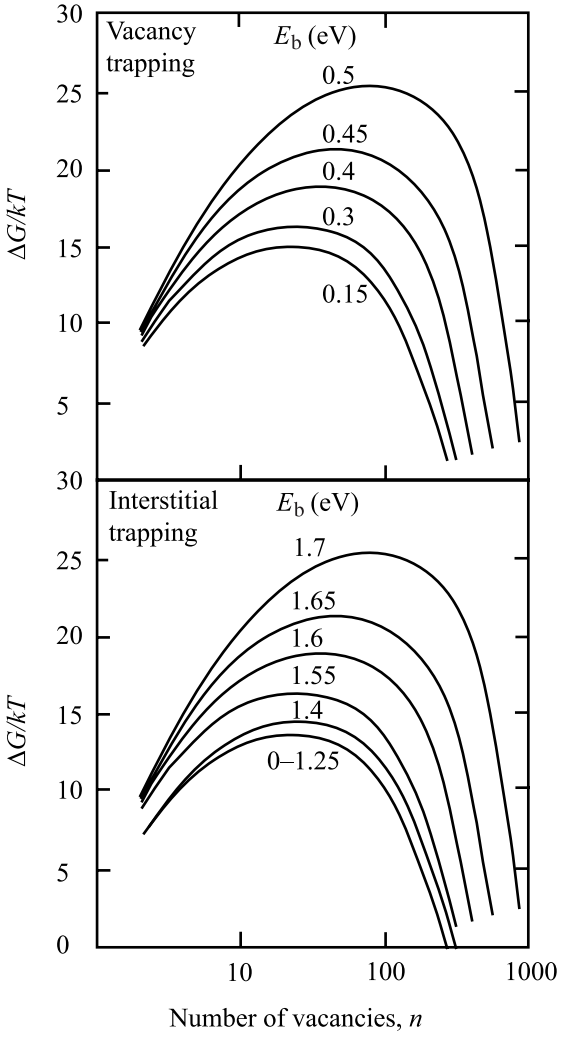

Fig. 8.45. The effect of impurity trapping on the free energy of void nucleation. Upper curves are for vacancy trapping and lower curves for interstitial trapping. The nucleation rates calculated from the curves are given as a function of binding energy in eV (after [42])

While the potential exists for precipitates to strongly influence void growth through their action as sinks or recombination sites, measurements of the effect of precipitation on void growth have failed to show that they play a significant role.

8.3.11 Effect of Reactor Operating History

Much of our understanding of void behavior in metals comes from irradiation in reactors. The experimental data is used to validate models and to provide material parameters to benchmark the models. Given that most models assume that reactor parameters (temperature, dose rate, stress) are constant over time, it is often

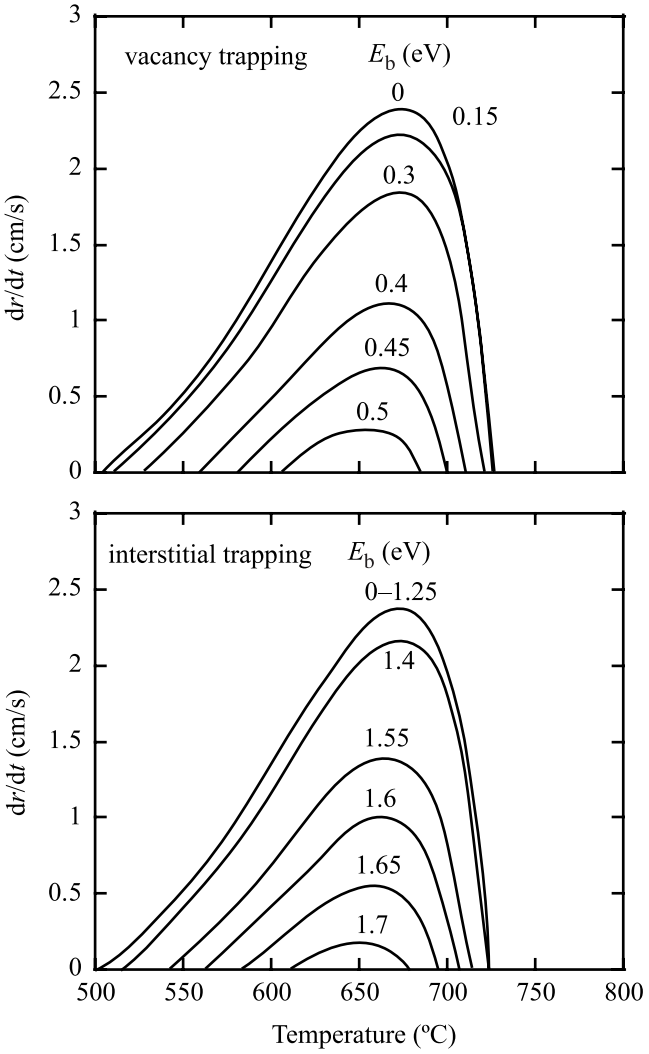

Fig. 8.46. The effect of impurity trapping on void growth rates. *Upper curves* are for vacancy trapping and *lower curves* are for interstitial trapping (after [42])

true that in both commercial and test reactors, these parameters can vary considerably during operation and due to the shutdown-startup cycle. It is not unusual for irradiation experiments to experience numerous power (and hence, temperatures) reductions over the course of a sixth month to one year irradiation. Garner [47] cites one instance in which a 600 °C, three-year irradiation experienced 237 temperature setbacks in the first year, during which the temperature fell to as low as 50 °C. While the dose accumulated at these lower than target temperatures is low (0.12 dpa in the 3.5 dpa accumulated in year 1), they can have a profound effect on the mi-

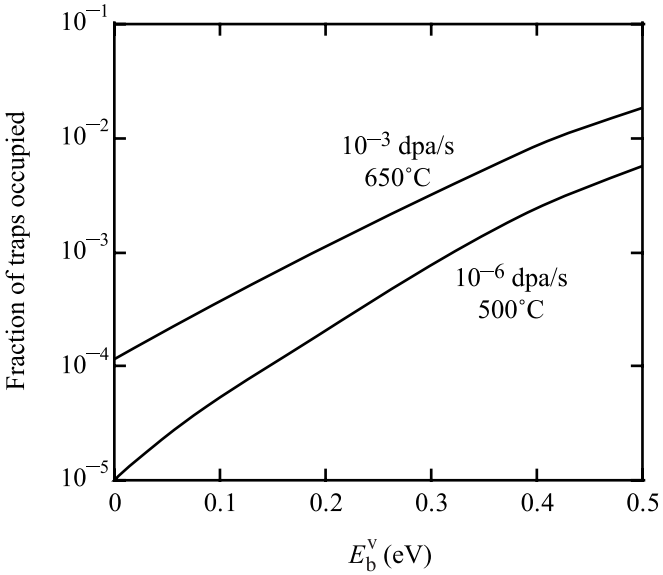

Fig. 8.47. The fraction of traps occupied for vacancy trapping at typical charged particle and fast reactor dose rates and temperatures vs. binding energy. Under these conditions, the fraction of traps occupied is small even at high vacancy binding energies (after [42])

crostructure. Figure 8.51a shows the difference of dislocation loop size and number density in Ni–2.0Si samples irradiated in JMTR at 400 ℃ for the case of "conventional" temperature control vs. one where the temperature control was considerably improved. The smaller mean loop size and larger density is likely the result of additional loop nucleation during the periods where temperature was low but the neutron flux was non-zero. This low-temperature microstructure persisted at the nominal irradiation temperature and resulted in an alteration of the loop size distribution as compared to the case in which temperature was controlled. Low-temperature loop nucleation in a high temperature microstructure can also affect the evolution of the void microstructure.

Figure 8.51b shows the microstructure of a Fe–15Cr–16Ni alloy irradiated at 600 ℃ in the Materials Open Test Assembly (MOTA) in the Fast Flux Test Facility (FFTF) to comparable doses. The sample on the left was in an assembly, reactor shutdown occurred over a six-hour period during which the temperature was reduced by 50 – 100 ℃ and then to gradually over the six-hour period during which the flux was also decreased. Irradiation during cooling is responsible for the formation of the fine dislocation loop structure. Following rapid shutdown during which the neutron flux and temperature is decreased over a several minute period, no fine loop structure is observed. The fast drop in temperature does not provide an opportunity to accumulate enough dose in this intermediate temperature regime to cause loop nucleation.

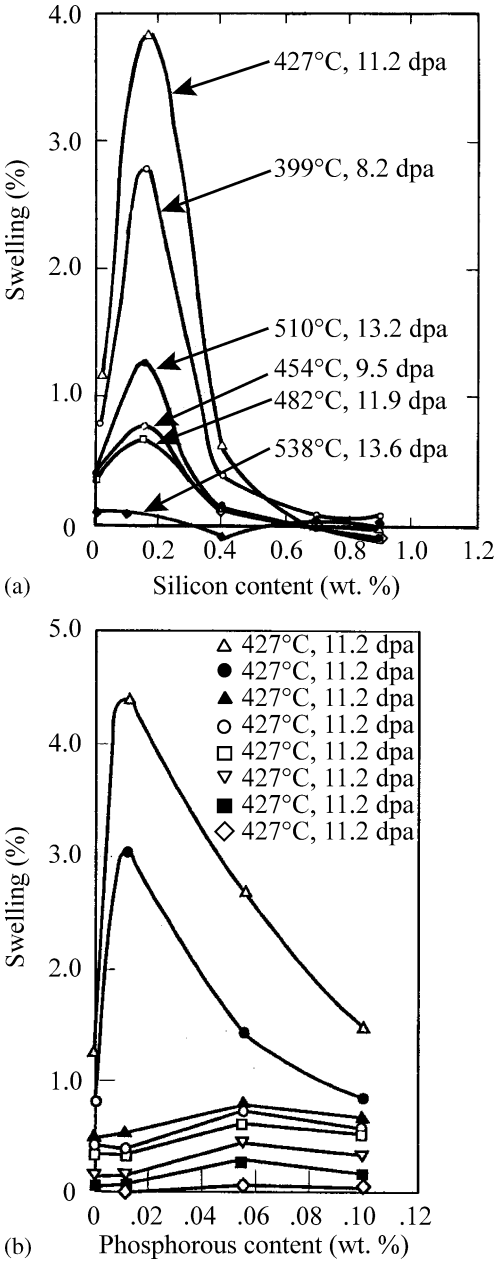

Fig. 8.48. Influence of (a) silicon and (b) phosphorus on the swelling in EBR-II of annealed Fe–25Ni–15Cr at various combinations of temperature and fluence (after [43])

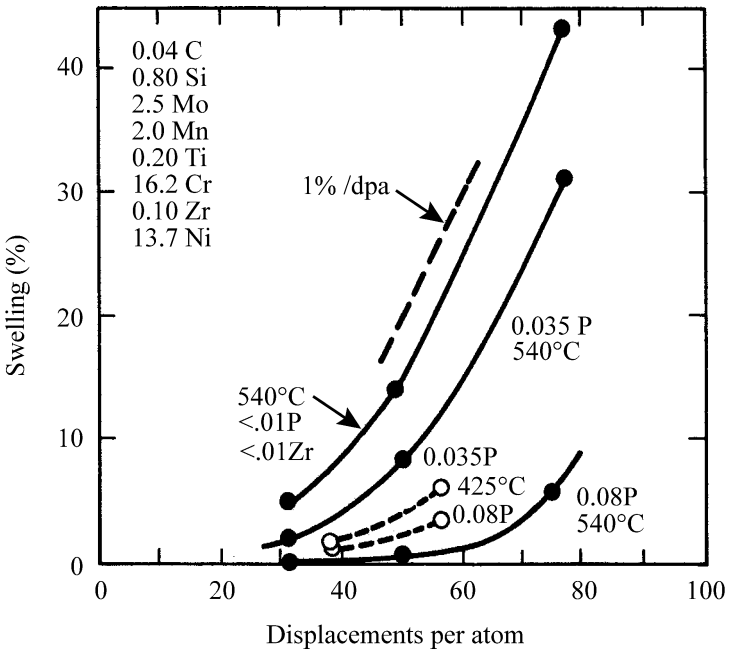

Fig. 8.49. Influence of phosphorus level on swelling in EBR-II for a titanium-modified 316 steel at 425 and 540 °C (after [44])

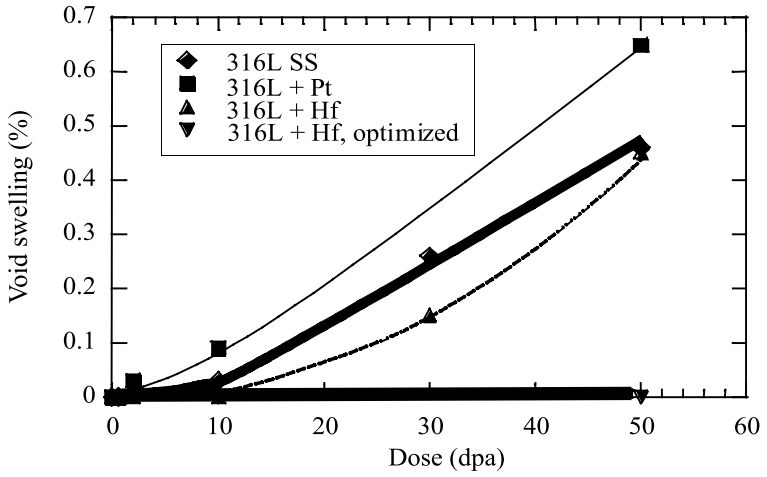

Fig. 8.50. Suppression of swelling to at least 50 dpa in 316 SS doped with ~ 1 wt% Hf after irradiation with 5 MeV Ni^{++} ions at 500 °C (after [45])

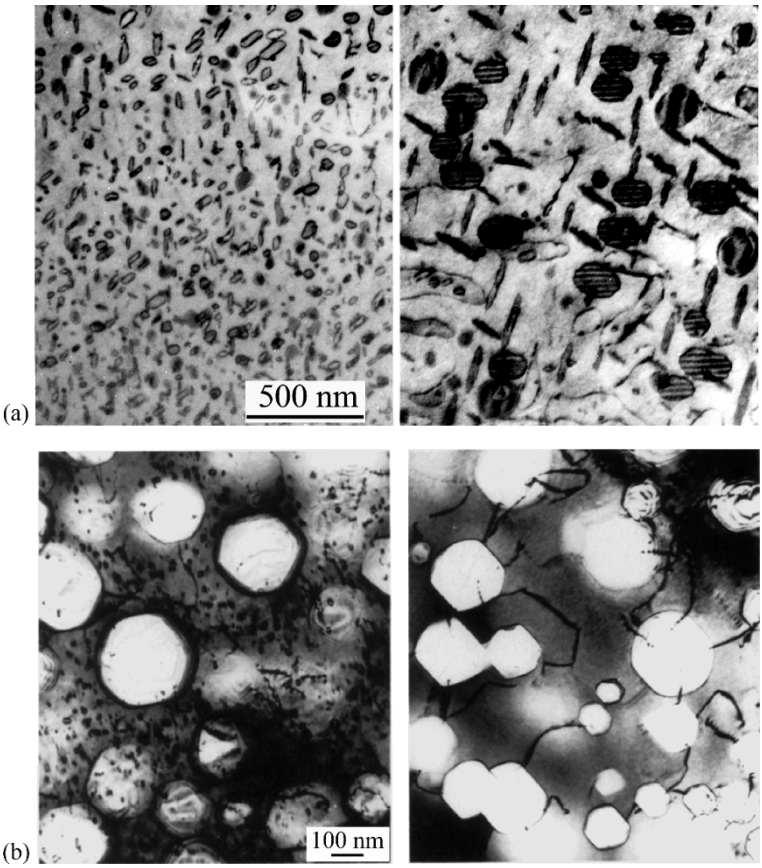

Fig. 8.51. (a) Effect of temperature control on dislocation loop formation and growth in Ni–2%Si irradiated at 400 °C in the Japan Materials Test Reactor (JMTR) to a dose of $\sim 10^{24}\,\mathrm{n/m^2}$. LHS is convential control ($0.92\times10^{24}\,\mathrm{n/m^2}$, $E > 1,0\,\mathrm{MeV}$), RHS is improved control ($0.96\times10^{24}\,\mathrm{n/m^2}$). (b) Effect of shutdown rate on the formation of small dislocation loops in Fe–15Cr–16Ni irradiated at in FFTF at 600 °C. The image *on the left* underwent a slow temperature decrease during power shutdowns compared to a very rapid reduction in temperature at shutdown for the sample *on the right* (after [47])

The significance of these observations is twofold. First, that a low-temperature dislocation microstructure introduced into a high-temperature microstructure can alter the further development of that microstructure, affecting both loop and void evolution. Second, only very small doses ($< 0.1\,\mathrm{dpa}$) are required to nucleate the fine loop structure that remains stable during the continuation of the irradiation at high temperature. This data also provides additional information on the loop nucleation rate, indicating that it is perhaps higher than current models can explain.

8.4 Bubble Growth

Up to this point, we have been treating voids as essentially empty cavities that grow and shrink by the absorption of vacancies. We have accounted for the effect of gas atoms on the nucleation of voids and also on the equilibrium vacancy concentration at the void surface. But we have not discussed the magnitude of the pressure in the void due to the gas and the effect this may have on the growth of the void. We also have made no distinction between a void and a bubble. One question that we would like to answer is how much gas must a void have in order to be considered a bubble? In a practical sense, the distinction is largely one of degree and character. A cavity is considered to be a bubble if the effect of the gas (on the surface energy and due to the pressure) causes the cavity to become spherical. This is essentially how voids and bubbles are distinguished in transmission electron microscopy. Due to the periodicity of the lattice, cavities will be faceted with the facets lying on the close-packed planes. But if the surface energy is changed by the gas, or if the gas pressure is high enough, then the cavity will become spherical in shape. Of course, very large voids will approach a spherical shape as the contribution of the facets diminishes with increasing void radius.

Because insoluble gases are often formed by transmutation when certain elements are irradiated, inert gas bubbles form, which alter the mechanical and physical properties of an alloy. Bubble formation depends on the mobility of the gas (either in the form of individual atoms or complexes), the minimum number of gas atoms which are able to form a stable nucleus and the rate at which lattice vacancies can be supplied to enhance the stability of a nucleated core.

Bubbles nucleate under irradiation and then grow or redissolve. The criterion is that nucleation ceases when a gas atom diffusing at random is most likely to encounter a pre-existing nucleus rather than take part in creating a new one. The resulting bubble density varies inversely as the square root of the gas atom diffusion coefficient and thus increases with decreasing temperature.

The following assumptions about bubble nucleation under irradiation are made. Homogeneous nucleation is predicated on the premise that bubbles grow by the interaction of gas atoms from a background atomic population on a random basis. Thus, no account is taken of local effects such as cascade processes or precipitation on lattice defects or impurity agglomerates. Concerning stable nuclei, we assume that a pair of gas atoms is stable against thermal dissociation and that its activation energy is such that its motion may be ignored with respect to that of single gas atoms.

In this section, we will first consider the mechanics of bubbles followed by the development of bubble growth models that will closely parallel void growth.

8.4.1 Bubble Mechanics

For a gas-filled bubble of radius R, embedded in a solid medium, the change in the free energy of the solid due to the bubble is:

$$\mathrm{d}G = V\,\mathrm{d}p + \gamma \mathrm{d}A\ . \tag{8.188}$$

Since

$$V\,\mathrm{d}p = \mathrm{d}(pV) - p\,\mathrm{d}V\,, \tag{8.189}$$

and for an ideal gas, $pV =$ constant and $V = 4/3\pi R^3$, then:

$$\frac{\mathrm{d}G}{\mathrm{d}r} = -4\pi R^2\left(p - \frac{2\gamma}{R}\right)\,. \tag{8.190}$$

Setting $\mathrm{d}G/\mathrm{d}r = 0$ yields:

$$p = 2\gamma/R\,. \tag{8.191}$$

Thus, the equilibrium condition for a bubble is expressed by the force balance $p = 2\gamma/R$, in which the force due to the outward pressure of the gas, p, is balanced by the inward-acting force due to the surface tension, $2\gamma/R$. In the presence of a stress, the force balance becomes:

$$p = \frac{2\gamma}{R} - \sigma\,. \tag{8.192}$$

where positive stress is tension.

All bubble models require a specific relation between the number of gas atoms in a bubble and its radius. The van der Waals equation of state is used to describe the thermodynamic state of inert gas in bubbles. Letting n_x be the number of gas atoms in a spherical bubble of radius R and the gas density is ρ_g. Then:

$$n_x = (4/3\pi R^3)\rho_\mathrm{g}\,. \tag{8.193}$$

From the idea gas law ($pV = nkT$), we have:

$$p\frac{V}{n} = kT \quad \text{or} \quad \frac{p}{\rho_\mathrm{g}} = kT \quad \text{or} \quad p = \frac{3nkT}{4\pi R^3}\,. \tag{8.194}$$

Using Eq. (8.191) for mechanical equilibrium to eliminate ρ_g and p in Eqs. (8.193) and (8.194) gives:

$$\begin{aligned} n_x &= 4/3\pi R^3\frac{2\gamma}{RkT} \\ &= \frac{8\pi R^2\gamma}{3kT}\,. \end{aligned} \tag{8.195}$$

For small R, $1/\rho_\mathrm{g}$ is not proportional to R and we must account for the volume occupied by the gas atoms themselves. We do this by modifying Eq. (8.194) to include a term B which is a function of temperature and pressure. This gives us van der Waals equation of state:

$$P\left(\frac{1}{\rho_\mathrm{g}} - B\right) = kT \quad \text{or} \quad \frac{1}{\rho_\mathrm{g}} = B + \left(\frac{kT}{2\gamma}\right)R\,, \tag{8.196}$$

and Eq. (8.195) becomes:

$$n_x = \frac{8\pi R^2\gamma}{3(kT + 2B\gamma/R)} = \frac{4/3\pi R^3}{B + (kT/2\gamma)R}\,. \tag{8.197}$$

For large R, the perfect gas approximation applies, and for very small R, the dense gas limit applies. Physically, there is a minimum volume occupied by each atom, B and as R decreases, the volume per atom approaches this limit. The result is:

$$\frac{1}{\rho_g} = B\frac{\text{nm}^3}{\text{atom}} : \text{ dense gas limit} , \tag{8.198}$$

and

$$\frac{1}{\rho_g} \cong \left(\frac{kT}{2\gamma}\right) R : \text{ ideal gas limit} . \tag{8.199}$$

Note that for stainless steel at 500 ℃, where $\gamma \sim 1.75\,\text{J/m}^2$, $2\gamma/kT \sim 328\,\text{nm}^{-2}$ and $\frac{1}{\rho_g} \cong 3\times 10^{-4} R\frac{\text{nm}^3}{\text{atom}}$.

The limiting cases corresponding to Eqs. (8.198) and (8.199) are:

$$n_x = \left(\frac{4\pi R^3}{3B}\right) \text{ for small } R \tag{8.200}$$

$$= \left(\frac{4\pi R^2}{3}\right)\left(\frac{2\gamma}{kT}\right) \text{ for large } R . \tag{8.201}$$

If Eq. (8.191) is not satisfied, then the bubble is described as a non-equilibrium bubble. That is, the bubble is not in equilibrium with the solid. Mechanical equilibrium is usually maintained by a flow of vacancies to the bubble to provide the additional volume needed to accommodate the influx of gas atoms. Whether Eq. (8.191) is satisfied depends on the relative absorption rates of vacancies and gas atoms by the bubble. A bubble of radius R can be considered as the absence of $(4/3\pi R^3)/\Omega$ matrix atoms where Ω is the atomic volume. The empty sphere of radius R can be thought of as consisting of n_v vacancies given by:

$$n_v = \frac{4/3\pi R^3}{\Omega} . \tag{8.202}$$

The number of gas atoms in a sphere of radius R in mechanical equilibrium is given by Eq. (8.197). The number of vacancies per gas atom in an equilibrium bubble is then:

$$\frac{n_v}{n_x} = \left(\frac{kT}{2\gamma}\right)\frac{R}{\Omega} + \frac{B}{\Omega} . \tag{8.203}$$

Note that n_x increases as R^2 but n_v increases as R^3, so increasing numbers of vacancies are needed per gas atom in order to maintain equilibrium.

Stress is accounted for by taking Eq. (8.192) and substituting in from Eq. (8.194) for p gives:

$$\sigma = \frac{2\gamma}{R} - \frac{3n_x kT}{4\pi R^3} , \tag{8.204}$$

where σ is the hydrostatic tensile stress. The critical bubble radius for unstable bubble growth is determined by setting $\mathrm{d}\sigma/\mathrm{d}r = 0$ and solving for R, yielding:

$$R_\mathrm{c} = \left(\frac{9n_x kT}{8\pi\gamma}\right)^{1/2} . \tag{8.205}$$

Substituting for R_c in Eq. (8.205) into Eq. (8.204) gives:

$$\sigma_\mathrm{c} = \left(\frac{128\pi\gamma^3}{81n_x kT}\right)^{1/2} , \quad \text{or} \quad n_x = \frac{128\pi\gamma^3}{81\sigma_\mathrm{c}^2 kT} . \tag{8.206}$$

The critical bubble radius, R_c is related to the equilibrium bubble radius, R_0 by expressing Eqs. (8.201) and (8.205) in terms of the number of gas atoms in the bubble, n_x and eliminating n_x, giving:

$$R_\mathrm{c} = \sqrt{3}R_0 , \tag{8.207}$$

and the critical stress in terms of R_0 is:

$$\sigma_\mathrm{c} = \frac{4\sqrt{3}\gamma}{9R_0} . \tag{8.208}$$

Substituting for Eq. (8.201) into Eq. (8.204) to eliminate n_x gives a relation between the applied stress, the initial bubble size and the critical bubble size:

$$\sigma_\mathrm{c} = \frac{2\gamma}{R_\mathrm{c}}\left(1 - \frac{R_0^2}{R_\mathrm{c}^2}\right) . \tag{8.209}$$

Equations (8.208) and (8.209) provide the bubble stability criterion in terms of the applied stress and the bubble size. For bubbles of size R_0, Eq. (8.208) gives the critical stress for stability. For a solid with bubbles of size $R_0 < R_\mathrm{c}$, application of a tensile stress σ_c will cause the bubble to grow to size R_c specified by Eq. (8.209). If $R_0 > R$ or if σ_c is greater than the right hand side of Eq. (8.208), then the bubble will grow without bound. Or, for a given applied stress, Eq. (8.208) gives the critical bubble radius for stability. Equation (8.205) can be compared to the stability equation for a gas-free void in a solid subject to a stress, σ. For $p = 0$ in Eq. (8.192), we have that $\sigma = 2\gamma/R$. The numerical coefficient in Eq. (8.208) is about 0.77, which is less by about a factor of 3 than the coefficient for the void. The difference is due to the effect of the gas pressure in the bubble that assists the stress.

8.4.2 Growth Law

Analogous to void growth, the time rate of change of the volume of a bubble is equal to the difference in the rates at which vacancies and interstitials are absorbed and to the volume carried by each of these point defects:

$$\frac{\mathrm{d}}{\mathrm{d}t}\left(\frac{4}{3}\pi R^3\right) = \Omega\left[4\pi R D_\mathrm{v}\left(C_\mathrm{v} - C_\mathrm{v}^\mathrm{V}\right) - 4\pi R D_\mathrm{i}\left(C_\mathrm{i} - C_\mathrm{i}^\mathrm{V}\right)\right] , \tag{8.210}$$

and so the growth law is:

$$\frac{\mathrm{d}R}{\mathrm{d}t} \equiv \dot{R} = \frac{\Omega}{R}\left[D_\mathrm{v}\left(C_\mathrm{v} - C_\mathrm{v}^\mathrm{V}\right) - D_\mathrm{i}\left(C_\mathrm{i} - C_\mathrm{i}^\mathrm{V}\right)\right] , \tag{8.211}$$

where C_v^V and C_i^V are the concentrations of vacancies and interstitials at the bubble surface and $C_\mathrm{v}$and C_i are the point defect concentrations in the bulk solid. The thermodynamic vacancy concentration at the bubble surface given by Eq. (8.85) is modified to include the effect of gas pressure in the bubble:

$$C_\mathrm{v}^\mathrm{V} = C_\mathrm{v}^0 \exp\left[\frac{-\Omega}{kT}\left(p - \frac{2\gamma}{R}\right)\right] , \tag{8.212}$$

and for interstitials

$$C_\mathrm{i}^\mathrm{V} = C_\mathrm{i}^0 \exp\left[\frac{\Omega}{kT}\left(p - \frac{2\gamma}{R}\right)\right] , \tag{8.213}$$

where C_v^0 and C_i^0 are the thermodynamic equilibrium concentrations of vacancies and interstitials respectively for a stress-free solid and the exponential terms reflect the presence of a mechanical stress acting on the solid equal in magnitude to $p - 2\gamma/R$. Because C_i^0 is so small, the interstitial term, Eq. (8.213) can be neglected.

Setting $\mathrm{d}R/\mathrm{d}t = 0$ in Eq. (8.211) and substituting Eq. (8.212) for C_v^V into the resulting expression, taking logarithms and re-arranging gives [48, 49]:

$$R_\mathrm{c} = \frac{2\gamma}{p + \dfrac{kT}{\Omega}\ln S_\mathrm{v}} , \tag{8.214}$$

where S_v is the effective vacancy supersaturation given by:

$$S_\mathrm{v} = \frac{D_\mathrm{v}C_\mathrm{v} - D_\mathrm{i}C_\mathrm{i}}{D_\mathrm{v}C_\mathrm{v}^0} . \tag{8.215}$$

Now, substituting Eq. (8.194) for p into Eq. (8.214) and re-arranging gives:

$$g(R_\mathrm{c}) = R_\mathrm{c}^3 - \frac{2\gamma\Omega}{kT\ln S_\mathrm{v}}R_\mathrm{c}^2 + \frac{3n_x\Omega}{4\pi\ln S_\mathrm{v}} = 0 , \tag{8.216}$$

where the expression is denoted by the function $g(R_\mathrm{c})$, which is zero when R_c is a root. The growth rate is plotted as a function of void radius in Fig. 8.52 for three conditions. The lower curve is the case where Eq. (8.216) has three real roots, the middle curve shows the case in which at least two of the roots are equal and the upper curve has one real root [49]. In case I, the roots are denoted $R_\mathrm{c}^\mathrm{B}$and R_c^V. A void containing enough gas atoms that it is between R_c^B and R_c^Vwill shrink back to R_c^B. A void with the same number of gas atoms but with radius below R_c^B will grow to R_c^B and stop. Finally, a void with the same number of gas atoms and with radius above R_c^Vwill grow without limit by bias-driven growth. As the number of gas atoms increases, Eq. (8.216) is represented by curves that progress from I to II to III. In

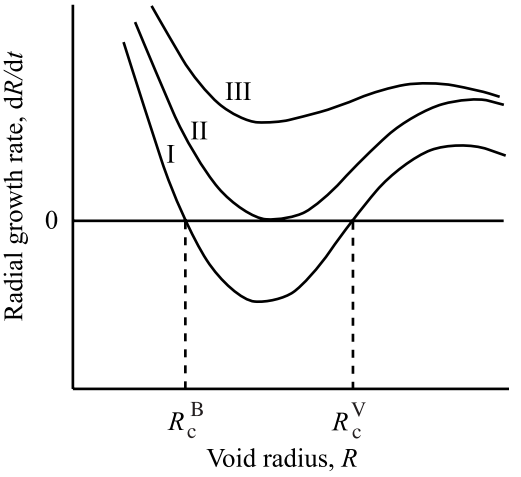

Fig. 8.52. Schematic plot of cavity growth rate as a function of cavity radius for increasing amount of helium gas in the void or S_v (after [48])

the case of curve III, the number of gas atoms is large enough that there will be no intersections with the $dR/dt = 0$ axis and these cavities will only grow by bias-driven growth. At some critical number of gas atoms, there is just one intersection of the function dR/dt with the $dR/dt = 0$ axis. This case is represented by curve II. In this case, the corresponding number of gas atoms is denoted as n_x^* and the corresponding minimum critical radius where R_c^B and R_c^V coincide is denoted as R_c^*. The quantity, n_x^* is the maximum number of gas atoms that may be contained in a cavity for there to still exist a critical radius, with a minimum value of R_c^*.

The minimum critical radius, R_c^* can be found by taking the derivative of Eq. (8.216) with respect to R_c, giving:

$$\frac{dg(R_c)}{dR_c} = 3R_c^2 - \frac{4\gamma\Omega}{kT\ln S_v}R_c \,. \tag{8.217}$$

Setting Eqs. (8.216) and (8.217) to zero simultaneously yields the minimum critical radius:

$$R_c^* = \frac{4\gamma\Omega}{3kT\ln S_v} \,, \tag{8.218}$$

and from Eq. (8.205):

$$n_x^* = \frac{128\pi\gamma^3\Omega^2}{81(kT)^3(\ln S_v)^2} \,. \tag{8.219}$$

Stoller et al. [49] noted that Eq. (8.219) can be written for non-spherical cavities using a shape factor, F_V such that:

$$n_x^* = \frac{32F_V\gamma^3\Omega^2}{27(kT)^3(\ln S_v)^2} \,, \tag{8.220}$$

where $F_V = 4\pi/3$ for a spherical void. He also notes that more physically reasonable solutions are obtained using a hard-sphere equation of state rather than the ideal gas law, which tends to overpredict swelling incubation times.

It should also be noted that Eqs. (8.219) and (8.206) are the same when σ is replaced with $\Omega/\ln S$, indicating that the stability criterion is the same regardless of whether the solid is acted on by an actual stress or an effective stress defined by the irradiation-induced vacancy supersaturation. A bubble is stable for negative vacancy supersaturation and can be stable or metastable for positive vacancy supersaturation depending on the magnitude of the supersaturation, the gas content and the bubble size according to Fig. 8.52. For a constant stress or irradiation-induced vacancy supersaturation, when the stability limit is reached by gas absorption, a bubble starts to grow by vacancy absorption and is transformed into a cavity. Equations (8.218) and (8.205) describe the bubble-to-void conversion criterion.

Equation (8.211) can be used to calculate the swelling rate due to bubble swelling by assuming all gas to be in the bubbles, re-solution to be insignificant and the gas to be ideal such that:

$$p = \frac{n_x kT}{4/3\pi R^3 \rho_B} , \tag{8.221}$$

where ρ_B is the total bubble density and $n_x = \dot{x}t$ is the gas concentration in the solid being produced by transmutation at a rate of $\dot{x}$. The swelling rate due to bubble growth is:

$$\mathrm{d}(\Delta V/V)/\mathrm{d}t = (4\pi R^2 \rho_B/\Omega)\,\mathrm{d}R/\mathrm{d}t . \tag{8.222}$$

8.4.3 Bubble Growth by Dislocation Loop Punching

While vacancy diffusion is the prime mechanism contributing to bubble growth on a fine scale, an additional mechanism for bubble growth in the case of high gas pressure is dislocation loop punching. If the pressure in the bubble is large enough, the stress in the solid nearby may reach a level where dislocation sources can be activated, resulting in the growth of the bubble by *punching out* a dislocation loop (Fig. 8.53). Recall that the stress required to operate a Frank–Read source is $\sim \mu b/l$, where l is the spacing between pinning points. Dislocation sources that are easiest to activate will be those with $l \sim r_0$, where r_0 is the radius of the bubble. So the excess pressure required for the bubble to generate dislocations is then $\sim \mu b/r_0$. The magnitude of the excess pressure required to generate prismatic dislocations can be determined by comparing the free energy change of the bubble upon creation of a dislocation loop of size equal to the bubble, to the energy of the loop itself [51]. The work to increase the bubble size is:

$$\Delta F = -p\,\mathrm{d}V = -\left(p - \frac{2\gamma}{r_0}\right)\pi r_0^2 b , \tag{8.223}$$

where p is the pressure in the bubble, V is the bubble volume, γ is the surface energy and b is the Burgers vector. Neglecting the stacking fault energy contribution, the

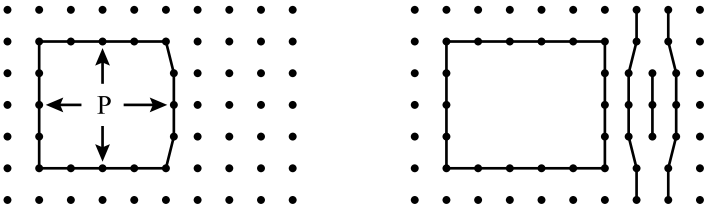

Fig. 8.53. Schematic illustration of the growth of a bubble by dislocation loop punching (after [50])

energy of the prismatic dislocation loop of radius r_0 given by Eq. (7.64) is approximated as:

$$E_{\mathrm{L}} = \frac{\mu b^2 r_0}{2(1-\nu)} \ln \frac{4r_0}{r_{\mathrm{c}}} \,, \tag{8.224}$$

so that for dislocation loop formation to be energetically possible:

$$\left(p - \frac{2\gamma}{r}\right) \pi r_0^2 b > \frac{\mu b^2 r_0}{2(1-\nu)} \ln \frac{4r_0}{r_{\mathrm{c}}} \,, \tag{8.225}$$

or approximating E_{L} as $\pi \mu b^2 r_0$:

$$p > (2\gamma + \mu b)/r_0 \,. \tag{8.226}$$

For typical values of γ and μ, the gas pressure in the bubble must be about an order of magnitude greater that $2\gamma/r_0$ before dislocations can be generated and allow the bubble to expand.

8.4.4 Bubble Lattices

Similar to void lattices described earlier, high levels of He can result in the organization of gas bubble lattices. In fact, gas bubble lattice formation has been observed in bcc, fcc and hcp metals following He injection at temperatures $< 0.3T_{\mathrm{m}}$ [52]. Helium bubbles in Cu are aligned with dense-packed rows parallel to matrix $\{111\}$ directions. Johnson et al. [52] measured the lattice constant of the He bubble superlattice in Cu to be $a_{\mathrm{He}} = 7.6\,\mathrm{nm}$, corresponding to a bubble density of 10^{25} bubbles/m^3. Figure 8.54 shows a bright field transmission electron micrograph of a helium gas bubble lattice in molybdenum following 40 keV He^+ irradiation to a dose of 5×10^{21} He^+/m^2 at 500 °C. While the same forces driving the formation of void lattices is expected to apply to bubble lattices, additional interactions may arise due to the close spacing of overpressurized bubbles, such as bubble growth by dislocation loop punching.

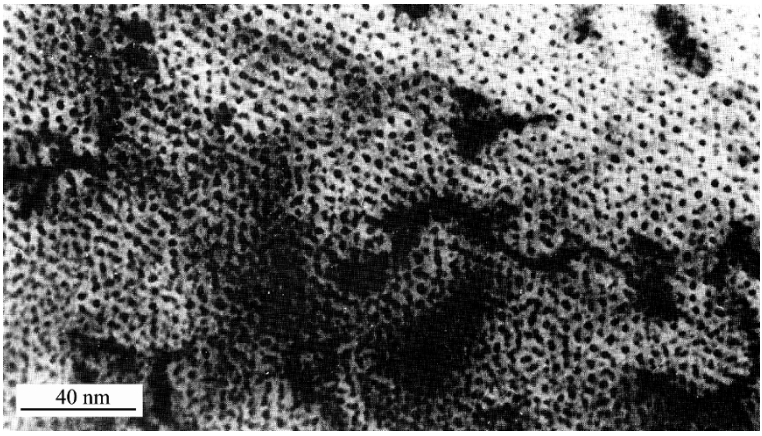

Fig. 8.54. He gas bubble superlattice formed in molybdenum following 40 keV He^+ irradiation to a dose of 5×10^{21} He^+/m^2 at 500 °C (after [39])

8.4.5 Helium Production

An important ingredient in bubble formation and growth is the production of helium. In a reactor, He production is governed by the boron and nickel contents of the alloy through the reactions:

$$^{10}\mathrm{B}(n,\alpha)^{7}\mathrm{Li}\,, \tag{8.227}$$

and the two-step reaction:

$$^{58}\mathrm{Ni}(n,\gamma)^{59}\mathrm{Ni}(n,\alpha)^{56}\mathrm{Fe}\,. \tag{8.228}$$

The thermal neutron (n,α) cross section for ^{10}B is very large, about 3837b, while the cross section for ^{59}Ni is for fast neutrons and is only about 4.3b. For thermal reactors then, a large amount of helium is produced early in life from transmutation of boron, but this source burns out by about 1 dpa ($\sim 10^{21}\,\mathrm{n/cm^2}$). The presence of nickel in stainless steels provides a smaller but sustained source of helium at higher dose. In this regard, thermal reactors produce greater amounts of helium at low dose and in a lower dose rate environment, making low dose helium-induced swelling a greater problem in a thermal reactor than in a fast reactor. Figure 8.55 shows the production rate of helium from an alloy containing ^{58}Ni and ^{10}B in the HFIR (thermal) reactor. Note that the production rate of helium is dominated at low fluence by the contribution from ^{10}B, and at higher fluence by ^{58}Ni. Helium buildup for the same alloy in a fast reactor and a fusion reactor are shown for comparison. Note that the helium buildup in a fusion reactor matches that in HFIR, and both are higher than that in a fast reactor.

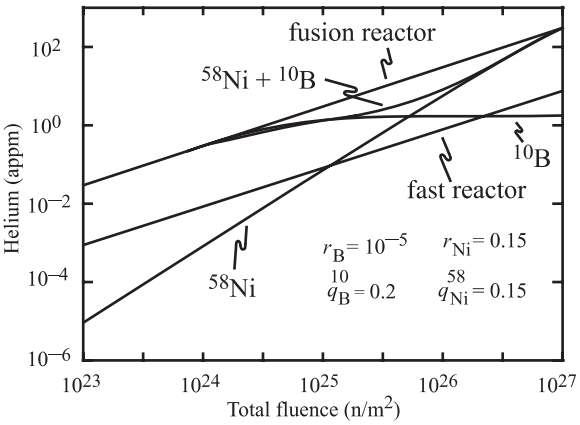

Fig. 8.55. Helium buildup vs. fluence for stainless steel in HFIR (thermal reactor), a fusion reactor spectrum and a fast reactor spectrum. In the figure, r is the atom fraction of boron or nickel in the alloy and q is the initial fraction of the isotope listed in the figure (after [27])

Nomenclature

a	Lattice constant
$A_{\mathrm{v,i}}^X$	Absorption rate of vacancies, interstitials by sink X
B	Volume occupied by a gas atom in a lattice
C_j	Concentration of species j
C_j^0	Thermal equilibrium concentration of species j
$C_{\mathrm{v}}^{\mathrm{L}}$	Vacancy concentration in equilibrium with a dislocation loop
d_{abs}	Effective diameter of dislocations for absorbing glissile SIA clusters
$d^{\mathrm{c,e}}$	Strength of diffusive spread for clusters (c) or for vacancy emission (e) relative to single point defects
D_j	Diffusion coefficient of species j
D^{c}	Diffusive spread due to cascades
D^{e}	Diffusive spread due to vacancy emission
D^{s}	Diffusive spread due to single defect jumps
E	Energy
E_{b}^j	Binding energy of specie j
E_{f}^j	Formation energy of specie j
E_{m}^j	Migration energy of specie j
F_{V}	Shape factor ($= 4\pi/3$ for spherical void)
$g(R_{\mathrm{c}})$	Void growth rate factor, defined in Eq. (8.216)
G	Free energy
G_0	Free energy of perfect lattice
ΔG	Change in free energy
ΔG_n^0	Activation barrier for void nucleation without interstitials
$\Delta G_n'$	Activation barrier for void nucleation with interstitials
H	Enthalpy, also Henry's law constant Eq. (8.57)
J	Nucleation current
k	Boltzmann's constant

k_{g}^2	Sink strength for 1D diffusing SIA clusters
k_X^2	Sink strength of sink X
k_j^2	Total sink strength species j
$K_{\mathrm{cl}}^{\mathrm{eff}}$	Effective production rate of defects in clusters and free form
K_j	Loss rate of species j
K_{iv}	Vacancy–interstitial recombination rate
K_j^{eff}	Effective production rate of free defects of type j
K_0	Defect production rate
K_0^{eff}	Effective Frenkel Pair production rate accounting for recombination
K_x^{c}	Rate of gas atom re-solution
l	Distance of cluster to a grain boundary
L_j	Thermal emission rate of species j
m_{i}	Number of interstitial in an interstitial loop
M	Helium concentration
M_x	Helium cluster of x gas atoms
n	Number of vacancies in a void
n_{cr}	Number of vacancies in a void of critical size
$n_{\mathrm{k}}, n'_{\mathrm{k}}$	Critical void nucleus cluster size
$n_{\mathrm{v,i}}$	Number of vacancies, interstitials
$N_{\mathrm{d}j}$	Average number of defects of type j generated in a single cascade
N_0	Number of lattice sites per unit volume
N_{R}	See Eq. (8.151)
N_{S}	See Eq. (8.154)
p	Gas pressure
p_{cl}	Defined in Eq. (8.186)
p_l	Defined in Eq. (8.185)
P_{m}	Probability of nucleating a void embryo of size m
Q	Defined in Eq. (8.148)
r	Radius
r_0	Prismatic dislocation loop radius
R	Void or bubble radius
R_{g}	Grain radius
R_{c}	Critical bubble radius
R_{cr}	Critical void radius
R_{iv}	Vacancy–interstitial recombination rate
R_{max}	Saturation void size
R_0	Equilibrium bubble radius
$\dot{R}$	Rate of change of radius, growth rate
r_k, r'_k	Critical void nucleus radius
S	Entropy
S_j	Supersaturation of species j
T	Temperature
V	Volume

$\Delta V/V$	Fractional volume
w_n	Number of ways of removing $\rho^0(n)$ voids of size n from a solid
x	Number of gas atoms in a void
x_g	Mean glissile cluster size
z_v	Vacancy bias factor
z_i	Interstitial bias factor
Z	Zeldovich factor
Z'	Zeldovich factor in the presence of interstitials or in a stressed solid
α_j	Emission rate of species j
β	$2\gamma\Omega/kT$ defined in Eq. (8.71)
β_j	Absorption rate of species j
δ	Thickness of void shell
ε_i^g	Fraction of interstitials in glissile clusters
ε_T	Fraction of Frenkel pairs that recombines during cascade cooling
Φ	Fluence or dose
γ	Surface energy
η	Defined in Eq. (8.117)
μ	Shear modulus
μ_x	Chemical potential of species x
ν	Poisson's ratio
θ	Angle between surface and tangent to void, Eq. (8.81)
Θ	Defined in Eq. (8.98)
ρ	Void size distribution
ρ_x	Density of entity x
σ	Hydrostatic stress
τ	Time
Ω	Atomic volume
ξ	Defined in Eq. (8.15)
ζ	Defined in Eq. (8.130)

Subscripts

B	Bubbles
cr	Critical size
CP	Coherent precipitates
D	Total dislocations
g	Glissile clusters or gas
gb	Grain boundary
hom	Homogeneous
i	Interstitials
j	Defect specie representation
IP	Incoherent precipitates
L	Dislocation loops
N	Network dislocations

s	Sinks
v	Vacancies
V	Void
0	Equilibrium

Superscripts

c	Cascades
e	Vacancy emission
L	Loops
m	Number of vacancies in a void embryo of size m
s	Single defects
V	Voids
0	Equilibrium
*	Minimum critical value
′	In presence of interstitials

Problems

8.1 In a solid where the effect of interstitials are neglected (i.e., where $\beta_i/\beta_v = 0$),
   a) Determine the critical void embryo size (in terms of the number of vacancies *and* void radius).
   b) Show schematically how the number of vacancies in the critical size void embryo varies with:
      i) Temperature
      ii) Degree of vacancy supersaturation
      iii) Void surface energy
      iv) The presence of interstitials
   c) How do your answers to parts (a) *and* (b) change when an inert gas is present?

8.2 Determine the critical void embryo size for 316 stainless steel ($a = 0.3\,\text{nm}$, $\gamma = 1.75\,\text{J/m}^2$) irradiated at 500 °C so as to produce a vacancy supersaturation of 10^3.

8.3 Derive Eq. (8.40).

8.4 Calculate and plot the relative void growth rate $\dot{R}/R_o$ for stainless steel ($T_m = 1823\,\text{K}$) as a function of T/T_m, given that

$$Q_f^v = 1.4\,\text{eV}$$
$$Q_m^v = 1.09\,\text{eV}$$
$$\rho_d = 10^{10}\,\text{cm}^{-2}$$
$$\Sigma_s = 0.3\,\text{cm}^{-1}$$
$$\phi = 10^{14}\,\text{n/cm}^2\,\text{s}$$
$$\nu = 100\,\text{displacements/neutron}$$

$$z_{iv} = 30$$
$$Z_i = 1.02$$
$$Z_v = 1.00$$
$$a^3 = \Omega = 0.011\,\mathrm{nm}^3$$
$$kT/2\gamma = 0.01\,\mathrm{nm}^2$$
$$\nu = 10^{13}\,\mathrm{s}^{-1}$$

Neglect voids as sinks ($\rho_V \simeq 0$) and precipitates ($\rho_{CP} \sim 0$) and loops as sinks ($\rho_L \simeq 0$). Assume the vacancy diffusion coefficient is given by

$$D_v = \nu a_0^2 \exp(-Q_m^v/kT)$$

and the equilibrium vacancy concentration is given by

$$C_v = \Omega^{-1} \exp(-Q_f^v/kT)\ .$$

Assume the void diameter is 50 nm.

8.5 The equation for growth of a cavity is given by:

$$\frac{dR}{dt} = \frac{\Omega}{R}\left[D_v(C_v - C_r^V) - D_i C_i\right]\ .$$

Explain what happens to the cavity growth rate if the radiation dose rate doubles. Assume low sink strength and low temperature. Explain what happens if the radiation stops but the sample is held at the same temperature that existed during the radiation.

8.6 A solid is subjected to a neutron flux, resulting in void formation and growth. At time t_1, a condition is reached where the dislocation density is $10^9\,\mathrm{cm}^{-2}$, the voids are all 100 nm in diameter at a density of $10^{14}\,\mathrm{cm}^{-3}$ and the void growth rate is zero. In the absence of thermal emission, however, $\dot{R} = 10^{-2}\,\mathrm{nm/s}$. The metal is instantaneously strained such that the dislocation density increases by a factor of 10 and the void growth rate in the absence of thermal emission increases to $8 \times 10^{-2}\,\mathrm{nm/s}$. Determine the direction and magnitude of the hydrostatic stress needed to suppress void growth.
Assume that the solid contains no dislocation loops or precipitates and that the voids are gas-free.

8.7 Pure nickel has been found to be highly susceptible to void formation when irradiated in a fast neutron spectrum. Along with voids, perfect dislocation loops are found in nickel. In comparison, Fe–18Cr–8Ni stainless steel is less susceptible to void formation and faulted Frank loops are found; but voids are also present.
As the nickel content in the stainless steel is increased, two other observations are made. The susceptibility to void formation decreases, and voids that are present are surrounded by a nickel-rich shell.

Given the following information, explain each of these observations.

$$\sigma/\gamma|_{\mathrm{Ni}} < \sigma/\gamma|_{\mathrm{Fe}}\,, \quad R_{\mathrm{Ni}} < R_{\mathrm{Fe}}$$

Element	Cr	Fe	Ni
$\sigma_{\mathrm{eff}}(n,\alpha)$	0.20	0.23	4.20

8.8 a) Explain the reason for the characteristic bell-shaped plot of swelling vs. irradiation temperature.
b) How and why is the shape changed by:
i) Cold-work prior to irradiation
ii) The addition of impurities
iii) Grain size
c) Explain why swelling and creep can affect each other.

8.9 You are designing the stainless steel fuel cladding for the Advanced Breeder Reactor. Your objective is to delay void nucleation *and* minimize void growth. Concerning cladding fabrication, you can control:
a) Grain size
b) Degree of cold-work
c) Precipitate density
d) Impurity content
of the steel.
From a design standpoint, you can control the normal operating temperature of the cladding over a window of 100 °C.
Using void nucleation and growth theory, how can you utilize these *five* parameters to reach this goal? Be quantitative where possible.

8.10 Annealing is a means of removing radiation damage from an alloy. For stainless steel with both dislocation loop and void populations, explain what will occur when the steel is annealed at 600 °C for several hours. In describing the changes during annealing, indicate relative rates and endpoints.

8.11 In the absence of gas atoms, we wish to eliminate voids in Cu by thermal treatment at 400 °C. Calculate the length of time needed to accomplish this for an initial void radius of 5 nm and 30 nm. The surface free energy of copper is $1.73\,\mathrm{J/m^2}$.

8.12 Given that the number of gas atoms in a bubble can be described as

$$m = (4/3\pi R^3)\rho_{\mathrm{g}}$$

and that the gas atom density, ρ_{g}, can be described by

$$1/\rho_{\mathrm{g}} = B + (kT/2\gamma)R$$

where B is the dense gas limit:
a) Show that the volume increase that accompanies coalescence of equal size gas bubbles is given as

$$(\Delta V/V)_{\mathrm{final}}/(\Delta V/V)_{\mathrm{initial}} = /2\,.$$

b) Assuming that the overall gas balance in UO_2 can be given as

$$YF't = mN$$

where
Y = noble gas yield of a fission event
F' = fission rate density
m = gas atoms per bubble
N = bubble density,
and all the gas remains in bubbles. Develop an expression for the volumetric swelling rate and indicate the dependence on burnup.

c) How would you account for
   i) Gas remaining in the matrix?
   ii) Re-solution?

References

1. Cauthorne C, Fulton E (1967) Nature 216:575
2. Jenkins ML, Kirk MA (2001) Characterization of Radiation Damage by Transmission Electron Microscopy. Institute of Physics Publishing, Philadelphia, PA
3. Adda U (1972) In: Corbett JW, Ianiello LC (eds) Proceedings of Radiation-Induced Voids in Metals, CONF-710601, USAEC Technical Information Center, Oak Ridge, TN, 1972, p 31
4. Olander DR (1976) Fundamental Aspects of Nuclear Reactor Fuel Elements, TID-26711-P1. Technical Information Center, USERDA, Washington, DC
5. Mansur LK (1994) J Nucl Mater 216:97–123
6. Russell KC (1971) Acta Met 19:753
7. Powell RW, Russell KC (1972) Rad Eff 12:127
8. Katz JL, Wiedersich H (1972) In: Corbett JW, Ianiello LC (eds) Proceedings of Radiation-Induced Voids in Metals, CONF-710601, USAEC Technical Information Center, Oak Ridge, TN, 1972, p 825
9. Russell KC (1979) Acta Met 26:1615
10. Packan NH, Farrell K, Stregler JO (1978) J Nucl Mater 78:143
11. Wiedersich H, Katy JL (1979) Adv Colloid Interface Sci 10:33
12. Russell KC (1972) Acta Met 20:899
13. Katz JL, Wiedersich H (1973) J Nucl Mater 46:41
14. Semenov AA, Woo CH (2002) Phys Rev B 66:024118
15. Brailsford AD, Bullough R (1972) J Nucl Mater 44:121–135
16. Mansur LK (1978) Nucl Technol 40:5–34
17. Brimhall JL, Kissinger HE, Kulcinski GL (1972) In: Corbett JW, Ianiello LC (eds) Proceedings of Radiation-Induced Voids in Metals, CONF-710601, USAEC Technical Information Center, Oak Ridge, TN, 1972, p 338
18. Garner FA, Porollo SI, Vorobjev AN, Konobeev YuV, Dvoriashin AM (1999) In: Ford FP, Bruemmer SM, Was GS (eds) Proceedings of the 9th International Symposium on Environmental Degradation of Materials in Nuclear Power Systems: Water Reactors, The Minerals, Metals and Materials Society, Warrendale, PA p. 1051
19. Garner FA (1984) Irradiation performance of cladding and structural steels in liquid metal reactors, chap 6. In: Frost BRT (ed) Materials Science and Technology, vol 10A, Nuclear Materials, part I. VCH, New York

20. Krasnoselov VA, Prokhorov VI, Koleskikov AN, Ostrovskii ZA (1983) Atomnaya Energiya 54(2)111–114
21. Garner FA, Bates JF, Mitchell MA (1992) J Nucl Mater 189:201–209
22. Brager HR, Garner FA (1979) Effects of Radiation on Structural Materials the 9th International Symposium, STP 683. America Society for Testing and Materials, Philadelphia, PA, 1979, pp 207–232
23. Dupouy JM, Lehmann J, Boutard JL (1978) In: Proceedings of the Conference on Reactor Materials Science, vol. 5, Alushta, USSR. Moscow, USSR Government, pp 280–296
24. Busboom HJ, McClelland GC, Bell WL, Appleby WK (1975) Swelling of Types 304 and 316 Stainless Steel Irradiated to 8×10^{22} n/cm^2, General Electric Company Report GEAP-14062. General Electric Co., Sunnyvale, CA
25. Seran LJ, Dupouy JM (1982) In: Effects of Radiation on Materials the 11th International Symposium, STP 782. American Society for Testing and Materials, Philadelphia, PA, 1982, pp 5–16
26. Seran LJ, Dupouy JM (1983) In: Proceedings of the Conference on Dimensional Stability and Mechanical Behavior of Irradiated Metals and Alloys, vol 1, Brighton. British Nuclear Energy Society, London, 1983, pp 22–28
27. Mansur LK (1993) J Nucl Mater 206:306–323
28. Brailsford AD, Bullough R (1973) J Nucl Mater 48:87
29. Brailsford AD, Bullough R (1972) British Rep AERE-TB-542
30. Dubuisson P, Maillard A, Delalande C, Gilbon D, Seran JL (1992) Effects of Radiation on Materials the 15th International Symposium, STP 1125. American Society for Testing and Materials, Philadelphia, PA, 1992, pp 995–1014
31. Brager HR, Garner FA, Guthrie GL (1977) J Nucl Mater 66:301–321
32. Wolfer WG, Foster JP, Garner FA (1972) Nucl Technol 16:55
33. Brailsford AD (1975) J Nucl Mater 56:7
34. Wolfer WG, Mansur LK (1980) J Nucl Mater 91:265
35. Allen TR, Cole JI, Gan J, Was GS, Dropek R, Kenik EA (2005) J Nucl Mater 341:90–100
36. Singh BN, Golubov SI, Trinkaus H, Serra A, Osetsky Y, Baraskev AV (1997) J Nucl Mater 251:107–122
37. Golubov SI, Singh BN, Trinkaus H (2000) J Nucl Mater 276:78–89
38. Abromeit C (1994) J Nucl Mater 216:78–96
39. Ghoniem NM, Walgraef DJ, Zinkle S (2002) Comput Aided Mater Des 8:1–38
40. Woo CH, Frank W (1985) J Nucl Mater 137:7
41. Garner FA (1984) J Nucl Mater 122–123:459–471
42. Mansur LK, Yoo MH (1978) J Nucl Mater 74:228–241
43. Garner FA, Kumar AS (1987) Radiation-Induced Changes in Microstructure the 13th International Symposium, STP 955 (Part 1). American Society for Testing and Materials, Philadelphia, PA, 1987, pp 289–314
44. Garner FA, Brager HR (1985) J Nucl Mater 133–134:511–514
45. Gan J, Simonen EP, Bruemmer SM, Fournier L, Sencer BH, Was GS (2004) J Nucl Mater 325:94–106
46. Brailsford AD, Mansur LK (1981) J Nucl Mater 103–104:1403–1408
47. Garner FA, Sekimura N, Grossbeck ML, Ermi AM, Newkirk JW, Watanabe H, Kiritani M (1993) J Nucl Mater 205:206–218
48. Mansur LK, Coghlan WA (1983) J Nucl Mater 119:1–25
49. Stoller RE, Odette GR (1985) J Nucl Mater 131:118–125
50. Evans JH (1978) J Nucl Mater 76–77:228–234
51. Trinkaus H (1983) Rad Eff 78:189–211
52. Johnson PB, Mazey DJ, Evans JH (1983) Rad Eff 78:147–156

9 Phase Stability Under Irradiation

Irradiation can have profound effects on the formation or dissolution of phases by alteration of the stability of those phases. The most direct way in which irradiation can alter phase stability is by causing local enrichment or depletion of solute such that the solubility limit is crossed. But irradiation can also dissolve phases by recoil dissolution, cause disordering by creating anti-site defects, and lead to nucleation and growth of distinct phases. Under specific conditions, irradiation can also lead to the formation of metastable phases including amorphization. Because the phase structure of an alloy can significantly affect the physical and mechanical properties of the material, understanding how irradiation affects phase stability is of great importance for engineering materials.

9.1 Radiation-Induced Segregation and Radiation-Induced Precipitation

Radiation-enhanced diffusion (RED), discussed in Chap. 4, and radiation-induced segregation (RIS), presented in Chap. 6, explain how irradiation can increase the atomic transport of atoms in the alloy, and how the coupling between the vacancy and interstitial fluxes and the solute and solvent atoms can lead to enrichment or depletion of solute atoms at defect sinks such as the free surface, grain boundaries, dislocations, precipitate interfaces, etc. Enrichment or depletion of solute can lead directly to precipitate formation if the local solute concentration exceeds the solubility limit, or precipitate dissolution if the solute content is driven below the solubility limit. Recall that the temperature dependence of RIS is such that at low temperatures, RIS is minimal due to low defect mobility and the high recombination rate of vacancies and interstitials, limiting the number available to annihilate at sinks. At high temperature, the high equilibrium vacancy concentration leads to enhanced recombination and faster back diffusion, limiting the degree of RIS. However, at intermediate temperatures, significant participation of the solute in the defect fluxes results in pronounced segregation at sinks. Figure 9.1 shows how RIS can lead to precipitate formation or dissolution at a sink. Enrichment of a solute at a sink can raise the local concentration (Fig. 9.1a) above the solubility limit (shown as a dashed line in Fig. 9.1b) locally. The excess solute can then precipitate as a second phase. If a second phase is already present, then depletion of the solute (Fig. 9.1c) can lead to dissolution of that phase locally (Fig. 9.1d).

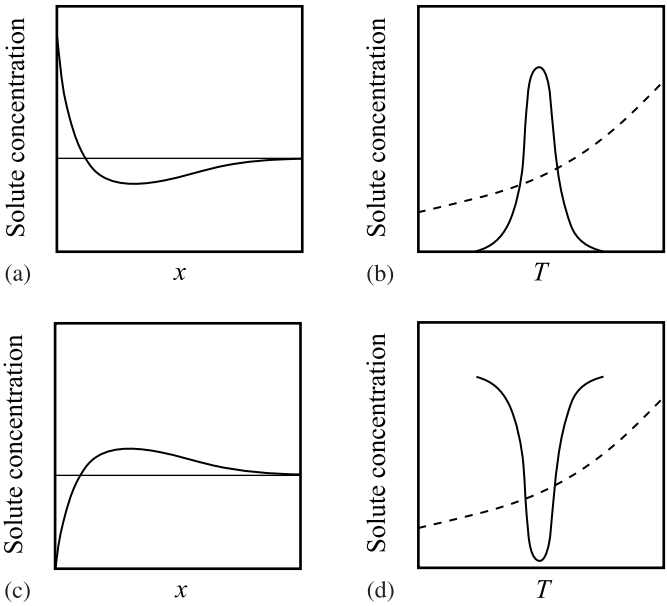

Fig. 9.1. Schematic illustration showing (a) enrichment of solute at a sink and (b) its corresponding elevation above the solubility limit, and (c) depletion of a solute at a sink and (d) its corresponding suppression below the solubility limit

A classic example of radiation-induced precipitate formation and dissolution is described in Sect. 6.1.2 and Fig. 9.2 and Fig. 9.3 for the case of RIS in solid solution Ni–Si and Ni–Al alloys. The consequence of a large amount of solute enrichment at sinks is precipitation of a second phase. In the Ni–Si system, Si is undersized relative to Ni and enriches at sinks during irradiation (Fig. 9.2). RIS causes segregation to levels that are well above the solubility of Si in Ni, resulting in formation of a Ni_3Si, γ' precipitate. Ni_3Si precipitates at the surface, grain boundaries and dislocation loops. Conversely, in the case of Ni–Al, Al is oversized with respect to Ni and depletes at sinks under irradiation as shown in Fig. 9.3. The result is the dissolution of existing precipitates at those locations. Since the Ni–Al alloy is an initially homogeneous alloy and the Al content is below the solubility limit for Al, no precipitates are present before irradiation. However, as shown in Fig. 9.3, the region *behind* the depleted zone is enriched in Al and this amount of enrichment exceeds the solubility level at locations that are displaced from the sink interface, resulting in precipitation of Ni_3Al in a subsurface layer a small distance away from the grain boundary and dislocation loops. Both of these examples are consequences of crossing the solubility line for an element in solution by solute enrichment or depletion due to RIS, and constitute a primary mechanism of phase instability under irradiation.

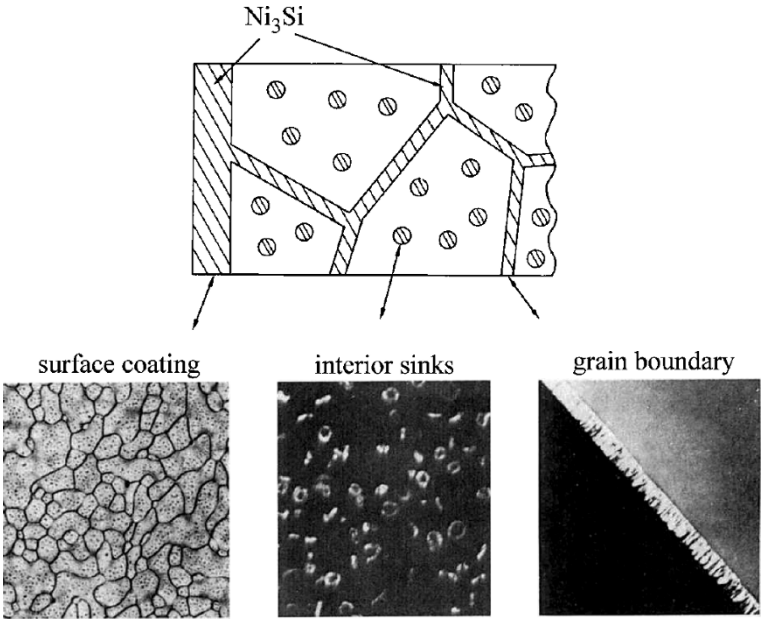

Fig. 9.2. Formation of γ'-Ni_3Si on defect sinks in a solid solution of Ni–6at% Si alloy showing (a) a surface coating of Ni_3Si, (b) toroidal γ' precipitates at dislocation loops and (c) a grain boundary coated with Ni_3Si (from [1])

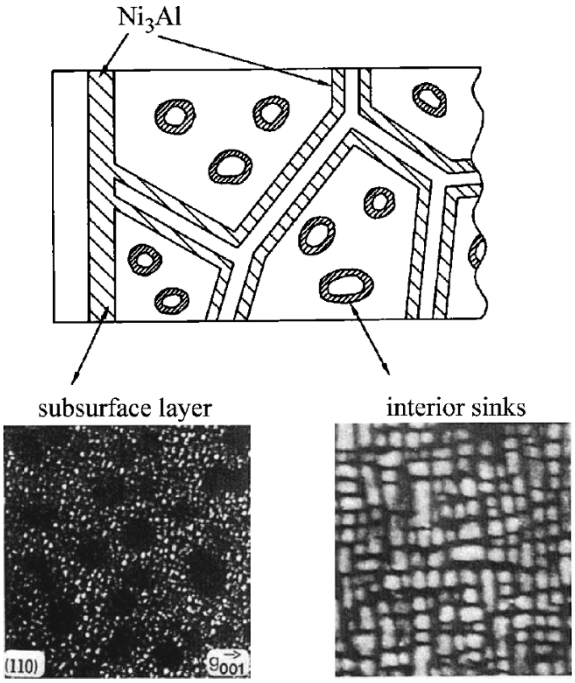

Fig. 9.3. Formation of γ'-Ni_3Al away from defect sinks in a solid solution of Ni–12.8 at% Al showing (a) a subsurface layer of γ'-Ni_3Al, and (b) formation of Ni_3Al away from dislocation loops (from [1])

9.2 Recoil Dissolution

Atom displacements created within collision cascades can cause the atoms in a precipitate to be ballistically driven into the surrounding matrix, thus contributing to the dissolution of the precipitate. Nelson, Hudson and Mazey [2] developed a model (NHM) for recoil dissolution of precipitates that will be summarized here. For a displacement rate in the solid of K_0 dpa/s, the flux of atoms (atoms per unit area per second) from the precipitate surface can be written as ζK_0. For a spherical precipitate of radius r_p, the dissolution rate expressed as the rate of volume shrinkage is given by:

$$\frac{dV}{dt} = -4\pi r_p^2 \zeta K_0 \Omega \ , \tag{9.1}$$

where Ω is the atomic volume.

Dissolution by recoil re-solution of the solute is balanced by growth of the precipitate due to diffusion of the solute atoms to the precipitate. Even though the solute is being re-distributed between the precipitate and the matrix, the total concentration of solute, C is fixed, and can be expressed as:

$$C = 4/3\pi r_p^3 \rho C_p + C_s \ , \tag{9.2}$$

where ρ is the precipitate density and C_p is the concentration of solute in the precipitates and C_s is the concentration of solute in solution. The growth rate of precipitates due to the solute flux is given by:

$$\frac{dV}{dt} = \frac{3DC_s r_p}{C_p} \ , \tag{9.3}$$

where D is the solute diffusion coefficient.

The net growth rate of the precipitate is then the sum of terms due to recoil dissolution, Eq. (9.1) and precipitate growth due to diffusion of solute from solution, Eq. (9.3) and can be written as:

$$\frac{dV}{dt} = -4\pi r_p^2 \zeta K_0 \Omega + \frac{3DC_s r_p}{C_p} \ . \tag{9.4}$$

Substituting for C_s from Eq. (9.2) gives:

$$\frac{dV}{dt} = -4\pi r_p^2 \zeta K_0 \Omega + \frac{3DCr_p}{C_p} - 4\pi r_p^4 D\rho \ , \tag{9.5}$$

and writing Eq. (9.5) as a radial growth law gives:

$$\frac{dr_p}{dt} = -\zeta K_0 \Omega + \frac{3DC}{4\pi r_p C_p} - r_p^2 D\rho \ . \tag{9.6}$$

Equation (9.6) is plotted in Fig. 9.4 and shows that for small precipitate sizes, the growth rate is positive, but at larger sizes where the surface area becomes large, precipitates will dissolve. At the size dictated by zero growth rate, dissolution is balanced by re-precipitation. Note that the effect of irradiation is to result in a type

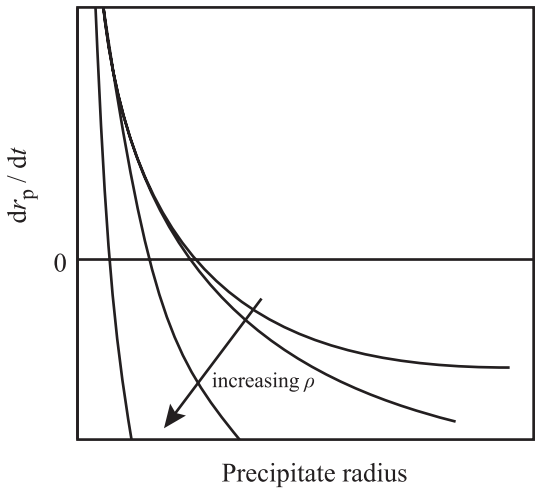

Fig. 9.4. Growth rates for precipitates undergoing irradiation-induced dissolution (from [2])

of *inverse* coarsening in which smaller particles are more stable than larger ones, which is opposite that which occurs by Ostwald ripening.

The solute concentration profile can be determined with the use of a cell model in which all precipitates are of the same size and each is in a matrix cell of radius, L with $4/3\pi L^3\rho = 1$. In the Wilkes model [3] re-solution deposits the solute atoms homogeneously throughout the cell and constitutes a *source* term in the steady state solution of the diffusion equation. Figure 9.5 shows the solute source term in the matrix surrounding the precipitate. The diffusion equation is $\dfrac{\partial C}{\partial t} = D\nabla^2 C + \zeta K_0$,

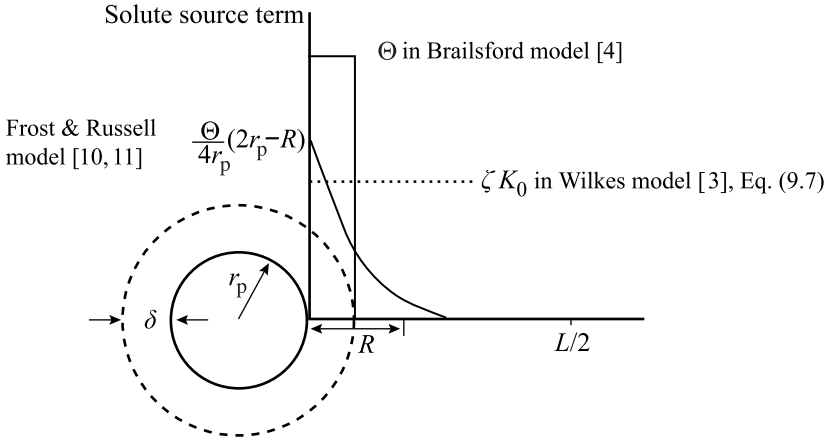

Fig. 9.5. Source terms for irradiation-induced re-solution of solute from the precipitate, according to various models. The term r_p is the precipitate radius, L is the precipitate spacing, R is the recoil radius in the Frost–Russell model [10, 11], and δ is the shell about r_p in the Brailsford model [4]

and subject to the boundary conditions: $\left.\frac{\partial C}{\partial r}\right|_{r=L} = 0$ at the cell boundary ($r = L$), and the solute concentration at the precipitate surface equals the equilibrium concentration, $C(r_\mathrm{p}) = C_\mathrm{e}$, the concentration is then:

$$C(r) = C_\mathrm{e} + \frac{\zeta K_0 r_\mathrm{p}^2}{2\Omega D(L^3 - r_\mathrm{p}^3)} \left[\frac{2L^3(r - r_\mathrm{p})}{r r_\mathrm{p}} - r^2 + r_\mathrm{p}^2 \right] . \tag{9.7}$$

The concentration profile of Eq. (9.7) is plotted in Fig. 9.6a and shows that the solute concentration rises from the precipitate boundary, r_p and levels out as it approaches the cell boundary, L. The steady state cell boundary concentration, $C(L)$ can be written as an excess concentration:

$$\begin{aligned} \chi &= \frac{2D\Omega}{\zeta K_0}(C(L) - C_\mathrm{e}) \\ &= L\frac{2(r_\mathrm{p}/L) - 3(r_\mathrm{p}/L)^2 + (r_\mathrm{p}/L)^4}{1 - (r_\mathrm{p}/L)^2} , \end{aligned} \tag{9.8}$$

and is shown in Fig. 9.6b as a function of precipitate-to-cell radius ratio (r_0/L). Note that for a fixed cell size the cell boundary concentration initially increases since the steady state solute supersaturation is increasing with precipitate surface area. When the precipitate is large, the precipitate surface is close to the cell wall and the back diffusion becomes significant, thus causing a reduction in the concentration. For most practical situations, the volume fraction of precipitate is small so that the precipitate size distribution is to the left of the peak in Fig. 9.6b. As a result, small precipitates will experience a net loss of solute until steady state is reached.

An improvement in the treatment of the source term in the simple NHM model is obtained by assuming that particles are spaced infinitely far from each other (dissolution–re-precipitation at one particle is unaffected by others), and that re-solution occurs at a uniform rate in a shell of thickness δ around the particle of radius, r_p (Fig. 9.5) [4]. For an initial precipitate size of r_0, the resulting size was found to be:

$$r_0^3 - r_\mathrm{p}^3 = \frac{3\delta^2 r_\mathrm{p}(3r_\mathrm{p} + 2\delta)}{8\pi D\rho_\mathrm{p}[(r_\mathrm{p} + \delta)^3 - r_\mathrm{p}^3)]} \left(-\frac{\Theta}{4\pi r_\mathrm{p}^2} \right) , \tag{9.9}$$

where Θ is the re-solution induced rate of precipitate volume change. The effect of irradiation in this model is to reduce the precipitate size from its original dimension by up to a factor of 2 [3]. Note that for the case where $\delta \to \infty$, the result reduces to that given in Eq. (9.6).

This result can be compared to the well-known thermal coarsening behavior of precipitates described by Wagner [5] and Lifshitz and Slyosov [6]:

$$\bar{r}_\mathrm{p}^3 - \bar{r}_0^3 = \frac{8DC_\mathrm{e}\gamma V_\mathrm{m}^2 t}{9\mathscr{R}T} , \tag{9.10}$$

where r_0 is the initial average precipitate radius, Ce is the solubility of the precipitate of infinite radius, V_m is the molar volume, γ is the particle-matrix interface

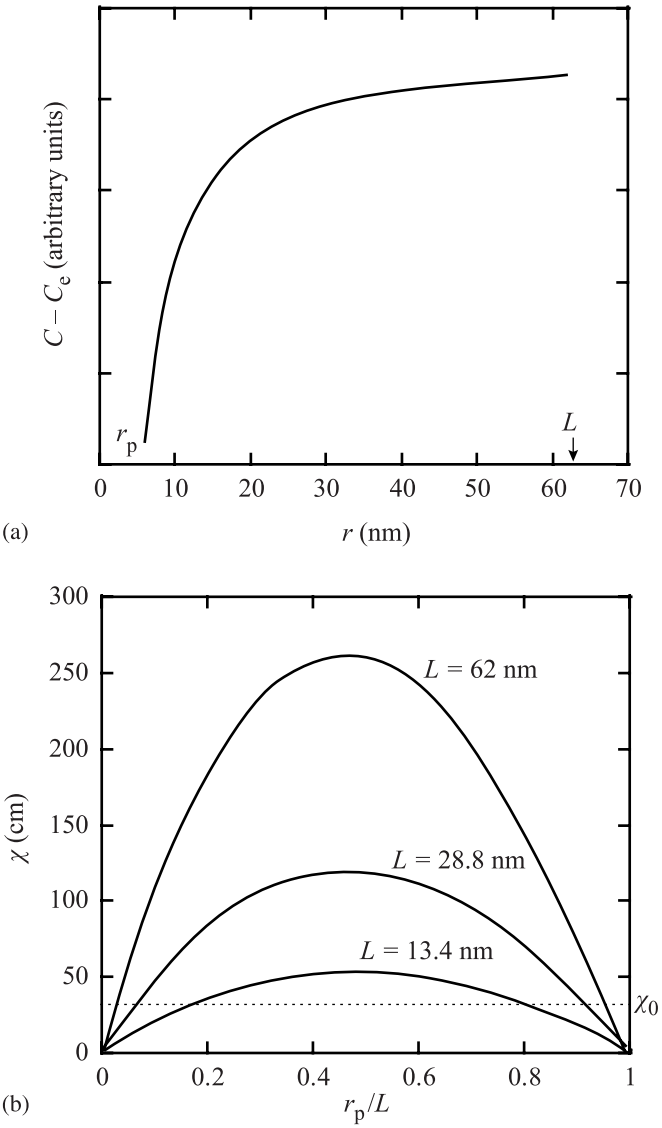

Fig. 9.6. (a) Steady state solute concentration in the matrix from Eq. (9.7), and (b) steady state boundary concentration from Eq. (9.8) (from [3])

energy and $\mathscr{R}$ is the gas constant. Accounting for irradiation-induced re-solution and irradiation-enhanced diffusion the maximum stable particle size [7, 8, 9] is shown to be:

$$r_{\max} = \left(\frac{3aD}{lfK_0} \right)^{1/2} , \tag{9.11}$$

where a is the lattice spacing, l is the linear dimension of the cascade, f is the fraction of solute atoms dissolved and the product lf is the shrinkage by re-solution [2]. When particles are initially larger than the maximum stable size, the maximum size decreases according to:

$$r_{\max}(K_0 t) - r_{\max}(K_0 t_0) = -lfK_0(t - t_0) \,, \tag{9.12a}$$

and when the initial particle sizes are much smaller than that given by the equilibrium size distribution, then the particle size increases according to:

$$r^3_{\max}(K_0 t) - r^3_{\max}(K_0 t_0) = 9aD(t - t_0) \,. \tag{9.12b}$$

Note that Eq. (9.12b) is similar to Eq. (9.10) for thermal coarsening.

A modification to the Wilkes's cell model is to provide a source term for the re-deposited solute that is more realistic than having it deposited uniformly in the cell (Wilkes [3]) or uniformly in a shell (Brailsford [4]). Frost and Russell [10, 11] model the rate of solute re-deposition in the matrix using the rate at which recoils originate in the matrix, which depends on the distance from the precipitate center, r according to:

$$G(r) = \frac{\Theta}{4rR}\left[r_{\mathrm{p}}^2 - (r - R)^2\right] \,, \tag{9.13}$$

where Θ is the re-solution rate per atom and R is the recoil distance (Fig. 9.5). Solving the diffusion equation with the spatially dependent source term, $G(r)$:

$$\frac{\partial C}{\partial t} = D\nabla^2 C + G \,, \tag{9.14}$$

gives:

$$\begin{aligned} C(r) = C_0 + \frac{\Theta}{48RD}\big[&r^3 - r_{\mathrm{p}}^3 - 4R\left(r^2 - r_{\mathrm{p}}^2\right) \\ &-6\left(r_{\mathrm{p}}^2 - R^2\right)(r - r_{\mathrm{p}}) - (3r_{\mathrm{p}} - R)(r_{\mathrm{p}} + R)^3\big]\left(\frac{1}{r} - \frac{1}{r_{\mathrm{p}}}\right) \,, \end{aligned} \tag{9.15}$$

and the maximum concentration is given by:

$$C_{\max} = C_0 + \frac{\Theta R^2}{12D}\left(1 - \frac{R}{4r_{\mathrm{p}}}\right) \,. \tag{9.16}$$

The maximum solute concentration is proportional to the re-solution rate and weakly dependent on the precipitate size.

The inverse coarsening rate of particles that are not of the same size can be determined by calculating the diffusion near each particle [10, 11]. The calculation assumes that the concentration at the edge of its cell is an average matrix concentration, and that there is no net flux to or away from a precipitate of some radius, r_{m} giving:

$$\frac{\mathrm{d}r_{\mathrm{p}}}{\mathrm{d}t} = \left(1 - \frac{r_{\mathrm{p}}}{r_{\mathrm{m}}}\right)\frac{1}{r_{\mathrm{p}}^2}\frac{L}{(L - r_{\mathrm{p}}^2)}\frac{\Theta R^3}{48} \,, \tag{9.17}$$

for which solutions exist depending on the value of r_m. Assuming that $r_p \ll L$ and the initial precipitate size is r_0, then:

$$\frac{r_p^3(t)}{r_0^3} = 1 + \frac{t}{\tau_A}\,, \quad \text{for} \quad r_p \ll r_m \quad \text{and} \quad \tau_A = \frac{48 r_0^3}{\Theta R^3}\,, \tag{9.18}$$

$$\frac{r_p^2(t)}{r_0^2} = 1 - \frac{t}{\tau_B}\,, \quad \text{for} \quad r_p \gg r_m \quad \text{and} \quad \tau_B = \frac{24 r_m r_0^2}{\Theta R^3}\,, \tag{9.19}$$

$$r_p - r_m = (r_0 - r_m)\exp(-t/\tau_C)\,, \quad \text{for} \quad r \cong r_m \quad \text{and} \quad \tau_C = \frac{48 r_m^3}{\Theta R^3}\,. \tag{9.20}$$

Note that the relation between the particle size and time is $r_p^3 \alpha t$ when the size is below r_m and $r_p^2 \alpha t$ when the size is greater than r_m. For all cases, when R, r_0 and r_m are of the order of 10 nm, t is between $10/\Theta$ and $100/\Theta$. For the case of fast reactor conditions, $\Theta \sim 10^{-7}$ dpa/s, so $10^8\,\text{s} \le t \le 10^9\,\text{s}$, which is equivalent to 3 to 30 years. Since the incubation time varies with r^3, larger precipitates would require even longer for inverse coarsening to occur. Consequently, irradiation-induced inverse coarsening by recoil re-solution is expected only after very long-term exposures.

The effect of irradiation on precipitate stability is shown schematically in Fig. 9.7 as a series of illustrations with increasing dose. Prior to irradiation, the precipitate is in equilibrium with the matrix solute concentration, C_e (Fig. 9.7a). Irradiation causes dissolution of the precipitate surface and an increase in the solute content near the interface that begins to diffuse away (Fig. 9.7b). Re-solution is balanced by re-precipitation and results in a steady state concentration profile (Fig. 9.7c). Local supersaturation of solute may lead to the nucleation of new precipitates in the matrix (Fig. 9.7d) or if the precipitates are very widely spaced, the matrix solute may not reach a value that results in steady state and the precipitate will continue to dissolve (Fig. 9.7e).

Determining the stability of a phase under irradiation is complicated by the influence of multiple parameters such as the displacement rate, temperature, and sink strength. An estimate for the stability of a precipitate can be obtained by considering two opposing processes, ballistic mixing and radiation-enhanced interdiffusion. This problem was analyzed by Abromeit [13] and the analysis is summarized here. Precipitates are assumed to be dissolved by ballistic mixing at a rate approximated by:

$$R_m = \beta \sigma_D \phi\,, \tag{9.21}$$

where the product of the displacement cross section, σ_D and the flux, ϕ is the displacement rate in dpa/s, and β is a factor that links displacement rate to solute loss from the precipitate. Similarly, the rate of formation or growth of a precipitate due to radiation-enhanced diffusion is given by:

$$R_g = \alpha \tilde{D}\,, \tag{9.22}$$

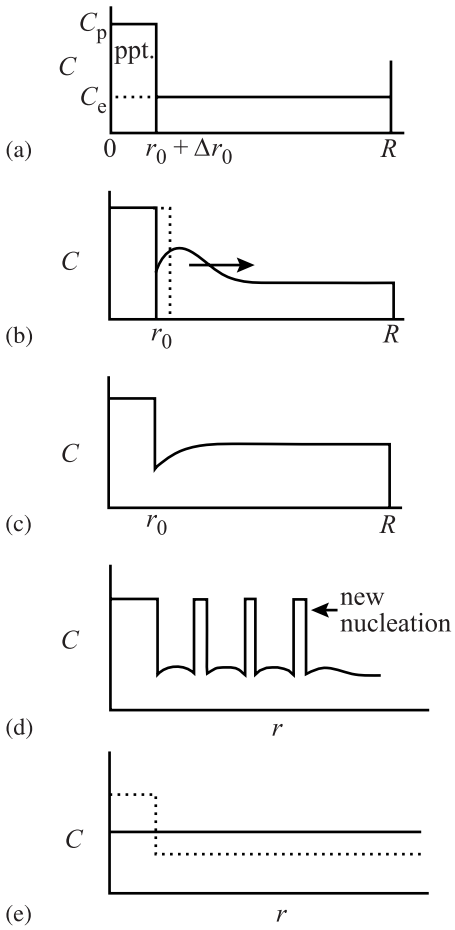

Fig. 9.7. Schematic illustration of radiation-induced precipitate dissolution and precipitation as a function of dose. (a) Unirradiated state, (b) surface dissolution at low dose, (c) steady state, and either (d) nucleation of new precipitates due to local solute supersaturation in the matrix, or (e) continued dissolution of the precipitate due to low precipitate density (from [12])

where α is a constant and $\tilde{D}$ is the interdiffusion coefficient. The solubility limit may be determined by equating the two processes, yielding:

$$\alpha\tilde{D} = \beta\sigma_{\mathrm{D}}\phi \; . \tag{9.23}$$

The steady state point defect balance equations are written as in Chap. 5:

$$\begin{aligned} &K_0 - K_{\mathrm{iv}}C_{\mathrm{i}}C_{\mathrm{v}} - D_{\mathrm{v}}k_{\mathrm{s}}^2 C_{\mathrm{v}} = 0 \\ &K_0 - K_{\mathrm{iv}}C_{\mathrm{i}}C_{\mathrm{v}} - D_{\mathrm{i}}k_{\mathrm{s}}^2 C_{\mathrm{i}} = 0 \; , \end{aligned} \tag{9.24}$$

and the variables are as defined in Chap. 5, where $K_{\mathrm{iv}} = 4\pi r_{\mathrm{v}} D_{\mathrm{i}}/\Omega$, and $k_{\mathrm{s}}^2 = 4\pi r_{\mathrm{s}} C_{\mathrm{s}}/\Omega$ is the sink strength. Note that in this analysis, no distinction is made in the sink strength for vacancies and interstitials.

When recombination dominates defect loss:

$$\tilde{D} = AK_0^{1/2} D_{\mathrm{v}}^{1/2} (\Omega/4\pi r_{\mathrm{v}})^{1/2} \; , \tag{9.25}$$

and when defect annihilation at sinks dominates, $\tilde{D}$ is temperature-independent and can be described as:

$$\tilde{D} = AK_0/k_s^2 \tag{9.26}$$

and A is a constant describing the transport efficiencies of the atoms via vacancies and interstitials. Eliminating $\tilde{D}$ from Eqs. (9.25) and (9.26) defines the boundary between the regimes where recombination is dominant and where annihilation at sinks is dominant and gives:

$$K_0 = k_s^4 D_v(\Omega/4\pi r_v) \, . \tag{9.27}$$

Equation (9.27) is shown by the plane, P_1 in Fig. 9.8 that plots the solubility as a function of damage rate, temperature and sink strength. Given that $\sigma_d\phi = K_0/N$ the contribution of defect annihilation at sinks to the solubility limit is determined by eliminating $\tilde{D}$ between Eqs. (9.21) and (9.26) and yields the critical sink strength:

$$k_c^2 = \mathrm{A}\alpha N/\beta \, . \tag{9.28}$$

Equation (9.28) is shown as the plane, P_2 in Fig. 9.8. Finally, according to Eqs. (9.23) and (9.25), a temperature-dependent boundary separates the two-phase from the one-phase regimes and is given as:

$$K_0 = (A\alpha N/\beta)^2 D_v \Omega/4\pi r_v \, , \tag{9.29}$$

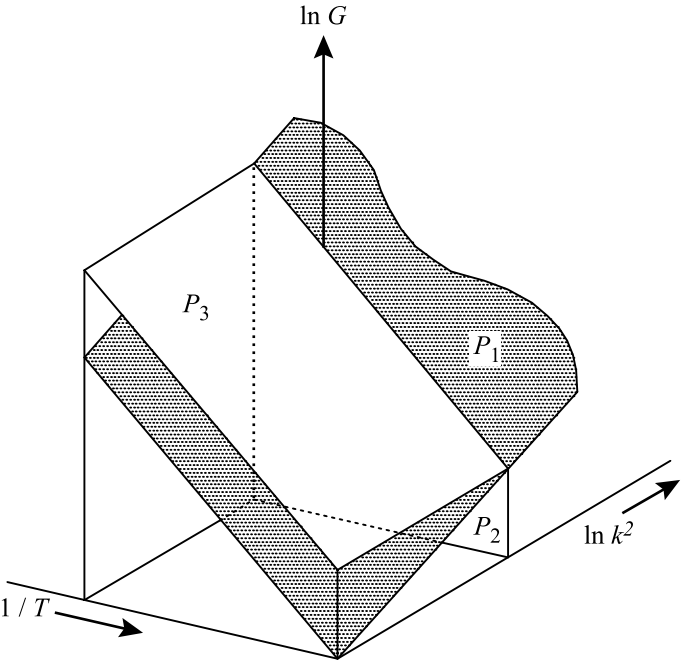

Fig. 9.8. Stability diagram for precipitates under irradiation in displacement rate-temperature-sink strength space. The plane P_1 separates recombination and annihilation regimes, and precipitates are stable below the plane P_3 and to the left of the plane P_2 (from [13])

and is shown as plane P_3 in Fig. 9.8. Precipitates are stable below P_3 and to the left of P_2. The region representing stability of the two-phase structure increases in size with increasing temperature due to increasing diffusivity and with increasing values of the critical sink strength, k_c^2.

The term β in Eq. (9.21) is approximated by $\beta = \beta_1 V_c/\Omega$, where β_1 is a constant and V_c is the volume of the collision cascade and is therefore proportional to the cube of the cascade radius, r_c [13]. Re-precipitation of the solute dissolved into the matrix by the cascade is controlled by interdiffusion with the rate constant given by Fick's law as $\alpha = 4\alpha_1/r_c^2$, where α_1 is a constant. Inserting these expressions for α and β into Eqs. (9.28) and (9.29) gives:

$$k_c^2 = \frac{3\pi A \alpha_1 \Omega N}{\beta_1} \frac{1}{r_c^5} , \tag{9.30}$$

$$K_0 = \left(\frac{A\alpha_1 N}{\beta_1}\right)^2 \frac{3D_v\Omega^3}{4\pi^3 r_v} \frac{1}{r_c^{10}} . \tag{9.31}$$

Note that both the critical sink strength and the production rate/temperature relationship exhibit a very strong dependence on the cascade size. The model was applied to the case of a Cu–48%Ni–8%Fe alloy irradiated with 300 keV Cu^+ ions over a range of temperatures and displacement rates. Figure 9.9 plots the primary recoil rate vs. $1/T$ with the open symbols denoting irradiation-induced dissolution of the two-phase structure. Note that there is a critical displacement rate for irradiation-induced dissolution that increases with temperature. The line in the graph is the optimal fit of Eq. (9.31) to the data, from which the cascade radius was determined to be ~ 2.7 nm.

In summary, radiation-induced dissolution is a key process affecting the stability of precipitates. Radiation results in re-solution of the precipitate outer surface and

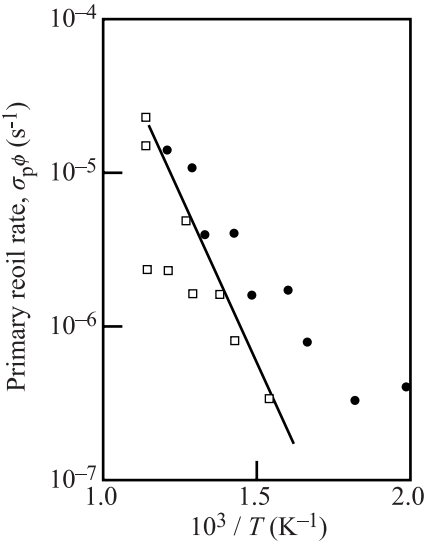

Fig. 9.9. Stability of the two-phase structure in Cu–48%Ni–8%Fe irradiated with 300 keV Cu^{++}. *Filled symbols* denote irradiation-induced disordering of the two-phase structure and *open symbols* denote no irradiation effect. The *line* is the best fit of Eq. (9.31) (from [13])

the evolution of the phase microstructure is then determined by the relative rates of re-solution and re-precipitation. In essence, phase stability is controlled by kinetic processes in the solid. Besides dissolution, precipitate stability is also affected by radiation-induced disordering, described in the next section.

9.3 Radiation Disordering

The NHM model described in the last section was originally developed for both recoil dissolution and disordering dissolution. Disordering involves the loss of long-range order due to irradiation. In the case of disordering, displacement is assumed to occur in a shell of thickness, l at the precipitate surface and result in the loss of solute atoms by diffusion to the matrix. It is also assumed that only a fraction, f of these solute atoms actually become dissolved. Defining $\xi = lf$ as the dissolution parameter, then the dissolution rate given in Eq. (9.1) becomes:

$$\frac{\mathrm{d}V}{\mathrm{d}t} = -4\pi r_{\mathrm{p}}^2 \xi K_0 \,, \tag{9.32}$$

and the rate of change of the precipitate size due to disordering dissolution is:

$$\frac{\mathrm{d}r}{\mathrm{d}t} = -\xi K_0 + \frac{3DC}{4\pi r_{\mathrm{p}} C_{\mathrm{p}}} - r_{\mathrm{p}}^2 D\rho \,, \tag{9.33}$$

which is identical to Eq. (9.6) except for the first term. Russell [14] points out that since $l \sim 10\,\mathrm{nm}$, then for $f \sim 1$, $\xi = lf \sim 10\,\mathrm{nm}$. Comparing this value to the corresponding term in Eq. (9.6) for recoil dissolution, where $\zeta\Omega \sim 10^{-4}\,\mathrm{nm}$, shows that the disordering dissolution rate is much higher than that due to recoil dissolution, so disordering dissolution is expected to be a much more effective process. Referring back to Fig. 9.4 shows that the stable precipitate size will be lower for disordering dissolution due to its greater efficiency.

Irradiation is known to disorder alloys by the creation of vacancies and interstitials and anti-site defects, in which the atoms are re-located to the complementary site, disrupting the order in the alloy. But disordered alloys will return to their equilibrium state as long as diffusion can occur. In fact, the high concentration of vacancies and interstitials produced by irradiation can enhance the ordering process by radiation-enhanced diffusion. Therefore, irradiation causes two opposing processes to occur: disordering and re-ordering. Liou and Wilkes [15] describe the rate of change of order in an alloy due to irradiation starting from the Bragg–Williams definition of long-range order for a binary alloy with atoms arranged on two sublattices, α and β, where the long-range order parameter is defined as:

$$S = \frac{(f_{A\alpha} - X_{\mathrm{A}})}{(1 - X_{\mathrm{A}})} \,, \tag{9.34}$$

where $f_{A\alpha}$ is the probability of an A atom being on an α lattice site, and X_{A} is the atomic fraction of A atoms. When $S = 1$, the alloy is completely ordered and when $S = 0$, the alloy is completely disordered.

Under irradiation, the rate of ordering can by written as a competition between radiation-induced disordering and thermal re-ordering:

$$\frac{\mathrm{d}S}{\mathrm{d}t} = \left(\frac{\mathrm{d}S}{\mathrm{d}t}\right)_{\mathrm{irr}} + \left(\frac{\mathrm{d}S}{\mathrm{d}t}\right)_{\mathrm{th}} . \tag{9.35}$$

The disordering rate due to irradiation can be written as:

$$\left(\frac{\mathrm{d}S}{\mathrm{d}t}\right)_{\mathrm{irr}} = -\varepsilon K_0 S , \tag{9.36}$$

where ε is the disordering *efficiency*, or the ratio of replacements to displacements, and is of the order 10–100 under neutron irradiation.

The thermal order-disorder transition can be written as a chemical reaction in which A and B atoms on the wrong lattice sites are interchanged so that the A–B pair is on the correct sites:

$$(A-B)_{\mathrm{wrong}} \underset{K_{\mathrm{w}}}{\overset{K_{\mathrm{c}}}{\rightleftharpoons}} (A-B)_{\mathrm{correct}} , \tag{9.37}$$

where the rate constants, K_{c} and K_{w} are given by:

$$K_{\mathrm{c}} = \nu_{\mathrm{c}} \exp(-U/kT) , \tag{9.38a}$$

$$K_{\mathrm{w}} = \nu_{\mathrm{w}} \exp[(-U+V_{\mathrm{T}})/kT] , \tag{9.38b}$$

where U is the energy barrier for the reaction and the activation energy, V_{T} is the energy reduction when the wrong A–B pair transforms to the correct A–B pair and the $\nu_{\mathrm{c,w}}$ are the frequency factors for the *correct* and *wrong* pairs, respectively. The solution of the chemical rate equations gives the following relation for the order parameter in terms of the equilibrium order parameter, S_{e} and the time, t:

$$\frac{(1-S)}{(1-S_{\mathrm{e}})} = \coth(k_{\mathrm{o}} t + y) , \tag{9.39}$$

where y is a constant and k_{o} is the rate constant defined as:

$$k_{\mathrm{o}} = \left[\nu_{\mathrm{v}} C_{\mathrm{v}} \exp(-E^{\mathrm{v}}_{\mathrm{m0}}/kT)(Z_\alpha + Z_\beta - 2) + \nu_{\mathrm{i}} \sigma C_{\mathrm{i}} \exp(-E^{\mathrm{i}}_{\mathrm{m0}}/kT)\right] (X_{\mathrm{A}}/X_{\mathrm{B}})^{1/2} \times Z_\beta \exp(-V_0/2kT) , \tag{9.40}$$

where $2\nu_{\mathrm{v}} = (\nu_{\mathrm{c}}\nu_{\mathrm{w}})^{1/2}_{\mathrm{v}}$ and $3\nu_{\mathrm{i}} = (\nu_{\mathrm{c}}\nu_{\mathrm{w}})^{1/2}_{\mathrm{i}}$ are the frequency factors for exchange by vacancies and interstitials, respectively, $E^{\mathrm{v}}_{\mathrm{m0}}$ and $E^{\mathrm{i}}_{\mathrm{m0}}$ are the vacancy and interstitial migration energies for ordering, Z_α is the number of α sites that are nearest neighbor to a β site and Z_β is the reverse, where α and β refer to the two sublattices, σ is a parameter accounting for the number of reaction paths and their probabilities and X_{A} and X_{B} are the atom fractions of A and B atoms, respectively. V_0 is the activation energy for ordering, $V_0 = AV$, where A is crystal structure dependent ($A = 6$

for fcc and $A = 14$ for bcc) and $V = V_{AB} - (V_{AA} + V_{BB})/2$, where the V_{XY} terms are the energies of the respective atom pairs. The time derivative of the thermal order parameter can be written as [15]:

$$\left(\frac{dS}{dt}\right)_{th} = \frac{k_o(1-S)^2}{(1-S_e)} - (1-S_e)k_o \,. \tag{9.41}$$

The steady state solution to Eq. (9.35), where the terms are given in Eqs. (9.36) and (9.41), is:

$$S = 1 + \varepsilon K_0 - \frac{(1-S_e)}{2k_o}\left(\varepsilon^2 K_0^2 + 4k_o^2 + \frac{4k_o \varepsilon K_0}{(1-S_e)}\right)^{1/2} . \tag{9.42}$$

Liou and Wilkes applied this formalism to the $AuCu_3$ system as a function of temperature and dose rate. Figure 9.10 shows that at any given temperature, the effect of increasing dose rate is a reduction in the order, as expected. Also, for a given dose rate, increasing temperatures results in greater order. Another way of showing the competing effects of irradiation and temperature on the alloy order is given in Fig. 9.11a. Here, the equilibrium value of S_e is 1.0, but the alloy is in a state where the order, $S_{observed}$ is less than S_e. At low temperature, where defect motion is restricted, the effect of irradiation is to disorder the alloy. At high temperature, the effect of irradiation is to increase defect mobility so that the order parameter approaches equilibrium, which lies above the original, incompletely equilibrated state. That is, irradiation assists ordering at high temperatures. This behavior is further illustrated by the example shown in Fig. 9.11b, which is a first-order transition of a solid solution alloy in the disordered α phase to an ordered α' phase. Under irradiation, the ordered phase becomes disordered at low temperatures, reverting to

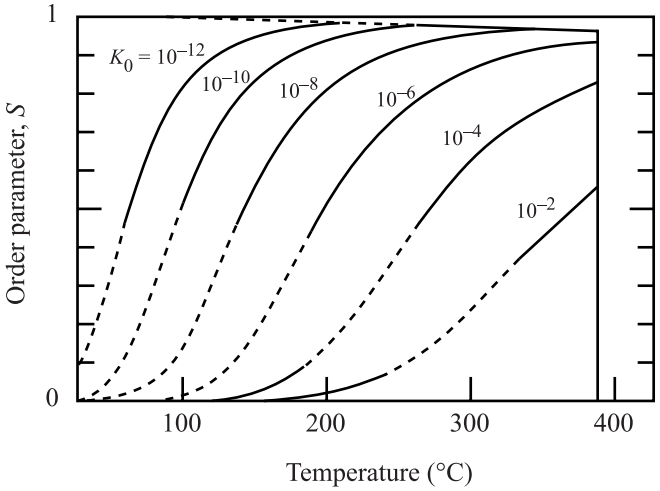

Fig. 9.10. Steady state long-range order parameter for Cu_3Au under irradiation for various dose rates (from [15])

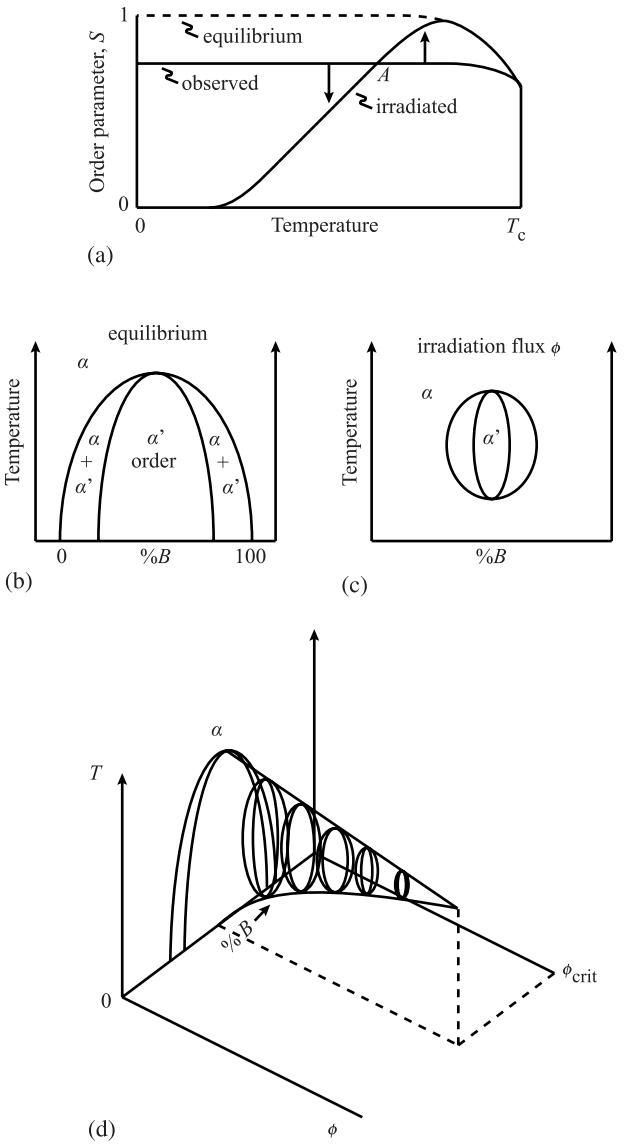

Fig. 9.11. (a) Effect of irradiation on the temperature dependence of the order parameter for a phase structure that is not at the equilibrium order, S_e. (b) Equilibrium phase diagram showing a first-order phase transformation of the disordered a phase to the ordered α'-phase. (c) Modification of the phase diagram by irradiation reflecting the change in order as given in (a). (d) Dependence on the irradiation-modified phase diagram with dose rate (from [3])

the α phase as shown in Fig. 9.11c. Since the degree of disordering is dependent on the dose rate, the shape of the phase fields shown in Fig. 9.11c will change at higher dose rate. The dependence of the phase fields on dose rate is shown schematically in Fig. 9.11d, in which the ordered region continues to shrink with increasing dose rate.

The change in the phase diagram caused by irradiation-induced disordering constitutes an irradiation modified phase transition as disordering can change the alloy phase structure. Recall that the ordered state is the arrangement of atoms that

minimizes the free energy of the solid. Consequently, radiation-induced disorder increases the free energy of the solid above the equilibrium value. Hence, under irradiation, a new free energy balance may be achieved between adjacent phases in the alloy. Figure 9.12 shows how the compositions of the α and γ phases determined by the common tangent of free energy curves can be changed when irradiation induces an increase in the free energy of the intermetallic β phase, resulting in a partially disordered phase, β'. Note that while the ordered β phase is in equilibrium with the α phase at a composition C_A, partial disordering by irradiation raises the free energy of the β phase to β' and the concentration of A in equilibrium with α and β' phases is now C'_A. Further irradiation can lead to complete disordering, β'' phase, such that the phase does not form. Note that order-disorder transformation energies are generally in the range of 0.1 to 0.6 eV/atom [16].

The effect of irradiation on ordering can also be understood with the aid of the thermal spike model of the cascade, discussed in Sects. 3.3 and 10.2.4. Recall that the energy density in the core of the cascade can reach values such that the region resembles a liquid-like structure. Wollenberger [12] determined the time dependence of the temperature in the cascade as a function of the distance from the center of the spike, where temperature is normalized to the disordering temperature, T_c and the result is shown in Fig. 9.13 for nickel. In this figure, r_c is the value of the cascade radius at which the temperature just reaches the disordering temperature at any time during the thermal spike, which in this case is 2.6 nm. As such, the temperature of the region inside this radius can be assumed to exceed T_c, resulting in disordering of the center of the cascade. Presumably, in the outer regions of the cascade where the temperature is below T_c but where the vacancy density is high, re-ordering will occur. In fact, when the re-ordered shell of a new cascade overlaps the disordered zone from an old cascade, the remaining disorder will be reduced, causing a reduction in the disordering efficiency per cascade with increasing fluence. The consequence of this overlap process is that the long-range order parameter will not completely vanish, even at high fluences.

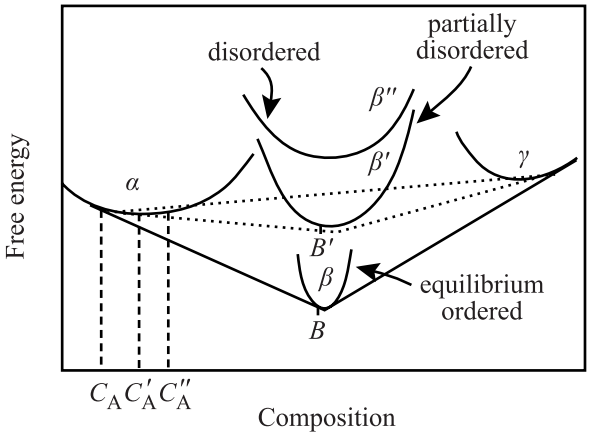

Fig. 9.12. Schematic illustration of a phase diagram for an alloy with an ordered intermetallic compound, β showing partial disordering to β', and complete disordering, β'' due to the increase in free energy caused by irradiation (from [14])

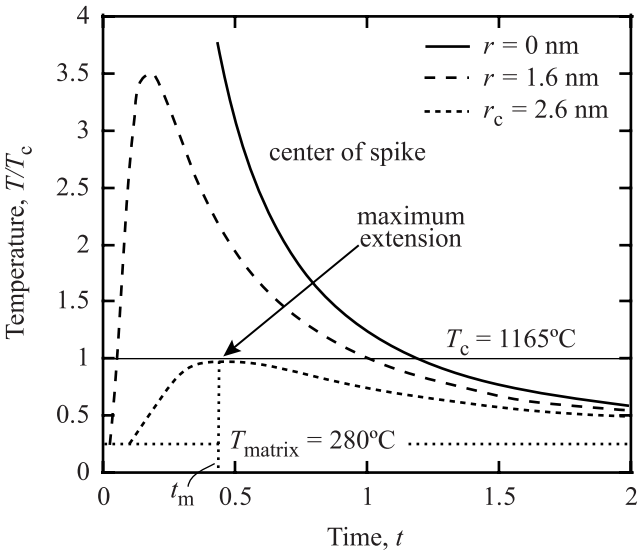

Fig. 9.13. Time dependence of the temperature of a thermal spike for different radial locations within the spike (from [12])

At low temperatures where vacancies are immobile, irradiation-induced disordering can occur very quickly in some systems. For example, the γ' phase ($L1_2$), $NiAl_3$, is extremely unstable under irradiation [17], becoming disordered following irradiation with 500 keV Kr at RT to a dose of 2×10^{14} i/cm^2 [18]. On the other hand, Fe_3Al (bcc) and FeAl (bcc-B2) undergo only partial disordering after 40 dpa of 2.5 MeV Ni^+ irradiation [19]. Hence, factors besides dose play a role in the order-disorder transformation reaction in alloys.

9.4 Incoherent Precipitate Nucleation

Irradiation can induce the formation of precipitates in an alloy. Precipitate growth and nucleation can be expressed as a *chemical* effect of vacancies and interstitials due to high levels of solute supersaturation under irradiation. The supersaturation provides the driving force for the reaction. Maydet and Russell [20] developed a model for the growth of spherical, incoherent precipitates under irradiation and that model is described here. The precipitate is characterized by two variables: the number of solute atoms, x and the number of excess vacancies, n, which is the difference in the number of matrix atoms displaced by the precipitate and x. Precipitates with greater atomic volume than the matrix must have $n > 0$ to relieve the strain energy, and undersized precipitates must have $n < 0$. The precipitate behavior is described by its movement in a phase space of coordinates n and x, much as was done with dislocation loops and voids in Chaps. 7 and 8. Figure 9.14 shows how the precipitate can move in phase space by capture of solute atoms, β_x, vacancies, β_v

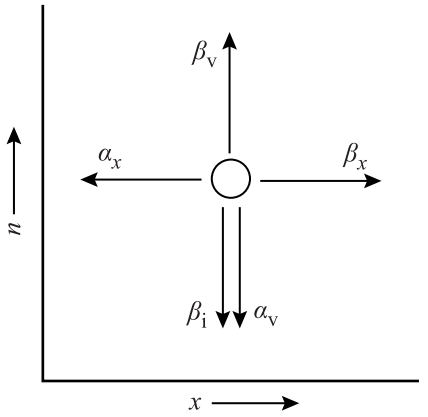

Fig. 9.14. Precipitate trajectories in (n,x) phase space showing the processes giving rise to its motion (from [20])

or interstitials, β_i, or the emission of solute atoms, α_x or vacancies, α_v. The particle moves in phase space with a velocity equal to the frequency of addition of solute or defect times the jump distance:

$$\dot{x} = \beta_x(n,x) - \alpha_x(n,x) \,, \tag{9.43}$$

$$\dot{n} = \beta_v(n,x) - \alpha_v(n,x) - \beta_i(n,x) \,. \tag{9.44}$$

The βs are determined from concentrations and diffusivities of the defects and solute and the αs are determined as follows.

As with void nucleation, there exists an energy barrier to the growth of the precipitate above some size, such that precipitates below this size equilibrate with each other and growth and shrinkage occur at the same rate. That is, the excess number of $(n,x-1)$-mer gaining a solute atom to become a (n,x)-mer is balanced by the reverse process. The same holds for the number of $(n-1,x)$-mer gaining a vacancy to become a (n,x)-mer. The equilibrium number of (n,x)-mer is then:

$$\rho_p^0(n,x) = \frac{1}{\Omega_m} \exp\left(-\frac{\Delta G_p^0(n,x)}{kT}\right) \,, \tag{9.45}$$

where Ω_m is the atomic volume of the matrix phase and $\Delta G_p^0(n,x)$ is the free energy of formation of a precipitate from n matrix vacancies and x solute atoms. The balance between $(n,x-1)$-mer and (n,x)-mer can be written as:

$$\beta_v(n-1,x)\rho_p^0(n-1,x) = \alpha_v(n,x)\rho_p^0(n,x) \,, \tag{9.46}$$

$$\beta_x(n,x-1)\rho_p^0(n,x-1) = \alpha_x(n,x)\rho_p^0(n,x) \,. \tag{9.47}$$

Substituting Eq. (9.45) into Eqs. (9.46) and (9.47) and replacing differences in $\Delta G_{\mathrm{p}}^{0}(n,x)$ by derivatives, gives:

$$\alpha_{\mathrm{v}}(n,x) \approx \beta_{\mathrm{v}}(n,x) \exp\left(\frac{1}{kT}\frac{\partial \Delta G_{\mathrm{p}}^{0}(n,x)}{\partial n}\right), \tag{9.48}$$

$$\alpha_{x}(n,x) \approx \beta_{x}(n,x) \exp\left(\frac{1}{kT}\frac{\partial \Delta G_{\mathrm{p}}^{0}(n,x)}{\partial x}\right), \tag{9.49}$$

where $\beta_{\mathrm{v}}(n-1,x)$ and $\beta_{x}(n,x-1)$ in Eqs. (9.46) and (9.47) vary slowly with n and x and have been replaced with their values at (n,x).

The free energy change upon formation of a precipitate from a solid solution that contains a supersaturation of solute and vacancies is given as:

$$\Delta G_{\mathrm{p}}^{0} = -nkT \ln S_{\mathrm{v}} + (36\pi\Omega^{2})^{1/3}\gamma x - xkT \ln S_{x} + \frac{\Omega E x(\delta - n/x)^{2}}{9(1-\nu)}, \tag{9.50}$$

where S_{v} is the vacancy supersaturation, S_{x} is the solute supersaturation, Ω is the atomic volume of the precipitate, $\delta = (\Omega - \Omega_{\mathrm{m}})/\Omega_{\mathrm{m}}$, γ is the matrix:precipitate surface energy, E is Young's modulus, ν is Poisson's ratio, and the remaining variables are as previously defined. The first two terms are the same as in the formation of a void from a supersaturation of vacancies given in Eq. (8.17) in which the first term is due to the vacancy supersaturation and the second term is the contribution of surface energy (with the number of solute atoms substituted for the number of vacancies in the aggregate). The third term reflects the effect of solute supersaturation, analogous to vacancy supersaturation, and the last term accounts for the elastic (volume) strain energy due to either an excess or deficit of vacancies from the stress-free condition (given by $\delta = n/x$). Substituting into Eqs. (9.48) and (9.49) for $\alpha_{\mathrm{v}}(n,x)$ and $\alpha_{x}(n,x)$ into Eqs. (9.43) and (9.44) gives:

$$\dot{x} = \beta_{x}(n,x) - \alpha_{x}(n,x) = \beta_{x}\left[1 - \exp\left(\frac{1}{kT}\frac{\partial \Delta G_{\mathrm{p}}^{0}}{\partial x}\right)\right], \tag{9.51}$$

$$\dot{n} = \beta_{\mathrm{v}}(n,x) - \alpha_{\mathrm{v}}(n,x) - \beta_{\mathrm{i}}(n,x) = \beta_{\mathrm{v}}\left[1 - \frac{\beta_{\mathrm{i}}}{\beta_{\mathrm{v}}} - \exp\left(\frac{1}{kT}\frac{\partial \Delta G_{\mathrm{p}}^{0}}{\partial n}\right)\right], \tag{9.52}$$

where from Eq. (9.50) the arguments of the exponents are determined to be:

$$\frac{1}{kT}\frac{\partial \Delta G_{\mathrm{p}}^{0}}{\partial x} = -\ln S_{x} + \frac{2Ax^{-1/3}}{3} + B(\delta^{2} - n^{2}/x^{2}), \tag{9.53}$$

$$\frac{1}{kT}\frac{\partial \Delta G_{\mathrm{p}}^{0}}{\partial n} = -\ln S_{\mathrm{v}} - 2B(\delta - n/x), \tag{9.54}$$

with $A = \dfrac{(36\pi\Omega^{2})^{1/3}\gamma}{kT}$ and $B = \dfrac{\Omega E}{9kT(1-\nu)}$.

The behavior of the precipitate in (n,x) space may be described by constructing nodal lines in (n,x) space along which $\dot{x}$ and $\dot{n}$ individually are set equal to zero as follows:

$$n = x\left[\delta + \frac{1}{2B}\ln\left\{S_{\mathrm{v}}\left(1-\frac{\beta_{\mathrm{i}}}{\beta_{\mathrm{v}}}\right)\right\}\right], \quad \text{for} \quad \dot{n}=0\,, \tag{9.55}$$

$$n = x\delta\left[1+\frac{2A}{3B\delta^2 x^{1/3}} - \frac{1}{\delta^2 B}\ln S_x\right]^{1/2}, \quad \text{for} \quad \dot{x}=0\,. \tag{9.56}$$

Figure 9.15 shows that the nodal lines in (n,x) space converge and cross at a critical point, beyond which they diverge. The critical point (n^*, x^*) is found by solving Eqs. (9.55) and (9.56) simultaneously to obtain:

$$x^* = -\frac{32\pi\gamma^3\Omega^2}{3(\Delta\phi)^3}, \quad \text{or} \quad r_{\mathrm{p}}^* = -\frac{2\gamma\Omega}{\Delta\phi} \tag{9.57}$$

$$n^* = x^*\left[\delta + \frac{1}{2B}\ln\left\{S_{\mathrm{v}}\left(1-\frac{\beta_{\mathrm{i}}}{\beta_{\mathrm{v}}}\right)\right\}\right], \tag{9.58}$$

where x^* and r_{p}^* are related by $x^* = \dfrac{4/3\pi r_{\mathrm{p}}^2}{\Omega}$, and the irradiation-modified free energy is given by:

$$\Delta\phi = -kT\ln S_x - \delta kT\ln[S_{\mathrm{v}}(1-\beta_{\mathrm{i}}/\beta_{\mathrm{v}})] - \frac{kT}{4B}[\ln S_{\mathrm{v}}(1-\beta_{\mathrm{i}}/\beta_{\mathrm{v}})]^2\,. \tag{9.59}$$

Figure 9.15 is constructed for the case where $\delta > 0$, that is an excess of vacancies relative to solute. Under this condition, the region above the $\dot{n}=0$ line contains an excess of vacancies and has a greater tendency for emission than capture, giving $\dot{n}<0$, or shrinkage. The opposite is true for the $\dot{x}=0$ nodal line in that the vacancy rich precipitate will increase its strain energy by solute emission, causing $\dot{x}<0$ and

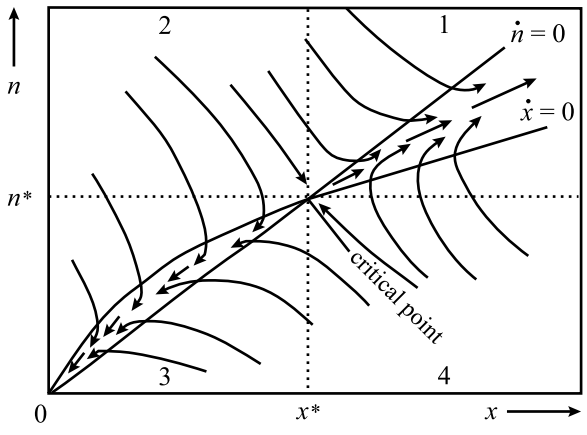

Fig. 9.15. Nodal lines, critical points and precipitate trajectories in (n, x) phase space for growth of an oversized, incoherent precipitate under irradiation (from [20])

supporting growth. As shown, particle growth is determined by the quadrants defined by the critical point. Precipitates grow in quadrant 1 and decay in quadrant 3 and behavior in quadrants 2 and 4 depend on the values of the capture terms. Precipitates that are between the nodal lines cannot escape. When with $x > x^*$, precipitates will grow and when $x < x^*$, they will decay. In general, irradiation will tend to stabilize a precipitate with $\delta > 0$ and destabilize ones with $\delta < 0$. Note that the unstable case of $\delta < 0$ means that $\Delta\phi > 0$, which can only occur if the first term in Eq. (9.59) is positive since the second term is always negative as long as $\beta_i/\beta_v < 1$. Physically, this means that since there is a *net* arrival of vacancies to the precipitate, those precipitates that need the vacancies to grow (e.g., an oversized precipitate, $\delta > 0$) will be stabilized by irradiation.

For an undersized precipitate phase ($\delta < 0$) to grow from a slightly supersaturated solid solution without prohibitive strain energy, the particle must emit vacancies into the matrix. In the absence of excess vacancies, this is easily done, as vacancies arrive at and leave the interface at the same rate (in the absence of growth or decay), and there is no trouble in establishing a net flux tout to allow growth. Under irradiation, the vacancy emission rate is not altered, but the arrival rate is increased by several orders of magnitude. It is then almost impossible to achieve a net emission of vacancies. There will instead tend to be a net gain of solute atoms in the face of the slight solute supersaturation. The excess vacancies thus destabilize the undersized precipitate phase. The same arguments may be used to understand stabilization of an oversized precipitate.

The potential function given in Eq. (9.59) has some of the properties of a free energy. It predicts whether precipitates of a given size will be stable under irradiation and provides the minimum stable precipitate size. In the absence of excess vacancies due to irradiation, $\Delta\phi$ in Eq. (9.59) becomes $\Delta\phi = -kT\ln S_x$, which is the Gibbs–Thompson equation. The effect of irradiation is to shift the effective free energy curve for the precipitate vertically by the amount $\delta kT\ln[S_v(1-\beta_i/\beta_v)]$. If $\Delta\phi < 0$, precipitates larger than x^* will be stable, and if $\Delta\phi > 0$, all precipitates will decay. Russell shows this schematically in Fig. 9.16. For this alloy, the θ phase is thermally stable and the ψ phase is not. The effect of irradiation is to destabilize the θ phase ($\delta < 0$) and stabilize the ψ phase ($\delta > 0$), by virtue of the sign of δ. Note that the order of stability is reversed by irradiation so that the θ phase would dissolve and the ψ phase would precipitate. The precipitation of the ψ phase under irradiation is an example of irradiation-induced precipitation in an undersaturated solid solution.

The nucleation rate of precipitates due to irradiation can also be estimated. The nucleation rate is the number of precipitate nuclei growing past a certain value of x per unit time and volume [22]. At steady state, the nucleation flux is independent of x, and the nucleation rate can be given at an arbitrary value of x as:

$$J_p(x) = \sum_{n=-\infty}^{\infty} [\beta_x(x)\rho_p(n,x) - \alpha_x(n,x)\rho_p(n,x+1)]\,, \tag{9.60}$$

and the summation converges rapidly for large values of n due to the effect of strain energy. Figure 9.17 shows how the nucleation rate varies with supersaturation of

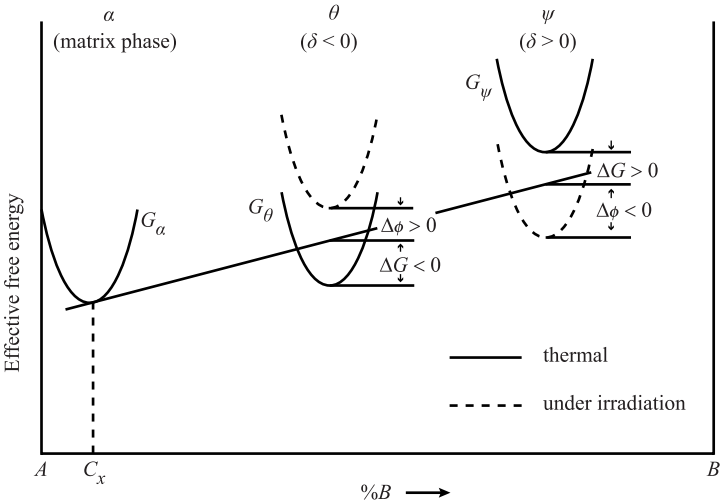

Fig. 9.16. Schematic phase diagram showing the effect of irradiation on the stability of incoherent precipitates in the case where the precipitate is thermally stable (θ) and thermally unstable (ψ) (from [21])

vacancies and solute in the Al–2%Ge system under irradiation. As expected, the nucleation rate increases with both S_x and S_v, but is more sensitive to S_x. Figure 9.17a shows the huge effect of excess vacancies alone on precipitate nucleation. Excess vacancies elevate the nucleation rate from infinitesimal to a high value giving a high precipitate density. Figure 9.17b shows that the effect of excess interstitials is to reduce the nucleation rate somewhat, but by factors small compared to the huge enhancements due to the vacancies. Irradiation is thus a tool for creating phases which otherwise might be impossible to obtain, and also for preventing the formation of phases that are otherwise stable.

9.5 Coherent Precipitate Nucleation

The preceding analysis applies for the precipitation of incoherent precipitates from a solid solution due to irradiation. We consider here the precipitation of *coherent* precipitates due to irradiation. The distinction between these two cases lies in the behavior of point defects at the precipitate surface. As shown in Chap. 8, incoherent precipitates behave like voids in that defects can be absorbed and emitted. However, the coherent precipitate interface acts as a defect trap such that the defect retains its identity. This feature has the result of reducing the problem of determining the energy change due to precipitation from a two-dimensional (n,x) problem to a one-dimensional (x) problem. Cauvin and Martin [23], as summarized by Russell [14] described the pseudo-equilibrium precipitate size distribution under irradi-

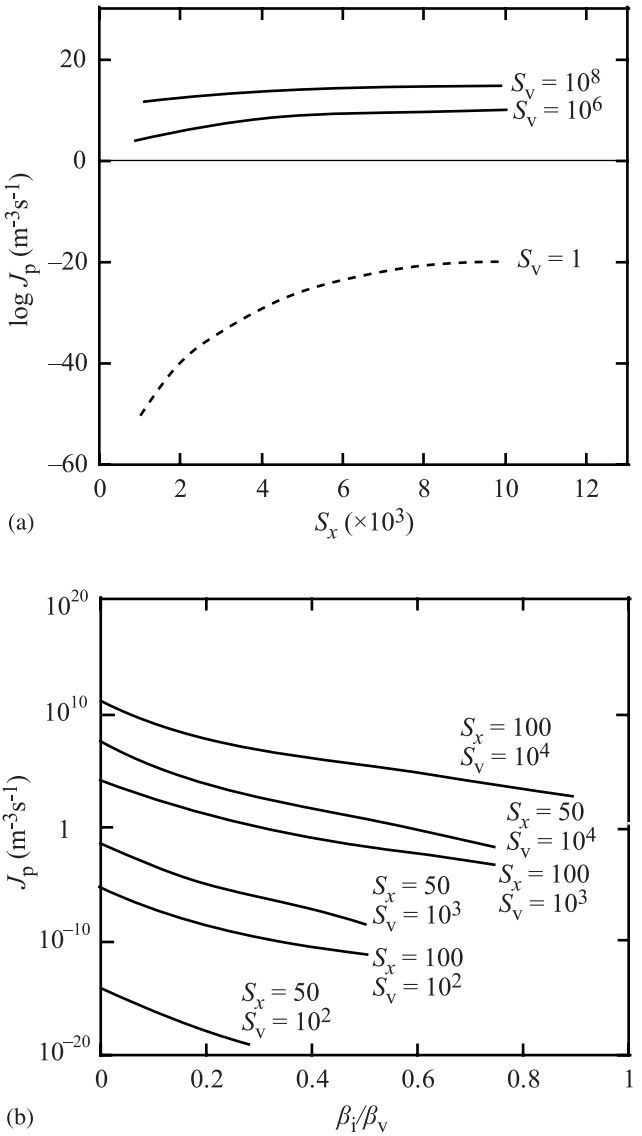

Fig. 9.17. (a) Dependence of nucleation rate on solute supersaturation for various vacancy supersaturation levels, based on a solid solution of Ge in Al at 23 °C. (b) Effect of interstitial–vacancy arrival rate ratio on the nucleation rate for several solute and vacancy supersaturation levels, based on a solid solution of Ge in Al at 123 °C (from [21])

ation, $\rho'(x)$ as:

$$\frac{\rho'(x)}{\rho'(x+1)} = \frac{\rho^0(x)}{\rho^0(x+1)} B(x) \,, \tag{9.61}$$

where $\rho^0(x)$ is the equilibrium size distribution in the absence of irradiation produced defects and $B(x)$ is defined by:

$$B(x) = \frac{\beta_{\rm v}(x)[\rho_{\rm v}(x) + \rho_n(x)] + \beta_{\rm i}(x)[\rho_{\rm i}(x) + \rho_n(x)]}{[\beta_{\rm v}(x) + \beta_{\rm i}(x)]\rho_{\rm t}(x)} \,, \tag{9.62}$$

where:

$\rho_{\rm i}(x) =$ number of clusters with trapped interstitials
$\rho_{\rm v}(x) =$ number of clusters with trapped vacancies
$\rho_n(x) =$ number of clusters with no trapped defects,
$\rho_{\rm t}(x) = \rho_{\rm i}(x) + \rho_{\rm v}(x) + \rho_n(x)$.

The quantity $B(x)$ is the fraction of solute arriving at the precipitate that does *not* result in defect annihilation. The thermal and irradiation-modified solubilities are related by: $C_{\rm irr} = C_0 B(\infty)$. In parallel with the equilibrium free energy, the pseudo-free energy, $\Delta G'(x)$ is given in terms of the pseudo-equilibrium precipitate size distribution, $\rho'(x)$ as:

$$\frac{\rho'(x)}{\rho'(x+1)} = \exp\left(\frac{1}{kT}\frac{\partial \Delta G'}{\partial x}\right) \,. \tag{9.63}$$

As with an unirradiated solid solution in which a metastable condition exists if $G(x)$ has a maximum in x, then $G'(x)$ must have a maximum in x for metastability in the irradiated state. Recalling that $\rho^0(x) = \exp(-G^0(x)/kT)$, then Eq. (9.61) can be rewritten using Eq. (9.63) as:

$$\frac{\partial G'(x)}{\partial x} = \frac{\partial \Delta G^0(x)}{\partial x} + kT \ln B(x) \,, \tag{9.64}$$

and $B(x)$ has one of two forms depending on the sign of the term, σ defined as:

$$\sigma = \frac{(1 - p_{\rm i}/p_{\rm v})}{(1 - \beta_{\rm i}/\beta_{\rm v})} \,. \tag{9.65}$$

where $p_{\rm i,v}$ is the probability of a particular trapping site being occupied by an interstitial or a vacancy. For either case, the value of B approaches a constant with increasing values of x, and in similar fashion for large x:

$$\frac{\partial \Delta G^0(x)}{\partial x} = -kT \ln S_x \,, \tag{9.66}$$

and Eq. (9.64) can be written as:

$$\frac{\partial G'(x)}{\partial x} = -kT \ln S_x + kT \ln B(x) \,. \tag{9.67}$$

Figure 9.18 shows the terms of the expression in Eq. (9.64) for the pseudo-free energy of the solid solution under irradiation for various values of σ. When $\sigma < 0$, if $-kT \ln B(\infty) > -kT \ln S_x$, then the solution will be metastable, as in Fig. 9.18a. If

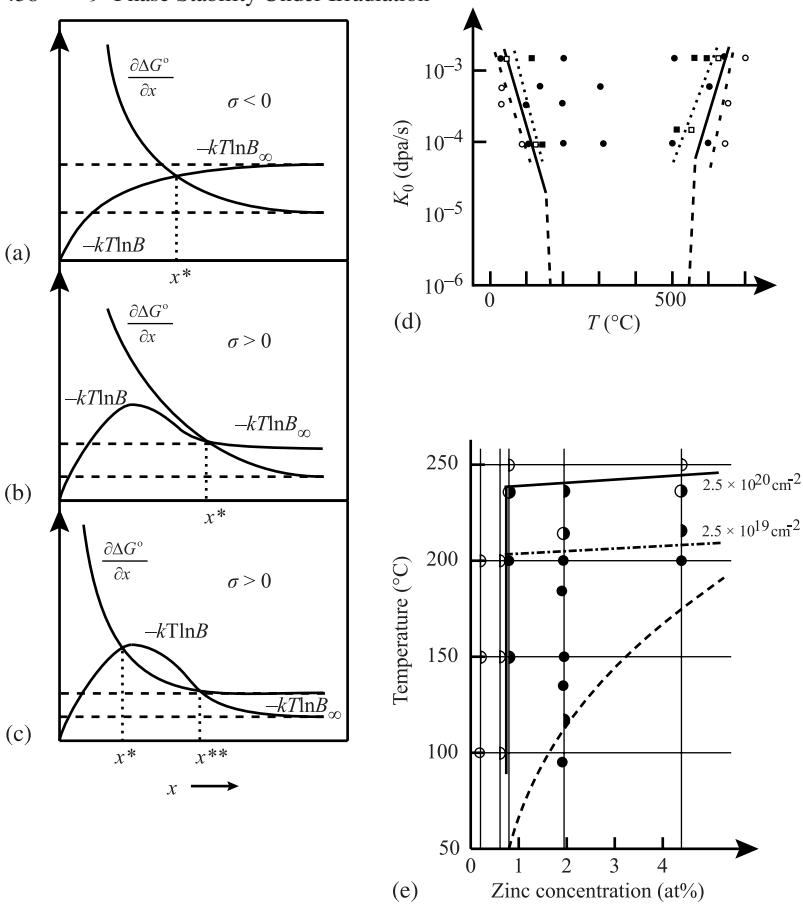

Fig. 9.18. Schematic illustration of stability altered by defect recombination at the particle-matrix interface. (a) $\sigma < 0$, 1 root. (b) $\sigma > 0$, 1 root. (c) $\sigma > 0$, 2 roots (from [23]). (d) Dose rate-temperature dependence of precipitation of Ni_3Si, γ' from undersaturated Ni–Si solid solution alloys irradiated with 1 MeV electrons, – Ni–6at%Si, Ni–4at%Si, – Ni–2at%Si. (e) Increase in temperature at which Zn rich clusters, or G.P. zones are stable with increasing irradiation dose rate by 1 MeV electrons over a range of Zn concentration in the Al–Zn phase diagram. *Half circles* to the *right* (*left*) indicate data at high (*low*) irradiation flux. *Full* (*open*) *symbols* indicated occurrence (absence) of irradiation-induced precipitation. *Dashed line* is the stability limit in the absence of irradiation (from [24])

$\sigma > 0$, then the solution to $\dfrac{\partial G'(x)}{\partial x} = 0$ may have 0, 1 or 2 roots. The solid solution is stable if there are 0 roots. With one root, the solution is metastable (Fig. 9.18b). But in the case of 2 roots (Fig. 9.18c) the solution is metastable below the value x^{**}, and the precipitate could never grow to large size. Note that in this model, irradiation will always decrease solid solubility.

Table 9.1. Irradiation-induced precipitation in undersaturated binary alloys (from [24])

Alloy	Projectile	Precipitate	Morphology
MgCd	e^-	Mg_3Cd	–
AlZn	n	β Zn	homogeneous precipitation
	e^-	G.P. zones and β Zn	homogeneous precipitation
AlAg	e^-	(100) Ag-rich platelets	homogeneous precipitation
NiBe	Ni^+	β NiBe	at interstitial dislocation loops
	e^-	β NiBe	homogeneous precipitation and at interstitial dislocation loops
NiSi	n	γ' Ni_3Si	at interstitial dislocation loops
	Ni^+	γ' Ni_3Si	"
	e^-	γ' Ni_3Si	"
	H^+	γ' Ni_3Si	coherent, triggered by inhomogenity of defect production
NiGe	e^-	γ' Ni_3Ge	at cavities and dislocation lines
CuBe	e^-	G.P. zones	homogeneous precipitation
	Cu^+	γ	at cascades
PdMo	Cu^+	M_o	at dislocation loops
PdFe	H^+	γ' Pd_3Fe	at dislocation loops
PdW	H^+N^+ e^-	bcc W	at dislocation loop s
WRe	n	WRe_3, W-Re	homogeneous precipitation
FeV	e^-	unidentified	homogeneous precipitation
FeCr	e^-	"	"
various ternaries	n, ions, e^-	changes of composition	–

A compilation of precipitates formed in undersaturated solid solutions due to irradiation is shown in Table 9.1. Note that precipitation can occur with many particle types and over large ranges of temperature and dose rate. The relation between these latter two variables is important and is highlighted in Figs. 9.18d,e. Figure 9.18d is constructed from 1 MeV irradiation of several undersaturated Ni–Si solid solution alloys and delineates the region of Ni_3Si, γ' precipitation from the solid solution, as shown by the filled circles. Figure 9.18e shows the dose dependence of solubility in Al–Zn. With increasing dose rate, formation of Guinier-Preston (GP) zones (Zn-rich clusters) in Al–Zn occurs at higher temperatures compared to the stability limit in the absence of irradiation (dashed line). Both of these examples show that irradiation of an undersaturated solid solution can lead to precipitation under irradiation at temperatures where the precipitate would not be thermally stable. They also underscore the strong coupling between temperature and dose rate in irradiation-induced precipitation.

In summary, irradiation can affect phase stability by numerous processes: solute enrichment or depletion, precipitate re-solution, precipitate disordering, and irradiation-induced nucleation of both incoherent and coherent precipitates. Irra-

diation can also induce the formation of phases that are not stable under equilibrium conditions or metastable phases. Metastable phase formation is discussed in the next section.

9.6 Metastable Phases

Since the term *metastable* implies a phase with a free energy higher than that of the stable phase under the prevailing conditions of temperature and pressure, it is natural to look to thermodynamics to explain their formation under irradiation. Experimental results seem to indicate a strong role of thermodynamics in the tendency to form metastable phases. Intermetallic compounds with small ranges of solubility and complex crystal structures are prime candidates for transformation to a metastable phase [19]. Also, the change in the free energy of the solid due to irradiation-induced defect buildup argues for a thermodynamic explanation [25]. However, not all transformations can be explained on a purely thermodynamic basis as solids under irradiation are generally far from equilibrium. Irradiation can be considered as similar to a quench process in which the atom configurations are essentially determined during the relaxation period following the collision events. At low temperatures, kinetics are restricted and the formation of complex crystalline structures is unlikely. Irradiation will usually result in solid solution, simple cubic structures or amorphous structures. The structure of the metastable system is, however, influenced by the equilibrium nature of the system. Those systems with many intermetallic compounds will form amorphous phases while those with no intermetallic alloys show a tendency to form solid solutions. At high temperature where atom mobility is significant, equilibrium phases will usually form.

Metastable phases can be formed by neutron irradiation or by ion irradiation, ion implantation and ion beam mixing. Differences in the transformation process between ion irradiation techniques can provide insight into the mechanism governing metastable phase formation. For example, in ion irradiation experiments, the main result of the radiation is imparting damage to the lattice. However, in ion implantation, the implanted species provides a chemical alteration to the target as well. Ion beam mixing experiments are designed to follow the transformation by rapidly (far from equilibrium) altering the bulk content of the film. Metastable phases formed by irradiation usually occur by one of four types of transformations [26]:

order → disorder
crystal structure transformation: A → B
crystal structure A → quasicrystal structure
crystal structure A → amorphous structure

The first three transformations will be briefly discussed and amorphization will be discussed in Sect. 9.7. For a more complete discussion of metastable phase formation, the reader is referred to [27].

9.6.1 Order–Disorder Transformations

The order-disorder transformation and its role in phase stability was discussed in Sect. 9.3. However, radiation-induced disorder has been linked to metastable phase formation. In fact, many compounds are believed to undergo chemical disordering prior to amorphization under electron irradiation. Luzzi and Meshii [28] showed that of 32 compounds irradiated, all underwent chemical disordering and 15 amorphized. They concluded that irradiation-induced chemical disordering provided the driving force for amorphization, and cited the difficulty in forming the amorphous structure in pure metals as support for this argument. The linkage between disordering and amorphization also depends on the irradiation conditions, in particular the mass of the particle and whether damage is introduced via Frenkel pairs (electron irradiation) or in cascades (heavy ion irradiation). Comparison of the enthalpy for the order-disorder transformation to that for the crystalline-to-amorphous transformation shows that $\Delta H_{\text{O-D}} \sim 5\Delta H_{\text{c-a}}$ [16]. So in fact, the enthalpy change for disordering may be sufficient to induce amorphization. The role of disordering in the onset of amorphization will be discussed in Sect. 9.7.

9.6.2 Crystal Structure Transformations

Numerous examples exist on the transformation from one crystal structure to another upon ion irradiation. One of the simplest examples is the transformation of pure nickel metal from fcc to hcp under irradiation. This transformation has been found to occur during irradiation with a variety of species including neutrons, chemically inert elements such as He and Ar, the metalloids P and As, as well as self-irradiation [29]. Observations on P-implanted high purity Ni [30] revealed an orientation relationship between the new hcp phase and the fcc matrix similar to that observed for martenistic fcc $\rightarrow$ hcp transformations. The transformation in Ni is thus believed to be martensitic. TEM examination of Sb-implanted Ni showed hcp particles extending 20 nm beyond the implanted depth, but dechanneling is present up to 130 nm, suggesting that the defect distribution is playing a role in the structure transformation.

Ion irradiation has also been found to induce phase transformations between bcc and fcc phases in iron-based austenitic alloys [31]. The most prominent example is the fcc-to-bcc transformation of 304 stainless steel following implantation with $3 \times 10^{16}\,\text{Fe}^{+}/\text{cm}^2$ at 160 keV. Although this dose amounted to an increase in the Fe alloy composition by only ~ 1 at% (67 at% Fe nominal), the structure transformed from fcc $\rightarrow$ bcc. The orientation relationship was neither the Kurdjumov–Sachs nor the Nishijima–Wasserman relationships typically found in ion-irradiated steels [31], but instead obeyed the following relationship:

$$(100)_{\text{bcc}} || (100)_{\text{fcc}} \quad \text{and} \quad [010]_{\text{bcc}} || [011]_{\text{fcc}} \,. \tag{9.68}$$

Follstaedt [32] suggested that the transformation need not be occurring martensitically, but that the increased defect concentration and hence, diffusivity, may be responsible for the transformation. It should also be noted that this transformation is

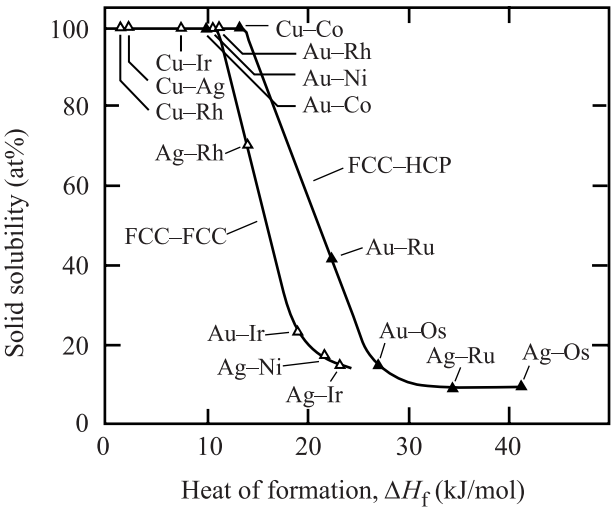

Fig. 9.19. Irradiation-induced solid solubilities for binary metal systems of positive heats of formation (from [33])

fundamentally different from that of nickel under irradiation in that the transformation is from the metastable state to the equilibrium structure, whereas in the case of Ni, the transformation is from the equilibrium fcc structure to a metastable hcp structure.

The heat of formation of an alloy can have a strong influence on whether a metastable phase forms. Figure 9.19 shows the irradiation-induced solubilities for several binary metal systems as a function of the heat of formation, ΔH_f. The samples were in the form of multilayers and were bombarded at 77 K by 400 keV Kr^+ ions. All systems had positive values of ΔH_f, meaning that in thermal equilibrium there is no, or only a limited miscibility of the components of the considered system. Note that the data points of the systems whose components have the same structures and of systems with components of different structure follow smooth curves. Both curves exhibit a rapid decrease from complete solubility to levels below 15 at% in a range of ΔH_f of about 12 kJ/mol. However, even at large values of ΔH_f, the solubility still has not disappeared.

Metastable solid solutions can also form by displacement mixing at temperatures at which radiation-enhanced diffusion is sufficiently slow to maintain the supersaturated solid solution phase. Ion beam mixing of multilayered Ag–Cu targets form a continuous series of metastable solid solutions across the phase diagram. Although the phase diagram of the Cu–Ag system is a simple eutectic one with rather small solubilities of Ag in Cu and Cu in Ag, irradiation produced a single phase, metastable solid solution with the fcc structure across the entire Cu–Ag system [34]. Since ion beam mixing takes place mainly in the solid state, extended solid solutions can be achieved in nearly immiscible systems such as Ag–Ni. Even in the binary Au–Fe and Au–V systems which have more complex phase diagrams exhibiting a large solubility gap and several intermetallic compounds, respectively, and the bcc structure at the Fe– and V-rich terminal solid solutions, metastable solid solu-

tions form across both systems during ion beam mixing [35]. In all cases, the lattice parameters of the solid solutions vary smoothly with composition and show small or moderate deviations from Vegard's law between the appropriate end-members.

9.6.3 Quasicrystal Formation

The most novel metastable phases are the quasicrystalline phases, produced by ion irradiation of specific Al alloys. These phases show long-range order, but possess forbidden crystalline symmetries such a five or sixfold symmetry. The phase was discovered by Shectman et al. [36] at the National Bureau of Standards. Quasicrystals have positional order, but are neither periodically nor randomly spaced; instead, they are quasiperiodically spaced. This means that, given the position of one unit cell, the positions of the other unit cells are determined according to a predictable but subtle sequence that never quite repeats. Because these structures are highly ordered like crystals but are quasiperiodic instead of periodic, they have been called quasiperiodic crystals, or quasicrystals for short.

The first quasicrystals formed by ion irradiation were in the Al–Mn system and examples extend into ternary and quaternary systems as well. In these initial experiments, the quasicrystal phase was formed by irradiating alternating layers of Al and Mn in the composition $Al_{84}Mn_{16}$ with 400 keV Xe ions to doses of $2–10 \times 10^{15}\,Xe/cm^2$ at 80 °C [37, 38]. Results showed that the icosahedral phase forms without a separate thermal treatment at or above 80 °C while the amorphous phase forms at 60 °C. The icosahedron is a regular polyhedron possessing twenty identical triangular faces, thirty edges and twelve vertices. The black pentagons on the surface of a soccer ball are centered on the vertices of an icosahedron. This observed dependence on sample temperature suggests that the icosahedral phase does not form within the dense ion cascade, but rather during subsequent defect evolution. Similar results have been achieved with freestanding Al–Fe multilayered samples [39], indicating that both multilayered and amorphous samples can be transformed to the quasicrystalline phase. In addition to temperature, the composition of the samples has an important effect on quasicrystal formation, establishing that quasicrystals are formed within a well-defined composition and temperature region.

9.7 Amorphization

Irradiation can induce the formation of amorphous phases in alloys. Although the phase space available to an alloy is extremely large, only one point corresponds to an absolute minimum in free energy. This point represents the equilibrium phase. Given sufficient time, at any temperature greater than zero, the system will find that point and settle into the equilibrium phase. Nonetheless, there are generally other minima in the free energy phase space, which are of varying depths. These other minima correspond to metastable phases. Certain of these phases exhibit compositional short-range order (CSRO) very similar to that of the equilibrium phase but with different compositional long-range order. Similarly, the spatial arrangements

of the atoms on a small scale (topological short-range order, TSRO) can be very similar to the equilibrium phase but with different long-range order (such as fcc vs. hcp phases). In general, there may exist many phases with CSRO and TSRO that are nearly identical to the equilibrium phase. Common examples of such metastable phases include glasses and crystalline solids with a slightly different unit cell than the equilibrium.

It has been suggested that in alloys with large negative heats of formation, disruption of chemical short-range order will lead to lattice destabilization and the formation of an amorphous phase [40]. In fact, the data on ion irradiation of intermetallic compounds supports just this sort of conclusion [22, 40]. Contradicting these observations are results of electron irradiation that show that complete long-range disordering often precedes the formation of an amorphous phase [26, 41]. For intermetallic compounds such as NiAl or FeTi, electron irradiation disorders but does not amorphize the compounds [42]. Irradiation with light ions produces much the same result as electron irradiation in that the amorphous phase is difficult to form, suggesting that disruption of CSRO is not adequate for lattice destabilization and that another mechanism must be responsible for amorphization such as topological disorder [42, 43, 44, 45, 46]. In fact, self-ion irradiation of Ni that induces a phase change from stable fcc to metastable hcp as discussed in Sect. 9.6, clearly has no chemical component and must be a result of the topological disorder introduced into the system by the Ni^+ beam. The next two sections discuss the roles of heat of compound formation, crystal structure differences, solubility range of intermetallic compounds and the critical defect density on the formation of the amorphous phase.

9.7.1 Heat of Compound Formation and Crystal Structure Differences

A good correlation exists between the heat of formation of a compound and the formation of amorphous phases in metal–metal systems [47], with large negative heats of formation tending to amorphize under irradiation. A plot of the ratio of the atomic radii vs. the heat of formation calculated using the Miedema model [48] shows where amorphization will occur (Fig. 9.20). In fact, alloys do not become amorphous if the heat of formation is greater than about $+10\,\mathrm{kJ/mol}$. However, the amorphous structure can be formed by ion mixing if the heat of formation is higher, e.g., Cr/Ag, Co/Cu, Fe/Cu and Co/Au. Specific compositions in the Au–Ir, Au–Ru and Au–Os systems, whose heats of formation range from $+19$ to $+27\,\mathrm{kJ/mol}$, were made amorphous by irradiation [33].

It has also been observed that crystalline phases of simple structures such as solid solutions or simple cubic structures form under irradiation, while amorphous phases are formed from more complex structures. This is explained by the short duration of the relaxation stage following the thermal spike. During the relaxation period, atoms attempt to re-arrange themselves. If the relaxation time is sufficient for precipitates to nucleate, crystalline phase formation may be achieved. The time required for nucleation is strongly influenced by the temperature, the crystalline structure of nuclei and the composition of the films that have been homogenized

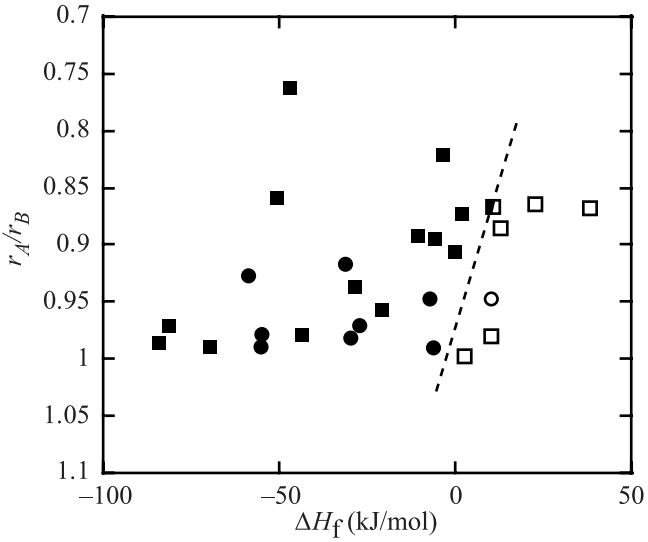

Fig. 9.20. Ratio of atomic radii vs. the heat of formation of an equiatomic compound (□ metal-metal crystalline, ■ metal-metal amorphous, ○ metal-metalloid crystalline, ● metal-metalloid amorphous) (from [47])

with thermal treatments or ion beams. If the overall composition is not close to a simple crystal structure in the equilibrium phase diagram and there is not a strong chemical driving force (as well as mobility) to promote significant atomic motion, then crystalline phase formation may be inhibited.

The role of structure difference in the propensity for irradiation-induced amorphization can be understood with the aid of a binary constitution diagram of an A–B alloy (Fig. 9.21a) a schematic free energy diagram for this alloy (Fig. 9.21b) and the corresponding polymorphic phase diagram (Fig. 9.21c) [49]. Note that the T_0 curves in Fig. 9.21c are obtained from the crossing of the solid free energy curve with that of the liquid (or amorphous) curve at a given temperature. The $T_{0\alpha}$ line defines the thermodynamic composition limits of the α-solution. When the concentration profile induced by mixing falls locally outside these limits, the α-solution is superheated with respect to the liquid (amorphous) phase and is not stable. Since melting is a local phenomenon not involving long-range diffusion, and since solids are not observed to withstand extensive superheating, it follows that observation of an α-phase outside these composition limits represents an unstable state. Such a state will likely melt or amorphize before thermal spike evolution is complete. This leads to the first fundamental rule for solid phase formation.

Johnson et al. [49] suggest that terminal solid solutions α and β can be formed up to the limits of the $T_{0\alpha}$ and $T_{0\beta}$ curves (i.e., within the polymorphic phase diagram limits of α and β). Solutions formed outside these limits are superheated and unstable against amorphization or melting. Secondly, intermetallic compounds with broad equilibrium homogeneity ranges (wide polymorphic limits in Fig. 9.21), and

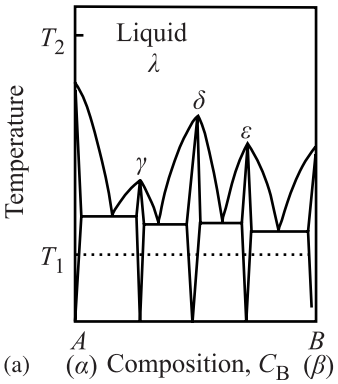

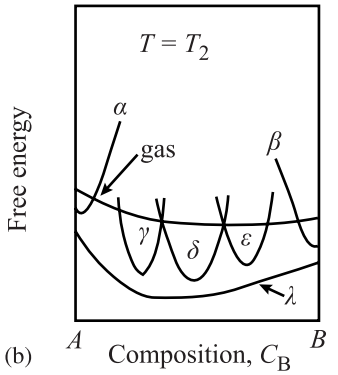

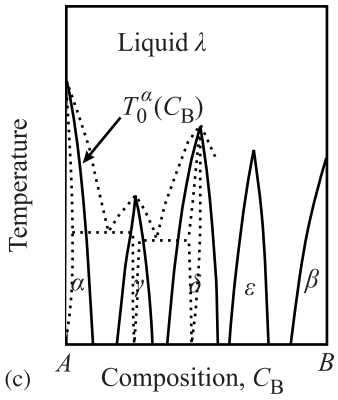

Fig. 9.21. (a) Binary constitution diagram of an A–B alloy. (b) Schematic free energy diagram for the alloy at temperature T_2. (c) Polymorphic phase diagram corresponding to the equilibrium phase diagram in part (a). The *dashed lines* show part of the original equilibrium diagram. *Solid lines* are representative T_0 lines of each phase. The T_0 lines define regions of polymorphic solid formation from the liquid state. Regions outside correspond to liquid or amorphous (polymorphic) states (from [49])

low-energy interfaces with α-solution or β-solution phases, may form in the prompt cascade provided that their respective growth kinetics allow high growth velocities. Compounds with narrow homogeneity range and complex chemically ordered unit cells should not form. Finally, amorphous phases are expected whenever the ion induced composition profile $C_B(z)$ lies outside the polymorphic limits of crystalline

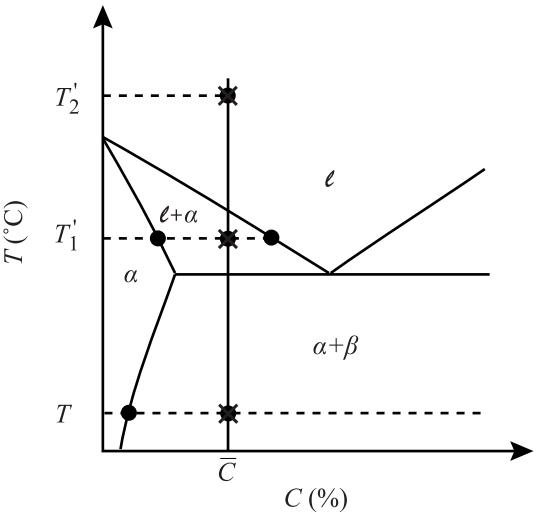

Fig. 9.22. Possible configurations of an equilibrium, two-phase alloy under irradiation at temperature T. Irradiation to an effective temperature, T_1' gives amorphous and crystalline phases of different composition, while more intense irradiation to an effective temperature, T_2' gives a single uniform amorphous phase (from [59])

phases. Amorphization may occur in addition when polymorphic limits permit compound formation but kinetics of compound formation or growth are slow.

Martin [50] proposed a theory for amorphization that is similar in nature to that of Johnson. In this model, he adds the ballistic radiation recoil re-solution displacement jumps to thermally activated jumps to obtain an irradiation-altered diffusion equation. The practical effect of irradiation is then to cause the system to assume the configuration at temperature T that would be stable at a temperature T' in the absence of irradiation: $T' = T(1 + D_B/D')$, where D' is the thermally activated diffusion coefficient and D_B is the diffusion coefficient including ballistic effects (Fig. 9.22). The theory predicts that irradiation of an equilibrium alloy of two solid phases at temperature T could raise the *effective* temperature to T_1', or under sufficiently intense irradiation to T_2'. At T_1' the irradiated alloy would at steady state be composed of amorphous and crystalline phases of different compositions. Irradiation intense enough to raise the effective temperature to T_2' would produce a uniform amorphous alloy.

9.7.2 Solubility Range of Compounds and Critical Defect Density

The tendency toward amorphization of the intermetallic compounds by irradiation correlates reasonably well with the degree of solubility within the phases. That is, alloys with limited solubility or a narrow compositional range show greater tendency for amorphous transformation. This correlation is also consistent with the concept that a critical energy or defect density must be created before the amorphous transformation can occur. If the total free energy of the defect crystalline state becomes greater than that of the amorphous state, a spontaneous transformation should occur. Associated with this critical free energy is a critical defect concentration. If this critical defect concentration can be reached under irradiation, then the crystal should

relax into the lower free energy (amorphous) state. This critical defect concentration has been estimated at 0.02 for silicon and germanium [51]. An estimate of the defect concentration required for amorphization can be made based on the increase in energy of lattice upon formation of a stable Frenkel pair. Each Frenkel pair will raise the energy of the alloy by an amount equal to the enthalpy of defect formation, $\Delta H_{\text{i-v}}$. The concentration of vacancy–interstitial pairs, $C_{\text{i-v}}$ needed to increase the energy of the alloy by $\Delta H_{\text{c-a}}$ can be estimated from the relationship:

$$\Delta H_{\text{c-a}} = C_{\text{i-v}} \Delta H_{\text{i-v}} \ . \tag{9.69}$$

The magnitude of $\Delta H_{\text{i-v}}$ for an fcc metal is approximately 5 eV, and $\Delta H_{\text{c-a}}$ is approximately 0.06 eV/atom [16], giving the critical vacancy–interstitial concentration for amorphization as ~ 0.01. However, such levels are not possible at reactor core component temperatures, but may be achievable in laboratory experiments conducted at temperatures where vacancies are immobile.

The link between defect density and degree of solubility can be understood by referring to the free energy diagram in Fig. 9.23. Compounds with no or limited compositional range will undergo a greater increase in free energy than those with wide compositional range. The greater increase in free energy is due to the inability of the compound to exist in equilibrium outside the designated composition range. This is manifest in the narrow and steeply rising free energy vs. composition curves. For ordered phases (intermetallics) the increase is not only due to point defects, but anti-site defects in regions of localized non-stoichiometry. This proposed solubility rule is very consistent with Johnson's thermodynamic analysis [49]. Note that for $NiAl_3$, only a slight deviation from stoichiometry is needed to result in a very large rise in the free energy. Therefore, the critical anti-site defect density would be low for $NiAl_3$ as compared to NiAl.

Anti-site defects may play a critical role in the amorphization process since calculations have shown that the critical defect density may be difficult to reach accounting for only point defects. However, since the defect concentration is strongly dependent on atom mobility and this is largely unknown in intermetallic compounds, accurate estimates of defect concentration are difficult to determine. Further, the critical defect density will be strongly temperature-dependent with higher concentrations required at higher temperatures.

Further support for the existence of a critical defect density is provided by the observation that compounds that become amorphous during irradiation do not show evidence of prior dislocation loop formation [25, 52]. Although it has been assumed that the attainment of a critical defect concentration will cause an amorphous transformation, the high free energy associated with the point defects can also be relieved through the formation of a dislocation structure through the collapse of interstitial or vacancy clusters into small loops. However, observations show that either a material transforms directly to the amorphous state or forms dislocation loops.

Since greater mobility is required for the formation of dislocation loops, and the maximum defect concentration associated with the nucleation of loops in irradiated metals is $\sim 10^{-4}$ [53], almost two orders of magnitude less than that for amorphization, indicates that defect mobility is a key factor in the amorphization process. This

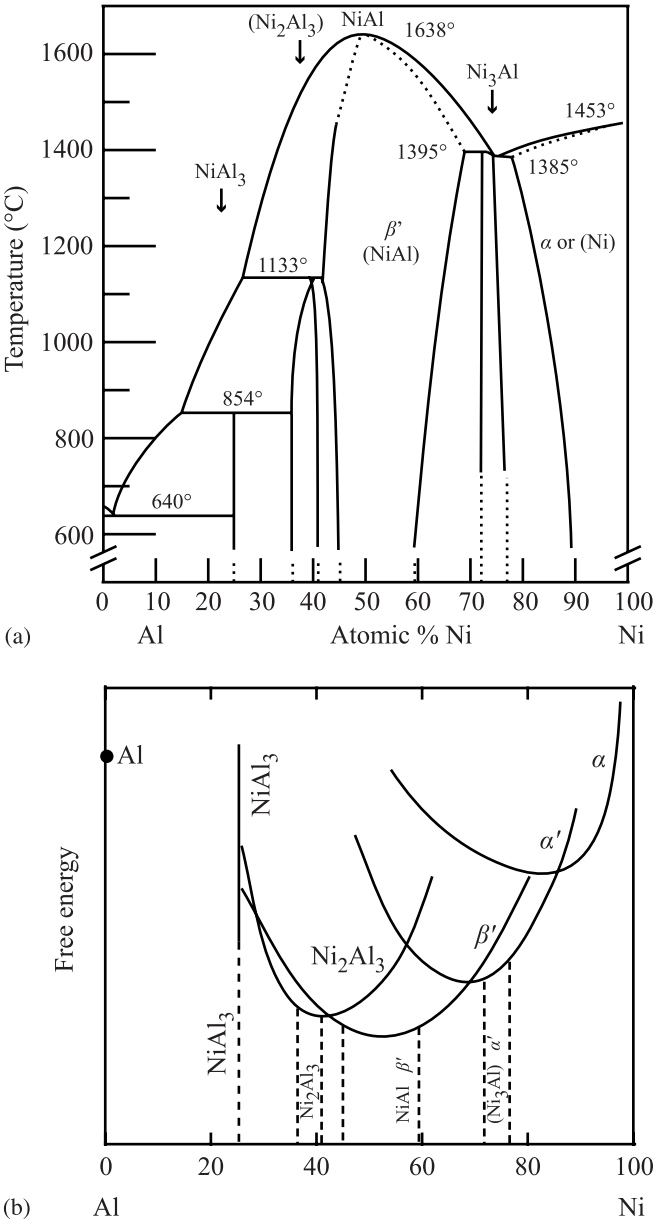

Fig. 9.23. Ni–Al phase diagram (a) with hypothetical free energy diagram (b) at the irradiation temperature (from [19])

observation is consistent with the ease of amorphization in intermetallics where defect mobility is low, and the preferential formation of dislocation loops in pure metals and solid solution alloys where the mobility is high.

9.7.3 Thermodynamics and Kinetics of Amorphization

In many respects, the C → A (crystalline-to-amorphous) transformation can be understood by relating it to melting by virtue of the similarity of these transformations. For example, amorphization is known to occur in a heterogeneous manner, similar to the first-order nucleation and growth process characteristic of melting. Also, Brillouin scattering studies have shown that intermetallics undergo a softening in the shear modulus, analogous to that observed at the onset of melting of many metals. As such, the C → A transformation can be considered to be a type of melting transformation. Okamoto et al. [54] wrote a comprehensive review of the physics of the crystalline-to-amorphous phase transformation. The role of irradiation in this transformation as presented in their paper is followed here.

The liquid to glass transition is characterized by a temperature called the glass transition temperature, T_g. The glass transition is not a thermodynamic phase transition, but rather the point in the relaxation process where configurational equilibrium can no longer be achieved during the experiment. In this regard, it is more of a kinetic parameter that depends on the time-scale of observation. Free energy plots of the glass transition for perfect and defected crystals are shown in Fig. 9.24. The perfect crystal is shown by the bottom line and the defected crystals, denoted by the dashed lines, have higher free energies. The melting temperatures are given by T_m^0 and T_m^d, respectively. Also shown are two glass transition temperatures, T_g corresponding to an unrelaxed glassy state and T_k corresponding to the ideal glass

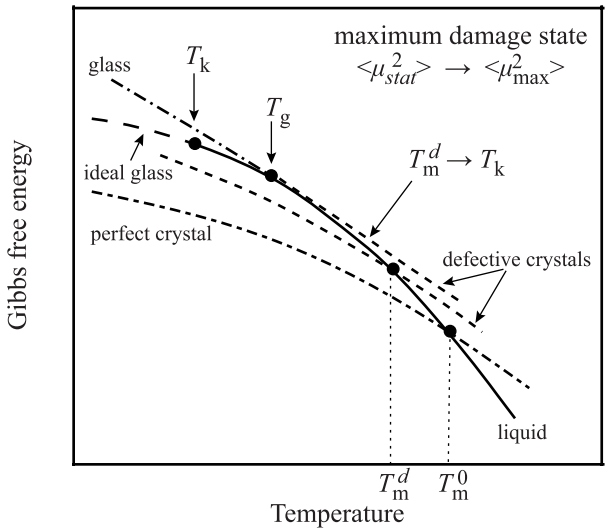

Fig. 9.24. Schematic plot of the Gibbs free energy as a function of temperature for a perfect crystal, the liquid phase and two defective crystalline states. T_m^0 and T_m^d are the thermodynamic melting temperatures of the perfect and defective crystals, respectively, T_g is the kinetic glass-transition temperature for the unrelaxed glassy phase and T_k is the ideal glass transition temperature (from [54])

transition temperature. Since the glass transition temperature is dependent on time, it is postulated that there exists some temperature, T_k below which the transition will never occur, and is known as the ideal glass temperature. Note that these points lie at a higher free energy than that of either the perfect crystal or the defected crystal.

As described by Okamoto et al. [54], one of the simplest models of melting is due to Lindemann [55] who proposed that crystals melt when the root-mean-square (rms) thermal displacement, $\langle \delta^2_{vib} \rangle^{1/2}$ of atoms from their equilibrium sites becomes large enough to encroach on nearest neighbors, or when the vibrational amplitude is about 50% of the interatomic spacing. Thus, melting occurs when $\langle \delta^2_{vib} \rangle^{1/2} / r_{nn}$ reaches a critical value equal to some fraction $\langle \delta^2_{crit} \rangle^{1/2} / r_{nn}$ of the nearest neighbor spacing, r_{nn}. In the harmonic Debye model of crystal lattices, the mean square thermal displacement for a perfect crystal at a temperature T above the Debye temperature, Θ_0 is:

$$\langle \delta^2_{vib} \rangle = \frac{36\pi^2\hbar^2 T}{Mk\Theta_0^2} , \tag{9.70}$$

where $\hbar$ is Planck's constant, k is Boltzmann's constant and M is the atomic mass. Since melting occurs when $\langle \delta^2_{vib} \rangle$ reaches some critical value. Then from Eq. (9.70) the melting temperature of the perfect crystal is:

$$T_m^0 = \frac{Mk\Theta_0^2}{36\pi^2\hbar^2} \langle \delta^2_{crit} \rangle . \tag{9.71}$$

The total mean-square atomic displacement is composed of thermal $\langle \delta^2_{vib} \rangle$ and static $\langle \delta^2_{stat} \rangle$ components, where the latter is due to defect structures such as point defects, anti-site defects, size mismatch between solute, solvent atoms in solid solution, defect clusters and impurities. The generalized form of the Lindemann melting criterion then becomes:

$$\langle \delta^2_{crit} \rangle = \langle \delta^2_{stat} \rangle + \langle \delta^2_{vib} \rangle , \tag{9.72}$$

where $\langle \delta^2_{crit} \rangle$ is a constant. Referring back to Fig. 9.24, this criterion shows that the crystal can be melted either by heating it to the melting point, T_m^0 ($\langle \delta^2_{vib} \rangle = \langle \delta^2_{crit} \rangle$) or by increasing the amount of static disorder, $\langle \delta^2_{stat} \rangle$ in the crystal until the free energy is equal to that of the liquid. As the damage level increases, the melting temperature of the defective crystal, T_m^d defined by the intersection of the free energy curve with that of the supercooled liquid, decreases, as shown in Fig. 9.24. The maximum damage state will occur when the free energy curve of the defective crystal is tangent to that of the supercooled liquid, shown as the upper most dashed line in Fig. 9.24.

The state of maximum damage, $\langle \delta^2_{vib} \rangle = \langle \delta^2_{crit} \rangle$, or where $T_m^d = 0$, is the theoretical upper limit for damage accumulation in a defective crystal. Figure 9.25 shows a polymorphous melting curve for a defective crystal in which $\langle \delta^2_{stat} \rangle$ represents the

sum total of the effect of all defects in the crystal. The linear region follows from Eq. (9.72). Along the melting curve, where $T = T_{\mathrm{m}}^{\mathrm{d}}$, Eq. (9.72) becomes:

$$\left\langle \delta_{\mathrm{crit}}^2 \right\rangle = \left\langle \delta_{\mathrm{stat}}^2 \right\rangle + \frac{36\pi^2\hbar^2 T_{\mathrm{m}}^{\mathrm{d}}}{Mk\Theta_0^2} \,, \tag{9.73}$$

which is written in the form of Eq. (9.71) as:

$$T_{\mathrm{m}}^{\mathrm{d}} = \frac{Mk\Theta_0^2}{36\pi^2\hbar^2} \left\langle \delta_{\mathrm{crit}}^2 \right\rangle \,, \tag{9.74}$$

where the Debye temperature of the defective crystal, Θ_{d} is given as:

$$\Theta_{\mathrm{d}}^2 = \Theta_0^2 \left(1 - \frac{\left\langle \delta_{\mathrm{stat}}^2 \right\rangle}{\left\langle \delta_{\mathrm{crit}}^2 \right\rangle} \right) \,. \tag{9.75}$$

In a perfect crystal, $\left\langle \delta_{\mathrm{stat}}^2 \right\rangle \to 0$, $\Theta_{\mathrm{d}}^2 \to \Theta_0^2$, and $T_{\mathrm{m}}^{\mathrm{d}} \to T_0^{\mathrm{d}}$. Note that Eq. (9.74) shows that the proportionality between the melting temperature and $\left\langle \delta_{\mathrm{stat}}^2 \right\rangle$, Fig. 9.25, is related to the Debye temperature given in Eq. (9.75). Also, since Θ_{d}^2 is proportional to the shear modulus, μ_{d}, the linear decrease in melting temperature also means that disorder-induced reduction of the shear modulus is occurring with the same functional dependence on $\left\langle \delta_{\mathrm{stat}}^2 \right\rangle$. From these proportionalities, we can

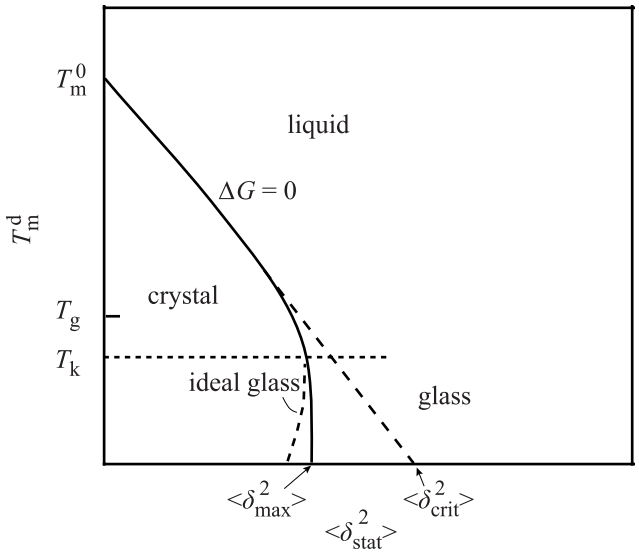

Fig. 9.25. Generalized T_0 curve showing schematically the effects of static atomic disorder as measured by $\left\langle \delta_{\mathrm{stat}}^2 \right\rangle$, on the melting temperature of the defective crystal, $T_{\mathrm{m}}^{\mathrm{d}}$. $\left\langle \delta_{\mathrm{max}}^2 \right\rangle$ and $\left\langle \delta_{\mathrm{crit}}^2 \right\rangle$ are the critical values of $\left\langle \delta_{\mathrm{stat}}^2 \right\rangle$ for thermodynamic and mechanical melting (from [54])

write:

$$\frac{T_{\mathrm{m}}^{\mathrm{d}}}{T_{\mathrm{m}}^{0}} = \frac{\mu_{\mathrm{d}}}{\mu_0} = \frac{\Theta_{\mathrm{d}}^2}{\Theta_0^2} = \left(1 - \frac{\langle \delta_{\mathrm{stat}}^2 \rangle}{\langle \delta_{\mathrm{crit}}^2 \rangle}\right) . \tag{9.76}$$

If it were possible to relate the defects created by irradiation to the mean square displacement in the solid, then we could use Eq. (9.76) to determine the amorphization criterion directly. Since this is not possible, there are two alternative ways of determining the amorphization criteria. One is through disordering and another is through free energy change.

Radiation-Induced Amorphization Driven by Disordering

Recall that in Sect. 9.6 we determined that the disordering energy should be sufficient to drive the C → A transformation. In fact, the chemical rate theory of radiation-induced order-disorder transformation can be used to determine the cut-off temperature, below which amorphization can occur. In this model [56], the rate of change in the long-range order parameter consists of a disordering term due to irradiation and a thermal re-ordering term, similar to that in Sect. 9.3:

$$\frac{\mathrm{d}S}{\mathrm{d}t} = -\varepsilon K_0 S + \nu \exp\left(\frac{-U}{kT}\right) \Big[C_{\mathrm{A}}(1-C_{\mathrm{A}})(1-S)^2 - \exp\left(\frac{-V}{kT}\right) \left(S + C_{\mathrm{A}}(1-C_{\mathrm{A}})(1-S)^2\right) \Big] \tag{9.77}$$

where U is the energy barrier for the A–B pair interchange, V is the ordering energy such that $V = V_{\mathrm{AB}} - 1/2\,(V_{\mathrm{AA}} + V_{\mathrm{BB}})$ where V_{AB}, V_{AA}, and V_{BB} are the bond energies for A–B, A–A and B–B pairs, respectively, and the remaining terms were defined in Sect. 9.3. The first term is the irradiation-induced disordering rate, and the second and third terms are the thermal re-ordering and disordering rates. An example of the variation of long-range order with temperature in the CuTi system is shown in Fig. 9.26 along with the variation of amorphization dose with temperature. Note that below about −53 °C, the order parameter drops to zero. This is the cut-off temperature, T_{C}, which coincides with the onset of amorphization, $T_{\text{c-a}}$. Just above the cutoff temperature, $\mathrm{d}S/\mathrm{d}t$ is ~ 0 and the relationship between the cutoff temperature and the damage rate, K_0, can be written by setting $\mathrm{d}S/\mathrm{d}t$ in Eq. (9.77) to zero:

$$\varepsilon K_0 S_0 = \nu \exp\left(\frac{-U}{kT_C}\right) \Big[C_{\mathrm{A}}(1-C_A)(1-S_0)^2 - \exp\left(\frac{-VS_0}{kT}\right) \left(S_0 + C_{\mathrm{A}}(1-C_{\mathrm{A}})(1-S_0)^2\right) \Big] , \tag{9.78}$$

where S_0 is the steady state value of the long-range order parameter. For typical values of V, the exponent inside the square brackets is of the order 10^{-5} to 10^{-21} and so the second term can be neglected, and the expression in Eq. (9.78) can be solved

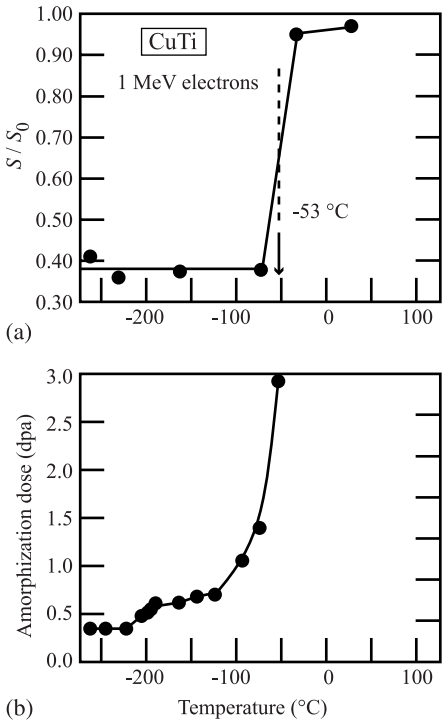

Fig. 9.26. Temperature dependence of (a) The long-range order parameter S/S_0, and (b) the critical amorphization dose for CuTi, irradiated with 1 MeV electrons (from [54])

for T_C:

$$T_C = U\left[k\ln\left(\frac{\nu C_A(1-C_A)(1-S_0)^2}{\varepsilon K_0 S_0}\right)\right]^{-1}. \tag{9.79}$$

Equation (9.79) gives an estimation of the cutoff temperature, or the $T_{c\text{-}a}$ temperature for a solid under irradiation. Note that it depends on the displacement rate and also on the number of replacements per displacement, ε. As such, the temperature at which amorphization will occur will depend on the irradiating particle and the dose rate. Figure 9.27 shows a schematic illustration of the temperature dependence of the critical dose for amorphization for various types of charged particles. $T_{c\text{-}a}$ is the temperature below which complete amorphization can be achieved. $T_{a\text{-}c}$ is the temperature beyond which the crystalline compound cannot be amorphized and is independent of irradiation conditions, and T_{th} is the thermal re-crystallization temperature. Okamoto et al. [54] describe the main kinetic features of irradiation-induced amorphization as follows:

– For a specified particle and dose rate, there is a temperature at which the two competing processes of damage production and recovery just balance. Below that temperature, damage production dominates recover and the crystal can be completely amorphized.

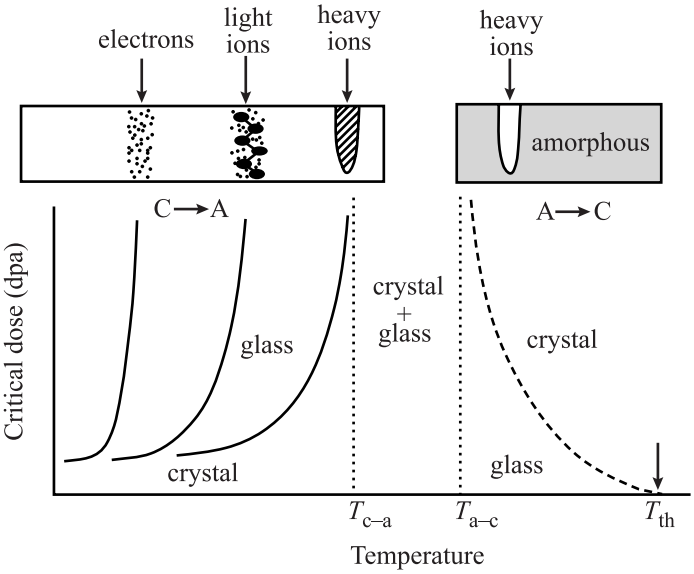

Fig. 9.27. Schematic illustration of the temperature dependence of the critical dose for amorphization for irradiation by various types of particles (from [54])

- Amorphization occurs homogeneously at low temperature, far from the critical dose rate and temperature. Heterogeneous amorphization occurs near the cutoff temperature.
- For fixed dose rate, T_{c-a} increases with increasing particle mass.
- T_{c-a} is a kinetic parameter that depends on the irradiation variables such as dose rate. Higher dose rates shift $T_{c\text{-}a}$ to higher values.
- There is a temperature, T_{a-c} above which amorphization is impossible. T_{a-c} depends on the target temperature but not irradiation variables.
- Between T_{a-c} and T_{th}, irradiation can induce the A → C transformation and the dose required for the transformation is dose-dependent.

Figures 9.28a,b show two examples of the temperature dependence of irradiation-induced amorphization in NiAl and NiTi, respectively. Figure 9.29 shows how T_{c-a} varies with particle type at nearly equal dose rates. Clearly, irradiation with heavy ions can induce amorphization over a much larger temperature range than is possible by irradiation with electrons because the ions can transfer much more energy in a much smaller volume than can electrons. While electron irradiation in the ∼ MeV range produces isolated displacements (single Frenkel pairs), heavy ion irradiation results in cascades in which the effective displacement rate is high such that the damage rate outweighs the recovery rate.

Relating the ordering process to the mean square static displacement, Okamoto et al. [54, 57] show that:

$$\left\langle \delta^2_{\text{stat}} \right\rangle \alpha (1 - S^2) \,, \tag{9.80}$$

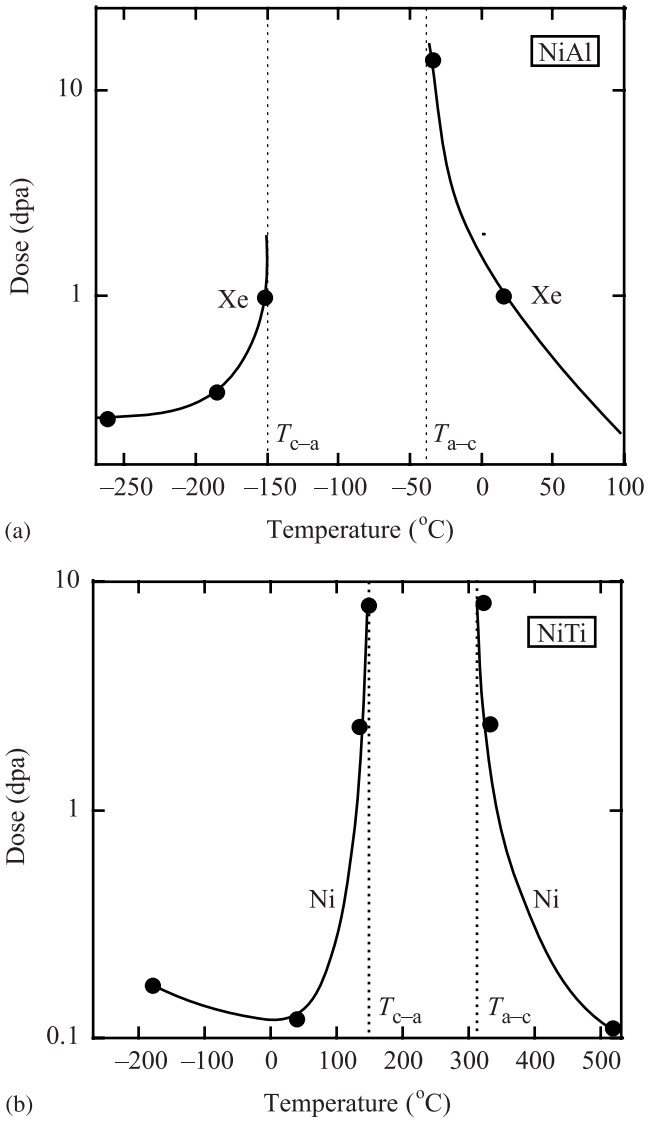

Fig. 9.28. Temperature dependence of the total displacement dose for ion-induced amorphization and crystallization of (a) crystalline and amorphous NiAl, and (b) crystalline and amorphous NiTi (from [54])

and since from Eq. (9.75), $\langle \delta^2_{\text{stat}} \rangle$ is proportional to the shear modulus, μ, then $\mu\alpha(1 - S^2)$. Figure 9.30 shows that amorphization of Zr_3Al occurs very near to the point where the straight line fit through data crosses the horizontal line for the amorphous alloy, showing that the onset of amorphization is related to a critical

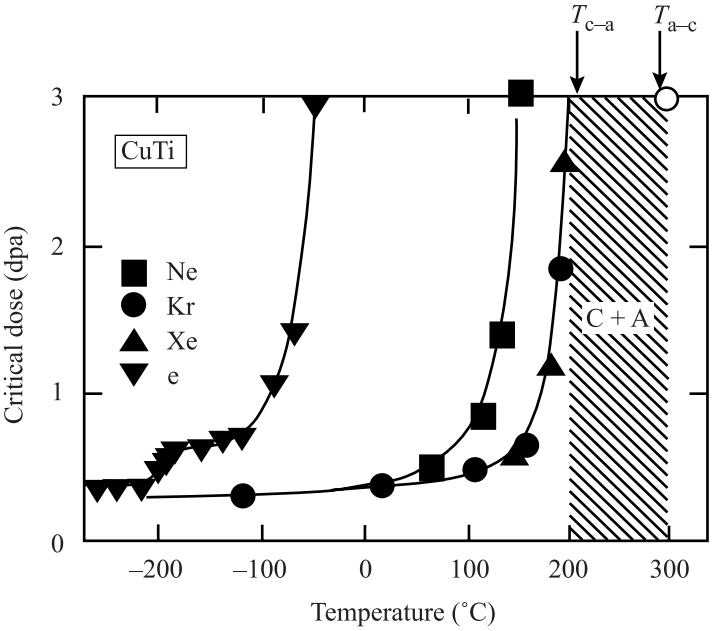

Fig. 9.29. Temperature dependence of the critical amorphization dose for CuTi during irradiation with 1 MeV electrons and 1 MeV Ne, Kr and Xe ions, all at a dose rate of 10^{-3} dpa/s (from [54])

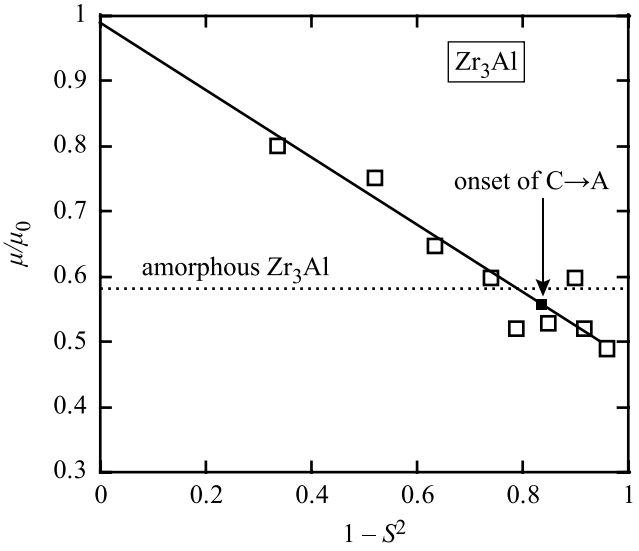

Fig. 9.30. Relative change in the shear modulus with increasing degree of disorder $(1 - S^2)$ in 1 MeV Kr^+ irradiated Zr_3Al. The *dashed line* represents the relative shear modulus in the amorphous phase, and the *vertical arrow* indicates the onset of amorphization (from [54])

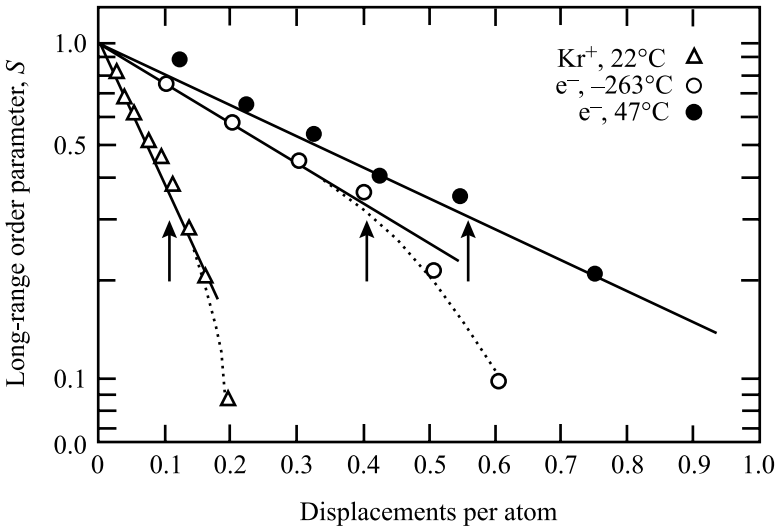

Fig. 9.31. Damage-dose dependence of the long-range order parameter, S in Zr_3Al during irradiation with 1 MeV electrons at 10 K and 320 K and with 1 MeV Kr at 295 K (from [54])

value of the mean-square chemical disorder $(1 - S^2)$ and from Eq. (9.80), the mean square static displacement. Another example of the role of disorder in amorphization is shown in Fig. 9.31 which gives the dose dependence of S for Zr_3Al during irradiation with 1 MeV electrons at two temperatures, and ions at 22 °C. The onset of amorphization is shown by the arrows, and although it occurs at different doses for the different particles and irradiation temperatures, the value of the order parameter is about the same. The significance of this observation is that while disordering kinetics differ between particles and temperatures, amorphization depends only on the magnitude of S and not how it is reached. Figure 9.32 [54, 57] shows an additional example of the correlation between the onset of amorphization and the rms static displacement for case of B implantation into Nb. When the mean square static displacement reaches a critical value, amorphization occurs.

Radiation-Induced Amorphization Driven by Free Energy

Amorphization can also be explained by considering the free energy of the transformation, as explained by Motta et al. [58, 59] and summarized here. The criteria for amorphization is that the free energy change upon irradiation, ΔG_{irr} must be greater than that for the C $\rightarrow$ A transformation, ΔG_{ac}:

$$\Delta G_{\text{irr}} \geq \Delta G_{\text{ac}} \, . \tag{9.81}$$

The term ΔG_{irr} includes all of the defects created by irradiation and can be written as the sum of terms representing chemical disordering, ΔG_{dis} and all other defects,

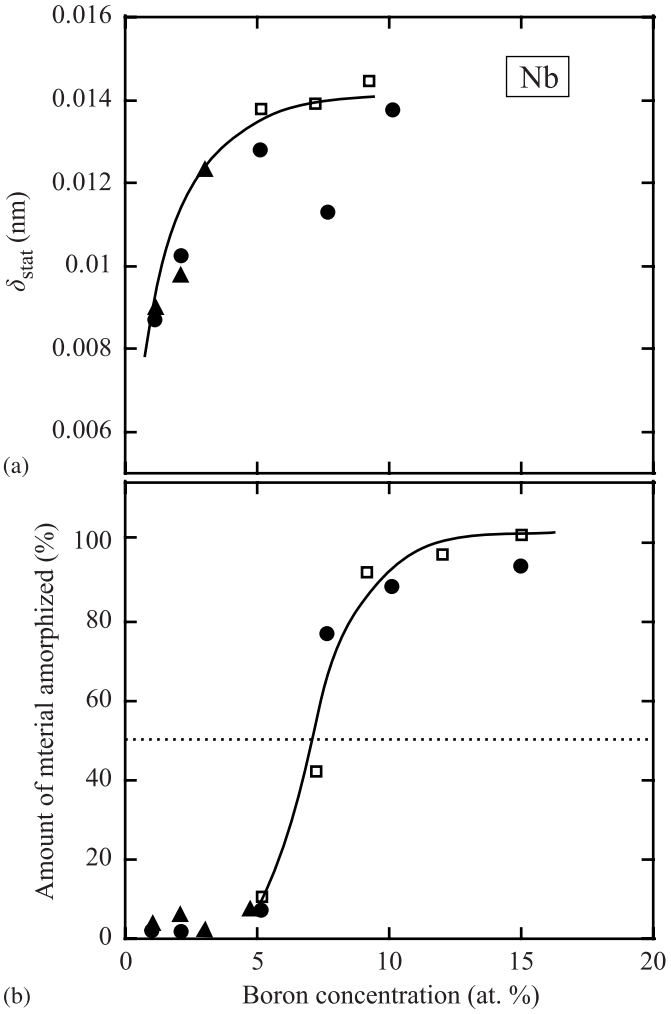

Fig. 9.32. Correlation between (a) average static displacement, δ_{stat} and (b) volume fraction of the amorphous phase vs. the concentration of B atoms implanted into Nb (after [32])

ΔG_{def}:

$$\Delta G_{irr} = \Delta G_{def} + \Delta G_{dis} = \sum_j (C_j E_j - T\Delta S_j) + \Delta C_{AB} NV - T\Delta S_{dis} \,, \tag{9.82}$$

where C_j is the concentration of defect j, E_j is the formation energy, V is the ordering energy (defined earlier) and ΔS_j and ΔS_{dis} are the configuration entropy changes due to point defects and anti-site defects, respectively. The term ΔC_{AB} is the change in the number of A–B pairs and is determined from the long-range order parameter,

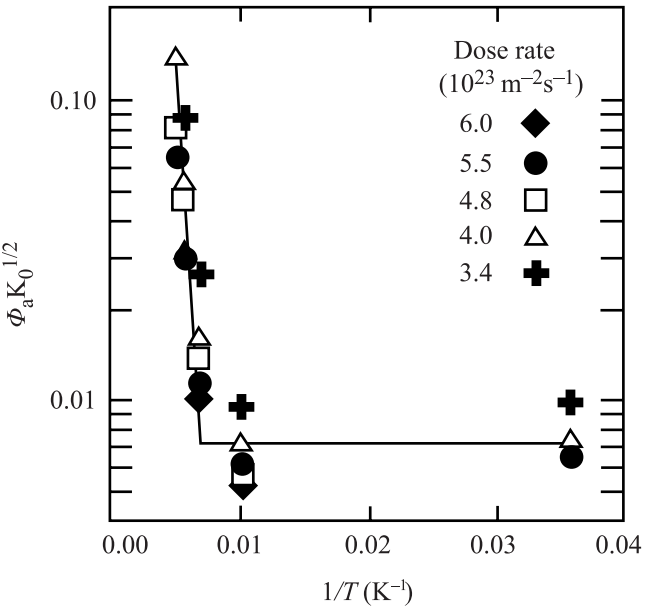

Fig. 9.33. Plot of the dose to amorphization × square root of dose rate vs. $1/T$. The lines are fit to the data and indicate that there are two regimes, an athermal regime at low temperature and a thermally activated regime at higher temperature (after [58])

S as:

$$\Delta C_{\mathrm{AB}} = N\left[A\left(1-S^2\right)+B(1-S)\right] , \tag{9.83}$$

where N is the number of lattice sites per mole and A and B are the fractions of atoms on the respective lattice sites in the ordered phase. The concentrations of defects is given by the defect balance equations given in Eq. (5.1). Equations (9.81), (9.82), and (9.83) and (5.1) can be used to determine a relationship between the dose to amorphization, the dose rate and the temperature. Motta determined this relationship for electron irradiation of Zr_3Fe to be:

$$\Phi_{\mathrm{a}}\, K_0^{1/2} = B\exp(-E_{\mathrm{m}}^{\mathrm{i}}/2kT) , \tag{9.84}$$

where Φ_{a} is the dose to amorphization, K_0 is the dose rate, $E_{\mathrm{m}}^{\mathrm{i}}$ is the interstitial migration energy and B is a constant, and the results shown in Fig. 9.33 are found to be in good agreement with observations, shown in Fig. 9.34.

9.8 Phase Stability in Reactor Core Component Alloys

The stability of phases in engineering alloys under irradiation is of great technological importance. Stainless steels are widely used in the cores of current

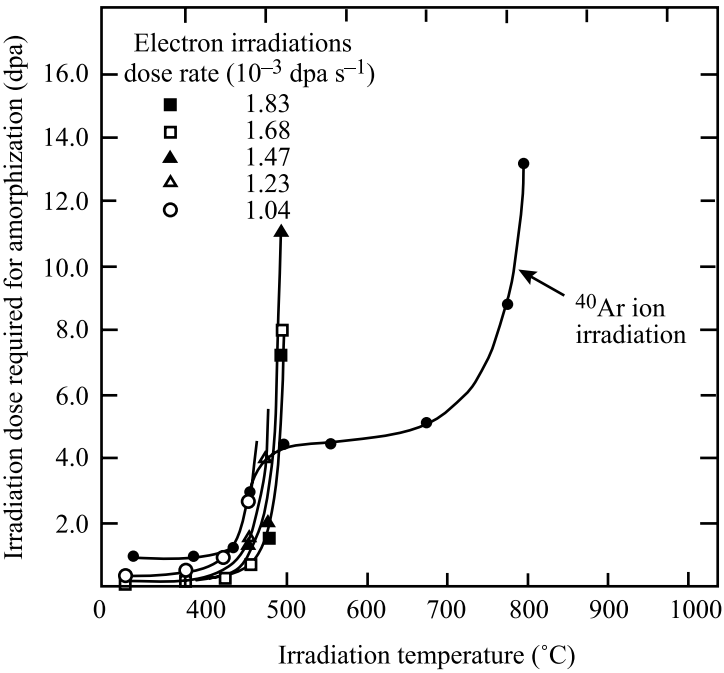

Fig. 9.34. Dose to amorphization for Zr_3Fe during electron and Ar^+ irradiation (after [58])

and advanced reactor systems and have also been studied most comprehensively. Some 10 phases are observed to be affected by irradiation of austenitic stainless steels [60, 61, 62]. These phases can be grouped into three categories [60]: *radiation-induced*, *radiation-modified*, and *radiation-enhanced*. Table 9.2 gives the phases belonging to each category along with a crystallographic and morphological description of the phases. The radiation-induced phases include γ', G and M_xP phases and appear only under irradiation, but not under thermal conditions. The radiation-modified group consists of phases that occur during both irradiation and thermal aging and includes η (M_6C), Laves and M_2P (FeTiP). The radiation-enhanced category consists of phases that regularly occur during thermal processing, but are either produced more rapidly or more abundantly at lower temperatures during reactor irradiation. Phases in this category include M_6C, $M_{23}C_6$ and MC carbides and σ and χ intermetallic phases.

Figure 9.35 provides a temperature-dose map in which the various phases listed in Table 9.2 are found to form. Note that while fluences of approximately 10 dpa are required for these phases to appear, the more important variable is temperature. In solution annealed and cold worked 316 SS, there is little evidence of significant radiation-induced precipitation below 370 °C. The only phase found to form in this regime is γ'–Ni_3Si, and it has been observed in both light water reactor core components and following proton irradiation at 360 °C [63]. The γ' phase has also been

Table 9.2. Phases observed in austenitic stainless steel alloys after neutron irradiation (from [60] and [61])

Radiation	Phase	Crystal structure	Lattice parameter (nm)	Morphology	Orientation in γ matrix	Volume misfit
-induced	γ' (Ni_3Si)	Cubic, A1 Fm3m	0.35	Spherical	Cube on cube	−0.1
	G ($M_6Ni_{16}Si_7$)	Cubic, A1 Fm3m	1.12	Small rod	Random	0.05
	M_2P (FeTiP)	Hexagonal, C22, P321	0.6 ($c/a = 0.6$)	Thin lath	$(1210)_{ppt}\|\|(001)_\gamma$	−0.4
	Cr_3P	Tetragonal, S_4^2 14	0.92 ($c/a = 0.5$)	–	–	~ 0
-modified	η (M_6C)	Cubic, E9, Fd3M	1.08	Rhombohedral	Cube on cube or twin	0.1
	Laves (A_2B)	Hexagonal, C14 $P6_3/mmc$	0.47 ($c/a = 0.77$)	Faulted lath	Various	−0.05
	M_2P (FeTiP)	Same	Same	Same	Same	Same
-enhanced	MC	Cubic, B1 Fm3m	0.43	Spherical	Spherical	0.7
	η (M_6C)	Same	Same	Same	Same	Same
	τ ($M_{23}C_6$)	Cubic, $D8_4$ Fm3m	1.06	Rhombohedral platelet	Cube on cube or twin	0.1
	Laves (A_2B)	Same	Same	Same	Same	Same
	σ	Tetragonal, $D8_b$ p4/mnm	0.88 ($c/a = 0.52$)	Various	Various	~ 0
	χ	Cubic, A12 143m	0.89	various	various	0.05

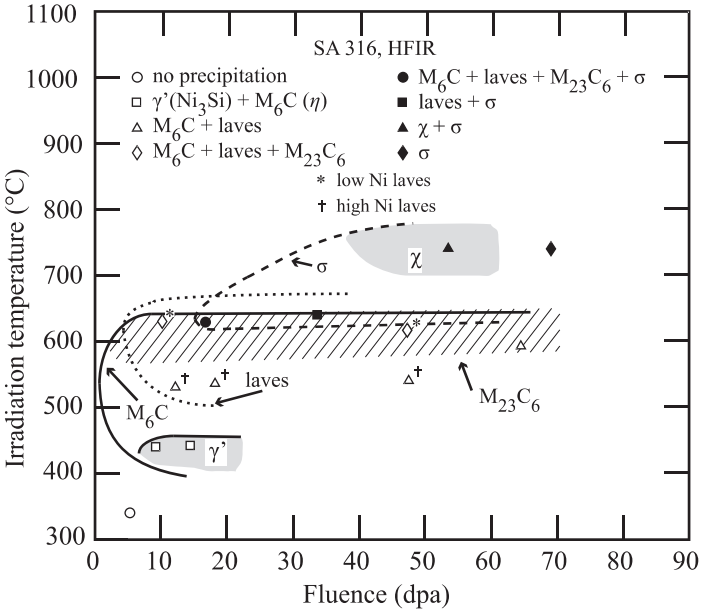

Fig. 9.35. Dose and temperature dependence of precipitate phase formation in solution annealed 316 stainless steel irradiated in HFIR (after [61])

detected in 316 stainless steel irradiated in a fast reactor as low as 270℃ [60]. Between 400 and 550℃, γ'-Ni_3Si readily forms during fast reactor irradiations and is greatest in steels with higher Si and Ti contents. In mixed spectrum reactors in this temperature range, fine Cr-rich phases such as $M_{23}C_6$ and M_6C form in 316 SS and Ti-rich MC forms in Ti-modified steels [60]. In the 500 to 600℃ temperature range, both radiation-induced and radiation-modified phases form, including the G-phase ($M_6Ni_{16}Si_7$), M_6C Laves and phosphides and silicides. The G-phase volume fraction is a function of the Si, Ti and Nb content of the steel with volume fraction increasing with alloy composition.

The appearance of these phases can be related to the effects of irradiation on phase stability. By far, the greatest effect of irradiation on precipitation in stainless steels is due to solute enrichment via radiation-induced segregation. Recall from Chap. 6 that irradiation of austenitic stainless steels causes the enrichment of Si and Ni at sinks and many of the phases appearing under irradiation are rich in one or both of these elements. Radiation-enhanced diffusion affects MC precipitation by enhancing its growth compared to that under thermal conditions. While it is expected that oversized phases are more stable under irradiation and undersized phases are less stable, of the phases given in Table 9.2, three have positive misfits of at least 10% and of those, only M_6C is stable under a wide range of irradiation conditions. Both MC and $M_{23}C_6$ are oversized and will benefit from vacancy supersaturation, but also from the depletion of their main constituent, Cr, due to RIS. Conversely,

several of the phases that are undersized are induced or enhanced by irradiation: Laves, M_2P, γ'. Clearly, the effect of solute segregation and other material and irradiation parameters play a large role in the phases that are stable under irradiation.

Nomenclature

a	Lattice spacing
A	Term relating to crystal structure dependence on ordering energy
C_e	Matrix solute concentration
C_i	Concentration of species i
C_p	Concentration of solute in the precipitate
D	Diffusion coefficient
$\tilde{D}$	Interdiffusion coefficient
E	Young's modulus
E_{m0}^{j}	Migration energy for ordering of defect j
G	Solute source term
ΔG_p	Free energy of formation of a precipitate
$\Delta G'$	Pseudo-free energy of formation of a precipitate
ΔG_{ac}	Free energy change due to amorphization
ΔG_{irr}	Free energy change due to irradiation
ΔG_{def}	Free energy change due to defects
ΔG_{dis}	Free energy change due to chemical disordering
$\hbar$	Planck's constant
ΔH_f	Heat of formation
$\Delta H_{i\text{-}v}$	Enthalpy of defect formation
$\Delta H_{c\text{-}a}$	Enthalpy for the crystalline to amorphous transition
J_p	Precipitate nucleation rate
k	Boltzmann's constant
k_o	Rate constant for the ordering reaction
k_s^2	Sink strength
K_{iv}	Recombination rate constant
K_0	Defect production rate
L	Cell size
M	Atomic mass
n	Excess number of vacancies in a precipitate
N	Atom number density
p_x	Probability that a trap site is occupied by species x
Q	Activation energy for ordering
r_c	Cascade radius
r_p	Precipitate radius
r_j	Recombination radius of specie j
r_{nn}	Nearest neighbor atom spacing
R	Metal:metalloid size ratio
R_m	Precipitate dissolution rate by ballistic mixing

R_s	Precipitate growth rate due to radiation-enhanced diffusion
R	Gas constant
S	Long-range order parameter
S_e	Equilibrium value of order parameter
S_j	Supersaturation of species j
$S_{observed}$	Observed long-range ordering parameter
S_0	Steady state value of order parameter
S_v	Vacancy supersaturation
S_x	Solute supersaturation
ΔS_{dis}	Configurational entropy change due to anti-site defects
ΔS_j	Configurational entropy change due to point defects
t	Time
T	Temperature
T_C	Cut-off temperature
T_{a-c}	Temperature above which crystal cannot be amorphized
T_{c-a}	Temperature below which complete amorphization can be achieved
T_g	Glass transition temperature
T_k	Ideal glass transition temperature
T_m	Melting temperature
U	Energy barrier for ordering reaction
V	Volume. Also, ordering parameter
V_0	Activation energy when the long-range order parameter, $S = 1$.
V_T	Energy reduction when a wrong A–B pair transforms to a correct A–B pair
V_c	Cascade volume
V_m	Molar volume
V_{ij}	Bond energy for species i and j
x	Number of solute atoms in a precipitate
X_j	Atom fraction of species j
Z_α	Number of α sites that are nearest neighbor to a β site
Z_β	Number of β sites that are nearest neighbor to a α site
α	Constant in Eq. (9.22)
α_j	Emission rate of species j
β	Constant in Eq. (9.21)
β_j	Capture rate of species j
δ	Fractional difference in volume of the precipitate relative to the matrix
$\left\langle \delta^2_{crit} \right\rangle^{1/2}$	Critical value of means square displacement
$\left\langle \delta^2_{stat} \right\rangle^{1/2}$	Amount of static disorder in the solid
$\left\langle \delta^2_{vib} \right\rangle^{1/2}$	Root-mean-square thermal displacement
ε	Disordering efficiency
ϕ	Neutron flux

γ	Particle-matrix interface energy. Also surface energy
μ	Shear modulus
ν	Poisson's ratio
ν_j	Frequency factor for defect j
ν_c	Frequency factor for correct A–B pair
ν_w	Frequency factor for wrong A–B pair
Θ	Re-solution rate of precipitate volume
Θ_0	Debye temperature
ρ	Density
ρ_p	Precipitate number density
ρ_p^0	Equilibrium precipitate number density
ρ'	Pseudo-equilibrium precipitate number density
σ	Parameter in Eq. (9.40)
σ_D	Displacement cross section
τ	Time constant
Ω	Atomic volume
ξ	Dissolution parameter in Eq. (9.32)
ζ	Constant in Eq. (9.1)

Superscripts

i	Interstitial
v	Vacancy

Subscripts

d	Defective
def	Defects
dis	Disordered
e	Solubility
i	Interstitials
irr	Irradiation
m	Matrix
max	Maximum
p	Precipitate
s	Solute
th	Thermal
v	Vacancies
x	Solute atom
0	Initial

Acronyms

CSRO	Compositional short-range order
HFIR	High Flux Isotope Reactor (Oak Ridge National Laboratory)
NHM	Nelson–Hudson–Mazey

RED	Radiation-enhanced diffusion
RIS	Radiation-induced segregation
TSRO	Topological short-range order

Problems

9.1 A spherical precipitate grows via a random nucleation process at temperature T. The same precipitate grows under irradiation at the same temperature T. Under irradiation, the time to obtain the same volume fraction of precipitate is half that during pure thermal aging. Calculate the difference in the activation energy at this temperature between thermal and irradiated conditions for this transformation process. State key assumptions.

9.2 What phase is 304 stainless steel? Does radiation-induced segregation in 304 stainless steel tend to stabilize or destabilize this phase? Explain why.

9.3 For 316 SS under irradiation with a vacancy supersaturation, $S_v = 10^4$ and a solute supersaturation, $S_x = 10^2$, find the interstitial to vacancy arrival rate ratio (β_i/β_v) that will stabilize a precipitate phase that is oversized by 5% ($\delta = 0.05$). Plot your results as a function of temperature from 573 to 873 K in increments of 100 K. Neglect the temperature dependence of Young's modulus.

9.4 For a Ni–5%Al alloy undergoing shrinkage by recoil dissolution and growth by diffusion of the solute from solution:

a) Determine the critical γ' precipitate radius, below which growth occurs and above which shrinkage will occur.

b) Compare your result to that expected when the precipitate size is governed by dissolution disordering.

Use the following irradiation parameters:

$$\phi_f = 10^{15}\,\mathrm{n/cm^2\,s} \quad (E \sim 0.5\,\mathrm{MeV})$$
$$\rho = 10^{15}\,\mathrm{cm^{-3}}$$
$$\zeta\Omega = 10^{-4}\,\mathrm{nm}$$
$$\xi = 10\,\mathrm{nm}$$
$$D = 10^{-15}\,\mathrm{cm^2/s}$$

9.5 For the same alloy as in the last problem, plot the dependence of the maximum stable particle size on f, the fraction of atoms dissolved by a cascade for precipitates undergoing irradiation-induced re-solution. Make the plot for the range $0 < f < 1$ and $l = 10\,\mathrm{nm}$.

9.6 Estimate the disordering rate due to irradiation for Ni–25Al (γ') irradiated with 5 MeV Ni^{++} ions at a displacement rate of 10^{-3} dpa/s and with a disordering efficiency of 30.

9.7 A recent paper reports the discovery of a new microstructural defect aggregate, termed a *black hole* because of its affinity for vacancies ($z_v^{BH} > z_i^{BH}$).

Describe how the presence of these black holes along with the usual array of defect sinks will affect:

a) Void nucleation rate
b) Critical void size
c) Void growth rate
d) Incoherent precipitate ($\delta > 0$) stability
e) Incoherent precipitate nucleation rate.

9.8 In the nickel-rich end of the Ni–Al system, a solid solution of Al in Ni, known as the γ phase, has an fcc crystal structure. Near a composition of Ni–50Al, the β phase (bcc) is the stable structure. Given the information below, determine the window on S_v and β_i/β_v needed to form the NiAl (β) phase from:

a) A saturated solution of Al in Ni
b) A supersaturated solution, $S_x = 2.0$
c) An undersaturated solution, $S_x = 0.5$.

Irradiation temperature = 500 °C

$$N = 0.35$$
$$E = 150\,\text{GPa}$$
$$a_\beta = 0.3574\,\text{nm}$$
$$a_\gamma = 0.490\,\text{nm}$$

9.9 Using the rules for amorphous phase formation, describe the relative ease of forming an amorphous phase in each single and two-phase region of the Ni–Al phase diagram. Explain your reasoning.

9.10 One of the theories of the formation of irradiation-induced amorphization requires that the vacancy and interstitial defect concentrations reach a level of 2%, at which point the affected volume will become amorphized. Determine whether this is possible in NiAl (β' – bcc) by determining the migration enthalpy for interstitials at 300 K which would allow the point defect concentrations to reach this point. Assume a low sink concentration in the material and a displacement rate of 10^{-4} dpa/s.

9.11 Estimate the crystalline-to-amorphous temperature for $NiAl_3$ for the following irradiation and material parameters under 5 MeV Ni^{++} ion irradiation:

$$K_0 = 10^{-3}\,\text{dpa/s}$$
$$U = 0.1\,\text{eV}$$
$$S_0 = 1.0$$
$$\nu = 10^{13}\,\text{s}^{-1}$$
$$\varepsilon = 30$$

References

1. Rehn LE (1982) In: Picraux ST, Choyke WJ (eds) Metastable Materials Formation by Ion Implantation. Elsevier Science, New York, pp 17–33

2. Nelson RS , Hudson JA, Mazey DJ (1972) M Nucl Mater 44:318–330
3. Wilkes P (1979) J Nucl Mater 83:166–175
4. Brailsford AD (1980) J Nucl Mater 91:221–222
5. Wagner C (1961) Z Elektrochem 65:581–591
6. Lifshitz IM, Slyozov VV (1961) Phys Chem Solids 19:35–50
7. Frost HJ, Russell KC (1983) In: Nolfi FV (ed) Phase Transformations During Irradiation. Applied Science, New York, p 75
8. Baron M, Chang H, Bleiberg ML (1977) In: Bleiberg ML, Bennett JW (eds) Radiation Effects in Breeder Reactor Structural Materials. TMS-AIME, New York, pp 395–404
9. Bilsby CF (1975) J Nucl Mater 55:125–133
10. Frost HJ, Russell KC (1982) Acta Metal 30:953–960
11. Frost HJ, Russell KC (1981) J Nucl Mater 103–104:1427–1432
12. Wollenberger H (1994) J Nucl Mater 2116:63–77
13. Abromeit C, Naundorf V, Wollenberger H (1988) J Nucl Mater 155–157:1174–1178
14. Russell KC (1984) Prog Mater Sci 28:229–434
15. Liou K-Y, Wilkes P (1979) J Nucl Mater 87:317–330
16. Nastasi M, Mayer JW, Hirvonen JK (1966) Ion-Solid Interactions: Fundamentals and Applications. Cambridge University Press, Cambridge, p 342
17. Potter DI (1983) In: Nolfi FV (ed) Phase Transformations During Irradiation. Applied Science, New York, p 213
18. Eridon J, Rehn L, Was G (1987) Nucl Instr Meth B 19/20:626
19. Brimhall JL, Kissinger HE, Charlot LA (1983) Rad Eff 77:273
20. Maydet SI, Russell KC (1977) J Nucl Mater 64:101–114
21. Russell KC (1979) J Nucl Mater 83:176–185
22. Mruzik MR, Russell KC (1978) J Nucl Mater 78:343–353
23. Cauvin R, Martin G (1981) Phys Rev B 32(7):3322–3332
24. Martin G, Bellon P, (1997) In: Ehrenreich H, Spaepen F (eds) Solid State Physics: Advances in Research and Applications, vol 50. Academic, New York, pp 189–332
25. Brimhall JL, Simonen EP (1986) Nucl Instr Meth B 16:187
26. Was GS, Eridon JM (1987) Nucl Instr Meth B 24/25:557
27. Was GS (1989) Prog Surf Sci 32(3/4):211
28. Luzzi DE, Meshii M (1986) Scr Metal 20:943
29. Johnson E, Wohlenberg T, Grant WA (1970) Phase Transitions 1:23
30. Grant WA (1981) Nucl Instr Meth 182/183:809
31. Johnson E, Littmark U, Johnson A, Christodoulides C (1982) Phil Mag A 45:803
32. Follstaedt DM (1985) Nucl Instr Meth B 78:11
33. Peiner E, Kopitzki K (1988) Nucl Instr Meth B 34:173
34. Tsaur BY, Lau SS, Mayer JW (1980) Appl Phys Lett 36:823
35. Tsaur BY, Lau SS, Hung LS, Mayer JW (1981) Nucl Instr Meth 182/813:1
36. Shectman D, Blech I, Gratias D, Cahn JW (1984) Phys Rev Lett 53:1951
37. Knapp JA, Follstaedt DM (1985) Phys Rev Lett 55(15):1591
38. Lilienfield DA, Nastasi M, Johnson HH, Ast AG, Mayer JW (1985) Phys Rev Lett 55(15):1587
39. Lilienfield DA, Mayer JW (1987) Mat Res Soc Symp 74. Materials Research Society, Pittsburgh, PA, p 339
40. Ossi PM (1977) Mater Sci Eng 90:55
41. Luzzi DE, Mori H, Fujita H, Meshii M (1984) Scr Metal 18:957
42. Pedraza DF (1987) Mater Sci Eng 90:69
43. Pedraza DF (1990) Rad Eff 112:11

44. Pedraza DF, Mansur LK (1986) Nucl Instr Meth B 16:203
45. Pedraza DF (1986) J Mater Res 1:425
46. Simonen EP (1986) Nucl Instr Meth B 16:198
47. Alonso JA, Somoza S (1983) Solid State Comm 48:765
48. Miedema AR (1973) J Less Comm Metals 32:117
49. Johnson WL, Cheng Y-T, Van Rossum M, Nicolet M-A (1985) Nucl Instr Meth B 7/8:657
50. Martin G (1984) Phys Rev B 30:1424
51. Swanson ML, Parsons JR, Hoelke CW (1971) Rad Eff 9:249
52. Brimhall JL, Kissinger HE, Pelton AR (1985) Rad Eff 90:241
53. Brimhall JL, Simonen EP, Kissinger HE (1973) J Nucl Mater 48:339
54. Okamoto PR, Lam NQ, Rehn LE (1999) In: Ehrenreich H, Spaepen F (eds) Solid State Physics: Advances in Research and Applications, vol 52. Academic, New York, pp 2–137
55. Lindemann FA (1910) Z Phys 11:609
56. Dienes GJ (1955) Acta Metal 3:549
57. Lam NQ, Okamoto PR, Li M (1997) J Nucl Mater 251:89–07
58. Motta AT, Howe LM, Okamoto PR (1999) J Nucl Mater 270:174–186
59. Motta AT (1997) J Nucl Mater 244:227–250
60. Mansur LK (1987) In: Freeman GR (ed) Kinetics of Nonhomogeneous Processes. Wiley, New York, pp 377–463
61. Maziasz PJ, McHargue CJ (1987) Int Mater Rev 32(4):190–218
62. Maziasz P (1993) J Nucl Mater 205:118–145
63. Was GS (2004) In: Proceedings of the 11th International Conference on Environmental Degradation of Materials in Nuclear Power Systems: Water Reactors, American Nuclear Society, La Grange Park, IL, pp 965–985

10 Unique Effects of Ion Irradiation

This chapter will focus on processes that are unique to ion bombardment of metals and alloys. Ion bombardment is important in fusion reactor systems in which the reaction products consist of energetic helium and hydrogen (deuterium or tritium) ions that impact the first wall and other components. In laboratory experiments, ion implantation, ion beam mixing and ion beam-assisted deposition are used to study ion–solid interactions and to create new phases and unique microstructures. The topic of ion beam modification of materials or ion–solid interactions in general is a broad subject, and a comprehensive treatment is beyond the scope of this text. (The reader is referred to several excellent texts and review articles on the subject, see for example, [1, 2, 3, 4, 5].) Rather, we will focus on processes that occur during ion–solid interactions and that result in unique microstructures or phases in the target, such as displacement mixing, preferential sputtering, Gibbsian adsorption, grain growth, etc., and the combination of these processes that together alter the target from its original state. Recall that ions not only create damage, but they contribute to a chemical change in the target by virtue of their presence. Processes affecting the surface structure and composition that are negligible under neutron irradiation (sputtering, recoil mixing, Gibbsian adsorption) can be very significant under ion irradiation.

We will start with a brief introduction of ion irradiation techniques to set the stage for understanding the effects to be described later. The effects of ion irradiation on composition, microstructure and phase formation will then be presented. A final topic is the effects due to bombardment by gases at high doses and high temperature as will be experienced in the first wall of a fusion reactor, or at low temperature in a laboratory.

10.1 Ion Irradiation Techniques

The modification of metal surfaces by ion beams can be accomplished by a variety of methods, each with its own advantages for particular situations. The principal methods include ion implantation, ion beam mixing, ion beam-assisted deposition and plasma ion implantation, and are shown schematically in Fig. 10.1a–d. Each of these techniques will be briefly described and considered for their capacity to alter the composition of the target.

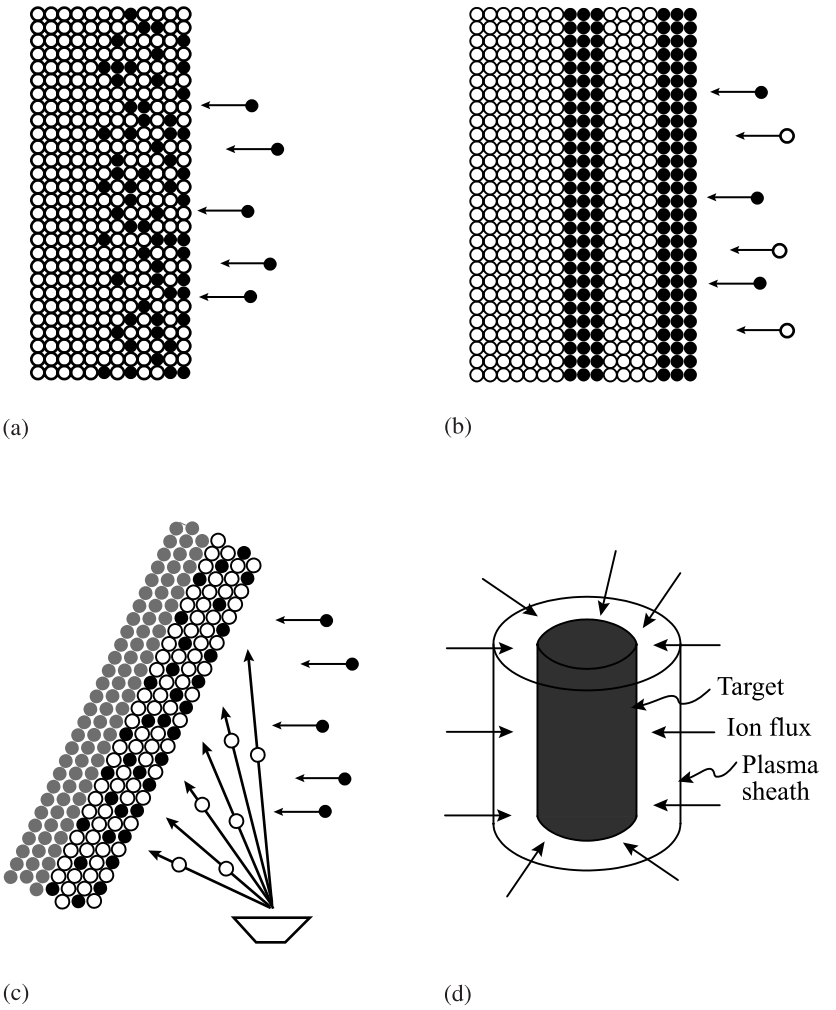

Fig. 10.1. Ion beam surface modification by (a) direct ion implantation, (b) ion beam mixing, (c) ion beam-assisted deposition, and (d) plasma source ion implantation (from [3])

Ion implantation (II) is the bombardment of a target with a beam of ions in the energy range from a few hundred keV to several MeV. The beam is usually monoenergetic, contains a single charge state and is generally (but not always) mass analyzed. Due to the stochastic nature of the elastic collision process, the ions come to rest in a Gaussian distribution with the mean of the Gaussian centered about R_p, the projected range, with the FWHM $\sim 2.35\Delta R_p$, where ΔR_p is the standard deviation from the mean.

Although it is a simple process, this technique has several disadvantages from the standpoint of modifying the surface composition. First, since the depth of the

implanted distribution varies as $E^{1/2}$, energies in the several hundred keV range that are achievable in the most common implanters, will result in projected ranges of less than 100 nm for most heavy ions. Energies in the MeV range are required to penetrate into the micrometer range. Second, sputtering will limit the concentration of the implanted specie to a value that is the reciprocal of the sputtering yield (see Sect. 10.2.1). Since sputtering yields of metals at these energies range from 2–5, the maximum concentration of implanted specie is 50 to 20%, respectively. The shape and location of the distribution can also be a drawback. In corrosion, where the composition of the top few monolayers is most important, the bulk of the modification occurs at considerably greater depths, leaving the surface lean in the implanted specie. When implantation induces a phase transformation, the effectiveness or efficiency of direct implantation is lesser still. Finally, it is often desirable to implant metal ions into pure metals or alloys to achieve a particular surface composition. As a practical matter, most commercial implanters can produce large currents of inert gases, but more elaborate measures are needed in order to produce metal ions at currents that are practical. Ion beam mixing provides an alternative to the shortcomings of direct ion implantation.

Ion beam mixing (IBM) refers to the homogenization of bilayers or multilayers of elements deposited onto the surface of a target prior to bombardment. The idea behind IBM is to create a surface alloy by homogenizing alternate layers of the alloy constituents deposited in a thickness ratio so as to result in the desired final composition following mixing. IBM greatly relieves several of the shortcomings of ion implantation. First, the requirement of producing a metal ion beam is eliminated since noble gases can be used for mixing. Noble gases will not contribute a chemical effect in the solid and yet can be made into high current beams in most commercial implanters. Second, there is no restriction on the composition range since the final composition is controlled by the ratio of layer thicknesses. This also removes two other shortfalls of ion implantation, that of uniformity and surface deficiency of the implanted specie. Ion beam mixing results in a very uniform composition throughout the depth of penetration of the ion, including the very near-surface region that is problematical for ion implantation. Finally, if the elemental layers are made thin enough, the dose needed to achieve complete mixing can be orders of magnitude lower than that needed to produce concentrated alloys by direct implantation.

If the process is carried out at low temperature, the result is often a metastable alloy in the form of either a supersaturated solid solution or an amorphous structure. The microstructure can then be controlled by subsequent annealing treatments. However, despite its many advantages, ion beam mixing still suffers from the same disadvantage of limited depth of penetration. The thickness of the surface is still governed by the projected range of the ion, which is in the 100 nm range for heavy ions of a few hundred keV. A solution to this problem lies in the technique of ion beam-assisted deposition.

Ion beam-assisted/enhanced deposition (IBAD/IBED) refers to the growth of a film with the assistance of an ion beam. In this technique, a film is grown onto a substrate by physical vapor deposition concurrently with the bombardment by an

ion beam of low ($\sim$1 keV) energy. The advantages of this method are numerous. First, there is virtually no limit to the thickness of film that can be modified since bombardment occurs during growth. Second, ion bombardment concurrent with vapor deposition provides for an atomically mixed interface, resulting in greater adherence. The composition gradient at the interface can be controlled by the deposition rate and the ion flux. Third, the enhanced mobility of the surface during growth allows for the control of grain size and morphology, texture, density, composition, and residual stress state. These properties are determined principally by controlling the atom deposition rate in conjunction with the ion flux (ion to atom arrival rate ratio), ion energy, fluence and species. Hence, pure metals, solid solution alloys, intermetallic compounds and a host of metal-based compounds can be grown by this technique.

A final technique is plasma surface ion implantation (PSII). In this technique, the target is placed directly in the plasma source and is then pulse biased to a high negative potential (-40 to -100 keV). A plasma sheath forms around the target and ions are accelerated normal to the target surface across the plasma sheath. PSII has several potential advantages relative to conventional line-of-sight implantation including elimination of the need for target manipulation and beam rastering, elimination of target masking (retained dose problem), operation of the ion source hardware and controls are near ground potential, and easier scaling to large and/or heavy targets.

All of these techniques involve energetic ion–solid interaction and the physical processes that constitute this interaction such as sputtering, Gibbsian adsorption, recoil implantation, displacement mixing, radiation-enhanced diffusion and radiation-induced segregation. These processes affect composition, microstructure and phase structure and form the basis for the observed changes in the physical and mechanical properties of the metal or alloy. Chapters 7, 8 and 9 described the microstructure and phase changes due to irradiation, and this chapter will focus on the composition effects and some additional effects unique to ion irradiation, such as grain growth, texture modification and surface morphology during high gas loading.

10.2 Composition Changes

Under ion bombardment, a variety of processes occur, some of which are much more pronounced than in the case of neutron irradiation and some that are the same. Bombardment by heavy ions results in sputtering of atoms from the surface, inducing compositional changes in the near-surface region of the target. At temperatures between 0.3 and 0.5 T_m, Gibbsian adsorption causes changes in the composition of the first two atom layers, which can impact the sputtering process. The primary disordering mechanism is collisional or ballistic mixing which can be qualitatively classified into recoil implantation and cascade (isotropic) mixing. Recoil implantation refers to the direct displacement of a target atom by a bombarding ion. Indirect processes involving other target atoms are collectively called cascade mixing. Referring to experiments involving the implantation into a bilayer or a thin marker layer

embedded in a monatomic solid, recoil implantation produces a shift and a broadening of a given initial profile while cascade mixing produces broadening. But in addition to collisional mixing, thermal processes may become important, leading to radiation-enhanced diffusion (Chap. 5). When the flux of defects to sinks becomes coupled to the flux of host atoms, radiation-induced segregation can occur, resulting in the accumulation or depletion of an alloy component at defect sinks (Chap. 6). The following subsections provide a development of the physical processes of sputtering, Gibbsian adsorption, recoil implantation and cascade mixing. Radiation-enhanced diffusion and radiation-induced segregation were described in earlier chapters and will be included only in combination with other processes to present a complete picture of composition changes under ion bombardment.

10.2.1 Sputtering

Sputtering is a key element in determining surface composition under ion bombardment, primarily through the action of preferential sputtering. Different elements sputter with different probabilities, and the surface composition is a function of these probabilities. This section will briefly describe the process of physical sputtering, followed by a discussion of preferential sputtering as it affects surface compositional changes in alloys.

Basic Model

Surfaces of solids erode under ion bombardment. The erosion rate is characterized by the sputtering yield, Y, which is defined as the mean number of emitted atoms per incident particle. Y depends on the structure and composition of the target, parameters of the incident beam and the experimental geometry. For medium mass ions and keV energies, $0.5 \leq Y < 20$.

In the sputtering process, atoms are ejected from the outer surface layers (Fig. 10.2). The bombarding ion transfers energy in collisions to the target atoms that recoil with enough energy to generate other recoils. Some of the backward-directed recoils will intersect the surface with enough energy to escape the solid. It is these recoils that make up most of the sputtered yield, which is proportional to the number of displaced or recoil atoms. In the linear cascade regime, the number of recoils is proportional to the energy deposited per unit depth in nuclear energy loss [6, 7, 8, 9]. A collision cascade is linear if only a minor fraction of the target atoms within the cascade volume is set in motion. For a bulk cascade, this implies a low density of point defects generated. As applied to sputtering, it means that the sputter yield must be small compared to the number of target atoms located within the surface area affected by a bombarding particle. In practice, cascades in metals are close to linear except those generated by rather heavy ions bombarding heavy targets in the energy range from $\sim$10 keV to $\sim$1 MeV. The sputtering yield for particles incident on the surface can be expressed as:

$$Y = \Lambda F_{\mathrm{D}}(E_0)\,, \tag{10.1}$$

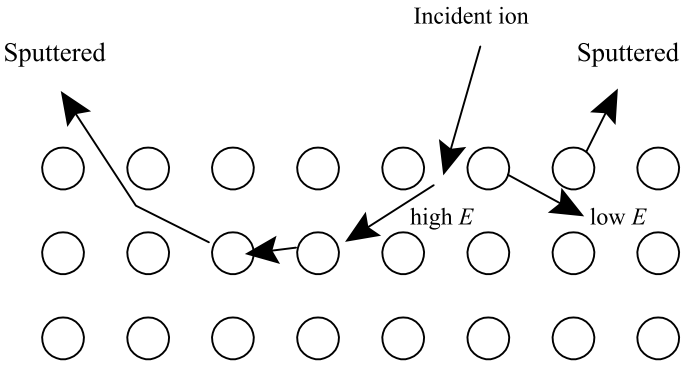

Fig. 10.2. Schematic illustration of the re-direction of momentum from an incident ion to the backward direction resulting in sputtering

where Y is the number of atoms emitted per incident particle, E_0 is the incident particle energy, Λ contains all the material properties such as surface binding energies and incident ion angular dependence, and F_D is the density of deposited energy per unit depth at the surface and depends on the type, energy and direction of the incident ion and the target parameters Z_2, M_2 and N. The derivation of Λ involves a description of the number of recoil atoms that can overcome the surface barrier and escape from the solid. Sigmund [6] has derived an expression for Λ using the Thomas–Fermi screening function:

$$\Lambda = 0.042/NU_0 \,, \tag{10.2}$$

where N is the atomic number density and U_0 is the surface binding energy and can be estimated from the heat of sublimation. The deposited energy, F_D is given as

$$F_\mathrm{D}(E_0) = \alpha \, \mathrm{d}E/\mathrm{d}x|_\mathrm{n} \,, \tag{10.3}$$

where $\mathrm{d}E/\mathrm{d}x|_\mathrm{n}$ is the energy loss rate due to nuclear stopping and α is a correction factor that accounts for the angle of incidence of the beam to the surface and contributions due to large angle scattering events. The factor α increases with the angle of incidence due to increased energy deposition in the surface, and α also increases with M_2/M_1, again, due to greater energy deposition in the surface. Using the inverse square potential (see Eq. (1.159)), $\mathrm{d}E/\mathrm{d}x|_\mathrm{n}$ is evaluated to be:

$$\mathrm{d}E/\mathrm{d}x|_\mathrm{n} = NS_\mathrm{n} = N\frac{\pi^2}{2}Z_1Z_2\varepsilon^2 a\frac{M_1}{M_1+M_2} \,, \tag{10.4}$$

where N is the atom number density, S_n is the nuclear stopping power, a is the screening radius, ε is the unit charge, Z and M are atomic number and atomic mass, respectively, and the subscripts 1 and 2 refer to incident and target atoms, respectively. The nuclear stopping power calculated using a Thomas–Fermi cross

section [10] is:

$$S_n(E) = 4\pi a N Z_1 Z_2 \varepsilon^2 \frac{M_1}{M_1 + M_2} S_n(\in) \,, \tag{10.5}$$

where $S_n(\in)$ is the reduced stopping power (from Eq. (1.142)), and the reduced energy, $\in$ (from Eq. (1.137)) is:

$$\in = \frac{M_2}{M_1 + M_2} \frac{a}{Z_1 Z_2 \varepsilon^2} E \,. \tag{10.6}$$

For 1 keV Ar incident on Cu, $a = 0.0103$ nm and $\in = 0.008$, and for 10 keV O incident on Cu, $a = 0.0115$ nm and $\in = 0.27$. For ion energies between 1 and 10 keV, values of $\in$ are in the range 0.01 to 0.3, or just below the plateau in $\mathrm{d}E/\mathrm{d}x|_n$. Using the energy-independent value of $S_n(\in)$ of $\sim 0.39\,\mathrm{eV\,cm^2}$ (from Eq. (1.162)), gives $\mathrm{d}E/\mathrm{d}x|_n \sim 1240\,\mathrm{eV/nm}$ for Ar incident on C, and $\mathrm{d}E/\mathrm{d}x|_n \sim 320\,\mathrm{eV/nm}$ for O incident on Cu. Using the expression for Λ in Eq. (10.2), the sputtering yield in Eq. (10.1) becomes:

$$Y = 0.528 \alpha Z_1 Z_2 \frac{M_1}{U_0 (M_1 + M_2)} S_n(\in) \,. \tag{10.7}$$

For Ar incident on Cu, $NS_n = \mathrm{d}E/\mathrm{d}x|_n = 1240\,\mathrm{eV/nm}$, $U_0 \sim 3\,\mathrm{eV}$, $\alpha \sim 0.25$, $\Lambda = 0.0165\,\mathrm{nm/eV}$ and $N = 85\,\mathrm{atoms/nm^3}$, giving $Y \sim 5.1$. Figure 10.3 shows the variation of the sputter yield with angle, atomic number of the ion, target atom–incident ion mass ratio and ion energy. Sputtering increases with departure from normal incidence because more of the ion energy is deposited close to the surface. The same is true for the dependence on Z of the ion for a fixed energy. Sputter yield is low at low energies because of the small amount of energy deposited in the surface. Similarly, since the elastic scattering cross section decreases with energy, the energy deposited in the surface region drops at high energies and the sputter yield falls. The result is a peak at intermediate energies where the energy deposition in the near-surface region is high.

The sputtering yield can be used to determine the steady state concentration of the implanted specie [1] as follows. We assume that we are implanting an ion of element A in to a target of element B, where $N_{A,B}$ is the atomic concentration and $S_{A,B}$ is the sputtered flux of elements A and B. Then at any time, we have that:

$$S_B / S_A = \chi (N_B / N_A) \,, \tag{10.8}$$

where χ is the ratio of probabilities for sputtering a B atom off the surface to that for an A atom. The flux of incident A atoms, ϕ_A is related to the total sputtered flux by the sputtering yield:

$$\phi_A Y = S_A + S_B \,. \tag{10.9}$$

At steady state, the addition of A atoms by implantation equals that lost by sputtering so there is no net change in the total number of A atoms in the target and

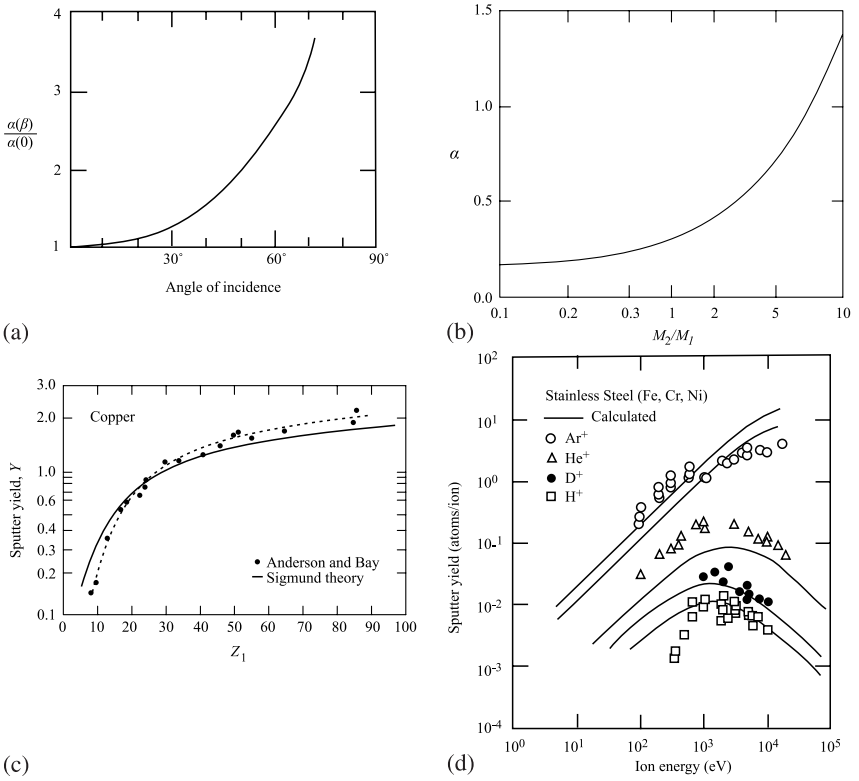

Fig. 10.3. Dependence of sputter yield on (a) angle of incidence, β, where β is measured from the surface normal (from [8]), (b) atomic number of the incident ion (from [9]), (c) target atom–incident ion mass ratio through the factor α in Eq. (10.3) (from [8]), and (d) incident ion energy (from [7])

$\phi_A = S_A$. Substituting for S_A into Eq. (10.9) yields $S_B = (Y-1)\phi_A$. Substituting for S_A and S_B into Eq. (10.8) gives the steady state surface composition:

$$N_A/N_B = \chi(Y-1)^{-1} . \tag{10.10}$$

For the case where $\chi = 1$, Eq. (10.10) becomes:

$$N_A/(N_A+N_B) = 1/Y , \tag{10.11}$$

which indicates that the concentration of the implanted specie is determined directly by the sputter yield.

Preferential Sputtering

When energetic ions strike a target consisting of an alloy, not all of the elements of the target will be sputtered with the same yield. The yield of A atoms of an alloy per

incident ion in the flux of sputtered atoms [11] is:

$$Y_{\mathrm{A}} = \int_0^{\infty} \sigma_{\mathrm{A}}(x)(C_{\mathrm{A}}(x)/\Omega)\,\mathrm{d}x\,, \tag{10.12}$$

where $\sigma_{\mathrm{A}}(x)$ is the cross section for A atoms at a depth $x \geq 0$ to be ejected from the surface, $x = 0$, into the region $x < 0$ per incoming ion, $C_{\mathrm{A}}(x)$ is the atomic fraction of A in the alloy at depth x, and Ω is the mean atomic volume. We can also define the probability per unit depth, $p_{\mathrm{A}}(x)$ that an A atom present at depth x is ejected by an incoming ion:

$$p_{\mathrm{A}}(x) \equiv \sigma_{\mathrm{A}}(x)/\Omega\,. \tag{10.13}$$

The yield of A atoms then takes the form:

$$Y_{\mathrm{A}} = \int_0^{\infty} C_{\mathrm{A}}(x)p_{\mathrm{A}}(x)\,\mathrm{d}x\,. \tag{10.14}$$

The primary effects in alloy sputtering are those related to the individual sputtering events and the physical variables contributing to the sputter yield, and are all contained in the sputter probability, p_{A}, which depends on the type and energy of the incoming ion, the type of the sputtered atom and its surface binding energy, etc. Since the values of the sputter probabilities, p_{i} will differ for differing atomic species, preferential sputtering will occur.

The secondary effects in alloy sputtering enter into Eq. (10.14) via the atomic concentration, C_{A}, which gives the probability that a site is occupied by an A atom. As a consequence, the sputter yields of the alloying components will be affected through the factor $C_{\mathrm{A}}(x)$ in Eq. (10.14). Practically, sputtered atoms come from a shallow layer (Fig. 10.1) with the contribution falling off exponentially with depth. The decay length is of the order of two atomic layers. Therefore, the integral in Eq. (10.14) can be replaced [6, 7, 12] by:

$$Y_{\mathrm{A}} = \overline{p}_{\mathrm{A}} C_{\mathrm{A}}^{\mathrm{s}}\,, \tag{10.15}$$

where $\overline{p}_{\mathrm{A}}$ is the average total probability for an A atom present in the surface layer to be sputtered off per incident ion and $C_{\mathrm{A}}^{\mathrm{s}}$ is the average atomic concentration of A in the surface layer, denoted by the superscript s. The thickness of this layer is not well-defined but should be taken as one or two atomic layers for determining $C_{\mathrm{A}}^{\mathrm{s}}$ since the origin of sputtered ions is heavily weighted toward the first atomic layer.

Differences in the sputter probabilities for component atoms in an alloy are caused by differences in the amounts of energy and momentum transferred to atoms of different masses, and surface binding energies. However, continued sputtering of a semi-infinite alloy target of uniform bulk composition must eventually lead to a steady state in which the composition of the flux of sputtered atoms leaving the surface equals the composition of the bulk alloy. Wiedersich et al. [11] have shown that bombardment of a binary alloy AB with a flux of ions ϕ (ions/cm^{2}s) leads to an

atom removal rate given by:

$$\frac{\mathrm{d}N}{\mathrm{d}t} = \phi(Y_\mathrm{A} + Y_\mathrm{B}) \,. \tag{10.16}$$

Therefore, the rate at which the sputtered surface recedes can be calculated from the total rate of atom loss per unit area:

$$\dot{\delta} = \mathrm{d}\delta/\mathrm{d}t = \phi\Omega\,\mathrm{d}N/\mathrm{d}t = \phi\Omega(\overline{p}_\mathrm{A}C^\mathrm{s}_\mathrm{A} + \overline{p}_\mathrm{B}C^\mathrm{s}_\mathrm{B}) \,, \tag{10.17}$$

where δ is the thickness of the surface layer removed by sputtering.

They also showed that the net accumulation rate of species, i in a slab of solid at the surface of the sample, $0 \leq x < x_0$ is:

$$\frac{\mathrm{d}N_i}{\mathrm{d}t} = \phi\left[C^b_i(\alpha/\Omega^b) - Y_i\right] \,, \tag{10.18}$$

where C^b_i is the atomic concentration of component i of the bulk alloy, denoted by the superscript b, α is the volume removed per incident ion and Ω^b is the average atomic volume of the bulk alloy. The net rate of accumulation of implanted ions is:

$$\frac{\mathrm{d}N_0}{\mathrm{d}t} = \phi\left[1 - Y_0\right] \,. \tag{10.19}$$

At steady state, the terms in the square brackets of Eqs. (10.18) and (10.19) must equal zero, giving:

$$Y_1 : Y_2 : Y_3 .... = C^\mathrm{b}_1 : C^\mathrm{b}_2 : C^\mathrm{b}_3 ..., \tag{10.20}$$

and

$$Y_0 = 1 \,. \tag{10.21}$$

That is, the ratios of the alloy components in the sputtered flux are the same as those of the bulk alloy and their concentrations are just uniformly *diluted* by the re-emitted sputter ions. Note that the steady state flux of sputtered atoms contains *no information* on preferential sputtering. Information about preferential sputtering can be obtained from the steady state concentrations in the near-surface region via the approximation given in Eq. (10.15). Substituting Eq. (10.15) into Eq. (10.20) yields:

$$\frac{p_1}{p_2} = \frac{C^\mathrm{b}_1}{C^\mathrm{s}_1}\frac{C^\mathrm{s}_2}{C^\mathrm{b}_2} \,, \quad \text{or} \quad \frac{C^\mathrm{s}_1}{C^\mathrm{s}_2} = \frac{C^\mathrm{b}_1}{C^\mathrm{b}_2}\frac{p_2}{p_1} \,. \tag{10.22}$$

That is, after steady state is attained, the sputter probabilities are proportional to the ratio of the bulk and surface concentrations of the element in question. The sputter probability of the sputter ions can be obtained from the surface concentration:

$$p_0 \cong \frac{1}{C^\mathrm{s}_0} \,. \tag{10.23}$$

Lam and Wiedersich [13] have described the time evolution of preferential sputtering, PS on the near-surface composition for a binary alloy AB with $p^\mathrm{s}_\mathrm{A} > p^\mathrm{s}_\mathrm{B}$, i.e.,

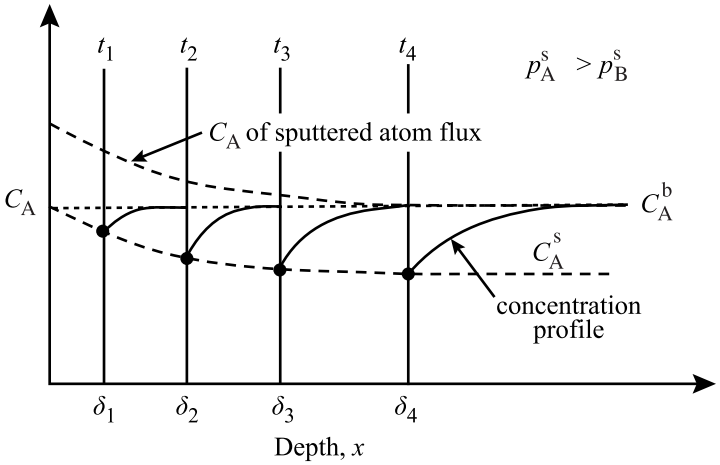

Fig. 10.4. Schematic description of the effect of preferential sputtering on the time evolution of the composition of the near-surface region of the sample and of the sputtered atom flux (from [13])

for the case where PS of A atoms occurs (see Fig. 10.4). Note that initially, the concentration of A atoms in the sputtered flux (top dashed line) is larger than in the bulk. However, as the surface composition changes (bottom dashed line) and the near-surface layer composition is altered, a steady state will be achieved after a certain bombardment time, when the composition of the sputtered atom flux becomes equal to the bulk composition, as dictated by the law of conservation of matter. That is, the surface concentration of A atoms will evolve to a steady state at which the higher sputtering probability of element A relative to element B, is offset by a lower A atom concentration.

Consider a binary alloy, A:B such that $C^b_A = C^b_B = 0.5$. Then from Eq. (10.22) we have:

$$\frac{C^s_A}{C^s_B} = \frac{\overline{p}_B}{\overline{p}_A} \,. \tag{10.24}$$

If the surface concentrations are measured to be $C^s_A = 0.33$ and $C^s_B = 0.67$, then we know that $\overline{p}_A : \overline{p}_B = 2.0$. Conversely, if we measure a steady state sputtered atom flux of A atoms to B atoms of 1.0 ($Y_A : Y_B = 1.0$), then all this tells us is that $S_A : S_B = 1.0$. That is, measuring the sputtered atom flux tells us nothing about the surface composition. We must make surface composition measurements directly and independently.

10.2.2 Gibbsian Adsorption

Gibbsian adsorption (or thermal surface segregation) is the process by which the surface of an alloy re-adjusts itself to a composition different from that of the

bulk in order to lower the free energy of the alloy [14]. In metallic systems the change can be quite substantial, but the effect is confined to one or two atomic layers. The bulk composition is essentially unaffected because of the large bulk-to-surface volume ratio. The re-adjustment occurs spontaneously at temperatures sufficiently high for diffusion to proceed at reasonable speed. Consider a surface layer of composition$C_{\mathrm{A}}^{\mathrm{s}}$and $C_{\mathrm{B}}^{\mathrm{s}}$ that differs from the bulk composition $C_{\mathrm{A}}^{\mathrm{b}}$ and $C_{\mathrm{B}}^{\mathrm{b}}$. At equilibrium, the surface composition is related to the bulk composition [14] by:

$$\frac{C_{\mathrm{A}}^{\mathrm{s}}}{C_{\mathrm{B}}^{\mathrm{s}}} = \frac{C_{\mathrm{A}}^{\mathrm{b}}}{C_{\mathrm{B}}^{\mathrm{b}}} \exp\left(-\frac{\Delta H_{\mathrm{A}}}{kT}\right) , \tag{10.25}$$

where ΔH_{A} is the heat of adsorption, defined as the enthalpy change associated with the exchange of an A atom in the bulk with a B atom at the surface. At elevated temperature, equilibrium is approached by a net flux, J_{A} of A atoms described by:

$$J_{\mathrm{A}}\Omega = \left[(\nu_{\mathrm{A}}^{\mathrm{b}\to\mathrm{s}} C_{\mathrm{A}}^{\mathrm{b}} C_{\mathrm{B}}^{\mathrm{s}}) - (\nu_{\mathrm{A}}^{\mathrm{s}\to\mathrm{b}} C_{\mathrm{A}}^{\mathrm{s}} C_{\mathrm{B}}^{\mathrm{b}})\right] \xi , \tag{10.26}$$

where ξ is the atomic layer thickness, $\nu_{\mathrm{A}}^{\mathrm{b}\to\mathrm{s}}$ is the bulk-to-surface jump frequency and $\nu_{\mathrm{A}}^{\mathrm{s}\to\mathrm{b}}$ is the surface-to-bulk jump frequency for atom A. The first term on the right is the flux of A atoms from the bulk to the surface and the second term is the flux of A atoms from the surface to the bulk. At equilibrium ($J_{\mathrm{A}} = 0$), or:

$$\frac{\nu_{\mathrm{A}}^{\mathrm{b}\to\mathrm{s}}}{\nu_{\mathrm{A}}^{\mathrm{s}\to\mathrm{b}}} = \frac{C_{\mathrm{A}}^{\mathrm{s}}}{C_{\mathrm{A}}^{\mathrm{b}}} \frac{C_{\mathrm{B}}^{\mathrm{b}}}{C_{\mathrm{B}}^{\mathrm{s}}} , \tag{10.27}$$

and substituting into Eq. (10.25) gives:

$$\nu_{\mathrm{A}}^{\mathrm{s}\to\mathrm{b}} = \nu_{\mathrm{A}}^{\mathrm{b}\to\mathrm{s}} \exp\left(-\frac{\Delta H_{\mathrm{A}}}{kT}\right) . \tag{10.28}$$

This says that the activation enthalpy for a surface segregating element (one that must have $\Delta H_{\mathrm{A}} < 0$) for the jump back into the bulk is effectively increased by the heat of adsorption relative to the migration enthalpy in the bulk. The difference in concentration between the surface layer and the bulk is established and maintained by the reduced probability of thermally activated jumps of A atoms from the surface into the bulk. The enhanced surface concentration due to Gibbsian adsorption, GA will result in an increased loss of the segregated elements due to sputtering. Continued preferential loss of an element by GA requires that diffusion be high ($T \geq 0.5T_{\mathrm{m}}$), but because sputtering enhances thermal diffusion, the effect of GA becomes significant at $T \cong 0.3T_{\mathrm{m}}$. However, the athermal displacement mixing process will oppose GA. The effect of GA at steady state is to suppress the concentration in the alloy just below the surface layer to a value that maintains the surface layer concentration at the value dictated by preferential sputtering. Hence, under ion bombardment, the surface composition will be affected by both of these processes. Lam and Wiedersich [13] provided a schematic description of the dynamic behavior of the surface composition during ion bombardment resulting from the simultaneous effects of GA and PS. In the example shown in Fig. 10.5, Gibbsian adsorption

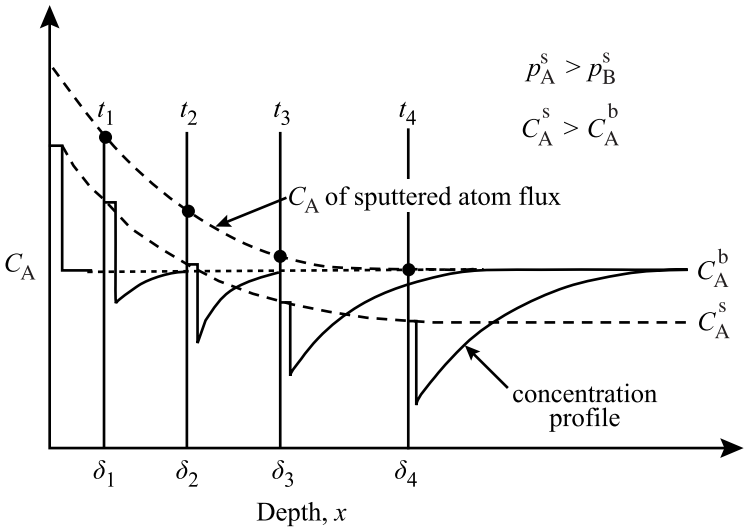

Fig. 10.5. Schematic description of the simultaneous effects of GA and PS on the time evolution of the near-surface composition and of the sputtered atom flux (from [13])

results in a surface concentration of A atoms that is initially greater than the bulk level, shown by the step change in A atom concentration at the surface. This leads to enhanced preferential sputtering of A atoms since the sputtered atom flux is primarily from the first atom layer. Consequently, the concentration of A atoms in the subsurface layer will be reduced in an effort to re-establish thermodynamic equilibrium. After a time, t_1, the A atom concentration profile resembles the original in that there is a step-wise enrichment of A at the surface, but the surface concentration is reduced relative to the original and the concentration behind the step is reduced as well. With increasing bombardment time, the surface concentration of A continues to drop and the zone depleted in atom A increases in depth and width. Steady state is reached when the composition of the sputtered atom flux is equal to the bulk composition of the alloy.

10.2.3 Recoil Implantation

The incoming ion beam imparts its momentum to the atoms (and electrons) of the solid. Hence, the momentum distribution of atoms during the displacement process is not isotropic and atoms will be re-located preferentially in the beam direction. This does *not* lead to any significant net atom transport in the beam direction because the solid will relax to approximately its normal density, i.e., the flux of recoiling atoms in the beam direction is compensated by a uniform flux of atoms due to relaxation in the opposite direction. In alloys, the relocation cross section and the range of the recoiling atoms depend on the charge and mass of the nucleus in such a way that generally the lighter component atoms will be transported relative to the

heavier components in the beam direction. This can be described as a flux of atoms of some of the alloy components toward deeper regions in the target, compensated by an opposite flux of the remainder of components to maintain atomic density at the proper value, i.e., the net flux of atoms is approximately zero across any plane parallel to the surface inside the target. The expression "recoil implantation" is used to describe the net transport parallel to the beam direction of some types of atoms relative to other types. The mechanics of recoil implantation have been developed by Sigmund et al. [15, 16, 17] and are summarized here.

Consider the average implantation effect of a single ion (M_0, Z_0) slowing down along a straight line to a well-defined range, R in a homogeneous binary alloy of components 1 and 2 , characterized by M_i,Z_i, and C_i with $i = 1, 2$, and $C_1 + C_2 = 1$. The number of i recoils created with energy $(T, \mathrm{d}T)$ in element $(x, \mathrm{d}x)$ along its path is:

$$NC_i \,\mathrm{d}x \sigma_{0i}(E(x)\,, T)\,, \tag{10.29}$$

where $E(x)$ is the ion energy at depth x and σ_{0i} is the elastic scattering cross section between ions and i atoms. From LSS theory, the projected range of a recoil, R_p is:

$$R_\mathrm{p} = R_i(T) \left(\frac{T}{\gamma_{0i} E(x)} \right)^{1/2}, \tag{10.30}$$

where R_i is the path length and recoils are assumed to slow down on a straight line to a well-defined range, and $\gamma_{ij} = 4M_iM_j/(M_i + M_j)^2$. Then the total *effect*, P_i of the knock-on implantation is the integral of the *number* of recoils and their *range*:

$$P_i = NC_i \int_0^R \mathrm{d}x \int_0^{\gamma_{0i} E(x)} \sigma_{0i}(E(x), T) R_i(T) \left(\frac{T}{\gamma_{0i} E(x)} \right)^{1/2} \mathrm{d}T\,. \tag{10.31}$$

Equation (10.31) is evaluated on the basis of power law scattering:

$$\begin{aligned} \sigma_{ij}(E,T) &= C_{ij} E^{-m} T^{-1-m}\,, \quad i,j = 0,1,2, \quad 0 < m < 1 \\ C_{ij} &= B_1 a_{ij}^{2(1-m)} \left(\frac{M_i}{M_j} \right)^m (Z_i Z_j)^{2m} \\ a_{ij} &= B_2 \left(Z_i^{2/3} Z_j^{2/3} \right)^{-1/2}\,, \end{aligned} \tag{10.32}$$

where B_1 and B_2 are constants. The range $R_i(T)$ is determined, as in Chap. 1, from the partial stopping cross section:

$$S_{ij}(E) = \int T' \,\mathrm{d}\sigma_{ij}(E, T')\,. \tag{10.33}$$

Performing the integration in Eqs. (10.31) and (10.33) and dividing by the projected range yields:

$$Q_i = \frac{P_i}{R_p} = \frac{1-m}{m(1+2m)} \gamma_{01}^{2m-1} \frac{c_i}{(A_{i1} + A_{i2})}\,, \tag{10.34}$$

where

$$A_{ij} = c_j \left(\frac{\gamma_{ij}}{\gamma_{0i}}\right)^{1-m} \left(\frac{a_{ij}}{a_{0i}}\right)^{2(1-m)} \left(\frac{M_i^2}{M_0 M_j}\right)^{m} \left(\frac{Z_j}{Z_0}\right)^{2m} , \tag{10.35}$$

where 0 is the incoming ion, i is the atom struck by the ion, and j is the subsequent atoms struck by the ith atom.

Q_i is the *equivalent* number of i atoms recoil implanted over the depth R_p (i.e., the ion range) in the direction of the ion beam, per incident ion. The dominating term in Q_i with regard to its dependence on i is the factor M_i^{2m} in Eq. (10.35). It shows that recoil implantation prefers the *lighter* species since the number of i recoils at a given energy $(T, \mathrm{d}T)$ is proportional to $M_i^{-m} Z_i^{2m}$, so it is greatest for the heavy component. But the *range* of i recoils at a given T is proportional to $M_i^{-m} Z_i^{-2m}$, so it is greatest for the light component. Hence, the combined effect, or the number $\times$ range, is proportional to M_i^{-2m}.

As an example, consider Ar^+ bombardment of PtSi. The resulting values for the equivalent number of each atom type recoil implanted over the range of the ion [15] are:

$$Q_\mathrm{Pt} = 0.034\,, Q_\mathrm{Si} = 0.37 \quad \text{for} \quad m = 0.5$$
$$Q_\mathrm{Pt} = 0.019\,, Q_\mathrm{Si} = 0.94 \quad \text{for} \quad m = 0.33\,.$$

In both cases, there is a net transport of Si relative to that of Pt. Results for a similar experiment in which Si containing a marker layer of Pt was bombarded with 300 keV

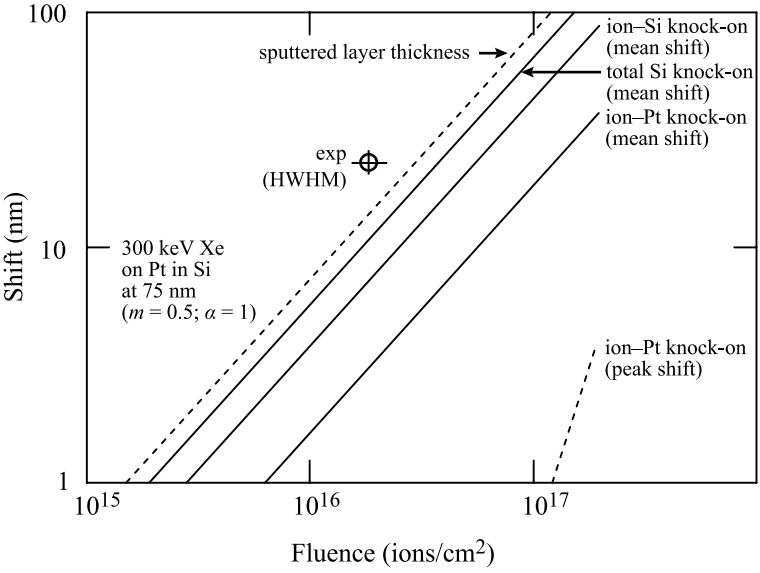

Fig. 10.6. Marker layer shift for 300 keV Xe ions incident on a thin Pt layer at 75 nm in Si, calculated using Sigmund's recoil implantation model (from [16])

Xe^+ are shown in Fig. 10.6. Note that the shift of the ion-Si knock-on is greater than that for the ion–Pt knock-on, resulting in a net transport of Si away from the surface, relative to that for Pt. The significance of this result is that preferential transport of a specie in a target based on its mass can contribute to mixing of the solid.

10.2.4 Cascade (Isotropic, Displacement) Mixing

The rapid transfer of energy from recoiling atoms of the solid to other atoms leads to an efficient randomization of recoil directions within cascades. As a consequence, most of the relocation events of atoms in energetic cascades lead to *isotropic* mixing rather than to recoil implantation. Molecular dynamics calculations indicate that the number of replacements in a displacement event results in a mean square diffusion distance of atoms, $\langle x^2 \rangle \sim 30\, a^2$ per defect pair produced (where a is the nearest neighbor distance). Thus, an atomically sharp interface is broadened by $\langle x^2 \rangle^{1/2}$, or about 5 atom planes for a dose of one dpa. Broadening increases proportionally to the square root of dose, so ion beam mixing of multilayer targets is an efficient means of homogenizing the solid.

As with neutron irradiation, ion irradiation of a target results in the production of a collision cascade. Depending on the ion mass and its energy, the energy density in the cascade can range from 10^{-3} to 10 eV/atom. The cascade propagation time is of the order 10^{-14} s and the quench time, is 10^{-12} s. It is important to distinguish between individual cascades and cascade overlap. In a target undergoing ion bombardment at a current density (proportional to dose rate) of $1\,\mu A/cm^2$ ($\sim 6 \times 10^{12}$ ions/cm^{2}s for singly charged ions), successive cascades will occur in a given region of material at roughly 1 second intervals for cascade diameters of $\sim$4 nm. That is, each volume of material will experience a cascade once each second. In order for cascade overlap to be avoided, the total dose must be kept below $\sim 10^{13}$ ions/cm^2. Realize that even in the cascade overlap regime, the cascade lifetime is $\sim 10^{-12}$ s, so there is no temporal communication between cascades unless there is some thermal diffusion. Within a single cascade, the mean displacement distance is always insignificantly small. For example, if each Frenkel pair is displaced an average of $\sim$1 nm (R_{recoil}), because the ratio of the number of displaced atoms, N_d to the total number of atoms within the central core of the cascade, N_v, is much less than unity, the mean atomic displacement within the cascade ($R_{\text{recoil}} \times N_d/N_v$) is negligible. Only with the aid of radiation-enhanced diffusion after the cascade has ended, could significant mixing occur. At doses of $\sim 10^{16}$ ions/cm^2, the implanted region receives over 10^3 successive overlapping cascades and the cumulative effect of ballistic mixing is no longer negligible.

Ballistic Mixing

Recall that the atomic model of thermal diffusion resulted in a diffusion coefficient of the form, Eq. (4.44):

$$D = 1/6\lambda^2\Gamma\,, \tag{10.36}$$

where Γ is the total jump frequency and λ is the jump length. If we assume that the distribution of momentum transfers in cascade mixing is isotropic, then the result is a cumulative random walk-like displacement process. We can characterize the transport process by introducing an *effective diffusion coefficient*, D^* [18, 19] where:

$$D^* = 1/6R^2F \,, \tag{10.37}$$

where R is the root-mean-square displacement of an atom in the collision cascade and $F(x)$ is the atomic displacement rate in dpa/s. F can be estimated from the K–P displacement model as follows. Recall from Chap. 2 Eqs. (2.1) and (2.2) that:

$$\frac{R_\mathrm{d}}{N} = F = \int \phi(E)\sigma_\mathrm{D}(E_\mathrm{i})\,\mathrm{d}E_\mathrm{i} \,, \tag{10.38}$$

$$\text{and} \quad \sigma_\mathrm{D}(E_\mathrm{i}) = \int \sigma_\mathrm{s}(E_\mathrm{i}, T)\nu(T)\,\mathrm{d}T \,. \tag{10.39}$$

Assuming a monoenergetic particle flux and isotropic elastic scattering gives:

$$\nu = \overline{T}/2E_\mathrm{d} \,, \tag{10.40}$$

$$\text{and} \quad \sigma_\mathrm{D} = \frac{\overline{T}}{2E_\mathrm{d}}\sigma_\mathrm{s} \,, \tag{10.41}$$

$$\text{giving} \quad F = \phi\sigma_\mathrm{s}\frac{\overline{T}}{2E_\mathrm{d}} \,. \tag{10.42}$$

By the definition of average energy loss, $\mathrm{d}E/\mathrm{d}x|_\mathrm{n} = \dfrac{\overline{T}}{\lambda} = N\sigma_\mathrm{s}\overline{T}$, and substituting for $\overline{T}$ into Eq. (10.42) gives:

$$F = \frac{\phi\ \mathrm{d}E/\mathrm{d}x|_\mathrm{n}}{2E_\mathrm{d}N} \,, \tag{10.43}$$

where $\mathrm{d}E/\mathrm{d}x|_\mathrm{n}$ is the ion energy deposited per unit depth into atomic processes and E_d is the displacement energy. Substituting the expression for F in Eq. (10.43) into Eq. (10.37) for D^* gives:

$$D^* \cong \frac{R^2\phi\ \mathrm{d}E/\mathrm{d}x|_\mathrm{n}}{12E_\mathrm{d}N} \,. \tag{10.44}$$

As mentioned earlier, the effect of cascade mixing is to smear out an originally sharp interface or to broaden a delta function to a Gaussian distribution. Let us consider the effect of cascade mixing on three different composition profiles in a target. Recall that Fick's second law states that:

$$\frac{\partial C}{\partial t} = -\nabla\cdot D\nabla C = -D\nabla^2 C, \quad \text{for} \quad D \neq f(C) \,. \tag{10.45}$$

Case 1: Thin film

For the geometry shown in Fig. 10.7a, the boundary conditions are:

$$C \to 0 \quad \text{as} \quad t \to 0 \quad \text{for} \quad |x| > 0$$
$$C \to 1 \quad \text{as} \quad t \to 0 \quad \text{for} \quad x = 0$$

$\int_{-\infty}^{\infty} C(x,t)\,\mathrm{d}x = \alpha$, where α is the total amount of solute in the target. Assuming that the layer is infinitely thin, the solution to Fick's second law is:

$$C(x,t) = \frac{\alpha}{\sqrt{4\pi Dt}} \exp\left(\frac{-x^2}{4Dt}\right), \tag{10.46}$$

where the variance, $\sigma^2 = 4Dt$, the standard deviation, $\sigma = \sqrt{4Dt}$, and the full width at half maximum, FWHM $= 2.35\sigma$. From Eq. (10.44), the increment of FWHM due to cascade mixing is then:

$$\Delta\text{FWHM} = 2.35\sqrt{4D^*t} \cong R\left[\frac{2\,\mathrm{d}E/\mathrm{d}x|_{\mathrm{n}}\,\phi t}{E_{\mathrm{d}}N}\right]^{1/2}. \tag{10.47}$$

Note that the broadening of the thin film as described by ΔFWHM is proportional to $(\phi t)^{1/2}$, or the effective ion mixing coefficient, $4Dt$ is proportional to ϕt. Figure 10.8 shows that as predicted by Eq. (10.47), mixing given by $4Dt$ is proportional to the dose.

Taking the example of 150 keV Kr^+ bombardment of a Ni sample containing a thin film as in Fig. 10.7a, the dose needed to produce a ΔFWHM of 10 nm is:

$$\Delta\text{FWHM} = 10\ \text{nm} \cong R\left[\frac{2\,\mathrm{d}E/\mathrm{d}x|_{\mathrm{n}}\,\phi t}{E_{\mathrm{d}}N}\right]^{1/2}. \tag{10.48}$$

For $\mathrm{d}E/\mathrm{d}x|_{\mathrm{n}} = N\sigma_{\mathrm{s}}\overline{T}$, then Eq. (10.48) becomes:

$$\Delta\text{FWHM} = 10\,\text{nm} \cong R\left[\frac{2\sigma_{\mathrm{s}}\overline{T}\phi t}{E_{\mathrm{d}}}\right]^{1/2}. \tag{10.49}$$

For $\sigma_{\mathrm{s}} \sim 10^{16}\,\mathrm{cm}^2$, $\overline{T} \sim E_i = 150\,\mathrm{keV}$, $E_{\mathrm{d}} \sim 15\,\mathrm{eV}$ and $R \sim 1.5\,\mathrm{nm}$, and the dose to cause a ΔFWHM of 10 nm is $8.5 \times 10^{14}\,\mathrm{i/cm}^2$. If He^+ is used instead of Kr^+, then the required dose is $3.5 \times 10^{15}\,\mathrm{i/cm}^2$.

Case 2: Pair of semi-infinite solids (bilayer)

For a bilayer as shown in Fig. 10.7b, the boundary conditions are:

$$C = 0 \quad \text{for} \quad x < 0 \quad \text{at} \quad t = 0,$$
$$C = C' \quad \text{for} \quad x > 0 \quad \text{at} \quad t = 0.$$

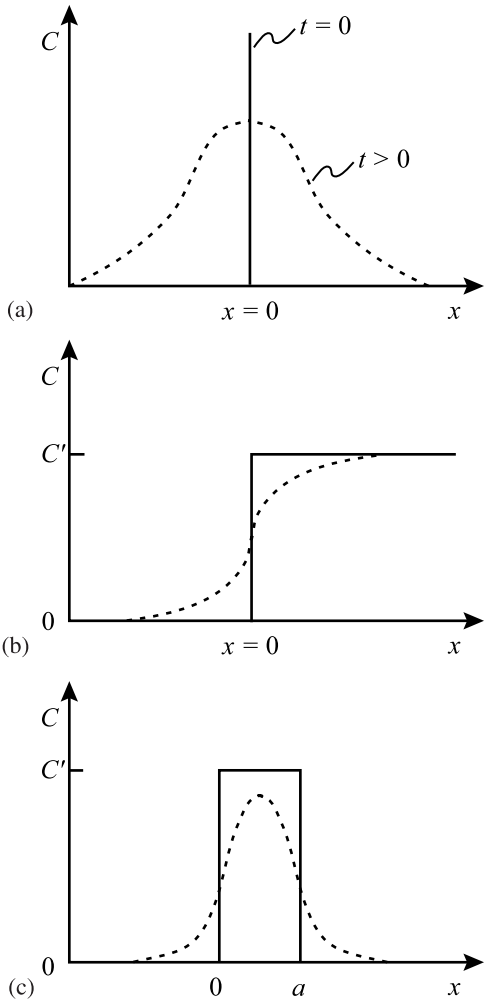

Fig. 10.7. Schematic illustration of the effect of ion beam mixing on (a) a thin film, (b) a pair of semi-infinite solids (bilayer), and (c) a thin film of finite thickness (multilayer)

The solution to Fick's second law subject to the boundary conditions is:

$$C(x,t) = \frac{C'}{2}\left[1 + \mathrm{erf}\left(\frac{x}{\sqrt{4Dt}}\right)\right] . \tag{10.50}$$

Figure 10.9 shows that as predicted by Eq. (10.50), mixing across a bilayer interface as described by $4Dt$ is, indeed, linear with dose for several bilayers systems, although the proportionality constant is system-dependent, as will be discussed later.

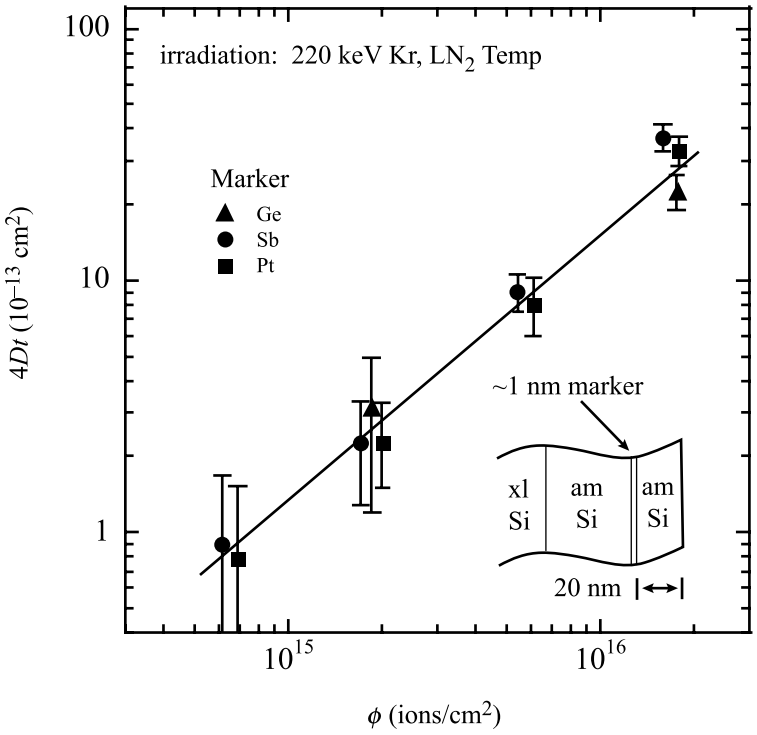

Fig. 10.8. Marker mixing data for several different markers in amorphous Si showing the relationship between the effective ion mixing diffusion coefficient, $4Dt$, and the dose, ϕt (from [1])

Case 3: Thin film of finite thickness (multilayer)

For a layer of finite thickness, as shown in Fig. 10.7c, the boundary conditions are:

$$C = C' \quad \text{for} \quad 0 < x < a \quad \text{and} \quad t = 0\,,$$
$$C = 0 \quad \text{for} \quad x < 0\,, x > a \quad \text{and} \quad t = 0\,.$$

The solution is:

$$C(x,t) = \frac{C'}{2}\left[\operatorname{erf}\left(\frac{x}{\sqrt{4Dt}}\right) - \operatorname{erf}\left(\frac{x-a}{\sqrt{4Dt}}\right)\right]\,. \tag{10.51}$$

Chemical Effects on Ion Beam Mixing

Observations of mixing in binary systems reveals large differences in the amount of mixing that cannot be explained by ballistic effects. For example, mixing in the Cu–Au system is an order of magnitude higher than that in the Cu–W system [21, 22] and mixing of marker layers in Si and Ge varies significantly for elements of similar

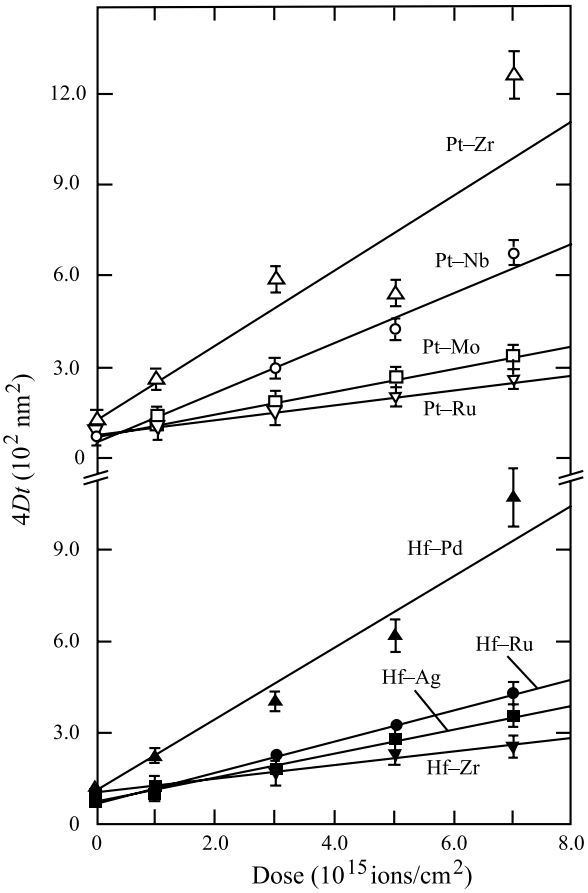

Fig. 10.9. Mixing of the interface vs. dose for several bilayer samples irradiated with 600 keV Xe^{++} ions at 77 K (from [20])

mass [23]. These systems are *collisionally similar* systems in that the ratio of the masses of the constituents is similar and so in a ballistic mixing model, they should behave similarly. Quite to the contrary, Fig. 10.9 showed that collisionally similar binary systems exhibited very different mixing rates. Further, mixing was occurring at 77 K where radiation-enhanced diffusion is suppressed.

Johnson [24, 25, 26, 27, 28, 29] accounted for the chemical nature of the binary alloy components by first realizing that fundamentally, diffusion is driven by a chemical potential gradient, $\nabla\mu(x)$ and only for ideal solutions does Fick's law apply. More generally, for interdiffusion of two metals which form non-ideal solutions, one must relate $\nabla\mu(x)$ to $\nabla C(x)$. This can be accomplished by replacing D by a modified D' that accounts for the Kirkendall effect and describes diffusional

intermixing:

$$D' = \left[D_{\mathrm{A}}^{0} C_{\mathrm{B}} + D_{\mathrm{B}}^{0} C_{\mathrm{A}}\right]\left[1 + \frac{\partial \ln \gamma(C_{\mathrm{A}})}{\partial \ln C_{\mathrm{A}}}\right]$$
$$= D\left[1 - \frac{2\Delta H_{\mathrm{mix}}}{kT}\right] . \tag{10.52}$$

where D is the rate coefficient of unbiased mixing, γ is the activity coefficient and ΔH_{mix} is the enthalpy of mixing given by:

$$\Delta H_{\mathrm{mix}} = 2\delta C_{\mathrm{A}} C_{\mathrm{B}} ,$$
$$\delta = z[H_{\mathrm{AB}} - (H_{\mathrm{AA}} + H_{\mathrm{BB}})/2] , \tag{10.53}$$

where z is the coordination number (number of nearest neighbors) and H_{ij} is the potential between atom pairs, or pair enthalpies. Equation (10.52) simply says that random walk will be *biased* when the potential energy depends on the configuration. So mixing rates depend not only on the number of random walk steps per unit time, but also on the degree of Darken biasing. Figure 10.10 highlights the effect of ΔH_{mix} on mixing rates for several bilayer systems. Equation Eq. (10.52) can be used to obtain a value of kT_{eff}, the effective temperature at which diffusion occurs. [28] In the Pt–Au system, the value for kT_{eff} is 1–2 eV. This means that the dominant contribution to ion mixing occurs when particle kinetic energies are of the order 1 eV!

If mixing depends on the thermodynamic properties of the solid, then it should depend on the cohesive energy, ΔH_{coh}, which is a measure of how tightly bound

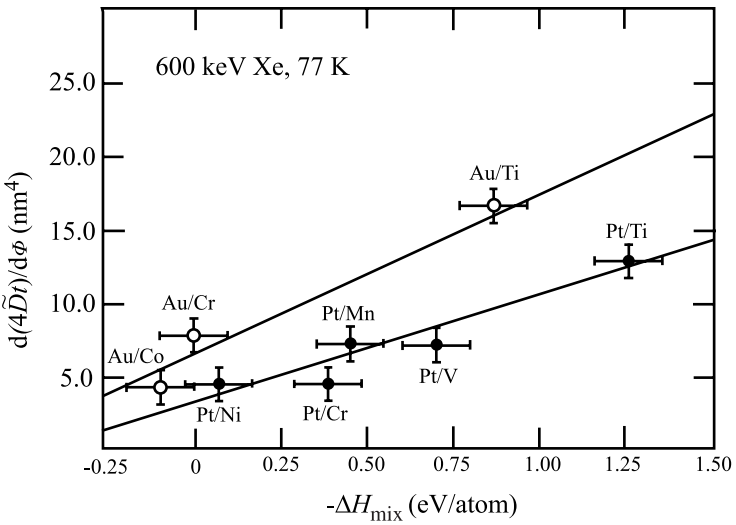

Fig. 10.10. Effect of the heat of mixing on the observed mixing rates for several binary metal systems following irradiation with 600 keV Xe^{++} ions at 77 K (from [24])

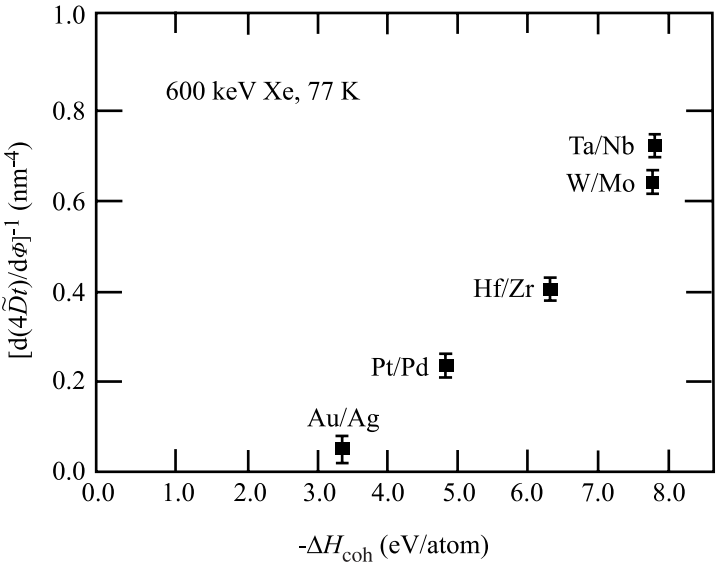

Fig. 10.11. Effect of the average cohesive energy on ion mixing in several binary metal systems following irradiation with 600 keV Xe^{++} at 77 K (from [29])

atoms are in a solid. Indeed, if we plot $\mathrm{d}(4Dt)/\mathrm{d}\phi$ vs. ΔH_{coh}, we note a strong correlation (Fig. 10.11). The energy range of interest, $\sim$1 eV correlates with the thermalized regime of a displacement cascade, which can be depicted as a thermal spike. The effect of thermal spikes on diffusion was treated by Rossi and Nastasi [30] starting with Vineyard's thermal spike model [31] in which the non-linear Fourier equation for heat conduction in an isotropic and uniform medium is given as:

$$\nabla\kappa\cdot\nabla T = c\frac{\partial T}{\partial t}\,, \tag{10.54}$$

where $\kappa = \kappa_0 T^{n-1}$ is the thermal diffusivity, $c = c_0 T^{n-1}$ is the specific heat capacity, κ_0 and c_0 are constants and $n \geq 1$. At time $t = 0$, a cylindrical spike is introduced along an infinite straight line at constant energy density, ε, where the distance perpendicular to the axis of the cylinder is r. The initial condition for the temperature distribution is given by:

$$Q = \int c\,\mathrm{d}T = (c_0/n)T^n(r,0)\,. \tag{10.55}$$

For zero initial ambient temperature, solution of Eq. (10.54) subject to boundary condition in Eq. (10.55), gives the temperature distribution in space and time:

$$T(r,t) = \left[\frac{n\varepsilon}{4\pi\kappa_0 t}\right]^{1/n}\exp(-c_0 r^2/4\pi\kappa_0 t)\,. \tag{10.56}$$

Defining η as the total number of atom jumps in one spike per unit length of the spike, then analogous to thermal diffusion, we assume Arrhenius behavior for the jump rate, R such that $R = A\exp(-Q/kT)$, then η is:

$$\eta = \int 2\pi r\,\mathrm{d}r \int A\exp(-Q/T(r,t))\,\mathrm{d}t\ . \tag{10.57}$$

Integration of Eq. (10.56) yields:

$$\eta = \frac{n^3\Gamma(2n)A\varepsilon^2}{8\pi\kappa_0 c_0 Q^{2n}}\ , \tag{10.58}$$

where $\Gamma(2n)$ is the gamma function with argument $2n$. For moderate temperatures, $n = 1$ and Eq. (10.58) becomes:

$$\eta = \frac{A\varepsilon^2}{8\pi\kappa c Q^2}\ . \tag{10.59}$$

Referring back to Eq. (10.52) for a binary system with $|\Delta H_{\mathrm{mix}}| > 0$, the *effective* jump rate at temperature T can be written as:

$$R_{\mathrm{eff}} = A\exp(-Q/kT)\left[1 - 2\Delta H_{\mathrm{mix}}/kT\right]\ , \tag{10.60}$$

and Eq. (10.57) becomes;

$$\eta_{\mathrm{c}} = \int 2\pi r\,\mathrm{d}r \int A\exp(-Q/kT(r,t))\left[1 - 2\Delta H_{\mathrm{mix}}/kT(r,t)\right]\mathrm{d}t\ , \tag{10.61}$$

where the subscript on η denotes chemical biasing. Taking $n = 1$ and carrying out the integral over the size and lifetime of the spike yields:

$$\eta_{\mathrm{c}} = \frac{A\varepsilon^2}{8\pi\kappa c Q^2}(1 - 4\Delta H_{\mathrm{mix}}/Q)\ . \tag{10.62}$$

Since the activation energy scales with the cohesive energy, we take $Q = -s_2\Delta H_{\mathrm{coh}}$, where s_2 is a constant. After a dose Φ (i/cm^2), the total number of jumps in the solid is equal to $\eta_{\mathrm{c}}\Phi/\rho$, where ρ is the atomic density. The mixing rate is then given by:

$$\frac{\mathrm{d}(4Dt)}{\mathrm{d}\Phi} = \eta_{\mathrm{c}} r_{\mathrm{c}}^2/\rho\ , \tag{10.63}$$

where r_{c} is a characteristic jump distance. Assuming that r_{c} scales with the interatomic distance as $r_{\mathrm{c}} = s_1\rho^{-1/3}$, we obtain:

$$\frac{\mathrm{d}(4Dt)}{\mathrm{d}\Phi} = \frac{K_1\varepsilon^2}{\rho^{5/3}(\Delta H_{\mathrm{coh}})^2}(1 + K_2\Delta H_{\mathrm{mix}}/\Delta H_{\mathrm{coh}})\ , \tag{10.64}$$

where K_1 depends on κ, c and A, and $K_2 = 4/s_2$. Equation (10.64) is plotted in Fig. 10.12 as the mixing vs. the ratio of $\Delta H_{\mathrm{mix}}/\Delta H_{\mathrm{coh}}$ for a large number of binary

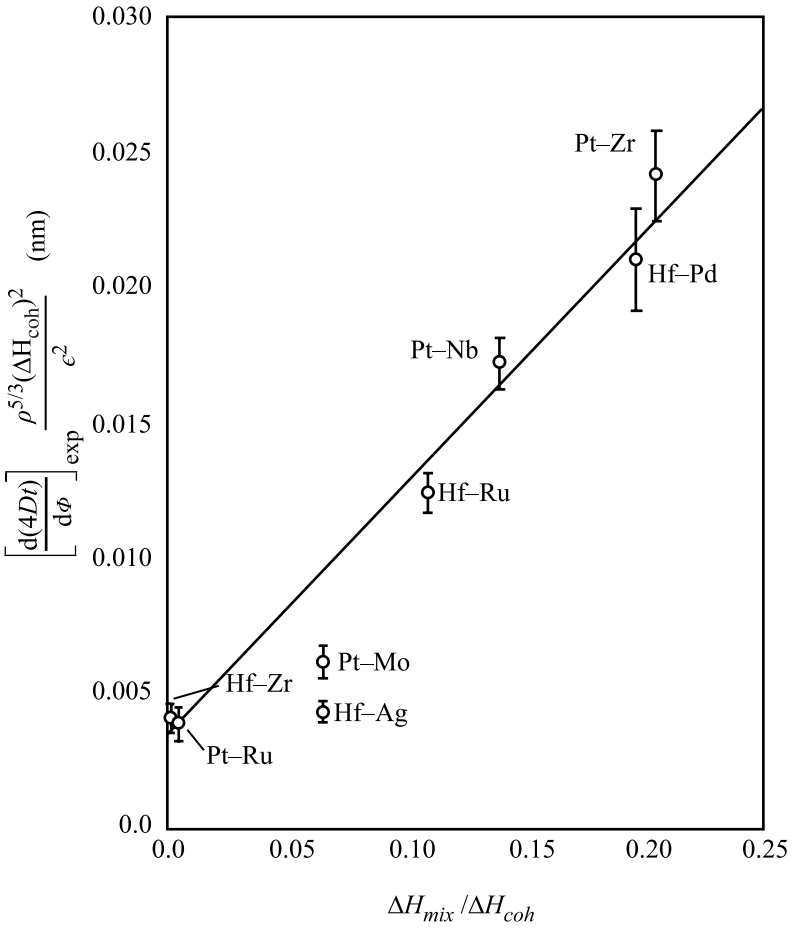

Fig. 10.12. Correlation between mixing and the ratio of $\Delta H_{\mathrm{mix}}/\Delta H_{\mathrm{coh}}$ for several metal bilayers irradiated with 600 keV Xe^{++} at 77 K (from [20])

systems and shows excellent correlation, indicating that the chemical effect of on beam mixing is indeed, strong even at temperatures where RED does not occur. With increasing temperature, RED contributes to mixing as well.

Figure 10.13 shows the amount of intermixed silicon in a Si–Nb bilayer sample that was irradiated with Si^{+} ions [32]. At high temperature, the data follow an Arrhenius-type behavior with an activation energy of 0.9 eV. As the temperature is lowered, the amount of intermixing does not continue to drop, but levels out at a value that is determined by the ballistic mixing of the elements, which is temperature-dependent. Mixing induced by temperature only (thermal mixing) is shown by the solid curve on the left with an activation energy of 2.7 eV. The effect of radiation-enhanced diffusion is then the difference between the two plots that display Arrhenius behavior. Note that the low-temperature mixing is not due to

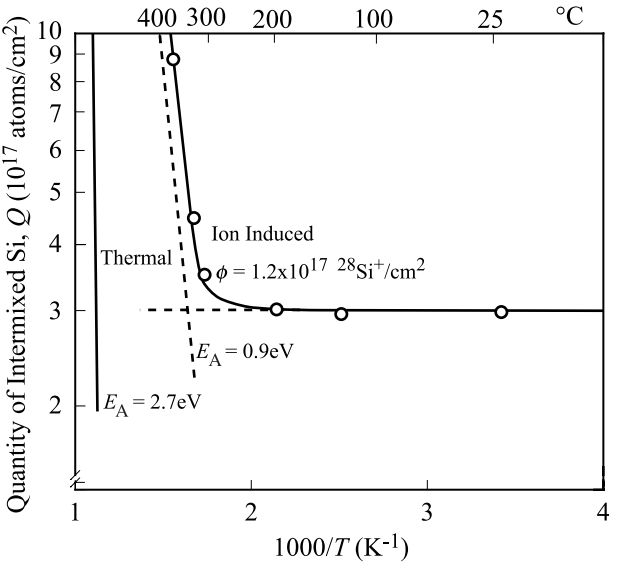

Fig. 10.13. Logarithm of the quantity of intermixed silicon vs. reciprocal temperature for a Nb–Si bilayer sample after a fluence of $1.2 \times 10^{17}\ ^{28}Si^{+}/cm^{2}$. The solid line is fit to the data points of the sum of a temperature-independent part (nearly horizontal dotted line) and a thermally activated part (high slope dotted line) with an activation energy $E_A \sim 0.9\,eV$ (from [32])

an enhancement of diffusion by radiation, but rather to ballistic mixing. The total amount of mixing can be described by an effective diffusion coefficient [25] of the form:

$$D = D_{\text{ballistic}} + D_{\text{rad}} \exp(-Q/kT)\ , \tag{10.65}$$

where the first term on the right hand side is due to ballistic mixing and is temperature-independent, and the second term is due to radiation-enhanced diffusion and has an Arrhenius-type temperature dependence, where Q is an apparent activation energy. The temperature at which the two terms contribute equally to diffusion can be determined from Eq. (10.65) to be:

$$T_c = \frac{Q}{k\,[\ln(D_{\text{rad}}/D_{\text{ballistic}})]}\ . \tag{10.66}$$

Assuming that there is a scaling relationship between the apparent activation energy and the cohesive energy of the matrix, ΔH_{coh}, i.e., $Q = S\Delta H_{\text{coh}}$, where S is a constant, then we obtain:

$$T_c = \frac{S\Delta H_{\text{coh}}}{k\,[\ln(D_{\text{rad}}/D_{\text{ballistic}})]}\ . \tag{10.67}$$

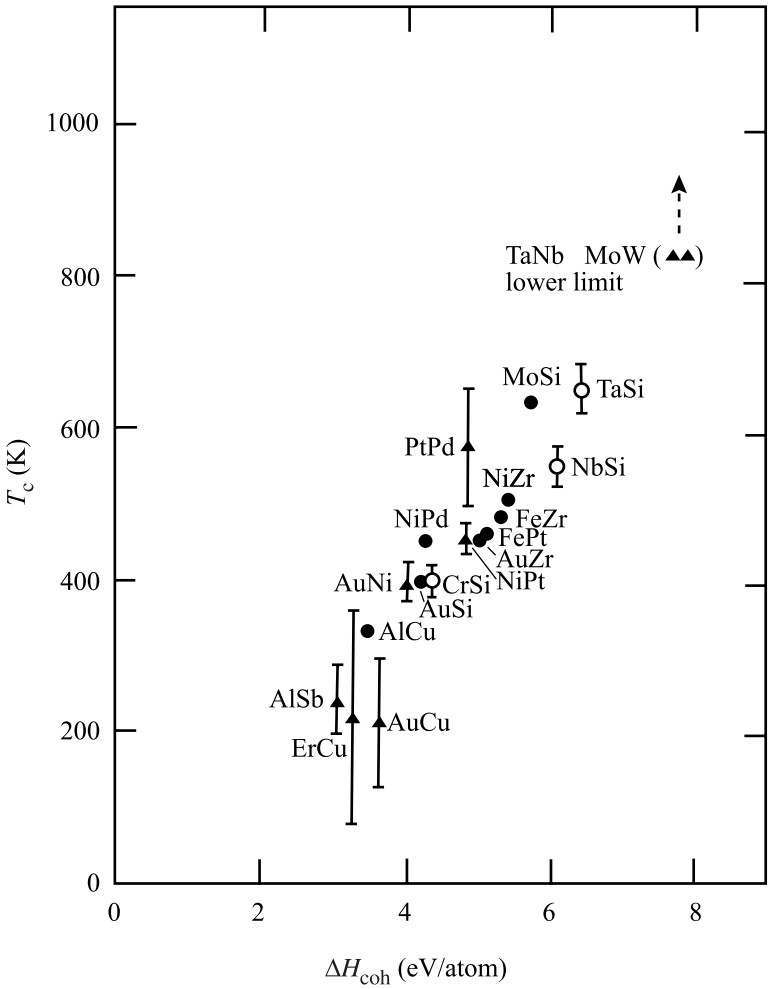

Fig. 10.14. Correlation between the average cohesive energy and the critical temperature, T_c at which mixing by radiation-enhanced diffusion equals that due to ballistic processes (from [33])

Figure 10.14 shows the critical temperature as a function of the average cohesive energy for several bilayer systems using a scaling factor, $S = 0.1$ [33]. Note that the critical temperature is linear with the cohesive energy, as predicted by Eq. (10.67). That the vacancy migration energy also scales with the cohesive energy means that radiation-enhanced diffusion is due to vacancy migration.

In addition to homogenization of a target, displacement mixing is a very effective tool to study phase transformations under irradiation. Phase stability under irradiation was covered in Chap. 9, but ion beam mixing provides a unique opportunity to study ion-induced phase formation. Figure 10.15 shows how bilayer wedge

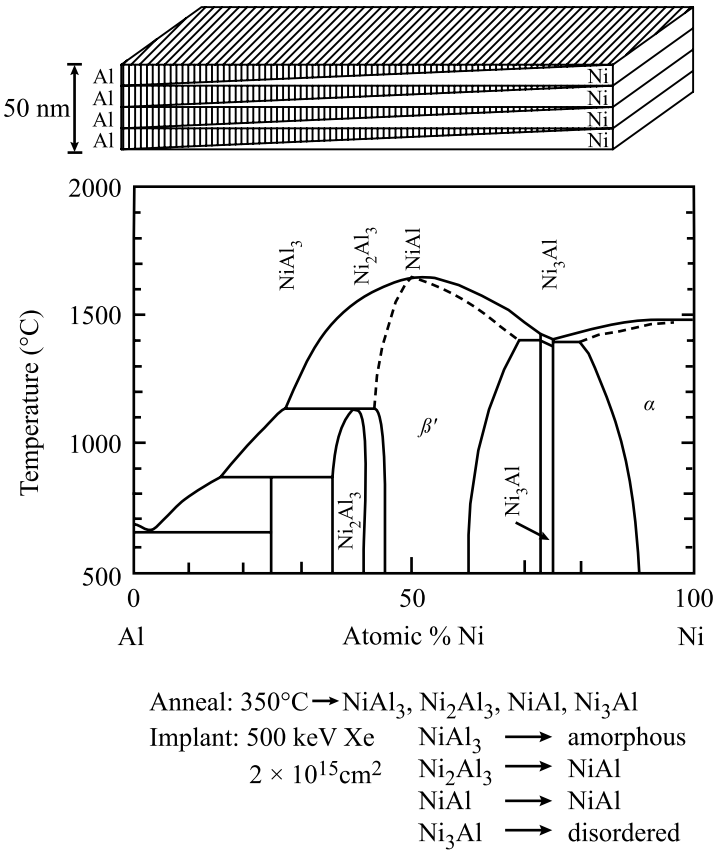

Fig. 10.15. Sample configuration, equilibrium phase diagram of Ni–Al and results of multilayered samples pre-annealed at 350 °C followed by irradiation with 500 keV Xe^+ to a dose of 2×10^{15} cm^2 (from [34])

samples can be made to cover the full range of composition in the Ni–Al binary system and how the phases develop as a function of composition. Figure 10.16 also shows that in most cases the phases formed are independent of whether the irradiation is by ion beam mixing, direct ion implantation of an inert element, or direct implantation of A into B or B into A.

10.2.5 Combination of Processes Affecting Surface Compositional Changes

Accounting for the effects of all the processes described in the previous sections, Lam and Wiedersich [13] constructed a phenomenological model for bombardment-induced composition modification by formulating a set of coupled partial differential equations describing the temporal and spatial evolution of defect and atom concentrations during ion bombardment of a binary alloy. The formulation was based on

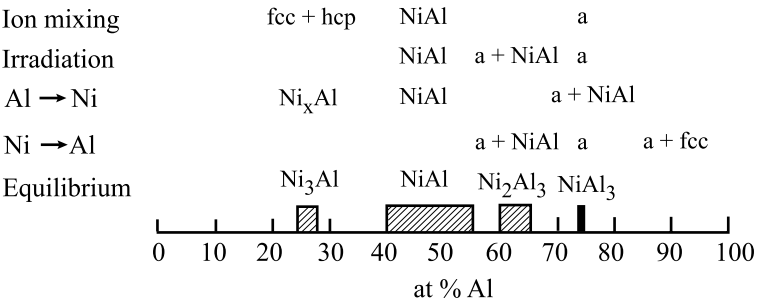

Fig. 10.16. Summary of microstructures in the Ni–Al system prepared by various ion beam treatments (from [35])

the set of diffusion and reaction rate equations, i.e., Fick's second law with source and sink terms, describing the time rate of change of the alloy composition and defect concentrations,

$$\frac{\partial C_\mathrm{v}}{\partial t} = -\nabla \cdot (\Omega J_\mathrm{v}) + K_0 - R \,, \tag{10.68}$$

$$\frac{\partial C_\mathrm{i}}{\partial t} = -\nabla \cdot (\Omega J_\mathrm{i}) + K_0 - R \,, \tag{10.69}$$

$$\frac{\partial C_\mathrm{A}}{\partial t} = -\nabla \cdot [(\Omega J_\mathrm{A}) - D_\mathrm{A}^\mathrm{disp} \nabla C_\mathrm{A}] \,, \tag{10.70}$$

where K_0 and R are the locally and spatially dependent rates of production and recombination of vacancies and interstitials and $D_\mathrm{A}^\mathrm{disp}$ is the diffusion coefficient caused solely by the displacement process. The time-dependent atom and defect concentration distributions can be determined by solving Eqs. (10.68) through (10.70) numerically for a semi-infinite target using appropriate starting and boundary conditions as described by Lam. [13, 36, 37, 38] This formulation covers the processes of DM, RED and RIS. Gibbsian adsorption and preferential sputtering can be accommodated in the model by treating the surface layer as a separate phase. Because of the structure of the phenomenological model, calculations can be made to determine the dependence of surface and subsurface compositional changes on material and irradiation variables as well as isolating the contributions of individual processes. However, because many of the parameters needed in the models are unknown, quantitative comparisons with experiment are difficult. Nevertheless, semi-quantitative modeling of bombardment-induced compositional redistribution in several binary alloys have been made.

Wiedersich et al. [11, 34] provided a nice description of the effects of the different processes that occur during bombardment of an alloy and how those processes affect the surface composition. The calculations were performed with various combinations of preferential sputtering, displacement mixing, radiation-enhanced diffusion, Gibbsian adsorption and radiation-induced segregation included. Figure 10.17 shows the time evolution of the Cu concentration profiles and the location of the

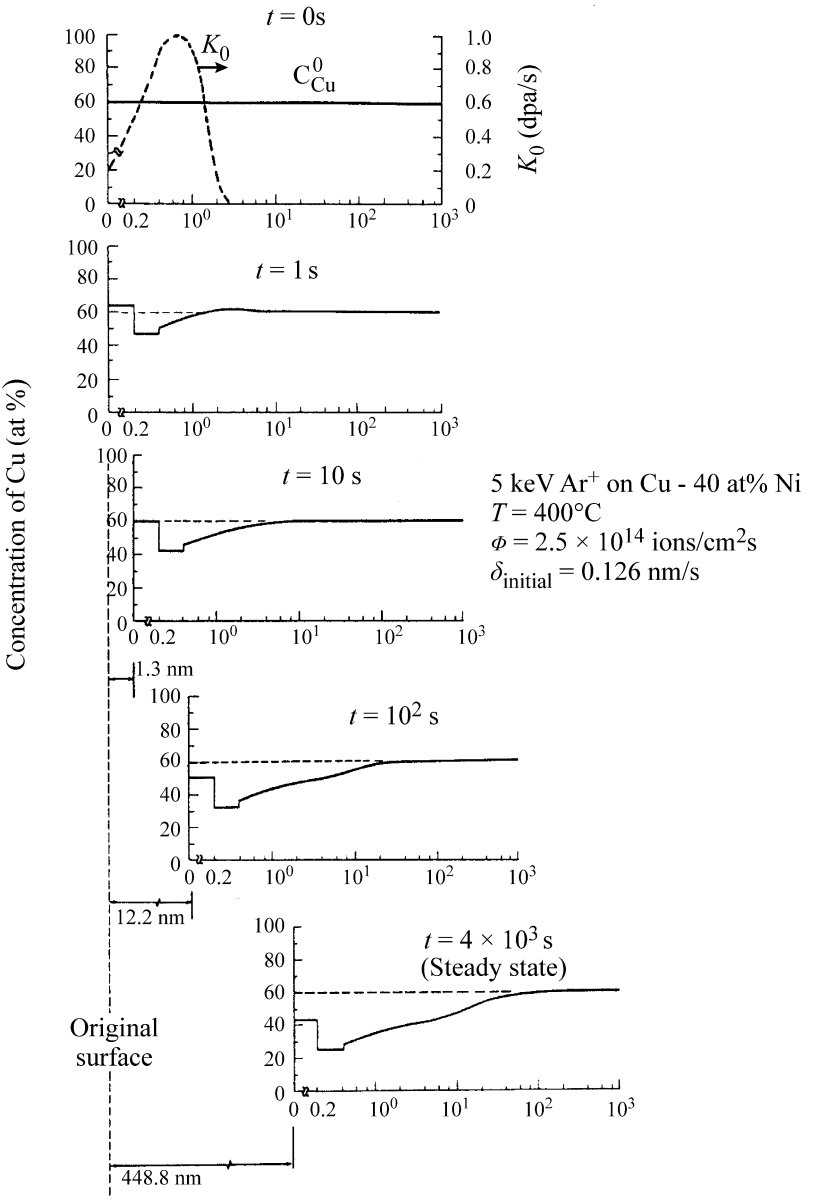

Fig. 10.17. Time evolution of Cu concentration and the location of the surface in a Cu–40 at%Ni alloy bombarded with 5 keV Ar^+ at 400 °C (from [11])

sample surface in Cu–40at%Ni bombarded with 5 keV Ar ions at 400 °C. Gibbsian adsorption causes an initial enrichment in the surface concentration of Cu (1 s). After 10^2 s, sputtering has preferentially removed Cu from the surface, resulting in a depletion of surface Cu relative to the bulk. After 4×10^3 s, steady state is achieved

and the Cu concentration is depleted at the surface, but the depth profile continues to reflect the effect of GA. Note also the recession of the surface with increasing dose due to sputtering.

Figure 10.18 shows the time dependence of the Cu concentration at the alloy surface. Note that in the absence of irradiation (curve 1), GA leads to a strong Cu enrichment in the first atom layer. Accounting only for PS and RED during irradiation (2) causes a monotonic decrease in C^{s}_{Cu} to the steady state value, defined by the sputtering probability ratio and the bulk composition. If GA is included (3), C^{s}_{Cu} increases rapidly at short times owing to radiation-enhanced adsorption, and then decreases slowly to the steady state value. The inclusion of DM reduces the effect of GA (4). Considering only PS, RED and RIS (5), C^{s}_{Cu} decreases rapidly to the steady state value due to the dominant effect of segregation. If GA is added (6) then the effect of RIS is masked. Finally, with the addition of DM (7), or when all processes are included, C^{s}_{Cu} increases initially and then decreases toward the steady state value. The effect of different combinations of processes on the steady state Cu concentration profile is illustrated in Fig. 10.19.

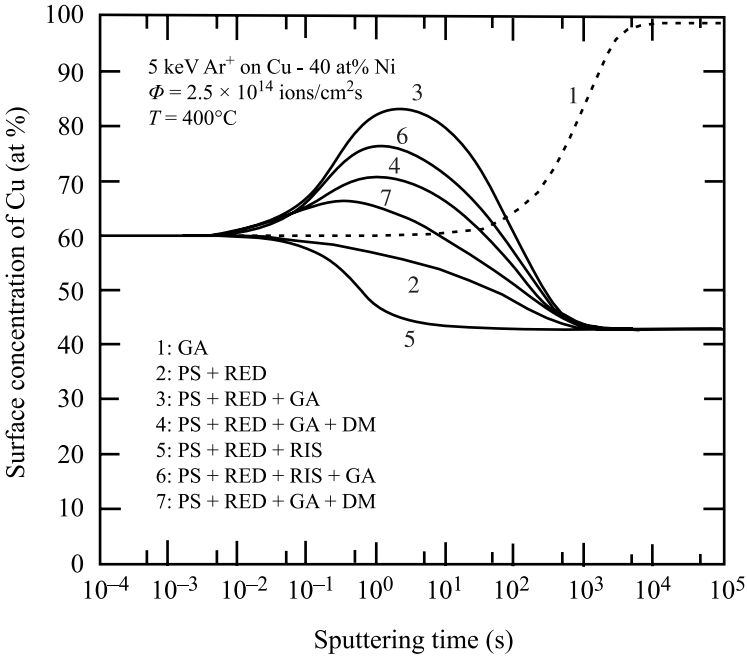

Fig. 10.18. Effects of various combinations of Gibbsian adsorption (GA), preferential sputtering (PS), radiation-enhanced diffusion (RED), displacement mixing (DM), and radiation-induced segregation (RIS) on the time evolution of the surface concentration of Cu in Cu–40 at%Ni described in Fig. 10.17 (from [11])

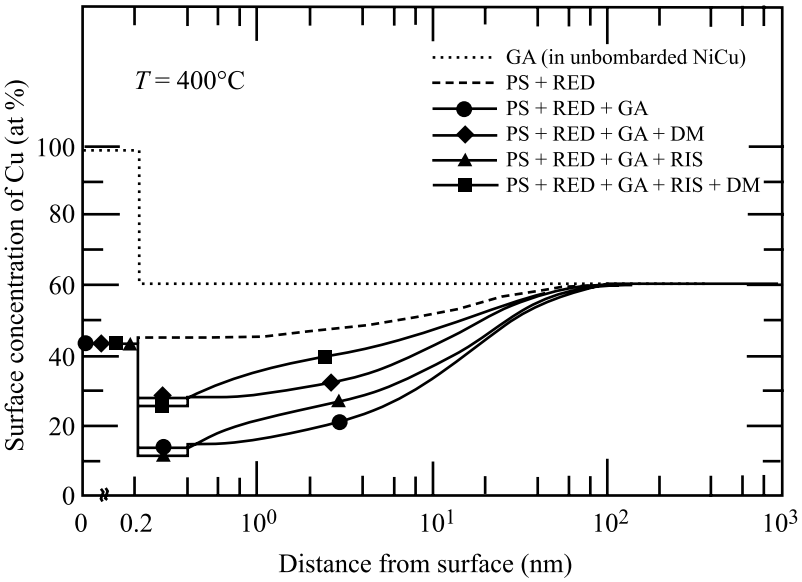

Fig. 10.19. Effects of various combinations of the same five processes described in Fig. 10.18 on the steady state Cu concentration profiles (from [11])

10.2.6 Implant Re-Distribution During Ion Implantation

The implantation example given in Fig. 10.17 to Fig. 10.19 was for bombardment of an alloy with an inert gas ion that plays no role as a chemical constituent of the alloy. In ion implantation, the concentration of the implanted ion is important to track, in addition to the effects of the various surfaces processes. A kinetic model was developed recently by Lam and Leaf [39] to describe the effects of these kinetic processes on the spatial re-distribution of implanted atoms during the implantation process. The effects of spatially non-uniform rates of damage and ion deposition, as well as the movement of the bombarded surface as a result of sputtering and introduction of foreign atoms into the system, were taken into account. The evolution of the implant concentration profile in time and space was calculated for various temperatures, ion energies, and ion–target combinations for a metal substrate B into which A atoms are implanted at a flux ϕ. The local concentrations of vacancies, B interstitial, A interstitials, A–vacancy complexes and free substitutional (A) solutes change with implantation time according to a system of kinetic equations [39] similar to those of Eqs. (10.68) through (10.70). Concurrently with the buildup of solute concentration in the host matrix, the surface is subjected to displacements both from sputtering and the introduction of foreign atoms into the system. Sputtering causes a recession of the surface while implantation causes an expansion. The net surface displacement rate is controlled by the competition between the rates of ion collection and sputtering.

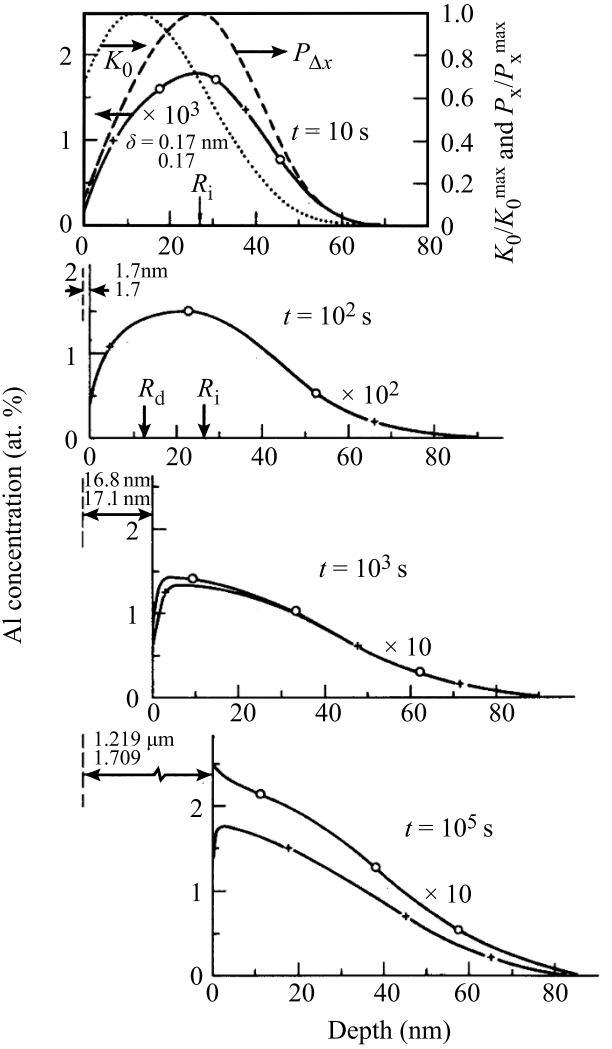

Fig. 10.20. Development of Al concentration profiles during 50 keV implantation at 500 °C. The normalized damage rate, K_0 and ion deposition rate P are shown in the top plot and the surface displacements resulting from sputtering are indicated. Note that the concentration profiles are multiplied by factors shown in each plot (from [13])

The temporal and spatial evolution of the surface and subsurface alloy composition is obtained by solving this set of equations for a semi-infinite medium, starting from the thermodynamic equilibrium conditions. Sample calculations were performed for low and high-energy Al^+ and Si^+ implantations into Ni, since it is known from earlier studies that in irradiated Ni, Si segregates in the same direction as the defect fluxes whereas Al opposes the defect fluxes [40]. Re-distributions of Al and Si solutes in Ni during 50 keV implantation at 500 °C are shown in Fig. 10.20 and Fig. 10.21, respectively.

In the Al-implantation case, C^s_{Al} increases with time to a steady state value of ~50 at%, which is governed by the partial sputtering yield of the implant. This value

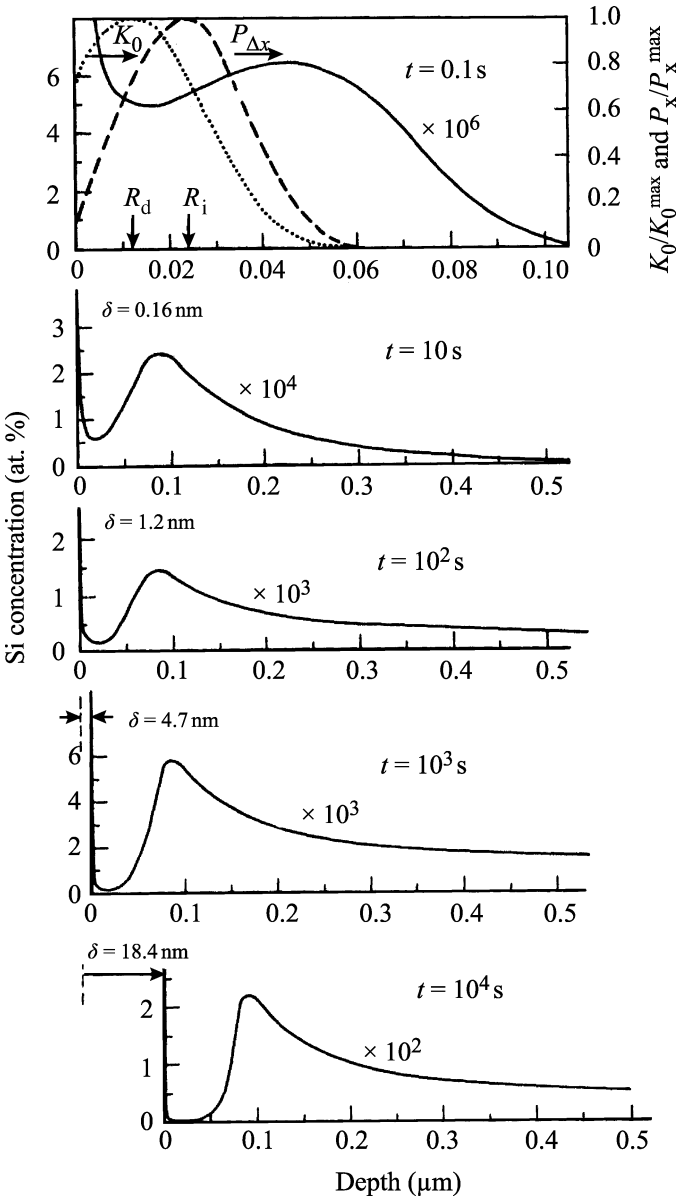

Fig. 10.21. Time evolution of the Si concentration profile during 50 keV implantation at 500 °C. The normalized damage rate, K_0 and ion deposition rate, P are shown in the top plot. Surface displacements resulting from sputtering are indicated (from [13])

is substantially larger than that obtained in very high-energy implantation, where sputtering is negligible and C_{Al}^{s} is controlled by RIS. However, the total implant concentration remaining in the sample is significantly smaller because of sputtering.

Furthermore, the shape of the steady state implant profile is dictated by PS, which controls the boundary condition at the surface, and by RED and RIS.

The evolution of the Si profile is rather different from that of Al, because of the different RIS behaviors. After a short implantation time, Si enrichment occurs at the surface because of RIS, and the Si distribution peak starts moving into the sample interior (Fig. 10.21). With increasing time, $C_{\mathrm{Si}}^{\mathrm{s}}$ increases monotonically, attaining a steady state value of $\sim$100 at% at $t \geq 2 \times 10^4$ s. Unlike the Al case, the Si profile shows a significant shift of the implant distribution into the beyond-range region. This predicted translation of the Si distribution peak into the sample interior was consistent with experimental measurements by Mayer et al. [41] in Si-implanted Ni at elevated temperatures.

10.3 Other Effects of Ion Implantation

10.3.1 Grain Growth

Ion-induced grain growth has been observed during irradiation of pure metals and multilayers. Liu and Mayer [42] observed the growth of grains of pure nickel films upon irradiation with inert gas ions, Ar, Kr and Xe in the energy range 150 to 580 keV. In their experiments, the grain size increased with dose until saturation at about 1×10^{16} i/cm^2. They found a nearly homogeneous grain size in the irradiated samples as compared to a wide spread in the grain size of thermally annealed samples. They also observed a dependence of the saturated grain size on ion species and only a weak dependence of grain size on ion dose at high doses (Fig. 10.22). The localized damage caused by the displacement spike in the vicinity of the grain boundary is the likely driving force for grain growth. The observed grain growth is explained by the re-ordering or growth of heavily damaged grains into neighboring, undamaged grains. The reduction in energy at a localized growing grain is equivalent to the difference between the energy released from the consumed region and the energy required to expand the grain boundary. The initially rapid grain growth can be explained by a larger probability of damaging an entire grain when the grains are small. As the irradiation process continues, the large grains consume the small ones and the average grain size increases. When the average diameter of the growing grains approaches the dimension of the damaged volume, the probability of highly damaging an entire grain by a single collision cascade is reduced, as is the chance of growing certain grains at the expense of others. Therefore, the grain growth rate gradually decreases with the increase of grain size.

The grain growth rate during mixing of multilayered Ni–Al films is enhanced over that due to bombardment of co-deposited Ni–Al films of the same average composition by a factor of 2.2 (Fig. 10.23). This enhancement can be understood using the concept of the heat of mixing, using Johnson's expression for the total number of atom jumps induced in a spike per unit length of a cylindrical thermal spike, η. Assuming that this value is proportional to grain boundary mobility, the

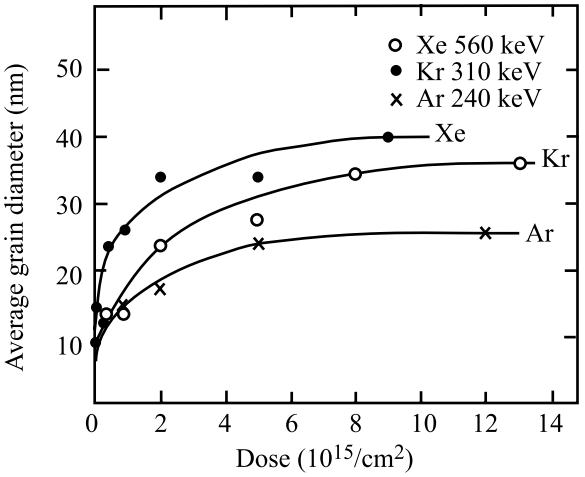

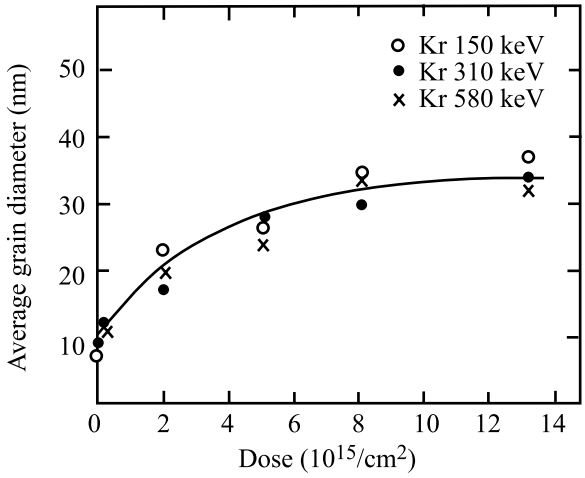

Fig. 10.22. Average grain diameter vs. dose for (a) 240keV Ar, 310keV Kr and 560keV Xe ion irradiations of polycrystalline nickel films, and (b) 150keV, 310keV and 580keV Kr ion irradiations of polycrystalline nickel films (from [42])

grain size, d can be related to the initial grain size, d_0 and η in Eq. (10.64) as follows:

$$(d^3 - d_0^3)/\phi\alpha\varepsilon^2\Delta H_{\text{coh}}^2[1 + K_2(\Delta H_{\text{mix}}/\Delta H_{\text{coh}})] \,. \tag{10.71}$$

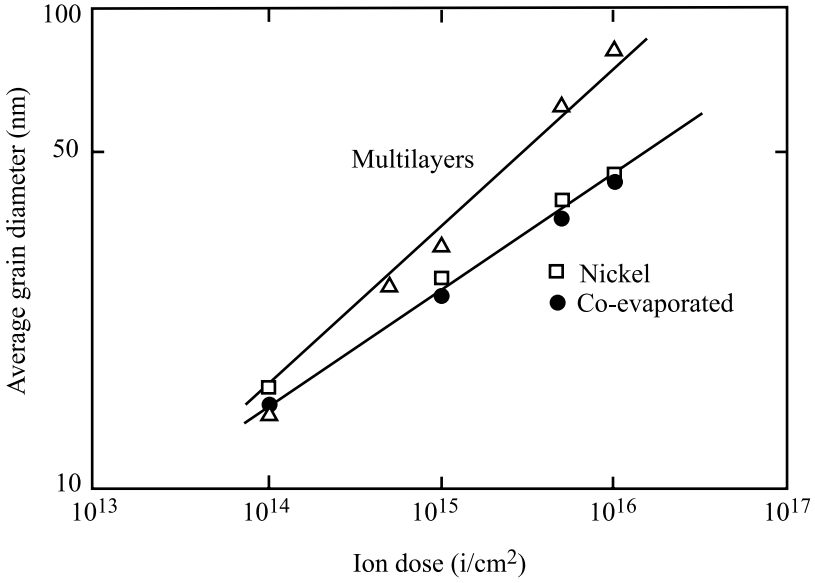

Fig. 10.23. Ion-induced grain growth observed in 40 nm thick nickel, Ni–20at%Al multilayers and Ni–20at%Al co-evaporated films irradiated with 700 keV Xe^{++} ions (from [43])

Since $\Delta H_{\text{mix}} = 0$ for the irradiated co-evaporated films, the ratio of measured values of mobilities should be:

$$\frac{(d^3 - d_0^3)\big|_{\text{ML}} / \phi|_{\text{ML}}}{(d^3 - d_0^3)\big|_{\text{CO}} / \phi|_{\text{CO}}} = 1 + K_2(\Delta H_{\text{mix}}/\Delta H_{\text{coh}}) \,. \tag{10.72}$$

Given the cohesive energy and heat of mixing of a Ni–20at%Al alloy, the ratio in Eq. (10.72) is 3.0, as compared with the measured value of 2.2. These results indicate that the heat of mixing appears to play a role in ion-induced grain growth as well as ion beam mixing.

10.3.2 Texture

There have been many reports of texture effects in ion beam mixed or ion beam-assisted deposition of films. Alexander et al. [43] and Eridon et al. [44] found that mixing multilayers of Ni and Al in the composition Ni–20%Al resulted in the formation of the hcp and fcc (γ) phases. The γ phase had a strong $\langle 111 \rangle$ texture and the hcp phase had a $\langle 001 \rangle$ texture. The textures were such that the close-packed planes of both phases were parallel to the film surface. These textures formed regardless of the angle of the ion irradiation with respect to the film. The formation of the texture seemed to be driven by the matching of the close packed planes. Ahmed and Potter [45] found that irradiation of Ni with Al to 1.2×10^{18} /cm^2 resulted in 350 nm

grains of β' phase oriented with respect to the underlying fcc nickel in accord with the Nishiyama relationship [46].

The development of texture during ion beam-assisted deposition can be correlated with the channeling directions of ions in the crystal lattice and the density of energy deposition would be inversely related to the depth of channeling. Thus, in an fcc crystal, the ease of channeling is in the order $\langle 110\rangle$, $\langle 200\rangle$, $\langle 111\rangle$. Bradley et al. [47] have developed a model to explain the development of preferred orientation due to low-energy ion bombardment during film growth which is based on the difference in sputtering yields for different orientations rather than reorientation during recrystallization. Both effects are of course based on the same phenomenon of the variation of energy density with channeling direction. In this model, crystallites with high sputtering orientations are removed more rapidly and newly deposited material grows epitaxially in the low sputtering yield orientations.

Thin films of PVD deposited materials normally grow with the planes of highest atomic density parallel to the substrate so fcc films have a $\langle 111\rangle$ texture, bcc films have a $\langle 110\rangle$ texture and hcp films have a $\langle 0002\rangle$ texture (for ideal c/a ratios). The easiest channeling directions in each structure are as follows:

fcc $\langle 110\rangle, \langle 100\rangle, \langle 111\rangle$

bcc $\langle 111\rangle, \langle 100\rangle, \langle 110\rangle$

hcp $\langle 1120\rangle, \langle 0002\rangle$

Ion bombardment causes a shift in the preferred orientation to alignment of the easiest channeling direction along the ion beam axis. Thus, an ion beam at normal incidence on an fcc film will cause a shift in orientation from $\langle 111\rangle$ to $\rangle 110\langle$ texture. A beam incident at an angle will produce a different texture depending on the crystallography. The texturing effect appears to be most sensitive to high-energy beams because of the larger volume affected per ion and the deeper penetration. Experiments on ion bombardment during deposition of an Al film show that while Al forms a very strong $\langle 111\rangle$ texture during physical vapor deposition, bombardment during deposition can induce an equally strong $\langle 110\rangle$ texture that is driven by ion channeling [48].

10.3.3 Dislocation Microstructure

Ion implantation can induce the formation of a high dislocation density well beyond the implanted layer in response to high surface stresses caused by high doses of the implanted element [49]. Figure 10.24 shows the depth profile of the dislocation density in α-Fe resulting from implantation of various ions (C, Fe, W, Ar) at energies between 40 and 68 keV and to doses up to $10^{18}\,\mathrm{cm}^{-2}$. Note that while the projected ion range is less than 50 nm in all cases, the induced dislocation density peaks at between 5 and 10 μm and extends out to over 100 μm or more. The substructure is characterized by a dense dislocation network in which the dislocation density increases with dose and with the radius of the implanted ion. X-ray diffraction measurements show that the stresses exceed the yield stress and cause plastic strains in the range of 10%.

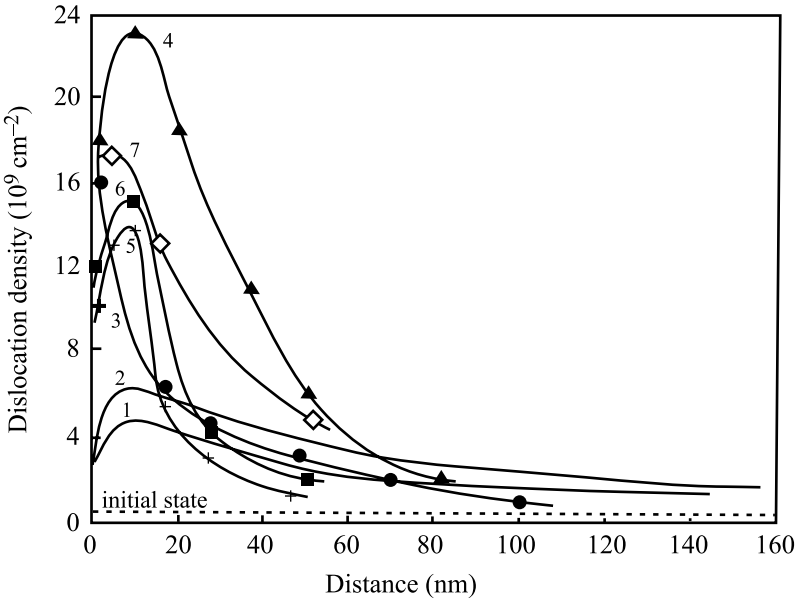

Fig. 10.24. Dislocation density vs. depth in α-Fe irradiated with 1) C: 40 keV, 1×10^{16} cm^{-2}, 2) C: 40 keV, 1×10^{18} cm^{-2}, 3) Fe: 68 keV, 1×10^{18} cm^{-2}, 4) W: 110 keV, 2×10^{17} cm^{-2}, 5) Ar: 50 keV, 2×10^{16} cm^{-2}, 6) Ar: 50 keV, 5×10^{16} cm^{-2}, 7) Ar: 50 keV, 1×10^{17} cm^{-2}. Irradiations 1–4 were pulsed and irradiations 5–7 were continuous (from [49])

The high density dislocation network created by ion implantation can induce recrystallization which can then affect the distribution of the implanted specie. Ahmed and Potter [45] performed a study of 180 keV Al implantation into pure Ni at 25 °C and at elevated temperatures (300–600 °C). At elevated temperatures, individual dislocation loops dominate the microstructure at the lowest fluences ($\sim 10^{15}$ cm^{-2}). These loops bound collections of interstitial atoms or vacancies, defects caused by the energetic Al ions penetrating the nickel structure and displacing atoms from their lattice sites. The loops climb with further implantation, intersect and react with other loops, and form complex dislocation networks after a dose of 2.1×10^{17} Al/cm^2. By a dose of 3×10^{17} Al/cm^2, three-dimensional aggregates of vacancies are present.

The composition profile of Al implanted into Ni is relatively independent of temperature between 23 and 600 °C and for doses less than 10^{18} cm^{-2}. However, at higher doses, gross changes in the implanted distribution occur with the profile flattening and a considerable amount of Al transported to greater depths (Fig. 10.25). The same occurs following aging of room temperature implantations at 600 °C for 15 min. The microstructures developed at depths greater than the range of the 180 keV Al^+ ions, ~100 nm, play an important role in determining the stability of the implanted concentration profiles.

Dislocation loops are present at depths near 300 nm following room temperature implantation. These loops are faulted Frank loops, 5–10 nm in diameter and their number density increases with fluence, reaching $\sim 4 \times 10^{16}$ cm^{-2} at 3×10^{18} cm^{-2}.

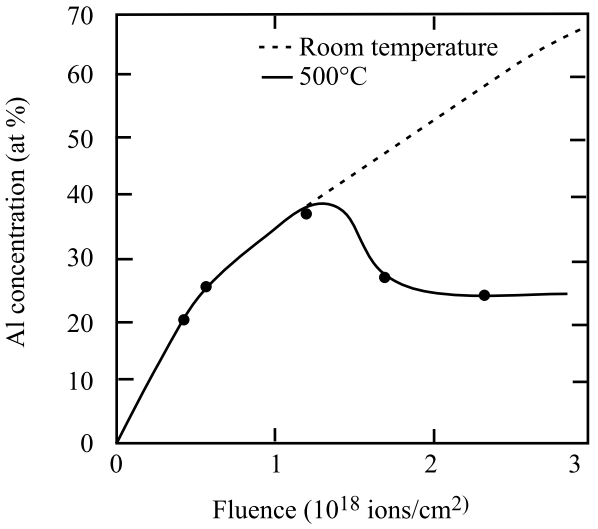

Fig. 10.25. Peak aluminum concentration plotted vs. fluence for implantation of aluminum into nickel at 500 °C (from [45])

However, the dislocations behind the implanted layer are removed when the material is heated to 600 °C. This occurs by re-crystallization, which is also responsible for the re-distribution of implanted Al. The following describes the processes occurring.

Following room temperature implantation, an amorphous phase extends to a depth of ∼160 nm. Small crystal of β' and γ extend from 160 nm to ∼300 nm and from ∼300 nm to ∼400 nm, respectively. Dislocations and dislocation loops extend beyond this to depths of >800 nm. Aging at 600 °C following room temperature implantation or implanting at high temperatures causes re-crystallization of the fine grain structure to depths of ∼ 800 nm to ∼1000 nm. In both instances, aluminum atoms must move through relatively pure nickel to accomplish the re-distribution, which is only possible if some fast diffusion process occurs. This is afforded by the small grains which form upon re-crystallization of the heavily dislocated region beyond the implanted layer and provide high angle grain boundaries for abnormally fast diffusion. The composition reaches a plateau by virtue of the limited extent of the re-crystallization. Figure 10.26 shows that the re-distribution only occurs above a threshold dose indicating the role of the radiation damage in the re-crystallization process. This example serves to tie together the roles of the implanted specie, the character of the radiation damage and the processes (re-crystallization and abnormally fast diffusion) that can be affected by implantation fields.

10.4 High Dose Gas Loading: Blistering and Exfoilation

The first wall and divertor of a fusion reactor are expected to be subject to high fluxes of moderate to low-energy deuterium and helium ions created as fusion reaction products. Below 1 MeV, helium comes to rest approximately 1 μm below the surface and extended exposure at high flux can lead to very high levels of

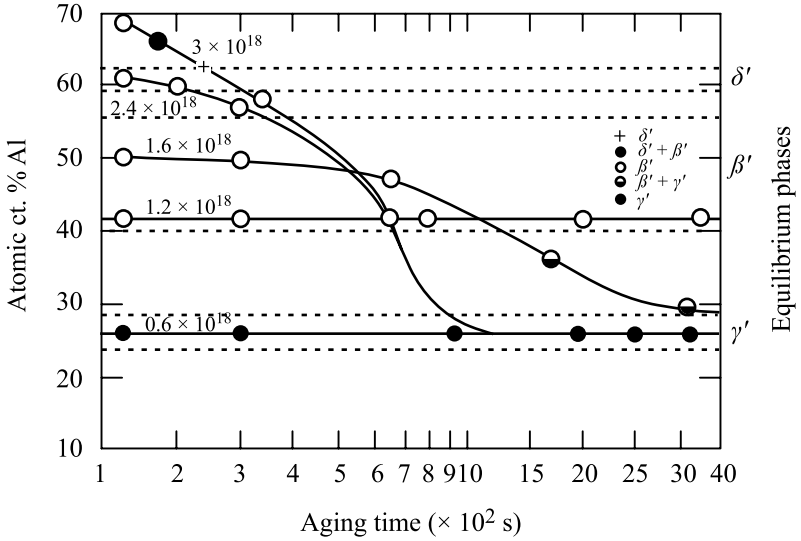

Fig. 10.26. Aluminum concentration vs. time at 600°C for fluences between 0.6 and 3.0×10^{18} i/cm^2. The phases observed in the implanted layers, symbols on curves, and those expected based on the equilibrium phase diagram (right side ordinate) are shown (from [45])

helium. At the expected temperatures (400–700°C) and aided by the high defect concentration due to radiation damage, He will be mobile and will form bubbles as discussed in Chap. 8. The growth and coalescence of bubbles leads to the formation of blisters resulting in exfoliation of the surface as shown in Fig. 10.27. Figure 10.28a illustrates the result of high He loading a short distance beneath the surface of a metal. The bubbles are constrained to a narrow band of solid beneath the surface. There, they may grow and either coalesce to form larger bubbles or cause interbubble fracture due to the stresses between the bubbles (Fig. 10.28a). A cross sectional image of the subsurface region of a nickel sample bombarded with a high dose of He, Fig. 10.28b shows that the bubble microstructure is confined to the near-surface region. Stresses arise because the bubbles are not in equilibrium. That is, pressure due to the gas in the bubble is not balanced by the stress due to the surface tension, resulting in a radially directed stress, σ_{rr} on the bubble:

$$\sigma_{rr} = p - (2\gamma/r) \,. \tag{10.73}$$

Wolfer [52] developed an expression for the average stress field between bubbles:

$$\frac{\overline{\sigma}}{\mu} = \left[f_{He} \frac{p}{\mu \rho \Omega} - \frac{2\gamma}{\mu \Omega} \left(\frac{4\pi \rho_B}{3} \right)^{1/3} S^{2/3} \right] F(S) \,, \tag{10.74}$$

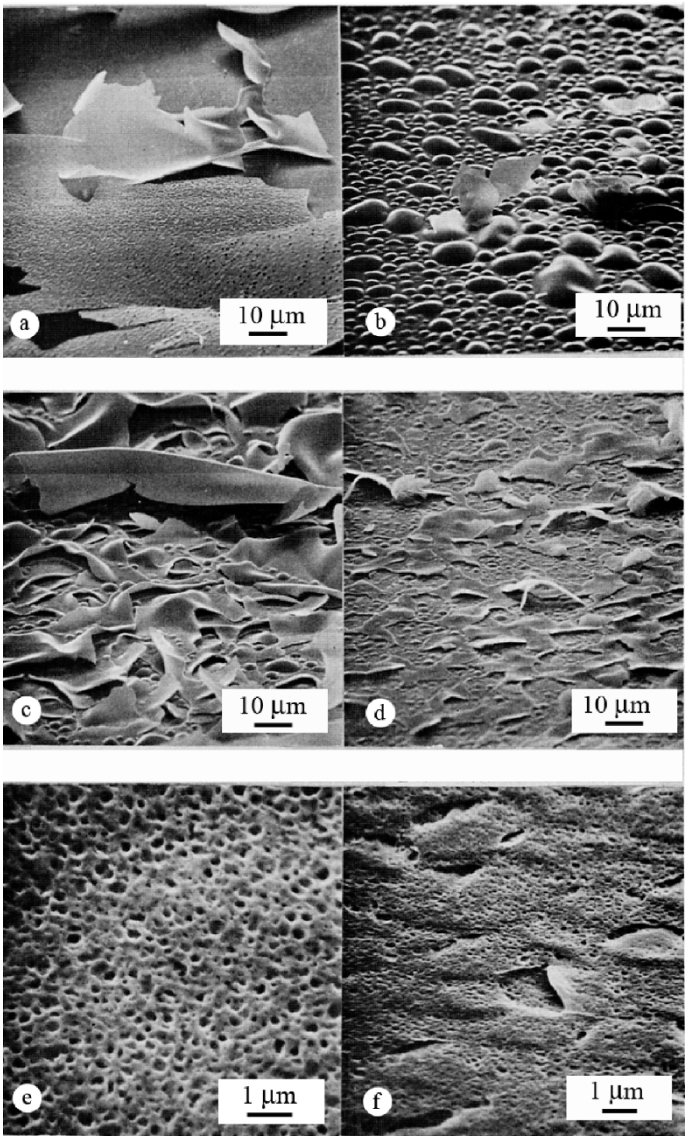

Fig. 10.27. Surface topography of polycrystalline nickel irradiated with different doses of 100 keV He^+ ions: (a) 2×10^{18} $^4He/cm^2$ at normal incidence, (b) 2×10^{18} $^3He/cm^2$ at normal incidence, (c) 1×10^{19} $^3He/cm^2$ at normal incidence, (d) 2×10^{19} $^3He/cm^2$ at 60° from normal, (e) 1.2×10^{20} $^4He/cm^2$ at normal, and (f) 3.4×10^{19} $^3He/cm^2$ at 60° from normal (from [50])

where μ is the shear modulus, $f_{He} = m\rho_B\Omega$, m is the number of gas atoms in a bubble, ρ_B is the bubble density, Ω is the atomic volume of the metal atoms, ρ is the helium density in the bubbles, γ is the surface energy and $S = f_{He}/\rho$ The function

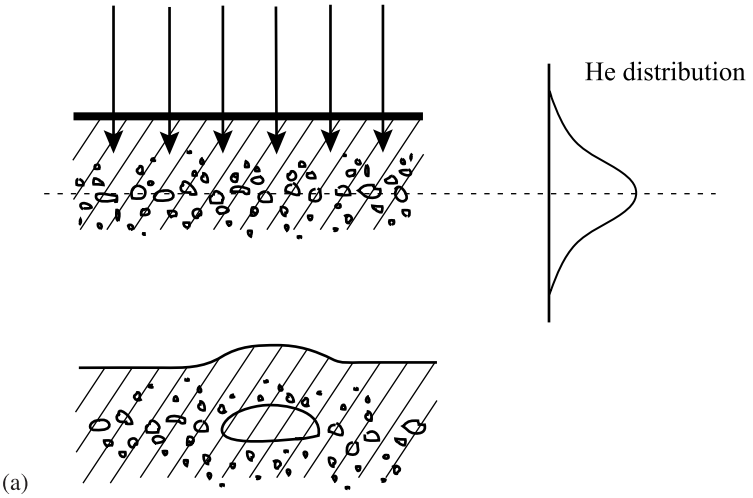

(a)

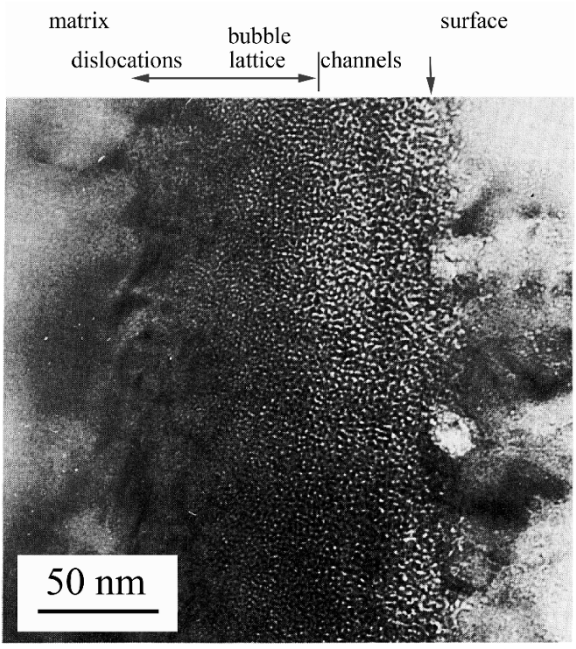

(b)

Fig. 10.28. (a) Coalescence of bubbles below the surface of a sample loaded with a high dose of helium. (b) Cross section of a high dose, He-implanted surface layer of nickel showing the dislocations (deep), bubble lattice (middle) and connected channels (near-surface) (from [51])

$F(S)$ is defined for a random array of bubbles and for $\rho \sim 1.0$ as:

$$F(S) = (0.827S^{1/3} - S)^{-1} \,. \tag{10.75}$$

Since the ultimate tensile strength determines both the ductile, transgranular fracture of fcc metals and the transgranular cleavage fracture of bcc and hcp metals, and is about 0.003μ for fcc metals and roughly 0.01μ for bcc metals, then $\overline{\sigma} \sim 0.01\mu$. The corresponding helium concentrations needed to reach the stress to cause fracture between bubbles due to the stress are shown in Fig. 10.29, and for $\rho = 1$, the critical helium concentration is $\sim 20 - 40\%$. Wolfer also identifies another stress, the lateral stress, σ_L that is in the plane of the bubbles parallel to the surface (Fig. 10.30). The lateral stress depends on the swelling rate, $\dot{S}$ according to:

$$\sigma_L = \frac{-\dot{S}E}{(1-\nu)}\,, \tag{10.76}$$

where E is the elastic modulus and ν is Poisson's ratio. Blister formation is then a two-step process. Fracture starts at the depth, t_B below the surface where $\overline{\sigma}$ is a maximum by growth of the bubbles to a point where the local stresses are sufficient to crack open the plane adjoining the bubbles. The penny-shaped crack then spreads until a diameter, D_B is reached where the buckling condition is satisfied by the existing lateral load:

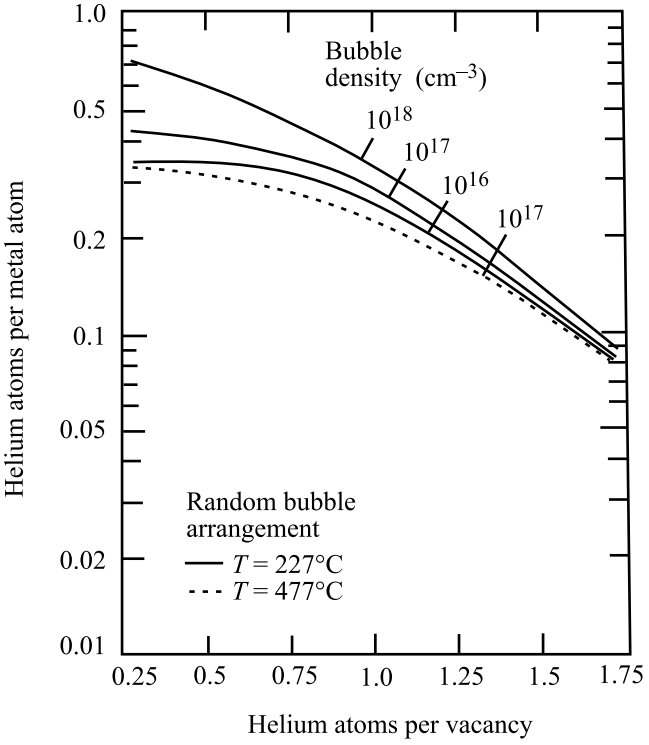

Fig. 10.29. Critical implanted He concentration vs. He concentration in the bubbles for the case of random bubbles (from [52])

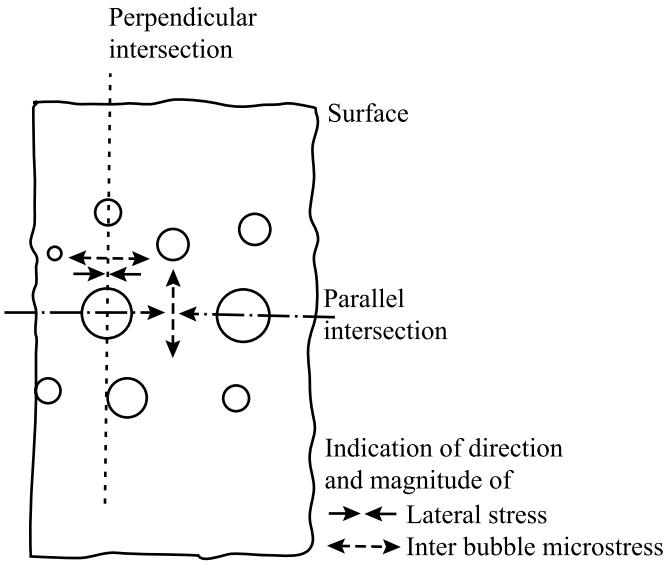

Fig. 10.30. Schematic cross section of the He-implanted layer with gas bubbles and definitions of the lateral stress and the interbubble stress (from [52])

$$D_{\mathrm{B}} = 1.55\frac{\mu}{(1-\nu)P}\,, \tag{10.77}$$

$$\text{where} \quad P = -\int_0^{t_{\mathrm{B}}} \sigma_L \,\mathrm{d}t_{\mathrm{B}} \tag{10.78}$$

Note that experiment has identified the relationship between the blister base diameter and its thickness to be $D_{\mathrm{B}} \sim t_{\mathrm{B}}^{\mathrm{m}}$, and this relation supports the lateral stress as the cause of blister formation [52]. Alternatively, the penny-shaped crack can continue to extend until detachment occurs, resulting in flaking and exfoliation as shown in Fig. 10.27.

Very high doses of helium or implantation at high temperature often result in a *sponge*-type structure in which the surface consists of a series of pits as shown in Fig. 10.31. At very high temperature where bubbles are mobile, the pits may be the result of bubble intersection with the surface. However, high dose ion implantation can led to severe topological surface changes and this is the subject of much investigation.

10.5 Solid Phases and Inert Gas Bubble Lattices

Implantation of noble gases to high doses at room temperature can lead to a different phenomenon: solid bubbles. Ar, Kr and Xe implanted into a variety of host metals have been observed to form solid bubbles consisting of crystals of the implanted

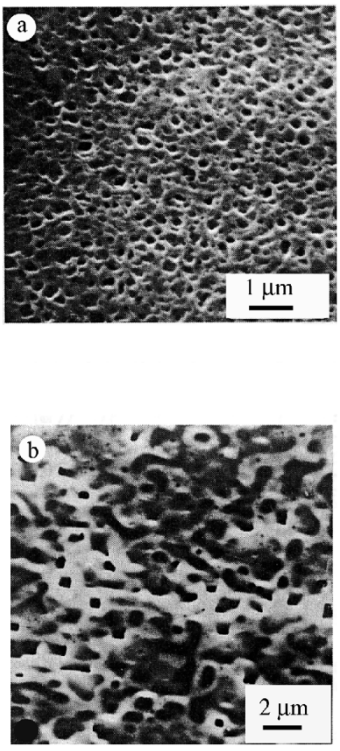

Fig. 10.31. Holes in the surface of Nb irradiated with (a) 1.2×10^{20} He/cm^2 at 23 °C and (b) 3×10^{17} He/cm^2 at 823 °C (from [53])

noble gas. In Ni and Al, gases precipitate as solids with the same crystal structure as the host lattice and epitaxially aligned with the matrix. The solid phase forms at doses in the range of $10^{20}\,m^{-2}$ and the precipitate size is about 1.5 nm in Ni and up to 4.7 nm in Al [54, 55]. The lattice parameter of the precipitates is larger than that of the host and increases with the atomic mass of the inert gas. The lattice parameter increases with dose and tends toward a saturation value as shown in Fig. 10.32. Precipitate densities can be very high, in the range of $10^{24}\,m^{-3}$. The average pressure of the solid gas can be determined from the average gas density, the lattice constant and the equation of state for the gas and is estimated to reach values in excess of 40 kbar. While the pressure required to solidify the gas at room temperature depends on the gas (8 kbar for Kr and 11.5 kbar for Ar), the calculated values are in excess of these amounts by several times. The inert gas is held in the solid state by the interatomic forces between the Kr–Kr and the Kr–Ni atoms, for the case of Kr in Ni. As the precipitate size increases, the average spacing between the gas atoms increases, decreasing the magnitude of the Kr–Kr interaction. Eventually, the decrease in gas pressure allows melting of the solid Kr. Implantation of high doses of Kr into amorphous TiCr resulted in the precipitation of crystalline Kr as in the case of crystalline

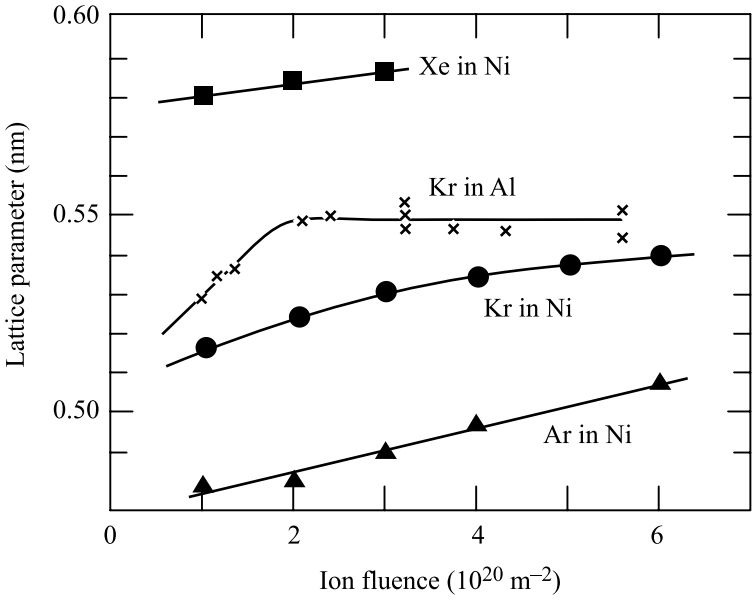

Fig. 10.32. Lattice parameter of solid noble gas precipitates of Xe, Kr and Ar in nickel and of Kr in aluminum, as a function of fluence and implanted at room temperature (from [54] and [55])

metal hosts, but in this case, the solid Kr precipitates induced local crystallization of the host as a bcc structure.

High dose implantation at room temperature can also lead to bubble lattice formation similar to the void lattices described in Chap. 8. Bubble lattices have been observed in Cu, Ni, Au, Ti and stainless steel irradiated with He or Kr. In fcc lattices, the bubbles form in densely packed rows parallel to the matrix $\{111\}$ trace directions [56], and can be described by a lattice constant of order 7.6 nm, corresponding to a bubble density of $\sim 10^{25}\,\mathrm{m}^{-3}$. In hcp lattices, the bubble alignment is parallel to the basal plane, similar to that found for void ordering [57]. The formation of a bubble lattice is independent of the inert gas used and whether the gas atoms are present in bubbles in a gaseous or solid form.

Nomenclature

a	Screening radius. Also nearest neighbor distance
c	Specific heat capacity C_i Concentration of atom of type i
$\mathrm{d}E/\mathrm{d}x\|_\mathrm{n}$	Energy loss rate due to nuclear stopping
d	Grain size
D	Diffusion coefficient
D_B	Blister diameter
D^*	Effective diffusion coefficient
D'	Modified diffusion coefficient accounting for diffusional intermixing

E	Energy. Also Young's modulus
E_{coh}	Cohesive energy
E_{d}	Displacement energy
E_{mix}	Energy of mixing
F	Displacement rate in dpa/s
F_{D}	Deposited energy
H_{ij}	Potential energy between atom pairs of type i and j
ΔH_{coh}	Cohesive energy
ΔH_{A}	Heat of adsorption
ΔH_{mix}	Heat of mixing
J_{i}	Flux of atoms of type i
k	Boltzmann's constant
K_0	Defect production rate
m	Number of gas atoms in a bubble
M	Atomic mass
N	Atom number density
p	Gas pressure in a bubble
p_{i}	Sputter probability of atom of type i
$\overline{p}_{\mathrm{i}}$	Average total sputter probability of atom of type i
P	Load
P_{i}	Total effect of recoil implantation, Eq. (10.31)
Q	Activation energy
Q_{i}	Equivalent number of i atoms recoil implanted over a depth R_{p}
r_{c}	Characteristic jump distance in a thermal spike
R	Ion range. Also root mean square of an atom in a collision cascade Also vacancy–interstitial recombination rate. Also jump rate in thermal spikes
R_{d}	Displacement rate in #/cm^{3}s
R_{p}	Projected range
R_{recoil}	Recoil range
ΔR_{p}	Standard deviation of the projected range
S	Scaling factor
S_{i}	Sputtered flux of atom of type i
S_{n}	Nuclear stopping power
S_{X}	Sputtered flux of element X
t	Time
t_{B}	Blister shell thickness
T	Temperature. Also energy transferred in a collision event
T_{eff}	Effective temperature at which diffusion occurs
U_0	Surface binding energy
Y	Sputter yield
z	Coordination number
Z	Atomic number

α	Constant in Eq. (10.3)
χ	Ratio of probability of sputtering a B atom to that for an A atom
δ	Thickness of surface layer removed by sputtering
ε	Unit charge. Also the energy density in the cascade
$\in$	Reduced energy
ϕ_ι	Flux of atoms of type *i*
γ	Activity coefficient. Also surface energy
Γ	Total jump frequency
η	Number of atom jumps in a thermal spike per unit length of the spike
κ	Thermal diffusivity
λ	Jump length
Λ	Factor in sputtering yield Eq. (10.2) containing material parameters
μ	Shear modulus. Also chemical potential
ν	Number of displacement per primary knock-on atom. Also Poisson's ratio
$\nu_i^{s\to b}$	Surface-to-bulk jump frequency for atom *i*
$\nu_i^{b\to s}$	Bulk-to-surface jump frequency for atom *i*
ρ	Atom density
ρ_B	Gas bubble density
σ_d	Displacement cross section
σ_s	Scattering cross section
$\sigma_{0,i}$	Elastic scattering cross section between ions and i atoms
σ_i	Surface ejection cross section for atoms of type *i*
σ_L	Lateral stress in the solid
$\overline{\sigma}$	Average stress
Ω	Atomic volume
ξ	Atomic layer thickness

Superscripts

b	Bulk
s	Surface

Subscripts

A	Adsorption
B	Bubble or blister
d	Displacement
P	Projected
s	Scattering

Acronyms

CO	Co-evaporated
DM	Displacement mixing
GA	Gibbsian adsorption
FWHM	Full width at half maximum
IBAD	Ion beam-assisted deposition
IBED	Ion beam-enhanced deposition
IBM	Ion beam mixing
II	Ion implantation
ML	Multilayered
PS	Preferential sputtering
PSII	Plasma source ion implantation
RED	Radiation-enhanced diffusion
RIS	Radiation-induced segregation

Problems

10.1 Use the description of how a delta function distribution of particles spreads by diffusion to calculate the width of an initially sharply peaked distribution of:
   a) Vacancies
   b) Interstitials
   c) Self-tracer diffusing by vacancy mechanism.
   in Pt, after a time $t = 1\,\text{min}$, for temperatures of 20 °C and 800 °C.

10.2 Consider a thin foil of a binary alloy in which the surface is the only defect sink. The foil is at thermal equilibrium at low temperature and is then heated instantaneously to near its melting point. Describe qualitatively the evolution of:
   a) The vacancy concentration
   b) The composition profile.

10.3 A bilayer of 50 nm Pd on top of 50 nm Ni is deposited on a silicon substrate. The layer is mixed with 300 keV Kr^+ at a current of $40\,\mu\text{A}/\text{cm}^2$. Determine the sputtering yield. What is the maximum amount of Kr which can be implanted into this sample?

10.4 A Ni–1%Si alloy is heated to a temperature of 500 °C during irradiation by 500 keV Kr ions at a current density of $1\,\mu\text{A}/\text{cm}^2$.
   a) What physical processes will be important in determining the surface concentration?
   b) If each process occurs independently of the others, what would be the effect of *each* on the surface composition?
   c) Estimate the *combined* effect of these processes on the surface composition and provide an argument to support your answer for the case where

i) Thermal processes dominate pure collisional processes
ii) Pure collisional processes dominate thermal processes.

Draw the composition vs. depth profile for cases (i) and (ii).

$$C_{\mathrm{Si}}^{\mathrm{B}} = 0.01$$
$$C_{\mathrm{Ni}}^{\mathrm{B}} = 0.99$$
$$\Delta H_{\mathrm{A}}^{\mathrm{Si}} = -0.1\,\mathrm{eV}$$
$$\overline{p}_{\mathrm{Si}}/\overline{p}_{\mathrm{Ni}} = 2.0$$
$$\Delta H_{\mathrm{m}}^{\mathrm{Ni,v}} = 0.77\,\mathrm{eV}$$

$$\Delta H_{\mathrm{m}}^{\mathrm{Ni,i}} = 0.1\,\mathrm{eV}$$
$$\Delta H_{\mathrm{m}}^{\mathrm{Si,v}} = 1.28\,\mathrm{eV}$$
$$\Delta H_{\mathrm{m}}^{\mathrm{Si,i}} = 0.15\,\mathrm{eV}$$
$$R_{\mathrm{S}t} = 0.1176\,\mathrm{nm}$$
$$R_{\mathrm{Ni}} = 0.1245\,\mathrm{nm}$$

$$\frac{C_{\mathrm{A}}^{\mathrm{surface}}}{C_{\mathrm{B}}^{\mathrm{surface}}} = \frac{C_{\mathrm{A}}^{\mathrm{bulk}}}{C_{\mathrm{B}}^{\mathrm{bulk}}} \exp\left(\frac{-\Delta H_{\mathrm{A}}}{kT}\right)$$
$$\frac{\overline{p}_{\mathrm{A}}}{\overline{p}_{\mathrm{B}}} = \frac{C_{\mathrm{A}}^{\mathrm{bulk}}}{C_{\mathrm{B}}^{\mathrm{surface}}} \frac{C_{\mathrm{B}}^{\mathrm{bulk}}}{C_{\mathrm{A}}^{\mathrm{surface}}}$$

10.5 A homogeneous A–B alloy of composition A–50 at%B is bombarded with 5 keV Ar ions at 400 ℃. Given that the surface concentration following bombardment is 30% A and 70% B, describe what processes or combinations of processes could give rise to such behavior and which processes are dominant?
$\Delta H_{\mathrm{m,A}}^{\mathrm{v}}$ = migration enthalpy for A atoms by vacancies = 0.7 eV
$\Delta H_{\mathrm{m,B}}^{\mathrm{v}}$ = migration enthalpy for B atoms by vacancies = 0.9 eV
$\Delta H_{\mathrm{m,A}}^{\mathrm{i}} = \Delta H_{\mathrm{m,B}}^{\mathrm{i}}$ = migration enthalpy for A and B atoms via interstitials = 0.1 eV
ΔH_{A} = enthalpy of adsorption of A in B = −0.3 eV
$p_{\mathrm{A}}^{\mathrm{s}}$ = sputtering probability for A atoms = 3 atoms/ion
$p_{\mathrm{B}}^{\mathrm{s}}$ = sputtering probability for B atoms = 4 atoms/ion
C_{A} = constant $\times (d_{\mathrm{Av}}/d_{\mathrm{Bv}} - d_{\mathrm{Ai}}/d_{\mathrm{Bi}})C_{\mathrm{v}}$
$d_{\mathrm{Av}}\alpha \exp(-\Delta H_{\mathrm{m,A}}/kT)$
$C_{\mathrm{A}}^{\mathrm{s}}/C_{\mathrm{B}}^{\mathrm{s}} = (C_{\mathrm{A}}^{\mathrm{b}}/C_{\mathrm{B}}^{\mathrm{b}})\exp(-\Delta H_{\mathrm{A}}/kT)$

10.6 Explain why ion beam mixing experiments often do not agree with the predictions from the ballistic theory of mixing. How would the temperature of the sample affect your answer?

10.7 A sample of polycrystalline Si is bombarded with 500 keV Al^+ ions to a dose of 5×10^{15} i/cm^2. Given that $R_p = 260$ nm and $\Delta R_p = 94$ nm and that the damage profile has the same shape but peaks at $0.8R_p$, calculate the peak damage in the material using reasonable assumptions.
The distribution of ions is given by $N(x) = N_p \exp(-X^2)$ where $X = (x - R_p)/\Delta R_p$, and $N_p = 0.4N_s/\Delta R_p$.
Assume that electronic stopping varies with energy as $kE^{1/2}$ where $k = 1.5 \times 10^{-16}$ eV$^{1/2}$cm^2.

Energy transfer cross section based on inverse square law:

$$\sigma(\mathrm{E,T}) = \frac{\pi^2 a^2 E_a \gamma^{1/2}}{8E^{1/2}T^{3/2}}$$

Energy transfer cross section based on Rutherford scattering:

$$\sigma(\mathrm{E,T}) = \frac{\pi b_0^2 E\gamma}{4T^2}$$

$N = 3 \times 10^{22}$ a/cm^3

$E_c = 28$ keV
$E_a = 14$ keV
$E_b = 14$ MeV
$E_d = 30$ eV
$a = a_B/(z_1 z_2)^{1/6}$
$a_B = 0.053$ nm
$b_0 = z_1 z_2 \varepsilon^2/\eta E$
$\varepsilon^2 = 2a_B E_R$

10.8 Explain the roles of cohesive energy and migration energy in ion beam mixing. What are the magnitudes of these energies and how can they influence ion beam mixing? Could a homogeneous alloy be *unmixed*?

10.9 A Cu–40%Ni target is irradiated with 100 keV Ar^+ at a current density of 40 μA/cm^2.

a) Determine which element will segregate to the surface under irradiation at 500 °C.
b) On a single graph, draw the surface concentration as a function of time at 400 °C for the following processes:
   i) GA only
   ii) PS + RED
   iii) PS + RED + GA
   iv) PS + RED + RIS.

GA = Gibbsian adsorption
PS = Preferential sputtering
RED = Radiation-enhanced diffusion
RIS = Radiation-induced segregation
$\Delta H_{m,v}^{Cu} = 0.77$ eV
$\Delta H_{m,v}^{Ni} = 0.82$ eV
$\Delta H_{m,i}^{Cu,Ni} = 0.12$ eV

$\Delta H_{\mathrm{A}}^{\mathrm{Cu}} = -0.25\,\mathrm{eV}$
$P_{\mathrm{Cu}} = 5.5$, $P_{\mathrm{Ni}} = 2.75$ atoms/ion per unit concentration.

10.10 Determine the lateral load at which helium bubbles cause blistering in 316 stainless steel under the condition that the blister diameter $\sim t_{\mathrm{B}}^2$, where t_{B} is the blister cap thickness.

References

1. Nastasi M, Mayer JW, Hirvonen JK (1996) Ion-Solid Interactions: Fundamentals and Applications. Cambridge University Press, Cambridge
2. Komarov F (1992) Ion Beam Modification of Materials. Gordon and Breach, Philadelphia
3. Was GS (1989) Prog Surf Sci 32(3/4):211–312
4. Smidt F (1990) Int Mater Rev 35(2):61–128
5. Hirvonen JK (1991) Mater Sci Rep 6:251–274
6. Sigmund P (1969) Phys Rev 184:383
7. Smith DL (1978) J Nucl Mater 75:20–31
8. Sigmund P (1981) In: Sputtering by Particle Bombardment I. Springer, Berlin Heidelberg New York, p 9
9. Winters HF (1976) In: Kaminsky M (ed) Radiation Effects in Solid Surfaces. American Chemical Society, Washington, DC, p 1
10. Lindhard J, Nielsen V, Scharff M (1968) Kgl Danske Videnskab Selskab Mat Fys Medd 36(10):1
11. Wiedersich H, Andersen HH, Lam NQ, Rehn LE, Pickering HW (1983) In: Poate JM, Foti G, Jacobson DC (eds) Surface Modification and Alloying, NATO Series on Materials Science. Plenum, New York, p 261
12. Falcone G, Sigmund P (1981) Appl Phys 25:307
13. Lam NQ, Wiedersich H (1987) Nucl Instr Meth B 18:471
14. Wynblatt P, Ku RC (1979) In: Johnson WC, Blakely JM (eds) Interfacial Segregation. American Society for Metals, Metals Park, OH, p 115
15. Sigmund P (1979) J Appl Phys 50(11):7261
16. Sigmund P, Gras-Marti A (1981) Nucl Instr Meth 182/183:25
17. Gras-Marti A, Sigmund P (1981) Nucl Instr Meth 180:211
18. Myers SM (1980) Nucl Instr Meth 168:265
19. Anderson HH (1979) Appl Phys (Germany) 18:131
20. Workman TW, Cheng YT, Johnson WL, Nicolet MA (1987) Appl Phys Lett 50(21):1485
21. Westendorp H, Wang ZL, Saris FW (1982) Nucl Instr Meth 194:453
22. Wang ZL, Westendorp JFM, Doorn S, Saris FW (1982) In: Picraux ST, Choyke WJ (eds) Metastable Materials Formation by Ion Implantation. Elsevier, New York, p 59
23. Paine BM, Averback RS (1985) Nucl Instr Meth B 7/8:666
24. Johnson WL, Cheng Y-T, Van Rossum M, Nicolet M-A (1985) Nucl Instr Meth B 7/8:657
25. Van Rossum M, Cheng Y-T (1988) Defect Diffusion Forum 57/58:1
26. Cheng Y-T, Workman TW, Nicolet M-A, Johnson WL (1987) In: Beam-Solid Interactions and Transient Processes, vol 74. Materials Research Society, Pittsburgh, PA, p 419
27. Ma E, Workman TW, Johnson WL, Nicolet M-A (1989) Appl Phys Lett 54(5):413
28. Cheng Y-T, Van Rossum M, Nicolet M-A, Johnson WL (1984) Appl Phys Lett 45(2):185
29. Van Rossum M, Cheng Y-T, Nicolet M-A, Johnson WL (1985) Appl Phys Lett 46(6):610

30. Rossi F, Nastasi M (1991) J Appl Phys 69(3):1310
31. Vineyard GH (1976) Rad Eff 29:245
32. Matteson S, Roth J, Nicolet M, Rad Eff 42 (1979) 217–226
33. Cheng Y-T (1989) Phys Rev B 40(10):7403–7405
34. Hung LS, Mayer JW (1985) Nucl Instr Meth B 7/8:676
35. Was GS, Eridon JM (1987) Nucl Instr Meth B 24/25:557
36. Lam NQ, Leaf GK, Wiedersich H (1980) J Nucl Mater 88:289
37. Lam NQ, Wiedersich H (1982) In: Picraux ST, Choyke WJ (eds) Metastable Materials Formation by Ion Implantation. Elsevier, New York, p 35
38. Lam NQ, Wiedersich H (1981) J Nucl Mater 103/104:433
39. Lam NQ, Leaf GK (1986) J Mater Res 1:251
40. Rehn LE, Okamoto PR (1983) In: Nolfi FV (ed) Phase Transformations During Irradiation. Applied Science, New York, p 247
41. Mayer SGB, Milillo FF, Potter DI (1985) In: Koch CC, Liu CT, Stoloff NS (eds) High-Temperature Ordered Intermetallic Alloys, vol 39. Materials Research Society, Pittsburgh, PA, p 521
42. Liu JC, Mayer JW (1987) Nucl Instr Meth B 19/29:538
43. Alexander D, Was G, Rehn LE (1990) Materials Research Symposium, vol 157. Materials Research Society, Pittsburgh, PA, p 155
44. Eridon J, Rehn L, Was GS (1987) Nucl Instr Meth B 19/20:626
45. Ahmed M, Potter DI (1987) Acta Metal 35(9):2341
46. Nishiyama Z (1978) In: Fine ME, Meshii M, Wayman CM (eds) Martensitic Transformations, vol 7. Academic, New York
47. Bradley RM, Harper JME, Smith DA (1986) J Appl Phys 60:4160
48. Ma Z, Was GS (1999) J Mater Res 14(10):4051–4061
49. Didenko AN, Kozlov EV, Sharkeev YuN, Tailashev AS, Rajabchikov AI, Pranjavichus L, Augulis L (1993) Surf Coat Technol 56:97–104
50. Behrisch R, Risch M, Roth J, Scherzer BMU (1976) Proceedings of the 9th Symposium on Fusion Technology. Pergamon, New York, pp 531–539
51. Ullmaier H (1983) Rad Eff 78:1–10
52. Wolfer WG (1980) J Nucl Mater 93/94:713–720
53. Behrisch R, Scherzer BMU (1983) Rad Eff 78:393–403
54. Birtcher RC, Jäger W (1987) Ultramicroscopy 22:267–280
55. Liu AS, Birtcher RC (1989) Mat Res Soc Symp, vol 128. Materials Research Society, Pittsburgh, PA, pp 303–308
56. Johnson PR (1983) Rad Eff 78:147–156
57. Mazey DJ, Evans JH (1986) J Nucl Mater 138:16–18

11 Simulation of Neutron Irradiation Effects with Ions

Radiation effects research is conducted with a variety of energetic particles: neutrons, electrons, light ions and heavy ions. Energetic ions can be used to understand the effects of neutron irradiation in reactor components, and interest in this application of ion irradiation has grown in recent years for several reasons that include the avoidance of high residual radioactivity and the decline of neutron sources for materials irradiation. The damage state and microstructure resulting from ion irradiation, and thus the degree to which ion irradiation emulates neutron irradiation, depend upon the particle type and the damage rate. This chapter will begin with a brief review of the damage function, primary recoil spectrum and efficiency of defect production for various particle types. Effects of particle type on both microstructure and microchemistry will be discussed, followed by the effects of the irradiated microstructure on mechanical properties. The roles of dose, dose rate, and temperature parameters and the constraints on parameter space by each particle source will be discussed and compared against the effects of neutron irradiation.

11.1 Motivation for Using Ion Irradiation as a Surrogate for Neutron Irradiation

In the 1960s and 1970s, heavy ion irradiation was developed for the purpose of simulating neutron damage in support of the fast breeder reactor program [1, 2, 3]. Ion irradiation and simultaneous He injection have also been used to simulate the effects of 14 MeV neutron damage in conjunction with the fusion reactor engineering program. The application of ion irradiation (defined here as any charged particle, including electrons) to the study of neutron irradiation damage is of interest to the light water reactor community to address issues such as stress corrosion cracking of core materials that are affected by irradiation [4, 5, 6]. Ion irradiation is also being used to understand the irradiated microstructure of reactor pressure vessel steels, Zircaloy fuel cladding, and materials for advanced reactor concepts.

There is significant incentive to use ion irradiation to study neutron damage as this technique has the potential for yielding answers on basic processes in addition to the potential for enormous savings in time and money. Neutron irradiation experiments are not amenable to studies involving a wide range of conditions, which is precisely what is required for investigations of the basic damage processes. Radi-

ation damage simulation by ions allows easy variation of the irradiation parameters such as dose, dose rate and temperature over a wide range of values.

Typical neutron irradiation experiments in test reactors require 1–3 years of in-core exposure to reach appreciable fluence levels for accelerated post-irradiation testing. However, this is accompanied by at least another year of capsule design and preparation as well as disassembly and cooling. Analysis of microchemical changes by Auger electron spectroscopy (AES) or microstructural changes by energy dispersive spectroscopy via scanning transmission electron microscopy (STEM-EDS) and mechanical property or stress corrosion cracking (SCC) evaluation can take several additional years because of the precautions, special facilities and instrumentation required for handling radioactive samples. The result is that a single cycle from irradiation through microanalysis and mechanical property/SCC testing may take between three and five years. Such a long cycle length does not permit for iteration on irradiation or material conditions that is critical in any experimental research program. The long lead time required for design and irradiation also reduces flexibility in altering irradiation programs as new data becomes available. Because of the long cycle time, the requirement of special facilities and special sample handling, the costs for neutron irradiation experiments are very high.

In contrast to neutron irradiation, ion (heavy, light or electrons) irradiation enjoys considerable advantages in both cycle length and cost. Ion irradiations of any type rarely require more than several tens of hours to reach damage levels in the 1–10 dpa range. Ion irradiation produces little or no residual radioactivity, allowing handling of samples without the need for special precautions. These features translate into significantly reduced cycle length and cost. The challenge is then to verify the equivalency of the results of neutron and ion irradiation.

The key question that needs to be answered is how do results from neutron and charged particle irradiation experiments compare? How, for example is one to compare the results of a component irradiated in-core at 288 °C to a fluence of 1×10^{21} n/cm^2 ($E > 1$ MeV) over a period of 8.5 months, with an ion irradiation experiment using 3 MeV protons at 400 °C to 1 dpa (displacements per atom) at a dose rate of 10^{-5} dpa/s ($\sim$1 day), or 5 MeV Ni^{++} at 500 °C to 10 dpa at a dose rate of 5×10^{-3} dpa/s ($\sim$1 hr)? The first question to resolve is the measure of radiation effect. In the irradiation assisted stress corrision cracking (IASCC) problem in LWRs, concern has centered on two effects of irradiation: *segregation* of major alloying elements or impurities to grain boundaries, which then cause embrittlement or enhance the intergranular stress corrosion cracking (IGSCC) process, and *hardening* of the matrix that results in localized deformation and embrittlement. The appropriate *measure* of the radiation effect in the former case would then be the alloy concentration at the grain boundary or the amount of impurity segregated to the grain boundary. This quantity is *measurable* by analytical techniques such as AES or STEM-EDS. For the latter case, the *measure* of the radiation effect would be the nature, size, density and distribution of dislocation loops, black dots and the total dislocation network, and how they impact the deformation of the alloy. Hence, spe-

cific and measurable effects of irradiation can be determined for both neutron and ion irradiation experiments.

The next concern is determining how ion irradiation translates into the environment describing neutron irradiation. That is, what are the irradiation conditions required for ion irradiation to yield the same *measure* of radiation effect as that for neutron irradiation? This is the key question, for in a post-irradiation test program, it is only the *final state* of the material that is important in the determination of equivalence, and not the path taken. Therefore, if one could devise ion irradiation experiments that yielded the same *measures* of irradiation effects as observed in neutron irradiation experiments, then the data obtained in post-irradiation experiments will be equivalent. In such a case, ion irradiation experiments can provide a direct substitute for neutron irradiation. While neutron irradiation will always be required to qualify materials for reactor application, ion irradiation provides a low cost and rapid means of elucidating mechanisms and screening materials for the most important variables.

11.2 Review of Aspects of Radiation Damage Relevant to Ion Irradiation

The first problem in determining the equivalence between the measure of radiation effect in charged particle and neutron irradiation is the use of a common dose unit. Recall from the introduction that irradiated materials properties can be more successfully compared using dpa as a measure of exposure. The basic (measurable) dose unit for neutron irradiation is the fluence in (n/cm^2) above some energy threshold ($E > x$ MeV), where x is the energy threshold. For charged particles it is the integrated current or charge in units of Q/cm^2. Both of these measures can be converted to dose in units of *dpa* and dose rate as *dpa/s* using one of several models for the determination of *dpa*, as shown in Chap. 2. A fundamental difference between ion and neutron irradiation effects is the particle energy spectrum that arises due to the difference in how the particles are produced. Ions are produced in accelerators and emerge in monoenergetic beams with vary narrow energy widths. However, the neutron energy spectrum in a reactor extends over several orders of magnitude in energy, thus presenting a much more complicated source term for radiation damage. Figure 11.1 shows the considerable difference in neutron and ion energy spectra and also between neutron spectra in different reactors and at different locations within the reactor vessel.

Another major difference in the characteristics of ions and neutrons is their depth of penetration. As shown in Fig. 2.25 of Chap. 2, ions lose energy quickly because of high electronic energy loss, giving rise to a spatially non-uniform energy deposition profile caused by the varying importance of electronic and nuclear energy loss during the slowing down process. Their penetration distances range between 0.1 and 100 μm for ion energies that can practically be achieved by laboratory-scale accelerators or implanters. By virtue of their electrical neutrality, neutrons can penetrate

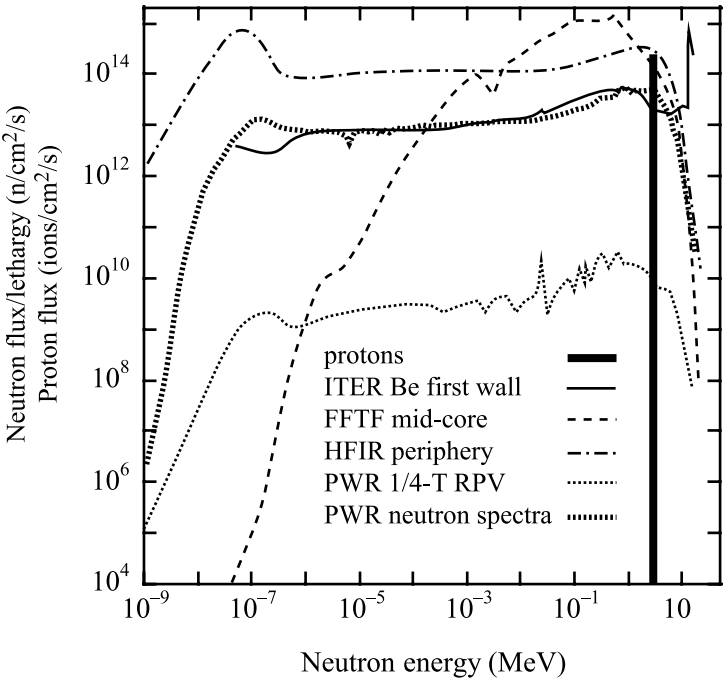

Fig. 11.1. Energy spectra of incident ions in a monoenergetic ion beam, and neutrons from a variety of reactor types (from [7])

very large distances and produce spatially flat damage profiles over many millimeters of material.

As discussed in Chap. 2, the total number of displacements per atom is given by the K–P [8] or NRT [9] models. This quantity provides an adequate measure of the number of displacements created by the incoming particle irrespective of the mass of the particle. In addition to dpa, the primary recoil spectrum describes the relative number of collisions in which an energy between T and $T + \mathrm{d}T$ is transferred from the primary recoil atom to other target atoms. The fraction of recoils between the displacement energy E_d, and T is, from Eq. (3.11):

$$P(E_\mathrm{i}, T) = \frac{1}{N} \int_{E_\mathrm{d}}^{T} \sigma(E_\mathrm{i}, T')\,\mathrm{d}T' \tag{11.1}$$

where N is the total number of primary recoils and $\sigma(E_\mathrm{i}, T)$ is the differential cross section for a particle of energy E_i to create a recoil of energy T, and E_d is the displacement energy. The recoil fraction is shown in Fig. 3.5, which reveals only a small difference between ions of very different masses.

But there is a substantial difference in the damage morphology between particles of different mass. Light ions such as electrons and protons will produce damage as isolated Frenkel pairs or in small clusters while heavy ions and neutrons produce

damage in large clusters (see Fig. 3.7). For 1 MeV particle irradiation of copper, half the recoils for protons are produced with energies less than ~60 eV while the same number for Kr occurs at about 150 eV. Recoils are weighted toward lower energies because of the screened Coulomb potential that controls the interactions of charged particles. For an unscreened Coulomb interaction, the probability of creating a recoil of energy T varies as $1/T^2$. However, neutrons interact as hard spheres and the probability of a creating a recoil of energy T is independent of recoil energy. In fact, a more important parameter describing the distribution of damage over the energy range is a combination of the fraction of defects of a particular energy and the damage energy. Described in Chap. 3, the *weighted average* recoil spectrum, $W(E_\mathrm{i}, T)$ weights the primary recoil spectrum by the number of defects or the damage energy produced in each recoil:

$$W(E_\mathrm{i}, T) = \frac{1}{E_\mathrm{D}(E_\mathrm{i})} \int_{E_\mathrm{d}}^{T} \sigma(E_\mathrm{i}, T') E_\mathrm{D}(T')\, \mathrm{d}T' \,, \tag{11.2}$$

$$E_\mathrm{D}(E_\mathrm{i}) = \int_{E_\mathrm{d}}^{\hat{T}} \sigma(E_\mathrm{i}, T') E_\mathrm{D}(T')\, \mathrm{d}T' \,, \tag{11.3}$$

where $\hat{T}$ is the maximum recoil energy given by $\hat{T} = E_i = 4E_\mathrm{i}M_1M_2/(M_1 + M_2)^2$. As described in Chap. 3, for the extremes of Coulomb and hard-sphere interactions, the weighted average recoil spectra for each type of interaction is:

$$W_\mathrm{Coul}(E_\mathrm{i}, T) = \frac{\ln T - \ln E_\mathrm{d}}{\ln \hat{T} - \ln E_\mathrm{d}} \tag{11.4a}$$

$$W_\mathrm{HS}(E_\mathrm{i}, T) = \frac{T^2 - E_\mathrm{d}^2}{E_\mathrm{d}^2} \,. \tag{11.4b}$$

Equations (11.4a) and (11.4b) are graphed in Fig. 3.6 for 1 MeV particle irradiations of copper. The Coulomb forces extend to infinity and slowly increase as the particle approaches the target, hence the slow increase with energy. In a hard-sphere interaction, the particles and target do not *feel* each other until their separation reaches the hard-sphere radius at which point the repulsive force goes to infinity. A screened Coulomb potential is most appropriate for heavy ion irradiation. Note the large difference in $W(E_\mathrm{i}, T)$ between the various types of irradiations. While heavy ions come closer to reproducing the energy distribution of recoils of neutrons than do light ions, neither is accurate in the *tails* of the distribution. This does not mean that ions are poor simulations of radiation damage, but it does mean that damage is produced differently and this difference will need to be considered when designing an irradiation program that is intended to produce microchemical and microstructural changes that match those from neutron irradiation.

The actual number of defects that survive the displacement cascade and their spatial distribution in the solid will determine the effect on the irradiated microstructure. This topic was covered in Chaps. 3 and 7 by classification of defects according

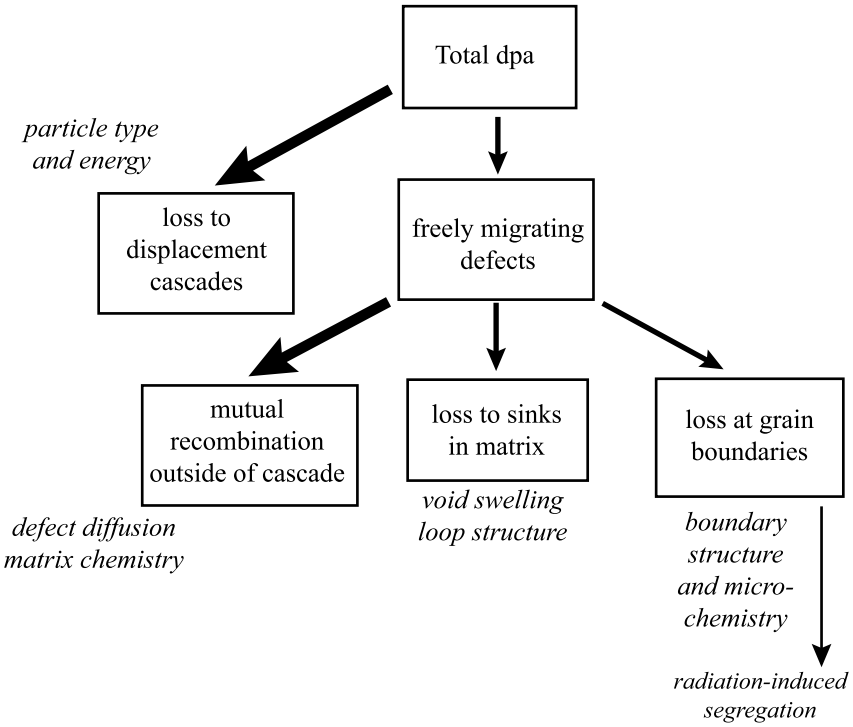

Fig. 11.2. History of point defects after creation in the displacement cascade

to their behavior in the solid. Figure 11.2 summarizes the effect of damage morphology from the viewpoint of the grain boundary and how the defect flow affects radiation-induced grain boundary segregation. Despite the equivalence in energy among the four particle types described in Fig. 3.7, the average energy transferred and the defect production efficiencies vary by almost two orders of magnitude! This is explained by the differences in the cascade morphology among the different particle types. Neutrons and heavy ions produce dense cascades that result in substantial recombination during the cooling or quenching phase. However, electrons are just capable of producing a few widely spaced Frenkel pairs that have a low probability of recombination. Protons produce small widely spaced cascades and many isolated FPs due to the Coulomb interaction and therefore, fall between the extremes in displacement efficiency defined by electrons and neutrons.

11.3 Particle Type Dependence of RIS

We will focus on the comparison between four types of particle irradiation in order to outline a methodology for establishing equivalence between neutron and charged particle irradiation. We will further focus on radiation-induced segregation as the

measure of the effect of irradiation in order to compare the particles. RIS is selected because it depends only on the action of point defects, and not on their agglomeration. The irradiation parameters for the four particle types are given in Table 11.1. Each experiment is characterized by the particle type, energy and irradiation temperature, reported dose rate and reported total dose. The last column is the dose to reach a steady state RIS profile using the Perk's model [11]. The columns labeled *reported* and *corrected* refer to RIS calculations using the nominal dose rate (*reported* value) and the efficiency-corrected (*corrected* value), respectively. The displacement efficiency is calculated using Naundorf's model, described in Chap. 3.

A quantity of interest in RIS for LWR core materials is the amount of chromium depleted from the grain boundary, or the area inside the Cr concentration profile (Fig. 11.3). In other reactor systems, other elements may be of interest due to the potential for in-reactor precipitation. The appropriate measure of depletion is somewhat questionable. One could use the grain boundary chromium value as the measure of the extent of chromium depletion. Alternatively, the FWHM of the depletion profile has been used. In fact both of these quantities are useful and can be obtained from measured depletion profiles. However, the area inside the Cr concentration profile represents changes to a volume of material and is more sensitive to changes in the profile shape than either the grain boundary value or the FWHM alone. The amount of Cr depletion is determined by integrating the concentration profile for

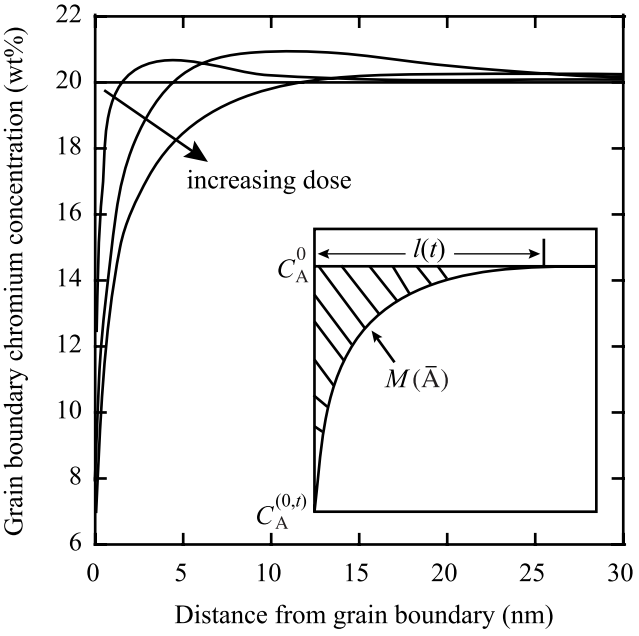

Fig. 11.3. Definition of the segregated area, M in a quantitative assessment of RIS

Table 11.1. Comparison of irradiation parameters and RIS for different particle types (from [10])

Particle type	Energy (MeV)	Temp (°C)	Effic.	Dose rate (dpa/s)		Total dose (dpa)		Dose to steady state** (dpa)	
				rept'd	corr'd*	rept'd	corr'd	rept'd	corr'd
Electrons	1.0	450	1.0	2×10^{-3}	2×10^{-3}	10	10	28	28
Protons	3.4	360	0.2	7×10^{-6}	1×10^{-6}	1	0.2	7	3
Ni ions	5.0	500	0.04	5×10^{-3}	2×10^{-4}	10	0.4	25	7
Neutrons	Fission reactor	288	0.02	$\sim5\times0^{-8}$	9×10^{-10}	1	0.02	4	1.4

* Efficiency corrected value

** As calculated by the Perks model [11] for RIS

that element with distance from the grain boundary:

$$M = \int_0^{l(t)} \left[C_A^0 - C_A(x,t)\right] \mathrm{d}x \,, \tag{11.5}$$

where M is the segregated area, C_A^0 is the bulk atom concentration, $C_A(x,t)$ is the atom concentration near the surface, and $l(t)$ is the half width of the depleted zone.

Figures 11.4a,b show the amount of grain boundary chromium depletion as a function of irradiation dose (Fig. 11.4a) and time (Fig. 11.4b) for each of the four particles described in Table 11.1. The calculated values of Cr depletion for each of the particle types using *reported* and *corrected* dose rates, according to the freely migrating defect production efficiencies, are shown by the open and closed symbols, respectively. Since electrons are assumed to be 100% efficient in producing defects available to affect segregation, there is no change in the segregated area after accounting for efficiency. However, there is a difference with protons, heavy ions and neutrons, which amounts to a reduction in the amount of segregation. The difference is largest for neutrons and smallest for protons. The difference is a function of not only the displacement efficiency, but also the slope of the dose rate curves. Nevertheless, substantial differences result in the expected amounts of grain boundary segregation when the displacement efficiency is taken into account.

Figure 11.5a shows the calculated amount of Cr depletion as a function of temperature for several displacement rates at *steady state*. Steady state is reached at different dose levels for each experiment. At a given displacement rate, the segregated area peaks at some intermediate temperature and falls off at both higher and lower temperatures. This is due to the dominance of recombination at low temperatures and back diffusion at high temperatures [10]. Also note that the effect of a decreasing displacement rate is to shift the curves to higher maxima at lower temperatures. For a given dose, a lower displacement rate yields lower steady state defect concentrations, reducing the number of defects lost to recombination, and shifting the curve to lower temperatures while increasing the degree of segregation. Figure 11.5a also shows the effect of three of the four parameters defining an experiment:

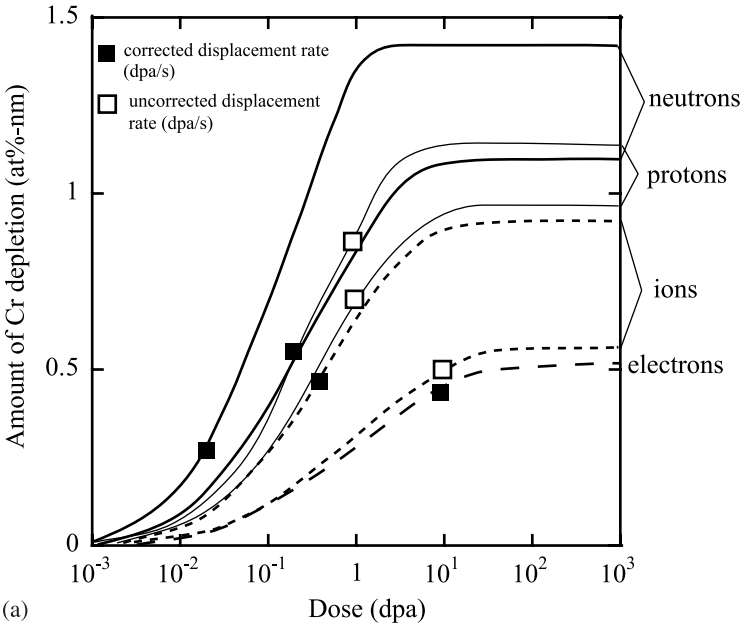

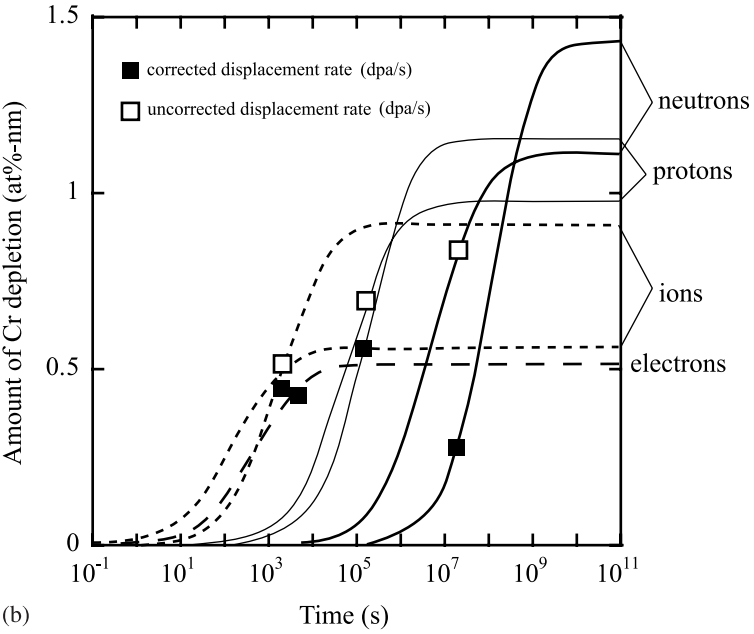

Fig. 11.4. Chromium depletion vs. (a) dose and (b) irradiation time, for several particle types, and the effect of correcting for particle efficiency (from [10])

particle type, temperature and dose rate. It does not show the effect of dose since this is a steady state result that is achieved at different doses for each of the experiments described in Table 11.1.

Figure 11.5b shows the dose required to reach steady state as a function of temperature and dose rate. Each of the experiments is plotted for both the reported and the corrected displacement rates. Note the large difference in the dose to reach steady state between electrons and neutrons. In general, irradiation at a lower dpa rate will result in a lower dose to reach steady state and the difference is greatest for this comparison. Correspondingly, proton and heavy ion irradiation fall between neutrons and electrons for the experiments described in Table 11.1. This can be understood by considering the chemical rate equations given in Eq. (5.1), where the first term is the production rate, the second is the loss by mutual recombination and the third is the loss by annihilation of defects at sinks. At steady state, $C_{\mathrm{i,v}}\alpha K_0^{1/2}$ at low temperature and $C_{\mathrm{i,v}}\alpha K_0$ at high temperature (see Chap. 5). So the resulting point defect concentrations are strong functions of the production rate.

Figure 11.6 shows a plot of segregation as a function of temperature for particles with displacement rates characteristic of their sources. Note that the temperature at which segregation is a maximum (concentration is a minimum) shifts to higher values with increasing dose rate. This is due to the trade-off between temperature and dose rate. The temperature-dose rate interdependence for stainless steel over a wide range of temperatures and dose rates is shown in Fig. 11.7. Also noted are the regions in which reactor irradiation by neutrons, and where proton and Ni ion irradiations occur. This graph explains why the experiments conducted at the highest dose rates are also conducted at the highest temperatures.

A simple method for examining the trade-off between dose rate and temperature in comparing irradiation effects from different particle types is found in the invariance requirements discussed in Chap. 8. For a given change in dose rate, we would like to know what change in temperature (at the same dose) is required to cause the same number of defects to be absorbed at sinks. The number of defects per unit volume that are lost to sinks up to time τ is:

$$N_{\mathrm{Sj}} = \int_0^{\tau} k_{\mathrm{Sj}}^2 C_{\mathrm{j}}\,\mathrm{d}t\ , \tag{11.6}$$

and the ratio of ratio of vacancy loss to interstitial loss is:

$$R_{\mathrm{S}} = \frac{N_{\mathrm{Sv}}}{N_{\mathrm{Si}}}\ , \tag{11.7}$$

where $j = \mathrm{v}$ or i, and k_{S}^2 is the sink strength. The quantity N_{S} is important in describing microstructure development involving total point defect flux to sinks (e.g., RIS). The number of defects per unit volume that have recombined up to time τ is given by:

$$N_{\mathrm{R}} = K_{\mathrm{iv}} \int_0^{\tau} C_{\mathrm{i}} C_{\mathrm{v}}\,\mathrm{d}t\ , \tag{11.8}$$

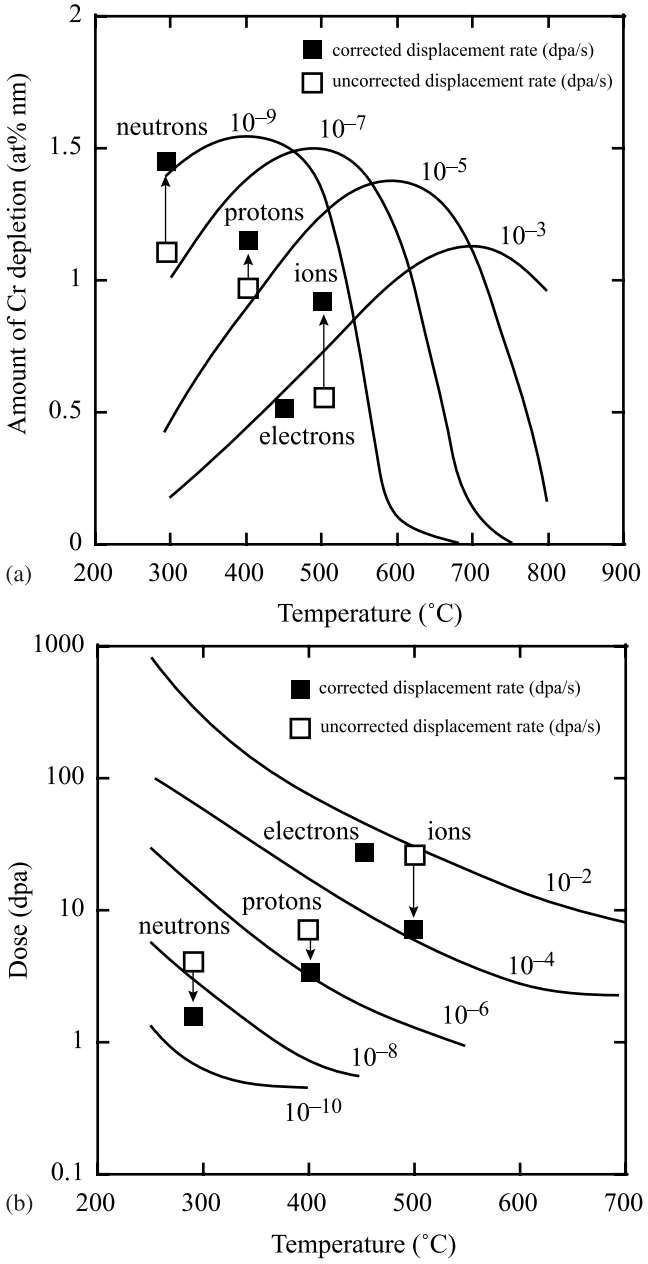

Fig. 11.5. (a) Chromium depletion, and (b) dose to reach steady state, as functions of temperature, dose rate and particle efficiency (from [10])

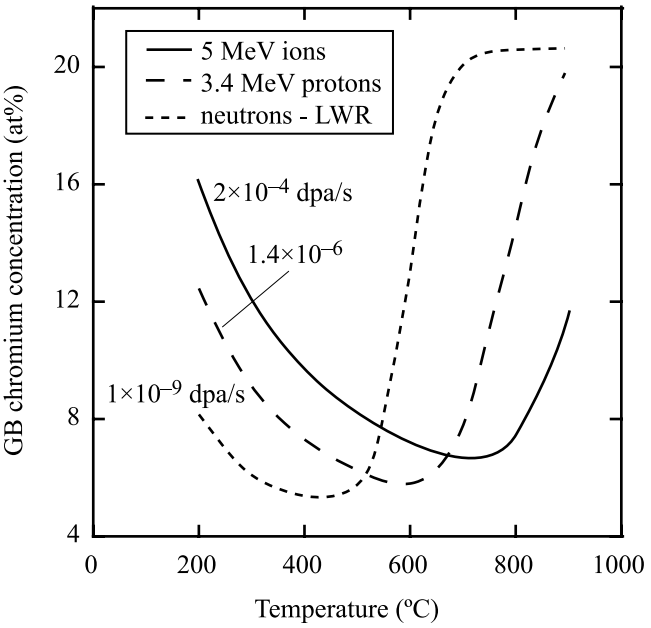

Fig. 11.6. Dependence of grain boundary chromium concentration on temperature for particles with various dose rates and defect generation efficiencies (from [10])

where K_{iv} is the vacancy–interstitial recombination coefficient. N_R is the relevant quantity for the growth of defect aggregates such as voids and loops that require partitioning of point defects to allow growth.

The invariance requirements can be used to prescribe an ion irradiation temperature-dose rate combination that simulates neutron radiation. We take the example of irradiation of stainless steel under typical boiling water reactor (BWR) core irradiation conditions of $\sim 4.5 \times 10^{-8}$ dpa/s at 288 °C. If we were to conduct a proton irradiation with a characteristic dose rate of 7.0×10^{-6} dpa/s, then using Eq. (8.158) with a vacancy formation energy of 1.9 eV and a vacancy migration energy of 1.3 eV, the experiment will be invariant in N_S with the BWR core irradiation (e.g., RIS), for a proton irradiation at 400 °C. Similarly, using Eq. (8.162), an irradiation temperature of 300 °C will result in an invariant N_R (e.g., swelling or loop growth). For a Ni^{++} ion irradiation at a dose rate of 10^{-3} dpa/s, the respective temperatures are 675 °C (N_S invariant) and 340 °C (N_R invariant). In other words, the temperature "shift" due to the higher dose rate is dependent on the microstructure feature of interest. Also, with increasing difference in dose rate, the ΔT between proton and ion irradiation increases substantially. The nominal irradiation temperatures selected for proton irradiation, 360 °C and for Ni^{++} irradiation, 500 °C represent compromises between the extremes for invariant N_s and N_R.

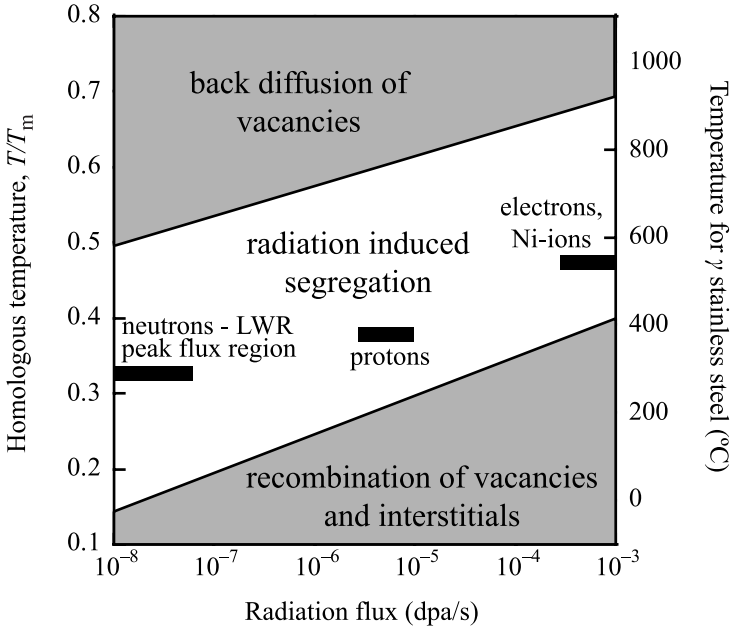

Fig. 11.7. Relation between temperature and dose rate in the context of radiation-induced segregation, and the locations of neutron, proton and nickel ion irradiations

11.4 Advantages and Disadvantages of the Various Particle Types

Each particle type has its advantages and disadvantages for use in the study or emulation of radiation effects. Common disadvantages of charged particle beams are the lack of transmutation reactions and the need to use a raster-scanned beam. With the exception of some minor transmutation reactions that can occur with light ion irradiation, charged particles do not reproduce the types of transmutation reactions that occur in reactor core materials due to interaction with neutrons. The most important of these is the production of He by transmutation of Ni or B. But a second consideration is that of a raster-scanned beam in which any volume element of the target is exposed to the beam for only a fraction of the raster-scan cycle. For a typical beam scanner and beam parameters, the fraction of time that any particular volume element in the solid is being bombarded is $\sim$0.025. Thus, the instantaneous dose rate during the *beam-on* portion of the cycle is 40 times that of the average (Fig. 11.8). The result is that the defect production rate is very high and defects can anneal out in the remaining 0.975 portion of the cycle before the beam again passes through the volume element. As such, the effective defect production rate in raster-scanned systems will be less, and must be accounted for.

While one objective of ion irradiation is to emulate the effect of neutrons, a second is to understand basic physical radiation damage processes, for which neutron

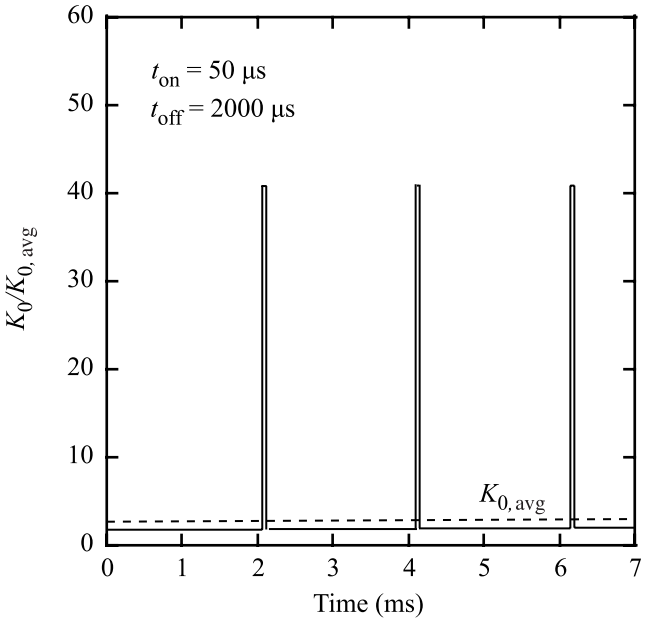

Fig. 11.8. The effect of a raster-scanned beam on the instantaneous production rate of point defects with the same time averaged rate as a continuous source (from [12])

irradiation is often less well-suited. While ion irradiation can be conducted with great control over temperature, dose rate and total dose, such control is a challenge to reactor irradiations. For example, instrumented tubes with active temperature control are expensive to design, build and operate. Even so, frequent power changes can be difficult to handle as the flux-temperature relationship will change and this can result in artifacts in the irradiated microstructure (see Sect. 8.3.11 and Fig. 8.51). On the other hand, cheaper "rabbit" tube irradiations use passive gamma heating and temperatures are not known with any certainty. Similarly, doses and dose rates are most often determined by neutronic models of the core locations and are not verifiable. As such, ion irradiations enjoy the advantage of better control and verification of irradiation conditions as compared to neutron irradiation. Table 11.2 provides a list of advantages and disadvantages for each of three particle types; electrons, heavy ions and light ions (protons), and they are discussed in detail in the following sections.

11.4.1 Electrons

Electron irradiation is easily conducted in a high voltage transmission electron microscope and as such, it uses a rather simple ion source, that being either a hot filament or a field emission gun. An advantage is that the same instrument used for irradiation damage can be used to image the damage. Another advantage is that the

Table 11.2. Advantages and disadvantages of irradiations with various particle types (from [12])

Electrons	
Advantages	*Disadvantages*
Relatively "simple" source – TEM	Energy limited to ∼1 MeV
Uses standard TEM sample	no cascades
High dose rate – short irradiation times	Very high beam current (high dpa rate) requires high temperature
	Poor control of sample temperature
	Strong "Gaussian" shape (nonuniform intensity profile) to beam
	No transmutation
Heavy Ions	
Advantages	*Disadvantages*
High dose rate – short irradiation times	Very limited depth of penetration
High T_{avg}	Strongly peaked damage profile
Cascade production	Very high beam current (high dpa rate) requires high temperature
	No transmutation
	Potential for composition changes at high dose via implanted ion
Protons	
Advantages	*Disadvantages*
Accelerated dose rate – moderate irradiation times	Minor sample activation
Modest ΔT required	Smaller, widely separated cascades
Good depth of penetration	No transmutation
Flat damage profile over tens of μ m	

high dose rate requires very short irradiation time, but this will also require a large temperature shift as explained in the previous section.

There are several disadvantages to electron irradiation using a TEM. First, energies are generally limited to 1 MeV. This energy is sufficient to produce an isolated Frenkel pair in transition metals, but not cascades. The high dose rate requires high temperatures that must be closely monitored and controlled, which is difficult to do precisely in a typical TEM sample stage. Another drawback is that since irradiations are often conducted on thin foils, defects are created in close proximity to the surface and their behavior may be affected by the presence of the surface. Perhaps the most serious drawback is the Gaussian shape to the electron beam that can give rise to strong dose rate gradients across the irradiated region. Figure 11.9 shows the composition profile of copper around a grain boundary in Ni–39%Cu following electron irradiation. Note that while there is local depletion at the grain boundary (as expected), the region adjacent to the minimum is strongly enriched in copper due to the strong defect flux *out* of the irradiated zone defined by the horizontal line below the spectrum. This outward-directed defect flux causes a reversal in the

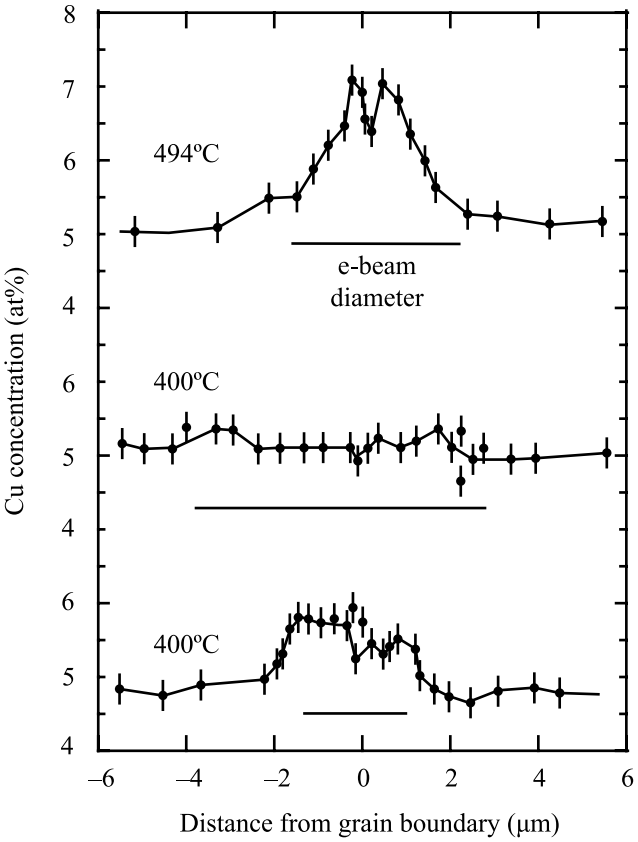

Fig. 11.9. Enrichment of copper surrounding a local depletion at the grain boundary. The enrichment is caused by the high defect flux away from the irradiated region defined by the horizontal line (from [13])

direction of segregation from that caused by a defect flux *to* the sink. Another often observed artifact in electron irradiation is very broad grain boundary enrichment and depletion profiles. Figure 11.10 shows that the enrichment profile for Ni and the depletion profiles for Fe and Cr in stainless steel have widths on the order of 75–100 nm, which is much greater than the 5–10 nm widths observed following neutron irradiation under similar conditions and all model simulations of radiation-induced segregation. A similar effect was noted by Wakai [15] in electron and D^+ irradiation of the same alloy in which it was observed that the segregation was much greater and narrower around the grain boundary in the deuteron-irradiated sample as compared to the electron irradiation (Fig. 11.11).

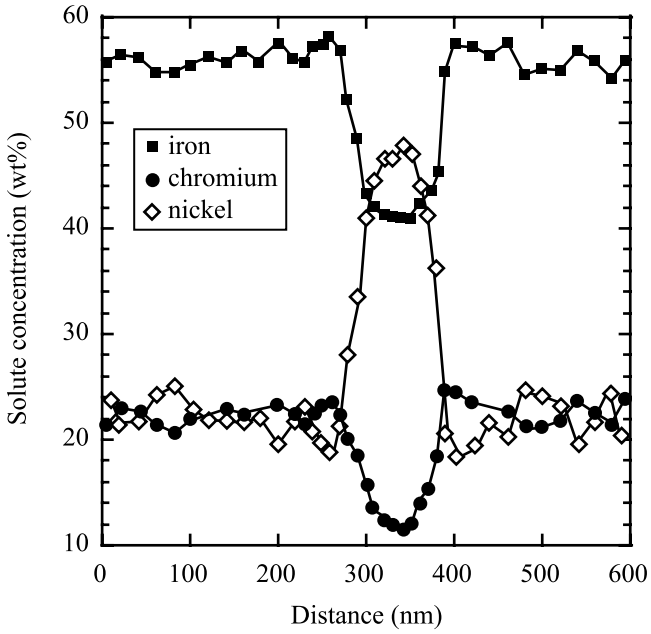

Fig. 11.10. Broad grain boundary enrichment and depletion profiles in Fe–20Cr–25Ni–0.75Nb–0.5Si following irradiation with electrons at 420 °C to 7.2 dpa (from [14])

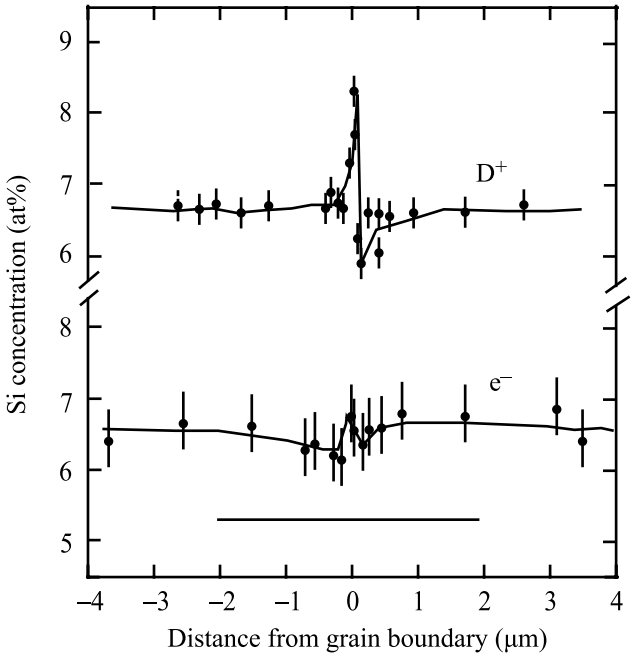

Fig. 11.11. Comparison of deuteron and electron irradiation showing the greater amount of segregation and the narrower profile for the deuteron irradiation (from [15])

11.4.2 Heavy Ions

Heavy ions enjoy the benefit of high dose rates resulting in the accumulation of high doses in short times. Also, because they are typically produced in the energy range of a few MeV, they are very efficient at producing dense cascades, similar to those produced by neutrons (Fig. 3.7). The disadvantage is that as with electrons, the high dose rates require large temperature shifts so that irradiations must be conducted at temperatures of order ∼500 °C in order to create similar effects as neutron irradiation at ∼300 °C. Clearly, there is not much temperature margin for studying neutron irradiations at high temperature since higher ion irradiation temperatures will cause annealing. Another drawback is the short penetration depth and the continuously varying dose rate over the penetration depth. Figure 11.12 shows the damage profile for several heavy ions incident on nickel. Note that the damage rate varies continuously and peaks sharply at only 2 µm below the surface. As a result, regions at well-defined depths from the surface must be able to be reproducibly sampled in order to avoid dose or dose rate variations. Small errors (500 nm) made in locating the volume to be characterized can result in a dose that varies by a factor of two from the target value.

A problem that is rather unique to nickel ion irradiation of stainless steel or nickel-base alloys is that in addition to the damage they create, each bombarding Ni ion constitutes an interstitial. Figure 11.13a shows that 5 MeV Ni^{++} irradiation of a Fe–15Cr–35Ni alloy resulted in high swelling in the immediate subsurface region

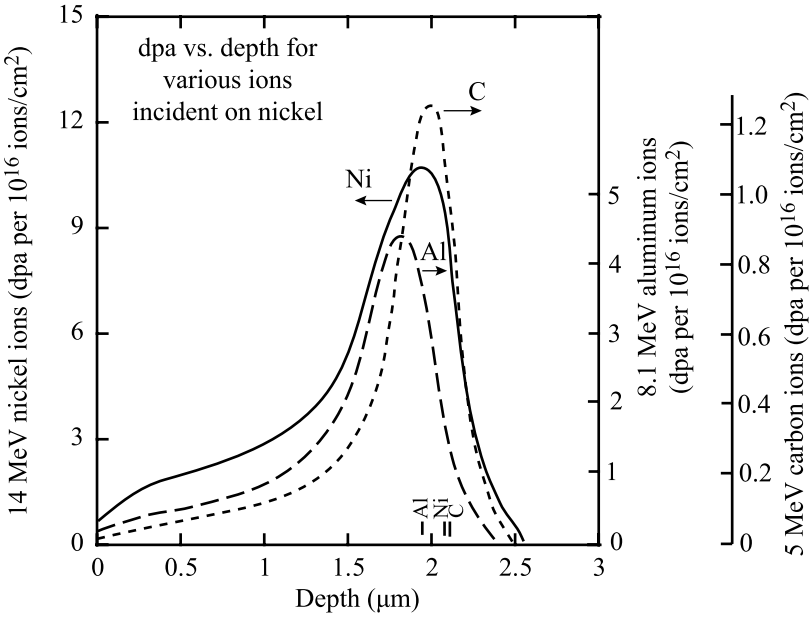

Fig. 11.12. Damage profiles for C, Al and Ni irradiation of a nickel target at energies selected to result in the same penetration depth (from [16])

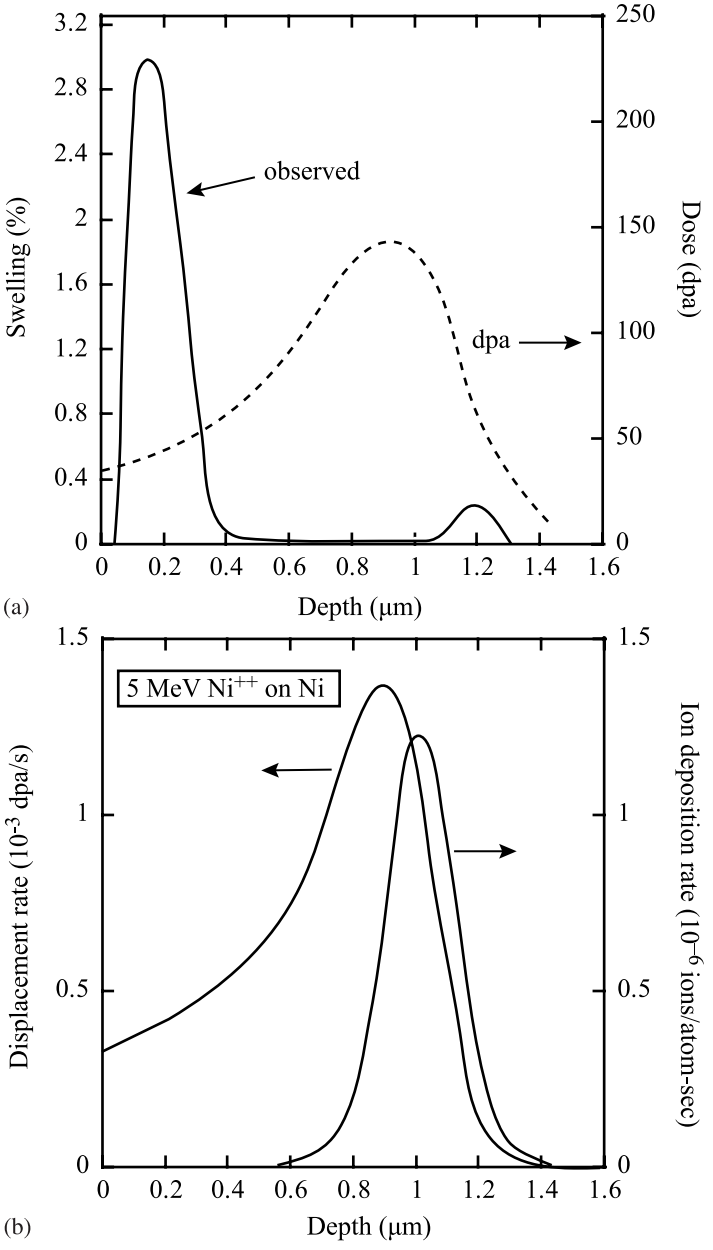

Fig. 11.13. (a) Subsurface swelling resulting from 5 MeV Ni^{+} ion irradiation of Fe–15Cr–35Ni at 625 °C (from [17]). (b) Displacement rate and ion deposition rate calculated for 5 MeV Ni^{++} on nickel (from [18])

compared to that near the damage peak. As shown in Fig. 11.13b, the Ni^{++} ions come to rest at a position just beyond the peak damage range. So even though the peak damage rate is about $3\times$ that at the surface, swelling at that location is suppressed by about a factor of 5 compared to the surface [17]. The reason is that the bombarding Ni^{++} ions constitute interstitials and the surplus of interstitials near the damage peak results in a reduction of the void growth rate [18, 19]. In the dose rate-temperature regime where recombination is the dominant point defect loss mechanism, interstitials injected by Ni^{++} ion bombardment may never recombine since there is no corresponding vacancy production. Therefore, injected interstitials comprise a larger fraction of the point defects absorbed at sinks whenever the fraction of point defects recombining is large, such as in the peak swelling regime.

11.4.3 Protons

In many ways, proton irradiation overcomes the drawbacks of electron and neutron irradiation. At only a few MeV, the penetration depth can exceed 40 μm and the damage profile is relatively flat such that the dose rate varies by less than a factor of 2 over several tens of μm. Further, the depth of penetration is sufficient to assess such properties as irradiation hardening through microhardness measurements, and stress corrosion cracking through crack initiation tests such as the slow strain rate test. Figure 11.14 (and Fig. 2.25) shows schematics of 3.2 MeV proton and 5 MeV

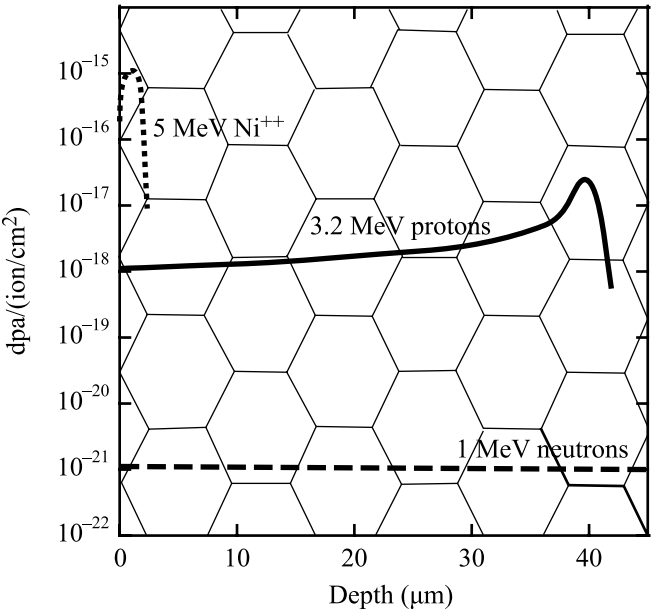

Fig. 11.14. Damage profiles for 1 MeV neutrons, 3.2 MeV protons and 5 MeV Ni^{++} ions in stainless steel (from [12])

Ni^{++} damage profiles in stainless steel. Superimposed on the depth scale is a grain structure with a grain size of 10 μm. Note that with this grain size, there are numerous grain boundaries and a significant irradiated volume over which the proton damage rate is flat. The dose rate for proton irradiations is 2 to 3 orders of magnitude lower than that for electrons or ions, thus requiring only a modest temperature shift, but since it is still 10^2 to 10^3 times higher than neutron irradiation, modest doses can be achieved in a reasonably short irradiation time.

The advantages are that because of the small mass of the proton compared to heavy ions, the recoil energy is smaller and the resulting damage morphology is characterized by smaller, more widely spaced cascades than with ions or neutrons (see Fig. 3.7). Also, since only a few MeV are required to surmount the Coulomb barrier for light ions, there is also a minor amount of sample activation that increases with proton energy.

11.5 Irradiation Parameters for Particle Irradiations

In the process of setting up an ion irradiation experiment, a number of parameters that involve beam characteristics (energy, current/dose) and beam–target interaction must be considered. One of the most important considerations is the depth of penetration. Figure 11.15 shows the range vs. particle energy for protons, helium ions and nickel ions in stainless steel as calculated by SRIM [20]. The difference in penetration depth between light and heavy ions is over an order of magnitude in this energy range. Figure 11.16 shows how several other parameters describing the target behavior during proton irradiation vary with energy; dose rate, the time to reach

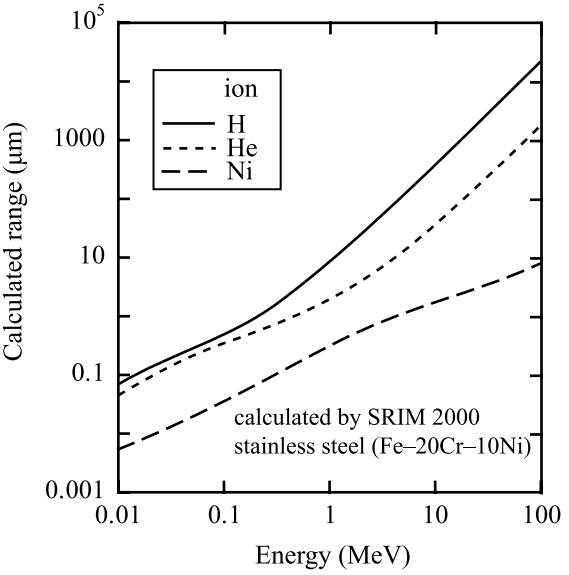

Fig. 11.15. Range of protons, helium atoms and nickel ions in stainless steel as a function of ion energy (from [12])

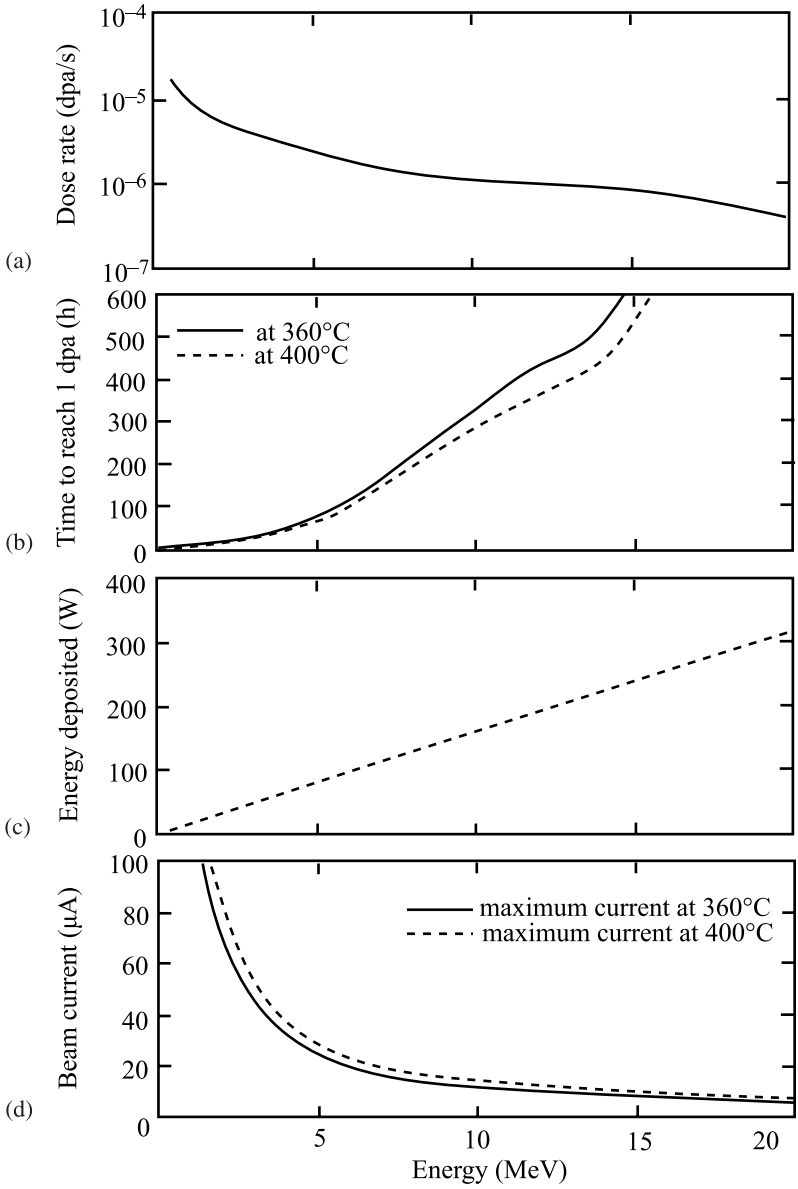

Fig. 11.16. Behavior of beam–target parameters as a function of beam energy proton irradiation at 360 °C. (a) Dose rate. (b) Time to reach 1 dpa. (c) Energy deposition and (d) Beam current limit to maintain a sample temperature of 360 °C (from [12])

1 dpa, deposited energy and the maximum permissible beam current (which will determine the dose rate and total dose) given a temperature limitation of 360 °C. With increasing energy, the dose rate at the surface decreases due to the drop in the elastic

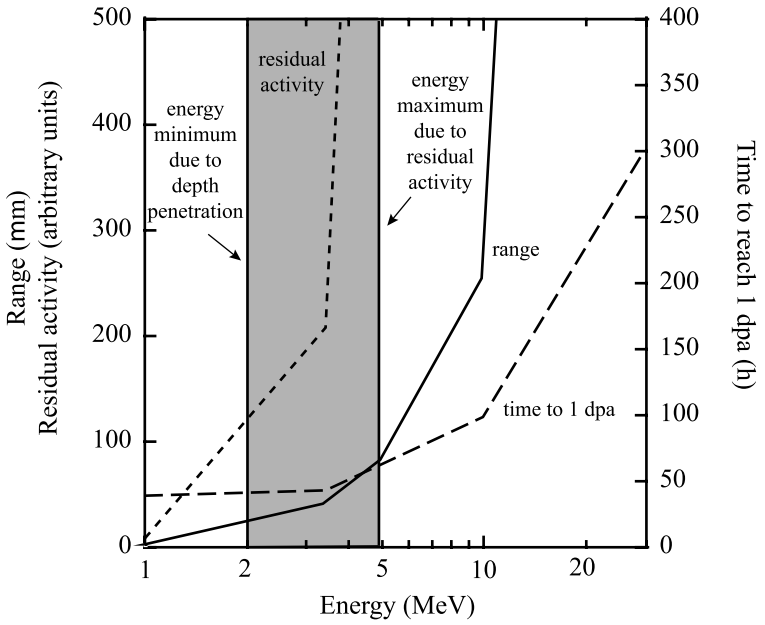

Fig. 11.17. Variation of ion range, residual activity and time to reach 1 dpa as a function of proton energy (from [12])

scattering cross section (Fig. 11.16a). Consequently, the time to reach a target dose level, and hence the length of an irradiation, increases rapidly (Fig. 11.16b). Energy deposition scales linearly with the beam energy, raising the burden of removing the added heat in order to control the temperature of the irradiated region (Fig. 11.16c). The need to remove the heat due to higher energies will limit the beam current for a specific target temperature (Fig. 11.16d) and a limit on the beam current (or dose rate) will result in a longer irradiation to achieve the specified dose. Figure 11.17 summarizes how competing features of an irradiation vary with beam energy, creating trade-offs in the beam parameters. For example, while greater depth is generally favored in order to increase the volume of irradiated material, the higher energy required leads to lower dose rates near the surface and higher residual radioactivity. For proton irradiation, the optimum energy range, achieved by balancing these factors, lies between 2 and 5 MeV as shown by the shaded region.

11.6 Emulation of Neutron Irradiation Damage with Proton Irradiation

Proton irradiation has undergone considerable refinement as a radiation damage tool. Numerous experiments have been conducted and compared to equivalent neutron irradiation experiments in order to determine if proton irradiation can capture

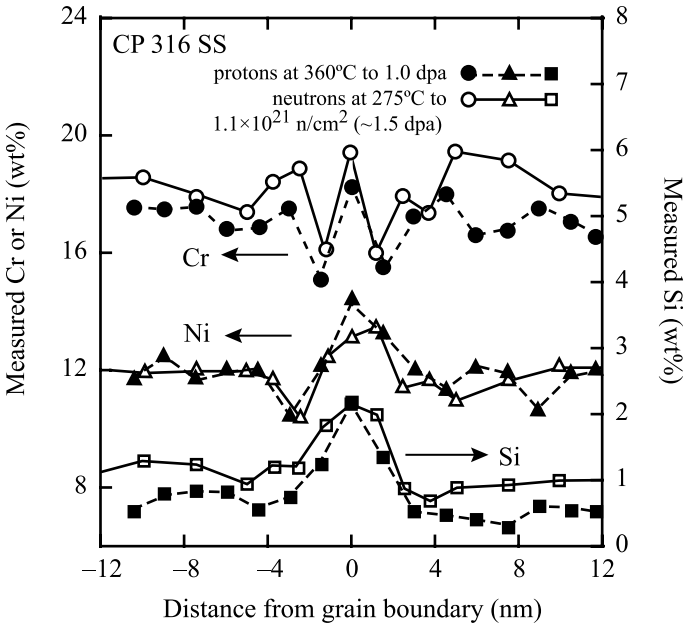

Fig. 11.18. Comparison of grain boundary segregation of Cr, Ni and Si in commercial purity 316 stainless steel following irradiation with either protons or neutrons to similar doses (from [21])

the effects of neutron irradiation on microstructure, microchemistry and hardening. In some cases, benchmarking exercises were conducted on the same native heat as neutron irradiation in order to eliminate heat-to-heat variations that may obscure comparison of the effects of the two types of irradiating particles. The following examples cover a number of irradiation effects on several alloys in an effort to demonstrate the capability of proton irradiation to capture the critical effects of neutron irradiation.

Figures 11.18 to 11.24 show direct comparisons of the *same* irradiation feature on the *same* alloy heats (commercial purity (CP) 304 and 316 stainless steels) following either neutron irradiation at 275 °C or proton irradiation at 360 °C to similar doses. Figure 11.18 compares the RIS behavior of Cr, Ni and Si in a 316 stainless steel alloy following irradiation to approximately 1 dpa. Neutron irradiation results are in open symbols and proton irradiation results are in solid symbols. This dose range was chosen as an extreme test of proton irradiation to capture the "W"-shaped chromium depletion profile caused by irradiation of a microstructure containing grain boundary chromium enrichment prior to irradiation. Note that the two profiles trace each other extremely closely both in magnitude and spatial extent. The agreement extends across all three elements. Figure 11.19 shows the agreement in the dislocation microstructure as measured by the dislocation loop size distribution (Fig. 11.19a) and the size and number density of dislocation loops (Fig. 11.19b) for

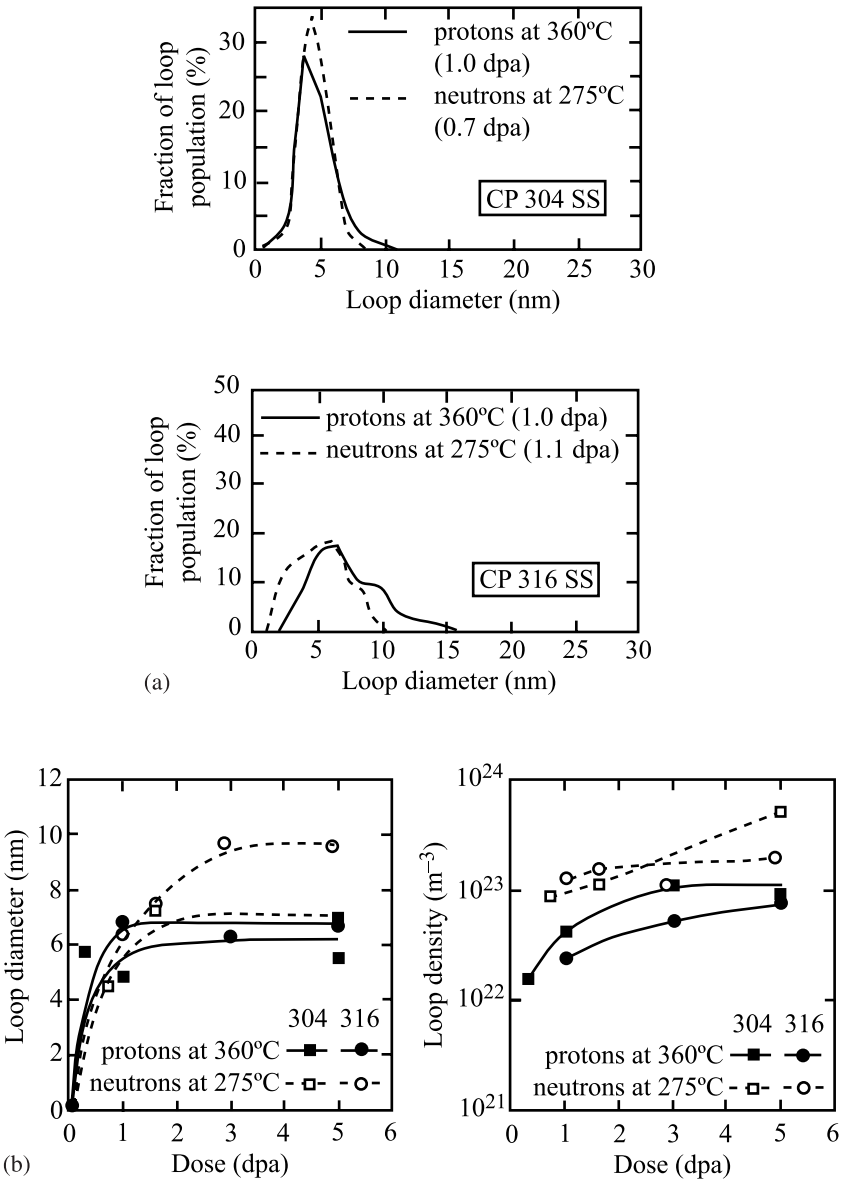

Fig. 11.19. Comparison of (a) loop size distributions and (b) loop diameter and loop number density for commercial purity 304 and 316 stainless steels irradiated with neutrons or protons to similar doses (from [21])

304 SS and 316 SS. Note that the main features of the loop size distributions are captured by both irradiations:; sharply peaked distribution in the case of 304 SS and a flatter distribution with a tail for the case of 316 SS. The agreement in loop size is

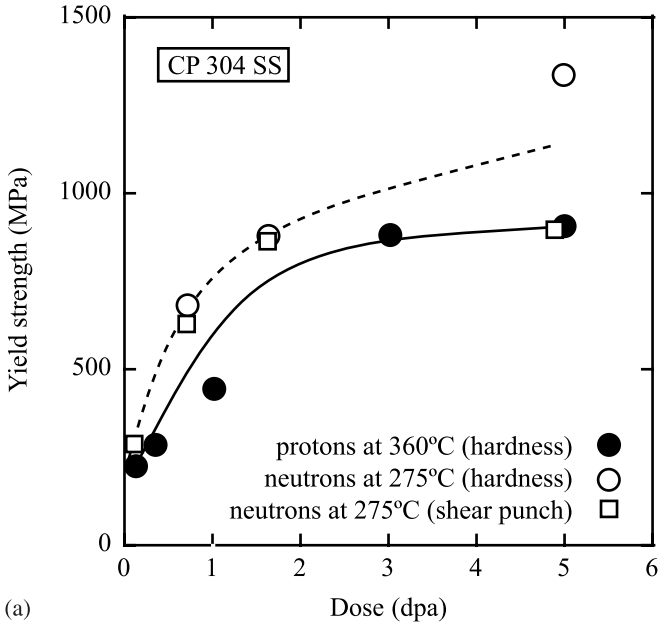

(a)

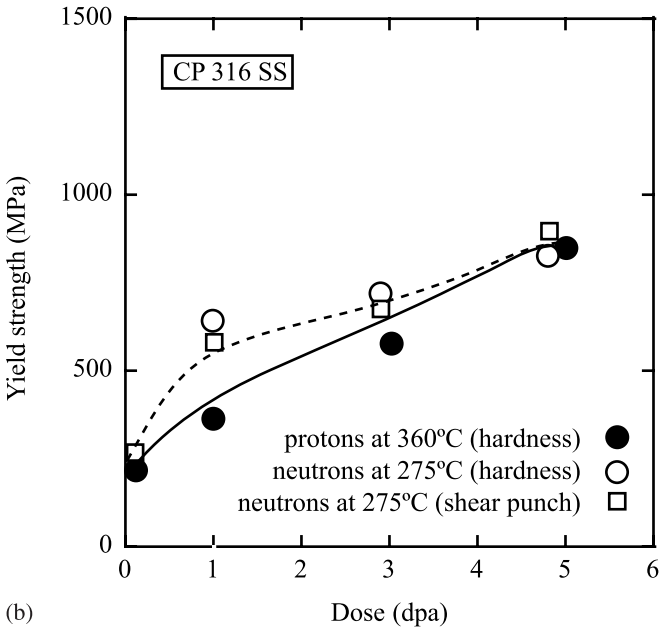

(b)

Fig. 11.20. (a), (b) Comparison of hardening in commercial purity 304 and 316 stainless steel irradiated with neutrons or protons to similar doses (from [21])

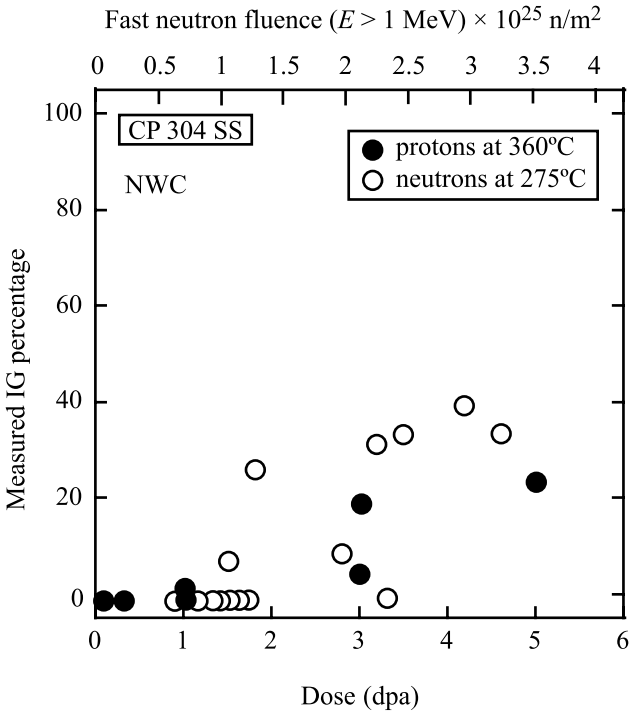

Fig. 11.21. Comparison of the extent of intergranular stress corrosion cracking in commercial purity 304 stainless steel following similar SCC tests of either neutron or proton-irradiated samples from the same heat (from [21])

good for the 304 SS alloy, while loops are smaller for the proton-irradiated 316 alloy. The loop density is about a factor of 3 less for the proton-irradiated case than for the neutron irradiated case, which is expected since the proton irradiation temperature was optimized to track RIS (higher temperature) rather than the dislocation loop microstructure. That the loop sizes and densities are this close is somewhat remarkable considering that loop density is driven by in-cascade clustering, and cascades from proton irradiation are much smaller than those from neutron irradiation. However, the surviving fraction of interstitial loops is greater for proton irradiation, partially compensating the greater loop formation rate under neutron irradiation and resulting in loop densities that are within a factor of 3 [22].

Figure 11.20 shows the comparison of irradiation hardening between the two types of irradiation. The results are close, with proton irradiation resulting in slightly lower hardness. Figure 11.21 shows the IASCC susceptibility of CP 304SS as measured by the %IG on the fracture surface following constant load testing (neutron-irradiated samples) and constant extension rate testing (proton-irradiated samples) in BWR normal water chemistry. Despite the significantly different testing mode, the results are in excellent agreement in that both proton and neutron irradiation result in the onset of IGSCC at about 1 dpa (see Chap. 15).

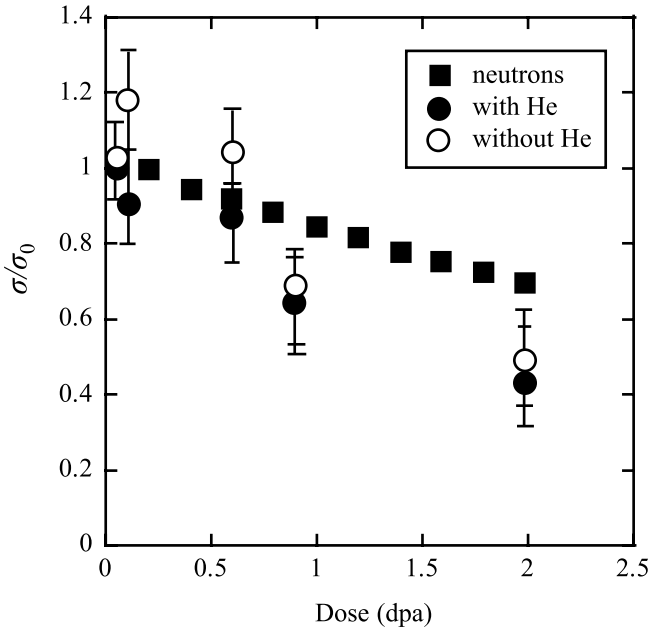

Fig. 11.22. Comparison of relaxation in residual stresses between neutron and proton-irradiated stainless steel after removing the effect of thermally induced relaxation (from [23])

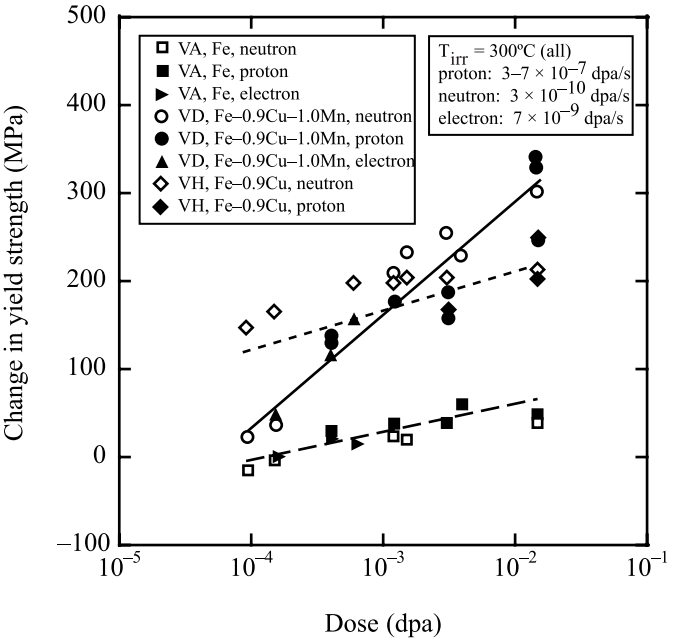

Fig. 11.23. Irradiation hardening in model reactor pressure vessel steels following neutron, proton and electron irradiation at about 300 °C (from [24])

Figure 8.40 in Chap. 8 shows the swelling behavior in austenitic stainless steels as a function of alloy nickel content for proton, Ni ion and neutron irradiation. While these experiments were conducted on different sets of alloys, and under highly disparate irradiation conditions, they all show the same dependence of swelling on nickel content. In the two commercial purity alloys, no voids were formed in either neutron or proton-irradiated samples.

In the last example on stainless steel alloys, Fig. 11.22 shows the relaxation of residual stress by neutron and proton irradiation. Here again, results are on different alloys and are from different types of tests, but both show the same dependence of stress relaxation on dose.

The next examples are from reactor pressure vessel steel and Zircaloy. Figure 11.23 shows an experiment on model reactor pressure vessel alloys in which the same heats were irradiated with neutrons, electrons or protons at around 300 °C to doses spanning two orders of magnitude. The alloys include a high purity Fe heat (VA) that hardens very little under irradiation, an Fe–0.9Cu (VH) heat that hardens rapidly initially, followed by a slower hardening rate above 0.1 mpda, and a Fe–0.9Ce–1.0Mn alloy (VD) in which the hardening rate is greatest over the dose range studied. Despite the very different compositions and hardening rates, the results of the three types of irradiation agree extremely well. Figure 11.24 shows hardening for Zircaloy-2 and Zircaloy-4 irradiated with either neutrons or protons. Although the irradiations were not conducted on the same heats of material, nor using simi-

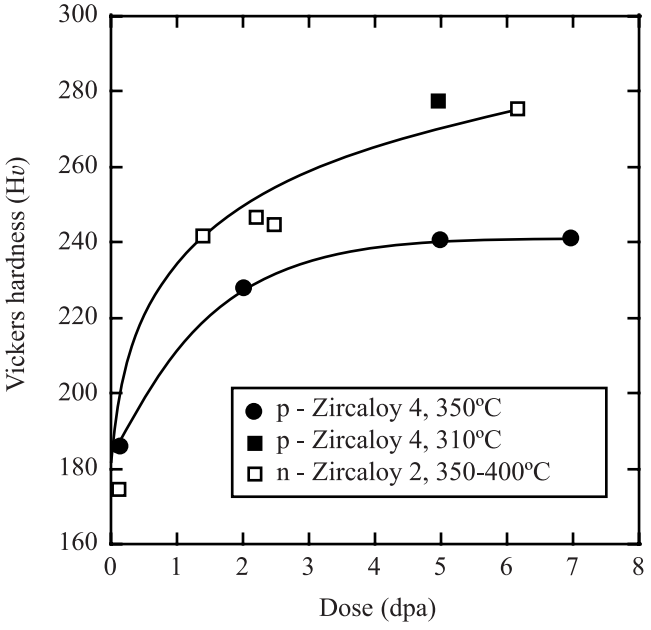

Fig. 11.24. Hardening of Zircaloy-4 irradiated with 3 MeV protons at 310 °C and 350 °C and comparison to neutron-irradiated Zircaloy-2 (from [25])

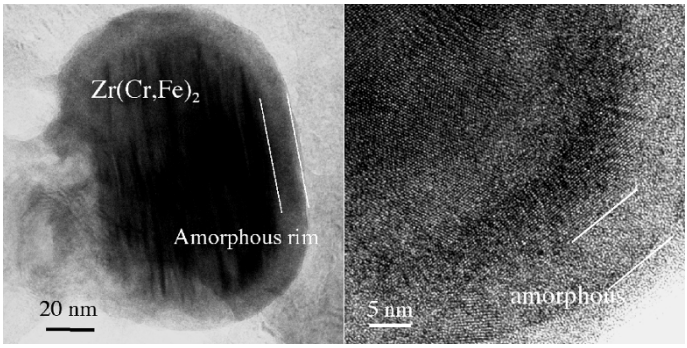

Fig. 11.25. Conventional (left) and high-resolution (right) image of a $Zr(Cr,Fe)_2$ precipitate after proton irradiation to 5 dpa at 310 °C, showing amorphization of the precipitate (from [25])

lar irradiation parameters, there is good agreement in the magnitude and dose dependence of hardening. Figure 11.25 also shows proton-induced amorphization of a $Zr(Fe,Cr)_2$ precipitate after irradiation to 5 dpa at 310 °C, similar to that observed in reactor. These examples represent a comprehensive collection of comparison data between proton and neutron irradiation and taken together, serve as a good example of the capability for charged particles to emulate the effect of neutron irradiation on the alloy microstructure.

Nomenclature

C_i	Concentration of atom of type i
E_d	Displacement energy
k_S^2	Sink strength
$l(t)$	Half width of the chromium depleted zone
M	Amount of grain boundary chromium depletion defined by Eq. (11.5)
N_S	Number of defects per unit volume lost to sinks
N_R	Number of defects per unit volume lost to recombination
R_S	Ratio of vacancy loss to interstitial loss
T	Energy transferred
$P(T)$	Fraction of recoils between E_d and T
$W(E_i, T)$	Weighted average recoil spectrum
$\sigma(E_i, T)$	Scattering cross section for the transfer of energy in $T + dT$
$\sigma_D(E_i)$	Displacement cross section

Acronyms

AES	Auger electron spectroscopy
CP	Commercial purity

IASCC	Irradiation-assisted stress corrosion cracking
IGSCC	Intergranular stress corrosion cracking
K–P	Kinchen–Pease
NRT	Norgett, Robinson, Torrens
SCC	Stress corrosion cracking
SRIM	Stopping power and ranges of ions in matter
STEM-EDS	Scanning transmission electron microscopy-energy dispersive spectroscopy

Problems

11.1 Radiation effects experiments can be conducted with a variety of energetic particles. However, the result is sometimes dependent on the nature of the irradiating particle and the conditions under which the irradiation occurs.

a) Explain (as quantitatively as possible) the differences in the effects of irradiation for a 1 MeV particle of the following types: electron, proton, neutron, Ni ion. In your answer, make sure you address the following:
   a) The recoil spectrum
   b) The damage function
   c) The spatial distribution of defects and the form of the defects
   d) The subsequent behavior of freely migrating defects and defect clusters.

b) Unfortunately, irradiations with the various types of particles do not occur under identical conditions. The following are typical temperatures and dose rates for irradiation with each particle type, as dictated by the facility needed to produce such particles:
   Electrons: 500 °C, 10^{-3} dpa/s
   Protons: 400 °C, 10^{-5} dpa/s
   Ni ions: 500 °C, 10^{-3} dpa/s
   Neutrons: 300 °C, 10^{-8} dpa/s
   Answer part (a) again given these irradiation conditions.

11.2 Three separate particles travel through a pure iron slab, specifically 1 MeV neutrons, 1 MeV gammas, and 1 MeV electrons. For each:

a) Calculate the maximum possible energy transfer to an Fe atom from each particle.
b) State any assumptions you made in part (a).
c) Explain the relative damage consequences for each particle.
d) To minimize damage to the iron, would it be a good idea to place shielding between the radiation source and the iron slab?

11.3 Calculate and graph the weighted recoil spectra for 1 MeV protons and 1 MeV neutrons incident on copper.

11.4 Using the invariance requirements, determine the temperature at which proton irradiations should be conducted in order to produce:

a) The same amount of RIS

b) The same dislocation microstructure
as irradiation in a fast reactor at a temperature of 500 °C, given that the proton damage rate is 10^{-5} dpa/s and the damage rate in a fast reactor is 8×10^{-8} dpa/s.

11.5 Determine the optimum ion irradiation technique for the following objectives:
a) High dose (100 dpa) microstructure investigation at high (500 °C) temperature
b) Investigation of effect of irradiation on stress corrosion cracking of a zirconium alloy in water
c) Tracking the evolution of amorphization with dose.

References

1. Abromeit C (1994) J. Nucl Mater 216:78–96
2. Mazey DJ (1990) J. Nucl Mater 174:196
3. Active Standard (1989) Standard Practice for Neutron Irradiation Damage Simulation by Charged Particle Irradiation, Designation E521-89. American Standards for Testing and Materials, Philadelphia, PA 1989, p D-9
4. Was GS, Andresen PL (1992) JOM 44(4):8
5. Andresen PL, Ford FP, Murphy SM, Perks JM (1990) Proceedings of the 4th International Symposium on Environmental Degradation of Materials in Nuclear Power Systems: Water Reactors. National Association of Corrosion Engineers, Houston, TX, pp 1–83
6. Andresen PL (1992) In: Jones RH (ed) Stress Corrosion Cracking, Materials Performance and Evaluation. ASM International, Meals Park, OH, p 181
7. Sterbentz JW (2004) Neutronic Evaluation of a 21×21 Supercritical Water Reactor Fuel Assembly Design with Water Rods and SiC Clad/Duct Materials, INEEL/EXT-04-02096, Idaho National Engineering and Environmental Laboratory. Bechtel BWXT Idaho, LLC, Idaho Fall, ID
8. Kinchin GH, Pease RS (1955) Prog Phys 18:1
9. Norgett MJ, Robinson MT, Torrens IM (1974) Nucl Eng Des 33:50
10. Was GS, Allen T (1993) J Nucl Mater 205:332–338
11. Perks JM, Marwick AD, English CA (1986) AERE R 12121 June
12. Was GS, Allen TR (2007): In Sickefus KE Kotomin EA Obervaga BP (eds). Radiation Effects in Solids, NATO Science Series II: Mathematics, physics and chemistry, Vol 235, Springer, Berlin, pp 65–98
13. Ezawa T, Wakai E (1991) Ultramicroscopy 39:187
14. Ashworth JA, Norris DIR, Jones IP (1992) JNM 189:289
15. Wakai E (1992) Trans JIM 33(10):884
16. Whitley JB (1978) Dissertation. Nuclear Engineering, University of Wisconsin-Madison
17. Garner FA (1983) J Nucl Mater 117:177–197
18. Lee EH, Mansur LK, Yoo MH (1979) J Nucl Mater 85/86:577–581
19. Brailsford AD, Mansur LK (1977) J Nucl Mater 71:110–116
20. Ziegler JF, Biersack JP, Littmark U (1996) The Stopping and Range of Ions in Matter. Pergamon, New York

21. Was GS, Busby JT, Allen T, Kenik EA, Jenssen A, Bruemmer SM, Gan J, Edwards AD, Scott P, Andresen PL (2002) J Nucl Mater 300:198–216
22. Gan J, Was GS, Stoller R (2001) J Nucl Mater 299:53–67
23. Sencer BH, Was GS, Yuya H, Isobe Y, Sagasaka M, Garner FA (2005) J Nucl Mater 336:314–322
24. Was GS, Hash M, Odette GR (2005) Phil Mag 85(4–7):703–722
25. Zu XT, Sun K, Atzmon M, Wang LM, You LP, Wan FR, Busby JT, Was GS, Adamson RB (2005) Phil Mag 85(4–7):649–659

Part III

Mechanical Effects of Radiation Damage

12 Irradiation Hardening and Deformation

Exposure of metals to irradiation results in an increase in the yield strength over a wide temperature range, and is most pronounced at $T_{irr} < 0.3T_m$. Typical engineering stress-stress curves for fcc and bcc steels are shown in Fig. 12.1. Note that for both crystal structures, in addition to increasing the yield strength, the ductility (measured either by total elongation or by uniform elongation) is reduced. Irradiation also increases the yield strength, σ_y much more than it does the ultimate tensile strength, σ_{UTS} for both fcc and bcc metals. The approach of σ_y to σ_{UTS} results in a loss of ductility to the limit where $\sigma_y = \sigma_{UTS}$ and uniform elongation is zero. In bcc metals tested at low temperature, high fluences may even result in the disappearance of necking deformation with fracture occurring on the elastic line, rendering them totally brittle.

Irradiation-induced hardening in both fcc and bcc metals is caused by the production of the various defects discussed in Chaps. 3, 7, 8 and 9:

- Defect clusters
- Impurity–defect cluster complexes
- Dislocation loops (faulted or unfaulted, vacancy or interstitial type)
- Dislocation lines (dislocation loops that have unfaulted and joined the dislocation network of the original microstructure)
- Voids and bubbles
- Precipitates

This chapter will focus on the mechanisms of irradiation hardening in metals due to the various irradiation-produced defects. Before beginning a discussion of hardening, it is helpful to briefly review the basic elements of elasticity and plasticity theory [1], which will serve as a basis for understanding the effect of irradiation on hardening.

12.1 Elastic and Plastic Deformation

12.1.1 Elasticity

In the elastic region, deformation is proportional to load, and the relation is known as Hooke's law:

$$\sigma = E\varepsilon \,, \tag{12.1}$$

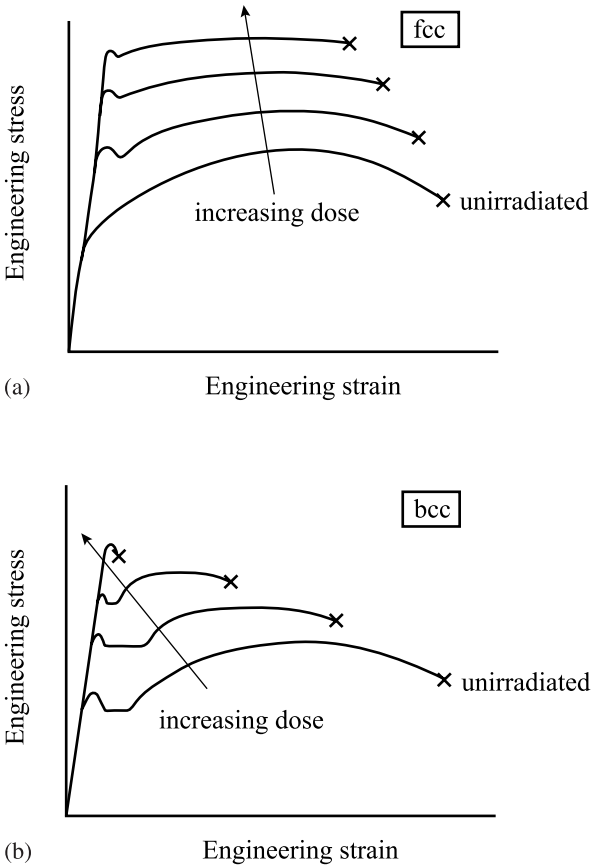

Fig. 12.1. Effect of irradiation on the stress-strain behavior in (a) an austenitic (fcc) stainless steel and (b) a ferritic (bcc) steel

where σ is stress, ε is strain and E is the modulus of elasticity in tension or compression. While a tensile force in the x-direction produces extension along the x-axis, it also produces a contraction along the transverse y and z-directions. The transverse strain is a constant fraction of the longitudinal strain:

$$\varepsilon_{yy} = \varepsilon_{zz} = -\nu\varepsilon_{xx} = \frac{-\nu\sigma_{xx}}{E}, \tag{12.2}$$

where ν is Poisson's ratio and has a value of 0.25 for perfectly isotropic elastic materials, but is approximately 0.33 for most metals. For a three-dimensional state of stress, the resulting strains are:

Stress	x-Strain	y-Strain	z-Strain
σ_{xx}	$\varepsilon_{xx} = \dfrac{\sigma_{xx}}{E}$	$\varepsilon_{yy} = \dfrac{-\nu\sigma_{xx}}{E}$	$\varepsilon_{zz} = \dfrac{-\nu\sigma_{xx}}{E}$
σ_{yy}	$\varepsilon_{xx} = \dfrac{-\nu\sigma_{yy}}{E}$	$\varepsilon_{yy} = \dfrac{\sigma_{yy}}{E}$	$\varepsilon_{zz} = \dfrac{-\nu\sigma_{xx}}{E}$
σ_{zz}	$\varepsilon_{xx} = \dfrac{-\nu\sigma_{zz}}{E}$	$\varepsilon_{yy} = \dfrac{-\nu\sigma_{zz}}{E}$	$\varepsilon_{zz} = \dfrac{\sigma_{zz}}{E}$

Superposition of strain components yields:

$$\begin{aligned}
\varepsilon_{xx} &= \frac{1}{E}[\sigma_{xx} - \nu(\sigma_{yy} + \sigma_{zz})] \\
\varepsilon_{yy} &= \frac{1}{E}[\sigma_{yy} - \nu(\sigma_{xx} + \sigma_{zz})] \\
\varepsilon_{zz} &= \frac{1}{E}[\sigma_{zz} - \nu(\sigma_{xx} + \sigma y_y)] \,.
\end{aligned} \tag{12.3}$$

Adding the strain components gives:

$$\varepsilon_{xx} + \varepsilon_{yy} + \varepsilon_{zz} = \frac{1-2\nu}{E}(\sigma_{xx} + \sigma_{yy} + \sigma_{zz}) \,, \tag{12.4}$$

and

$$\sigma_m = 1/3(\sigma_{xx} + \sigma_{yy} + \sigma_{zz}) \tag{12.5}$$

is the hydrostatic or mean stress, and

$$\Delta = \varepsilon_{xx} + \varepsilon_{yy} + \varepsilon_{zz} \tag{12.6}$$

is the volume strain. Shear stresses produce shear strains according to the following relations:

$$\varepsilon_{xy} = \frac{\sigma_{xy}}{\mu} \,, \quad \varepsilon_{yz} = \frac{\sigma_{yz}}{\mu} \,, \quad \varepsilon_{xz} = \frac{\sigma_{xz}}{\mu} \,, \tag{12.7}$$

where μ is the shear modulus.

The stress-strain relations for an isotropic solid involve three elastic constants, ν, E and μ, that are related as follows:

$$\mu = \frac{E}{2(1+\nu)} \,. \tag{12.8}$$

In a general anisotropic linear elastic solid, there are up to 21 independent elastic constants. Since the constants must obey various geometrical constraints for a given crystal structure, the number of independent elastic constants is reduced considerably in structures possessing a high degree of symmetry.

For small elastic strains there is no coupling between the expressions for normal stress and strain and the equations for shear stress and shear strain and we can solve

for stress in terms of strain. Writing Eq. (12.4) in terms of stress:

$$\sigma_{xx} + \sigma_{yy} + \sigma_{zz} = \frac{E}{1-2\nu}(\varepsilon_{xx} + \varepsilon_{yy} + \varepsilon_{zz}) , \tag{12.9}$$

and rewriting the first equation in Eq. (12.3) as:

$$\varepsilon_{xx} = \frac{1+\nu}{E}\sigma_{xx} - \frac{\nu}{E}(\varepsilon_{xx} + \varepsilon_{yy} + \varepsilon_{zz}) , \tag{12.10}$$

and substituting Eq. (12.10) into Eq. (12.8) to eliminate σ_{yy} and σ_{zz} gives:

$$\sigma_{xx} = \frac{E}{1+\nu}\varepsilon_{xx} + \frac{\nu E}{(1+\nu)(1-2\nu)}(\varepsilon_{xx} + \varepsilon_{yy} + \varepsilon_{zz}) , \tag{12.11}$$

or in tensor notation:

$$\sigma_{ij} = \frac{E}{1+\nu}\varepsilon_{ij} + \frac{\nu E}{(1+\nu)(1-2\nu)}\varepsilon_{ij}\delta_{ij} , \tag{12.12}$$

were δ_{ij} is the Kronecker delta with values $\delta_{ij} = 1$ for $i = j$and $\delta_{ij} = 0$ for $i \neq j$. Upon expansion, this expression yields three equations for normal stress and six equations for shear stress. Equation (12.12) is often written in briefer notation using the Lamé constant, defined as:

$$\lambda = \frac{\nu E}{(1+\nu)(1-2\nu)} . \tag{12.13}$$

Substituting for Eqs. (12.6), (12.8) and (12.13) for Δ, μ and λ, respectively, into Eq. (12.11) gives:

$$\sigma_{xx} = 2\mu\varepsilon_{xx} + \lambda\Delta . \tag{12.14}$$

The stresses and strains can be broken into hydrostatic and deviatoric components. Hydrostatic stress involves only pure tension and compression while deviatoric stress represents the shear stresses in the total state of stress. The distortion is related to the stress deviator by:

$$\sigma'_{ij} = \frac{E}{1+\nu}\varepsilon'_{ij} = 2\mu\varepsilon'_{ij} , \tag{12.15}$$

while the relationship between hydrostatic stress and mean strain is:

$$\sigma_{ii} = \frac{E}{1-2\nu}\varepsilon_{ii} = 3K\varepsilon_{ii} , \tag{12.16}$$

where $K = \dfrac{E}{3(1-2\nu)}$ is the bulk modulus or volumetric modulus of elasticity. The bulk modulus is the ratio of the hydrostatic pressure to the dilatation that it produces:

$$K = \frac{\sigma_m}{\Delta} = \frac{-p}{\Delta} = \frac{1}{\beta} , \tag{12.17}$$

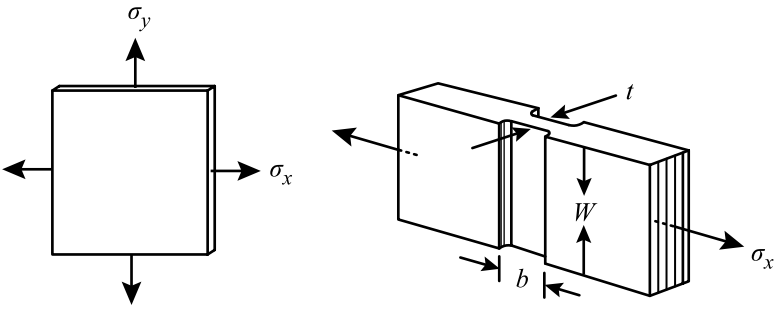

Fig. 12.2. Examples of (a) plane stress state and (b) plane strain state

where $-p$ is the hydrostatic pressure and β is the compressibility of the solid. Note that the hydrostatic component of the stress tensor produces only elastic volume changes and does not cause plastic deformation. So the yield stress of a solid is independent of the hydrostatic stress. The stress deviator involves shear stress and is responsible for plastic deformation.

Two special cases of engineering importance are plane stress and plane strain. The plane stress state occurs when one of the principal stresses is zero, such as in a thin sheet loaded in the plane of the sheet (Fig. 12.2a) or an internally pressurized, thin-walled tube. In this case, the principal stresses are:

$$\begin{aligned}
\sigma_1 &= \frac{E}{1-\nu^2}(\varepsilon_1 + \nu\varepsilon_2)\,, \\
\sigma_2 &= \frac{E}{1-\nu^2}(\varepsilon_2 + \nu\varepsilon_1)\,, \\
\sigma_3 &= 0\,.
\end{aligned} \tag{12.18}$$

The plane strain state is one in which one of the principal strains is zero such as occurs when one dimension is much greater than the other two (Fig. 12.2b). In this case, we have $\varepsilon_3 = \frac{1}{E}[\sigma_3 - \nu(\sigma_1 + \sigma_2)]$, and combining with $\sigma_3 = \nu(\sigma_1 + \sigma_2)$ gives:

$$\begin{aligned}
\varepsilon_1 &= \frac{1}{E}[(1-\nu^2)\sigma_1 - \nu(1+\nu)\sigma_2]\,, \\
\varepsilon_2 &= \frac{1}{E}[(1-\nu^2)\sigma_2 - \nu(1+\nu)\sigma_1]\,, \\
\varepsilon_3 &= 0\,.
\end{aligned} \tag{12.19}$$

Note that the expressions in Eqs. (12.18) and (12.19) were written in terms of principal stresses and principal strains, which act normal to the principal planes. Principal planes are those on which the maximum normal stresses act and on which no shearing stresses act.

The strain energy, U is the energy expended by the action of external forces in deforming an elastic body. The work performed during elastic deformation is stored as elastic energy and is recovered upon release of the applied forces. Energy is the product of force, F through the distance, δ over which it acts. In deformation of an elastic solid, the force and deformation increase linearly from zero to a value of $1/2F\delta$. This quantity is the area under the elastic portion of the stress-strain curve that was presented in Chap. 7 (Fig. 7.22). If we subject a cube to a tensile stress in the x-direction, then we can write an expression for the change in strain energy of the solid:

$$\begin{aligned} \mathrm{d}U &= 1/2F\,\mathrm{d}\delta \\ &= 1/2(\sigma_{xx}A)(\varepsilon_{xx}\,\mathrm{d}x) \\ &= 1/2(\sigma_{xx}\varepsilon_{xx})(A\,\mathrm{d}x)\ . \end{aligned} \tag{12.20}$$

Since $A\,\mathrm{d}x$ is the volume increment, the strain energy per unit volume or strain energy density is:

$$\begin{aligned} U &= 1/2\sigma_{xx}\varepsilon_{xx} \\ &= 1/2\frac{\sigma_{xx}^2}{E} \\ &= 1/2\varepsilon_{xx}^2 E\ . \end{aligned} \tag{12.21}$$

For pure shear stress:

$$\begin{aligned} U &= 1/2\sigma_{xy}\varepsilon_{xy} \\ &= 1/2\frac{\sigma_{xy}^2}{\mu} \\ &= 1/2\varepsilon_{xy}^2\mu\ . \end{aligned} \tag{12.22}$$

Elastic strain energy for a three-dimensional stress state is obtained by superposition of Eqs. (12.21) and (12.22):

$$\begin{aligned} U &= 1/2(\sigma_{xx}\varepsilon_{xx} + \sigma_{yy}\varepsilon_{yy} + \sigma_{zz}\varepsilon_{zz} + \sigma_{xy}\varepsilon_{xy} + \sigma_{yz}\varepsilon_{yz} + \sigma_{xz}\varepsilon_{xz}) \\ &= 1/2\sigma_{ij}\varepsilon_{ij}\ . \end{aligned} \tag{12.23}$$

Substituting expressions for strains from Eqs. (12.3) and (12.7) gives:

$$\begin{aligned} U =& \frac{1}{2E}(\sigma_{xx}^2 + \sigma_{yy}^2 + \sigma_{zz}^2) - \frac{\nu}{E}(\sigma_{xx}\sigma_{yy} + \sigma_{yy}\sigma_{zz} + \sigma_{xx}\sigma_{zz}) \\ &+ \frac{1}{2\mu}(\sigma_{xy}^2 + \sigma_{yz}^2 + \sigma_{xz}^2)\ , \end{aligned} \tag{12.24}$$

and substituting Eq. (12.4) into Eq. (12.24) gives:

$$U = 1/2\lambda\Delta^2 + \mu(\varepsilon_{xx}^2 + \varepsilon_{yy}^2 + \varepsilon_{zz}^2) + 1/2\mu(\varepsilon_{xy}^2 + \varepsilon_{yz}^2 + \varepsilon_{xz}^2)\ . \tag{12.25}$$

Note that the derivative of U with respect to any strain component gives the corresponding stress component:

$$\frac{\partial U}{\partial \varepsilon_{xx}} = \lambda\Delta + 2\mu\varepsilon_{xx} = \sigma_{xx} \quad \text{and} \quad \frac{\partial U}{\partial \sigma_{xx}} = \varepsilon_{xx} \,. \tag{12.26}$$

12.1.2 Plasticity

Elastic deformation depends only on the initial and final states of stress and strain, while plastic strain depends on the loading path by which the final state is achieved. The stress required to cause metal to flow plastically to any given strain describes the flow curve, which is given by the power-law hardening relationship:

$$\sigma = K\varepsilon_{\mathrm{p}}^{n} \,, \tag{12.27}$$

where ε_{p} is the plastic strain, K is the stress at $\varepsilon_{\mathrm{p}} = 1.0$, and n is the strain hardening exponent. Note that $n = 0$ for perfectly plastic behavior and $n = 1$ for elastic behavior. Typically, n is between 0.1 and 0.5. The shape of the power-law hardening curve for various values of n is shown in Fig. 12.3. The yield strength is easy to find in a tension test. We would like to develop mathematical relations for predicting the conditions under which plastic yielding begins when a material is subject to any possible combination of stresses. However, there is currently no way of calculating the relationship between the stress components to correlate yield in a three-dimensional state of stress with yield in uniaxial tension. All yielding criteria are empirical.

Von Mises proposed that yielding will occur when the second invariant of the stress deviator (see for example [1]) exceeded some critical value, k^2, or:

$$k^2 = 1/6\left[(\sigma_1 - \sigma_2)^2 + (\sigma_2 - \sigma_3)^2 + (\sigma_3 - \sigma_1)^2\right] \,. \tag{12.28}$$

The value of k is determined by applying this expression to a uniaxial tension test in which $\sigma_1 = \sigma_{\mathrm{y}}$, $\sigma_2 = \sigma_3 = 0$, (σ_{y} is the yield stress) giving:

$$\sigma_{\mathrm{y}}^2 + \sigma_{\mathrm{y}}^2 = 6k^2 \,, \quad \text{or} \quad \sigma_{\mathrm{y}} = \sqrt{3}k \,. \tag{12.29}$$

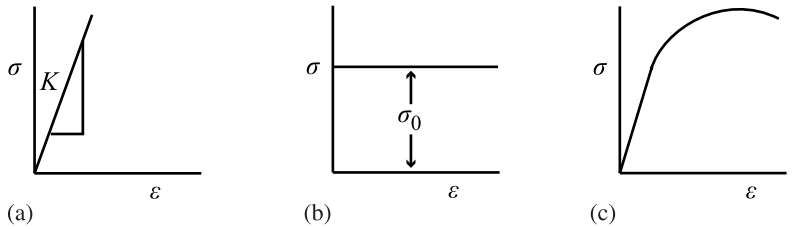

Fig. 12.3. Flow curves drawn from Eq. (12.27) for the cases (a) elastic behavior, $n = 1$, (b) perfectly plastic behavior, $n = 0$, (c) plastic behavior with intermediate value of n

Substituting Eq. (12.29) into Eq. (12.28) gives the familiar form of the von Mises yield criterion:

$$\sigma_y = 1/\sqrt{2}\left[(\sigma_1-\sigma_2)^2+(\sigma_2-\sigma_3)^2+(\sigma_3-\sigma_1)^2\right]^{1/2}, \tag{12.30}$$

and if shear stresses are present:

$$\sigma_y = 1/\sqrt{2}\left[(\sigma_{xx}-\sigma_{yy})^2+(\sigma_{yy}-\sigma_{zz})^2+(\sigma_{zz}-\sigma_{xx})^2+6(\sigma_{xy}+\sigma_{yz}+\sigma_{xz})\right]^{1/2}. \tag{12.31}$$

Yielding will occur when the differences in stresses on the right side of the equation exceed the yield stress in uniaxial tension, σ_y. For a pure shear stress state (as in a torsion test), the shear stress, σ_s is related to the principal stresses by:

$$\sigma_1 = -\sigma_3 = \sigma_s\,, \quad \sigma_2 = 0\,, \tag{12.32}$$

and at yield:

$$\sigma_1^2+\sigma_1^2+4\sigma_1^2 = 6k^2\,, \quad \text{and} \quad \sigma_1 = k\,, \tag{12.33}$$

so k is the yield stress in pure shear. The von Mises criterion predicts that the yield stress in torsion will be less than that in uniaxial tension by:

$$k = \frac{1}{\sqrt{3}}\sigma_y = 0.577\sigma_y\,. \tag{12.34}$$

Another criterion used for yielding due to a multiaxial stress state is the Tresca (or maximum shear stress) criterion, which says that yielding occurs when the maximum shear stress reaches the value of the shear stress in the uniaxial tension test:

$$\sigma_s^{\max} = \frac{\sigma_1-\sigma_3}{2}\,, \tag{12.35}$$

where σ_1 is the algebraically largest principal stress and σ_3 is the algebraically smallest principal stress. For uniaxial tension, $\sigma_1 = \sigma_y$, $\sigma_2 = \sigma_3 = 0$, and the shearing yield stress, σ_{sy} is equal to $\sigma_y/2$, and (12.35) becomes:

$$\sigma_s^{\max} = \frac{\sigma_1-\sigma_3}{2} = \frac{\sigma_y}{2} = \sigma_{sy}\,, \tag{12.36}$$

so the maximum shear stress criterion is then given by:

$$\sigma_1-\sigma_3 = \sigma_y\,. \tag{12.37}$$

For a pure shear stress state, $\sigma_1 = -\sigma_3 = k$, and $\sigma_2 = 0$, so the maximum shear stress criterion states that yielding will occur when:

$$\sigma_1-\sigma_3 = 2k = \sigma_y\,, \quad \text{or} \quad k = \frac{\sigma_y}{2}\,. \tag{12.38}$$

The Tresca yield criterion has been observed to hold fairly well in alloys that exhibit a yield drop [2]. Alloys that yield by homogeneous plastic flow generally obey the von Mises criterion or deviate from it only slightly. In fact, in many real materials, the yield surface is "between" the Tresca and von Mises criteria [2].

12.1.3 Tension Test

The tension test is perhaps the best way to demonstrate the elastic and plastic behavior of metals. In a tension test, a specimen is subjected to a continually increasing uniaxial tensile force, while simultaneous observations are made of the elongation of the specimen. Data are plotted in a stress-strain diagram from load-elongation measurements, resulting in an engineering stress-engineering strain curve. The parameters used to describe the stress-strain curve are:

- Yield strength
- Tensile strength
- Fracture strength
- Uniform strain
- Fracture strain
- Reduction in area

Figure 12.4 illustrates the engineering stress-engineering strain curve and the parameters used to describe the behavior of the sample. The average longitudinal stress, S is the load, P divided by the *original* area, A_0:

$$S = \frac{P}{A_0} \,. \tag{12.39}$$

The average linear strain, e is the ratio of the change in length, δ to the original length, L_0:

$$e = \frac{\delta}{L_0} = \frac{\Delta L}{L_0} = \frac{L - L_0}{L_0} \,. \tag{12.40}$$

The engineering stress-engineering strain curve is not a true indication of the deformation characteristics of a material because it is based entirely on the original dimensions of the specimen that change continuously during a test.

The true stress, σ and true strain, ε are based on the instantaneous values of cross sectional area and length and are given by:

$$\sigma = \frac{P}{A} = S\frac{A}{A_0} \,, \tag{12.41}$$

$$\begin{aligned} \varepsilon &= \int_{L_0}^{L_f} \frac{\mathrm{d}L}{L} \\ &= \ln \frac{L_f}{L_0} = \ln(e+1) \,. \end{aligned} \tag{12.42}$$

While the true strain and engineering strain are close at small values of strain (<0.2), they diverge significantly at large values of strain. The relationship between true and engineering stress is determined by invoking conservation of volume:

$$\frac{A_0}{A} = \frac{L_0}{L} = e + 1 \,, \quad \text{and} \quad S = \frac{P}{A_0}(e+1) = S(e+1) \,. \tag{12.43}$$

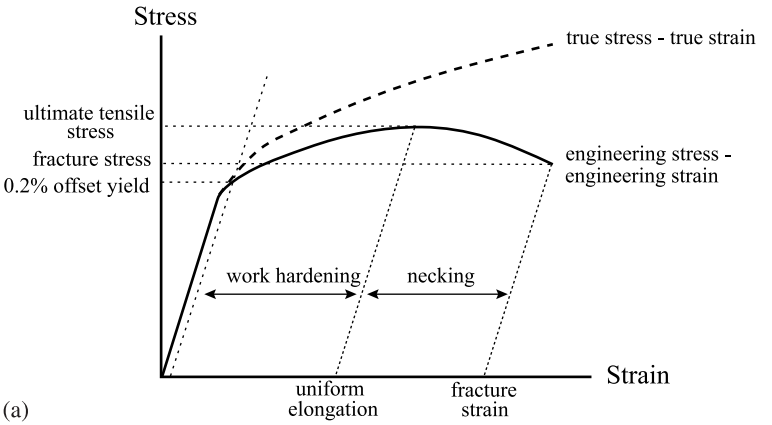

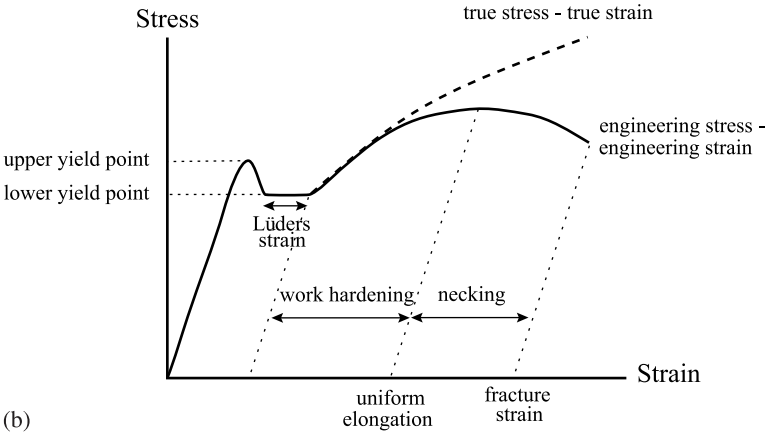

Fig. 12.4. Engineering stress-engineering strain and true stress-true strain curves resulting from a uniaxial tensile test and key parameters defining the curves for (a) fcc metals and (b) bcc metals

Up to a certain limiting load, a solid will recover its original dimensions when the load is removed. The load beyond which the material no longer behaves elastically is the *elastic limit*. If the elastic limit is exceeded, the body will retain a permanent set upon removal of the load. The stress at which plasticity begins is called the *yield stress*, σ_y or YS. Various definitions exist for the yield stress but the commonly accepted one is the offset yield strength, determined by the stress corresponding to the intersection of the stress-strain curve and a line parallel to the elastic part of the

curve and offset by a strain of 0.2%. The yield strength is written as follows:

$$\sigma_{\mathrm{y}} = \frac{P_{(\text{strain offset}=0.2\%)}}{A_0} \,. \tag{12.44}$$

The *tensile strength* or *ultimate tensile strength* (UTS) is the maximum load divided by the original cross sectional area of the sample:

$$s_{\mathrm{u}} = \frac{P_{\max}}{A_0} \,. \tag{12.45}$$

The true stress at maximum load is the true tensile strength and is given by the maximum load divided by the sample cross sectional area at maximum load:

$$\sigma_{\mathrm{u}} = \frac{P_{\max}}{A_{\mathrm{u}}} \,, \quad \varepsilon_{\mathrm{u}} = \ln \frac{A_0}{A_{\mathrm{u}}} \,. \tag{12.46}$$

Eliminating $P_{\max}$ from Eqs. (12.45) and (12.46) gives:

$$\begin{aligned} \sigma_{\mathrm{u}} &= S_{\mathrm{u}} \frac{A_0}{A_{\mathrm{u}}} \\ &= S_{\mathrm{u}} \exp(\varepsilon_{\mathrm{u}}) \,. \end{aligned} \tag{12.47}$$

The *fracture stress* is the stress at the point of failure and is given by:

$$\begin{aligned} S_{\mathrm{f}} &= \frac{P_{\mathrm{f}}}{A_0} \,, \quad e_{\mathrm{f}} = \frac{L_{\mathrm{f}} - L_0}{L_0} \\ \sigma_{\mathrm{f}} &= \frac{P_{\mathrm{f}}}{A_{\mathrm{f}}} \,, \quad \varepsilon_{\mathrm{f}} = \ln \frac{A_0}{A_{\mathrm{f}}} \,. \end{aligned} \tag{12.48}$$

Strain occurs uniformly in the gage section of the sample up to the UTS, which is when necking or localized deformation begins to occur. The true uniform strain, ε_{u} is given by the strain at maximum load:

$$\varepsilon_{\mathrm{u}} = \ln \frac{A_0}{A_{\mathrm{u}}} \,. \tag{12.49}$$

The true fracture strain, ε_{f} is the true strain based on the original area and the area after fracture, A_{f}:

$$\varepsilon_{\mathrm{f}} = \ln \frac{A_0}{A_{\mathrm{f}}} = \ln \frac{1}{1 - RA} \,, \tag{12.50}$$

where RA is the reduction in area at fracture:

$$RA = \frac{A_0 - A_{\mathrm{f}}}{A_0} \,. \tag{12.51}$$

Finally, the local necking strain, ε_n is the strain required to deform the specimen from the maximum load to fracture:

$$\varepsilon_n = \ln \frac{A_u}{A_f} . \tag{12.52}$$

A final quantity of importance in the tensile test is the onset of plastic instability, which occurs when the increase in stress due to the decreasing cross sectional area becomes greater than the load-carrying ability of the metal. This necking or localized deformation begins at the point of maximum load and is defined by the condition that $dP = 0$:

$$P = \sigma A$$

$$dP = \sigma\, dA + A\, d\sigma = 0 , \quad \text{and} \quad -\frac{dA}{A} = \frac{d\sigma}{\sigma} \tag{12.53}$$

and from conservation of volume:

$$\frac{dL}{L} = -\frac{dA}{A} = d\varepsilon , \tag{12.54}$$

so that at the point of tensile instability:

$$\sigma = \frac{d\sigma}{d\varepsilon} . \tag{12.55}$$

That is, the point of necking at maximum load is obtained from the true stress-true strain curve by finding the point on the curve where the rate of strain hardening equals the stress. Referring back to the flow curve relation given in Eq. (12.27), the strain hardening exponent is defined by:

$$n = \frac{d\ln\sigma}{d\ln\varepsilon} = \frac{\varepsilon\, d\sigma}{\sigma\, d\varepsilon} , \quad \text{and} \quad \frac{d\sigma}{d\varepsilon} = n\frac{\sigma}{\varepsilon} . \tag{12.56}$$

Substituting Eq. (12.55) into Eq. (12.56) gives a simple expression for the true uniform strain:

$$\varepsilon_u = n . \tag{12.57}$$

That is, the true uniform strain is equal to the strain hardening exponent in the power-law hardening expression, Eq. (12.27).

12.1.4 Yield Strength

The yield strength represents the onset of plasticity and hence, is a key parameter in determining the mechanical behavior of metals. Yielding can be understood by examining the behavior of dislocations in a metal under stress. Dislocations formed by sources such as the Frank–Read source, frequently pile up on slip planes at barriers such as grain boundaries, precipitates or sessile dislocations. The leading dislocation is acted on not only by the applied shear stress, but also by the interaction with other dislocations on the slip plane, leading to a high stress concentration on the lead dislocation in the pile-up. The pile-up of dislocations also exerts a back

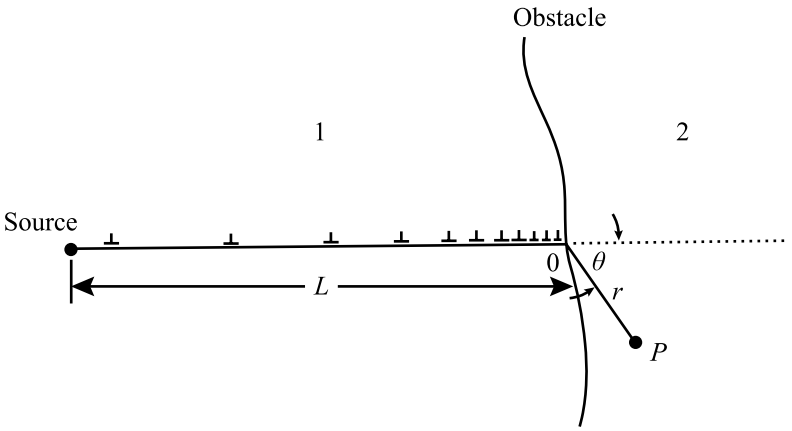

Fig. 12.5. Dislocation pile-up at an obstacle in a solid

stress on dislocations further from the barrier, opposing their motion on the slip plane (Fig. 12.5). The high stress at the head of the pile-up can initiate yielding on the other side of the barrier (or it may nucleate a crack at the barrier, see Chap. 13).

The number of dislocations in the pile-up can be estimated by summing the x-direction forces between each dislocation in the pile-up under the condition of mechanical equilibrium. The number of dislocations in a pile-up of length L under a shear stress σ_s on the slip plane [3] is:

$$n = \frac{\pi(1-\nu)L\sigma_s}{\mu b} . \tag{12.58}$$

At large distances from the pile-up, the array of n dislocations can be considered to act like a single dislocation with Burgers vector nb with a force equal to $nb\sigma_s$. A more complete analysis of the stress at the head of the pile-up was made by Stroh [4] who showed that the tensile stress normal to the line OP in the neighboring grain is:

$$\sigma = \frac{3}{2}\left(\frac{L}{r}\right)^{1/2} \sigma_s \sin\theta \cos\theta/2 . \tag{12.59}$$

The maximum value of σ occurs at $\theta = 70.5°$ and yields:

$$\sigma = \frac{2}{\sqrt{3}}\left(\frac{L}{r}\right)^{1/2} \sigma_s , \tag{12.60}$$

and the shear stress acting in the plane OP is given by:

$$\sigma_P = \beta\sigma_s \left(\frac{L}{r}\right)^{1/2} . \tag{12.61}$$

If the obstacle is a grain boundary, and the distance from the head of the pile-up in grain 1 to the nearest dislocation source in grain 2 in Fig. 12.5 is r, and the length of the pile-up, L is taken to be equal to the grain diameter, d then yielding will occur when the shear stress in the pile-up, σ_s reaches the shear stress to cause yielding, σ_{sy} or $\sigma_s = \sigma_{sy}$. If σ_{sd} is the stress required to nucleate slip in grain 2, then the shear stress causing yielding can be written as follows:

$$(\sigma_{sy} - \sigma_{si}) \left(\frac{d}{r}\right)^{1/2} = \sigma_{sd} \,, \tag{12.62}$$

where σ_{si} is the friction stress, or the stress opposing dislocation motion in the slip plane. Equation Eq. (12.62) can be written in terms of the normal stress where $\sigma_s = \sigma/m$ where m is the Schmidt factor defined as the ratio of the resolved shear stress to the axial stress:

$$\begin{aligned} \sigma_y &= \sigma_i + m\sigma_{sd} \left(\frac{r}{d}\right)^{1/2} \\ &= \sigma_i + k_y d^{-1/2} \,. \end{aligned} \tag{12.63}$$

Equation (12.63) is the Hall–Petch equation, which describes the grain size dependence of the yield stress. Note that the yield strength increases with decreasing grain size. Yield behavior in metals is generally found to follow this relation for nominal grain sizes (few to hundreds of micrometers), but fails at very low grain sizes in the nanometer range.

12.2 Irradiation Hardening

Irradiation of a metal causes strengthening by *source hardening* and *friction hardening*. Source hardening is the increase in stress required to start a dislocation moving on its glide plane. The applied stress required to release a dislocation into its slip plane is called the *unpinning* or unlocking stress. Once moving, the dislocation can be impeded by natural or radiation-produced obstacles lying close to or in the slip plane. The resistance to motion caused by these obstacles is referred to as friction hardening. Both of these concepts will be discussed and then applied to describe the hardening resulting from each of the radiation-induced defects listed earlier. It should be noted, however, that the true distinction between source and friction hardening is unclear, as lattice hardening produces all the characteristics of the deformation that has been attributed to source hardening. The loss of distinction is due to the fact that the distance between defect clusters is less than the source length that would produce the observed critical shear stress. Therefore, the *source* cannot operate without interference from the lattice clusters [5]. Nevertheless, we will treat them separately in the following sections. Hardening mechanisms will first be discussed for single crystals containing an obstacle of a single type. The superposition of hardening from different origins in a single crystal will be treated next followed by an extension of theory to the polycrystalline solid.

12.2.1 Source Hardening

Source hardening is found in irradiated fcc and both unirradiated and irradiated bcc metals. In unirradiated bcc metals, source hardening is manifest by the upper and lower yield points in the stress-strain curve (Fig. 12.4b) and is thought to be caused by the pinning or locking of dislocation lines by impurity atoms. Before a Frank–Read source can operate under an applied stress, the dislocation line must be unpinned from the impurities. This requires a larger stress than that to move the dislocation, causing a drop in the yield stress. Yield then continues at a constant *flow stress* (*Lüders* strain region) until the onset of work hardening which progresses in the same manner as in fcc metals.

Source hardening is found in irradiated fcc metals in which irradiation-produced defect clusters in the vicinity of Frank–Read sources raise the stress required to expand the loops and to permit source multiplication. Once the stress level is sufficient to release the source, the moving dislocations can destroy the small clusters and reduce the stress needed to continue the deformation.

In unirradiated fcc metals, the stress required to initiate dislocation motion is the unpinning stress of the Frank–Read sources in the metal and is given by Eq. (7.32a) as $\sigma_{FR} = \dfrac{\mu b}{l}$, where μ is the shear modulus, b is the Burgers vector and $l(= 2R)$ is the distance between pinning points shown in Fig. 7.25. Note that the stress is inversely proportional to the distance between pinning points. The gradual onset of yielding characteristic in fcc metals is generally explained by a distribution of stresses required to operate the sources. At low applied stress, dislocation sources easiest to operate (with large separation between pinning points) begin to generate dislocations. As dislocations are generated and move through the lattice, they begin to pile up and exert a back stress on the dislocation source, ceasing its operation and hence the plastic strain. With increasing applied stress, more dislocation sources are activated and dislocation multiplication increases.

Source hardening, as described by Eq. (7.32b) requires the dislocation line segment to bow out between the pinning points, which requires strong pinning. However, release of the dislocation will occur at lower values of applied stress if the dislocation segment is able to unlock itself before bowing occurs. That is, applied stresses below that required to operate a Frank–Read source are able to push the dislocation line segment past the pinning points. This process could occur, for example, if the pinning points consisted of small dislocation loops or defect clusters. The stress necessary to unlock a dislocation line segment from a small loop can be estimated using the analysis in [3].

Consider a group of edge character loops arranged in a row, each having Burgers vector b_ℓ, radius r, and spacing, l and are at a stand-off distance y from the straight edge dislocation of Burgers vector b_{seg}, as shown in Fig. 12.6. Referring to the interaction between edge dislocations presented in Sect. 7.1.6, only the σ_{yy} term exerts a stress on the loop that acts to expand or contract it. The force on the loop due to the σ_{yy} component of stress from the straight edge dislocation is $2\pi r\sigma_{yy}b_\ell$,

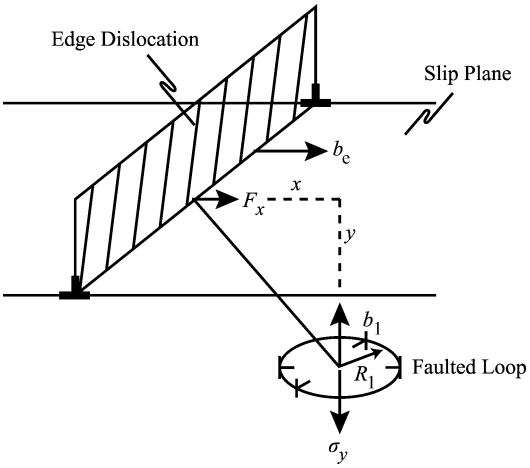

Fig. 12.6. Hardening by faulted loops caused by the interaction of stress fields between an edge dislocation moving on its slip plane located parallel to and displaced a distance y from the plane of the loop (after [3])

and the work to expand the loop is:

$$\frac{\mathrm{d}W}{\mathrm{d}r} = 2\pi r \sigma_{yy} b_\ell$$
$$W = \pi r^2 \sigma_{yy} b_\ell \,. \tag{12.64}$$

Substituting for the stress, $\sigma_{yy.}$ given by Eq. (7.15), into Eq. (12.64) and differentiating with respect to x gives the force between the loop and the edge segment in the x-direction:

$$F_x = \frac{-\partial W}{\partial x} = -\frac{\mu b_\ell b_{\mathrm{seg}} r^2}{1-\nu} \frac{xy(3y^2 - x^2)}{(x^2+y^2)^3} \,. \tag{12.65}$$

Singh et al. [6] noted that the force is a maximum at an angle of about 40° between the distance vector and the glide plane of the dislocation and the value of the force can be written as a function of r/y:

$$F_x^{\max} \approx \frac{0.28\mu b^2}{(1-\nu)} \left(\frac{r}{y}\right)^2 \approx 0.4\mu b^2 \left(\frac{r}{y}\right)^2 \,, \tag{12.66}$$

for $\nu = 1/3$ and $b_\ell = b_{\mathrm{seg}}$. Given that $F = \sigma_{\mathrm{s}} b l$, then:

$$\sigma_{\mathrm{s}} = \frac{0.4\mu b}{l} \left(\frac{r}{y}\right)^2 \,. \tag{12.67}$$

Singh suggests that $y = 1.5r$ is consistent with the observed microstructure, yielding a relation for the shear stress in terms of the loop spacing as:

$$\sigma_{\mathrm{s}} = \frac{0.09\mu b}{l} \,. \tag{12.68}$$

Note that this value of shear stress is considerably less than that to initiate a Frank–Read source by bowing of the dislocation segment of $\sigma_{FR} = \dfrac{\mu b}{l}$.

Singh et al. also postulated that the unlocking process occurred by interaction between an edge segment and a network of loops that are no longer well-separated, but have lost their individuality and act as a network. For this case, the yield stress can be estimated by the stress necessary to overcome the interaction between dislocation dipoles. This problem is treated in more detail in Chap. 14, in which the shear stress is provided in Eq. (14.23) as:

$$\sigma_s = \frac{\mu b}{8\pi(1-\nu)y} \approx \frac{0.06\mu b}{y}\,, \tag{12.69}$$

for $\nu = 1/3$.

12.2.2 Friction Hardening

Friction hardening refers to the stress required to sustain plastic deformation, which is often termed the flow stress, or friction stress. The forces responsible for resisting dislocation motion through a crystal lattice arise from the dislocation network and obstacles such as defect clusters, loops, precipitates, voids, etc. These sources of hardening are characterized as either long-range or short-range. Long-range stresses are caused by dislocation–dislocation interaction by virtue of their stress fields. Short-range stresses have their origin in the interaction between the moving dislocation and discrete obstacles in the slip plane. The total applied shear stress necessary to overcome both long-range and short-range forces in order to move the dislocation is:

$$\sigma_F = \sigma_{LR} + \sigma_{SR} \tag{12.70}$$

where σ_F is the friction stress and the subscripts *LR* and *SR* represent long and short-range contributions, respectively, and σ_{SR} is given by:

$$\sigma_{SR} = \sigma_{ppt} + \sigma_{void} + \sigma_{loops}\,, \tag{12.71}$$

where the terms on the right hand side of the equality correspond to precipitates, voids and loops, respectively.

Long-Range Stresses

Long-range forces arise from the repulsive interaction between a moving dislocation and components of the dislocation network of the solid. Dislocations on parallel glide planes exert forces on each other due to their stress fields, which constitute the long-range stress fields. Referring back to Eq. (7.51) describing the force between edge dislocations, the maximum force occurs at an angle $\theta = 0°$, which

yields a value of:

$$F_x(0^\circ) = F_{\mathrm{LR}} = \frac{\mu b^2}{2\pi(1-\nu)r} \,. \tag{12.72}$$

Taking $\nu = 1/3$, and the distance between dislocations, r from Eq. (5.75) as $1/\sqrt{\pi\rho_{\mathrm{d}}}$, where ρ_{d} is the dislocation density gives:

$$F_{\mathrm{LR}} = \frac{\mu b^2\sqrt{\pi\rho_{\mathrm{d}}}}{\pi 4/3} \approx \frac{\sqrt{\pi}\mu b^2\sqrt{\rho_{\mathrm{d}}}}{4} \approx \alpha\mu b^2\sqrt{\rho_{\mathrm{d}}} \,, \tag{12.73}$$

where α is a constant with a value ~ 0.44. The stress needed to overcome this force is $\sigma_{\mathrm{LR}} = F_{\mathrm{LR}}/b$, giving:

$$\sigma_{\mathrm{LR}} = \alpha\mu b\sqrt{\rho_{\mathrm{d}}} \,. \tag{12.74}$$

Note that if the long-range stress is equated to the unpinning stress given as the grain size-dependent term in Eq. (12.63), then the yield strength can be written as:

$$\sigma_{\mathrm{y}} = \sigma_{\mathrm{i}} + \alpha\mu b\rho_{\mathrm{d}}^{1/2} \,. \tag{12.75}$$

Equation (12.75) actually represents a different way of obtaining the grain size dependence of the yield stress, since the dislocation density has been observed to vary with grain size, d as $\rho_{\mathrm{d}} = 1/d$.

Short-Range Stresses

Short-range forces are due to the interaction between a moving dislocation and an obstacle that lies in its slip plane. Short-range forces arise only when the dislocation contacts the obstacle. Short-range forces can be classified into athermal and thermally activated interactions. An athermal stress interaction is independent of temperature and results in the dislocation bowing around the obstacle. In thermally activated processes, the dislocation will overcome the obstacle either by cutting through, or climbing over it. Both processes require the addition of energy through an increase in temperature. We will discuss dislocation bowing around the obstacle and obstacle cutting in this section, and the process of climb will be described in detail in Chap. 14 on creep.

The friction stress due to a dispersion of barriers depends on the average separation between the obstacles in the slip plane of the moving dislocation. Figure 12.7 shows a unit area of a slip plane that is intersected by portions of spherical objects of diameter d, which are randomly distributed throughout the solid at a concentration of N cm^{-3}. Any sphere that has its center within the slab of volume d centered on the slip plane intersects the slip plane. The number of obstacles in this volume element is Nd, which is also the number of intersections per unit area on the slip plane. The product of the number of intersections per unit area, Nd and the square of the distance between obstacles, l^2 is unity, yielding the distance between obstacles:

$$l = (Nd)^{-1/2} \,. \tag{12.76}$$

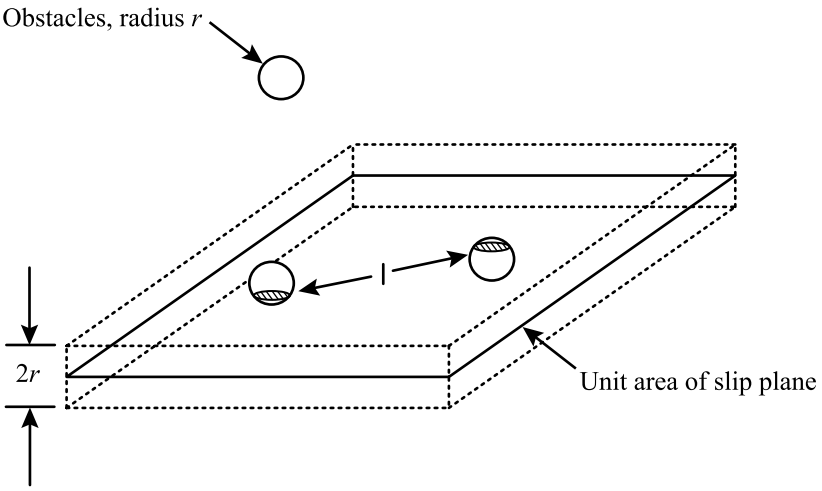

Fig. 12.7. Schematic showing the intersection of spherical obstacles of radius r and spacing l with a unit area of slip plane (after [3])

Precipitates

When a dislocation encounters an obstacle such as an incoherent precipitate, the short-range interaction occurs when it physically contacts the obstacle. For strong obstacles, an applied stress will cause the dislocation to bow out between the obstacles. Bowing will continue until adjacent segments touch and annihilate each other. This "pinch-off" process is exactly the same as occurs in a Frank–Read source. Following pinch-off, the dislocation is free to continue along its glide plane until it encounters the next obstacle and the process repeats itself. The obstacles are left with a dislocation loop surrounding them, which presents a stronger obstacle to the next dislocation that comes along (Fig. 12.8a). The short-range stress due to an array of obstacles of density N and size d is determined as follows. The line tension of an edge dislocation was given in Eq. (7.22) as $\Gamma \approx \dfrac{\mu b^2}{4\pi} \ln\left(\dfrac{R}{r_c}\right)$, where R is equated to the grain radius and r_c is the dislocation core radius and the dislocation core energy is neglected. From Eq. (7.31), the shear stress is related to the line tension by $\sigma_s = \Gamma / bR$. Substituting for Γ from Eq. (7.22) and setting $R = l/2$ where l is the obstacle spacing gives:

$$\sigma_s \approx \frac{\mu b}{l} \frac{1}{2\pi} \ln\left(\frac{l}{2r_c}\right) . \tag{12.77}$$

Substituting in for l from Eq. (12.75) gives:

$$\sigma_s \approx \alpha \mu b \sqrt{Nd} , \tag{12.78}$$

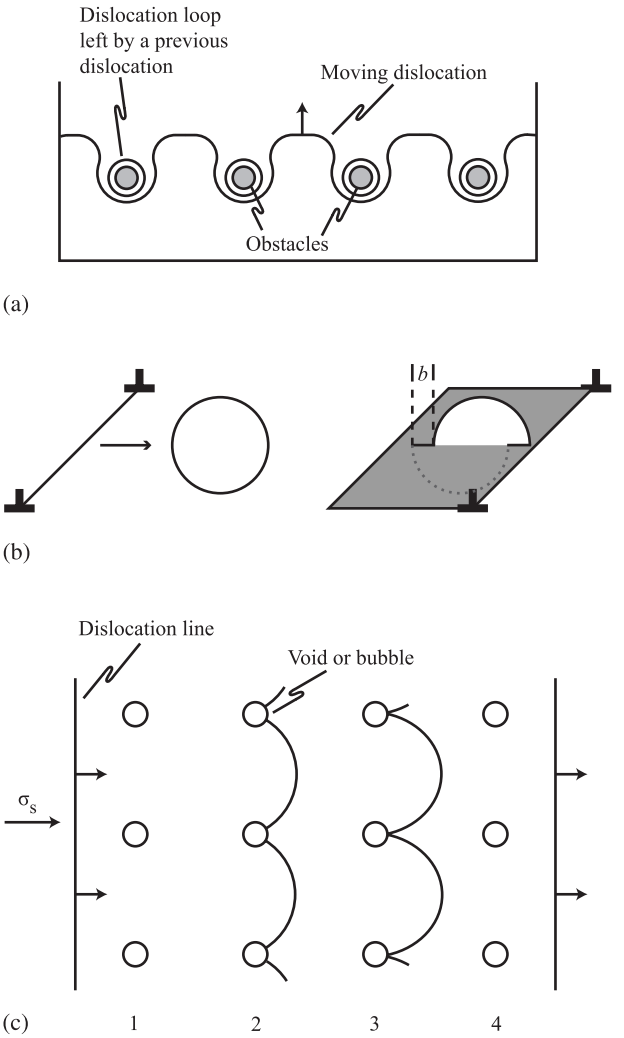

Fig. 12.8. (a) Dislocation bowing around hard obstacles such as precipitates. (b) Dislocation cutting of an obstacle such as a precipitate. (c) Dislocation interaction with voids

where $\alpha = \frac{1}{2\pi} \ln\left(\frac{l}{2r_c}\right)$. The applied stress at yield, σ_y is related to the resolved shear stress, σ_s by the Taylor factor, M such that $\sigma_y = M\sigma_s$, and Eq. (12.77) can be written in terms of the applied stress as:

$$\sigma_y = \alpha M \mu b \sqrt{Nd} \,. \tag{12.79}$$

Stoller and Zinkle [7] have shown that M is actually an upper limit for the ratio of uniaxial yield strength to resolved shear strength and has the value of 3.06 for both

fcc and bcc lattices. Equation (12.79) is generally written as:

$$\Delta\sigma_y = \alpha M \mu b \sqrt{Nd}\,, \tag{12.80}$$

where $\Delta\sigma_y$ represents the *increment* in the yield strength due to the obstacles of size d, number density, N and strength α. In fact, the term α represents the strength of the specific barrier in terms of the Orowan hardening model. A perfectly hard barrier would have a value of $\alpha = 1$. Hardening according to Eq. (12.80) is often termed *dispersed barrier* hardening after the original formulation of Seeger [8].

Dislocation bowing provides the greatest strengthening by obstacles. However, obstacle cutting can also provide strengthening. Obstacle cutting results in hardening by a variety of mechanisms, summarized by Dieter [1] as follows:

1. Shearing of the particle creates a step of width b on either side of the particle and the increase in surface area requires additional work be done to shear the particle.
2. If the particles are ordered structures, such as intermetallic compounds, then the shearing will also produce a new interface within the particle that will require extra energy.
3. Hardening also arises from the difference between the elastic moduli of the matrix and particle, which affects the line tension of the dislocation requiring additional stress to cut the particle.
4. Strengthening also occurs due to the difference in Peierls stress between the particle and matrix.

Figure 12.8b shows the result of a dislocation cutting an obstacle. The resulting obstacle is sheared and the top and bottom halves are displaced along the glide plane by an amount equal to the magnitude of the Burgers vector of the dislocation. Successive shearing of the obstacle on the same plane can result in complete separation of the two parts resulting in two smaller obstacles.

Molecular dynamics (MD) simulation of dislocation–obstacle interaction provides a means of visualizing complicated microstructural processes as shown in the following sections. It is important to note, however, that simulations are only as good as the interatomic potentials that define them and they may be influenced by other factors such as the size of the simulated volume and the strain rate. Hence, their value is largely in their qualitative description rather than as a strict quantitative interpretation.

Movies 12.1–12.3 show molecular dynamics simulations of the interaction between a dissociated edge dislocation and a cobalt precipitate in copper as a function of precipitate size at a temperature of 10 K and a under an applied stress of 100 MPa. The precipitate size in Movie 12.1 is 1.5 nm in size and is sheared by both partials of the edge dislocation. Movies 12.2 and 12.3 are for 3 and 5 nm precipitates, respectively, and show that while the first partial shears the precipitate, the trailing partial undergoes Orowan bowing and pinch-off, leaving a ring around the precipitate as shown in the schematic illustration in Fig. 12.8a. Movie 12.4 shows the shearing of a 2 nm copper precipitate. The first part of the movie shows the behavior of the

dislocation line in the shearing process, and the second part shows the shearing of the precipitate to result in an offset of the part of the precipitate above the slip plane relative to that below, as illustrated in Fig. 12.8b.

For the case where hardening results from the difference in moduli between the precipitate and the matrix, such as for large vacancy clusters or copper-rich precipitates in ferritic pressure vessel steels, the Russell and Brown model [9] has been found to best describe hardening. They showed that the yield stress in shear is a function of the obstacle spacing in the slip plane, l and the critical angle at which the dislocation can cut an obstacle, ϕ:

$$\sigma_{sy} = 0.8\frac{\mu b}{l}\cos\frac{\phi}{2} \quad \text{for} \quad \phi \leq 100^\circ$$
$$\sigma_{sy} = 0.8\frac{\mu b}{l}\left(\cos\frac{\phi}{2}\right)^{3/2} \quad \text{for} \quad \phi > 100^\circ\,, \tag{12.81}$$

and when $\phi = 0$, the stress is the Orowan stress. They showed that if a dislocation crosses an interface and has energy E_1 per unit length on one side and energy E_2 per unit length on the other, then the equilibrium of the dislocation requires that $E_1 \sin\theta_1 = E_2 \sin\theta_2$, where θ_1 and θ_2 are the angles between the dislocation and the normal to the interface. When the energy of the dislocation is lower in the precipitate than it is in the matrix ($E_1 < E_2$), then the angle ϕ has a minimum value when the dislocation is about to break away, given by $\phi_{min} = 2\sin^{-1}(E_1/E_2)$, and the strength from Eq. (12.81) is given by:

$$\sigma_{sy} = 0.8\frac{\mu b}{l}\left[1 - \frac{E_1^2}{E_2^2}\right]^{1/2} \quad \text{for} \quad \sin^{-1}\frac{E_1}{E_2} < 50^\circ$$
$$\sigma_{sy} = 0.8\frac{\mu b}{l}\left[1 - \frac{E_1^2}{E_2^2}\right]^{3/4} \quad \text{for} \quad \sin^{-1}\frac{E_1}{E_2} \geq 50^\circ\,, \tag{12.82}$$

where:

$$\frac{E_1}{E_2} = \frac{E_1^\infty \log\dfrac{r}{r_c}}{E_2^\infty \log\dfrac{R}{r_c}} + \frac{\log\dfrac{R}{r}}{\log\dfrac{R}{r_c}}\,, \tag{12.83}$$

and E^∞ is the energy per unit length of dislocation in the infinite media, R is an outer cut-off radius (taken as half the distance to the next obstacle) and r_c is the dislocation core radius. The stresses in Eq. (12.82) depend inversely on the particle spacing, l and therefore decrease as the particle radius increases (for constant volume fraction of precipitate). However, combining Eq. (12.83) with Eq. (12.82) yields a maximum in the relation between strength and precipitate size. For voids or for precipitates in pressure vessel steels, the maximum is at about $2r_c$ ($\sim$5a) or $\sim$1.5 nm.

Voids

Dislocations can also cut through voids, although the structure of the void is the same before and after the cut. Precipitates and voids are generally considered to

be hard barriers with $\alpha \sim 1$. The only difference between passage of a mobile dislocation through precipitates and voids is that in the case of voids, the dislocation segments always meet the void surface at right angles and leave no dislocation ring after passage through the void (Fig. 12.8c). As described by Olander [3], the force to cut through a void is:

$$F = \frac{U_\mathrm{V}}{R} = \sigma_\mathrm{s} b l \,, \tag{12.84}$$

where U_V is the elastic strain energy in a volume of solid equal to the cavity, R is the radius of the cavity and l is the void spacing on the slip plane. From Eq. (7.21), the elastic energy per unit volume for a screw dislocation is given as $W = \dfrac{\mu b^2}{8\pi^2 r^2}$. The elastic energy of the void–dislocation interaction energy can be approximated by the elastic energy in the volume of the void:

$$\begin{aligned} U_\mathrm{V} &= \int_{r_\mathrm{c}}^{R} 4\pi r^2 W \,\mathrm{d}r \\ &= 4\pi \int_{r_\mathrm{c}}^{R} \frac{\mu b^2}{8\pi^2} \,\mathrm{d}r \\ &= \frac{\mu b^2}{2\pi}(R - r_\mathrm{c}) \approx \frac{\mu b^2 R}{2\pi} \,. \end{aligned} \tag{12.85}$$

Substituting into Eq. (12.84) and solving for σ_s gives:

$$\sigma_\mathrm{s} = \frac{1}{2\pi}\frac{\mu b}{l}, \tag{12.86}$$

which is smaller than the Orowan stress, Eq. (7.32a) by a factor of $1/2\pi$ indicating that cutting of voids requires less energy than bowing around them. Written in the form of Eq. (12.80) gives:

$$\Delta\sigma_\mathrm{y} = \alpha M \mu b \sqrt{Nd} \,, \quad \alpha \approx 0.16 \tag{12.87}$$

A more complete treatment of dislocation–void interaction accounts for image stresses, dislocation self-interaction and elastic anisotropy of the crystal. The image stress must be added to the dislocation stress in order to make the void surfaces traction free. Dislocation self-interaction refers to the dipole-like attractive forces between the dislocation branches termination at a void, which can aid in pulling the branches together around the void, thus diminishing strengthening effects. Finally, elastic anisotropy of the crystal containing the void row must be accounted for in the dislocation stress field calculation. Inclusion of these factors in the calculation of the stress necessary for a dislocation to cut a void shows that the void is a very strong obstacle, approaching the Orowan stress value for impenetrable obstacles. A detailed treatment of these effects is given in [10].

The interaction between dislocations and voids is illustrated in Movies 12.5–12.7. Movie 12.5 shows the interaction of leading and trailing partials of a dissociated edge dislocation with a 3 nm void in copper at 0 K. Note that the dislocation

lines maintain a right angle with the void surface throughout the interaction. Movie 12.6 shows the shearing of a 1 nm void in iron by a dislocation and the resulting stress-strain behavior due to the dislocation–void interaction. In these three perspectives, the displacement of the top half of the void relative to the bottom half is evident. Finally, Movie 12.7 shows the repeated shearing by multiple dislocations of a 2.6 nm He bubble under an applied shear stress of 100 MPa. Note that the bubble appears to elongate in the direction of the applied stress, due to the offset of the half above the slip plane relative to that below, similar to that shown in Fig. 12.8b.

Loops

The interaction between a mobile dislocation and a loop was described in Sect. 12.2.2 where it was shown that the stress in Eq. (12.68) is of the order $\sigma_s = \dfrac{0.1\mu b}{l}$, and for l given by Eq. (12.76) the stress becomes:

$$\sigma_s = 0.1\mu b\sqrt{Nd}\,, \tag{12.88}$$

which is well below the Orowan stress. Written in the form of Eq. (12.80), the yield strength increment due to loops is:

$$\Delta\sigma_y = \alpha M\mu b\sqrt{Nd}\,, \quad \text{with} \quad \alpha \approx 0.1\,. \tag{12.89}$$

The types of interactions between dislocation lines and loops described in this chapter are illustrated in Movies 12.8–12.12. In Movies 12.8 and 12.9, the interaction between the dislocation and the loop is through the stress fields. Movie 12.8 shows an edge dislocation in copper (edge on: red spheres are the partials), interacting with a 37 SIA perfect loop (green spheres) a distance 2 loop diameters from the dislocation. Both have Burgers vector $1/2[110]$. Note that as the dislocation moves, the interacting strain fields drag the loop in the direction of the moving dislocation. Movie 12.9 shows an edge dislocation bypassing a 153 SIA Frank loop at 100 K under an applied stress of 300 MPa in copper. The blue spheres are atoms in the fcc crystal and the yellow spheres are atoms in the stacking fault. During the non-intersecting interaction, the Frank loop rotates to become a mobile perfect loop and glides to annihilation at the free surface.

Movies 12.10–12.12 illustrate interactions in which the dislocation contacts the loop. Movie 12.10 shows a dissociated screw dislocation shearing the same Frank loop under the same conditions as that shown in Movie 12.9. Note that the sheared loop is absorbed into the screw dislocation core. Movie 12.11 is another example of a screw dislocation interacting with a perfect loop (same Burgers vector) in which the loop is absorbed and then re-emitted a distance away from the original absorption point, and the dislocation cross slips onto a different glide plane. Movie 12.12 shows an edge dislocation interacting with and unfaulting a Frank loop (5 nm, 331 SIA) in iron at 300 K, resulting in near destruction of the loop.

Another type of faulted defect, the stacking fault tetrahedron, described in Chap. 7, also interacts with dislocations and can contribute to hardening. Movie

12.13 shows the interaction of successive edge dislocations with a 153 vacancy SFT at 100 K under an applied stress of 100 MPa in copper. The SFT is sheared into a smaller SFT and a truncated base and subsequent interactions result in absorption of the truncated base into the dislocation. Movie 12.14 shows the details of the interaction between edge partials shown in Movie 12.13 but at a slower rate and with a 45-vacancy SFT.

Movies 12.15–12.17 show the interaction of a screw dislocation with an SFT in Cu. In Movie 12.15, the 45-vacancy SFT is sheared and in Movie 12.16, the 98-vacancy SFT is absorbed and then re-emitted. Movie 12.17 shows a 78-vacancy SFT being absorbed and re-emitted as a smaller SFT and a separate truncated base. A real-time movie of a dislocation-SFT interaction in copper was conducted on a sample under dynamic loading in the stage of a transmission electron microscope at room temperature, Movie 12.18. The SFTs were introduced by quenching the copper specimen in iced brine after a 2 h anneal at 1073 K. The weak-beam dark-field movie shows a dislocation being pinned by a stacking-fault tetrahedron. The result of the interaction is the formation of a perfect loop. Finally, Movies 12.19 and 12.20 show the interaction of a screw dislocation in copper with multiple defects: a 78-vacancy SFT and a perfect loop consisting of 61 interstitials in Movie 12.19 and 91 interstitials in Movie 12.20.

Effect of Temperature

As described in the preceding section, obstacle strength and density determine the velocity of dislocations in a polycrystal. If the Gibbs free energy of activation for cutting or bypassing an obstacle is $\Delta G(\sigma_s)$, then the mean velocity of a dislocation segment, $\bar{v}$, is given by [11]:

$$\bar{v} = \beta b \nu \exp\left(-\frac{\Delta G(\sigma_s)}{kT}\right) , \tag{12.90}$$

where β is a dimensionless parameter, b is the magnitude of the Burgers vector, ν is the frequency and σ_s is the shear stress. The term $\Delta G(\sigma_s)$ is a function of the internal stress and the distribution of obstacles and for a regular array of obstacles, it can be expressed as:

$$\Delta G(\sigma_s) = \Delta F\left(1 - \frac{\sigma_s}{\sigma_s^0}\right) , \tag{12.91}$$

where ΔF is the total free energy (activation energy) required to overcome the obstacle without aid from an external stress. The term σ_s^0 is the stress at which a dislocation can move through the obstacle with no help from thermal energy, or essentially, the flow stress at 0 K where $\Delta G = 0$:

Generalizing to a random array of obstacles [11], Eq. (12.91) becomes:

$$\Delta G(\sigma_s) = \Delta F\left[1 - \left(\frac{\sigma_s}{\sigma_s^0}\right)^p\right]^q , \tag{12.92}$$

Table 12.1. Strength of various obstacle types causing source and friction hardening in irradiated metals

Type of strengthening	Obstacle classification	Obstacle type	Stress increment	α
Source		Loops	$\sigma_s = \frac{0.09\mu b}{l}$ isolated loops	
			$\sigma_s \approx \frac{0.06\mu b}{y}$ loop network	
Friction	Long-range	Dislocation network	$\sigma_{LR} = \alpha\mu b\sqrt{\rho_d}$	< 0.2
	Short-range	Precipitates and voids	$\Delta\sigma_y = \alpha M\mu b\sqrt{Nd}$	1.0 bowing 0.3–0.5 cutting
		Dislocation loops		0.25–0.5
		Black dots		< 0.2

where $0 \leq p \leq 1$ and $1 \leq q \leq 2$, and where σ_s^0 is given phenomenologically by:

$$\frac{\sigma_s}{\sigma_s^0} = \left[1 - \left(\frac{T}{T_0}\right)^p\right]^q , \tag{12.93}$$

where reasonable limiting behavior is found with $p = 2/3$ and $q = 3/2$ [12]. Since the strain rate is proportional to the average dislocation velocity (see Sect. 14.1), the rate equation for discrete obstacle controlled plasticity is given by:

$$\dot{\varepsilon} = \dot{\varepsilon}_0 \exp\left\{-\frac{\Delta F}{kT}\left[1 - \left(\frac{\sigma_s}{\sigma_s^0}\right)^p\right]^q\right\} , \tag{12.94}$$

which captures both the stress and temperature dependence of dislocation passage through a random array of obstacles.

Hardening due to long-range and short-range obstacles is summarized in Table 12.1 using Eq. (12.80) to describe short-range obstacles. Note that the values of α can vary by a significant amount depending on obstacle type. Much work has been done to determine the value of α experimentally, and column 5 in Table 12.1 gives the generally accepted values for α based on experimental work.

12.2.3 Superposition of Hardening Mechanisms

As discussed in Chaps. 7, 8, and 9, the microstructure of an irradiated metal can be quite complicated. At very low dose, it consists of defect clusters and small loops. With increasing dose, the loop microstructure saturates at a particular number density and loop size and as loops unfault and become part of the dislocation line network, the dislocation density rises. At higher temperatures, voids and bubbles contribute to the microstructure, and irradiation-induced precipitation can also contribute at high temperature. Each of these features presents a different type of

obstacle to the moving dislocation. In order to assess the hardening of a true irradiated microstructure, we must have some way of accounting for obstacles of different types, sizes and number densities. Below, we treat several special cases of various combinations of short-range and long-range obstacles as originally described by Bement [13].

Long-Range Stresses and Short-Range Obstacles

If long-range internal stresses exist in the lattice, as caused for example by groups of dislocations of predominantly the same sign of Burgers vector, and if in addition, dispersed barriers with a short-range interaction and an average distance, l_S smaller than the average "wavelength" of the long-range stresses, are present, on average the effective stress available for pushing the dislocation over the short-range obstacles (σ_{SR}) is the difference between the applied stress, σ_a and the stress σ_{LR} necessary for moving the dislocations through the long-range stress field :

$$\sigma_a = \sigma_{LR} + \sigma_{SR} , \quad l_{SR} < l_{LR} . \tag{12.95}$$

Thus, the total stress is composed of the stress due to the two types of hardening as if each acted independently. Such is not the case if two types of short-range obstacles are present.

Two Types of Short-Range Obstacles

In an irradiated microstructure consisting of two types of short-range obstacles the superposition depends sensitively on the strengths and relative concentrations of the two types of obstacles.

Two Strong Obstacles

If both types of obstacles are strong such that dislocations interact by means of the Orowan mechanism, the moving dislocation cannot distinguish between them, and the sum of the area densities, N of the two obstacles in the glide plane determines the effective obstacle distance:

$$l = \frac{1}{\sqrt{N_1 + N_2}} , \tag{12.96}$$

$$\text{and} \quad \frac{1}{l^2} = \frac{1}{l_1^2} + \frac{1}{l_2^2} , \tag{12.97}$$

$$\text{giving} \quad \sigma_a^2 = \sigma_1^2 + \sigma_2^2 , \tag{12.98}$$

where σ_1 and σ_2 are the critical (short-range) stresses if the obstacles of type 1 or 2 with average distances l_1 and l_2 respectively, would act separately. This root-sum-square (RSS) model was shown by Foreman and Makin [14] to apply for a population of obstacles with similar strengths. However, the behavior of the dislocation

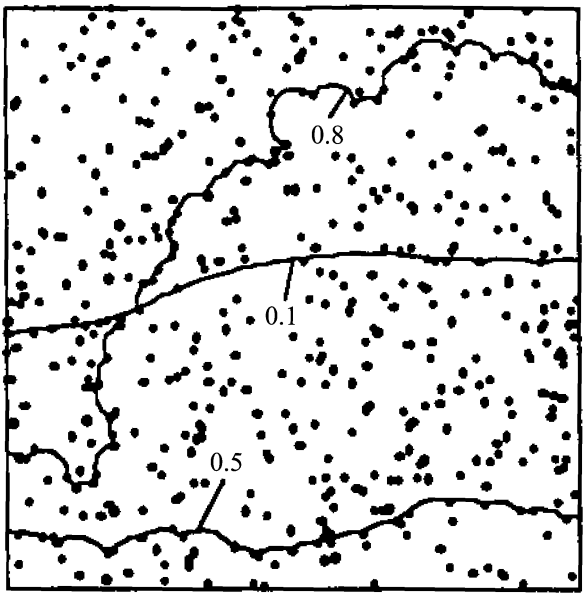

Fig. 12.9. Result of computer simulation of the shape of a dislocation line just prior to yielding for various fixed values of a (0.1, 0.5, 0.8) (after [15])

differs depending on the strength of the obstacle. Figure 12.9 shows the final configuration of a dislocation line just prior to yielding for obstacle strength, α of 0.1, 0.5 and 0.8 [15].

If there are types of obstacles in the lattice which can be surmounted with the help of thermal activation and for which the forces (F_1 and F_2) are nearly the same, Eq. (12.98) holds for the same reasons given above.

Two Obstacles with Different Strengths

There exist several subcases for combinations of weak and strong particles. Kocks [16] considered the case of many weak and a few strong obstacles giving the conditions:

$$F_1 \ll F_2 \quad \text{with} \quad l_1 \ll l_2 \,. \tag{12.99}$$

If a dislocation segment bows out under the applied stress between two strong obstacles, it cuts through many weak ones in its path. The more it bows out the larger the angle becomes between neighboring branches of the dislocation at the weak obstacles and the smaller (at a given stress) the force is with which the dislocation is pressed against the weak obstacles. Simultaneously, the angle between the neighboring branches of the dislocation at the strong obstacles becomes smaller and the force acting on them increases (Fig. 12.10). The critical situation is reached when the dislocation can break through weak and strong obstacles simultaneously.

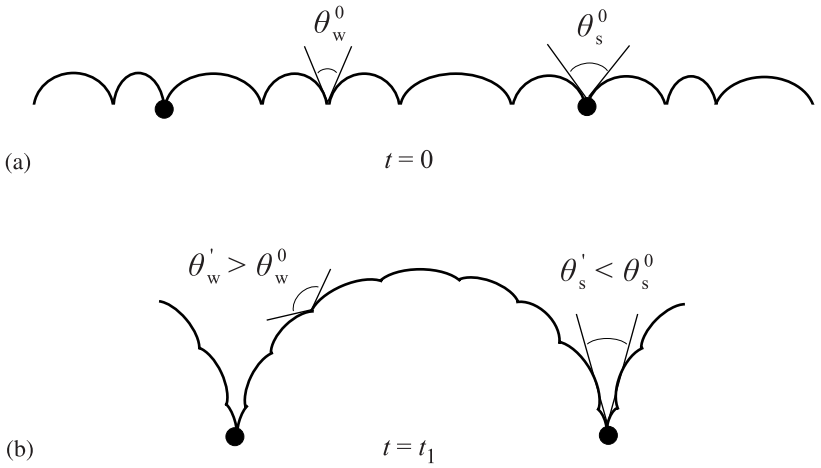

Fig. 12.10. Movement of a dislocation in an obstacle field consisting of many weak and a few strong obstacles (a) before application of a stress and (b) after the dislocation has moved past many of the weak barriers

The stress necessary to push the dislocation through this critical configuration is:

$$\sigma_a = \sigma_1 + \sigma_2 \, . \tag{12.100}$$

Movie 12.21 is a real-time movie of dislocation–defect interaction during straining of an irradiated copper sample. The sample was irradiated with 200 keV Kr^+ to a dose of about 10^{12} i/cm^2 at room temperature in the IVEM at Argonne National Laboratory. The defects consist predominantly of Frank loops with Burgers vector $a/3\langle 111\rangle$ and a smaller density ($\sim$10%) of stacking fault tetrahedra. As shown, the dislocation moves in a jerky manner with small segments breaking free from individual pining points and no observable defect absorption.

If no extreme condition exists as in Eq. (12.99), the thermally activated surmounting of the two types of obstacles must be treated in terms of so-called dependent processes. For such processes the waiting time t_s (average time during which a dislocation is pressed against an obstacle of type s until it gets enough thermal energy to overcome it) enters the theoretical treatment additively, so that the time a dislocation needs for moving over a given area is proportional to $N_1 t_1 + N_2 t_2$. If $N_1 t_1 \gg N_2 t_2$ the effective flow stress is determined almost exclusively by the obstacles of type 1; type 2 is "transparent" for the dislocation under the stress necessary to overcome type 1:

$$\sigma_a \approx \sigma_1 \quad \text{for} \quad N_1 t_1 \gg N_2 t_2; \sigma_1 \gg \sigma_2 \tag{12.101a}$$

$$\sigma_a \approx \sigma_2 \quad \text{for} \quad N_1 t_1 \ll N_2 t_2; \sigma_1 \ll \sigma_2 \, . \tag{12.101b}$$

This means that if type 2 obstacles are added to a constant concentration of type 1 obstacles, Eq. (12.101a) holds for small concentration and Eq. (12.101b) for

high concentrations of type 2 obstacles so that a transition occurs in the effective flow stress from σ_1 to σ_2. In extreme cases of very low or very high concentrations of type 2 obstacles, the stresses that the two types of obstacles would demand separately, determine the effective flow stress.

In summary, the root-sum-square superposition law, $\Delta\sigma_{yr} = \sqrt{\sum_i (\Delta\sigma_{y,i})^2}$works well when obstacles have similar strengths, and the linear superposition law, $\Delta\sigma_{yl} = \sum_i \Delta\sigma_{y,i}$ is better as the strengths become more dissimilar. Odette [16] has shown that hardening in a microstructure consisting of a wide range of obstacle strength is best fit by a combination of the root-square-sum and linear sum models, with the following weighting parameter, S:

$$(\sigma_y - \sigma_{yr}) = S(\sigma_{yl} - \sigma_{yr}) \tag{12.102}$$

and S can be related to the obstacle strengths by:

$$S \approx \alpha_s - 5\alpha_w + 3.3\alpha_s\alpha_w \,, \tag{12.103}$$

such that $S = 1$ for the linear sum law and $S = 0$ for the root sum square law. According to Eq. (12.103), S decreases with increasing α_w (stronger weak obstacles) and decreasing α_s (weaker strong obstacles). The superposition rules for different hardening mechanisms are summarized in Table 12.2.

Using Eqs. (12.80) and (12.75), observed trends in the dose and temperature dependence for ρ_d and $\sqrt{Nd}$, and the obstacle strengths ($\alpha_{voids} = 1.0$) listed in Table 12.1, Lucas [17] estimated the hardening as a function of dose for three temperatures, as shown in Fig. 12.11. While these are only predictions, they serve to

Table 12.2. Superposition rules for hardening

I. Long-range stresses and short-range obstacles
$\sigma_a = \sigma_{LR} + \sigma_{SR}$

II. Two types of short-range obstacles
A. Both types strong
$l = \dfrac{1}{\sqrt{N_1 + N_2}}$
$\sigma_a^2 = \sigma_1^2 + \sigma_2^2$
B. Many weak and few strong
$F_1 < F_2; \quad l_1 < l_2$
$\sigma_a = \sigma_1 + \sigma_2$
C. Thermally activated motion over barrier
$\sigma_a \approx \sigma_1$ for $N_1 t_1 \gg N_2 t_2$; $\tau_1 \gg \tau_2$
$\sigma_a \approx \sigma_2$ for $N_1 t_1 \ll N_2 t_2$; $\tau_1 \ll \tau_2$

III. Wide range of obstacle strength
$(\sigma_y - \sigma_{yr}) = S(\sigma_{yl} - \sigma_{yr})$
$S \approx \alpha_s - 5\alpha_w + 3.3\alpha_s\alpha_w$

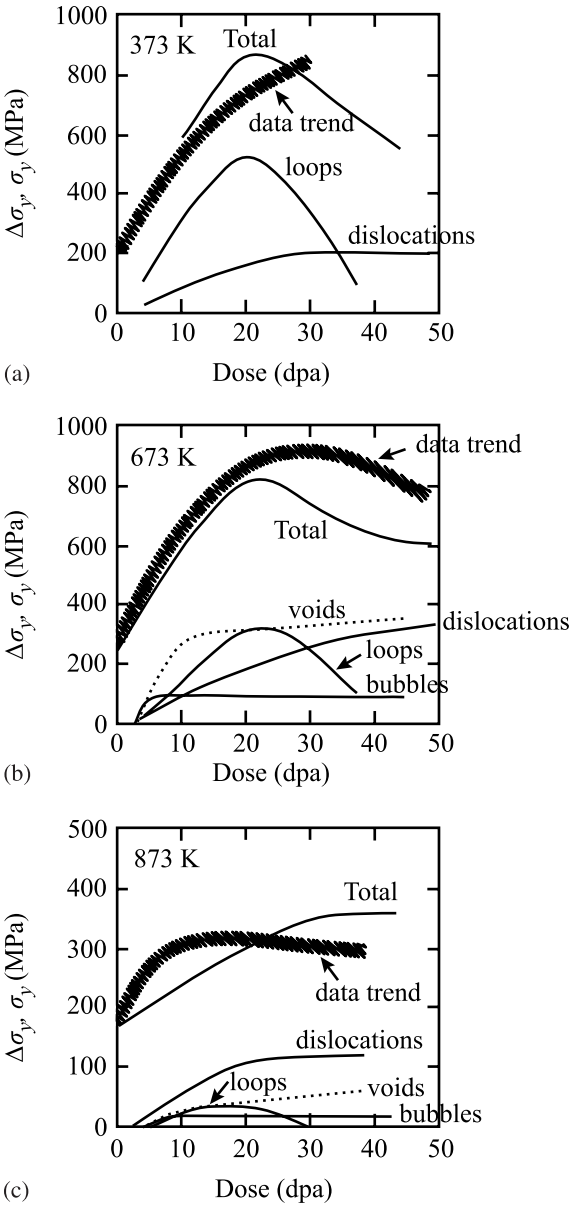

Fig. 12.11. Comparison of model predictions of the contribution to hardening from various microstructure features to data trends at (a) 100 °C, (b) 400 °C and (c) 600 °C (after [17])

illustrate the relative contributions to hardening of the various microstructure features. In stainless steels, low temperature (100 °C) hardening is dominated by black dot damage and small loops at low doses and the network density at higher doses.

Above about 400 °C, voids and bubbles can begin to make a contribution to the hardening. Intermediate to these temperatures, hardening is a maximum (near 300 °C) due to the combination of black dots, loops and He bubbles. At lower doses, voids and loops contribute the majority of hardening, but at higher doses, the dislocation microstructure and voids become the major source of hardening. These predictions differ somewhat from LWR data at ~ 300 °C [19] and even up to 400 °C [20, 21] in that the peak in hardness is not observed. This is likely due to the stability of the loop microstructure to high doses at temperatures below 400 °C. At high temperature (600 °C), hardening is dominated by network dislocations. The contribution from voids can be significant at very high doses.

12.2.4 Hardening in Polycrystals

Up to this point, we have considered hardening only in single crystals and have not accounted for the effect of grain boundaries in polycrystalline metals. In polycrystals [13], the flow stress is increased by the influence of the different grain orientations and of the grain boundaries. As described by Eq. (12.63), the *tensile* yield stress depends on the grain size d according to Hall–Petch relation given by $\sigma_y = \sigma_i + k_y d^{-1/2}$, where σ_i is the friction stress and k_y is the unpinning stress. The term k_y is based on the premise that a slip band is a stress concentration and that plastic flow between grains and therefore, throughout the polycrystalline solid occurs when the stress concentration due to a dislocation pile-up at a boundary is sufficient to activate a dislocation source in the neighboring grain. In the case of iron, steel and molybdenum, the effect of irradiation on the Hall–Petch relationship is to increase the friction stress σ_i, with little effect on k_y for small grain sizes. For larger grain sizes, samples undergo a greater increase in yield strength which reduces k_y to almost zero (Fig. 12.12).

The dislocation density in a solid undergoing plastic deformation increases linearly with strain, ε according to:

$$\rho = \rho_0 + A\varepsilon \,, \tag{12.104}$$

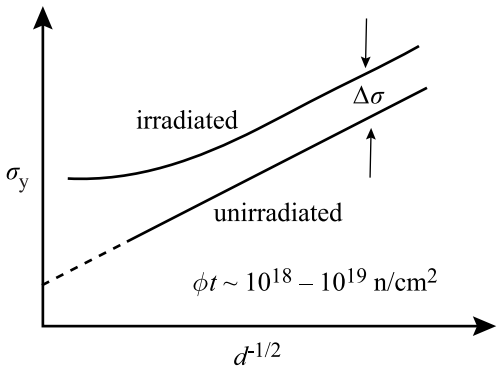

Fig. 12.12. Effects of irradiation on the Hall–Petch relationship for ferritic steel (after [13])

and

$$A = \beta / d \,, \tag{12.105}$$

where β is a constant and d is the grain diameter. Recall from Eq. (12.75) that the yield strength is related to the dislocation density by: $\sigma_y = \sigma_i + \mu b \rho_d^{1/2}$, and using Eqs. (12.104) and (12.105), the yield strength can be written as:

$$\sigma_y = \sigma_i + \mu b \left(\frac{\beta \varepsilon}{d} \right)^{1/2} \,, \tag{12.106}$$

which is equivalent to the Hall–Petch equation with:

$$k_y = \mu b (\beta \varepsilon)^{1/2} \,. \tag{12.107}$$

In this work hardening model, β is a measure of work hardenability due to dislocation channeling. As β approaches zero in irradiated material because of loss of strain hardenability due to dislocation channeling, the term $\beta\varepsilon$/d becomes very small and k_y approaches zero.

Data from a low alloy, Fe–Mn–C steel was used to chronicle the development of radiation hardening using the Hall–Petch parameters, as well as the strength coefficient K and the strain hardening exponent, n from the power law hardening equation given in Eq. (12.27). Four stages of radiation-hardening of a Fe–Cr–Mn steel with progressively increasing dose are shown in Fig. 12.13. Stage A occurs for very low does (10^{15} to 10^{16} n/cm^2) and involves an increase in k_y with negligible increase in stress σ_i, and no change in n and K. The result is an increase in the upper yield point and the Lüder's strain. Stage B occurs around $10^{18}\,\mathrm{n/cm^2}$ and represents an increase in σ_i but little change in k_y. In this stage, both n and K decrease, resulting in a reduced slope of the stress-strain curve and an increase in the Lüder's strain. Stage C appears at fluences of about $3 \times 10^{18}\,\mathrm{n/cm^2}$ and is characterized by a continued increase in σ_i and a decrease in k_y. The strain hardening exponent, n continues to decrease but K increases slightly, resulting in a small change in the slope of the stress-strain curve and a small decrease in Lüder's strain. In stage D, σ_i continues to increase and k_y falls nearly to zero. Also both n and K decrease, resulting in a further decrease in the slope of the stress-strain curve and the near disappearance of Lüder's strain. Although this description of the effects of irradiation on stress-strain behavior is specific to the iron alloy system, the changes in the parameters σ_i and k_y are consistent with the current understanding of barrier-hardening interactions, dislocation channeling and grain size effects and highlight the changing nature of the fluence-dependence of irradiation hardening in polycrystals. However, experimentally, k_y has been observed to either increase or decrease [22] suggesting that the grain size effect is not as well-established as suggested in Fig. 12.12.

12.2.5 Saturation of Irradiation Hardening

According to the dispersed barrier hardening model, Eq. (12.80), the increment in yield strength, $\Delta\sigma_y$ increases as $N^{1/2}$. In the absence of mechanisms for the destruction of obstacles, N is proportional to the total fluence and hence irradiation

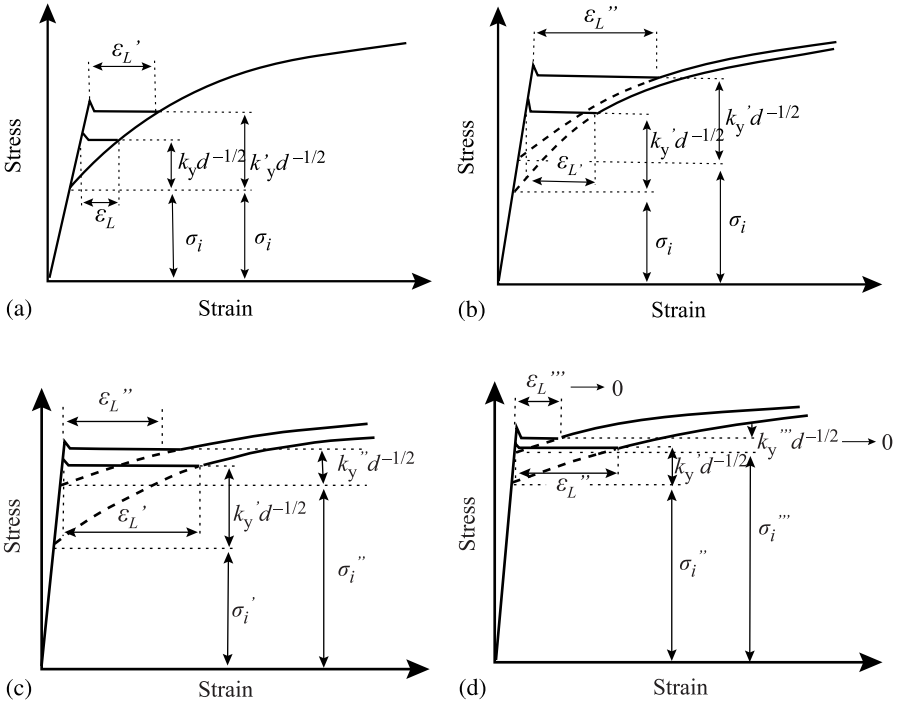

Fig. 12.13. Changes in the stress-strain curves for iron irradiated at 80 to 100 °C to neutron doses of (a) 10^{16} n/cm^2, (b) 10^{18} n/cm^2, (c) 3×10^{18} n/cm^2, (d) $>5\times10^{18}$ n/cm^2 (after [13])

hardening should be proportional to $(\phi t)^{1/2}$:

$$\Delta\sigma_S \propto (\phi t)^{1/2} . \tag{12.108}$$

That is, the number of obstacles continues to increase with fluence without bound. This is clearly counter to observations of the dislocation microstructure evolution at LWR temperatures, Chap. 7, in which the dislocation loop density and size are observed to saturate by several dpa. However, at low doses, the hardening described by Eq. (12.108) is reasonably accurate. Figure 12.14 shows the irradiation hardening in 300 series stainless steels irradiated at about 300 °C and tested at about that same temperature. Note that the hardening can be fit with a $(\phi t^{1/2})$ dependence quite well through about 5 dpa. However, the model described by Eq. (12.108) will clearly overestimate the hardening once saturation of the dislocation microstructure occurs.

In trying to account for saturation of hardening at higher doses, Makin and Minter [23] postulated that if a displacement cascade occurs in the neighborhood of an existing zone or cluster, no new zone is formed. This "prohibited" zone has a volume V. According to this model, as the concentration increases, it becomes harder to form new zones because of the reduced volume available for new zone

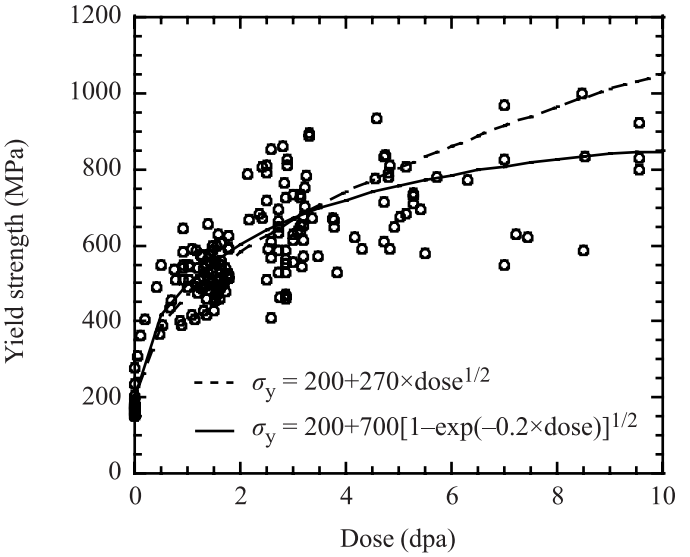

Fig. 12.14. Effect of irradiation dose on measured tensile yield strength for several 300 series stainless steels irradiated and tested at a temperature of about 300 °C (after [19])

formation. The time rate of change of the density of zones, N is then given by:

$$\frac{\mathrm{d}N}{\mathrm{d}t} = \zeta \Sigma_\mathrm{s} \phi \, (1 - VN) \ , \tag{12.109}$$

where ζ is the number of zones created per neutron collision ($\sim$1), Σ_s is the macroscopic scattering cross section and ϕ is the fast neutron flux. The term in parenthesis represents the fraction of solid volume available for the creation of new zones. Integration of Eq. (12.109) gives:

$$N = \frac{1}{V} \left[1 - \exp(-\zeta V \Sigma_\mathrm{s} \phi t) \right] \ , \tag{12.110}$$

and substitution of Eq. (12.106) into Eq. (12.80) yields

$$\Delta\sigma_\mathrm{y} = A \left[1 - \exp(-B\phi t) \right]^{1/2} . \tag{12.111}$$

where $A = \alpha M \mu b \left(\dfrac{d}{V} \right)^{1/2}$, and $B = \zeta V \Sigma_\mathrm{s}$. Higgy and Hammad [24] found that for 304 SS, 316 SS and 347 SS above fluences of about $5 \times 10^{19}\,\mathrm{n/cm^2}$, the irradiation hardening increment due can be described by Eq. (12.111) with $B = 2\text{–}3 \times 10^{-21}\,\mathrm{cm^2/n}$. Odette and Lucas [25] found that this same equation fit the data for hardening in 300 series stainless steels irradiated and tested at about 300 °C, with A $\approx$ 670 MPa and $B \approx 0.5$ with ϕt in units of dpa or $B \approx 7 \times 10^{-22}\,\mathrm{cm^2/n}$ with

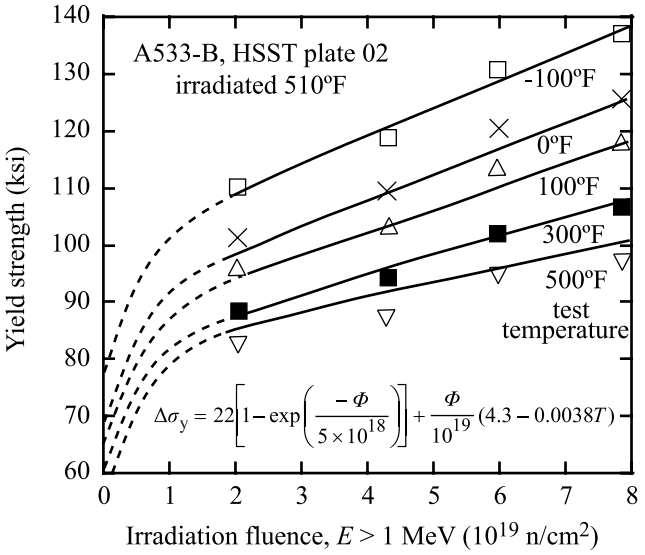

Fig. 12.15. Effect of irradiation fluence on the yield strength of A533-B steel for different test temperatures. Curves are the fits to the yield strength increment given by Eq. (12.113) (after [28])

ϕt in units of n/cm^2 and assuming that 1 dpa $\approx 7\times10^{20}$ n/cm^2. Note that application of Eq. (12.111) with similar values of A and B produces a good fit to the data in Fig. 12.14 Bement [26] found that for Zircaloy-2, $B = 2.99\times10^{-21}$ cm^2/n at 280 ℃.

Fluence exponents of less than 0.5 are commonly observed. Eason [27] found in analyzing a sizable database consisting of several stainless steels that the yield strength increment at 288 ℃ followed a fluence dependence of the form:

$$\Delta\sigma_y = a(\phi/10^{20})^b \,, \tag{12.112}$$

where:

- for type 304 and 304L stainless steel, $a \sim 2.05$ and $b = 0.124$,
- for type 316 stainless steel $a = 0.595$ and $b = 0.491$,
- for type 316L stainless steel $a = 0.517$ and $b = 0.562$,
- for type 347 stainless steel $a = 1.627$ and $b = 0.124$.

Williams and Hunter [21] used a modified form of Eq. (12.111):

$$\Delta\sigma_y = A\left[1-\exp(-B\phi t)\right] \,, \tag{12.113}$$

to fit hardening in an A533-B steel plate using $A = 22$ ksi (152 MPa) and $B = 2\times10^{-19}$ cm^2/n (Fig. 12.15).

Saturation occurs when a balance is reached between the creation and destruction of obstacles. Interstitial and vacancy loops are created from defect clusters. Interstitial loops grow in size as their number increase. However, vacancy loops

are generally unstable and shrink due to vacancy emission. Interstitial loops are removed by unfaulting. So an alternative formulation for the number of obstacles is to associate a lifetime, τ to these defects, [29] in which case, their density should develop according to:

$$\frac{\mathrm{d}N}{\mathrm{d}t} = \zeta \Sigma_\mathrm{s} \phi - \frac{N}{\tau} \,, \tag{12.114}$$

with a solution of the form:

$$N = \zeta \Sigma_\mathrm{s} \phi \, \tau \left[1 - \exp\left(-t/\tau\right)\right] \,. \tag{12.115}$$

12.2.6 Comparison of Measured and Predicted Hardening

The dispersed barrier hardening model has been applied to irradiation hardening of alloys in several systems. The most successful application is in the case of austenitic stainless steels and for irradiated microstructures that are dominated by loops. Figure 12.16 shows the correlation between measured and calculated yield strength for a set of solid solution alloys, which were all derived from a base alloy of composition Fe–18Cr–12Ni–1Mn, and differ in the single element added to the alloy. The alloys were irradiated with 3.2 MeV protons at 360 °C to a dose of 5.5 dpa and the microstructure was characterized by TEM. Loop and void size and density were determined for each alloy. Only the base 316 stainless steel alloy, 316+Mo and 316+Ni/Cr contained voids. The measurements of yield strength in Fig. 12.16 actually come from microhardness indentations (discussed in Sect. 12.2.8) and the calculated hardness values are determined from the dispersed barrier hardening model, Eq. (12.80). In this case, $\alpha = 0.25$ for loops and $\alpha = 0.5$ for voids produced the best fit with the data.

The loop strength of 0.25 is consistent with, although on the low side, of what has been observed in the literature [3, 13, 17, 31, 32, 33, 34]. Values of α for loops as high as 0.5 have been deduced from strengthening data [35]. The value of α for voids (0.5) is half that of the theoretical value for Orowan strengthening. However, Ando et al. [36] have shown that cavity shearing is more likely than Orowan pinning, resulting in a value of $\alpha = 0.5$ rather than 1.0. They concluded that the high value of α observed in some experiments is likely due to cavity-precipitate association. Electron microscopy has revealed that bubbles and MC precipitates nucleate and grow together in austenitic stainless steels [37]. Kelly [38] considered the hardening to be due to two spheres in contact rather than a single obstacle and derived the following relation for the bubble–precipitate pair:

$$\Delta\sigma_{\text{bubble-ppt}} = \frac{0.16 M \mu b \sqrt{Nd}}{1 - \dfrac{\sqrt{6}}{3}\sqrt{Nd}} \ln\left(\frac{\sqrt{6}d}{3b}\right) \,. \tag{12.116}$$

Hardening in ferritic steels used in reactor pressure vessels can be very complicated due to the role of solutes such as copper, nickel and manganese and the

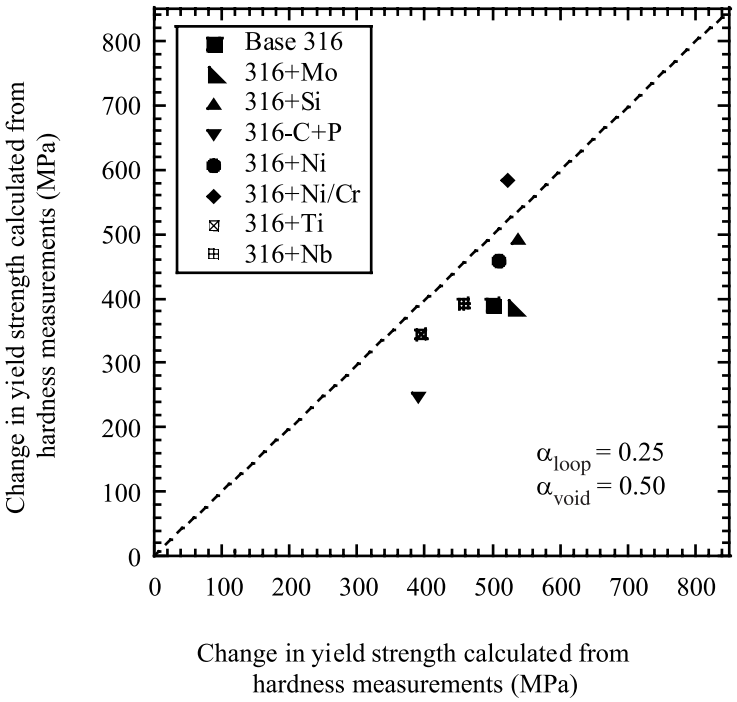

Fig. 12.16. Correlation between measured and calculated yield strength using Eq. (12.80) (after [30])

roles of temperature and irradiation flux. Hardening in RPV steels is controlled by the evolution of two primary classes of ultrafine scale features: copper rich precipitates (CRP), and matrix features (MF) [39]. The latter class can be subdivided into unstable matrix features (UMF) and stable matrix features (SMF), such that MF = UMF + SMF. CRPs form from a supersaturated solid solution as a consequence of radiation-enhanced diffusion. These precipitates are extremely small, and are best described as nanoscale defects and contribute the largest amount to hardening (Fig. 12.17). They are the dominant feature in irradiated RPV steels that have Cu contents greater than about 1% Cu. Their size and volume fraction increase with Cu content above about 1%, but the number density is relatively insensitive to copper in the range 0.2 to 0.4%. As such, their significance in hardening increases up to about 0.25 to 0.35% Cu [16]. CRPs can also become enhanced in Ni and Mn depending on the amount of these solutes in the steel.

SMFs are not completely understood, but likely consist of a range of defect cluster–solute complexes whose exact natures depend on the metallurgical variables and irradiation conditions. Phosphides, carbonitrides, manganese rich phases, large vacancy clusters and immobile interstitial loops are all likely candidates for the SMFs. SMFs account for the residual hardening in low Cu steels. UMFs undergo re-

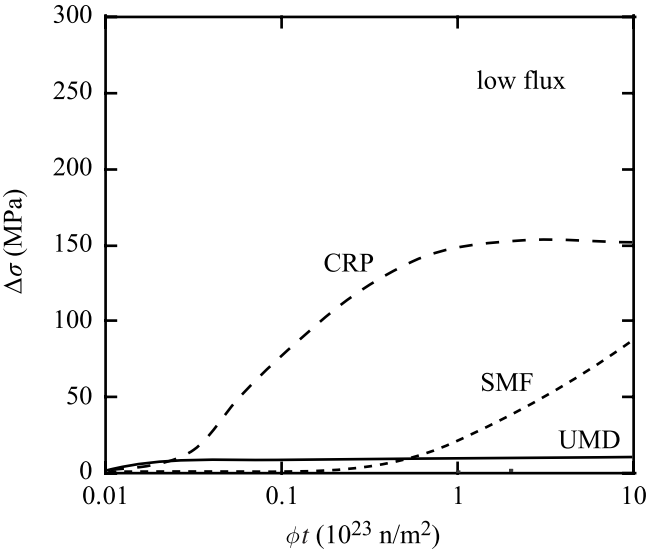

Fig. 12.17. Components of the microstructure contributing to hardening of a ferritic pressure vessel steel (after [40])

covery during irradiation and likely consist of small vacancy and interstitial clusters produced directly in displacement cascades.

The increase in yield strength in RPV steels due to irradiation can be described by the following [41]:

$$\Delta\sigma_{\mathrm{y}} = \Delta\sigma_{\mathrm{yp}} + B\sqrt{\phi t}\,, \tag{12.117}$$

where $\Delta\sigma_{\mathrm{yp}}$ is the contribution from CRPs and $B\sqrt{\phi t}$ is due to SMFs. The parameter B in the second term contains the composition dependence of hardening due to SMFs and will vary between steels. Odette et al. [41] have identified the composition dependence of B for low Cu steels ($< 0.1\%$) to be:

$$B = 681\mathrm{P} + 460\mathrm{Cu} + 10.4\mathrm{Ni} + 10.7\mathrm{Mn} - 10[\mathrm{MPa}]\,. \tag{12.118}$$

Figure 12.18 shows the very strong dependence of hardening on copper content, which has a profound impact on RPV steels and welds.

Dose rate affects the yield strength increment through the term $\Delta\sigma_{\mathrm{yp}}$. Odette [41] has shown that higher dose rates shift the yield strength to higher fluences (Fig. 12.19a) in the pre-plateau region. The CRP term can be written as:

$$\Delta\sigma_{\mathrm{yp}}(\phi t_{\mathrm{e}}) = \Delta\sigma_{\mathrm{ypm}}\sqrt{X}\,, \tag{12.119}$$

where $\Delta\sigma_{\mathrm{ypm}}$ is the plateau value of hardening (relatively insensitive to dose rate), ϕt_{e} is an effective fluence defined by $\phi t_{\mathrm{e}} \approx \phi t(\phi_{\mathrm{r}}/\phi)^{1/2}$, and ϕ_{r} is a reference flux.

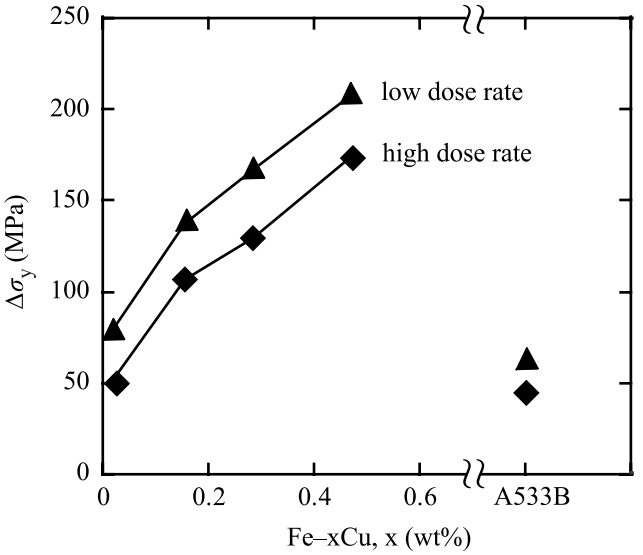

Fig. 12.18. Effect of copper on the hardening of ferritic steel alloys (after [42])

The term X is given by:

$$X = \left\{1 - \exp\left[-(F\phi t_e)^{\beta}\right]\right\} , \tag{12.120}$$

where F and β are fitting parameters. The result is that the CRP contribution to yield strength can be expressed as a function of ϕt_e (Fig. 12.19b) which shows that the CRP increment can be accounted for by using the effective fluence.

Attempts to apply the dispersed barrier hardening model to predict hardening in irradiated ferritic-martensitic steels have met with less success as the result is generally less than the measured value by a significant amount [43, 44].

12.2.7 Radiation Anneal Hardening

An additional hardening mechanism occurs upon annealing of bcc metals following irradiation and is known as radiation anneal hardening (RAH) [45]. Figure 12.20 shows the yield strength as a function of annealing temperature following irradiation of niobium containing 35 wppm C and 41 wppm O to a fluence of $2 \times 10^{18}\,\mathrm{n/cm^2}$. Note that hardening begins at a temperature of about 120 °C and increases to a maximum at about 180 °C before decreasing. However, a second peak in hardening appears at a temperature of 300 °C before the yield strength drops due to recovery. These peaks in the hardness are attributed to the oxygen and carbon impurities in the metal. It is well-known that interstitial impurities increase the yield strength of bcc metals. In the irradiated state, the radiation-prodced defects serve as trapping centers for interstitial impurities. Annealing enables the migration of the interstitials to defect clusters resulting in the formation of impurity–defect complexes or

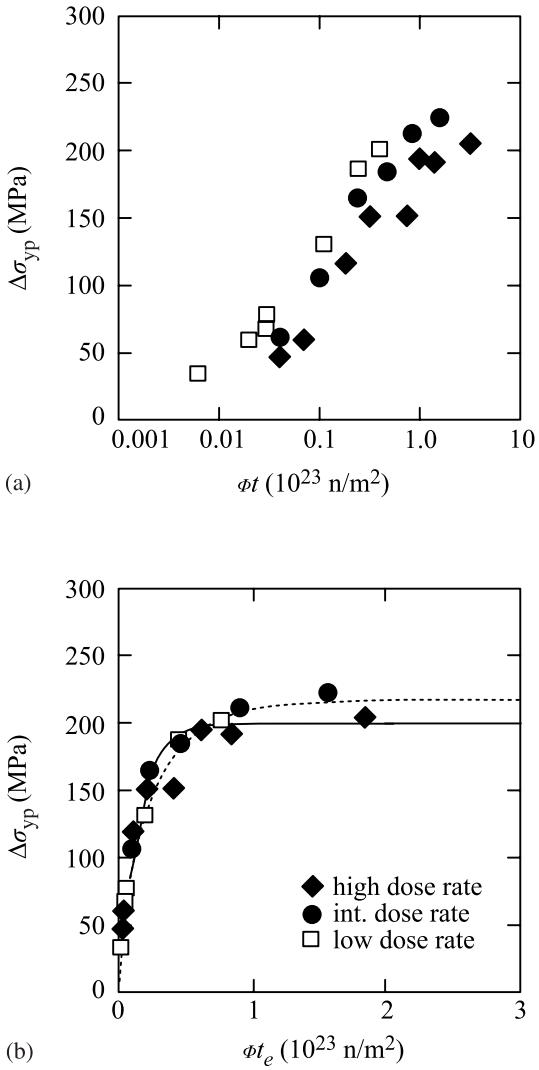

Fig. 12.19. Hardening of an A533B-type bainitic steel containing 0.4% Cu and 1.25% Ni following irradiation at 290°C (a) due to copper-rich precipitates vs. fluence, and (b) due to copper-rich precipitates vs. *effective* fluence (after [41])

the strengthening of existing defect clusters, both of which act as barriers to slip dislocation motion.

In the example shown in Fig. 12.20, the first peak is due to the migration of oxygen to defect clusters and the second peak is due to the migration of carbon. Measurements of the change in resistivity with time at temperature can be used to determine the activation energy for resistivity change, which can then be compared

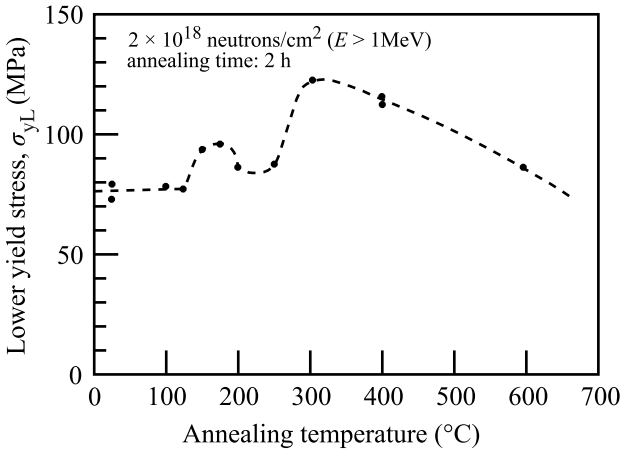

Fig. 12.20. Radiation anneal hardening in niobium containing 35 wppm C, 41 wppm O and 5 wppm N following irradiation to 2×10^{18} n/cm^2 and annealing for 2 h. Unirradiated yield strength is ~40 MPa (after [46])

with the activation energy for diffusion of the impurities to determine their identity. In niobium, vanadium and iron alloys, the primary agents responsible for radiation anneal hardening are oxygen, carbon and nitrogen.

12.2.8 The Correlation Between Hardness and Yield Strength

Much data on hardening comes from indentation or shear punch measurements of irradiated samples. Indentation techniques include Vickers microhardness and ball indentation. The Vickers microhardness technique uses a diamond pyramid-shaped indenter tip that is pressed against the sample with a pre-determined load (Fig. 12.21a). The shape of the indent and the magnitude of the load determine the value of hardness, which is a measure of the resistance of the solid to deformation, or hardness. The shear punch test is essentially a blanking operation in which a flat punch is driven at a constant rate, *s* through a TEM-sized disk. The disk is constrained along both its upper and lower surfaces in a test fixture, which also guides the punch. The load on the punch is measured as a function of specimen displacement, which is taken to be equivalent to the crosshead displacement. The yield and maximum loads are taken from a plot of punch load versus punch displacement. All of these techniques enjoy advantages over tensile testing in that they are relatively simple and quick, require much smaller volumes of irradiated materials, and in the case of microhardness indentation, are compatible with ion irradiation in which the damage is confined to the surface region. However, as hardening is generally defined as the increment in the yield strength due to the irradiated microstructure, there is much interest in relating hardness measurements to yield strength in order to increase their utility.

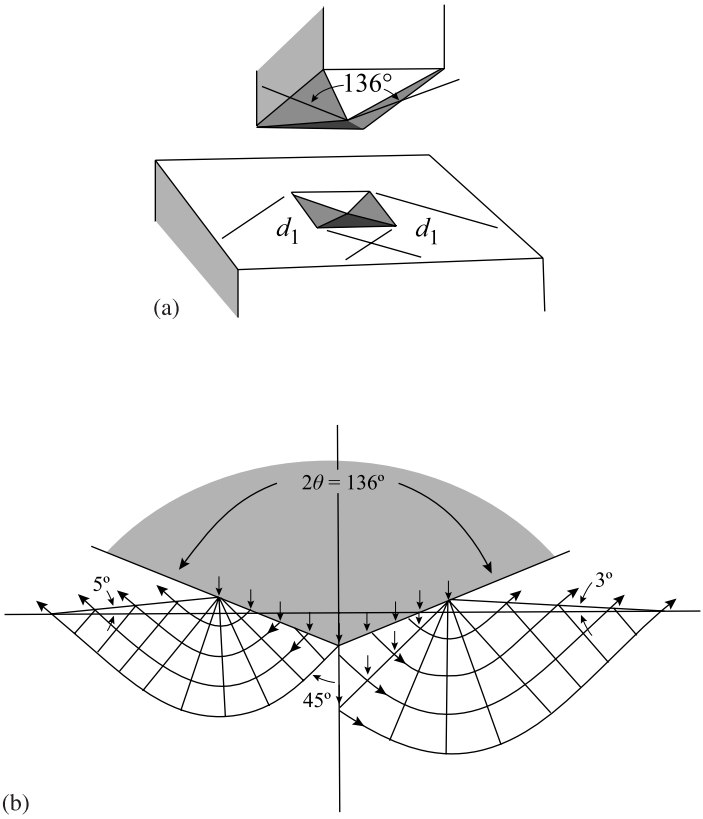

Fig. 12.21. Illustration of (a) the diamond pyramid tip used in Vickers microhardness measurement and the tip impression in the sample, and (b) flow pattern during Vickers indentation of a metal (after [47])

As originally described by Tabor [48] the indentations made during hardness tests are discernible as permanent impressions in the metal, so that the indentation must be primarily a measure of the plastic properties of the metal. While it is true that some change in shape and size occurs when the indenter is removed, the overriding effect is the plastic flow of the metal around the indenter tip, implying that the mean pressure over the indenter is connected to the plastic rather than elastic properties of the metal. Tabor [48] showed that this is indeed the case for a variety of different hardness and scratch tests, based on the work of Prandtl [49] and Hencky [50] and that the hardness measurement can also be used as a measure of the yield stress of the metal.

During indentation, stress is applied to the metal surface through the indenter tip. However, since the tip surface is not parallel to the sample surface, the stress state during indentation is not simply compressive. Instead, the stresses must be examined in two dimensions (along and perpendicular to the axis of the indenter

tip). Plastic deformation during indentation occurs when the Huber–Mises criterion is satisfied, which in the two-dimensional case, occurs when the maximum shear stress reaches a critical value, k:

$$2k = 1.15\sigma_y \,, \tag{12.121}$$

where σ_y is the yield stress.

The pyramidal shape of the indenter tip can be treated as a wedge during indentation. The pattern of plastic flow around the indenter tip during indentation can be determined using the Prandtl solution [49]. The flow pattern is shown schematically in Fig. 12.21b for a Vickers indentation. The pressure normal to the surface of the indenter tip, P can be calculated as:

$$P = 2k(1 + \pi/2) \,. \tag{12.122}$$

Equations (12.121) and (12.122) can be combined to yield:

$$P = 2k(1 + \pi/2) = 1.15\sigma_y(1 + \pi/2) = 2.96\sigma_y \,. \tag{12.123}$$

For a Vickers indenter:

$$H_v \equiv \frac{\text{load}}{\text{contact area}} = 0.927P \,, \tag{12.124}$$

where 0.927 is the ratio of the area of the base of the pyramid (the projected area) to the area of the sides of the pyramid (contact area). Combining Eqs. (12.123) and (12.124) gives:

$$H_v = 0.927P = 0.927 \times 2.96\sigma_y = 2.74\sigma_y \,. \tag{12.125}$$

Writing this expression in terms of yield strength gives the correlation:

$$\sigma_y = CH_v \,, \quad \text{with} \tag{12.126}$$

$C = 0.364$ for σ_y and H_v in units of kg/mm^2 , and

$C = 3.55$ for σ_y in MPa and H_v in kg/mm^2.

Tabor found the same result experimentally for a variety of metals (aluminum, copper, and mild steel). More recently, Larsson [51] studied indentation tests both theoretically and numerically. Specifically, he used finite element analysis to examine elastic-plastic material behavior under sharp contact situations (nanoindenters, Vickers or cone indenters, or even gear contact). Larsson's finite element results were in good agreement with the results of Tabor, validating the assertion that yield stress can, indeed, be determined from Vickers hardness measurements.

Busby et al. [52] reviewed existing correlations and compiled hardness data on austenitic stainless steels and ferritic steels to empirically determine the correlation between hardness and yield strength. They found that in general austenitic stainless steels follow a relation of the form:

$$\Delta\sigma_y = 3.03H_v \,, \tag{12.127}$$

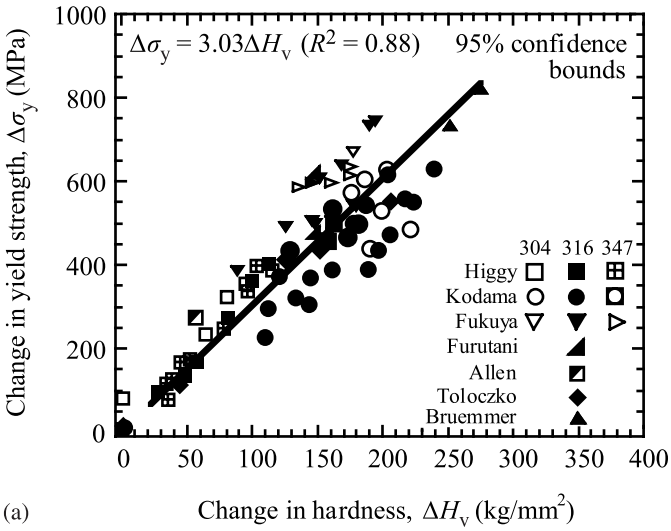

(a)

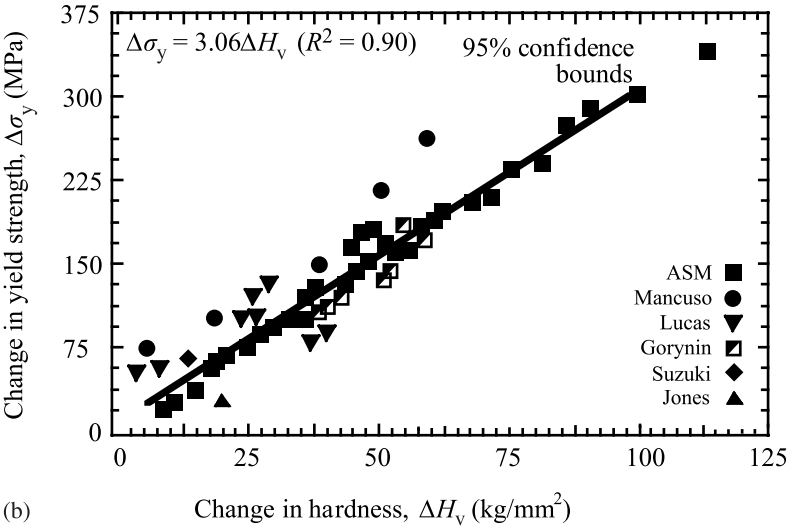

(b)

Fig. 12.22. Experimental data plotted as a change in yield stress vs. change in hardness for (a) austenitic stainless steels and (b) ferritic steels. The hardness-yield stress correlation is also plotted along with 95% confidence bounds (after [52])

and ferritic steels obey a correlation of the form:

$$\Delta\sigma_y = 3.06 H_v \, . \tag{12.128}$$

Figures 12.22a,b shows these correlations for the two classes of steels. The correlations are extremely close and can be taken to be equivalent given the confidence

interval used. While the dataset is best fit with a linear relation, the authors noted that for the austenitic stainless steels, there is some indication of a reduction in slope with increasing values of hardness. A two-slope fit resulted in:

$$\begin{aligned} \Delta\sigma_y &= 3.63\Delta H_v \quad \Delta H_v < 100\,\mathrm{kg/mm^2} \\ \Delta\sigma_y &= 2.13\Delta H_v \quad \Delta H_v > 100\,\mathrm{kg/mm^2}\,. \end{aligned} \tag{12.129}$$

The slope of the correlation in the low load regime is close to Tabor's theoretical value of 3.55 with the difference attributed to scatter in the database. The lower value of the slope at higher loads may reflect the differences between a hardness test and a tensile test. While the yield stress is measured at approximately 0.2% strain, the hardness test involves much higher strains, estimated to be between 8 and 18% [48, 51]. Thus, the nature of deformation of the irradiated metal will influence the correlation between hardness and yield strength at the higher hardness levels.

Lucas et al. [53] found that a correlation coefficient of 3.5 fit a wide range of RPV steel data. He also noted that this data is best fit with a simple linear regression that intersects the ordinate at about 30 MPa at a ΔH_v of zero, which could be a consequence of the fact that ΔH_v values correspond to a flow stress of several percent plastic strain. At low levels of hardening, σ_y may increase due to dislocation cutting of small defects, without a measurable increase in ΔH_v. At the higher levels of hardening, reached when defects are harder, the flow stress rises in proportion to the yield stress.

12.3 Deformation in Irradiated Metals

In addition to undergoing hardening, irradiated metals experience a loss of ductility and a loss of work hardening. The loss of ductility with dose in irradiated austenitic steels irradiated and tested at ~300 °C is shown in Fig. 12.23. Note that ductility drops from some 20–30% to values of less than 1% by ~4 dpa. The decrease in work hardening is evident by the decrease in the difference between σ_{UTS} and σ_y with increasing irradiation dose as shown in Fig. 12.1a,b. If the stress-strain behavior of the metal follows the power-law hardening model given in Eq. (12.27), $\sigma = K\varepsilon^n$, then, as shown in Eq. (12.57), the true uniform elongation ε_u is equal to n. So to first order, variations in ε_u with irradiation follow the changes that occur to the work hardening behavior described by n. Lucas [17] has shown that the behavior of ε_u vs. dose for stainless steel over the temperature range 300–500 °C can be described by the curves in Fig. 12.24a. The uniform elongation decreases significantly and approaches a minimum at a dose that decreases with temperature down to 300 °C. The temperature dependence of the loss of ductility is shown more clearly in Fig. 12.24b. As core components in light water reactors are generally at temperatures around 300 °C, the minimum in ductility at that temperature is a major concern.

The loss of uniform ductility and work hardening are due to the same cause: the interaction between dislocations and the irradiated microstructure. Up to this point,

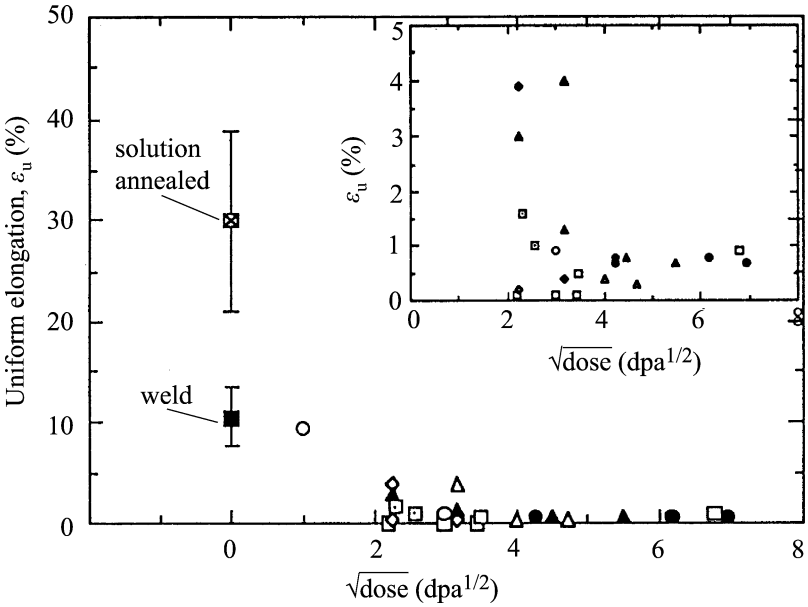

Fig. 12.23. Uniform elongation as a function of the square root of dose for 300 series austenitic stainless steels irradiated and tested at ~300 °C (after [25])

we have only discussed how irradiation can lead to hardening by pinning of dislocations by obstacles. However, dislocation–loop interaction can result in unfaulting of the loop and incorporation into the dislocation network. In fcc metals, unfaulting of a Frank loop can occur by several mechanisms. In one such mechanism [54] a mobile dislocation with Burgers vector $a/2[\bar{1}01]$ (shown as DB in Fig. 12.25a) intersects a small Frank loop with Burgers vector $a/3[\bar{1}11]$ ($D\delta$ in Fig. 12.25a) to form a Schockley partial on the loop plane with Burgers vector $a/6[\bar{1}\bar{2}1]$ (δB in Fig. 12.25a). The interaction of the Shockley partial with the faulted loop generates a helical segment on the original dislocation with Burgers vector $DB = D\delta + \delta B$, and eliminates the loop. A second type of reaction occurs when a glissile, perfect dislocation, $a/2[\bar{1}\bar{1}0]$ interacts with a sessile $a/3[111]$ Frank loop creating an $a/6[\bar{1}\bar{1}2]$ dislocation according to $a/2[\bar{1}\bar{1}0]+a/3[111]=a/6[\bar{1}\bar{1}2]$ [55]. The Shockley partial created by the interaction can sweep across the Frank loop, removing the stacking fault and reacting with the opposite side of the Frank loop according to $a/6[\bar{1}\bar{1}2]+a/3[\bar{1}\bar{1}\bar{1}]=a/2[\bar{1}\bar{1}0]$. Figure 12.25b shows the process by which the Frank loop lying in the plane of the figure interacts with a perfect dislocation moving on some other plane. The Frank loop is annihilated and the only remnant is a coil in the $a/2[\bar{1}\bar{1}0]$ dislocation approximately on the Frank loop $\{111\}$ plane. The result is that the unfaulting product of a perfect dislocation–Frank loop interaction immediately becomes part of the perfect dislocation network. A third mechanism [56] involves intersection of a mobile dislocation with a loop in which the loop glides on itself and becomes part of the glide dislocation as shown in Fig. 12.25c. Finally, un-

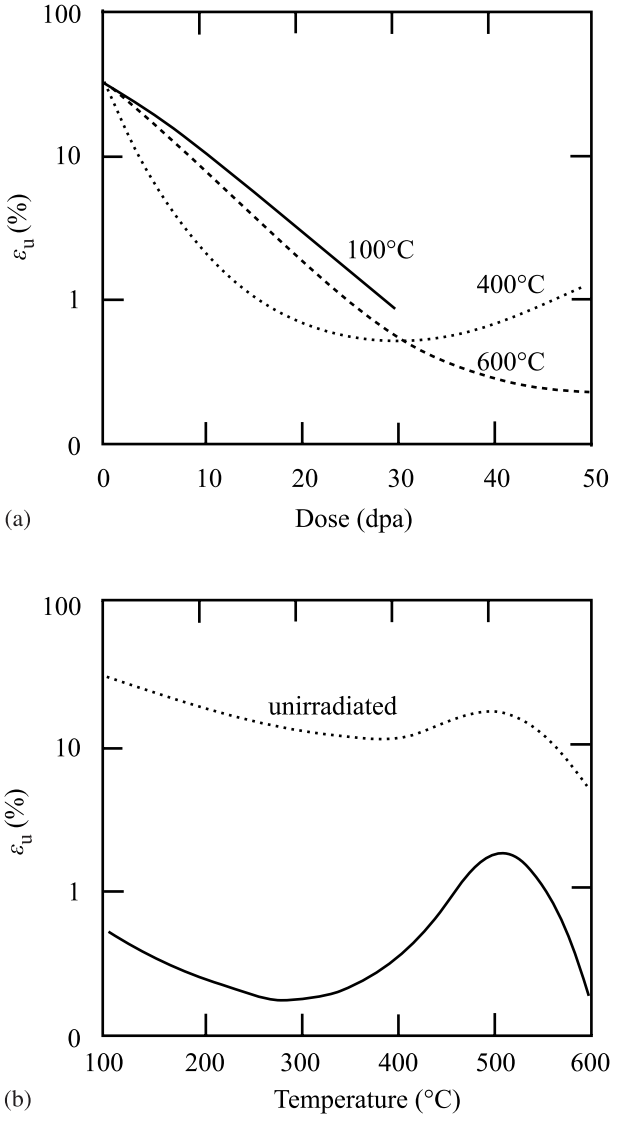

Fig. 12.24. Variation of uniform ductility in austenitic stainless steel with (a) dose and temperature, and (b) temperature (after [17])

faulting can be triggered by the formation of a Shockley partial loop inside a Frank loop [57]. Reaction between the Shockley partial loop of the type $a/6[11\bar{2}]$, and the Frank loop proceeds according to: $a/6[11\bar{2}] + a/3[111] = a/2[110]$, and is shown in Fig. 12.25d.

In bcc metals, faulted loops are rarely observed because of the high stacking fault energy that causes unfaulting at very small loop sizes. The Frank loop is of the form

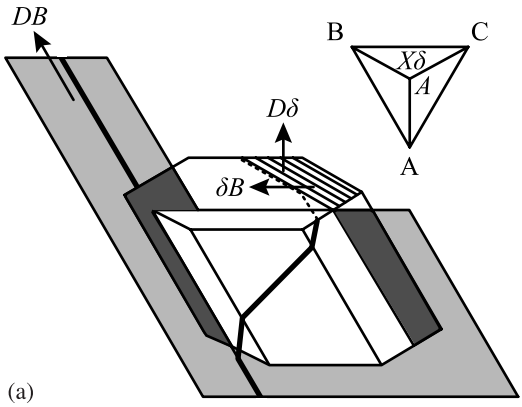

(a)

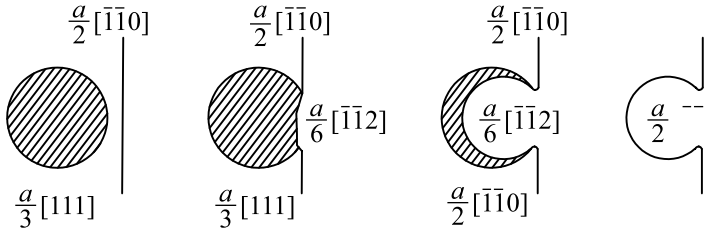

(b)

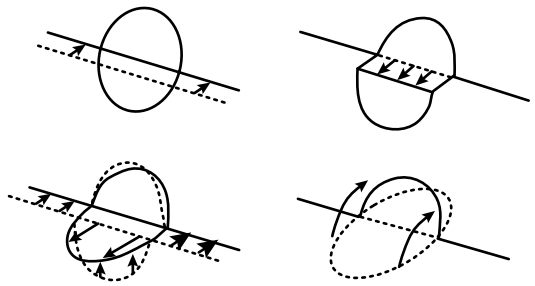

(c)

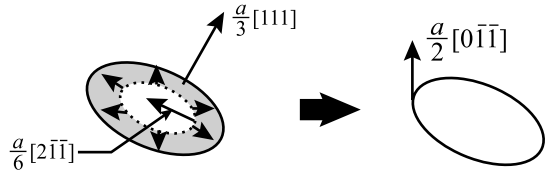

(d)

Fig. 12.25. Loop unfaulting mechanisms proposed by (a) Strudel and Washburn [54]. (b) Gelles [55]. (c) Foreman and Sharp [56] and Tanigawa [57]

$a/2[110]>$, and the stacking fault can be removed by two possible unfaulting reactions [58]: $a/2[110]+a/2[00\bar{1}] \rightarrow a/2[11\bar{1}]$, or $a/2[110]+a/2[\bar{1}10] \rightarrow a/2[010]$, with the result being a perfect loop in either case. The result of each of these unfaulting reactions is the removal of the dislocation loop from the microstructure and the growth of the dislocation network density.

12.3.1 Deformation Mechanism Maps

As described in Chap. 7, plastic deformation is characterized by the shear stress, strain or strain rate and temperature. Frost and Ashby [59] classified deformation mechanisms into five groups:

1. Flow above the ideal shear strength
2. Low-temperature plasticity by dislocation glide
3. Low-temperature plasticity by twinning
4. Power-law creep by dislocation glide or climb and glide
5. Diffusional creep

Each of these mechanisms can be subdivided into additional mechanisms. When stress and temperature are the independent variables, then the response of the metal is the strain rate and strain. Alternatively, the temperature and strain rate could be selected as the independent variables and the stress constitutes the response of the metal.

If strain rate is selected as the dependent variable, a convenient method of relating the strain rate of a metal to the independent variables of shear stress and temperature is the deformation mechanism map. A deformation mechanism map is a representation of the mechanism of deformation in stress-temperature space where stress is represented by the normalized stress σ_s/μ and the temperature is represented by the homologous temperature T/T_m, where μ is the shear modulus and T_m is the melting temperature. The map provides a relationship between the two independent variables, σ_{xy} and T and the dependent variable, $\dot{\varepsilon}$. An example of such a map for 316 stainless steel is given in Fig. 12.26a, in which the normalized stress is plotted on the ordinate and the homologous temperature is plotted on the abscissa. The various deformation mechanisms are denoted by labeled regions in the map, and the strain rate response of the metal to the stress/temperature combinations are given by contours of equistrain rate. Essentially, the strain rate contours provide the constitutive law in the form of a single equation:

$$\dot{\varepsilon} = f(\sigma_s, T)\,. \tag{12.130}$$

Figure 12.26a shows that above the ideal shear strength, plastic collapse occurs and the strain rate approaches infinity:

$$\begin{aligned} \dot{\varepsilon} &= \infty \quad \text{for} \quad \sigma_s \geq \alpha\mu \\ \dot{\varepsilon} &= 0 \quad \text{for} \quad \sigma_s < \alpha\mu\,, \end{aligned} \tag{12.131}$$

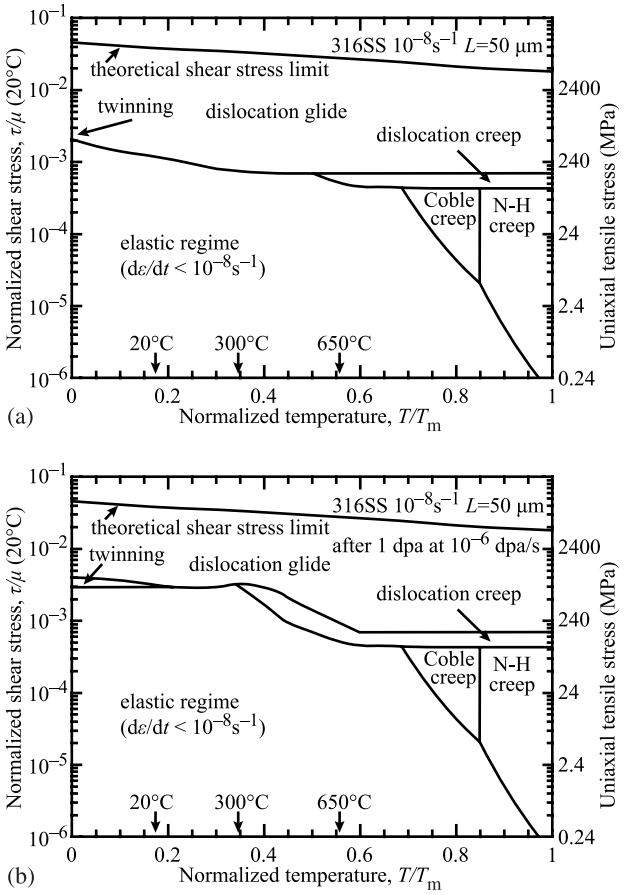

Fig. 12.26. Deformation mechanism map for 316 stainless steel with a grain size of 50 μm and deformed at a strain rate of $10^{-8}\,s^{-1}$ for (a) unirradiated condition, and (b) irradiated to 1 dpa at 10^{-6} dpa/s (after [60])

where α depends on the crystal structure and instability criterion but is generally between 0.05 and 0.1. Below the ideal shear strength, flow can occur by glide of dislocations that is generally limited by obstacles. Ashby gives the strain rate in the discrete obstacle controlled plasticity regime as:

$$\dot{\varepsilon} = \dot{\varepsilon}_0 \exp\left[-\frac{Q}{kT}\left(1 - \frac{\sigma_s}{\sigma_s^0}\right)\right], \tag{12.132}$$

where Q is the activation energy required to overcome the obstacle without aid from external stress, and σ_s^0 is the athermal component of the flow stress. At low temperature and high normalized stress, twinning is observed to occur. Byun et al. [61] have characterized the deformation in terms of the stress and strain, and have determined that the twinning stress, σ_t in polycrystalline metals could be defined by the critical

stress for infinite separation of partials:

$$\sigma_t = 6.14 \frac{\gamma_{SFE}}{b} , \tag{12.133}$$

where b is the Burgers vector of the partial dislocation. The strain rate equation for twinning [59] is:

$$\dot{\varepsilon} = \dot{\varepsilon}_t \exp\left[-\frac{Q_t}{kT} \left(1 - \frac{\sigma_s}{\sigma_t} \right) \right] , \tag{12.134}$$

where Q_t is the activation free energy to nucleate a twin without the aid of external stress, σ_t is the stress required to nucleate twinning in the absence of thermal activation and $\dot{\varepsilon}_t$ is a constant. The balance of the deformation map refers to creep mechanisms and these are discussed in detail in Chap. 14.

Under irradiation at the strain rate of $10^{-8}\,s^{-1}$ the effect of irradiation is shown in Fig. 12.26b. Due to irradiation hardening at temperatures below about $0.5T/T_m$, the stress for dislocation glide is increased, reducing the dislocation glide regime. Above this temperature, irradiation-enhanced softening can occur, causing a reduction in the stress for dislocation glide and an expansion of the glide regime at high temperature. Second, at low temperatures and high stresses, twinning can occur.

12.3.2 Localized Deformation

For defect clusters and coherent precipitates, multiple shearing can eliminate these obstacles in the dislocation glide plane. So in fact, passage of an initial group of dislocations down a particular slip plane can result in the clearing of the obstacles in that slip plane so that subsequent dislocations can pass relatively unimpeded. First observed in the 1960s in bcc metals [62, 63], this process is referred to as *dislocation channeling* and is observed to occur in fcc, bcc and hcp crystal lattices. As a result of channeling, work hardening in channels drops to nearly zero along with the macroscopic uniform strain, as the deformation becomes highly localized within the channels. Byun et al. [64] have pointed out that channel deformation occurs in unirradiated metals at high stress, and that the common feature between channel deformation in irradiated and unirradiated metals is the high stress.

Dislocation channels are characterized by width, spacing and the amount of strain in the channel. Figure 12.27 shows TEM images of dislocation channels in Fe18Cr–12Ni irradiated to 5.5 dpa at 360 °C with 3 MeV protons and strained to 7% at 288 °C. Channel width is generally on the order of 0.1 μm and channels are typically spaced 1 to 3 μm apart. Channels propagate across grains, initiating and terminating at grain boundaries. In a tensile sample, the channels of surface grains propagate to the surface and produce a step on the surface. Figure 12.28 shows an SEM image of the surface of irradiated stainless steel samples strained to 7%, from which the magnitude of the surface step can be characterized using Atomic Force Microscopy (AFM). Figure 12.29 shows how the intersection of a channel with the

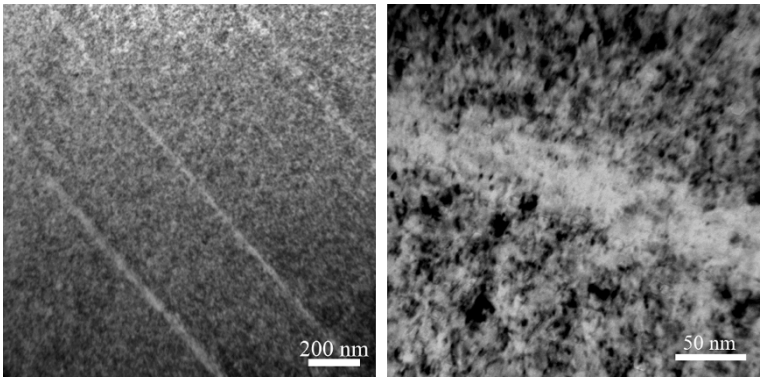

Fig. 12.27. Transmission electron micrographs of dislocation channels in Fe–18Cr–12Ni irradiated to 5.5 dpa at 360 °C with 3 MeV protons and strained to 7% at 288 °C [courtesy of Z Jiao, University of Michigan]

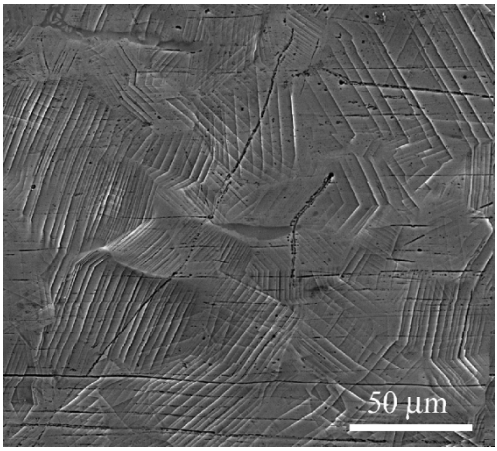

Fig. 12.28. Scanning electron micrograph of dislocation channels intersecting the surface of austenitic stainless steels irradiated to 5.5 dpa with 3.2 MeV protons at 360 °C followed by straining at $3 \times 10^{-7}\,\mathrm{s}^{-1}$ to 7% plastic strain in 288 °C argon [courtesy of Z Jiao, University of Michigan]

surface produces a step of height, h due to the passage of dislocations down the channel. For a height h, and a width, w, the channel strain, γ is simply:

$$\gamma = h/w\,. \tag{12.135}$$

The number of dislocations in a channel, n can be related to the step height by $n = h/b$, where b is the Burgers vector. Was et al. [65] have shown that straining 316L stainless steel to about 7% applied strain following irradiation to 5.5 dpa at 360 °C resulted in an average channel strain of close to 100% caused by the passage

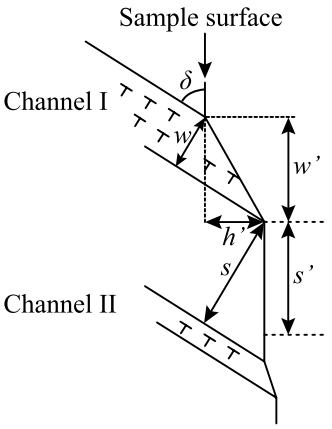

Fig. 12.29. Intersection of dislocation channels with a surface creating *step s* on the surface and defined by the height *h* and width *w*. Primed quantities are *apparent* values of height and width that are measured directly and must be converted to true height and true width in order to determine the strain in the channel (after [65])

of over 1000 dislocations down the channels. However, observations and model calculations indicate that many fewer dislocations (a few to 50) remain in the channels [61, 65]. Two possible reasons for the low number of residual dislocations in the channels are slip transfer to neighboring grains in cases where the slip planes are closely aligned between grains, or reaction of the dislocation with the grain boundary. When a dislocation channel intersects a grain boundary, dislocations in the channel either transfer to an adjoining grain or pile up at the grain boundary. When a dislocation transfers, it leaves a residual dislocation in the grain boundary. The reaction of dislocations involving grain boundaries can be expressed as: $\boldsymbol{b}_\mathrm{r} = \boldsymbol{b}_1 - \boldsymbol{b}_2$, where $\boldsymbol{b}_\mathrm{r}$ is the Burgers vector of the residual dislocation left behind in the grain boundary, and $\boldsymbol{b}_1$ and $\boldsymbol{b}_2$ are Burgers vectors of dislocations in grains 1 and 2, respectively. The number of residual dislocations in a grain boundary is likely proportional to the channel height or channel strain as the portion of dislocations piled up at a grain boundary is relatively small.

In addition to channeling caused by defect-clearing by gliding dislocations, deformation twinning is also observed to occur. Deformation twinning or mechanical twinning is a localized deformation mechanism caused by partial dislocations. In fcc metals with low stacking fault energy (SFE), deformation twins are formed by the glide of Shockley partial dislocation of the same sign on successive $\{111\}$ planes. In these twins, the shear strain is 70.7% and the defects are cleared by glide of the partial dislocations [66]. The Shockley partials are formed from dissociation of the ordinary dislocation with Burgers vector $1/2\langle 110\rangle$ into leading and trailing partial dislocations with Burgers vector of the type $1/6\langle 112\rangle$. The separation of the partials, or the width of the stacking fault, d is given by:

$$d \approx \frac{\mu b^2}{4\pi\gamma_\mathrm{SFE}} \,, \tag{12.136}$$

where γ_SFE is the stacking fault energy. In low stacking fault energy metals, the separation of partials is large. Was et al. [65] have observed the formation of twins at the intersection of dislocation channels with grain boundaries where the stress and

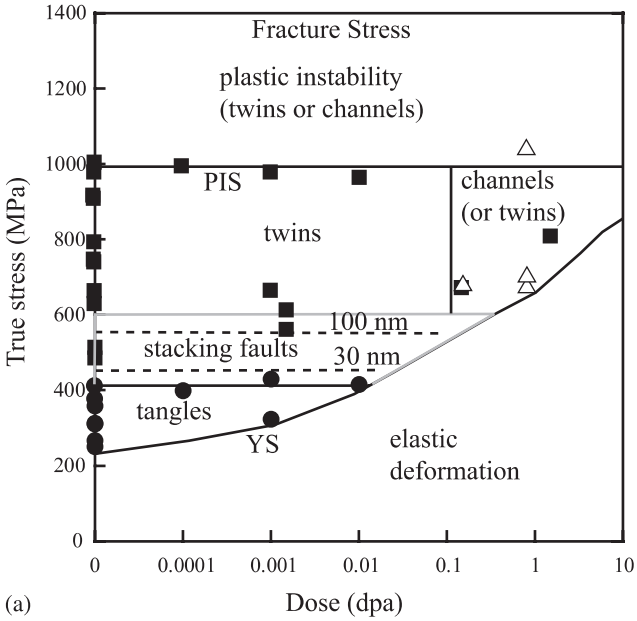

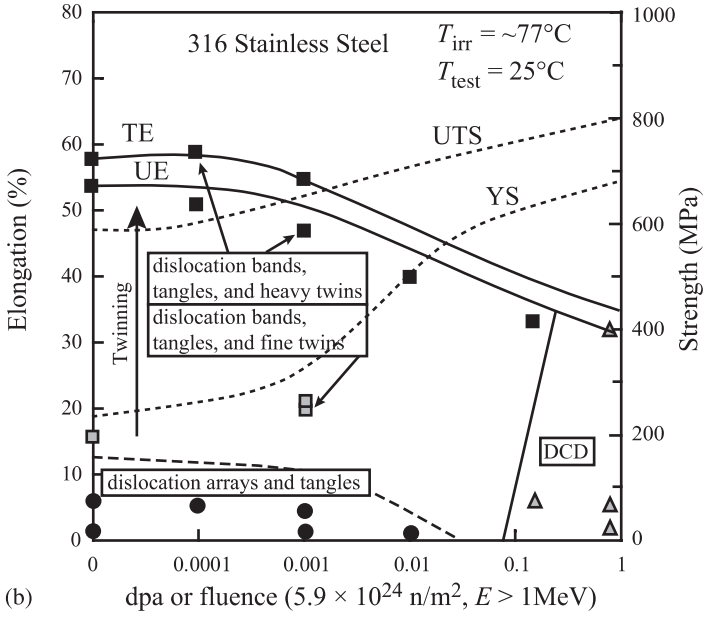

Fig. 12.30. (a) Stress-based deformation mode map for 316 stainless steel in true stress-dose space (PIS = plastic instability stress) (after [67]). (b) Strain-based deformation mode map for 316 stainless steel neutron irradiated at 65–100 °C and tested at room temperature (TE = total elongation, UE = uniform elongation, DCD = dislocation channeling deformation) (after [68])

strain is the greatest. Whether by channeling or twinning, localized deformation is a strong function of dose with localization of deformation increasing with dose. Twinning is also favored at low temperatures.

Byun and Hashimoto [67] and Farrell et al. [68] have constructed deformation mode maps for irradiated alloys that describe the mode of deformation as a function of applied strain. A stress-based map is shown in Fig. 12.30a and a strain-based map is shown in Fig. 12.30b for 316 austenitic stainless steel. In the stress-based map, higher dose leads to an increase in yield strength and an increase in the elastic deformation regime.

Nomenclature

A	Area of slip plane or dislocation loop or cross sectional area of a tensile sample after straining
A_0	Original cross sectional area in a tensile sample
$\boldsymbol{b}$	Burgers vector
d	Grain size or obstacle diameter or separation distance of partial dislocations
e	Elastic strain
E	Elastic modulus
F	Force
h	Dislocation channel height
H_v	Vickers hardness
K	Bulk modulus or constant in power law hardening equation
k	Square root of second invariant of the stress deviator used for the von Mises yield criterion
k_y	Unpinning stress
L_0, L	Original and deformed length of a tensile sample. L is also length of dislocation pile-up on a slip plane
l	Distance between obstacles on the slip plane
m	Schmidt factor
M	Taylor factor
N	Number density of obstacles on a slip plane
n	Number of dislocations in a pile-up
p	Hydrostatic pressure
P	Load
r	Distance from obstacle to Frank–Read source
r_d	Dislocation core radius
R	Radius of an obstacle
S	Engineering stress, or weighting parameter from Eq. (12.103)
t	Time
T	Temperature
U	Elastic strain energy

U_V	Elastic strain energy of volume of a void
V	Volume
w	Dislocation channel width
W	Work
α	Obstacle hardness
β	Compressibility, work hardenability
ϕ	Neutron flux
ϕt	Neutron fluence
ϕt_e	Effective neutron fluence
Δ	Volume strain
δ	Increment of distance
ε, ε_{ij}	Strain and components of strain
γ	Dislocation channel strain
γ_{SFE}	Stacking fault energy
Γ	Dislocation line tension
λ	Lamé coefficient
μ	Shear modulus
ν	Poisson's ratio
ρ_d	Dislocation density
σ	Tensile stress
σ_i	Friction stress
σ_m	Mean stress
σ_s	Shear stress
σ_s^0	Athermal component of flow stress
σ_y	Yield stress
σ_{yp}	CRP contribution to yield stress
σ_{ypm}	Yield strength plateau
τ	Defect lifetime
ζ	Number of damage zones created per neutron collision

Subscripts

d	Dislocation
f	Fracture
i,j or x,y,z	Stress and strain components
loop	Loops
LR	Long-range
n	Necking
ppt	Precipitates
s	Shear or strong
SR	Short-range
u	Uniform
void	Voids
V	Void
w	Weak

y	Yield
yr	Root-sum-square
yl	Linear sum

Superscripts

n	Strain hardening exponent

Acronyms

AFM	Atomic force microscope
CRP	Copper-rich precipitates
MF	Matrix features
RA	Reduction in area
RAH	Radiation anneal hardening
RPV	Reactor pressure vessel
RSS	Root-sum-square
SEM	Scanning electron microscopy
SFE	Stacking fault energy
SMF	Stable matrix features
TEM	Transmission electron microscope
UMF	Unstable matrix features
UTS	Ultimate tensile strength
YS	Yield strength

Problems

12.1 The irradiated microstructure will determine the extent of hardening in an alloy. Your goal is to limit the radiation hardening in a metal. Assume in your material that all hardening comes from voids and that no transmutation gas is present. For a fixed number of vacancies trapped in cavities, would you prefer a large density of small voids or a small density of large voids? Explain your reasoning.

12.2 If an alloy swells by increasing the radius of constant density voids, by how much does a doubling of the swelling harden the alloy? For this scenario, is the swelling or the hardening from voids more of a concern?

12.3 Electron microscopic examination of a 316 stainless steel specimen that has been irradiated at 400 °C to a fast neutron fluence of $1 \times 10^{22}\,\mathrm{n/cm^2}$ ($E > 0.1\,\mathrm{MeV}$) reveals voids with an average diameter of 40 nm and a volume density of $2.2 \times 10^{15}\,\mathrm{cm^{-3}}$. In addition, faulted loops of a diameter 16 nm are present at a volume density of $1.8 \times 10^{15}\,\mathrm{cm^{-3}}$. The incremental increase in the shear stress caused by a barrier can be expressed as:

$$\Delta\tau = \alpha\mu b/l (\mu = 80\,\mathrm{GPa}\,, b = 2.5 \times 10^{-10}\,\mathrm{m})$$

Assuming that both types of defects act as hard barriers ($\alpha = 1$ for voids, $\alpha = 1/2$ for faulted loops) and are distributed in regular, square arrays:

a) Calculate the change in the critical resolved shear stress ($\Delta\tau$) due to irradiation.
b) What is the interparticle spacing of the square arrays?
c) Which causes greater hardening, voids or loops?

12.4 For 316 stainless steel irradiated at 400 °C to a fast neutron fluence of $1 \times 10^{22}\,\mathrm{n/cm^2}$ ($E > 0.1\,\mathrm{MeV}$), determine the dislocation loop size and density required to produce the same hardening as the void population given in Problem 12.4.

12.5 A pressure vessel steel is irradiated at 300 °C to a fluence of $10^{20}\,\mathrm{n/cm^2}$. We wish to determine the change in NDT due to such an irradiation. NDT is defined by the condition that $\sigma_\mathrm{f} = \sigma_\mathrm{y}$ or $\sigma_\mathrm{y} k_\mathrm{y} = 4\mu\gamma d^{-1/2}$. The effect of irradiation on source hardening can be determined as follows:

$$d(\sigma_\mathrm{y} k_\mathrm{y}) = \sigma_\mathrm{y} dk_\mathrm{y} + k_\mathrm{y} d\sigma_\mathrm{y} = 0\,,$$

since the term $4\mu\gamma d^{-1/2}$ is essentially constant during irradiation.
The changes in k_y and σ_y due to the variables T and ϕt (where ϕt is manifest by radiation hardening or an increase in the friction stress σ_i) are:

$$\mathrm{d}k_\mathrm{y} = \frac{\partial k_\mathrm{y}}{\partial T}\,\mathrm{d}T + \frac{\partial k_\mathrm{y}}{\partial \sigma_i}\,\mathrm{d}\sigma_i$$
$$\mathrm{d}\sigma_\mathrm{y} = \frac{\partial \sigma_\mathrm{y}}{\partial T}\,\mathrm{d}T + \frac{\partial \sigma_\mathrm{y}}{\partial \sigma_i}\,\mathrm{d}\sigma_i\,.$$

Combining these expressions and neglecting the effect of radiation on source hardening ($\partial k_\mathrm{y}/\partial\sigma_i = 0$ and $\partial\sigma_\mathrm{y}/\partial\sigma_i = 1$) we obtain an increase in transition temperature $\mathrm{d}T_\mathrm{D}$;

$$\frac{\mathrm{d}T_\mathrm{D}}{\mathrm{d}\sigma_i} = -\left(\frac{\sigma_\mathrm{y}}{k_\mathrm{y}}\frac{\partial k_\mathrm{y}}{\partial T} + \frac{\partial \sigma_\mathrm{y}}{\partial T}\right)^{-1}\,.$$

To find the increase in transition temperature $\mathrm{d}T_\mathrm{D}$ as a function of fluence, we need the dependence of friction stress σ_i on ϕt. This will give us:

$$\mathrm{d}T_\mathrm{D} = \frac{\mathrm{d}T_\mathrm{D}}{\mathrm{d}\sigma_i}\frac{\mathrm{d}\sigma_i}{\mathrm{d}(\phi t)}\,\mathrm{d}(\phi t)\,.$$

Using Makin's theory for hardening by depleted zones,

$$\sigma_i = \sigma_i^0\,[1 - \exp(-\alpha\nu\Sigma_\mathrm{s}\phi t)]^{1/2}$$

and that

$$\sigma_i^0 = 6.64\,\mathrm{GPa}$$
$$\alpha = 1$$
$$\Sigma_\mathrm{s} = 0.26\,\mathrm{cm^{-1}}$$

and a cluster size of 6 nm, calculate the increase in transition temperature dT_D after a fluence increment of $10^{20}\,n/cm^2$, given that $dT_D/d\sigma_i \sim 0.3\,°C/MPa$.

12.6 The work hardening region of the stress-strain curve can be represented by the relation $\sigma = k\varepsilon^n$, where n is the work hardening coefficient. By increasing the yield stress more than the ultimate tensile stress, irradiation effectively reduces the work hardening coefficient. Using the criterion for plastic instability, $d\sigma/d\varepsilon = \sigma$, calculate the reduction in uniform elongation due to an irradiation that decreases n by an amount Δn.

12.7 A specimen of Ni–1Al is irradiated at 550 °C with 3.5 MeV nickel ions to a dose of 9 dpa. The resulting structure contains a void distribution consisting of $3 \times 10^{14}\,voids/cm^3$ at an average diameter of 50 nm.

a) What is the required stress for a dislocation to cut through an array of these barriers and what fraction is this of the full Orowan stress?
b) Assuming a constant total void volume, what is the stress if void growth causes the average void size to double?

Use the elastic constants for pure nickel and assume a grain size of $10\,\mu m$.

12.8 Consider a dislocation line in a solid containing N bubbles of radius R per cubic centimeter. A shear stress, τ_{xy} is applied to the solid, which causes the dislocation to glide along its slip plane. Under what conditions will the bubbles be swept along by the dislocation rather than be bypassed by it?

12.9 You have 3 tensile samples of 316 stainless steel. Two were irradiated in a reactor to $10^{21}\,n/cm^2$ at 300 °C and one was left unirradiated. The three samples are tested in a tensile test in the lab in the following manner: One irradiated sample is tested at room temperature, another at 300 °C and the unirradiated sample is tested at 300 °C, all at the same strain rate. Draw the engineering stress-engineering strain curves (on the same graph) that would result, labeling the points σ_y, σ_{UTS}, σ_f, ε_u, ε_f. Provide a brief explanation justifying the relative positions of the curves.

12.10 Draw the engineering stress-engineering strain curves that would result from a tensile test in the lab on the samples in Problem 12.9 following irradiation to $10^{21}\,n/cm^2$ at 300 °C and 700 °C. Label the points σ_y, σ_{UTS}, σ_f, ε_u, ε_f.

References

1. Dieter GE (1976) Mechanical Metallurgy, 2nd edn. McGraw-Hill, New York
2. Kocks UF (1970) Metal Trans 1:1121–1143
3. Olander DR (1976) Fundamental Aspects of Nuclear Reactor Fuel Elements, TLD-26711-Pl. Technical Information Center, ERDA, Washington, DC, chap 18
4. Stroh AN (1954) Proc Roy Soc Vol London 223:404–414
5. Makin MJ, Sharp JV (1965) Phys Stat Sol 9:109
6. Singh BN, Foreman AJE, Trinkaus H (1997) J Nucl Mater 249:103–115
7. Stoller RE, SJ Zinkle (2000) J Nucl Mater 283–287:349–352
8. Seeger A (1958) Proceedings of 2nd United Nations International Conference on the Peaceful Uses of Atomic Energy, Geneva, vol 6, United Nations, NY, p 250
9. Russell KC, Brown LM (1972) Acta Metal 20:969–974

10. Scattergood RO, Bacon DJ (1982) Acta Metal 30:1665–1677
11. Kocks UF, Arbon AS, Ashby MF (1975) Prog Mater Sci 19:1
12. Kocks UF (1977) Mater Sci Eng 27:291–298
13. Bement AL (1972) Rev Roum Phys 17(3):361–380
14. Foreman AJE, Makin MJ (1967) Can J Physics 45:511
15. Kocks UF (1969) Physics of Strength and Plasticity. MIT Press, Cambridge, p 13
16. Odette GR, Lucas GE (1998) Rad Eff Defects Solid 44:189
17. Lucas GE (1993) J Nucl Mater 206:287–305
18. Was GS, Busby JT, Andresen PL (2006) Corrosion in the Nuclear Power Industry, ASM Handbook, vol 13C, ASM International, pp 386–414
19. Was GS, Andresen PL (2007) Effect of Irradiation and Corrosion on SCC in LWRs, Corrosion in the Nuclear Power Industry, vol 13 B, chap 5-A3. American Society for Metals, Metals Park, OH (in press)
20. Zinkle SJ, Maziasz PJ, Stoller RE (1993) J Nucl Mater 206:266–286
21. Garner FA (1993) J Nucl Mater 205:98–117
22. Kojima S, Zinkle SJ, Heinisch HL (1989) Grain Size Effect on Radiation Hardening in Neutron-Irradiated Polycrystalline Copper, Fusion Reactor Materials Semiannual Progress Report for Period ending March 31, 1989, DOE/ER-0313/6: 43–49
23. Makin MJ, Minter FJ (1957) J Inst Metals 24:399
24. Higgy HR, Hammad FH (1975) J Nucl Mater 55:177–186
25. Odette GR, Lucas GE (1991) J Nucl Mater 179–181:572–576
26. Bement AL (1963) HW-74955, p 181
27. Eason ED (1998) Development, Evaluation and Analysis of the Initial CIR-IASCC Database, EPRI Report TR-108749, Oct 1998, pp 3–7 to 3–10
28. Williams JA, Hunter CW (1972) Effects of Radiation on Substructure and Mechanical Properties of Metals and Alloys, STM STP 529. American Society for Testing and Materials, Philadelphia, PA, p 13
29. Pettersson K (1992) Radiation Effects on Mechanical Properties of Light Water Reactor Structural Materials, TR1TA-MAC-0461. Materials Research Center, The Royal Institute of Technology, Stockholm, March 1992
30. Was GS, Busby JT (2003) Use of Proton Irradiation to Determine IASCC Mechanisms in Light Water Reactors: Solute Addition Alloys, Final Report, Project EP-P3038/C1434, Report #1007440. Electric Power Research Institute, Palo Alto, CA, April, 2003
31. Garner FA, Hamilton ML, Panayotou NF, Johnson GD (1981) J Nucl Mater 103/104:803–808
32. Grossbeck ML, Maziasz PJ, Rowcliffe AF (1992) J Nucl Mater 191–194:808–812
33. Zinkle SJ (1992) In: Stoller RE, Kumar AS, Gelles DS (eds) Effects of Radiation on Materials the 15th International Symposium, ASTM STP 1125. American Society for Testing and Materials, Philadelphia, PA, 1992, pp 813–834
34. Bloom EE (1976) Irradiation strengthening and embrittlement. In: Radiation Damage in Metals. American Society for Metals, Metals Park, OH, pp 295–329
35. Hashimoto N, Wakai E, Robertson JP (1999) J Nucl Mater 273:95–101
36. Ando M, Katoh Y, Tanigawa H, Kohyama A, Iwai T (2000) J Nucl Mater 283–287:423–427
37. Maziasz PJ (1993) J Nucl Mater 205:118–145
38. Kelly PM (1972) Scr Metal 6:647
39. Odette GR, Lucas GE, Klingensmith RD, Stoller RE (1996) In: Gelles DS, Nanstad RK, Kumar AS, Little EA (eds) Effects of Radiation on Materials the 17th International Symposium, STM STP 1270. American Society for Testing and Materials, Philadelphia, PA, 1996, pp 606–636

40. Odette GR, Mader EV, Lucas GE, Phythian W, English CA (1993) In: Kumar AS, Gelles DS, Nanstad RK, Little EA (eds) Effects of Radiation on Materials the 16th International Symposium, ASTM STP 1175. American Society for Testing and Materials, Philadelphia, PA, 1993, p 373
41. Odette GR, Yamamoto T, Klingensmith D (2005) Phil Mag 85(4–7):779–797
42. Kasada R, Kitao T, Morishita K, Matsui H, Kimura A (2001) In: Rosinski ST, Grossbeck ML, Allen TR, Kumar AS (eds) Effects of Radiation on Materials the 20th International Symposium, ASTM STP 1405. American Society for Testing and Materials, West Conshohocken, PA, 2001, p 237
43. Schaeublin R, Gelles D, Victoria M (2002) J Nucl Mater 307–311:197–202
44. Gupta G, Jiao Z, Ham AN, Busby JT, Was GS (2006) Microstructural evolution of proton irradiated T91. J Nucl Mater 351(1–3):162–173
45. Wechsler MS, Murty KL (1989) Metal Trans A 20A:2637–2649
46. Ohr SM, Tucker RP, Wechsler MS (1970) Phys Status Solidi A 2:559–569
47. McClintock FA, Argon AS (1966) Mechanical Metallurgy of Materials. Addison-Wesley, New York
48. Tabor D (1956) The physical meaning of indentation and scratch hardness. Brit J of App Phy 7:159 May
49. Prandtl L (1920) Nachr Ges Wiss, Gottingen, p 74
50. Hencky H, Agnew Z (1923) Math Mech 3:250
51. Larsson PL (2001) Investigation of sharp contact at rigid-plastic conditions. Int J Mech Sci 43:895–920
52. Busby JT, Hash MC, Was GS (2005) J Nucl Mater 336:267–278
53. Lucas GE, Odette GR, Maiti R, Sheckherd JW (1987) In: Garner FA, Henagar CH, Igata N (eds) Influence of Radiation on Materials Properties the 13th International Symposium (Part II), STM STP 956. American Society for Testing and Materials, Philadelphia, PA, 1987, pp 379–394
54. Strudel JL, Washburn J (1964) Phil Mag 9:491
55. Gelles DS (1981) In: Ashby MF, Bullough R, Hartley CS, Hirth JP (eds) Proceedings of Dislocation Modeling of Physical Systems. Pergamon, Oxford, p 158
56. Foreman AJE, Sharp JV (1969) Phil Mag 19:931
57. Tanigawa H, Kohyama A, Katoh Y (1996) J Nucl Mater 239:80
58. Eyre BL, Bullough R (1965) Phil Mag 12:31
59. Frost HJ, Ashby MJ (1982) Deformation-Mechanism Maps: The Plasticity and Creep of Metals and Ceramics. Pergamon, New York
60. Zinkle SJ, Lucas GE (2003) Deformation and Fracture Mechanisms in Irradiated fcc and bcc Metals, US Department of Energy, Semi-annual Report, DOE-ER-0313/34, p 117
61. Byun TS, Hashimoto N (2006) J Nucl Mater 354:123–130
62. Eyre BL (1962) Phil Mag 7:2107
63. Tucker RP, Wechsler MS, Ohr SM (1969) J Appl Phys 40(1):400–408
64. Byun TS, Farrell K (2004) Acta Materialia 52:1597–1608
65. Was GS, Jiao Z, Busby JT (2006) In: Gdoutos EE (ed) Proceedings of the 16th European Conference of Fracture. Springer, Berlin Heidelberg New York
66. Byun TS, Hashimoto N, Farrell K, Lee EH (2006) J Nucl Mater 354:251–264
67. Byun TS, Hashimoto N, Farrell K (2006) J Nucl Mater 351:303–315
68. Farrell K, Byun TS, Hashimoto N (2004) J Nucl Mater 335:471–486

13 Fracture and Embrittlement

Embrittlement of a metal is measured by the amount of plastic or creep deformation that occurs before fracture. Irradiation invariably renders a metal less ductile than the unirradiated condition. Fracture can be of the brittle type in which a small crack rapidly propagates across an entire component, or it can occur after long times at stress and after appreciable plastic deformation. Failure by stress rupture takes place by linkage of small intergranular cracks or cavities that have developed throughout the interior of the metal.

The fracture behavior of irradiated structural materials is of vital interest not only for reasons of public safety in the case of pressure containment systems but also for reasons of economy, in the case of fuel performance and plant reliability. Consequently, major efforts have been made to determine the mechanics and engineering limits for fracture of pressure vessel steels and reactor core component alloys under various metallurgical and operational conditions. Although considerable properties data have been developed to provide guidance for design and safeguards analysis, the effects of irradiation on basic fracture initiation and propagation mechanisms is still under investigation.

In this chapter, we will first develop the formulation for the theoretical cohesive strength of metals, followed by an introduction to fracture mechanics. Using these tools we will address the theory of brittle fracture and merge this theory with the theory of yielding in metals to describe the fracture behavior of metals spanning the elastic-plastic transition. The influence of irradiation combined with other embrittling effects on the fracture behavior of pressure vessel steels will be treated, followed by an application of fracture mechanics to crack propagation and fatigue crack growth. Finally, high-temperature embrittlement and fracture mechanisms will be discussed.

13.1 Types of Fracture

Metals can exhibit different types of fracture depending on the alloy, temperature, state of stress and rate of loading. Fracture can be classified into two general categories: *ductile fracture* and *brittle fracture*. A ductile fracture is characterized by appreciable plastic deformation prior to and during the propagation of a crack. Brittle fracture in metals is characterized by a rapid rate of crack propagation, with

no gross deformation and very little microdeformation. Actually, the boundary between a ductile and brittle fracture is arbitrary and depends on the situation being considered.

Brittle fracture often occurs by cleavage, or separation along a crystallographic plane of low index. The cleavage mode of fracture is controlled by tensile stresses acting normal to a crystallographic cleavage plane. Brittle fractures have been observed in bcc and hcp metals, but not in fcc metals except by grain boundary embrittlement. In polycrystalline samples, fractures are classified as either *transgranular*, in which the crack propagates through the grains, or *intergranular*, in which the crack propagates along the grain boundaries.

13.2 The Cohesive Strength of Metals

In most basic terms, the strength of metals is due to the cohesive forces between atoms. Figure 1.8 in Chap. 1 showed the variation in the potential function for an atom about its equilibrium site. Figure 13.1 shows the corresponding variation in cohesive force between two atoms as a function of the separation between theses atoms. This curve results from the attractive and repulsive forces between atoms. The interatomic spacing of the atoms in the unstrained condition is indicated by the length increment, a. If the crystal is subjected to a tensile load, the separation between atoms increases. The repulsive force decreases more rapidly with increased separation than does the attractive force, so that a net force between atoms balances the tensile load. As the tensile load is increased still further, the repulsive force is negligible and the attractive force begins to decrease because of the increased separation of the atoms. This point corresponds to the maximum in the curve, which is equal to the theoretical cohesive strength of the material.

A good approximation to the theoretical cohesive strength can be obtained if it is assumed that the cohesive force curve can be represented by a sine curve [1]:

$$\sigma = \sigma_{\text{th}} \sin \frac{2\pi x}{\gamma} \tag{13.1}$$

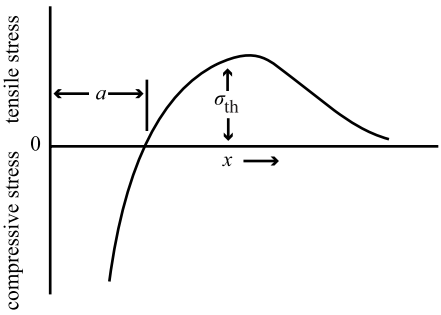

Fig. 13.1. Cohesive force on an atom relative to the separation distance between atoms (from [1])

where σ_{th} is the theoretical cohesive strength and x is the displacement in atomic spacing in a lattice with wavelength λ . For small displacements $\sin x \approx x$, and:

$$\sigma = \sigma_{th} \frac{2\pi x}{\lambda} . \tag{13.2}$$

Limiting consideration to a brittle elastic solid, from Hooke's law we have:

$$\sigma = E\varepsilon = \frac{Ex}{a} . \tag{13.3}$$

Eliminating x from Eqs. (13.2) and (13.3) gives:

$$\sigma_{th} = \frac{\lambda}{2\pi} \frac{E}{a}. \tag{13.4}$$

When fracture occurs in a brittle solid, all of the work expended in producing the fracture goes into the creation of two new surfaces. Each of these surfaces has a *surface energy* of γ in units of energy/unit area. The work done per unit area of surface in creating the fracture, U_f is the area under the stress-displacement curve of Fig. 13.1:

$$U_f = \int_0^{\lambda/2} \sigma_{th} \sin \frac{2\pi x}{\lambda} \, dx = \frac{\lambda \sigma_{th}}{\pi} \tag{13.5}$$

where λ is the wavelength. This energy is that required to create the two new fracture surfaces:

$$\frac{\lambda \sigma_{th}}{\pi} = 2\gamma , \quad \text{or} \quad \lambda = \frac{2\pi\gamma}{\sigma_{th}} , \tag{13.6}$$

and substituting into Eq. (13.4) gives:

$$\sigma_{th} = \left(\frac{E\gamma}{a} \right)^{1/2} . \tag{13.7}$$

Equation (13.6) provides an estimate of the theoretical stress required to create two new surfaces with surface energy, γ. Taking typical values for the parameters in Eq. (13.7) yields values for the theoretical fracture strength that are 10 to 1000 times that found in engineering materials. To resolve this discrepancy, Griffith [2] proposed that a brittle material contains a population of fine cracks that produce a stress concentration of sufficient magnitude so that the theoretical cohesive strength is reached in localized regions at a nominal stress, which is well below the theoretical value.

When a crack increases its length in the process of brittle fracture, it produces an increase in the surface area of the sides of the crack. Energy is required to overcome the cohesive force of the atoms, or expressed in another way, crack growth requires an increase in surface energy. The source of the increased surface energy is the elastic strain energy which is released as the crack spreads. Griffith established the

following criterion for the propagation of a crack: "A crack will propagate when the decrease in elastic strain energy is at least equal to the energy required to create the new crack surface." This criterion can be used to determine the magnitude of the tensile stress, which will just cause a crack of a certain size to propagate as a brittle fracture.

If we consider an elliptical crack of length $2c$ in a flat plate of unit thickness under an applied stress, σ acting normal to the crack plane, then the presence of a crack reduces the total strain energy by the amount [3]:

$$U_{\mathrm{E}} = -\frac{\pi c^2 \sigma^2}{E} \,. \tag{13.8}$$

The decrease in strain energy is available for creation of the two crack surfaces that requires the energy:

$$U_{\mathrm{S}} = 4\gamma c. \tag{13.9}$$

According to Griffith's criterion, the crack will propagate under a constant applied stress, σ if an incremental increase in crack length produces no change in the total energy of the system, i.e., the increased surface energy is compensated by a decrease in elastic strain energy. Using Eqs. (13.8) and (13.9), this criterion can be expressed by the following:

$$\frac{\partial}{\partial c}\left(4\gamma c - \frac{\pi \sigma^2 c^2}{E}\right) = 0 \,, \tag{13.10}$$

and solving for the stress gives:

$$\sigma_{\mathrm{f}} = \left(\frac{2E\gamma_s}{\pi c}\right)^{1/2} \,. \tag{13.11a}$$

For the plane strain condition, E is replaced by $E/(1-\nu)^2$ giving:

$$\sigma_{\mathrm{f}} = \left(\frac{4E\gamma_s}{(1-\nu)^2 \pi c}\right)^{1/2} \,. \tag{13.11b}$$

Equations (13.11) give the stress, σ_{f} required to propagate a crack in a brittle material as a function of the size of the microcrack.

It is well-established that even metals which fail in a completely brittle manner have undergone some plastic deformation prior to fracture. Therefore, in the strictest sense, Grittith's equation for the fracture stress does not apply for metals. Orowan [4] suggested that the Griffith equation would be made more compatible with brittle fracture in metals by the inclusion of a term expressing the plastic work required to extend the crack wall, γ_{p}. In this case, Eq. (13.11a) is modified as follows:

$$\sigma_{\mathrm{f}} = \left[\frac{2E\left(\gamma + \gamma_{\mathrm{p}}\right)}{\pi c}\right]^{1/2} \approx \left(\frac{E\gamma_{\mathrm{p}}}{c}\right)^{1/2} \,. \tag{13.12}$$

The surface energy term can be neglected since estimates of the plastic-work term are about 10^2 to $10^3\,\mathrm{J/m^2}$ compared with values of about $1\,\mathrm{J/m^2}$ for γ.

13.3 Fracture Mechanics

Fracture mechanics seeks to describe the relative toughness of engineering materials under conditions similar to those encountered in engineering practice. In considering this subject we shall use the approach of Irwin [5] as described by Read-Hill [6], who considers the work done in moving a crack a small distance, Δx, in order to determine the effective force resisting its movement. In computing this work, he assumes, for ease of presentation, that the crack moves backward and closes rather than opens. Thus, we assume that Fig. 13.2a represents one end of a crack that extends through the thickness of an infinitely wide plate of unit thickness, and that the plate is loaded by a uniform tensile stress σ. As indicated in Fig. 13.2b, a tensile stress, σ_{yy}, is applied in the y-direction on the upper and lower surfaces of the crack over a distance, Δx measured from the crack tip. This stress will close up the crack over the distance Δx if σ_{yy} is increased at all points to the same value that it had when the crack was originally at point a. The extension of the crack from point a to point b is shown in Fig. 13.2c.

Considering a small element, dx of the interval Δx, as shown in Fig. 13.2c, the opposite sides of this element move through a distance $2Y$ as the crack closes. Elasticity theory assumes that the displacement of the crack surfaces varies linearly with the hypothetical stress σ_{yy} applied to the crack surfaces. The work done on the small element dx, as σ_{yy} is raised to the value that closes the crack, is then:

$$\mathrm{d}W = \frac{2Y}{2}\sigma_{yy}\,\mathrm{d}x = Y\sigma_{yy}\,\mathrm{d}x\,, \tag{13.13}$$

and the work required to close the crack over the entire distance Δx is:

$$\Delta W = \int_0^{\Delta x} Y\sigma_{yy}\,\mathrm{d}x\,. \tag{13.14}$$

We further assume that the material ahead of the crack is subjected to a condition of plane stress. As discussed in Sect. 12.1, this means that the stress component, σ_{zz}, parallel to the edge of the crack is zero so that all the stress components lie in the plane of the plate. With this condition, elasticity theory predicts that:

$$\sigma_{yy} = \frac{\sigma\sqrt{c}}{\sqrt{2x}}\,, \tag{13.15}$$

and

$$Y = \frac{2\sigma\sqrt{c}}{E}\sqrt{2\,(\Delta x - x)}\,, \tag{13.16}$$

where x is the distance measured from point a in Fig. 13.2c, c is the half-crack length, and σ is the applied external stress. Evaluation of ΔW in Eq. (13.14) gives:

$$\Delta W = \frac{\sigma^2 c\pi\Delta x}{E}\,. \tag{13.17}$$

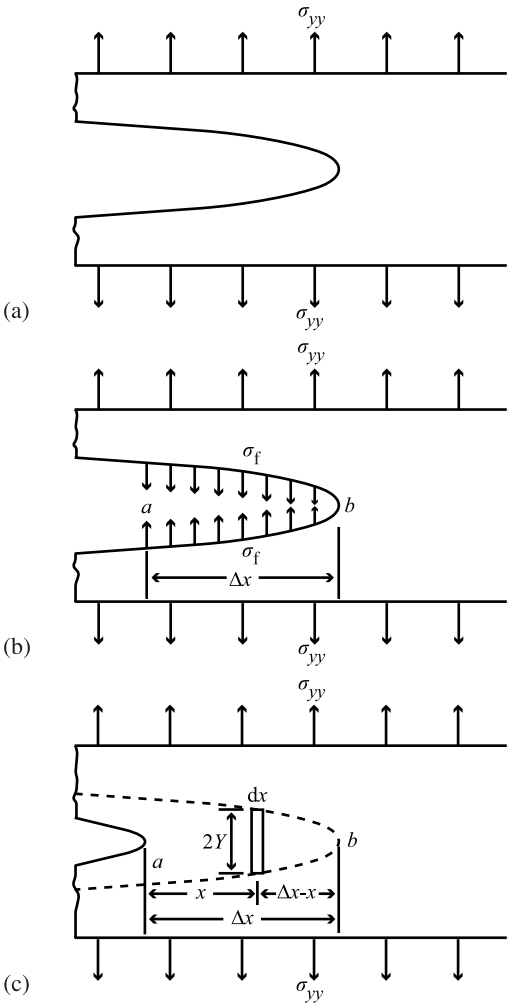

Fig. 13.2. Illustration of the Irwin method for determining the conditions for fracture (adapted from [6])

Since the derivative of the work with respect to the distance corresponds to a force, Irwin defines a *crack extension force* as:

$$G = \frac{\Delta W}{\Delta x} = \sigma_f^2 \frac{c\pi}{E}\,, \tag{13.18}$$

where σ_f is the applied stress at fracture. This force may be considered as that necessary to move the crack through the metal. Note that if this expression is compared to the Griffith relationship given in Eq. (13.11a), we have:

$$G = \frac{\sigma_f^2 c\pi}{E} = 2\gamma\,, \tag{13.19}$$

which suggests that the force per unit length exerted on the crack front as it advances is equal to twice the specific surface energy, γ. This result is expected since, according to the Griffith concept, the work expended in advancing the crack is converted into the surface energy of the two crack surfaces.

In this example, the Irwin analysis has been applied to a crack in a brittle elastic solid where its movement does not involve plastic deformation ahead of the crack. However, the Irwin approach can also be applied to problems where crack advance involves plastic deformation, in which Eq. (13.19) becomes::

$$G = 2(\gamma_p + \gamma)\,, \tag{13.20}$$

where γ is the true surface energy and γ_p is the plastic work per unit area involved in the creation of the surface. However, as described earlier, in most practical examples, $\gamma_p >> \gamma$, and γ can be neglected in comparison to γ_p, so that:

$$G \approx 2\gamma_p\,. \tag{13.21}$$

In Eq. (13.21), the right hand side of the equation represents the energy per unit plate thickness to make a crack grow in an elastic solid. Accordingly it is called the *crack resistance force* and is designated by R. So, crack growth begins when the critical energy release rate, G_c equals the crack resistance force R. Since R represents the rate at which energy is expended in growing a crack, then:

$$R = \mathrm{d}W/\mathrm{d}c = 2\gamma\,. \tag{13.22}$$

As indicated above for fracture in a brittle elastic plate, the vertical component of the stress ahead of the crack is given by the expression:

$$\sigma_{yy} = \frac{\sigma\sqrt{c}}{\sqrt{2x}}\,, \tag{13.23}$$

where x is the distance ahead of the crack. Note that in the numerator of the term on the RHS of the equation we have the product of the applied stress, σ, and the square root of c, the half-crack length. These two factors determine the general level of the stress at points ahead of the crack. The larger the applied stress or the greater the crack length, the more severe will be the stress at any point in front of the crack. Because of this, it is common practice in fracture analysis to use a parameter known as the *stress intensity factor*, which contains the product $\sigma\sqrt{c}$. In the case of a crack in a brittle elastic plate where the stress components ahead of the crack correspond to a condition of plane stress, the stress intensity factor K is defined as:

$$K = \sigma\sqrt{c\pi}\,. \tag{13.24}$$

At this point, it is convenient to define the three basic modes of fracture, as shown in Fig. 13.3. Mode *I* corresponds to fracture where the crack surfaces are displaced normal to themselves. This is a typical tensile type of fracture. In the second mode, Mode *II*, the crack surfaces are sheared relative to each other in a direction normal to the crack front; while in Mode *III*, the shearing action is parallel to the crack front.

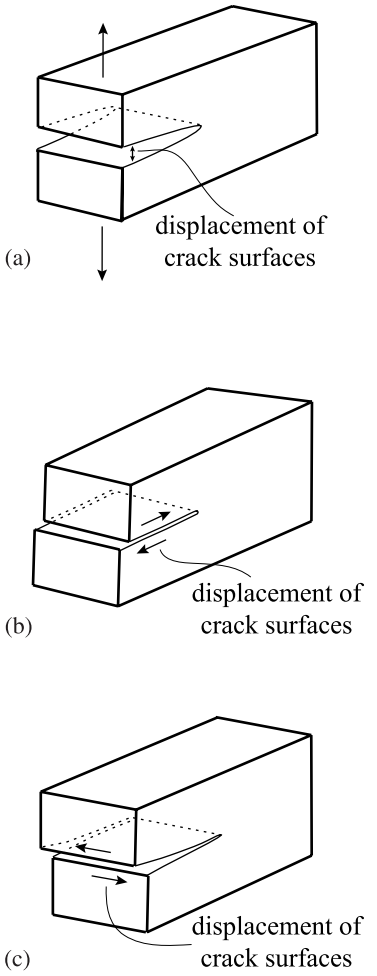

Fig. 13.3. The three basic modes of fracture (a) Mode I, tensile, (b) Mode II, shear in the direction normal to the crack front, and (c) Mode III, shear in the direction parallel to the crack front

The stress field around a crack in a solid depends on the mode. In the case of Mode *I* fracture in a plate with a center crack of length $2c$, the equations are expressed in terms of polar coordinate, r and θ, where r is the distance in the xy-plane from the crack tip to an element in space, and θ is the angle between r and the x-axis (as shown in Fig. 13.4):

$$\sigma_{xx} = \sigma(c/2r)^{1/2}\cos\frac{\theta}{2}\left[1-\sin\frac{\theta}{2}\cos\frac{3\theta}{2}\right]$$

$$\sigma_{yy} = \sigma(c/2r)^{1/2}\cos\frac{\theta}{2}\left[1+\sin\frac{\theta}{2}\cos\frac{3\theta}{2}\right]$$

$$\sigma_{zz} = 0\,, \quad \text{for plane stress crack growth}$$

$$\sigma_{zz} = \nu(\sigma_{xx}+\sigma_{yy})\,, \quad \text{for plane strain crack growth} \tag{13.25}$$

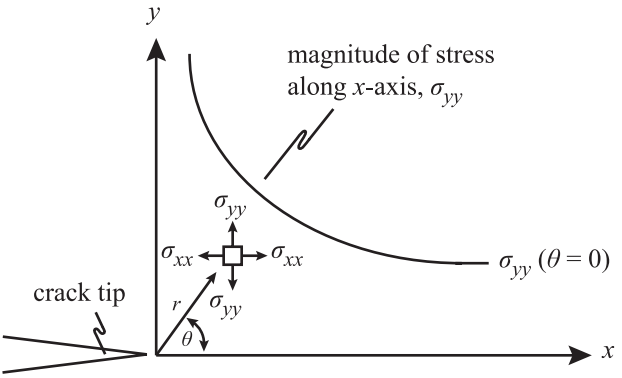

Fig. 13.4. Coordinate system for description of the stress field ahead of the crack as given by Eq. (13.25)

$$\sigma_{xy} = \sigma(c/2r)^{1/2} \sin\frac{\theta}{2}\cos\frac{\theta}{2}\cos\frac{3\theta}{2}$$
$$\sigma_{yz} = \sigma_{xz} = 0\,. \tag{13.25}$$

These equations are valid within a limited region around the crack tip. The stress field can be written in terms of the stress intensity factor using Eq. (13.24). For Mode *I*, the stress field around a crack trip is written as follows:

$$\sigma_{xx} = K_{\mathrm{I}}/(2\pi r)^{1/2}\cos\frac{\theta}{2}\left[1 - \sin\frac{\theta}{2}\cos\frac{3\theta}{2}\right]$$
$$\sigma_{yy} = K_{\mathrm{I}}/(2\pi r)^{1/2}\cos\frac{\theta}{2}\left[1 + \sin\frac{\theta}{2}\cos\frac{3\theta}{2}\right]$$
$$\sigma_{xy} = K_{\mathrm{I}}/(2\pi r)^{1/2}\sin\frac{\theta}{2}\cos\frac{\theta}{2}\cos\frac{3\theta}{2}\,. \tag{13.26}$$

When the applied stress is raised to the point where the crack is able to move rapidly, a critical value of the stress intensity factor is obtained above which unstable crack propagation occurs. This condition is written:

$$K_{\mathrm{c}} = \sigma_{\mathrm{f}}\sqrt{c\pi}\,. \tag{13.27}$$

The quantity K_{c} is called the *fracture toughness* and is rather simply related to the crack extension force:

$$G_{\mathrm{c}} = \frac{\sigma_{\mathrm{f}}^2 c\pi}{E} = \frac{K_{\mathrm{c}}^2}{E}\,, \tag{13.28}$$

for the case of plane stress, and for plane strain, Eq. (13.28) becomes:

$$G_c = \frac{\sigma_f^2 c\pi(1-\nu^2)}{E} = \frac{K_c^2(1-\nu^2)}{E} \,. \tag{13.29}$$

Both G_c and K_c may be considered to be parameters that measure the resistance of a metal to crack extension. It is important to note, however, that the relations between G_c and K_c refer specifically to a particular set of fracture conditions: where the crack advances elastically in a plate under the action of a simple tensile stress, and the stress components in front of the crack correspond to a condition of either plane stress or plane strain. For other fracture conditions, the relationship between G_c and K_c will normally be different. In fact, from Eq. (13.21), we can write:

$$G_c = \frac{\sigma_f^2 c\pi(1-\nu^2)}{E} = 2\gamma_p = R \,. \tag{13.30}$$

For fracture in Mode I loading, it is normal practice to add the subscript I to the symbols K_c and G_c. The relationship given earlier is, accordingly, more properly written:

$$G_{Ic} = \frac{\sigma_f^2 c\pi}{E} = \frac{K_{Ic}^2}{E} \quad \text{or} \quad G_{Ic} = \frac{K_{Ic}^2(1-\nu^2)}{E} \,. \tag{13.31}$$

The crack tip stresses due to an applied stress can result in plastic flow at the tip of the crack. The plastic zone ahead of the crack tip is kidney-shaped with lobes extending above and below the plane of fracture. A cross section through the plastic zone in the xy-plane is shown in Fig. 13.5. The extent of the zone in the crack plane (xz-plane in Fig. 13.5) is often used as an estimate of the plastic zone size. Using the expression for σ_{yy} in Eq. (13.26) and evaluating it at $\theta = 0$ gives $\sigma_{yy} = K_I/(2\pi r_p)^{1/2}$. Solving for r_p and using $\sigma_{yy} = \sigma_y$ for plane stress and $\sigma_{yy} = \sqrt{3}\sigma_y$ for plane strain,

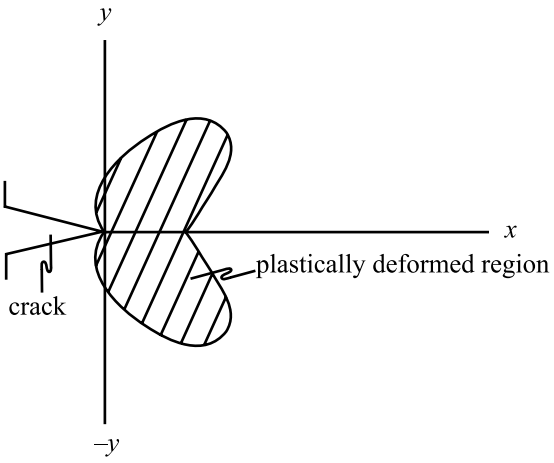

Fig. 13.5. Cross section (in the xy-plane) of the plastic zone in front of a crack tip

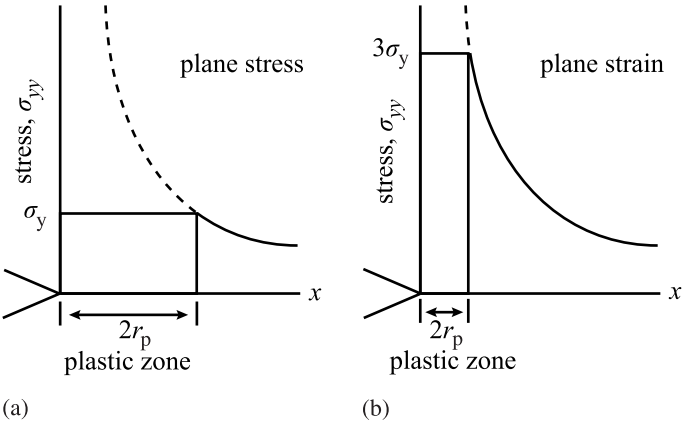

Fig. 13.6. Stress distribution ahead of a crack assuming that σ_{yy} cannot exceed σ_y for the cases of (a) plane stress and (b) plane strain

where σ_y is the yield stress, gives:

$$r_p = K_I^2/2\pi\sigma_y^2\,; \quad \text{plane stress} \tag{13.32}$$

$$r_p = K_I^2/6\pi\sigma_y^2\,; \quad \text{plane strain}\,. \tag{13.33}$$

Figures 13.6 shows the stress distributions ahead of the crack in plane stress (a), and plane strain (b), assuming that the stress σ_{yy} does not exceed the yield stress, σ_y. Note that the plastic zone size in the case of plane strain is about a factor of 3 less than that in plane stress as dictated by Eqs. (13.32) and (13.33).

13.4 Fracture Mechanics Tests

The objective of a fracture mechanics test is to determine the fracture parameters describing the resistance of the metal to crack advance. The Mode *I* fracture toughness is such a parameter and standard sample design and test methods have been developed to determine the plane strain fracture toughness of a metal. This standardized method is described by ASTM standard E399 [7] and applies to two sample designs, the 3-point loaded notched beam specimen and the compact tension specimen. The compact tension specimen is a common sample design and is shown in Fig. 13.7. Plane strain fracture toughness measurements rely on the validity of *linear elastic fracture mechanics* (LEFM). That is, Eq. (13.26) are assumed to be valid during plane strain fracture as they were derived using elasticity theory and do not account for plasticity. Therefore, for LEFM to hold, the size of the plastic zone, as given by Eq. (13.33) ahead of the crack tip must be small. Since $r_p \alpha 1/\sigma_y^2$, the yield strength plays a large role in the size of the plastic zone, and hence, the validity of the test. ASTM standard E399 requires that the thickness of the sample be of a minimum

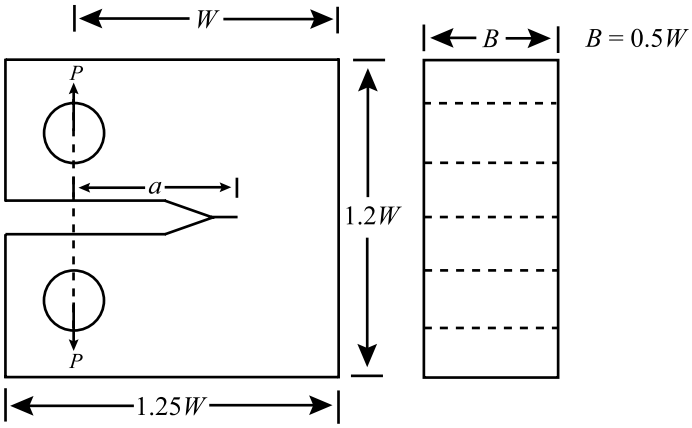

Fig. 13.7. ASTM compact tension sample design for plane strain fracture toughness measurements

size in order to ensure plane strain fracture. That size is given as:

$$B \geq 2.5(K_{\mathrm{Ic}}/\sigma_{\mathrm{y}})^2 \,, \tag{13.34}$$

where B is the specimen thickness. In addition, the size of the ligament, which is the length of uncracked material in the sample defined by $(W - a)$ in Fig. 13.7, must also be larger than the plastic zone size by the same amount as the sample thickness, B and the crack length, resulting in the following size requirements:

$$\begin{aligned} a &\geq 2.5(K_{\mathrm{Ic}}/\sigma_{\mathrm{y}})^2 \\ B &\geq 2.5(K_{\mathrm{Ic}}/\sigma_{\mathrm{y}})^2 \\ W &\geq 5.0(K_{\mathrm{Ic}}/\sigma_{\mathrm{y}})^2 \,, \end{aligned} \tag{13.35}$$

where a is used here to denote crack length. Note that Eq. (13.35) require a value for K_{Ic} in order to determine validity of the sample that will be used to measure K_{Ic}. So in practice, the magnitude of K_{Ic} is estimated in order to determine if the sample made from the metal to be tested will meet the requirements of Eq. (13.35). For a compact tension specimen, the stress intensity factor can be written in terms of the applied load, P, the sample dimensions, B and W and the ratio of crack length to sample width, a/W, and has the following form:

$$K = \frac{P}{BW^{1/2}} \times \\ \times \frac{\left(2 + \frac{a}{W}\right)\left[0.886 + 4.64\left(\frac{a}{W}\right) - 13.32\left(\frac{a}{W}\right)^2 + 14.72\left(\frac{a}{W}\right)^3 - 5.6\left(\frac{a}{W}\right)^4\right]}{\left(1 - \frac{a}{W}\right)^{3/2}} \,, \tag{13.36}$$

where the first term on the RHS is essentially the applied stress, and the second term reflects the effect of crack length.

13.5 Elastic-Plastic Fracture Mechanics

The determination of plane strain fracture toughness depends on the validity of LEFM for the particular test. If the yield strength is very high and the sample thickness is great enough, LEFM is satisfied. However, the low strength and high toughness for most metals (even in the irradiated state) requires thicknesses that could approach a meter in order to satisfy LEFM. When the plastic zone size in a sample is large enough to distort the elastic stress field, determination of fracture toughness using K_{Ic} is impractical. To obtain a measure of the resistance of a metal to fracture when significant plasticity is involved, other methods have been developed. The *J integral* and *crack opening displacement* methods as described by Read-Hill [8], is one such method that will be briefly reviewed.

The J integral proposed by Rice is a method for characterizing the stress-strain field at the tip of a crack by an integration path taken sufficiently far from the crack tip to be substituted for a path close to the crack tip region.

Formally, the J integral is defined for either elastic or elastic-plastic behavior as:

$$J = \int_{\zeta} W \,\mathrm{d}y - T\left(\frac{\partial u}{\partial x}\right)\mathrm{d}x\,, \tag{13.37}$$

where ζ is a contour around the crack tip, taken in a counterclockwise direction, W is the strain energy density ($\int_0^{\varepsilon} \sigma\,\mathrm{d}\varepsilon$), T is the traction vector normal to an element $\mathrm{d}s$ of the path ζ ($T_i = \sigma_{ij} n_{ij}$) and u is the displacement vector, Fig. 13.8a.

From a more physical viewpoint, J is the potential energy difference between two identically loaded bodies having slightly different crack lengths, or:

$$J = -\,\mathrm{d}V/\mathrm{d}c\,, \tag{13.38}$$

where V is the potential energy of the system, J is the negative of the rate of change of the potential energy with respect to the change in crack length. In experiments, $\mathrm{d}V/\mathrm{d}c$ is determined by plotting the load-displacement curves of two specimens with different initial crack lengths. As shown in Fig. 13.8b, loading to a constant load results in crack growth of the crack of initial length c to $c + \mathrm{d}c$, that produces an increment in the displacement, δ. The area between the two $P - \delta$ curves is the energy difference $\mathrm{d}V$ and when divided by $\mathrm{d}c$, gives J.

The crack opening displacement approach assumes that crack growth occurs when the magnitude of the plastic strain at the end of a crack reaches a critical value that depends on the specific metal or alloy. This critical strain can also be used as a failure criterion. The crack tip opening displacement for a crack of length $2c$ in an infinite thin plate subjected to uniform tensile stress, σ in a metal where plastic deformation occurs at the crack tip, Fig. 13.8c, was determined by Dugdale [9] as:

$$\delta_t = \frac{\pi c \sigma^2}{E \sigma_{\mathrm{y}}}\,. \tag{13.39}$$

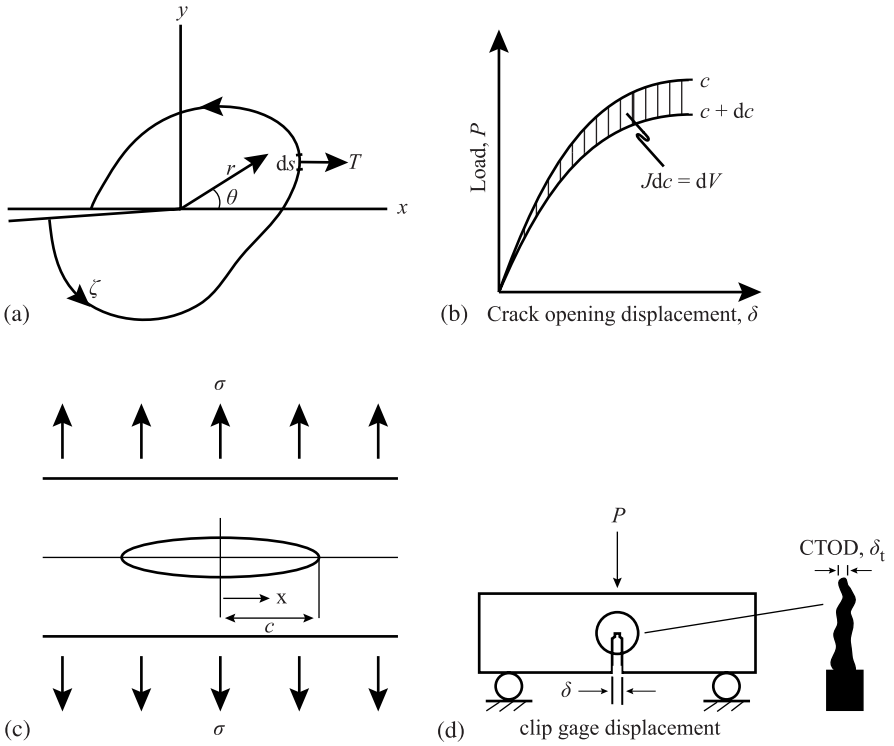

Fig. 13.8. (a) Crack-tip geometry and line integral contor. (b) Load-displacement curves for a constant displacement test on a plate containing cracks with slightly different initial lengths used to determine the *J* integral. (c) Crack geometry for COD analysis. (d) COD test setup in which displacement is measured using a clip gage

Re-writing the expression for the crack extension force, Eq. (13.31) by dividing both sides by σ_y gives:

$$\frac{G}{\sigma_y} = \frac{\pi c \sigma_f^2}{E \sigma_y} , \tag{13.40}$$

and substituting Eq. (13.39) into Eq. (13.40) gives:

$$G = \sigma_y \delta_t , \tag{13.41}$$

resulting in the following expression for the stress in terms of the critical crack tip opening displacement, δ_{ct} for fracture:

$$\sigma_f = \left(\frac{E}{\pi c} \sigma_y \delta_{ct} \right)^{1/2} . \tag{13.42}$$

The *crack opening displacement* (COD), δ at a distance x from the center of the crack is related to the crack tip opening displacement, δ_t by:

$$\delta = \frac{4\sigma}{E}\sqrt{c^2 - x^2 + E^2\delta_t^2/16\sigma^2}\,, \tag{13.43}$$

and can be measured by a clip gage attached to the faces of the sample, as shown in Fig. 13.8d, resulting in the load-displacement curve shown in Fig. 13.8b. Note that $x = 0$ when the measurement is taken on the surface of the sample shown in Fig. 13.8c.

For linear elastic behavior, the J integral is identical to G. Therefore, a J failure criterion for the linear elastic case is identical to the K_{Ic} failure criterion, so that for linear elastic plane strain conditions:

$$J_{Ic} = G_{Ic} = \frac{(1-\nu^2)K_{Ic}^2}{E}\,. \tag{13.44}$$

With increasing toughness, many materials do not fail catastrophically at a particular value of J or δ. Rather, they exhibit a gradual increase in J and δ with increasing crack length. A plot of J vs. crack length, c, is termed the *R curve*. Figure 13.9 illustrates a typical R curve for a ductile metal. Initially, the slope is very steep and there is a small amount of apparent crack growth due to tip blunting. As J increases, the material at the tip fails locally and crack advance occurs. A measure of the fracture toughness for elastic-plastic deformation is J_{Ic}, defined as the initiation of stable crack growth. From Fig. 13.9, J_{Ic} occurs when the crack begins to grow, but the precise point where this occurs is often poorly defined, resulting in a somewhat arbitrary definition.

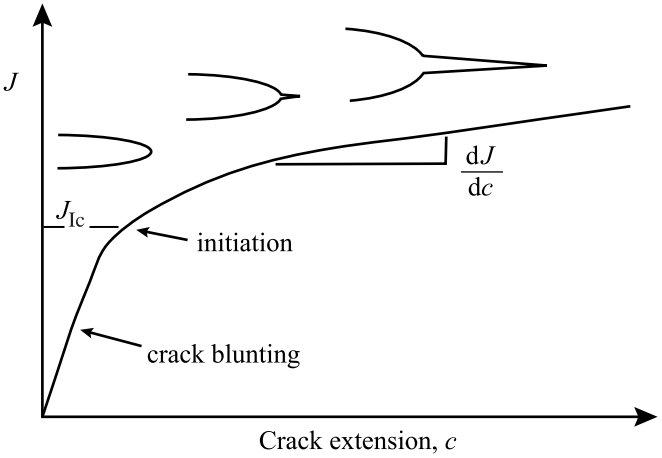

Fig. 13.9. Schematic R curve for a ductile metal (from [10])

13.6 Brittle Fracture

The greatest success of the application of the concept of fracture mechanics has been in the case of brittle fracture. Three basic factors contribute to cleavage-type fracture that is characteristic of brittle fracture: (1) a triaxial state of stress, (2) a low temperature, and (3) a high strain rate. All three of these factors do not have to be present at the same time to produce brittle fracture. A triaxial state of stress, such as exists at a notch, and low temperature are responsible for most service failures of the brittle type. However, since these effects are accentuated at a high rate of loading, many types of tests have been used to determine the susceptibility of materials to brittle fracture.

The process of brittle fracture consists of three stages:

1. Plastic deformation involving the pile-up of dislocations along their slip planes at an obstacle
2. The buildup of shear stress at the head of the pile-up to nucleate a microcrack
3. In some cases the stored elastic strain energy drives the microcrack to complete fracture without further dislocation movement in the pile-up. More typically in metals, a distinct growth stage is observed in which an increased stress is required to propagate the microcrack.

Plastic deformation by dislocation pile-up is treated in a theory of yielding in metals proposed by Cottrell [11]. This theory applies to metals exhibiting a distinct yield point and can be used to determine the fracture stress. Knowledge of both the yield stress and fracture strength permits the conditions for brittle fracture to be deduced.

The lower yield point in bcc metals or in irradiated fcc metals contains contributions due to source hardening and friction hardening. Cottrell assumes that dislocations in a few isolated grains have been unlocked either because the orientation of these grains relative to the load is such as to produce the maximum resolved shear stress on active slip planes or because a few sources in these grains have particularly low unpinning stresses. In either case, the dislocations produced in the prematurely yielded grains pile up against the grain boundary. The enhanced shear stress in the neighborhood of the pile-up triggers the sources in the adjacent grain. As such, yielding propagates across the entire specimen as the material flows.

The shear stress exerted on the slip plane in a grain next to one that has yielded and released an avalanche of dislocations which are stopped by the grain boundary is shown in Fig. 12.5. The shear stress acting on the sources in grain 2 consists of two components, the applied shear stress σ_a and the shear stress due to the proximity of the pile-up in grain 1. The latter is given in Eq. (12.62), which is re-written as:

$$\sigma_2 = \left(\frac{d}{r}\right)^{1/2} (\sigma_a - \sigma_i) \tag{13.45}$$

where σ_a is reduced by σ_i to account for the friction stress experienced by dislocations in the pile-up in grain+1. Writing Eq. (13.45) in terms of the applied stress and grouping terms containing $d^{-1/2}$ yields the Hall–Petch equation for the effect

of grain size on yielding, Eq. (12.63), $\sigma_y = \sigma_i + k_y d^{-1/2}$, where the second term on the right gives the source-hardening contribution to the yield stress.

Zener first proposed that the idea that the high stresses produced at the head of a dislocation pile-up could produce fracture [12]. The model is shown in Fig. 13.10. The shear stress acting on the slip plan squeezes the dislocations together. At some critical value of stress the dislocations at the head of the pile-up are pushed so close together that they coalesce into a wedge crack or cavity dislocation of height nb and length $2c$. Stroh [13] has shown that provided the stress concentration at the head of the pile-up is not relieved by plastic deformation, and then the tensile stress at the pile-up is given by:

$$\sigma = (\sigma_a - \sigma_i)\left(\frac{L}{r}\right)^{1/2}, \tag{13.46}$$

where σ_a is the applied shear stress, L is the length of the blocked slip band and r is the distance in the slip plane from the lead dislocation. Equation (13.46) (similar to Eq. (13.45)) can be equated with the theoretical cohesive strength, Eq. (13.7):

$$(\sigma_a - \sigma_i)\left(\frac{L}{r}\right)^{1/2} = \left(\frac{E\gamma}{a}\right)^{1/2}, \tag{13.47}$$

such that microcrack nucleation occurs at:

$$\sigma_a - \sigma_i = \left(\frac{Er\gamma}{La}\right)^{1/2}. \tag{13.48}$$

If we let and $r \approx a/2$ and $E \approx 2\mu$ then Eq. (13.48) becomes:

$$\sigma_a - \sigma_i = \left(\frac{2\mu\gamma}{L}\right)^{1/2}. \tag{13.49}$$

But from Eq. (12.58), the number of dislocations in the slip band can be expressed as:

$$n \approx 2(\sigma_a - \sigma_i)\frac{L}{\mu b}, \tag{13.50}$$

so eliminating L from Eqs. (13.49) and (13.50) gives:

$$(\sigma_a - \sigma_i)nb \approx 2\gamma. \tag{13.51}$$

This form of the equation for microcrack nucleation was proposed by Cottrell [11]. It has the direct physical significance that a crack will form when the work done by the applied shear stress in producing a displacement nb equals the work done in moving the dislocations against the friction stress plus the work in producing the new fracture surfaces. In terms of the normal stress:

$$\sigma(nb) \approx 4\gamma. \tag{13.52}$$

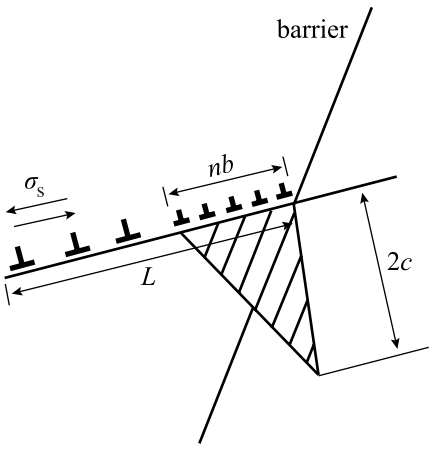

Fig. 13.10. Schematic of the formation of a microcrack at a pile-up of edge dislocations against a barrier

Assuming that the dislocation source is at the center of a grain of diameter d, so that $L = d/2$, and substituting Eq. (13.51) into Eq. (13.52) gives:

$$\sigma(\sigma_a - \sigma_i) = \frac{4\mu\gamma_s}{d} \,. \tag{13.53}$$

But since at the yield stress, σ_y is identified with σ_a and $(\sigma_y - \sigma_i) = k_y d^{-1/2}$ (see Eq. (12.63)), then from Eq. (13.32) we have the Cottrell–Petch equation:

$$\sigma = \sigma_f = \frac{4\mu\gamma}{k_y} d^{-1/2} \,. \tag{13.54}$$

This equation represents the stress required to propagate a microcrack of length d in brittle fracture.

The dependence of yield stress and fracture stress on grain size typical of a low-carbon steel are plotted in Fig. 13.11. Note that the two lines cross at a particular value of d and σ, and this intersection is the ductile-to-brittle transition. To the left of the transition, fracture and yielding occur simultaneously. However, the fracture occurs at the yield stress since in our model, yielding must occur first. To the right of the transition, yielding occurs first and the incremental strain between σ_f and σ_y is due to work hardening of the metal. During this process, the metal is deforming plastically and the fracture stress increases with decreasing d. The parameter, k_y determines the number of dislocations that are released into a pile-up when a source is unlocked. Materials with a high value of k_y (e.g., ferritic steels and molybdenum) are more prone to brittle fracture than materials with lower values (e.g., niobium and tantalum). In bcc metals, the frictional resistance increases rapidly as the temperature falls below room temperature and thus leads to a ductile-to-brittle transition.

The Cottrell–Petch theory provides an explanation of why irradiation embrittles steels. The irradiation-induced defects and defect clusters raise the frictional component to the yield stress, σ_i by increasing the resistance to dislocation motion. However, in unirradiated bcc metals, the sources are strongly pinned by impurity

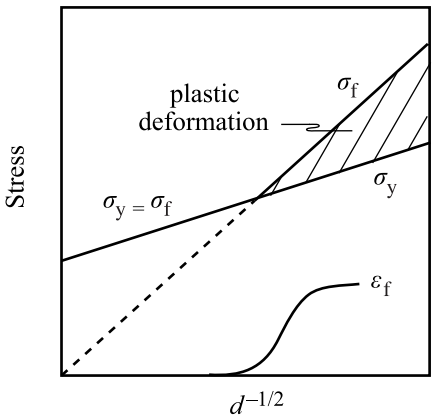

Fig. 13.11. Effect of grain size on yield and fracture stress of a typical low-carbon steel tested at low temperature

atoms in the absence of neutron-produced point defects (resulting in the upper and lower-yield point phenomenon), so irradiation has only a small effect on k_y. The net effect of these different dependencies on irradiation is that the yield strength is increased much more than the fracture strength. Figure 13.12 shows the effect of irradiation on the temperature dependence of the yield and fracture strengths. Note that the increase in the yield strength due to irradiation displaces the temperature at which brittle fracture occurs to higher temperatures. The drastic loss in ductility at low temperature results from the different sensitivities of σ_y and σ_f to neutron damage. The *ductile-brittle transition temperature* (DBTT) or the *nil-ductility temperature* (NDT) is defined by the condition that $\sigma_f = \sigma_y$, which from Eq. (13.54) is:

$$\sigma_y k_y = 4\mu\gamma d^{-1/2} . \tag{13.55}$$

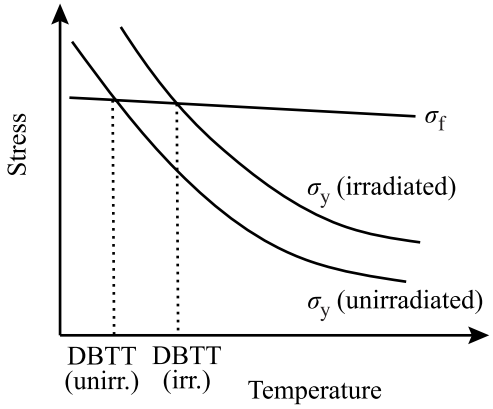

Fig. 13.12. The relationship between temperature dependence of yield stress and fracture strength and the ductile-to-brittle transition temperature

Table 13.1. Effect of irradiation on parameters in the Cottrell–Petch Eq. (13.56) after [14]

Term	Description	Effect of irradiation
σ_y	Yield stress	Increase
$\Delta\sigma = \sigma_f - \sigma_y$	Stress increment for fracture	Decrease
β	Triaxiality of applied stress	.....
μ	Shear modulus	.....
γ_e	Effective surface energy $(\gamma + \gamma_p)$	Decrease
d	Grain size	.....
k_y	Petch slope	Decrease (d large) Little change (d small)
M	Taylor orientation factor	Increase (?) due to channeling
σ_c	Source operating stress	Increase
r	Distance from source to pile-up	Decrease (?) due to channeling

Bement [14] has written the Cottrell–Petch equation for the fracture stress as:

$$\sigma_f = \frac{\beta\mu\gamma_e}{k_S} d^{-1/2} , \tag{13.56}$$

where β is a constant related to the degree of triaxiality of the applied stress, γ_e is the effective surface energy of the crack $(\gamma + \gamma_p)$ and $k_S = M^{-1}k_y$, where M is the Taylor orientation factor and k_y is the constant expressing the grain boundary contribution to the strength in the Hall–Petch expression given in Eq. (12.63).

From the Cottrell–Petch equation an irradiation-induced increase in yield strength, increase in k_S, or decrease in the effective surface energy, γ_e can promote embrittlement. Since the fracture stress, σ_f is not greatly affected by irradiation and is much less dependent upon temperature than is σ_y, the above irradiation-induced property changes can also cause a significant increase in the DBTT (under the criteria $\sigma_y = \sigma_f$) [15] as expressed by:

$$T_c = C^{-1}\left[\ln Bk_s d^{1/2}/(\beta\mu\gamma - k_y k_s)\right] , \tag{13.57}$$

where B and C are constants for expressing the temperature dependence of σ_i (neglecting long-range stresses) given by:

$$\sigma_i = B\exp(-CT) , \tag{13.58}$$

with T as the absolute temperature.

The expected effects of irradiation on the individual parameters of the Cottrell–Petch equation are given by Bement in Table 13.1. Although σ_y definitely increases with irradiation, which alone accounts for a substantial shift in the ductile-brittle transition temperature for steel, the effects of residual elements and dislocation channeling on σ_i and k_S are not as well-established.

Investigations of the effects of irradiation on the Hall–Petch relationship for iron, steel, and molybdenum have given varying results; however, the trend indicates that there is little effect of irradiation on k_y, at relatively small grain size

($d^{-1/2} > 4\,\mathrm{mm}^{-1/2}$) and a reduction of k_y, to small values at larger grain sizes. Irradiation of Armco-iron (50 μm grain size) to a dose of $3 \times 10^{18}\,\mathrm{n/cm^2}$ ($E > 1\,\mathrm{MeV}$) at 50 °C results in a decrease in k_y from $396\,\mathrm{MPa}(\mu\mathrm{m})^{1/2}$ to $305\,\mathrm{MPa}(\mu\mathrm{m})^{1/2}$ [16]. The significant reduction in k_y for large grain size occurs at neutron fluences greater than $\sim 10^{18}\,\mathrm{n/cm^2}$, which is the threshold for large increases in yield strength and correspondingly large increases in the ductile-brittle transition temperature. At these neutron exposures well-defined defect clusters and dislocation channels are observed in the electron microscope.

Contrary to observations, dislocation channeling might be expected to increase the value of k_y by restricting dislocation cross slip and by restricting the number of operating slip systems required to maintain continuity across grain boundaries. It is possible that in fine-grained material radiation defect clusters offer little additional impedance to forced slip near the boundaries in accordance with Johnson's model for k_y [17] and that in coarse-grained material the contributions of long-range stresses due to dislocation pile-ups at channel intersections or other barriers (such as carbides) override back stresses due to boundaries. That is, the flow stress becomes grain-size independent of k_y on post-yield strain and the amount of dislocation multiplication that occurs during channel formation is not known, so that grain size effects on the yielding and fracture of irradiated bcc metals are still uncertain.

From the above analysis, not only the assumption for the number of coalesced dislocations, nb in the wedge crack but also the surface energy term is important to the application of fracture models. The surface energy is also a critical parameter in the analysis of the propagation of existing cracks as described by the theories of Griffith [2], Orowan [4], and Irwin [5]. Reduction in the plane strain fracture toughness, K_{Ic}, for irradiated steel [18] would result partly from reduction in the critical crack extension force, $G_c = K_{Ic}^2/E$ which would result from reduction in effective surface energy ($G_c = 2\gamma_e$ when $\sigma = \sigma_f$).

The effective surface energy, γ_e for polycrystalline metals consists of the intrinsic surface energy, γ for a given cleavage plane and a term, γ_p which represents plastic relaxation at the tip of a flaw. Plastic relaxation at a crack tip can occur by either source multiplication or by extensive cross slip and both processes are strongly restricted by radiation damage in the early stages of plastic strain. Therefore, the effective surface energy at yielding should approach the intrinsic surface energy with increasing neutron fluence. However, measurements of γ_e have not been made for irradiated metals.

An extension of fracture theory relative to contributions of the intrinsic surface energy, γ and the plastic work energy, γ_p on cleavage fracture in bcc metals is the work of Stein reported by Bement [14]. It was found that the cleavage plane along which cracks propagate is the one for which the plastic work is the least and is not the one determined by differences in the intrinsic surface energy. If one were to consider two potential fracture planes before irradiation, the cleavage plane having the lowest work energy, γ_p would be the operating plane in cleavage fracture, even though its intrinsic energy, γ might be higher. After irradiation, however, if γ_p approaches a very low value, the intrinsic surface energy might then assume a control-

ling role in cleavage fracture, and the order of preference between the two (or more) potential cleavage planes might be reversed. As yet this possibility is unexplored.

13.7 Irradiation-Induced Embrittlement in Ferritic Steels

Most reactor pressure vessel steels have in common the characteristic of undergoing a transition from ductility to brittle fracture as the temperature is reduced. This transition usually occurs in a temperature range of only about 80 °C [19]. Over this range, the micro- and macroscopic nature of the fracture gradually changes from ductile dimpled rupture to cleavage along crystallographic boundaries with a broad range of mixed fracture modes in between. An important element of assessing the fracture characteristics of irradiated pressure vessel steels is the notched bar impact test. This test and the interpretation of its outcome in terms of the fracture mechanisms are discussed next.

13.7.1 Notched Bar Impact Testing

Despite the development of well-designed fracture mechanics methodology and test samples, the Charpy impact test has historically served as the primary basis for defining radiation effects on ductility. However, the results obtained from notched bar tests, such as the Charpy test, are not readily expressed in terms of design requirements, since it is not possible to measure the components of the triaxial stress condition at the notch. Nevertheless, the Charpy impact test has become widely used throughout the world as a severe test for brittle fracture.

The Charpy specimen has a square cross section (10×10 mm) and contains a 45° V-notch, 2 mm deep with a 0.25 mm root radius (Fig. 13.13). The specimen is supported in a horizontal position and loaded behind the notch by the impact of a heavy swinging pendulum (the impact velocity is approximately 5 m/s). The specimen is forced to bend and fracture at a high strain rate on the order of $10^3\,\mathrm{s}^{-1}$.

The principal measurement from the impact test is the energy absorbed in fracturing the specimen. After breaking the test bar, the pendulum continues on to a height, which decreases as the energy absorbed in fracture increases. The energy absorbed in fracture, usually expressed in J or ft-lbs, is read directly from a calibrated dial on the impact tester. If the fracture is completely ductile, the energy expended will be high; when it is completely brittle, the energy expended will be low. The energy required for fracture of a Charpy specimen is often designated C_V followed by the value, for example, C_V 41 J or C_{41}. Since the energy-absorbing capacity of the steel varies with temperature, the impact test provides a simple method of following the change in the fracture mode of a steel as a function of temperature. A representative curve, showing the transition from ductile to brittle behavior, is given in Fig. 13.14. One of its important features is that the transition is not sharp but occurs over a range of temperatures. If the fracture surfaces of the impact specimen are examined after fracture, it is generally found that there is a reasonable correlation between the amount of the cross section that has broken in a ductile fashion and the

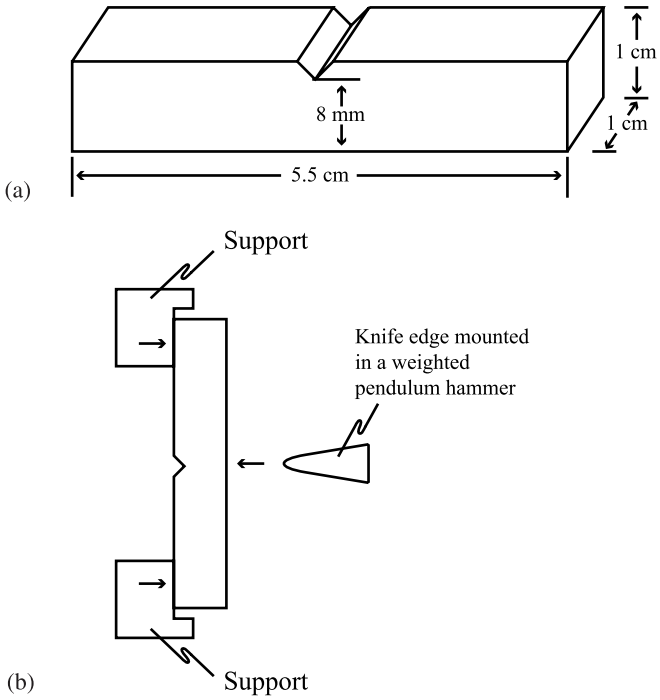

Fig. 13.13. (a) The Charpy V-notch impact test specimen. (b) Method of applying the impact load to the specimen

energy expended in breaking the specimen. Completely ductile specimens exhibit surfaces that are rough or fibrous, while those of brittle specimens contain an irregular array of small bright facets, each corresponding to the surface of a cleaved crystal. In those specimens where the fracture is part ductile and part brittle, the brittle, or bright area is found at the center of the cross section. Two measures of the transition from brittle to ductile behavior are the percent shear fracture and the lateral expansion, and both follow the same dependence on temperature as does the absorbed energy plot given in Fig. 13.14. Therefore, the shift from ductile to brittle behavior can also be followed by examining the fracture surfaces of impact specimens.

The Charpy impact test has been widely used to measure the effect of a number of variables on the brittle-to-ductile transition. The lack of a sharp transition in absorbed energy to mark the separation of ductile and brittle behavior poses a difficulty in interpretation of the Charpy test result. Still, as a matter of convenience, it is common practice to speak of the transition temperature of a metal. This term, however, needs to be carefully defined, as there are a number of different ways of expressing it. One is to take the temperature at which an impact specimen fractures with a half-brittle and half-ductile fracture surface. A second way of defining the transition temperature uses the average energy criterion: the temperature at which the energy absorbed falls to one-half the difference between that needed to fracture

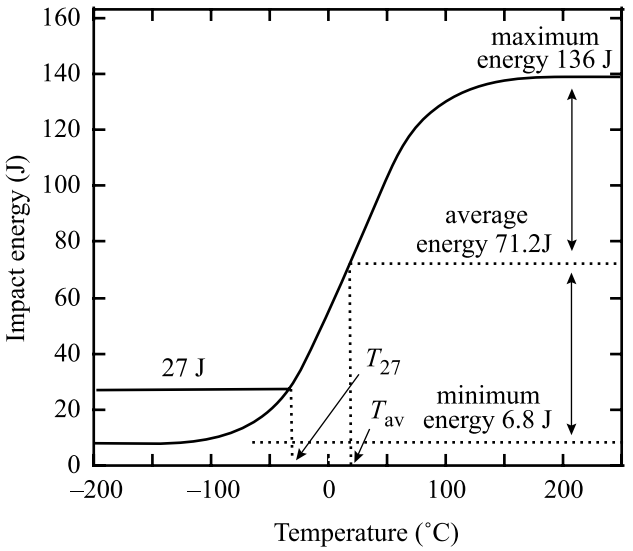

Fig. 13.14. Illustration of the effect of irradiation on the Charpy impact curve for a reactor pressure vessel steels, showing a shift in DBTT and a decrease in the upper shelf energy

a completely ductile specimen, and that needed to fracture a completely brittle specimen. The temperature at which a Charpy specimen breaks with a fixed amount of energy, e.g., 41 J, is also a widely employed basis for the transition temperature. The nil-ductility temperature is defined as the temperature at which fracture initiates with essentially no prior plastic deformation. The true NDT temperature is determined from drop weight tests as prescribed by ASTM E208-95a. From this temperature, the reference temperature, RT_{NDT} is given by $RT_{\mathrm{NDT}} = T_{\mathrm{NDT}} - 60^{\circ}\mathrm{F}$ [20].

Figure 13.15 illustrates the effect of irradiation on a Charpy curve for a typical pressure vessel steel. Note that irradiation causes a shift of the curve to higher temperatures and a reduction in the upper shelf energy (USE). Further, the slope of the curve is reduced with irradiation. All three of these features change with increasing fluence and hardening.

13.7.2 DBTT and Reduction in the Upper Shelf Energy

The shift from ductile to brittle fracture was discussed earlier with the aid of the Hall–Petch relationship. It was shown that the yield strength decreases with temperature and the fracture stress is roughly temperature-independent, so the intersection of the fracture stress curve and the flow stress curve is taken as the ductile-to-brittle transition temperature (DBTT). Irradiation causes an increase in the yield stress, shifting the point at which the fracture stress and flow stress curves intersect to higher temperature, thus increasing the DBTT as was shown in Fig. 13.12. The transition from ductile to brittle behavior is most commonly characterized by the intersection of the Charpy curve with the 41 J line, denoted C_{41}, and the corresponding

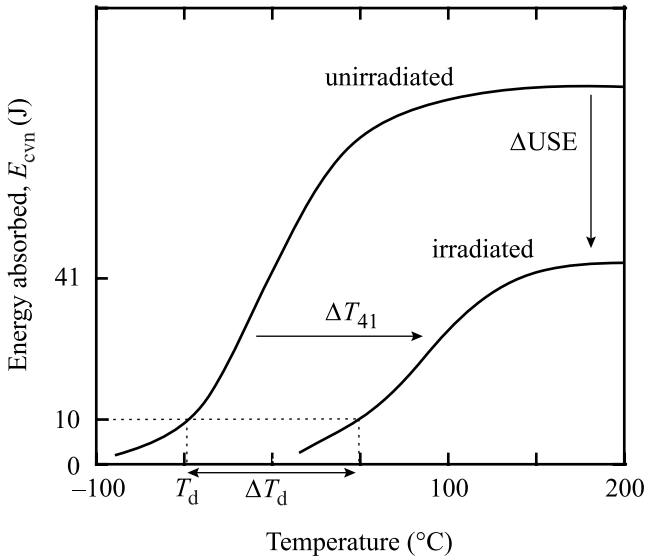

Fig. 13.15. Transition temperature shift as a function of yield stress resulting from irradiation

temperature shift between unirradiated and irradiated condition is designated ΔT_{41}. Odette [21] noted that ΔT_{41} is a non-linear function of $\Delta\sigma_y$, with $\Delta T_{41}/\Delta\sigma_y$ increasing with $\Delta\sigma_y$ and T^* , where T^* is the temperature at which the fracture and flow stress curves intersect. Thus the DBTT increases faster than linear with increases in hardening due to irradiation.

Irradiation-induced segregation of embrittling elements such as phosphorus can also lead to a drop in the fracture stress, causing an additional shift in the DBTT. Phosphorus segregates to grain boundaries during irradiation as described in Chap. 6, where it is believed to reduce grain boundary cohesion, resulting in an increase in the DBTT or a decrease in the lower shelf toughness. The additional increase in the DBTT is shown as ΔT_3 in Fig. 13.16. If both mechanisms are operative, the combined shift of ΔT occurs where the two components are combined by linear addition as in Fig. 13.16.

Irradiation not only increases the DBTT but also reduces the energy absorption for fracture at the ductile shelf of the transition curve (Fig. 13.15). The change in upper shelf energy also appears to result from the increase in yield stress due to irradiation. Figure 13.17 shows the fractional change in upper shelf energy, f with the change in yield stress and is described by:

$$\begin{aligned} f &= 9\times10^{-4}\Delta\sigma_y \quad \text{for} \quad 0<\Delta\sigma_y<40\,\text{MPa} \\ &= 9\times10^{-4}\Delta\sigma_y+\sqrt{0.02\Delta\sigma_y-40} \quad \text{for} \quad \Delta\sigma_y>40\,\text{MPa}\,. \end{aligned} \tag{13.59}$$

In addition to shifting the yield stress curve to higher temperatures, irradiation also reduces the slope of the curve, and represents an additional contribution to

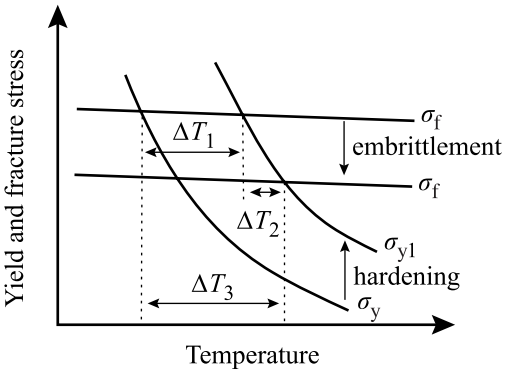

Fig. 13.16. Variation of the yield stress and fracture stress with temperature and irradiation, resulting in independent contributions to the transition temperature shift (from [22])

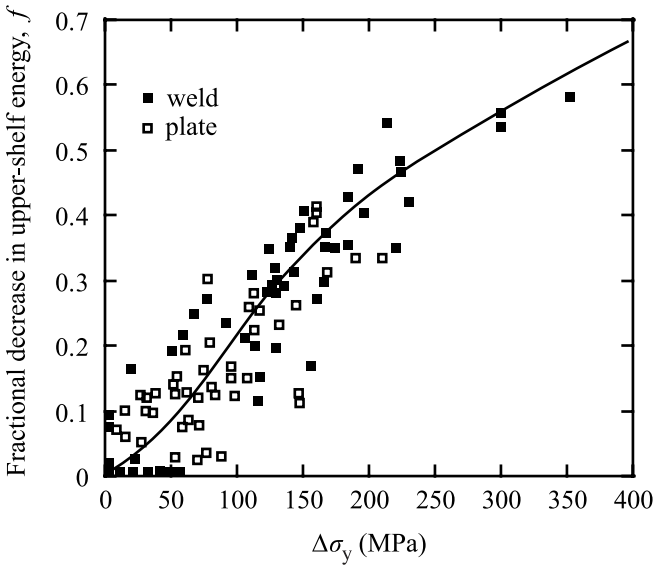

Fig. 13.17. Fractional decrease in the Charpy upper shelf energy as a function of yield strength increase due to irradiation (from [21])

the temperature shift. Odette [21] showed that the energy-temperature slope change can be related to the decrease in the upper shelf energy (E_U), and that the ratio of irradiated to unirradiated upper shelf energy ($f_{E_u} = E_{U,i}/E_U$) empirically correlates with $\Delta\sigma_y$:

$$\Delta T_s(^\circ C) \approx \frac{3720}{E_u}\left(\frac{1-f_{E_u}}{f_{E_u}}\right) . \tag{13.60}$$

The resulting transition temperature can be expressed as:

$$\Delta T = \Delta T_1 + \Delta T_2 + \Delta T_s . \tag{13.61}$$

Decreases in the upper shelf energy have been linked to an increase in the amount of shear fracture on the fracture surface [23]. Nevertheless, the effect of irradiation on the upper shelf energy is believed to be due to a reduction in strain hardening and flow localization leading to lower ductility and an increased triaxial stress state due to strength increases [21]. As discussed in Chap. 12, flow localization in the form of dislocation channeling occurs in irradiated ferritic steels and this may contribute to the reduced ductility in the ductile fracture regime.

13.7.3 Master Curve Approach

Of greatest importance in ensuring the integrity of reactor pressure vessel steels under irradiation is to be able to quantitatively determine how the fracture toughness of the steel is affected by irradiation. Irradiation shifts the fracture toughness curve to higher temperatures. Figure 13.18 shows that the effect of irradiation is to displace the fracture toughness curve to the right on the temperature scale. Interestingly, the shape of the curve is similar before and after irradiation. In fact, it has been observed that over a range of ferritic steels, the fracture toughness transition curves have a characteristic shape. The fixed shape implies that the fracture toughness for these materials can be described by a series of curves that differ only in their location on the temperature scale. This is the basis for the *Master Curve* concept. According to this concept a fracture toughness curve can be determined by a single parameter that fixes the position of the Master Curve on the temperature scale. This parameter is termed, T_0 and is defined as the temperature at which the median fracture toughness for a 1T (25.4 mm thick) fracture toughness specimen

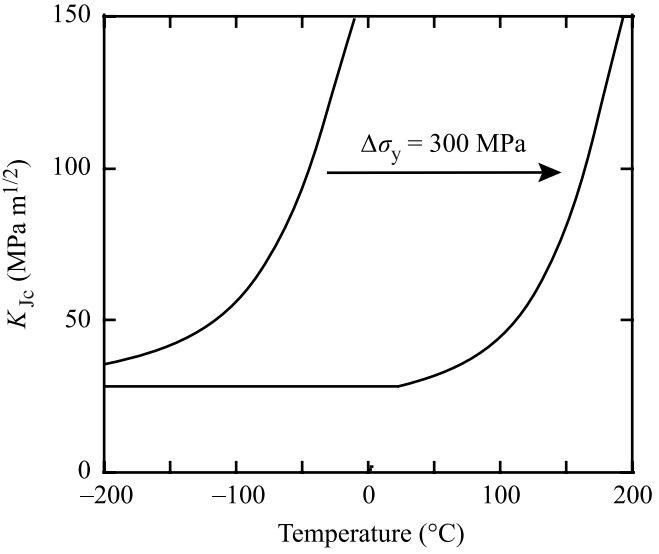

Fig. 13.18. Displacement of the fracture toughness curve with irradiation

equals 100 MPa m$^{1/2}$ (91 ksi in$^{1/2}$). The Master Curve is given as:

$$K_{\mathrm{Jc(med)}} = 30 + 70\exp(0.019(T - T_0)) \tag{13.62}$$

where T is the test temperature, T_0 is the reference temperature defined above, and $K_{\mathrm{Jc(med)}}$ is the median fracture toughness in MPa m$^{1/2}$. The median fracture toughness is defined as:

$$K_{\mathrm{Jc(med)}} = \sqrt{\frac{J_c E}{(1-\nu^2)}}\,, \tag{13.63}$$

where E is Young's Modulus, ν is Poisson's ratio and J_c is the value of the J integral at the onset of cleavage fracture and is determined from the area under the load-displacement curve.

Reactor surveillance programs have historically used Charpy V-notch specimens rather than fracture toughness specimens. These specimens are exposed in surveillance capsules, after which they are tested, and the shift in impact energy due to irradiation is calculated. These temperature shifts are all that is available to determine the shift in fracture toughness due to irradiation. Figure 13.19 shows that in principle, the change in DBTT measured in a Charpy test should be relatable to the shift of the fracture toughness curve.

Sokolov et al. [25] conducted a series of experiments on weld material containing high Cu, Ni and Mn contents and irradiated at 288 ℃ to 0.74×10^{19} n/cm^2 ($E > 1$ MeV). The Charpy curves before and after irradiation are shown in Fig. 13.20 and exhibit an increase in the ΔT_{41} by 169 ℃ and a substantial reduction in the upper shelf energy of some 40 J. Fracture toughness experiments were conducted on 0.5T and 1T CT specimens made from the same alloy and irradiated under the same conditions. The unloading compliance method was used to determine the J integral vs. crack extension, from which a value of J_c was determined. That was converted to the critical value of the stress intensity factor using Eq. (13.63), and replicate tests were used to determine $K_{\mathrm{Jc(med)}}$. The median fracture toughness is plotted in Fig. 13.21 and from the Master Curve definition, the shift of the value of T_0 is determined at

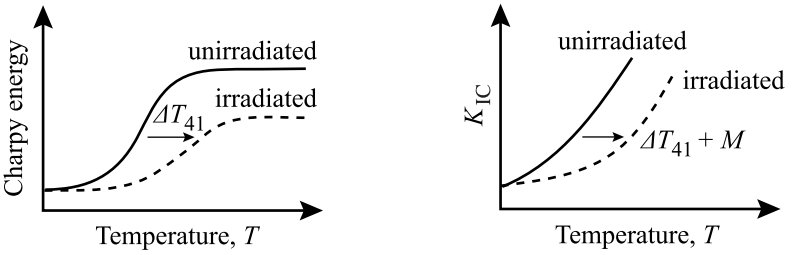

(a) (b)

Fig. 13.19. Application of the transition temperature shift in a Charpy test to the fracture toughness test. (a) Charpy impact energy, and (b) fracture toughness (from [24])

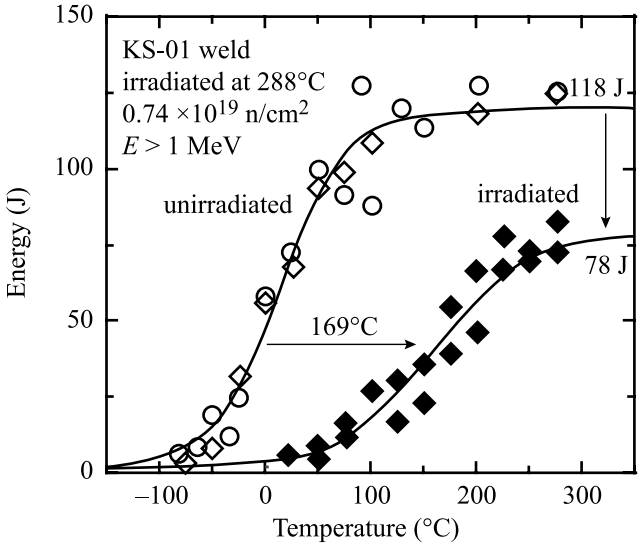

Fig. 13.20. Charpy impact energy vs. test temperature for weld metal in the unirradiated condition and following irradiation to 0.74×10^{19} n/cm^2 ($E > 1.0$ MeV) at 288 °C (from [25])

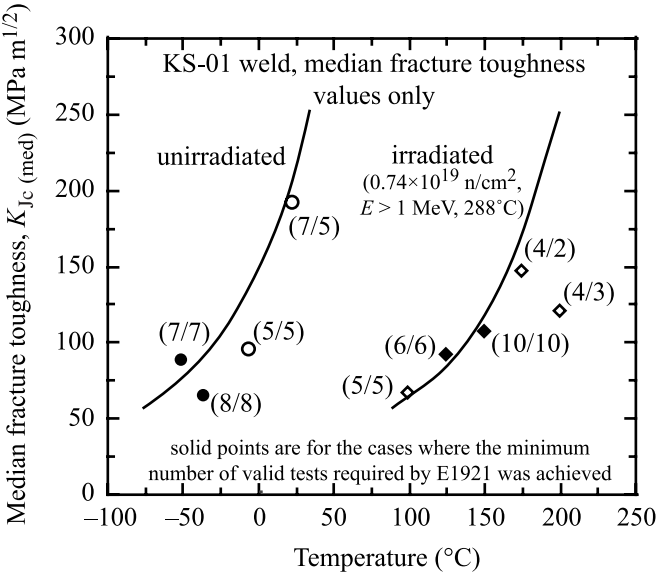

Fig. 13.21. Median fracture toughness of the same weld metal in the unirradiated condition and following irradiation under the same conditions as for the Charpy test in Fig. 13.20 (from [25])

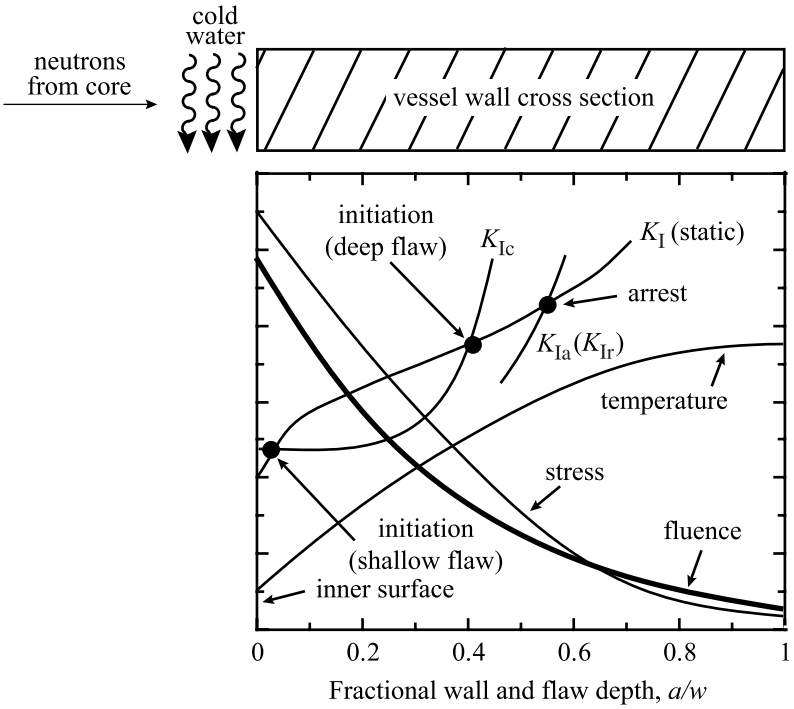

Fig. 13.22. Temperature, fluence, stress and resulting toughness gradient through the thickness of a reactor pressure vessel wall (courtesy of ST Rosinski, EPRI)

100 MPa $m^{1/2}$ to be 165 °C, which is in excellent agreement with the Charpy ΔT_{41} value of 169 °C.

The approach of estimating fracture toughness based on a reference temperature employs what is termed the *adjusted reference temperature* (ART) [26], which is a function of the Charpy temperature shift as follows:

$$ART = RT_{NDT} + \Delta T_{41} + M \,, \tag{13.64}$$

where RT_{NDT} is a reference nil-ductility temperature for the unirradiated material, ΔT_{41} is the Charpy temperature shift at $C_V = 41$ J, and M is a margin-of-safety term that has a value of 36 °C for welds to account for uncertainties in RT_{NDT} and ΔT_{41}. In this way, the large amount of surveillance data collected on Charpy samples can be used to determine the fracture toughness of the irradiated steel, which is crucial for ensuring the integrity of the pressure vessel as it ages.

An additional consideration in assessing the integrity of the pressure vessel is the establishment of gradients due to its thickness. Since the pressure vessel wall thickness can exceed 200 mm, neutron fluence, temperature and stress will all vary through the thickness of the vessel wall. Variation in the temperature and neutron fluence will cause the microstructure to differ as a function of position in the vessel. Since fluence is at a maximum and temperature is at a minimum at the inner diameter

of the vessel, the hardening and embrittlement will be greatest there. That stress is a maximum at the surface means that the fracture toughness will be lowest at the vessel inner surface (Fig. 13.22). For flaws initiating at the inner surface, they will be growing into material with increasing toughness, which provides an additional margin of safety against through-wall cracking.

13.7.4 Factors Affecting the Degree of Embrittlement

Because irradiation hardening is the principal factor affecting embrittlement, the same factors that influence hardening will influence embrittlement. These include:

- Steel composition and microstructure
- Exposure temperature
- Neutron environment

Effects of Microstructure and Composition

Of considerable importance to the improvement of the ductile-brittle transition temperature of pressure vessel steel is the influence of the microstructure on the fracture stress. The critical fracture stress can be increased by decreasing the mean dislocation path length (λ) in steel, which can be accomplished by reducing the grain size ($d = 2\lambda$) in pearlitic steels or by reducing the interparticle spacing ($l = \lambda$) among dispersed carbides (hard barriers) in tempered steels [26]. Although refinements in grain size and carbide dispersion can increase the fracture stress to a greater extent than yield stress, thereby reducing both the static and dynamic transition temperatures, irradiation hardening can reverse these beneficial effects.

It has also been suggested that the abundance of grain boundaries in fine-grain steel act as a more efficient trap for defects. This role is thought to be especially important where free interstitial (and embrittling) elements such as nitrogen may be more homogeneously trapped, thereby lessening the effects on macroscopic properties of the irradiated steel. However, as discussed earlier, grain boundary segregation of elements such as phosphorus can result in embrittlement of the grain boundary.

As in the case of hardening, the presence of substitutional elements, such as copper, nickel, manganese and phosphorus, controls the level of embrittlement in the Mn–Mo steels used in the USA for reactor pressure vessels. The dominant hardening and hence, embrittling feature is the copper-rich precipitate (CRP), which consists of very small ($1 - 3\,\text{nm}$) coherent precipitates with high Cu content that can form at number densities exceeding $10^{23}\,\text{m}^{-3}$. CRPs are enriched in Mn and Ni as well as smaller amounts of P and Si. Both Ni and Mn form strong bonds with Cu in the precipitate and increase the volume of the precipitate. As such, increasing amounts of Ni and Mn amplify the hardening effect of Cu. The effect of Cu on the embrittlement of A533B steel is shown in Fig. 13.23. As a result of a large NRL study on the role of residuals in radiation embrittlement, it was concluded some time ago that clean steels (low residuals P, S, Cu, Sn, As, Sb, etc.) mean low radiation

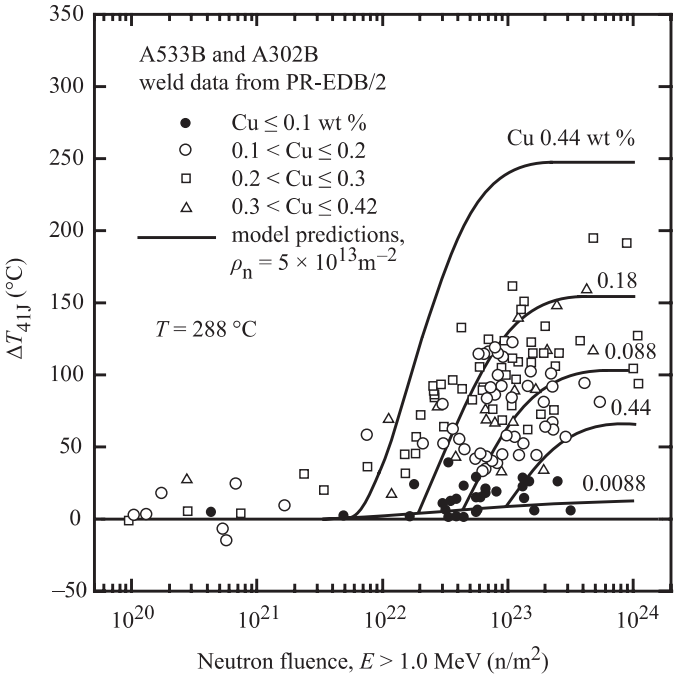

Fig. 13.23. Effect of copper content on the temperature shift of A533-B and A302-B welds irradiated at 288 °C (from [28])

sensitivity [28]. In fact, it is possible to develop steels with low residual content that show very low response to irradiation to end-of-life fluences (Fig. 13.24).

Notwithstanding the influence of residual elements on radiation defect stabilization, there are other intrinsic effects of these elements on impact behavior, which may prove to be important in radiation embrittlement sensitivity. Those residual elements which restrict cross slip, cause significant matrix strengthening, and reduce fracture surface energy are primarily suspect. Phosphorus contributes strongly to all three processes, copper is a potent solid solution hardener and silicon, vanadium, aluminum and cobalt diminish the ease of cross slip.

Effect of Temperature

As shown by both Charpy and fracture toughness curves, the level of embrittlement is progressively reduced with higher irradiation temperature. This effect is a manifestation of the annealing process that is accelerated at higher temperatures. The mechanisms responsible for affecting the strength of pressure vessel steels (dislocation impedance by irradiation-induced precipitates, defect-solute clusters) are essentially low-temperature processes and are annealed out at temperatures approaching 400 °C in steel. Figure 13.25 shows the drop in the transition temperature increase for a given fluence as the irradiation temperature is raised. The implication is that

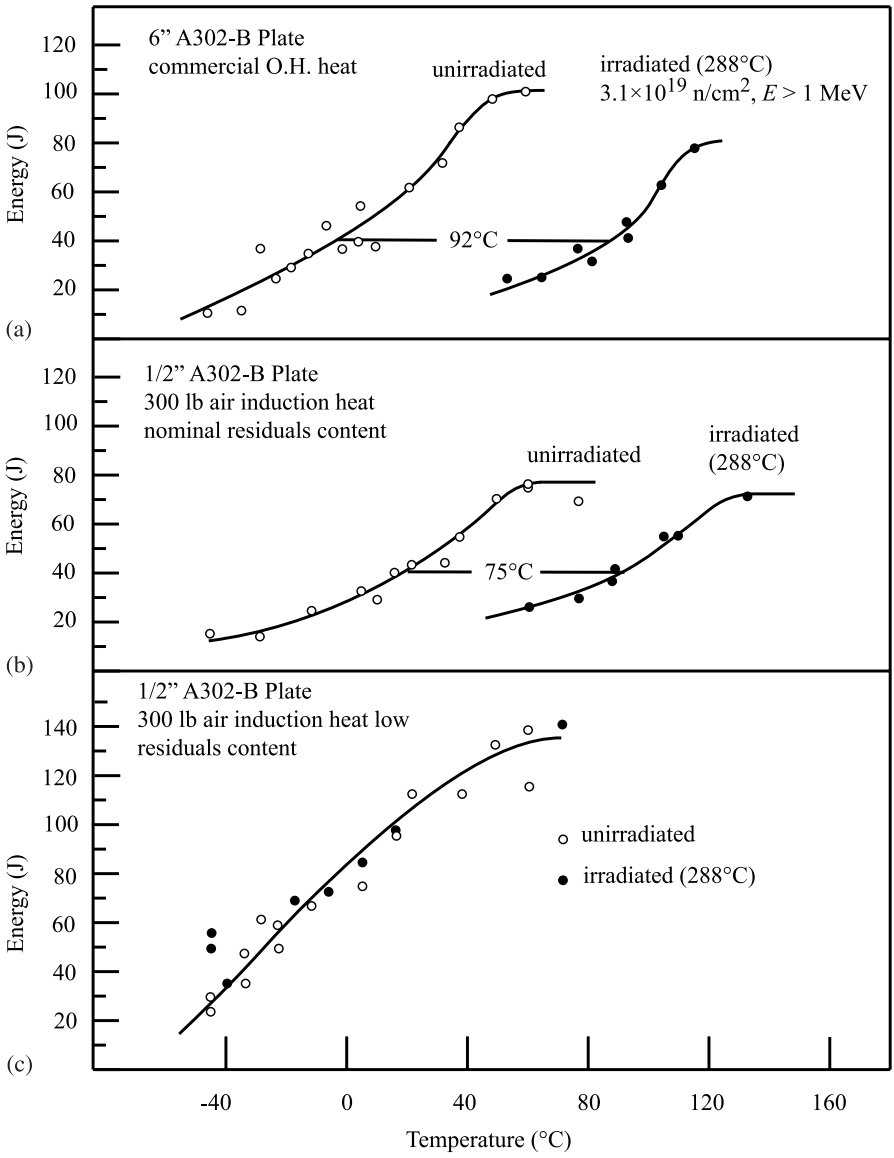

Fig. 13.24. Comparison of radiation embrittlement sensitivity in A302-B plate. (a) Commercial heat. (b) Air-induction heat with nominal residuals. (c) Air-induction heat with low residuals (from [29])

irradiation at higher temperature will result in less embrittlement than at low temperature.

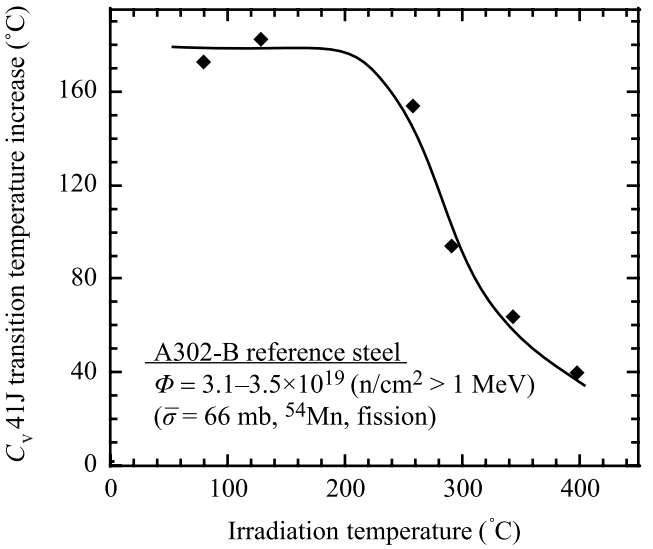

Fig. 13.25. Effect of irradiation temperature on transition temperature increase for an A302-B steel (from [19])

Effect of Neutron Environment

It is well-established that the magnitude of embrittlement is a strong function of the neutron fluence with the transition temperature increasingly rapidly with fluence. Attempts have been made to characterize the transition temperature shift as a function of neutron fluence. A simple model is:

$$\Delta T_{41} = A(\varphi t)^n \,, \tag{13.65}$$

where ΔT_{41} is the transition temperature shift of Charpy energy at 41 J or the fracture toughness at 100 MPa m$^{1/2}$ and ϕt is the neutron fluence in units of n/cm^2 ($E >$ 1.0 MeV). The value of the exponent, n will vary depending on the type of steel. The average value of n for advanced US steels is 0.5 [30], but the value is closer to 0.33 for Russian steels [31]. The US Nuclear Regulatory Commission (NRC) Regulatory Guide 1.99 (RG 1.99), Rev. 2 [32] provides the following relation:

$$\Delta T_{41} = A\Phi^{(0.28-0.1\log\Phi)} \,, \tag{13.66}$$

where Φ is neutron fluence in units of 10^{19} n/cm^2 ($E > 1$ MeV). An example of the behavior of the transition temperature with fluence is shown in Fig. 13.26 for a 0.24%Cu–1.6%Ni weld irradiated at 290 °C [33] and compared to the NRC Regulatory Guide 1.99 specification [32]. Unfortunately the response of different steels, and the influence of other factors is reflected in the value of A and causes a large scatter. Further, there does appear to be a tendency towards saturation, which is also

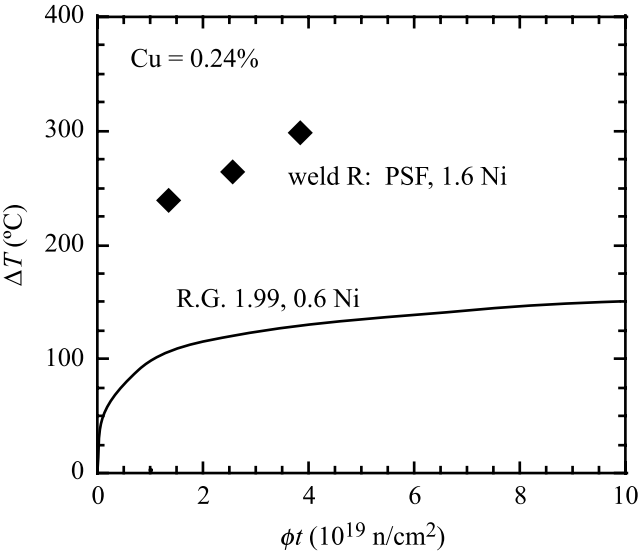

Fig. 13.26. Effect of neutron fluence ($E > 1.0\,\text{MeV}$) on the transition temperature in a 0.24Cu–1.6Ni weld metal irradiated at 290°C (from [33])

strongly influenced by many factors. As shown in Figs. 12.17 and 13.27, the effect of CRPs on hardening and embrittlement saturates at high doses due to depletion of copper from the matrix.

Of greater importance is the role of flux or dose rate on embrittlement. At very low fluxes ($<10^{14}\,\text{n/m}^2\,\text{s}$), CRP growth is increased due to enhanced copper diffusion due mainly to thermal processes. At very high fluxes ($\gg 10^{16}\,\text{n/m}^2\text{s}$), a high density of unstable matrix defects becomes significant. These defects increase vacancy and interstitial loss, reducing radiation-enhanced diffusion and slowing the growth of CRPs. In the intermediate flux regime (10^{15}–$10^{16}\,\text{n/m}^2\text{s}$), there is a significant influence of flux on embrittlement in which hardening and embrittlement vary with $\phi^{-1/2}$ (see Fig. 12.19a). The mechanism for this effect is believed to involve enhanced solute trapping as well as enhanced recombination and a high efficiency for radiation-enhanced diffusion.

13.7.5 Embrittlement of Ferritic-Martensitic Steels

Ferritic-martensitic steels have been considered for use in both fusion and advanced fission reactor systems because of their resistance to swelling and helium embrittlement, and the potential for low activation. The steels are used in the two-phase, ferritic-martensitic structure, and can be heat treated to optimize toughness and high-temperature strength. The standard heat treatment consists of a solution anneal to completely austenitize the microstructure and to dissolve the carbides, as well as a tempering treatment to relieve the stresses and enhance toughness. The

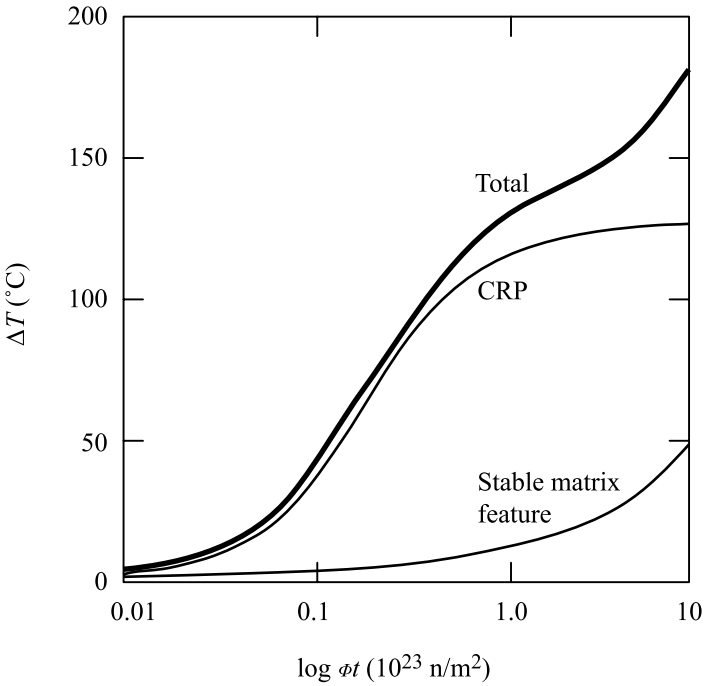

Fig. 13.27. Effect of copper-rich precipitates (CRP) on the fluence dependence of the transition temperature (from [34])

resulting microstructure consists of tempered martensitic laths forming subgrains in a ferrite matrix with a high dislocation density.

However, as with low alloy steels used for thermal reactor pressure vessels, these steels are also susceptible to brittle fracture. Figure 13.28 shows a set of Charpy curves for three F-M steels: modified 9Cr–1Mo, NF616 (12Cr–2W), and HCM12A (12Cr–2W–1Cu) before and after irradiation in the high flux reactor in Petten (Netherlands) to 2.5 dpa at 300 °C. Note that all three alloys show substantial transition temperature shifts. The shift for the modified 9Cr–1Mo steel was 175 °C, compared to 225 °C for HCM12A and 249 °C for NF616. All steels exhibited reductions in the upper shelf energy of between 2.2 and 4.0 J. As with the low alloy steels, the yield strength can be correlated with DBTT as shown in Fig. 13.29a. However, the drop in upper shelf energy can also be correlated with the reduction in area as shown in Fig. 13.29b.

13.7.6 Annealing and Re-Irradiation

One way of reversing the embrittling effects of irradiation is to thermally anneal out the defects to restore the toughness properties that were degraded by neutron irradiation. However, the success of annealing depends on the rate of embrittlement upon

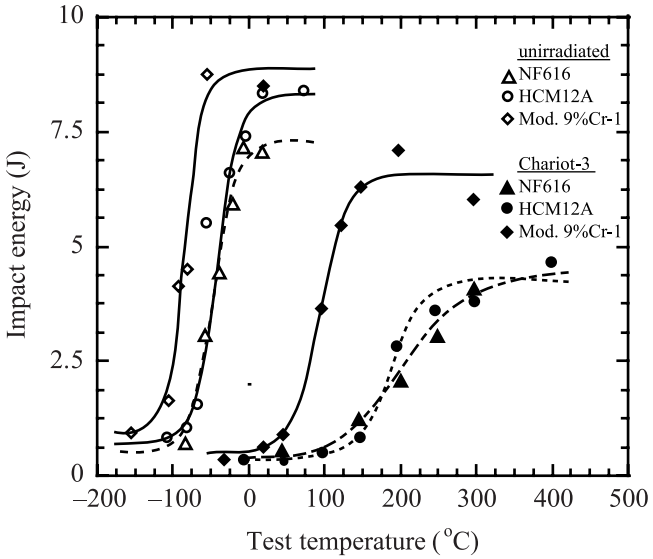

Fig. 13.28. Transition temperature curves for different F-M steels measured using miniaturized Charpy specimens (from [35])

re-irradiation of the steel. Annealing of irradiated pressure vessel steels at temperatures near 450 °C for 70 to 150 h will provide nearly complete recovery of the transition temperature, even after irradiation to very high fluences ($>1\times10^{20}\,\mathrm{n/cm^2}$) [30]. Annealing under these conditions produces a significant drop in the density and volume fraction of copper-rich precipitates. The annealing treatment also coarsens the remaining precipitates and results in an overall reduction of Cu in solution [31]. The lower amount of Cu in solution makes the annealed alloy less susceptible to embrittlement and it exhibits a lower re-embrittlement rate than in the unirradiated condition. Figure 13.30a–c show the effect of annealing and re-irradiation on the embrittlement of an A533B, class 1 plate. Figure 13.30a shows the increase in ΔT_{41} with fluence to almost $1.4\times10^{20}\,\mathrm{n/cm^2}$. Annealing at 454 °C for times between 72 and 168 h (Fig. 13.30b) results in Charpy curves that are indistinguishable from that of the unirradiated curve. Re-irradiation to $4.7\times10^{19}\,\mathrm{n/cm^2}$, of a sample initially irradiated to $2\times10^{19}\,\mathrm{n/cm^2}$ and then annealed at 454 °C for 72 h, produced less hardening that the original irradiation. The measured transition temperature shift is shown in Fig. 13.30c by the solid symbol, which is well below the re-embrittlement *lateral shift* (dotted line) predicted by NRC Regulatory Guide 1.162.

13.7.7 Fatigue

Basic structural changes occur in a metal when it is subjected to cyclic stress. These changes divide the fatigue process into stages:

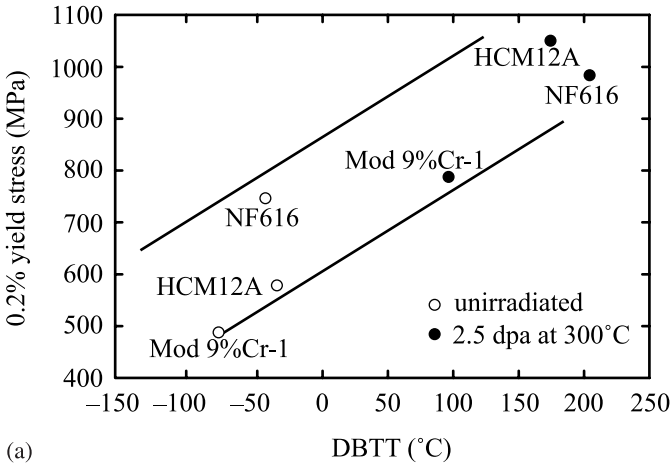

(a)

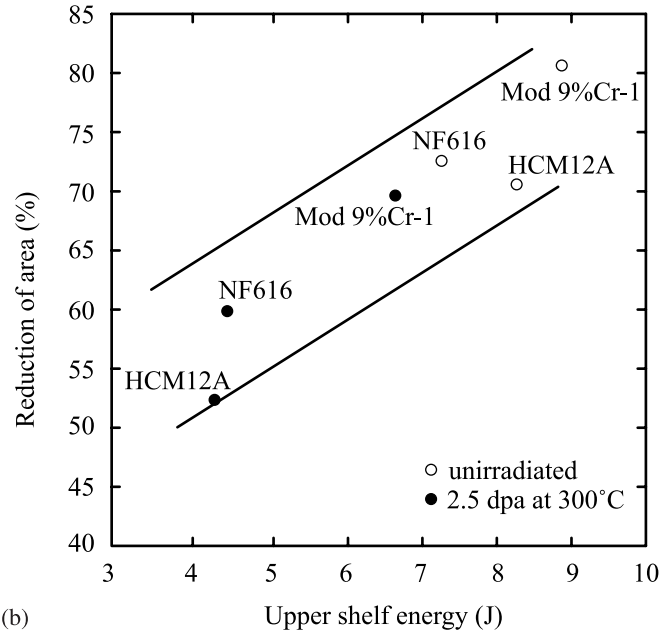

(b)

Fig. 13.29. Relationship between (a) yield strength and DBTT and (b) reduction in area and upper shelf energy (from [35])

1. *Crack initiation* is the early development of fatigue damage which can be removed by suitable thermal annealing.
2. *Slip band crack growth* involves the deepening of the initial crack on planes of high shear stress, frequently referred to as *stage I crack growth.*

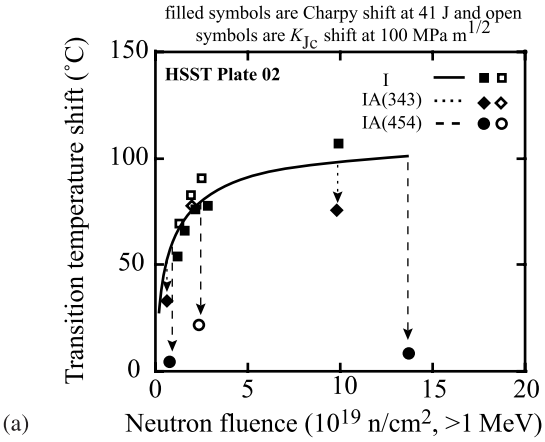

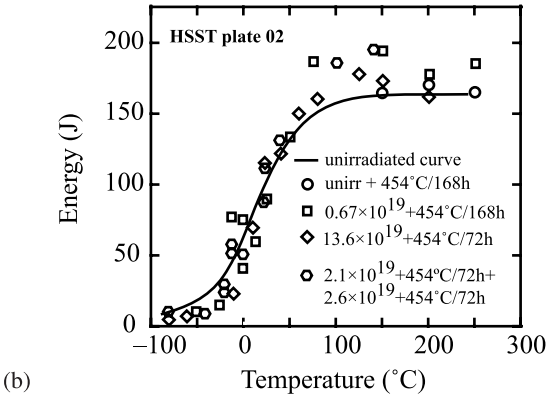

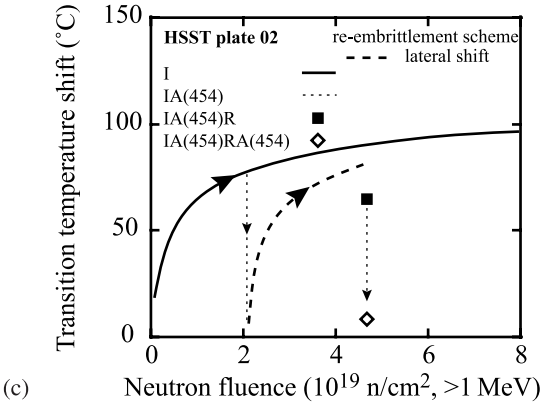

Fig. 13.30. Effect of irradiation and annealing in an A533B steel plate on (a) transition temperature shift, (b) Charpy curve, and (c) transition temperature shift following re-irradiation (from [31])

3. *Crack growth on planes of high tensile stress* involves growth of a well-defined crack in a direction normal to the maximum tensile stress, called *stage II crack growth.*
4. *Ultimate ductile failure* occurs when the crack reaches sufficient length that the remaining cross section cannot support the applied load, *stage III.*

Fatigue life is measured by the S-N curve in which the number of cycles to failure is plotted vs. the stress (maximum or average). S-N curves generally apply to fatigue failure at a high number of cycles ($N > 10^5$) and at these lives, the stress is generally elastic, though plastic deformation occurs on a microscale. At higher stresses, deformation is characterized by gross plasticity and strain-controlled, low cycle fatigue tests are most appropriate for assessing fatigue life in this regime. While the stress amplitude is fixed in a high cycle fatigue test, the stress intensity factor will increase as the crack length increases with the number of cycles, as prescribed by Eq. (13.27). The increase in crack length is therefore related to the change in ΔK by:

$$\Delta K = K_{\max} - K_{\min} = (\sigma_{\max} - \sigma_{\min})\sqrt{\pi c}\,. \tag{13.67}$$

The fatigue crack growth process is divided into stages that depend on the magnitude of ΔK. The rate of crack propagation in fatigue is denoted as $\mathrm{d}a/\mathrm{d}N$ and varies with ΔK in an inert environment as shown in Fig. 13.31a. The stage I crack propagates initially along the persistent slip bands. In polycrystalline metal, the crack may extend for only a few grain diameters before the crack propagation changes to stage II. The rate of crack propagation in stage I is generally very low, on the order of nanometers per cycle. The fracture surface of stage I fracture is highly faceted. Figure 13.31b shows a schematic illustration of stages I and II during fatigue crack propagation in metals.

Stage II crack propagation occurs by a plastic blunting process [37] that is illustrated in Fig. 13.32. At the start of the loading cycle the crack tip is sharp (Fig. 13.32a). As the tensile load is applied the small double notch at the crack tip concentrates the slip along planes at 45 ℃ to the plane of the crack (Fig. 13.32b). As the crack widens to its maximum extension (Fig. 13.32c) it grows longer by plastic shearing and at the same time its tip becomes blunter. When the load is changed to compression the slip direction in the end zones is reversed (Fig. 13.32d). The crack faces are pressed together and the new crack surface created in tension is forced into the plane of the crack (Fig. 13.32e) where it partly folds by buckling to form a re-sharpened crack tip. The re-sharpened crack is then ready to advance and be blunted in the next stress cycle (Fig. 13.32f).

Considerable research has gone into determining the laws of fatigue crack propagation for stage II growth. In general, the aim in fatigue crack growth rate testing is to maintain a predominantly elastic condition in the test specimen, thereby allowing results to be interpreted in terms of the crack tip stress intensity defined by linear-elastic fracture mechanics. The crack propagation rate in stage II is described by the

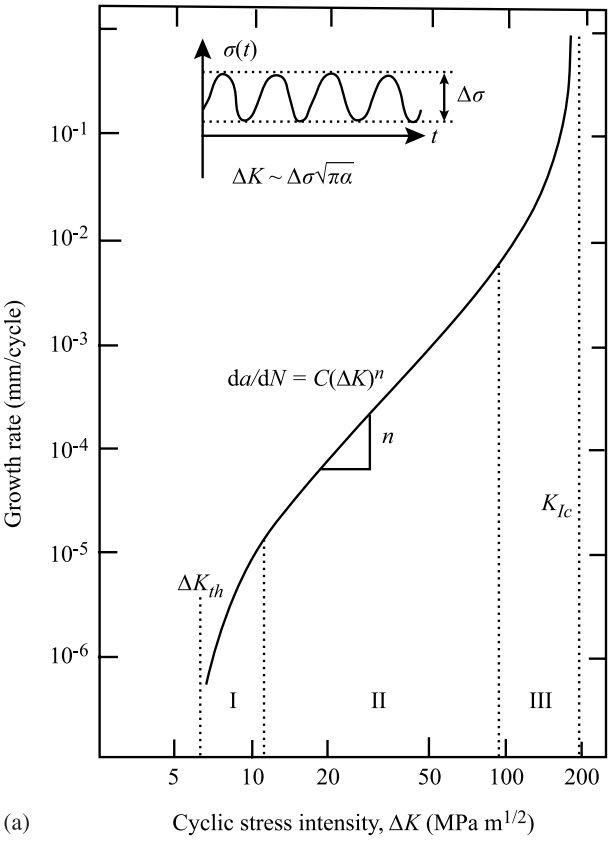

(a)

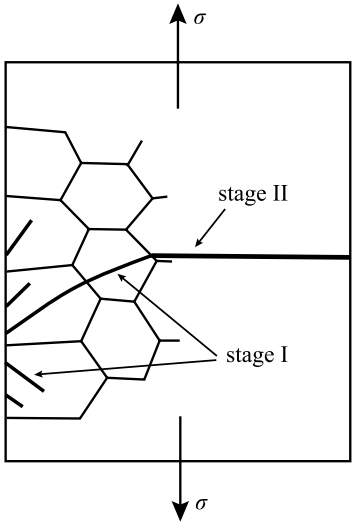

(b)

Fig. 13.31. (a) Schematic illustration of fatigue crack growth behavior in an inert environment as a function of the stress intensity factor range, ΔK, and (b) schematic representation of stages I and II in fatigue crack propagation in a metal (from [36])

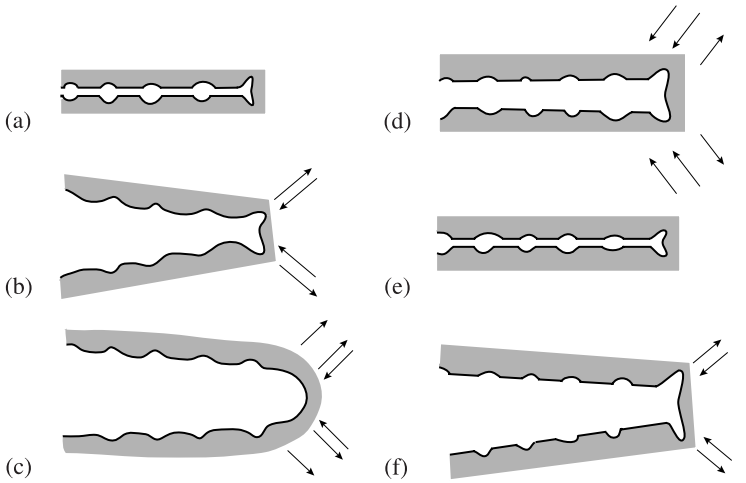

Fig. 13.32. Plastic blunting process for growth of stage II fatigue cracks (from [37])

Paris equation:

$$\frac{\mathrm{d}a}{\mathrm{d}N} = C(\Delta K)^n \tag{13.68}$$

where $\dfrac{\mathrm{d}a}{\mathrm{d}N}$ is the incremental increase in the crack length per cycle, C and n are constants and ΔK is the stress intensity factor range given in Eq. (13.67). (Note that it is common to represent the crack growth per cycle as $\mathrm{d}a/\mathrm{d}N$ and the crack growth rate as $\mathrm{d}a/\mathrm{d}t$, where a is the crack length). In addition to the specification of ΔK, the ratio of $K_{\max}$ to $K_{\min}$ is an important parameter describing the mean stress during cyclic loading and is designated as the R ratio, such that $\Delta K = K_{\max}(1-R)$. Note that stage III fatigue crack growth is limited by the static fracture toughness, K_{Ic}. The initiation of fatigue crack growth is defined by the threshold value of the stress intensity increment, ΔK_{th}, below which a fatigue crack cannot propagate. Fracture toughness behavior is closely related to the concepts of fatigue crack growth, since the fracture toughness provides the "end-of-life" criteria for terminating fatigue crack growth. One of the more profound changes induced by neutron irradiation is the decrease in fracture toughness. Hence, the effect of neutron irradiation on the fatigue crack growth of pressure vessel steels is of considerable importance.

Considerable progress has been made in using LEFM techniques to characterize the effect of neutron irradiation on the fatigue crack propagation behavior of reactor pressure vessel steels. The general observation is that neutron irradiation, in most cases, does not have a significant detrimental effect on the fatigue crack growth behavior of pressure vessel steels in an air environment (Fig. 13.33). In pressurized water environments, irradiation has not been found to increase the growth rates beyond those, which are due to the environment itself (Fig. 13.34).

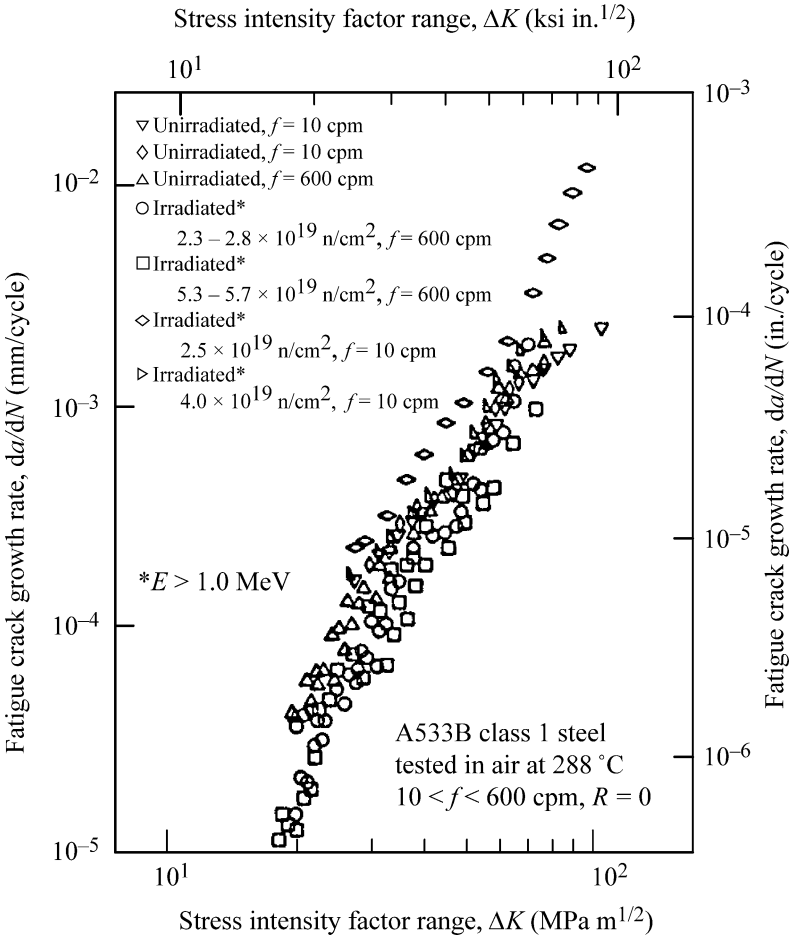

Fig. 13.33. Fatigue crack growth behavior of irradiated and unirradiated A533-B class 1 steel tested in air at 288 ° C (from [38])

Thus, after considerable testing, there is no detectable effect of irradiation on the fatigue crack growth rate of pressure vessel steels. However, a wider range of external variables, such as waveform, temperatures, load ratios, and especially the environment, may well combine to synergistically worsen the situation. The role of the environment in crack growth will be discussed in Chap. 15.

13.8 Fracture and Fatigue of Austenitic Alloys at Low to Intermediate Temperatures

Austenitic stainless steels are used in numerous core structures in light water reactors that operate in the low to intermediate temperature range (<400 °C). As shown

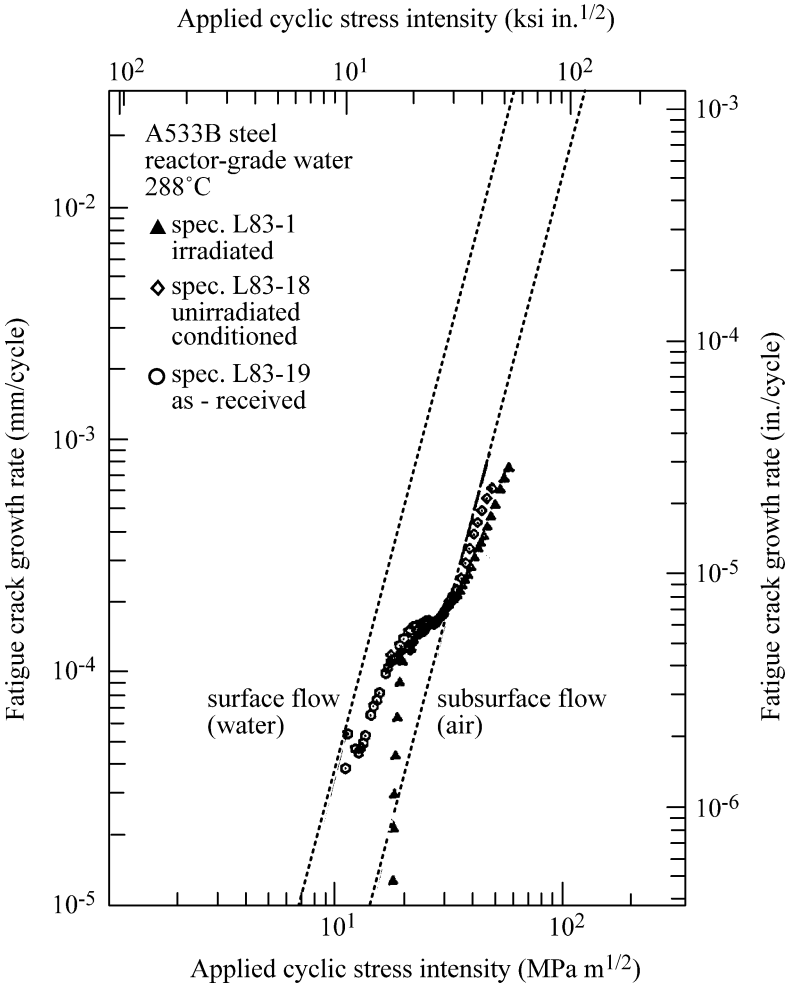

Fig. 13.34. Fatigue crack growth rates for unirradiated and irradiated A533-B steel in high temperature, pressurized reactor grade water (from [39])

in Chap. 12, in this temperature range significant increases in yield strength occur (up to a factor of 5) that are accompanied by a drastic loss of ductility (from ∼30% to <1%). The implication of these mechanical property changes on fracture and fatigue are discussed next.

13.8.1 Effect of Irradiation on Fracture Toughness

The fracture toughness of irradiated stainless steels in the intermediate temperature range decreases sharply with irradiation dose. Figure 13.35a summarizes the trend in the fracture toughness for solution annealed and cold-worked conditions, where

K_{Ic} is given by Eq. (13.27). Figure 13.35b shows the drop in K_{Ic} as a function of neutron exposure up to 40 dpa for 304 and 316 stainless steel irradiated and tested between 205 and 427 °C. In fact, the value of J_{Ic} drops from values between 600 and 823 kJ/cm^2 in the unirradiated condition to values as low as 20 kJ/cm^2 for ~6 dpa 304 stainless steel irradiated and tested at 288 °C [42]. In elastic-plastic fracture, the resistance to crack growth is also described by the tearing modulus, T_m defined as:

$$T_m = \frac{dJ}{da}\frac{E}{\sigma_0^2}\,, \tag{13.69}$$

where dJ/da is the slope of the resistance curve of J vs. increase in crack length, a and σ_0 is the flow stress which is approximated by the average of the yield and ultimate strengths. The tearing modulus also decreases significantly as a result of neutron irradiation in this temperature range.

Odette and Lucas [43] used a scaling relationship to describe the dependence of fracture toughness on irradiation:

$$\frac{K_{Ic}^{irr}}{K_{Ic}^{unirr}} = \sqrt{\frac{e_u^{irr}}{e_u^{unirr}}\frac{\sigma_0^{irr}}{\sigma_0^{unirr}}}\,, \tag{13.70}$$

where e_u is the uniform engineering strain. The fit of this equation to the fracture toughness data for several austenitic steels is shown by the solid line in Fig. 13.35b. While it tracks the data well, this relation does not provide a physical basis for the reduction in toughness. Instead, it has been proposed that the loss of fracture toughness with irradiation is due to a change in fracture mode.

In the unirradiated condition, ductile metals such as stainless steels fracture by ductile-dimple rupture in which voids nucleate and grow in the plastic region ahead of the crack tip until they eventually linkup with the crack tip by necking of the remaining ligament (Fig. 13.36a) [41]. At low dose, irradiation may accelerate void linkage by work softening and localized deformation. Coalescence can occur by diffuse necking (DN) when the microvoid height is approximately equal to the distance from its edge to the blunted crack tip. Coalescence may also occur at lower strain by localized necking (LN) between the void and the crack tip. In either case, the fracture toughness can be related to deformation parameters by:

$$K_{Jc} = \sqrt{1.5\beta r^* \sigma_0 E'}\,, \tag{13.71}$$

where β is the ratio of crack opening to the distance to the next void at the point of crack-void linkage ($\beta = \delta/r^*$), and $E' = E/(1-\nu^2)$. The value of β decreases as deformation becomes increasingly localized. At high doses, crack advance is more likely controlled by heterogeneous deformation in the zone ahead of the crack due to intense dislocation channeling in the solid. In this case, fracture occurs by a decohesion process in which deformation is concentrated into a series of plastic ligaments behind the crack tip (Fig. 13.36b) and extending over a process zone of length, L_z. Crack growth occurs when the displacement capacity of the last ligament, Δ_z is reached under a local stress σ_z:

$$K_{Jc} = \sqrt{0.5\Delta_z \sigma_z E'}\,. \tag{13.72}$$

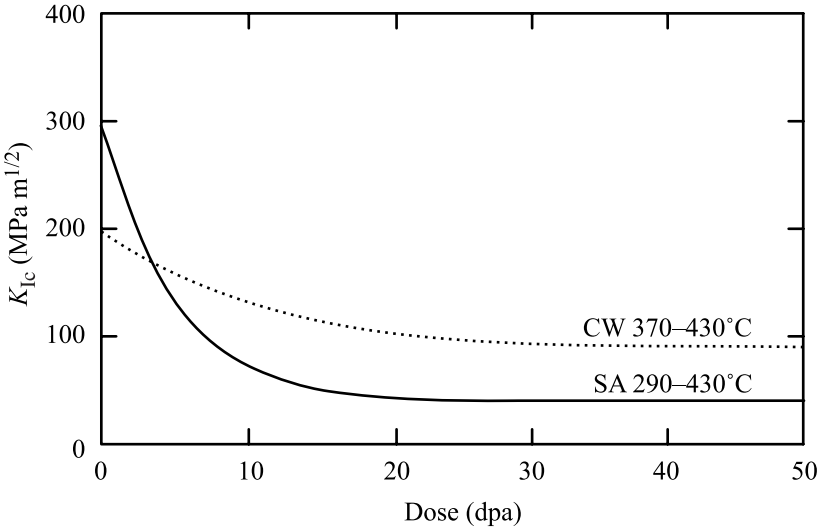

(a)

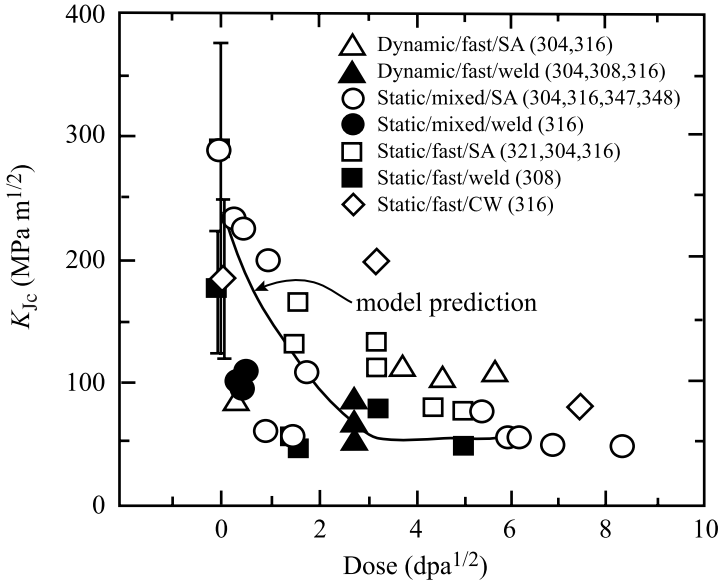

(b)

Fig. 13.35. Variation of fracture toughness with dose for (a) cold-worked and solution annealed austenitic stainless steels (from [40]), and (b) for various austenitic stainless steels irradiated and tested between 205 and 427 °C (from [41])

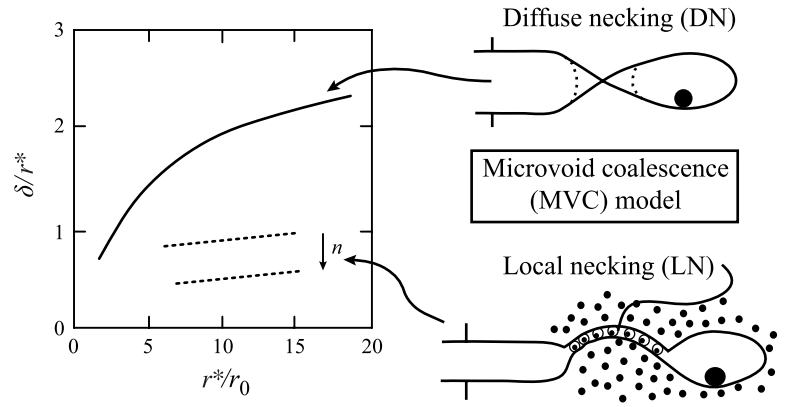

(a)

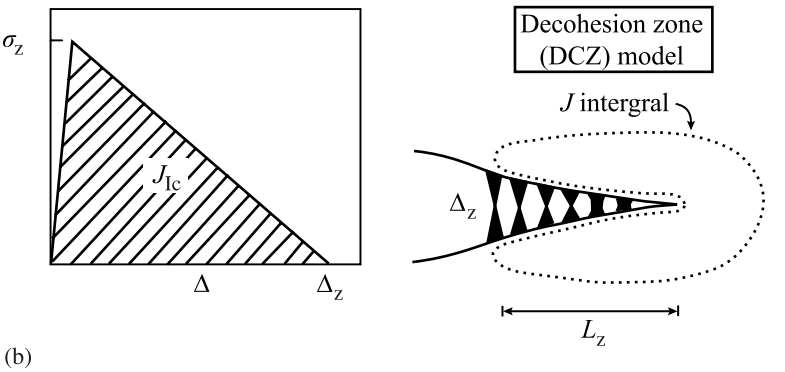

(b)

Fig. 13.36. Models ofductile fracture. (a) Microvoid coalescence model: ratio of crack opening, δ to distance to next void at point of crack linkage, r^* vs. the latter quantity normalized by the initial inclusion radius, r_0. (b) Decohesion zone model: crack growth by the failure of plastic ligaments bridging the faces of a virtual crack. (from [41])

While these models are consistent with the role of the increased localization of plastic flow with irradiation dose, confirming experiments have yet to be conducted.

In addition to altering the ductile fracture process, irradiation may also result in a change in fracture mode from ductile-dimple rupture to cleavage. It is well-known that plasticity can induce martensite formation in austenitic stainless steels that may fracture by a quasi-cleavage mechanism. However, such processes are unlikely when deformation occurs at temperatures $>300\,^{\circ}\mathrm{C}$.

13.8.2 Effect of Irradiation on Fatigue

Due to the reduced uniform strain and increasing localization of plastic deformation resulting from irradiation, it may be expected that fatigue crack growth should re-

spond accordingly. In particular, in stage III fatigue crack growth, where the growth rate is limited by the fracture toughness, Fig. 13.31a, reduction in fracture toughness due to irradiation will result in an increase in crack growth rate. In stage I, the threshold stress intensity range ΔK_{th} is sensitive to the chemical environment, the R ratio, grain boundary impurity segregation and to the tendency for high strength materials to undergo flow localization. This latter sensitivity is supported by empirical data that show that ΔK_{th} decreases with increasing yield strength in unirradiated 316 SS [44]. Consequently, the severe localization of plasticity caused by irradiation may be expected to lead to decreases in the threshold stress intensity.

However, the data on the effect of irradiation on fatigue in austenitic stainless steels in the low to intermediate temperature range is mostly in stage II that is described by the Paris equation. In this regime, crack propagation is primarily dependent on the elastic properties of the solid, and less so on the microstructure and on plastic deformation processes. Limited data shows that the crack growth rate is, in fact, relatively insensitive to irradiation to doses of up to about 30 dpa. Figure 13.37 shows that the crack growth rate of 316 stainless steel irradiated to $2.03 \times 10^{21}\,\mathrm{n/cm^2}$ at 380 °C is bounded on the high side by crack growth in mill-annealed plate and on the low side by 20% cold-worked plate, both in the unirradiated condition. As such, irradiation of austenitic stainless steels to low or intermediate doses does not result in measurable increases in fatigue crack growth. However, with increasing temperature, the generation and accumulation of helium into bubbles can affect the fatigue crack propagation, as will be discussed in the next section.

Nevertheless, it may be expected that under irradiation, low cycle fatigue life should decrease due to decreased ductility, and high cycle fatigue life should increase due to increased strength. This behavior was indeed measured for 304 stainless steel at both room temperature and 325 °C following irradiation to $8 \times 10^{22}\,\mathrm{n/cm^2}$ ($E > 0.1\,\mathrm{MeV}$) at a temperature of 400 °C [46]. The beneficial effect of irradiation in HCF is likely due to the fact that despite significant hardening, and a reduction in work hardening coefficient by a factor of 2.7, the alloy retained ductility to 4–5% elongation.

13.9 High-Temperature Embrittlement

Nuclear systems that operate in the high-temperature regime include fast reactors, advanced fission reactors, fusion reactors, and systems for accelerator-based transmutation of wastes. Among these systems, three alloy classes, austenitic stainless steels, ferritic-martensitic steels and vanadium alloys, are among the primary candidate alloys for core components. These alloys are selected based on their high-temperature strength. However, degradation mechanisms unique to the high-temperature regime can limit their usefulness.

The nature of fracture at high temperatures is quite different from the mode of fracture exhibited by metals and alloys following tensile tests at low temperatures. At low temperatures fracture tends to result from shearing through grains of

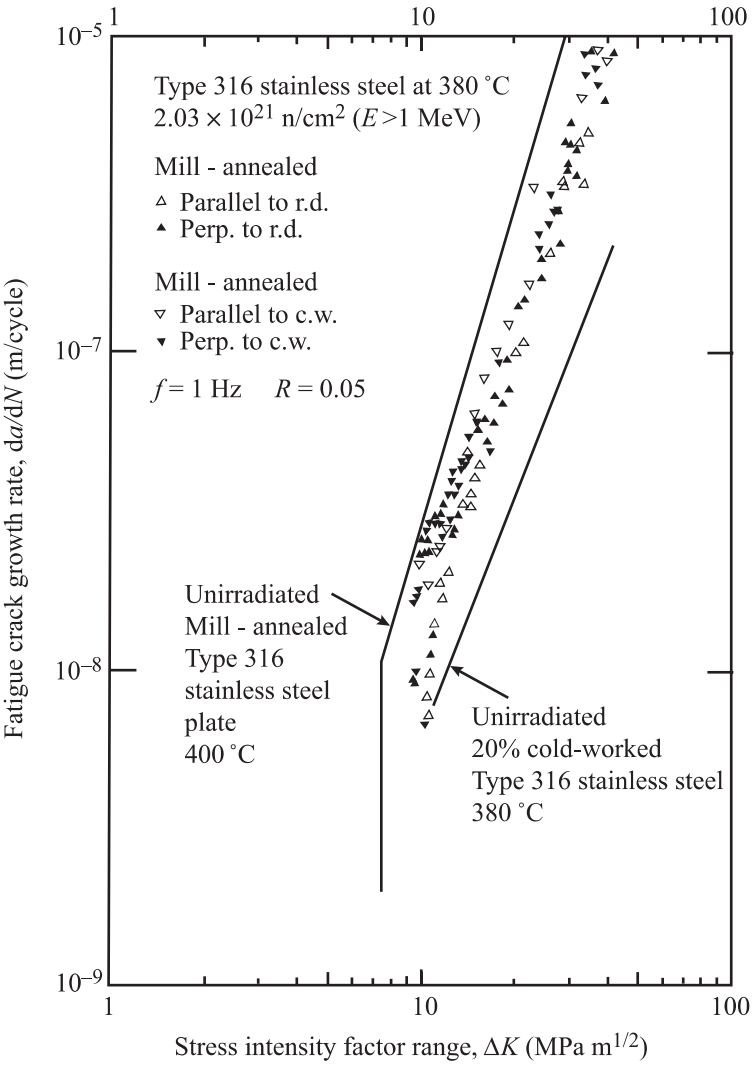

Fig. 13.37. Effect of irradiation to 2.03×10^{21} n/cm^2 ($E > 1$ MeV) at 380 °C on fatigue crack propagation rate in mill-annealed and 20% cold-worked type 316 SS (from [45])

the metal (i.e., transgranular fracture) and often occurs only after appreciable deformation. The fracture mode that terminates the third stage of high-temperature creep or the deformation in a high-temperature tensile test is usually of the intergranular type. As the temperature increases (above 0.3 T/T_m), the grain boundary loses strength relative to the matrix. At these temperatures, grain boundary sliding is prevalent and intergranular fracture can occur by Zener wedge cracking at grain boundary junctures (higher stresses and lower temperatures), by the fracture of con-

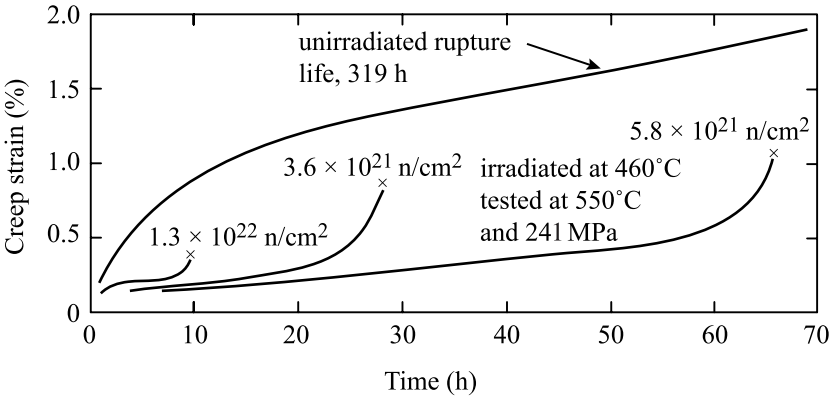

Fig. 13.38. Effect of irradiation on the creep rupture of annealed 304 stainless steel irradiated at 370 – 460 °C and tested at 550 °C and 241 MPa (from [47])

tinuous, brittle boundary phases, by grain boundary void formation (lower stresses and higher temperatures), or by helium embrittlement via grain boundary bubbles.

The effect of irradiation on the high-temperature embrittlement of alloys is measured in a creep rupture test. Creep rupture refers to the failure of a specimen that has been subject to stresses well below the yield stress for long periods of time. Deformation occurs by creep (Chap. 14) rather than by rapid plastic deformation characteristic of a tensile test. In a creep rupture test, the time to failure, or the *rupture life*, t_f, and the *elongation at failure*, ε_f, are measured. Provided that steady state creep prevails for the major portion of the test, these two quantities are related by:

$$t_f = \frac{\varepsilon_f}{\dot{\varepsilon}} \tag{13.73}$$

were $\dot{\varepsilon}$ is the steady state creep rate. The creep rupture properties depend on the extent of irradiation, the irradiation and testing temperatures and on the degree of cold-work of the specimens. These variables directly control the creep rate and the elongation at fracture ε_f. The rupture life, t_f, is indirectly affected by the same variables because it is the ratio of ε_f to $\dot{\varepsilon}$. Figure 13.38 shows the effect of fast neutron fluence on the creep rupture properties of an austenitic stainless steel. The data indicate that both the creep rate $\dot{\varepsilon}$ and the elongation to fracture ε_f are reduced in the irradiated specimens. Those processes which affect the former are discussed in Chap. 14 (Irradiation Creep), while the mechanisms that reduce the elongation to fracture ε_f, i.e., grain boundary voids, grain boundary sliding and helium embrittlement, are the subject of this section.

13.9.1 Grain Boundary Voids and Bubbles

At high temperature, diffusion is rapid and the application of a stress can result in the nucleation and growth of voids on grain boundaries that are aligned perpendicular

to the applied stress. Void nucleation and growth are aided by creep that is important at temperatures above about $0.3\,T_m$. Stresses well below those required for the formation of wedge cracks can lead to formation and growth of grain boundary voids. Once formed, the voids grow by rapid diffusion along grain boundaries until the remaining cross sectional area is too low to support the load and fracture occurs either by linkage of bubbles, or more likely, crack propagation through the grain boundary void array. If helium is present, it can accelerate void growth through the effect of pressure on the void surfaces, resulting in a reduction in the time to failure.

In analyzing embrittlement due to void or bubble growth on the grain boundaries, we will first consider purely diffusive growth of the voids. However, the presence of a tensile stress at high temperature will produce creep, which can couple with diffusion to accelerate growth of the voids. In the limit, void growth is controlled by the overall creep rate. Finally, we will consider grain boundary cavity growth by grain boundary sliding, a process that becomes more favorable at higher temperatures where grain boundary strength drops.

Diffuse Growth of Voids and Bubbles

Diffusive growth of voids on grain boundaries was first analyzed by Hull and Rimmer [48] and was based on the assumptions that:

- Diffusion through the cavity surface is sufficiently fast for the cavity to remain spherical in shape.
- Grain boundary diffusion dominates volume diffusion.
- The grains themselves are rigid and their movement in the direction normal to the boundary is not constrained.
- Vacancies are supplied by the grain boundary and the void is in equilibrium with the applied stress; $\sigma = 2\gamma/R$.

Voids are assumed to be arranged on a square grid in the grain boundary plane where the spacing between the neighboring voids is $2b$. The grain boundary is considered to have a thickness designated as δ_{gb}, and vacancies created in the annulus around the grain boundary diffuse to and are absorbed by the void causing it to grow. From the preceding assumptions, the vacancy concentration at the void surface is given, with $p = 0$, by;

$$C_{\mathrm{v}}(R) = C_{\mathrm{v}}^{0} \exp\left(\frac{2\gamma}{R}\frac{\Omega}{kT}\right) . \tag{13.74}$$

The flux of vacancies to the void is:

$$J_{\mathrm{gb}} = \frac{D_{\mathrm{gb}}\nabla\mu}{kT\Omega} , \tag{13.75}$$

where $\nabla\mu$ is the gradient of the chemical potential and D_{gb} is the grain boundary diffusion coefficient. For a void of radius R, the chemical potential is $\mu = \sigma\Omega$ and

the gradient is:

$$\nabla\mu = \frac{\Omega}{b}\left(\sigma - \frac{2\gamma}{R}\right) , \tag{13.76}$$

and the vacancy flux to the void is:

$$J_{\rm gb} = \frac{D_{\rm gb}}{kTb}\left(\sigma - \frac{2\gamma}{R}\right) . \tag{13.77}$$

Assuming the void remains spherical, the time rate of change of the void volume is:

$$\begin{aligned}\frac{{\rm d}V}{{\rm d}t} &= \left(2\pi R\delta_{\rm gb}\right) J_{\rm gb}\Omega \\ &= \frac{2\pi D_{\rm gb}\delta_{\rm gb}\Omega R}{kTb}\left(\sigma - \frac{2\gamma}{R}\right) ,\end{aligned} \tag{13.78}$$

and the rate of growth of the void size is:

$$\frac{{\rm d}R}{{\rm d}t} = \dot{R} = \frac{D_{\rm gb}\delta_{\rm gb}\Omega}{kTRb}\left(\sigma - \frac{2\gamma}{R}\right) . \tag{13.79}$$

This diffusive cavity growth model assumes that diffusion at the cavity surface is much faster than along the grain boundary, allowing the void to maintain its spherical shape. However, if this is not true, then the void will assume a *lens* shape and growth depends more strongly on the stress. It can be shown [49] that for low stresses:

$$\dot{R} = \frac{D_{\rm S}\delta_{\rm S}\Omega\sigma^3}{2kT\gamma^2} , \quad \text{for} \quad 3.5\frac{\sigma b}{\gamma}X \ll 1 , \tag{13.80}$$

and

$$\dot{R} = \frac{(D_{\rm gb}\delta_{\rm gb})^{3/2}}{2(D_{\rm S}\delta_{\rm S})^{1/2}}\frac{\Omega\sigma^{3/2}}{kTb^{3/2}\gamma^{1/2}} , \quad \text{for} \quad 3.5\frac{\sigma b}{\gamma}X \gg 1 , \tag{13.81}$$

where $X = D_{\rm S}\delta_{\rm S}/D_{\rm gb}\delta_{\rm gb}$, $D_{\rm s}$ is the surface diffusion coefficient and $\delta_{\rm s}$ is the surface thickness, or the depth over which surface diffusion occurs.

If helium accumulates in the voids, then it can assist in void growth by virtue of the internal pressure. In this case, Eq. (13.74) is modified to account for the pressure in the void:

$$C_{\rm v}(R) = C_{\rm v}^0 \exp\frac{\Omega}{kT}\left[\left(\frac{2\gamma}{R} - p\right)\right] , \tag{13.82}$$

and the growth law for helium filled bubbles becomes:

$$\dot{R} = \frac{D_{\rm gb}\delta_{\rm gb}\Omega}{kTRb}\left(\sigma - \frac{2\gamma}{R} + p\right) . \tag{13.83}$$

Power-Law Creep-Controlled Void Growth

Cadek [50] reviewed the role of creep in grain boundary void growth and that treatment will be summarized here. Void growth on an isolated grain boundary can only occur if the displacements of the grain in response to cavity growth are accommodated by creep flow in the surrounding grain. In the temperature range of interest for materials in nuclear systems, dislocation creep is the dominant creep mode and both thermal and irradiation-induced dislocation creep mechanisms are described more fully in Chap. 14. Nevertheless, if void growth is occurring faster than can be accommodated by the creep rate, load is shed by the voids to the surroundings until the stress on the cavities is reduced to a value that is compatible with the flow of the solid by creep. The net effect is a reduction in the void growth rate such that the void growth rate is controlled by the creep rate. In this case [46], constrained cavity growth occurs according to the following rate:

$$\dot{R} = \frac{1}{2.5}\left(\frac{b}{R}\right)^2 d_f \dot{\varepsilon}\,, \tag{13.84}$$

where $\dot{\varepsilon}$ is the creep rate and d_f is the grain facet diameter. Compared to the linear stress dependence for diffusional growth of cavities, power-law creep constrained growth is proportional to σ^n through the power-law creep relation: $\dot{\varepsilon} = A(\sigma/B)^n$, giving:

$$\dot{R} = \frac{A}{2.5}\left(\frac{b}{R}\right)^2 \left(\frac{\sigma}{B}\right)^n d_f\,, \tag{13.85}$$

where n is typically between 2 and 3.

Coupled Diffusion and Power-Law Creep

Intermediate to purely diffusive or power-law constrained cavity growth is coupled diffusive and power-law creep-driven growth. In this mode, diffusive cavity growth can be affected by power-law creep of the surrounding matrix such that the diffusion distance in the boundary is reduced and growth is accelerated. In this regime, the volumetric cavity growth rate is:

$$\dot{V} = 2\pi R^3 A \left(\frac{\sigma b^2}{B(b^2 - R^2)}\right)^n\,, \tag{13.86}$$

and the growth law becomes:

$$\dot{R} = \frac{RA}{2}\left(\frac{\sigma b^2}{B(b^2 - R^2)}\right)^n\,. \tag{13.87}$$

From the power-law creep relation, Eq. (13.87) can be written in terms of the creep rate, $\dot{\varepsilon}$ as:

$$\dot{R} = \frac{R}{2}\dot{\varepsilon}\left(\frac{b^2}{b^2 - R^2}\right)^n\,. \tag{13.88}$$

Equations (13.87) and (13.88) apply at high stresses where creep deformation dominates. At low stresses, the rate of growth is controlled by diffusion and the void growth rate is described by Eqs. (13.84) and (13.85).

Failure Strain and Time to Rupture

The time to failure is obtained by integration of the growth law from $R = R_0$, the initial void size to $R = R_f$, where R_f is the void size at failure:

$$t_f = \int_{R_0}^{R_f} \frac{dR}{\dot{R}} \,. \tag{13.89}$$

Alternatively, Eq. (13.89) can be written in terms of the area fraction of cavities as:

$$t_f = \int_{f_0}^{f_f} \frac{df}{f} \,, \tag{13.90}$$

where $f = R^2/b^2$ is the area fraction of cavities. The fractional area occupied by the voids at the point where the voids touch is shown in Fig. 13.39. When voids touch, the separation distance, $b = 2R$, and the fraction of the grain boundary covered by the voids is given by the shaded area in Fig. 13.39. The cross sectional area of the voids on the grain boundary is $4 \times (\pi R^2/4)$, and the grain boundary area is $b^2 = (2R)^2$, so the ratio is $f = \pi R^2/(2R)^2 = \pi/4$. However, rupture will occur sooner as the remaining cross sectional area cannot support the increasing stress. The fracture criterion $f_f = 0.25$ is typically adopted [51]. The strain at failure is determined as follows. For a void of volume $4/3\pi R^3$ at a grain boundary of area $\pi b^2 - \pi R^2$, the relative displacement of the grains is $u = \dfrac{4/3\pi R^3}{\pi b^2}$, and the strain at failure is u/d, where d is the mean grain diameter, giving:

$$\varepsilon_f = 4/3 f_f^{3/2} \frac{b}{d} \,, \tag{13.91}$$

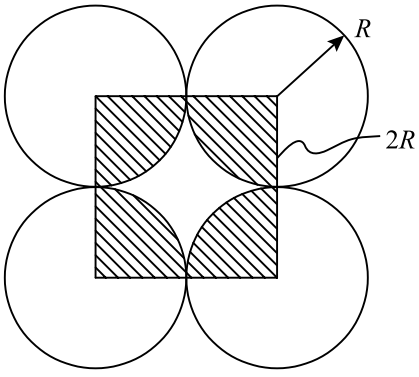

Fig. 13.39. Illustration of grain boundary voids at the point in time where the void surfaces touch

and applying the fracture criterion $f_f = 0.25$ gives:

$$\varepsilon_f \cong 0.17\frac{b}{d} . \tag{13.92}$$

Cocks and Ashby [47] have determined expressions for the failure time for each of the growth mechanisms described in this section. For purely diffusional void growth, the failure time is:

$$t_f \cong t_n + \frac{0.17}{\phi_0 A}\left(\frac{B}{\sigma}\right) , \tag{13.93}$$

$$\text{where} \quad \phi_0 = \frac{2D_{gb}\delta_{gb}\Omega}{kTb^3}\frac{B}{A} , \tag{13.94}$$

and t_n is the void nucleation time. For the power-law creep regime or due to coupled grain boundary diffusion and power-law creep, the failure strain is given by the strain due to creep in the specimen as a whole plus that due specifically to the voids [47]:

$$\varepsilon_f = t_f\dot{\varepsilon} + 0.17\frac{b}{d} , \quad \text{and} \tag{13.95}$$

$$t_f = t_n + \frac{1}{n\dot{\varepsilon}} . \tag{13.96}$$

13.9.2 Grain Boundary Sliding

As the temperature of a metal is increased, fracture under applied stress changes from transgranular to intergranular. Figure 13.40 shows the relationship between strength of the grain matrix and grain boundaries as a function of temperature and strain rate. The intersection between the strength of the grains and that of the grain boundaries is termed the *equicohesive temperature* (ECT) denoting the temperature at which they have equal strength. Above the ECT, grain boundary facture is more likely, while below it, transgranular fracture is preferred. Also shown in Fig. 13.40 is the role of strain rate on the ECT. Decreasing strain rate moves the ECT to lower temperatures, reflecting the increasing importance of grain boundary processes in determining the fracture strength of the metal.

At temperatures in the creep regime, low stresses or strain rates cause fracture to be dominated by wedge cracks leading to fracture across the grain facet and possibly interaction and linkage to final fracture. At still lower stresses, intergranular creep fracture is dominated by the formation, growth and coalescence of grain boundary cavities, as discussed in the previous section. The low to intermediate stress regime is where grain boundary sliding (GBS) can lead to cracking and fracture. Under these conditions, grains are able to slide along grain boundaries resulting in the formation of voids or cracks at triple points as shown in Fig. 13.41. This process is similar to wedge crack formation in brittle fracture discussed in Sect. 13.6, but at high temperature, the source of strain is in the grain boundary rather than in

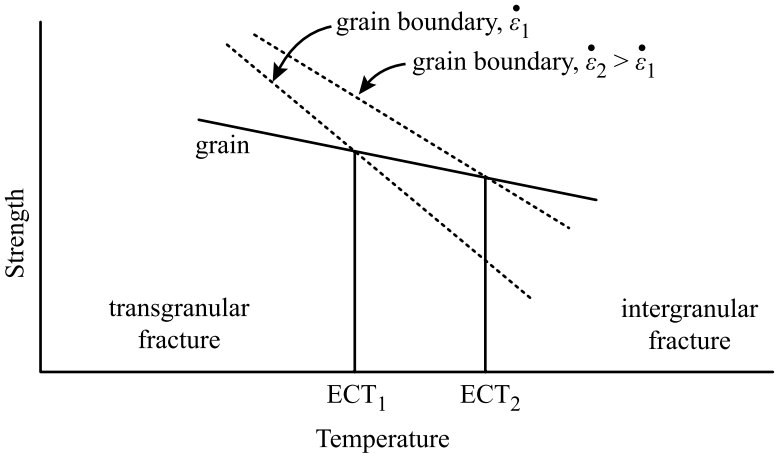

Fig. 13.40. Equicohesive temperature delineating transgranular fracture from intergranular fracture as a function of temperature, and the role of strain rate on the ECT

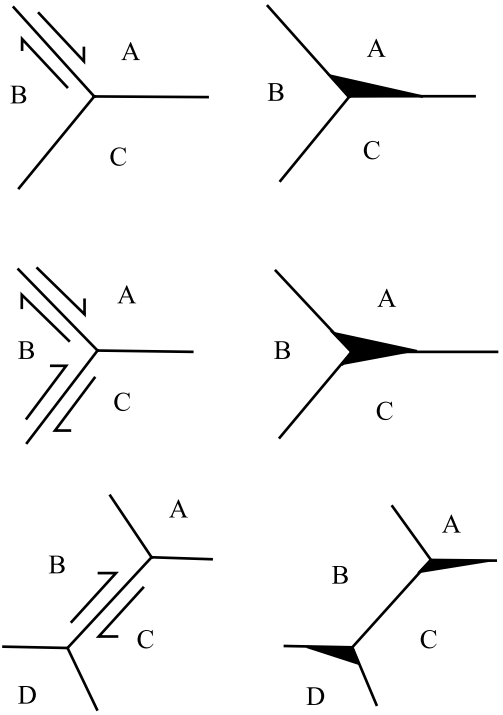

Fig. 13.41. Intergranular cracking due to grain boundary sliding

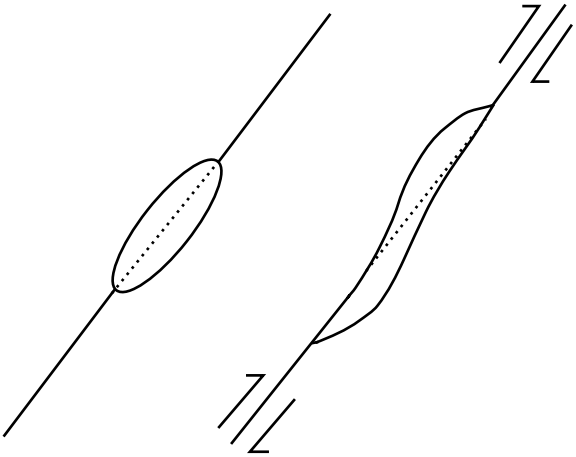

Fig. 13.42. The effect of grain boundary sliding on the shape of the grain boundary cavities

a slip band in the matrix. Grain boundary void formation relieves the localized high stresses at triple points. In fact, GBS is responsible for both grain boundary void formation and growth.

Grain boundary sliding has its origin in the dislocation creep process. Dislocations generated in a neighboring grain due to power-law creep may be incorporated into a grain boundary by glide. These dislocations can move by a combination of glide and climb along the grain boundary. Sliding is accommodated by the opening up of grain boundary voids and the rate of GBS is proportion to the Burgers vector component parallel to the grain boundary plane and controlled by climb [50]. Since GBS is caused by the glide of the same dislocations that causes grain deformation, there is a linear relationship between the strain due to GBS, ε_{gbs} and the total creep strain, ε. The strain rate due to GBS was determined by Langdon [52] to be:

$$\dot{\varepsilon}_{\text{gbs}} = AD_{\text{vol}} \frac{b^2 \sigma^2}{\mu \, \mathrm{d} kT} \,, \tag{13.97}$$

where D_{vol} is the volume diffusion coefficient and d is the mean grain diameter.

Grain boundary sliding can result in crack-like growth of cavities due to distortion and sharpening of the shape of the cavity such that surface diffusion is stimulated. As shown in Fig. 13.42, sliding of the grain boundary produces a more distinct acicular shape to the cavity in which surface diffusion plays a larger role in growth. As such, the rate of cavity growth is linked to the rate of grain boundary sliding. The net effect of GBS is to enhance the transport of matter along the grain boundary, in effect, enhancing the grain boundary diffusion coefficient and accelerating void growth.

13.9.3 Grain Boundary Crack Growth

While link-up of cavities on grain boundary facets results in fracture of the grain boundary, cavity growth and coalescence occur at very different rates due to their non-uniform distribution on grain boundaries. Therefore, local link-up and the formation of a crack that propagates to adjacent grain boundaries is a likely mechanism for intergranular creep crack growth. The cracks propagate by either diffusion of vacancies to the crack tip and deposition of atoms in the grain boundary facet, plastic flow or plastic flow-enhanced diffusion. In either of these cases, the cracks grow in steps by nucleation and growth of cavities that successively link-up with the crack.

Figure 13.43 shows the propagation of a crack along a cavitated grain boundary. As shown in Sect. 13.3, the stress field ahead of the crack tip of a stressed solid is amplified by the presence of the crack, and this stress will enhance growth of cavities closest to the tip. Figure 13.44a shows the stress distributions ahead of grain boundary cracks, cavities and the intermediate case of crack-like cavities leading to subcritical crack growth by cavity growth and coalescence ahead of the crack tip (Fig. 13.44b). When helium is present, the growth of cracks and bubbles is driven by gas absorption and the supply of helium becomes and key factor in limiting their growth. Trinkhaus [53] has shown that subcritical crack growth by void coalescence is favored at high He pressure and low temperatures, while stress-driven void growth dominates at high temperature and low He content, with gas-driven bubble growth becoming important at higher helium contents in the solid (Fig. 13.45).

The mechanisms of high-temperature embrittlement and fracture discussed in the preceding sections apply to unirradiated as well as irradiated solids. So it is appropriate to reiterate the mechanisms by which irradiation can accelerate the embrittlement and fracture processes. First, the nucleation of voids in a solid under stress occurs more easily by virtue of irradiation-induced void growth. As shown earlier, helium produced by transmutation reduces the critical void size for stability and thus enhances void and bubble growth. Both of these processes will accelerate the growth of grain boundary cavities, reducing the time to rupture. At high temperature, where grain boundary strength is reduced relative to the matrix, irradiation hardening can accentuate that difference, favoring fracture along grain boundaries. The occurrence of dislocation channeling results in localized deformation and the efficient transmission of plasticity to the grain boundary that can accelerate grain boundary sliding

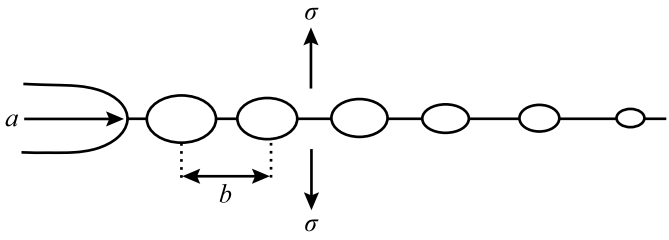

Fig. 13.43. Propagation of a crack by the growth of cavities ahead of the crack tip

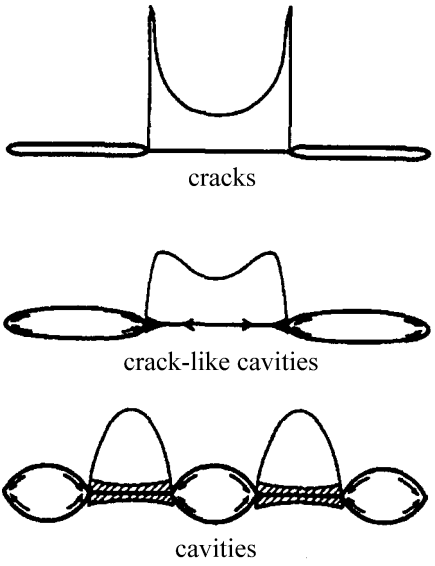

(a)

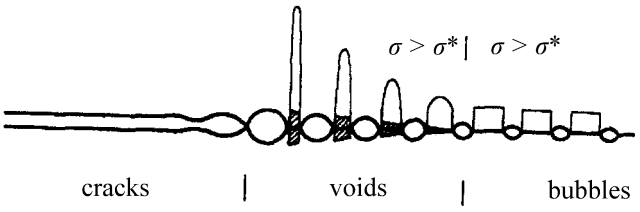

(b)

Fig. 13.44. Schematic illustration of (a) the stress distribution between cracks, cavities and crack-like cavities, and (b) the growth of a crack by unstable void growth and coalescence ahead of the crack tip (from [53])

and contribute to grain boundary void formation and growth. Finally, the incorporation of transmutation helium into grain boundary voids can assist in grain boundary crack growth by link-up of voids. So in summary, while high-temperature grain boundary embrittlement is characteristic of deformation and fracture in unirradiated metals, irradiation during deformation can significantly enhances these processes and shorten the time to failure.

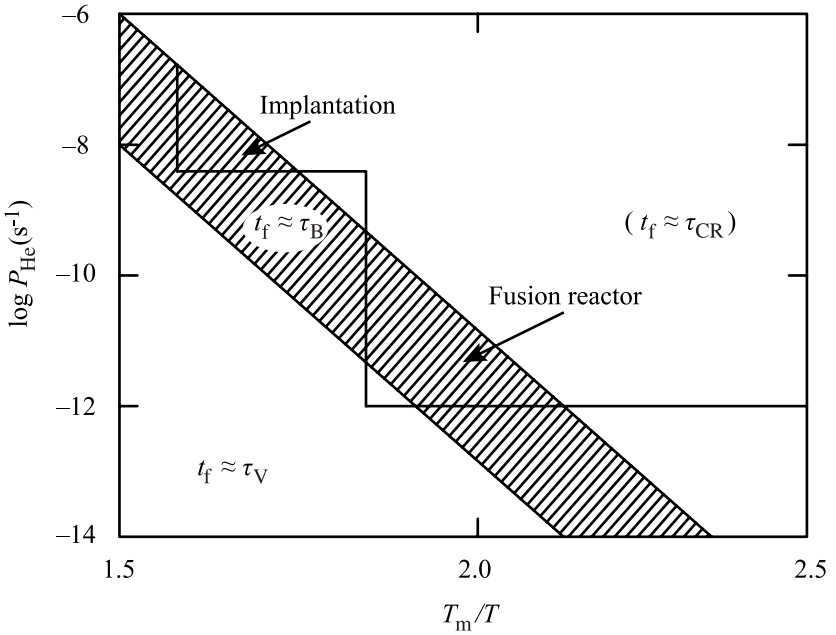

Fig. 13.45. Mechanisms controlling the lifetime, t_f of a sample under stress, gas-driven stable bubble growth, τ_B, stress-driven unstable void growth, τ_V and subcritical crack growth by void coalescence, τ_{CR} (from [53])

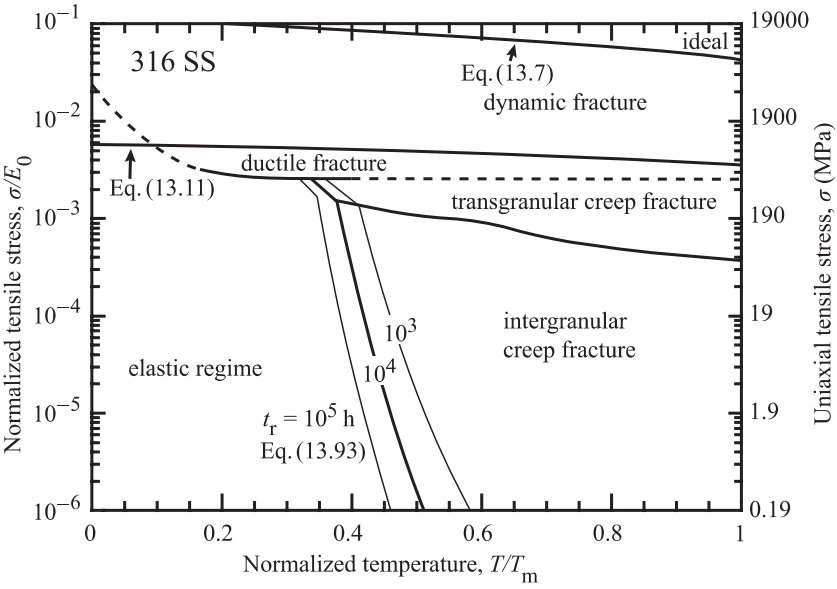

Fig. 13.46. Fracture mechanism map for 316 stainless steel (from [55])

13.9.4 Fracture Mechanism Maps

Similar to deformation mechanism maps described in Chap. 12, Ashby-type maps of fracture mechanisms can be constructed to show the regimes for the different types of fracture as a function of normalized stress and homologous temperature [54]. In these maps, the rupture time is used to determine the boundaries between various fracture mechanisms. Unfortunately, the constitutive equations describing fracture are not as well-established for the various fracture mechanisms. A fracture map for stainless steel constructed by Zinkle [55] is shown in Fig. 13.46. The upper most line describes the ideal fracture strength of the alloy as given by Eq. (13.7). The fracture stress separating the elastic regime from cleavage is given by Eq. (13.11). The boundary between the elastic regime and the intergranular creep fracture regime is described by Eq. (13.93). The effect of irradiation on the fracture mechanism map is through changes in time to rupture defining the regime boundaries. In fcc metals, the primary effect of irradiation is on the intergranular creep fracture regime due to high-temperature helium embrittlement. In bcc metals, radiation hardening will increase the cleavage regime.

Nomenclature

a	Lattice parameter. Also crack length
B	Compact tension sample thickness
b	Half spacing between voids on a grain boundary
c	Half-crack length
C_v	Energy absorbed in a Charpy V-notch test. Also vacancy concentration
d	Grain size or obstacle diameter or separation distance of partial dislocations
d_f	Grain facet diameter
D	Diffusion coefficient
e_u	Engineering uniform elongation strain
E	Elastic modulus
E_U	Charpy upper shelf energy
f	Fractional change in upper shelf energy. Also area fraction of cavities on grain boundaries
f_f	Fracture criterion for area fraction of grain boundaries
F	Work done by an external force
G	Crack extension force
G_c	Crack extension force corresponding to fracture toughness
J	Value of the J integral, defined in Eq. (13.37)
k	Boltzmann's constant
K	Stress intensity factor
K_c	Fracture toughness
K_{Jc}	Fracture toughness equivalent to J_c
$K_{Jc(med)}$	Median fracture toughness

k_s	Irradiation-induced increase in yield stress
k_y	Unpinning parameter or source hardening contribution to the yield stress
L	Length of dislocation pile-up on a slip plane
M	Taylor factor
n	Number of dislocations in a pile-up
P	Load
r_p	Plastic zone size
RT_{NDT}	Reference nil-ductility temperature
R	Void radius
t	Time
t_f	Creep rupture life
t_n	Void nucleation time
T	Temperature
T^*	Temperature at which flow stress and fracture stress curves intersect
T_m	Tearing modulus
T_0	Reference temperature for Master curve
ΔT_{xy}	Charpy transition temperature shift at a C_V value of xy
U_E	Elastic strain energy
U_f	Work to create a surface by fracture
U_S	Decrease in strain energy due to formation of crack surfaces
V	Volume. Also potential energy of the system.
W	Work. Also width parameter for the compact tension sample
β	Constant related to the degree of triaxiality of the applied stress. Also ratio of crack opening to void spacing, Eq. (13.71)
ε	Strain
ε_f	Fracture strain
$\dot{\varepsilon}$	Creep strain
ϕ	Neutron flux
ϕt	Neutron fluence
Δ_z	Displacement of last ligament at a crack tip
δ	Crack opening displacement, COD
δ_t	Crack tip opening displacement, CTOD
γ	Surface energy
γ_e	Effective surface energy
γ_p	Plastic work term
λ	Lattice wavelength spacing
μ	Shear modulus. Also chemical potential
ν	Poisson's ratio
Ω	Atomic volume
σ	Tensile stress
σ_a	Applied stress
σ_f	Fracture stress

σ_i	Friction stress
σ_0	Flow stress
σ_{th}	Theoretical cohesive strength
σ_y	Yield stress
τ	Defect lifetime

Subscripts

c	Critical value of K, G or J for onset of fracture
f	Fracture. Also final
gb	Grain boundary
gbs	Grain boundary sliding
I, *II*, *III*	Fracture mode
R	Rupture
S	Surface
u	Uniform, also displacement
v	Vacancy
V	Void
vol	Volume
0	Initial

Superscripts

n	Exponent on stress in the creep equation. Also exponent on ΔK in the crack growth rate equation Eq. (13.68)

Acronyms

COD	Crack opening displacement
CRP	Copper-rich precipitates
DBTT	Ductile-to-brittle transition temperature
ECT	Equicohesive temperature
GBS	Grain boundary sliding
LEFM	Linear elastic fracture mechanics
NDT	Nil-ductility temperature
RPV	Reactor pressure vessel
USE	Upper shelf energy

Problems

13.1 In an AISI 4340 steel, γ_e, the effective surface energy that takes into account the work done in expanding the crack, is about 1.5×10^3 Pa m. Assuming a grain size of ASTM 8:

a) Compute the stress to propagate a crack equal in length to an average grain diameter. Take $E = 200$ GPa.

b) Using the value computed in part (a), calculate the crack length for unstable fracture in AISI 4340 given that $K_{IC} = 58\,\text{MPa}\,\text{m}^{1/2}$.

13.2 A fracture toughness measurement conducted at $-40\,^{\circ}\text{C}$ gave a crack extension force G_{IC} value of $7.08\,\text{N/m}$ for a low-carbon steel of grain size $23\,\mu\text{m}$ and $E = 207\,\text{GPa}$. Compute the effective surface energy $\gamma_e = \gamma_s + \gamma_p$, in (Pa m) associated with the crack propagation.

13.3 From the knowledge that the yield strength of a pressure vessel steel can be described by the Hall–Petch relationship Eq. (12.63) and that the fracture strength can be described by the Cottrell–Petch Eq. (13.54) and the temperature dependence of each of these terms, explain:

a) Why the fracture toughness increases with increasing temperature while the yield strength decreases

b) How the fracture toughness and yield strength curves plotted as a function of temperature would change if the sample were irradiated.

13.4 A steel plate is 305 mm wide and 6.35 mm thick. It contains a 25.4 mm long crack along each edge.

a) Calculate the force required to propagate the crack the remaining 254 mm across the width of the plane.

b) Calculate the force required to break the plate in tension if there were no crack. Assume the fracture strength is $7 \times 10^6\,\text{MPa}$ (10^5 psi).

c) Calculate the force required to break the plate in tension at the theoretical cohesive strength.

For steel, use: $E = 100\,\text{GPa}$ ($14.5 \times 10^6\,\text{psi}$)

$\gamma_s = 1\,\text{J/m}^2$

$a = 3 \times 10^{-10}\,\text{m}$

13.5 Draw a Charpy impact energy curve for a carbon steel before and after irradiation at $300\,^{\circ}\text{C}$ to $2 \times 10^{19}\,\text{n/cm}^2$.

a) Explain the behavior of irradiation in terms of σ_y and σ_f.

b) List the factors that may influence the NDT and ductile shelf energy. Explain the mechanism and the direction of change.

13.6 Consider helium bubbles 100 nm in radius located on a grain boundary.

a) To what size do the bubbles grow under the influence of a tensile stress one-half the critical value for instability?

b) Two of the bubbles coalesce. What is the equilibrium size of the new bubble?

13.7 A fusion first wall made of austenitic stainless steel is subjected to a fast neutron flux of $5 \times 10^{14}\,\text{n/cm}^2\text{s}$ ($E > 1\,\text{MeV}$) and a stress of one-half of the unirradiated yield strength. After 300 days, the pin is removed and analyzed by transmission electron microscopy (TEM). It is revealed that 30% of the grain boundary is covered with either voids or bubbles (undiscernable in the TEM) with an average size of 50 nm. Given the following information, make a prediction of the time to rupture and the failure mechanism:

$\sigma_y = 280\,\text{MPa}$
$d = 20\,\mu\text{m}$
$\gamma_{ss} = 5\,\text{MPa}$
$\dot{\varepsilon} = C\sigma\phi =$ steady state creep rate
$C = 1.3 \times 10^{-27}\,\text{cm}^2/\text{MPa}$

13.8 At 300 °C, 2% of the volume of a solid is occupied by equilibrium bubbles, all of which have radius R_i. The number of gas atoms is assumed to remain unchanged for all cases described below. Ideal gas behavior is assumed, so that the number of gas atoms in an equilibrium bubble is $m = \frac{4\pi R^2}{3}\frac{2\gamma}{kT}$.

a) Impurity atoms segregate to the bubble surfaces, leading to a 30% reduction in the surface free energy, γ. Calculate the volume fraction occupied by bubbles after equilibrium is re-established.

b) The temperature is then raised to T = 800 °C, which leads to diffusion of the impurities into the bulk, restoring the original value of γ. Calculate the volume fraction occupied by bubbles after equilibrium is re-established.

c) For the same initial conditions (2% at 300 °C), bubbles coalesce in groups of ten and reach equilibrium. What is the resulting volume fraction occupied by bubbles?

13.9 A fuel pin under an applied stress of 140 MPa fails, owing to helium embrittlement at a strain of 1%. What concentration (in atomic ppm) of helium in the metal is necessary to cause fracture at this value of the strain? The irradiation temperature is 700 °C.

References

1. Dieter GE (1976) Mechanical Metallurgy, 2nd edn. McGraw-Hill, New York
2. Griffith AA (1968) Trans Am Soc Met 61:871–906
3. Inglis CE (1913) Trans Inst Nav Archit 55(1):219–230
4. Orowan E (1950) In: Fatigue and Fracture of Metals. Wiley, New York
5. Irwin GR (1958) Encyclopedia of Physics, IV. Springer, Berlin Heidelberg New York
6. Reed-Hill RE (1973) Physical Metallurgy Principles, 2ndedn. D Van Nostrandm New York
7. ASTM (2005) E399-05 Standard Test Method for Linear-Elastic Plane-Strain Fracture Toughness K_{Ic} of Metallic Materials. ASTM International, West Conshohocken, PA
8. Reed-Hill RE (1992) Physical Metallurgy Principles, 3rd edn. PWS, Boston
9. Dugdale DS (1960) J Mech Phys Solids 8:100
10. Anderson TL (1995) Fracture Mechanics, 2nd edn. CRC, New York, p 142
11. Cottrell AH (1958) Trans AIME 212:192
12. Zener C (1948) In: Fracturing of Metals. American Society for Metals, Metals Park, Ohio
13. Stroh AH (1957) Adv Phys 6:418

14. Bement AL (1972) Rev Roum Phys 17(4):505
15. Petch NJ (1957) Fracture. Wiley, New York, p 54
16. Murty KL (1999) J Nucl Mater 270:115–128
17. Johnson AA (1962) Phil Mag 7:177
18. Mager TR, Hazelton WS (1969) Radiation Damage in Reactor Materials, vol I. IAEA, Vienna, p 317
19. Steele LE (1975) Neutron Irradiation Embrittlement of Reactor Pressure Vessel Steels. IAEA, Vienna,
20. ASTM (2000) E 208-95, Standard Test Method for Conducting Drop-Weight Test to Determine Nil-Ductility Transition Temperature of Ferritic Steels. ASTM International, West Conshohocken, PA
21. Odette GR, Lambrozo PM, Wullaert RA (1985) In: Garner FA, Perrin JS (eds) Effects of Irradiation on Materials the 12th International Symposium, ASTM STP 870. American Society for Testing and Materials, Philadelphia, PA, pp 840–850
22. English CA, Ortner SR, Cage G, Server WL, Rosinski ST (2001) In: Rosinski ST, Grossbeck ML, Allen TR, Kumar AS (eds) Effects of Radiation on Materials the 20th International Symposium, ASTM STP 1405. American Society for Testing and Materials, West Conshohocken, PA, 2001, pp 151–173
23. Hausild P, Kyta M, Karlik M, Pesck P (2005) JNM 341:184–188
24. Odette GR, Lucas GE (1996) J Non Destructive Eval 15:137
25. Sokolov MA, Nanstad RK, Miller MK (2004) J ASTM Int 1(9):123–137
26. Lott RG, Rosinski ST, Server WL (2004) J ASTM Int 1(5):300–310
27. Hahn GT, Rosenfield AR (1966) Acta Metal 14:815
28. Stoller RE (2004) J ASTM Int 1(4):326–337
29. Steele LE, Hawthorne JR (1967) ASTM STP-426, Effects of Irradiation on Structural Materials. American Society for Testing and Materials, Philadelphia, PA, p 534
30. Steele LE, Davies LM, Ingham T, Brumovsky M (1985) Garner FA, Perrin JS (eds) Effects of Irradiation on Materials the 12th International Symposium. American Society for Testing and Materials, Philadelphia, PA, 1985, pp 863–899
31. Sokolov MA, Chernobaeva AA, Nanstad RK, Nikolaev YA, Korolev YN (2000) In: Hamilton ML, Kumar AS, Rosinski ST, Grossbeck ML (eds) Effects of Radiation on Materials the 19th International Symposium, ASTM STP 1366. American Society for Testing and Materials, West Conshohocken, PA, 2000, pp 415–434
32. U S Nuclear Regulatory Commission (1998) Regulatory Guide 199, Radiation Embrittlement of Reactor Vessel Materials, Revision 2. US Nuclear Regulatory Commission, Washington, DC, May 1998
33. Odette GR, Lucas GE (1998) Rad Eff Defects Solid 44:189
34. Odette GR, Lucas GE (2001) JOM July:18–22
35. Horsten MG, van Osch EV, Gelles DS, Hamilton ML (2000) In: Hamilton ML, Kumar AS, Rosinski ST, Grossbeck ML (eds) Effects of Radiation on Materials the 19th International Symposium, ASTM STP 1366. American Society for Testing and Materials, West Conshohocken, PA, 2000, pp 579–593
36. Callister WD (1991) Materials Science and Engineering, an Introduction. Wiley, New York
37. Laird C (1967) Fatigue Crack Propagation, ASTM STP-415. American Society for Testing and Materials, Philadelphia, PA, 1967, p 131
38. James LA (1977) Nucl Safety 18(6):791
39. Cullen WH, Watson HE, Taylor RE, Loss FJ (1981) J Nucl Mater 96:261
40. Lucas GE (1993) J Nucl Mater 206:287–305

41. Odette GR, Lucas GE (1992) J Nucl Mater 191–194:50–57
42. US Nuclear Regulatory Commission (2003) Fracture Toughness and Crack Growth Rates of Irradiated Austenitic Stainless Steels, NUREG/CR-6826. US Nuclear Regulatory Commission, Washington, DC, p 21
43. Odette GR, Lucas GE (1991) J Nucl Mater 179–181:572
44. Wolfer WG, Jones RH (1981) J Nucl Mater 103/104:1305–1314
45. Lloyd G (1982) J Nucl Mater 110:20–27
46. Murty KL, Holland FR (1982) Nucl Technol 58:530–537
47. Bloom EE (1976) Irradiation strengthening and embrittlement. In: Radiation Damage in Metals. American Society for Metals, Metals Park, OH, pp 295–329
48. Hull D, Rimmer DE (1959) Phil Mag 4:673
49. Nix WD, Yu KS, Wang JS (1983) Metal Trans 14A:563
50. Cadek J (1988) Creep in Metallic Materials, Materials Science Monographs 48. Elsevier, New York
51. Cocks ACF, Ashby MF (1982) Prog Int Mat Sci 27:189–244
52. Langdon TG, Vastava RB (1982) In: Rhode RW, Swearengen JC (eds) Mechanical Testing for Deformation Model Development, ASTM STP 765. American Society for Testing and Materials, Philadelphia, PA, 1982, p 435
53. Trinkaus H, Ullmaier H (1994) J Nucl Mater 212–215:303–309
54. Teirlinck D, Zok F, Embury JD, Ashby MF (1988) Acta Metal 36:1213–1228
55. Li M, Zinkle SJ (2007) J Nucl Mater 361(2–3) 192–205

14 Irradiation Creep and Growth

Creep is the time-dependent deformation of a metal under constant load and at high temperature ($T/T_m > 0.3$). The metal responds by elongating with a strain defined as either the nominal strain, ε, calculated from the original length of the sample:

$$\varepsilon = \int_{l_0}^{l} \frac{\mathrm{d}l}{l_0} = \frac{l - l_0}{l_0} , \tag{14.1}$$

or as the true strain, ε_T, determined from the instantaneous length of the sample:

$$\varepsilon_T = \int_{l_0}^{l} \frac{\mathrm{d}l}{l} = \ln \frac{l}{l_0} = \ln(1 + \varepsilon) . \tag{14.2}$$

The nominal or engineering strain is related to the nominal or engineering stress corresponding to the initial cross section of the sample, while the true strain is related to the true stress corresponding to the instantaneous cross section. The components of strain are elastic, anelastic, and plastic. Elastic strain is instantaneous, time-independent and reversible upon release of the stress. An elastic strain is also reversible but depends on strain rate. Plastic strain is time-dependent, irreversible and is characterized by a volume conservative change in shape, or distortion of the sample. Creep refers to the time-dependent component of plastic strain.

In general, creep is a very temperature-dependent process, requiring the thermal formation of vacancies and the motion of vacancies by volume or grain boundary diffusion, or the climb of dislocations over obstacles and glide along slip planes. The probability of vacancy formation and of vacancy or dislocation motion is proportional to $\exp(-Q/kT)$, where Q is the activation energy for the rate limiting process. Increased temperature provides the thermal energy required to overcome obstacles and barriers to dislocation motion. Creep is also dependent on the stress and the nature of the stress dependence provides information about the mechanism by which it occurs. Due the production of excess defects, irradiation can accelerate creep. Irradiation creep is not strongly dependent on temperature, primarily because the formation of vacancies and self-interstitials is provided by energetic atomic displacement rather than by thermal processes. Creep is most important in reactor applications in regions of intermediate temperature, high neutron/ion flux and low stress. However, before we attempt to understand the role of irradiation in creep, we will review the main thermal creep mechanisms, as they will constitute the foundation for understanding irradiation creep.

14.1 Thermal Creep

In most alloys, thermal creep proceeds through a sequence of stages as shown in Fig. 14.1. In stage I, the metal undergoes strain hardening leading to a decrease in strain rate with time. At long times, necking occurs due to localized deformation resulting in an increase in the strain rate, stage III. Between these two stages is stage II, during which the creep rate is either constant or a minimum. In this region, strain hardening is balanced by recovery so that the creep rate is relatively constant. Creep in this regime is designated as steady state or secondary creep. This is also the region of most technological importance and in which the majority of service life is spent. The variables describing plastic deformation are the shear stress σ_s, temperature T, strain rate $\dot{\varepsilon}$, and strain ε, or time, t. The key-independent variables governing creep in metals in practical applications are temperature and stress, and the deformation mechanisms can be characterized according to these variables. As discussed in Chap. 12, Sect. 12.3, the Ashby-type deformation mechanism map can be used to describe the various deformation processes as a function of normalized stress and homologous temperature. In that chapter we focused on the regions described by plastic collapse and dislocation glide. Here we will focus on the regions that exhibit rate-dependent plasticity, or creep.

Figure 14.2 shows a deformation mechanism map for pure nickel. We begin by developing the equations for the strain rate. The strain rate in the region of dislocation glide is given by the Orowan equation, which is a relationship between the strain rate and dislocation velocity and is determined as follows. When an edge dislocation moves completely across a slip plane, the upper half of the crystal is sheared relative to the lower half by an amount equal to one Burgers vector, b (Fig. 14.3a and 14.3b). If the dislocation moves only part way across the crystal, or a distance Δx, then the top surface is translated by an amount $b\Delta x/x$ relative to the bottom

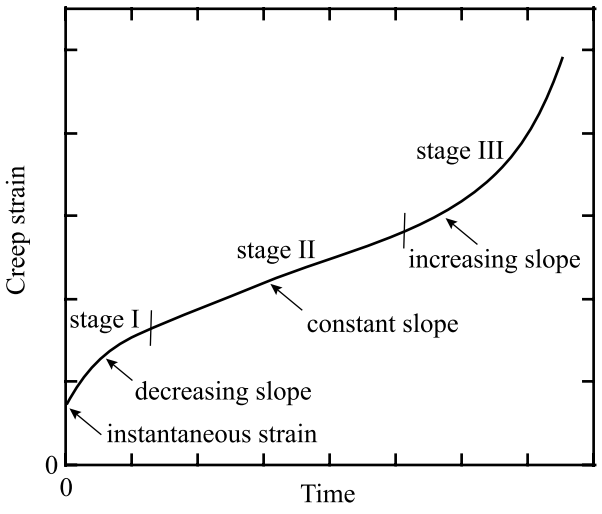

Fig. 14.1. Creep curve of a metal exhibiting the classical three stages of creep

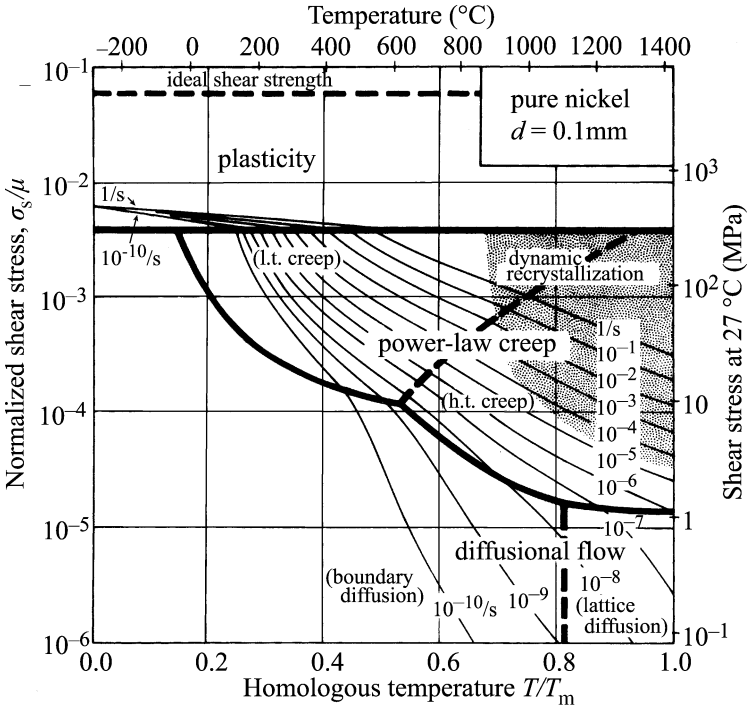

Fig. 14.2. Deformation mechanism map for pure nickel in which the strain rates and deformation mechanisms are given as a function of the normalized shear stress and the homologous temperature (after [1])

surface (Fig. 14.3c). So the displacement of the top half of the crystal relative to the bottom half is in relation to the fraction of the length the crystal has slipped. If the area of the slip plane is A, then $b\Delta A/A$ is the equivalent expression. The shear strain, ε_s is the displacement divided by the height, z of the crystal and is then given by:

$$\varepsilon_s = \frac{b\Delta A}{A}\frac{1}{z}. \tag{14.3}$$

The term zA is the volume of the crystal, V. For n dislocations of length, l moving an average distance $\overline{\Delta x}$ on the slip plane, the area swept out by the dislocation, ΔA, can be written as $nl\overline{\Delta x}$, giving:

$$\varepsilon_s = \frac{nbl\overline{\Delta x}}{V}\,. \tag{14.4}$$

The term nl/V is the mobile dislocation density, ρ_m, and if the dislocations move over the distance in a time interval Δt, Eq. (14.4) can be written as a strain rate:

$$\dot{\varepsilon}_s = \rho_m b v_d\,, \tag{14.5}$$

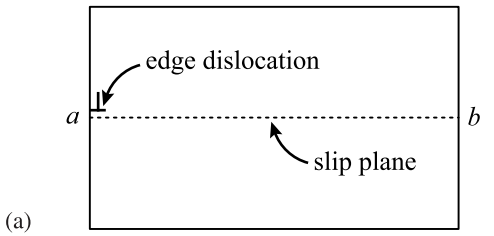

(a)

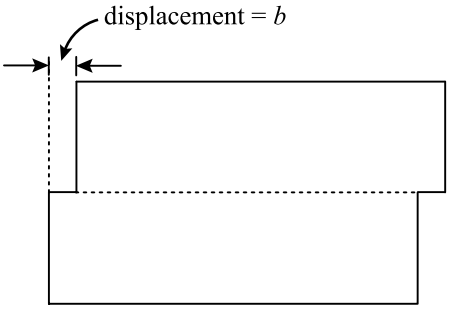

(b)

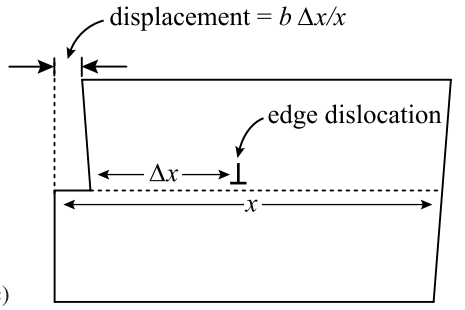

(c)

Fig. 14.3. Displacement of halves of a crystal due to passage of a dislocation along its slip plane

where $\dot{\varepsilon}_s$ is the shear strain rate and v_d is the average dislocation velocity. Equation (14.5) can be expressed in terms of the tensile strain rate, $\dot{\varepsilon}$ as:

$$\dot{\varepsilon} = 1/2\rho_m b v_d \,, \tag{14.6}$$

where 1/2 is an approximate Schmid orientation factor.

At steady state, ρ_m is a function of stress and temperature only. As given in Eq. (7.32b), the shear stress $\sigma_s = \mu b/R$, where μ is the shear modulus, R is half the distance to the next dislocation. Since R is proportional to $\rho^{-1/2}$, then Eq. (7.32b) becomes:

$$\rho_m = \alpha \left(\frac{\sigma_s}{\mu b} \right)^2 , \tag{14.7}$$

where α is a constant of order unity. The form of Eq. (14.7) depends on the process limiting plasticity at low temperature, discrete obstacles, lattice resistance or phonon/electron drag [1].

High-temperature plasticity is described by the following:

$$\dot{\varepsilon} = c\left(\frac{\sigma_s}{\mu}\right)^n , \tag{14.8}$$

where n varies between 3 and 10 and is termed power-law creep. Power-law creep can occur by glide, climb-enabled glide, or Harper–Dorn creep, each process characterized by a different dependence on the stress. At very high stresses (above $10^{-3}\mu$), the strain rate is higher than predicted by power-law creep and this regime is termed power-law breakdown where the creep rate is given in the following form:

$$\dot{\varepsilon} = B\exp(A\sigma_s)\exp\left(\frac{-Q}{kT}\right) , \tag{14.9}$$

where the activation energy, Q often exceeds values for self-diffusion.

At high temperatures (lower right portion of the map in Fig. 14.2), diffusional flow can drive creep. For creep controlled by lattice diffusion, the creep rate is described by:

$$\dot{\varepsilon} = \frac{A\sigma_s\Omega D_{vol}}{kTd^2} , \tag{14.10}$$

where D_{vol} is the volume diffusion coefficient and d is the grain size. When grain boundary diffusion dominates, then the creep rate varies as d^{-3}:

$$\dot{\varepsilon} = \frac{A\pi\delta_{gb}\sigma_s\Omega D_{gb}}{kTd^3} , \tag{14.11}$$

and D_{gb} is the grain boundary diffusivity and δ_{gb} is the effective thickness of the grain boundary. Equations (14.10) and (14.11) can be combined into a single equation describing creep as:

$$\dot{\varepsilon} = \frac{A\sigma_s\Omega D_{eff}}{kTd^2} , \tag{14.12}$$

where the effective diffusion coefficient, D_{eff} is given by:

$$D_{eff} = D_{vol}\left[1 + \frac{\pi\delta gb}{d}\frac{D_{gb}}{D_{vol}}\right] . \tag{14.13}$$

A more complete discussion of diffusional creep will be given in Sect. 14.1.2. We will focus first on dislocation creep as this is the mechanism of primary relevance to irradiation creep.

14.1.1 Dislocation Creep

Climb and Glide

In the climb and glide model, creep is controlled by the time required for a dislocation, blocked by an obstacle, such as a void, loop, etc., to climb to a slip plane that does not intersect the obstacle so it is free to glide. The obstacle blocking the slip of a dislocation on its glide plane causes additional dislocations generated by a nearby source to pile up behind it, as shown in Fig. 14.4. The stress fields of the dislocations overlap and create an increasing stress on the dislocation at the head of the pile-up. For a solid with a mobile dislocation density, ρ_m, each dislocation, driven by a stress σ, travels a mean distance, l by glide, resulting in a strain:

$$\varepsilon = \rho_m b l \, . \tag{14.14}$$

The strain rate is:

$$\dot{\varepsilon} = b\frac{\mathrm{d}}{\mathrm{d}t}(\rho_m l) = b\rho_m \frac{\mathrm{d}l}{\mathrm{d}t} + bl\frac{\mathrm{d}\rho_m}{\mathrm{d}t} \, , \tag{14.15}$$

where $\bar{v} = \dfrac{\mathrm{d}l}{\mathrm{d}t}$ is the mean glide velocity, and $\dfrac{\mathrm{d}\rho_m}{\mathrm{d}t}$ is the generation rate of dislocations. We will assume that $\rho_m \bar{v} \gg l\dfrac{\mathrm{d}\rho_m}{\mathrm{d}t}$, so that creep is controlled by dislocation velocity and not dislocation generation, then the creep rate is the same as that given in Eq. (14.5), $\dot{\varepsilon} = \rho_m b \bar{v}$. However, if the moving dislocation encounters obstacles along its path, which it must overcome, then the velocity must account for the time that the dislocation is held up by the obstacle and not just its motion on the glide plane. The effective velocity can be written as:

$$\bar{v} = \frac{l}{t} = \frac{l}{t_c + t_g} \, , \tag{14.16}$$

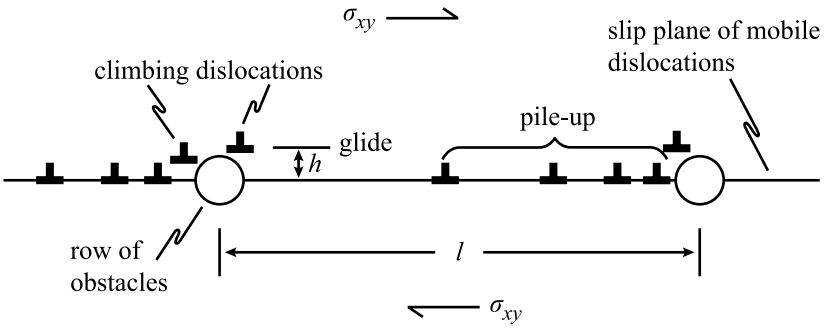

Fig. 14.4. Schematic showing the pile-up of dislocations behind an obstacle on the glide plane of the dislocations

where t_g is the time spent in glide and t_c is the time spent pinned at the obstacle and l is the distance between obstacles. As will be discussed in the next section, the dislocation overcomes the obstacle by climbing to a slip plane that bypasses the obstacle. The time required for climb is much greater than that for glide, so that Eq. (14.16) reduces to:

$$\bar{v} \approx \frac{l}{t_c} . \tag{14.17}$$

For an obstacle of height h, the time that the dislocation spends climbing to a slip plane that bypasses the obstacle can be written as:

$$t_c = \frac{h}{v_c} , \tag{14.18}$$

where v_c is the climb velocity. Substituting Eqs. (14.17) and (14.18) into Eq. (14.6) gives:

$$\dot{\varepsilon} = \rho_m b l \frac{v_c}{h} . \tag{14.19}$$

Equation (14.19) shows that determination of the creep rate amounts to determining the obstacle height and the climb velocity of the dislocation. The obstacle height is determined in the next section.

Obstacle Height

Obstacles to dislocations are often other dislocations. Equation Eq. (7.51) described the force on a moving edge dislocation due to a stationary edge dislocation. That force has two components, one in the x-direction (along the glide plane) and one in the y-direction (perpendicular to the glide plane). From Eq. (7.51), those forces are:

$$F_x = \frac{\mu b^2}{2\pi(1-\nu)r}(\cos\theta\cos 2\theta) \tag{14.20a}$$

$$F_y = -\frac{\mu b^2}{2\pi(1-\nu)r}\sin\theta(2+\cos 2\theta) , \tag{14.20b}$$

where we have dropped the individual designations on the Burgers vectors. Substituting for r using $y = r\cos\theta$ gives:

$$F_x = \frac{G}{y}\sin\theta\cos\theta\cos 2\theta = \frac{G}{y}g_x(\theta) \tag{14.21a}$$

$$F_y = -\frac{G}{y}\sin^2\theta(2+\cos 2\theta) = -\frac{G}{y}g_y(\theta) . \tag{14.21b}$$

where $G = \dfrac{\mu b^2}{2\pi(1-\nu)}$ and $g_{x,y}(\theta)$ are functions of θ in Eq. (14.21). The force on the moving dislocation due to the applied shear stress is $F = \sigma_{xy} b$. This force is

balanced by that due to the repulsion from the stationary dislocation, Eq. (14.21a) giving:

$$\sigma_{xy} b = F_x = \frac{G}{y} g_x(\theta) \, . \tag{14.22}$$

The blocked dislocation is also subjected to a climb force provided by F_y Eq. (14.21b). Under this force, the dislocation will climb in a direction perpendicular to its slip plane until it reaches the point where the glide plane no longer intersects the obstacle. During its climb, the angle between the two dislocations increases starting from a value near $\theta = 0$. Referring back to the variation in force between the two dislocations as a function of angle and separation distance, r, shown in Fig. 7.33, we re-plot the angular dependence of the forces in Fig. 14.5 over the range $0 \leq \theta \leq \pi$ for a separation given by y, where the angular dependence is given by $g_{x,y}(\theta)$ in Eq. (14.21) and $y = r \sin\theta$. Note that the restraining force between the two dislocations increases with θ initially. Once the angle reaches $\pi/8$ the restraining force is at a maximum. If the force due to the applied stress has remained in balance with the restraining force, then for values of θ above $\pi/8$, the applied stress will exceed the restraining force and the dislocation will be free to move beyond the obstacle. Setting $g_x(\theta)$ to its maximum value in Eq. (14.22), and designating the value of y at this point as the height of the obstacle, h that must be overcome for the dislocation

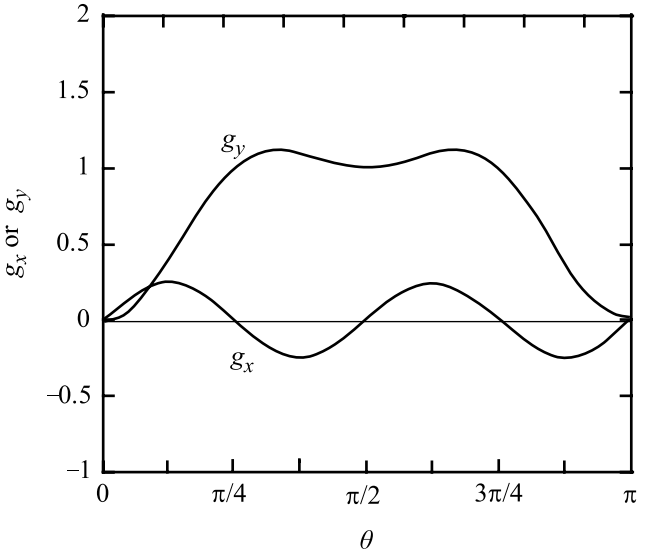

Fig. 14.5. Plot of the angular components, $g_x(\theta)$ and $g_y(\theta)$ of the force on an edge dislocation due to a stationary edge dislocation where y is the vertical separation distance between the two

to be able to continue to glide yields an expression for h:

$$h = y = \frac{G}{4\sigma_{xy} b}$$
$$= \frac{\mu b}{8\pi(1-\nu)\sigma_{xy}} \sim \frac{\mu b}{16\sigma_{xy}} \quad \text{for} \quad \nu \sim 1/3 \,. \tag{14.23}$$

When there are n dislocations in a pile-up against the obstacle, the stress in Eq. (14.23) is multiplied by n.

Climb Velocity

An edge dislocation of Burgers vector b, subjected to a normal stress, σ perpendicular to the extra plane of atoms, climbs in the direction normal to the slip plane. Climb occurs by absorption or emission of vacancies at the dislocation core. We will assume that this process occurs along the entire length of the dislocation line. When the solid is under an applied stress, σ (tensile is positive) the vacancy concentration in equilibrium with the dislocation is given by:

$$C(R) = C_{\mathrm{v}}^0 \exp\left(\frac{\sigma\Omega}{kT}\right) \,, \tag{14.24}$$

where Ω is the atomic volume and C_{v}^0 is the equilibrium vacancy concentration in the solid, a distance R away, where R is the distance between dislocations in the solid and is given by $R = 1/\sqrt{\pi\rho_{\mathrm{d}}}$, where ρ_{d} is the dislocation density such that $\pi R^2 \rho_{\mathrm{d}} = 1$ (area per dislocation $\times$ dislocations per unity area $= 1$). The distance R also defines the *unit cell* that reproduces, on average, the collection of ρ_{d} dislocations in the solid.

Driven by the difference in vacancy concentration between the dislocation core and the radius of the cylinder of the unit cell, defined by R, the vacancy flux to the dislocation is:

$$J = 2\pi r D_{\mathrm{v}} \frac{\mathrm{d}C_{\mathrm{v}}}{\mathrm{d}r} \,, \tag{14.25}$$

where C_{v} is the vacancy concentration in the region $r_{\mathrm{c}} < r < R$, (r_{c} is the dislocation core radius), and is described by the diffusion equation in cylindrical coordinates:

$$\frac{1}{r}\frac{\mathrm{d}}{\mathrm{d}r}\left(r\frac{\mathrm{d}C_{\mathrm{v}}}{\mathrm{d}r}\right) = 0 \,, \tag{14.26}$$

with boundary conditions:

$$C_{\mathrm{v}}(R) = C_{\mathrm{v}}^0 \exp\left(\frac{\sigma\Omega}{kT}\right)$$
$$C_{\mathrm{v}}(r_{\mathrm{c}}) = C_{\mathrm{v}}^0 \,. \tag{14.27}$$

The solution to Eq. (14.26) subject to boundary conditions in Eq. (14.27) is:

$$C_\mathrm{v} = C_\mathrm{v}^0 - C_\mathrm{v}^0 \left[1 - \exp\left(\frac{\sigma\Omega}{kT}\right)\right] \frac{\ln R/r}{\ln R/r_\mathrm{c}} \,. \tag{14.28}$$

For $\dfrac{\sigma\Omega}{kT}$ small, we can approximate the exponent by $e^x \sim x + 1$, and Eq. (14.28) becomes:

$$C_\mathrm{v} = C_\mathrm{v}^0 \left(1 + \frac{\sigma\Omega}{kT}\right) \frac{\ln R/r}{\ln R/r_\mathrm{c}} \,. \tag{14.29}$$

Evaluating the gradient of the concentration profile at $r = r_\mathrm{c}$ gives:

$$\frac{\mathrm{d}C_\mathrm{v}}{\mathrm{d}r} = C_\mathrm{v}^0 \frac{\sigma\Omega}{kT} \frac{1}{\ln R/r_\mathrm{c}} \frac{1}{r_\mathrm{c}} \,, \tag{14.30}$$

and the flux, Eq. (14.25) becomes:

$$J_\mathrm{v} = \frac{2\pi D_\mathrm{v} C_\mathrm{v}^0 \sigma\Omega}{kT \ln R/r_\mathrm{c}} \,. \tag{14.31}$$

The flow of vacancies to the dislocation per unit length is $J\Omega$, or Jb^3, where $\Omega \sim b^3$. The sheet of atoms has a thickness of b so dividing by b gives the flow of volume per unit length per unit thickness, or the flow per unit distance perpendicular to the glide plane, which is just the climb velocity:

$$\begin{aligned} v_\mathrm{c} &= \frac{2\pi D_\mathrm{v} C_\mathrm{v}^0 \sigma\Omega b^2}{kT \ln R/r_\mathrm{c}} \\ &= \frac{2\pi D_\mathrm{vol} \sigma b^2}{kT \ln R/r_\mathrm{c}} \,, \end{aligned} \tag{14.32}$$

for $D_\mathrm{v} C_\mathrm{v}^0 \Omega = D_\mathrm{vol}$.

We now have all the elements required to derive the creep rate due to dislocation climb and glide over obstacles. Recall that the creep rate is given by Eq. (14.19) as $\dot{\varepsilon} = \rho_\mathrm{m} b l \dfrac{v_\mathrm{c}}{h}$. For the case where the dislocations are being created by Frank–Read sources, the creep rate can be expressed as the product of the Frank–Read source density, ρ_FR, the area swept out by the source times the Burgers vector, Ab, and the inverse of the waiting time, v_c/h or:

$$\dot{\varepsilon} = \rho_\mathrm{FR} A b \frac{v_\mathrm{c}}{h} \,. \tag{14.33}$$

Substituting in for h from Eq. (14.23) and v_c from Eq. (14.32) gives:

$$\dot{\varepsilon} = \frac{16\pi^2 \rho_\mathrm{FR} A b^3 D_\mathrm{vol} \sigma (1-\nu) n \sigma_{xy}}{\mu b k T \ln R/r_\mathrm{c}} \,. \tag{14.34}$$

The number of dislocations, n in a pile-up is given by [2]:

$$n = \frac{\pi(1-\nu)l\sigma_{xy}}{\mu b}\,, \tag{14.35}$$

where l is the length of the pile-up, and the stress $\sigma = n\sigma_{xy}$ [2]. Substituting into Eq. (14.34) gives:

$$\dot{\varepsilon} = \frac{16\pi^2\rho_{\mathrm{FR}}AD_{\mathrm{vol}}(1-\nu)^3 l^2\sigma_{xy}^4}{\mu^3 kT\ln R/r_{\mathrm{c}}}. \tag{14.36}$$

Weertman [3, 4] suggests that the quantity $\rho_{\mathrm{FR}}Al^2$ is proportional to σ_{xy}^{-1}, yielding:

$$\dot{\varepsilon} = \frac{C\pi^2 D_{\mathrm{vol}}(1-\nu)^3\sigma_{xy}^3}{\mu^3 kT\ln R/r_{\mathrm{c}}}\,, \tag{14.37}$$

where C is a constant. According to Eq. (14.37), the creep rate due to climb and glide is proportional to the self-diffusion coefficient and the stress to the power 3.

Climb and Annihilation

Climbing dislocations can also encounter other dislocations of opposite sign, creating an attractive force between them that drives the climb and results in mutual annihilation of the dislocations [5]. Figure 14.6 shows dislocation loops spaced apart from each other and on different slip planes. Dislocations of opposite sign will experience an attractive force that will cause them to climb toward each other and to annihilate. This is an important mechanism in that it provides a means for limiting the dislocation density in the solid. The creep rate is determined using the same equation as for climb over obstacles and is caused by glide of dislocations, piled up behind the lead dislocation, once annihilation has occurred (Fig. 14.7). That is:

$$\dot{\varepsilon} = \rho_{\mathrm{FR}}Ab\frac{v_{\mathrm{c}}}{h} = \dot{\varepsilon} = \frac{\rho_{\mathrm{FR}}Ab}{t_{\mathrm{c}}}\,, \tag{14.38}$$

where t_{c} is the waiting time defined by v_{c}/h. The climb velocity is the same as determined in Eq. (14.32), but the height is now the distance between two dislocations that are climbing toward each other. Referring back to the climb force caused by a normal stress, Eq. (14.22) showed that:

$$\sigma = \frac{F_y}{b} \cong -\frac{G}{by}\,. \tag{14.39}$$

The rate of approach of the two dislocations of opposite sign is $2v_{\mathrm{c}}$, and combining Eq. (14.32) for v_{c} and Eq. (14.39) for σ, gives

$$\mathrm{d}y/\mathrm{d}t = 2v_{\mathrm{c}} = -2\left(\frac{2\pi bD_{\mathrm{vol}}G}{kT\ln R/r_{\mathrm{c}}y}\right)\,, \tag{14.40}$$

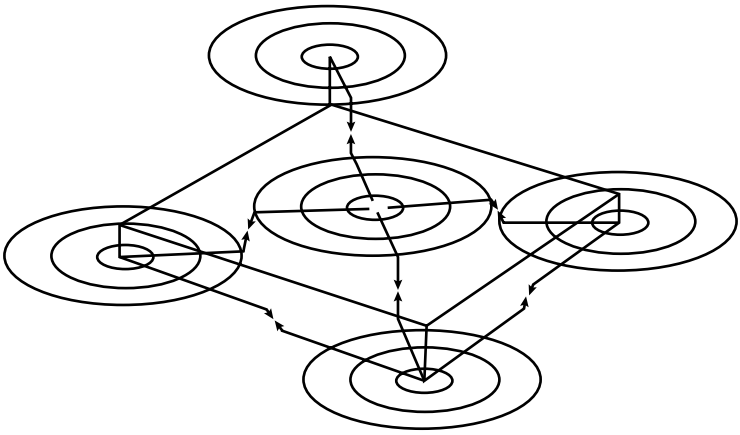

Fig. 14.6. Dislocations climbing toward each other to mutual annihilation

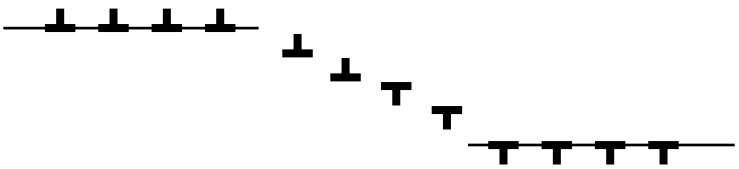

Fig. 14.7. Arrangement of a network of Frank–Read sources that produce dislocations that climb to annihilation (after [5])

and integrating Eq. (14.40) between the limits $y = h$ at $t = 0$ and $y = 0$ at $t = t_c$ gives:

$$t_c = \frac{kT \ln R/r_c h^2}{8\pi b D_{vol} G} \,. \tag{14.41}$$

For n dislocations produced by each Frank–Read source, the waiting time per dislocation is t_c/n, where n is approximated by l/h [3]. Substituting Eq. (14.41) into Eq. (14.38) gives:

$$\dot{\varepsilon} = \frac{\rho_{FR} A b^2 8\pi l D_{vol} G}{kT \ln R/r_c h^3} \,. \tag{14.42}$$

In Eq. (14.42), A is the area swept out by the dislocation and can be approximated by πl^2, where the distance l between sources on a slip plane is given as $(h \cdot \rho_{FR})^{-1/2}$, where ρ_{FR} is the source density and h is the separation between sources normal to their slip planes. Substituting the expressions for A and l in Eq. (14.42) gives:

$$\dot{\varepsilon} = \frac{8\pi^2 b^2 D_{vol} G}{kT \rho_{FR}^{0.5} \ln R/r_c h^{4.5}} \,. \tag{14.43}$$

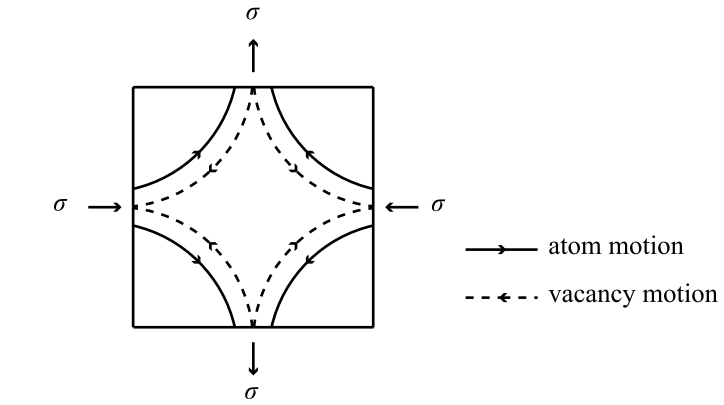

(a)

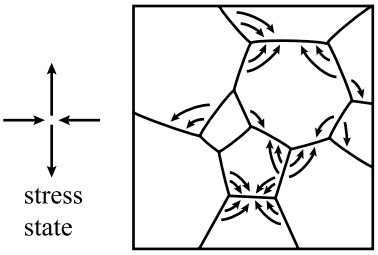

(b)

Fig. 14.8. Idealization (a) of a more realistic picture of vacancy and atom flow between grain faces (b) aligned with tensile or compressive directions of the applied stresses

Substituting for h Eq. (14.23), and G Eq. (14.21) gives:

$$\dot{\varepsilon} = \frac{C\pi^{5.5}(1-\nu)^{3.5} D_{\text{vol}} \sigma_{xy}^{4.5}}{kT\rho_{\text{FR}}^{0.5} b^{0.5} \mu^{3.5} \ln R/r_{\text{c}}} , \tag{14.44}$$

where C is a constant that contains the numerical terms. Note that the stress dependence in this model is 4.5 rather than 3.0 in the climb to glide mode. In both climb models, the creep rate is proportional to D_{vol} or $\exp(-E_{\text{vol}}/kT)$.

14.1.2 Diffusional Creep

In the high temperature, low stress regime of the deformation mechanism map, if we ignore the role of dislocations, then atom diffusion by way of vacancies controls creep. Consider the case of an idealized, cuboidal grain of edge length d, on which a stress is applied as shown in Fig. 14.8a. The faces will act as the sources and sinks for vacancies. Under the applied stress, vacancies will follow the paths

described by the dashed lines and atoms will move in the opposite direction (solid lines). Note that the vacancy flow is from the faces acted on by the tensile stress to those acted on by the compressive stress. The atom flow is in the opposite direction, from the faces acted on by a compressive stress to those acted on by a tensile stress. A more realistic picture of the process is shown in Fig. 14.8b. The creation of a vacancy on the face acted on by a compressive stress, σ due to thermal activation requires that the free energy of vacancy creation be increased by $\sigma\Omega$, the work expended on transferring a volume Ω. A vacancy created on the face acted on by the tensile stress, σ means that the free energy will be lowered by the same amount, $\sigma\Omega$. Therefore, at equilibrium, the vacancy concentration at the respective faces is:

$$\begin{aligned} C_{\mathrm{v}}^{\mathrm{t}} &= C_{\mathrm{v}}^{0} \exp\left(\frac{\sigma\Omega}{kT}\right) \\ C_{\mathrm{v}}^{\mathrm{c}} &= C_{\mathrm{v}}^{0} \exp\left(\frac{-\sigma\Omega}{kT}\right) , \end{aligned} \tag{14.45}$$

where σ is the magnitude of the stress and the superscripts t and c refer to tensile and compressive, respectively. The vacancy flow rate, A across the area d^2 acted on by the stress is:

$$A = J_{\mathrm{v}} d^2 . \tag{14.46}$$

The magnitude of the vacancy flux, J_{v} is given by Fick's law:

$$\begin{aligned} J_{\mathrm{v}} &= D_{\mathrm{v}} \frac{\mathrm{d}C}{\mathrm{d}x} \\ &\approx \kappa D_{\mathrm{v}} \frac{C_{\mathrm{v}}^{\mathrm{t}} - C_{\mathrm{v}}^{\mathrm{c}}}{d} , \end{aligned} \tag{14.47}$$

where D_{v} is the vacancy diffusion coefficient and κ is a coefficient of proportionality between the mean vacancy diffusion path and the cube edge d. Substituting Eqs. (14.45) and (14.47) into Eq. (14.46) gives:

$$A = D_{\mathrm{v}} C_{\mathrm{v}}^{0} \kappa d \left[\exp\left(\frac{\sigma\Omega}{kT}\right) - \exp\left(\frac{-\sigma\Omega}{kT}\right)\right] . \tag{14.48}$$

Recognizing that $D_{\mathrm{vol}} = D_{\mathrm{v}} C_{\mathrm{v}}^{0} \Omega$, and that the difference in exponentials can be written using the hyperbolic sine function, Eq. (14.48) becomes:

$$A = \frac{2\kappa \mathrm{d} D_{\mathrm{vol}}}{\Omega} \sinh(\sigma\Omega/kT) . \tag{14.49}$$

The strain is just the atom volume, Ω transferred to the compressive faces per unit area (d^2) divided by the dimension, d:

$$\varepsilon = \frac{\Omega}{d^2} \frac{1}{d} . \tag{14.50}$$

Since the flow rate of vacancies to the boundary is A, then the strain rate becomes:

$$\dot{\varepsilon} = A\frac{\Omega}{d^3} = \frac{2\kappa D_{\text{vol}}}{d^2}\sinh(\sigma\Omega/kT)\,, \tag{14.51}$$

and for $\sigma\Omega kT$ small ($\sim$1), the sinh term can be approximated by its argument, yielding:

$$\dot{\varepsilon} = B_{\text{vol}}\frac{D_{\text{vol}}\sigma\Omega}{d^2kT}\,, \tag{14.52}$$

where B_{vol} is the constant 2κ. Note that the creep rate is controlled by stress to the power $n = 1$, and is inversely proportional to the square of the grain size. The temperature dependence is governed by the volume diffusion coefficient D_{vol} or $\exp(-E_{\text{vol}}/kT)$ and is identical to that due to dislocation creep described in the last section. Extension of this mechanism to polycrystals [6] results in the exact same expression. Diffusional creep due to volume or lattice diffusion of atoms by way of vacancies is termed Nabarro–Herring (N–H) creep after the individuals who first derived the creep expression [7, 8].

At temperatures below the range where Nabarro–Herring creep occurs, grain boundary diffusion dominates mass transport. Coble [9] first derived an expression for grain boundary-dominated diffusion assuming spherical grains, yielding the following expression:

$$\dot{\varepsilon} = B_{\text{gb}}\frac{D_{\text{gb}}\delta_{\text{gb}}\sigma\Omega}{\pi d^3kT}\,. \tag{14.53}$$

In this expression, D_{gb} is the grain boundary diffusion coefficient, δ_{gb} is the grain boundary width, and the constant $B_{\text{gb}} \sim 148$ [6]. Note that while the stress dependence is the same as for N–H creep, the grain size dependence is d^{-3} rather than d^{-2}. Due to the nature of grain boundary diffusion vs. volume diffusion, Coble creep will dominate at lower temperatures and N–H creep will dominate at higher temperatures, and both will contribute in the intermediate temperature range. The diffusional creep rate can therefore be described by a common equation:

$$\dot{\varepsilon} = B\frac{\sigma\Omega}{d^2kT}D_{\text{eff}}\,, \tag{14.54}$$

where, as was shown earlier, D_{eff} is the effective diffusion coefficient given by:

$$D_{\text{eff}} = D_{\text{vol}}\left(1 + \frac{\pi}{d}\frac{D_{\text{gb}}\delta_{\text{gb}}}{D_{\text{vol}}}\right)\,, \tag{14.55}$$

and the constant $B = 14$ [6]. It follows then, that grain boundary diffusion will contribute to the creep rate at larger values of $D_{\text{gb}}/D_{\text{vol}}$ and for smaller grain sizes d.

14.2 Irradiation Creep

Irradiation significantly increases the creep rate over that due to thermal creep, or induces creep in temperature regimes where thermal creep is negligible. Both stainless steels and zirconium alloys exhibit irradiation creep rates that are significantly

larger than thermal creep rates at the same temperature. In fact, at light water reactor core temperatures, thermal creep is negligible, but the irradiation creep rate can exceed $10^{-6}\,s^{-1}$. Irradiation increases the numbers of interstitials and vacancies in the solid, but the effect of this increase is not merely to accelerate thermal creep. In fact, as will be shown, irradiation does not accelerate diffusional creep rates. Rather, irradiation creep needs to be understood in the context of enhanced defect production, the application of a stress and the developing irradiation microstructure. The formation and growth of loops and voids play important roles in the creep process. As will be shown, the stress-induced nucleation of dislocation loops and the bowing of dislocation lines by stress-assisted preferential absorption of interstitials can account for the transient portion of the creep behavior, but climb and glide are required to explain steady state creep. The following sections present the mechanisms responsible for creep in metals under irradiation and their dependencies on the independent variables of dose rate, temperature and stress as well as the developing microstructure.

14.2.1 Stress-Induced Preferential Nucleation of Loops (SIPN)

The application of an external stress can enhance the probability of interstitial loops nucleating on planes with a preferred orientation. Interstitial loops will be more likely to nucleate on planes perpendicular to an applied tensile stress than parallel to the stress. Vacancy loops will be less likely to nucleate on planes perpendicular (non-aligned) to the tensile stress and more likely to nucleate on planes parallel (aligned) to the stress. In either case, such preferential loop nucleation will cause the solid to increase in length in the direction of the applied tensile stress (Fig. 14.9). This process is termed the *stress-induced preferential nucleation*, SIPN mechanism of irradiation creep [10]. If f is the excess fraction of aligned interstitial loops, then the concentration of aligned loops, N_{AL}, [11] is:

$$N_{AL} = 1/3(1-f)N_L + fN_L\,, \tag{14.56}$$

and the concentration of non-aligned loops, N_{NL}, is:

$$N_{NL} = 2/3(1-f)N_L\,, \tag{14.57}$$

where N_L is the total loop concentration. The excess fraction of aligned interstitial loops is determined as follows.

If n interstitials are required before the interstitial aggregate is able to form an interstitial loop, then the probability that such an aggregate will form, p, in response to a normal stress is:

$$p_i = \exp\frac{\sigma_i n\Omega}{kT} \Bigg/ \sum_{j=1}^{n_0} \exp\frac{\sigma_j n\Omega}{kT}\,, \tag{14.58}$$

where the subscript i refers to the ith orientation of n_0 possible loop orientations, and the number of loops in the ith orientation is:

$$N_L^i = p_i N_L\,. \tag{14.59}$$

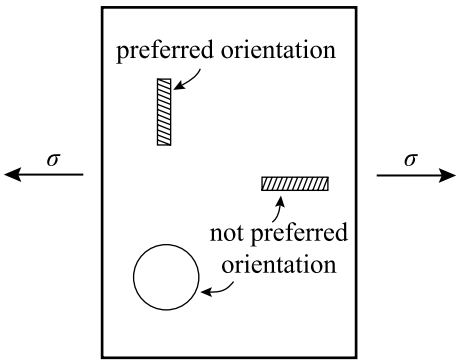

Fig. 14.9. Schematic of the influence of stress on the nucleation of dislocation loops

Defining f_i as the excess fraction of interstitial loops in the ith orientation, then:

$$p_i N_{\mathrm{L}} = \frac{1}{n_0}\left(1 - \sum_{j=1}^{n_0} f_j\right) N_{\mathrm{L}} + f_i N_{\mathrm{L}}, i = 1 \ldots n_0 \,, \tag{14.60}$$

giving:

$$f_i = \left(\exp \frac{\sigma_i n \Omega}{kT} - 1\right) \Bigg/ \sum_{j=1}^{n_0} \exp \frac{\sigma_j n \Omega}{kT} \,. \tag{14.61}$$

We can simplify the description by reducing the n_0 possible orientations to the three orthogonal directions. Then, for a uniaxial tensile stress orthogonal to the i = 1 orientation, the other two orthogonal orientations (i = 2, 3) will have $p_2 = p_3 = 0$, and:

$$f_1 = \left(\exp \frac{\sigma_1 n \Omega}{kT} - 1\right) \Bigg/ \left(\exp \frac{\sigma_1 n \Omega}{kT} + 2\right) , \tag{14.62}$$

and $f_2 = f_3 = 0$.

Using the result from Eq. (14.62), the creep strain due to the asymmetry in the loop population is:

$$\varepsilon = 2/3 \left[\pi r_{\mathrm{L}}^2 b N_{\mathrm{AL}} - 1/2 \pi r_{\mathrm{L}}^2 b N_{\mathrm{NL}}\right] \,. \tag{14.63}$$

Substituting for N_{AL} and N_{NL} from Eqs. (14.56) and (14.57) gives:

$$\varepsilon = 2/3 f \pi r_{\mathrm{L}}^2 b N_{\mathrm{L}} \,, \tag{14.64}$$

where b is the Burgers vector and r_{L} is the average loop radius. The creep rate is obtained by taking the time derivative of the creep strain given in Eq. (14.64), yielding:

$$\dot{\varepsilon} = 4/3 f b \pi r_{\mathrm{L}} N_{\mathrm{L}} \dot{r}_{\mathrm{L}} \,, \tag{14.65}$$

and defining $\rho_L = 2\pi r_L N_L$ as the loop line length per unit volume gives:

$$\dot{\varepsilon} = 2/3 f b \rho_L \dot{r}_L \,. \tag{14.66}$$

If the argument of the exponential term in the expression for f in Eq. (14.62) is small compared to 1, then the exponent can be replaced by $\exp(x) \sim x + 1$, yielding:

$$f = \frac{\sigma n \Omega}{3kT} \,, \tag{14.67}$$

where the subscript on the stress is dropped, and Eq. (14.66) becomes:

$$\dot{\varepsilon} = \frac{2}{9} \frac{\sigma n b \Omega}{kT} \rho_L \dot{r}_L \,. \tag{14.68}$$

Note that the creep rate is proportional to stress and the loop growth rate, $\dot{r}_L$. Brailsford and Bullough [10] have shown that the creep rate can be related to swelling if the irradiated microstructure consists of only loops and voids as sinks and the absorption rate of vacancies by voids equals the absorption rate of interstitials by loops. In Eq. (14.65), the product of $2\pi r_L b$ (edge area of loop of thickness b) and $\dot{r}_L$is the interstitial volume added to the loop. Multiplying by N_L loop/unit volume gives the volume fraction increase of the loop due to the net absorption of interstitials. If this is balanced by a corresponding and equal net absorption of vacancies to voids to produce a fractional swelling rate, $\dot{S}$, then Eq. (14.65) becomes:

$$\dot{\varepsilon} = 2/3 f \dot{S} \,. \tag{14.69}$$

Substituting for f using Eq. (14.67) for the case where n is small yields:

$$\dot{\varepsilon} = \frac{2}{9} \frac{\sigma n \Omega}{kT} \dot{S} \,, \tag{14.70}$$

and generalizing for the case where the total dislocation density is $\rho = \rho_L + \rho_N$, gives:

$$\dot{\varepsilon} = \frac{2}{9} \frac{\sigma n \Omega}{kT} \frac{\rho_L}{\rho} \dot{S} \,. \tag{14.71}$$

Whether SIPN can accurately account for the observed creep strains is a matter of considerable debate. Matthews and Finnis [12] reviewed the arguments for and against SIPN and noted that while observations have supported an increase in preferred loop orientation with tensile stress, the magnitude of the measured creep strain is higher than can be accounted for by preferred orientation by a factor of 2–4, even if n is assumed to large (10–30). The greatest limitation of the model is that once a loop is nucleated, the strain rate is determined by the irradiation dose, but is independent of stress. Thus, creep should continue if the stress is removed once nucleation has been completed. Also, if nucleation occurs before the stress is applied, then creep should not occur. Clearly, SIPN cannot account for all of the observed creep, but it may be a viable mechanism for a portion of the observed creep strain rate. A compliment to loop nucleation is preferential absorption of defects by loops caused by the applied stress, discussed in the next section.

14.2.2 Stress-Induced Preferential Absorption (SIPA)

At steady state, there are several distinct processes that may result in creep of a solid under irradiation and stress. They are (1) the transfer of atoms from planes parallel to the applied stress to those perpendicular to the applied stress, (2) the glide of dislocations on planes inclined to the stress direction, and (3) the climb and glide of dislocations due to the interstitial bias of the dislocation. The first is termed *stress-induced preferential absorption* (SIPA) and the second process is termed *preferred absorption glide* (PAG) [13]. PAG results from preferred absorption (SIPA) but is an additional component to the creep strain since it describes the glide contribution to the creep strain whereas SIPA describes only the climb contribution to creep strain. The third mechanism is creep strain from the climb and glide process due to the net absorption of interstitials on dislocations of all orientations (i.e., unassisted by stress) and is essentially the same process as the climb and glide model described in Sect. 14.1 but for the case where the defect source is the excess interstitials. Note that this process is tied to swelling as the corresponding net excess of vacancies accumulates at cavities causing swelling.

The origin of the preferred absorption is the interaction between the dislocation and defects. In conventional SIPA, the origin is the elastic interaction between the long-range stress field of the dislocation and that of the defect. Other origins for SIPA are anisotropic diffusion and elastodiffusion. While differing in the details of the origin of the interaction, all of these mechanisms result in a preferred absorption of interstitials by dislocations.

The flux of excess interstitials absorbed by dislocations with orientation described by j and density ρ_j is:

$$J_j = \rho_j \Omega \left(z_{\mathrm{i}}^{dj} D_{\mathrm{i}} C_{\mathrm{i}} - z_{\mathrm{v}}^{\mathrm{d}j} D_{\mathrm{v}} C_{\mathrm{v}} + z_{\mathrm{v}}^{\mathrm{d}j} D_{\mathrm{v}} C_{\mathrm{v}}^{\mathrm{d}j} \right) , \tag{14.72}$$

where $z_{\mathrm{i,v}}^{\mathrm{d}j}$ are the capture efficiencies of dislocations of orientation, j, D_{iv} are the diffusion coefficients, and C_{iv} are the bulk concentrations of interstitials and vacancies, respectively. The variable, $C_{\mathrm{v}}^{\mathrm{d}j}$ is the vacancy concentration in equilibrium with a dislocation of orientation j. For a uniaxial tensile stress where $j = 1$:

$$C_{\mathrm{v}}^{\mathrm{d}1} = C_{\mathrm{v}}^{0} \exp\left(\frac{\sigma \Omega}{kT} \right) \tag{14.73}$$

$$C_{\mathrm{v}}^{\mathrm{d}2} = C_{\mathrm{v}}^{\mathrm{d}3} = C_{\mathrm{v}}^{0} . \tag{14.74}$$

The interstitial flux, J_j can also be related to the climb velocity as follows:

$$J_j = b \rho_j v_j , \tag{14.75}$$

where ρ_j is the density of dislocations with their planes perpendicular to j. Substituting for J_j from Eq. (14.75) into Eq. (14.72) and solving for v_j gives:

$$v_j = \frac{\Omega}{b} \left(z_{\mathrm{i}}^{\mathrm{d}j} D_{\mathrm{i}} C_{\mathrm{i}} - z_{\mathrm{v}}^{\mathrm{d}j} D_{\mathrm{v}} C_{\mathrm{v}} + z_{\mathrm{v}}^{\mathrm{d}j} D_{\mathrm{v}} C_{\mathrm{v}}^{\mathrm{d}j} \right) . \tag{14.76}$$

Substituting Eq. (14.76) into Eq. (14.5) gives the total creep rate as:

$$\dot{\varepsilon}_j = \Omega \left(z_{\mathrm{i}}^{\mathrm{d}j} D_{\mathrm{i}} C_{\mathrm{i}} - z_{\mathrm{v}}^{\mathrm{d}j} D_{\mathrm{v}} C_{\mathrm{v}} + z_{\mathrm{v}}^{\mathrm{d}j} D_{\mathrm{v}} C_{\mathrm{v}}^{\mathrm{d}j} \right) \rho_j \,. \tag{14.77}$$

But Eq. (14.77) also includes contributions due to void swelling. That component of the strain is just one-third of the volumetric swelling, or $\varepsilon = 1/3(\varepsilon_1 + \varepsilon_2 + \varepsilon_3)$ and the swelling strain rate, $\dot{\varepsilon}_S$ is:

$$\dot{\varepsilon}_S = \frac{\Omega}{3} \sum_{n=1}^{3} \left(z_{\mathrm{i}}^{\mathrm{d}n} D_{\mathrm{i}} C_{\mathrm{i}} - z_{\mathrm{v}}^{\mathrm{d}n} D_{\mathrm{v}} C_{\mathrm{v}} + z_{\mathrm{v}}^{\mathrm{d}n} D_{\mathrm{v}} C_{\mathrm{v}}^{\mathrm{d}n} \right) \rho_n \,. \tag{14.78}$$

The creep by climb due to preferential absorption of interstitials at dislocations is then:

$$\begin{aligned} \dot{\varepsilon}_j =& \Omega (z_{\mathrm{i}}^{\mathrm{d}j} D_{\mathrm{i}} C_{\mathrm{i}} - z_{\mathrm{v}}^{\mathrm{d}j} D_{\mathrm{v}} C_{\mathrm{v}} + z_{\mathrm{v}}^{\mathrm{d}j} D_{\mathrm{v}} C_{\mathrm{v}}^{\mathrm{d}j}) \rho_j \\ & - \frac{\Omega}{3} \sum_{n=1}^{3} \left(z_{\mathrm{i}}^{\mathrm{d}n} D_{\mathrm{i}} C_{\mathrm{i}} - z_{\mathrm{v}}^{\mathrm{d}n} D_{\mathrm{v}} C_{\mathrm{v}} + z_{\mathrm{v}}^{\mathrm{d}n} D_{\mathrm{v}} C_{\mathrm{v}}^{\mathrm{d}n} n \right) \rho_n \,. \end{aligned} \tag{14.79}$$

For dislocations distributed isotropically among the three orthogonal directions:

$$\rho_1 = \rho_2 = \rho_3 = \rho/3 \,. \tag{14.80}$$

Substituting Eqs. (14.73) and (14.74) for the equilibrium vacancy concentration and Eq. (14.80) for the dislocation density into Eq. (14.79) for the stress direction $j = 1 = A$ (aligned dislocations) gives:

$$\dot{\varepsilon}_{\mathrm{climb}} = \frac{2}{9} \Omega \rho \left\{ \underbrace{\left[\Delta z_{\mathrm{i}}^{\mathrm{d}} D_{\mathrm{i}} C_{\mathrm{i}} - \Delta z_{\mathrm{v}}^{\mathrm{d}} D_{\mathrm{v}} C_{\mathrm{v}} \right]}_{\mathrm{SIPA}} + \underbrace{D_{\mathrm{v}} C_{\mathrm{v}}^{0} \left[z_{\mathrm{v}}^{\mathrm{dA}} \exp\left(\frac{\sigma \Omega}{kT} \right) - z_{\mathrm{v}}^{\mathrm{dN}} \right]}_{\mathrm{PE}} \right\} \,, \tag{14.81}$$

where $\Delta z_{\mathrm{i,v}}^{d} = z_{\mathrm{i,v}}^{\mathrm{dA}} - z_{\mathrm{i,v}}^{\mathrm{dN}}$, and $z_{\mathrm{i,v}}^{\mathrm{dA}}$ denotes the capture efficiency of aligned dislocations and $z_{\mathrm{i,v}}^{\mathrm{dN}}$ denotes the capture efficiency of non-aligned dislocations ($j = 2$). The first term in square brackets is the dislocation climb creep rate due to preferential absorption of interstitials, or SIPA:

$$\dot{\varepsilon}_{\mathrm{SIPA}} = \frac{2}{9} \Omega \rho \left[\Delta z_{\mathrm{i}}^{\mathrm{d}} D_{\mathrm{i}} C_{\mathrm{i}} - \Delta z_{\mathrm{v}}^{\mathrm{d}} D_{\mathrm{v}} C_{\mathrm{v}} \right] \,. \tag{14.82}$$

The second term in square brackets is the dislocation climb creep rate due to preferred emission, PE [13] of vacancies:

$$\dot{\varepsilon}_{\mathrm{PE}} = \frac{2}{9} \Omega \rho D_{\mathrm{v}} C_{\mathrm{v}}^{0} \left[z_{\mathrm{v}}^{\mathrm{dA}} \exp\left(\frac{\sigma \Omega}{kT} \right) - z_{\mathrm{v}}^{\mathrm{dN}} \right] \,. \tag{14.83}$$

If the differences in capture efficiencies (preference) of the dislocations in different orientations were removed, i.e., $\Delta z_{\mathrm{i}}^{\mathrm{d}} = \Delta z_{\mathrm{v}}^{\mathrm{d}} = 0$, then the first term disappears and the creep rate is then due solely to thermal processes.

14.2.3 Climb and Glide due to Preferential Absorption (PAG)

While SIPA provides a mechanism for creep by dislocation climb, dislocations can also contribute to creep by glide if they are able to overcome obstacles in their slip plane by the climb process [13]. Under an applied stress, pinned dislocations will glide until they reach a configuration where the restoring force due to line tension is balanced by the applied stress. Since dislocations are pinned, creep is limited to the elastic stress given by $\varepsilon = \sigma/E$. Climb enables the dislocation to overcome the initial pinning points. The released segments bow out between new pinning points until, again, the line tension balances the applied stress. Figure 14.10 shows the process by which dislocation segments bow out between pinning points, are released from the pinning points and are then pinned again. Each cycle of climb and glide to pinning results in an elastic deflection in addition to the strain due to climb, which together, account for the total creep strain in the solid, all the while, the dislocation network maintains its configuration. This mechanism has also been referred to as "transient creep" because of its occurrence at low dose. However, since the dislocation lines can continue to bow out after climbing over pinning points, it can also account for steady state creep.

Similar to Eq. (14.19), the creep rate due to climb and glide can be written as:

$$\dot{\varepsilon}_{\mathrm{CG}} = \varepsilon \frac{v_{\mathrm{c}}}{l} \,, \tag{14.84}$$

where ε is the strain due to elastic deflection, v_{c} is the climb velocity and l is the distance between pinning points. When pinning is caused by the network dislocation density, l is given by $l = 1/\sqrt{\pi\rho_{\mathrm{d}}}$, and ρ_{d} is the dislocation density. Equation Eq. (14.84) then becomes:

$$\dot{\varepsilon}_{\mathrm{CG}} = \varepsilon(\pi\rho_{\mathrm{d}})^{1/2} v_{\mathrm{c}} \,. \tag{14.85}$$

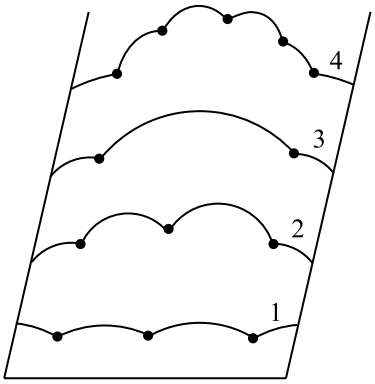

Fig. 14.10. Schematic of glide by dislocation bowing and the pinning and unpinning of dislocation segments

The climb velocity can be determined from Eq. (14.76) by adding and subtracting the velocity component due to volumetric swelling:

$$v_j = \frac{\Omega}{b}\left[\left(z_{\mathrm{i}}^{\mathrm{d}j} D_{\mathrm{i}} C_{\mathrm{i}} - z_{\mathrm{v}}^{\mathrm{d}j} D_{\mathrm{v}} C_{\mathrm{v}} + z_{\mathrm{v}}^{\mathrm{d}j} D_{\mathrm{v}} C_{\mathrm{v}}^{\mathrm{d}j}\right) - \frac{1}{3\rho_j}\sum_{n=1}^{3}\left(z_{\mathrm{i}}^{\mathrm{d}n} D_{\mathrm{i}} C_{\mathrm{i}} - z_{\mathrm{v}}^{\mathrm{d}n} D_{\mathrm{v}} C_{\mathrm{v}} + z_{\mathrm{v}}^{\mathrm{d}n} D_{\mathrm{v}} C_{\mathrm{v}}^{\mathrm{d}n}\right)\rho_n\right] + \frac{\Omega}{3b\rho_j}\sum_{n=1}^{3}\left(z_{\mathrm{i}}^{\mathrm{d}n} D_{\mathrm{i}} C_{\mathrm{i}} - z_{\mathrm{v}}^{\mathrm{d}n} D_{\mathrm{v}} C_{\mathrm{v}} + z_{\mathrm{v}}^{\mathrm{d}n} D_{\mathrm{v}} C_{\mathrm{v}}^{\mathrm{d}n}\right)\rho_n \,. \tag{14.86}$$

The physical meanings of the terms in Eq. (14.86) are as follows. The first term in square brackets is the climb velocity due to all processes contributing to vacancy and interstitial absorption and vacancy emission. The second term in the square brackets is the climb due to net point defect absorption and emission at dislocations attributable only to swelling. Subtracting this term from the first term yields the net result, enclosed in square brackets, being the climb velocity due only to the volume conserving processes of stress-induced preferred absorption and to preferred vacancy emission. The last term in Eq. (14.86) is the dislocation climb velocity due to isotropic swelling. It is the terms in square brackets that are responsible for the climb and glide process in the absence of swelling. Using Eq. (14.80) and the average velocity of the dislocations given by:

$$v = \frac{|v_1| + |v_2| + |v_3|}{3}\,, \tag{14.87}$$

Equation (14.86) becomes:

$$v = \frac{\Omega}{3b}\left\{\left|z_{\mathrm{i}}^{\mathrm{d}1} D_{\mathrm{i}} C_{\mathrm{i}} - z_{\mathrm{v}}^{\mathrm{d}1} D_{\mathrm{v}} C_{\mathrm{v}} + z_{\mathrm{v}}^{\mathrm{d}1} D_{\mathrm{v}} C_{\mathrm{v}}^{d1}\right| + 2\left|z_{\mathrm{i}}^{\mathrm{d}2} D_{\mathrm{i}} C_{\mathrm{i}} - z_{\mathrm{v}}^{\mathrm{d}2} D_{\mathrm{v}} C_{\mathrm{v}} + z_{\mathrm{v}}^{\mathrm{d}2} D_{\mathrm{v}} C_{\mathrm{v}}^{\mathrm{d}2}\right|\right\}. \tag{14.88}$$

When preferential absorption and preferential emission occur without the occurrence of swelling, the number of interstitials absorbed must be balanced by the number of vacancies absorbed, so:

$$\left(z_{\mathrm{i}}^{\mathrm{d}1} D_{\mathrm{i}} C_{\mathrm{i}} - z_{\mathrm{v}}^{\mathrm{d}1} D_{\mathrm{v}} C_{\mathrm{v}} + z_{\mathrm{v}}^{\mathrm{d}1} D_{\mathrm{v}} C_{\mathrm{v}}^{\mathrm{d}1}\right) = 2\left(z_{\mathrm{i}}^{\mathrm{d}2} D_{\mathrm{i}} C_{\mathrm{i}} - z_{\mathrm{v}}^{\mathrm{d}2} D_{\mathrm{v}} C_{\mathrm{v}} + z_{\mathrm{v}}^{\mathrm{d}2} D_{\mathrm{v}} C_{\mathrm{v}}^{\mathrm{d}2}\right)\,, \tag{14.89}$$

and Eq. (14.88) becomes:

$$v = \frac{2}{3}\frac{\Omega}{b}\left(z_{\mathrm{i}}^{\mathrm{d}1} D_{\mathrm{i}} C_{\mathrm{i}} - z_{\mathrm{v}}^{\mathrm{d}1} D_{\mathrm{v}} C_{\mathrm{v}} + z_{\mathrm{v}}^{\mathrm{d}1} D_{\mathrm{v}} C_{\mathrm{v}}^{\mathrm{d}1}\right)\,. \tag{14.90}$$

Substituting the climb velocity given in Eq. (14.90) into the creep equation for climb and glide Eq. (14.85) gives:

$$\dot{\varepsilon}_{\mathrm{CG}} = \frac{2}{3}\frac{\varepsilon}{b}\Omega\left(\pi\rho_{\mathrm{d}}\right)^{1/2}\left(z_{\mathrm{i}}^{\mathrm{d1}}D_{\mathrm{i}}C_{\mathrm{i}} - z_{\mathrm{v}}^{\mathrm{d1}}D_{\mathrm{v}}C_{\mathrm{v}} + z_{\mathrm{v}}^{\mathrm{d1}}D_{\mathrm{v}}C_{\mathrm{v}}^{\mathrm{d1}}\right) . \tag{14.91}$$

After some manipulation of Eq. (14.91), Mansur [13] showed that the climb and glide creep rate can be written as:

$$\dot{\varepsilon}_{\mathrm{CG}} = \frac{4}{9}\frac{\varepsilon\Omega}{b}\Omega(\pi\rho_{\mathrm{d}})^{1/2}D_{\mathrm{i}}C_{\mathrm{i}}\Delta z_{\mathrm{i}}^{\mathrm{d}} , \tag{14.92}$$

where $\Delta z_{\mathrm{i}}^{\mathrm{d}}$is defined after Eq. (14.81). Note that in both Eqs. (14.82) and (14.92), the term $\Delta z_{\mathrm{i}}^{\mathrm{d}}$ appears, which represents the difference in capture efficiencies between aligned and non-aligned dislocations, and is therefore dependent on stress. Mansur writes $\Delta z_{\mathrm{i}}^{\mathrm{d}} = \Delta z_{\mathrm{i}}'\varepsilon$ (where $\Delta z_{\mathrm{i}}'$ is independent of stress) so that $\dot{\varepsilon}_{\mathrm{SIPA}}\alpha\varepsilon$ and $\dot{\varepsilon}_{\mathrm{CG}}\alpha\varepsilon^2$, and since $\varepsilon = \sigma/E$, we have $\dot{\varepsilon}_{\mathrm{SIPA}}\alpha\sigma$ and $\dot{\varepsilon}_{\mathrm{CG}}\alpha\sigma^2$. Also, as shown in Sect. 5.1.3, the term C_{i} is proportional to the defect production rate, K_0, for sink-dominated cases, and to $K_0^{1/2}$ for recombination-dominated cases. It should also be noted that since there is no need for a net preferential absorption of interstitials at all edge dislocations, creep can proceed in the absence of swelling.

14.2.4 Climb and Glide Driven by Dislocation Bias

The preceding analysis describes creep that is driven by stress-induced preferential absorption of interstitials at dislocations. The creep rate has both climb and glide components and the creep process is governed by dislocation segment bowing following climb to free the segment from the pinning points. Here we consider creep that is driven by the dislocation bias rather than preferential absorption. Clearly in order for there to be a net absorption of interstitials by dislocations requires that there is an equivalent net absorption of vacancies by other sinks in the solid. These sinks are assumed to be voids. Creep due to the excess absorption of interstitials at dislocations is equivalent to the thermal creep climb and glide mechanisms discussed in Sect. 14.2, but with interstitial absorption replacing vacancy absorption. For this case, we return to Eq. (14.19), which expresses the creep rate in terms of the climb velocity, v_{c} and the obstacle height, h. Equation (14.75) gives the climb velocity in terms of the absorption flux of interstitials at dislocations. For climb due solely to dislocation bias, Eq. (14.72) for the interstitial flux becomes:

$$J = \rho_{\mathrm{m}}\Omega\left[z_{\mathrm{i}}^{\mathrm{d}}D_{\mathrm{i}}C_{\mathrm{i}} - z_{\mathrm{v}}^{\mathrm{d}}D_{\mathrm{v}}C_{\mathrm{v}}^{\mathrm{d}}\right] , \tag{14.93}$$

and substituting the expression for J in Eq. (14.93) into Eq. (14.75) and solving for v_{c} gives:

$$v_{\mathrm{c}} = \frac{\Omega}{b}\left[z_{\mathrm{i}}^{\mathrm{d}}D_{\mathrm{i}}C_{\mathrm{i}} - z_{\mathrm{v}}^{\mathrm{d}}D_{\mathrm{v}}C_{\mathrm{v}}^{\mathrm{d}}\right] . \tag{14.94}$$

Equation (14.94) also can be obtained directly from Eq. (14.86) by neglecting thermal emission, $C_{\mathrm{v}}^{\mathrm{d}j} \sim 0$, and requiring that the zs for dislocations do not have an orientation dependence, so that $z_{\mathrm{v}}^{\mathrm{d}j} = z_{\mathrm{v}}^{\mathrm{d}}$ and $z_{\mathrm{i}}^{\mathrm{d}j} = z_{\mathrm{i}}^{\mathrm{d}}$. The obstacle height is given in Eq. (14.23) and in the case of a dislocation pile-up against an obstacle, the stress σ_{xy} is replaced by $n\sigma_{xy}$ where n is the number of dislocations in the pile-up and as given by Eq. (14.35). Substituting Eq. (14.94) for v_{c}, Eq. (14.23) for h and Eq. (14.35) for n into Eq. (14.19) gives:

$$\dot{\varepsilon} = \frac{\rho_{\mathrm{m}} l^2 \Omega 8\pi^2 (1-\nu)^2 \sigma_{xy}^2}{(\mu b)^2} \left[z_{\mathrm{i}}^{\mathrm{d}} D_{\mathrm{i}} C_{\mathrm{i}} - z_{\mathrm{v}}^{\mathrm{d}} D_{\mathrm{v}} C_{\mathrm{v}}^{\mathrm{d}} \right] . \tag{14.95}$$

When creep is driven by swelling, the absorption rate of interstitials at dislocations is balanced by the same absorption rate of vacancies by voids:

$$\rho_{\mathrm{m}} (J_{\mathrm{i}}^{\mathrm{d}} - J_{\mathrm{v}}^{\mathrm{d}}) = A_{\mathrm{v}}^{\mathrm{V}} - A_{\mathrm{i}}^{\mathrm{V}} = \frac{1}{\Omega} \frac{\Delta \dot{V}}{V} . \tag{14.96}$$

Substituting Eq. (14.96) into Eq. (14.95) gives:

$$\dot{\varepsilon} = \frac{\rho_{\mathrm{m}}}{\rho_{\mathrm{d}}} \frac{8\pi^2 l^2 (1-\nu)^2 \sigma_{xy}^2}{(\mu b)^2} \frac{\Delta \dot{V}}{V} , \tag{14.97}$$

where the term $\rho_{\mathrm{m}}/\rho_{\mathrm{d}}$ is the fraction of the dislocation density that is mobile and can contribute to creep. It should also be noted that irradiated metals often do not exhibit pile-ups at obstacles. In this case, the number of dislocations in a pile-up, n is set equal to 1 and the creep rate is proportional to the stress. Wolfer et al. [14] showed that when Frank loops are the obstacles, the creep rate is proportional to stress to the power $n = 1$.

14.2.5 Transient Creep

Creep can occur prior to the achievement of steady state by the vacancy and interstitial concentrations. Such creep is referred to as *transient creep*. Three transient creep processes are of greatest importance: *glide-induced transient absorption*, *start up-induced transient absorption*, and *cascade creep*.

Glide-Induced Transient Absorption

In climb and glide creep, the climb process is the limiting step as glide occurs extremely rapidly. In fact, the glide process is so rapid that steady state concentrations of point defects cannot be maintained at the dislocation. As a result, the dislocation absorbs both vacancies and interstitials rapidly in an effort to re-establish the steady state point defect diffusion profiles at its new location [15]. However, vacancies and interstitials are not absorbed in equal numbers and the imbalance in absorption rate gives rise to a form of transient creep termed glide-induced transient absorption.

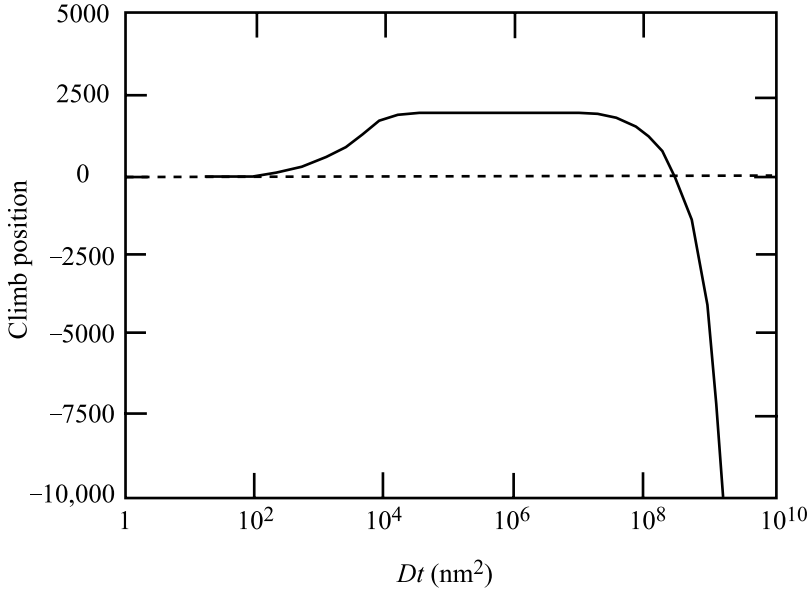

Fig. 14.11. Dislocation climb for a unit length of dislocation in units normalized to the steady state vacancy concentration divided by 10^{18}. The diffusion coefficients are in units of nm^2/s and a steady state climb rate corresponding to 1% of the total interstitial flux is assumed (after [15])

Figure 5.3 in Chap. 5 shows that at steady state, the bulk vacancy concentration exceeds the interstitial concentration by orders of magnitude. Consequently, the flow of vacancies to the dislocation causes an increment of positive climb, releasing the dislocation from an obstacle and producing creep by glide. Figure 14.11 shows the increment of climb caused by excess vacancy absorption prior to achievement of steady state diffusion profiles. The initial climb shown in the positive direction is the transient vacancy climb, and the negative climb at longer times ($Dt > 10^8\,nm^2$) is the bias-driven interstitial climb. If the transient positive climb is large enough to escape the barrier, the dislocation glides to the next barrier. If the transient climb is inadequate, the steady state climb eventually reverses the dislocation motion and escape occurs in the negative direction. Once steady state has been achieved, then climb is controlled by the small net excess of interstitials due to stress-induced preferential absorption described in the preceding section. This form of transient climb can cause high creep rates at low temperatures, where the steady state vacancy concentration is high, as long as the temperature is not too low so that vacancy diffusion is limiting.

Start Up-Induced Transient Absorption

Significant creep can also occur at low temperatures coincident with the start of the irradiation. This creep process, referred to as start up-induced transient absorp-

tion, occurs by the absorption of interstitials prior to steady state when interstitials are mobile but vacancy diffusion is too slow for them to interact with the dislocations [16]. Referring again to Fig. 5.3, at the start of irradiation at low temperature, the concentrations of both vacancies and interstitials increase linearly with time until interstitials begin to be absorbed at sinks. At this point in time, defined by the time constant τ_2, the interstitial concentration reaches a quasi-steady state while the vacancy concentration continues to climb. The continued buildup of vacancies causes recombination to occur, resulting in a decrease in the interstitial concentration and a slower rate of vacancy buildup with time. With additional increase in the vacancy concentration, recombination dominates the loss process (at $t = \tau_4$) causing a steeper decline in the interstitial loss rate and a smaller rate of vacancy buildup. Eventually, steady state is reached when the vacancy concentration is high enough that vacancies interact with sinks.

The contribution of interstitials to creep during this start up transient can be estimated by determining the number of excess interstitials, N_i, that are absorbed by the dislocations in each time interval in Fig. 5.3. For example, in the time interval $\tau_4 - \tau_2$, the number of interstitials produced is $K_0(\tau_4 - \tau_2)$, and the number remaining is $K_0/K_\mathrm{is}C_\mathrm{s}$, so the number absorbed by the dislocation is:

$$N_\mathrm{i} = K_0(\tau_4 - \tau_2) - K_0/K_\mathrm{is}C_\mathrm{s} \; . \tag{14.98}$$

Using the same analysis, estimates can be made for the number of interstitials absorbed during the time interval $\tau_3 - \tau_4$, or until steady state is reached, at which point the transient ends. Interstitial absorption results in climb-enabled glide as described by Eq. (14.92), with N_i substituted for C_i. Figure 14.12 shows that the total creep strain in austenitic stainless steels can be dominated by start up-induced transient absorption at temperatures into the 300 ℃ range, and near the 200 ℃ range for ferritic alloys. As such, it is an important mechanism of creep at low temperature and during the start up phase of an irradiation.

Cascade Creep

One of the simplest transient creep models is based on the effect of stress on the displacement spike volume. As described by Brinkman and Wiedersich [17], if a load is applied to a solid during the occurrence of a displacement spike, then elastic strain in the spike region is relaxed locally and frozen in. The strain rate from this process is given by:

$$\dot{\varepsilon}_\mathrm{cas} = \varepsilon_\mathrm{e} V_\mathrm{cas} \alpha N \sigma_\mathrm{s} \phi \; , \tag{14.99}$$

where the elastic strain $\varepsilon_\mathrm{e} = \sigma/E$, V_cas is the volume of the cascade, α is the number of spikes per neutron scattering event, N is the atom number density in the solid, σ_s is the neutron scattering cross section and ϕ is the fast neutron flux. Matthews and Finnis [12] noted that this creep rate underestimates the observed irradiation creep in neutron-irradiated structural materials. However, since defect generation does not

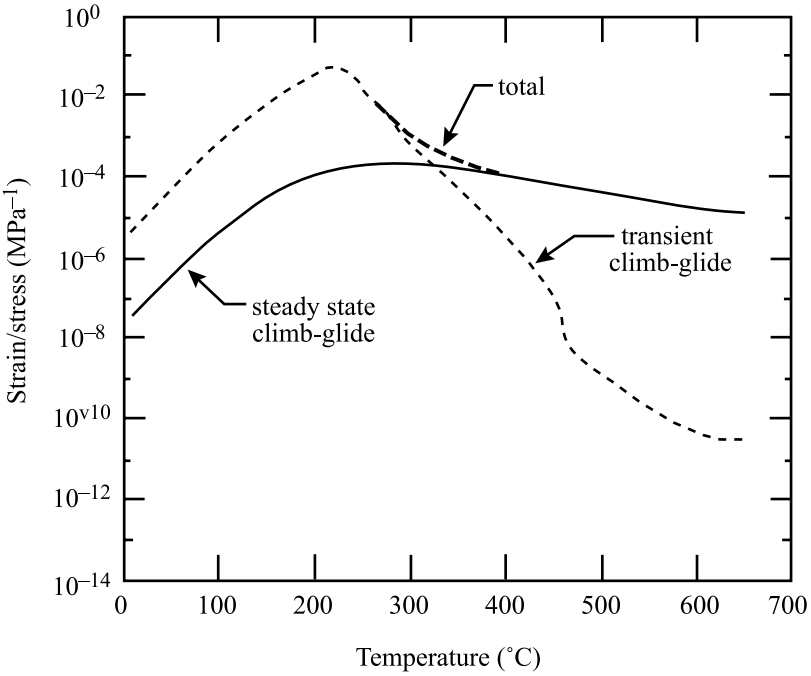

Fig. 14.12. Creep deformation per unit stress as a function of temperature for austenitic alloys using the conventional climb-enabled glide model (steady state condition) and the start up-induced transient absorption model (from [16])

occur continuously over space and time, and not all defects escape the damage region, strain caused by cascade effects may be important to consider. A dislocation segment will make climb excursions in response to fluctuations in the local vacancy concentration caused by a nearby cascade. During an excursion, there is a probability that the segment will be unpinned. Mansur [18] accounted for cascade effects in the climb-enabled glide model by replacing v_c/h in Eq. (14.19) by the release frequency of pinned dislocation segments, ω:

$$\dot{\varepsilon} = \rho b l \omega \,, \tag{14.100}$$

where:

$$\omega = \sum_{j-1}^{h} R_j F_j \,, \tag{14.101}$$

and F_j is the frequency with which a dislocation segment climbs to a height of at least h:

$$F_j = 4\pi N \sigma_s \phi \int_0^\infty \rho^2 P_j \, \mathrm{d}r \,, \tag{14.102}$$

and P_j is the probability of climb of j or greater. The term, R_j is the probability of finding a dislocation a distance jb from the unpinning point, and is given by:

$$R_j = \rho_j/\rho \ . \tag{14.103}$$

The release frequencies, and hence the creep rates determined using this model are comparable to those from preferred absorption-driven climb or swelling-driven climb [18].

14.2.6 Loop Unfaulting

Another possible interaction between an applied stress and interstitial loops that could produce creep strain is loop unfaulting. As discussed in Chap. 7, dislocation loops grow in size and eventually become unstable and unfault to become part of the dislocation network. This process is equivalent to the production of mobile dislocations which may then participate in the creep process by SIPA, PAG or climb and glide driven by interstitial bias. The maximum radius to which a loop can grow, $R_{\max}$, is governed by the loop density and is given by:

$$\frac{4\pi}{3}\rho_\ell R_{\max}^3 = 1 \ . \tag{14.104}$$

When loops interact, they coalesce and contribute to the network dislocation density. Interaction between individual dislocations and loops results in loop unfaulting that also contributes to the network (see Chap. 12, Sect. 12.3). As the dislocation density increases, the rate of loop interaction with the network increases and the loop radius is limited to a value of the order of the network mesh length, $\rho_{\mathrm{N}}^{-1/2}$, where ρ_{N} is the network dislocation density. Loop unfaulting can contribute to irradiation creep strain since the presence of a stress will assist the nucleation of the unfaulting dislocations with favorable orientations resulting in an increased probability of unfaulting. The application of a shear stress in the plane of the loops will induce a greater number of loops to shear in the direction favored by the stress to produce a net shear of the crystal, which will appear as creep. If ρ is the total dislocation density and ρ_{s} is the number of dislocation loops lying on a plane for which the shear stress is a maximum, then the number of loops shearing in that direction is given by Lewthwaite [19] as:

$$\rho_1 = \frac{\rho_{\mathrm{s}} \exp\left(\dfrac{\pi R_{\mathrm{c}}^2 b\sigma}{kT}\right)}{\exp\left(\dfrac{\pi R_{\mathrm{c}}^2 b\sigma}{kT}\right) + \exp\left(-\dfrac{\pi R_{\mathrm{c}}^2 b\sigma}{kT}\right)} \ , \tag{14.105}$$

where, R_{c} is the critical loop size for unfaulting (the maximum value is given by Eq. (14.104)), and σ is the stress. The number of loops shearing in the opposite direction is $\rho_2 = \rho_{\mathrm{s}} - \rho_1$, and the strain due to the loop unfaulting is then:

$$\varepsilon = \bar{A} b_{\mathrm{s}} (\rho_1 - \rho_2) \ , \tag{14.106}$$

where $\bar{A}$ is the average loop area, b_s is the magnitude of the Burgers vector of the reaction producing the strain. Substituting in for ρ_1 and ρ_2 in Eq. (14.106) and averaging the strain over all possible loop orientations (which gives a factor of 1/30) yields:

$$\varepsilon = \frac{\rho \bar{A} b_s}{30} \left[\frac{\exp\left(\frac{\pi R_c^2 b\sigma}{kT}\right) - \exp\left(\frac{\pi R_c^2 b\sigma}{kT}\right)}{\exp\left(\frac{\pi R_c^2 b\sigma}{kT}\right) + \exp\left(-\frac{\pi R_c^2 b\sigma}{kT}\right)} \right] . \tag{14.107}$$

The term in brackets can be written as the hyperbolic tangent of the argument, giving:

$$\varepsilon = \frac{\rho \bar{A} b_s}{30} \tanh(\pi R_c^2 b\sigma / kT) . \tag{14.108}$$

If the argument is small compared to 1, then $\tanh x \sim x$ and Eq. (14.108) becomes:

$$\varepsilon = \frac{\rho \bar{A} b_s}{30} \pi R_c^2 b\sigma / kT . \tag{14.109}$$

If loop growth is driven by swelling, then $\rho \bar{A} b_s$ is replaced with $\Delta \dot{V}/V$, the loop volume $\pi R_c^2 b$ is equated with the volume of the defects in the loop, $n_c \Omega$, and the term $\dfrac{k_L^2}{k_L^2 + k_N^2}$ is added to account for the network dislocation density as well, to yield the creep rate in terms of the swelling rate:

$$\dot{\varepsilon} = \frac{\Delta \dot{V}}{V} \frac{k_L^2}{k_L^2 + k_N^2} \frac{\pi R_c^2 b\sigma / kT}{30} . \tag{14.110}$$

Matthews and Finnis [12] noted that the unfaulting radius is large in austenitic alloys and the creep rate can be significant, but because of the small critical loop size in bcc metals, the contribution will be small.

14.2.7 Recovery Creep

All of the irradiation creep mechanisms discussed thus far allow for, or contribute to the growth of the dislocation density, but do not account for the removal of dislocations, as must occur during creep. Matthews and Finnis [12] expressed the rate of change in dislocation density in terms of the creep rate as:

$$\dot{\rho} = \frac{\dot{\varepsilon}}{bl} - 2\rho^{3/2} v_c , \tag{14.111}$$

where l is the mean dislocation glide length and v_c is the climb velocity. The first term is the production rate of dislocations due to creep, obtained from Eq. (14.14), and the second term is the loss due to annihilation. Taking the steady state limit of

$\dot{\rho} = 0$, the steady state creep rate is expressed in terms of the dislocation density as:

$$\dot{\varepsilon} = 2bl\rho^{3/2}v_{\mathrm{c}} \,. \tag{14.112}$$

The stress dependence is determined by the dislocation density, the climb velocity and the slip length. The dislocation density varies with stress according to Eq. (14.7) (in which the term, α appears in the denominator inside the brackets), $\rho = \dfrac{\sigma^2}{\alpha^2\mu^2b^2}$ and contributes a σ^3 term to the creep rate given in Eq. (14.112). For stress-induced preferential absorption, we have from Eq. (14.82):

$$v_{\mathrm{SIPA}} = \frac{2}{9}\frac{\Omega}{b}\left(z_{\mathrm{i}}^{\mathrm{d}}D_{\mathrm{i}}C_{\mathrm{i}} - z_{\mathrm{v}}^{\mathrm{d}}D_{\mathrm{v}}C_{\mathrm{v}} + z_{\mathrm{v}}^{\mathrm{d}}D_{\mathrm{v}}C_{\mathrm{v}}^{\mathrm{d}}\right) \,, \tag{14.113}$$

and substituting into Eq. (14.112) and equating $\Omega = b^3$ gives:

$$\dot{\varepsilon} = \frac{4}{9}\frac{\sigma^3 l}{\alpha^3\mu^3}\left(z_{\mathrm{i}}^{\mathrm{d}}D_{\mathrm{i}}C_{\mathrm{i}} - z_{\mathrm{v}}^{\mathrm{d}}D_{\mathrm{v}}C_{\mathrm{v}} + z_{\mathrm{v}}^{\mathrm{d}}D_{\mathrm{v}}C_{\mathrm{v}}^{\mathrm{d}}\right) \,. \tag{14.114}$$

If l is fixed by impenetrable obstacles and is therefore independent of stress, then the stress dependence of the creep rate is σ^3. However, if l is determined by the dislocation density, then substituting for l from Eq. (14.84) and expressing the dislocation density in terms of stress, Eq. (14.7) gives:

$$\dot{\varepsilon} = \frac{4}{9}\frac{\sigma^2 b}{\sqrt{\pi}\alpha^2\mu^2}\left(z_{\mathrm{i}}^{\mathrm{d}}D_{\mathrm{i}}C_{\mathrm{i}} - z_{\mathrm{v}}^{\mathrm{d}}D_{\mathrm{v}}C_{\mathrm{v}} + z_{\mathrm{v}}^{\mathrm{d}}D_{\mathrm{v}}C_{\mathrm{v}}^{\mathrm{d}}\right) \,, \tag{14.115}$$

where the stress dependence is σ^2, which is the same stress dependence as in preferential absorption climb and glide given by Eq. (14.95).

14.2.8 Diffusional Creep: Why There is no Effect of Irradiation

All of the mechanisms of irradiation creep discussed thus far are based on the actions of dislocations. The reason is that while diffusional creep is a viable thermal creep mechanism, it is unaffected by irradiation, and can be understood as follows. Consider the discussion of Nabarro–Herring creep in Sect. 14.1.2. There it was shown that creep is driven by a difference in the equilibrium vacancy concentrations at the grain boundaries oriented parallel to the tensile and compressive stress directions, Eq. (14.45). Under irradiation, Eq. (14.47) is modified to include interstitials:

$$J_{\mathrm{v}} = D_{\mathrm{v}}\frac{\mathrm{d}C_{\mathrm{v}}}{\mathrm{d}x} - D_{\mathrm{i}}\frac{\mathrm{d}C_{\mathrm{i}}}{\mathrm{d}x} \approx \kappa D_{\mathrm{v}}\frac{C_{\mathrm{v}}^{\mathrm{t}} - C_{\mathrm{v}}^{\mathrm{c}}}{d} - \kappa D_{\mathrm{i}}\frac{C_{\mathrm{i}}^{\mathrm{t}} - C_{\mathrm{i}}^{\mathrm{c}}}{d} \,. \tag{14.116}$$

Substituting in for $C_{\mathrm{v}}^{\mathrm{t}}$ and $C_{\mathrm{v}}^{\mathrm{c}}$ from Eq. (14.45) and for $C_{\mathrm{i}}^{\mathrm{t}}$ and for $C_{\mathrm{i}}^{\mathrm{c}}$ using the same equations but with the signs on the arguments of the exponential terms re-

versed because of the opposite effect of stress on interstitials, gives:

$$J_{\mathrm{v}} = \kappa D_{\mathrm{v}} \frac{C_{\mathrm{v}}^0 \exp\left(\frac{\sigma\Omega}{kT}\right) - C_{\mathrm{v}}^0 \exp\left(-\frac{\sigma\Omega}{kT}\right)}{d} - \kappa D_{\mathrm{i}} \frac{C_{\mathrm{i}}^0 \exp\left(-\frac{\sigma\Omega}{kT}\right) - C_{\mathrm{i}}^0 \exp\left(\frac{\sigma\Omega}{kT}\right)}{d} . \tag{14.117}$$

Applying the approximation that the term $\frac{\sigma\Omega}{kT}$ is small compared to 1 yields:

$$J_{\mathrm{v}} = \frac{2\kappa\sigma\Omega}{dkT}\left(D_{\mathrm{v}}C_{\mathrm{v}}^0 + D_{\mathrm{i}}C_{\mathrm{i}}^0\right) \approx \frac{2\kappa\sigma\Omega}{dkT} D_{\mathrm{v}}C_{\mathrm{v}}^0 , \tag{14.118}$$

where the approximation is due to the fact that although D_{i} is greater than D_{v}, C_{v}^0 is much greater than C_{i}^0. The vacancy flux given in Eq. (14.118) is the same as that in Eq. (14.47) and thus, there is no effect of irradiation on Nabarro–Herring creep. The reason is that the creep rate is driven by the *difference* in the equilibrium values of defects at the grain boundaries, and these values do not depend on the concentration of vacancies or interstitials in the matrix. Irradiation simply serves to increase the flow of defects to each boundary equally without a change in the net amount. The same argument applies to Coble creep. As such, diffusional creep is unaffected by irradiation and does not contribute to irradiation creep.

14.2.9 Comparison of Theory with Creep Data

Much like thermal creep, primary creep is characterized by an initially high creep rate that declines with irradiation dose or fluence and transitions into steady state or secondary creep that is generally linear with dose. The difference between irradiation creep and thermal creep is in the magnitudes. The irradiation creep rates are much larger than those due solely to thermal processes. Of the mechanisms discussed, SIPN accounts best for the transitory nature of the primary creep regime, but cannot explain steady state creep. During steady state creep, the creep rate is proportional to the swelling rate and the relationship has been described by the following empirical equation [20]:

$$\dot{\bar{\varepsilon}}/\bar{\sigma} = B_0 + D\dot{S} , \tag{14.119}$$

where $\dot{\bar{\varepsilon}}/\bar{\sigma}$ is the effective strain rate per unit stress and dpa, and $\bar{\sigma}$ is the effective stress, B_0 is the creep compliance, D is the creep-swelling coupling coefficient and $\dot{S}$ is the instantaneous volumetric swelling rate per dpa. In the absence of swelling, only the first term is relevant and the equation predicts a dependence of creep on stress to the power $n = 1$:

$$\dot{\bar{\varepsilon}} = B_0\bar{\sigma}\phi . \tag{14.120}$$

While Eq. (14.119) is empirical, the relationship can also be determined from theory as well. Recall Eq. (8.122) for swelling in which thermal emission of vacancies is negligible and recombination is negligible. Assuming that the only point defect sinks are voids and dislocations and that the dislocation sink strength is much greater than the void sink strength, then Eq. (8.122) becomes:

$$\dot{R} = \frac{K_0(z_\mathrm{i} - z_\mathrm{v})\Omega}{R z_\mathrm{i} z_\mathrm{v} \rho_\mathrm{d}} , \tag{14.121}$$

and the void swelling rate is:

$$\dot{V} = 4\pi R^2 \dot{R} \rho_V = \frac{4\pi R K_0 \rho_V \Omega (z_\mathrm{i}^\mathrm{d} - z_\mathrm{v}^\mathrm{d})}{z_\mathrm{i}^\mathrm{d} z_\mathrm{v}^\mathrm{d} \rho_\mathrm{d}} . \tag{14.122}$$

Substituting the expression for C_i from Eqs. (5.31) and (5.64) into Eq. (14.82) for SIPA creep, where only the first term is retained, the creep rate can be written as:

$$\dot{\varepsilon}_\mathrm{SIPA} = \frac{2}{9} \frac{\Omega \rho_\mathrm{d} \Delta z_\mathrm{i}^\mathrm{d} K_0}{z_\mathrm{i}^\mathrm{d} \rho_\mathrm{d}} , \tag{14.123}$$

and the ratio of the creep rate to the swelling rate is:

$$\frac{\dot{\varepsilon}_\mathrm{SIPA}}{\dot{V}} = \frac{2}{9} \delta \frac{z_\mathrm{v}^\mathrm{d} \rho_\mathrm{d}}{4\pi R_\mathrm{V} \rho_\mathrm{V}} , \tag{14.124}$$

where $\delta = \dfrac{\Delta z_\mathrm{i}^\mathrm{d}}{(z_\mathrm{i}^\mathrm{d} - z_\mathrm{v}^\mathrm{d})}$. The linear dependence of creep rate on void swelling applies as well to climb-glide creep.

There is also significant data to support this dependence, some of the most convincing provided in Fig. 14.13, that gives a value of B_0 of $\sim 3 \times 10^{-6}\,\mathrm{MPa}^{-1}\mathrm{dpa}^{-1}$. The dependence of creep rate on stress to the power $n = 1$ provides support for the SIPA mechanism of creep. Note also that the strains appear to be independent of temperature over the range studied, supporting irradiation creep as the mechanism behind the strain rate rather than thermal creep, which has a very steep temperature dependence. The creep rate has also been observed to vary as $\phi^{1/2}$ at low temperature, Fig. 14.14, yielding a B_0 dependence on flux of (dpa rate)$^{-1/2}$. When swelling begins, the creep rate is driven by swelling according to the term $D\dot{S}$ in Eq. (14.119). Some of the earliest and most convincing results supporting this coupling between creep and swelling is shown in Fig. 14.15 for annealed 304 SS irradiated in EBR-II. The coupling was further supported by the strong correlation between creep and swelling in pressurized tube experiments in the PHENIX reactor (Fig. 14.16). Typical values for D are $\sim 10^{-2}\,\mathrm{MPa}^{-1}$. Garner [20] presents a more complete description of the dependencies of B_0 and D on the various parameters affecting creep. While the creep compliance and the coupling term are not strict constants, the relation between creep, stress, flux and swelling is well-described by Eq. (14.119).

The complexity of irradiation creep and its strong dependence on the irradiated microstructure is illustrated by the observation by Garner et al. [21] that at high levels of irradiation dose, the irradiation creep rate can drop to zero. This phenomenon

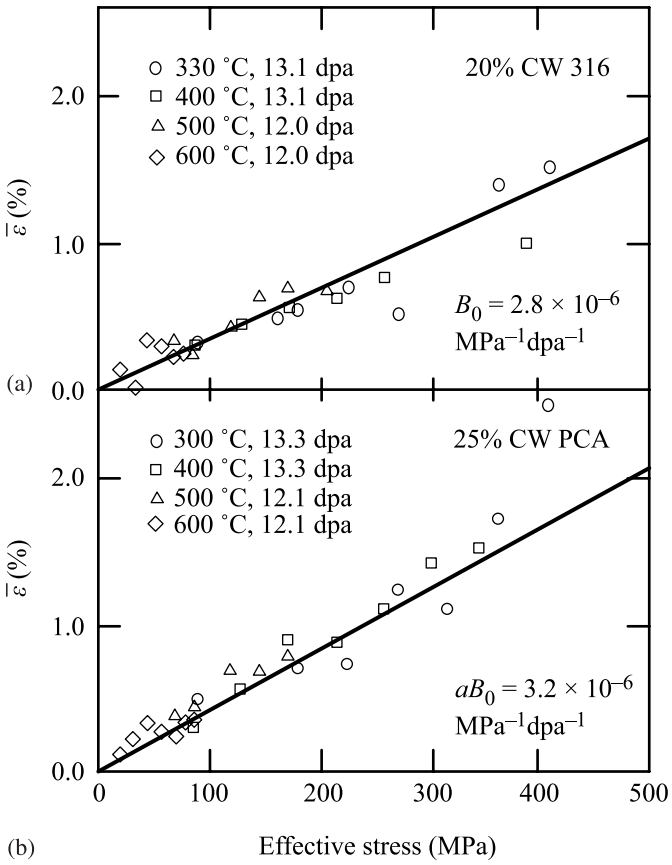

Fig. 14.13. Dependence of the normalized creep strain on effective stress in (a) 20% CW 316 and (b) 25% CW PCA, over a range of temperatures and within a narrow dose range of 12.0 to 13.3 dpa [20]

is illustrated in Fig. 14.17 in which instantaneous creep coefficient in a stainless steel irradiated in EBR-II at 550 °C is observed to increase to a maximum, and then drop to zero at high dose. Note that deformation has not stopped, rather at the point where the creep compliance goes to zero, the deformation can be totally accounted for by the strain due to swelling, $\varepsilon_{\text{linear}} = \varepsilon_{\text{swelling}}/3$. This occurrence has its origin in the development of the dislocation network and loop microstructure. Under irradiation and an applied stress, creep is sensitive to the anisotropy of the dislocation microstructure and accounts for processes such as SIPA and PAG, in addition to SIPN. In the absence of swelling, the degree of anisotropy increases with dose. When voids begin to form, they consume vacancies and the matching interstitial flux to dislocations overwhelms that in the void-free, dislocation-dominated case, causing an increase in the creep rate that is coincident with the onset of swelling. When voids become the dominant sink, they absorb both vacancies and interstitials

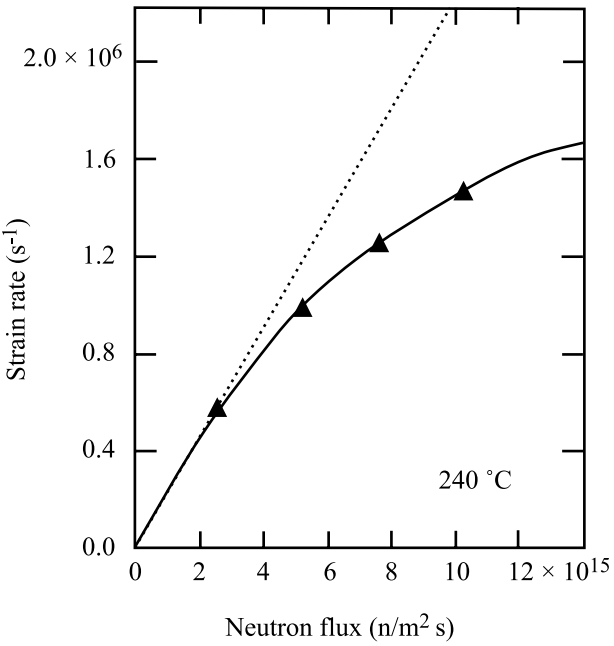

Fig. 14.14. Irradiation creep in annealed polycrystalline nickel irradiated at 240 °C in RTNS-II with 14 MeV neutrons (after [20])

in large numbers. The consequence is twofold: a reduction in the creep rate caused by the small excess interstitial flux to dislocations and a saturation in swelling due to low excess vacancy absorption. The dependence of creep on composition and metallurgical condition is largely determined by the response of swelling to those factors in the regime where creep is driven by swelling.

14.2.10 Irradiation-Modified Deformation Mechanism Map

The deformation mechanism map for 316 stainless steel can be modified to account for irradiation creep. Figure 14.18 shows the deformation map for 316 SS constructed in a manner identical to that for Fig. 12.26, but at a strain rate of $10^{-10}\,s^{-1}$ [22]. At this strain rate, irradiation creep is observable in the intermediate temperature regime. Below 20 °C, interstitial mobility drops and so does the irradiation creep rate. Above about 600 °C, Coble creep is the dominant creep mechanism. The irradiation creep regime, therefore, lies at intermediate temperature and intermediate stresses and can be described by the constitutive equation for the strain rate dependence of irradiation creep given by Eq. (14.119) in which the first term is due to dislocation creep (lower temperature portion of irradiation creep regime) and the second term is due to swelling-driven creep (higher temperature portion). The net effect of irradiation is to extend rate-dependent deformation to lower stresses.

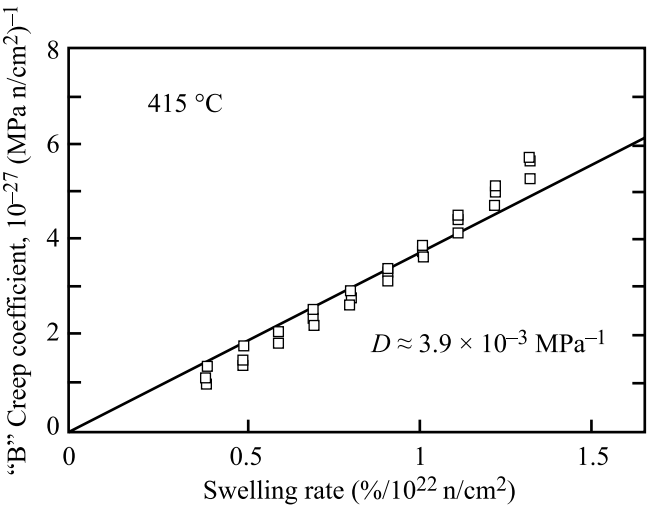

Fig. 14.15. Correlation of irradiation creep coefficients with swelling rates for annealed 304 L stainless steel irradiated in EBR-II (after [20])

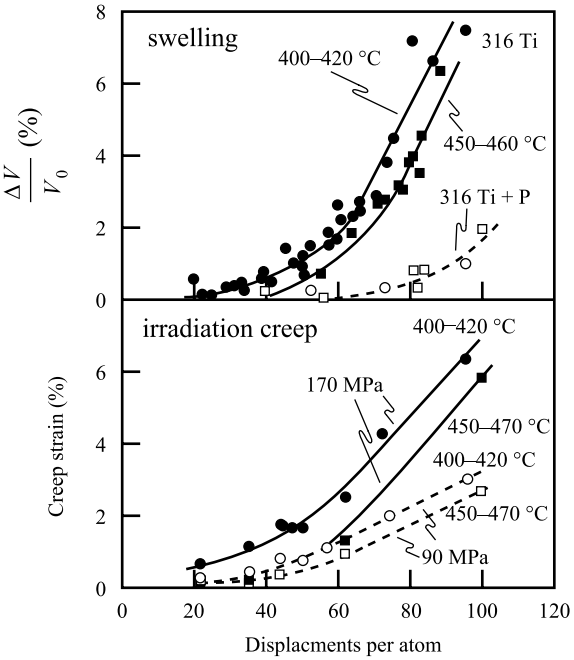

Fig. 14.16. Swelling and creep strains in two French steels irradiated as pressurized tubes in the PHENIX reactor (after [20])

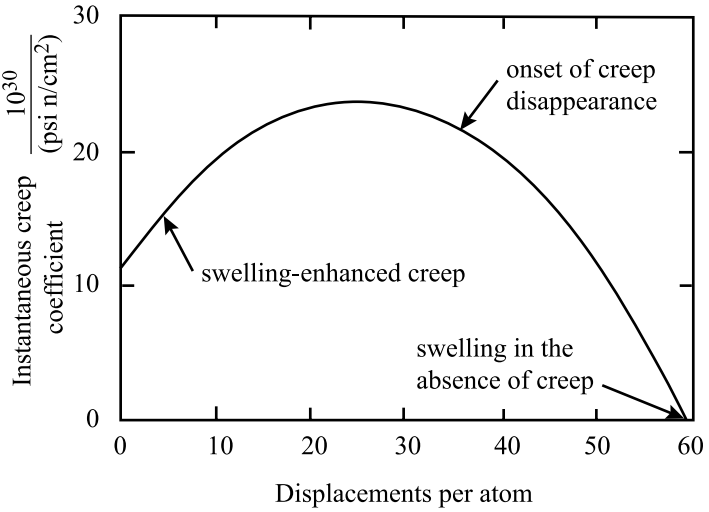

Fig. 14.17. The instantaneous creep coefficient determined from strain measurements of pressurized tubes of stainless steel, irradiated in the EBR-II reactor at 550 °C (after [20])

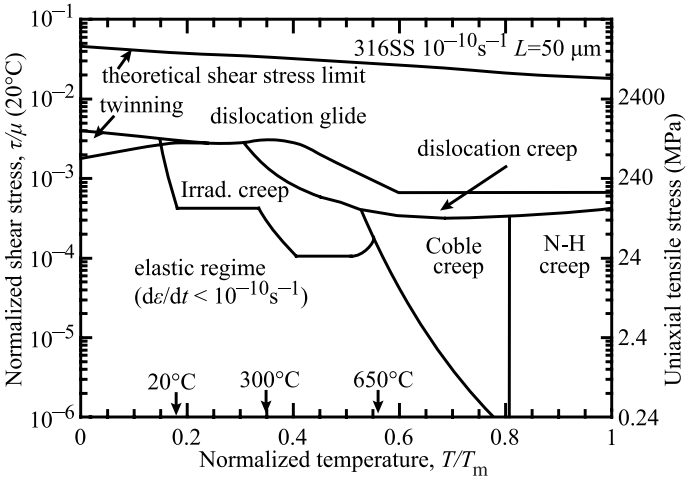

Fig. 14.18. Deformation mechanism map for 316 stainless steel irradiated to 1 dpa for a plastic strain rate of $10^{-10}\,\text{s}^{-1}$ (after [22])

14.3 Irradiation Growth and Creep in Zirconium Alloys

In addition to swelling and creep, another phenomenon occurs that leads to strains in some solids under irradiation. This phenomenon is termed *growth*. *Swelling* is the isotropic volume expansion of a solid without an external stress. *Creep* is the volume conservative distortion of a solid under an applied stress. *Growth* is the volume conservative distortion of a solid without an applied stress. Growth is only

Table 14.1. Slip systems for deformation in zirconium

	Tension (c-axis)		Compression (c-axis)	
Temp	Plane	Direction	Plane	Direction
Low	$(11\bar{2}1)$	$<\bar{1}\bar{1}26>$	$(11\bar{2}2)$	$<\bar{1}\bar{1}23>$
High	$(10\bar{1}2)$	$<\bar{1}011>$	$(10\bar{1}1)$	$<\bar{1}012>$

observed in non-cubic systems as it is highly dependent on anisotropy of the crystal structure. For this reason, irradiation growth can be significant in hcp metals such as zirconium and magnesium. Zirconium is stable in the α phase (hcp) below 863 °C and in the β phase (bcc) between 863 °C and T_{m}. Alpha-Zr has an ideal c/a ratio of 1.589. Three types of planes play key roles in the deformation and growth behavior of α-zirconium and its alloys:

- Prism I $(10\bar{1}0)$ and prism II $(11\bar{2}0)$
- Pyramidal $(11\bar{2}1)$, $(11\bar{2}2)$, $(10\bar{1}2)$
- Basal (0001)

Also of importance are the $(10\bar{1}2)$ and $(11\bar{2}2)$ planes. The prism, pyramidal and basal planes are shown in Fig. 14.19.

Deformation in hcp metals occurs by both slip and twinning. For stresses along the a-axis, slip occurs primarily on the $(10\bar{1}0)$ prism I plane in the $<11\bar{2}0>$ direction. At higher stress, slip occurs on the $(10\bar{1}1)$ and $(11\bar{2}1)$ pyramidal planes and in a $<c+a>$ direction, or along $<11\bar{2}3>$. At high temperatures, slip can occur on the (0001) basal plane in the a-direction, $<1\bar{2}10>$. Twinning is also a common deformation mode in hcp metals. Twinning will occur for stresses that have a component in the c-direction on one of the four pyramidal planes. The slip systems for deformation along the c-direction and as a function of temperature are given in Table 14.1. Note that different levels of stress are required to activate different deformation mechanisms. Hence, the stress needed to cause plastic deformation is a function of direction. A crystal possessing properties that are directionally dependent is called anisotropic.

Commercial production techniques result in Zr components in which the grains are aligned along preferential directions of the crystal. The preferential orientation of crystal directions is known as texture. The implication of texture in Zr components is that the anisotropic nature of the single crystal is exhibited in the polycrystalline material. Further, the texture changes with deformation and this is known as texture rotation. The texture is quantified by the f_{i} number or the fraction of basal poles in the ith direction, where $i = L$, T or N for longitudinal, transverse and normal, respectively. Note that $f_{\mathrm{L}} + f_{\mathrm{T}} + f_{\mathrm{N}} = 1$ always.

14.3.1 Microstructure of Irradiated Zirconium Alloys

In order to understand growth and creep in an anisotropic solid, we must have an understanding of the nature of the irradiated microstructure. One of the prime con-

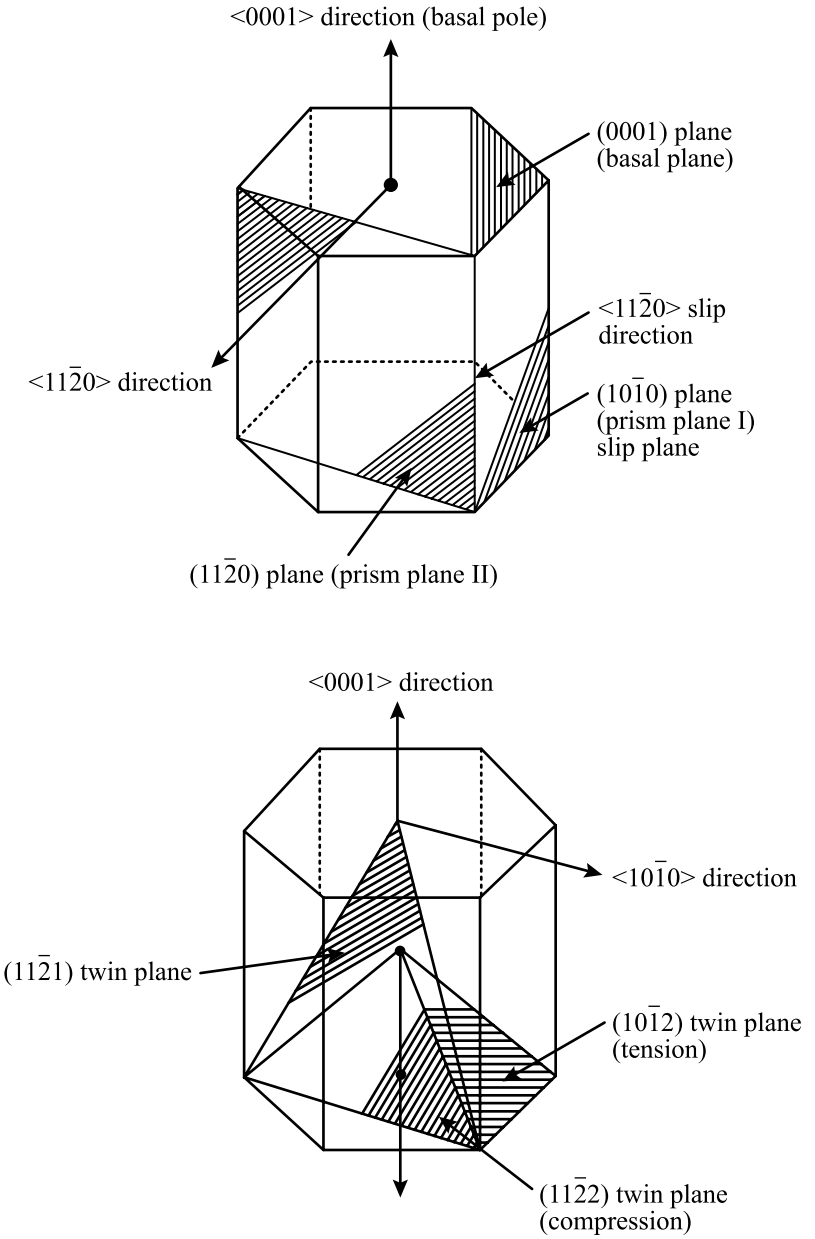

Fig. 14.19. Prism, pyramidal and basal planes in an hcp structure (after [23])

sequences of the crystal structure of zirconium and its alloys is anisotropic diffusion [24]. Another is that the dilatational strain of the self-interstitial is smaller in Zr than in most cubic solids, resulting in smaller elastic interaction between dislo-

cations and interstitials, which gives rise to vacancy loop stability. In fact, this small dilatational misfit may also explain the ease of Zr in accommodating interstitial gas atoms. The irradiation microstructure of Zr alloys can be summarized as follows.

Vacancy and interstitial $< a >$-type $1/3 < 1120 >$ (prism plane) loops nucleate and grow during neutron irradiation. Both are present in approximately equal numbers between temperatures of 300 and 450 °C, but vacancy loops are unstable above this range due to thermal emission. The relative numbers of vacancy and interstitial loops is dependent on the proximity of biased sinks for either interstitials or vacancies. The $< a >$-type dislocation loops arrange themselves in layers parallel to the basal plane, as shown in Fig. 14.20.

At doses above about $2.5 \times 10^{25}\,\mathrm{n/m^2}$, in the temperature range 300 to 500 °C, $< c >$-component dislocations start to develop on both the pyramidal and basal planes. The latter consist of vacancy loops having Burgers vector $1/6 < 20\bar{2}3 >$. The basal vacancy loops are believed to nucleate in collision cascades, and owe their stability to solutes that lower the stacking fault energy and stabilize them at small size. Impurity segregation at dislocations near the loops or anisotropic diffusion are likely to be the most important factors governing loop growth. Additional factors

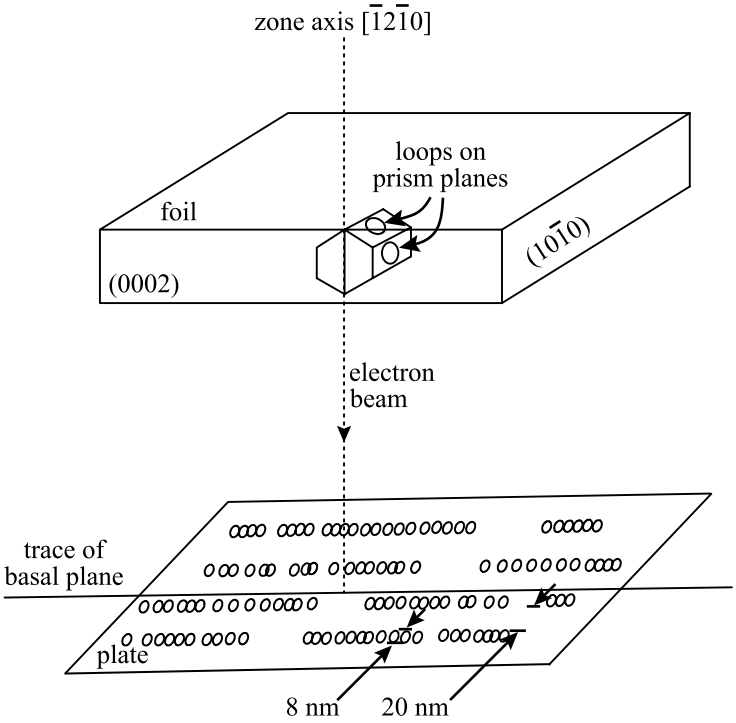

Fig. 14.20. Schematic diagram of the arrangement of dislocation loops on prism planes in irradiated zirconium (after [25])

that are important in $< c >$-component loops are stress and the magnitude of the Burgers vector.

At all temperatures, dislocation loop growth contributes to the network during irradiation, and recovery of the dislocation network is not significant below 400℃. The $< c >$-component vacancy sinks are likely net vacancy sinks and $< a >$-type dislocations are probably net interstitial sinks. The fact that $< c >$-component loops on basal planes are generally of vacancy character also indicates that the $< c >$-component network dislocations are also vacancy sinks since they climb in a similar manner.

Grain boundaries serve as sinks for interstitial defects during irradiation of annealed Zr. The bias is dependent on the grain boundary orientation and is a minimum for boundary planes that are parallel to the basal plane (0001). Voids can form in Zr at temperatures between 350 and 500℃, and their formation is a strong function of impurities and on the presence of insoluble gases. When they form, they also tend to be located at second phase particles. In fact, the lack of insoluble gases is likely one of the reasons for the instability of voids and the stability of $< c >$-component loops instead. As in cubic metals, insoluble gases play an important role in stabilizing small vacancy clusters against collapse to vacancy loops.

Lastly, radiation induces the formation (of ZrSn or ZrNb) or the dissolution or re-distribution and re-precipitation of intermetallic phases containing Zr and Fe, Cr or Ni depending on temperature, solute content and dose. The re-balancing of solute in the matrix can have an impact on the processes of creep and growth.

14.3.2 Irradiation Growth

Growth is easiest to understand first in single crystal zirconium. Measurements of growth of single crystal zirconium were first reported by Buckley in 1962 [26]. The shape change that occurred involved an expansion along the a-axis and a contraction along the c-axis, with magnitudes that resulted in zero net volume change, consistent with the concept of growth as a volume conservative distortion process. Results of these observations led to one of the first models of irradiation growth which held that interstitials condensed as dislocation loops lying on the prism planes and vacancies from depleted zones collapsed to form vacancy loops lying on the basal planes. This process is equivalent to a transfer of atoms from basal planes to prism planes via the irradiation-induced point defects, as shown schematically in Fig. 14.21. The growth strains of single crystal zirconium as a function of neutron fluence is shown in Fig. 14.22 in which there is a large positive growth strain in the $< a >$-direction, a negative growth strain in the $< c >$-direction and near zero strain in the $< c + a >$-direction. But subsequent, detailed TEM observations [28, 29] of the dislocation loop structure of Zr that had undergone irradiation growth showed that all of the irradiation-induced dislocation loops had Burgers vectors of the type, $b = 1/3 < 11\bar{2}0 >$, or $< a >$-type loops and no indication of $< c >$-component loops. While the loops with $< a >$-type Burgers vector could account for the a-axis expansion, they do not account for the c-axis contraction. In fact, after an initial strain of about 10^{-4}, the growth quickly saturated. Irradiation to much higher

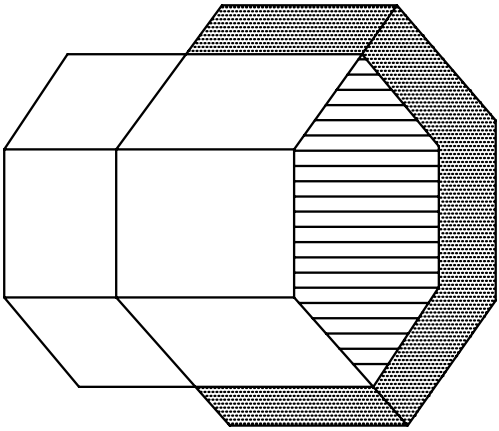

Fig. 14.21. Schematic of the change in shape of a single crystal of α-zirconium produced by interstitial condensation on prism planes and vacancy depleted zone collapse on basal planes

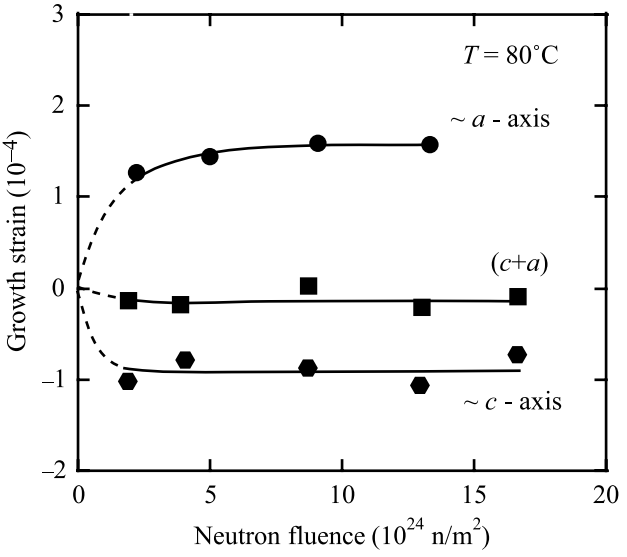

Fig. 14.22. Growth strains of annealed single crystals of zirconium as a function of neutron fluence at 80 °C (after [27])

doses showed that the saturation was in fact, temporary, and that the growth strain exhibited a *breakaway* behavior above $\sim 2.5 \times 10^{25}\,\mathrm{n/m^2}$ (Fig. 14.23). Breakaway growth has been ascribed to the nucleation and growth of $< c >$-component vacancy loops [27]. The current evidence supports the nucleation of a low density of loops with $1/6 < 20\bar{2}3 >$ Burgers vectors that grow to relatively large sizes ($> 100\,\mathrm{nm}$). In fact, much of the growth strain in Zircaloy-2 at high fluence can be accounted for by excess interstitial annihilation at $< a >$-type loops and network dislocations with the corresponding vacancies annihilating at the $< c >$-component loops [30].

In polycrystalline zirconium alloys, irradiation growth consists of three components: (1) a short-term transient due to irradiation-induced microstructure changes such as defect clusters or loops, (2) a crystallographic texture-dependent steady state

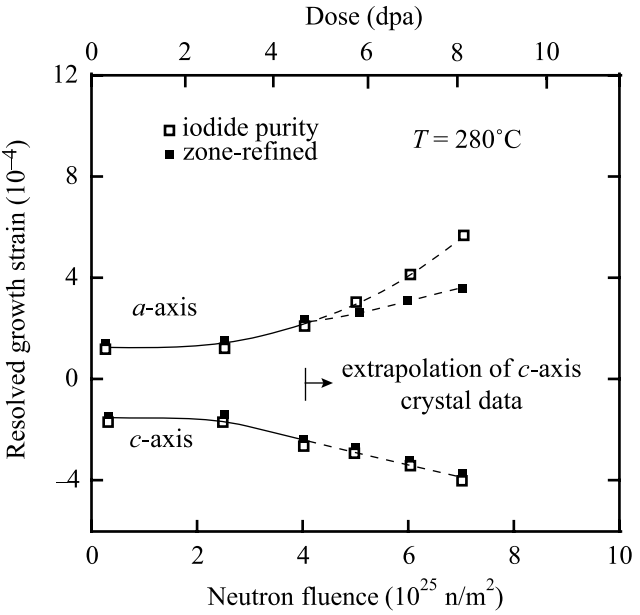

Fig. 14.23. Growth at high fluence for annealed zirconium single crystals at 273 °C showing the onset of breakaway growth at a fluence of 2.5×10^{25} n/m^2 (after [27])

growth component, and (3) a texture-dependent long-term transient arising from breakaway growth [29]. The growth strain in a given direction of a polycrystal, $\boldsymbol{d}$ can be related to its crystallographic texture by the f numbers and is proportional to the growth anisotropy factor, G_d:

$$G_\mathrm{d} = 1 - 3f_\mathrm{d}^b \,, \tag{14.125}$$

where f_d^b is the resolved fraction of basal poles in the direction $\boldsymbol{d}$. The values of f_d^b are determined from basal pole figures obtained by X-ray diffraction using the relationship:

$$f_\mathrm{d}^b = \sum_q V_q \cos^2 q \,, \tag{14.126}$$

where V_q is the volume fraction of grains with their basal poles at an angle q from the direction $\boldsymbol{d}$. If the resolved fraction of basal poles in a given direction is equal to 1/3, then according to Eq. (14.125), the growth in that direction should be zero. Adamson [32] showed that the growth strain in the longitudinal, transverse and thickness directions of re-crystallized and cold-worked Zircaloy-2 irradiated at 287 °C and 327 °C fit the behavior rather well. Figure 14.24 shows that the growth behavior of re-crystallized Zircaloy-2 at 57 °C also follows Eq. (14.125).

Irradiation growth is weakly dependent on grain size with smaller grains giving rise to larger growth. It is also dependent on cold-work with higher cold-work

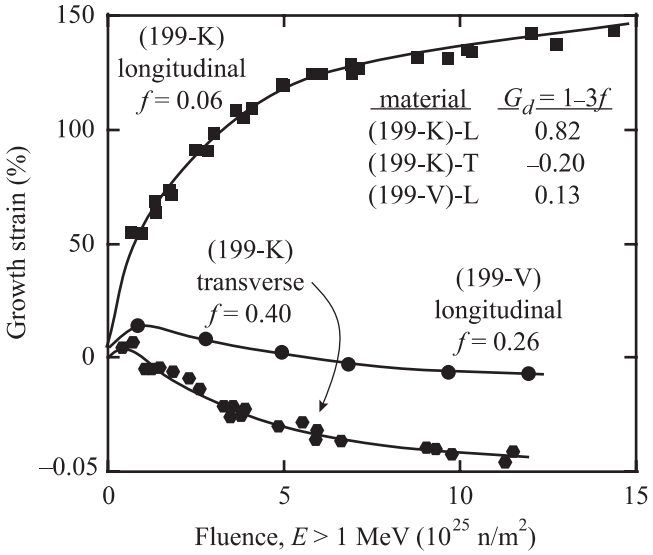

Fig. 14.24. Texture dependence of irradiation growth of Zircaloy-2 sheet at 57 °C [33]

resulting in a greater growth strain (Fig. 14.25). Growth appears to be dependent on fluence but there is not much evidence to support a flux dependence. Finally, growth is observed to increase with temperature, with a rapid increase above about 400 °C due in part to an increase in volume. It has also been proposed that impurity elements, such as Fe, can stabilize $< c >$-component loop embryos and enable their growth. Irradiation has been observed to amorphize Fe- and Cr-rich precipitates [34] causing the re-distribution of iron into the matrix [35]. This dissolution process may be a source of iron for $< c >$-component loop stabilization at high fluences.

Holt [36] describes a model that attempts to capture the sensitivity of the growth rate to the microstructure by estimating the annihilation probabilities for interstitials, and for vacancies at the various microstructural sinks. It holds that growth is driven by the difference in the anisotropy of interstitial and vacancy migration in which $(1 - 3f)$ growth can occur in cold-worked microstructures by vacancy partitioning to the $< c + a >$-network dislocations and interstitial partitioning to the a-type dislocations. The linear dependence of the growth rate of cold-worked and stress-relieved Zircaloy-2 is controlled by fast vacancy migration with a low migration energy of 0.7 eV. The breakaway growth at high fluences is due to the appearance of basal plane loops which act as strong vacancy sinks.

14.3.3 Irradiation Creep

Time-dependent deformation in zirconium alloys is a combination of thermal creep, irradiation creep and growth. While the thermal creep component at reactor temperatures is generally small if not negligible, irradiation creep and growth components are not easily separable. The dependence of unirradiated zirconium tensile

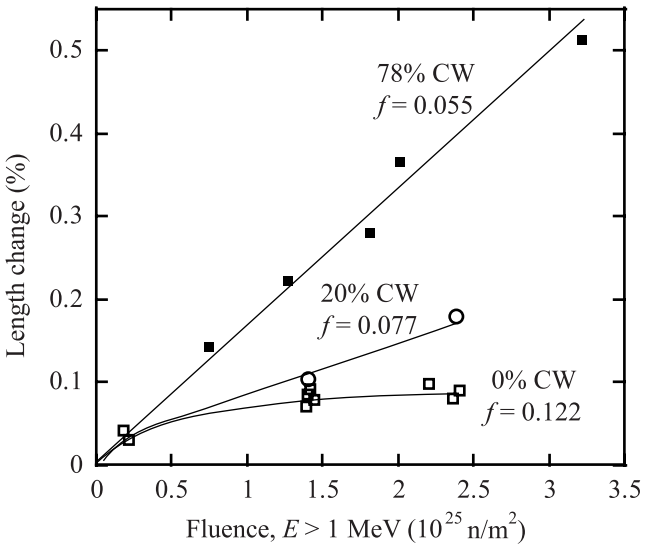

Fig. 14.25. Effect of cold-work on irradiation growth in Zircaloy-4 irradiated near 282 °C (after [31])

and creep properties on temperature can be subdivided into three regions as shown in Fig. 14.26. Below about 175 °C, the yield stress decreases with temperature, but creep below the yield stress does not depend strongly on temperature. Region II is the *athermal* region of creep and extends between about 175 to 523 °C in which mechanical recovery balances strain aging and the net effect is that creep is independent of temperature but does not readily reach steady state creep. Above 523 °C, the strong dependence of yield strength on temperature and the increased recovery leads to steady state creep rates at constant stress.

In reactor, creep follows the phenomenological equation:

$$\dot{\varepsilon} = A\sigma^n \phi^p G_{\mathrm{d}} \exp(-Q/kT)[f(t) \text{ or } g(\varepsilon)] \,, \tag{14.127}$$

where $f(t)$ and $g(\varepsilon)$ are functions of time and strain, respectively, and other terms are as previously defined. While the flux dependence is generally taken to be linear, correlations show that the value of p varies between 0.25 and 0.85 at low fluxes (10^{16} n/m^{2}s) and rises to an asymptotic value of 1.0 at high fluxes (10^{18} n/m^{2}s) [31]. The flux exponent also was found to decrease with temperature and become negligible above 523 °C (region III) [37]. The fluence dependence is generally linear, but data exists to show that at high fluence ($>\sim 2 \times 10^{25}$ n/m^2), there is an upturn in the creep rate (Fig. 14.27).

Creep of zirconium alloys is highly dependent on the stress. At 300 °C and low stress ($< 1/3\sigma_y$), $n = 1$. With increasing stress to values between 200 and 400 MPa, n rises to a value of 2, and then increases rapidly at higher stresses and can reach a value of 100 at a stress of 600 MPa (Fig. 14.28). Below about 300 °C,

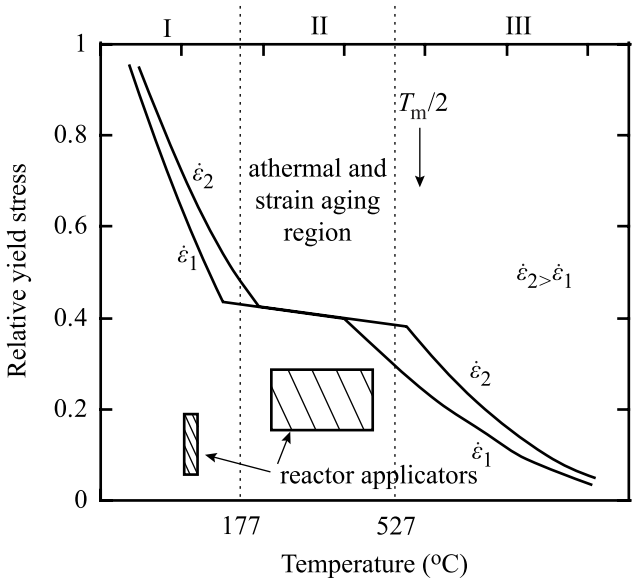

Fig. 14.26. Temperature dependence of the yield strength of zirconium alloys (after [31])

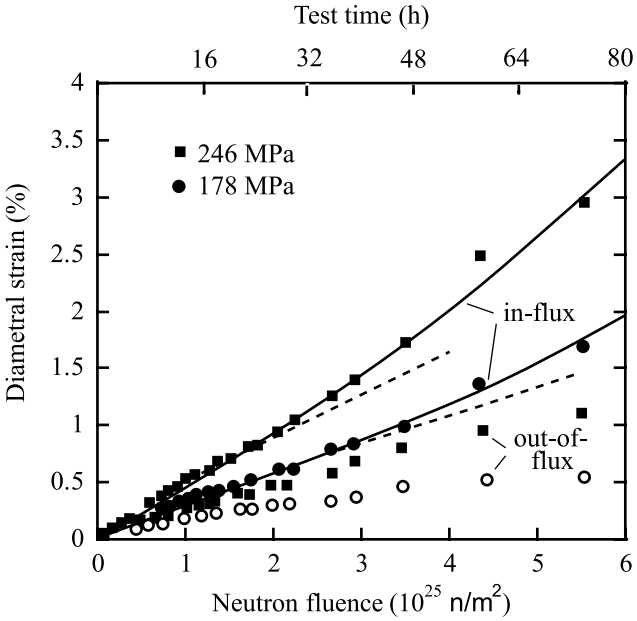

Fig. 14.27. Diametral creep strain in cold-worked Zr–1.5Nb tubes irradiated at 297 °C and a fast neutron flux of 2.1×10^{17} n/m^{2}s (after [31])

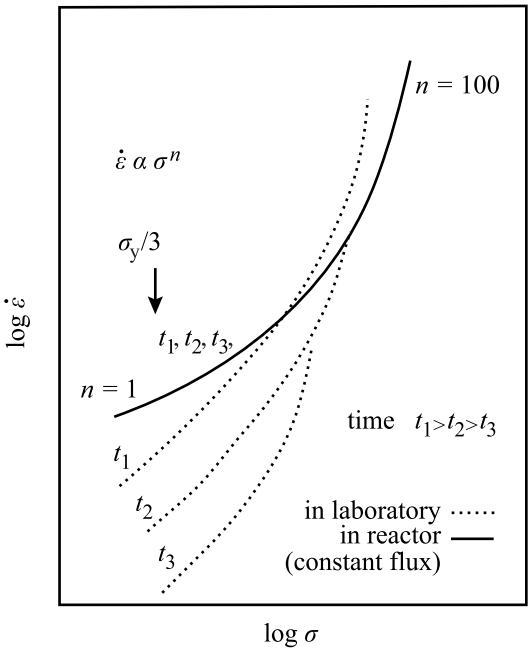

Fig. 14.28. Schematic of the stress dependence of in-reactor creep in zirconium alloys at about 300°C (after [31])

the temperature dependence of creep is weak and the activation energy is between 16 and 40 kJ/mol (Fig. 14.29). The temperature dependence increases rapidly with temperature and Q can exceed 200 kJ/mol. However, the transition temperature for Q is dependent on alloy content, metallurgical condition and stress [31]. As with texture, creep is highly dependent on the texture, which is included as the anisotropy coefficient in Eq. (14.127). However, as shown in Fig. 14.30, the texture dependence is greatest in the primary creep range. Creep in zirconium alloys is believed to be due to slip of $< a >$-type dislocations on prism planes with secondary slip of $< c + a >$-type dislocations on pyramidal planes. In Zircaloy-2 and Zr–2.5%Nb, slip of $< a >$-type dislocations contributed over 90% of the total strain [38]. The most likely mechanism to explain creep at low stress is the SIPA mechanism. As discussed earlier, this mechanism has an $n = 1$ stress dependence, which is consistent with creep at low stress. The elastodiffusion origin of SIPA [39] in which diffusion of interstitials is anisotropic in an applied stress field is consistent with the partitioning of interstitials to $< a >$-type loops, facilitating their climb and glide.

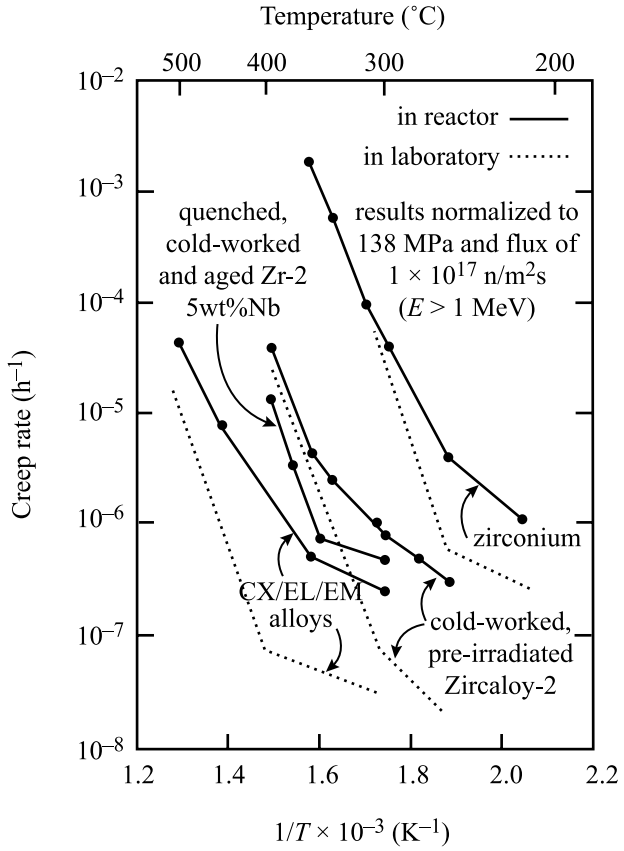

Fig. 14.29. Temperature dependence of in-reactor creep in zirconium alloys (after [31])

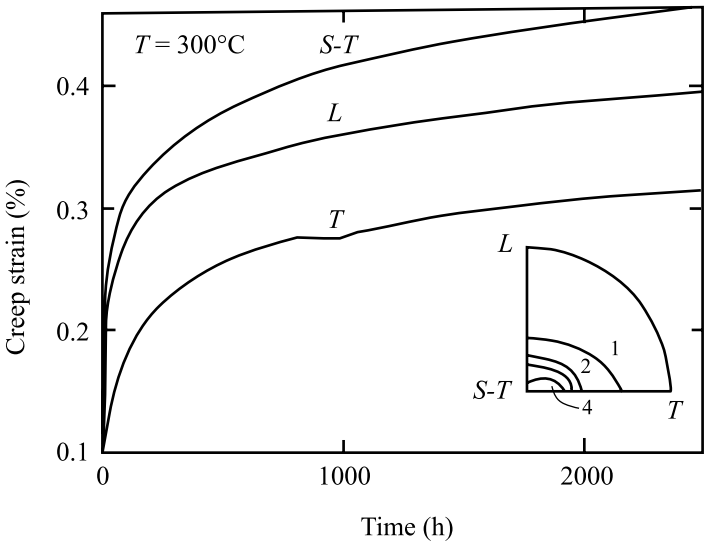

Fig. 14.30. Creep of cold-worked Zircaloy-2 at 207 MPa and 300 °C after [31]

Nomenclature

A	Area of slip plane or dislocation loop
$\bar{A}$	Average loop area
a	Lattice constant
$\boldsymbol{b}$	Burgers vector
B_0	Creep compliance
$C_{\mathrm{v,i}}$	Concentration of vacancies, interstitials
$C^0_{\mathrm{v,i}}$	Thermal equilibrium concentration of vacancies, interstitials
d	Grain size
D	Creep-swelling coupling coefficient
D_{eff}	Effective diffusion coefficient
D_{gb}	Grain boundary diffusion coefficient
$D_{\mathrm{i,v}}$	Interstitial, vacancy diffusion coefficient
D_{vol}	Volume diffusion coefficient
E	Energy or elastic modulus
E_{vol}	Activation energy for volume diffusion
f^b_{d}	Resolved fraction of basal poles in the d direction
f_{i}	Fraction of interstitial loops aligned in direction i. Also resolved fraction of basal poles of hcp unit cells in the i direction.
F_{i}	Component of force in the ith direction
F_j	Frequency with which a dislocation climbs a height, h
G_{d}	Anisotropy factor
h	Obstacle height on glide plane
k	Boltzmann's constant
$k^2_{\mathrm{v,i}}$	Total sink strength for vacancies, interstitials
$k^2_{\mathrm{L,N}}$	Sink strengths for loops, networks
l	Glide length on the slip plane
J	Flux
n	Number of interstitials are required to form an interstitial loop Also, number of dislocations in a pile-up
n_0	Number of possible loop orientations
N	Atom number density
N_{L}	Number density of dislocation loops
P_j	Probability of a dislocation climb of j or greater
r_{c}	Dislocation core radius
r_{L}	Dislocation loop radius
R_{c}	Critical loop size for survival
R_j	Probability of finding a dislocation a distance j from unpinning point
R_{max}	Maximum dislocation loop radius
$\dot{S}$	Swelling rate
t	Time
T	Temperature
T_{m}	Melting temperature
v_{c}	Dislocation climb velocity

v_{d}	Average dislocation velocity
V	Volume
V_{cas}	Volume of cascade
V_q	Volume fraction of grains with their basal poles at an angle q with respect to a direction, d
$\frac{\Delta \dot{V}}{V}$	Swelling rate
$z_{\mathrm{i,v}}^{\mathrm{d}j}$	Capture efficiencies of dislocation of orientation j
$\Delta z_{\mathrm{i,v}}^{\mathrm{d}}$	Difference in capture efficiencies between aligned and non-aligned loops
α	Number of spikes per neutron scattering event
ϕ	Neutron flux
δ	Effective thickness of the grain boundary
ε_{s}	Shear strain
$\dot{\varepsilon}$	Strain rate
$\dot{\bar{\varepsilon}}$	Effective strain (or creep) rate
$\dot{\varepsilon}_{\mathrm{m}}$	Swelling strain
$\varepsilon, \varepsilon_{ij}$	Strain and components of strain
ε_{e}	Elastic strain
μ	Shear modulus
ν	Poisson's ratio
ω	Release frequency of pinned dislocation segments
Ω	Atomic volume
ρ, $\rho_{\mathrm{m,L,N}}$	Total dislocation density, mobile, loop and network components
ρ_{FR}	Frank–Read source density
σ, σ_{ij}	Stress and components of stress
σ_{s}	Neutron scattering cross section. Also shear stress
$\bar{\sigma}$	Effective stress

Subscripts

c	Climb
d	Dislocation
eff	Effective
FR	Frank–Read
g	Glide
gb	Grain boundary
i, v	Interstitial, vacancy
NL	Non-aligned loop
L	Loop
m	Mobile
N	Network
s	Shear
S	Swelling
vol	Volume

Superscripts

c	Compressive
dA	Aligned dislocation loops
dN	Non-aligned dislocation loops
D	Dislocation
V	Void
n	Stress exponent
p	Flux exponent
t	Tensile

Acronyms

GC	Glide and climb
FR	Frank–Read
N-H	Nabarro–Herring
PA	Preferential absorption
PAG	Preferential absorption glide
PE	Preferential emission
SIPA	Stress-induced preferential absorption
SIPN	Stress-induced preferential nucleation

Problems

14.1 Referring back to the void growth rate calculation in Problem 8.4 of Chap. 8:
- a) Calculate the irradiation creep rate for stainless steel as a function of temperature and applied shear stress. Assume a void number density of $2 \times 10^{15}\,\mathrm{cm}^{-3}$ for the creep rate calculation.
- b) Identify the window in stress-temperature space in which the creep rate remains below 0.01%/hour.

14.2 In the Hesketh model of irradiation creep by stress-enhanced vacancy–loop collapse, depleted zones with less than $m_c \sim 200$ vacancies remain in the solid as vacancy platelets. For $m < m_c$, the volume per platelet of size m is $m\Omega$. Using the inverse square distribution function for vacancy platelet (or depleted zone) size produced by a neutron collision, compute the swelling due to uncollapsed platelets in the absence of applied stress at a fast fluence of $10^{20}\,\mathrm{neutrons/cm}^2$. Assume $\Sigma_s = 0.2\,\mathrm{cm}^{-1}$, $\Omega = 0.012\,\mathrm{nm}^3$, and $\nu = 500$ Frenkel pairs per fast neutron collision.

14.3 An Inconel-718 bolt is used to hold a reactor mechanical component in place. The lifetime of the bolt is determined by the stress relaxation (due to irradiation creep). The bolt must be replaced if the load drops to 10% of the initial load. For the small irradiation dose received by the bolt, assume the creep strain rate ($\dot{\varepsilon}$) during irradiation is proportional to the displacement damage rate ($\dot{\phi}$) and the effective stress (σ):

$$\dot{\varepsilon} = -B\dot{\phi}\sigma \tag{14.128}$$

a) Calculate the radiation dose (in dpa) when the bolt stress drops to 10% of the initial value. Assume the elastic modulus E is a constant value of 7.6×10^{10} Pa and the creep coefficient B is a constant value of $1.6 \times 10^{-6}\,\mathrm{MPa^{-1}dpa^{-1}}$.

b) Due to changes in fuel loading patterns, the dpa rate at the bolt decreases by 50% after 5 dpa. Recalculate the total dose to reach 10% of the initial pre-load. Does this change the time to replace the bolt?

14.4 A dislocation which absorbs vacancies and interstitials at different rates will exhibit climb. The climb velocity v_c is given by $v_c = (J_i^d - J_v^d)b^2$ where J_i^d is the flux of interstitials to a unit length of dislocation line and b is the Burgers vector.

If the average obstacle size is 100 nm, calculate the mean time needed for dislocations to climb over obstacles in fcc aluminum at 200 °C in a monoenergetic neutron flux of $10^{14}\,\mathrm{n/cm^2s}$ ($E = 1$ MeV). Assume that the obstacles are *not* sinks for point defects and that kinetics are diffusion-limited.

$$
\begin{aligned}
T_m &= 660\,^\circ\mathrm{C} \\
a &= 0.30\,\mathrm{nm} \\
Q_f^v &= 3.2\,\mathrm{eV} \\
Q_m^v &= 0.62\,\mathrm{eV} \\
Q_i^v &= 0.66\,\mathrm{eV} \\
Q_i^v &= 0.12\,\mathrm{eV} \\
S_{th}^v &= 0.7\,\mathrm{k} \\
S_{th}^i &= 8\,\mathrm{k} \\
S_m^v &= S_m^i = 0 \\
\nu &= 10^{13}\,\mathrm{s^{-1}} \\
\rho_d &= 10^9\,\mathrm{cm^{-2}} \\
b &= 0.2\,\mathrm{nm}
\end{aligned}
$$

14.5 A creep experiment is performed on unirradiated 316 stainless steel ($T_m = 1750$ K) samples at 300 °C and 700 °C in the laboratory at low stress. Comparison experiments are performed on a second pair of 316 SS samples at the same temperatures, but *during* irradiation at a neutron flux of $1 \times 10^{14}\,\mathrm{n/cm^2s}$ ($E > 1$ MeV). A third pair of samples is tested in the lab at the same temperatures but after being irradiated to a fluence of $10^{21}\,\mathrm{n/cm^2}$ at the test temperatures.

a) Make two plots, one for each temperature. Draw, label and explain the expected creep curves for each of these experiments.

b) What mechanisms would you expect to control creep in each of these experiments?

14.6 The 316 stainless steel sample irradiated at 700 °C in Problem 14.5 above fails at 1% strain in a creep test. The failure is attributed to helium embrit-

tlement and calculations show that the total helium content in the metal was 10^{17} at/cm^3, the grain size was 20 μm and the swelling at failure was 30%. What is the stress at failure?

14.7 The generalized equation for thermal creep is:

$$\dot{\varepsilon} = \frac{ADb}{kT}\left(\frac{\sigma}{\mu}\right)^n \left(\frac{b}{d}\right)^p, \quad \text{where} \quad D = D_0 \exp(-Q/kT)$$

D = Diffusion coefficient
d = Grain size
b = Burgers vector
k = Boltzmann's constant
T = Temperature (K)
μ = Shear modulus
σ = Applied stress
n = Stress exponent
p = Inverse grain size exponent
A = Dimensionless parameter

a) Are any of the variables that describe the creep affected by irradiation?
b) If so, how would increasing the displacement rate during an irradiation by an order of magnitude change the creep rate in a pure alloy with very low sink density?

14.8 The generalized correlation between creep and swelling is written as:

$$\dot{\bar{\varepsilon}}/\bar{\sigma} = B_0 + D\dot{S} \tag{14.119}$$

Comparing this equation to the generalized creep equation in Problem 14.7, implies that the stress exponent is 1. What does that tell you about the likely mechanisms of creep?

References

1. Frost HJ, Ashby MJ (1982) Deformation Mechanism Maps: The Plasticity and Creep of Metals and Ceramics. Pergamon, New York
2. Olander DR (1976) Fundamental Aspects of Nuclear Reactor Fuel Elements, TLD-26711-Pl. Technical Information Center, ERDA, Washington, DC chap 19
3. Weertman J (1955) J Appl Phys 26(10):1213
4. Weertman J (1968) Trans ASM 61:681
5. Weertman J (1957) J Appl Phys 28(3):362
6. Cadek J (1988) Creep in Metallic Materials. Elsevier, New York
7. Nabarro FRN (1948) Report on Conference on Strength of Solids. Physical Society, London, p 75
8. Herring C (1950) J Appl Phys 21:437
9. Coble RL (1963) J Appl Phys 34:1679
10. Brailsford AD, Bullough R (1973) Phil Mag 27:49

11. Bullough R (1985) In: Dislocations and Properties of Real Materials, Proceedings of Royal Society, London. The Institute of Metals, London, p 283
12. Matthews JR, Finnis MW (1988) J Nucl Mater 159:257
13. Mansur LK (1979) Phil Mag A 39(4):497
14. Wolfer WG, Foster JP, Garner FA (1972) Nucl Technol 16:55
15. Mansur LK (1992) Mater Sci Forum 97–99:489–498
16. Grossbeck ML, Mansur LK (1991) JNM 179–181:130–134
17. Lewthwaite GW (1973) Scr Metal 7:75
18. Brinkman JA, Wiedersich H (1964) In: Proceedings of the Symposium on Flow and Fracture of Metals and Alloys in Nuclear Environment, STP 380. American Society for Testing and Materials, West Conshohocken, PA, p 3
19. Mansur LK, Coghlan WA, Reiley TC, Wolfer WG (1981) J Nucl Mater 103/104:1257
20. Garner FA (1994) In: BRT Frost (ed) Materials Science and Technology, chap. 6, vol 10A. VCH, New York, p 419
21. Garner FA, Grossbeck ML (1994) Fusion Materials Semi-annual Progress Report DE/ER-0313/16. US DOE, Oak Ridge, TN, March 1994
22. Zinkle S, Lucas GE (2003) Deformation and Fracture Mechanisms in Irradiated FCC and BCC Metals, US Department of Energy, Semi-annual Report, DOE-ER-0313/34. US DOE, Washington, DC
23. Klepfer HH (ed) (1962) Proceedings of the USAEC Symposium on Zirconium Alloy Development, US Atomic Energy Commission, GEAP4089, vol II, p 13–11
24. Griffiths M (1988) J Nucl Mater 159:190
25. Northwood DO (1977) At Energy Rev 15(4):547
26. Buckley SN (1962) Uranium and Graphite. Institute of Metals, London, p 445
27. Carpenter GJC, Zee RH, Rogerson A (1988) J Nucl Mater 159:86
28. Fidleris V (1975) At Energy Rev 13:51
29. Northwood DO, Fidleris V, Gilbert RW, Carpenter GJC (1976) J Nucl Mater 61:123
30. Griffiths M, Gilbert RW (1987) J Nucl Mater 150:169
31. Fidleris V (1988) J Nucl Mater 159:22
32. Adamson RB, Tucker RP, Fidleris V (1982) In: Zirconium in the Nuclear Industry the 5th Symposium, STP 754. American Society for Testing and Materials, West Conshohocken, PA, p 208
33. Fidleris V, Tucker RP, Adamson RB (1987) Zirconium in the Nuclear Industry the 7th Symposium, STP 939. American Society for Testing and Materials, West Conshohocken, PA, 1987, p 49
34. Lemaignan C, Motta AT (1994) In: Frost BRT (ed) Materials Science and Technology, chap 7, vol 10B. VCH, New York, p 1
35. Zu XT, Sun K, Atzmon M, Wang LM, You LP, Wan FR, Busby JT, Was GS, Adamson RB (2005) Phil Mag 85(4–7):649–659
36. Holt RA (1988) J Nucl Mater 159:310
37. Nichols FA (1969) J Nucl Mater 20:249
38. Christodoulou N, Causey AR, Woo CH, Tome CN, Klassen RJ, Holt RA (1993) In: Kumar AS, Gelles DS, Nanstad RK, Little EA (eds) Proceedings of the 16th International Symposium on Effects of Radiation on Materials, ASTM STP 1175. American Society for Testing and Materials, West Conshohocken, PA, 1993, pp 1111–1128
39. Woo CH (1984) J Nucl Mater 120:55

15 Environmentally Assisted Cracking of Irradiated Metals and Alloys

A growing concern for electric power utilities worldwide has been the degradation of core components in nuclear power reactors, which provide approximately 17% of the world's electric power production. Service failures have occurred in boiling water reactor (BWR) core components and, to a somewhat lesser extent, in pressurized water reactor (PWR) core components consisting of iron and nickel-base stainless alloys that have achieved a significant neutron fluence in environments that span oxygenated to hydrogenated water at 270–340 °C. Because cracking susceptibility depends on many factors, such as alloy composition and microstructure, stress, radiation, and the environment, the failure mechanism has been termed irradiation-assisted stress corrosion cracking (IASCC). Initially, the affected components were either relatively small (bolts, springs, etc.) or those designed for replacement (fuel rods, control blades, or instrumentation tubes). Since these early observations, many more structural components (PWR baffle bolts and BWR core shrouds) have been identified to be susceptible to IASCC. Recent reviews [1, 2, 3, 4, 5] describe the current knowledge related to IASCC service experience and laboratory investigations and highlight the limited amount of well-controlled experimentation that exists on well-characterized materials.

The importance of neutron fluence on IASCC has been well-established (Fig. 15.1). Intergranular (IG) SCC is promoted in austenitic stainless steels as a critical *pseudo-threshold* fluence is exceeded. The dose to cracking is referred to as a *pseudo-threshold* because the value depends on the environmental and material parameters. Cracking is observed in BWR oxygenated water at fluences above about $2–5 \times 10^{20}\,\mathrm{n/cm^2}$ ($E > 1\,\mathrm{MeV}$), which corresponds to about 0.3–0.7 displacements per atom (dpa) (Fig. 15.2). While the fluence dependence on cracking is not strong, cracking does occur during ex situ, slow-strain-rate SCC testing of stainless steels irradiated in core. The occurrence of cracking in post-irradiation tests indicates that *persistent* radiation effects (material changes) are primarily responsible for IASCC susceptibility, although in situ effects like radiation creep relaxation of weld residual stresses and increased stress from differential swelling can be important. In fact, IASCC only occurs with the confluence of irradiation and an aggressive environment. If either is absent, cracking is either eliminated or greatly reduced.

IASCC can be categorized into radiation effects on (1) water chemistry (radiolysis), and (2) material properties, as summarized in Fig. 15.3. The cracking response to changes in water chemistry is similar for both irradiated and unirradiated materi-

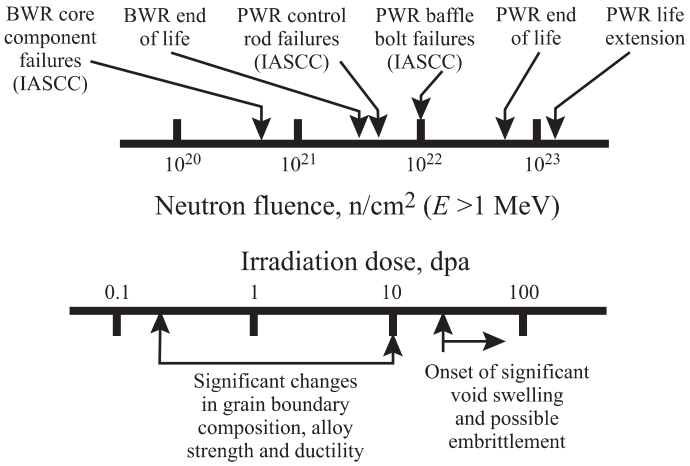

Fig. 15.1. Neutron fluence effects on irradiation-assisted stress corrosion cracking susceptibility of stainless steels in LWR environments (from [6])

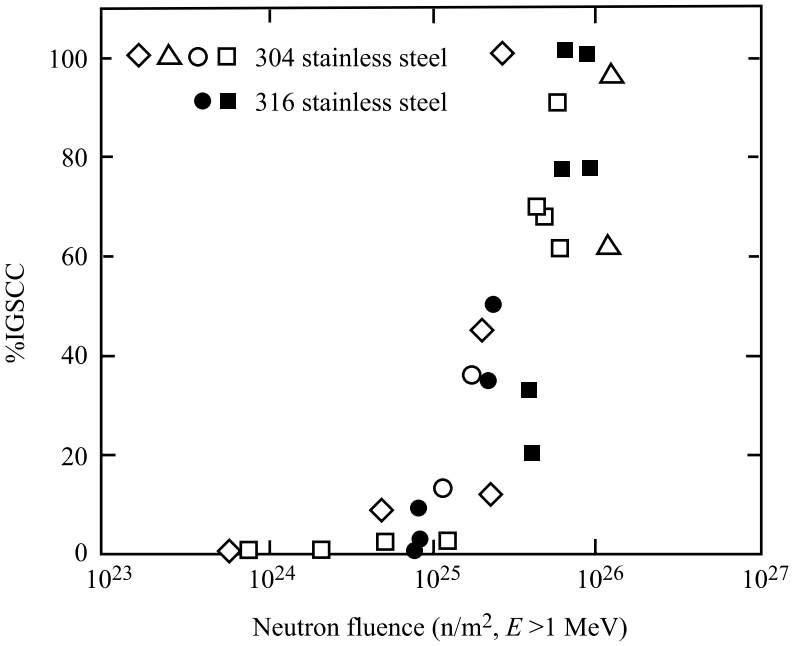

Fig. 15.2. Dependence of cracking in neutron-irradiated high-purity 304 SS and 316 SS on accumulated high-energy neutron fluence (from [4])

als. In both cases, there is a steep increase in environmental cracking kinetics with a rise in the corrosion potential above about $100 mV_{SHE}$ [7, 8, 9]. At high corrosion potential, the crack growth rate also increases sharply as impurities (especially chlo-

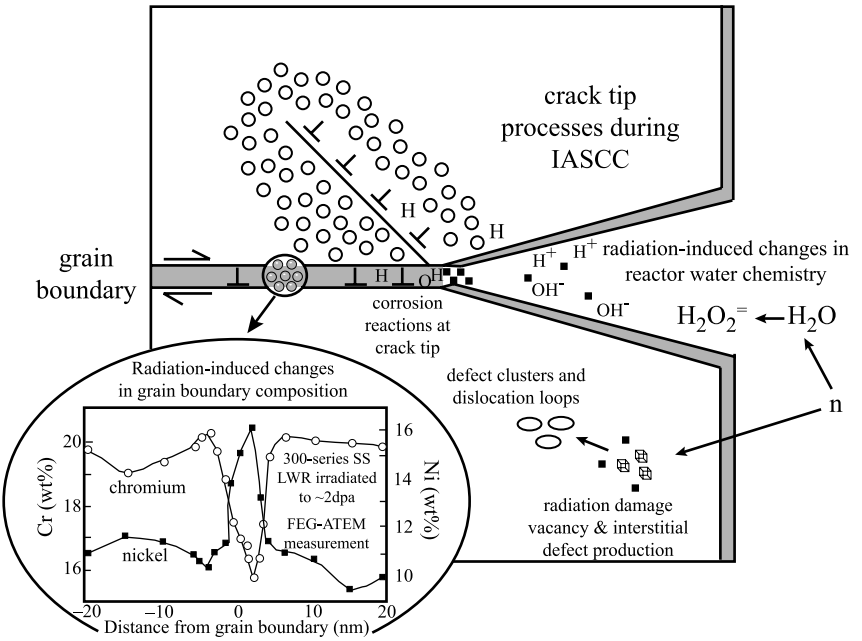

Fig. 15.3. Schematic illustration of mechanistic issues believed to influence crack advance during IASCC of austenitic stainless steels in LWRs (from [6])

ride and sulfate) are added to pure water in either the irradiated or unirradiated cases. In post-irradiation tests, the dominant radiation-related factors are microstructural and microchemical changes, which can be responsible for *threshold-like* behavior in much the same way as corrosion potential, impurities, degree of sensitization, stress, temperature, etc. Other radiation phenomena, like radiation creep relaxation and differential swelling, could also have *persistent* effects if the sources of stress present during radiation (e.g., weld residual stresses, or loading from differential swelling) were also present during post-irradiation testing. The effects of radiation rapidly (in seconds) achieve a dynamic equilibrium in water, primarily because of the high mobility of species in water. In metals, dynamic equilibrium is achieved only after many dpa, typically requiring years of exposure. As both radiation-induced segregation (RIS) of major elements, and radiation hardening (RH) and the associated microstructural development asymptotically approach a dynamic equilibrium, other factors (e.g., RIS of Si, or precipitate formation or dissolution) may become important. Data on post-irradiation slow strain rate tests (SSRT) on stainless steels show that there is a distinct (although not invariant) threshold fluence at which IASCC is observed under LWR conditions [8]. The term "threshold" is used here to characterize the regime where cracking increases steeply with fluence, but it does not mean that cracking is absent below the threshold or that cracking saturates at the threshold. Because this threshold occurs at a fraction to several dpa (depending on the alloy, stress, water chemistry, etc.), Fig. 15.2, in situ effects (corrosion potential,

conductivity, temperature) may be important, but only persistent radiation effects (microstructural and microchemical changes) can be responsible for the threshold-like behavior vs. fluence in post-irradiation tests.

The following sections begin with a tutorial on stress corrosion cracking, followed by a treatment of the effects of irradiation on water chemistry and the alloy itself. The effect of irradiation on SCC is discussed first in the context of commercial experience, and then from a mechanistic perspective through its effect on water chemistry and the alloy microstructure.

15.1 Stress Corrosion Cracking: A Tutorial

Stress corrosion cracking is the premature cracking of an alloy in the presence of a tensile stress and a corrosive environment. Historically, SCC was believed to occur only when three conditions were fulfilled: a susceptible alloy, a specific environment, and a tensile stress. In practice, most alloys are susceptible to SCC over a range of environments. The term *alloy* should be interpreted broadly so as to incorporate commercial purity metals since SCC is known to be a strong function of impurity content of pure metals. Similarly, the environment needs to be broadly interpreted to potentially all environments other than noble gases, since many gases, aqueous solutions and liquid metals can promote SCC. The distinguishing characteristic of SCC is the requirement of a stress. While localized corrosion can occur in a stress-free environment, SCC can only occur with the imposition of a tensile stress. Figure 15.4 shows a stress-strain curve for an alloy in an inert environment compared to one in which the alloy is susceptible to stress corrosion cracking. SCC reduces the strain to failure as well as the maximum stress. Cracking may be either transgranular (TG) (e.g., 304 stainless steel in boiling $MgCl_2$ at 154 °C) or intergranular, IG (e.g., 304 stainless steel in 288 °C water, Fig. 15.5). Typically, when the general corrosion rate is high, SCC susceptibility is low and when the general corrosion rate is low, the SCC susceptibility is high.

A distinction is often made between stress corrosion cracking, hydrogen embrittlement and corrosion fatigue. Stress corrosion cracking is used here to refer to the broad category of cracking in a metal or alloy due to chemical or electrochemical

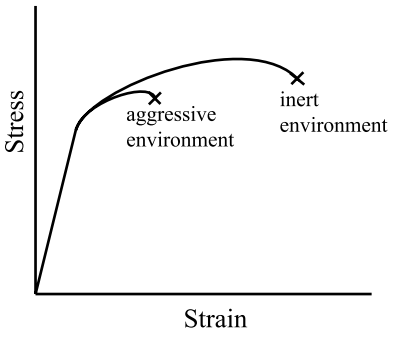

Fig. 15.4. Effect of the environment on stress-strain behavior of metals undergoing stress corrosion cracking

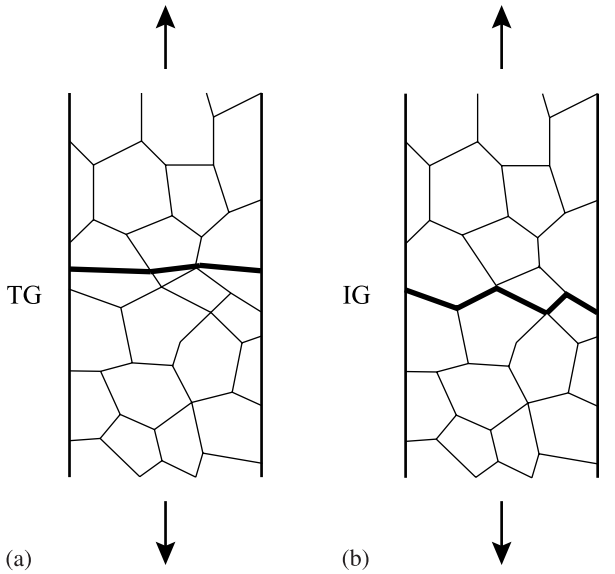

Fig. 15.5. Schematic illustrations of (a) transgranular stress corrosion cracking and (b) intergranular stress corrosion cracking

processes involving the combination of environment and stress. In this context, hydrogen produced by the corrosion reaction is a form of stress corrosion cracking, yet hydrogen absorption from the gaseous state is not. SCC is often distinguished from corrosion fatigue by constant or monotonically increasing loading vs. cyclic loading. Corrosion fatigue and hydrogen embrittlement will be discussed later in the chapter. Stress corrosion cracking often exhibits some of the following characteristics [10]:

- Localization of damage in the form of TG or IG cracks
- Some of the most susceptible alloys are often very corrosion resistant (e.g., the corrosion rate of stainless steel in boiling $MgCl_2$ is essentially zero, but it is highly susceptible to TGSCC)
- Resistance to SCC depends on alloy composition
- SCC exhibits a strong dependence on microstructure
- Alloys that are ductile in an inert environment, fail in a brittle manner
- Cathodic polarization mitigates the initiation of SCC

Stress corrosion cracking often takes some time to occur, requiring an incubation period. Following initiation, cracks propagate at a slow rate until the stresses in the remaining ligament exceed the fracture stress and failure occurs due to overload. The SCC process is often characterized by the following stages:

- Crack initiation followed by stage 1 propagation
- Stage 2 or steady state crack propagation
- Stage 3 crack propagation or final failure

However, not all alloys exhibit these stages or the stages may not be distinct or easily identifiable. To distinguish and quantify these stages of fracture, various SCC tests have been developed and are briefly summarized here.

15.1.1 SCC Tests

Stress corrosion cracking tests fall into three basic categories: static loading of smooth samples, static loading of pre-cracked samples, and slow strain rate testing. Static loading of smooth samples provides the time to failure as a function of applied stress as the measure of the degree of stress corrosion cracking susceptibility. Figure 15.6 shows a plot of the time to failure vs. stress for an alloy undergoing stress corrosion cracking. The minimum stress at which failure occurs is known as the threshold stress, σ_{th} for SCC. The failure time includes both the initiation time, t_{init} and the propagation time, t_{prop}, so that $t_{\text{fail}} = t_{\text{init}} + t_{\text{prop}}$. This test is useful for determining the maximum stress that can be applied without SCC failure in a specific environment. Examples of this test are the C-ring, U-bend and the O-ring tests shown in Fig. 15.7. In these tests, the sample is stressed to a fixed deflection and then held at that displacement for the duration of the test. In this mode, stress relaxation can occur so that the stress will decrease as the test progresses. As such, fixed load tests have been developed in which the load remains constant for the duration of the test.

In static loading of pre-cracked samples, a constant load or fixed crack opening displacement is applied to a sample with a pre-crack such as a compact tension (CT) or a double cantilever beam (DCB) specimen. The crack length is measured as a function of time, yielding a crack propagation rate (or crack velocity) that can be described as a function of the stress intensity, K. Figure 15.8 shows a plot of a $\mathrm{d}a/\mathrm{d}t$ vs. K curve in which the three stages of cracking are shown. As discussed in Chap. 13, K is a function of applied stress, specimen geometry and the square root of crack length. In the absence of a corrosive environment, fracture occurs when $K \geq K_{\text{Ic}}$, the plane strain fracture toughness. The effect of the corrosion environment is to lower the value of K at which cracking occurs. The existence of the plateau characteristic of stage II cracks can be due to the environment. That is, in the regime where the environment has a strong impact, crack velocity is independent of the stress intensity factor.

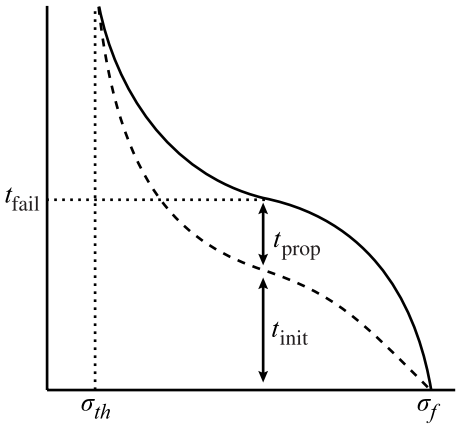

Fig. 15.6. Failure time as a function of stress for an alloy undergoing stress corrosion cracking. Failure time is the sum of the crack initiation time and the crack propagation time

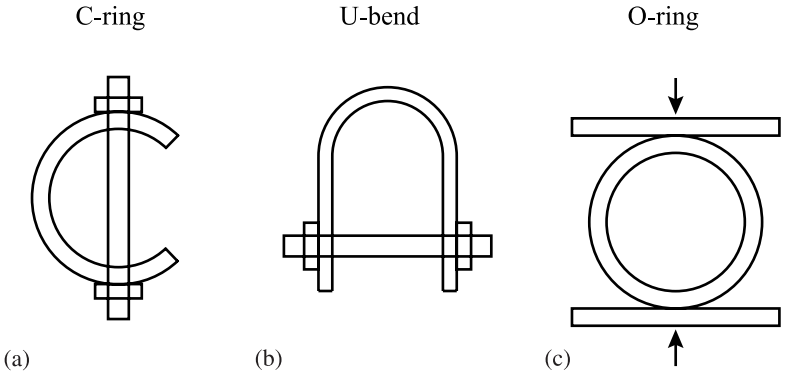

Fig. 15.7. Common constant-deflection tests used to assess the relative susceptibility of an alloy to stress corrosion cracking. (a) C-ring, and (b) reverse U-bend

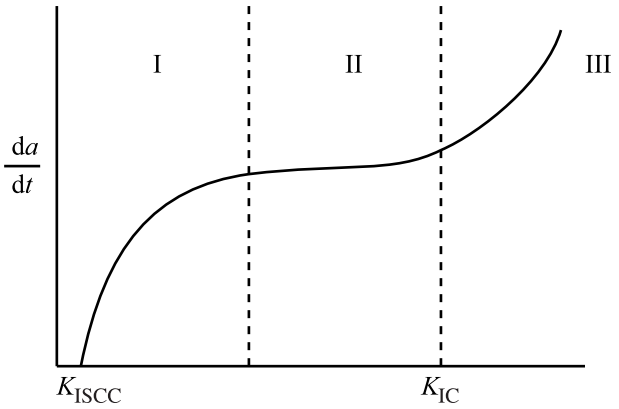

Fig. 15.8. Crack growth rate as a function of the crack tip stress intensity. Note that region II is independent of stress intensity, indicating the effect of the aggressive environment

The slow strain rate test involves the application of a slowly increasing strain, usually by applying a constant displacement rate, on a smooth bar or pre-cracked sample. The ductility in the corrosive environment is a measure of SCC susceptibility and is plotted against the strain rate and can be compared with that in an inert environment (Fig. 15.9). As shown, various measures can be used to indicate susceptibility, such as strain to failure, reduction in area, fracture energy or percent of the fracture surface that is due to SCC (TG or IG). Stress corrosion cracking susceptibility is manifest in a reduction in ductility at lower strain rates since there is sufficient time for the environment to induce SCC. As the strain rate rises, the time available for corrosion is reduced and the ductility approaches that in an inert environment. At very low rates, ductility can also increase as the strain rate is too slow to keep up with the effect of the environment. Known as constant extension rate tensile (CERT) or slow strain rate tensile (SSRT) tests, these tests are excellent indicators of the relative susceptibility of alloys to cracking in an environment, or for studying the influence of metallurgical variables. How-

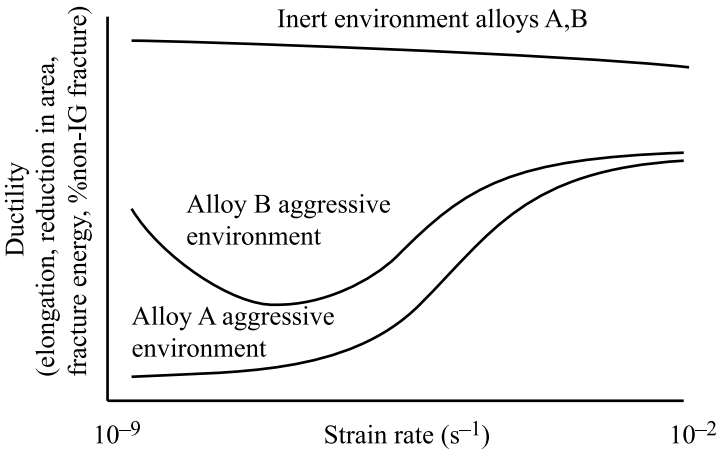

Fig. 15.9. Strain rate dependence of various measures of ductility. Alloys with no environmental effect have minimal strain rate dependence. In an aggressive environment, low strain rates are the most aggressive and cause the greatest reduction in ductility (from [10])

ever, since they combine both the initiation and propagation stages, they are not as effective in determining the initiation stage, which is how they have traditionally be used. In most cases, they are effective in evaluating moderate to severe SCC.

15.1.2 SCC Processes

Specific mechanisms of SCC will be discussed later, but it is instructive here to consider the basic processes behind these mechanisms. Many proposed mechanisms are based on either anodic or cathodic processes, but some are purely chemical oxidation. A mechanism must explain the actual crack propagation rates, fractographic features and the formation of cracks. Atomistically, this amounts to explaining how atomic bonds are broken, which is believed to occur by either chemical oxidation or chemical solvation and dissolution or mechanical fracture (ductile or brittle). Ultimately, mechanical fracture is assumed to be stimulated or induced by interactions between the material and the environment. Certain processes or events must occur for sustained crack propagation to be possible. Figure 15.10 illustrates a crack tip in which crack propagation results from reactions in the metal ahead of the propagating crack. The potential rate-determining steps include [10]:

1. Mass transport along the crack to the crack tip
2. Reactions in the solution near the crack
3. Surface adsorption at or near the crack tip
4. Surface diffusion
5. Surface reactions
6. Adsorption into the bulk
7. Bulk diffusion to the plastic zone ahead of the crack tip

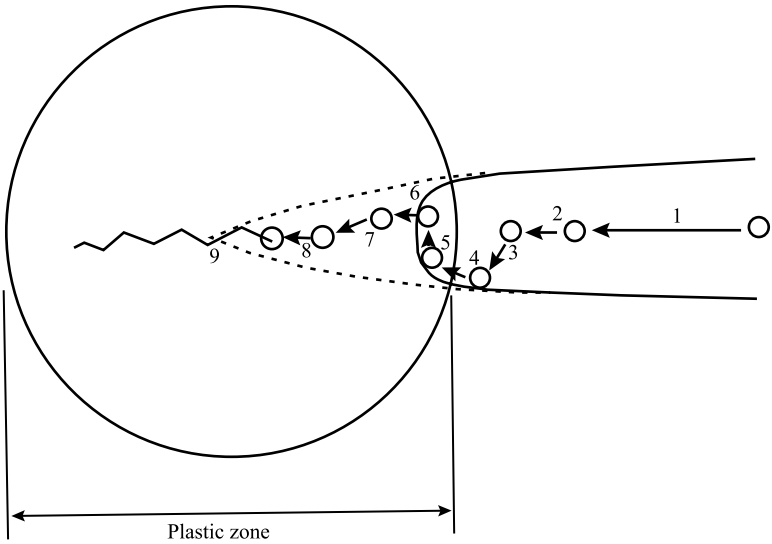

Fig. 15.10. Schematic illustration of crack tip processes that may be occur during environmentally assisted crack propagation (from [10])

8. Chemical reactions in the bulk
9. Rate of interatomic bond rupture

In addition to these processes, the passivation of the surface layer by a protective oxide is an important process that can strongly affect stress corrosion cracking. Environmental parameters that affect crack propagation in aqueous solutions include:

– Temperature
– Pressure
– Solute species
– Solute concentration and activity
– pH
– Electrochemical potential
– Solution viscosity
– Agitation/flow rate

An important factor in the cracking process is that the environment in occluded sites such as a crack tip can differ significantly from that in the bulk solution. If an alteration to the bulk environment allows the formation of a critical SCC environment at the crack nuclei, then crack propagation will result. If the bulk cannot maintain this local crack tip environment, then crack propagation will be retarded. SCC propagation rates are also influenced by a variety of mechanical and metallurgical factors, such as:

– The magnitude of the applied stress or the stress intensity factor, K
– Stress state: plane stress vs. plane strain

- Loading mode at the crack tip
- Alloy composition (nominal and local)
- Metallurgical condition (second phases in the grain boundary and matrix, phase composition and shape, grain size, grain boundary segregation, strength level, residual stress)
- Crack geometry (length, aspect ratio, crack opening)

15.1.3 Metallurgical Condition

As stated earlier, pure metals are much less susceptible to SCC than alloys or commercial purity metals [11]. However, "pure" may mean 99.9999% or better, so it is a very loose term. Conversely, grain boundary chemistry and structure often play significant roles in SCC. Intergranular cracking of high purity iron is due to grain boundary impurities. Aluminum alloy 7075 (Al–Zn–Mg) fails intergranularly in chlorides and halides due to grain boundary depletion of magnesium and zinc caused by precipitation of $MgZn_2$ at the boundary (Fig. 15.11). The $MgZn_2$ phase dissolves preferentially, leaving holes in the grain boundary and the weak aluminum bridges rupture mechanically.

The strong dependence of cracking in Fe–18Cr–xNi alloys on the nickel content in boiling $MgCl_2$ is an example of the effect of bulk alloy content on SCC. The greatest susceptibility occurs at a concentration of about 8 wt% nickel, Fig. 15.12, which is also the concentration at which the general corrosion rate is the lowest. Grain size can influence SCC, with susceptibility increasing with grain size. As grains become larger, dislocation pile-ups at grain boundaries become longer, producing higher local stresses and strains (according to the Hall–Petch relation), and higher susceptibility to SCC (Fig. 15.13).

15.1.4 Crack Initiation and Crack Propagation

The stress corrosion cracking process is often subdivided into initiation and propagation stages. Common sites for SCC crack initiation are:

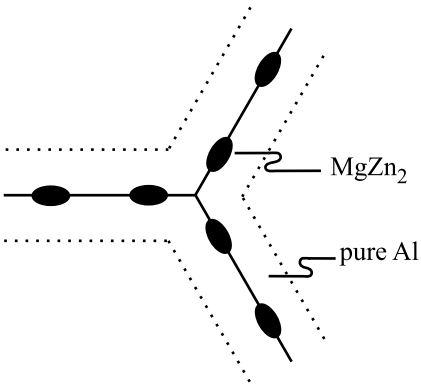

Fig. 15.11. Formation of $MgZn_2$ and depletion of Mg and Zn from the grain boundary, leading to a weak grain boundary and intergranular stress corrosion cracking in an Al–Zn–Mg alloy

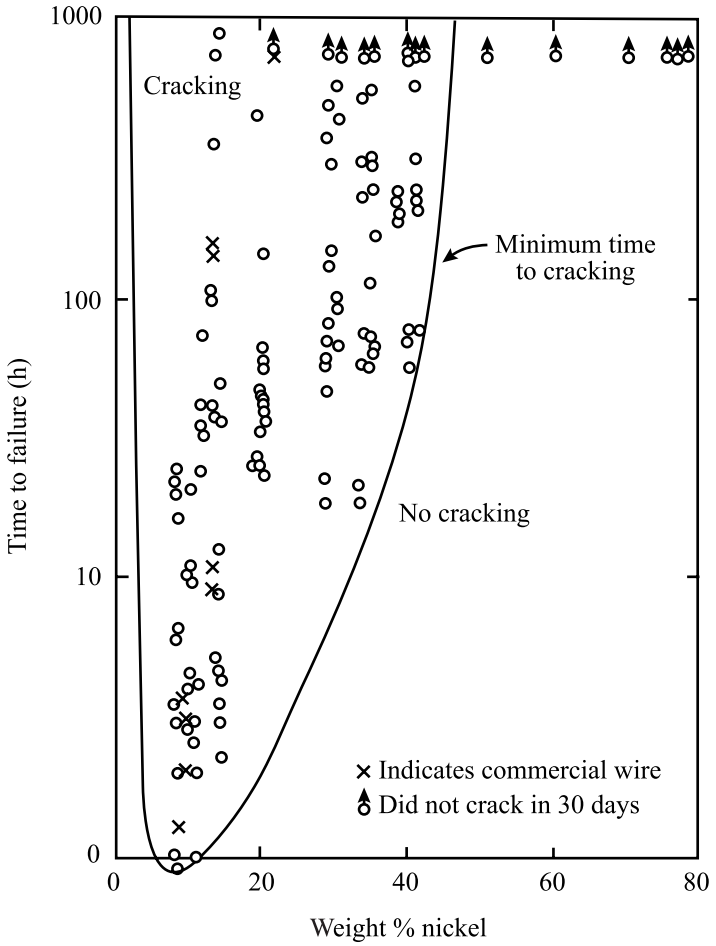

Fig. 15.12. Effect of nickel content on stress corrosion cracking in Fe–Cr–Ni alloys exposed to boiling 42% $MgCl_2$ solution at 154 °C (from [12])

- Pre-existing or corrosion-induced surface features such as grooves and burrs
- Corrosion-induced pits
- Intergranular corrosion or slip-dissolution processes. Intergranular corrosion-initiated SCC requires differing local grain boundary chemistry (e.g., sensitized stainless steels for grain boundary segregation). Slip dissolution-initiated SCC requires local corrosion at emerging slip planes in primarily, low stacking fault materials

While crack initiation is of great concern, there is a distinct lack of understanding of the initiation of SCC cracks due to the complexity of the process and the difficulty in defining the initiation phase. Further, the distinction between crack initiation and propagation phases is unclear. Nevertheless, the importance of the crack initiation

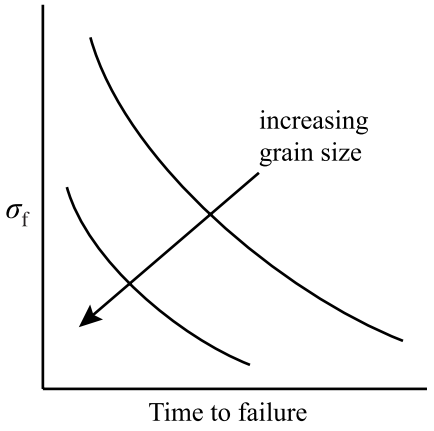

Fig. 15.13. Effect of grain size on the relation between failure stress and time to failure by SCC

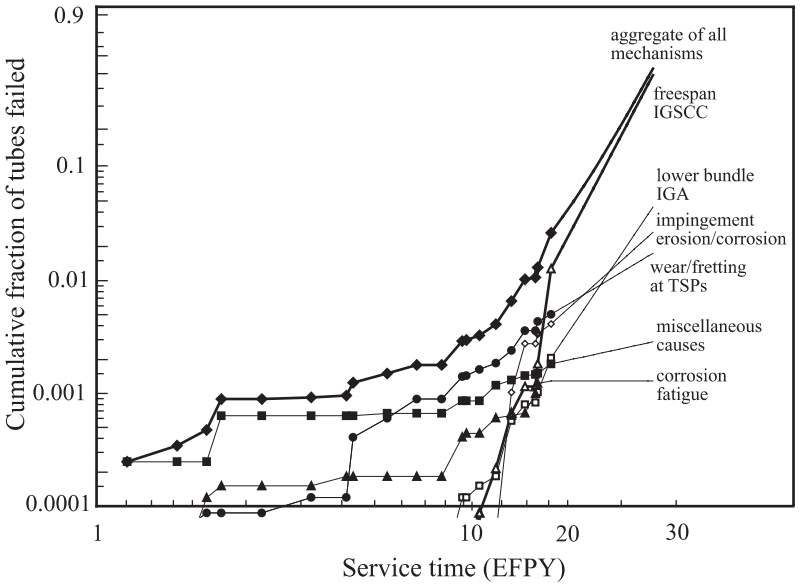

Fig. 15.14. Cumulative fraction of failed steam generator tubes for various modes of degradation of a typical once-through steam generator. Note that freespan IGSCC (*thick line*) did not become measurable until about 10 years, and after 13 years, it accounted for more failures than all other modes combined

phase cannot be overstated. Figure 15.14 shows a plot of the cumulative failure fraction of Inconel alloy 600 (Ni–16Cr–9Fe) steam generator tubes in a typical once-through steam generator as a function of effective full power years (EFPY). Note that cracking on the secondary side (freespan IGSCC) in the hot leg does not appear until about 10 years after startup. Yet, by the 13-year mark, this degradation mode grew to dominate all other failure modes in the steam generator combined. In fact,

the growth rate was so fast that the decision was made to replace the steam generator within two years after this data was accumulated. Clearly, in this case, initiation required considerable time, but once it occurred, propagation of the crack proceeded rapidly.

Cracks may initiate at pre-existing surface flaws, or corrosion processes may create a surface flaw by pitting or localized corrosion, e.g., grain boundary attack or crevice corrosion. However, the conditions under which a crack will propagate are not necessarily the same. Both thermodynamic requirements and kinetic conditions must be met for a crack to initiate or to grow.

Thermodynamics of SCC

The thermodynamic conditions for oxidation-related SCC are that dissolution of the metal in the electrolyte must be thermodynamically possible, and that a protective film, such as an oxide or salt, must be thermodynamically stable and quite insoluble. The tendency for a metal to corrode is given by the Nernst equation, which expresses the electromotive force potential, EMF of a cell in terms of the activities of the products and reactants of the cell:

$$E - E^0 = \frac{-RT}{nF} \ln \frac{a_{\text{product}}}{a_{\text{reactant}}} , \tag{15.1}$$

where E is the equilibrium electrode potential and E^0 is the standard electrode potential, T is the temperature, n is the number of electrons involved in the reaction, F is Faraday's constant and a is the activity. The electrode potential is related to the free energy according to:

$$\Delta G = -nFE . \tag{15.2}$$

Thus, the measure of whether a metal will corrode is whether its actual electrode potential is above or below its equilibrium electrode potential. If the electrode potential is above the equilibrium potential, then the oxidation reaction will proceed. Reactions can be arranged according to their EMF in what is known as the electromotive force series shown in Table 15.1. In this table, reactions are written as reduction reactions that proceed from left to right, with the corresponding standard potential. The noble end of the series contains the "noble" metals, Au and Pt, while the active end contains "active" elements such as K and Na. These reactions are referred to as "half-cell" reactions because they constitute only "half" of the complete reaction involving both anodic and cathodic reactions. However, the table is a convenient tool for comparing the relative position of reactions with respect to a standard scale.

An example of the determination of the EMF of a cell is the corrosion of zinc with the cathodic reduction of hydrogen (or oxygen). The anodic and cathodic reac-

Table 15.1. Standard electromotive force potentials (reduction potentials) (after [11])

	Reaction	Standard potential, E^0 (volts vs. SHE)
Noble	$Au^{3+} + 3e^- = Au$	+1.498
	$Cl_2 + 2e^- = 2Cl^-$	+1.358
	$O_2 + 4H^+ + 4e^- = 2H_2O$ (pH 0)	+1.229
	$Pt^{3+} + 3e^- = Pt$	+1.2
	$O_2 + 2H_2O + 4e^- = 4OH^-$ (pH 7)	+0.82
	$Ag^+ + e^- = Ag$	+0.799
	$Hg_2^{2+} + 4e^- = 2Hg$	+0.788
	$Fe^{3+} + e^- = Fe^{2+}$	+0.771
	$O_2 + 2H_2O + 4e^- = 4OH^-$ (pH 14)	+0.401
	$Cu^{2+} + 2e^- = Cu$	+0.337
	$Sn^4 + 2e^- = Sn^{2+}$	+0.15
	$2H^+ + 2e^- = H_2$	0.000
	$Pb^{2+} + 2e^- = Pb$	−0.126
	$Sn^{2+} + 2e^- = Sn$	−0.136
	$Ni^{2+} + 2e^- = Ni$	−0.250
	$Co^{2+} + 2e^- = Co$	−0.277
	$Cd^{2+} + 2e^- = Cd$	−0.403
	$Fe^{2+} + 2e^- = Fe$	−0.440
	$Cr^{3+} + 3e^- = Cr$	−0.744
	$Zn^{2+} + 2e^- = Zn$	−0.763
	$2H_2O + 2e^- = H_2 + 2OH^-$	−0.828
	$Al^{3+} + 3e^- = Al$	−1.662
	$Mg^{2+} + 2e^- = Mg$	−2.363
	$Na^+ + e^- = Na$	−2.714
Active	$K^+ + e^- = K$	−2.925

tions and the total reactions are written as:

Anodic: $Zn \rightarrow Zn^{2+} + 2e^-$
Cathodic: $2H^+ + 2e^- \rightarrow H_2$ (or $O_2 + 4H^+ + 4e^- \rightarrow 2H_2O$)
Total: $Zn + 2H^+ \rightarrow Zn^{2+} + H_2(g)$

The equilibrium electrode potentials and cell potentials corresponding to the reactions are then written according to Eq. (15.1) as:

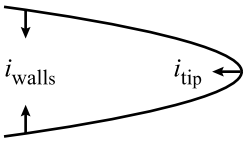

Fig. 15.15. Schematic illustration showing corrosion current from the walls and the tip of a crack

$$E_{\text{Zn}} = E^0_{\text{Zn}} - \frac{0.0257}{2} \ln \frac{a_{\text{Zn}^{2+}}}{a_{\text{Zn}}}, \quad a_{\text{Zn}} = 1 \,,$$

$$E_{\text{H}_2} = E^0_{\text{H}_2} - \frac{0.0257}{2} \ln \frac{p_{\text{H}_2}}{a^2_{\text{H}^+}} \,,$$

$$\begin{aligned} E_{\text{cell}} &= E_{\text{Zn}} + E_{\text{H}_2} \\ &= E^0_{\text{Zn}} + E^0_{\text{H}_2} - \frac{0.0257}{2} \ln a_{\text{Zn}^{2+}} + 0.0257 pH - \frac{0.0257}{2} \ln p_{\text{H}_2} \,. \end{aligned}$$

Hence, the cell potential for the total reaction is a function of the pH, the activity of Zn^{2+} ions and the hydrogen gas pressure.

Without oxidation or anodic dissolution, cracks would not advance. The occurrence of simultaneous film formation and oxidation during stress corrosion crack growth can be understood from Fig. 15.15, which shows a crack in which dissolution is occurring at both the crack tip and crack walls. The ratio of anodic currents from the walls relative to the crack tip is the critical parameter. The ratio $i_{\text{walls}}/i_{\text{tip}}$ must be $\ll 1$ for a crack to propagate, otherwise the crack will blunt.

Figure 15.16 shows a polarization curve for an active-passive alloy. Note that there are two zones where SCC is most likely to occur. In zone 1, the alloy is in the active-to-passive film transition so that the simultaneous condition for film formation on crack walls and corrosion at the crack tip are met. In zone 2, similar conditions are met with the added factor that these potentials are above the pitting potential and cracks can initiate from pits. Practically, IGSCC can occur over the entire range between and including zones 1 and 2 because chemical inhomogeneities at the grain boundary produce a different electrochemical response relative to the bulk material.

Pourbaix Diagrams

The domains of stability of the various forms of a metal; metallic state, metal ions, oxides, etc., can be represented by a graphical representation known as the stability or Pourbaix diagram after Marcel Pourbaix [14]. The diagram is based on thermodynamic computations for a number of selected chemical species and the equilibria between them. It is possible to predict from a potential-pH diagram if a metal will corrode or not. It is *not* possible to determine how long a metal will last or how fast it will corrode. Figure 15.17a shows the Pourbaix diagram for iron in water at 25 °C where the ionic activities are set at 10^{-6}. The stability diagram is analogous to the equilibrium phase diagram, Fig. 15.17b, in that it portrays phase equilibria between metal, metal ions and metal oxide in aqueous solutions. In these diagrams, horizontal lines represent pure charge transfer reactions involving only electrons and the

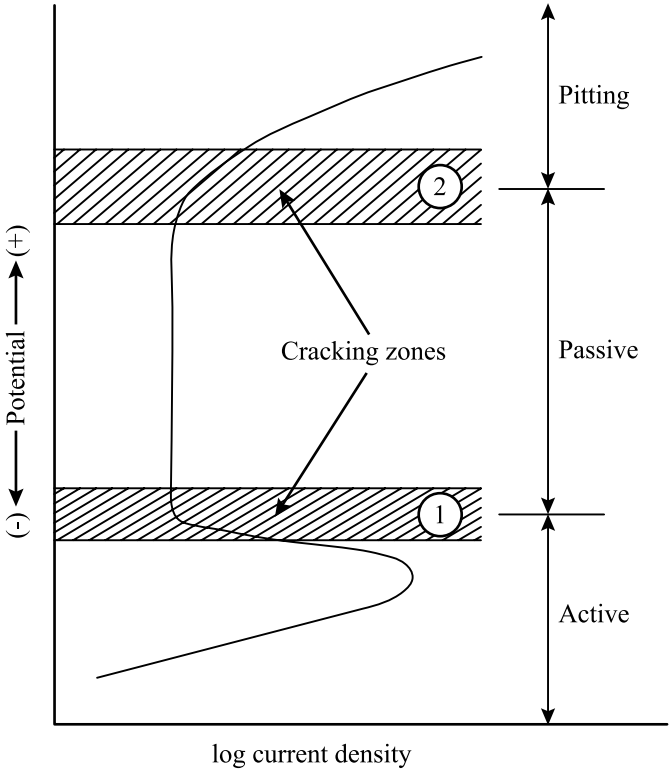

Fig. 15.16. Schematic anodic polarization curve showing the potential ranges over which susceptibility to stress corrosion cracking occurs (from [13])

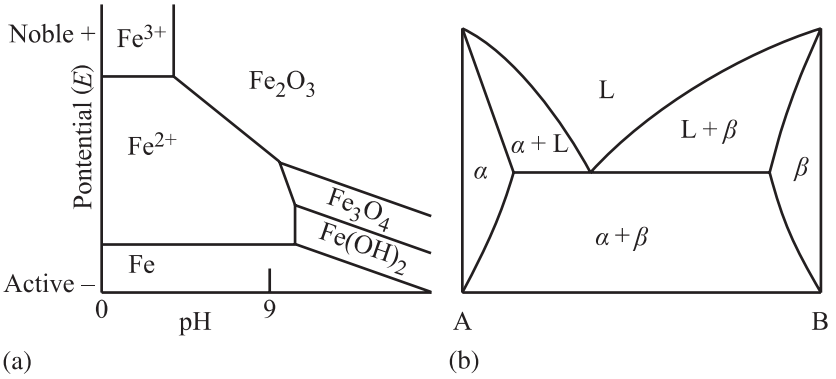

Fig. 15.17. Comparison of (a) a Pourbaix diagram with (b) a phase diagram. Both diagrams describe regions in which the various phases are thermodynamically stable

reduced and oxidized species, but not protons. Hence, they are not influenced by pH. Vertical lines represent acid-base reactions where there is no charge transfer, hence they are independent of potential. Reactions involving both electron transfer and protons are indicated by sloping lines.

An overlay of the regimes in which SCC occurs on the Pourbaix diagram will identify the phases that correlate with cracking. Figure 15.18 shows a Pourbaix diagram for nickel and iron in 300℃ water in which SCC is associated with potentials and pHs that follow the Ni/NiO stability line. The effect of many environmental parameters such as pH, oxygen concentration and temperature on the thermodynamic conditions for SCC can be related to their effect on the potential-pH diagram. For materials in which SCC occurs by a hydrogen-induced subcritical crack growth mechanism, the thermodynamic requirement for crack growth is governed by the hydrogen reduction line (a). The range of potentials at which H is available to cause crack growth increases and becomes more oxidizing with decreasing pH. However, the potential and pH at the tip of a crack can differ substantially from that at the free surface due to production, reaction and diffusion of oxygen or metal ions within the crack. These processes result in a drop in the potential and a shift in the pH. In acidic environments, the anodic and cathodic reactions are:

Anodic: $M \rightarrow M^{2+} + 2e^-$
Cathodic: $O_2 + 4H^+ + 4e^- \rightarrow 2H_2O$

The consumption of H^+ causes an increase in the pH. In basic environments, the anodic and cathodic reactions are:

Anodic: $M \rightarrow M^{2+} + 2e^-$
Cathodic: $O_2 + 2H_2O + 4e^- \rightarrow 4OH^-$

But due to metal hydrolysis in a basic electrolyte, we have $M^{2+} + 2H_2O \rightarrow M(OH)_2 + 2H^+$ and the pH decreases. In both cases, increased resistance in the crack or crevice due to gas bubbles, for example, leads to an ohmic drop causing a decrease in potential at the tip of the crack relative to the sample surface by up to several hundred millivolts. The result of these processes is shown in Fig. 15.19 for aerated water in which the crack tip condition is driven to a lower potential and an intermediate pH, both of which are considerably different than those at the sample surface.

Kinetics of SCC

As in the thermodynamic conditions for SCC, environmental parameters such as potential, pH, oxygen concentration and temperature along with crack geometry and crack tip chemistry strongly affect crack growth kinetics. The rate of corrosion, or the corrosion current is given by $i_{corr} = i_a = i_c$, where i_a is the anodic current and i_c is the cathodic current. That is, due to charge conservation, the rate of anodic oxidation must equal the cathodic rate of reduction. The anodic and cathodic currents are equal

in magnitude at a potential known as the corrosion potential E_{corr}. The corrosion rates are related to the corrosion potential through:

$$i_{\mathrm{a}} = i_0 \mathrm{e}^{(1-\beta)\eta F/RT}, \quad i_{\mathrm{c}} = i_0 \mathrm{e}^{-\beta\eta F/RT}, \tag{15.3}$$

where i_0 is the exchange current density, β is a symmetry factor, and η is the overpotential defined by $\eta = E_{\mathrm{corr}} - E$, where E is the equilibrium potential for the cathodic or anodic reactions. Hence, Eq. (15.3) shows that the anodic and cathodic currents are driven by the difference between the corrosion potential and the equilibrium potentials.

For the case of a crack growing by anodic dissolution alone, the total crack advance is a function of the total anodic charge transfer (integral of current over time) at the crack tip, and therefore, the crack velocity is a function of the average crack tip current density. A limiting velocity can be described for a crack advancing under pure anodic dissolution by the following Faradaic relationship:

$$\dot{a} = \frac{\mathrm{d}a}{\mathrm{d}t} = \frac{i_{\mathrm{a}} M}{nF\rho}, \tag{15.4}$$

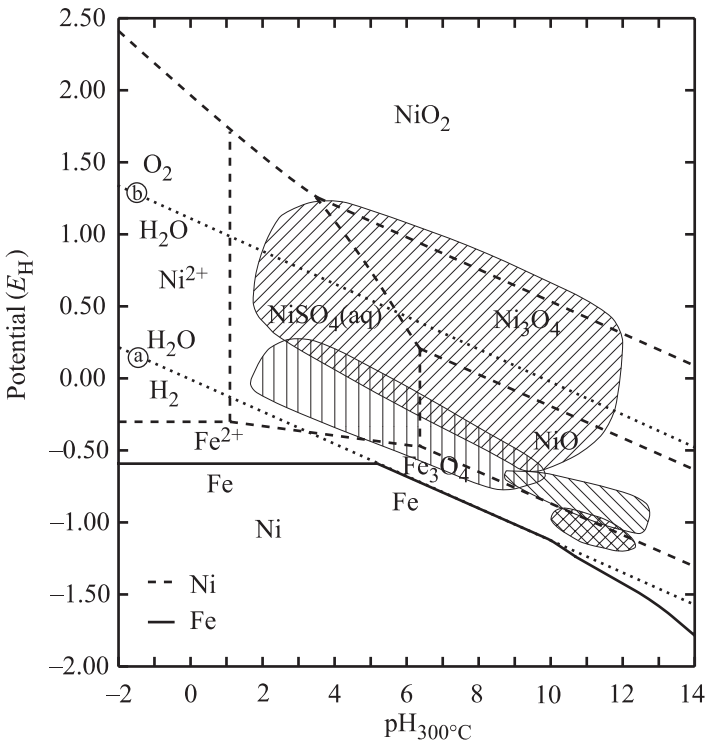

Fig. 15.18. Various SCC submodes as a function of potential and pH plotted over the Ni and Fe stability diagrams at 300 °C (from [15])

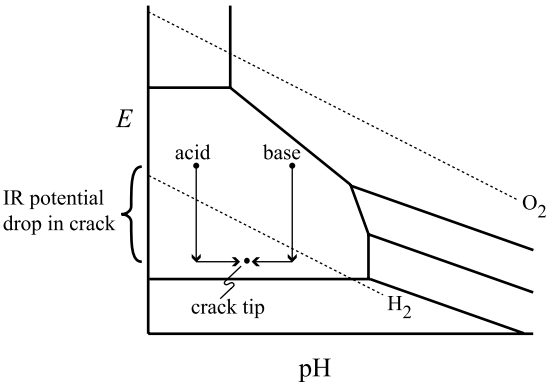

Fig. 15.19. Schematic Pourbaix diagram showing the change in potential and pH of basic and acidic bulk solutions vs. the crack tip

where i_a is the anodic current density of a bare surface, M is the atomic weight, n is the valence, F is Faraday's constant and ρ is the density. Equation (15.4) assumes that the crack tip is maintained in a bare condition while the crack walls are relatively inactive (to prevent blunting). A number of factors can reduce crack velocity, principle among them is the formation of a film which covers the crack tip. Other factors that can limit crack velocity are:

- Limits on diffusion of species into or out of the crack
- Crack growth away from the principal stress
- Changes in local alloy chemistry
- Corrosion of the crack walls

15.1.5 Mechanisms of Stress Corrosion Cracking

By virtue of its nature, stress corrosion cracking refers to a chemical or electrochemical process involving oxidation and reduction reactions where the thermodynamic tendency is described by the Nernst equation. Under certain conditions, these reactions can manifest themselves in the form of a stress corrosion crack. The mechanisms by which these cracks form and propagate is not completely agreed upon. The leading theories are active path SCC and the film rupture model.

Active Path SCC

Active path SCC was first proposed in the 1940s to explain rapid grain boundary attack, and is based on the establishment of galvanic cells between the base metal and anodic paths set up by heterogeneous phases (or segregated elements) along grain boundaries or slip planes. Active path SCC also refers to preferential dissolution of a phase in the alloy. The applied stress ruptures oxide films and exposes fresh metal to dissolution. The idea behind this theory is that preferred dissolution occurs at slip planes due to the increased number of preferred sites. Plastic

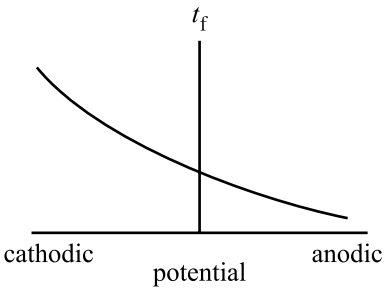

Fig. 15.20. Behavior of time to failure for an active path stress corrosion cracking mechanism

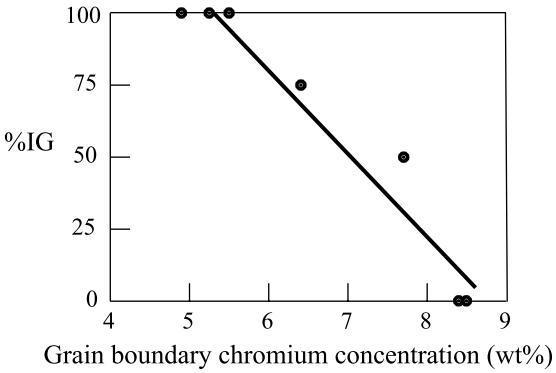

Fig. 15.21. Percent IG fracture vs. grain boundary chromium concentration for Ni–16Cr–9Fe stressed in 0.017 M $Na_2S_4O_6$ at 25 °C (from [16])

deformation is essentially "feeding" bare material to the electrolyte for consumption with the net effect being an increase in the exchange current density, and hence, the rate of corrosion. Active path SCC should follow a time-to-failure dependence on current described by the plot in Fig. 15.20. However, electrochemical dissolution at a crack tip will tend to blunt the crack rather than contribute to its advance. So active path SCC is not a plausible explanation for observed stress corrosion cracks.

It should be noted, however, that active path corrosion can contribute to intergranular separation. The intergranular fracture of Ni–Cr–Fe alloys in sodium tetrathionate, $Na_2S_4O_6$ (pH $\sim 3-4$), depends strongly on the grain boundary chromium level (Fig. 15.21). Cracking is believed to occur by stress-assisted intergranular attack in which the role of stress is to open the crack tip for access by the bulk solution, which then causes preferential dissolution along the grain boundary. This is an example of a stress-assisted anodic dissolution-driven process and is not based on film rupture.

Film Rupture Model

The corrosion resistance of most alloys is attributed to the passive film on the surface. When sufficient stress is applied, the film is ruptured or damaged by shear stresses on properly oriented glide planes (Fig. 15.22). But SCC susceptibility depends on the nature of slip. In alloys with high stacking fault energy (SFE) the

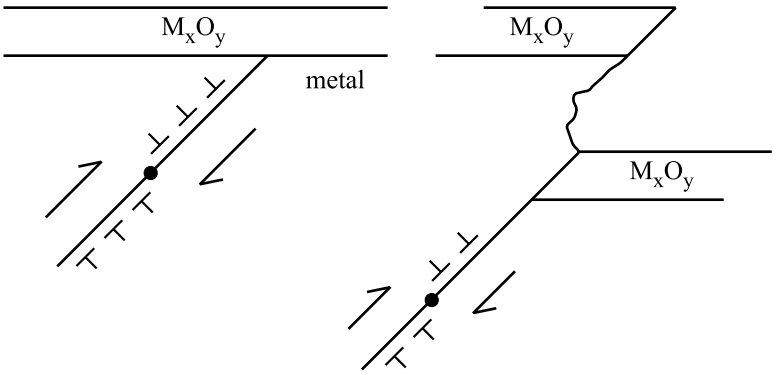

Fig. 15.22. Schematic illustration of the process by which slip can cause rupture of an oxide film, leading to accelerated corrosion before re-passivation

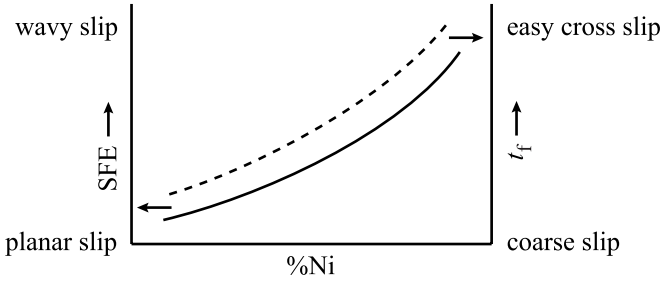

Fig. 15.23. Dependence of stacking fault energy (which determines the slip character) and time to failure on the nickel content in an austenitic, Fe–Cr–Ni alloy

separation of total dislocations into partials is unlikely. Since partials must recombine in order to cross slip, high SFE alloys exhibit easy cross slip while low SFE alloys do not exhibit cross slip. As a result, low SFE alloys exhibit planar slip in which the deformation occurs on relatively few slip planes and is characterized by regularly spaced slip bands, not unlike the morphology of dislocation channels discussed in Chap. 12. Figure 15.23 shows the effect of Ni content in austenitic alloys on the SFE and time-to-failure along with the role of the nature of slip. Low SFE alloys (low Ni content) exhibit coarse or *planar* slip and low time-to-failure, while high SFE alloys (higher Ni content) can cross slip exhibiting *wavy* slip and a longer time-to-failure.

Re-passivation of the exposed surface will likely occur, but the rate of re-passivation will control the rate of crack propagation. If re-passivation occurs too quickly, the corrosion attack causes only a very small increment of crack growth. If re-passivation occurs too slowly, corrosion blunts the crack tip. Hence, there is an intermediate rate at which corrosion occurs to maximize growth crack without blunting it. Figure 15.24 shows how the rate of re-passivation at a potential, E_1 can vary with the environment. Chloride ions are effective in slowing re-passivation. So

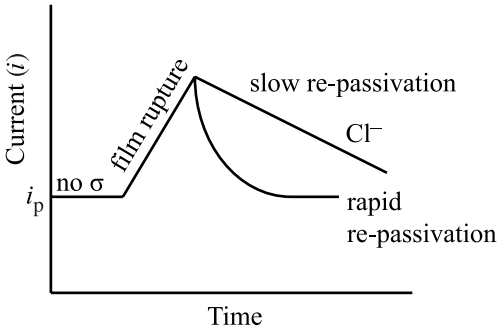

Fig. 15.24. Behavior of the corrosion current in a re-passivation test in which an applied stress results in film rupture and re-passivation. Aggressive species in the solution can cause slow re-passivation, allowing for a greater amount of corrosion

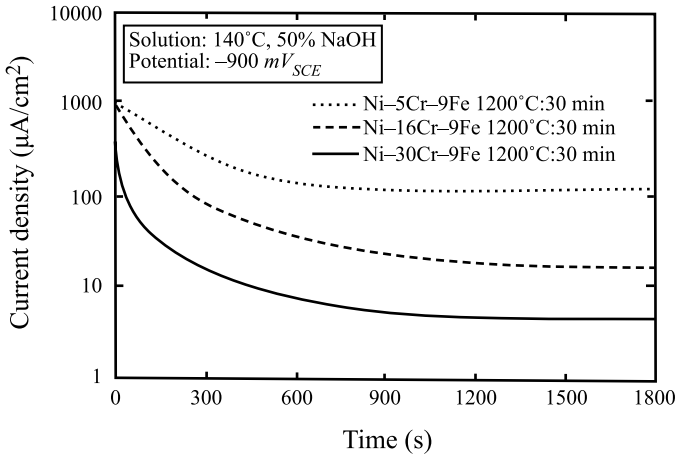

Fig. 15.25. Current decay, or re-passivation rate of Ni–Cr–Fe alloys as a function of chromium content, showing that re-passivation occurs much more quickly with higher alloy chromium contents (from [17])

while SCC of stainless steels does not occur in sulfuric acid at room temperature, the addition of Cl^- to sulfuric acid induces susceptibility to SCC, presumably by reducing the re-passivation rate. In fact, alloy composition can strongly affect re-passivation rate as well. Figure 15.25 shows that increasing Cr in a Ni–Cr–Fe alloy substantially increases the re-passivation rate, which leads to a reduction in the SCC susceptibility.

15.1.6 Predictive Model for Crack Propagation

Structural components manufactured from stainless steels, nickel-base alloys and ferritic steels are all susceptible to environmentally assisted cracking in light water reactor environments. The phenomenology of cracking in these environments is well-recognized in terms of the effect that various material, stress and environmental parameters have on the cracking susceptibility. For these systems, Ford and

Andresen [7, 8, 9, 18] have developed a working hypothesis for the cracking mechanism that is based on the slip oxidation/film rupture model and the relevant crack tip environment. In this model, crack advance is related to the oxidation reactions that occur at the crack tip as the protective film is ruptured by increasing strain in the underlying matrix. Rupture events occur with a periodicity, t_f, which is determined by the fracture strain of the oxide and the strain rate at the crack tip. The extent of crack advance is related (by Faraday's law) to the oxidation charge density associated with dissolution and oxide growth (passivation) on the bare metal surface, similar to that described by Eq. (15.4):

$$\dot{a} = \frac{M}{nF\rho}\frac{Q_f}{t_f}\,, \tag{15.5}$$

where

$$t_f = \frac{\varepsilon_f}{\dot{\varepsilon}_{ct}}\,, \tag{15.6}$$

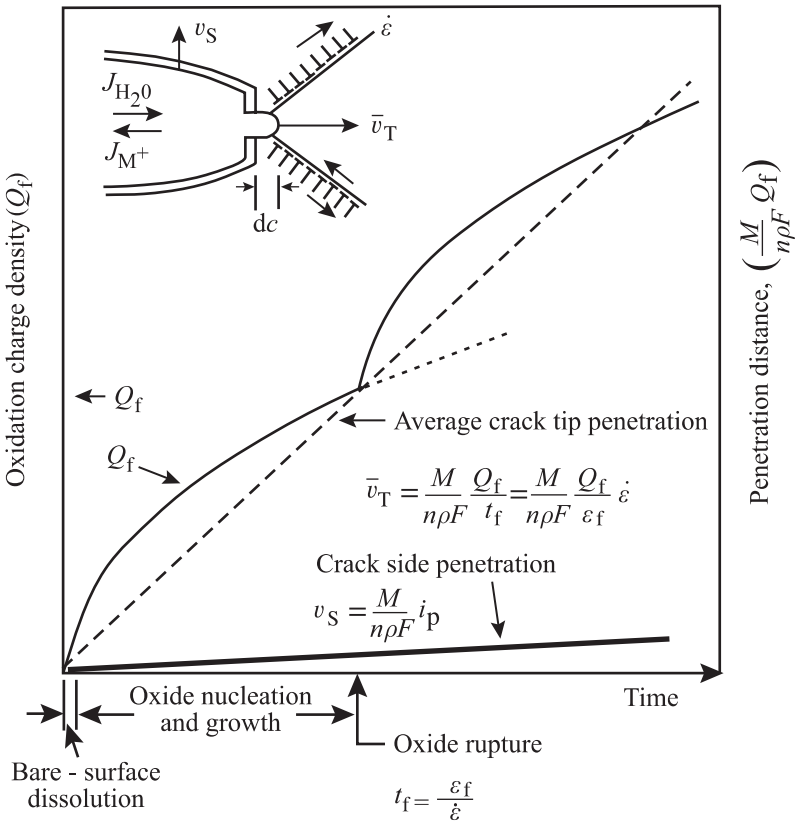

Fig. 15.26. Schematic of the oxidation charge density vs. time relationship for a strained crack tip and unstrained crack sides obeying the film rupture model (from [18])

giving the average crack velocity in terms of the crack tip strain rate:

$$\bar{v}_{\mathrm{T}} = \dot{a} = \frac{M}{nF\rho}\frac{Q_{\mathrm{f}}}{\varepsilon_{\mathrm{f}}}\dot{\varepsilon}_{\mathrm{ct}}\,, \tag{15.7}$$

where Q_{f} is the charge transfer at fracture, ε_{f} is the fracture strain and $\dot{\varepsilon}_{\mathrm{ct}}$ is the crack tip strain rate. The oxidation charge density and crack penetration rate are shown as a function of time in the schematic diagram of Fig. 15.26. Note that the oxidation charge density varies in a parabolic fashion with time according to a solid state oxidation model [19], and the velocity of crack propagation is an average over time. The reactions at the crack tip vary with time in a complex manner for different environments and material chemistries, and the resultant average crack growth rate, $\bar{v}_{\mathrm{T}}$, is re-stated in a general form:

$$\bar{v}_{\mathrm{T}} = \frac{M}{nF\rho}\frac{i_{\mathrm{a}}t_0^{\mathrm{m}}}{(1-m)\varepsilon_{\mathrm{f}}^{\mathrm{m}}}\dot{\varepsilon}_{\mathrm{ct}}^{\mathrm{m}} \tag{15.8}$$

$$= f(m)\dot{\varepsilon}_{\mathrm{ct}}^{\mathrm{m}}\,, \tag{15.9}$$

where $\dot{\varepsilon}_{\mathrm{ct}}$ is the strain rate at the crack tip and embodies the mechanical contributions to cracking, i_{a} is the bare surface dissolution current, and t_0 and m are re-passivation parameters that represent the effects of the environment and material chemistries on environmentally assisted crack growth.

The model is composed of three primary conceptual and predictive elements: (1) the rate of film rupture (proportional to the crack tip strain rate), (2) the solution chemistry at the crack tip, and (3) the resultant kinetics of oxidation/re-passivation in the crack tip environment following a film rupture event. Most of the parameters that comprise the water and material chemistry effects distill into a single parameter, m, that represents the slope of the re-passivation current on a log-log plot. The crack tip strain rate formulations then permit the calculation of the frequency of film rupture *events* and in turn, the prediction of the environmental crack growth rate over a continuum of loading, water and material characteristics. For example, the function, f in Eq. (15.8) may be of the form, $f(m) \sim Am^{3.6}$, where m is a function of water chemistry and material chemistry and is an indicator of the level of susceptibility, where $m \to 0.3$ for high susceptibility and $m \to 1$ for low susceptibility. The crack tip strain rate is a function of the stress intensity of the crack tip and may be expressed in the form $\dot{\varepsilon}_{\mathrm{ct}} = BK^4$. So the crack growth rate is then:

$$\bar{v}_{\mathrm{T}} = Am^{3.6}(BK^4)^{\mathrm{m}}\,. \tag{15.10}$$

15.1.7 Mechanical Fracture Models

Cracks can also occur as a result of corrosion reactions, but when their behavior is driven by the stress rather than corrosion reactions, they are considered to fail by mechanical fracture. Several models exist to explain cracking by mechanical fracture processes.

Under certain conditions, a fine array of corrosion-induced tunnels are observed at the point where slip steps emerge on the sample surface. The tunnels grow in diameter and length until stress in the remaining ligaments rises to the point where the load can no longer be sustained with the reduced cross section and fracture occurs by overload. According to the *corrosion tunnel model*, cracks propagate by alternate tunnel growth and ductile fracture. Cracks propagating by this mechanism should result in grooved fracture surfaces with evidence of microvoid coalescence. That this morphology is generally not observed suggests that the application of a tensile stress results in thin, flat slots instead of tunnels. This morphology is very consistent with transgranular SCC fracture morphology.

Based on fractographic studies, it was concluded that cleavage fracture is not an atomically brittle process, but occurs by alternate slip at the crack tip in conjunction with formation of very small voids ahead of the crack. It was also proposed that chemisorption of environmental species facilitated the nucleation of dislocations at the crack tip, promoting shear processes responsible for brittle cleavage-like fracture. The *adsorption-enhanced plasticity* mechanism relies on adsorption of aggressive species to promote cleavage fracture.

In the *tarnish rupture* model, a brittle surface forms on the metal and fractures under an applied stress. Fracture exposes bare metal, which rapidly reacts with the environment to re-form the film. The crack propagates by successive cycles of film growth and fracture. Assuming that the film penetrates along the grain boundary ahead of the crack tip, the model has been applied to intergranular cracking. The key feature of this mechanism is that fracture occurs entirely within the oxide film and not in the metal.

The *film-induced cleavage* mechanism holds that a thin surface film or layer forms on the surface, followed by the formation of a brittle crack in the layer. The crack crosses the film-matrix interface without loss of velocity and continues to propagate in the ductile matrix along a particular crystallographic direction. The crack eventually blunts and arrests and the cycle then repeats. This model can also explain crack arrest markings, cleavage-like facets on the fracture surface and the discontinuous nature of crack propagation. The assumption that a brittle crack continues to propagate in a ductile matrix can be justified if the crack is sharp and propagates at high velocities.

First proposed by Uhlig, the *adsorption*(*stress-sorption*) mechanism is related to the Griffith criterion for crack formation in glass and other brittle solids. It holds that adsorption of a species of any kind that reduces surface energy should favor crack formation. Recalling the expression for fracture stress, σ_f from Chap. 13:

$$\sigma_f = \left(\frac{2E\gamma}{\pi c}\right)^{1/2}, \tag{15.11}$$

where E is Young's modulus, γ is the surface energy and $2c$ is the crack length, then a reduction in the surface energy, e.g., as might occur by adsorption of Cl^- on a stainless steel surface, results in a lowering in the stress required for fracture. Unfortunately, the plausibility of this model is hard to establish because of the difficulty of determining the energy in the environment.

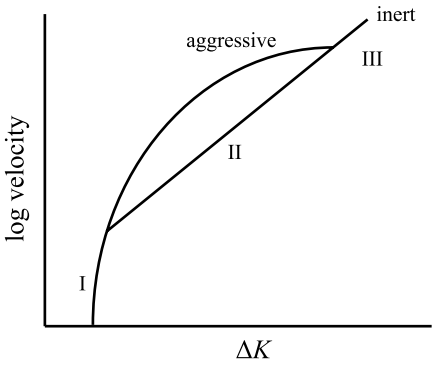

Fig. 15.27. Effect of an aggressive environment on the behavior of crack velocity with ΔK in a corrosion fatigue test

15.1.8 Corrosion Fatigue

Damage by corrosion fatigue is a conjoint action of corrosion and fatigue that is greater than that caused by the sum of both processes acting separately. In air, fatigue proceeds by localized slip within grains of the metal caused by alternating stress, resulting in slip steps at the metal surface. Adsorption of air on the exposed metal surfaces prevents re-welding on the reverse cycle (slip irreversibility). Continued application of stress produces protrusions above the metal surface (extrusions) and intrusions below. Corrosion accelerates plastic deformation by the formation of surface lattice vacancies, in particular, di-vacancies that rapidly diffuse into the metal at room temperature and accelerate plastic deformation by facilitating dislocation climb. The higher the rate of corrosion, the greater is the availability of di-vacancies and the more pronounced is the formation of intrusions and extrusions. Lower frequencies produce greater degradation since more time is available per cycle for corrosion to occur. Figure 15.27 shows that the effect of the environment is greatest at intermediate values of ΔK.

15.1.9 Hydrogen Embrittlement

Hydrogen embrittlement is caused by the entry of hydrogen into the alloy by the corrosion process, cathodic protection or high hydrogen overpressures. A common characteristic of hydrogen cracking is a specific delay in time for appearance of cracks after stress is applied. This is due to the time required for hydrogen to diffuse to a specific area near a crack nucleus and reach a critical concentration. Hydrogen embrittlement usually results in intergranular fracture and tends to be greatest at low strain rates.

There are several mechanisms by which hydrogen is believed to cause embrittlement. The *decohesion mechanism* holds that atomic hydrogen lowers or reduces the metal-metal bond strength. The *pressure theory* is based on precipitation of hydrogen as a gas at internal defects. The pressure developed by precipitation is added to the applied stress to lower the apparent fracture stress. Blisters can form if the process occurs close enough to the surface to deform the thin layer of metal above it.

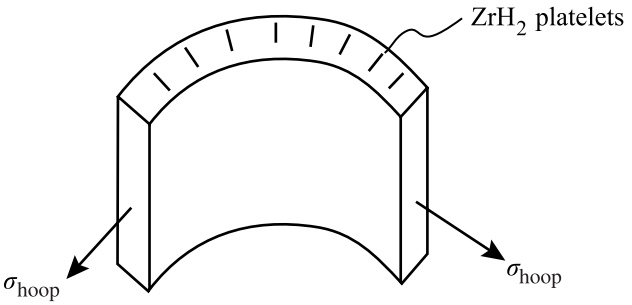

Fig. 15.28. Orientation of ZrH_2 platelets in Zircaloy fuel cladding under the application of a hoop stress

A variation of the pressure theory is the *hydrogen attack* mechanism, which is due to the reaction between hydrogen and carbon to form methane. In addition to the formation of high pressure methane gas bubbles, the reaction causes de-carburization and a weakening of the metal. Uhlig proposed that *direct adsorption* of hydrogen reduces the surface energy required to form a crack, thus lowering the fracture stress. The formation of a brittle *hydride* phase, e.g., ZrH_2 or TiH_2, can also induce embrittlement of the metal. The specific volume of the hydride is greater than the metal from which it came. Combined with the plate-like morphology of the hydride, the metal at the edge of the hydride platelet experiences a high tensile stress if the applied stress is perpendicular to the plane of the platelet. In zirconium alloys, platelets form on basal planes that are aligned in the radial direction of fuel cladding, causing a high tensile stress in the metal at the edges of the platelet due to the pressure in the cladding (Fig. 15.28). Hydrogen also interacts with dislocations. A high hydrogen fugacity at the metal surface and along grain boundaries can induce plasticity by activation of dislocation sources. The chemical driving force is responsible for the formation of dislocations, which then spread additional hydrogen into the lattice and exert a large stress intensity factor at the crack tip. This *hydrogen-induced localized plasticity* (HELP) mechanism can explain high temperature effects of hydrogen. Hydrogen-induced cracking is an important mechanism in ferritic steels, nickel-base alloys and titanium and aluminum alloys.

15.2 Effects of Irradiation on Water Chemistry

15.2.1 Radiolysis and its Effect on Corrosion Potential

It is widely acknowledged that SCC susceptibility is fundamentally influenced by the corrosion potential [1, 7, 20, 21]. In this regard, what distinguishes BWRs from PWRs is the low H_2 concentration in BWRs, which permits the radiolytic formation of oxidants. Above $\approx 500\,\text{ppb}$ ($5.6\,\text{cc/kg}$) H_2, radiolytic formation of oxidants is effectively suppressed and the corrosion potential remains close to its thermodynamic minimum (which is a function of temperature, H_2 fugacity, and pH). BWRs cannot

achieve this H_2 level because H_2 partitions to the steam phase, which begins to form about a quarter of the way up the fuel rods. Thus, radiolysis has a greater impact on BWRs, and is the focus of this section.

Water is decomposed by ionizing radiation into various primary species [22, 23, 24, 25] including both radicals (e.g., e^-_{aq}, H, OH, HO_2) and molecules (e.g., H_2O_2, H_2, O_2), which can be oxidizing (e.g., O_2, H_2O_2, HO_2) or reducing (e.g., e^-_{aq}, H, H_2). The predominant species that are stable for more than a few seconds are H_2O_2 and H_2, with O_2 forming primarily from the decomposition of H_2O_2. Because H_2 partitions to the steam phase and H_2O_2 is not volatile, the re-circulated water in a BWR ($\approx$ 87% of the total water flow) is oxidant-rich. The concentrations of radiolytic species are roughly proportional to the square root of the radiation flux in pure water. The radiation energy-intensity spectrum influences the concentration of each radiolytic specie, which is described in terms of a yield, or G value (molecules produced per 100 eV absorbed by water). In LWRs, the G values for most species are within a factor of ≈ 3 for fast neutron vs. gamma radiation. Despite this similarity, the influence of fast neutron radiation is much stronger than gamma radiation primarily because the energy deposition rate, or mean linear energy transfer (LET), is greater (40 eV/nm for fast neutrons vs. 0.01 eV/nm for gamma radiation [25]). Also, the neutron flux in LWRs (e.g., $\approx 1.03 \times 10^9$ Rad/h core average and $\approx 1.68 \times 10^9$ Rad/h peak in a BWR4 of 51 W/cc power density) is also higher than the gamma flux ($\approx 0.34 \times 10^9$ Rad/h) [5]. In fact, the moderate gamma levels present in the downcomer in the outside annulus of a BWR core actually promote recombination of hydrogen and various oxidants [23, 26]. Overall, the contribution of thermal neutrons and beta particles to radiolysis is small in LWRs.

As in many electrochemical processes, the integrated effects of various oxidants and reductants on environmental cracking is best described via changes in corrosion potential, which controls the thermodynamics and influences the kinetics of most reactions. Since electrochemical potentials are logarithmically dependent on local oxidant, reductant, and ionic concentrations via the Nernst relationship, Eq. (15.1), radiation-induced increases in concentrations of various species by many orders of magnitude may have comparatively small effects on the corrosion potential in hot water. Further, corrosion potentials are mixed potentials involving a balance of anodic and cathodic reactions on the metal surface, which depend on the concentrations of both oxidizing and reducing species. At low oxidant concentrations, low corrosion potentials of $\approx -0.5 V_{SHE}$ result from mass transport-limited kinetics (e.g., oxygen transport to the metal surface). In this regime, more pronounced shifts in corrosion potential with radiation can occur, presumably from the radiolytic formation of oxidizing species within the mass transport-limited stagnant layer.

The relationship between dissolved oxygen and corrosion potential in hot water as a function of radiation type and flux is shown in Fig. 15.29, in which the connected points represent data obtained in controlled, radiation on/off experiments. The curves in Fig. 15.29 represent the scatter band for the data obtained under unirradiated conditions. Similar scatter also exists in the irradiated corrosion potential

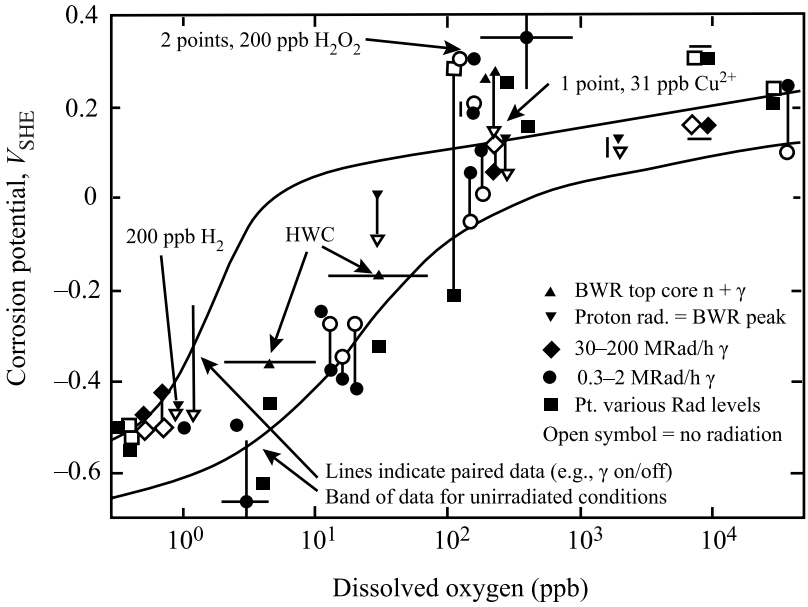

Fig. 15.29. Effect of radiation on the corrosion potential of type 304 stainless steel in 288 °C water. The curves denote the range of typical values in the unirradiated corrosion potential data (from [1])

data in Fig. 15.29 and is comprised of contributions from both real effects and experimental error. Figure 15.29 shows that little, if any, elevation in corrosion potential results from irradiation sources which do not include neutrons or simulate their contribution (e.g., using high-energy protons). Some studies using gamma radiation [1, 20] showed a significant decrease in corrosion potential, especially in the intermediate (e.g., 10 to 200 ppb) range of dissolved oxygen. This is consistent with enhanced recombination of oxidizing and reducing species, which occurs in the downcomer region of BWRs [26] and is relied upon to produce SCC mitigation using *hydrogen water chemistry* (HWC).

In instances where neutrons or protons have been used, a consistent, significant elevation in corrosion potential is observed. It is more pronounced in hot water containing low dissolved oxygen concentrations and no dissolved hydrogen where increases of over +0.25 V occur. At higher inlet oxygen concentrations (e.g., ≈ 200 ppb), the data still show a significant shift (typically +0.1 to 0.15 V) in corrosion potential for radiation conditions representative of peak LWR core fluxes; less increase is observed for inlet oxygen concentrations associated, e.g., with air saturation (≈ 8.8 ppm O_2) or oxygen saturation (≈ 42 ppm O_2 at STP). A similar elevation in corrosion potential is observed for additions of hydrogen peroxide (200 ppb H_2O_2, Fig. 15.29), which suggests that H_2O_2 may be a major factor in increasing the corrosion potential under irradiated conditions.

In-core, in situ measurements in BWRs show that the corrosion potential, which is $\approx +0.2$ to $+0.25 V_{SHE}$ in normal water chemistry, can be decreased by > 0.5 V by sufficient additions of dissolved hydrogen in a BWR [27]. This is corroborated by other measurements [28], which show very little radiation-induced elevation in corrosion potential when the fully de-aerated inlet water contains moderate dissolved hydrogen (> 200 ppb H_2, 0 ppb O_2). However, at high H_2 levels, the core becomes reducing, and the small concentration of ^{16}N (transmuted from ^{16}O) changes from soluble NO_3^- to volatile NO_x and NH_3, causing a large increase in radiation level in the steam lines and turbine.

The effect of radiation on the corrosion potential within a crack or crevice is also of interest, with the possibility that a net oxidizing environment in the crack could be created that could elevate the corrosion potential above the potential at the crack mouth. In the absence of radiation, measurements in high-temperature water in artificial crevices (e.g., tubing), at the tip of growing cracks, and of short crack growth behavior show that the corrosion potential remains low (i.e., $-0.5 \pm 0.1 V_{SHE}$ in 288 °C pure water) for all bulk oxygen concentrations, indicating that complete oxygen consumption occurs within the crack, as discussed in Sect. 15.1.4 on page 779. Recent measurements of radiation effects in crevices show that the elevation in corrosion potential is limited to < 0.05 V in-core; this is consistent with the interpretation of available corrosion potential data on free surfaces [1, 7, 20, 29]. These small changes will not significantly affect the ≈ 0.75 V ($+0.25 V_{SHE}$ (near mouth) minus $-0.5 V_{SHE}$ (in crack)) potential difference in the crack under irradiated normal BWR water chemistry conditions. The potential difference, along with other factors, controls the enhancement mechanism that can lead to an increased anion activity and altered pH at the crack tip [8, 9, 21].

15.2.2 Effect of Corrosion Potential on IASCC

Laboratory tests have been conducted on pre-irradiated alloys using slow strain rate testing (SSRT) in hot water with addition of oxygen and/or hydrogen peroxide to elevate the corrosion potential to simulate the effect of radiation. Tests by Jacobs et al. [30] on stainless steel irradiated to $\approx 3 \times 10^{21}$ n/cm^2 showed a strong effect of dissolved oxygen (and, by inference, corrosion potential) on IASCC (Fig. 15.30a). Similarly, Ljungberg [31] showed a strong effect of corrosion potential on crack growth rate (Fig. 15.30b). Since the corrosion potential is a sensitive function of oxygen content, increasing oxygen content results in elevated corrosion potential and higher crack growth rates.

In situ data on fracture mechanics specimens of furnace sensitized type 304 stainless steel exposed in the Nine Mile Point Unit 1 BWR showed that the higher corrosion potentials measured in-core vs. in the re-circulation water piping induced significantly higher measured crack growth rates. Ex situ crack growth rate testing on irradiated (4 dpa) type 304 SS is one of many examples of well-behaved crack growth rate at high corrosion potential, along with the strong effect of re-

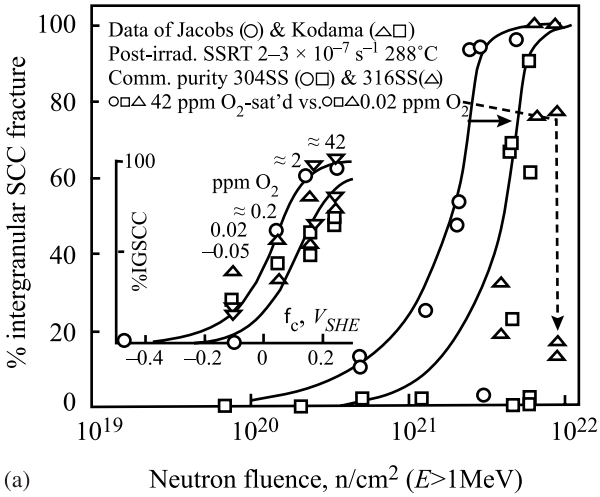

(a)

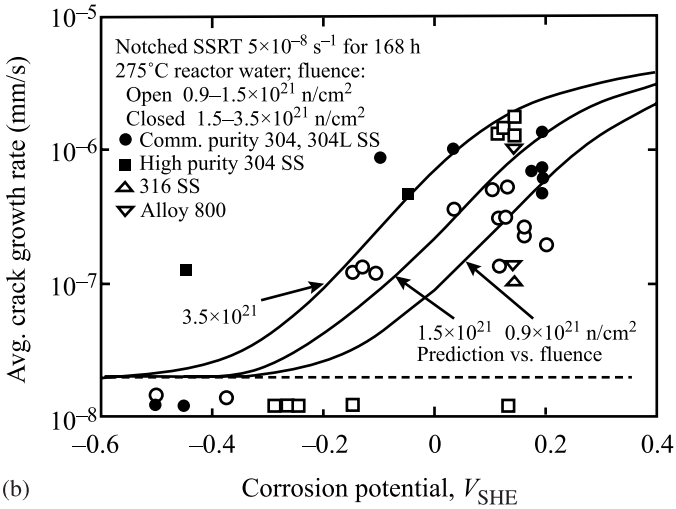

(b)

Fig. 15.30. (a) Dependence of IASCC on fast neutron fluence as measured in slow strain rate tests at $3.7 \times 10^7\,\mathrm{s}^{-1}$ in 288 °C water on pre-irradiated type 304 stainless steel. The effect of corrosion potential via changes in dissolved oxygen is shown at a fluence of $\approx 2 \times 10^{21}\,\mathrm{n/cm}^2$ (from [30]). (b) Comparison of predicted and observed crack growth rates for stainless steels irradiated in a BWR at 288 °C to various fluences. Notched tensile specimens were tested at a slow strain rate in 288 °C pure water and interrupted after a given strain/time (from [31])

duced corrosion potential. These data are compared with other irradiated and unirradiated data in Fig. 15.31 based on simultaneous measurements of corrosion potential and crack growth rate in fracture mechanics specimens; the accompanying curves represent model predictions [5]. Clearly the in situ data compare favorably

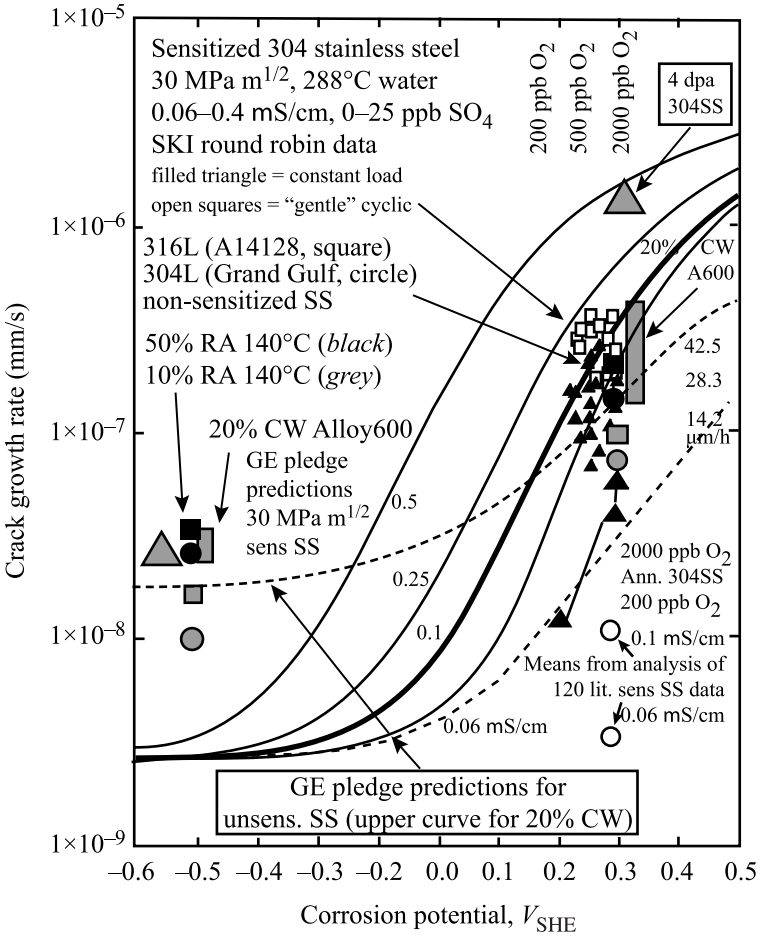

Fig. 15.31. Observed and predicted relationships of crack growth rate vs. corrosion potential for furnace sensitized type 304 stainless steel at a constant K of $\approx 27.5\,\mathrm{MPa}\sqrt{\mathrm{m}}$. The observed data were obtained in water of conductivity between 0.1 to $0.3\,\mu\mathrm{S/cm}$. The predicted relationships show the sensitivity of the crack growth rate to changes in combinations of corrosion potential and water purity (0.1 to $0.5\,\mu\mathrm{S/cm}$). The large triangles were obtained on 304 SS irradiated to 4 dpa. The larger circles and rectangles represent cold-worked stainless steel and alloy 600 (from [7, 8, 9, 32, 33])

with the spectrum of unirradiated data and data obtained on a fracture mechanics specimen of furnace sensitized type 304 stainless steel using high-energy proton irradiation to simulate the mix of neutron and gamma radiation present in power reactors. These data support the premise that increasing corrosion potential leads to higher crack growth rate and the effect of irradiation on water chemistry is to elevate corrosion potential through formation of radicals and higher oxygen concentration.

15.3 Service and Laboratory Observations of Irradiation Effects on SCC

15.3.1 Austenitic Alloys

A historical perspective of IASCC service experience is instructive, as the phenomenon extends back to the 1960s, and the early observations and conclusions projected an accurate image of the important characteristics, generic nature, and broad relevance to plant components. As with other instances of environmental cracking, occasional early observations pointed the way toward a growing incidence with time and neutron fluence. IASCC was first reported in the early 1960s [1, 7, 20] and involved intergranular cracking of stainless steel fuel cladding. The findings and conclusions were that intergranular cracking morphology predominated, with initiation of multiple cracks occurring from the waterside. By contrast, only ductile, transgranular cracking was observed in post-irradiation mechanical tests performed in inert environments and at various temperatures and strain rates. Grain boundary carbide precipitation was generally not observed by optical or transmission electron microscopy (although pre-existing thermal sensitization was present in some cases). A correlation between time-to-failure and stress level was reported, with failure occurring first in thin-walled rods with small fuel-to-cladding gaps, where swelling strains were largest. The highest incidence of cracking occurred in peak heat flux regions, corresponding to the highest fluence and the greatest fuel-cladding interaction (highest stresses and strains). Similar stainless steel cladding in PWR service exhibited fewer instances of intergranular failure. At that time the PWR failures were attributed to off-chemistry conditions or stress rupture.

IASCC has since been observed in a growing number of other stainless steel (and nickel alloy) core components, such as neutron source holders in 1976 and control rod absorber tubes in 1978 [1]. Instrument dry tubes and control blade handles and sheaths, which are subject to very low stresses also cracked, although generally in creviced locations and at higher fluences [5]. Following an initial trickle of failures in the most susceptible components, numerous incidents of IASCC have been observed since the early 1990s, perhaps most notably in BWR core shrouds [1, 7, 20, 29] and PWR baffle bolts [34, 35].

Table 15.2 presents a broad summary of reported failures of reactor internal components, showing that IASCC is not confined to a particular reactor design. For example, stainless steel fuel cladding failures were reported in early commercial PWRs and in PWR test reactors. At the West Milton PWR test loop, intergranular failure of vacuum annealed type 304 stainless steel fuel cladding was observed in 316 °C ammoniated water (pH 10) when the cladding was stressed above yield. Similarly, IASCC was observed in creviced stainless steel fuel element ferrules in the Winfrith SGHWR, a 100 MWe plant in which light water is boiled within pressure tubes, giving rise to a coolant chemistry similar to other boiling water reactor designs.

Reactor type comparisons were also made in swelling tube tests performed in the core of a BWR and a PWR on a variety of commercial and high purity heats of

Table 15.2. IASCC service experience (after [5])

Component	Alloy	Reactor type	Possible sources of stress
Fuel cladding	304 SS	BWR	Fuel swelling
Fuel cladding	304 SS	PWR	Fuel swelling
Fuel cladding*	20%Cr/25%Ni/Nb	AGR	Fuel swelling
Fuel cladding ferrules	20%Cr/25%Ni/Nb	SGHWR	Fabrication
Neutron source holders	304 SS	BWR	Welding & Be swelling
Instrument dry tubes	304 SS	BWR	Fabrication
Control rod absorber tubes	304/304L/316L SS	BWR	B_4C swelling
Fuel bundle cap screws	304 SS	BWR	Fabrication
Control rod follower rivets	304 SS	BWR	Fabrication
Control blade handle	304 SS	BWR	Low stress
Control blade sheath	304 SS	BWR	Low stress
Control blades	304 SS	PWR	Low stress
Plate type control blade	304 SS	BWR	Low stress
Various bolts**	A-286	PWR & BWR	Service
Steam separator dryer bolts**	A-286	BWR	Service
Shroud head bolts**	600	BWR	Service
Various bolts	X-750	BWR & PWR	Service
Guide tube support pins	X-750	PWR	Service
Jet pump beams	X-750	BWR	Service
Various springs	X-750	BWR & PWR	Service
Various springs	718	PWR	Service
Baffle former bolts	316 SS Cold-work	PWR	Torque, differential swelling
Core shroud	304/316/347 /L SS	BWR	Weld residual stress
Top guide	304 SS	BWR	Low stress (bending)

* Cracking in AGR fuel occurred during storage in spent fuel pool

** Cracking of core internals occurred away from high neutron and gamma fluxes

types 304, 316 and 348 stainless steel and Alloys X-750, 718 and 625. Swelling was controlled by varying the mix of Al_2O_3 and B_4C within the tubes; the latter swells as neutrons transmute B to He. Nominally identical strings of specimens were inserted into the core in place of fuel rods. The distinction in the IASCC response between the two reactor types was small. While the available data clearly support a linkage between IASCC in BWRs and PWRs, it is clear that the elevated corrosion potential in BWRs accelerates SCC, and to a lesser extent, the generally higher flux and temperature in PWRs also accelerates SCC.

Laboratory data support that obtained in the plant in terms of the accelerating effect of irradiation. Since laboratory data is collected post-irradiation in which radiolysis of the water is not a factor, the effects of irradiation that are responsible for the observed cracking is deduced to come from changes in the microstructure. Figure 15.32 shows the effect of irradiation on the crack growth rate of 304 and 316 stainless steel under continuous cycling in 289 °C high purity water with ~ 300 ppb dissolved oxygen as compared to that in air. The 45° line indicates no effect of the environment on cracking and the two curves represent the expected crack growth rates for unirradiated austenitic stainless steels in high-purity water

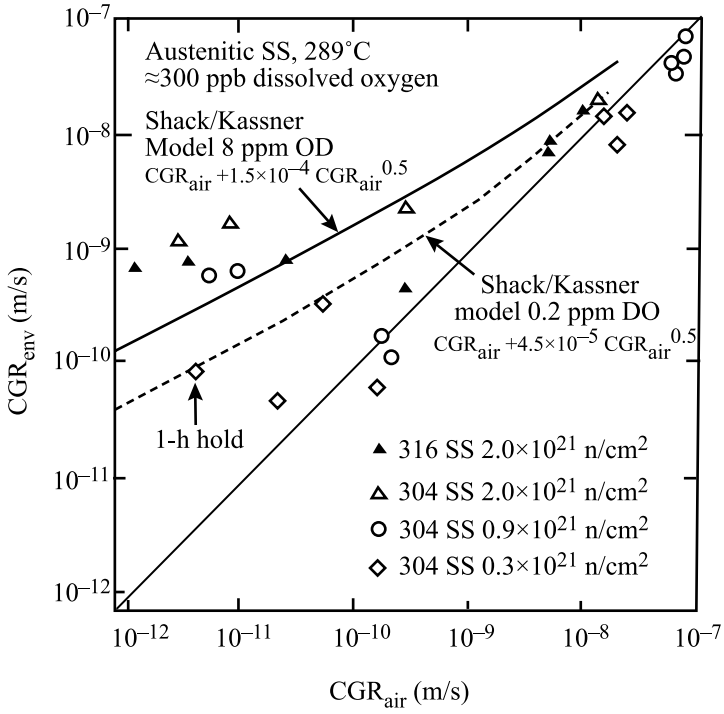

Fig. 15.32. Comparison of the crack growth rate in irradiated austenitic stainless steels under continuous cycling in 288 °C high purity water containing 300 ppb O_2 compared to that in air (from [36])

with either 8 ppm (solid) or 0.2 ppm (dashed) dissolved oxygen [36]. By comparing the data at different neutron fluence levels, it is clear that both the environment and the fluence level affect the crack growth rate. The crack growth rate in 304 SS irradiated to $2 \times 10^{21}\,\mathrm{n/cm^2}$ is over an order of magnitude greater than that for irradiation at $0.3 \times 10^{21}\,\mathrm{n/cm^2}$.

Since the early 1990s, the plant and laboratory evidence of IASCC makes a compelling case that cracking is environmentally assisted and that there is a well-behaved continuum in response over ranges in fluence, corrosion potential, temperature, stress, etc. Since there is a consistent trend toward increasing IASCC susceptibility with increasing corrosion potential in BWRs (e.g., Figs. 15.30a and 15.31), PWRs should be less susceptible to IASCC. However, other factors distinguish PWRs from BWRs, including their higher temperatures, $\approx 10\times$ higher neutron fluence in core structural components, higher hydrogen fugacity, and the borated-lithiated water chemistry (including the possibility of localized boiling and thermal concentration cells in crevices from gamma heating which could lead to aggressive local chemistries). The possible role of radiation-induced segregation of Si may be especially important in accounting for the limited difference in SCC response at high potential (BWR) vs. low potential (PWR) at high fluence.

The two most widespread examples of irradiation-assisted SCC are in BWR core shrouds and PWR baffled bolts although susceptibility clearly exists in other areas, such as control blade components, fuel components, the BWR top guide, etc., SCC in the BWR core shroud occurs almost exclusively near the welds (both circumferential and vertical), and initiation is observed from both the inside (ID) and outside (OD) surfaces (the shroud separates the upward core flow from the downward re-circulation flow that occurs in the annulus between the shroud and the pressure vessel). This large diameter welded "pipe" has inherent susceptibility to SCC, related primarily to weld residual stresses and weld shrinkage strains, and cracking is observed in both low fluence and moderate fluence areas. Severe surface working has also been found to aggravate IASCC in core shrouds. The extent of the enhancement in SCC susceptibility by irradiation is limited, because while radiation hardening and radiation-induced segregation occur, radiation creep relaxes the weld residuals stress.

Extensive failures of PWR baffle bolts have occurred beginning in the 1990s [34, 35] although large plant-to-plant and heat-to-heat differences are observed. Most baffle bolts are fabricated from type 316 stainless steel cold-worked to $\approx 15\%$ to increase their yield strength. The complex baffle former structure exists in a PWR because the fuel does not have a surrounding "channel", so the baffle former structure must conform closely to the geometry of the fuel to provide well-distributed water flow. The baffle former plates are usually made from annealed type 304 stainless steel. Because of their proximity to the fuel, very high fluences can develop, up to ~ 80 dpa by the end of the original design life. The high gamma flux produces significant heating in the components, in some instances estimated at 40 °C above the coolant temperature, especially in designs where the PWR coolant does not have good access to the bolt shank. Figure 15.33 shows micrographs of IG cracking in

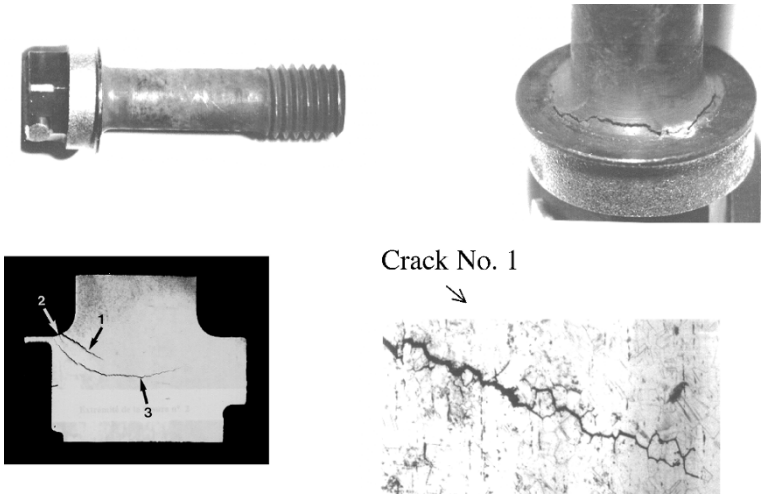

Fig. 15.33. Cracks in cold-worked 316 stainless steel baffle bolt. The location of the cracks received a neutron dose of about 7 dpa at $\sim 310\,^{\circ}\mathrm{C}$ (courtesy, Electrabel)

the baffle bolt described earlier in Chap. 8 on swelling. Note that the cracks are occurring where the shank meets the head. Cracks are completely intergranular and penetrate greater than half the thickness of the bolt.

The number of IASCC incidents has continued to grow as more and more components in LWRs are revealed to be susceptible. The overall trends and correlations for IASCC can be summarized as follows:

- While intergranular cracks related to radiation effects in solution annealed stainless steel were once thought to occur only at fluences above $\approx 0.3 \times 10^{21}\,\mathrm{n/cm^2}$, significant intergranular cracking in BWR core shrouds over a broad range of fluences make it clear that such a distinction (a true fluence threshold) is not justified. Of course, observations of SCC in unsensitized stainless steel (with or without cold-work) also render untenable the concept of a threshold fluence, below which no SCC occurs. This also holds for thresholds in corrosion potential, water impurities, etc.
- Fluence affects SCC susceptibility, but almost always in a complex fashion. SCC in BWR shrouds and PWR baffle bolts does not always correlate strongly with fluence, one important reason for this is that radiation creep produces relaxation of the stresses from welding and in bolts.
- High stresses or dynamic strains were involved in most early incidents; however, cracking has been observed at quite low stresses at high fluences and longer operating exposure. Laboratory and field data indicate that IASCC occurs at stresses below 20% of the irradiated yield stress, and at stress intensities below $10\,\mathrm{MPa\,m^{1/2}}$.
- A strong effect of corrosion potential is clear from extensive laboratory and field data. Its effect is generally consistent from low to high fluence, although the

quantitative change associated with changes in potential vary. Materials prone to high radiation-induced changes in Si level may exhibit a very limited effect of corrosion potential. A true threshold potential clearly does not exist, as irradiated materials exhibit IASCC in de-aerated water.
- Solution conductivity (i.e., impurities, especially chloride and sulfate) strongly affects cracking propensity in BWR water. This correlation applies equally to low and high flux regions and to stainless steels and nickel-base alloys. Indeed, the correlation closely parallels that from out-of-core.
- Crevice geometries exacerbate cracking due primarily to their ability to create a more aggressive crevice chemistry from the gradient in corrosion potential (in BWRs) or in temperature (most relevant to PWRs).
- Cold-work often exacerbates cracking (esp. abusive surface grinding), although it can also delay the onset of some radiation effects.
- Temperature has an important effect on IASCC, enhancing both crack initiation and growth rate.
- Grain boundary carbides and chromium depletion are not required for susceptibility, although furnace sensitized stainless steels are clearly highly susceptible to cracking in-core. Cr depletion remains a primary culprit, although its effect is most pronounced in pH-shifted environments, as can develop when potential or thermal gradients exist. The role of N, S, P, and other grain boundary segregants is less clear.
- The fluence at which IASCC is observed is dependent on applied stress and strain, corrosion potential, solution conductivity, crevice geometry, etc. At sufficiently high conductivities, cracking has been observed in solution annealed stainless steel in the field and in the laboratory. Thus, while convenient in a practical engineering sense, the concept of a "threshold" fluence (or stress, corrosion potential, etc.) is scientifically misleading as cracking susceptibility and morphology are properly considered an interdependent continuum over many relevant parameters.

The field and laboratory data available in the early 1980s, coupled with broader fundamental understanding of environmental cracking in hot water, led to the hypothesis that among innumerable possible radiation effects the most significant factors were radiation-induced segregation at grain boundaries, radiation hardening (elevation of the yield strength), deformation mode, radiation creep relaxation (of constant displacement stresses, e.g., in welds and bolts), and radiolysis (elevated corrosion potential in BWRs). Other factors could also be important in some instances, such as void formation, which may also affect fracture toughness, and can produce differential swelling that causes re-loading of components like baffle bolts.

15.3.2 Ferritic Alloys

Ferritic alloys are also susceptible to environmentally enhanced cracking in high-temperature water. The role of irradiation alone on the fatigue crack growth rate in pressure vessel steels was discussed in Chap. 13, where it was determined that

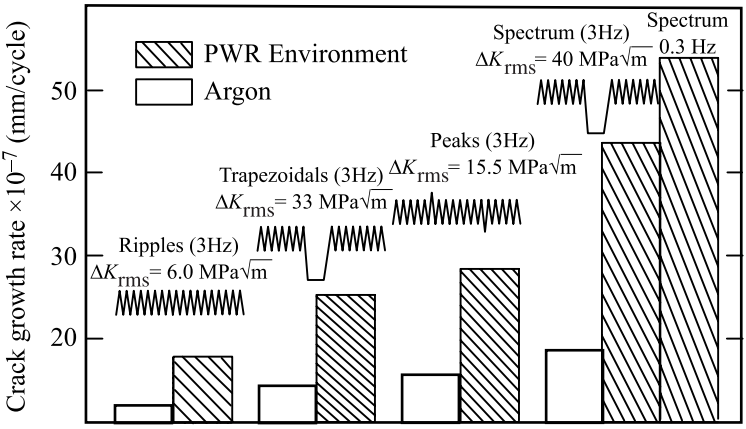

Fig. 15.34. The effect of environment, frequency and transients on the fatigue crack growth behavior of A533B steel subjected to various loading sequences (from [37])

irradiation alone did not accelerate crack growth rate. However, crack growth rates *are* affected by the environment. In fact, the environment, loading parameters and material parameters all affect the crack growth rate in high-temperature water. In general, crack growth per cycle increases with:

Environmental parameters
- Increased oxygen concentration
- Increased conductivity
- Increased temperature

Loading parameters
- Increased R ratio (higher mean stress)
- Decreasing frequency
- Transients and hold periods in the waveform

Material parameters
- Increasing sulfur content in the alloy

For example, Fig. 15.34 shows the effect of environment, frequency and load waveforms on the fatigue crack growth rate in A508 steel. In a PWR environment, lower frequency, transients and hold times in the waveforms increase the crack growth rate. The effect of the environment on cracking is shown in Fig. 15.35a, which gives the fatigue crack growth rate as a function of ΔK for A533B steels and welds in PWR water. The solid line at right is the ASME Boiler and Pressure Vessel Code bounding crack growth rate in air. As is evident, the environment has a significant effect on both the growth rate and the dependence of $\mathrm{d}a/\mathrm{d}N$ on ΔK. Figure 15.35b also shows that in reactor grade water at 288°C, the effect of irradiation only minimally augments the crack growth rate due to the environment.

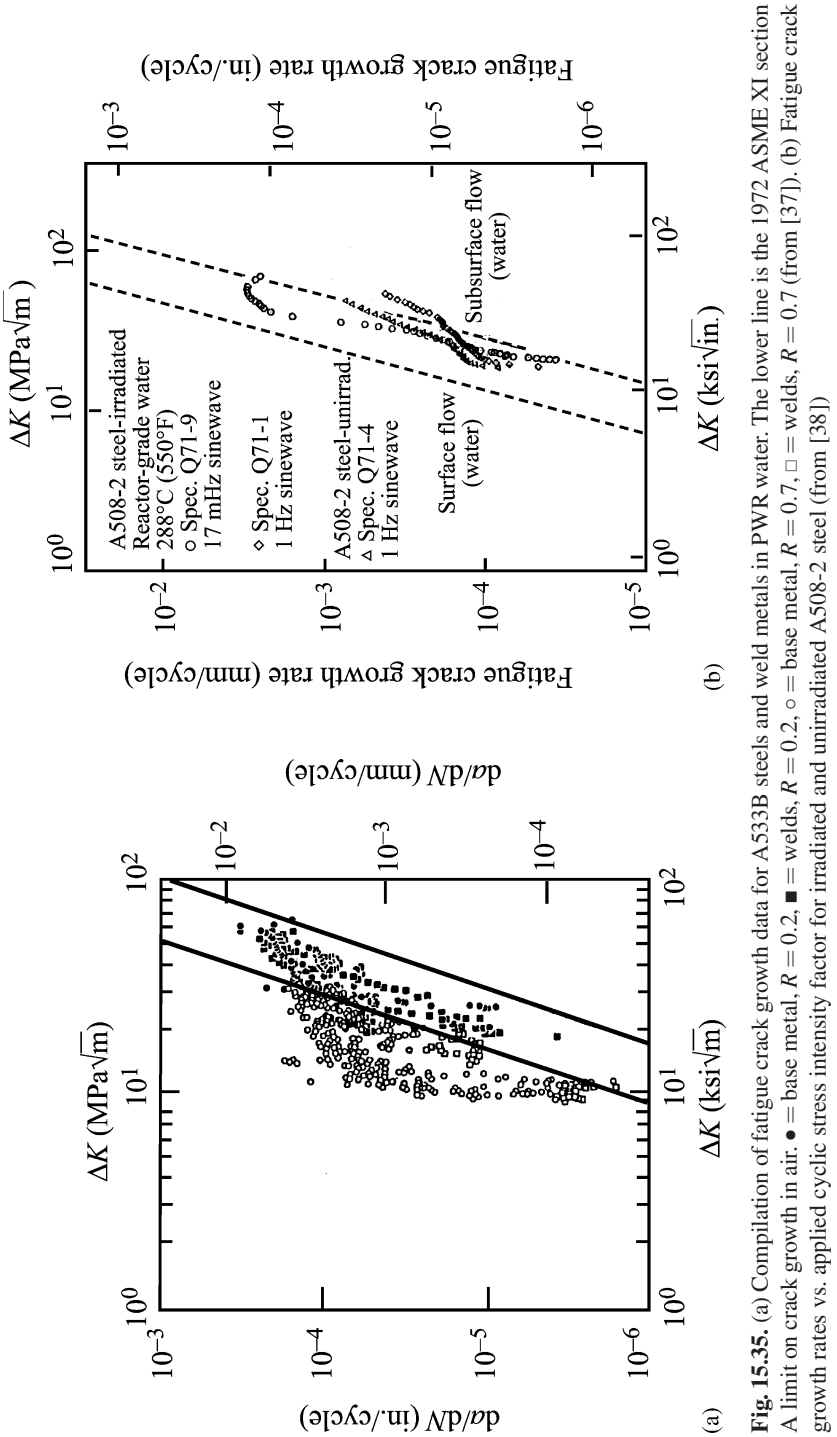

Fig. 15.35. (a) Compilation of fatigue crack growth data for A533B steels and weld metals in PWR water. The lower line is the 1972 ASME XI section A limit on crack growth in air. ● = base metal, $R = 0.2$, ■ = welds, $R = 0.2$, ○ = base metal, $R = 0.7$, □ = welds, $R = 0.7$ (from [37]). (b) Fatigue crack growth rates vs. applied cyclic stress intensity factor for irradiated and unirradiated A508-2 steel (from [38])

15.4 Mechanisms of IASCC

While the mechanism by which irradiation affects stress corrosion cracking is not precisely known, existing theories fall into five categories: (1) radiation-induced grain boundary chromium depletion, (2) radiation hardening, (3) localized deformation, (4) selective internal oxidation and (5) irradiation creep. The difficulty in determining the role of irradiation in SCC stems from the simultaneous occurrence of several effects. Figure 15.36 shows a schematic representation of the increase in RIS, dislocation microstructure and radiation hardening, and that all of these factors increase with approximately the same relationship with irradiation dose. Thus, the attribution of one or a combination of effects to the observed increase in cracking is complicated. The following sections describe the mechanisms by which these processes can influence IGSCC.

15.4.1 Grain Boundary Chromium Depletion

As described in Chap. 6, irradiation in the temperature range relevant to LWR core components results in grain boundary segregation, marked by a significant decrease in the chromium concentration. Chromium imparts passivity to austenitic alloys by formation of a chromium oxide film, and its loss from the grain boundary can result in loss of passivation locally. The depletion of chromium from grain boundaries in austenitic stainless steels and nickel-base alloys is a well-known cause of IGSCC in high-temperature water [39]. By analogy, the loss of chromium due to RIS is implicated as a cause of IASCC in the irradiated condition. Existing data supports this premise in part, by showing that there is a general trend in increasing %IGSCC

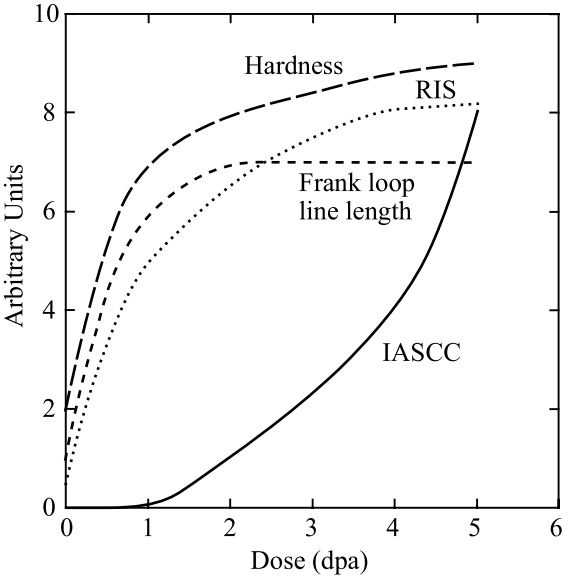

Fig. 15.36. Schematic diagram showing the increase in all parameters (RIS, loops, hardness) and SCC susceptibility with dose (from [4])

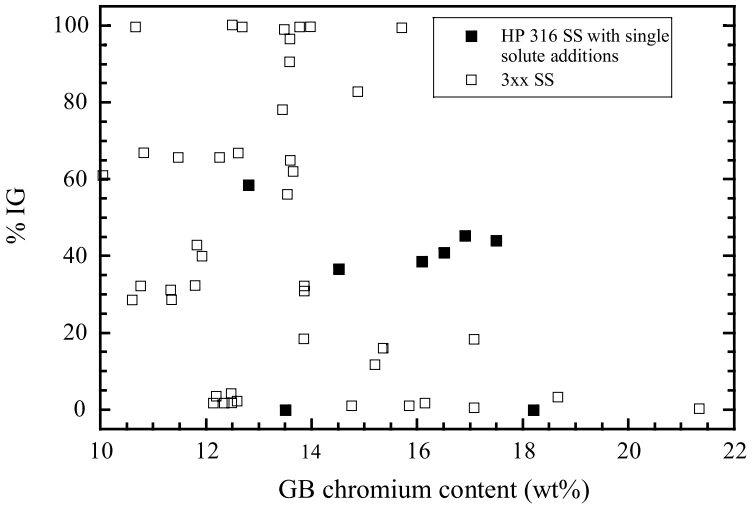

Fig. 15.37. Effect of grain boundary chromium content on IGSCC for irradiated 300 series stainless steels (from [4])

as the grain boundary chromium concentration decreases (Fig. 15.37). However, the data exhibit considerable scatter, some of which may be attributed to the stochastic nature of crack initiation that is inherent in a straining electrode test, but is unlikely to explain all of the variability.

Recently, post-irradiation annealing experiments have been utilized to separate the various effects of irradiation due to differences in their annealing characteristics. Figure 15.38 shows that of the principal irradiation-induced microstructure features, RIS is slowest to recover in isothermal anneals and is essentially unchanged over the time period during which the SCC susceptibility is completely eliminated. This result, which is consistent across several studies using different types of irradiation, has focused attention on hardening and deformation as potential primary factors in IASCC.

15.4.2 Irradiation Hardening

IGSCC has been observed to correlate with hardness as evidenced by the increase in crack growth rate with cold-work in 300 series austenitic stainless steels tested in high-temperature water (Fig. 15.39a). IGSCC as measured by %IG in constant extension rate tests also correlates with hardening due to irradiation, shown in Fig. 15.39b. However, as mentioned earlier, other effects occur during irradiation that makes it difficult to attribute the increased cracking to hardening alone. Hash et al. [41] conducted a series of experiments on a heat of stainless steel that showed that in the absence of significant grain boundary chromium depletion, hardening due to irradiation results in more IGSCC than hardening from cold-work. This result suggests that hardness alone is not the cause of IASCC, but rather another effect

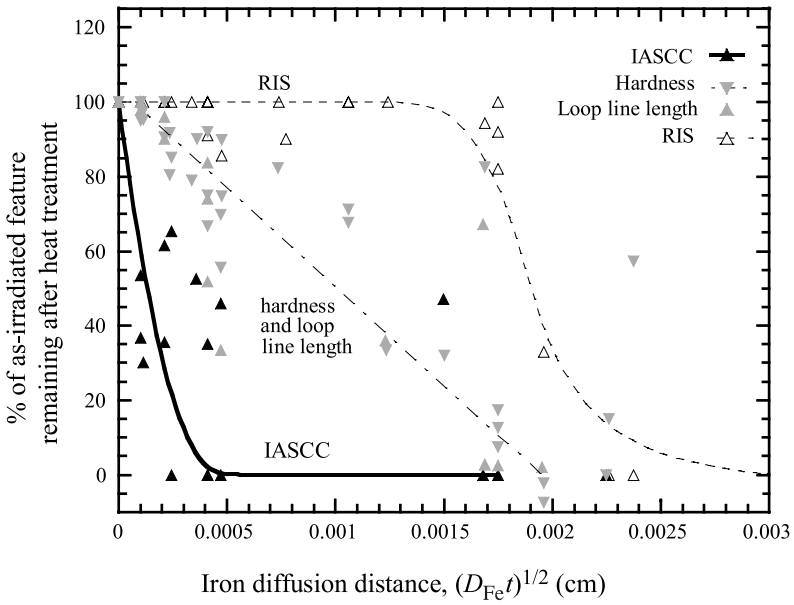

Fig. 15.38. Removal of RIS, dislocation microstructure as measured by loop line length and hardness with annealing as measured by $(Dt)^{1/2}$ for iron, to account for annealing at different times and temperatures (from [4])

related to hardness may be operating. That factor is suspected to be the deformation mode.

15.4.3 Deformation Mode

As discussed in Chap. 12, irradiated metals exhibit localized deformation characterized by the concentration of strain into dislocation channels. The strain in these channels can exceed 100%, and while channels are believed to initiate at grain boundaries, they also must terminate there as well. As such, the considerable amount of localized strain in the channels must be accommodated by the boundary to avoid mechanical fracture. Accommodation can occur by several mechanisms including the transfer of slip across the boundary, cross slip in the grain boundary region, and reaction of the dislocations in the channels with grain boundary dislocations to produce a resultant dislocation in the grain boundary plane that can lead to grain boundary sliding if it is mobile. The sliding of a grain boundary will rupture the oxide film above it and expose the underlying metal to the solution, allowing for dissolution and re-oxidation. Repeated cycles of sliding, rupture, dissolution and re-passivation can then propagate a grain boundary crack by a slip oxidation-type process, as shown in Fig. 15.40. In addition to grain boundary sliding, the formation of wedge cracks due to dislocation pile-up at the grain boundary can also rupture the oxide and promote IGSCC in much the same manner. This mechanism has support

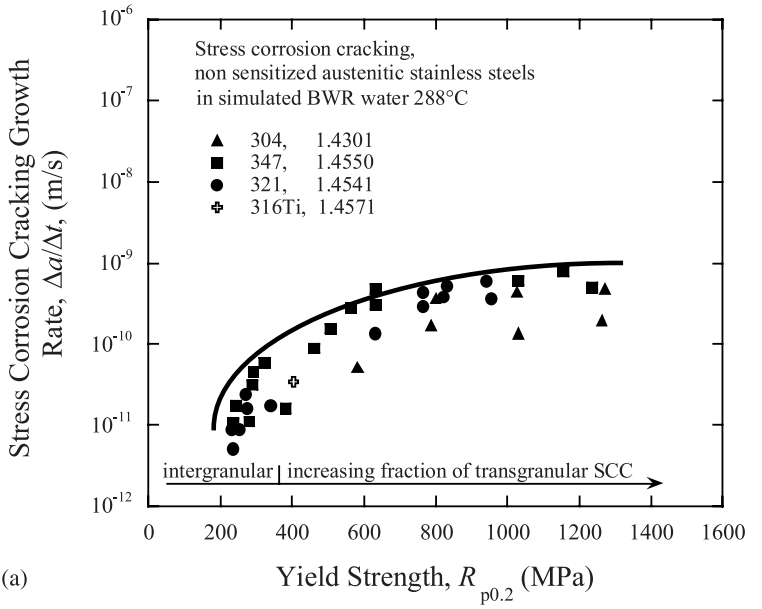

(a)

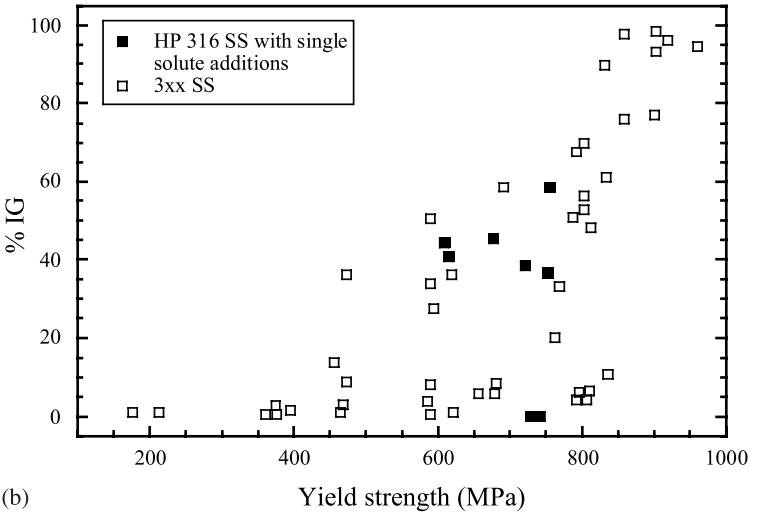

(b)

Fig. 15.39. Effect of yield strength on IGSCC. (a) Crack growth rates for 316L and 347 stainless steel in primary water as a function of yield strength due to cold-work (from [40]). (b) %IGSCC in SSRT tests on 300 series stainless steels where hardening is by irradiation (from [4])

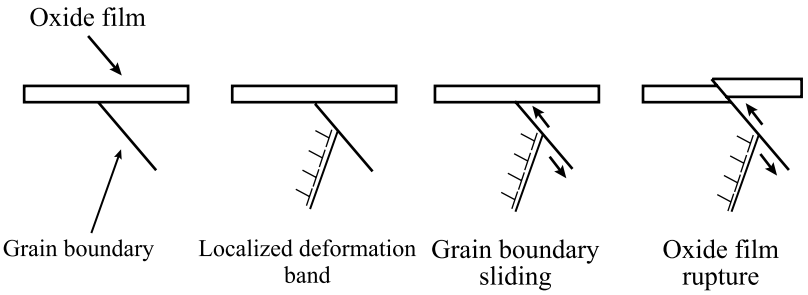

Fig. 15.40. Schematic of the process by which dislocation channels can transfer slip to the grain boundary and result in rupture of the oxide film at the grain boundary, causing IGSCC

in the role of stacking fault energy in IGSCC discussed in Sect. 15.1.5, in which low SFE alloys undergo planar slip, which is conducive to grain boundary dislocation pile-ups similar to, but not as severe as that in dislocation channels. Thus, as the fluence increases, localized deformation becomes more severe and IG cracking severity should follow.

15.4.4 Selective Internal Oxidation

A final mechanism that has the potential for causing IG cracking is selective internal oxidation, which is based on the rapid transport of oxygen along grain boundaries that then oxidizes and embrittles the metal ahead of the crack tip, resulting in increased cracking along the grain boundaries [42]. Internal oxidation is observed in nickel-base alloys at temperatures above 600 °C [43, 44, 45] but it is not expected to occur in iron or nickel-base alloys at LWR core temperatures. However, the combination of short circuit diffusion paths (grain boundaries) and radiation-enhanced diffusion have increased the plausibility of this mechanism operating in the lower temperature range. Observation of oxygen penetrating ahead of an active crack tip in stainless steel core components [46] provides support to this mechanism.

15.4.5 Irradiation-Induced Creep

In contrast to the previous four effects of irradiation on SCC, irradiation-induced creep will relax residual stress, thus effectively removing the driving force for SCC. As shown in Chap. 11, the relaxation of stress depends on the dose. Figure 15.41 shows the reduction in the stress on a bolt as a function of neutron flux. Note that the relaxation follows a roughly exponential behavior with neutron dose, such that the stress is reduced to about half of its original value after only 2 dpa. Stress relaxation by irradiation-induced creep is an important process to relieve stress in baffle bolts of PWRs that could see additional stresses if swelling occurs in the plates.

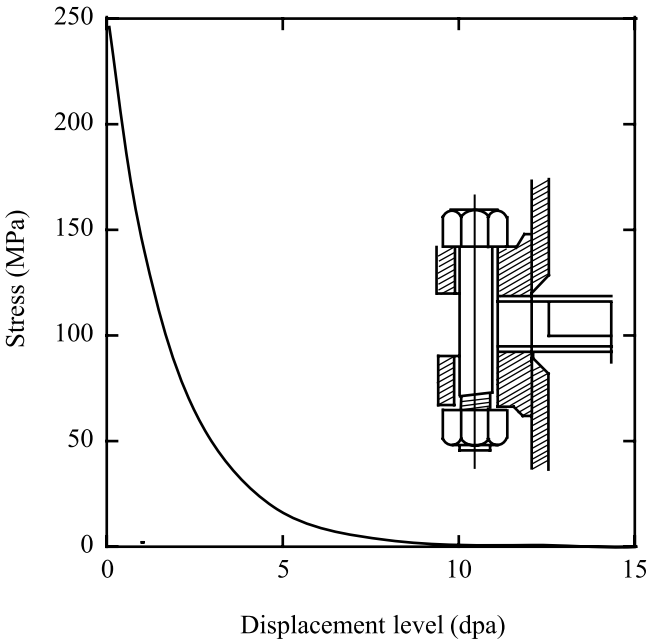

Fig. 15.41. Irradiation-induced creep causing stress relief in a bolt that was originally torqued to 250 MPa and then exposed to a neutron flux (from [47])

Nomenclature

a	Activity of reactants/products
$\dot{a}$	Crack growth rate
$\mathrm{d}a/\mathrm{d}n$	Crack growth per cycle
$\mathrm{d}a/\mathrm{d}t$	Crack growth rate
c	Crack length
i_{corr}	Corrosion current
$i_{0,\mathrm{a,c}}$	Current: exchange, anodic, cathodic
E	Equilibrium electrode potential
E^0	Standard equilibrium electrode potential (at STP)
E_{corr}	Corrosion potential
F	Faraday's constant, 96,500 Coulombs/charge
G	Yield of radiolysis product
ΔG	Free energy change for a reaction
K	Stress intensity
ΔK	Stress intensity range
K_{Ic}	Mode I fracture toughness
K_{th} or K_{SCC}	Threshold stress intensity for SCC
m	Re-passivation parameter

M	Atomic mass
n	Charge transfer in oxidation/reduction reaction
Q_f	Charge transferred during a reaction
R	Gas constant
$t_{init,prop,fail}$	Time of: crack initiation, crack propagation, failure
t_0	Re-passivation parameter
$\bar{v}_T$	Average crack velocity
β	Symmetry factor in expression for corrosion current
ε_f	Fracture strain
$\dot{\varepsilon}_{ct}$	Crack tip strain rate
γ	Surface energy
η	Overpotential
ρ	Density
σ_f	Fracture stress
σ_{th} or σ_{SCC}	Threshold stress for SCC

Acronyms

AGR	Advanced gas reactor
BWR	Boiling water reactor
CT	Compact tension
CERT	Constant extension rate test
DCB	Double cantilever beam
EFPY	Effective full power years
EMF	Electromotive force
HWC	Hydrogen water chemistry
IASCC	Irradiation-assisted stress corrosion cracking
IGSCC	Intergranular stress corrosion cracking
LET	Linear energy transfer
LWR	Light water reactor
NWC	Normal water chemistry
PWR	Pressurized water reactor
RH	Radiation hardening
RIS	Radiation-induced segregation
SCC	Stress corrosion cracking
SFE	Stacking fault energy
SGHWR	Steam generating heavy water reactor
SSRT	Slow strain rate test
STP	Standard temperature and pressure
TGSCC	Transgranular stress corrosion cracking

Problems

15.1 Discuss the relative advantages and disadvantages of constant load, constant deflection and constant extension rate tensile tests for assessing:

a) The relative susceptibility of a variety of alloys to stress corrosion cracking
b) The susceptibility of one alloy to stress corrosion cracking in several environments
c) The stress and strain dependence of stress corrosion cracking.

15.2 a) Calculate the minimum specimen width necessary for a valid fracture mechanics test of a steel of yield strength 700 MPa and fracture toughness of $170\,\mathrm{MPa}\sqrt{\mathrm{m}}$.
b) Would it be practical to measure the fracture toughness of this alloy?
c) If a corrosive environment makes hydrogen embrittlement possible with K_{Ihic} of $23\,\mathrm{MPa}\sqrt{\mathrm{m}}$, what is the minimum specimen width?

15.3 Plot the crack growth rate of an alloy over the range $10 \leq K \leq 60\,\mathrm{MPa}\sqrt{\mathrm{m}}$, for a crack tip strain rate given by BK^4, where B is $2 \times 10^{-22}\,\mathrm{MPa}^{-1/4}\mathrm{m}^{-1/8}$, and $A = 10\,\mathrm{m/s}$ for values of $m = 0.1$, 0.5 and 1.0.

15.4 Consider a low alloy steel in contact with a stainless steel and determine the potential difference under STP.
a) Which will corrode?
b) Where could such a situation arise locally due to the effects of irradiation?

15.5 For the alloys described in Problem 15.4, describe how irradiation can alter the corrosion potential of the system.

15.6 What are the possible ways in which irradiation can lead to the onset of IASCC?

References

1. Andresen PL, Ford FP, Murphy SM, JM Perks (1990) In: Proceedings of the 4th International Symposium on Environmental Degradation of Materials in Nuclear Power Systems: Water Reactors. NACE International, Houston, TX, pp 1–83 to 1–121
2. Scott P (1994) J Nucl Mater 211:101–122
3. Bruemmer SM (2002) In: Proceedings of the 10th International Conference on Environmental Degradation of Materials in Nuclear Power Systems: Water Reactors. NACE International, Houston, TX
4. Was GS (2004) In: Proceedings of the 11th International Conference on Environmental Degradation of Materials in Nuclear Power Systems: Water Reactors. American Nuclear Society, La Grange Park, IL, pp 965–985
5. Was GS, Busby JT, Andresen PL (2006) Effect of irradiation on stress corrosion cracking and corrosion in light water reactors: corrosion in the nuclear industry. In: Corrosion: Environments and Industries, ASM Handbook, vol 13c. ASM International, Metals Park, OH, pp 386–414
6. Bruemmer SM, Simonen EP, Scott PM, Andresen PL, Was GS, Nelson JL (1999) J Nucl Mater 274:299–314
7. Ford FP, Andresen PL (1994) Corrosion in nuclear systems: environmentally assisted cracking in light water reactors. In: Marcus P, Oudar J (eds) Corrosion Mechanisms. Dekker, New York, pp 501–546

8. Ford FP, Andresen PL (1988) In: Theus GJ, Weeks JR (eds) Proceedings of the 3rd International Symposium on Environmental Degradation of Materials in Nuclear Power Systems: Water Reactors. The Metallurgical Society of AIME, Warrendale, PA, p 789
9. Andresen PL, Ford FP (1988) Mat Sci Eng vol A 1103:167
10. Jones RH (1987) Stress Corrosion Cracking in ASM Handbook, vol 13, 9th edn. ASM International, Metals Park, OH, p 145
11. Jones DA (1992) Principles and Prevention of Corrosion. Macmillan, New York
12. Copson HR (1959) In: Rhodin TN (ed) Physical Metallurgy of Stress Corrosion Fracture. Interscience, New York, p 247
13. Staehle RW (1977) In: Staehle RW (ed) Stress Corrosion and Hydrogen Embrittlement of Iron Base Alloys, NACE-5. NACE, Houston, TX, p 193
14. Pourbaix M (1974) Atlas of Electrochemical Equilibria in Aqueous Solutions. NACE, Houston, TX
15. Staehle RW, Gorman JA (2002) In: Proceedings of the 10th International Conference on Environmental Degradation of Materials in Nuclear Power Systems: Water Reactors. NACE International, Houston, TX, bonus paper
16. Was GS, Rajan VB (1987) Metal Trans A 18A:1313–1323
17. Sung JK, Koch J, Angeliu T, Was GS (1992) Metal Trans A 23A:2887–2804
18. Ford FP, Andresen PL, Solomon HD, Gordon GM, Ranganath S, Weinstein D, Pathania R (1990) In: Proceedings of the 4th International Symposium on Environmental Degradation of Materials in Nuclear Power Systems: Water Reactors. NACE, Houston, TX, pp 4–26 to 4–51
19. Wagner C (1959) Z Electrochem 63:772–782
20. Andresen PL (1992) In: Jones RH (ed) Stress Corrosion Cracking: Materials Performance and Evaluation. ASM, Materials Park, OH, pp 181–210
21. Andresen PL, Young LM (1995) In: Proceedings of the 7th International Symposium on Environmental Degradation of Materials in Nuclear Power Systems: Water Reactors. NACE International, Houston, TX, pp 579–596
22. Lin CC (1986) Proceedings of the 2nd International Symposium on Environmental Degradation of Materials in Nuclear Power Systems: Water Reactors. American Nuclear Society, La Grange Park, IL, pp 160–172
23. Burns WG, Moore PB (1976) Rad Eff 30:233
24. Cohen P (1969) Water Coolant Technology of Power Reactors. Gordon and Breach Science, New York
25. British Nuclear Energy Society (1989) Proceedings of the Conference on Water Chemistry of Nuclear Reactor Systems 5, Bournemouth, UK, 23–27 October 1989, British Nuclear Energy Society, London
26. Taylor DF (1990) Paper 90501, Corrosion/90, Las Vegas. NACE, Houston, TX
27. Head RA, Indig ME, Andresen PL (1989) Measurement of In-core and Recirculation System Responses to Hydrogen Water Chemistry at Nine Mile Point Unit 1 BWR, EPRI Contract RP2680-5, Final Report. EPRI, Palo Alto, CA
28. Gordon BM (1985) Hydrogen Water Chemistry for BWR, Task 27, Materials and Environmental Monitoring with in the Duane Arnold BWR, Contract RP1930-1, Project Manager, JL Nelson. EPRI, Palo Alto, CA
29. Andresen PL, Ford FP (1995) In: Proceedings of the 7th International Symposium on Environmental Degradation of Materials in Nuclear Power Systems: Water Reactors. NACE, Houston, TX, pp 893–908
30. Jacobs AJ, Hale DA, Siegler M (1986) Unpublished Data. GE Nuclear Energy, San Jose, CA, January 1986

31. Ljungberg LG (1991) Communication, ABB Atom, Vasteras, Sweden, March 1991
32. Ford FP, Taylor DF, Andresen DL, Ballinger RG (1987) Environmentally Controlled Cracking of Stainless and Low Alloy Steels in LWR Environments, NP-5064M (RP2006-6). EPRI, Palo Alto, CA
33. Angeliu TM, Andresen PL, Sutliff JA, Horn RM (1999) In: Proceedings of the 9th International Symposium on Environmental Degradation of Materials in Nuclear Power Systems. The Minerals, Metals and Materials Society, Warrendale, PA, p 311
34. Scott PM (1994) J Nucl Mat 211:101
35. Scott PM, Meunier M-C, Deydier D, Silvestre S, Trenty A (2000) In: Kane RD (ed) ASTM STP 1401, Environmentally Assisted Cracking: Predictive Methods for Risk Assessment and Evaluation of Materials, Equipment and Structures. American Society for Testing and Materials, West Conshohocken, PA, pp 210–223
36. Chopra OK, Gruber EE, Shack WJ (2003) Fracture Toughness and Crack Growth Rates of Irradiated Austenitic Steels. US Nuclear Regulatory Commission, NUREG/CR-6826, 2003, p 37
37. Bulloch JH (1989) Res Mechanica 26:95–172
38. Cullen WH, Watson, HE, Taylor RE, Loss FJ (1981) J Nucl Mater 96:261–268
39. Bruemmer SM, Was GS (1994) J Nucl Mater 216:348–363
40. Speidel MO, Magdowski R (1999) In Ford FP, Bruemmer SM, Was GS (eds) Proceedings of the 9th International Conference in Environmental Degradation of Materials in Nuclear Power Systems: Water Reactors, the Minerals, Metals and Materials Society, Warrendale, PA, p 325
41. Hash MC, Wang LM, Busby JT, Was GS (2004) In: Grossbeck ML, Allen TR, Lott RG, Kumar AS (eds) Effects of Radiation on Materials the 21st International Symposium, ASTM STP. American Society for Testing and Materials, West Conshohocken, PA, pp 92–104
42. Scott PM (2002) In: Ford FP, Bruemmer SM, Was GS (eds) Proceedings of the 9th International Conference on Environmental Degradation of Materials in Nuclear Power Systems: Water Reactors. The Minerals, Metals and Materials Society, Warrendale, PA, pp 3–14
43. Bricknell RH, Woodford DA (1982) Acta Metal 30:257–264
44. Iacocca RG, Woodford DA (1988) Metal Trans A 19A:2305–2313
45. Woodford DA, Bricknell RH (1983) Treatise on Materials Science and Technology, vol 25. Academic, New York
46. Thomas LE, Gertsman VY, Bruemmer SM (2002) In: Nelson L, Was GS, King P (eds) Proceedings of the 10th International Conference on Environmental Degradation of Materials in Nuclear Systems: Water Reactors. NACE International, Houston, TX, p 117
47. Grossbeck ML, Mansur LK (1991) J Nucl Mater 179–181:130–134

Index